

REPORT DOCUMENTATION PAGE				Form Approved OMB No. 0704-0188	
The public reporting burden for this collection of information is estimated to average 1 hour per response, including the time for reviewing instructions, searching existing data sources, gathering and maintaining the data needed, and completing and reviewing the collection of information. Send comments regarding this burden estimate or any other aspect of this collection of information, including suggestions for reducing the burden, to Department of Defense, Washington Headquarters Services, Directorate for Information Operations and Reports (0704-0188), 1215 Jefferson Davis Highway, Suite 1204, Arlington, VA 22202-4302. Respondents should be aware that notwithstanding any other provision of law, no person shall be subject to any penalty for failing to comply with a collection of information if it does not display a currently valid OMB control number. PLEASE DO NOT RETURN YOUR FORM TO THE ABOVE ADDRESS.					
1. REPORT DATE (DD-MM-YYYY) 04-01-2002		2. REPORT TYPE Conference Proceedings		3. DATES COVERED (From - To) 06-05-01 - 09-05-01	
4. TITLE AND SUBTITLE Light Materials for Transportation System (LiMat-2001)				5a. CONTRACT NUMBER F6256200M9105	
				5b. GRANT NUMBER	
				5c. PROGRAM ELEMENT NUMBER	
6. AUTHOR(S) Conference Committee				5d. PROJECT NUMBER	
				5e. TASK NUMBER	
				5f. WORK UNIT NUMBER	
7. PERFORMING ORGANIZATION NAME(S) AND ADDRESS(ES) Pohang Univeristy of Science and Technology San 31, Hyoja-dong, Nam-gu Pohang 790-784 Korea (South)				8. PERFORMING ORGANIZATION REPORT NUMBER N/A	
9. SPONSORING/MONITORING AGENCY NAME(S) AND ADDRESS(ES) AOARD UNIT 45002 APO AP 96337-5002				10. SPONSOR/MONITOR'S ACRONYM(S) AOARD	
				11. SPONSOR/MONITOR'S REPORT NUMBER(S) CSP-001013	
12. DISTRIBUTION/AVAILABILITY STATEMENT Approved for public release; distribution is unlimited.					
13. SUPPLEMENTARY NOTES					
14. ABSTRACT This proceedings emanates from an interdisciplinary materials conference, the objective of which was to provide a forum for scientific exchange among materials researchers from the aerospace, automotive, civil, marine, and rail-transportation industries. The theme of need to develop improved lightweight materials is common to each of those industries. Papers within the proceedings focus on titanium, magnesium, and aluminum alloys, intermetallics, and metal/ceramic composites. Emphasis is placed on fabrication, mechanical properties, microstructural studies, corrosion, and fundamental modeling.					
15. SUBJECT TERMS Aerospace Materials					
16. SECURITY CLASSIFICATION OF:			17. LIMITATION OF ABSTRACT	18. NUMBER OF PAGES	19a. NAME OF RESPONSIBLE PERSON
a. REPORT	b. ABSTRACT	c. THIS PAGE			Thomas D. Kim
U	U	U	UU	1144	19b. TELEPHONE NUMBER (Include area code) +81-3-5410-4409

The Second International Conference on
Light Materials for Transportation Systems

LiMAT-2001



Volume II

Edited by
Nack J. Kim, C. S. Lee and D. Eylon

DISTRIBUTION STATEMENT A:
Approved for Public Release -
Distribution Unlimited

LiMAT-2001

**Proceedings of the Second International Conference on
Light Materials for Transportation Systems (LiMAT-2001)
held at Pusan, Korea, May 6~10, 2001**

Volume II

Edited by

Nack J. Kim, POSTECH

C.S. Lee, POSTECH

D. Eylon, University of Dayton

20020114 164

Organized by

Center for Advanced Aerospace Materials
Pohang University of Science and Technology

Co-organized by

Korea Institute of Machinery and Materials
Research Center for Aircraft Parts Technology, Gyeongsang National Univ.

Sponsored by

The Korean Institute of Metals and Materials (KIM)
The Minerals, Metals and Materials Society (TMS)
US Air Force Office of Scientific Research/Asian Office of
Aerospace Research and Development (AFOSR/AOARD)
The Office of Naval Research International Field Office (ONRIFO)
Korea Science and Engineering Foundation (KOSEF)
Technology Innovation Center for Metals and Materials (TICM), POSTECH
Pohang Iron and Steel Company
Hyundai Motor Company

Published in Aug., 2001 by:

Center for Advanced Aerospace Materials
Pohang University of Science and Technology
San31, Hyoja-dong, Pohang 790-784, Korea
Tel: +82-54-279-2141, 2820
Fax: +82-54-279-2399

ISBN 89-85510-01-0

Printed in The Republic of Korea

PREFACE

During the last several decades, considerable efforts have been made in light materials research for applications in transportation systems. Although the impetus for this comes from the various needs depending on the type of transportation system, one common goal is to develop transportation system with improved performance. For the automotive industry in particular, ever increasing restrictions on the fuel consumption and pollutant emission have placed a great demand to the automobile manufacturers to produce automobiles with reduced weight. Using light materials can be a viable solution to this challenge and it is expected that the demand for the light materials will continue to grow.

As such, this conference aims to review and update all aspects of the science and technology of light materials for applications in various transportation systems. The first conference on Light Materials for Transportation Systems was held in Kyoungju, Korea in 1993 (LiMAT-93). After 8 years following the first conference, the second conference is being held under the theme of "Development of Better Air, Sea and Land Transportation Light Materials for the 2000's" with an emphasis on technology transfer from aerospace to sea and land transport to help improve performance, cost and reliability. We believe that it is timely appropriate and also important to review our efforts on the light materials research, and to redirect our future research efforts.

We would like to express our deep gratitude to The Korean Institute of Metals and Materials (KIM), The Minerals, Metals and Materials Society of USA (TMS), US Air Force Office of Scientific Research/Asian Office of Aerospace Research and Development (AFOSR/AOARD), The Office of Naval Research International Field Office (ONRIFO), Korea Science and Engineering Foundation, Pohang Iron and Steel Co., Hyundai Motor Co., Technology Innovation Center for Metals and Materials (TICM) of Pohang University of Science and Technology, who have co-sponsored our conference.

Aug., 2001

Nack J. Kim
C.S. Lee
D. Eylon

LiMAT-2001 Organizing Committee

SESSION CHAIRMEN

S.H. Ahn

Research Institute of Industrial
Science and Technology
(KOREA)

S. Ankem

University of Maryland
(USA)

E.S. Balmuth

Lockheed Martin Aeronautics Co.
(USA)

Y.W. Chang

Pohang Univ. of Science and Technology
(KOREA)

K.M. Cho

Pusan National University
(KOREA)

W.S. Cho

Hyundai Motor Company
(KOREA)

D.M. Dimiduk

Air Force Research Laboratory
(USA)

D. Eliezer

Ben Gurion University of the Negev
(ISRAEL)

O.S. Es-Said

Loyola Marymount University
(USA)

E. Evangelista

University of Ancona
(ITALY)

D. Eylon

University of Dayton
(USA)

D.S. Han

Hyundai Motor Company
(KOREA)

D. Hua

Northeastern University
(P.R.CHINA)

S.M. Hur

Agency for Defense Development
(KOREA)

S.K. Hwang

Inha University
(KOREA)

O.M. Ivasishin

Institute for Metal Physics
(UKRAINE)

C.G. Kang
Pusan National University
(KOREA)

H. Kikukawa
Japan Aircraft Development
Corporation
(JAPAN)

J.G. Kim
Sungkyunkwan University
(KOREA)

S.S. Kim
Gyeongsang National University
(KOREA)

H. Kwon
Kookmin University
(KOREA)

E.W. Lee
Naval Air Systems Command
(USA)

J.C. Lee
Korea Institute of Science and
Technology
(KOREA)

S.Y. Lee
Korea Institute of Machinery and
Materials
(KOREA)

K. Nakasa
Hiroshima University
(JAPAN)

M. Niinomi
Toyohashi University of Technology
(JAPAN)

C.G. Park
Pohang Univ. of Science and Technology
(KOREA)

Y.H. Park
Tohoku National Industrial Research
Institute
(JAPAN)

S.L. Semiatin
Air Force Research Laboratory
(USA)

K.S. Shin
Seoul National University
(KOREA)

T. Shinoda
Nagoya University
(JAPAN)

C. Suryanarayana
University of Central Florida
(USA)

H.G. Suzuki
National Research Institute for Metals
(JAPAN)

L. Wagner
Technical Univ. of Brandenburg at
Cottbus
(GERMANY)

TABLE OF CONTENTS

Volume I

PLENARY LECTURES

The Advanced Materials and Technology in the Next Generation Vehicles (INVITED) <i>W.S. Cho</i>	3
Applications, Benefits, and Implementation of Ti-6Al-4V Castings (INVITED) <i>E.W. Lee, C.S.C. Lei and W.E. Frazier</i>	5
Friction Stir Welding: Emphasis on Aircraft and Space Applications (INVITED) <i>K.V. Jata</i>	15
The R&D Actives on Light Alloys and Their Applications in Transport Systems in China (INVITED) <i>Z. Lian</i>	23
Structural In-Situ Composites at Very High Temperatures (INVITED) <i>S. Hanada, T. Suzuki, K. Yoshimi and N. Nomura</i>	31

Session I : TITANIUM ALLOYS

Enhancement of Mechanical Properties by Alloying and Processing in Titanium Base Alloys (INVITED) <i>Y.T. Lee, S.E. Kim, Y.T. Hyun and H.W. Jeong</i>	41
Thermomechanical Control Processes of Titanium Alloys (INVITED) <i>H.G. Suzuki</i>	49
High Strength Microstructural Forms in Beta Alloys Intended for Automotive Application (INVITED) <i>O.M. Ivasishin and S. Fox</i>	57
The Ordering Behavior of Supersaturated Metastable Phase in Beta-Ti Alloys <i>B.H. Choe, B.H. Lee, B.G. Jung, T.H. Lee, C.G. Lee, S.J. Kim and Y.T. Lee</i>	65
Influence of Cooling Rate From a Temperature within the Beta Phase Region on Tensile Properties and Phase Constitution of Ti-Fe-Cr Alloys for Technical Aids <i>M. Ikeda, S. Komatsu, M. Ueda, T. Imose and K. Inoue</i>	73
Effect of Preform Microstructure on Constitutive Behavior of Ti-6Al-4V under Conventional Hot-Working Conditions (INVITED) <i>S.L. Semiatin and T.R. Bieler</i>	79

Characteristics of Titanium Silicides Formed by Hip in Ti-Fe-Si Alloys <i>H.W. Jeong, S.E. Kim, Y.T. Hyun and Y.T. Lee</i>	91
The Role of Filler Material in 360°C Cold Bending Ti-6Al-4V Large-Diameter Seamless Tube <i>S.M. Hur and J.S. Park</i>	97
Microstructure and Properties of Titanium-Based Materials Sintered from TiH ₂ Powder <i>H.H. Shin, H.L. Park and S.N. Chang</i>	105
Effects of Precipitated Intermetallics on Fracture Characteristics of Ti-6Al-2Sn-2Zr-2Mo-2Cr-Si (INVITED) <i>M. Niinomi, K. Fukunaga, G. Tono, J. Koike, D. Eylon and S. Fujishiro</i>	111
Correlation of Microstructure with Quasi-Static and Dynamic Deformation Properties of Ti-6Al-4V Alloy <i>D.G. Lee, C.-S. Lee, S.H. Kim, S.H. Lee and C.S. Lee</i>	119
Effect of Microstructure on Fracture Behavior of β -Rich $\alpha+\beta$ Type Titanium Alloy with High Superplastic Formability <i>Gunawarman, M. Niinomi, K. Fukunaga, D. Eylon, S. Fujishiro and C. Ouchi</i>	127
A New Method for Detection and Quantification of Fretting Fatigue Damage (INVITED) <i>E.B. Shell and D. Eylon</i>	133
Characterization of Accumulated Fatigue Damage in Ti-6Al-4V Using Nonlinear Acoustics and TEM <i>J.L. Maurer, J. Frouin, S. Sathish and D. Eylon</i>	141
Cycle Deforming Behavior and Structure Observation of Ti-2Al-2.5Zr Alloy at -196 °C <i>Y. Zhentao and D. Ju</i>	147
Recent Developments on the Low-Temperature (298 – 458K) Creep Deformation Behavior of Titanium Alloys (INVITED) <i>S. Ankem and D. Doraiswamy</i>	153
High Temperature Deformation Behavior of Ti40 Burn Resistant Titanium Alloy <i>Y.Q. Zhao, K.Y. Zhu, H.L. Qu, H. Wu and L. Zhou</i>	161
A Study on the Machining Characteristics in Turning of Ti-6Al-4V Alloy – Tool Wear Experiment with Carbide Tool K10 – <i>W.P. Hong, H.C. Kim and D.J. Lee</i>	167

Session II : MAGNESIUM ALLOYS

New Magnesium Alloys for Automobile Applications (INVITED) <i>D. Eliezer and E. Aghion</i>	175
---	-----

New Semisolid Process of Magnesium Alloys <i>T. Motegi, E. Yano and N. Nishikawa</i>	185
Rheological and Flow Behavior of Semi-Solid AZ91D Magnesium Alloy (INVITED) <i>C.D. Yim, S.H. Lee and K.S. Shin</i>	191
Fabrication of Bulk Mg-Cu-Ag-Y Glassy Alloy by Squeese Casting <i>E.S. Park, H.K. Lim, W.T. Kim and D.H. Kim</i>	199
Fatigue in Wrought and Cast Magnesium Alloys (INVITED) <i>L. Wagner, J. Wendt and M. Hilpert</i>	205
Effect of Test Environment on Fatigue Crack Propagation Behavior of AZ91D Magnesium Alloy <i>H.C. Jung and K.S. Shin</i>	215
The Effect of Ca Addition on the Microstructure, Mechanical and Corrosion Properties in Mg-Zn Alloy <i>B.Y. Hur, J.P. Eom, S.G. Lim and K.W. Kimm</i>	221
Strip Casting of Mg Alloys <i>S.S. Park, Y.S. Park and Nack J. Kim</i>	225

Session III : FUNDAMENTAL ISSUES

Copper Concentration inside Guinier-Preston (I) Zone Formed in an Al-Cu Alloy <i>M. Takeda, Y. Nagura and A. Igarashi</i>	235
Effect of Damage Growth on Sheet Metals Forming <i>Y.S. Kim and S.Y. Won</i>	241
Advanced Indentation Approach to Characterize Micro-Mechanical Properties of Small-Volume Materials <i>Y. Choi, Y.H. Lee, J.H. Ahn and D. Kwon</i>	247
<i>Ab Initio</i> Study on Generalized Stacking Fault Energy of Basal Plane in Magnesium <i>T. Uesugi, M. Kohyama, M. Kohzu and K. Higashi</i>	255
Mechanically Alloyed Magnesium Alloys for Hydrogen Storage <i>C. Suryanarayana, E. Ivanov and I.G. Konstantchuk</i>	261
A Microstructural Model for the Prediction of High Cycle Fatigue Life Based on the Small Crack Theory <i>J.S. Park, S.H. Park and C.S. Lee</i>	269
Trace and Control of Binder Removal Processes from MIM Compacts by Simultaneous Application of Thermogravimetry and Mass Spectrometry <i>T. Senda, K. Suzuki and Y. Kankawa</i>	275

Addressing Urgent Mass Reduction Requirements by the Use of Lightweight Components <i>M. Leary and C. Burvill</i>	281
Optimal Material Selection for Finite Life Automotive Suspension Applications <i>M. Leary and C. Burvill</i>	287

Session IV : FORMING

Textures and Structures of Asymmetrically Rolled Aluminum Sheets (INVITED) <i>D.N. Lee, S.H. Kim and K.H. Kim</i>	297
Evolution of Anisotropy in Precipitation Hardening Al-Li 2090-T8E41 Alloy <i>H. Garmestani, S. R. Kalidindi, C. Fountain, L. Williams, E.W. Lee and O.S. Es-Said</i>	305
Through-Thickness Variation of Microstructure and Texture in High Speed Hot Rolling of Aluminum and Aluminum Alloy Sheet <i>T. Sakai, S.H. Lee and Y. Saito</i>	311
Texture Evolution of the Al Sheet Processed by Continuous Confined Strip Shearing Based on Equal Channel Angular Pressing <i>J. Lee, H.K. Seok, J.H. Han, J.Y. Suh and H.I. Lee</i>	317
Elongation-Control Rolling of Wires with Asymmetric Cross Section <i>H. Utsunomiya, Y. Saito, M. Ueyama and R. Souba</i>	325
Effect of Preform Shape on a Surface Grain Coarsening Behavior at the Hammer-Forged Al7050 <i>Y.S. Lee, J.H. Lee and Y.S. Choi</i>	331
Light Weight Aluminum Forged Suspension Parts for Automobile <i>Y. Inagaki</i>	337
Characteristics of Strain Profile at Hydroformed Al Tubes <i>S.Y. Lee, Y.J. Jo, S.M. Sohn, M.Y. Lee and Y.S. Kim</i>	343
The Hemming Process for Aluminum Body Sheet <i>K. Noda, Y. Takaki and H. Konishi</i>	349
Inhomogeneous Deformation Behaviour during Equal Channel Multi-Angular Pressing <i>H.S. Kim and M.H. Seo</i>	355
Plastic and Superplastic Forming of Aluminium Based Metal Matrix Composites for Transport Applications (INVITED) <i>F.Bardi, P. Cavaliere, L. Ceschini, A. Morri, S. Spigarelli and E. Evangelista</i>	361
An Analysis of Gas Pressure Forming of Superplastic Al 5083 Alloy <i>C.K. Syn, M.J. O'Brien, D.R. Lesuer and O.D. Sherby</i>	369

Hot Forming Related Properties of Al 6061/Al ₂ O ₃ and Al 2618/Al ₂ O ₃ Composites <i>M. Vedani and E. Gariboldi</i>	375
Particle Weakenging in High-Strain-Rate Superplastic Powder-Metallurgy Processed 2124 and 6061 Aluminum Composites <i>W.J. Kim and K.B. Kim</i>	381
Determination of Superplastic Properties of AlCuAgMgZr Alloys Prepared from Various Techniques <i>J. Dutkiewicz, P. Malczewski J. Kuśnierz and T.G. Nieh</i>	387
Fracture and Superplasticity in Hyper-eutectic Al-20Si Alloy with Coarse Primary Silicon Phase <i>A. Shan, I.G. Moon, J.W. Park and Y.H. Park</i>	393
Improving the Superplastic Properties of an Aluminum Alloy Using Equal-Channel Angular Pressing <i>S.W. Lee, M. Furukawa, Z. Horita and T.G. Langdon</i>	399
High Strain Rate Superplasticity (HSRS) in Aluminum Based Alloys and Composites for Automotive and Aircraft Applications <i>Y.H. Han, R.S. Mishra and A.K. Mukherjee</i>	405
High Strain Rate Superplasticity of Mg-Li- Zn Alloy <i>S.W. Lim, T. Imai, J. Mao, T. Choh and Y. Nishida</i>	411
Superplastic Formability of Fine-Grained AZ61 and AZ31 Magnesium Alloy Sheets and Deformation Mechanism Maps for Magnesium Alloys <i>S.W. Chung and W.J. Kim</i>	417
Superplastic Deformation Behavior of Fe-Al Intermetallic Alloys <i>J.H. Song, T.K. Ha, H.T. Lim and Y.W. Chang</i>	423

Session V : JOINING

Development of High Deposition Rate Double Wire MIG Welding Process For Aluminum Alloy (INVITED) <i>T. Shinoda, J. Nakata and H. Miyauchi</i>	431
Effect of Alloy Elements on Solidification Discontinuities of EB Welded High Tensile Aluminum Alloys <i>S.W. Kim and C.H. Lee</i>	439
Underwater Friction Welding of A6061 Aluminum Alloy <i>K. Katoh and H. Tokisue</i>	445
Diffusion Bonding in Pure Magnesium <i>H. Somekawa, M. Kohzu and K. Higashi</i>	451

Effect of the Pulse Frequency on Solidification Crack Sensitivity of TIG Welded AZ31 Magnesium Alloy <i>T. Asahina, H. Tokisue and K. Katoh</i>	457
Mechanical Properties and Interface Reaction in Brazed Joint of Titanium and Stainless Steel <i>S.C. Kwon, H.J. Yim, S.H. Kim and Y.Y. Kim</i>	463
Brazing Process and Microstructures of Al/Ti Brazed Joint <i>W.H. Sohn, S.I. Cha, H.H. Bong and S.H. Hong</i>	469

Session VI : SPECIAL SESSION ON JAPAN'S NEDO

Nedo'S R&D Program on Key Technology for Innovative Low-Cost and Lightweight Structures <i>Y. Ito</i>	477
R&D Scheme and Objectives for Innovative Aircraft Structures <i>A. Yahata, M. Kadoya and H. Kikukawa</i>	483
Innovative Nose Section of Fuselage Structures Applied by Friction Stir Welding (FSW) of the Aluminum Alloy and Large Thin Casting of Improved Aluminum Alloy <i>Y. Hirose, T. Tsujimoto, K. Kosugi, M. Imuta and H. Fukagawa</i>	489
Application of Manufacturing Processes for Monolithic Structure to Wing Leading Edge <i>T. Jinishi, M. Matoba, S. Ohashi, M. Ochi and A. Yahata</i>	495

Volume II

Session VII : ALUMINUM ALLOYS

Enhancement in Strength and Fatigue Resistance of 6061Al Alloy Produced by Equal-Channel Angular Pressing <i>J.K. Kim, C.S. Chung, T.Y. Park, C.W. An and W.J. Kim</i>	503
Computational Thermodynamic Optimization of Aluminum Base Metallic Glass Systems <i>M.C. Gao, R.E. Hackenberg and G.J. Shiflet</i>	509
Crystallization Behavior of Al-Mn-Ni-Fe Amorphous Alloys <i>H.W. Jin, K.M. Lim and C.G. Park</i>	517
Synthesis and Thermal Stability of Nanocrystalline Al-Mg Alloys <i>F. Zhou, D.H. Shin and E.J. Lavernia</i>	523

Growth Kinetics of Primary Al Nanocrystals in Al-Ni-Nd Alloy <i>S.H. Kim, S.B. Lee and Nack J. Kim</i>	529
DSC and HRTEM Study of Precipitation in Al-Mg-Si Alloys <i>K. Matsuda, H. Matsui, K. Terayama, Y. Uetani and S. Ikeno</i>	535
Stress-Assisted Nucleation of Ω Precipitate in Al-Cu-Mg-Ag Alloys <i>S. Muraishi, S. Kumai and A. Sato</i>	541
A Study on the Structural Characteristics and Tensile Properties of Al-Si Alloys Utilizing Strip Casting Method <i>S.L. Kuan, T.S. Lui, L.H. Chen and J.M. Song</i>	547
Effects of Mn Addition on Microstructure and Mechanical Properties of Strip Cast Al6061 Alloy <i>Y.S. Park and Nack J. Kim</i>	553
A Review of the Effect of Retrogression and Reaging on Aluminum Alloy 7249 <i>K. Koziar, P. Fleck, G. Davila, E. Fromer, M. Leal, H. Pech, J. Foyos, E.W. Lee, B. Sarkar and O.S. Es-Said</i>	559
Effect of Retrogression and Reaging on Bake Hardenability in Al-Mg-Si-(Cr, Be) Alloys <i>K.D. Woo, J.S. Lee, C.H. Yang, H.C. Park and S.W. Kim</i>	565
Influence of Retrogression and Reaging (RRA) Treatments to an Al-Li-Cu-Mg-Zr Alloy on Mechanical Properties and Stress Corrosion Cracking Behaviour. <i>K.S. Ghosh, K. Das and U. K. Chatterjee</i>	571
Effects of Excess Silicon Content on the Ageing Behaviour of Solution-Treated Al-Mg-Si Alloys <i>Y. Ohmori, Y. Matsuura, K. Nakai and S. Kobayashi</i>	577
Effect of Over-Aging on the Microstructure and Mechanical Properties of Cu, Ni Containing AC8A Aluminum Casting Alloy <i>S.W. Kwon, D.W. Suh, Y.R. Im, H.C. Lee, J.K. Yang and K.H. Ryu</i>	583
Application of Aluminum Alloy 2297 in Fighter Aircraft Structures (INVITED) <i>E.S. Balmuth</i>	589
Mechanical Property of Super-High Strength Aluminum Alloys <i>K. Osamura, H. Adachi, J. Kusui and K. Yokoe</i>	597
The Effects of Chemical and Microstructure on Axial Compressing Property of Extruded Al-Mg-Si Alloys <i>H. Kawai and M. Hirano</i>	603
Microstructure and Elevated-Temperature Strength of P/M $\text{Al}_{96-x}\text{Fe}_x\text{Cr}_2\text{Ti}_2$ (x=3, 4, 5) Alloys <i>H.M. Kimura, A. Inoue and K. Sasamori</i>	609

Effect of Si Addition on the Microstructure and Creep Properties of the Mechanically Alloyed Al-10Ti Alloy <i>C.J. Choi, J.K. Park and B.K. Kim</i>	615
Texture Analysis of Aluminum Plate Produced by ECAP <i>S.M. Baeck, H.K. Seok, J.C. Lee, D.I. Kim, H.C. Lee and K.H. Oh</i>	621
Microstructural Evolution during ECA Pressing of Commercial 5083 Al Alloy and Its Mechanical Properties (INVITED) <i>S.Y. Chang, J.G. Lee, K.T. Park and D.H. Shin</i>	627
Grain Refinement and Strengthening of 6061 Aluminum Alloy by Accumulative Roll-Bonding Process <i>S.H. Lee, Y. Saito, T. Sakai, H. Utsunomiya and N. Tsuji</i>	635
Refinement of Intermetallic Compounds in Al-Fe Alloys by LTMT Process <i>C.Y. Lim, H.W. Kim, J.M. Lee and S.B. Kang</i>	641
Mechanical Properties of Al-Mg-Sc and Commercial Aluminum Alloys after Equal-Channel Angular Pressing <i>M. Furukawa, S.W. Lee, Z. Horita and T.G. Langdon</i>	647
Fracture Toughness of Various Zones in Weldments of 6082 Al Alloys <i>V.A. Mosneaga, T. Kobayashi and H. Toda</i>	653
Study on Microstructures and Mechanical Properties in Electromagnetic Cast and Direct Chill Cast Al Alloys <i>S.W. Kim, H. Hao, U.J. Lee, K.D. Woo and J.Z. Jin</i>	659
Tensile Ductility and Tear Resistance of A356 Aluminum Alloys Fabricated by Conventional and Semi-Liquid Casting Process <i>S. Kumai, T. Tanaka, S.W. Han, A. Sato and S.W. Kim</i>	665
A Study on the Fabrication Process, Compression Strength and Sound Absorption Properties of Al Foam in Pot Furnace <i>B.Y. Hur, H.J. Ahn, D.C. Choi and S.Y. Kim</i>	671
Development of Light-Weight Al Scroll Compressor for Car Air Conditioner <i>J.M. Park, J.K. Ahn, H.B. Im, C.S. Ha, I.D. Choi, K.M. Cho and I.M. Park</i>	675
Hydrogen-Assisted Deformation and Fracture Behavior of Al8090 <i>W.K. Jang, S.S. Kim and K.S. Shin</i>	681
Fracture Behavior of AA6061 Aluminum Alloy Under Resonant Vibration <i>J.H. Horng, J.L. Hu, T.S. Lui and L.H. Chen</i>	689
Deformation Behavior of a Spray-Cast Hypereutectic Al-25Si Alloy <i>T.K. Ha, J. Kim, W.J. Park, E.S. Lee, S.H. Ahn and Y.W. Chang</i>	695
Acoustic Emission from Fatigue Crack Extension in Corroded Aluminum Alloys <i>K.W. Nam, S.H. Ahn and A.K. Mal</i>	701

Short and Long Fatigue Crack Growth Behavior in Al-7%Si-0.4%Mg Alloy Castings <i>S.W. Han, S. Kumai and A. Sato</i>	707
Fatigue Crack Propagation Behavior of A356 Squeeze Cast Alloy <i>S.H. Kim and K.H. Rhee</i>	713

Session VIII : INTERMETALLICS

Gamma Titanium Aluminides: Alloys, Processing & Scale-Up (INVITED) <i>D.M. Dimiduk, H.A. Lipsitt and M.J. Blackburn</i>	721
Advances in Synthesizing Methods of Ti-Based Intermetallics from Elemental Powders (INVITED) <i>H.S. Park, Y. Wu, Y. Park, D. Lee and S.K. Hwang</i>	729
Mechanical Properties and Microstructure Observation of TiAl+Nb Alloy <i>Y.Q. Yan, L. Zhou, W.S. Wang and G.Z. Luo</i>	737
Effect of B Addition on the Continuous Cooling Transformation Behavior of Ti-45.5at.%Al Alloy <i>S.K. Kim, J.S. Kim and J.K. Park</i>	743
Effects of Low Cycle Fatigue Test Parameters on $\alpha_2 \rightarrow \gamma$ Phase Transformation at the Grain Boundary in Lamellar TiAl Alloy <i>Y.S. Park and S.W. Nam</i>	749
High Temperature Deformation Behavior of Fine Duplex Gamma TiAl Alloy <i>J.H. Kim, D.H. Shin and C.S. Lee</i>	755
Creep, Creep-Fatigue and Continuous Fatigue Deformation Characteristics of Lamellar TiAl Alloy (INVITED) <i>S.W. Nam, Y.S. Park and S.J. Yang</i>	761
A Comparative Study of the Creep Resistance Improvement between the Interstitial Alloying Elements and Different Heat Treatments for TiAl Alloys <i>S.J. Yang, S.W. Nam and S.K. Hwang</i>	769
Effect of Lamellar Spacing on the Fatigue Crack Propagation Resistance of Fully Lamellar γ -TiAl Alloy <i>H.J. Kim and C.S. Lee</i>	775
In-Situ Observation of Fatigue Crack Propagation of Ti-Al Intermetallics <i>H. Suzuki, A. Nozue and M.N. Tamin</i>	781
The Optimum Thickness of Coating Film for the Fatigue Strength of Surface Modified TiAl Intermetallic Alloy <i>H. Suzuki, Y. Watanabe, M. Ikenaga and K. Ikenaga</i>	787

Surface Strengthening for Optimizing Fatigue Performance of Gamma Titanium Aluminides at Ambient and Elevated Temperatures <i>J. Lindemann, D. Fagaraseanu and L. Wagner</i>	793
Alloy Design of Gamma Titanium Aluminides <i>K. Hashimoto</i>	799
Fabrication of $Ti_3Al-xNb$ ($x=0, 3, 7, 11, 13$ at%) Powder Compacts Manufactured by Pulse Discharge Sintering <i>W. Fang, S.H. Ko and Y.H. Park</i>	805
Synthesis of Ti-Based Intermetallic Compounds and Their Composite Using Shock Compression <i>J.S. Lee, K. Hokamoto and K.S. Kumar</i>	811
Improved Room and High Temperature Mechanical Properties of an Orthorhombic Ti_2AlNb -Based Alloy <i>M. Hagiwara, S. Emura and F. Tang</i>	817
Microstructure and Tensile Ductility of Fe-40Al with High Boron Content <i>J.H. Lee, S.I. Kwun, W.S. Lee, Y.H. Kim and J.W. Byeon</i>	823
Synthesis of Nickel Aluminides via Vacuum Plasma Spraying with Self-Propagating High-Temperature Synthesis <i>Y.G. Jeong, S.J. Park and H.K. Lee</i>	829

Session IX : COMPOSITE MATERIALS

Methodologies to Design the Interfaces in SiC/Al Composites (INVITED) <i>J.C. Lee</i>	837
Tensile Properties and Microstructures of 7075 Al/SiC _p Composite Fabricated by Pressureless Infiltration Technique <i>K.B. Lee, H.S. Sim and H. Kwon</i>	845
Microstructure and Thermal Properties of Compositionally Graded Al-SiC _p Composites <i>N.B. Choi, J.I. Hwang, I.M. Park, I.D. Choi and K.M. Cho</i>	851
Preparation of SiC/2024 Composites by Semisolid Casting <i>X. Meng, H. Ding, Y. Chen and J. Wen</i>	857
Influence of ECA Pressing on Microstructure and Mechanical Properties of P/M SiC _w /6061 Al Alloy Composite <i>S.Y. Chang, S.K. Ryu, D.H. Shin, H. Tezuka and T. Sato</i>	863
In-Situ Synthesis of Al/Al ₃ Ti Composites by MA-PDS Process <i>Z. Sun, Q. Wang, H. Hashimoto, Y.H. Park and T. Abe</i>	869
Microstructural Evolution of Al/Al ₃ Fe Composites by Plasma Synthesis Method <i>J.M. Lee, S.B. Kang, C.Y. Lim, C.Y. Eum, T. Sato, H. Tezuka and A. Kamio</i>	875

Dynamic Softening of Al-18Si Composite during Hot Deformation <i>S.I. Kim, C.H. Han, H.I. Lee and Y.C. Yoo</i>	881
Tailoring the Hypereutectic Al-Si-Xs Composites as a Structural Material Requiring High Young's Modulus <i>H.K. Seok, J.Y. Suh, D.S. Shin, H.I. Lee and J.C. Lee</i>	887
Particles Refinement in Aluminum Composite Slurry Formed by Liquid/Particles Reaction and Its Wear Properties <i>M. Tsujikawa, M. Hino and M. Kawamoto</i>	893
Dry Sliding Wear Behavior of Aluminum Alloy Matrix Composites Reinforced with Carbide Particles Produced by a Pressureless Infiltration Technique <i>S.H. Kim, H.C. Park, H. Kwon and Y.S. Kim</i>	899
Effect of Residual Stress on the Wear Properties of SiC _p /6061Al Composites <i>H.J. Kim, C.G. Kim, L.S. Oh and J.H. Cheon</i>	905
Active Control of Crack Closure Acts by the Shrinkage Effect of Shape Memory TiNi Fiber Embedded/Polymer Matrix Composite <i>A. Shimamoto, C.C. Lee and H. Isui</i>	911
The Properties and Microstructures of TiC _p Particle Reinforced Titanium Matrix Composites <i>Z. Lian, M. Xiaonan, Z. Yongqing, Z. Liying and A. Vassel</i>	917
Mechanical Properties of SCS-6/Ti-15V-3Cr-3Sn-3Al Titanium Matrix Composites <i>H. Izui, A. Tada and T. Furukawa</i>	923
Mechanical and Fracture Behaviors of (Al ₂ O ₃ +SiC _p)/AZ91 Hybrid Mg Matrix Composite <i>I.M. Park, K.M. Cho, I.D. Choi and C.S. Ha</i>	929

Session X : CORROSION & SURFACE TREATMENT

Corrosion Attacks of Aluminum Wire in a Solution Contaminated by Combustion Gas of Chemical Waste <i>O. Seri</i>	937
Changes in Oxide Film Characteristics of Magnesium Alloy by the Addition of Calcium and Minor Element <i>B.S. You, M.H. Kim, W.W. Park and I.S. Chung</i>	943
Corrosion Models in Mg Alloys with Residual and Concentrated Stresses <i>S.I. Tanaka and S. Iwata</i>	949
The Effect of SiC and Si ₃ N ₄ Additions on the Oxidation Resistance of TiAl Alloys <i>D.B. Lee, K.B. Park and J.J. Moon</i>	955

TEM Observation of Initial Oxidation Behaviour of Nb Ion Implanted TiAl <i>S. Taniguchi, Y.C. Zhu, K. Fujita and N. Iwamoto</i>	961
Investigation of Passivity and Its Breakdown on Al ₃ Ti Alloys in 3.5 wt.% NaCl Solution <i>Y.J. Yu and J.G. Kim</i>	967
High Temperature Sulfidation and Oxidation of Sputter-Deposited Nb-Al-Si Coatings <i>D.B. Lee, G.Y. Kim and W.S. Shim</i>	973
Effect of Molybdenum on the Corrosion Behavior of Iron-Aluminides in Thiosulfate-Chloride Solution <i>Y.S. Choi and J.G. Kim</i>	977
A Study of Composite Coating of Cr Evaporation and Pack Cementation to Improve High Temperature Oxidation Resistance of TiAl Alloys <i>D.J. Jung, H.G. Jung and K.Y. Kim</i>	983
Titanium and Aluminum Coatings with Supersonic Free-Jet PVD <i>A. Yumoto, F. Hiroki, I. Shiota and N. Niwa</i>	991
Fabrication and Thermo-Mechanical Properties of Functionally Graded Thermal Barrier Coatings <i>J.H. Kim, Y.M. Rhyim and C.G. Park</i>	997
Low Pressure Carburizing of Ti-6Al-4V Alloy <i>J.H. Kim, C.H. Shin and S.W. Kim</i>	1003
Nitriding and Boronizing of Titanium and Titanium Alloys and Evaluation of Surface Strength <i>K. Nakasa, X. Yan and M. Kato</i>	1009
Intensified Plasma-Assisted Processing of Pure Ti and Ti-6Al-4V Alloy <i>E.I. Meletis</i>	1015
Evaluation of Corrosion on Aluminum Alloy Airframe Structures under Protective Coatings Using Acoustic and Thermographic Techniques <i>J. Hoffmann, S. Sathish and N. Meyendorf</i>	1021
Microstructure and Mechanical Properties of Ti-6Al-4V Alloy Surface-Alloyed Materials Fabricated by High-Energy Electron Beam Irradiation <i>K.J. Euh, J.M. Lee and S.H. Lee</i>	1027

Session XI : MELTING/CASTING

The Expanding Family of Aluminium Grain Refiners for the Wrought and Foundry Industries <i>D.A. Boot and P. Fisher</i>	1037
---	------

Filling Limitation and Mechanical Properties for Different Gate Positions in Semi-Solid Forming Process of Aluminum Alloys <i>C.G. Kang, P.K. Seo and Y.I. Son</i>	1043
Comparison of Innovative Induction Heating for Aluminum Alloys and Metal Matrix Composites in Semi-Solid Forming Process <i>H.K. Jung and C.G. Kang</i>	1049
Microstructural Evolution and Deformation Behaviour of 2014 Aluminium Alloys in the Semi-Solid State <i>D.S. Han, I.C. Stone and B. Cantor</i>	1055
Microstructural Control for Thixotropic Al Alloy by Horizontal Continuous Casting Process Using Electromagnetic Stirring <i>K.B. Kim, D.Y. Lee, Y.K. Seon, H.I. Lee and D.S. Shin</i>	1061
Interfacial Reactions between Mold Materials and Molten Titanium Aluminide <i>M.G. Kim, S.Y. Sung, T.W. Hong, Y.I. Bae and Y.J. Kim</i>	1067
POSTER PRESENTATION	
Effect of Silicon on Microstructure and Mechanical Properties of TiAl Base Alloys <i>S.E. Kim, F. Sun, Y.T. Lee and M. Yamaguchi</i>	1075
Development of Fine Microstructure of B.390 Casting Alloy by the Modification of Ca Amount <i>H.J. Kim, M.K. Kim, B.H. Jung and K.J. Son</i>	1081
Plasma Nitriding Properties of Ti-aluminide Intermetallic Compounds Fabricated by Hot-Pressing <i>J.Y. Son and Y.W. Park</i>	1087
High Resolution Electron Microscopic Study of the $\delta'/G.P.$ zone Complex Precipitate Structure in an Al-Li-Cu-Mg-Zr Alloy <i>K.H. Lee, Y.H. Lee, Y.J. Lee and K. Hiraga</i>	1093
Eutectic Bonding of Al6061 Alloy Using Cu Insert Metal <i>S.Y. Shin, D.C. Cho, C.H. Lee, M.W. Ko and K.S. Shin</i>	1101
Rotation-Cylinder Method for Mass-Production of Lightweight Mg-Ni Hydrogen Absorbing Alloys <i>W. Ha, T.W. Hong, S.K. Kim, S.G. Lee and Y.J. Kim</i>	1109
Drilling of Magnesium AM60B Alloy by Use of PVD Coated Tools <i>E. Gariboldi, P. Locati and M. Vedani</i>	1115
High Efficient Drilling of Aluminum Alloys <i>K. Sakurai, K. Adachi, G. Kawai and K. Ogawa</i>	1121
Selection of Optimum Welding Conditions for A6061 Aluminum Alloy Friction Welding by Neural Networks <i>G. Kawai, T. Sawai, T. Kurozawa, Y. Yamamoto, H. Yamaguchi and K. Ogawa</i>	1127
Evaluation of Corrosion Fatigue Pitting Damage on 2024-T3 <i>Y.I. Yoon, V. Chandrasekaran, D.W. Hoepfner and Y.H. Hwang</i>	1133
Characteristics of Semi-Solid Processed Al-Based Alloys for Automobile Applications <i>S.Y. Lee, B.S. Kim, B.Y. Lee, S.Y. Lee and H.J. Lee</i>	1139

AUTHOR INDEX

Session VII

ALUMINUM ALLOYS

Session VII

ENHANCEMENT IN STRENGTH AND FATIGUE RESISTANCE OF 6061Al ALLOY PRODUCED BY EQUAL-CHANNEL ANGULAR PRESSING

J. K. Kim, C. S. Chung, T. Y. Park, C. W. An, and W. J. Kim

Dept. of Materials Science and Engineering, Hong-Ik University
72-1, Sangsu-dong, Mapo-ku, Seoul, 121-791, Korea

ABSTRACT

The ECAP process has the potential for significantly refining the grains of polycrystalline materials to within the submicrometer. In this investigation, this ECA pressing technique has been applied to a commercial 6061 aluminum and alloy. The grain size has been significantly decreased by ECAP process. Pre-ECAP solid-solution treatment plus post-ECAP aging treatment has been found to be more effective in enhancing the strength of a commercial 6061 Al alloy than pre-ECAP peak-aging treatment. Large increase of ~40% in UTS and yield stress was obtained in the post-ECAP aged material compared to the peak-aged commercial 6061 Al alloy. Fatigue performance of the ECAP processed 6061 Al alloy was discussed in terms of fatigue life, crack nucleation and propagation. The improvement of fatigue properties was observed and attributed to a higher resistance to crack nucleation in the ultrafine-grained material.

1. INTRODUCTION

It has been well demonstrated that equal channel angular pressing (ECAP) is a prospective method of producing very fine grain size (sub-micrometer or nano-meter) in ingot-processed metallic alloys [1-6] without reduction in the cross-sectional dimensions of a sample. Fine grains are beneficial in viewpoints of increased strength, toughness and fatigue life, and improved superplasticity. Ferrasse et al.[7] studied the effect of pre-ECAP heat treatment (i.e., peak-aging and over-aging) on development of sub-microstructure in the ECAP processed 6061 Al alloy. They found that the ECAP processed peak-aged material exhibited much higher strength than the ECAP processed over-aged material, although both materials had the similar subgrain sizes of ~ 0.4 μ m.

In the present study, another heat-treatment method linked with ECAP process has been proposed to enhance the strength of a commercial 6061 Al alloy. Before ECAP process, the alloy was solid-solution treated, quenched into water, and after the ECAP process the material was aged at relatively low temperature. The solid-solution treated alloy has an advantage over the peak-aged material in viewpoint of lowering load and temperature for ECAP process.

Another objective of this study is to investigate enhancement in fatigue properties after ECAP processing. There have been relatively few studies for the fatigue behavior of ECAP processed aluminum alloys. Vinogradov et al.[8] studied the fatigue property of the ECAP processed 5056Al alloy. The material exhibited a slight enhanced fatigue life at high stress amplitudes but no improvement in the fatigue limit was observed. It was also found that the

crack growth rate was greater in the ECAP processed material than the coarse-grained material.

2. Experimental Procedure

For the sample preparation, a 6061 Al billet was extruded to a diameter of 18mm at 450°C and cut to the length of 100mm. The bar was solution treated at 530°C for 4 hrs. and then quenched into water. The grain size measured after the heat treatment was 40~80µm. The ECA pressing was conducted on a solid die with an internal angle (Φ) of 90° between the two separate portions of the channel at the pressing speed of 4mm s⁻¹. For this die design, it has been shown that the true strain accrued on a single pass through the die is ~1 [9]. A 6061Al sample was held at 125°C for 20 min. and then pressed through the die preheated to 125°C. Repetitive pressings of the same sample were performed up to 12 passes, equivalent to strain of ~12. All pressings were conducted by rotating each sample about the longitudinal axis by 90° in the same direction between consecutive passes (designated as route B_c [10]). After the ECA pressing, the 6061Al bar was aged at 175°C or 100°C as a function of time. Microhardness and tensile tests were carried out to characterize the strength and ductility of the ECAP processed materials. Tensile test was conducted in air at room temperature, using a testing machine operating at a constant cross-head speed with an initial strain rate of 5x10⁻⁴s⁻¹.

The microstructure of each sample was examined using transmission electron microscopy(TEM). Samples for TEM were cut from the y plane and selected area electron diffraction(SAED) patterns were taken from areas having a diameter of ~10µm.

The fatigue life experiments were carried out under the complete unloading condition R (the ratio of the minimum to maximum stress for a cyclic stress)=0. The crack nucleation and propagation was characterized using miniature single edge notched samples at the stress ratio R=0.1 and initial stress intensity factor range of $\Delta K_0=3\text{MPa}\times\text{m}^{1/2}$. For the fatigue life and crack propagation tests, a sinusoidal waveform load control mode was employed with a frequency of 10Hz.

3. Results and Discussion

TEM micrographs of the as-ECAP processed samples are shown in Fig. 1, together with SAED patterns taken from regions within these areas. Fig. 1(a) is the microstructure after 1 pass, where parallel bands of elongated subgrains have formed. Further deformation (12 pass) has broken elongated band structure, without reduction of the thickness, to equiaxed subgrains by forming the boundaries perpendicular to the direction of the bands (Fig. 1(b)). The subgrain size was measured to be 0.3~0.4µm, which is very similar to those measured in the ECAP processed peak-aged and over-aged 6061 Al alloy studied by Ferrasse et al. [7]. This result implies that the size of subgrains formed during ECAP process is little affected by the density and size of precipitate particles. The SAED pattern shown in Fig. 1(b) exhibits diffracted beams scattered more uniformly around rings compared to that for the 1 passed material, thus indicating the presence of structure of grains separated by boundaries having higher angles of misorientation.

The effect of number of pass on hardness of the solid-solution treated materials is shown in Fig. 2. The hardness has increased by about 55% after 1 pass. After 4 pass, the increase in hardness was near 85%. This large increase in hardness can be directly attributed to the considerable grain refinement made through severe deformation (Fig. 1). However, after 4–6

pass, the hardness gradually continues to decrease, indicating softening occurs after the critical strain accumulation.

The hardness of the ECAP processed materials was measured after aging treatment at 175°C as a function of time up to 8hrs. In the unpressed state, there is a significant increase in hardness with time (50% after 8hrs). In the pressed materials, on the other hand, the opposite trend. This result attests that in the pressed material, the effect of recovery or/and grain coarsening of heavily deformed substructure by annealing overwhelms the effect of precipitate hardening by aging. To reduce the softening effect by annealing, a lower aging temperature of 100°C was used. The effect of aging at 100°C is shown in Fig. 2. The strengthening with aging is now recognized. All the pressed materials exhibit large increase in hardness. The optimum aging time at 100°C was determined to be near 48hrs. since the hardness started to fall after 48hrs. This enhancement in strength indicates that the aging effect is more dominant than the softening effect at 100°C.

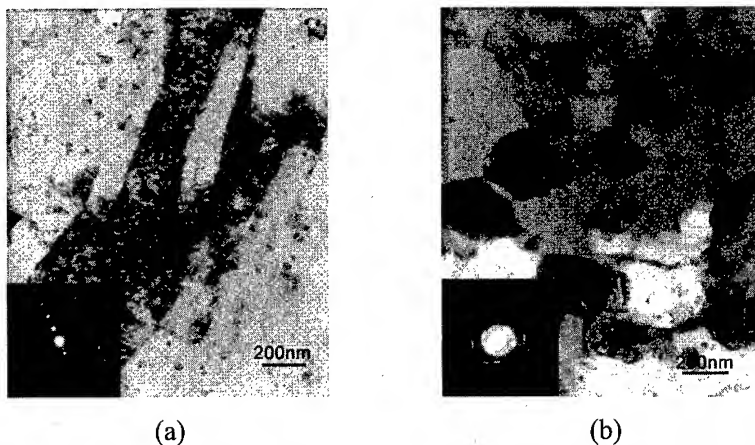


Figure 1. TEM micrographs of the solid-solution treated 6061 Al alloys after ECAP process (a) 1 pass (b) 12 pass.

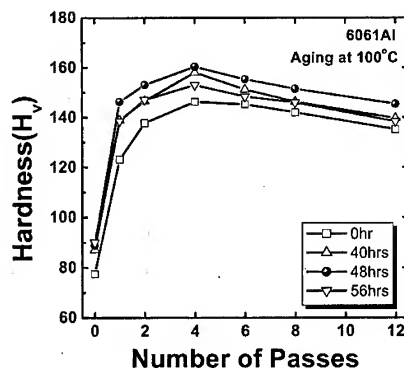


Figure 2. Vickers hardness of the ECAP processed materials with aging treatment.

The engineering stress-strain curves obtained by tensile testing on the peak-aged commercial 6061Al alloy and 1, 4 and 12 passed ECAP 6061Al alloy with and without aging

treatment at 100°C for 48hrs. are compared in Fig. 3. The combination of ECAP process with aging treatment at 100°C results in a significant increase in tensile strength. There is an increase in yield stress and UTS by ~40% at 4 pass compared to that of the peak-aged (T6) commercial 6061Al alloy, which agrees with the hardness result. It should be noted here that even the 4 passed solid-solution 6061 Al alloy (425 MPa) is stronger than that of 4 passed peak-aged 6061 Al alloy (400 MPa) reported by Ferrasse et al. [7]. This result may be linked with the difference in dislocation accumulation rate and stability of precipitates during ECAP. It was suggested by Hong et al. [11,12] that the hardening rates of the under-aged and solid-solution treated Al alloys are higher than those of peak-aged and overaged Al alloys because dynamic recovery is more effectively suppressed by the high solute content in the matrix. Furthermore, needle-shaped θ' precipitates in Al-Cu alloys were found to be sheared into fine particles after a few passes of ECAP [13], which may weaken the strengthening effect of precipitates in the pre-ECAP aged material. Tensile ductility, on the other hand, shows the trend to decrease with increase in number of pass. Beyond 4 pass, however, no further decrease in ductility was observed.

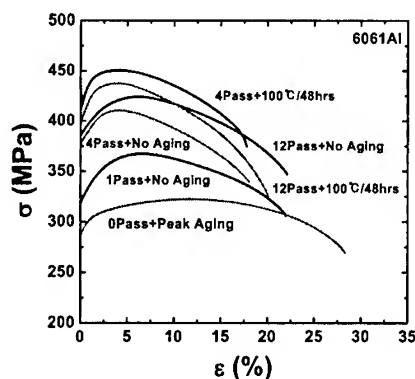


Figure 3. Comparison of engineering stress-engineering strain curves between the T6 treated commercial 6061 Al alloy and ECAP processed 6061 Al alloy (1, 4 and 12 pass) with and without the low-temperature aging.

To assess general fatigue performance one needs to consider two factors: the resistance to crack nucleation and crack propagation. Fatigue life, which is determined by both factors, is usually evaluated through the stress amplitude versus number of cycles (S-N) curve, while the resistance of crack propagation is evaluated in terms of crack growth rate and its relation with a stress intensity factor K . Fig. 4(a) is the S-N curves for the solid solution 6061 Al alloy at 0 and 1 passes. The fatigue data for the T6 treated commercial 6061 Al alloy are also presented for comparison. The ECAP processed 6061Al alloy shows a significant improvement in fatigue life (more than a factor of 10!) compared to the 0 passed solid-solution and T6 treated alloys that are similar in fatigue behavior. This result is remarkable since this improvement can be achieved in both low and high-cyclic fatigue region ($N \sim 10^7$). Vinogradov et al. [8] also reported the enhancement in fatigue life in the ECAP processed 5056 alloy (4 pass) but it was only valid in the low-cycle region and the improvement was

relatively slight (about factor of 2). Vinogradov et al. [8] explained the increase in fatigue life in the ECAP processed 5056 Al alloy in terms of higher yield stress in the ECAP alloy that prevents macroscopic plastic deformation at the beginning of load controlled cycling in contrast to the low-strength initial alloy. Therefore, the incubation period for crack nucleation is increased and longer fatigue life is the result.

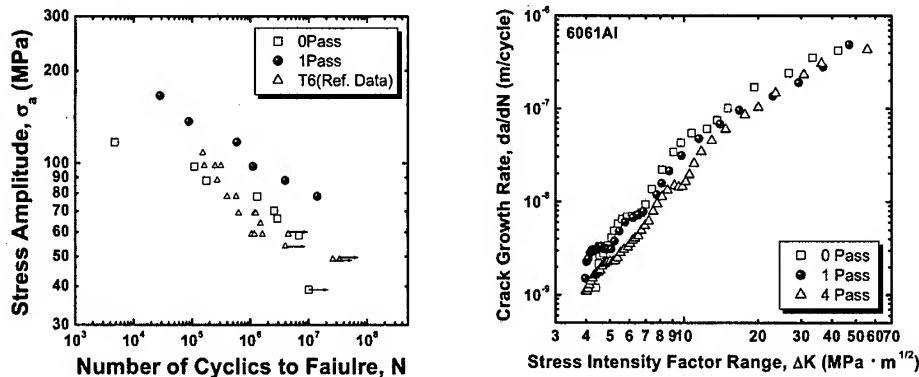


Figure 4. (a) S-N curves and (b) Fatigue crack growth rate as a function of ΔK value.

The crack growth rate, da/dN , where a is the crack size, is plotted in logarithmic coordinate in Fig. 4(b) as a function of the stress intensity factor range ΔK . In the intermediate range, the crack propagation reasonably well obeys the Paris law:

$$da/dN = C(\Delta K)^m \quad (1)$$

where C and m are material parameters depending on loading conditions.

The following can be inferred from the plot in Figure 4(b). First, values of C and m in Eq. (1) do not change significantly after 1 pass. However, C value distinctly decreases at 4 pass. Second, there is crossover in crack growth rate at small ΔK values: higher crack growth rate is higher number of passes. This result agrees well with the known effect of grain size on fatigue threshold at low load ratios where the material with fine grains shows a lower apparent fatigue threshold[14].

4. Summary and conclusion

In the present study, an effective heat-treatment method linked with ECAP process has been proposed to enhance the strength of a commercial 6061 Al alloy. Before ECAP process, the alloy was solid-solution treated and quenched into water and after the ECAP process, the material was aged at 100°C . The large increase of $\sim 40\%$ in UTS and yield stress was obtained in the post-ECAP aged material compared to the peak-aged (T6) commercial 6061 Al alloy.

Large enhancement in fatigue life was observed after ECAP processing. Judging from the S-N curve and crack propagation rate measurement, it is concluded that increased resistance to crack nucleation improves the fatigue life of the ECAP processed 6061 Al alloy.

Acknowledgement

This work was supported by the Korea Science and Engineering foundation (KOSEF 2000).

Reference

1. R. S. Mishra, R. Z. Valiev, S. X. McFadden and A. K. Mukherjee, *Mater. Sci. Eng. A*, Vol. 252 (1998), pp. 174.
2. R. Z. Valiev, A. V. Kornikov and R. R. Mulyokov, *Mater. Sci. Eng. A*, Vol. 168 (1993), pp. 141.
3. M. Furukawa, Y. Ma, Z. Horita, M. Nemoto, R. Z. Valiev and T. G. Langdon, *Mater. Sci. Eng. A*, Vol. 241 (1998), pp. 122.
4. P. B. Berbon, N. K. Tsenev, R. Z. Valiev, M. Furukawa, Z. Horita, M. Nemoto and T. G. Langdon, *Metall. Mater. Trans. A*, Vol. 29 (1998), pp. 2237.
5. Y. Iwahashi, Z. Horita, M. Nemoto and T. G. Langdon, *Acta Mater.*, Vol. 46 (1998), pp. 3317.
6. R. Z. Valiev, N. A. Krasilnikov and N. K. Tsenev, *Mater. Sci. Eng. A*, Vol. 137 (1991), pp. 35.
7. S. Ferrasse, V. M. Segal, K. T. Hartwig and R. E. Goforth, *J. Mater. Res.*, Vol. 12 (1997), pp. 1253.
8. A. Vinogradov, S. Nagasaki, V. Patlan, K. Kitagawa and N. Kawazoe, *NanoStructured Mat.*, Vol. 11 (1999), pp. 925.
9. A. Vinogradov, T. Mimaki, S. Hashimoto and R. Valiev, *Scripta Mater.*, Vol. 41 (1999), pp. 319.
10. R. Z. Valiev, R. K. Islamgaliev and I. V. Alexandrov, *Progress in Materials Science*, Vol. 74 (1999), pp. 1.
11. S. I. Hong, G. T. Gray III and Z. Wang, *Mater. Sci. Eng. A*, Vol. 221 (1996), pp. 38.
12. S. I. Hong, G. T. Gray III and J. J. Lewandowski, *Acta Metall. Mater.*, Vol. 41 (1993), pp. 2337.
13. M. Murayama, K. Hono and Z. Horita, in *Ultrafine Grained Materials*, R. S. Mishra, S. L. Semiatin, C. Suryanarayana, N. N. Thadhani and T. C. Lowe, eds., TMS, Warrendale, PA, (2000), pp. 145.
14. S. Suresh: *Fatigue of Materials*, Cambridge University Press, Cambridge, UK(1998), pp. 679.

COMPUTATIONAL THERMODYNAMIC OPTIMIZATION OF ALUMINUM BASE METALLIC GLASS SYSTEMS

M.C. Gao, R.E. Hackenberg, and G.J. Shiflet
Department of Materials Science and Engineering
University of Virginia, Charlottesville, VA 22903

Abstract

As important glass-forming alloys, the ternary Al-Fe-Gd and Al-Ni-Gd systems in their Al-rich corner were examined experimentally to assist in a thermodynamic assessment of these systems. The solid-state phase equilibria were determined using XRD and TEM-EDS techniques. While this work confirmed the solid-state equilibria in Al-Fe-Gd reported previously, the ternary phase in Al-Ni-Gd system was identified to be $\text{Al}_{15}\text{Ni}_3\text{Gd}_2$ rather than $\text{Al}_{16}\text{Ni}_3\text{Gd}$ reported in literature, and its morphology changes from rods to irregular particles in different tie triangles. Differential thermal analysis of 24 alloys in Al-Fe-Gd system and 42 alloys in Al-Ni-Gd system yielded critical temperatures pertaining to the solid-liquid equilibria. A self-consistent thermodynamic database for these systems was developed using the CALPHAD approach. Parameters describing the Gibbs free energy of various phases of the Al-Gd, Al-Ni, Al-Fe-Gd and Al-Ni-Gd systems were manually optimized in this study. Topics about metallic glass formation are discussed in light of these results.

1. INTRODUCTION

Aluminum-based glasses, discovered by our group in 1988 [1] were recognized to form in a nontraditional manner [2, 3]. Several empirical factors favoring metallic glass formation include a multicomponent system with atomic size differences larger than 10%, a low temperature deep eutectic in the binary (or ternary) phase diagram, negative heats of mixing between the components and high viscosity of the melt (see [4]). Aluminum-based glasses, in particular, do not appear to follow these rules, since alloys exhibiting the best glass formation ability tend to lie relatively far from the eutectic region [3]. The glass-forming range of Al-rare earth binary alloys lies on the solute-rich side of the eutectic where the liquidus temperature increases rapidly as the rare-earth is added. In fact, in a recent study of the Al-Ni-Gd system, Guo et al. [3] identified alloys which exhibit positive glass forming ability (GFA)-related parameters but which experimentally don't exhibit good GFA. Extending the composition range to four [5] and even seven components [6] does extend the composition range but does not improve the GFA, hence the confusion principle [7] and atomic size effects [8] are not applicable. Little thermodynamic information is available for the Al-transition metal-rare earth glass-forming alloys, in part due to the unusual combination of elements in these Al-transition metal-rare earth systems, and to date, no thermodynamic databases have been developed. A self-consistent thermodynamic database would be a useful tool in analyzing the composition dependence of GFA in these systems.

2. EXPERIMENTAL PROCEDURE AND RESULTS

2.1 Experimental procedure

All the alloys were synthesized from pieces of Al (99.9% purity), Gd (99.9%) and Fe (99.995%) or Ni(99.9945%) of about 2-5 grams in a Ti-gettered arc-melter in an argon atmosphere. (Note that all compositions reported in this study are in atomic %.) Alloys selected for isothermal annealing studies first underwent rapid solidification using a melt-spinning technique to obtain ribbons of 10-30 micron thickness. These ribbons were then sealed inside silica tubes under a partial pressure of argon and annealed at 500°C for times up to 64 days. The annealed ribbons were analyzed with X-ray diffraction (XRD) using CuK α radiation. Specimens for transmission electron microscopy were made by electropolishing melt-spun and annealed ribbons in a solution of 1 part nitric acid to 3.5 parts methanol at 8-12 volts and -30°C. These thin foils were first examined in a conventional TEM, where the phases were identified using selected area diffraction (SAD). The chemical composition of each phase present was then determined using small probe quantitative energy-dispersive x-ray spectroscopy (EDS) in a field-emission TEM. The composition of each phase was determined using Cliff-Lorimer equations [9]. Neither k-factor showed a substantial thickness dependence; this indicates that preferential x-ray absorption was negligible for the x-ray lines employed and for the thicknesses of the specimens analyzed in the FEG-TEM [10]. A minimum of 10 particles from each phase were probed, and their average value determined for each annealing condition. Differential thermal analysis (DTA) was performed by heating and cooling the alloy in alumina crucibles under a flowing argon environment at a rate of 10°C/minute. It was found that the resolution of the weaker thermal events did not improve with scan rates of 5°C/minute. The apparatus was periodically calibrated with high purity standards of Al and Au. The initial sample state (as arc-melted ingot, as melt-spun or as spun-and-annealed ribbon) was seen to have no effect whatsoever on the DTA profiles in the temperatures of interest, so specimens with all 3 conditions were analyzed. All the alloy compositions were analyzed 2-5 times, with the DTA profiles showing good reproducibility.

2.2 Al-Fe-Gd system at 500°C

Fig. 1 shows TEM images from Al₉₀Fe₅Gd₅ annealed 30 days at 500°C. The original amorphous phase has completely decomposed into fcc-Al, M₃Gd (M = Al, Fe) and τ_1 (Al₁₀Fe₂Gd).

Fig. 2 shows the typical XRD patterns of annealed alloys for 7 days at 500°C. Notice that alloy Al₈₅Fe₁₀Gd₅ show neither M₃Gd nor Al₁₃Fe₄, indicating it locates on the boundary connecting fcc Al and τ_1 . The EDS results are reported elsewhere [12]. It was found that the phase

compositions differ little with annealing time at 500°C when comparing 7, 30 and 64 days. The fcc-Al matrix is essentially depleted of both Fe and Gd, at least within the experimental uncertainty of these measurements. The M₃Gd phase, originating from the Al-Gd binary system as Al₃Gd (DO₁₉ structure), is seen to have about 1 at% solubility for Fe, which is different than the isothermal section by Vivchar *et al.* [11], which assigned no Fe solubility to this phase. The τ_1 phase, however, is seen to have a composition close to its reported value [11]. The DTA data were published elsewhere [12].

2.3 Al-Ni-Gd system at 500°C

Twelve alloys were heat treated at 500°C for 1 day, 7 days, 18 days, 30 days and 60 days respectively. Fig. 3 shows the TEM images of alloys $\text{Al}_{90}\text{Ni}_3\text{Gd}_7$ and $\text{Al}_{82}\text{Ni}_{15}\text{Gd}_3$ annealed at 500°C for 30 days. Note the difference in morphology of the ternary phase. It is rod-shaped for alloys with Ni/Gd ratio < 1.5 and has an irregular shape for alloys with Ni/Gd ratio > 1.5. Typical XRD patterns of annealed alloys are shown in Fig. 4. Strong diffraction peaks of fcc Al from $\text{Al}_{16}\text{Ni}_3\text{Gd}$ ($=\text{Al}_{80}\text{Ni}_{15}\text{Gd}_5$) indicates that this reported chemistry is not the correct composition of the ternary phase. The identical diffraction peak positions from $\text{Al}_{16}\text{Ni}_3\text{Gd}$ and $\text{Al}_{82}\text{Ni}_{15}\text{Gd}_3$ indicate that they *both* must be located in the same tie triangle. XRD of alloy $\text{Al}_{15}\text{Ni}_3\text{Gd}_2$ ($=\text{Al}_{75}\text{Ni}_{15}\text{Gd}_{10}$) shows neither Al_3Gd nor Al peaks. The EDS results of the equilibrium ternary phases at 500°C are listed in Table 1. Note that the consistency in composition for different alloys under different annealing times. According to these results, the chemistry of this ternary phase was tentatively determined to be $\text{Al}_{15}\text{Ni}_3\text{Gd}_2$. Both the XRD and EDS results from this work disagree with the reported value, $\text{Al}_{16}\text{Ni}_3\text{Gd}$ [13]. The only literature pertaining to the Al-Ni-Gd system is the isothermal section at 800°C in the range 0 to 33.3 at.% Gd [13]. The ternary phase closest to the Al-rich corner was reported to be $\text{Al}_{16}\text{Ni}_3\text{Gd}$ with an orthorhombic crystal structure. Currently, the crystal structure of this compound is under investigation.

3. THERMODYNAMIC ASSESSMENT

The Gibbs energy of individual phases is described by sublattice models [14] and is defined relative to the Standard Element Reference (SER), i.e., the enthalpies of the pure elements in their defined reference phase at 298.15K and 1 atm. The detailed formulation and the magnetic contribution for Al-Fe-Gd are listed in [12]. The description of Gibbs energy of Al-Ni-Gd [15] follow in a similar way as Al-Fe-Gd system. The excess Gibbs energy is expressed in Redlich-Kister-Muggianu polynomial form [16, 17]. All the ternary mixing parameters were set to zero. Lacking compositional data from ternary alloys, the stable intermetallic compounds $\text{Al}_{13}\text{Fe}_4$, Al_5Fe_2 , Al_2Fe , AlFe were assumed to have no solubility of Gd. Thus, their (binary) sublattice models and parameters are accepted without alteration [18, 19]. The stable intermetallic compounds previously assessed for the Fe-Gd binary system that impact the equilibria in the Al-rich corner are: $\text{Fe}_{17}\text{Gd}_2$ and Fe_2Gd , and the 2-sublattice models and parameters reported by Liu *et al.* [20]. They are described as M_{17}Gd_2 and M_2Gd in this work since prior work [18] indicates that Al and Fe mix on the first (M) sublattice, while Gd is confined by itself to the second (rare-earth) sublattice. The parameters for Gd-Ni binary assessed previously [21] was used in this work without modification except for the Ni_5Gd compound. Ni_5Gd was modeled as M_5Gd with Al and Ni occupy the first sublattice and Gd the second. The Al-Gd binary compounds of interest to this study are Al_3Gd and Al_2Gd ; the AlGd , Al_2Gd_3 and AlGd_2 do not affect the phase equilibria in the Al-rich corner and will not be considered further. Al_2Gd has the same C15 Laves phase structure as Fe_2Gd and Ni_2Gd , so they are all described as M_2Gd . The Al_3Gd phase (DO_{19} structure) shows some solubility of Fe/Ni in the ternary system, thus the M_3Gd phase is defined as having the DO_{19} structure, with Al and Fe/Ni mixing on the M sublattice. A magnetic contribution to the Gibbs energies of Fe_2Gd and $\text{Fe}_{17}\text{Gd}_2$ was made as described by Liu *et al.* [20]. No magnetic contribution was made for the

other binary and ternary compounds of interest since they magnetically order at temperatures far below ambient, if at all. The ternary phases optimized in this work include $\text{Al}_{10}\text{Fe}_2\text{Gd}$ and $\text{Al}_8\text{Fe}_4\text{Gd}$ for the Al-Fe-Gd system, and $\text{Al}_{15}\text{Ni}_3\text{Gd}_2$, Al_4NiGd , $\text{Al}_3\text{Ni}_2\text{Gd}_1$, $\text{Al}_7\text{Ni}_3\text{Gd}_2$, Al_2NiGd , AlNiGd for the Al-Ni-Gd system. They are all modeled as stoichiometric compounds with 3 sublattices which are exclusively occupied by Al, Fe/Ni and Gd, respectively. Both ternary systems were optimized by trial and error and the parameters for Al-Fe-Gd are listed in Table 2. All calculations during and after optimization were carried out using the Thermo-Calc software package [22]. Currently Al-Ni-Gd system is still undergoing manual optimization, and the results associating with Al-Ni-Gd in this paper are tentative.

4. RESULTS AND DISCUSSION

The calculated Al-Gd binary phase diagram [12] was done in the range of 65-100 at.% Al. Good agreement is obtained against experimental data from 3 independent sources: Buschow [23], Saccone *et al.* [24] and this study. This thermochemical comparison gives an important cross-check of the validity of the parameters for Al_3Gd and Al_2Gd , and by consequence, the binary Al-Gd liquid mixing parameters. The only literature data pertaining to the Al-Fe-Gd system is the partial isotherm at 500°C [11]. Since the ternary mixing parameter in the liquid was set to zero, the solid-liquid equilibria in ternary alloys are determined through (1) the binary stability and mixing parameters (2) the mixing parameters for Al and Fe/Ni on the M sublattice of M_AGd_B compounds (${}^0L_{\text{Al,Fe/Ni;Gd}}^{\text{M}_A\text{Gd}_B}$) and (3) the stabilities of the ternary compounds. In assessing the ternary systems, (1) the binary parameters were left untouched (2) ${}^0L_{\text{Al,Fe/Ni;Gd}}^{\text{M}_A\text{Gd}_B}$ were determined to give agreement at 500°C and to avoid improbable solubilities at higher temperatures, and (3) the parameters for ternary compound phases were determined to obtain the best agreement between the solid-liquid phase boundaries and the DTA heating onset temperature values [12,15].

Figures 5 and 6 show calculated isopleths through the Al-Fe-Gd phase diagram at 5 at.% Fe and 5 at.% Gd, respectively. Reasonable agreement is obtained with the experimental DTA data for these and other compositions. The intermediate phase boundaries (those between the initial and final melting) often did not appear as a thermal event in the DTA data; this is attributed to the low volume fractions and/or low latent heats of melting of the particular compound phases in question. Figures 7 and 8 show tentatively calculated isopleths through the Al-Ni-Gd phase diagram at 3 at.% Ni and 3 at.% Gd, respectively. Figures 9 and 10 show the 500°C isothermal sections for Al-Fe-Gd and Al-Ni-Gd respectively, with the glass forming range marked.

The results of this study reinforce two main ideas: firstly, that there are no deep eutectics in the Al-rich corner and secondly, that the occurrence of intermetallic compounds (especially $\text{Al}_{10}\text{Fe}_2\text{Gd}$), determine to a large degree in the solid-liquid equilibria in the Al-rich corner where metallic glass formation has been observed. This has important consequences for the compositional dependence of amorphous phase retention during rapid solidification and the decomposition of this phase into fcc-Al and/or compounds upon heating.

ACKNOWLEDGEMENTS

MCG and GJS acknowledge financial support from the Air Force Office of Scientific Research (grant F49620-97-1-0105). REH acknowledges support from the National Science Foundation (grant DMR-9904034). Additional support was provided by the University of Virginia Academic Enhancement Program.

REFERENCES

1. He, Y., Poon, S.J. and Shiflet, G.J., *Science*, 1988, **241**, 1640.
2. He, Y., Dougherty, G.M., Shiflet, G.J., and Poon, S.J., *Acta Metall. Mater.*, 1993, **41**, 337.
3. Guo, F.Q., Poon, S.J. and Shiflet, G.J., *Scripta Mater.*, 2000, **43**, 1089.
4. Johnson, W.L., Inoue, A., and Liu, C.T., eds., *Bulk Metallic Glasses*, Materials Research Society Symposium Proceedings, Vol. 554, MRS, Warrendale, PA, 1999.
5. Guo, F.Q., Enouf, S.J., Shiflet, G.J. and Poon, S.J., *Mater. Trans. JIM*, 2000, **41**, 1406.
6. Guo, F.Q., Poon, S.J. and Shiflet, G.J., *Mater. Sci. Forum*, 2000, **331**, 31.
7. Greer, A.L., *Nature*, 1993, **366**, 303.
8. Inoue, A., *Sci. Rep. RITU*, 1996, **A42**, 1.
9. Cliff, G. and Lorimer, G.W., *J. Microscopy*, 1975, **103**, 203.
10. Horita, Z., Sano, T. and Nemoto, M., *Ultramicroscopy*, 1987, **21**, 271.
11. Vivchar, O.I., Zarechnyuk, O.S. and Ryabov, V.R., *Dopov. Akad. Nauk RSR (A)*, 1973, **11**, 1040.
12. Hackerberg, R.E., Gao M.C. and Shiflet, G.J., *Acta Metall.*, submitted, 2001.
13. Rykhal, R.m., Zarechnyuk, O.S., Marich, O.M., *Dopov. Akad. Nauk Ukr. RSR. (A)*, (9), 835-855, 1978.
14. Hillert, M. and Staffanson, L.I., *Acta Chem. Scand.*, 1970, **24**, 3618.
15. Gao, MC, Hackerberg, R.E., and Shiflet, G.J., to be published.
16. Redlich, O. and Kister, A.T., *Ind. Eng. Chem.*, 1948, **40**, 345.
17. Muggianu, Y.M., Gambino, M. and Bros, J.P., *J. Chim. Phys.*, 1975, **22**, 83.
18. Seiersten, M.: Unpublished Research, Thermo-Calc AB, Stockholm, 1991; also COST 507 Report, European Commission, Brussels, 1995.
19. SGTE SSOL Solution Database version M, Thermo-Calc AB, Stockholm, 1999.
20. Liu, Z.K., Zhang, W. and Sundman, B., *J. Alloys Compounds*, 1995, **226**, 33.
21. Su, X., Zhang W., and Du Z., *Rare Metals*, 1996, **15**(4), 275.
22. Sundman, B., Jansson, B. and Andersson, J.-O., *Calphad*, 1985, **9**, 153.
23. Buschow, K.H.J., *J. Less-Common Metals*, 1965, **9**, 452.
24. Saccone, A., Cardinale, A.M., Delfino, S. and Ferro, R., *Z. Metallkunde*, 2000, **91**, 17.

Table 1: Composition (at%) of the equilibrium ternary phase in 3 Al-Ni-Gd alloys annealed at 500°C, determined using TEM-EDS on thin-foil TEM specimens.

bulk alloy	Al ₉₀ Ni ₇ Gd ₃	Al ₉₀ Ni ₃ Gd ₇	Al ₈₂ Ni ₁₅ Gd ₃
annealing time	18 days	60 days	30 days
Al	75.5±0.7	73.5±1.0	75.5±1.2
Ni	14.5±1.0	15.9±1.3	15.2±1.9
Gd	10.0±0.9	10.6±0.7	9.4±1.0

Table 2: Thermodynamic parameters obtained in the present work for Al-Fe-Gd system (SI units)

Phase	Parameter	Value
Liquid	${}^0L_{\text{Al,Gd}}^{\text{liquid}}$	-235000+55T
	${}^1L_{\text{Al,Gd}}^{\text{liquid}}$	0
	${}^2L_{\text{Al,Gd}}^{\text{liquid}}$	+38000+8T
FCC	${}^0L_{\text{Al,Gd}}^{\text{fcc}}$	+5000
BCC	${}^0L_{\text{Al,Gd}}^{\text{bcc}}$	+100000
HCP	${}^0L_{\text{Al,Gd}}^{\text{hcp}}$	0
M ₃ Gd	$G_{\text{Al:Gd}}^{\text{M}_3\text{Gd}} - 0.75 {}^0G_{\text{Al}}^{\text{fcc}} - 0.25 {}^0G_{\text{Gd}}^{\text{hcp}}$	-43100+3.43T
	$G_{\text{Fe:Gd}}^{\text{M}_3\text{Gd}} - 0.75 {}^0G_{\text{Fe}}^{\text{bcc}} - 0.25 {}^0G_{\text{Gd}}^{\text{hcp}}$	0
	${}^0L_{\text{Al,Fe:Gd}}^{\text{M}_3\text{Gd}}$	-150500+73T
M ₂ Gd	$G_{\text{Al:Gd}}^{\text{M}_2\text{Gd}} - 0.667 {}^0G_{\text{Al}}^{\text{fcc}} - 0.333 {}^0G_{\text{Gd}}^{\text{hcp}}$	-57900+6.88T
	${}^0L_{\text{Al,Fe:Gd}}^{\text{M}_2\text{Gd}}$	-104000+37T
M ₁₇ Gd ₂	$G_{\text{Al:Gd}}^{\text{M}_{17}\text{Gd}_2} - 0.8947 {}^0G_{\text{Al}}^{\text{fcc}} - 0.1053 {}^0G_{\text{Gd}}^{\text{hcp}}$	-5000
	${}^0L_{\text{Al,Fe:Gd}}^{\text{M}_{17}\text{Gd}_2}$	-200000+65T
Al ₁₀ Fe ₂ Gd (τ ₁)	$G^{\tau_1} - 0.769 {}^0G_{\text{Al}}^{\text{fcc}} - 0.154 {}^0G_{\text{Fe}}^{\text{bcc}} - 0.077 {}^0G_{\text{Gd}}^{\text{hcp}}$	-35000+6.73T
Al ₈ Fe ₄ Gd (τ ₂)	$G^{\tau_2} - 0.615 {}^0G_{\text{Al}}^{\text{fcc}} - 0.308 {}^0G_{\text{Fe}}^{\text{bcc}} - 0.077 {}^0G_{\text{Gd}}^{\text{hcp}}$	-59000+18.75T

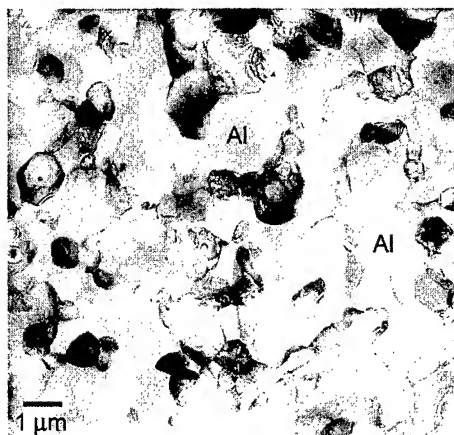


Fig. 1 TEM image of $\text{Al}_{90}\text{Fe}_5\text{Gd}_5$ after 30 days annealed at 500C

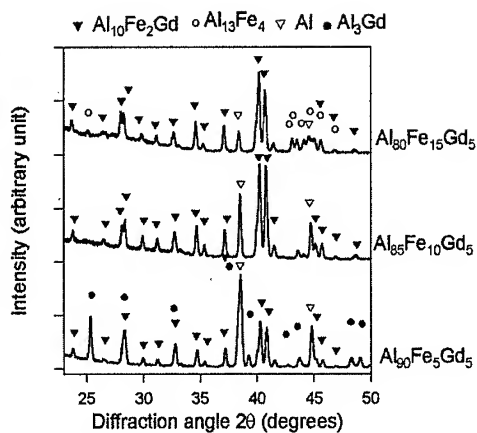


Fig. 2 XRD of Al-Fe-Gd alloys after 7 days annealed at 500C

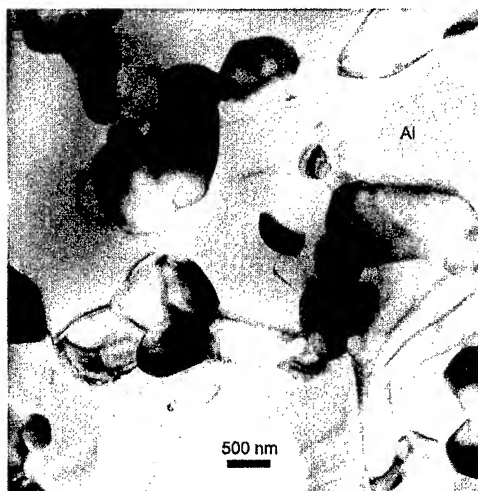
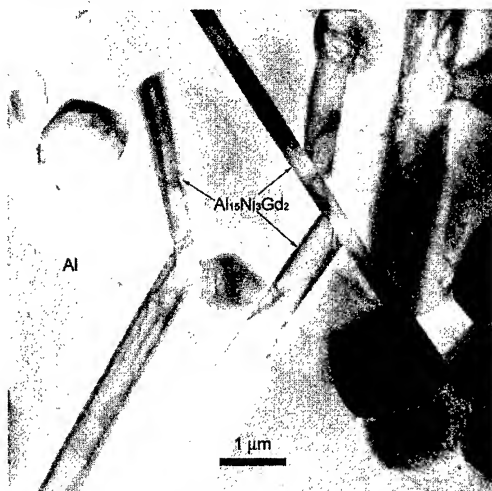


Fig. 3 TEM images of $\text{Al}_{90}\text{Ni}_3\text{Gd}_7$ (left) and $\text{Al}_{82}\text{Ni}_{15}\text{Gd}_3$ (right) after annealing at 500C for 30 days

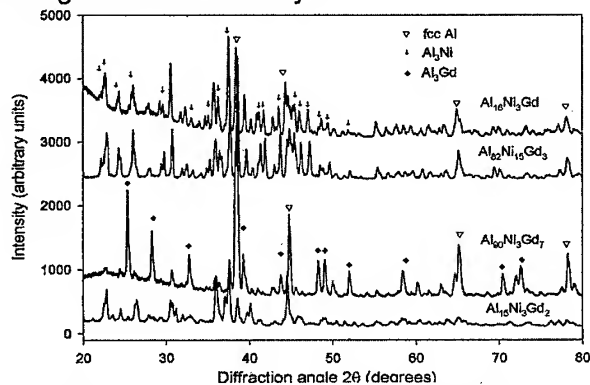


Fig. 4 XRD of Al-Ni-Gd alloys after annealing at 500C for 30 days

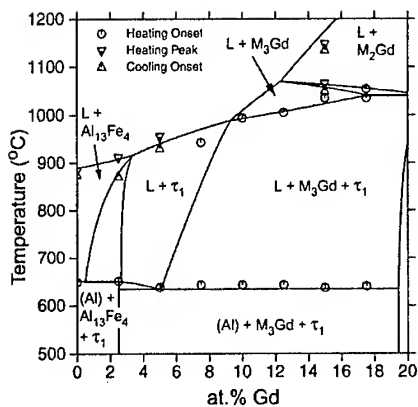


Fig. 5 Calculated Al-5Fe-Gd isopleth

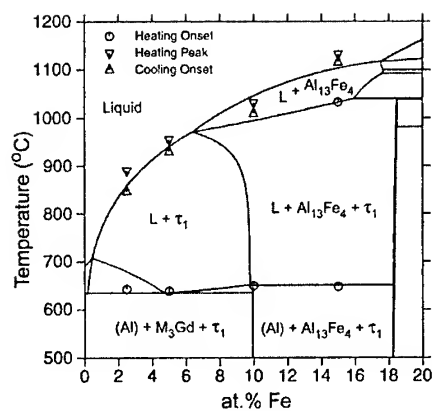


Fig. 6 Calculated Al-Fe-5Gd isopleth

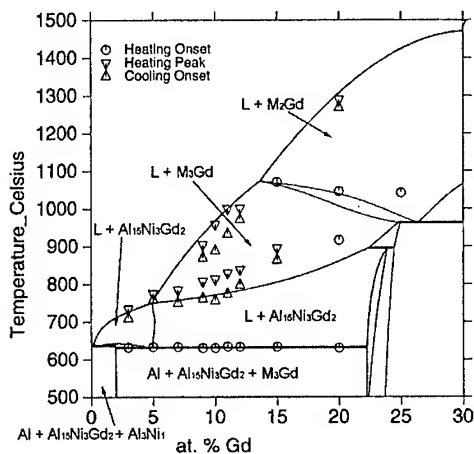


Fig. 7 Calculated Al-3Ni-Gd isopleth.

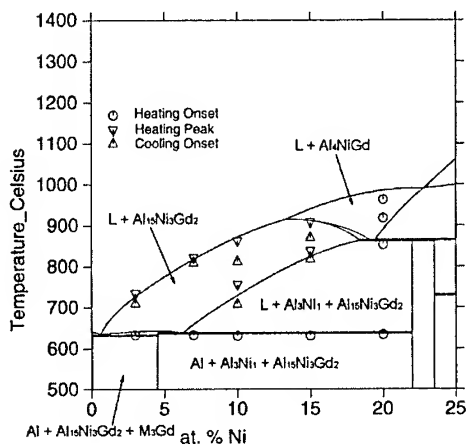


Fig. 8 Calculated Al-Ni-3Gd isopleth

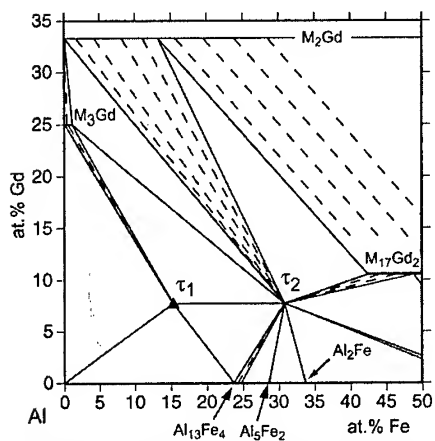


Fig. 9 Calculated Al-Fe-Gd isotherm at 500°C with glass forming region shaded.

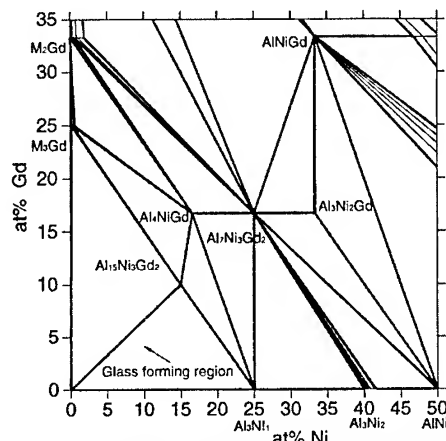


Fig. 10 Calculated Al-Ni-Gd isotherm at 500°C with glass forming region marked.

CRYSTALLIZATION BEHAVIOR OF Al-Mm-Ni-Fe AMORPHOUS ALLOYS

H. W. Jin, K.M. Lim and C.G. Park

Center for Advanced Aerospace Materials
Pohang University of Science and Technology, Pohang 790-784, KOREA

ABSTRACT

The crystallization behavior of amorphous $\text{Al}_{86}\text{Mm}_4\text{Ni}_{10-x}\text{Fe}_x$ ($x=0,2,3,5,8$) alloys have been investigated to examine the effect of Fe addition. The thermal stability of the amorphous phase significantly increased by the addition of Fe. Two-step crystallization was observed in the present alloy system. That is, first crystallization of α -Al was followed by the crystallization of intermetallic phases, such as $\text{Al}_3(\text{Ni},\text{Fe})$ and $\text{Al}_{11}\text{Ce}_3$. The activation energy for the crystallization of α -Al increased from 2.47eV to 3.70eV as the Fe content increased from 0 at.% to 5 at.%. Simultaneous precipitation of α -Al and intermetallic phase was observed in $\text{Al}_{86}\text{Mm}_4\text{Ni}_5\text{Fe}_5$ and $\text{Al}_{86}\text{Mm}_4\text{Ni}_2\text{Fe}_8$ alloys. Glass transition was obscured by exothermic heat evolutions prior to crystallization and could be observed in DSC thermogram only after proper annealing treatment to remove exothermic structural relaxation.

1. INTRODUCTION

Amorphous aluminum alloys have been an attractive candidate for transportation applications because of their high tensile strength and low density. Amorphous ribbons of Al-RE-TM (RE: rare earth element and TM: transition metal) ternary system show the tensile strength up to 1560MPa, which is approximately 3 times higher than that of commercial crystalline Al-based alloys [1~4]. Applications of these amorphous alloys are limited to relatively lower application temperatures (below 200°C) due to an embrittlement upon crystallization when exposed at high temperature.

It was reported that the thermal stability of Al-RE-Ni ternary amorphous alloys was substantially improved by partial substitution of Ni with other transition metals, such as Fe, Mn and Co [4,5]. However the crystallization behavior of Al-base amorphous alloys is not clearly understood yet. In this article, we have been investigated the effect of Fe addition on the crystallization behavior of amorphous Al-Mm-(Ni,Fe) alloys with a systematic change in the relative composition of TM elements.

2. EXPERIMENTAL PROCEDURE

$\text{Al}_{86}\text{Mm}_4\text{Ni}_{10-x}\text{Fe}_x$ ($x=0,2,3,5,8$ at.%) alloy ingots were prepared by arc melting under argon atmosphere. Starting materials were highly pure elemental granules (99.99% Al, Ni, Fe) and Ce-rich misch-metal(Mm). Alloy ingots were remelted several times in order to homogenize alloy compositions. The alloy ingots were melt-quenched into an amorphous state using a

single-roll vacuum melt-spinner to fabricate alloy ribbons with 2 mm in width and $30\mu\text{m}$ in thickness. Amorphous structure of rapidly solidified ribbons was examined by Rigaku X-ray diffractometer. Thermal analysis was carried out in the differential scanning calorimetry (Perkin-Elmer DSC-7) under N_2 gas flow. Some alloy specimens are isothermally annealed for 20 minutes at several different annealing temperature below T_{x1} . Isothermal annealing treatment was carried out in DSC and each sample was cooled down to 50°C at a cooling rate of 200 K/min. After isothermal heating treatment the sample was reheated at 20K/min or 40K/min of scanning rate. TEM observation was performed on a JEOL 200CX equipped with an in-situ heating holder. Thin foil samples were obtained by twin-jet polishing in a solution of 25% HNO_3 +75% CH_3OH at 243K. X-ray photoemission spectroscopy(XPS) spectra were also obtained from the some alloy ribbons with a Perkin-Elmer PHI 5400 system using Mg K_α radiation.

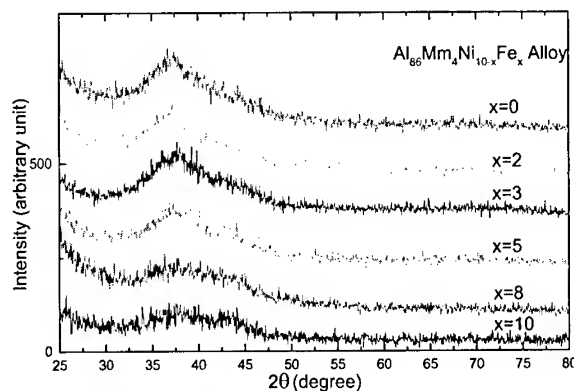


Fig. 1. X-ray diffraction patterns of the rapidly solidified $\text{Al}_{86}\text{Mm}_4\text{Ni}_{10-x}\text{Fe}_x$ alloys with varied x values : (a) $x=0$, (b) $x=2$, (c) $x=3$, (d) $x=5$, (e) $x=8$ and (f) $x=10$.

3. RESULTS AND DISCUSSION

X-ray diffraction patterns of the melt-spun $\text{Al}_{86}\text{Mm}_4\text{Ni}_{10-x}\text{Fe}_x$ ($x=0, 2, 3, 5, 8, 10$) amorphous ribbons are shown in Fig. 1. Only broad diffusive peaks were observed in every specimens, indicating that fully amorphous structure was obtained in the rapidly solidified alloy ribbons.

Figure 2 shows the DSC thermograms of the present amorphous alloy ribbons. The first crystallization temperature (T_{x1}) increased with an increase in Fe content. Significant differences in crystallization behavior were observed depending on the Fe content. That is, in the alloys containing less than 5at.% Fe, a small exothermic peak was followed by a sharp exothermic peak. The second sharp exothermic peak appeared at a temperature about 100K higher than that of the first small peak. X-ray diffraction results revealed that the first small exothermic peak corresponded to the crystallization of α -Al from the amorphous matrix and the following exothermic peaks corresponded to the

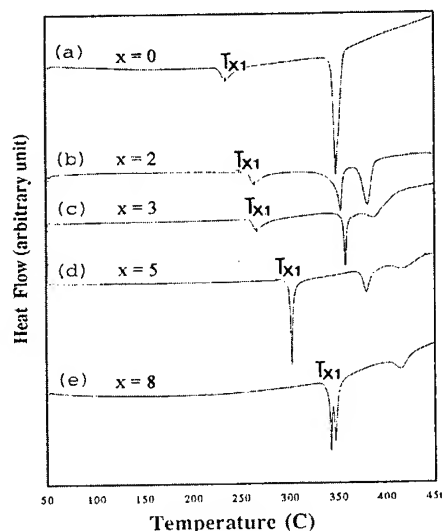


Fig. 2. DSC thermograms for $\text{Al}_{86}\text{Mm}_4\text{Ni}_{10-x}\text{Fe}_x$ amorphous alloys at a constant heating rate of 20K/min ; (a) $x=0$, (b) $x=2$, (c) $x=3$, (d) $x=5$ and (e) $x=8$.

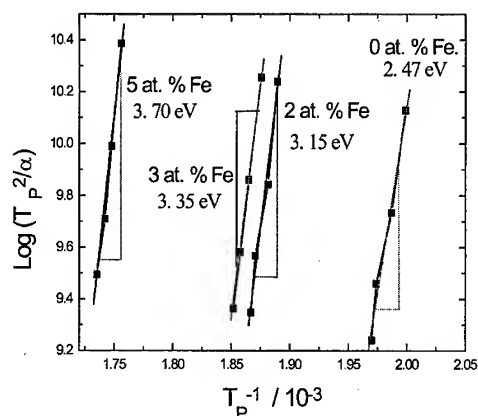


Fig. 3. Kissinger plots for the first exothermic peaks in DSC thermograms of the present alloy ribbons

crystallization of some intermetallic phases such as $\text{Al}_3(\text{Ni,Fe})$ and $\text{Al}_{11}\text{Ce}_3$ [6]. On the other hand, alloys containing more than 5 at.% Fe exhibited sharp overlapped exothermic peaks, indicating a simultaneous crystallization of α -Al and an intermetallic phase [8].

The lowest crystallization temperature, T_{x1} , defined as the onset temperature of the first exothermic peaks in Fig. 2 (a)~(d), exhibited a nearly linear relationship with the Fe content. Fig. 3 shows the Kissinger's plot of the first exothermic peaks in the DSC results. The activation energy of the α -Al precipitation, evaluated from the slope of linearity in Kissinger's plot, is 2.47 eV for the $\text{Al}_{86}\text{Mm}_4\text{Ni}_{10}$ alloy and increases substantially with increasing Fe content, x . The activation

energy of the first crystallization reaches a value of 3.70 eV in $\text{Al}_{86}\text{Mm}_4\text{Ni}_5\text{Fe}_5$ alloy. In some of the Al-based amorphous alloys, the growth of α -Al without nucleation was proposed as a first crystallization reaction due to the presence of quenched-in nuclei [7]. In the present study, however, the activation energy of crystallization is much higher than that of Al self-diffusion (~1.45 eV). Thus, the quenched-in nuclei theory cannot explain the crystallization of α -Al in the present study.

Figure 4 shows the microstructure of the alloy ribbons observed just after the first crystallization peak. Only α -Al crystallites were observed in the $\text{Al}_{86}\text{Mm}_4\text{Ni}_7\text{Fe}_3$ alloy ribbons. The presence of some dendritic particles in alloys indicated the relatively low nucleation frequency of α -Al. However, some intermetallic phases such as $\text{Al}_3(\text{Ni,Fe})$ were observed in the $\text{Al}_{86}\text{Mm}_4\text{Ni}_5\text{Fe}_5$ alloy ribbons, as indicated by arrows in electron diffraction pattern of Fig. 4(b) [8]. The *in-situ* isothermal annealing results also revealed that α -Al and intermetallic phases precipitated simultaneously during the crystallization process of $\text{Al}_{86}\text{Mm}_4\text{Ni}_5\text{Fe}_5$ amorphous alloy ribbons. Thus the first exothermic peak observed in

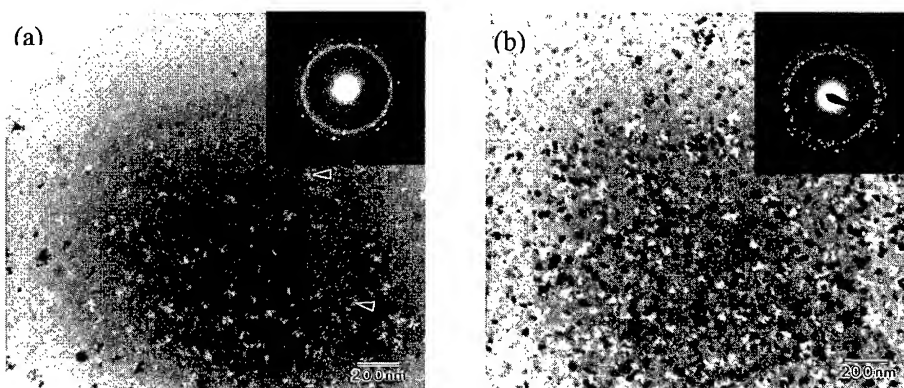


Fig. 4. Bright-field TEM micrographs and electron diffraction patterns showing the crystallization products after first exothermic peak in DSC curves of $\text{Al}_{86}\text{Mm}_4\text{Ni}_7\text{Fe}_3$ (a) and $\text{Al}_{86}\text{Mm}_4\text{Ni}_5\text{Fe}_5$ (b).

$\text{Al}_{86}\text{Mm}_4\text{Ni}_5\text{Fe}_5$ alloy can be regarded as overlapping of the peaks for the precipitation of α -Al and intermetallic phases.

It was noted in DSC thermogram shown in Fig. 2, that the specimen did not show any distinct endothermic step of glass transition(T_g) before crystallization. The glass transition during differential scanning calorimetry can be described as a kinetic phenomenon caused by the continuous approach of free volume towards an equilibrium during the warming up. The glass transition has been the most widely used calorimetric evidence of amorphous materials. However, the absence of this glass transition in DSC scans does not necessarily imply that the material is not really amorphous. In fact, for some amorphous alloys, glass transition was not observed though they were absolutely fully amorphous[9~11].

It has been suggested that the absence of glass transition temperature(T_g) implies that glass transition temperature is higher than the crystallization temperature(T_x)[9]. However, it seems out of reason to consider that crystallization can take place, which requires long-range diffusion of constitute atoms and the formation of critical size of nuclei, while maintaining excess free volume far from the equilibrium state. Some researchers supposed that T_g might not be observed if crystallization occurred only by growth mechanism from the quenched-in α -Al nuclei[10, 11]. In the present study, however, the activation energy for the first α -Al crystallization, evaluated in the present investigation, is much greater than that of Al self-diffusion. Thus, a new viewpoint is necessary in order to explain the crystallization behavior of the present alloy system. The present authors suggest that glass transition may be obscured by other exothermic reactions since the glass transition of a particular material partly depends on its thermal history. That is, small endothermic peak due to the glass transition may be obscured when certain heat evolving reactions - such as structural relaxation - occur near the glass transition. Fortunately, these heat evolving reactions can be removed by proper pre-annealing heat treatment.

Fig. 5 shows the DSC scans of the alloy containing 3 at.% Fe obtained before and after

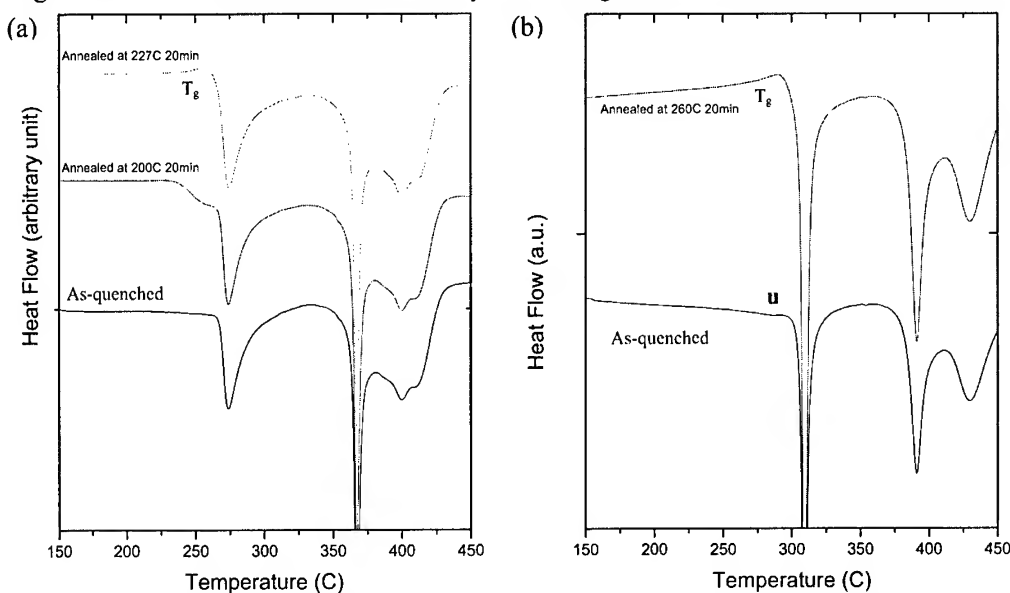


Fig. 5. (a) DSC thermograms recorded after an isothermal annealing at the different annealing temperatures of $\text{Al}_{86}\text{Mm}_4\text{Ni}_7\text{Fe}_3$ amorphous alloy. (b) DSC thermograms recorded after an isothermal annealing at 260°C for 20 min with a scanning rate of 40 K/min in the $\text{Al}_{86}\text{Mm}_4\text{Ni}_5\text{Fe}_5$ amorphous alloy.

annealing treatment. The DSC scan of as-quenched specimen exhibits almost steady heat flow, i.e. nearly flat baseline, before crystallization. However, DSC scans of isothermally annealed specimen exhibited an endothermic step of the glass transition. These results imply that the glass transition occurs on heating the present alloy ribbons, although it was not detected in conventional DSC scans, and that the endothermic step of glass transition can be masked by some exothermic reactions near the crystallization temperature range. The observation of endothermic step(T_g) was more pronounced at higher annealing temperature because the exothermic reaction could be effectively eliminated by annealing at higher temperature.

In the crystallization by nucleation and growth mechanism, pre-annealing heat treatment may result in partial crystallization[12]. Thus, a peak shift to low temperature would be observed in subsequent DSC scanning. In case of crystallization by growth mechanism, on the other hand, peak shift toward high temperature would be observed because pre-annealing increase the grain size of quenched-in nuclei[12]. In the present investigation, no peak shift could be recognized in the subsequent DSC scanning after pre-annealing heat treatment. This result, thus, excludes the possibility of partial crystallization of amorphous phase or the growth of quenched-in nuclei during the pre-annealing heat treatment.

The glass transition was also observed in the alloys containing 5 at. % Fe after pre-annealing heat treatment, as shown in Fig. 5(b). An increase in scanning rate revealed a broad exotherm, designated as 'u', in the DSC thermogram from as-quenched specimen. And this broad exotherm disappeared after isothermal the pre-annealing heat treatment. This result is a strong evidence for the masking of glass transition by exothermic structural relaxation.

Figure 6 shows the XPS spectra obtained from some alloy ribbons near the Al 2p level(72.9 eV). Only one sharp peak, designated as " α ", appears in as-quenched ribbons. The binding energy of " α " peak corresponds to 72.8eV, which is quite close to that of pure Al(72.9eV). In pre-annealed specimens, a new peak, denoted as " β ", is observed in addition to the original " α " peak. The binding energy of " β " peak is about 75.4eV, 2.6eV higher than that of " α " peak. And the " β " peak exhibited higher intensity than " α " peak in fully crystallized alloy

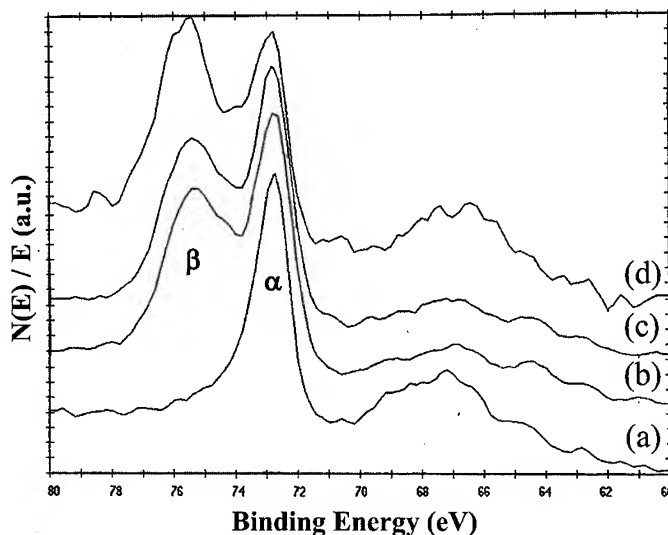


Fig. 6. XPS spectra of the Al₈₆Mm₄Ni₇Fe₃ alloy ribbons with different heat treatment conditions. (a) as-quenched, (b) annealed at 200°C for 20min., (c) annealed at 227°C for 20min., (d) annealed to 450°C.

ribbons after DSC scanning to 450°C. These results indicated that pre-annealing heat treatment caused the structural relaxation of amorphous phase to evolve two different chemical environments of Al, i.e. Al-rich region and Al-poor region. And the evolution of structural relaxation is followed by the precipitation of α -Al and intermetallic phase such as $(\text{Ni,Fe})\text{Al}_3$ and $\text{Al}_{11}\text{Mm}_3$ in the two chemically different regions respectively. The substitution of Ni with Fe enhances this kind of structural relaxation since Fe has stronger interaction with Al than Ni has.

4. CONCLUSION

1. The thermal stability of the present amorphous alloys was enhanced by the addition of Fe.
2. Primary crystallization of α -Al was the first crystallization product in the alloys containing small fraction of Fe upto 3 at.%. Further increase of Fe content above 5 at.% induced simultaneous crystallization of α -Al and intermetallic phases as a first crystallization reaction.
3. The glass transition was obscured by exothermic heat evolution caused by structural relaxation. By applying suitable heat treatment, the glass transition could be observed in DSC thermograms.

REFERENCES

1. A. Inoue, Y.H. Kim and T. Masumoto, Mater. Trans., JIM, 33 (1992) pp. 487.
2. A. Inoue, Y. Horio, Y.H. Kim and T. Masumoto, Mater. Trans., JIM, 33 (1992) pp. 669.
3. Y. He, G.M. Dougherty, G.J. Shiflet and S.J. Poon, Acta metall. mater., 41 (1993) pp. 337.
4. Y.H. Kim, A. Inoue and T. Masumoto, Mater. Trans., JIM, 32 (1991) pp. 559.
5. M. Yewondwossen, R.A. Dunlap and D.J. Lloyd, J.Phys. : Condens. Matter., 4 (1992) pp. 461.
6. H.W. Jin, Y.J. Kim, C.G. Park and M.C. Kim, Light Weight Alloys for Aerospace Applications IV, edited by E.W. Lee, W.E. Frazier, N.J. Kim and J. Nata, (1996) pp. 31.
7. A.P. Tsai, T. Kamiyama, Y. Kawamura, A. Inoue and T. Masumoto, Acta mater. 45, (1997) pp. 1477.
8. H.W. Jin, Y.J. Kim and C.G. Park, J. Mater. Sci., (2001) In Press.
9. A. Inoue, T. Zhang, W. Zhang and A. Takeuchi, Materials Transactions JIM 37 (1996) pp. 108.
10. R.F. Cochrane, P. Schumacher, A.L. Greer, Mat. Sci. & Eng. A133 (1991) pp. 367.
11. K.Nakazato, Y.Kawamura, A.P. Tsai, A. Inoue, Appl. Phys. Lett. 63 (1993) pp. 2644.
12. L.C. Chen, F. Spaepen, Mat. Sci. & Eng. A133 (1991) pp. 367.

SYNTHESIS AND THERMAL STABILITY OF NANOCRYSTALLINE Al-Mg ALLOYS

Fei Zhou¹, Dong H. Shin² and Enrique J. Lavernia¹

1. Department of Chemical and Biochemical Engineering and Materials Science,
University of California at Irvine, Irvine, CA 92697-2575

2. Department of Metallurgy & Materials Science,
Hanyang University, Ansan, Kyunggi-Do 425-791, Korea

ABSTRACT

Nanocrystalline Al-Mg alloy powders have been synthesized by a mechanical attrition technique with low milling energy under liquid nitrogen in a process known as cryomilling. Two classes of powder blends of nominal composition Al-7.5Mg (wt.%) were used as starting materials for cryomilling: (i) a mixture of spray-atomized Al-50Mg powders and pure Al blends, and (ii) spray-atomized Al-7.5Mg alloy powder. The microstructural evolution during cryomilling has been characterized by X-ray diffractometry in detail. The cryomilling reduced the grain size down to about 25 nm and produced a supersaturated Al-Mg face-centered cubic (fcc) solid solution having approximately 7.5 wt.% Mg in solution. Formation of the nanostructures in the Al-Mg samples was found to be dominated by the total lattice strain of fcc Al, which is similar to other conventional milling processes with high or low milling energy levels. The nanocrystalline Al-Mg alloy powders produced by cryomilling exhibited a high resistance against grain growth, which facilitates processing of bulk nanocrystalline Al alloys at elevated temperatures.

1. INTRODUCTION

In the past decade mechanical attrition (MA) [1, 2] has demonstrated to be an effective method to process nanocrystalline (nc) materials, which are materials with a microstructure the characteristic length scale of typically less than 100 nanometers [3]. The formation of nanostructures during MA was found to be total strain dominant regardless of material systems and processing variables (*e.g.*, mill energy, milling temperature) [1]. In the case of ductile materials, for example, aluminum-based alloys, the relatively strong tendency to adhere to the container walls and to sinter to larger particles with several millimeters in diameter during milling leads to difficulties during processing by conventional MA techniques. With the introduction of cryogenic liquid media to MA, the cryogenic ball milling, or "cryomilling" process [4], has been successfully employed in solving this challenge. A number of nc alloys, such as Fe-Al [5], 5083 Al alloy [6], stainless steel [7], and Inconel alloy [8] were produced.

This study is to investigate the microstructural evolution during cryomilling and thereby to enhance our understanding of the possible mechanisms that govern the crystal refinement process. Al-7.5Mg (wt.%) was chosen as a model system in this study and X-ray diffractometry was used to examine the development of grain size and microstrain during

milling process. In addition, thermal stability of the nc alloy powders produced by cryomilling was also assessed with respect to possible applications.

2. EXPERIMENTAL

Two classes of Al-7.5Mg (wt.%) powder blends were used as starting materials for cryomilling: (A) a mixture of spray-atomized Al-50Mg (wt.%) alloy powders and pure Al blends in the proper ratio, and (B) spray-atomized Al-7.5Mg alloy powders. The milling was carried out in a modified Union Process 01-HD attritor with a stainless steel vial and balls (with 6.4-mm-diameter) at a rate of 180 rpm. The ball-to-powder ratio was 36:1. During the milling operation, liquid nitrogen was added into the mill to maintain complete immersion of the milling media that keeps a temperature of -190°C . Prior to milling ~ 0.25 wt % of stearic acid ($\text{CH}_3(\text{CH}_2)_{16}\text{CO}_2\text{H}$) was added to the powders as a process control agent to moderate the cold welding process. After different milling times a small quantity of materials was removed from the attritor for microstructure analysis. The x-ray diffraction (XRD) measurements were carried out by a Siemens D 5000 diffractometer equipped with a graphite monochromating crystal using Cu $K\alpha$ radiation. The grain size and lattice microstrain of fcc-Al in the cryomilled samples were determined following the method described in ref. [9] from peaking broadening of the five intense diffraction peaks ($\{111\}$, $\{200\}$, $\{220\}$, $\{311\}$ and $\{222\}$) with subtraction of the instrumental broadening and $K\alpha_2$ components.

3. RESULTS AND DISCUSSION

3.1. Evolution of microstructure during cryomilling

The structural evolution of the two types of Al-Mg powders during cryomilling is shown in Figure 1. At the initial stage of milling (1 h), the type A sample displayed sharp peaks from fcc-Al and evident peaks of the γ phase ($\text{Al}_{12}\text{Mg}_{17}$), an intermetallic compound that was present in the unmilled spray atomized Al-50Mg powders (see Figure 1a). The reflection peaks of both phases diminished rapidly with increasing milling time and the γ phase becomes undetectable in the pattern after 8 h of milling. Simultaneously, the fcc-Al peaks shifted toward lower diffraction angles, indicating a lattice expansion. Figure 1(b) shows the XRD

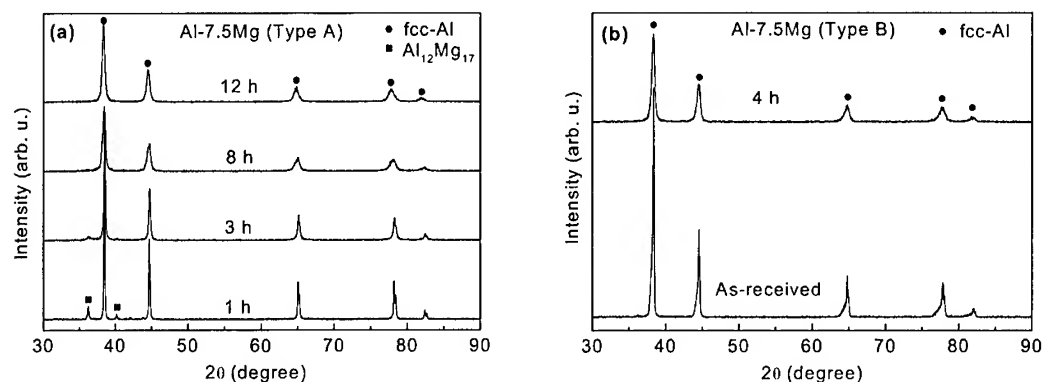


Fig.1. XRD patterns for Al-7.5Mg samples milled for various times: (a) a mixture of Al and spray-atomized Al-50Mg alloy (Type A), and (b) spray-atomized powders (Type B).

patterns of the type B sample in the spray-atomized state and after cryomilling of 4 h. Only fcc Al was found in these samples, indicating formation of a fcc Al-Mg solid solution.

The variation of the lattice parameter of α -Al with milling time for the two types of Al-7.5Mg powders is shown in Figure 2. Before cryomilling, the lattice constant value of the sample B was considerably larger than that of the sample A, suggesting Mg atoms were trapped in fcc-Al lattice in the spray-atomized powders. For both of the samples, the lattice constant value remained stable in the initial stage of milling and then increased substantially upon further milling. Finally it approached to a value of about 0.4085 nm. Assuming that the expansion of the fcc-Al lattice can be singularly attributed to the dissolved Mg atoms, one may estimate the Mg concentrations in Al-Mg solid solutions based on the literature data available in ref.[10]. The Mg content in the fcc-Al lattice was found to be approximately 7.5 (in wt. %) after cryomilling of 12 h, indicating that all Mg atoms were essentially dissolved after a sufficiently long time of cryomilling. With respect to the solubility in the equilibrium state [11], the fcc Al-Mg solid solution formed was supersaturated.

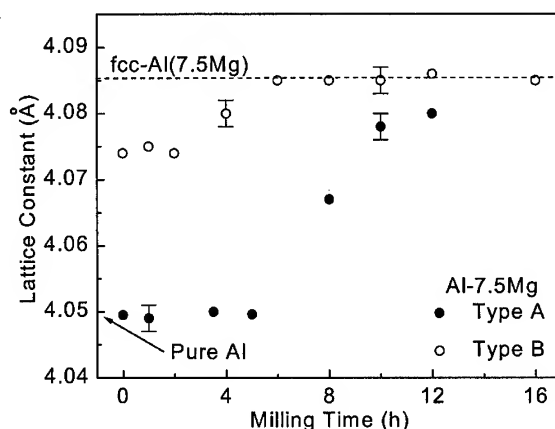


Fig. 2. Estimated lattice constant of α -Al (Mg) in Al-7.5Mg with milling time.

The extension of terminal solid solubility has been reported for a number of alloys by mechanical alloying [12]. In the case of Al-Mg binary alloy, it was reported [13] that a terminal solid solubility of 23 at. % of Mg in Al was obtained by high energy MA at room temperature while only about 1.0 at. % of Mg is miscible in the solid state under equilibrium conditions [11]. This extension of solid solubility was attributed to the nc structure formed during the MA process. The large volume fraction of grain boundary present in the nc state are thought to enhance the solid solubility in these materials. In the case of cryomilled Al-Mg, it was seen that the solid solubility of Mg increased remarkably after milling of 6 h, at which the crystalline size of fcc-Al reduced down to about 80 nm (see Figure 3 in the next section). On one hand, this finding suggests that the enhanced dissolution of Mg content in Al is associated with the formation of nanostructure by MA, which may give rise to the high diffusion activity in the alloy. On the other hand, the maximum solid solubility of Mg in the supersaturated Al-Mg solid solutions formed by the cryomilling process in the present study was found to be about 13 at. % [14]; this value is much lower than that dissolved by the milling conducted at ambient temperature. This may be expected as a result of the extremely slow diffusion kinetics at the process temperature (diffusivity of Mg in Al at -190°C is much lower than that at room temperature) as well as the relatively low energy imparted by the vibratory mill, for example, in comparison to high energy SPEX shaker mill.

3.2. Grain size and lattice microstrain

The crystallite size and the lattice microstrain in the milled samples were estimated by XRD line broadening. Figure 3(a) depicts the development of the average grain size of fcc-Al

phase during the cryomilling process for the two types of Al-7.5Mg samples. The cryomilling reduced the grain size values rapidly during the first hours of milling and then decreased it much slowly to a constant value for long milling times (*i.e.*, $t \geq 8$ h). After 12 h of milling, the grain size reached a steady state, being about 25 nm for the both samples studied herein, despite a large difference between them in starting stage of the cryomilling. The grain size measurements by XRD were also confirmed by the TEM observations. The minimum grain size value that achieved in the Al-Mg alloys is comparable with the literature data reported for pure Al. For example, a final grain size of 22 ± 2 nm was found by Eckert *et al.* [15] in ball-milled Al prepared by high energy ball milling (with Spex 8000 at a ball-to-powder ratio of 4:1). Similar results have been also reported earlier by Oleszak *et al.* [16] for a nc Al prepared by ball milling with a low energy level.

The lattice microstrain estimated from the XRD reflections is plotted against milling time in Figure 3(b). A maximum strain value was observed during the milling process, *i.e.*, the strain increased at the early stage of milling and reached a maximum before it dropped in the final stage of the milling process. For the two classes of Al-Mg samples, the maximum strain was found to be around 0.4%. The samples milled for 8, 10 and 12 h exhibited a much higher strain value, which may be speculated to originate from the formation of a supersaturated fcc Al(Mg) solid solution. The strain in the steady state of cryomilling was seen to be about 0.3%, which is comparable to the values reported for milled Al [15, 16].

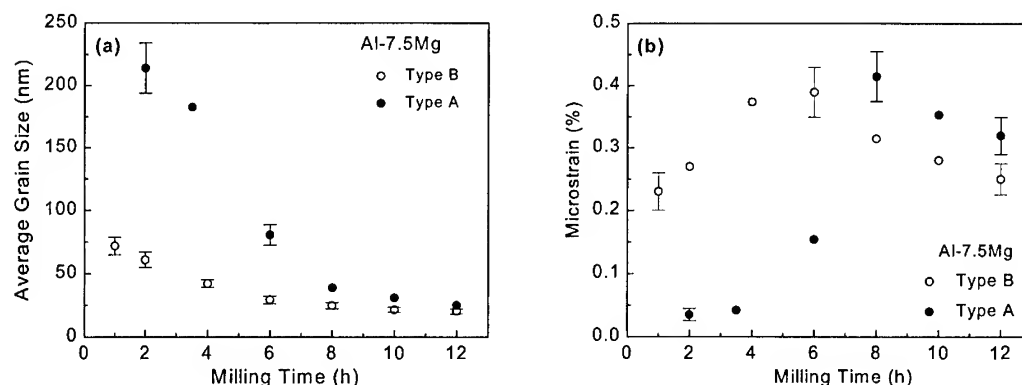


Fig. 3. The variation of (a) grain size and (b) lattice microstrain with milling time.

The lattice microstrain was found to be responsible for determining the nc grain size [1]. For the materials in the present study, it was noted that the strain increased with decreasing grain size and reached a maximum before it decreased to low values at the smallest grain size. The maximum was found to correspond to the milling time of which the crystallite size approached to the final steady state value. This is consistent with the study of Oleszak *et al.* [16] that indicated a broad maximum in strain vs. $1/d$ for a number of elements including Al and several other fcc metals in a low energy mill. It has been suggested in previous studies [1, 2] that the microstrain is due to dislocation density which rapidly increases with initial milling time. As the grain size becomes nanoscale within shear bands and as the number of such shear bands increases and the average grain size decreases, the dislocation-free nanograins and the absorption of dislocations at the increasing number of grain boundaries results in a decrease in dislocation density and therefore in microstrain.

In comparison to the low energy milling process at ambient temperature, it was noted that for cryomilling the milling time needed to reach the final steady state in Al was much shorter. This may be explained by the effect of milling parameters on the microstructure of the final product. It has been shown that lower milling temperatures typically result in smaller minimum grain sizes [1], as the minimum grain size obtained by milling has been attributed to a balance between the defect/dislocation structure introduced by the plastic deformation of milling and its recovery by thermal processes. In light of the cryogenic temperature of the milling in the present study, it is therefore expected that the recovery is not as effective as the milling at the ambient temperature and subsequently the milling time to reach a steady state is relatively shorter.

3.3. Grain size stability

Thermal annealing was carried out at various temperatures for the milled nc Al-7.5Mg alloy powders in order to evaluate grain growth behavior. Figure 4 shows the grain size vs. the annealing temperature for 1, 2, 4, and 6 hours. On heating the as-milled sample, limited grain growth occurred. The grain size in the powder sample annealed at 200°C for 1 hour was measured to be around 40 nm, an increase by a factor of less than 2. With increasing temperature up to 450°C, only limited growth was observed. No considerable growth was detected for an increase in the annealing time from 1 h to 6 h at each temperature. It is worth noting that in all of the Al-7.5Mg samples isothermally annealed within the time limits applied in this study the grain size of fcc-Al was maintained below 100 nm. It should be also pointed out that in a related study [6] the grain size in a bulk Al-7.5Mg sample produced by hot isostatic pressing and extrusion at 300°C was around 50 nm, consistent well with the results for the powder sample. In practice enhanced grain size stability was also observed in other nc materials produced by cryomilling (*e.g.*, in Al [17]). It was revealed that the high grain size stability may be mainly attributed to the pinning effect arising from the following two sources existing in milled samples: (i) grain boundary segregation of solute or/and impurities, and (ii) the second phase (such as ultrafine Al oxide and nitride). In the case of Al-Mg, the segregation of solute atoms of Mg to the grain boundaries in the supersaturated fcc Al(Mg) solid solution may result in the pinning force inhibiting grain growth process. Microstructural analyses are needed to support this suggestion. In reference to possible applications, the high grain size stability of the cryomilled Al-Mg alloy powders renders cryomilling a promising route to produce large quantity of powder materials for processing of bulk nc Al alloys by means of hot consolidation techniques.

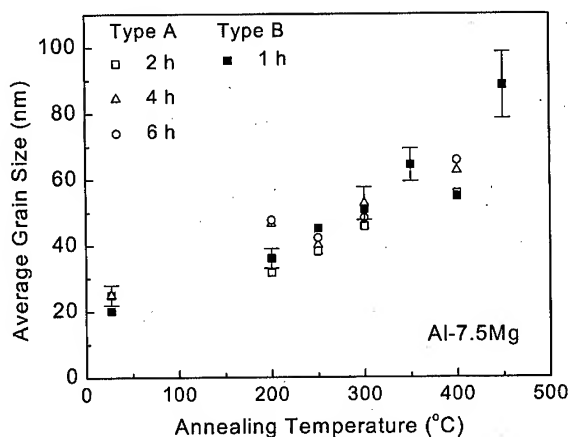


Fig. 4. The grain size in the Al-7.5Mg samples as a function of annealing temperature.

4. CONCLUSION

A supersaturated Al-Mg solid solution with grain size of about 25nm was produced by mechanical attrition under liquid nitrogen (*i.e.*, cryomilling). The cryomilling of the Al-7.5Mg mixture consisted of two phases of fcc-Al and γ -Al₁₂Mg₁₇ gives rise to a supersaturated fcc Al-Mg solid solution. Similar Al-Mg solid solution was also formed by cryomilling of spray-atomized Al-7.5Mg alloy powders. The formation of nanostructures during cryomilling was found to be the total microstrain dominant process, which is similar to other conventional milling processes with high or low milling energy levels. A high degree of stability of nanostructures was found in the cryomilled materials.

ACKNOWLEDGEMENTS

Financial support for this research work was provided by the Office of Naval Research under grant N00014-00-1-0109 with Dr. L. Kabacoff as program officer. Partial materials used in this work were provided by Rocketdyne Propulsion and Powder, the Boeing Company. One of the authors thanks to 2000 National Research Laboratory Program by Korea Ministry of Science and Technology.

REFERENCES

1. C. C. Koch, Nanostr. Mater., 9 (1997), 13.
2. H. J. Fecht, Nanostr. Mater., 6 (1995), 33.
3. H. Gleiter, Acta Mater., 48 (2000), 1.
4. M. J. Luton et al.: Multicomponent Ultrafine Microstructures, eds. by L. E. McCandish, et al., MRS Symposium Proceedings Vol.132, Pittsburgh, PA (1989), 79.
5. R. J. Perez, H. G. Jiang, C. P. Dogan, and E. J. Lavernia, Metall. Trans. A, 29 (1998), 2469.
6. R. Hayes, V. Tellkamp, and E. J. Lavernia, Scripta Mater., 41 (1999), 743; J. Mater. Res., 15 (2000), 2215.
7. H. G. Jiang, M. L. Lau, and E. J. Lavernia, Nanostr. Mater., 10 (1998), 169.
8. D. Cheng, J. He, R. Rodriguez, M. Ice, and E. J. Lavernia: Surface Engineering in Materials Science I, eds. by S. Seal, N. B. Dahotre, J. J. Moore and B. Mishra, The Minerals, Metals & Materials Society (2000), 13.
9. H. P. Klug and L. Alexander: X-ray Diffraction Procedures for Polycrystalline and Amorphous Materials, 2nd ed., John Wiley and Sons, New York, NY (1974), 661.
10. H. L. Luo, C. C. Chao, and P. Duwez, Trans. of Metall. Soc. of AIME, 230 (1964), 1488.
11. T. B. Massalski (ed.): Binary Alloy Phase Diagram, ASM International, Metals Park, OH (1991), 170.
12. C. Suryanarayana, Prog. Mater. Sci., 46 (2000), 1.
13. D. L. Zhang, T. B. Massalski, and M. R. Paruchuri, Metall. Mater. Trans. 25A (1994), 73.
14. F. Zhou, E. J. Lavernia, to be published results (2001).
15. J. Eckert, J. C. Holzer, C. E. Krill, III, and W. L. Johnson, J. Mater. Res., 7 (1992), 1751.
16. D. Oleszak and P. H. Shingu, J. Appl. Phys., 79 (1996), 2975.
17. F. Zhou, J. Lee, S. Dallek, and E. J. Lavernia, J. Mater. Res., (2001, in press).

GROWTH KINETICS OF PRIMARY AL NANOCRYSTALS IN Al-Ni-ND ALLOY

Sang Hyuk Kim, Sang Bock Lee* and Nack J. Kim*

Research Institute of Industrial Science and Technology, Pohang 790-330, Korea

*Center for Advanced Aerospace Materials

Pohang University of Science and Technology, Pohang 790-784, Korea

ABSTRACT

The purpose of this study is to predict the growth behavior of the primary Al nanocrystals with the application of appropriate model. From the JMA analysis of the crystallization of an $\text{Al}_{85}\text{Ni}_{10}\text{Nd}_5$ amorphous alloy it was shown that the early nucleation sites saturation of primary Al phases was occurred and that with the crystallization proceeding the nucleation rate was gradually decreased.

The Ham analysis from this study predicts quite well the measured crystal size and growth rate. The predicted crystal size (the Ham model) becomes less than that given by $S\sqrt{Dt}$ (parabolic growth law) after only a few seconds for temperatures above the glass transition, emphasizing the need to consider diffusion-field impingement in a growth kinetics analysis involving high particle densities.

1. INTRODUCTION

Nanocrystalline materials, namely, polycrystals with <100 nm-sized crystalline grains, have attracted much attention in recent years since the first report by Gleiter and his co-workers was published [1]. Of special importance is the recent discovery of Al rich glasses containing ~85 at. % Al and a combination of transition and rare-earth element additions [2-3]. These materials yield microstructures consisting of a high volume fraction of Al nanocrystals in an amorphous matrix. The volume fraction of nanocrystals approaches 30%, which offer remarkably high strength.

Some researches on the growth kinetics of Al nanocrystal have been conducted using the parabolic growth model. However, the results are rather unsatisfactory since the parabolic growth model doesn't consider the diffusion field impingement. In the metallic glass alloy system, which reveals a high nucleation density after annealing above glass transition such as the most Al-base metallic glasses, the diffusion field impingement has to be considered for the growth kinetics. The focus of the present study is to expand upon the analysis of the growth rate considering diffusion field impingement.

2. EXPERIMENTS

The alloy investigated in the present study was prepared by melting and casting high-purity metals in a vacuum induction furnace under an Ar gas atmosphere. Nominal composition was $\text{Al}_{85}\text{Ni}_{10}\text{Nd}_5$. The alloy of $\text{Al}_{85}\text{Ni}_{10}\text{Nd}_5$ was rapidly solidified by remelting under an Ar gas atmosphere, and then melt-spinning onto the outer surface of the rotating

copper wheel. The melt-spun ribbons exhibit thickness of about $20\mu\text{m}$ and width of about 2mm . Crystallization behavior of the amorphous ribbons was investigated by using differential scanning calorimetry (Perkin-Elmer DSC7). Heat treatment of the melt-spun ribbons was conducted at various temperatures. Microstructural changes during heat treatment of amorphous ribbons were studied by using X-ray diffractometry with Cu K α radiation and transmission electron microscopy (JEOL 2010F).

3. RESULTS AND DISCUSSION

A DSC heating curve of melt-spun $\text{Al}_{85}\text{Ni}_{10}\text{Nd}_5$ alloy for the entire course of crystallization is shown in Fig. 1. The glass transition onset temperature is about 242°C and the first observable crystallization reaction occurs at about 252°C . From this work, XRD and TEM analyses indicate that the microstructure of as-melt-spun ribbon is amorphous. TEM analysis of the sample isothermally held at 251°C for 2 min (Fig. 2) indicates the development of Al nanocrystals of 23 nm average size and about $4.9 \times 10^{21}\text{m}^{-3}$ particle density.

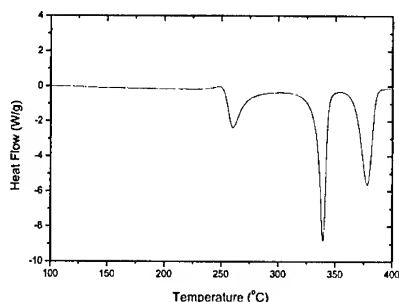


Fig. 1 DSC continuous heating curve at $40^\circ\text{C}/\text{min}$ of amorphous $\text{Al}_{85}\text{Ni}_{10}\text{Nd}_5$ alloy



Fig 2 TEM bright-field micrograph and SADP (inserted) of $\text{Al}_{85}\text{Ni}_{10}\text{Nd}_5$ sample held at 251°C for 2 min.

Fig. 3 shows the change in the first exothermic reaction with annealing time at different annealing temperatures below the onset temperature of the first exothermic reaction in Fig. 1. The exothermic reaction for the $\text{Al}_{85}\text{Ni}_{10}\text{Nd}_5$ alloy begins to appear after an incubation period, followed by a maximum exothermic peak and then a rapid decrease in the reaction. With increasing annealing temperature the exothermic peak becomes sharp and moves to left-hand side indicating acceleration of transformation kinetics.

In the theory of solid state phase transformation, the Johnson-Mehl-Avrami (JMA) equation is widely used in modeling the isothermal phase transformation mechanism [4-6]. The JMA equation relates the transformed volume fraction x at a constant annealing temperature T and time t [4-6] :

$$x(t) = 1 - \exp[-K_T(t - \tau)^n] \quad (1)$$

where K_T , τ and n are the temperature dependent kinetic constant, incubation time and Avrami exponent, respectively. Avrami exponent n reflects the characteristics of nucleation and growth process during the transformation. Normally, for an isothermal crystallization of an

amorphous alloy, a mean value of the Avrami exponent was used to interpret the process. Recently as an alternative method of analysis of the isothermal DSC results of amorphous alloys crystallization the local value of the Avrami exponent has been proposed by Calka et al [7]. The local Avrami exponent $n(x)$ is defined as

$$n(x) = \frac{\partial \ln(-\ln(1-x))}{\partial \ln(t-\tau)} \quad (2)$$

Fig. 4 shows the relationship between the crystallized volume fraction of primary Al $x(t)$ and anneal time t at annealing temperature of 247°C . Plotting $\ln(-\ln(1-x))$ against $\ln(t-\tau)$, as in Fig. 5 (a), we can get the local Avrami exponents in the whole transformation range using the definition of $n(x)$ in equation (2). Fig. 5(b) shows a plot on $n(x)$ vs x at 247°C isothermal annealing the as-quenched $\text{Al}_{85}\text{Ni}_{10}\text{Nd}_5$ glass, in a range of 0.5%~99.5%. It can be seen from the plot (Fig. 5 (a)) that in the whole transformation, there are three distinct stages with different Avrami exponents. This evident variation of the mean value of Avrami exponent indicates that there are different dominating mechanisms at the different transformation stages.

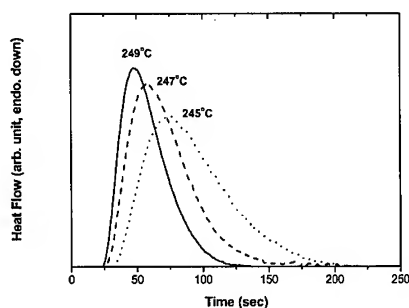


Fig. 3 Change in the first exothermic peak of $\text{Al}_{85}\text{Ni}_{10}\text{Nd}_5$ alloy with annealing time.

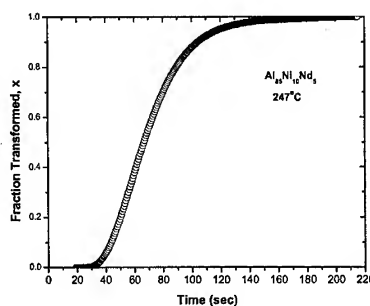


Fig. 4 Isothermal transformation curve for nanocrystallization of primary Al phase of $\text{Al}_{85}\text{Ni}_{10}\text{Nd}_5$ alloy at 247°C .

According to the classical phase transformation theory [8], that the Avrami exponent in the early stage of crystallization is smaller than 1 means the surface crystallization dominates, and such a process frequently occurs in the crystallization of amorphous melt-spun ribbon of metallic system [9, 10]. With the crystallization proceeding, the value of n increases and tends to an average value of about 2, indicating that 3-dimensional nucleation and growth becomes dominating. Finally, the n value decreases and tends to about 1, which implies that in the final stage of crystallization, the growth of primary Al phases with a considerable volume is dominant.

As shown in Fig. 5 (b), the local Avrami exponent value $n(x)$ increases up to the maximum value of about 2 in the very early stage of transformation and decrease continuously to about 1. Decreases of $n(x)$ values shows a decrease of the increasing rate of nucleation, and reaching to the maximum value in such a short time indicates the early sites saturation of nucleation (heterogeneous nucleation).

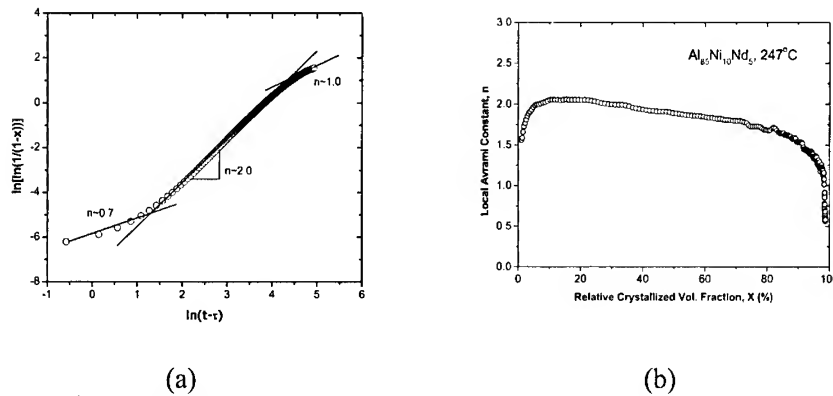


Fig. 5 (a) plot of $\ln[-\ln(1-x)]$ vs $\ln(t-\tau)$ for nanocrystallization of primary Al phase, and (b) plot of local Avrami exponent ($n(x)$) vs crystallized volume fraction (x) of primary Al phase.

Generally, in the analysis of diffusion controlled precipitate growth, the parabolic growth model has been applied. But because this type of law does not consider the diffusion field impingement effect, so it is not rigorous to describe the growth behavior during non-polymorphic transformation. In a recent research, the adoption of Ham model [11], which considers spherical precipitate growth including diffusion field impingement, for describing the growth behavior during the non-polymorphic transformation has reported [12]. In this study, Ham model is adopted to predict the growth behavior of primary Al nanocrystals developed from the $\text{Al}_{85}\text{Ni}_{10}\text{Nd}_5$ amorphous alloy. The brief description of Ham model is as follows.

For a precipitate size $R(t)$ and spacing $2r_s$, Ham gives the growth rate as

$$\frac{dR}{dt} = \left[\frac{\bar{C}(t) - C_m}{C_p - C_m} \right] \frac{D}{R(t)} \quad (3)$$

where D is the matrix diffusivity, \bar{C} is the average solute content in the matrix, and C_p and C_m are the precipitate and matrix compositions at the interface, respectively. The parameters needed for the Ham model include the Al nanocrystal particle density, which is obtained from TEM analysis ($N_v \sim 4.9 \times 10^{21} \text{m}^{-3}$, Fig. 2); the enthalpy of crystallization and the interface compositions, which can be obtained from thermodynamic model; and the diffusivity, which can be obtained from modeling the DSC exotherm.

In order to obtain the interface composition of the matrix and the precipitate, Coates Model, which accounts for diffusion limited growth of precipitates in ternary systems with unequal component diffusion coefficients [13, 14], is adopted in this study. For purpose of this analysis, the ratio $D_{\text{Ni}}/D_{\text{Nd}}=100$ has been used which is reasonable for the large observed differences in composition profiles of rare-earth and transition metal [15]. The calculated metastable fcc-liquid equilibria at 524K is given in Fig. 6. The alloy composition of interest (Al-10Ni-5Nd) is on the tie line joining the fcc phase and liquid phase of composition Al-10.1Ni-7.3Nd. The calculated enthalpy change (ΔH_v) is $-1.20 \times 10^9 \text{ J/m}^3$.

In order to estimate the diffusivity of Nd the Ham analysis was applied to the continuous heating curve with the starting time for the peak onset and the values of $N_v=4.9 \times 10^{21} \text{m}^{-3}$ and $\Delta H_v=-1.20 \times 10^9 \text{ J/m}^3$ (eqn. (4)).

$$\frac{dH}{dt} \equiv (N_v V) \cdot \Delta H_v \cdot 4\pi R^2 D_{Nd} r_s \left(\frac{\bar{C}(t) - C_m}{C_p - C_m} \right) \left(\frac{C_i - \bar{C}(t)}{C_p - C_m} \right)^{\frac{1}{3}} \quad (4)$$

Fig. 7 shows the calculated heat evolution rates for the continuous heating curve for three different D_{Nd} values. For the case of $D_{Nd} \sim 5.6 \times 10^{-17} \text{ m}^2/\text{s}$, the calculated heat evolution rate shows relatively good agreement with the experimental data except for the higher temperature region. The Ham model is based on the assumption of a constant diffusivity, but in fact the diffusivity varies with the temperature and the composition. These are the reasons why there are some discrepancies between calculated and experimental data in the higher temperature region as shown in Fig. 7.

In Fig. 8, the crystal size of primary Al as a function of time calculated from parabolic growth model and Ham model was compared. The Ham analysis predicts a rapid deviation from parabolic growth behavior when the high observed particle density and the estimated diffusion coefficient are used in calculation. Fig. 9 shows the measured crystal size variation with annealing time t at 260°C and 280°C . As shown in Fig. 9, the crystal size of primary Al nanocrystals was very stable as about $25\sim 30 \text{ nm}$ size even after annealing for 3 hours.

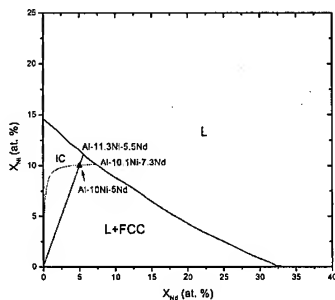


Fig. 6 Calculated metastable phase diagram (524K) of Al-Ni-Nd showing fcc-L equilibria.

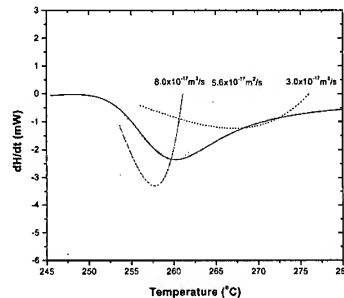


Fig. 7 Modeling of continuous heating curve of Al-10Ni-5Nd from Fig. 1. The peak has been fitted with three values for the neodymium diffusion coefficient.

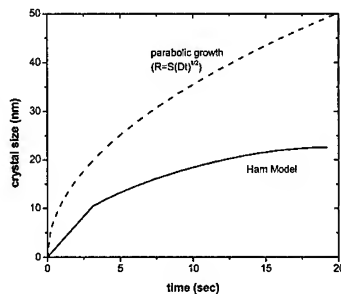


Fig. 8 Calculated crystal size as a function of time given by the Ham model (solid line).

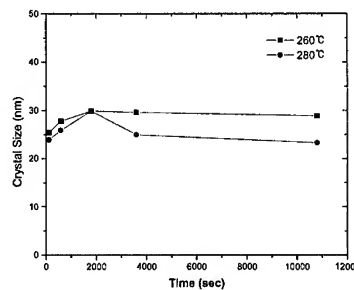


Fig. 9 Measured crystal size by XRD method after annealing at 260°C and 280°C for various holding time.

The Ham analysis predicts quite well the measured crystal size and growth rate in the present study. The predicted crystal size (the Ham model) becomes less than that given by $S\sqrt{Dt}$ after only a few seconds for temperatures above the glass transition, emphasizing the need to consider the diffusion-field impingement in a growth kinetics analysis when particle density are high.

4. CONCLUSION

In this study, the nucleation and growth behavior of primary Al nanocrystals in Al-Ni-Nd amorphous alloy was investigated using the JMA analysis and Ham model.

Avrami exponents for crystallization of primary Al phase were obtained. In early stage, it was about 0.7. This indicates that the crystallization mechanism in the early stage is surface nucleation and growth. In the middle stage, the obtained Avrami exponent was about 2. From this result, it was found that the dominant mechanism is bulk nucleation and growth. In the last stage, the Avrami exponent was about 1.0 and this means that the primary Al nanocrystals grow in bulk.

In order to investigate the growth behavior of primary Al nanocrystals, the variations of primary Al crystal sizes with annealing temperatures and time were measured by XRD method (Scherrer equation). Before the formation of intermetallic compounds, the growth rate of primary Al nanocrystals reaches nearly zero in a very short time. This behavior cannot be predicted by the conventional diffusion-controlled parabolic growth law, which doesn't consider the diffusion field impingement effect. However, the Ham analysis from this study predicts quite well the measured crystal size and growth rate. The predicted crystal size (the Ham model) becomes less than that given by $S\sqrt{Dt}$ (parabolic growth law) after only a few seconds for temperatures above the glass transition, emphasizing the need to consider diffusion-field impingement in a growth kinetics analysis involving high particle densities.

REFERENCES

1. R. Birringer, U. Herr, and H. Gleiter ; *Trans. Japan Inst. Met. Suppl.*, 27, 43 (1986)
2. A. Inoue, K. Ohtera, A. P. Tsai, and T. Masumoto ; *Japan J. Appl. Phys. Chem.*, 35 (1984) p. 241.
3. Y. He, S. J. Poon, and G. J. Shiflet ; *Science*, 241 (1988) p. 1640.
4. W. A. Johnson and R. F. Mehl ; *Trans. AIME*, 135 (1939) p. 416.
5. M. J. Avrami ; *J. Chem. Phys.*, 7 (1939) p. 1103.
6. A. N. Kolmogorov ; *Bull. Acad. Sci. USSR*, 3 (1937) p. 355.
7. A. Calka and A. P. Radinski ; *MRS Symp. Proc.* 80 (1987) p. 203.
8. J. W. Christian : *The theory of transformation in metals and alloys*, Pergamon Press, Oxford, (1975).
9. A. Calka and A. P. Radinski ; *J. Mater. Res.* 3 (1988) p. 59.
10. M. A. Gibson and G. W. Delamore ; *J. Mat. Sci.* 22 (1987) p. 4550
11. F. S. Ham ; *J. Phys. Chem. Solids*, 6 (1958) p. 335.
12. D. R. Allen, J. C. Foley and J. H. Perepezko ; *Acta. Mat.*, 46 2 (1998) pp. 431-440.
13. D. E. Coates ; *Metall. Trans.*, 3A (1972) p. 1203.
14. D. E. Coates ; *Metall. Trans.*, 4A (1973) p. 1077.
15. K. Hono, Y. Zhang, A. Inoue and T. Sakurai ; *Mat. Trans. Jim*, 36 (1995) p. 909.

DSC AND HRTEM STUDY OF PRECIPITATION IN Al-Mg-Si ALLOYS

Kenji Matsuda*, Hiroaki Matsui**, Kiyoshi Terayama*, Yasuhiro Uetani***
and Susumu Ikeno*

*Faculty of Engineering, Toyama University, Toyama, 930-8555, Japan .

**Graduate student, Toyama University, Toyama, 930-8555, Japan .

***Research Institute of Technology, Toyama Prefectural University, Toyama,
939-0398, Japan.

ABSTRACT

A differential scanning calorimeter (DSC) measurement and high- resolution transmission electron microscopy (HRTEM) were performed to confirm the precipitation sequence of Al-Mg₂Si alloys containing Mg₂Si 0.6, 1.0 and 1.6 mass% during heating. 4 exothermic (peaks A, C, D and E) and 1 endothermic (peak B) peaks were clearly detected on a DSC curve of Al-1.6 mass% Mg₂Si alloy. These peaks were unclear when Mg₂Si contents decreased from 1.6 to 0.6 mass%. Needle-shaped and rod-shaped precipitates were observed in alloys heated to temperature peak B or more by TEM. HRTEM observation was also performed for samples heated upto each peak. The mono-layer GP zone was observed in the sample heated to temperature between peaks A and B. The precipitation sequence of 1.0 and 0.6 % alloys were also confirmed and precipitation sequence of Al-Mg₂Si alloys during heating are as follows:

G.P. zones → Random-type → Parallelogram-type → β' phase → β phase

No β" phase existed in these alloys what did not include Si in excess.

1. INTRODUCTION

The precipitation sequence of Al-Mg-Si alloys has been studied by several techniques, especially by the thermal analysis, which can obtain information about precipitation from its early stage to the equilibrium stage. Since Al-Mg-Si alloys have been focused on as materials for body sheets of vehicles and structural materials with weldability, there are many reports about precipitation sequence of this alloy system by the deferential scanning calorimetry (DSC)[1-11]. There are, however, no reports that were clarified relationship between peaks on DSC curves and precipitates caused during heating by to be classified crystal structures or types of precipitates. We are studying

precipitation sequence by high-resolution transmission electron microscopy (HRTEM) [12-17]. In this study, DSC curves of Al-Mg₂Si alloys containing several amount of Mg₂Si were measured and precipitates in these alloys were observed by HRTEM in order to confirm corresponding between results peaks on DSC curves and precipitates in the matrix.

2. EXPERIMENTAL PROCEDURE

Alloys used were prepared using 99.99 %Al and 99.9 %Mg and Si ingots. Alloys included Mg₂Si of 0.6, 1.0 and 1.6 mass% and they are called as 0.6, 1.0 and 1.6 % alloys in the present work. Ingots were hot- and cold-rolled to 0.2 mm thick sheets. These sheets were solution heat treated at 848 K for 3.6 ks DSC samples were prepared from sheets to discs of 4 mm in diameter and 0.05mm in thickness, and its weight was 15 mg. These discs were heated from the room temperature to 773 K at the heating rate of 10 K/min after solution heat treatment at 848 K for 3.6 ks. 99.99 % aluminum disc was used as the blank sample. TEM samples were prepared by the electrolytic polishing method. DSC was used a DSC-3300S (Mac Science), and HRTEM was used EM-002B (Topcon) at 200 kV.

3. RESULTS AND DISCUSSION

Figure 1 shows DSC curves obtained from the 0.6, 1.0 and 1.6 % alloys heated at 10 K/min. There are 4 endothermic peaks A, C, D and E, and 1 exothermic peak B. It has been reported that peak A is the formation of G.P. zones, peak B is the dissolution of G.P. zones, and C, D and E are corresponding to the formation of β'' , β' and β phase, respectively [1-11]. Peaks in Fig.1 were similar to previous reports. Peaks on the DSC curve of 0.6 % alloy were unclear compared with that of 1.6 % alloy.

Figure 2 shows microstructures obtained from the 1.6 % alloy heated up to near peaks B, C, D and E. Needle-shaped and rod-shaped precipitates, which are parallel to [100] and [010] directions of the matrix, were observed in TEM images of Figs. 2(b), (c), (d) and (e). Fig. 2(a) shows TEM image of the sample heated to 463 K between peaks A and B. There are no needle- or rod-shaped precipitates in this figure when the sample observed in this magnification. Fig. 2(f) shows an optical micrograph of the sample heated to 723K and a lot of plate-shaped β -phase was observed in there.

Figure 3 shows typical HRTEM images of Fig. 2(a) - (d). The mono-layer G.P. zones [12,17] were observed in Fig. 3(a), although there were no precipitate in Fig. 2(a). The mono-layer G.P. zone shows arrangement of bright and dark dots along the (200) plane of the matrix alternately. Fig. 3(b) shows a cross-section of the needle-shaped precipitate and there were no periodicity in there. This is the random-type precipitate what is a transition phase from G.P. zones to metastable phases [12,17]. There were many random-type precipitates in this temperature. The parallelogram-type precipitate, which is a precursor of the β' phase and different from the β'' phase [13,16,17], was observed in

Fig. 3(c). It can be seen a parallelogram network of bright dots in its cross-section. Fig. 3(d) shows a typical HRTEM image of the β' phase [14] in the 1.6 % alloy heated upto peak D. In the 1.6 % alloy, namely, it was confirmed that the G.P. zones, the random-type, the parallelogram-type precipitates, the β' phase and the β phase are observed during heating.

Figure 4 shows TEM images of 1.0 % and 0.6 % alloys heated to 533 and 573K. Needle- and rod-shaped precipitates were also confirmed in those samples. It was also confirmed by HRTEM that the precipitation sequence of 1.0 % and 0.6 % alloys was similar to that of 1.6 % alloy. Figure 5 shows a typical HRTEM image of the β'' -phase in an Al-1.0 mass% Mg_2Si - 0.4 mass% Si alloy (excess Si-type) aged at 423 K for 2400 ks[13,15]. This phase was never observed in this study. As 6000 series aluminum alloys of excess Si-type have been generally used for studies of precipitation sequence in this alloy system [1-11], it is expected that the β'' phase was observed in samples heated upto the maximum exothermic peak of DSC curve in their reports.

4. CONCLUSIONS

DSC curves of Al- Mg_2Si alloys were obtained, and HRTEM observation was performed for peaks in their DSC curves to clarify their precipitation sequence. Results obtained are summarized as follows:

1. There are 4 endothermic peaks A, C, D and E, and 1 exothermic peak B in the 1.6 % alloy as the same as that reported in previous works. These peaks were unclear when Mg_2Si contents decreased from 1.6 to .06 mass%.
2. The 1.6% alloy heated to temperatures near or between each peak was observed by TEM. Needle-shaped and rod-shaped precipitates were observed in samples heated to temperature peak B or more. There are no needle- or rod-shaped precipitates in the sample heated to temperature between peaks A and B. HRTEM observation was performed for samples heated upto each peak and found out the random-type, the parallelogram-type, the β' phase. The β phase was also confirmed in the sample heated to peak E. The mono-layer GP zone was observed in the sample heated to temperature between peaks A and B.
3. The precipitation sequence of 1.0 and 0.6 % alloys were also confirmed and those were similar to that of 1.6 % alloy, namely it is as follows;

G.P. zones \rightarrow Random-type \rightarrow Parallelogram-type \rightarrow β' phase \rightarrow β phase

4. No β'' phase existed in these alloys what did not include Si in excess.

REFERENCES

1. J.D.Bryant, Metall. Mater. Trans.A, Vol.30A (1999), pp.1999 - 2006.
2. S.P.Chen, et al., J.Mater. Sci., Vol.33(1998), pp.4477-4483.
3. I.Dutta, S.M.Allen and J.L.Hafley, Met. Trans.A, Vol.22A(1991), pp.2553-2563.

4. A.K.Gupta and D.J.Lloyd, *Met.Mater.Trans.A*, Vol.30A (1999), pp.879-884.
5. I.Dutta and S.M.Allen, *J.Mater.Sci.Letters*, Vol.10(1991),pp. 323-326.
6. T.Das,P.R.Munroe and S.Bandyopadhyay, *J.Mater.Sci.*, Vol.31(1996), pp.5351-5361.
7. A.Borrego and G.Gonzalez-Doncel, *Mater.Sci.Eng.*, Vol.A245 (1998), pp.10-18.
8. T.Das,S.Bandyopadhyay and S.Blairs, *J.Mater. Sci.*, Vol.29 (1994), pp.5680-5688.
9. G.A.Edwards,K.Stiller et al., *Acta Mater.*, Vol.40(1998), pp.3893-3904.
10. L.Zhen,S.B.Kang and H.W.Kim, *Mater.Sci.Tech.*, Vol.13 (1997), pp.905-910.
11. L.C.Doan,Y.Ohmori and K.Nakai, *Mater. Trans. JIM.*, Vol.41(2000), pp.300-305.
12. K.Matsuda,H.Gamada et al., *Met.Mater.Trans.A.*, Vol.29A (1998), pp.1161-1167.
13. K.Matsuda,T.Naoi et al., *Mater.Sci.Eng.*, Vol.A262 (1999), pp.232- 237.
14. K.Matsuda, S.Ikeno and S.Tada, *J.Japan Inst.Metals*, Vol.57(1993), pp.1107-1113.
15. K.Matsuda,Y.Sakaguchi et al., *J. Mater. Sci.*, Vol.35 (2000), pp.179- 189.
16. K.Matsuda, H.Gamada et al., *J.Japan Inst.Light Metals*, Vol.47(1997), pp.493-499.
17. K.Matsuda,T.Yoshida et al., *J.Japan Inst. Metals*, Vol.62 (1998), pp.133- 139.

ACKNOWLEDGEMENT

The authors are grateful to staff of Hokuriku Fabrication center, Shin-Nikkei Co. Ltd. for analysis of chemical composition of alloys.

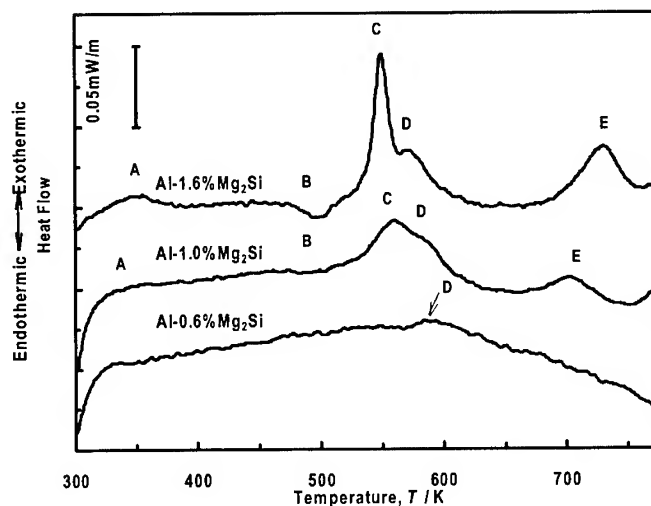


Fig. 1 DSC curves obtained from the 0.6, 1.0 and 1.6 % alloys heated at 10 K/min.

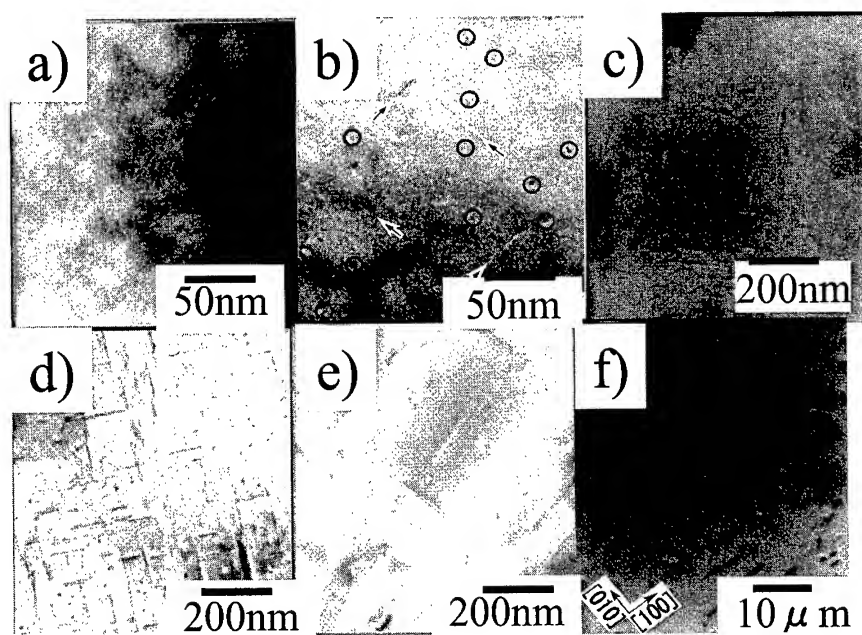


Fig.2 TEM images obtained from the 1.6 % alloy heated at 10 K/min up to (a) 463, (b) 498 (c) 547, (d) 573 and (e) 623 K. Fig. 2(f) shows an optical micrograph of the 1.6 % alloy heated to 723 K.

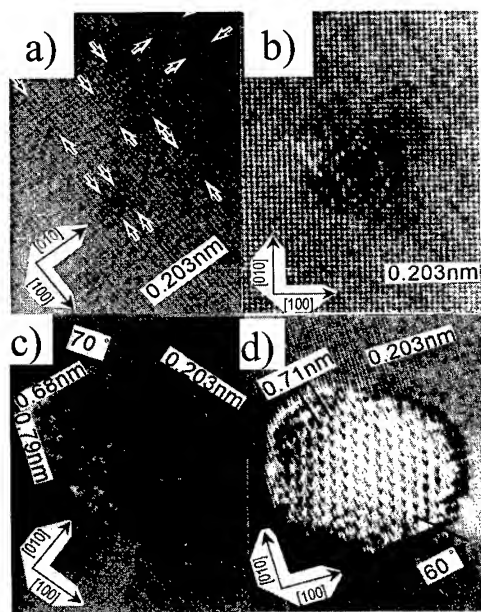


Fig.3 HRTEM images of Fig. 2 (a) - (d). Samples were heated to (a) 463, (b) 498 (c) 547 and (d) 573 K.

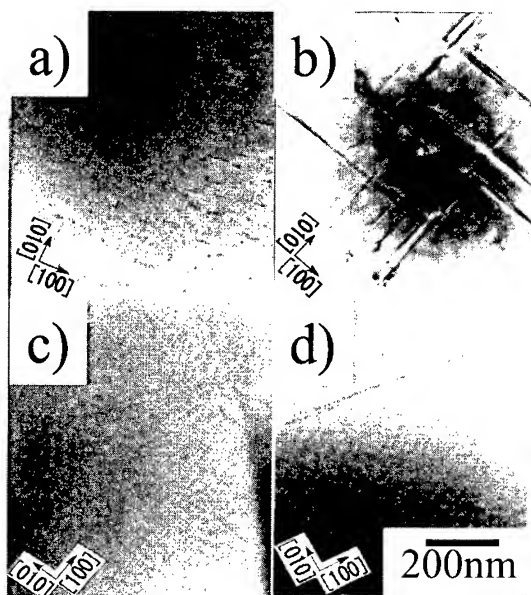


Fig. 4 TEM images in 1.0 and 0.6 % alloys heated to 533 (a) and (c), and 573 K (b) and (d).

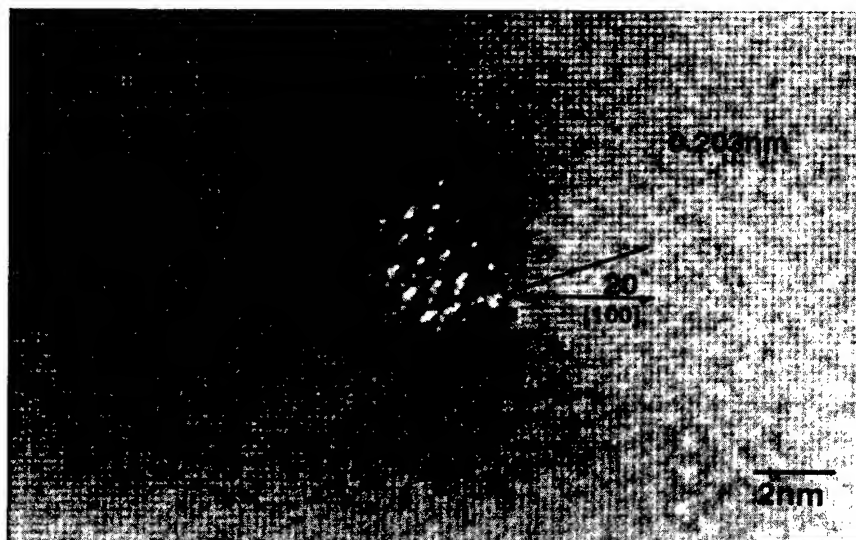


Fig. 5 HRTEM image of the β'' phase in an Al-1.0 mass% Mg_2Si - 0.4 mass% Si alloy aged at 423 K for 2400 ks [13].

STRESS-ASSISTED NUCLEATION OF Ω PRECIPITATE

IN Al-Cu-Mg-Ag ALLOYS

S. Muraishi, S. Kumai and A. Sato

Department of Materials Science and Engineering, Tokyo Institute of Technology
4259 Nagatsuta, Midori-ku, Yokohama 226-8502, Japan

ABSTRACT

Effect of the external stress on precipitation of Ω plates and G.P. zone in an Al-Cu-Mg-Ag polycrystalline was examined. Compressive stress during ageing promoted the nucleation of particular variants of Ω and G.P. zone. During the early stage of aging, the number density of G.P. zone was increased under stress aged condition than that of stress-free aged condition. In contrast to that, the number density of Ω under stress-aged condition is quite small at the beginning of ageing. The Ω plate was hardly observed by conventional TEM. However, HRTEM observation revealed that small Ω plate exists with weak contrast in the dark strain contrast. These results indicate that the growth of Ω is suppressed by excess nucleation of G.P. zone at the early stage of ageing.

1. INTRODUCTION

Addition of Mg and Ag to an Al-Cu binary alloy introduces finely dispersed Ω precipitates on $\{111\}_{\text{Al}}$ habit planes replacing G.P. zone and θ' on $\{001\}_{\text{Al}}$. Muddle et al [1] have reported that the crystallographic structure of Ω precipitate is orthorhombic ($a=0.496$, $b=0.895$, $c=0.848$) similar to θ' (Al_2Cu). Recently Murayama et al [2] investigated nucleation of the Ω precipitates using 3DAPFIM method. They found that Mg-Ag co-clusters form at the very early stage of ageing, and then Cu atoms aggregate to these clusters to form Ω nuclei. In this point of view, the precipitate sequence of Ω is closely related to G.P. zone which consists of Cu atoms. In the mean time, stress effect on nucleation and growth was treated by Eto et al [3] concerning G.P. zones in Al-Cu binary alloys. They suggested that the particular variant of G.P. zone nucleated under the external stress will grow to θ' through G.P. [II].

In the present study, the stress effect on the precipitation sequence of Ω together with G.P. zone in Al-Cu-Mg-Ag polycrystalline alloy was investigated. Applying the stress during ageing, the stress effect on the precipitation behavior of Ω and G.P. zone was examined. Two-step ageing (combination of stressed and stress-free ageing) was also conducted for further investigation. Ω precipitates at the very early stage of aging were observed by HRTEM.

2. EXPERIMENTAL PROCEDURES

Chemical composition of the alloy was Al-6.3 Cu-0.3 Mg-0.5 Ag (wt.%). The alloy cast plate of 40 mm in thickness was homogenized at 743 K for 8 h in air, and hot-rolled down to the plate of 15 mm thick. Grain size was about 100 μm . Rectangular specimens bar ($2 \times 2 \times 4 \text{ mm}^3$) were used in compressive stress aging. The longest axis of the specimen along which the external stress applied, corresponds to a rolling direction. Specimens were quenched into iced water after solution heat treatment at 793 K for 1h. Subsequently they were aged either under compressive stress in the range from 75MPa to 150MPa or under stress-free condition at 450 K for 1 ~ 10 h. Two-step ageing (combination of stressed and stress-free ageing) was also made. TEM specimens were cut from the aged specimen and mechanically thinned down to 200 μm , and twin-jet-polished to a few μm in a solution of 10 % perchloric acid and 90 % methanol at 238 K and 14V. Final polishing was made in a solution of 33% nitric acid and 66 % methanol. The TEM observation was carried out using JEOL 2011 and PHILIPS CM200.

3. EXPERIMENTAL RESULTS AND DISCUSSION

3.1 Stress effects on the number density of Ω and G.P. zone

Figures 1 (a) - (c) show the TEM microstructures of the specimens, which were aged at 450K for 1 h under stress free condition (a), the compressive stress of 150MPa along near [111] direction (b) and along near [011] direction (c). Stress axis is indicated with arrows in the figures. Ω plates were finely dispersed on {111} Al matrix together with G.P. zone on {001} Al matrix (Fig.1 (a)). The number of Ω is about the same as that of G.P. zone at 1hour.

Stress effect on Ω plates and G.P. zone is shown in Figs 1 (b) and (c). Under the compressive stress along near [111] direction, Ω precipitates are hardly observed. The number density of the G.P. zone variant perpendicular to the stress axis is very high (Fig. 1(b)). On the

other hand, in Fig.1 (c), small Ω precipitates are observed along near $[011]$ direction. The number density of G.P. zone variant parallel to the compressive stress axis is quite low. These results are explained by misfit-effect [3-5]. The nucleation of the G.P. zone variant perpendicular to the stress axis is promoted in early stage of aging. The nucleation and growth of Ω is seemed to be suppressed by excessively nucleated G.P. zone.

The number density of Ω and G.P. zone was measured for the specimens aged from 1 to 10 hour. Changing the total number density of G.P.

zone and Ω was shown as a function of aging time in Figs 2 (a) and (b), for stress-free and stress-aged condition respectively. For stress-free aged specimens, the total number density of G.P. zone was estimated from the number density obtained for one of the three variants using TEM image. It should be mentioned that omega has four equivalent variants. For the stress-aged specimen, the obtained total number density of G.P. zone was from only one (001) variant whose precipitation is facilitated by compressive stress along $[001]$. On the other hand, the total number density of Ω is estimated from the number density obtained for one of four variant, because no preferable Ω variant exist for the external stress along $[001]$ direction. In Fig. 2 (a), the number density of G.P. zone aged under stress is higher than that of free-aged. As increasing the time, the number density of G.P. zone decrease to 1/30 for both stress and

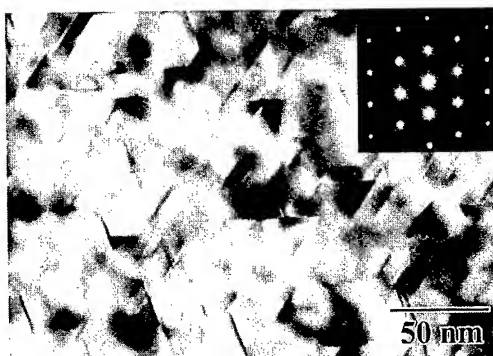


Fig. 1(a) TEM microstructure of the specimen stress-free aged for 1 h. Ω and G.P. zone are finely dispersed.

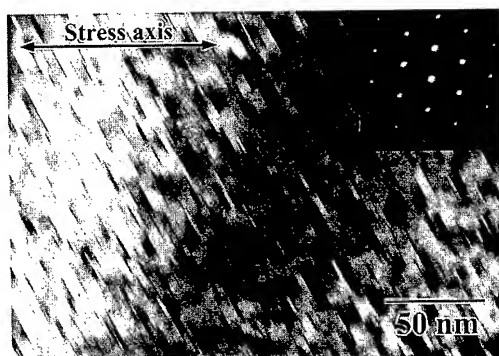


Fig. 1(b) Stress-aged for 1h. The preferential nucleation of G.P zones perpendicular to stress axis is evident. Ω is hardly observed.

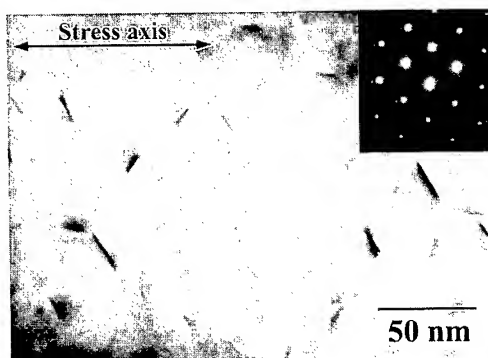


Fig. 1(c) Stress-aged for 1h. Small Ω plates are exhibited. The nucleation of G.P zones parallel to stress axis is seemed to be suppressed.

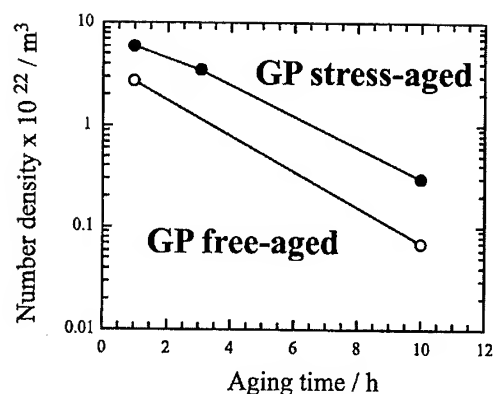


Fig. 2(a) The change in the total number density of G.P. zones as a function of ageing time. Stress aging increases the number density of G.P. zones.

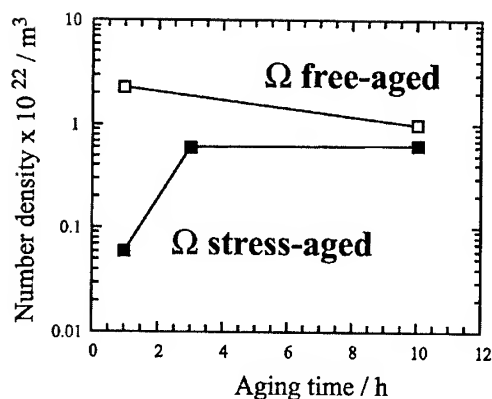


Fig. 2(b) the change in the total number density of Ω as a function of ageing time. Stress aging decreases the number density of Ω at early stage.

stress-free condition. Meanwhile, in Fig. 2 (b), decrease in the number density of Ω in stress-free condition is moderate. In contrast to that, at 1 hour, the number density of Ω aged under stress is quite low compared to free-aged one. In the present compressive stress direction was chosen so that none of the four variant of Ω show preferential nucleation and growth. Therefore, decrease in the number density of Ω is considered to be due to the excess nucleation of G.P. zones.

3.2 HRTEM observation of the early stage of Ω plates

In order to find the early stage of Ω , HRTEM observation was carried out. Figure 3 shows the HREM image of the specimen aged for 1 h under stress. A small Ω plate with a slight contrast is visible in the strong strain contrast. They could not be detected by the conventional TEM as shown before. Muddle et al [1] reported the crystallographic structure of Ω is orthorhombic and the c axis of Ω corresponds to four $\{111\}$ Al planes. However, the thickness of this thin Ω plate in Fig. 3 has only two layers of $\{111\}$ Al planes. This

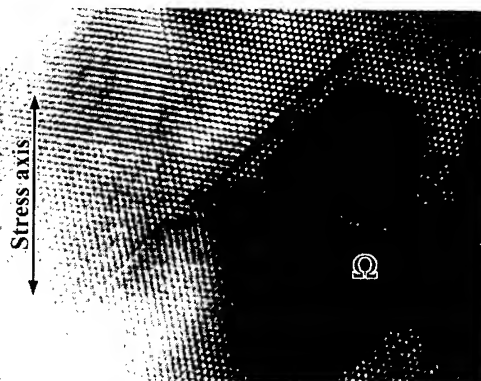


Fig. 3 HRTEM observation of thin Ω plate with weak contrast.

corresponds to the 1/2 of the Ω unit cell. Similar Ω morphology was reported by Cui et al [6]. Such Ω plates give fairly weak contrast. So it is generally difficult to observe them by conventional TEM. Considering these facts, the number density of Ω at 1 hour of stress aging, as shown in Fig.2(b), is considered to be underestimated. This result also suggests that the precipitation of Ω is suppressed by excess G.P. zones.

3.3 The effect of external stress on the nucleation of Ω and GP-zone

It is found that the small Ω nuclei exist at the time of 1 hour of stress aging. To examine the stress effect on the Ω nuclei existed at the time of 1 hour of stress ageing, two-step ageing (stress aging + stress-free ageing.) was performed. Figure 4 shows the microstructure of the specimen stress-aged for 1h and then stress-free aged at 450 K for 10 h. Applying the stress at the beginning of ageing, the number density of Ω_1 variant perpendicular to the stress axis became twice as that of Ω_2 variant. The present authors reported the preferential alignment of Ω plates by stress-aging for 10h at the same temperature [7]. The stress-orienting effect obtained here was comparable to that. This indicates that the stress effect for Ω is dominated by the first step of stress-aging for 1h.

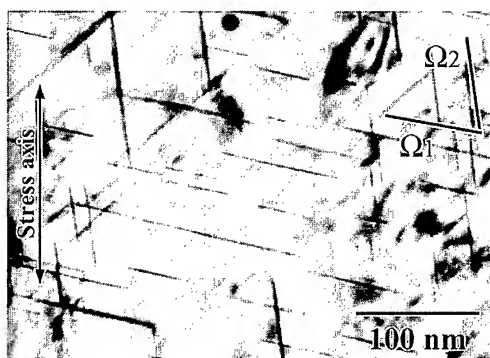


Fig. 4 Stress orienting effect of Ω in the two-step aged specimen. (stress ageing for 1h followed by stress-free ageing).

This study found that the nucleation of G.P. zone is facilitated by compressive stress. Consequently, the growth of Ω is suppressed by excess G.P. zone at early stage of stress aging. These results suggest that the precipitation sequence of Ω and G.P. zone are closely related. Generally, the precipitation sequence of θ' in Al-Cu alloy is known as follows, $\alpha' \rightarrow$ G.P. (I) \rightarrow G.P. (II) $\rightarrow \theta'$. On the other hand, for Al-Cu-Mg-Ag alloys, it is considered that Ω and G.P. zone independently nucleate in the early stage of ageing [8] and the volume fraction of θ' is about 10% of all the precipitates ($\Omega + \theta'$). This indicates that the growth of Ω on $\{111\}$ habit planes is preferred rather than the continuous growth of G.P. zones to θ' on $\{001\}$ habit planes in Al-Cu-Mg-Ag alloys. Recently, Murayama et al. [2] found that the Mg and Ag co-clusters formed in early stage of ageing, and Cu atoms aggregate to these co-clusters to form Ω nucleus. Lower number density of Ω in early stage of stress-aging (Fig. 2(b)) and very fine Ω plates observed by HRTEM (Fig. 3) demonstrated that the growth kinetics of Ω

precipitate is closely related to G.P. zones.

5. SUMMARY

Stress-assisted nucleation of Ω precipitate and G.P. zone was investigated. Applying the stress at the early stage of ageing, the number density of G.P. zone was higher than that of stress-free aged. In contrast to that, the number density of detectable Ω in stress-aged condition was observed to be quite low at the beginning of ageing. It is found that the nucleation of G.P. zone is facilitated by compressive stress. HRTEM observation and the experimental results of two-step aging suggest that the precipitation of Ω is suppressed by excessively nucleated G.P. zones.

REFERENCES

1. B. C. Muddle and I. J. Polmear, *Acta Met.*, Vol. 37 (1989), pp. 777-789.
2. M. Murayama and K. Hono, 1998, *Scripta Met.*, Vol. 38 (1998), pp. 1315-1319.
3. T. Eto, A. Sato and T. Mori, 1978, *Acta Met.*, Vol. 26 (1978), pp. 499-508.
4. J. D. Eshelby, *Pro. R. Soc. A*, Vol. 241 (1957), pp. 376-396.
5. T. Mura, *Micromechanics of Defects in Solids*, Martinus Nijhoff Publishers (1987), p1.
6. Q. Cui, G. Itoh and M. Kanno, *J. Japan Inst. Metals*, Vol. 59 (1995), pp. 492-501
7. S. Muraishi, S. Kumai and A. Sato, *Phil. Mag. A*, submitted.
8. K. Hono, N. Sano, S. S. Babu, R. Okano and T. Sakurai, *Acta Metall. Mater.*, Vol. 41 (1993), pp. 829-838.

A STUDY ON THE STRUCTURAL CHARACTERISTICS AND TENSILE PROPERTIES OF Al-Si ALLOYS UTILIZING STRIP CASTING METHOD

S. L. Kuan, T. S. Lui, L. H. Chen and J. M. Song

Dept. of Materials Science and Engineering, National Cheng-Kung University,
Tainan, Taiwan 701, R.O.C.

ABSTRACT

Al-Si alloys in a thin strip form can be produced using the strip casting with a low production cost, which apparently broaden its usability. A fine solidification structure of hypoeutectic strips can be classified into four zones along the through-thickness direction, namely, the upper dendritic zone, the mixed zone of dendritic and equiaxed-dendritic, the equiaxed-cell zone and the lower dendritic zone. With hypereutectic strips, the primary silicon particles exist in the vicinity of the subsurface, and the matrix microstructure can be divided into eutectic structure in the center of the strips and off-eutectic structure near the surface.

The results of tensile test show that the cracks of the hypoeutectic Al-Si strips initiate from the broken acicular silicon particles, which only appear in the equiaxed-cell zone, and the low ductility of hypereutectic strips can be resulted from crack initiation on the massive primary silicon particles.

Performing a proper TMT process is essential to enhance the ductility of hypoeutectic Al-Si strip.

Keyword: Strip Casting, Al-Si Strip, Solidification Structure, Tensile Property, Solution Treatment, TMT process

1. INTRODUCTION

Binary Al-Si alloys combine the advantages of excellent castability, high corrosion resistance and good mechanical properties, accounting for their extensive use as engineering materials [1,2]. It is difficult to produce Al-Si plates due to the problem with plastic working, e.g. rolling, especially for the materials with high silicon content. Using strip casting, 1 mm to 3 mm plate can be produced by direct casting, thereby eliminating the hot rolling and annealing processes [3,4]. According to our previous study [3,4], the solidification rate in the center of the strip is slower than that near the strip surface; thus a multi-layer solidification structure of Al-Si strip was produced.

Because the Al-Si strips not only possess a multi-layer microstructure but also different kinds of eutectic silicon, therefore, the tensile properties of Al-Si strip are worthy to investigate. In addition, the effects of the solution treatment and thermal mechanical treatment (TMT) were also examined.

2. EXPERIMENTAL PROCEDURES

As illustrated schematically in Fig. 1, the unequal-diameter twin-roller strip caster used in this study. Table 1 lists the composition of Al-Si strips. To prepare the strips, commercial pure aluminum (99.7wt% purity) and metallic silicon (99.9wt% purity) were melted in an induction furnace and poured into the strip caster after degassing by argon. Small amount of refiner containing Ti, B, P was applied in hypereutectic compositions.

Solution treatment was held in the salt bath furnace at 530°C for 1 to 12 hours. The TMT samples were cold-worked by rolling parallel to the casting direction prior to the solution treatment, and the rolling reductions were 10%, 30% and 75% (denoted as "C.W.10%",

“C.W.30%” and “C.W.75%” in the text and figures).

The dimension of tensile specimens was illustrated in Fig. 2. The longitudinal direction of the specimens is parallel to the casting direction. The initial tensile strain rate of the tensile testing was $6 \times 10^{-4} \text{ sec}^{-1}$.

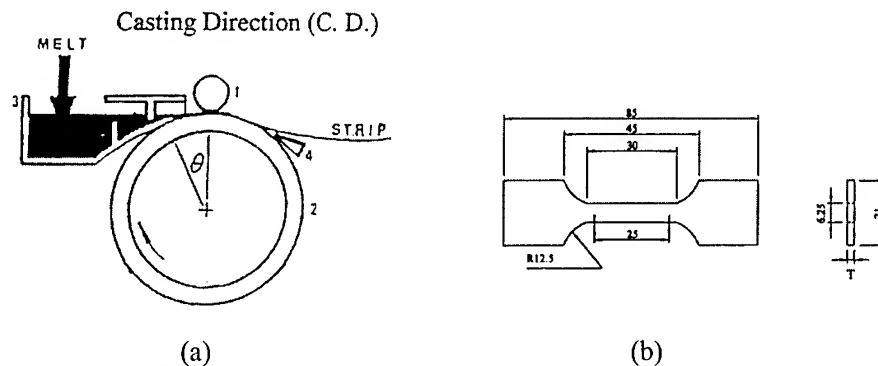


Fig. 1 Schematic diagrams of (a) the unequal-diameter twin-roller strip caster, showing 1: upper roller (200mm diameter), 2: main roller (625mm diameter), 3: tundish, 4: knife for detaching the strip from the main roller, and θ : contact angle; (b) the tensile specimen (unit: mm).

Table 1 Chemical compositions of Al-Si strips (wt%).

	Si	Fe	Ti	B	P	Al
7.1Si	7.1	0.36	—	—	—	Bal.
14.1Si	14.1	0.18	0.23	0.046	0.03	Bal.
17.0Si	17.0	0.22	0.26	0.052	0.03	Bal.

3. RESULTS AND DISCUSSION

To illustrate the overall solidification structure, Fig. 3(a) displays a through-thickness optical micrograph of the Al-7.10wt%Si strip that was produced at the pouring temperature of 630°C. As depicted in this figure, there are distinct zones with structural morphologies, namely the upper and lower columnar-dendrite zones near the top and bottom surfaces (denoted as “UCD” and “LCD” in the figure and text), mixed zone of the columnar-dendrites and equiaxed cells below the upper columnar-dendrite zone (denoted as “M” in this figure and the text), and a euqiaxed-cell zone in-between the mixed zone and lower columnar-dendrite zone (denoted as “E” in this figure and the text). Magnified microstructures of the M-Zone, E-Zone and LCD-Zone are shown in Figs. 3(b), (c) and (d), respectively. As revealed in these micrographs, eutectic silicon particles are acicular in the E-Zone and granular in the other zones. Therefore, we can recognize that the hypoeutectic strip possesses a multi-layer structure and the eutectic silicon can be divided into a granular form and a acicular form.

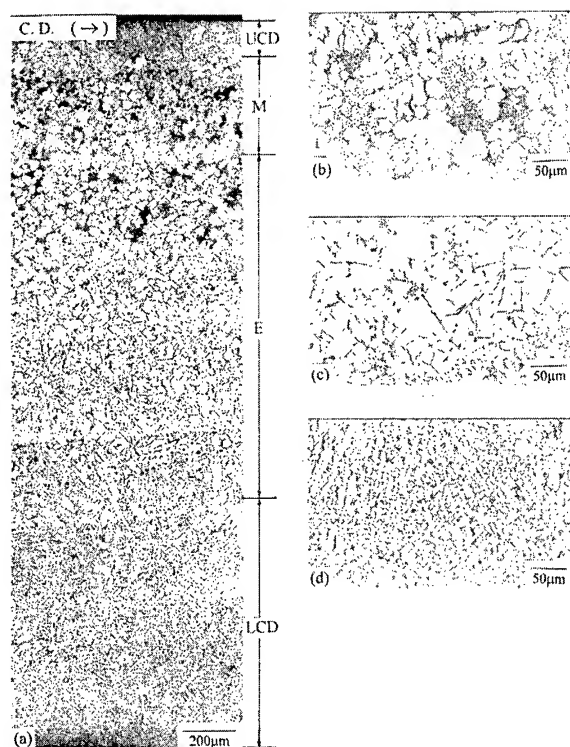


Fig. 2 Micrographs of hypoeutectic 7.1 Si strip produced at the roller speed with 23.4 m/min: (a) through-thickness microstructure (C. D.: casting direction); (b) mixed zone (M-Zone); (c) equiaxed-cell zone (E-Zone) and (d) lower columnar-dendrite zone (LCD-Zone).

To investigate in which zone crack initiates during tensile deformation, Figs. 3 (a) through (c) illustrate the magnified microstructures of as-cast strip that has been strained to nearly necking stage. Figure 3(b) show several cracks have been developed from the broken acicular particle into matrix in the E-Zone (marked by the arrows). Meanwhile, although the broken granular particles was observed (marked by the arrows), it should be noted that no cracks can be observed to extent into the matrix of the M-Zone and LCD-Zone, as shown in Figs. 3(a) and (c). The examination of the fracture surface of the same specimen after fracturing shows that the fracture surfaces of M-Zone and LCD-Zone both show dimple pattern (see Figs. 3(d) and (f)), and the fracture surface of the E-Zone reveals a combination of quasi-cleavage and dimple pattern as illustrated in Fig. 3(e).

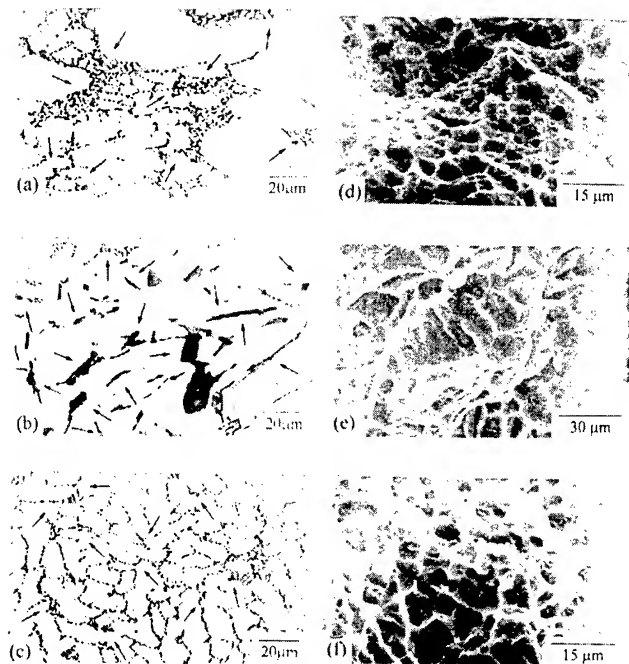


Fig. 3 (a)-(c) Microstructures of hypoeutectic 7.1Si strip strained nearly necking: (a) M zone, (b) E zone and (c) LCD zone; (d)-(f) SEM fractography of hypoeutectic strip after fracturing: (d) M-Zone; (e) E-Zone; (f) LCD-Zone.

The aforementioned features imply that the acicular particles predominantly cause inferior elongation of hypoeutectic strip.

The effects of S.T. and TMT process on the morphology of eutectic silicon in the E-Zone and tensile elongation of specimen are summarized in Fig. 4. As depicted in Fig. 4(a), the longitude size of acicular particle decreases with increasing the rolling reduction, but the transverse size is not affected. Consequently, the aspect ratio of acicular particles decreases with a higher rolling reduction, as illustrated in Fig. 4(b). Additionally, it can be correlated to the part cleavage/part dimple fracture pattern appeared at the E-Zone as shown in Fig. 3(e). To realize the influence of the shape change of the acicular particles on the fracture pattern in the E-Zone, the area fraction ratio of the quasi-cleavage and dimple patterns of the fractured specimens are given in Fig4 (c). According to the results, the area fraction ratio of dimple and quasi-cleavage patterns increase with decreasing the aspect ratio of acicular particles and thus the elongation of specimens is improved.

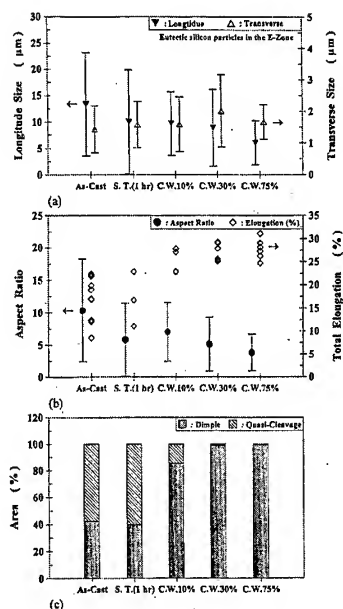


Fig. 4 The effects of solution treatment and TMT process on the properties of strip, plotted against five different specimen conditions for (a) the longitude and transverse size of acicular particle, (b) the aspect ratio of acicular particle and total elongation and (c) area percentage of dimple/quasi-cleavage in E-Zone on fracture surface.

Fig. 5 displays the tensile properties of hypereutectic 17.0Si strip produced under different rolling speed, indicating that the elongation of each strip is about 1.0%. Fig. 6 shows the microstructure of refined hypereutectic strip, indicating that the microstructure of the hypereutectic strip consists of the eutectic structure, off-eutectic structure and primary silicon particles. The off-eutectic structure is mainly formed near the surfaces of the strip, and the eutectic structure locates in the center of the strip. Due to the formation of off-eutectic structure near the top surface, the primary silicon particles are constrained to sub-surface of the hypereutectic strip. We infer that the cracking on the massive primary silicon particles (see Fig. 6 (a) and (b)) leads to the deterioration in elongation of refined hypereutectic Al-Si strips.

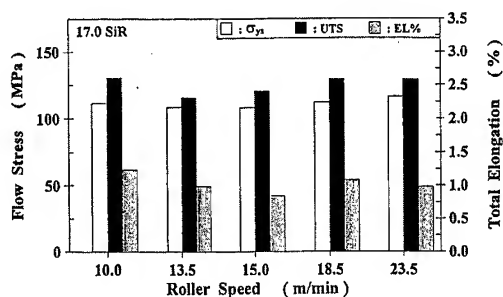


Fig. 5 Tensile properties of hypereutectic strips against the roller speed.

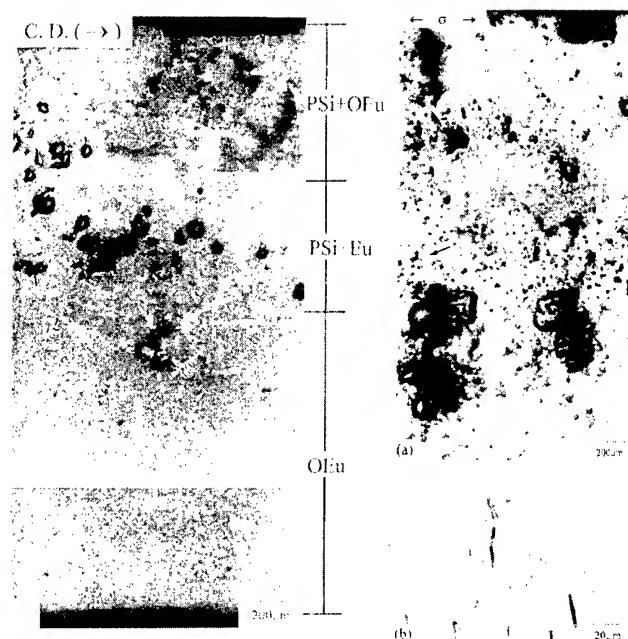


Fig. 6 Microstructure of hypereutectic strip and the cracking on the primary silicon particles under 0.6% strain.

4. CONCLUSIONS

1. During the tensile deformation, the cracks initiate easily on the broken acicular particles in the equiaxed-cell zone of the strip. The acicular particle is a major factor to cause inferior elongation of the hypoeutectic Al-Si strip.
2. Increasing the rolling reduction of TMT process will improve the ductility of hypoeutectic Al-Si strip by reducing the longitude size and the aspect ratio of the acicular silicon particles.
3. Low ductility of hypereutectic Al-Si strip can be attributed to massive primary silicon particles.

5. REFERENCE

1. W. R. D. Jones, W. L. Bartlett, *J. Inst. Metals*, 1952~1953, **81**, 145~151.
2. J. E. Hatch, *ALUMINUM: Properties and Physical Metallurgy*, (ASM, Metals Park, Ohio, U.S.A., 1st ed., 1984).
3. S. L. Kuan, T. S. Lui and L. H. Chen, *AFS Trans.*, 1996, **104**, 735~741.
4. S. L. Kuan, T. S. Lui and L. H. Chen, *Int. J. Cast Metal Res.*, 1999, **12**, 167~177.

EFFECTS OF Mn ADDITION ON MICROSTRUCTURE AND MECHANICAL PROPERTIES OF STRIP CAST Al6061 ALLOY

Young S. Park and Nack J. Kim

Center for Advanced Aerospace Materials and
Dept. of Materials Science and Engineering
Pohang University of Science and Technology, Pohang 790-784, KOREA

ABSTRACT

A study has been on the microstructure and mechanical properties of strip cast Al6061 alloy with and without 0.5Mn addition. The microstructures of the as-cast alloys are characterized by the presence of Si particles along cell boundaries. It also shows that there is a development of well-defined subgrains caused by hot rolling effect during strip casting. Si particles present along the cell boundaries transform into fine α -AlFeSi particles during solution treatment in the base alloy. There is also a presence of α -AlFeSi particles in the Al matrix. The addition of Mn results in an increase in the volume fraction of α -AlFe(Mn)Si particles in the Al matrix. Due to the increased volume fraction of α -AlFe(Mn)Si particles in the Mn containing alloy, the Mn containing alloy has less amount of Mg_2Si precipitates in the Al matrix than the base alloy. Accordingly, the Mn containing alloy shows lower yield strength but higher ultimate tensile strength due to higher work hardening rate than the base alloy. The increased work hardening rate of the Mn containing alloy is due to the presence of fine α -AlFe(Mn)Si particles in the Al matrix.

1. INTRODUCTION

Twin-roll casting or strip casting is the preferred method for fabricating thin-gauge Al sheets and foils [1]. One of the main advantages of strip casting is that capital investment for a strip caster is much lower than the conventional ingot/hot rolling process. Since the strip casting process combines solidification and hot rolling into one operation, hot rolling needed for conventionally produced ingots can be eliminated or reduced, resulting in substantial savings in energy and cost. Besides such economic benefits of strip casting, it is also able to reduce segregation, to improve inclusion size distribution and to refine microstructural and textural homogeneity [2-5]. In fact, the steel industry is quite enthusiastic about the strip casting and several R&D efforts are currently underway to produce steels with high solute contents such as stainless steels by strip casting [6-11]. However, the application of strip casting in Al alloys is mostly limited to the alloys with low solute contents [12-14].

Recently, attempts have been made to fabricate the highly alloyed Al-6Fe-1V-2Si alloy by strip casting using single-roll caster [15-17]. Al-6Fe-1V-2Si alloy is a derivative of commercial non-heat treatable Al8009 alloy. Al8009 alloy derives its excellent high temperature properties from the finely distributed thermally stable dispersoids [18]; hence the rapid solidification/powder metallurgy (RS/PM) process is used to produce the alloy. The studies on the strip casting of Al-6Fe-1V-2Si alloy show that its microstructure is less than desirable since it has the coarser microstructure than the RS/PM alloy. However, the studies

show that otherwise non-existing metastable phases form in the microstructure of strip due to the fast solidification rate of strip casting, suggesting that strip casting can be applied for the production of relatively highly alloyed Al alloys.

The present research was aimed at studying the structure and properties of strip cast SC6061 alloy to see the feasibility of strip casting for the production of Al alloys with modest solute contents. In addition to Al6061 alloy, 0.5 wt.% Mn containing alloy was also studied to utilize the potentially beneficial effect of Mn on the formation of dispersoids.

2. EXPERIMENTAL PROCEDURE

The strip casting apparatus is schematically shown in Fig. 1. Molten metal is fed from the melting furnace through the tundish into twin rolls. Rolls are made of Cu-0.7wt%Be and 200mm in diameter and 100mm in width. The roll speed can be varied continuously in the range of 4 – 16m/min. Two alloys have been strip cast in the present study; Al6061 with and without 0.5Mn addition (SC6061Mn and SC6061, respectively). Their chemical compositions are shown in Table 1. These alloys were induction melted in Ar atmosphere at 1000°C. After melting, melt was transferred into tundish whose temperature was set at 750°C. Roll gap was set at 2mm and 2.5mm and roll speed was 4m/min. Produced strips were 2 – 2.5mm in thickness and 50 – 70mm in width.

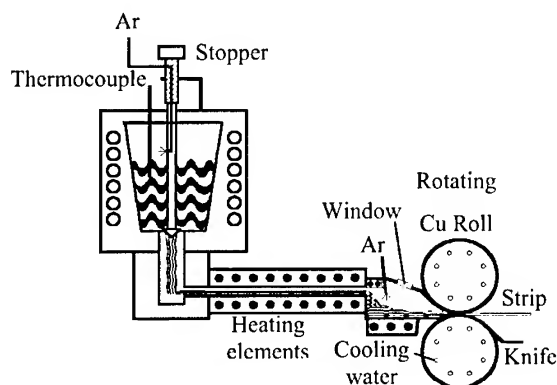


Fig. 1. Schematic drawing of the twin roll caster used in the present study.

Microstructural observation of the strip was conducted on the cross sections by optical microscopy (OM) and scanning electron microscopy (SEM). Details of the microstructural constituents were analyzed on the longitudinal sections by transmission electron microscopy (TEM). Thin foils for TEM were made by jet polishing in a solution of 33% HNO₃ and 67% methanol or ion milling. Strips were subjected to solution treatment at 540°C for 2 hours followed by aging. Tensile tests were conducted using flat tensile specimens with 12.6 mm gage length, 2 mm gage thickness and 5 mm gage width. Strain rate used was 8×10^{-5} /sec.

Table 1. Chemical Compositions of the Alloys Used in the Present Study

	Al	Mg	Si	Mn	Fe
SC6061	Bal.	0.89	0.50	0.06	0.43
SC6061Mn	Bal.	0.90	0.49	0.54	0.40

3. RESULTS AND DISCUSSION

3.1 As-cast Microstructure

TEM analysis has been conducted on the jet polished specimens and the results are shown in Fig. 2. Bright field micrograph of Fig. 2a shows that the 200 – 300 nm sized particles are present along the cell boundaries. EDS analysis shows that the particles mostly contain Si (Fig. 2b). It is not clear whether Al is present in the particles since Al peak can come from the surrounding matrix. Microdiffraction analysis of the particles shows that they have diamond cubic structure with $a = 0.357$ nm (Fig. 2c). These results indicate that the nature of the particles is Si. High magnification micrograph of the cell boundary area shows that the cluster of fine particles decorates the cell boundaries, besides the above mentioned Si particles. TEM analyses of these fine particles show that they are bcc phase containing Al, Si and Fe. Its lattice parameter has been calculated to be 1.258 nm. This phase is identical to the α -AlFeSi phase observed in our previous studies of rapidly solidified Al-Fe-V-Si alloys [17,18]. Fig. 3 shows the bright field TEM micrograph of the as-cast SC6061Mn alloy strip containing 0.5Mn. It shows that cell boundaries are decorated by particles, as in the case of the as-cast SC6061 alloy strip. Microdiffraction and EDS analyses again show that they consist of Si particles and cluster of fine α -AlFeSi particles.

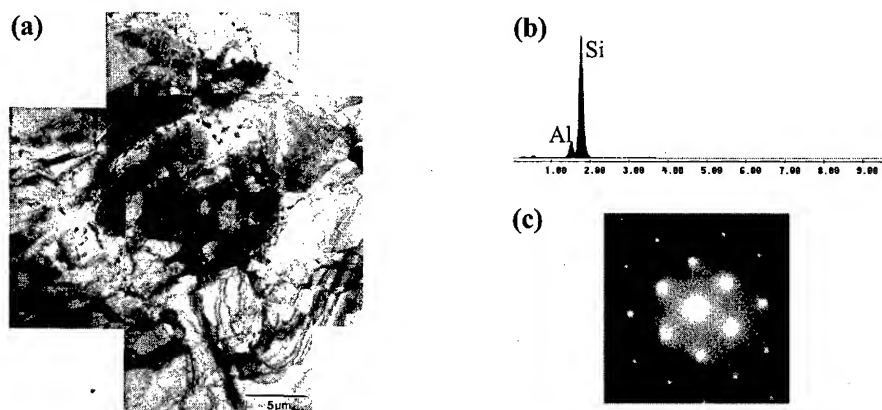


Fig. 2. a) BF micrograph of as-cast SC6061 alloy b) EDS spectra from Si containing particles (ion-milled specimen), and c) microdiffraction pattern of Si containing particles (ion-milled specimen).

It is also interesting to note that there is development of well-defined subgrains formed by recovery within the cell. During strip casting, solidified cells receive a large amount of rolling deformation. The presence of large amount of dislocations within the subgrains indicates that the temperature or the deformation was not enough for the recrystallization to occur. These subgrains are more or less oriented parallel to the casting direction.

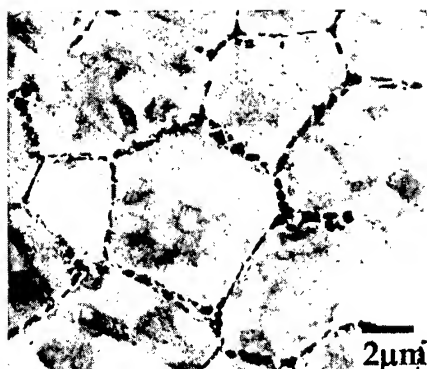


Fig. 3. BF micrograph of as-cast SC6061Mn alloy.

3.2 T6 Microstructure

Fig. 4a shows the microstructure of the T6 treated SC6061 strip. Morphologically, the microstructure of the T6 treated specimen is quite similar to that of the as-cast specimen. However, there is a very important difference between these two specimens; coarse Si particles present in the as-cast specimen disappear after heat treatment and are replaced by fine particles. Microdiffraction (insert in Fig. 4a) and EDS (Fig. 4b) analyses of the particles show that they are the α -AlFeSi phase. It indicates that Al and Fe diffuse onto boundaries and react with Si to form α -AlFeSi phase during heat treatment. There are also α -AlFeSi particles within the Al matrix, although their volume fraction is low. Besides the above mentioned α -AlFeSi particles, there is also a presence of very fine Mg_2Si particles within the Al matrix of the T6 treated SC6061 strip.

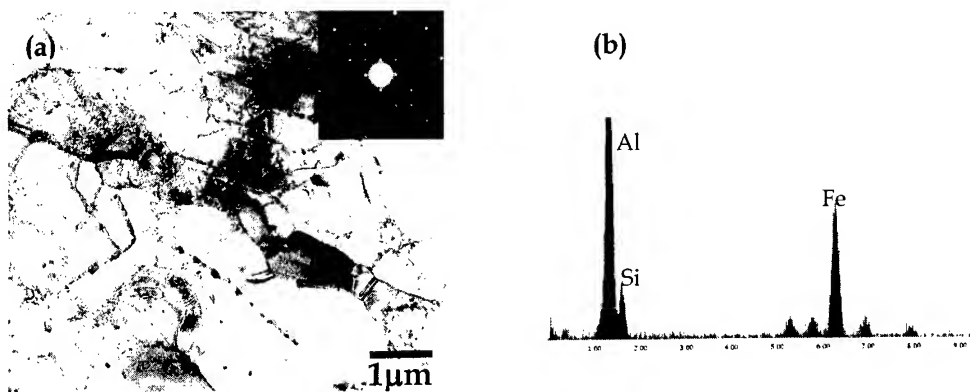


Fig. 4. a) BF micrograph of T6 treated SC6061 alloy showing α -AlFeSi particles along grain boundaries and b) EDS spectra from α -AlFeSi particles.

T6 heat treatment of the SC6061Mn alloy results in the similar microstructure to that of the base alloy. As shown in Fig. 5a, however, there is a larger volume fraction of second phase particles within the matrix in the SC6061Mn alloy than in the SC6061 alloy. These particles have the same crystal structure as α -AlFeSi particles observed in the SC6061 alloy but contain Mn besides Al, Si and Fe as shown in Fig. 5b. It can also be seen that there are some particles which are rod-shaped; however, diffraction analysis shows that these particles are

also α -AlFeSi particles. Although such type of particles are known to be detrimental to mechanical properties due to their asymmetric morphology, it might not be the case in the present study since they exist as fine particles. The volume fraction of Mg_2Si particles in the T6 treated SC6061Mn alloy is very small. This is mainly due to the fact that the SC6061Mn alloy contains a larger volume fraction of α -AlFe(Mn)Si particles than the SC6061 alloy, thereby decreasing the amount of Si available for the formation of Mg_2Si particles in the former.

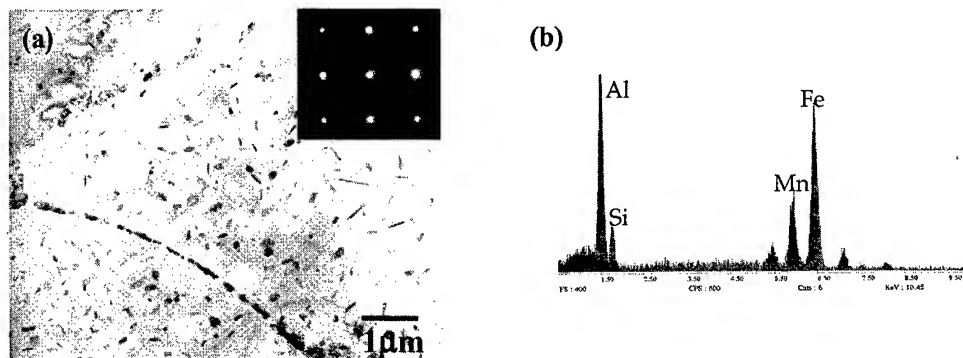


Fig. 5. a) BF micrograph of T6 treated SC6061Mn alloy showing α -AlFe(Mn)Si particles along grain boundaries and within Al matrix and b) EDS spectra from α -AlFe(Mn)Si particles.

4. Mechanical Properties

Tensile properties of the ingot cast and rolled commercial IM6061 alloy are also shown for comparison purposes (Table 2). It shows that the SC6061Mn alloy has a higher ultimate tensile strength than the SC6061 alloy with equivalent elongation. Ultimate tensile strength of the SC6061 alloy is slightly lower than that of the IM6061 alloy, but the addition of Mn results in higher ultimate tensile strength and elongation than the IM6061 alloy.

Table 2. Tensile Properties of Strip Cast Alloys

	YS (MPa)	UTS (MPa)	El. (%)
SC6061	197	326	23
SC6061Mn	176	350	24
IM6061	240	330	22

Although the exact contribution of each phase to the overall strength of the strip cast alloys is not known, it is expected that the yield strength of the strip cast alloys is mainly controlled by the more densely populated Mg_2Si particles. Therefore, the SC6061 alloy, which has a larger volume fraction of Mg_2Si particles, shows higher yield strength than the SC6061Mn alloy. It shows that the SC6061Mn alloy has higher ultimate tensile strength with equivalent elongation than the SC6061 alloy despite its lower yield strength. Analysis of the stress-strain curves shows that the SC6061Mn alloy has a higher work hardening rate than the SC6061 alloy. This is undoubtedly due to a larger volume fraction of α -AlFe(Mn)Si particles in the SC6061Mn alloy than in the SC6061 alloy. Unlike the Mg_2Si particles which are susceptible to shearing by dislocations, α -AlFe(Mn)Si particles are incoherent with Al matrix [19] and thus induce the bypassing of dislocations [20]. In general, shearable precipitates do not

contribute to work hardening significantly since there is no multiplication of dislocations around precipitates. Rather, they often cause severe planar slip. On the other hand, non-shearable dispersoids significantly contribute to work hardening since there is multiplication of dislocations around dispersoids. Hence the SC6061Mn alloy shows a higher work hardening rate and accordingly a higher ultimate tensile strength than the SC6061 alloy.

5. SUMMARY

1. The microstructure of the strip cast alloys consists of fine cell structure with Si particles along cell boundaries. Inside cell structure, there is a development of dislocation subgrains which are caused by hot rolling effect during strip casting.
2. During heat treatment, Si particles transform into α -AlFeSi particles, resulting in a dispersion of α -AlFeSi particles along grain boundaries in the base alloy. The addition of Mn results in an increase in the volume fraction of α -AlFe(Mn)Si particles in the Al matrix.
3. The base alloy has higher yield strength but lower ultimate tensile strength than the Mn containing alloy. The Mn containing alloy shows a much higher work hardening rate than the base alloy due to the presence of α -AlFe(Mn)Si dispersoids in the Al matrix of the former.

REFERENCES

1. Frishchkech, B. and Maiwald, K. P., *Light Metals 1988* (ed. by Boxall, L. G.), TMS, Warrendale, PA, 1988, 369.
2. Merchant, H. D., Kattamis, T. Z., and Morris, J. G., *Continuous Casting of Non-Ferrous Metals and Alloys* (eds. by Merchant, H. D., Taylor, D. E., and Chia, E. H.), TMS, Warrendale, PA, 1989, 1.
3. Hazalden, L. O., Geiast, G. J., and Parker, B. A., in Ref. 2, p.163.
4. Wood, J. V., *Materials Science and Technology*, 1988, **4**, 189.
5. Clyne, T. W., *Metals Technology*, 1984, **112**, 350.
6. Shibuya, K. and Ozawa, M., *ISIJ Int.*, 1991, **31**, 661.
7. Buchner, A. R. and Schmitz, J. W., *Steel Research*, 1991, **62**, 346.
8. Tsuji, N., Tsuzaki, K., and Maki, T., *ISIJ Int.*, 1992, **32**, 1319.
9. P. Vangala et al., *Melt-spinning and Strip Casting* (ed. by Matthys, E. F.), TMS, Warrendale, PA, 1992, 225.
10. Yasunaka, H., *ISIJ Int.*, 1995, **35**, 784.
11. Robson, A. L., Thompson, G. L., Longdon, P. and Wilkinson, A., *Thermec '97* (ed. by Chandra, T.), TMS, Warrendale, PA, 1997, 2263.
12. Petry, C. J., *Aluminum Alloys – Physical and Mechanical Properties* (eds. by Starke, Jr., E. A. and Sanders, Jr., T. H.), EMAS, U. K., 1986, 111.
13. Loria, E. A., *Aluminum Alloys – Physical and Mechanical Properties* (eds. by Starke, Jr., E. A. and Sanders, Jr., T. H.), EMAS, U. K., 1986, 133.
14. Saito, Y., Tsuji, N., Nagai, Y., and Sakai, T., *Thermec '97* (ed. by Chandra, T.), TMS, Warrendale, PA, 1997, 2381.
15. Koh, H. J. and Kim, N. J., *J. of the Korean Institute of Metals and Materials*, 1998, **36**, 2027.
16. Koh, H. J. and Kim, N. J., *J. of the Korean Institute of Metals and Materials*, 1998, **36**, 2035.
17. Koh, H. J., Park, W. J., and Kim, N. J., *Materials Transactions JIM*, 1998, **39**, 982.
18. Park, W. J., Ahn, S. and Kim, N. J., *Mat. Sci. Eng.*, 1994, **A189**, 291.
19. Kim, N. J., *International Journal of Rapid Solidification*, 1991, **6**, 175.
20. Kim, I. S., Kim, N. J., and Nam, S. W., *Scripta Metallurgica et Materialia*, 1995, **32**, 1813.

A REVIEW OF THE EFFECT OF RETROGRESSION AND REAGING ON ALUMINUM ALLOY 7249

Koziar, K., Fleck, P., Davila, G., Fromer, E., Leal, M., Pech, H., Foyos, J., Lee, E.W.*, Sarkar, B.*, and Es-Said, O.S.

National Science Foundation
Research Experience for Undergraduates Program
Loyola Marymount University
Los Angeles, CA 90045-8145

*Naval Air Systems Command
Naval Air Warfare Center Code 4342
MS Bldg 2188
Patuxent River, MD 20670-1908

ABSTRACT

Retrogression and reaging (RRA) consists of heating T6 samples at high temperatures below the solvus line for a short time and then reaging them to the original T6 treatment. The effect of RRA on improving the tensile strength and corrosion resistance properties of 7249-T76 aluminum alloy is reviewed. The retrogression heat treatments were carried out in the temperature range of 170°C to 210°C from 20 to 120 minutes. Reaging was done similar to the optimized T6 treatment.

1. INTRODUCTION

Retrogression and Reaging (RRA) is a multi-step process heat treatment which involves taking the 7xxx series aluminum alloy in the T-6 temper, retrogressing it by heating it to a high temperature for a short time, quenching, then reaging the alloy at a low temperature for a long, similar to the T-6 aging time [1, 2]. This results in an optimized combination of the stress corrosion cracking resistance of the T-7 temper and the strength of the T-6 temper.

If the material could be heated to a temperature high enough to allow the dislocations to disappear, but without causing overaging, the susceptibility to stress corrosion cracking should be decreased. Retrogression should be carried out at a temperature below the solvus line of the material, but high enough to allow the dislocations to disappear. Reaging is done to bring the material back to its original yield strength (i.e. that of the T-6 temper) [1, 3].

J.K. Park, [4], studied the influence of retrogression and reaging treatments on the stability of the various phases in aluminum alloy 7075-T6. The resistance to SCC of the retrogressed and reaged T-6 temper was due to coarsening of the grain boundary precipitates. The initial loss of strength, which was the result of the retrogression treatment, was due to the partial or complete dissolution of small η' particles. The crack growth rate for the RRA samples studied were both along the order of magnitude of that of the T73 condition, which is two orders of magnitude less than the T6 condition. The crack growth rate decreased with the

increase in the areal fraction of the grain boundaries covered by particles. It also decreased with the increase in particle size (i.e. coarsening) and the decrease in particle density, [4].

The resistance to stress corrosion cracking without loss of strength, which is obtained through the RRA process, is the coarsening of second-phase particles at the grain boundaries and the increase in volume fraction of second-phase particles at the grain interior, [4-6].

It was suggested that retrogression be carried out in the range of 200 to 260 °C, while reaging should be at 120°C, [3]. While original retrogression times ranged from a few seconds to a few minutes, subsequent research showed that retrogression times could be increased if the retrogression temperature were to be decreased, [7].

2. RRA HEAT TREATMENT OF 7249 ALLOY

Al-7249 is an Al-Zn-Mg-Cu-Cr alloy developed as a derivative from 7149; the chemistry of the alloying elements are shown in Table I. It was developed as a replacement material for 7075-T6 forgings, which are susceptible to SCC.

Table I: Composition of 7249:

	Wt. %
Zn	7.5-8.2
Mg	2.0-2.4
Cu	1.3-1.9
Cr	0.12-0.18
Fe	< 0.12
Si	< 0.10
Mn	< 0.10
Ti	< 0.06
other, each	< 0.06
other, total	< 0.15

7249 alloy was received as wide extrusions. The wide extrusions were received as plates with fins. The dimensions are as shown in figure 1. Samples were machined parallel to the extrusion direction, [8]. Additional samples were also machined in the 90°, 45° and fin 0° angles.

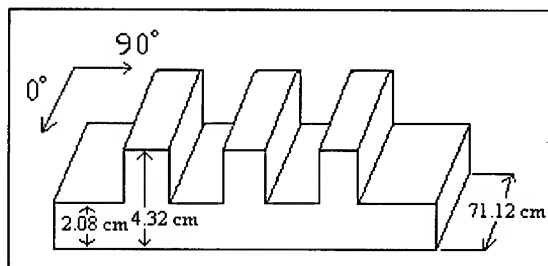


Fig. 1: Wide Extrusions, [8]

2.1 Optimization of T-6 Temper from the Wide Extrusions

Since this alloy system is relatively new, a T-6 optimization treatment needed to be established. T-6 optimization for the wide extrusions consisted of solution treating, naturally aging, then artificially aging samples at various temperatures and times, Tables (IIa) and (IIb), [8]. All samples were taken from the 08 direction from the wide extrusions.. There were three samples per combination. All samples were solution treated at their respective time and temperature, then water quenched. They were then naturally aged for 48 hour, after which they were kept in the freezer until they were artificially aged. All samples were artificially aged at 1218C at their respective times. After artificial aging, all samples were air-cooled, then tensile tested.

A multi-step solution treatments were performed to observe if there were any quantitative differences in the mechanical properties of the alloy from the different solution treatments.

Table IIa: Solution Treatment

1 hr @ 4638C
1 hr @ 4748C
1 hr @ 3638C + 1 hr @ 4138C + 2 hrs @ 4698C
1 hr @ 3748C + 1 hr @ 4248C + 2 hrs @ 4748C

Table IIb: Aging at 1218C

24 hrs
36 hrs
48 hrs
60 hrs

2.2 Retrogression and Reaging

After the optimum T-6 condition was performed (i.e. they were solution treated for 1 hour at 4748C, water quenched, naturally aged for 48 hours, then artificially aged at 1218C for 24 hours), the samples were retrogressed and reaged, [8]. Optimization of retrogression and reaging then consisted of various retrogression times and temperatures. The retrogression temperatures were 170, 180, 190, and 2108C and the times varied from 20 to 120 minutes. The reaging time and temperature was the same time and temperature used for the T-6 condition, (i.e. 1218C for 24 hours).

2.3 Results

The best results for the T-6 optimization was 1 hour at 474° C and 24 hours @ 121°C, respectively, [8]. The 0.2% yield and ultimate strength for this combination was 591.9 and 655.2 MPa respectively.

For the optimization of the T-6RRA temper, the best 0.2% yield and ultimate strengths were 640.1 and 662.1 MPa respectively. The retrogression time and temperature was 60 minutes at 170°C, figure 2. The percent elongation for this time and temperature was 7.60%; the conductivity was 35% IACS, with a corresponding resistivity of 5.7 micro-ohm-cm, figure 3.

Figure 3: Resistivity of RRA Treated 7249, [8]

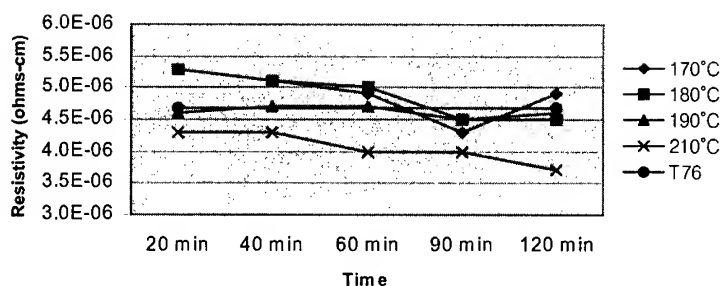
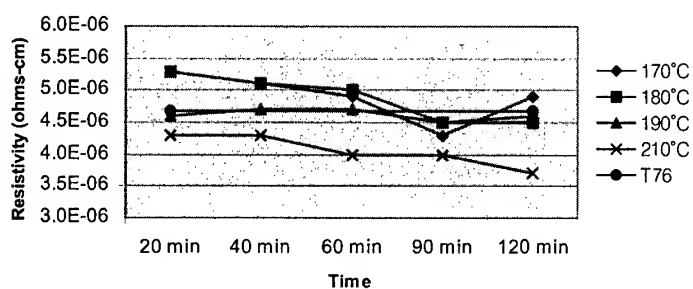


Figure 3: Resistivity of RRA Treated 7249, [8]



A set of 40 samples which were first brought to the T-6 temper, retrogressed, then reaged for 24 hours had mean 0.2% yield and ultimate strengths, standard deviations and percent anisotropy as shown in Table III.

Table III T6 Retrogressed and Reaged for 24 Hours

Degree Orientation (in regards to Extrusion Direction)	0.2% Yield Strength (MPa)			Ultimate Strength (Mpa)		
	Mean	Standard Deviation	Percent Anisotropy	Mean	Standard Deviation	Percent Anisotropy
45	571.9	1.8	12.5%	601.5	1.2	9.8%
90	608.4	2.7		638.7	1.4	
0	653.2	1.1		667.0	2.1	
0 - Fin	630.4	2.8		655.2	1.9	

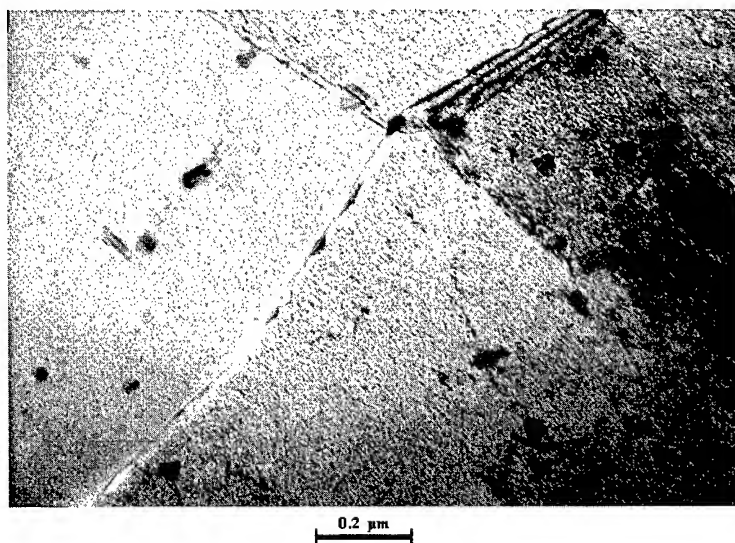
EXCO tests performed on samples retrogressed at 180C for 60 minutes indicated that the RRA samples had better exfoliation corrosion properties at short intervals as compared to the T-76 and T-6 tempers, Table IV [8].

Table IV EXCO Corrosion Test, [8]

5 Hrs	T6	Pitting & copper redepositing on the surface		
	T76	Light pitting & copper redepositing on the surface		
	RRA	Very light pitting with copper in the scratch pattern		
24 Hrs	T6	EB	EB	EB
	T76	EB	EB	EB
	RRA	EB	EB	EB
	All the EB surfaces with copper layers dissolved off or lifted and floated away from the surface			
48 Hrs	T6	EC	EC	EC
	T76	EC	EC	EC
	RRA	EC	EC	EC

A microstructural characterization study is underway to evaluate the particle size and distribution in the RRA sample. Figure 4 reveals relatively large sized precipitates on the grain boundaries and in the grain interior of RRA 7249 sample which was retrogressed at 170°C for 1 hour and reaged, [9].

Figure 4: 7249-RRA



3. CONCLUSIONS

The recommended T6 heat treatment for the wide extrusions is solution treating at 474°C for one hour, water quenching, naturally aging for 48 hours, then artificially aging for 24 hours at 121°C. For strength, the best retrogression time and temperature for the wide extrusions is 170°C for 1 hour.

The purpose of retrogression and reaging is to find the best strength and resistance to stress corrosion cracking; because of this, the best retrogression and reaging treatment is not always the one which exhibits the greatest strength. Therefore, the recommended retrogression treatment that might provide good strength and stress corrosion cracking resistance is 180°C for 60 minutes, then reage each for 24 hours at 121°C as shown in the EXCO test. Further optimization studies and microstructural characterization are underway.

Acknowledgements

This work was funded by the National Science Foundation (NSF) Grant No. EEC-9732046, Research Experiences for Undergraduates (REU) Site.

REFERENCES

1. B. Cina and R. Gan, "Reducing Stress Corrosion Cracking in Aluminum Alloys." U.S. Patent 3856584, December 24, 1974.
2. R.S. Kaneko, Metal Progress, 1980. Volume 117. pp 41-43.
3. M. Talianker and B. Cina, Metallurgical Transactions A, 1989. Volume 20A. pp 2087-2092.
4. J.K. Park, Materials Science and Engineering, 1988. Volume A103. pp 223-231.
5. J.K. Park and A.J. Ardell, Metallurgical Transactions A, 1983. Volume 14A. pp 1957-1965.
6. J.K. Park and A.J. Ardell, Metallurgical Transactions A, 1984. Volume 15A. pp 1531-1543.
7. P. Fleck, et al, in Aluminum Alloys, Their Physical and Mechanical Properties – eds E.A. Starke, Jr., T.H. Sanders, Jr. and W.A. Cassada Proceedings ICAA7, (2000). Part 1, pp 649-654.
8. P. Fleck, et al, in Light Weight Alloys for Aerospace Applications V, eds E.W. Lee, W. Frazier, N. Kim and K. Jata, TMS, Warrendale, PA (2001), in press.
9. K. Koziar, et al, to be submitted to the Journal of Materials Engineering and Performance.

EFFECT OF RETROGRESSION AND REAGING ON BAKE HARDENABILITY IN AL-MG-SI-(CR, BE) ALLOYS

K. D. WOO, J. S. LEE, C. H. Yang, H. C. Park and S.W.Kim

Division of Advanced Materials Engineering & The Research Institute of Industrial Technology, Chonbuk National University, 664-14, Dugjin-dong, Chonju 561-756, KOREA

ABSTRACT

The effect of additional elements, pre-aging and RRA treatment on the bake hardenability of Al-Mg-Si alloys will be investigated. RRA (retrogression and reaging) is useful heat treatment method to increase the SCC in Al-Zn-Mg-Cu (7XXX) system alloys. The bake hardenability of Al-Mg-Si alloy has been improved by the addition of Cr and Be due to increase of β'' (Mg_2Si) precipitate density. Moreover the bake hardening is also improved by retrogression and reaging (pre-aged at 120°C, followed by baked at 225°C for 3min and re-aged at 180°C for 30 min) and two-step aging treatment (pre-aged at 120°C, followed by re-aged at 180°C/30min) in Al-Mg-Si-(Cr,Be) alloys. The pre-aged time at 120°C in RRA influenced the mechanical properties like elongation and strength, and formability in Al-Mg-Si- (Cr, Be) alloys. Therefore, RRA (retrogression and reaging) is very useful heat treatment method to improve the bake hardenability in Al-Mg-Si system alloys.

1. INTRODUCTION

Al-Mg-Si system alloys are capable of providing a good combination of formability and paint bake response that has favored with automotive penal applications. Cr and Be are useful elements to increase the elongation and strength respectively. The strength of Al-Mg-Si system alloys aged at ambient temperature for a long time, followed by artificial aging at 170-180°C are lower than that of artificial aging at 170-180°C without pre-aging at ambient temperature. This effect is well known as negative effect of strength in Al-Mg-Si alloys [1,2] because of G.P.I zone formation during pre-aging treatment. The bake hardenability decreases with increase of G.P.I zone content in Al-Mg-Si system alloys. Therefore, it is important to decrease or remove the G.P.I zone before bake treatment at 170-180°C in Al-Mg-Si alloys. Retrogression at high temperature is well known to effective heat treatment method to remove the G.P.I zones formed at ambient or low aging temperature [3]. In this study, RRA effect in Al-Mg-Si- (Cr,Be) alloys on bake hardenability has been investigated using hardness and tensile test, DSC(differential scanning calorimetry), TEM(transmission electron microscopy) and Erichsen test.

2. EXPERIMENTAL

The Al-Mg-Si-X (Cr, Be) alloys were fabricated by a high frequency melting furnace under Ar atmosphere, with pure (99.99%) aluminum, high purity master alloys of Al-10%Mg, Al-20%Si, Al-2.5%Be and Al-75%Cr. The alloy designs and chemical compositions of the specimens are shown in Table 1.

Table 1 Alloy designs and chemical compositions of Al-Mg-Si-X (Be, Cr) alloys (wt.%)

Alloy designs	Mg	Si	Ti	Be	Cr	Al
Al-0.8%Mg-1.0%Si	0.85	1.02	-	-	-	Bal.
Al-0.8%Mg-1.0%Si-0.05%Be	0.86	1.09	0.01	0.054	-	Bal.
Al-0.8%Mg-1.0%Si-0.05%Be-0.1%Cr	0.98	0.95	0.01	0.057	0.1	Bal.

As-cast ingots were scalped, followed by homogenizing at 560 °C for 24 hrs, forged in thickness of 35 mm, and then were hot and cold rolled to strips of 1.2 mm. The specimens were solution treated at 550 °C for 0.5 hrs in salt bath, followed by quenched into iced water. Table 2 shows the processes of heat treatments used in this study.

Table 2 Aging processes used in this study.

Kinds of treatments	Processes
Preaging treatment	120 °C
Two step aging treatment	Pre-aging(120 °C) → Bake treatment(180 °C/30min)
RRA(Retrogression and Reaging) treatment	Pre-aging(120 °C) → Retrogression(225 °C/3min) → Bake treatment(180 °C/30min)

The hardness of specimens was conducted with Rockwell hardness tester. Using the automatic displacement measurement device-equipped Instron 25 ton multi purpose tester with the specimen of plate type carried out the tensile test. The crosshead speed of the tensile test was 2mm/min. To observe the fracture surface of the tensile tested specimens, SEM was used. The specimen size for Erichsen test is 100 x 100 x 1.7 (mm) plate. The experimental conditions of Erichsen test are as follows,

Diameter of tip of punch : 10±0.05 mm, Inner and outer diameter of dice : 27±0.05 mm, 55±0.05 mm, Inner and outer diameter of press plate: 33mm, 55mm

3. RESULTS AND DISCUSSION

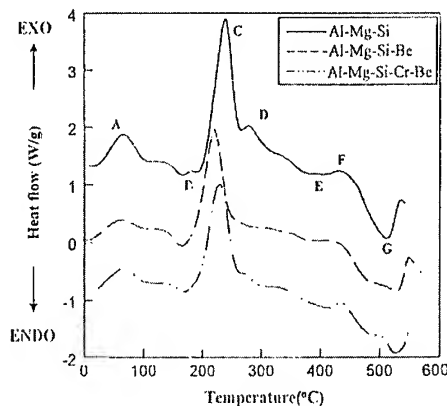


Fig. 1 DSC curve of as-quenched Al-0.8%Mg-1.0%Si-(Cr,Be) alloys(heating rate : 10 °C/min)

Fig. 1 shows the DSC thermograms of as quenched Al-Mg-Si-(Cr,Be) alloys analyzed with the heating rates of 10 °C/min. Four exothermic peaks A, C, D and F and three endothermic peaks B, E and G are shown. The four peaks A, C, D and F may be attributed to the precipitation of G.P.I zone, β'' , β' and β phase, respectively. The endothermic peaks B, E and G are due to the dissolution of G.P.I zone, β'' , β' and β phase respectively. By the addition of Be or Cr and Be in Al-Mg-Si alloy, the temperature of β'' precipitation shifts to the lower temperature. These results show that β'' phase in Al-Mg-Si-Be and Al-Mg-Si-Cr-Be alloys

precipitate at lower temperature than that in Al-Mg-Si alloy. Quantitative analysis of these peaks is shown in Table 3. The amounts of G.P.I zone formed during heat treatment in as-quenched Al-Mg-Si alloy were reduced by the addition of Be. And the onset temperature of G.P.I zone in Al-Mg-Si alloy is lower than that in Al-Mg-Si-

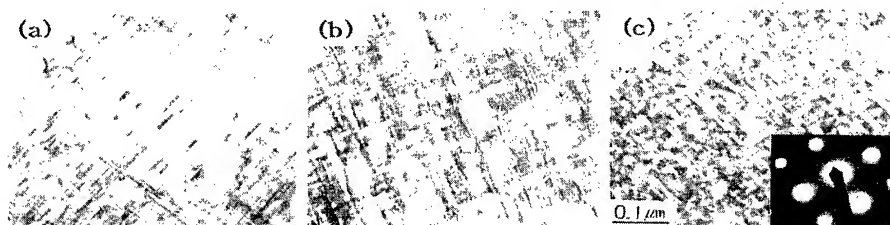


Fig. 2 Transmission electron micrographs of Al-0.8%Mg-1.0%Si(Cr,Be) alloys aged at 180°C for 4hr
(a) Al-Mg-Si alloy (b) Al-Mg-Si-Be alloy (c) Al-Mg-Si-Be-Cr alloy

Be or Al-Mg-Si-Be-Cr alloy due to Be addition.

Fig. 2 shows bright field TEM images of β'' phase, which obtained (100) zone axis, of Al-Mg-Si-(Cr,Be) alloys aged at 180°C for 4hrs. By the addition of Cr,Be in Al-Mg-Si alloy, needle-shaped β'' phases are shown the finer and denser distribution in comparison with the Be containing Al-Mg-Si alloy and Al-Mg-Si alloy. Be added Al-Mg-Si alloy aged at 180°C promoted the precipitation and growth of β'' phase.

Fig.3 shows the effect of pre-aging time in RRA treatment (as shown in Table 2) on hardness of Al-0.8%Mg-1.0%Si alloy and of Al-0.8%Mg-1.0%Si-0.1%Cr-0.05%Be alloy. The hardness of RRA treated Al-0.8%Mg-1.0%Si alloy increases with pre-aging time. The hardness of RRA treated specimen increased more than any other specimens and two-step aged specimens. This is because the content of β'' precipitate increases rather than that of other aging treatments (T6 and two-step aging) due to dissolution of G.P.I zone by retrogression at 225°C for 3min[4].

The effect of pre-aging time at 120°C on hardness of two-step aged and RRA treated Al-0.8%Mg-1.0%Si-0.1%Cr-0.05%Be alloy is similar to that of two-step aged and RRA treated Al-0.8%Mg-1.0%Si alloy. The hardness of two-step aged Al-0.8%Mg-1.0%Si-0.1%Cr-0.05%Be is higher than that of Al-0.8%Mg-1.0%Si alloy, especially for short pre-aging time at 120°C. This is because that the precipitation of G.P.I zone and β'' phase is promoted by the addition of Be in Al-0.8%Mg-1.0%Si alloy[4]. Also the hardness of RRA treated Al-0.8%Mg-1.0%Si-0.1%Cr-0.05%Be alloy is higher than any other hardness of ageing treated Al-0.8%Mg-

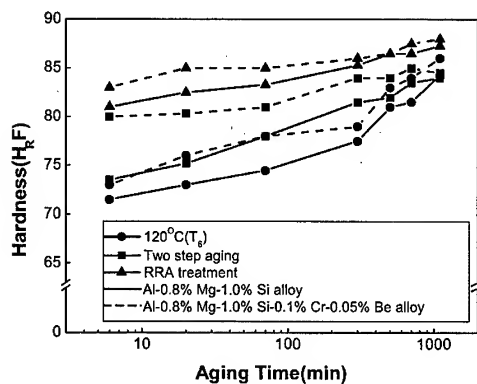


Fig. 3 Variation of hardness of two-step aging and RRA-treatment with pre-aging time of Al-0.8%Mg-1.0%Si and Al-0.8%Mg-1.0%Si-Cr-0.005%Be alloy pre-aged at 120°C.

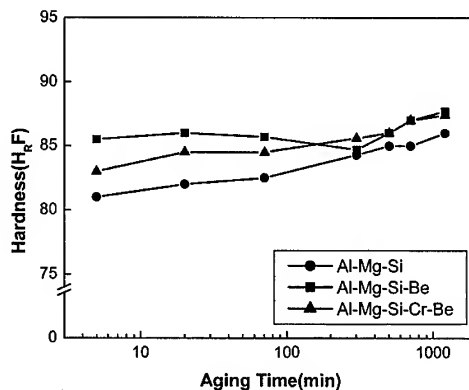


Fig. 4 Variation of hardness of Al-0.8%Mg-1.0%Si-(Cr,Be) alloys RRA treated 225°C for 3min after pre-aged at 120°C, and then aged at 180°C for 30min

1.0%Si alloy. Be is an effective element to dissolve the G.P.I zone retrogression aged at 225 °C.

Fig.4 shows the effect of pre-aging time at 120 °C in RRA treatment on hardness of Al-0.8%Mg-1.0%Si-(Cr, Be) alloy. The hardness increases with pre-aging time in all the alloys because the precipitation of G.P.I zone and β'' phase are suppressed by the formation of β'' phase during pre-aging at 120 °C. G.P.I zone deteriorated the bake hardenability at 180 °C, and β'' phase is an effective phase to increase hardness and strength. The hardness increases rapidly at early pre-aging time, but it increases slowly at long pre-aging time in Al-Mg-Si-Be. This is because the precipitation of GP I zones in Be added Al-Mg-Si alloy is accelerated due to decrease of the formation energy of G.P.I zone[4], but G.P.I zone formed at 120 °C is unstable at high temperature, so it is dissolved easily by aging at 225 °C. Therefore, the content of β'' precipitate in RRA treated Al-0.8%Mg-1.0%Si-(Cr, Be) alloy increases because of easy dissolution of G.P.I zone aged at 225 °C in Be added Al-Mg-Si alloy.

The hardness for short aging time of Cr and Be added Al-Mg-Si alloy is lower than that of Al-Mg-Si-Be alloy, because the precipitation of β'' phase is retarded because of lots of G.P.I zones which are stabilized by the addition of Cr in Al-Mg-Si-Be alloy[4], so the precipitation of β'' phase is difficult because the dissolution of G.P.I zone is difficult at early pre-aging time at 120 °C. But pre-aging at 120 °C for a long time, the hardness increase with formation of β'' phase and β' (Mg₂Si) phase. The hardness of all the RRA treated specimens is almost same if pre-aging time at 120 °C was long. This shows that RRA effect is not prominent if pre-aging

time at 120 °C is long.

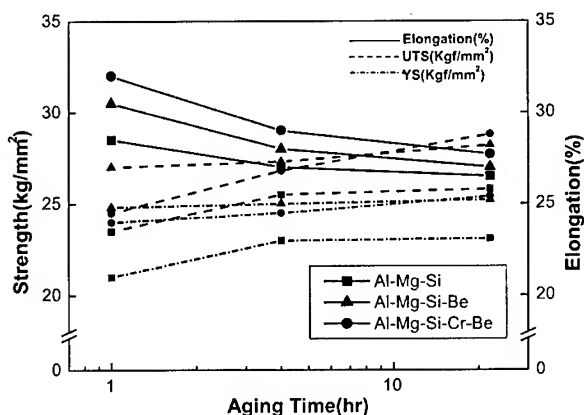


Fig. 5 Tensile Properties of Al-0.8%Mg-1.0%Si-(Cr,Be) alloys RRA treated after pre-aged at 120 °C.

1.0%Si-0.05%Be-0.1%Cr alloy is higher than those of commercial Al-Mg-Si system alloys (17- 22kgf/mm²)[5]. From this result, RRA treatment in Al-Mg-Si system alloys is very useful heat treatment method to enhance the bake hardenability for automobile body panels.

The formation of β'' phase and β' (Mg₂Si) phase in Al-0.8%Mg-1.0%Si-0.1%Cr-0.05%Be alloy, which is RRA treated after pre-aged at 120 for 1 hr, is easy due to increase of excess solute atoms by a dissolution of the G.P.I zone during retrogression at 225 °C for 3 min. Therefore, the strength and elongation of Al-0.8%Mg-1.0%Si-0.1%Cr-0.05%Be alloy, which is RRA treated after pre-aged at 120 °C for 1hr, are higher than those of the Al-0.8%Mg-1.0%Si-(Be) alloys two-step aged at 180 °C for 30min after pre-aged at 120 °C. Cr is known as an effective element to increase the strength and deformability in Al-Mg-Si alloy[6,7,8] due to decrease the grain size[8], increase nucleation rate of GP zone[7], but Choi [9] reported that Cr caused to decrease the strength in Al-Mg-Si alloy. In our study, Cr is also an effective element to increase the strength and toughness. The

Fig.5 shows tensile properties of Al-0.8%Mg-1.0%Si-(Cr, Be) alloy, which is RRA treated after pre-aged at 120 °C for 1, 4 and 24hrs. The strength of all the specimens increases slowly with increase of pre-aging time, but the fracture elongation decreases rapidly with increase of pre-aging time. The ultimate tensile strength (UTS) of Al-0.8%Mg-1.0%Si-0.05%Be-0.1%Cr alloy, which is RRA treated after pre-aged at 120 °C for 1 hr, is 27kgf/mm². And the yield strength (24-25kgf/mm²) of Al-0.8%Mg-1.0%Si-0.05%Be-0.1%Cr alloy, which is RRA treated after pre-aged at 120 °C, is similar to that of Al-0.8%Mg-1.0%Si-0.05%Be alloy, but yield strength of Al-0.8%Mg-

formation of G.P.I zone is retarded at the aging temperature of 120°C[9], so 120°C is useful pre-aging temperature to eliminate the negative effect of G.P.I zone for bake hardenability. Even if GPII zone (β'' phase) is formed being aged at 120°C, this GPII zone is easily dissolved into matrix by retrogression treated at 225 for 3 min due to instability by the addition of Cr in Al-Mg-Si[7]. As the structure of GPII zone is similar to the structure of G.P.I zone because Cr combines with the quenched-in vacancies.

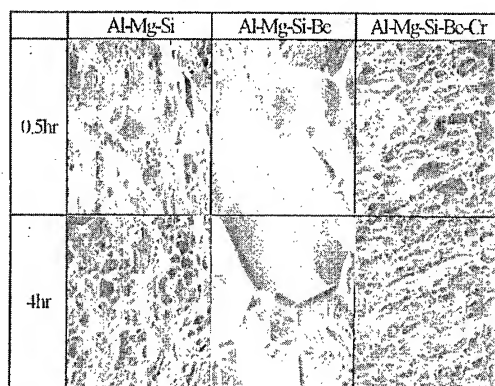


Fig. 6 Scanning electron micrographs of tensile fracture surfaces of Al-0.8%Mg-1.0%Si-(Cr,Be) alloys RRA-treated after pre-aged at 120°C

Fig.6 shows the fractographs of tensile fracture surfaces of Al-0.8%Mg-1.0%Si-(Cr, Be) alloys RRA treated after pre-aged at 120°C for 1 and 4hrs. The fracture surfaces of Al-0.8%Mg-1.0%Si and Al-0.8%Mg-1.0%Si-0.1%Cr-0.05%Be alloys are transgranular fracture surface. But the prominent intergranular fracture surfaces are shown in Be added Al-Mg-Si alloy aged at 120°C. From this result, Be is not effective element to increase the toughness and elongation.

Table 3 shows the relation between the yield strength, elongation and Erichsen value of Al-0.8%Mg-1.0%Si-0.1%Cr-0.05%Be alloy.

The strength of Al-0.8%Mg-1.0%Si-0.1%Cr-0.05%Be alloy by two-step aged at 180°C for 30min after pre-aged at 120°C for 4hr and RRA

treated after pre-aged at 120°C for 4hr is higher than two step aged at 60°C for 4hr followed by 180°C for 30 min in Al-0.8%Mg-1.0%Si-0.1%Cr-0.05%Be alloy. The Erichsen value of Al-0.8%Mg-1.0%Si-0.1%Cr-0.05%Be alloy is similar to other heat treatment methods like two-step aging treatment[4]. Cr, Be added alloy has good Erichsen value, which is 9.8, because Cr element decreases the grain sizes[7]. This Erichsen value is similar to that in commercial Al-Mg-Si system alloys which developed to use automobile panel materials [5]. Strain hardening exponent, n which is deformability factor, is 0.27 in RRA treated Al-0.8%Mg-1.0%Si-0.1%Cr-0.05%Be alloy[4]. This value is higher than that (n is 0.22 or 0.23) of commercialized Al-Mg-Si system alloys [5]. But in Be added Al-0.8%Mg-1.0%Si alloy, the Erichsen value(Er) and deformability factor (n) decrease because of increase the precipitates content at grain boundary[4]. This is because grain boundary precipitates enhance the intergranular fracture. Therefore, to improve the deformation property, it is important to decrease the grain size and reduce the grain boundary precipitate.

RRA treated Al-0.8%Mg-1.0%Si-0.1%Cr-0.05%Be alloy after pre-aged at 120°C has better combination of yield strength, elongation and Erichsen value than other.

Table. 3 Yield strength, Elongation, and Erichsen value of Al-0.8%Mg-1.0%Si-0.1%Cr-0.05%Be alloy

	Yield Strength (kg/mm ²)	Elongation (%)	Erichsen Value (Er : mm)
60°C/4hr → bake	23	31	10
120°C/4hr → bake	27	29	9.7
120°C/4hr 225°C/3min → bake	28	29	9.8

4. CONCLUSIONS

The effect of additional elements, pre-aging and RRA treatment on the bake hardenability of Al-Mg-Si alloys has been investigated. This study has been examined by means of measurement of hardness, tensile test, transmission electron microscope, differential scanning calorimetry, and Erichsen test.

The hardness, strength and deformability were enhanced by RRA(120°C for 1hr/225°C for 3min/180°C for 30min) treatment in of Al-0.8%Mg-1.0%Si-0.1%Cr-0.05%Be alloy, because G.P.I zone easily decomposed during retrogression treatment at 225°C for 3 min by the addition of Be and Cr in Al-Mg-Si alloy. The bake hardenability of Al-Mg-Si alloy has been improved by the addition of Cr and Be due to increase of β'' (Mg_2Si) precipitate density. Moreover, the bake hardening was also improved by RRA(pre-aged at 120°C, followed by baking at 225°C for 3min and re-aged at 180°C for 30 min) and two-step aging treatment (pre-aged at 120°C / re-aged at 180°C for 30min) in Al-Mg-Si-(Cr,Be) alloys. The pre-aged time at 120°C in RRA influenced the mechanical properties like elongation and strength, and formability in Al-Mg-Si- (Cr, Be) alloys. Therefore, RRA is very useful heat treatment method to improve the bake hardenability in Al-Mg-Si system alloys.

ACKNOWLEDGEMENTS

This work has been carried out with the financial supports of the Research Institute of Industrial Technology(RIIT) in Chonbuk National University.

REFERENCES

1. P.E.Fortin : Mat Prog., 86(1964) 119
2. D.W.Pashley, J.W.Rhodes and A.Sendorek : J.Inst.Metals, 94(1966) 41
3. M.U.Islam and W.Wallace, Metals Tech., 10(1983) 384
4. J.S.Lee, Ph D thesis, Chonbuk National University, Korea (1999)
5. M.Hino and M.Hirano, Kobe steel engineering reports, 38 (1988) 15-22
6. O.Engler and J.Hirsch, Mater. Sci. Forum, 217-222 (1996) 479
7. M.Yanagawa, M.Abe and S.Ohie, J. Jpn. Inst. Light Metal, 46 (1996) 27
8. M.Yanagawa, M.Abe and S.Ohie, J. Jpn. Inst. Light Metal, 46 (1996) 33
9. H.Choi, K.A.Kim, S.Y.Jeong, and D.N.Kim, J. Kor. Inst. Mat & Mater., 35(1997) 429

INFLUENCE OF RETROGRESSION AND REAGING (RRA) TREATMENTS TO AN Al-Li-Cu-Mg-Zr ALLOY ON MECHANICAL PROPERTIES AND STRESS CORROSION CRACKING BEHAVIOUR.

K. S. Ghosh, K. Das* and U. K. Chatterjee*

Department of Metallurgical Engineering, Regional Engineering College,
Warangal – 506 004, India. ksgghosh@metal.iitkgp.ernet.in

*Department of Metallurgical and Materials Engineering, Indian Institute
of Technology - Kharagpur- 721 302, India.

ABSTRACT

The high strength, aluminum alloys are susceptible to environmental induced cracking (EIC) in the peak aged tempers. A treatment, called retrogression and reaging (RRA), combining the beneficial effects of peak aging and over aging tempers, is a way to improve the EIC resistance. Retrogression was carried out for a 8090 Al-Li-Cu-Mg-Zr alloy at temperatures below and above the δ^1 solvus line for varying time ranging from 30 sec to 45 minutes and immediately reaging to peak aged temper. Hardness and tensile properties were studied. The susceptibility to stress corrosion cracking (SCC) has been studied on peak aged (T8), over aged (T7) and retrogression and reaging treated 8090 Al-Li-Cu-Mg-Zr alloys by using slow strain rate technique (SSRT) and constant load technique. The effects of applied potentials have also been studied. Retrogression and reaging (RRA) treatment on 8090 alloy have been found to improve the SCC resistance.

1. INTRODUCTION:

Aluminum alloys containing lithium are candidate alloys for aerospace industries because of reduction in density, increase in elastic modulus and increase in specific strength over the most widely used aluminum alloys 2024 and 7075 [1]. Their mechanical properties are strongly sensitive to processing conditions, and therefore, the product quality is more difficult to control than for conventional alloys. Al-Li alloys have unattractive fracture behaviour, especially poor ductility compared to traditional high strength alloys [2]. The weight saving and increased stiffness benefits of Al-Li alloys are much useful to the aerospace vehicle designers provided the alloys are relatively immune to environmental induced cracking (EIC). Alloys based on Al-Li-Cu-Zr and Al-Cu-Li-Zr systems are known to exhibit maximum resistance to stress corrosion crack initiation in the near peak aged condition, whereas the magnesium containing Al-Li-Cu-Mg-Zr alloys exhibit maximum resistance to crack initiation in the over aged condition. Various techniques are used for studying SCC susceptibility of 8090 systems. The literature shows that there are no consistent trends of SCC susceptibility of

Address of correspondence: K. S. Ghosh, RS(QIP), C/o Prof. U. K. Chatterjee, Professor,
Dept. of Met. & Mats. Engg., IIT-Kharagpur- 721 302, India

the different aging tempers. It has been proposed that the SCC susceptibility of 8090 alloys is due to film rupture by anodic dissolution and/or by hydrogen embrittlement [3,4,5,6,7]. Generally the high strength aluminum alloys are susceptible to stress corrosion cracking (SCC) in the peak aged (PA), T6x or T8x tempers. The over aging (OA) temper (T7x) has an acceptable SCC resistance, but has lower strength by 10-15%. Retrogression and reaging (RRA) treatments are ways to avoid this problem [8]. Commercial retrogression heat treatments could be identified by the T77xx designation. RRA treatments produce microstructures in the grain boundaries that closely match with those found in the T7x microstructures and with lower dislocations density compared to peak aged temper due to annihilation of some dislocations at the retrogression temperature [9,10]. Low-high-duplex ageing (LHDA) treatment comprises reaging the retrogressed alloy at lower temperature than the isothermal reaging temperature followed by higher temperature stage for short time [11]. The paper deals with the studies of mechanical and stress corrosion properties of a 8090 alloy in the peak aged, over aged and retrogressed and reaged tempers.

2. EXPERIMENTAL PROCEDURE:

The alloy 8090 was obtained from Defence Metallurgical Research Laboratory, Hyderabad, India, in sheet form having a thickness of 2.8 mm. The alloy was cast, homogenised, hot rolled and cold rolled to required thickness. The cold rolled sheets were solutionised at 530 - 535°C, water quenched, stretched 1.5- 2.5 %, followed by artificial aging at 170°C for 24 hours corresponding to peak aged (PA) temper. The chemical composition (in wt%) of the 8090 is 2.29% Li, 1.24% Cu, 0.82% Mg, 0.12% Zr, 0.09% Fe, 0.004% Si and balance Al. Coupons of approximate dimensions of 10 X 10 X 2.5 mm³ for hardness and tensile specimens for SSRT and constant load testing, cut from the as received 8090 alloy sheet, were retrogressed in air in a small vertical tube furnace. Retrogression temperatures were chosen above and below the δ^1 solvus line. After a precise time of holding in the furnace, specimens were quenched into ice-cold water followed by reaging to peak aged strength. Retrogression and reaging schedule to which the specimens were subjected are given in Table 1.

Table 1: Retrogression and Reaging treatments to 8090 peak aged as received alloy

Specimens	Retrogression temperatures, 0°C	Retrogression time	Isothermal reaging	Low-high-duplex reaging (LHDA)
For hardness	250 and 280	30 sec to 45 mins	170°C for 24 hours	150°C for 26 hours plus 210°C for 1 hour
Tensile specimens	250	12 mins	-do-	-do-
	280	8 mins		

Tensile specimens, transverse to rolling direction, obtained from as received sheet, had the following dimensions: 25 mm extended gauge length, 4 mm width and 2.5 mm thickness. The surfaces of the gauge portion of the tensile specimen were ground to 100 μ m minimum so as

to remove the lithium and magnesium depleted zones, developed during solutionising carried out in air at 535°C, followed by polishing of the gauge portion.

A constant elongation rate, CORRTEST machine was used for testing in laboratory air and in 3.5 % NaCl solution with a pH value of 6.9 under total immersion condition. SSRT tests with applied potentials were also studied, constructing an electrochemical cell with the specimen as a working electrode and a platinum counter electrode. Potentials were noted against saturated calomel reference electrode. Anodic and cathodic potentials were applied using an EG & G Princeton scanning potentiostat, model 362. Stress corrosion cracking studies were also carried out by constant load method using a Mayer's SC MK-2 testing unit with a lever ratio 30:1.

3. Results and Discussion

3.1 Hardness

Fig. 1 shows the variation of hardness vs. retrogression and reaging time at temperatures 250 and 280°C. The graphs exhibit the characteristic shape of retrogression and reaging. The hardness-retrogression curves have three distinct regions. There is an initial decrease in hardness, followed by an increase and again decrease in hardness. These stages are the result of the preferential dissolution of shearable coherent matrix δ' precipitates which are no longer stable at the retrogression temperature, the nucleation and growth of new stable phases and the overaging of the phases, respectively. The decrease in hardness on retrogression might also result due to the decrease of dislocation densities. The minimum in the retrogression curve is indicative of the maximum dissolution of δ' precipitates. Reaging the retrogressed alloy regained the hardness.

3.2 Tensile Properties

Table 2 gives the tensile properties of the alloy at various retrogression and reaging tempers at a strain rate of $3.5 \times 10^{-2} \text{ s}^{-1}$. The ultimate tensile strengths and plastic strains to fracture of the peak aged and retrogressed and reaged to peak aged tempers are of the same order. The strengths of only retrogressed alloys without reaging have decreased due to the dissolution of matrix strengthening δ' precipitates, but there is an increase of plastic strain to fracture compared to peak aged tempers.

3.3 Stress Corrosion Cracking

3.3.1 Slow Strain Rate Technique (SSRT)

The effect of strain rate on the SCC susceptibility was examined in the peak aged condition. Experiments were performed in air and in 3.5 % NaCl solution at five strain rates. Tests were repeated to confirm the results. The ratio of plastic strain to fracture in the environment to that in air ($\epsilon_{\text{NaCl}}/\epsilon_{\text{air}}$), called ductility ratio (DR), was used as a measure of SCC susceptibility. Fig. 2 shows the plot of ductility ratio (DR) vs. strain rates of 8090-T8 alloy. At high strain rates, the deformation rate is too rapid for electrochemical equilibrium to be achieved and hence there is limited susceptibility. At lower strain rates, the decrease of susceptibility is due to

higher repassivation rate at the crack tip than the process of slip step emergence and subsequent anodic dissolution.

The different aging treatments were the peak aging (PA), over aging (OA) and retrogression and reaging by isothermally and by low-high duplex ways corresponding to peak aged strength. Fig. 3, the bar diagram, shows the plastic strain to fracture in air and 3.5 % NaCl solution for peak aged, over aged and RRA treated samples. RRA and over aged samples showed more resistance to SCC susceptibility (using the strain to failure ratio criterion) compared to peak aged samples.

In the peak aged temper, the microstructure comprises a combination of equilibrium precipitates δ (AlLi), S (Al_2CuMg), T_2 (Al_6CuLi_3 or $\text{Al}_6\text{Cu}(\text{Li-Mg})_3$) on the high angle grain boundaries and fine δ' (Al_3Li), S' (Al_2CuMg) and T_1 within the grain matrix. The initiation of stress corrosion is apparently by the preferential dissolution of grain boundary precipitates accelerated by the propensity for planar slip leading to stress concentration at the grain boundary [11]. In isothermally over-aged tempers, equilibrium phases are additionally precipitated on sub-grain boundaries and heterogeneously within the matrix. As a result, the attack is more uniform, leading to an increase in SCC resistance. The low-high duplex reaging treatment also results in the development of fine and more homogenous distribution of δ' and S' precipitates and also formation of equilibrium phases at grain boundary and heterogeneously within the matrix, conferring the improved SCC resistance. The improvement in the SCC resistance is also attributed to the decrease of dislocation density [11].

Fig. 4 shows the stress strain curves of peak aged samples tested in air, 3.5% NaCl solution and with applied anodic and cathodic potentials. Under applied anodic potentials, both metal dissolution and hydrogen reduction take place while under applied cathodic potentials hydrogen reduction is the predominant reaction. Under anodic polarization, the susceptibility is most severe. Under applied anodic potential, the SCC susceptibility is severe, indicating that local anodic dissolution (LAD) plays an important role in the phenomenon.

3.3.2 Constant Load Test:

The constant load test results are given in Table 3. The results show that the time to fracture of retrogressed and reaged specimens is more compared to those with peak aged temper.

Table 3: Constant load test SCC results

Alloy Condition	Environment	Stress Applied, MPa	Time to fracture, h
Peak aged	3.5 % NaCl	370	528
R_280_170_-24	-do-	378	No failure till 528
Peak aged	3.5% NaCl + 0.1M LiCl + 0.3% H_2O_2	370	96
R 280 170 24	-do-	370	No failure till 150

4. CONCLUSIONS:

1) The higher the retrogression temperature and time, the more the decrease of hardness and strength values. This is due to an increased dissolution of δ^1 precipitates. 2) Retrogression and reaging treatments have been found to increase the resistance to SCC susceptibility of 8090 alloy. 3) SCC of 8090 alloy is aggravated under applied anodic potentials.

5. REFERENCES:

1. ASM Specialty Handbook, Aluminum and Aluminum Alloys, J. R. Davis, Davis & Associates, eds., ASM International, The Materials Information Society, (1998), pp 121-142.
2. K. T. Vekateswara Rao, W. Yu. and R. B. Ritchie, Metll. Trans. A, 19A(1988), pp. 563-569.
3. F. Binsfeld, M. Habashi, J. Galland, J. P. Fidelle, D. Miannay, P. Rofidal in 4th International Conference on Aluminum Lithium Alloys, G Champier, B Dupost, D Miannay, L Sabetay, eds., Les editions Journal de Physique, Paris, (1987), pp. C3:587-596.
4. A. Gray, *ibid*, pp. C3:891-904.
5. N. J. H. Holroyd, A. Gray, G. M. Scamans and R. Hermann, in the 3rd International Conference of Al-Li, C Baker, P.J. Gregson, S. J. Harris and C. J. Peel, eds., The Institution of Metals, London, (1986), pp. 310-320.
6. J. B. Lumsden and A. T. Allen, Corr. Sc. 44(1988), pp. 527 – 532.
7. C. Thakur and R. Balasubramaniam, Acta. Mater, 45(1997), pp. 1323-1332.
8. R. S. Kaneko, Metal Progress, April, (1980), pp. 41-43.
9. Z. Q. Hu, Y. Zhang, L. Liu and Z. Y. Zhu, Corrosion, 49(1993), pp. 491-498.
10. V. Kimosarov, M. Talianker and B. Cina, Mat. Sci. and Engg. A, 221(1996), pp. 113-121.
11. A. Gray, N. J. H. Holroyd, J white, in Vth International Conference on Aluminum and Lithium Alloys, Vol. III, Virginia, (1989), pp 1175-1186.

Table 2: Tensile Properties of 8090 at various tempers.

Tempers	UTS, MPa	Total Strain, %	Plastic Stain to fracture, %
Peak aged	446.17	7.92	5.28
R_280_8	335.43	12.352	8.24
R_250_12	345.9	10.796	8.04
(R_280_8_170_24)	446.12	8.656	5.79
(R_250_12_170_24)	434.11	7.02	5.08
(R_280_8_LHDA	418.12	9.056	6.01
(R_250_12_LHDA	413.7	7.724	5.67
Peak aged + 170_96	434.292	8.64	5.30

R_280_8: Retrogression at 280°C for 8 minutes; R_280_8_170_24: Retrogression at 280°C for 8 minutes and immediately reaging at 170°C for 24 hours. LHDA: low-high-duplex aging.

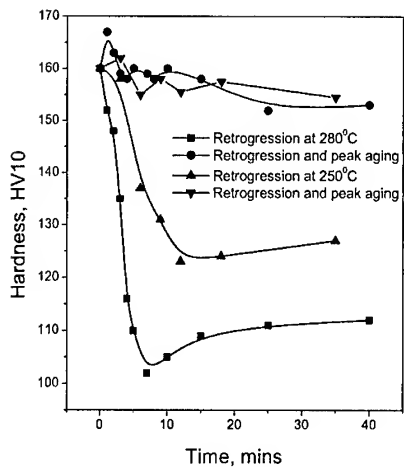


Fig 1: Plot of hardness vs retrogression time of 8090-T8

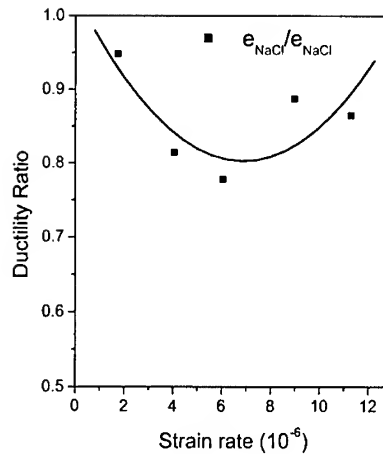


Fig 2: Ductility ratio vs strain rate

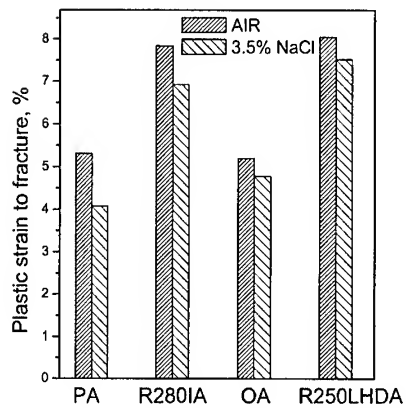


Fig 3: Plastic strain to fracture vs various temps

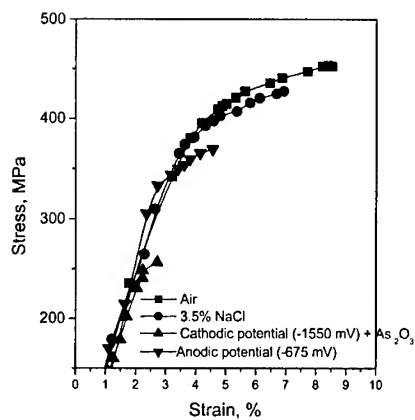


Fig 4: Plot of stress strain curves at a low strain rate.

EFFECTS OF EXCESS SILICON CONTENT ON THE AGEING BEHAVIOUR OF SOLUTION-TREATED Al-Mg-Si ALLOYS

Y. Ohmori, Y. Matsuura, K. Nakai and S. Kobayashi

Department of Materials Science & Engineering, Ehime University
3 Bunkyo-cho, Matsuyama 790-8577, Japan

ABSTRACT

The effects of excess Si and Mg contents on the precipitation behaviour of intermediate phases in Al-Mg₂Si alloys have been investigated by means of differential scanning calorimetry and transmission electron microscopy. At the ageing stage which has been identified as rodlike β' precipitation, the precipitation of cuboid β -Mg₂Si particles with the cube-cube β /Al orientation relationship was recognised. With the progress of ageing, thin β -Mg₂Si plates inclining either 45° or 18.4° from the cube-cube relationship about the $\{001\}_{\text{Al}} \parallel \{001\}_{\beta}$ habit plane normals formed. The morphological and the crystallographic changes of the precipitates can be explained in terms of elastic energy due to the precipitation and the misfits on the interfaces.

1. INTRODUCTION

In the Al-Mg-Si alloys, the formation of various intermediate phases such as monoclinic β'' needles^[1-7], hexagonal β' rods^[1, 4, 6, 8, 9] and small cuboid particles with f. c. c. structure has been reported in the aging processes prior to the stable β -Mg₂Si precipitation^[10]. Although these intermediate precipitates have been examined extensively by means of transmission electron microscopy, the results of the structural determinations are largely diversified and the details have not been well understood.

In the previous paper^[11], it has been pointed out that the DSC peak which has been so far identified as β' precipitation is probably due to that of cuboid β -Mg₂Si particles with the cube-cube orientation to the matrix. This type of β -Mg₂Si precipitation can clearly be recognized especially in the Al-Mg₂Si quasi binary and the excess Mg alloys. These results suggest that various modes of β -Mg₂Si precipitation can exist according to both chemical composition and precipitation condition.

In the present paper, therefore, the effects of excess Si content on the formation of the intermediate phases have been examined mainly by differential scanning calorimetry and transmission electron microscopy.

2. EXPERIMENTAL PROCEDURES

The nominal compositions of the Al-Mg-Si alloys are shown in Table 1. The ingots were rolled to plates at the reduction ratio of 90% and homogenized at 833K for 12h. The specimens solution-treated at 863K for 30 min were quenched into iced water prior to ageing.

DSC measurements were carried out at a heating rate of 20K/min under a dynamic N₂ atmosphere. All the DSC runs were started at room temperature and were ended at 853K. The microstructures of continuously heated specimens at 20K/min were examined by quenching from various temperatures.

The as-quenched specimens evacuated in quartz tubes were isothermally aged at 673K for various times. The observations of the microstructures and Vickers hardness measurements for them were conducted. The thin foil specimens were examined in a JEOL-2000EX microscope operating at 200kV.

Table 1 The nominal compositions of the alloys used. (at %)

Alloy	Mg	Si	Excess Si	Excess Mg
1	1.4	0.70	0	0
2	1.4	1.00	0.3	-0.6
3	1.4	0.55	-0.15	0.3

3. EXPERIMENTAL RESULTS

Figure 1 shows the results of DSC during continuous heating at 20K/min. As can be seen in Fig. 1 (a), five exothermic reactions and two endothermic reactions were detected in the excess Si alloy 2. Although the exothermic peaks A and E were commonly believed as clustering of solute atoms and the precipitation of β' rods, the previous results^[1] showed that the exothermic peaks A, B, D and E are probably due to the clustering of quenched-in vacancies, the solute atom clustering, the precipitation of β'' needles and the cuboid β -Mg₂Si precipitation, respectively. The reactions F may be the precipitation of stable β -Mg₂Si.

The effect of excess Si content on the peak height ratio of the reaction E to that of D, h_E/h_D , is shown in Fig.1 (b). The h_E/h_D value increases with decreasing the excess Si content linearly as reported in the previous study^[1].

In order to confirm various precipitation modes of intermediate phases, the microstructures formed during both continuous heating at 20K/min and isothermal aging were examined by means of transmission electron microscopy. Figure 2 shows the TEM micrograph for the excess Si alloy 2 aged up to the peak D, 548K. The bright field image and the selected area electron diffraction pattern are in Fig. 2 (a) and (b), respectively. The structure comprised mainly very fine β'' needles, but the structure could not be determined because of the extremely elongated reflections normal to the needle directions (Fig. 3 (b)). In the alloy 2 aged up to a higher temperature continuously, the formation of the so-called β' rods was recognised. The

reflections from the rods obtained by continuous heating, however, were still largely streaked, and the transformation from β'' to β' could not be confirmed in the present study.

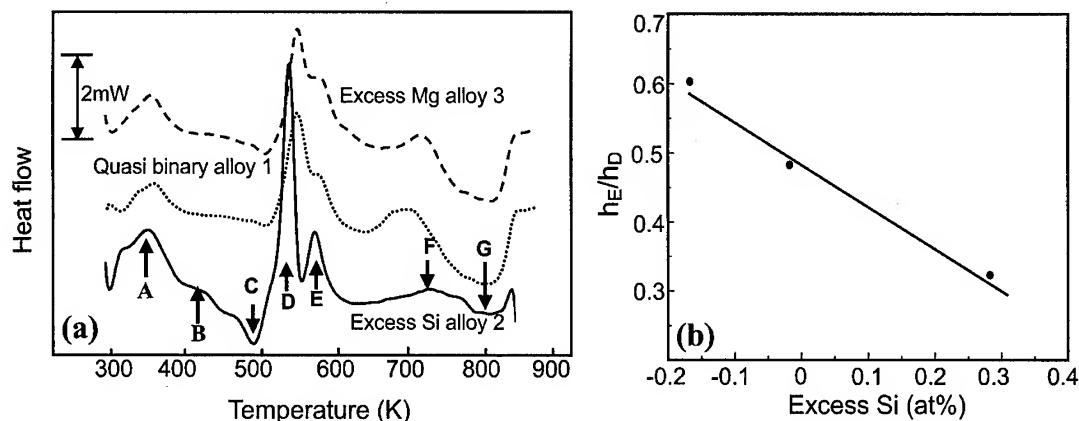


Fig.1 The results of DSC analysis

(a) DSC curves for the alloys used at the heating rate of 20K/min and (b) the effect of excess Si content on the peak height ratio of the reaction E to that of D

On the other hand, in the excess Mg and the Al-Mg₂Si quasi binary alloys aged up to the peak E, cuboid β -Mg₂Si particles were densely distributed in addition to the β'' needles. An example of such precipitations in the alloy 1 aged up to 603K is shown in Fig. 3. The bright field image, the selected area electron diffraction pattern and the key diagram for it are in Figs. (a), (b) and (c), respectively. As can be seen in the diffraction pattern (b) and the key diagram (c), the cuboid β -Mg₂Si particles are related to the matrix with the cube-cube orientation relationship^[9]:

$$[100]_{\text{Al}} \parallel [100]_{\beta}, [010]_{\text{Al}} \parallel [010]_{\beta}, [001]_{\text{Al}} \parallel [001]_{\beta}.$$

The cube plane normals are $\langle 100 \rangle_{\text{Al}}$ elastically soft directions.

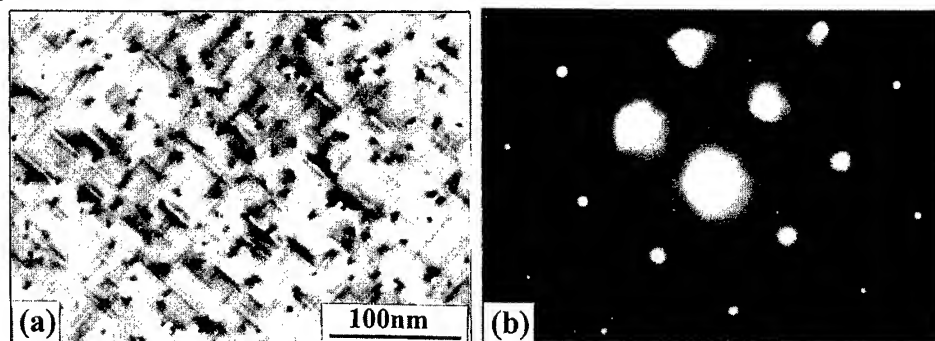


Fig. 2 Fine β'' needles formed in the alloy 2 by ageing up to 548K at 20K/min. (a) The bright field image and (b) the selected area electron diffraction pattern.

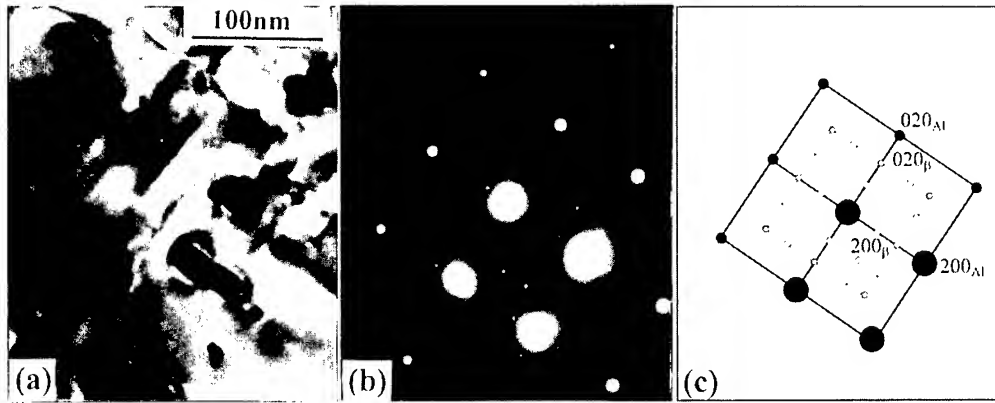


Fig. 3 Cuboid β and needlelike β'' precipitation in the alloy 1 heated up to 603K at 20K/min.

(a) The bright field image, (b) the selected area electron diffraction pattern, and (c) the schematic representation of (b).

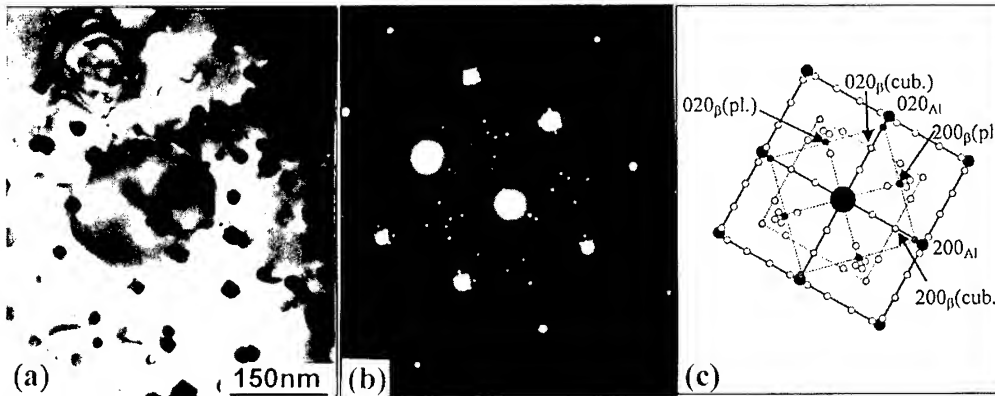


Fig. 4 The precipitation of β plates and cuboid particles in the alloy 1 aged at 573K for 20h.

(a) The bright field image, (b) the selected area electron diffraction pattern, and (c) the schematic representation of (b)

The isothermal ageing for long time at cuboid particle formation temperature induced the precipitation of β - Mg_2Si plates. These precipitates nucleated either separately or at the cuboid particles. In the intermediate stages of such an isothermal ageing, the β - Mg_2Si plate/matrix relationship was close to that obtained by Kanno et al^[10] as in Fig. 4:

$$(001)_{\text{Al}} \parallel (001)_{\beta} \cdots \text{habit plane}, [100]_{\text{Al}} \parallel [1\bar{1}0]_{\beta}, [010]_{\text{Al}} \parallel [110]_{\beta}.$$

The edges of the plates were parallel to $\langle 110 \rangle_{\text{Al}}$ and/or $\langle 100 \rangle_{\text{Al}}$ directions.

In the final stages of ageing, very large β - Mg_2Si thin plates were formed with 18.4° rotation about the $[001]_{\text{Al}} \parallel [001]_{\beta}$ direction from the cube-cube relationship as shown in Fig. 5 and the following relationship was obtained:

$$(001)_{\text{Al}} \parallel (001)_{\beta} \cdots \text{habit plane}, [110]_{\text{Al}} \parallel [120]_{\beta}, [\bar{1}10]_{\text{Al}} \parallel [\bar{2}10]_{\beta}$$

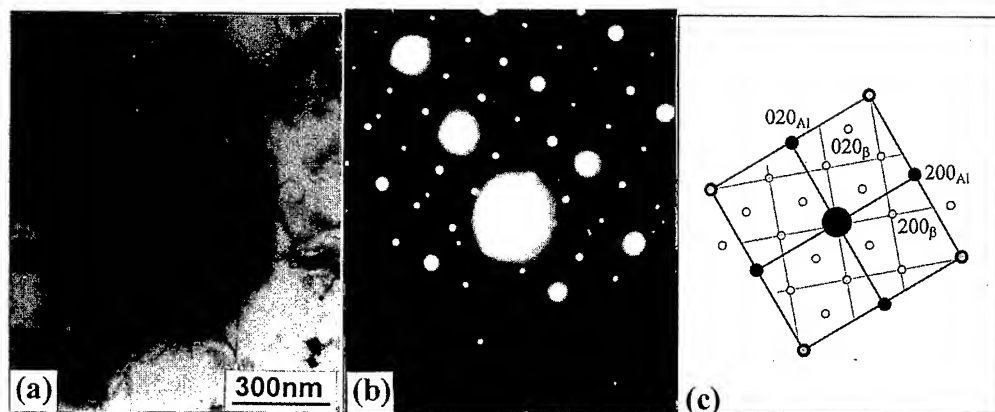


Fig. 5 The precipitation of β plates and cuboid particles in the alloy 1 aged at 573K for 50h.
(a) The bright field image, (b) the selected area electron diffraction pattern,
and (c) the schematic representation of (b)

4. DISCUSSIONS

Although the reaction E obtained in DSC has been believed to be the transformation from β'' needles to hexagonal β' rods, the previous results^[11] showed that the cuboid β -Mg₂Si particles form within the reaction E. The h_E/h_D ratio, which is proportional to the fraction of the reaction E, decreased with increasing excess Si content in keeping with the previous results^[11]. Therefore, the detection of β -Mg₂Si particles becomes difficult with increasing excess Si content though the reaction E arises from the precipitation of cuboid β -Mg₂Si particles. Thus, the reason for the morphological and the crystallographic variation of β -Mg₂Si phase with ageing condition should be revealed.

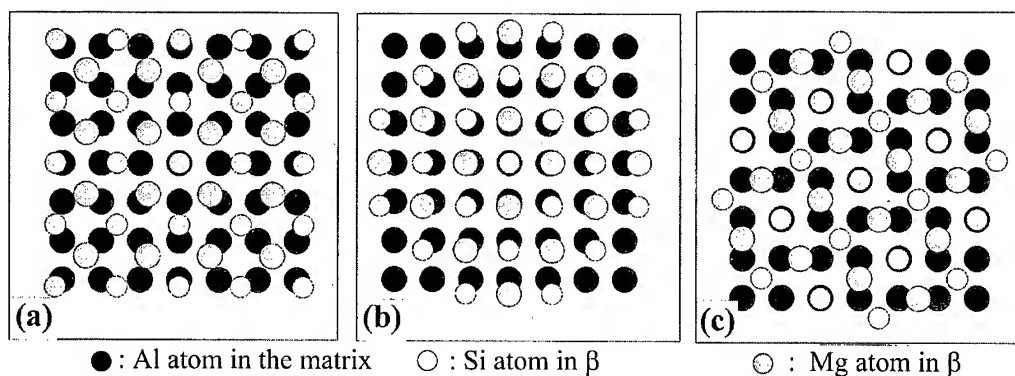


Fig. 6 Atomic correspondences between Al and β phase on the $(001)_{Al} \parallel (001)_{\beta}$ plane
(a) The cube-cube orientation relationship, (b) Kanno relationship^[10], and
(c) the relationship rotating about 18.4° from the cube-cube relationship.

At the initial ageing stage, coherent precipitates will form. The criterion to control such a precipitation is the elastic strain energy minimisation. In the case of cube-cube orientation relationship, the misfits along three $\langle 100 \rangle$ axes are only 4.5% as shown in Fig. 6 (a) and the $\langle 100 \rangle$ directions of both phases are elastically soft. Therefore, this relationship will provide the small elastic energy at least at the initial stage of precipitation.

With the growth of precipitates, the elastic strain energy proportional to the volume of an individual precipitate increases rapidly and the driving force for the coherent precipitation decreases. Then, the shape of the precipitate will change into plate with the habit plane of low surface energy. In the case of 45° rotation, although the misfits are slightly larger than those in the coherent case, the atomic arrangements of β phase and those of Al matrix on the $(001)_{\text{Al}} \parallel (001)_{\beta}$ plane are quite similar as shown in Fig. 6 (b), this plane being the habit plane. At later stage of ageing, the third orientation relationship (18.4° rotation) was obtained. In this case, the atomic arrangements on the $(001)_{\text{Al}} \parallel (001)_{\beta}$ plane of both phases are slightly different but the coincident site lattices are formed as shown in Fig. 6 (c). Thus, this can also be the habit plane. The precipitation sequence of plates will be determined by both the interface structures described above and the misfits normal to the habit plane.

5. CONCLUSIONS

At the ageing stage which has been identified as rodlike β' precipitation so far, the cuboid β - Mg_2Si particles with the cube-cube β/Al orientation relationship formed. With the progress of ageing, thin β - Mg_2Si plates inclining either 45° or 18.4° from the cube-cube relationship about the $\{001\}_{\text{Al}} \parallel \{001\}_{\beta}$ habit plane normals grew at the cuboid particle interfaces. The change in morphology and crystallography of the precipitates can be explained in terms of elastic energy due to the precipitation and the misfits on the interfaces.

6. REFERENCES

1. G. A. Edwards et al: Mater. Sci. Forum, **713**(1996), 217-222.
2. M. Murayama and K. Hono: Acta mater., **47**(1999), 1537-1548.
3. T. V. Shchegoleva: Phys. Met. Metallogr., **25**(1968), 56-59.
4. R. P. Wahi and M. von Heimendahl: Phys. Stat. Sol. (a), **24**(1974), 607-612.
5. K. Matsuda, S. Ikeno and S. Tada: J. Japan Inst. Metals, **57**(1993), 1107-1113.
6. J. P. Lynch, L. M. Brown and W. H. Jacobs: Acta Metall., **30**(1982), 1389-1395.
7. S. J. Andersen: Met. Mater. Trans. A, **26A**(1995), 1931-1937.
8. J. P. Lynch, L. M. Brown and W. H. Jacobs: Acta Metall., **30**(1982), 1389-1395.
9. K. Matsuda, S. Ikeno and S. Tada: J. Japan Inst. Metals, **57**(1993), 1107-1113.
10. M. Kanno, H. Suzuki and Y. Shiraishi: J. Japan Inst. Metals, **43**(1979), 81-86.
11. Chau Long Doan, Y. Ohmori and K. Nakai: to be published.

EFFECT OF OVER-AGING ON THE MICROSTRUCTURE AND MECHANICAL PROPERTIES OF Cu, Ni CONTAINING AC8A ALUMINUM CASTING ALLOY

S. W. Kwon, D. W. Suh, Y. R. Im, H. C. Lee, J. K. Yang*, K. H. Ryu*

School of Materials Science & Engineering,
Seoul National University, Seoul 151-742, KOREA

*R&D Institute, Dong Yang Piston Co. Ltd., Ansan B601-21, KOREA

ABSTRACT

The effects of the increased addition of alloying elements, Cu and Ni, on the microstructure and elevated temperature mechanical properties of a Al-12Si-CuMgNi (AC8A) piston alloy were investigated. Elevated temperature properties of AC8A cast alloys were improved by the increase of Cu and Ni content. Cu and Ni added alloy showed good elevated temperature stability of mechanical properties after over-aging at 350°C up to 1000 hours. θ' and θ'' phases are the main hardening precipitates in both alloys after aging for 5 hours at 210 °C. The θ' and θ'' precipitates changed to Q ($\text{Al}_5\text{Cu}_2\text{Mg}_8\text{Si}_6$) phase ($a=1.04\text{nm}$, $c=0.45\text{nm}$) after over-aging. Growth of fine silicon particles and precipitation of Cu-rich silicide were also observed after prolonged over-aging.

1. INTRODUCTION

Aluminum-silicon eutectic alloy shows excellent castability, low thermal expansion coefficient, good thermal conductivity, and excellent corrosion resistance[1]. They are well suited to aerospace structural applications, automobile industry, military applications, etc. And one of the well known AC8A(Al-12Si-CuMgNi wt.%) alloy has been widely used as a piston material for gasoline and diesel engine and referred to as 'piston alloy'. These alloys show good reliable strength and wear resistance. Hard silicon and intermetallic phases are known to provide good wear resistance in these alloys. Various alloying elements were introduced for further improvement of the alloy strength and to make alloys heat treatable[3]. But nowadays, pistons are getting exposed to higher gas pressure and temperature in combustion chamber and good elevated temperature strength and stability are required for piston materials. The purpose of this study is to investigate the effects of increased addition of Cu and Ni on the microstructure and elevated temperature mechanical properties of AC8A

alloy after prolonged over-aging at high temperatures.

2. EXPERIMENTAL PROCEDURE

The alloys were produced by a gravity casting process at Dong Yang Piston Co. Ltd., Ansan, KOREA. The chemical compositions of AC8A(A-alloy) and Cu, Ni added(B-alloy) alloys are given in Table 1. Both alloys were cast into automotive pistons and then artificially aged at 210°C for 5hr to a T6 condition. To simulate the prolonged use at elevated temperature, alloys were heat treated in a salt bath (KNO₃(55%)-NaNO₂(45%)) at 150°C, 250°C and 350°C for 1, 3, 6, 20, 40, 100, 200 and 1000 hours. Alloy hardness was measured using Brinell hardness tester with 2.5mm diameter ball indenter at the load of 62.5kg. The tensile tests were conducted using 10-ton capacity tensile testing machine (Instron 5582) at the cross-head speed of 0.3mm/min according to ASTM B557M. Cast structures were observed by scanning electron microscope JSM-5600 and XL-20 and chemistry of inter-dendritic precipitates were investigated by EDS analysis. The thin film specimens for TEM were prepared by twin-jet electro-polishing technique in a solution of 75% methanol and 25% nitric acid at -30°C. Philips CM-20 and JEM-200CX electron microscope were used for TEM observation.

3. RESULTS AND DISCUSSION

3.1 Mechanical properties of alloys

3.1.1 Variation of hardness on over-aging temperature and time

After T6 heat treatment, both A and B-alloys were over-aged at 150°C, 250°C and 350°C for up to 1000 hours. Fig.1 shows that variation of hardness with over-aging temperature and time. Alloy B which contains larger quantities of Cu and Ni shows higher hardness values not only after T6 aging but also after prolonged over-aging heat treatment. When aged at 150°C, alloy B shows second hardening, which is believed due to the precipitation of θ'' phase. After aging at 350 °C, both A and B alloy show rapid softening but the hardness of alloy B is about higher than that of A alloy even after 1000 hours of extended aging.

Table 1. Chemical composition of the alloys (weight percent (w/o))

Alloy	Si	Cu	Ni	Mg	Ti	V	Zr	Fe	Mn	Zn	Al
A	11.96	1.14	1.16	1.22	0.014			0.515	0.014		bal.
B	12.1	3.18	2.39	1.07	0.165	0.15	0.229	0.053	0.023	0.333	bal.

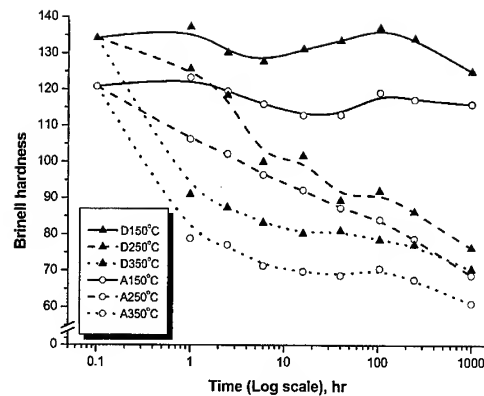


Fig.1 Variation of alloy hardness according to over-aging temperature and time.

3.1.2 Tensile test

Tensile behavior of two alloys are compared in Fig. 2. Fig.2(a) shows the room temperature tensile curves of alloy A and B. Both alloys fractured at similar strength level without significant plastic strains after T6 aging. Primary Si particles were the major fracture initiation sites. It is interesting to note that cracking of silicon particles frequently occurs along their longest dimension. This type of cracking can only be understood by the fact that primary silicon crystals as well as the eutectic silicon particle contain twin boundaries[5] which exhibit a significantly low resistance to cracking than single crystal. Fig 2(b) shows tensile curves of alloys at 350°C after over-aging at 350°C for 1000 hours. As expected from high hardness values, alloy B exhibited about 20% higher tensile strength than alloy A.

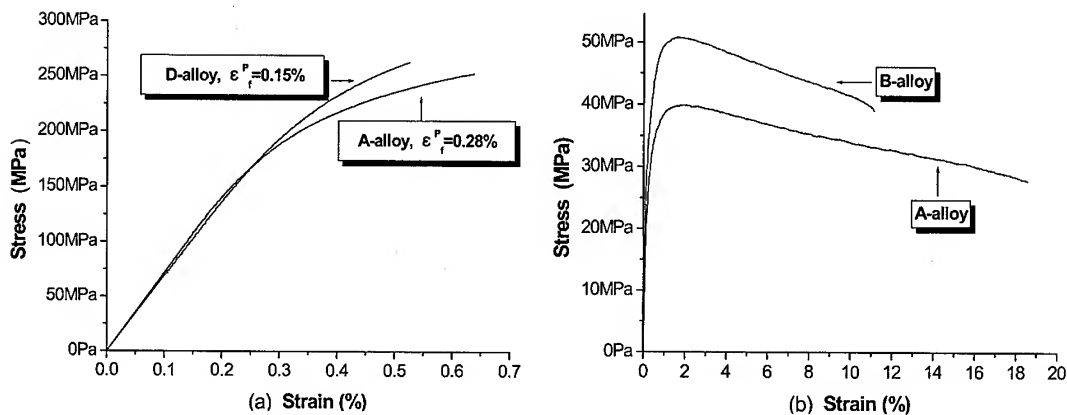


Fig. 2 Tensile curves of A and B alloys at room temperature(a), at 350°C after over-aging at 350°C for 1000 hours(b).

As will be discussed in next sections, both alloys shows similar microstructural variations during aging. Higher strength in alloy B may be a simple results of high volume fractions of precipitates and intermetallic phases in alloy B.

3.2 Microstructural variation during over-aging

3.2.1 Optical and SEM observation

In both A and B alloys investigated, aluminum dendrites, primary silicon, unmodified eutectic silicon, and intermetallic phase are commonly present (Fig. 3). There have been many reports on the intermetallic compounds in alloy systems having similar chemical composition[6-7]. In this study, observed intermetallic phases are (i)Al-Fe-Ni, (ii)Al-Mg-Si-Fe, (iii)Al-Si-Cu-Ni-Zr, and (iv)Al-Cu-Ni etc. The shape and distribution of these intermetallic compounds were not easy to characterize but abundant needle- and lath-like rich phases were observed in B-alloy(Fig.3(b)). During extended over-aging, aluminum dendritic structure was disappeared but over-aging had no effect on the microscopic appearance of microstructural features of primary silicons, eutectic silicons and multi-element intermetallic compounds. The intermetallic phases reduce the mean linear intercept length i.e. the mean free path for moving dislocations in the matrix. Alloy B showed heavier presence of intermetallic phases and smaller dendrite arm spacings than alloy A.

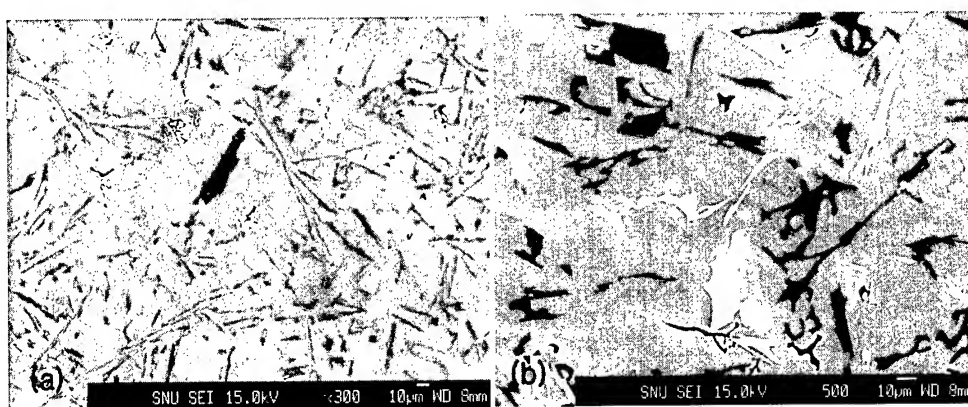


Fig. 3 Scanning electron micrographs shows intermetallic compounds in A(a) and B(b) alloys.

3.2.2 TEM observation

After T6 heat treatment, metastable plate-like θ'' or θ' (Al_2Cu) phases were formed in significant amount in both alloys as shown in Fig. 4. S'' or S' phases were not observed in even in alloy A which has lower Cu/Mg ratio. Formation of Mg containing intermetallics such

as Mg_2Si and Al-Mg-Fe-Si could reduce the Mg content in the alloys. Fine silicon particles (~50nm) were also observed in the matrix of both A- and B-alloys. In specimens over-aged at 350°C for 250 hours, rod-shaped and bulk hexagonal Q- $\text{Al}_5\text{Cu}_2\text{Mg}_8\text{Si}_6$ phases ($a=1.04\text{nm}$, $c=0.45\text{nm}$) and coarse Si particles (~250nm) were observed (Fig.5). Finely dispersed (less than 50nm) Cu-rich unknown Cu-Si phase was observed after significant over-aging (Fig. 6). When compared microstructural changes during elevated temperature aging, both alloys show identical aging behaviors. Increased amount of Cu may form larger quantities of Q phase and increased amount of Ni may contribute to larger volume fraction of Ni containing intermetallic phases which may results in smaller dendrite arm spacing.

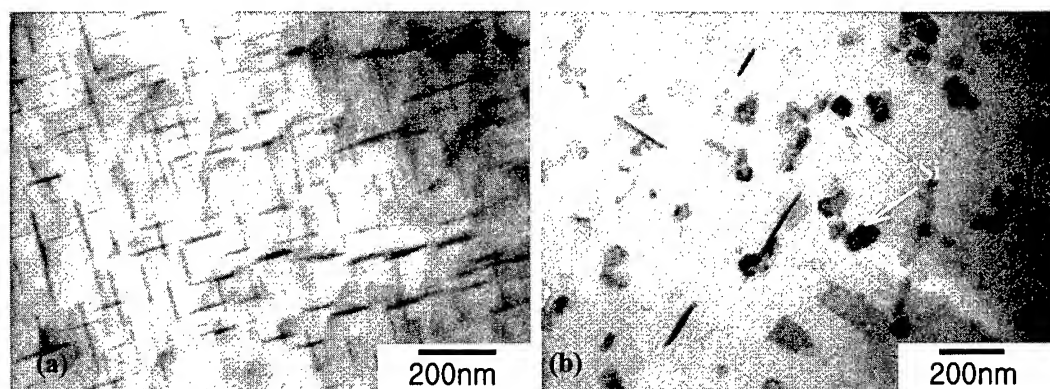


Fig. 4 Transmission electron microscophs shows θ'' or θ' (Al_2Cu) phases(a) and fine silicon particles(b).

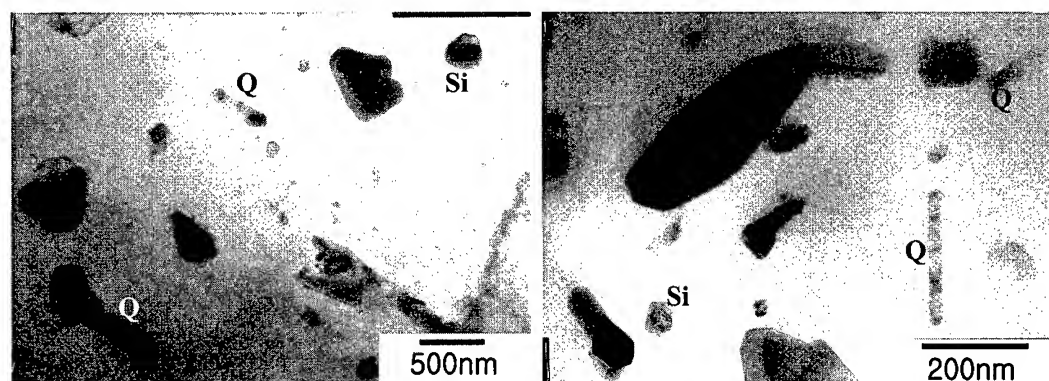


Fig. 5 Transmission electron microscophs shows rod-shaped and bulk hexagonal Q- $\text{Al}_5\text{Cu}_2\text{Mg}_8\text{Si}_6$ phases and coarse Si particles.

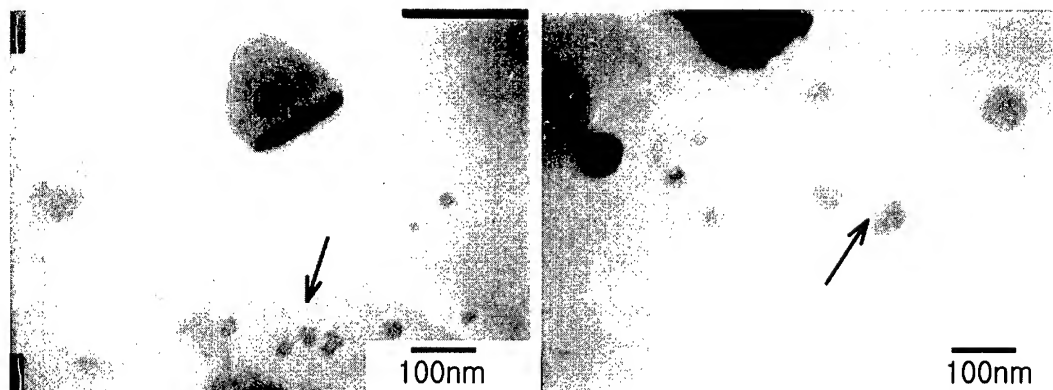


Fig. 6. Transmission electron micrographs shows Cu-rich unknown Cu-Si phase

4. CONCLUSIONS

The effects of increased addition of Cu and Ni on the over-aging behavior of AC8A piston alloys were investigated. Increased addition of Cu and Ni resulted in the improved tensile strength of T6 and over-aged alloys. Hardening of both alloys is believed due to the precipitation of θ'' and θ' phases and these precipitates turned to Q phase after extended aging at elevated temperature. Coarsening of fine Si particles also observed and precipitation of Cu rich silicon intermetallics also observed. Both alloys showed identical microstructural variations during aging and increased tensile strength of in alloy B may simply due to the large quantities of precipitates and Ni containing intermetallics.

REFERENCE

1. John E. Hatch: Aluminum Properties and Physical Metallurgy, 1st ed., American Society for Metals, Ohio(1984), pp. 338-350
2. S.Z. Lu and A. Hellawell, J. Crystal Growth, Vol.73(1985), pp. 316-
3. S. Gowri and F. H. Samuel, Metall. Trans. A, Vol.25A(1994), pp. 437-448
4. D. G. Eskin, Z. Metallkde, Vol.86(1995), pp 60-
5. K. F. Kobayashi and L. M. Hogan, J. Mater. Sci, Vol.20(1985), pp. 1961-1975
6. F. H. Samuel, A. M. Samuel and H. Liu, J. Mater. Sci, Vol.30(1995), pp. 2531-2540
7. A. M. Samuel, F. H. Samuel, J. Mater. Sci, Vol.30(1995), pp. 1698-1708
8. Jürgen Paul and Hans Eckart Exner, Z. Metallkde, Vol.81(1990), pp. 816-825.

APPLICATION OF ALUMINUM ALLOY 2297 IN FIGHTER AIRCRAFT STRUCTURES

E. S. Balmuth

Lockheed Martin Aeronautics Company
MZ 4273, P. O. Box 748, Fort Worth, TX 76101 USA

ABSTRACT

Aluminum alloy 2297-T87 is an Al-2.8Cu-1.3Li-0.3Mn-0.1Zr alloy, developed in the early 90's to provide a good combination of strength and toughness in thicknesses to 152mm, while offering advantages in density, modulus, and especially, fatigue crack growth resistance. Additionally, the alloy has excellent resistance to corrosion and fatigue crack initiation. Tensile properties show minimal variation with orientation. Both strength and toughness are quite stable after exposure to elevated temperatures. An extensive coupon and subcomponent test program verified that 2297 is a superior choice for fighter aircraft structure.

Initial applications of 2297-T87 were as replacements for fighter aircraft structural parts found to have limited fatigue life due to more severe flight spectra loading. The increased fatigue resistance and toughness of 2297-T87 provided a 5-fold increase in the spectrum fatigue performance compared to conventional aluminum alloys. As a result of the successful implementation on replacement bulkheads, frames, and fittings, additional production applications have been implemented to capture the weight savings and service life improvements available through direct substitution of 2297-T87. Over 3 million pounds of 2297-T87 has been successfully fabricated into aircraft structure since 1995. An AMS specification has been prepared for this alloy and properties have been submitted to Mil-Hdbk-5.

1. INTRODUCTION

The development effort for 2297 benefited from the Al-Li production development experience gained by the mill producers on earlier alloys [1,2]. The alloy design approach built on the experience from many scientific investigations of the microstructure and mechanical behavior of the early experimental and commercial Al-Li alloys. The demanding set of mechanical property goals set for 2297 were demonstrated in detailed coupon testing and evaluation. The damage tolerance advantages of 2297 were validated with a series of subcomponent tests [3,4].

1.1 Background

The promise of lithium-containing aluminum alloys with significantly lower density and higher elastic modulus was established in the 1970's [5]. In the 80's the major aluminum producers initiated alloy development efforts to define compositions and production processes to fulfill this promise. Al-Cu-(Mg)-Li alloys, 2090, 8090, and 2091 were introduced and evaluated by the aerospace industry. They offered an 8-10% lower density, strength levels

comparable to 7075 and 2124, and notably, unusually high resistance to fatigue crack growth [6]. While a number of applications were pursued in aircraft and launch vehicles, these alloys had shortcomings that limited their application in fighter aircraft structure. They were each formulated with solute contents near the maximum that could be dissolved in solid solution, resulting in pronounced quench sensitivity. Except for thin gages, embrittling equilibrium phases nucleated during the quench and coarsened during aging [7]. The alloys could be underaged to provide adequate fracture toughness with only small sacrifices in strength. However, thermal exposure from aerodynamic heating, engines, and other equipment would reduce toughness to unacceptable levels in most fighter aircraft applications. Other problems included anisotropic properties due to intense texture, resulting in 15-20% lower strength in 45-60° orientations, and relatively low stress corrosion resistance in 8090.

Despite their limitations, the early Al-Li alloys had useful properties in thin gages. But except for small parts like brackets, trade studies favored the use of advanced composites for most applications of thin gage materials in advanced fighter aircraft structures. The real need in these designs was for materials with improved performance that could be used for large, complex, multi-load path parts like bulkheads and frames, substituting for 7050-T7451 and 2124-T851. The design requirements for these are a good combination of strength and toughness in all orientations, thermally stable properties, and good corrosion resistance. Allowable stresses are largely controlled by the durability and damage tolerance properties of the material, making fatigue and fracture resistance the critical properties for sizing parts.

1.2 Alloy Development

An alloy development effort for thick plate products was begun in 1987 to overcome the problems observed in 2090, 8090, and 2091 [1,2]. This effort began with a collaborative producer-airframe company program to screen compositions based on plate made from small ingots, and progressed to scale-up of a selected composition with detailed characterization of mechanical and physical properties in 38 mm and 91mm-thick plate. Heat treat parameters were optimized, providing a peak aged condition. The alloy was given an experimental alloy designation and subsequently registered with the Aluminum Association as 2297. Its nominal composition is Al-2.8Cu-1.3Li-0.3Mn-0.1Zr. This alloy was incorporated in a USAF sponsored effort, Supportable Hybrid Fighter Structures, providing experience with the alloy in design and hardware fabrication [8]. In another collaborative effort, 140mm-thick plate was produced to demonstrate mechanical properties in sections typically used for airframe bulkheads [3]. Following the successful demonstration of alloy 2297, the USAF sponsored a Producibility, Reliability, Affordability, and Maintainability (PRAM) program to accelerate the qualification and implementation of 2297 for fatigue-prone aircraft structure [4]. Under the PRAM contract, additional lots of material were produced for full-scale qualification tests, aircraft component tests, aircraft strain-surveys, manufacturing trials, and aircraft flight evaluations. Alloy 2297 surpassed all expectations as a direct substitute for fatigue prone parts to extend the service life and was selected for production and spares applications.

1.3 Test and Evaluation

Properties of 2297 were extensively characterized with coupon tests [2]. To summarize the results of this work: Strength and fracture toughness is equal to, or better than, 2124-T851 in all orientations; there is no loss in toughness with thermal exposure; exfoliation resistance is high; stress corrosion resistance exceeds 172MPa; anisotropy in strength is minimal and

comparable to 2124; density is 5% lower than 2124; elastic modulus is 7% higher than 2124; stress-life fatigue tests show notched fatigue life equivalent to 2124 and 7475 with improved smooth specimen fatigue life; cyclic stress-strain tests show that 2297 is cyclically stable whereas 2124 cyclically softens and 7050 cyclically hardens; and, fatigue crack growth rates are significantly lower in constant amplitude and spectrum fatigue tests [1,2,3].

The coupon fatigue tests were conducted in different environments and covered a range of stress ratios. These provided the database needed for fatigue life calculations to predict the performance in structural components. Three subcomponents were selected to validate the improvement in fatigue life with 2297 over 2124 [4]. Figure 1 shows the setup for testing the joint between upper and lower FS341 bulkhead segments for the F-16. The loading is a tension-dominated wing bending moment spectrum. Cracks typically initiate at the bore of a cold-worked bolt hole joining the segments. A test simulating a shear web in an F-16 FS325 bulkhead also utilized a tension-dominated spectrum. In this case cracks develop at the systems penetration holes and the test was terminated when the crack extended completely from hole to hole. The third subcomponent in Figure 2 simulates the loading in the F-16 FS479 upper bulkhead segment where the vertical stabilizer is attached. For this test, a fully reversed spectrum is applied with periodic tensile loads well above the maximum design load.

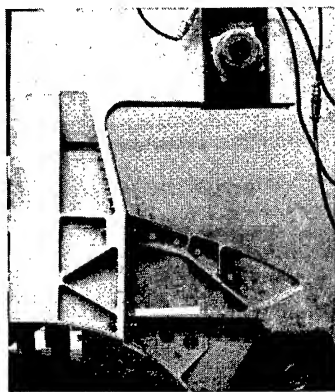


Fig.1 F-16 FS341 lower bulkhead test.

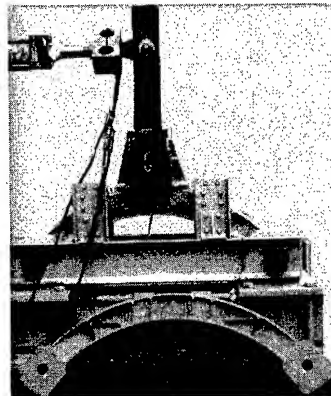


Fig.2 F-16 FS479 upper bulkhead test.

The subcomponent tests clearly illustrated the benefit of 2297 in highly loaded, fatigue critical applications. Fatigue cracks initiated from intentional preflaws early in the tests. The slower crack growth rates in 2297 typically resulted in a five-fold increase in life. Fatigue crack growth in the 2124 tests led to critical crack lengths and catastrophic failure of the FS341 and FS479 subcomponents. The 2297 tests were discontinued after 2 or 4 simulated lifetimes and tested for residual strength. Cracks had generally initiated at multiple locations, in addition to the preflawed location, and propagated to produce cracks several inches in length. Nevertheless, residual strength was well in excess of design limit load.

2. PRODUCTION APPLICATIONS

The initial production applications for alloy 2297-T87 were for military aircraft

replacement components that were subject to fatigue life limitations associated with a severe spectrum fatigue environment. Alloy 2297-T87 provided a “drop-in” substitute for alloy 2124-T851, thus minimizing the redesign/non-recurring costs as well as providing a 5-fold fatigue life enhancement and a 5% weight reduction. Even with the higher raw material costs compared to conventional Al alloys, the alloy substitution demonstrated life-cycle cost savings of over 100 million dollars associated with the reduced inspection and replacement of components manufactured with 2124-T851.

Additional fatigue testing and component testing demonstrated that 2297-T87 could replace higher strength alloys such as 7050-T7451 in parts that are sized primarily by durability and damage tolerance. As an example, recent trade studies for a part with 20% load transfer (5.1mm flange thickness, 6.35mm hole diameter) showed that a high strength alloy like 7050-T7451 offered a 163MPa durability/damage tolerance allowable stress compared to 200MPa for a similarly sized 2297-T87 part. The higher stress allowable in concert with a 7% density reduction compared to 7050 provides for weight savings potential in the range of 15-20% when 2297-T87 is specified in a new design for durability/damage tolerance designed parts.

Applications in fighter aircraft require good corrosion resistance. The corrosion behavior of 2297 and the application of standard corrosion preventive finish systems has been extensively studied. In both accelerated laboratory testing and in shipboard exposure testing, 2297 has demonstrated equal or better corrosion resistance than alloys currently in use. Alloy 2297-T87 has completed the requirements for inclusion in Mil-Hdbk-5 and has an industry AMS specification under development for design and procurement. The following paragraphs discuss specific applications where Al-Li alloy 2297-T87 provided a cost-effective solution for design.

2.1 Main Landing Gear Bulkhead

The Main Landing Gear bulkhead (Figure 3) is an example application where alloy 2297-T87 provided the only aluminum-based solution for a durability/fracture critical part. The main landing gear bulkhead is a primary wing-bending load path that has numerous penetrations for electrical and hydraulic systems. Cold-working, while successful in delaying fatigue crack initiation, was unsuccessful in providing for significant fatigue life enhancement, especially in areas such as flange radii. While it is always a consideration to add to the part thickness to account for stress reductions, the main landing gear bulkhead joint configuration was limited by geometry constraints. In this case, to meet the service life requirement, the only available options were to produce the part with 2297-T87 or convert to titanium. A change to titanium would result in a 4-fold increase in the part manufacturing and raw material costs compared to 2297-T87 in addition to the non-recurring costs associated with a redesign.

In 2124-T851, component testing and service life experience indicated that under a severe spectrum fatigue loading (100% tension/30%compression), the part would not meet the 8,000 hours required service life. Using 2297-T87, component testing and fatigue life analyses showed that the material provided a 5-fold life improvement using the most severe fatigue spectra anticipated (Figure 4) [9].

While 2297-T87 showed the necessary life improvement, other manufacturing and design considerations also needed to be addressed. First, the effect of the increased stiffness of Al-Li alloys on the overall load-path was evaluated using a static aircraft strain survey to make sure that the increase in material stiffness would not adversely impact the stress levels in the part. Strain survey results indicated that the load path was not altered more than 5% over the

baseline configuration due to the increased material stiffness [9]. Also, concerns regarding cold-working Al-Li alloys were considered. The joint configuration requires that the upper and lower bulkhead be cold-worked during assembly with the fuel shelf. Component tests were conducted using standard production tooling that indicated that the 5% cold-work during assembly was not an issue with Al-Li alloys. Other concerns that were addressed included the ability to utilize standard 2124 machining tooling and finishing operations. As a result of these evaluations and the successful component testing, alloy 2297-T87 was selected for production.

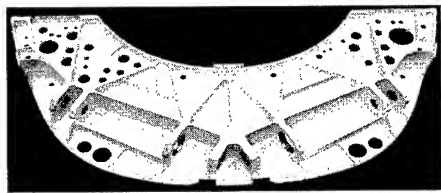


Fig.3 F-16 FS341 Main Landing Gear Bulkhead.

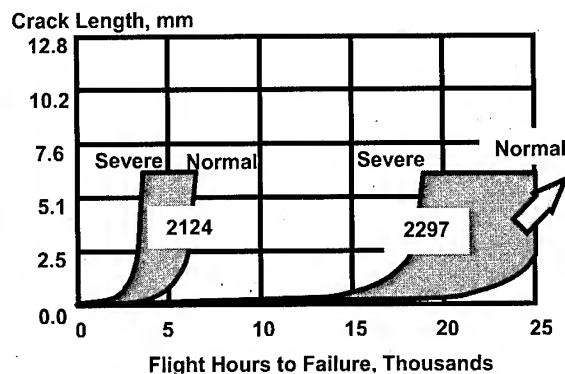


Fig.4 Spectrum Fatigue Crack Growth Life.

2.2 Vertical Stabilizer Attach Bulkhead

The vertical stabilizer attachment is a multiple load path design, however, the rudder hinge moment is applied primarily to the aft-most bulkhead. The high rudder loads transferred through to the bulkhead produced a very highly loaded joint. The flight spectra is also completely reversed (100% in both tension and compression), minimizing the potential benefits of cold-work through shot-peening processes. As with the main landing gear bulkhead, geometry limitations precluded flange thickness increases as an option for redesign. In this case, component testing comparing 2124-T851 and 2297-T87 again showed a 5X improvement in fatigue life for 2297-T87. This bulkhead (Figure 5) was converted to 2297-T87 in 1996 and has provided a significant increase in life compared to the original bulkhead.

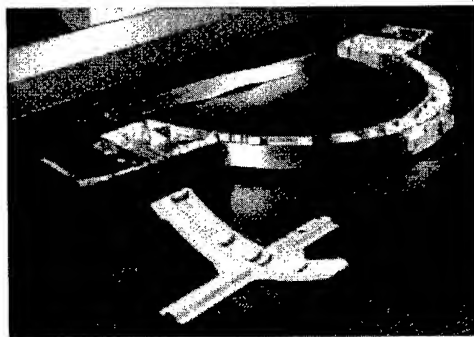


Fig.5 Alloy 2297 Production parts include the Upper Longeron at top, Vertical Tail Attach Bulkhead at center, and Engine Access Cover Stiffener.

2.3 Engine Access Cover Stiffener

The engine access cover (Figure 5) provides for load transfer from the fixed ventral stabilizer fin into the aircraft. Due to the highly dynamic environment associated with the ventral fin, the engine access cover stiffener is primarily designed by high cycle fatigue. Through the use of analytical modeling tools combined with service experience, the crack growth of 2124-T851 was not adequate to meet the service life requirements of the part. Analytical evaluation of 2297-T87 provided for considerable additional margin of safety for this part in conjunction with redesign. As a result, 2297-T87 was selected for future production and spares requirements.

2.4 Lower Frame

The F-16 FS446 Lower Frame has highly loaded joints with mating structure. The joint locations are subject to loads induced by the engine, the horizontal stabilizer and the vertical stabilizer. The joints were redesigned for future production. To provide sufficient life for aircraft with original design, replacement parts were made from 2297.

2.5 Upper Longeron

This is a highly loaded part that was originally fabricated from a 2024-T62 stretch-formed extrusion. It developed fatigue cracks at stress concentrations and countersunk fastener holes. The part was redesigned to increase thickness and reduce the stress concentrations. However, cracks initiated at the fastener holes and the part failed from very short critical cracks. Life was further improved with a change to 7475-T7351, increasing critical crack length. Full service life was only attained with a change to 2297.

3 NEW APPLICATIONS

Based on the successful experience with 2297 to date, it is anticipated that applications as replacements in aging aircraft and as candidates for new design will continue to expand. Material selection is usually guided by a trade study. These generally show that the higher performance but higher cost nature of 2297 compared with conventional alloys is affordable when durability and damage tolerance are the principal design drivers. Affordability from lower cost is also demonstrated when comparing with titanium or advanced composites for these kinds of applications. The cost of structure fabricated from aluminum alloys is being dramatically reduced with the use of high speed machining, again providing an advantage over titanium alloy structures. And, the availability of 2297 in thick plate enables the use of large, unitized structure that saves both weight and cost by eliminating joints and assembly. Weight savings are maximized in new design applications. In aging aircraft, the cost avoidance from eliminating redesign and eliminating inspections and more frequent repairs have favored replacements with 2297.

Raw material cost is an important element in the material selection trade studies. As illustrated in Figure 6, cost has decreased significantly as production requirements have increased. Further reduction in cost is anticipated.

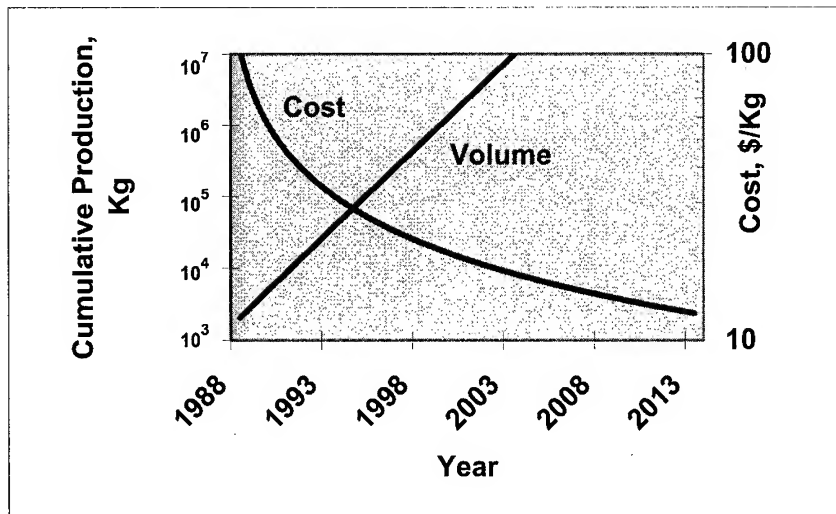


Fig.6 Alloy 2297 Raw Material Production and Cost

4. CONCLUSIONS

The problems of brittle fracture behavior, poor thermal stability, anisotropy, and low stress corrosion resistance that were found in the early Al-Li alloys have been overcome with the development of 2297-T87. Alloy 2297 thick plate has proven an excellent choice for replacing fatigue prone parts in aging aircraft. It can be used effectively where other kinds of repair, like cold working, or redesign are not sufficient or may not be practical. The higher strain allowable associated with the higher fatigue strength may enable alternate load paths, further increasing structural life. In replacing parts with 2297 significant cost avoidance has been realized by eliminating continued periodic inspections and more frequent repair or replacement. Fatigue problems can be resolved with minimal nonrecurring cost. In new applications, alloy 2297 offers affordable weight savings compared with other high strength aluminum alloys and large cost savings compared with titanium or advanced composites. Weight savings are greatest in structure sized by durability and damage tolerance. In these cases, weight savings of 15-20% can be expected. Large quantities of plate material have been produced, accompanied by a continuing decrease in raw material cost.

REFERENCES

1. M.H. Skillingberg, et al., in *Light-Weight Alloys for Aerospace Applications II*, E.W.Lee and N.J. Kim, eds., TMS-AIME, Warrendale, PA, USA (1991) pp.17-25.
2. D.J. Chellman, et al., in *Aluminum-Lithium*, M. Peters and P.-J. Winkler, eds., DGM Informationsgesellschaft mbH, Oberursel, Germany, (1992), pp. 1335-1340.
3. D.J. Chellman and E.S. Balmuth, "Durability and Damage Tolerance Behavior of Thick Plate Al-Li Alloy Product," LiMat '93, Kyongju, Korea, June 1993.
4. M.G. Filips, et al., "Fatigue Resistant Bulkheads," US Air Force Contract F42620-92-D-0316 Final Report, (1996).
5. E.S. Balmuth and R. Schmidt, in *Aluminum-Lithium Alloys*, T.H. Sanders, Jr. and E.A. Starke, Jr., eds., TMS-AIME, Warrendale, PA, USA (1981) pp. 69-88.

6. K.T.V. Rao, et al., in Aluminum-Lithium Alloys, T.H. Sanders, Jr. and E.A. Starke, Jr., eds., Materials and Component Engineering Publications Ltd., Birmingham, UK, (1989), pp. 955-971.
7. J.T. Staley, et al., Metall. Trans. 24A (1993) p. 2417.
8. F.W. Auld, et al., "Supportable Hybrid Fighter Structures," US Air Force Contract F33615-87-C-3207 Interim Report, (1990).
9. L.K. Austin, M. van den Bergh, A. Cho, and M. Niedzinski, in Workshop on New Metallic Materials for the Structure of Aging Aircraft, NATO RTO MP-25, (1999), pp. 2-1 – 2-10.

MECHANICAL PROPERTY OF SUPER-HIGH STRENGTH ALUMINUM ALLOYS

Kozo Osamura, Hiroki Adachi, Jun Kusui* and Kazuhiko Yokoe*

Department of Materials Science and Engineering,
Kyoto University, Sakyo-ku, Kyoto 606-8501, Japan

* Research and Development Laboratory, Toyo Aluminium K.K.,
Shiga 529-16, Japan

ABSTRACT

Recently our group reported the development of extremely high strength AlZnMgCu alloys (Mesoalite), which contain additional Mn and Ag elements. The major mechanical property of Mesoalite is characterized in terms of precipitation hardening, where fine T' metastable precipitates act as pinning centers. One of interaction mechanisms between precipitate and dislocation is described by the cut-through regime. According to our analysis, the coherency strain model contributes for the hardening due to T' precipitates. Another mechanism is the so-called Orowan model. The Orowan stress decreases with increasing the average precipitate radius, while the yield stress due to the coherency strain model increases. The maximum yield strength is expected to realize at the cross-over point for both mechanisms. The total strength to the present Mesoalite was made clear to be given by the multiple effect due to optimal precipitation hardening together with fiber reinforcement due to Mn intermetallic compounds as well as fine grain strengthening. The highest tensile strength have been observed as 910 MPa by the tensile test and 1033 MPa by the compression test. The superior anti-SCC and environmental characteristics have been revealed.

1. INTRODUCTION

The relationship between the specific strength and the tensile strength for several structure materials is shown in Fig. 1, where the specific strength is the tensile strength divided by the specific weight. The data seem to be divided into two groups. Ti and Fe based alloys show the high specific strength and heavy specific weight. On the other hand, Mg and Al alloys give light specific weight, but their specific strength tends to become higher for the same tensile strength. The second category of materials is greatly interesting for the transportation systems.

While the industrial high strength aluminum alloys are well known as 2024 and 7075, many efforts have been continuously paid to develop higher performance alloys. Recently some high strength alloys have been commercialized as their trade names, GIGAS, Weldalite and Mesoalite are given in Fig. 1. Our group developed extremely high strength AlZnMgCu alloys (Mesoalite) by means of powder metallurgy[1].

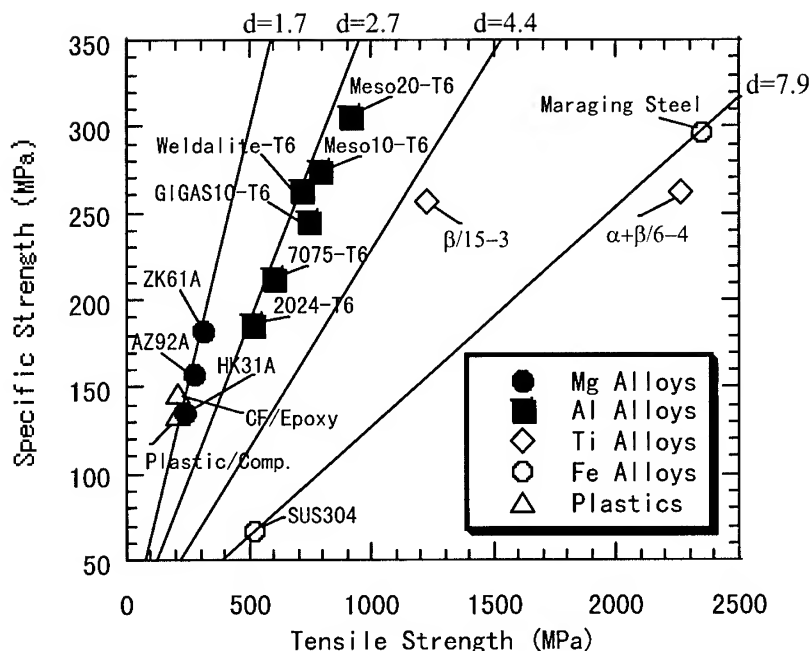


Fig. 1 Specific strength vs tensile strength for several structure materials. Here d is the specific weight and the specific weight is defined as the tensile strength divided by d .

The present study has been focused on discussing several possible strengthening mechanisms and clarifying their contribution to the strength. Also the environmental properties important to the application have been investigated.

2. EXPERIMENTAL PROCEDURE

The present powder was manufactured by air atomization technique. The powder used here had an average particle diameter of $40\ \mu\text{m}$. The cooling rate was estimated to be 10^4 to $10^5\ \text{K/s}$ from the dendrite arm spacing. The preparation technique is shown in Fig. 2. The powder was canned into the aluminum container and then pressed under hydrostatic pressure of 392 MPa. After degassing, the compact piece was hot-extruded at 773K. The extrusion ratio was selected as 10 or 20.

Table 1 Chemical composition of the samples used here

	Zn	Mg	Cu	Mn	Zr	Ag	Fe	Si	Al
I/M 7075	5.70	2.36	1.5	0.03			0.18		bal.
P/M 7075	5.58	2.60	1.6		0.01				bal.
Meso10	9.64	3.09	1.64			0.048	0.02		bal.
Meso20	9.08	2.90	1.79	3.74		0.038	0.09	0.03	bal.

In the present study, several kinds of alloys with different chemical composition were used as listed in Table 1, where the commercial I/M 7075 alloy was also tested as a reference material.

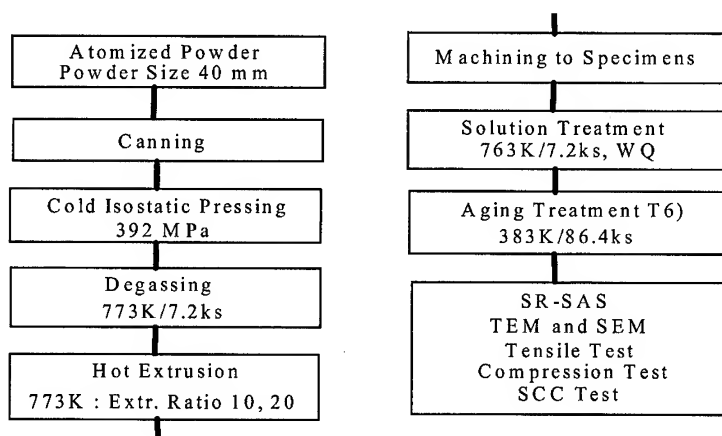


Fig. 2 Experimental procedure

Depending on the purpose, the round bar or the plate was prepared. The present technique can provide a large scale product, for instance, the rod with dimension of 75 mm dia and 1200 mm length. As a standard procedure of heat treatment, the solution treatment was carried out at 763 K for 7.2ks and followed by water quenching. The standard condition of aging treatment as T6 was 393 K and 86.4 ks.

The synchrotron radiation -small angle scattering measurements were carried out at BL15 of Photon Factory – KEK. Their data can provide the structure parameters of small particles dispersed in the matrix. The Guinier radius (R_g) is an average size parameter. The interparticle distance (L_p) means the nearest neighbor distance among particles distributed in the matrix. The volume fraction of particles per unit volume (V_f) is assessed using both size parameters of R_g and L_p . Further the microstructure characterization was carried out by means of TEM and SEM. Tensile test, compression test and hardness measurements were performed. The SCC test was also carried out.

3. EXPERIMENTAL RESULTS AND DISCUSSION

3.1 Microstructure Characterization

According to TEM observation, the microstructure of Meso20 after T6 heat treatment was made clear as follows. The average grain size was about 0.9 μm . At the grain boundaries, the Mn compounds ($\text{Al}_{20}(\text{Cu}, \text{Zn})_2\text{Mn}_3$) distribute, which formed during the hot extrusion. In each grain, the T' metastable precipitates distribute homogeneously[2,3]. In Meso10 without Mn addition, the fine MgZn_2 phase precipitates at grain boundaries and the average grain size was in the range between 2 and 5 μm . In the matrix, the T' metastable precipitates distribute homogeneously. In 7075 alloys, the fine MgZn_2 phase precipitates at grain boundaries and the η' metastable precipitates distribute homogeneously.

Table 2 shows Guinier radius and the interparticle distance of metastable precipitates in

the matrix for three alloys after T6 treatment. It was found that the radius of precipitates is about 2 nm and the nearest neighbor distance is between 8 and 12 nm. The nearest neighbor distance is just 2 ~ 3 times of the particle diameter. The metastable precipitates distribute so densely in the matrix.

Table 2 Microstructure of metastable precipitates after T6 treatment.

	R_p (nm)	L_p (nm)	V_f (%)
Meso20	2.7	8.0	6.3
Meso10	2.4	8.2	4.4
P/M7075	2.1	11.8	0.92

3.2 Mechanical Properties

Table 3 shows the mechanical property of high strength aluminum alloys. Meso20 showed very high tensile strength, but the elongation was low less than 1%. The yield strength of Meso10 was larger by 50% than that of commercial 7075 alloy. The small elongation of Meso20 is suggested to be induced by the fiber-like Mn compounds. In order to avoid the local stress concentration as much as possible, the compression test was carried out. Table 4 indicates the mechanical property determined from the compression test. Both samples showed enough large elongation. The tensile strength of Meso20 exceeded 1000 MPa.

Table 3 Tensile properties after T6 treatment

	YS (MPa)	UTS (MPa)	Elongation (%)	Microvickers Hardness
Meso20	900	910	0.7	230
Meso10	780	790	9.5	211
1/M7075	505	573	11.4	178

Various types of strengthening mechanism contribute to the yield strength. When there is no fibre reinforcing, the yield strength is typically given by three following terms;

$$\sigma_m = \sigma_{mo} + \sigma_{ppt} + \sigma_{HP}. \quad (1)$$

Here σ_{mo} is the contribution from the matrix including the solute atom strengthening and work-hardening. This contribution is not high for the samples after T6 treatment. The σ_{ppt} is the precipitation hardening obeying the coherency strain model[1] as

$$\sigma_{ppt} = 3MG |\varepsilon|^{3/2} (R_g V_f / b)^{1/2}. \quad (2)$$

The σ_{HP} indicates the fine grain strengthening and is expressed by the Hall-Petch type relation,

$$\sigma_{HP} = kM / d^{1/2}, \quad (3)$$

where M is Schmid factor, G is the shear modulus, ε is the coherency strain, b is the Burgers vector, k is the constant and d is the grain size. By fitting Eq. (1) to the data of Table 2, the

observed yield strength of Meso10 (780 MPa) was divided in three contributions of $\sigma_{mo}=48$ MPa, $\sigma_{ppt}=630$ MPa and $\sigma_{HP}=102$ MPa.

In the case of Meso20, an additional fiber reinforcing contributes to the yield strength according to the rule of mixture,

$$\sigma_c = (1-f)\sigma_m + f\sigma_f, \quad (4)$$

where f and σ_f are the volume fraction and strength of Mn intermetallics, respectively. The yield strength jumps from 780 to 900 MPa when comparing two samples of Meso10 and Meso20. This increment is attributed to the fiber reinforcement. When the total strength obeys the rule of mixture, each contribution has been estimated as follows; $\sigma_{mo}=50$ MPa, $\sigma_{ppt}=639$ MPa, $\sigma_{HP}=178$ MPa and $f\sigma_f=120$ MPa.

Table 4 Mechanical property determined from the compression test.

	YS (MPa)	UTS (MPa)	Elongation (%)
Meso20	698	1033	31
Meso10	598	907	35

Figure 3 shows the temperature dependence of tensile strength and elongation for three high strength aluminum alloys. At 423 K, both Meso10 and Meso20 showed superior mechanical property, that is, tensile strength higher than 440 MPa and elongation larger than 9%.

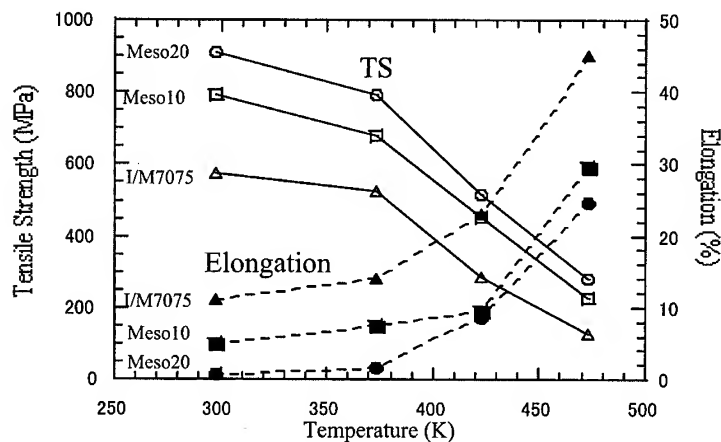


Fig. 3 Temperature dependence of tensile strength and elongation.

3.3 Characteristics for Environments

The SCC test was carried out for the T6 treated samples by being immersed in 3.5%NaCl aqueous solution. During test, the tensile load corresponding to 70% of the tensile strength

was applied to the sample, of which value is listed in Table 5. The test was continued up to 720 hours at room temperature.

Meso10 comprises the fine grains less than a few μm that contains rich solutes in excess of the equilibrium, while the present Mesoalites have GB segregation-free and PFZ-free microstructure after T6 treatment. This characteristic microstructure can avoid local stress concentration and GB solute segregation. As a result, the long life time for SCC attack should be realized for Meso10. Meso20 has still good anti-SCC property, because the life time exceeded 400 hrs even though so high applied load of 637 MPa. As shown in Table 2, the small elongation to fracture suggests an inhomogeneous local stress concentration around the Mn intermetallics and accordingly SCC might be accelerated.

Also the environmental test (JIS H0521) in atmosphere near seashore was carried out for one year[4]. The corrosion rate for both Meso10 and Meso20 was 0.30 and 0.36 $\mu\text{g}/\text{m}^2\text{sec}$, respectively, which was faster than 0.087 $\mu\text{g}/\text{m}^2\text{sec}$ of I/M7075. The degree of corrosion pits was observed to be the same for Meso20, Meso10 and I/M7075. The anodic oxidation film on Meso20 and Meso10 was confirmed to be very tight.

Table 5 Result of SCC test.

	Amount of Zn + Mg (w%)	Applied Load (MPa)	Time to Failure (h)
Meso20	12.0	637	447
Meso10	12.7	524	>720
I/M7075	8.1	462	>720

4. CONCLUSION

The powder metallurgy (P/M) allows a product of rapidly solidified powder that contains rich solutes in excess of the equilibrium, and also has segregation-free microstructure even in a very high solute alloy. Till now, several attempts have been carried out in order to improve the mechanical properties of AlZnMgCu P/M processed alloys. The strength was suggested to be related to the multiple effect due to precipitation hardening and fiber reinforcing as well as fine grain strengthening. The remarkable strengthening has been mainly attributed to the precipitation hardening.

The total strength was suggested to be given by the multiple effect due to optimal precipitation hardening together with fibre reinforcement due to Mn intermetallic compounds as well as fine grain strengthening. The highest tensile strength have been realized as 910 MPa by the tensile test and 1033 MPa by the compression test.

Mesoalite possesses also superior environmental characteristics against SCC, corrosion pits and so on.

REFERENCES

1. K.Osamura, K.Kohno, H.Okuda, S.Ochiai, J.Kusui, K.Fujii, K.Yokoe. T.Kotote and K.Hono, Mater. Sci. Forum, 217/222(1996), pp. 1829-1834.
2. K.Osamura, H.Adachi, H.Okuda, S.Ochiai, J.Kusui and K.Yokoe, Aluminum Alloys 3(1998), pp.1755-1760.
3. H.Adachi, K.Osamura and H.Okuda, Jap. J. Inst. Metals, 63(1999),pp.733-740.
4. J.Kusui and K.Yokoe, Research Activity Report of Toyo Aluminum, (1998), pp.50-62.

THE EFFECTS OF CHEMICAL AND MICROSTRUCTURE ON AXIAL COMPRESSING PROPERTY OF EXTRUDED Al-Mg-Si ALLOYS

Hitoshi KAWAI and Masakazu HIRANO

Aluminum Extrusion Research Section, KOBE STEEL, LTD.
Shimonoseki-City, Yamaguchi, 752-0953, Japan

ABSTRACT

The vehicle performance to ensure the safety against a collision becomes one of the major factors, both the weight reduction and the anti-collision safety are required in the current automobile industries.

In the case of the vehicle collision, energy absorption members, such as a side member, are to deform as bellows in the axial direction, and absorb the collision energy efficiently.

The aluminum alloy is an appropriate material to reduce the weight, presenting a small specific gravity about 1/3 of the steel. Especially, the Al-Mg-Si alloys feature in its well-balanced properties as well as its high workability to extrude into relatively a complicated section and enable the structure to sustain a high efficiency of energy absorption. The conventional extruded Al-Mg-Si alloys, however, tend to decrease the energy absorption, caused by a crack occurred under an axial compression if the yield stress increases.

In this research, the influence of a microstructure on the axial compressing property was studied for the extruded high-strength Al-Mg-Si alloys. As a result, we found a new measure to prevent the crack under the axial compression even the case of high-strength alloys, by controlling the grain to a fiber structure.

1. INTRODUCTION

Many studies have indicated the importance to reduce the weight of an automobile body, from the viewpoint of environmental protection. In recent years, to secure the safety against the automobile collision has become more important factor. The current vehicle absorbs the collision energy, by deforming the crushable zone such as an engine room and a luggage space. On the other hand, the main vehicle body is not deformed, securing the passenger's survival space.

The aluminum alloy is an effective candidate to reduce the vehicle weight, with a small specific gravity about 1/3 of the steel. Especially, the Al-Mg-Si alloys are favorable in its well-balanced properties. The energy absorption members, such as a side member allocated to the crushable zone, are required to absorb the collision energy efficiently by deforming itself as bellows in the axial direction. Here, the extruded Al-Mg-Si alloys are capable to extrude into relatively a complicated section and suitable as the structural members with a sufficient efficiency of the energy absorption. However, the conventional extruded Al-Mg-Si alloys tend to generate a crack under the axial compression when the yield stress increases, and decrease the energy absorption capacity.

In this study, the influence of a microstructure on the axial compressing property was investigated for the extruded high-strength Al-Mg-Si alloys.

2. SAMPLES

High-strength Al-Mg-Si alloys were prepared for the samples. Table 1 shows the chemical composition of the samples. A ϕ 155mm billet was produced by DC casting, and the billet was homogenized at 540°C for 4h. Then it was extruded into a square box shape of 40mmX40mmX2mm(thickness) using a 9.8kN extrusion press. Fig. 1 shows the cross-section. Here, the extrusion temperature was set at 500°C and the extrusion speed was 5m/min. The samples were finally prepared after the heat treatment as shown in Table 2.

Table 1 Chemical composition (mass%)

Symbol	Si	Fe	Cu	Mn	Mg	Ti	Zr
A	0.90	0.23	tr.	tr.	0.57	0.02	tr.
B	0.88	0.28	tr.	0.36	0.61	0.02	0.14

Table 2 Heat treatment conditions

Solution Treatment	Quenching	Aging	
		Temperature	Time
540°CX20min	Water Quench	180°C	9h

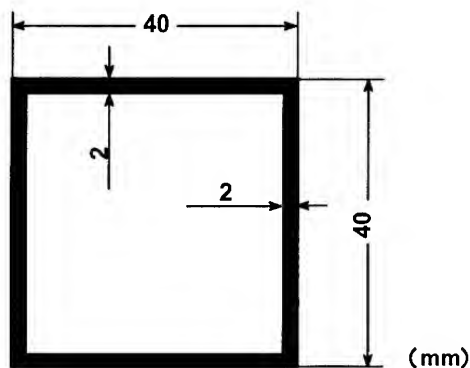


Fig. 1 Cross-section

3. TEST RESULTS

3.1 Results of Tensile Test and Microstructure Analysis

Table 3 shows the measured tensile properties, and the results of the microstructure analysis are shown in Fig. 2.

The sample A, which does not contain a transition metal, has an equiaxial grain of about 70 μm . On the other hand, the sample B, which contains the transition metal, has a fiber structure. The sample B presents a slightly higher property than the sample A in a tensile strength, yield stress and an elongation.

Table 3 Tensile property

Sample	TS (N/mm ²)	YS (N/mm ²)	El (%)
A	323	307	11.2
B	335	311	12.6

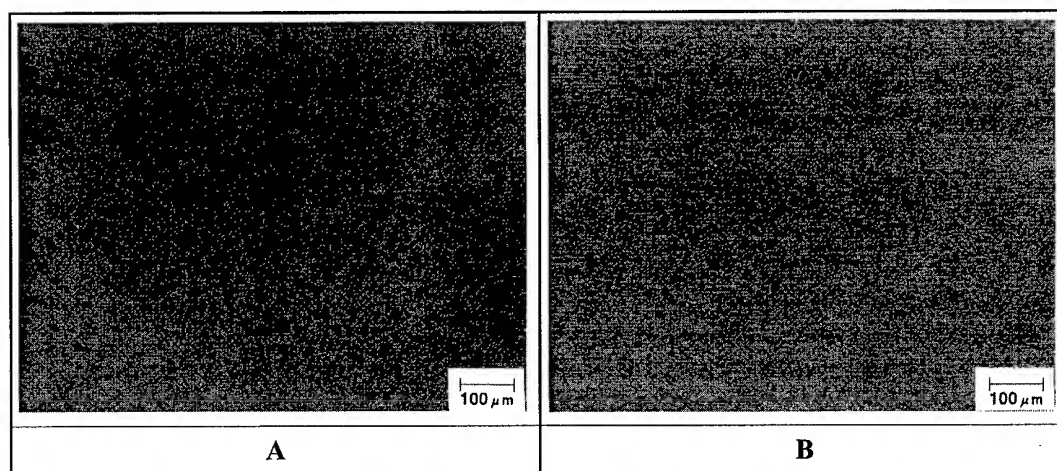


Fig. 2 Results of the microstructure analysis

3.2 Results of Axial Compression Test

Table 4 shows the results of the axial compression test. The load-displacement curve derived from the axial compression test is shown in Fig. 4 with photographs of the sample deformed during the test. The axial compression test was carried out using the 300kN universal testing machine according to the method shown in Fig. 3. Here, the average compression speed was 70mm/min.

There was no significant difference in the maximum load between each type of the sample. While the sample B deformed regularly as bellows, the sample A generated a crack without a bellows-deformation. Compared with the sample B, both the applied mean load and the absorbed energy were smaller for the sample A.

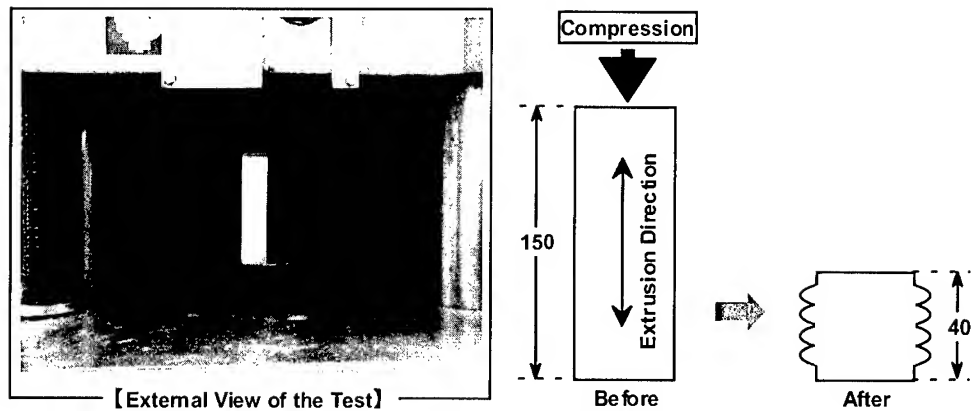


Fig. 3 Method of the axial compression test

Table 4 Results of the axial compression test

Sample	Maximum Load (kN)	Mean Load (kN)	Absorbed Energy* (J)	Deformation
A	93	20	1770	Poor
B	91	40	3040	Excellent

* Compression displacement : 0mm~75mm

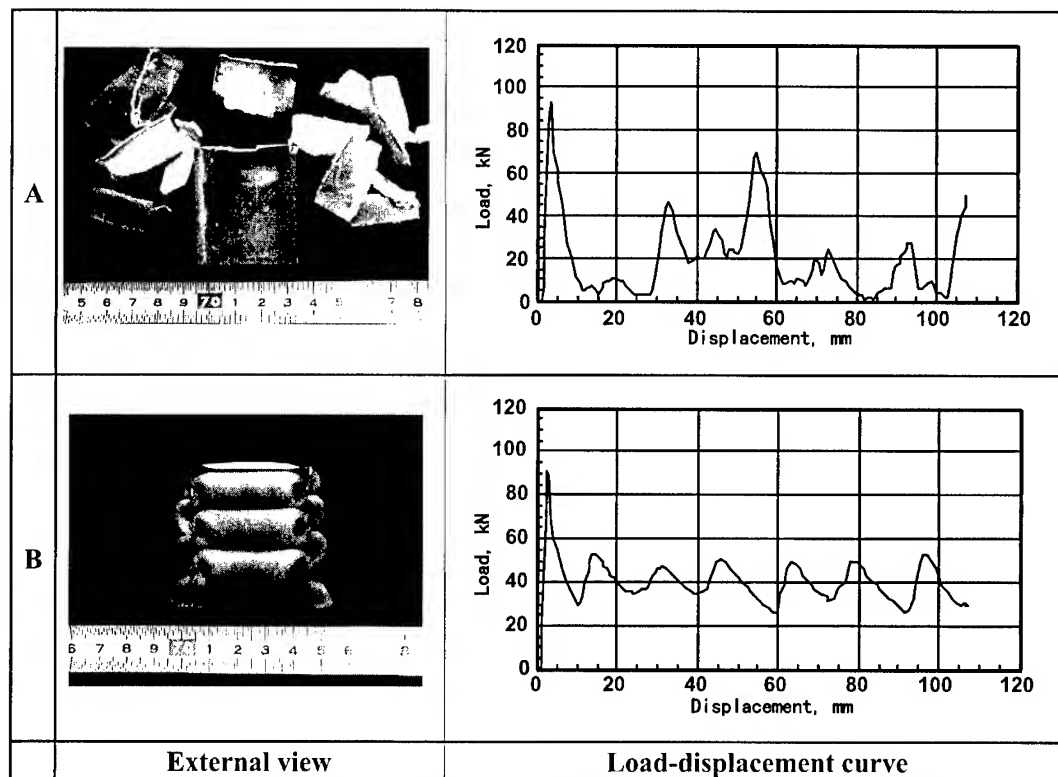


Fig. 4 Load-displacement curve and external view of the deformed sample

3.3 Results of Cross-sectional Microstructure Analysis

Fig. 5 shows the results of the cross-sectional microstructure analysis of the sample A on the fracture section of the axial compression test.

The crack propagated mainly along the grain boundary in the bellows-deformation section. Some cracks occurred along the grain boundary in depth, which did not appear on the surface.

Fig. 6 shows the results of the cross-sectional microstructure analysis of the sample B on the fracture section of the axial compression test.

Cracks, which were observed on a surface of the bellows-deformation, occurred within the grain and terminated before propagating into the depth.

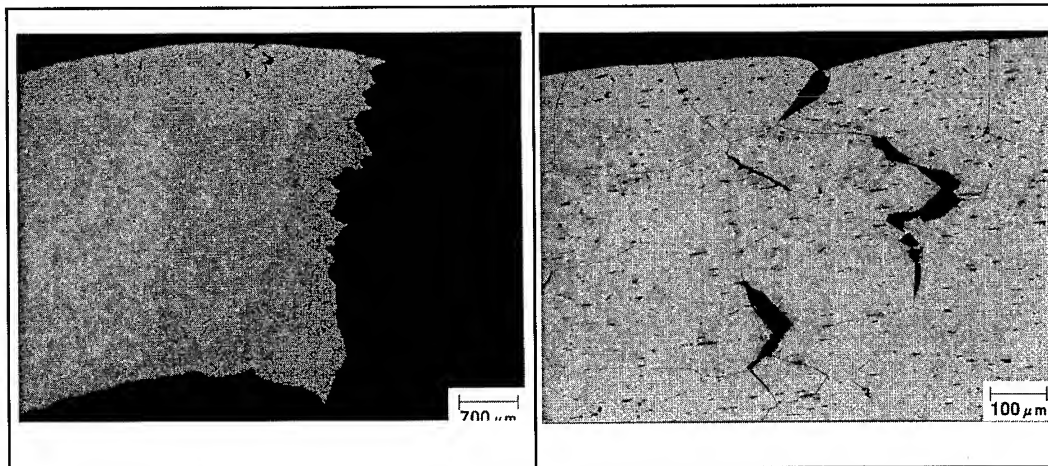


Fig. 5 Results of the cross-sectional microstructure analysis of the sample A on the fracture section of the axial compression test

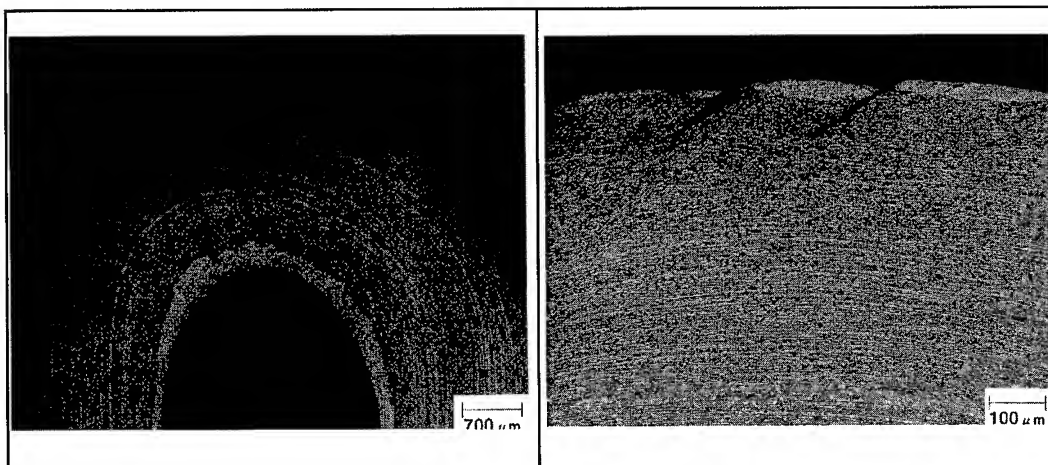


Fig. 6 Results of the cross-sectional microstructure analysis of the sample B on the fracture section of the axial compression test

4. DISCUSSION

The surface of the bellows-deformation, where the cracks initiated in the axial compression test, is of a tensile deformation. The SEM fractography on the fracture surface of the tensile test pieces, shown in Fig. 7, is to compare the fracture mechanics of each type of the tensile deformation.

As for the sample A, the intergranular fracture is dominant because the intergranular fractured surface occupies a major fraction where the grain boundary and dimples were intermingled. As for the sample B on the other hand, the transgranular fracture is dominant because of the dimple fractures over the whole surface.

From the above, controlling the grain to a fiber structure is judged to be effective to prevent the crack initiation under the axial compression deformation, by restraining the intergranular fracture.

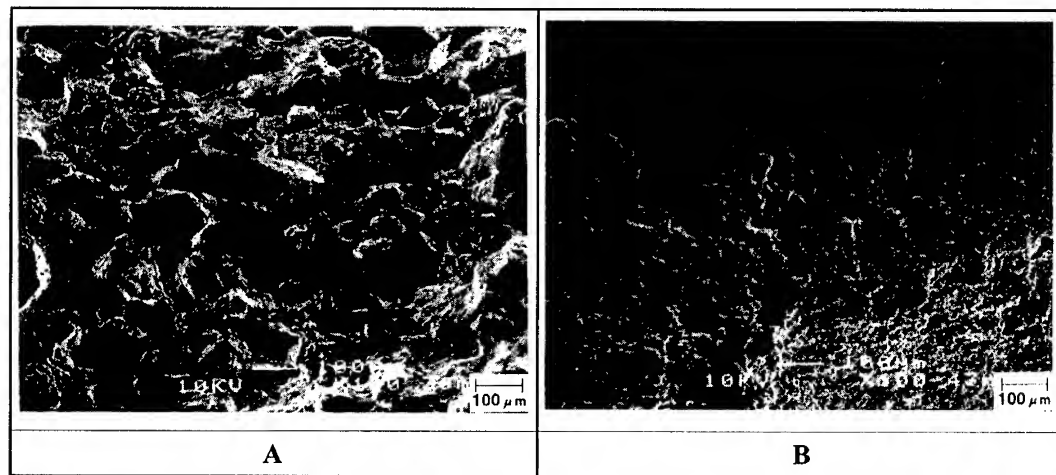


Fig. 7 SEM fractography on the fracture surface of the tensile test pieces

5. CONCLUSION

The influence of the microstructure on the axial compressing property was investigated for the extruded high-strength Al-Mg-Si alloys. Controlling the grain to a fiber structure is effective to prevent the crack under the axial compression deformation even in the case of the high-strength alloys. We judge that the fiber structure, controlled from the grain, contributes to restrain the intergranular fracture.

MICROSTRUCTURE AND ELEVATED-TEMPERATURE STRENGTH OF P/M $\text{Al}_{96-x}\text{Fe}_x\text{Cr}_2\text{Ti}_2$ ($x=3, 4, 5$) ALLOYS

Hisamichi M. Kimura, Akihisa Inoue and Kenichiro Sasamori
Institute for Materials Research, Tohoku University, Sendai 980-8577, Japan

ABSTRACT

Microstructure, mechanical properties and wear resistance were examined for powder metallurgy (P/M) $\text{Al}_{96-x}\text{Fe}_x\text{Cr}_2\text{Ti}_2$ ($x=3, 4, 5$) alloys prepared by extruding argon gas atomized powders at 673 K. Microstructure of the P/M $\text{Al}_{96-x}\text{Fe}_x\text{Cr}_2\text{Ti}_2$ ($x=3, 4, 5$) alloys consists of dispersed quasicrystalline (Q.C.) particles. The P/M alloys have ultimate tensile strength (σ_{UTS}) from 540 to 670 MPa, 0.2% proof strength ($\sigma_{0.2}$) from 450 to 580 MPa, plastic elongation (ϵ_{P}) from 1.1 to 7.3 %, Young's modulus (E) from 85 to 92 GPa and H_v from 165 to 200 at room temperature. The P/M alloys sustained high σ_{UTS} exceeding 300 MPa even after keeping for 100 hours at 573 K. The specific wear rate of the P/M $\text{Al}_{93}\text{Fe}_3\text{Cr}_2\text{Ti}_2$ alloy is as low as $2.7 \times 10^{-7} \text{ mm}^2/\text{kg}$ at the sliding velocity of 2 m/s.

1. INTRODUCTION

It is known that Q.C. alloys have high Vickers hardness (H_v) and extremely brittle nature. For example, H_v is 1010 for the $\text{Al}_{77.5}\text{Mn}_{22.5}$ alloy[1], 710 for the $\text{Al}_{85.6}\text{Cr}_{15.4}$ alloy[1] and 735 for the $\text{Al}_{86}\text{V}_{14}$ alloy[2] with a mostly single Q.C.. These alloys also have high thermal stability[1,3]. There is a possibility of synthesizing a new material with high specific strength, high elevated-temperature strength and high wear resistance by dispersing Q.C. particles into fcc-Al phase. Inoue et al. have found that a mixed microstructure consisting of Q.C. and fcc-Al phases is formed in the P/M $\text{Al}_{94}\text{V}_4\text{Fe}_2$ [4] and $\text{Al}_{93}\text{Fe}_3\text{Cr}_2\text{Ti}_2$ [5] alloys and their mixed phase alloys exhibit high elevated-temperature strength exceeding 300 MPa. This paper presents the microstructure, strength and wear resistance at room and elevated-temperatures for the P/M $\text{Al}_{96-x}\text{Fe}_x\text{Cr}_2\text{Ti}_2$ ($x=3, 4, 5$) alloys produced by P/M.

2. EXPERIMENTAL

The ingots of $\text{Al}_{96-x}\text{Fe}_x\text{Cr}_2\text{Ti}_2$ ($x=3, 4, 5$) alloys were prepared by induction melting of Al-4.82 mass%Ti, Al-4.89 mass%Cr and Al-51.09 mass%Fe and Al and Cr metals in an argon gas atmosphere. P/M $\text{Al}_{96-x}\text{Fe}_x\text{Cr}_2\text{Ti}_2$ ($x=3, 4, 5$) alloys with a diameter of 8 mm and a length of 300 mm were prepared by extruding argon gas atomized powders at 673 K and an extrusion ratio of 10. The atomized powders used for extrusion were sieved into the

sizes smaller than 26 μm , 75 μm and 125 μm , respectively. The structures of extruded alloys were examined by X-ray diffraction (XRD) and transmission electron microscopy (TEM). Tensile strength was measured at a strain rate of $4.0 \times 10^{-4} \text{ s}^{-1}$ in the temperature range from room temperature to 673 K with an Instron testing machine. Hardness was measured with a Vickers microhardness tester under a load of 9.8 N. Wear rate against hardened steel S50C ($H_v=680$) was measured in the sliding velocity range from 0.5 to 2 m/s with a wear testing machine. Specific wear rate (c) can be calculated using $c=w/Lx$, where w (mm^3), L (kg) and x (mm) are volume of wear, load and distance of wear, respectively.

3. RESULTS AND DISCUSSION

3.1 Microstructure

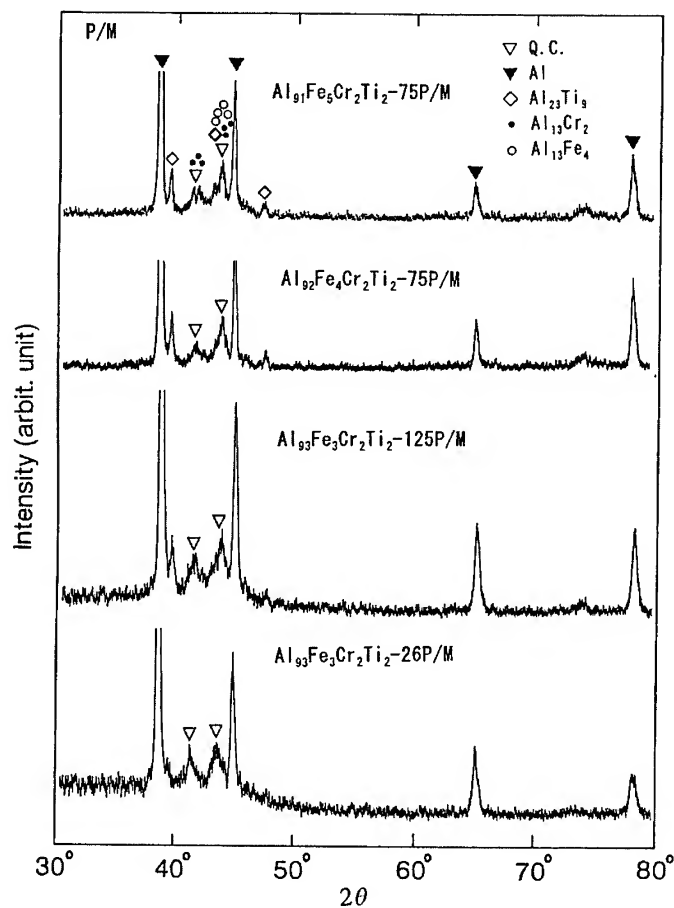


Fig. 1 XRD patterns of P/M $\text{Al}_{96-x}\text{Fe}_x\text{Cr}_2\text{Ti}_2$ ($x=3, 4, 5$) alloys produced by extrusion of atomized powders with sizes of ≤ 26 , ≤ 75 and $\leq 125 \mu\text{m}$, respectively.

Figure 1 shows the XRD patterns of the P/M $\text{Al}_{96-x}\text{Fe}_x\text{Cr}_2\text{Ti}_2$ ($x=3, 4, 5$) alloys produced by extruding atomized powders with the size smaller than 26, 75 and 125 μm at an extrusion temperatures (T_e) of 673 K and an extrusion ratio of 10. The structure of the alloy with $x=3$ consists of Al + Q.C. for the powder smaller than 26 μm ($\leq 26 \mu\text{m}$) and Al+Q.C.+ $\text{Al}_{23}\text{Ti}_9$ for the powder smaller than 125 μm ($\leq 125 \mu\text{m}$). The structure for the $x=4$ and 5 alloys consists of Al+Q.C.+ $\text{Al}_{13}\text{Fe}_4$ + $\text{Al}_{13}\text{Cr}_2$ for the powder smaller than 75 μm ($\leq 75 \mu\text{m}$). Figure 2 shows bright-field TEM images (a, b, c) and selected-area electron diffraction patterns (d, e, f) of the P/M $\text{Al}_{91}\text{Fe}_5\text{Cr}_2\text{Ti}_2$ alloy produced by extrusion of atomized powder with the powder size $\leq 75 \mu\text{m}$. The diffraction patterns of the precipitated particles have the five-, three- and two-fold symmetries of the Q.C. phase. An average size of the particle is estimated to be about 400 nm from TEM images.

All the prepared P/M $\text{Al}_{96-x}\text{Fe}_x\text{Cr}_2\text{Ti}_2$ ($x=3, 4, 5$) alloys had a mixed structure consisting of Q.C. dispersed particles in fcc-Al matrix and the size of dispersed particle ranges from 200 to 900 nm.

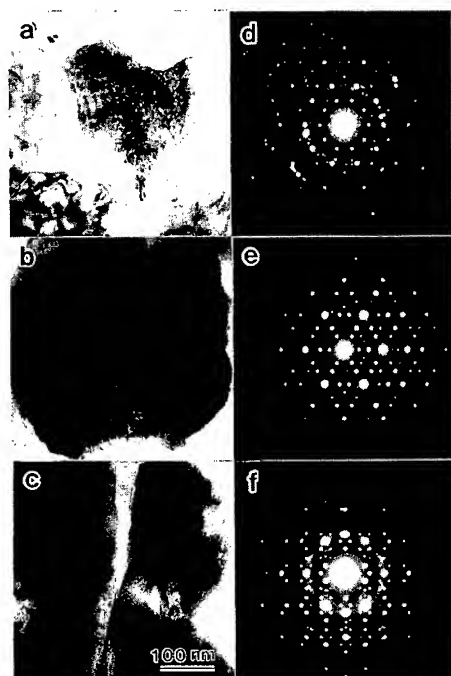


Fig. 2 TEM images and selected-area electron diffraction patterns of the P/M $\text{Al}_{91}\text{Fe}_5\text{Cr}_2\text{Ti}_2$ alloy produced by extrusion of atomized powder with a size $\leq 75 \mu\text{m}$.

3.2 Mechanical properties

Table 1 summarizes the ultimate tensile strength (σ_{UTS}), 0.2 % proof stress ($\sigma_{0.2}$) and plastic elongation (ϵ_p), Young's moduli (E) and Vickers hardness (H_v) at room temperature of the P/M $\text{Al}_{96-x}\text{Fe}_x\text{Cr}_2\text{Ti}_2$ ($x=3, 4, 5$) alloys, together with the data of the conventional

7075-T6 aluminum alloy. The σ_{UTS} , $\sigma_{0.2}$, E and Hv of the P/M $Al_{91}Fe_5Cr_2Ti_2$ alloy are higher than those for the conventional 7075-T6 aluminum alloy, while its ϵ_P is lower. For the P/M $Al_{96-x}Fe_xCr_2Ti_2$ ($x=3, 4, 5$) alloys, the σ_{UTS} , $\sigma_{0.2}$, E and Hv for

Table 1 Mechanical properties of the P/M alloys tested at room temperature. The data of the conventional 7075-T6 aluminum alloy also are shown for comparison.

P/M Alloy (at%)	Powder size (μm)	σ_{UTS} (MPa)	$\sigma_{0.2}$ (MPa)	ϵ_P (%)	E (GPa)	Hv
$Al_{93}Fe_3Cr_2Ti_2$	≤ 26	658 ± 9	545 ± 14	4.4 ± 0.5	85 ± 2	192 ± 3
$Al_{93}Fe_3Cr_2Ti_2$	≤ 125	537 ± 4	464 ± 5	5.4 ± 1.4	90 ± 1	165 ± 2
$Al_{92}Fe_4Cr_2Ti_2$	≤ 75	602 ± 2	521 ± 4	3.3 ± 0.4	88 ± 2	186 ± 3
$Al_{91}Fe_5Cr_2Ti_2$	≤ 75	664 ± 11	580 ± 11	1.1 ± 0.2	91 ± 1	199 ± 6
7075-T6	—	600	550	10.7	70	190 ± 3

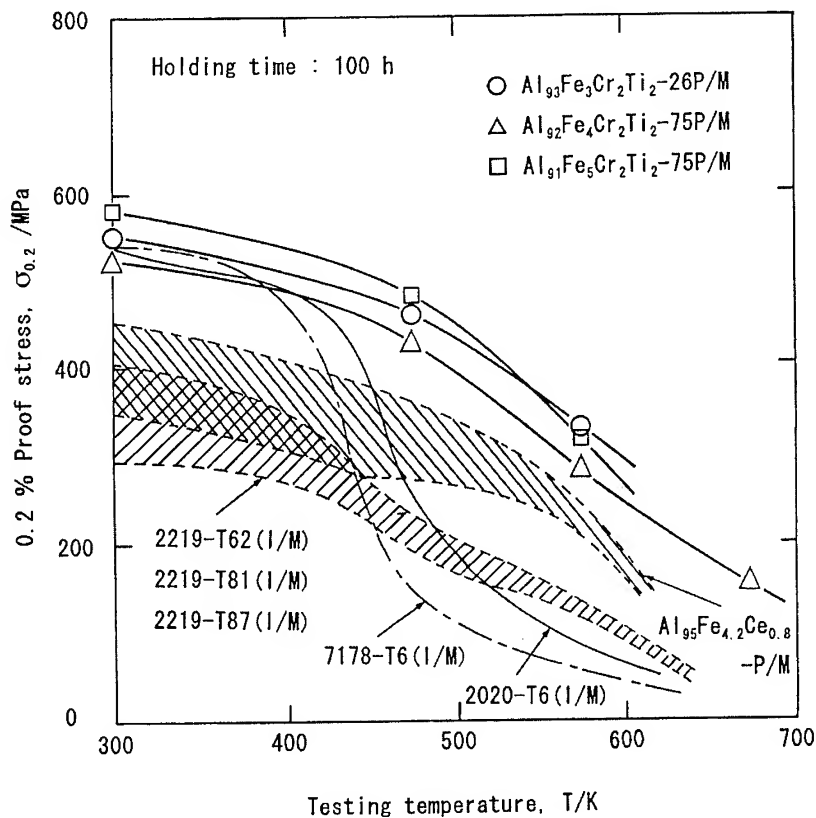


Fig. 3 0.2% proof strength ($\sigma_{0.2}$) of P/M $Al_{96-x}Fe_xCr_2Ti_2$ ($x=3, 4, 5$) alloys after keeping for 100 hours at various testing temperature. The data of the conventional aluminum alloy are also shown for comparison.

the powder with a size $\leq 26 \mu\text{m}$ are higher those for the powder with a size $\leq 125 \mu\text{m}$ and increase with an increase of x . On the other hand, the ϵ_p shows an opposite x dependence to that for σ_{UTS} , $\sigma_{0.2}$, E and H_v . The P/M alloys, exhibit σ_{UTS} in the range from 540 to 670 MPa, $\sigma_{0.2}$ from 450 to 580 MPa, ϵ_p from 1.1 to 7.3 %, E from 85 to 92 GPa and H_v from 165 to 200 at room temperature.

We examined the σ_{UTS} , $\sigma_{0.2}$ and ϵ_p after keeping for 100 hours at 573 K for the P/M $\text{Al}_{96-x}\text{Fe}_x\text{Cr}_2\text{Ti}_2$ ($x=3, 4$ and 5) alloys. The σ_{UTS} , $\sigma_{0.2}$ and ϵ_p of the P/M $\text{Al}_{96-x}\text{Fe}_x\text{Cr}_2\text{Ti}_2$ ($x=3, 4, 5$) alloys are in the range from 280 to 350 MPa, 260 to 320 MPa and 2.5 to 7.5 %, respectively. Figure 3 shows the $\sigma_{0.2}$ after keeping of 100 hours at various testing temperatures of the P/M $\text{Al}_{93}\text{Fe}_3\text{Cr}_2\text{Ti}_2$ ($\text{Al}_{93}\text{Fe}_3\text{Cr}_2\text{Ti}_2$ -26P/M) alloy produced by extrusion of atomized powder with the size $\leq 26 \mu\text{m}$ and the P/M $\text{Al}_{92}\text{Fe}_4\text{Cr}_2\text{Ti}_2$ ($\text{Al}_{92}\text{Fe}_4\text{Cr}_2\text{Ti}_2$ -75P/M) and $\text{Al}_{91}\text{Fe}_5\text{Cr}_2\text{Ti}_2$ ($\text{Al}_{91}\text{Fe}_5\text{Cr}_2\text{Ti}_2$ -75P/M) alloys produced by extrusion of atomized powders with the size $\leq 75 \mu\text{m}$. It is noticed that the present P/M alloys have high elevated-temperature strength with σ_{UTS} and $\sigma_{0.2}$ exceeding those of conventional P/M $\text{Al}_{95}\text{Fe}_{4.2}\text{Ce}_{0.8}$ alloy[6] and 2000 system aluminum alloys produced by ingot metallurgy[6]. In addition, these Al-based alloys do not include any expensive elements. Owing to these advantage points, the Al-Fe-Cr-Ti alloys with dispersed Q.C. particles are expected to be used as a new high elevated-temperature strength material.

3.3 Wear resistance

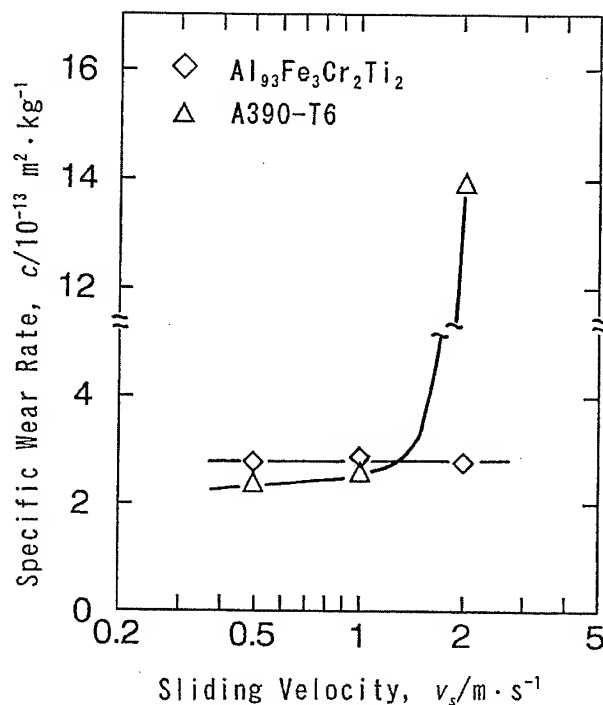


Fig. 4 The specific wear rate (c) against sliding velocity (v_s) for P/M $\text{Al}_{93}\text{Fe}_3\text{Cr}_2\text{Ti}_2$ alloy. The data of the conventional A390-T6 aluminum alloy are also shown for comparison.

Figure 4 shows the specific wear rate (c) of P/M $\text{Al}_{93}\text{Fe}_3\text{Cr}_2\text{Ti}_2$ alloy with dispersed quasicrystal particles produced by the powder with a particle size $\leq 26 \mu\text{m}$ against sliding velocity (v_s), together with the data of the conventional A-390 aluminum alloy. Although the specific wear rate of the conventional A-390 aluminum alloy increases rapidly at a sliding velocity of 1.5 m/s, the P/M $\text{Al}_{93}\text{Fe}_3\text{Cr}_2\text{Ti}_2$ alloy keeps the specific wear rate smaller than $3.0 \times 10^{-7} \text{ mm}^2/\text{kg}$ even at a velocity of 2 m/s. The good wear resistance of the P/M $\text{Al}_{93}\text{Fe}_3\text{Cr}_2\text{Ti}_2$ alloy is considered due to the dispersion of Q.C. particles with high hardness and high stability into the Al matrix.

4. CONCLUSIONS

The microstructure and mechanical properties of the P/M $\text{Al}_{96-x}\text{Fe}_x\text{Cr}_2\text{Ti}_2$ ($x=3, 4, 5$) alloys were examined. The results obtained are summarized as follows:

- 1) The P/M $\text{Al}_{96-x}\text{Fe}_x\text{Cr}_2\text{Ti}_2$ ($x=3, 4, 5$) alloys have a mixed structure consisting of dispersed Q.C. particles in fcc-Al matrix and size of the dispersed particle ranges from 200 to 900 nm.
- 2) The mixed phase alloys exhibit the ultimate tensile strength (σ_{UTS}) of 540 to 670 MPa, 0.2% proof strength ($\sigma_{0.2}$) of 450 to 580 MPa, plastic elongation (ϵ_p) of 1.1 to 7.3 %, Young's modulus (E) of 85 to 92 GPa and H_V of 165 to 200 at room temperature.
- 3) The P/M alloys sustained the high σ_{UTS} exceeding 300 MPa even after keeping for 100 hours at 573 K.
- 4) The specific wear rate of the P/M $\text{Al}_{93}\text{Fe}_3\text{Cr}_2\text{Ti}_2$ alloy is as low as $2.8 \times 10^{-7} \text{ mm}^2/\text{kg}$ at the sliding velocity of 0.5 m/s and $2.7 \times 10^{-7} \text{ mm}^2/\text{kg}$ at 2.0 m/s, being almost independent of sliding velocity.

REFERENCES

1. A. Inoue, H. M. Kimura and T. Masumoto: J. Mater. Sci., 22(1987), pp. 1758-1768.
2. H. M. Kimura, A. Inoue and K. Sasamori: J. Jpn. Inst. Light Met., 48(1988), pp. 127-131.
3. D. Shechtman, I. Blech, D. Gratias and J. W. Cahn: Phys. Rev. Lett., 53(1984), pp. 1951-1953.
4. H. M. Kimura, A. Inoue and K. Sasamori: J. Jpn. Inst. Light Met., 48(1997), pp. 539-544.
4. H. M. Kimura, A. Inoue and K. Sasamori: J. Jpn. Inst. Light Met., 48(1988), pp. 263-268.
5. P. R. Bridenbaugh, W. S. Cebulak, F. R. Billman and G. H. Hildeman: Light Metal Age, Oct., (1985), pp. 18-26.

EFFECT OF SI ADDITION ON THE MICROSTRUCTURE AND CREEP PROPERTIES OF THE MECHANICALLY ALLOYED AL-10Ti ALLOY

Chul-Jin Choi, Joong-Keun Park* and Byoung-Kee Kim

Korea Institute of Machinery and Materials
66, Sangnam-dong, Changwon, Kyungnam 641-010, KOREA

*Korea Advanced Institute of Science and Technology
373-1, Kusong-dong, Yusong-gu, Taejon 305-701, Korea

ABSTRACT

The microstructural evolution and creep properties were investigated in the mechanically alloyed Al-10Ti-xSi ($x=0, 2, 4$) alloy. In mechanically alloyed powders, Ti was dissolved, but Si was only crushed and embedded in Al matrix. After hot extrusion, the dissolved Ti reacted with Al to form the Al_3Ti particles, and Si was incorporated in them. Two distinctive creep mechanism have been observed depending on the test stress and temperature, i.e. Coble creep at low stresses and temperatures and dislocation creep at high stresses and temperatures. The transition stress from diffusion to dislocation creep has a tendency to shift to higher with increasing of Si content. This is due to the strengthening of Al_3Ti particles originated from Si incorporation into them. The creep properties of the mechanically alloyed Al-10Ti alloy were enhanced with an addition of Si.

1. INTRODUCTION

Mechanical Alloying (MA) offers the attractive advantages in the development of dispersion strengthened high temperature aluminum alloys because of its capability to largely extend the solid solubility of transition metal elements and uniformly disperse ultrafine dispersoids [1].

MA Al-Ti based alloy has drawn much attention as a promising candidate for high temperature structural components because of highly stable Al_3Ti phase and very low equilibrium solubility and diffusivity of Ti in Al [2]. Recently the addition of Si to MA Al-Ti has been reported to provide the improved strength at both ambient and elevated temperatures [3].

The objective of this study was to investigate the effect of Si addition on the microstructural evolution and creep properties of MA Al-10Ti alloy.

2. EXPERIMENTAL PROCEDURES

Elemental powders of Al, Ti and Si with 1 wt% stearic acid were mechanically alloyed using an attritor with Ar atmosphere, to obtain Al-10wt%Ti-xwt%Si ($x=0, 2, 4$) compositions. Table 1 shows the chemical composition of the MA powders. To consolidate them, aluminum

cans were filled with the MA powders and sealed. They were degassed and hot pressed at 450°C under 200 MPa. Decanned compacts were finally hot extruded to full density at 450°C with the extrusion ratio of 12 : 1. The specimens (8mm in diameter and 12 mm in height) for compression creep test were machined from the extruded rods. Creep tests were carried out in compression, using a linear variable differential transformer (LVDT) which was monitored in a strip charter recorder. The phases of MA powders and extruded compacts were analyzed by X-ray diffraction.

Table 1. Chemical composition of the MA Al-10Ti-xSi alloy powders

Element Alloy	Al	Ti	Si	C	O
Al-10Ti	Bal	9.52	-	0.61	1.81
Al-10Ti-2Si	Bal	9.53	1.56	0.61	1.04
Al-10Ti-4Si	Bal	9.47	3.79	0.71	1.21

3. RESULTS AND DISCUSSION

Fig 1. shows X-ray diffraction profiles of MA powders and hot extruded compacts of Al-10Ti-xSi alloy. The diffraction peaks of Ti are nearly invisible in all cases of MA powders (Fig 1(a)). This means that Ti is dissolved in the Al matrix by MA processing. On the contrary, Si peaks still remained for the MA Al-Ti-Si ternary powders. In the Al-Ti-Si ternary alloys, it is obvious that Si particles are not dissolved but dispersed uniformly in the Al matrix in a crushed state. After hot extrusion, new Al_3Ti phase can be observed. This indicates that the dissolved Ti react with Al to form the Al_3Ti phase. The Si peaks present in the X-ray patterns from the MA powders disappeared in the case of the Al-Ti-Si ternary alloys. It is noticeable that the diffraction angle of Al_3Ti phase shift to right with an increase of Si content in all alloys. This implies that Si is dissolved in Al_3Ti phase and changes its lattice parameter.

Table 2 shows a summary of the steady state creep rates for the extruded Al-10Ti-xSi alloys. Comparison of the steady state creep rates indicates that the creep rate becomes generally lower with increasing Si content at the same test temperature and stress.

Table 2 shows a summary of the steady state creep rates for the extruded Al-10Ti-xSi alloys. Comparison of the steady state creep rates indicates that the creep rate becomes generally lower with increasing Si content at the same test temperature and stress.

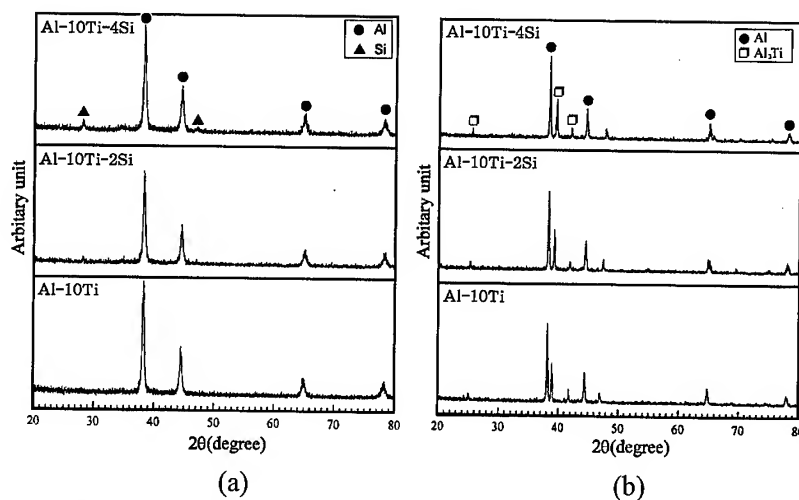


Fig. 1. X-ray diffraction profiles of Al-10Ti-xSi alloys : (a) MA powders ; (b) as-hot extruded.

Table 2. Measured steady state creep rates in Al-10Ti-xSi alloys

Temperature (°C)	Stress (MPa)	Creep rate (1/sec) for Al-10Ti	Creep rate (1/sec) for Al-10Ti-2Si	Creep rate (1/sec) for Al-10Ti-4Si
300	209	2.85×10^{-8}	1.52×10^{-8}	1.23×10^{-8}
	249	1.46×10^{-6}	1.52×10^{-7}	7.86×10^{-8}
400	119	3.60×10^{-7}	6.41×10^{-8}	5.95×10^{-8}
	139	2.43×10^{-6}	1.79×10^{-7}	8.35×10^{-8}
450	69	1.97×10^{-7}	1.28×10^{-7}	1.12×10^{-7}
	89	1.76×10^{-6}	2.58×10^{-7}	1.36×10^{-7}

Fig. 2 plots the stress dependence of the creep rate at various temperatures according to the conventional creep equation,

$$\dot{\epsilon} = A \sigma^n \exp(-Q/RT) \quad (1)$$

where A , σ , n , Q , R and T are a constant, the applied stress, the stress exponent, the activation energy for creep, the gas constant and the absolute temperature, respectively. One can notice that there are two distinctively different creep regimes depending on the magnitude of the applied stress. At low stress regime, the stress exponent, expressed as $n = (\ln \dot{\epsilon} / \ln \sigma)_T$ from equation (1), is low (1.2 ~ 1.9), while it is very high at high stress regime (10.0 ~ 19.0). This suggests that a transition from the diffusional creep to power law creep occurs as the applied stress increases. Table 3 summarizes the transition stresses for the Al-10Ti-xSi alloys. The comparison indicates that the transition stress tends to shift to a higher value with increasing Si content: for example, from 199 to 229 and 249 MPa at 300°C for Al-10Ti-xSi

alloys ($x=0, 2, 4$ wt%), respectively. It implies that the diffusional creep regime significantly enlarges to high stress with increasing Si content. We believe that such a tendency is primarily due to an enhancement of particle strength of Al_3Ti phase as a result of Si incorporation.

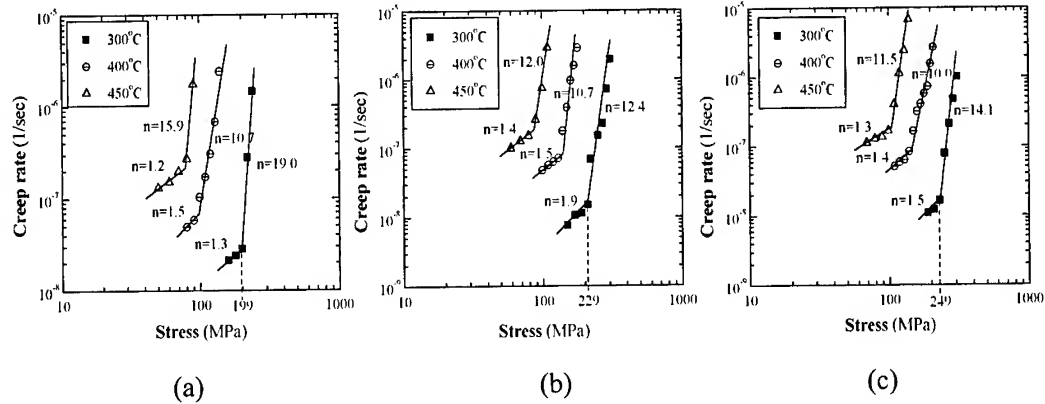


Fig. 2. Variation of steady state creep rate of Al-10Ti-xSi alloy as a function of an applied stress at various temperatures : (a) Al-10Ti ; (b) Al-10Ti-2Si ; (c) Al-10Ti-4Si. Note an appearance of two distinctively different creep regimes.

Table 3. Transition stresses from diffusional creep to dislocation one in MA Al-10Ti-xSi alloys

Material	Temperature(oC)	Transition stress(MPa)
Al-10Ti	300	199
	400	109
	450	70
Al-10Ti-2Si	300	229
	400	139
	450	79
Al-10Ti-4Si	300	249
	400	149
	450	99

Fig. 3 plots the steady state creep rates as a function of temperature: there are once again two distinctive regimes, now depending on two test stresses. At low temperature regime, the activation energy expressed as $Q = -R(\ln \dot{\epsilon} / \ln(1/T))_0$ from equation (1) is low (67~90 kJ/mole), whereas it is very high in high temperature regime (408~629 kJ/mole). The transition temperature is about 430°C at 99 MPa and decreases to about 380°C at 149 MPa for the Al-10Ti alloy. This temperature tends to shift to a higher one with increasing Si content. The activation energy in low temperature regime is close to that for the Al self diffusion (84 kJ/mole) at grain boundaries [4]. The activation energy in high temperature regime has no comparison : it is 3~4 times more than that of the Al self diffusion through the lattice (142 kJ/mole) [5]. However, this high activation energy together with the high stress exponent are

two characteristics frequently observed in the dislocation creep of dispersion strengthened alloys [6,7]. Therefore, this result suggests that the creep mechanism changes again from diffusional (Coble) to dislocation one as the test temperature increases. The tendency of the transition temperature to become higher with an increasing Si content means that diffusional creep regime extends to higher temperature. This is believed to arise from an enhancement of particle strength of the Al_3Ti phase with increasing Si content as a result of the dissolution of Si in Al_3Ti particles. Therefore, it could be concluded that the addition of Si enhanced the creep resistance of the MA Al-10Ti alloy due to the strengthening of Al_3Ti particles as a result of Si incorporation into them.

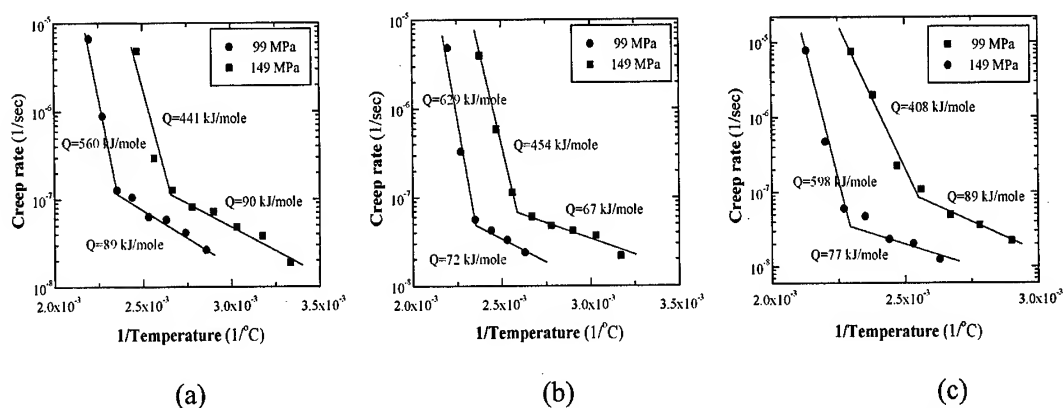


Fig. 5. Arrhenius plot of steady state creep rate of Al-10Ti-xSi alloy under two stress levels :
(a) Al-10Ti ; (b) Al-10Ti-2Si ; (c) Al-10Ti-4Si.

4. CONCLUSIONS

Through MA processing of Al-10Ti-xSi alloys ($x=0 \sim 4\text{wt}\%$), Ti was dissolved in the Al matrix, and Si particles were finely crushed and embedded in Al(Ti) powder particles. During hot extrusion, the dissolved Ti reacted with Al to form Al_3Ti phase, and Si particles were dissolved into the Al_3Ti phase.

Two distinctive creep mechanisms have been observed in the MA and extruded Al-10Ti-xSi alloys, i.e., Coble creep at low stresses and temperatures and dislocation creep at high stresses and temperatures. The transition stress and temperature from diffusion to dislocation creep tends to increase with increasing Si content. This is believed to arise from an enhancement of particle strength of Al_3Ti phases as a result of Si incorporation. This has an effect to enhance the creep resistance of the MA Al-10Ti alloy.

REFERENCES

- [1] P.S.Gilman and J.S.Benjamin, *Ann. Rev. Mat. Sci.*, Vol.13(1983) , pp.279
- [2] J.A.Hawk, P.K.Mirchandani, R.C.Benn and H.G.F.Wilsdorf, in *Dispersion Strengthened Aluminum Alloys*, Y.W.Kim and W.M.Griffith, eds., (1988), pp.551
- [3] A.S.Watwe, P.K.Mirchandani and W.E.Mattson, U.S.Patent, 5,169,461
- [4] H.J.Frost and M.F.Ashby: *Deformation Mechanism Maps, The Plasticity and Creep of Metals and Ceramics*, Pergamon Press, New York, NY (1982)
- [5] T.S. Lundy and J.F. Murdock, *J. Appl. Phys.*, Vol.33(1962), pp.1671
- [6] J.D. Whittenburger, *Metall. Trans.*, Vol.8A(1977), pp.1155
- [7] S.Purushothaman and J.K.Tien, *Acta Metall. Mater.*, Vol.26(1978), pp.519

TEXTURE ANALYSIS OF ALUMINUM PLATE PRODUCED BY ECAP

SukMin Baeck, Hyun-Kwang Seok*, Jae-Chul Lee*, Dong-Ik Kim,
Hu-Chul Lee and Kyu Hwan Oh

School of Materials Science and Engineering
Seoul National University, 151-742 Seoul, KOREA

*Div. Of Materials Science and Engineering
Korea Institute of Science and Technology, 130-650 Seoul, KOREA

ABSTRACT

Modified Equal Channel Angular Pressing(ECAP) process was used to make a plate from an annealed 1050 aluminum and the texture evolution of the plate was studied by using Electron Back Scattered Diffraction(EBSD) and the effects of texture evolution on the mechanical properties of the plate were investigated. By using rate sensitive model, texture evolution was simulated and calculation results were compared to the experimental results. It was found that the deformation texture of aluminum plate transformed from $\langle 100 \rangle // TD$ to $\langle 111 \rangle // TD$ and $\langle 110 \rangle // TD$ direction.

1. INTRODUCTION

A typical Equal Channel Angular Pressing(ECAP) is a process capable of introducing the shear deformation onto the plate continuously and is based on one-path Equal Channel Angular Extrusion. By using modified ECAP process, it is possible to make aluminum plates with high product rate compared to conventional ECAP and the shear flow is formed into the produced aluminum plate. The plastic strain ratio of ECAP aluminum plate is better than that of rolled aluminum plate due to the crystallographic texture evolution and micro-structural refinement. ECAP(Equal Channel Angular Pressing) was originally developed by Segal et al. [1-3]. During ECAP process the material is pressed through a die that consists of one guiding roll and one feeding roll with identical cross-sections intersecting at a given oblique angle. Fig.1 shows a schematic diagram of the ECAP process which can introduce shear strain into aluminum plate continuously.

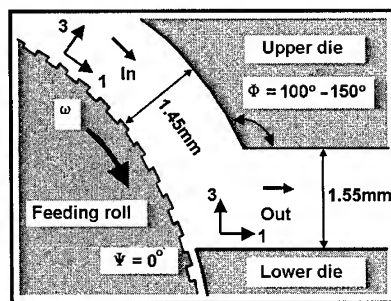


Fig. 1 Schematic representation of ECAP process

A specially designed feeding roll with knurls on its surface and a guiding roll were used. The oblique angle can be given the range of 100°~130°, and the oblique angle of this study is 120°, and an effective shear strain of 1.16 per pass of ECAP is introduced into aluminum plate[1,2]. And there are difference between inlet thickness and outlet thickness. When the plate of 1.55mm thickness is fed into the feeding roll, the thickness of plate is reduced into 1.45mm thick according inlet channel and proceeds toward the outlet channel along die gap(1.55mm). Such a die configuration makes a unique ECAP process which is different from the conventional ECAP process. Instead of feeding the aluminum plate using the ram type, roll type-feeding enables continuous operation and also makes various metal strip forming possible. In addition, there is no thickness change, the multi pass operation is possible in a continuous mode.

The purpose of ECAP is improvement of property of materials through texture change. Because it is known that plastic strain ratio is the major factor of formability[4], the improvement of plastic strain ratio(\bar{r}) was emphasized. Segal first noted that the use of repetitive pressing may provide different microstructures by rotating the sample orientation between consecutive pressing, by that means modifying the shear strain and shear directions. The studies about sample orientation had been demonstrated in several experiments[5-7]. And it is known that in case of metal plate plastic strain ratio(\bar{r}) depends on the texture of plate. The average plastic strain ratio of $\{111\}<110>$ is the highest as 1.91 and the planar anisotropy is the lowest. The ECAP process which can develop $\{111\}$ texture can improve the formability of aluminum plate[4]. Many researches have carried out to characterize micro structural and textural evolution in a polycrystalline materials[8-11]. In this research, single crystal like plates were used to see texture change doring modified ECAP process. Initial orientation and final orientation were measured by Electron Back Scattered Diffraction(EBSD). To analyze the texture evolution, rate sensitive model was used. The misorientation between experimentally measured orientation and calculative orientation was discussed.

2. RATE SENSITIVITY MODEL

Rate sensitive model assumes that the shear stress developed in crystallographic system is proportional to m square of shear strain on the slip system as given in Eq. (1). With schmid law as equilibrium in Eq. (2) and geometric relation of external strain and slip shear strain are compatibility Eq. (3). The relation between external strain and shear strain can be given as Eq.(4). By assuming external strain, external stress can be solved with non linear Newton-Raphson method.

$$\tau^s = \tau_o \operatorname{sgn}(\dot{\gamma}_s) \left| \frac{\dot{\gamma}_s}{\dot{\gamma}_o} \right|^m = \tau_o \frac{\dot{\gamma}_s}{\dot{\gamma}_o} \left| \frac{\dot{\gamma}_s}{\dot{\gamma}_o} \right|^{m-1} \quad (1)$$

$$\tau^s = m_{ij}^s \sigma_{ij} \quad (2)$$

$$\dot{\epsilon}_{ij} = \sum_s \frac{1}{2} (m_{ij}^s + m_{ji}^s) \dot{\gamma}_s \quad (3)$$

$$\dot{\epsilon}_{ij} = \frac{\dot{\gamma}_o}{\tau_o^{1/m}} \sum_s \frac{1}{2} (m_{ij}^s + m_{ji}^s) m_{kl}^s \sigma_{kl} \left| m_{pq}^s \sigma_{pq} \right|^{\frac{1}{m}-1} \quad (4)$$

Calculation was started from EBSD point measurement orientation data. The strain rate sensitivity was fixed 0.05 which is ideal constant for aluminum at room temperature and by effective shear strain was given 1.16 by calculation.

3. EXPERIMENTAL PROCEDURE

A commercial 5mm thick 1050 Al alloy plate, having the chemical composition of Al-

0.25Si-0.4Fe(in wt.%), was annealed at 500°C for 1.5 hours before rolling. Cold rolling was carried out unidirectionally to 1.55 mm without any intermittent annealing. The rolled sheets were annealed at 350°C for 1.5 hours. The strip with dimensions of 20(w) x 1.55(t) x 1000(l)mm was cut from the rolled sheet with their long axis parallel to the rolling direction. And single crystal specimen with demensions of 13(w) x 1.55(t) x 15(l)mm were inserted into rolled sheet and fed into the ECAP machine at an approximate speed of 12m/min. The oblique angles(Φ) of the ECAP die used in the study was 120°. The curvature angle(Ψ) of the channel was fixed to 0 to minimize the microstructural inhomogeneity, which can be developed at regions that had passed through the outer corner side. During ECAP the machine was shut downed and the single crystal specimen which have both deformed and undeformed region was get. In this study, one path ECAP was conducted. To examine the texture evolution, microscopic EBSD point measurement was conducted in Link Opal system in Jeol 6300 SEM.

4. RESULTS AND DISCUSSION

It is known that during planar compression Dillamore texture $\{4\ 4\ 11\}\langle 11\ 11\ 8\rangle$ and Goss texture $\{110\}\langle 001\rangle$ were stable. But after shear strain were added, stable orientation shift to shear deformation texture, rotC $\{001\}\langle 110\rangle$, shear texture $\{111\}\langle 112\rangle$. In this study shear deformation texture evolution were observed and typical orientation rotation data were given in Table. 1. In specimen 1(Fig. 2) (0.03 0.74 0.67)[0.99 0.01 -0.06] near goss texture(Fig. 2(a)) rotated to (0.62 0.55 0.54)[0.34 0.42 -0.83] near (Fig. 2.(b)) and calculation data were (0.49 0.61 0.61)[-0.86 0.38 0.30](Fig. 2(d)). In case of specimen 2(Fig. 3) (-0.36 0.89 -0.23)[0.76 0.43 0.46] texture (Fig. 3.(a)) rotated to (0.44 -0.57 0.68)[-0.1 -0.84 -0.55] near shear texture(Fig. 3(b)) from EBSD measurement and calculated value were (-0.68 0.57 -0.45)[0.49 0.82 0.29] (Fig. 3(d)). In case of specimen 3(Fig. 4) on observation before ECAP stable (0.59 0.43 0.67)[-0.64 -0.24 0.72] near shear texture (Fig. 4(a)) were observed and after ECAP process initial orientation were maintained. On EBSD observation initial (0.59 0.43 0.67)[-0.64 -0.24 0.72] (Fig. 4(c)) rotated to (0.58 0.48 0.65)[-0.16 -0.72 0.68] (Fig. 4(d)), and calculated data were (0.77 0.42 0.47)[-0.44 -0.17 0.87] texture(Fig. 4(d)). In case of specimen 4(Fig. 5) initial (0.98 0.16 0.02)[0.03 -0.06 -0.99] near cube texture $\{100\}\langle 001\rangle$ (Fig. 5(a)) rotated to (0.21 0.73 -0.64)[0.19 0.62 0.76] texture (Fig. 5(b)) experimentally and (0.78 0.28 0.55)[0.54 0.10 -0.83] texture(Fig. 5(d)) by calculation.

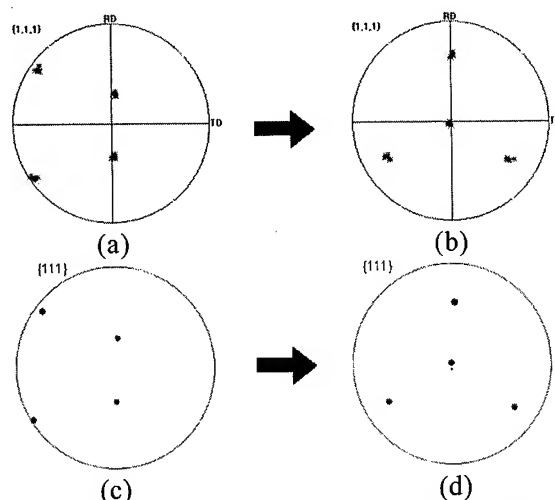


Fig. 2 Specimen 1. (a), (c) initial pole figure data from EBSD, (b) pole figure data from EBSD after ECAP, (d) calculated pole figure data

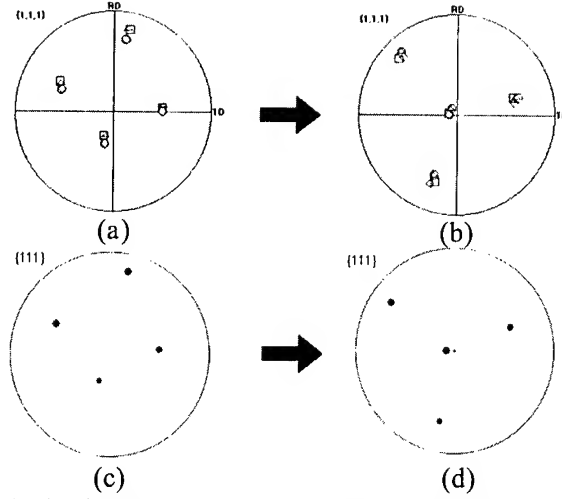


Fig. 3 Specimen 2. (a), (c) initial pole figure data from EBSD, (b) pole figure data from EBSD after ECAP, (d) calculated pole figure data

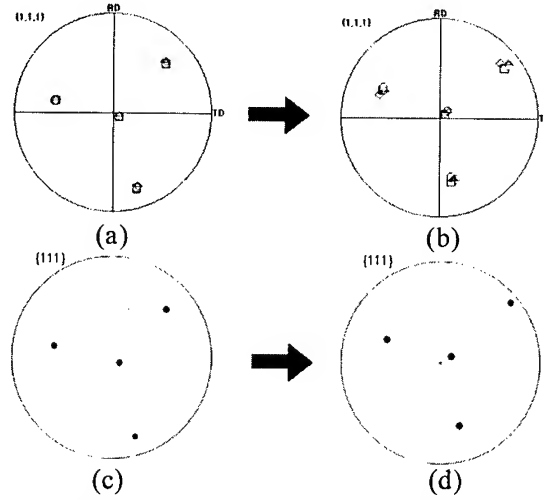


Fig. 4 Specimen 3. (a), (c) initial pole figure data from EBSD, (b) pole figure data from EBSD after ECAP, (d) calculated pole figure data

Misorientation calculation between measures and calculates orientations were evaluated. Eq. 5 complete misorientation matrix was reconstructed by using EBSD and calculated data by $\{hkl\}\langle uvw \rangle$ form. T is 24 symmetry operation matrix for cubic system. And misorientation(θ) were calculated through Eq. 6 and g_{exp} and g_{calc} were orientation matrix form experimentally measured and calculated orientations.

$$M = T g_{exp} g_{calc}^{-1} \quad (5)$$

$$\theta = \cos^{-1} \left\{ \frac{1}{2} (\text{Spur}(M) - 1) \right\} \quad (6)$$

In Table. 1 the calculated misorientation were within EBSD measurement accuracy. In Fig. 6 shows the predicted plastic strain ratio with angle to rolling direction in original aluminum plate. After ECAP, average plastic strain ratio increases two times and $\Delta\bar{r}$ reduces significantly. This improvement of plastic strain ratio is related to the texture.

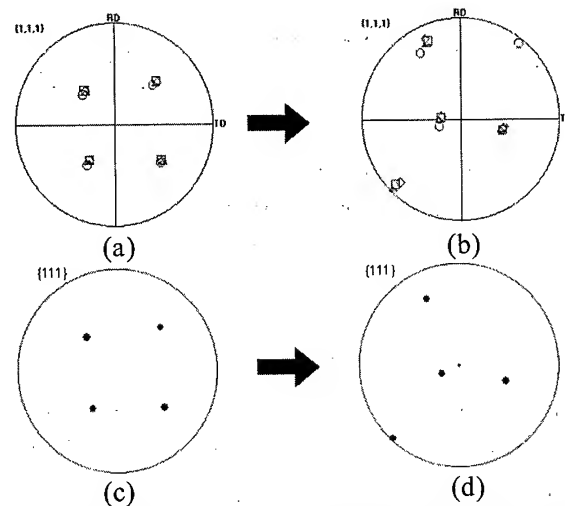


Fig. 5 Specimen 4. (a), (c) initial pole figure data from EBSD, (b) pole figure data from EBSD after ECAP, (d) calculated pole figure data

Table 1 orientation data by ECAP

Number of specimen	Initial index data	Experimental data After ECAP	Calculated data after ECAP	Misorientation between Exp. & Calc.
1	(0.03 0.74 0.67) [0.99 0.01 -0.06] ⁽¹⁾	(0.62 0.55 0.54) [0.34 0.42 -0.83] ⁽²⁾	(0.49 0.61 0.61) [-0.86 0.38 0.30] ⁽²⁾	3.87°
2	(-0.36 0.89 -0.23) [0.76 0.43 0.46]	(0.44 -0.57 0.68) [-0.1 -0.84 -0.55] ⁽²⁾	(-0.68 0.57 -0.45) [0.49 0.82 0.29] ⁽²⁾	2.33°
3	(0.59 0.43 0.67) [-0.64 -0.24 0.72] ⁽²⁾	(0.69 0.51 -0.50) [-0.44 0.85 0.26] ⁽²⁾	(0.77 0.42 0.47) [-0.44 -0.17 0.87] ⁽²⁾	5.75°
4	(0.98 0.16 0.02) [0.03 -0.06 -0.99] ⁽³⁾	(0.21 0.73 -0.64) [0.19 0.62 0.76]	(0.78 0.28 0.55) [0.54 0.10 -0.83]	7.21°

(1) near {110}<001> goss texture

(2) near {111}<112> shear texture

(3) near {100}<001> cube texture

5. CONCLUSION

In this study by using annealed aluminum plate, the deformation texture of ECAP aluminum plate were confirmed one-by-one. The initial texture of aluminum plate rotates to near {111} shear texture and it increases the plastic strain ratio(\bar{r}). And the increase of \bar{r} value improve the formability of aluminum plate. Comparing to calculation data by rate sensitive model, EBSD experimental data was well matched and the misorientation between experimental data and calculation data was within EBSD measurement accuracy.

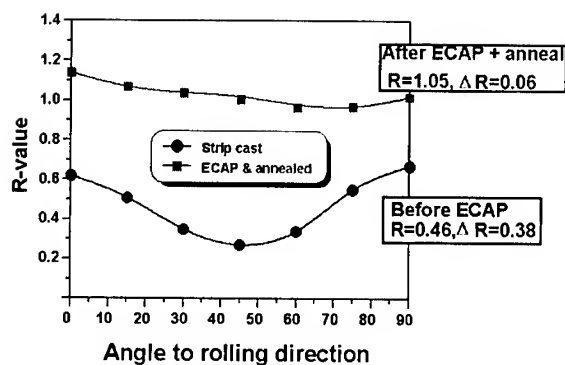


Fig. 6 Predicted plastic strain ratio

REFERENCES

- [1] V. M. Segal, V.I. Reznikov, A.E. Drobyshvskiy, V.I. Kopylov, Russ. Metall. Vol. 1 (1981) pp. 99.
- [2] V.M. Segal, in : H. Henein and T. Oki (Eds.), Proceedings of the First International Conference on Processing Materials for Properties, The minerals, Metals and Materials Society, 1993, pp.947.
- [3] V.M. Segal, Mater. Sci. Eng A Vol. 197 (1995), pp. 157.
- [4] S-H. Choi and K.H. Oh, Metals and Materials, 1997, Vol. 3, pp. 252.
- [5] Y. Iwahashi, Z. Horita, M. Nemoto, T.G. Langdon, Acta Mater. Vol. 45 (1997), pp. 4733.
- [6] S. Ferrasse, V.M. Segal, K.T. Hartwig, R.E. Goforth, Metall. Mater. Trans. Vol. A28(1997) pp. 1047.
- [7] Y. Iwahashi, Z. Horita, M. Nemoto, T.G. Langdon, Acta Mater. Vol. 46(1998), pp. 1589.
- [8] Z. Horita, D.J. Smith, M. Furukawa, M. Nemoto, R.Z. Valiev, T.G. Langdon, Ann. Chim. Fr. Vol. 21 (1996), pp. 417.
- [9] M. Furukawa, Z. Horita, M. Nemoto, R.Z. Valiev, T.G. Langdon, Mater. Sci. Forum Vol. 43 (1996), pp. 1204-1206
- [10] Y. Iwahashi, Z. Horita, M. Nemoto, T.G. Langdon, Acta Mater, Vol. 46 (1998), pp. 3317.
- [11] M. Nemoto, Z. Horita, M. Furukawa, T.G. Langdon, Mater. Sci. Forum Vol. 304-306(1999), pp. 59.
- [12] P. Van Houtte : Textures and Microstructures, 1988, Vol. 8-9, pp. 313.
- [13] G.R. Canova, C. Fressengeas, A. Molinari and U.F. Kocks, Acta metal., 1988, Vol. 36, pp. 1961.
- [14] L.S. Toth, P. Gilormini and J.J. Jonas, Acta metal., Vol. 36(1988), pp. 3077.

Microstructural Evolution During ECA Pressing of Commercial 5083 Al Alloy and Its Mechanical Properties

Si-Young Chang, Jung Guk Lee, Kyung-Tae Park* and Dong Hyuk Shin

Department of Metallurgy and Materials Science, Hanyang University,
Ansan, Kyunggi-do, Korea 425-791

*Division of Advanced Materials Science & Engineering, Taejon National
University of Technology, Taejon, Korea 300-717

ABSTRACT

An ultra-fine grained structure was introduced in a commercial 5083 Al alloy with an initial grain size of $\sim 200 \mu\text{m}$ using equal channel angular pressing technique. The equal channel angular pressing was successfully conducted at 373K and 473K on the same sample up to a total of 8 pressings using route C. An equiaxed ultra-fine grains with a grain size of $\sim 0.3 \mu\text{m}$ that were obtained in the present alloy after 4 pressings were thermally stable at 473 K and 523 K. The yield stress of as-received 5083 Al alloy was 129 MPa, whereas, at pressing temperature of 373 K, it increased to 330 MPa after a single pressing and finally became 389 MPa after 8 pressings. The sample pressed at 373 K showed much higher yield stress than one pressed at 473 K. The elongation of sample pressed at 473 K remained unchanged with the number of pressings. It was found that the 5083 Al alloy with a grain size of $\sim 0.3 \mu\text{m}$ exhibited a superplastic-like behavior with elongation to failure in excess of 200 % at 523 K.

1. Introduction

Al alloys have become attractive as a light and highly efficient material to overcome the problems of environment pollution and energy in all industrial fields. Among Al alloys, Al-Mg system alloys have been widely used in the form of wrought materials because they have high strength through solid solution hardening and work hardening and excellent corrosion resistance, formability, and weldability [1].

The superplasticity in metallic materials is strongly sensitive to the grain size. In general, the thermomechanical treatments (TMT) have been used to obtain the fine grained structure (UFG) in Al-Mg system alloys. Recently, a sub-micrometer ultra-fine grained structure was successfully introduced in a variety of bulk metallic materials without residual porosity by applying equal channel angular pressing (ECAP) technique [2]-[6]. It was recently reported that the ultrafine grained structure could be successfully obtained by ECAP in Al-3%Mg [7]-[9], Al-4.8%Mg (5056) [10] and Al-6%Mg-0.6%Mn [11] alloys. In addition, Horita et al. [12] obtained the average grain size of less than $1 \mu\text{m}$ in the commercial 5083 Al alloy with the highest strength out of non-heat treated type Al alloys using ECAP under special conditions. The research studies on the low temperature superplasticity for Al-Mg [7], [8], [13], [14] or Al-Mg-Mn [14]-[16] alloys have been also performed. However, the microstructure and

mechanical properties, in particular the low temperature superplasticity, of the ECA pressed commercial 5083 Al alloy at various conditions have been not well investigated.

Therefore, the aim in this study is to examine the microstructural and mechanical characteristics of commercial 5083 Al alloy with the UFG structure introduced by ECAP, and then to evaluate the feasibility of superplasticity at relatively low temperature.

2. Experimental Procedure

A commercial 5083Al alloy (Al-4.4%Mg-0.7%Mn-0.15%Cr (in mass %)) was supplied in the form of an extruded bar. Cylindrical samples of $\phi 18 \times 130$ mm were prepared from the extruded bar, followed by the annealing treatment at 723 K for 1 h. The annealed samples were used as as-received materials for ECAP. The average grain size of as-received 5083 Al alloy was approximately 200 μm . The ECAP was carried out using a press speed of 2 mm s⁻¹ with MoS₂ as a lubricant at 373 K and 473 K. The present ECAP die was designed to yield an effective strain of ~ 1 by a single pass: the inner angle and the arc of curvature at the outer point of contact between channels of the die were 90 and 20°, respectively [17], [18]. During the ECAP, the sample was rotated 180° around its longitudinal axis between individual pressings (Route C) [19].

Tensile tests were performed using an Instron machine on the full scale tensile specimens with 25 mm in gauge length at the initial strain rate of 1.00×10^{-3} s⁻¹ and at room temperature. In addition, the tensile specimens with 8 mm in gauge length were tensile-tested at the initial strain rate of 1.04×10^{-4} s⁻¹ and at 523 K. Microstructures of samples were investigated with a transmission electron microscope (TEM) utilizing a JEOL 2010 operated at 200 keV.

3. Results and Discussion

3.1 Microstructural characteristics

3.1.1 Microstructural evolution

Figure 1 represents TEM micrographs of 5083Al alloy after ECAP at 473 K with the number of pressing. After a single pressing, the microstructure mainly consisted of parallel bands of elongated grains, having a length of 0.8 μm and a width of ~ 0.2 μm . Its corresponding selected area electronical diffraction (SAED) pattern was characterized by relatively clear spots. This implies that most of the boundaries in fine grains formed by a single pressing would be low-angled.

The microstructure after 2 pressings showed fairly equiaxed fine grains and the subgrain bands parallel to the shear direction disappeared. The SAED pattern showed the appearance of the diffused spots and the extra spots indicating the formation of a high angle boundary. Near equiaxed ultra fine grains of approximately 0.3 μm were obtained by 4 and 8 pressings. In addition, the number of rings in the SAED pattern increased and the spots became more diffused compared to the previous ones. This also occurred after pressing at 373 K (Fig. 2). However, the sample pressed at 373 K showed more shear-deformed microstructure and the size of high angled grains was small compared with that pressed at higher temperature.

3.1.2 Annealed microstructure

Figure 3 represents TEM micrographs of 5083 Al alloy pressed at 473 K followed by annealing treatment at 523 K for 1h ((a), (b)) and at 373 K followed by annealing treatment at 473 K for 1h ((c), (d)). In the case of the four times pressed specimen apart from the as-ECA pressed specimen (see the Fig. 1(c) and Fig. 2(a)), the grain boundary was relatively clear after the annealing treatment. The grain sizes are approximately $0.5\ \mu\text{m}$ and $0.3\ \mu\text{m}$, indicating that there is almost no grain growth (Fig. 3(a) and (c)). For the eight times repetitively pressed specimens, some recrystallized grains of approximately $4\ \mu\text{m}$ in grain size are observed at pressing temperature of 473 K (Fig. 3(b)), whereas, at pressing temperature of 373 K, no grain growth occurred.

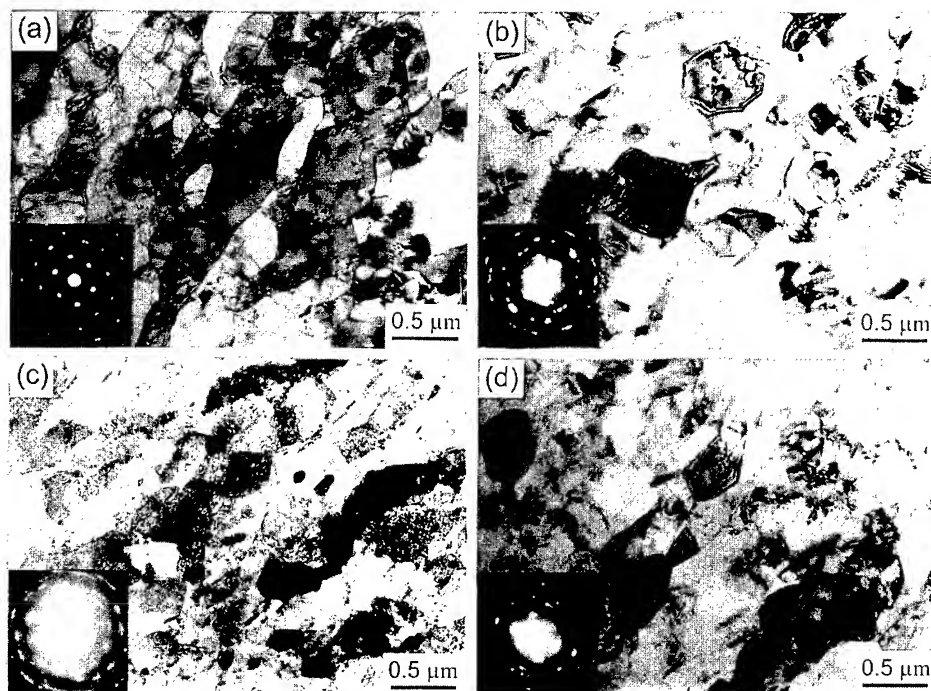


Fig. 1 TEM micrographs and corresponding SAED patterns of 5083 Al alloy pressed at 473 K; (a) 1 pressing, (b) 2 pressings, (c) 4 pressings, (d) 8 pressings.

Fig. 2 TEM micrographs and corresponding SAED patterns of 5083 Al alloy pressed 373 K; (a) 4 pressings, (b) 8 pressings.

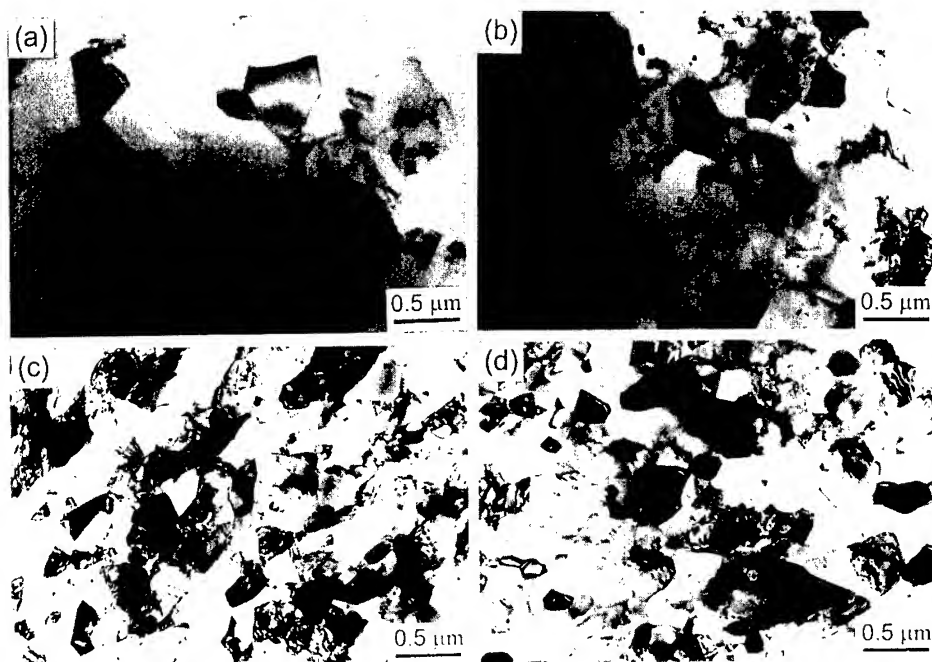


Fig. 3 TEM micrographs of 5083 Al alloy 4-pressed at 473 K (a) and 373 K (c), and 8-pressed at 473 K (b) and 373 K (d); annealed at 523 K ((a), (b)), at 473 K ((c), (d)) for 1 h.

It was previously known that the unclear grain boundaries in severely plastic-deformed metallic materials, included many facets and steps of regular or irregular alignment and the lattices near grain boundaries were severely distorted [20], [21]. Additionally, there were extrinsic dislocations with a density of approximately 10^{16} m^{-2} in the grain boundaries, resulting in the marked increase of grain boundary energy. Such grains with non-equilibrium grain boundaries could display grain growth even at relatively low temperatures [22], [23]. Hasegawa et al. [24] reported that the eight times repetitively ECA pressed Al-3Mg alloy, followed by the annealing treatment at 523 K for 1 h, revealed the presence of duplex structures with regions of both submicrometer grains and large grains. Accordingly, from the above results, it is apparent that the ultra-fine grains are more stable in the four times repetitively pressed 5083 Al alloy and the grain size remains small at 523 K ($\sim 0.5 \text{ Tm}$).

3.2 Mechanical characteristics

3.2.1 Tensile properties at room temperature

Figure 4 shows the variation of the tensile strength, yield strength and elongation with the number of pressings. The yield strength of as-received 5083 Al alloy drastically increased after a single pressing, for example, after pressing at 373 K, it increased from 129 MPa to 330 MPa. It gradually increased with the number of pressings and reached 389 MPa after 8 pressings. The tensile strength showed a gradual increase compared with the yield strength. In addition, the sample pressed at 373 K showed much higher yield stress and lower elongation than one pressed at 473 K. The elongation of sample pressed at 473 K remained unchanged after ECAP. The tensile strength, yield strength and elongation of the annealing-treated 5083 Al alloy after ECAP were in-between those of samples pressed at 373 K and at 473 K.

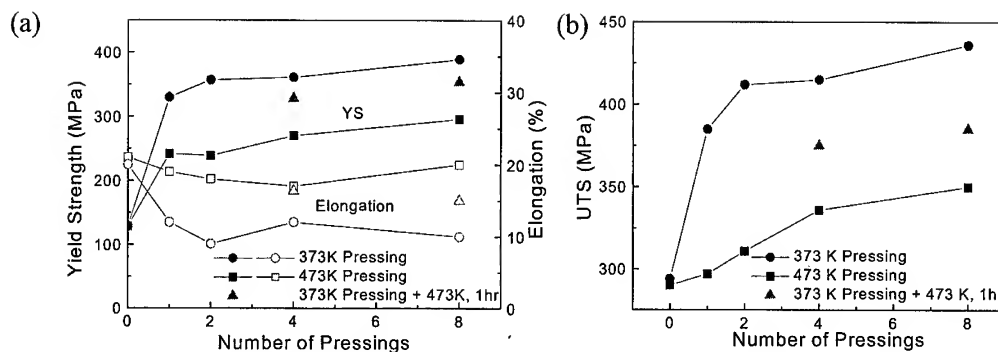


Fig. 4 Effect of the number of pressings on tensile properties of ECA pressed 5083 Al alloy.

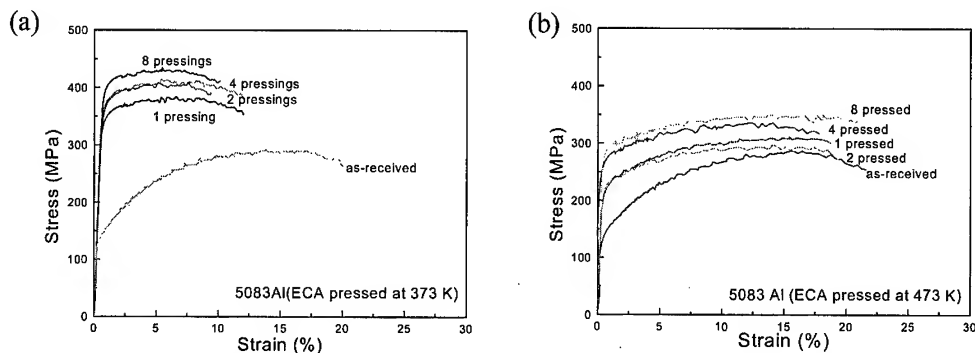


Fig. 5 Stress-strain curves of 5083 Al alloy pressed at (a) 373 K and (b) 473 K.

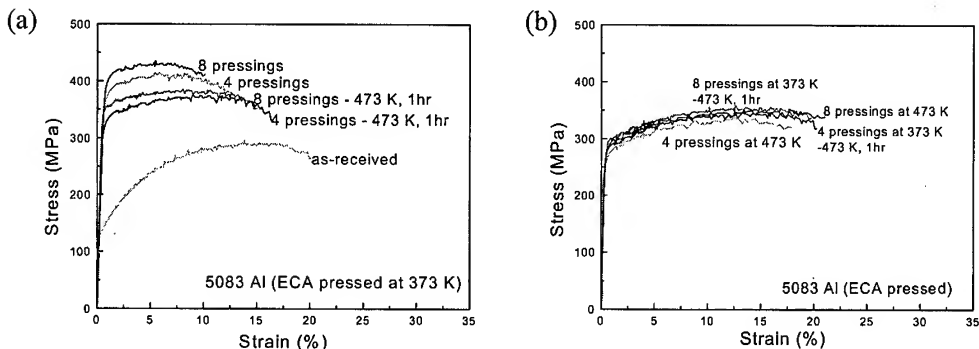


Fig.6 Stress-strain curves of ECA pressed (373 K) Al alloy after annealing treatment at 473 K for 1h, compared with those of 5083 Al alloys pressed at (a) 373 K and (b) 473 K.

Typical true stress - strain curves obtained for as ECA pressed Al alloys and as annealing-treated Al alloys after pressing at 373 K are shown in Fig. 5 and Fig. 6, respectively. The pre-material 5083 Al alloy exhibited the typical strain hardening behavior, whereas the ECA pressed one exhibited the small strain hardening. According to recent reports, it has a close relation to the annihilation kinetics of extrinsic grain boundary dislocation introduced by severe plastic deformation and the number of dislocation necessary to deform the ultra-fine grain [24]. On the other hand, there was no difference in strain hardening behavior with the number of pressings (Fig. 5) and annealing treatment (Fig. 6). In particular, it well agreed

with the Al alloy pressed at 473 K, as shown in Fig.6 (b). This corresponds to the microstructures shown in Fig. 1 and Fig. 3.

Consequently, there was a most significant (~15 %) increase in both yield strength and ultimate strength of the ECA pressed 5083 over the as-received 5083 with no decrease in elongation. This observation of increased strength with no corresponding decrease in elongation stands in stark contrast to the behavior of conventional materials. From this result, it is apparent that the improvement of the mechanical properties is attributable to the grain refining by the ECAP.

3.2.2 Tensile properties at 523 K

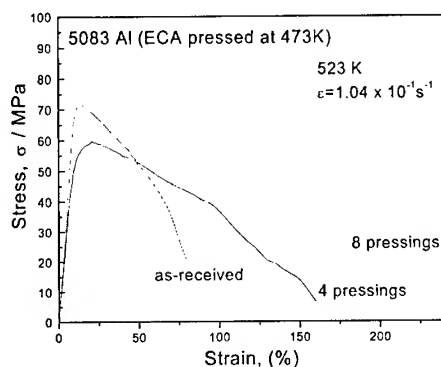


Fig. 7 Stress-strain curves for as ECA pressed Al alloy tensile-tested at an initial strain rate of $1.04 \times 10^{-4} \text{ s}^{-1}$ at 523K.

For the 5083 Al alloy pressed at 473 K, the tensile testing was performed at an initial strain rate of $1.04 \times 10^{-4} \text{ s}^{-1}$ at 523 K (0.53Tm). The stress-strain curves of are shown in Fig.7, together with that of the as-received 5083 Al alloy. The flow stress of as-received 5083 Al alloy was approximately 72 MPa, whereas the four and eight times pressed 5083 Al alloy revealed flow stress of 60 and 52 MPa, respectively. The elongation after four and eight ECAPs was 160 % and 220 % respectively. This is much higher than that of the as-received 5083 Al alloy.

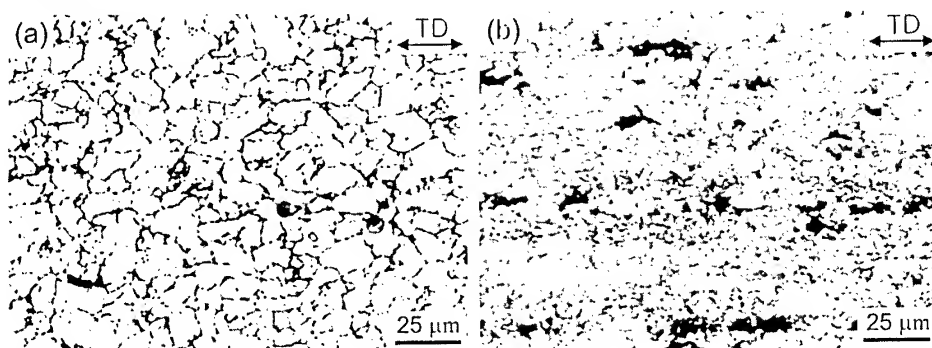


Fig. 8 OM micrograph of the grips section (a) and the deformed section (b), for 8 times ECA pressed 5083 Al alloy. TD indicates the tensile direction.

Figure 8 shows the OM microstructures of the grip section (a) and the deformed section (b), for eight times ECA pressed 5083 Al alloys after tensile deformation. The grain growth from

the initial grain size of $0.3\text{ }\mu\text{m}$ to approximately $8\text{ }\mu\text{m}$ occurs in the grip section and no cavities are observed. However, the local grain growth occurs in the deformed section, and the grains are elongated parallel to tensile direction. In addition, many cavities are observed in the deformed section. This is deduced to result from that, in general, the cavities could generate due to the stress concentration induced by the grain boundary sliding, and the growth of cavities occurs along the grain boundaries parallel to tensile direction. Nevertheless, it could be concluded that the decrease in flow stress and the increase in elongation result from the high-angled grain boundaries introduced by the repetitive ECAP. These boundaries could easily slide, which might play a dominant role in obtaining low temperature superplasticity.

Wang et al. [7] applied the ECAP to the Al-3Mg alloy, resulting in a grain size of approximately $0.2\text{ }\mu\text{m}$. In addition, Kawazoe et al. [10] obtained ultra-fine grained Al-4.8Mg alloy with a grain size of $0.3\text{ }\mu\text{m}$ with the ECAP. In both cases, however, the low temperature superplasticity still could not be obtained and the elongation did not exceed 200%. In contrast, the ECA pressed Al-4.4Mg-0.7Mn alloy in this study, showed the low temperature superplasticity property of elongation above 200 % at 523 K and $1\times 10^{-4}\text{ s}^{-1}$. This was comparable to the recent reports by Hsiao and Huang [15] that the Al-4.7Mg-0.7Mn alloy subjected to the improved TMTs possessed a 3D grain size of $0.5\times 0.5\times 0.2\text{ }\mu\text{m}$ and revealed an elongation of 230 % at 523 K and $2\times 10^{-4}\text{ s}^{-1}$, and by Tsuji et al. [16] that the small grain size of $0.28\text{ }\mu\text{m}$ for Al-4.45Mg-0.57Mn alloy was induced by the accumulative roll-bonding, resulting in a large elongation of 220% at 473 K and $1\times 10^{-3}\text{ s}^{-1}$. From the above results, consequently, it is apparent that the repetitive ECAP, which results in a high-angled grain boundary, is effective for obtaining the low temperature superplasticity in commercial 5083 Al alloy.

5. Conclusions

- (1) ECAP of commercial 5083 Al alloy was successfully conducted at 373 K and 473 K using route C. After a single pressing, the microstructure was reasonably homogeneous and consisted of parallel bands of elongated substructure with an average width of $0.2\text{ }\mu\text{m}$ and an average length of $0.8\text{ }\mu\text{m}$. An equiaxed ultra-fine grained structure of $\sim 0.3\text{ }\mu\text{m}$ was obtained after eight ECAPs.
- (2) The ultra-fine grains obtained by pressing at 373 K were thermally stable after annealing treatment at 473 K for 1h, whereas, after annealing treatment at 523 K for 1h, irregular grain growth occurred in the 8 pressed 5083 Al alloy at 473 K.
- (3) The yield strength of as-received 5083 Al alloy drastically increased from 129 MPa to 330 MPa after a single pressing and to 389 MPa after 8 pressings at 373 K. The sample pressed at 373 K showed much higher yield stress than one pressed at 473 K. The elongation of sample pressed at 473K remained unchanged with increasing the number of pressings.
- (4) At 523 K, the ECA pressed 5083 Al alloy with the grain size of $\sim 0.3\text{ }\mu\text{m}$ revealed a decrease in flow stress and an increase in elongation with increasing the number of pressings. Additionally, it exhibited a superplastic-like behavior with elongation to failure in excess of 200 %.

Acknowledgments

This work was supported by the 'National Research Laboratory Program' of Korea

REFERENCES

1. Microstructure and Properties of Aluminum Alloys, The Japan Institute of Light Metals, (1991), pp. 256-277.
2. R. Z. Valiev, R. K. Islamgaliev and I. V. Alexandrov, Progress in Materials Science, Vol.45(2000), pp. 103-189.
3. D. H. Shin, Y. S. Kim and E. J. Lavernia, Acta Materialia, Vol.49(2001), in press.
4. D. H. Shin, I. Y. Kim, J. Kim and K. T. Park, Acta Materialia, Vol.49(2001), pp. 1285-1292.
5. D. H. Shin, B. C. Kim, K. T. Park and W. Y. Choo, Acta Materialia, Vol.48(2000), pp. 3245-3252.
6. D. H. Shin, B. C. Kim, Y. S. Kim and K. T. Park, Acta Materialia, Vol.48(2000), pp. 2247-2255.
7. J. Wang, Z. Horita, M. Furukawa, M. Nemoto, N. K. Tsenev, R. Z. Valiev, Y. Ma and T. G. Langdon, J. Mater. Res., Vol.8(1993), pp. 2810-2818.
8. M. Furukawa, Z. Horita, M. Nemoto, R. Z. Valiev and T. G. Langdon, Mater. Characterization, Vol.37(1996), pp. 277-283.
9. J. Wang, M. Furukawa, Z. Horita, M. Nemoto, R. Z. Valiev and T. G. Langdon, Mater. Sci. Eng., Vol.A216(1996), pp. 41-46.
10. M. Kawazoe, T. Shibata, T. Mukai and K. Higashi, Scripta mater., Vol.36(1997), pp. 699-705.
11. M. V. Markushev, M. Yu. Murashkin, P. B. Prangnell, A. Gholinia and O. A. Maiorova, Nanostruct. Mater., Vol.12(1999), pp. 839-842.
12. Z. Horita, T. Fujinami, M. Nemoto and T. G. Langdon, Metall. Mater. Trans., Vol.31A(2000), pp. 691-701.
13. S. S. Woo, Y. R. Kim, D. H. Shin and W. J. Kim, Scripta mater., Vol.37(1997), pp. 1351-1358.
14. E. M. Taleff, G. A. Henshall, T. G. Nieh, D. R. Lesuer and J. Wadsworth, Metall. Mater., Vol.29A(1998), pp.1081-1091.
15. I. C. Hsiao and J. C. Huang, Scripta mater., Vol.40(1999), pp. 697-703.
16. N. Tsuji, K. Shiotsuki and Y. Saito, Mater. Trans. JIM, Vol.40(1999), pp. 765-771.
17. K. Nakashima, Z. Horita, M. Nemoto and T. G. Langdon, Acta Mater., Vol.46(1998), pp. 1589-1599.
18. Y. Iwahashi, J. Wang, Z. Horita, M. Nemoto and T. G. Langdon, Scripta mater., Vol.35(1996), pp. 143-145.
19. Y. Iwahashi, M. Furukawa, Z. Horita, M. Nemoto and T. G. Langdon, Metall. Mater. Trans., Vol.29A(1998), pp. 2245-2252.
20. Z. Horita, D.J. Smith, M. Furukawa, M. Nemoto and R.Z. Valiev and T.G. Langdon, J. Mater. Res., Vol.11(1996), pp.1880-1890.
21. Z. Horita, D.J. Smith, M. Nemoto and R.Z. Valiev and T.G. Langdon, J. Mater. Res., Vol.13(1998), pp. 446-450.
22. R. Z. Valiev, A. V. Korznikov and R. R. Mulyukov, Mater. Sci. Eng., Vol.A168(1993), pp. 141-148.
23. A. A. Nazarov, A. Z. Romanov and R. Z. Valiev, Nanostruct. Mater., Vol.4(1994), pp. 93-101.
24. H. Hasegawa, S. Komura, A. Utsunomiya, Z. Horita, M. Furukawa, M. Nemoto and T. G. Langdon, Mater. Sci. Eng., Vol.A256(1999), pp. 188-196.

GRAIN REFINEMENT AND STRENGTHENING OF 6061 ALUMINUM ALLOY BY ACCUMULATIVE ROLL-BONDING PROCESS

S. H. LEE, Y. SAITO, T. SAKAI, H. UTSUNOMIYA and N. TSUJI

Department of Materials Science and Engineering, Osaka University
2-1, Yamada-Oka, Suita, Osaka 565-0871, Japan

ABSTRACT

Accumulative Roll-Bonding (ARB) process, which is an intense plastic deformation process, is performed for a 6061 aluminum alloy to develop ultra-fine grains below $1\mu\text{m}$ in diameter and to improve the mechanical properties. The ARB process up to 8 cycles is performed at ambient temperature under unlubricated conditions. The ultra-fine grains surrounded by clear boundaries begin to appear at 3rd cycle, and the specimen after 8 cycles shows a microstructure covered with ultra-fine grains with a mean diameter of 310nm . The tensile strength of the ARB processed 6061 aluminum alloy increases with the number of ARB cycles (total equivalent strain), and after 8 cycles it reaches a maximum of 363MPa which is about three times of the initial. On the other hand, the elongation drops largely at the 1st cycle, however it hardly changes after the 2nd cycle. The results show that the ARB process is effective for grain refinement and strengthening of 6061 aluminum alloy.

1. INTRODUCTION

In recent years, aluminum alloys have attracted attention of many researchers, engineers and designers as promising structural materials for automotive industry or aerospace applications [1]. Especially, 6xxx aluminum alloys have been studied aggressively because of their benefits such as medium strength, formability, weldability, corrosion resistance, and low cost, comparing to other aluminum alloys [2]. It is expected that substitution of such aluminum alloys for steels will result in great improvements in energy economy, recyclability and life-cycle cost. However, it is necessary to improve the strength and the formability for further applications to the industries. Control of the microstructure and/or the texture is essential for improvement of their properties.

Much work has been done to develop the materials with ultra-fine grains less than $1\mu\text{m}$ in diameter because they would show outstanding strength at ambient temperature, high-strain-rate superplastic deformation at elevated temperatures and high corrosion resistance. Especially, the several unique processes such as equal channel angular extrusion (ECAE) [3,4], torsion straining under high pressure (TS) [5] and accumulative roll-bonding (ARB) process [6-8] were proposed to develop ultra-fine grains by introducing severe intense plastic strain in materials. These processes have great merit that the grain refinement and strengthening can be attained without additions of alloying elements or ceramic particles. Among such processes, the ARB process is mostly appropriate for the practical applications because it can be performed readily by the industrial rolling process. The authors applied the ARB process to 1100 commercial aluminum, 5083 alloy and Ti-added ultra low carbon interstitial free (IF) steel, and succeeded in obtaining ultra-fine grained materials with the grain diameter less than $1\mu\text{m}$ [7]. It was demonstrated that the ARB processed materials show outstanding tensile strength [7]. Furthermore, it was also clarified that the ARB processed 5083 sheet with submicrometer grains shows low-temperature superplasticity [9].

In the present study, the ARB process is applied to 6061 aluminum alloy, a typical Al-Mg-Si alloy. Since 6061 alloy is an age-hardening alloy, it can be strengthened appreciably

by heat treatment. The 6061 alloy has been also currently attracted interests of many researchers because its based metal matrix composite shows high-strain-rate superplasticity [10]. The objective of the present study is to investigate the feasibility of ARB to 6061 alloy and to clarify the evolution of the microstructures and the mechanical properties with number of ARB cycles.

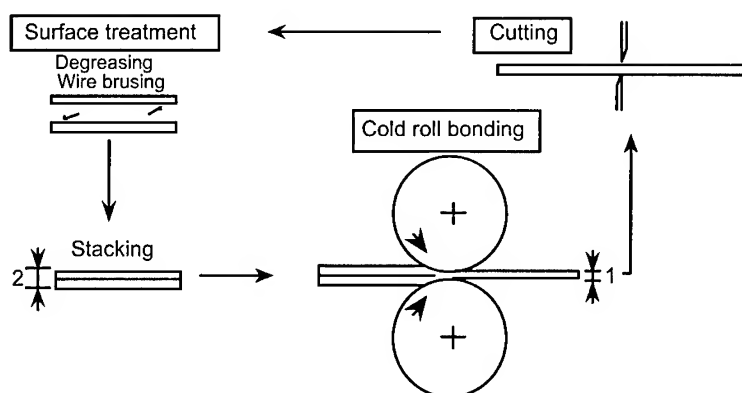
2. EXPERIMENTAL

The 6061 Al alloy sheet hot-rolled after hot extrusion was used for the present study. The sheet showed a recrystallized structure with the average grain diameter of 25 μ m. The chemical composition of the 6061 alloy is shown in **Table 1**.

Table 1 Chemical composition of 6061 aluminum alloy. (mass%)

Fe	Cu	Si	Zn	Mn	Mg	Cr	Ti	Al
0.16	0.19	0.71	0.04	0.02	0.94	0.08	0.03	Bal.

The schematic illustration of the ARB process is shown in **Fig. 1**. In the present ARB process, two sheets of 1mm in thickness and 20mm in width were stacked up and reduced to about 1mm by one-pass cold rolling. The two sheets were bonded during rolling. The bonded sheet was cut in half-length, stacked again and rolled to the thickness of 1mm. To obtain sufficient bonding strength, the surfaces of the two sheets to be bonded were degreased and scratch-brushed by a stainless-wire bevel brush beforehand. The ARB process up to 8 cycles was performed at ambient temperature without lubrication. The rolling reduction at the 1st cycle was almost 50%, however from the 2nd cycle it was below 50%, because of the elastic deformation of the rolling mill due to the increase in the flow stress of specimen increased at higher ARB cycles.



3. TESTING AND CHARACTERIZATION

The microstructure was investigated by transmission electron microscopy (TEM). TEM studies were conducted with a HITACHI H-800 microscope operated at 200kV. For TEM observation, thin disk-shaped foils parallel to the rolling plane and the thin rectangular foils perpendicular to the transverse direction were prepared by spark machining and twin-jet polishing. The mechanical properties of the ARB processed specimen were determined at ambient temperature by an Instron-type tensile testing machine. The test pieces were spark-machined so that the tensile direction was parallel to the rolling direction. The gauge

length was 10mm and the gauge width was 5mm. The initial strain rate was $8.3 \times 10^{-4} \text{ s}^{-1}$.

4. RESULTS AND DISCUSSION

4.1 Microstructures

TEM microstructures and the corresponding selected area diffraction (SAD) patterns observed at rolling plane of the specimens ARB-processed by 2, 4, 6 and 8 cycles are shown in Fig. 2. The SAD patterns were taken with an aperture of $1.6 \mu\text{m}$ in diameter. Many precipitates with equiaxed shape are seen in the specimens. The specimen after 2 cycles shows a typical dislocation cell structure of which the SAD pattern is a single net pattern (Fig. 2a). For the specimen after 4 cycles, the dislocation density in cells decreases and the cell size become fine, comparing to that after 2 cycles. The ultra-fine grains and subgrains are also seen in the specimen after 4 cycles, as indicated by the arrows in Fig. 2b. The fraction of these ultra-fine grains increased with the number of ARB cycles. The specimen after 6 cycles was covered with the ultra-fine grains of 500nm in average diameter surrounded by clear boundaries (Fig. 2c). The SAD pattern also shows more complex pattern than those after 2 or 4 cycles. This means that the grains formed in the specimen after 6 cycles have some misorientations to each other. The specimen after 8 cycles also showed an ultra-fine grained structure with average grain size of 310nm, smaller than that after 6 cycles (Fig. 2d). These ultra-fine grains began to appear at 3rd cycle. Figure 3 is TEM microstructure showing the ultra-fine grains developed on rolling plane of the specimen produced by 3 cycles. It is observed that the ultra-fine grains in which the dislocation density is very low, are surrounded by clear boundaries. This is quite different from that after 2 cycles shown in Fig. 2a. Its SAD pattern taken with an aperture of $1.6 \mu\text{m}$ in diameter shows a complex pattern, which indicates that the large misorientation exists between the ultra-fine grains.

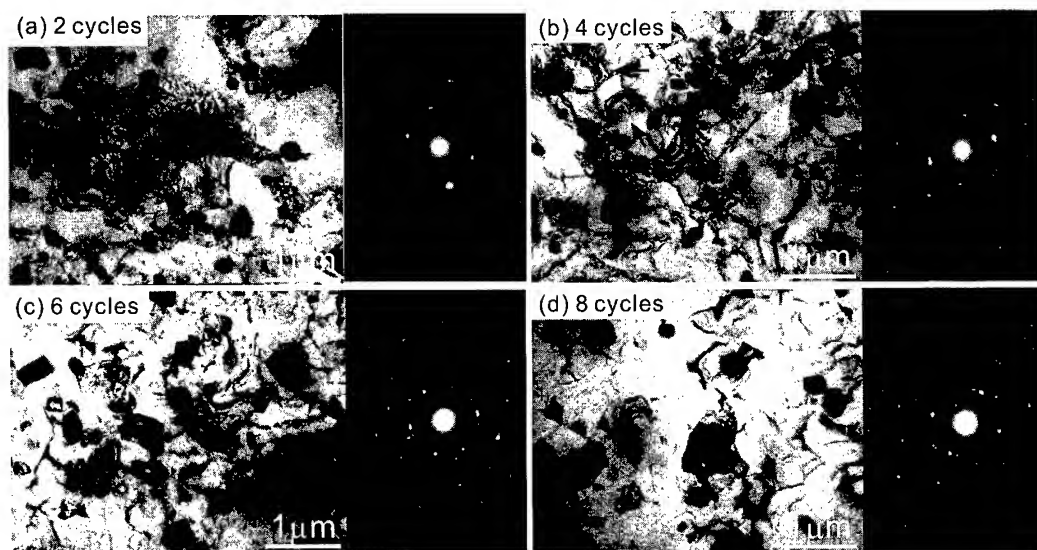


Fig. 2 Changes of TEM microstructures and the corresponding SAD patterns observed at rolling plane of the specimen with the number of ARB cycles.



Fig. 3 TEM microstructure showing ultra-fine grains formed in rolling plane of specimen after 3-cycle ARB.

Figure 4 shows TEM microstructures and the corresponding SAD patterns observed at the plane perpendicular to transverse direction (TD plane) of the specimens ARB-processed by 2, 4, 6 and 8 cycles. The specimen after 2 cycles shows a dislocation cell structure and the SAD pattern shows a single net pattern. The specimen after 4 cycles also shows primarily a dislocation cell structure, but some ultra-fine grains surrounded by clear boundaries as seen in Fig. 4b. The specimen after 6 cycles shows an ultra-fine grained structure covered by the grains elongated to the rolling direction over almost all regions. Its SAD pattern suggests that the large misorientation exists between the grains. Ito et al. demonstrated that the ultra-fine grains formed in 1100 pure aluminum by 6-cycle ARB have almost high-angle boundaries with large misorientations above 15 degrees to each other [8]. Therefore, it is thought that the ultra-fine grains formed after 6-cycle ARB in the present study have large misorientations to each other. The further ARB to 8 cycles makes the size and aspect ratio of the ultra-fine grains smaller. The results of TEM observation from ND and TD plane demonstrate that the ultra-fine grains developed by the ARB have a pancake-shape. The formation process of these ultra-fine grains with the number of ARB cycles is very similar to those of 1100 pure aluminum or a 5083 aluminum alloy [6].

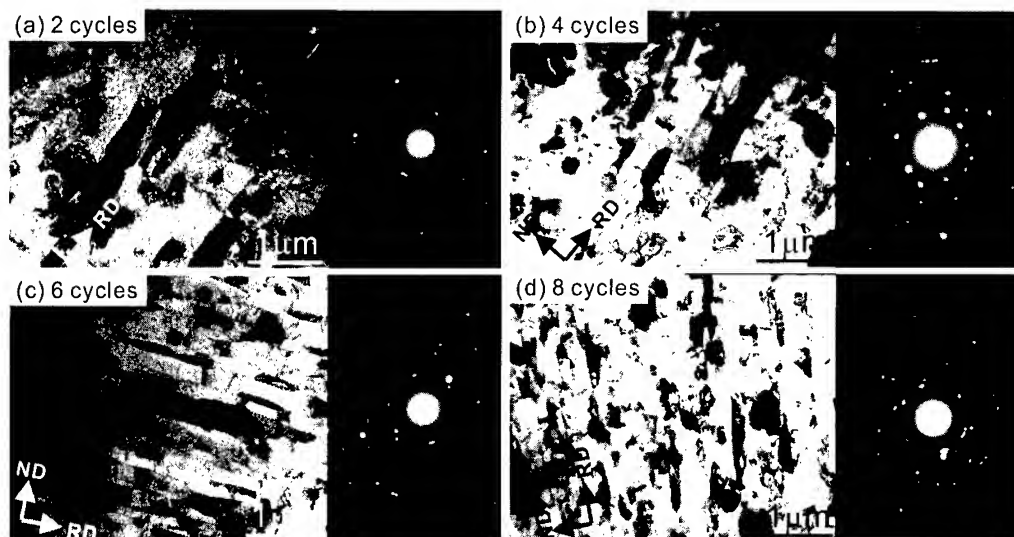


Fig. 4 Changes of TEM microstructures and the corresponding SAD patterns observed at TD plane of the specimen with the number of ARB cycles.

4.2 Mechanical properties

Changes in mechanical properties of the ARB processed 6061 alloy sheet with total equivalent strain are shown in Fig. 5. The results of 1100 pure aluminum, which have been reported by Saito et al. [7], are also plotted in the figure for comparison. The total equivalent strain (ϵ_{tn}) is given as follows,

$$\epsilon_{tn} = \frac{2}{\sqrt{3}} \ln \left(\frac{2^{n-1} h_0}{h_n} \right)$$

where n is the number of ARB cycles, h_0 is the thickness of the initial and h_n is the thickness of the specimen after n cycles. The tensile strength of the ARB processed 6061 alloy increases with the total equivalent strain, although the strengthening rate decreases at the higher strain. The tensile strength of the specimen after 8 cycles of the ARB is 363MPa, about three times of the initial value. In general, the T6-treated 6061 alloy shows the tensile strength of 310MPa and the elongation of 17% [11]. In the present study, the specimens were not heat-treated. It is notable that higher strength than the T6-treated 6061 alloy is achieved by the ARB process. However, the elongation shows only about 5%, which is much lower than that of the heat-treated 6061 alloy. Therefore, it is necessary to increase the elongation for practical use of the ARB processed materials.

By the way, the increment in strength of the ARB processed 6061 alloy with increase of strain is slightly different from that of 1100 aluminum, as Fig. 5 shows. The strength of 1100 aluminum increases largely with the strain up to a strain of 1.5, but above which the increment in the strength become smaller. On the other hand, the strength in the 6061 alloy increases almost linearly with the strain to a strain of 4, which is much larger than that of 1100 aluminum. This difference in tensile strength is probably due to the difference in work hardening behavior. The 6061 alloy contains the various solutes and many precipitates as shown in Fig. 4. These will contribute to the hardening of the 6061 alloy during the ARB. On the other hand, the elongation drops abruptly at the 1st cycle, above which it decreases progressively with the number of ARB cycles. This tendency is very similar to that of the ARB processed 1100 aluminum.

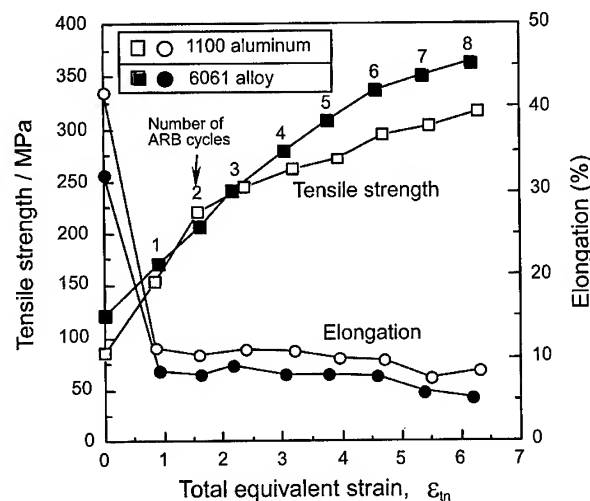


Fig. 5 Changes in mechanical properties of 1100 pure aluminum and 6061 alloy with total equivalent strain (the number of cycles) in the ARB

5. CONCLUSIONS

The ARB process up to 8 cycles has been performed successfully for 6061 Al-Mg-Si alloy. The results obtained are summarized as follows.

1. The ultra-fine grains with clear grain boundaries begin to appear at the 3rd cycle. The fraction of these ultra-fine grains increases with the number of ARB cycles. The specimen ARB-processed by 6-cycle ARB was almost covered with the ultra-fine grains of 500nm in average diameter over almost all regions. The further ARB process up to 8 cycles makes the size and aspect ratio of the ultra-fine grains smaller, results in ultra-fine grains with mean grain size of 310nm.
2. The tensile strength of the ARB-processed 6061 alloy increases with the number of ARB cycles, so that the specimen after 8 cycles shows tensile strength of 363MPa which is about three times of the initial. This value is higher than that of T6-treated 6061 alloy. On the other hand, the elongation decreases largely after 1 cycle, however it hardly changes after the 2nd cycle.

REFERENCES

- [1] L. P. Troeger and E. A. Starke Jr., Mater. Sci. Eng. Vol. A277(2000), pp. 102-113.
- [2] D. Marchive, Light Metal Age, April (1983), pp. 6-10.
- [3] V. M. Segal, Mat. Sci. Eng. Vol. A197(1995), pp. 157-164.
- [4] Y. Iwahashi, Z. Horita, M. Nemoto and T. G. Langdon, Acta Mater. Vol. 45(1997), pp. 3317-3331.
- [5] R.Z. Valiev, N. A. Krasilnikov and N. K. Tsenev, Mater. Sci. Eng. Vol. A137(1991), pp. 35-40.
- [6] Y. Saito, N. Tsuji, H. Utsunomiya, T. Sakai and R. G. Hong, Scrip. Mater. Vol. 39(1998), pp. 1221-1227.
- [7] Y. Saito, H. Utsunomiya, N. Tsuji and T. Sakai, Acta. Mater. Vol. 47(1999), pp. 579-583.
- [8] Y. Ito, N. Tsuji, Y. Saito, H. Utsunomiya and T. Sakai, J. of Jpn. Inst. Metals Vol. 64(2000), pp. 429-437.
- [9] N. Tsuji, K. Shiotsuki, H. Utsunomiya and Y. Saito, Mater. Sci. Forum Vol. 304-306 (1999), pp. 73-78.
- [10] T.G. Nieh, T. Imai, J. Wadsworth and S. Kojima, Scrip. Mater. Vol. 31(1994), pp. 1685-1690.
- [11] Metals handbook, ASM, Vol.1(1961), p. 946.

REFINEMENT OF INTERMETALLIC COMPOUNDS IN Al-Fe ALLOYS BY LTMT PROCESS

C. Y. Lim, H. W. Kim, J. M. Lee and S. B. Kang

Department of Materials Engineering,
Korea Institute of Machinery and Materials, Changwon 641-010, Korea

ABSTRACT

The severe plastic deformation at room or low temperatures and subsequent heat treatment is a feasible process capable of refining the sizes of grain/second phase particles in aluminum alloys. This study investigates the refinement of intermetallic compounds in Al-Fe alloys by low temperature thermomechanical treatment(LTMT) process. Hyper-eutectic Al-Fe alloys(3, 5, 7wt%) were manufactured by induction heating method. The as-cast structure was composed of coarse primary $Al_{13}Fe_4$ phase(acicular type, length 200~300 μ m) and fine eutectic phase(length 20 μ m) in aluminum matrix.

The severe plastic deformation of the alloys by swaging upto the equivalent true strain of 3.582 at low temperature led to a refinement of primary and eutectic phases less than 10 μ m. The matrix is also refined by this process. And the second phase was homogeneously distributed in the deformed alloy as particles. However, in the case of deformation at room temperature, brittle fracture occurred in Al-7Fe alloys.

After the plastic deformation, the hardness increased due to the internal stress and the fragmentation of the intermetallic compounds. Heat treatment(aging) of the as-deformed alloy at 150°C led to a further increase of the hardness due to the fine precipitation. The microstructure after heat treatment was analyzed.

1. INTRODUCTION

Conventional high strength Al alloys are generally precipitation hardened by aging at temperatures typically below 200°C. This heat treatment limits the maximum service temperature of these Al alloys to about 150°C. For higher temperature application, the precipitates made by aging should be replaced by dispersoids such as intermetallic compound, which is thermally stable. Suitable elements to form thermally stable dispersoids are transition elements, such as Fe and Ti, due to their low solubility in aluminum matrix. To achieve high strength at high temperature, a fine distribution of dispersoids with high volume fraction is needed [1].

Rapid solidification such as laser surface treatment, melt spinning and atomization is one of the processes to produce extremely fine dispersions of precipitates [2,3]. But, this process is not adequate for mass production due to the high cost and low productivity.

Severe plastic deformation(SPD) at low temperatures and subsequent heat treatment of aluminum alloys allows the production of materials with fine dispersions of precipitates [4].

The aim of this study was the production of Al-Ti, Al-Fe alloys with fine dispersions of intermetallic compounds by thermomechanical treatment at room(298K) and low(77K) temperatures. The matrix phase refined by the LTMT process is also investigated by TEM. Mechanical properties after this process is checked.

2. EXPERIMENTAL PROCEDURE

Three Al-(3,5,7)Fe alloys(wt%) and Al-5Ti alloy were prepared by induction melting. Rod shape samples with 35 mm diameter and 300 mm in length were casted for each alloy. Chemical composition of the alloys is listed in Table 1.

Table 1. Chemical composition of alloys(wt.%)

Alloys	Fe	Si	Ti	B	Al
Al-3Fe	3.24	0.23	-	-	Bal.
Al-5Fe	5.10	0.26	-	-	Bal.
Al-7Fe	7.18	0.25	-	-	Bal.
Al-5Ti	0.70	0.20	4.62	0.52	Bal.

The surface of cast bar of 35 mm in diameter was machined to 30 mm in diameter to erase the cast defects. Then processed swaging to 5 mm in diameter at 77 K with 16 steps without intermediate annealing. This working process creates an equivalent true strain of 3.58 after final swaged sample. The working process was also conducted at RT for comparison. The scanning electron micrographs were observed for the swaged specimens etched with the solution of 75 ml HCL + 25 ml HNO₃ + 5 ml HF + 25 ml H₂O. The phases were identified by EDS and X-ray diffraction methods. TEM samples were prepared by polishing the slices to a thickness of about 100µm and twin-jet electropolishing using a solution of 20 % perchloric acid and 80% metanol at -30°C. Transmission electron micrography observations were carried out using an JEOL JEM-2000FX II, operated at 200 kV. Tensile tests(gage length 10 mm) were carried out at RT, 200, 300, 400°C of as swaged condition. Hardness was measured on the longitudinal section of the samples using a micro-Vickers hardness tester with a load of 200 g and loading time of 10 sec.

3. RESULTS AND DISCUSSION

3.1 Microstructure Evolution

The as-cast microstructure of Al-Fe alloys is composed of Al-matrix and intermetallic compounds. Fig. 1 shows the scanning electron micrographs of Al-Fe alloys in as-cast condition. There are large primary phase and fine eutectic phase in aluminum matrix. The size of eutectic phase is about 20µm. The volume fraction of primary phase increases with increasing Fe contents. The results of x-ray diffraction show that both of eutectic and primary phases are monoclinic Al₁₃Fe₄. This is given in Fig. 2.



Fig. 1 SEM images of Al-Fe alloys in as-cast condition
(a) Al-3wt.%Fe, (b) Al-5wt.%Fe, (c) Al-7wt.%Fe

The microstructural change after swaging at cryogenic temperature (77 K) of the three Al-(3,5,7)Fe alloys is shown in the scanning electron micrographs (Fig. 3, 4, 5), respectively. Although the grain size is invisible in SEM image, a very fine dispersoids was produced by the cryogenic swaging deformation. At the deformation of equivalent true strain of 0.812, there is still large primary phase together with small eutectic one. With increasing the working to true strain 1.687, the coarse primary phase of $\text{Al}_{13}\text{Fe}_4$ is broken to small size, and homogeneously distributed in the Al matrix. At the true strain of 3.582, the primary phase is less than $10\mu\text{m}$ in size.

A very fine microstructure was produced in the matrix of Al-Fe alloy deformed at 77 K. Fig. 6 shows the typical microstructure of deformed matrix phase of Al-5Fe alloy, together with a selected area diffraction pattern (SADP) obtained from a area of $1.5\mu\text{m}$ in diameter. According to the ring pattern of SADP, there are many grains in the selected area of $1.5\mu\text{m}$ and they have high angle grain boundaries. The grain size of the aluminum matrix deformed at 77 K to the true strain of 3.582 was about less than 500nm . A high density dislocation tangle is observed along the subgrain boundaries.

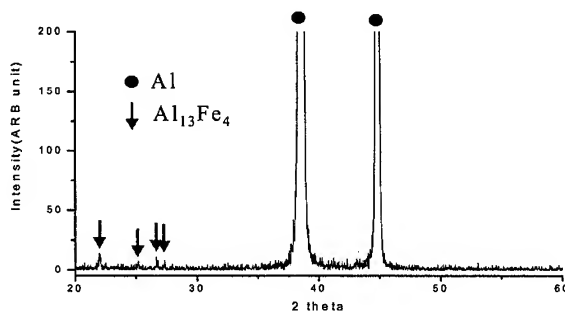


Fig. 2 X-ray diffraction pattern of as-cast Al-5Fe alloy.

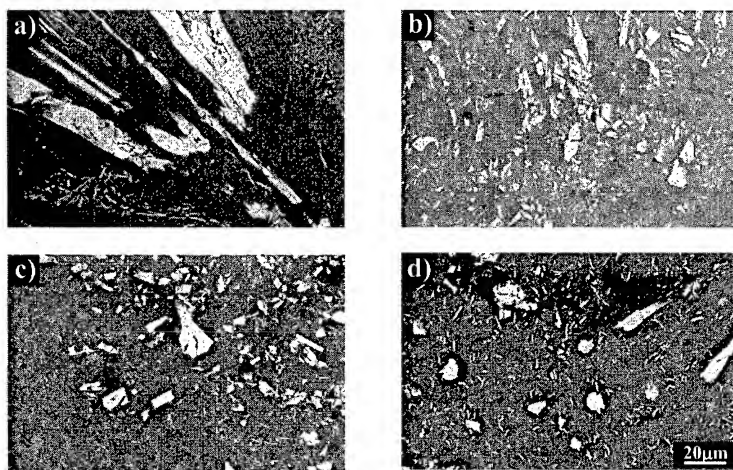


Fig. 3 SEM images of Al-3Fe alloy with cryogenic working at 77 K
(a) $\varepsilon = 0.812$, (b) $\varepsilon = 1.687$, (c) $\varepsilon = 2.669$, (d) $\varepsilon = 3.582$

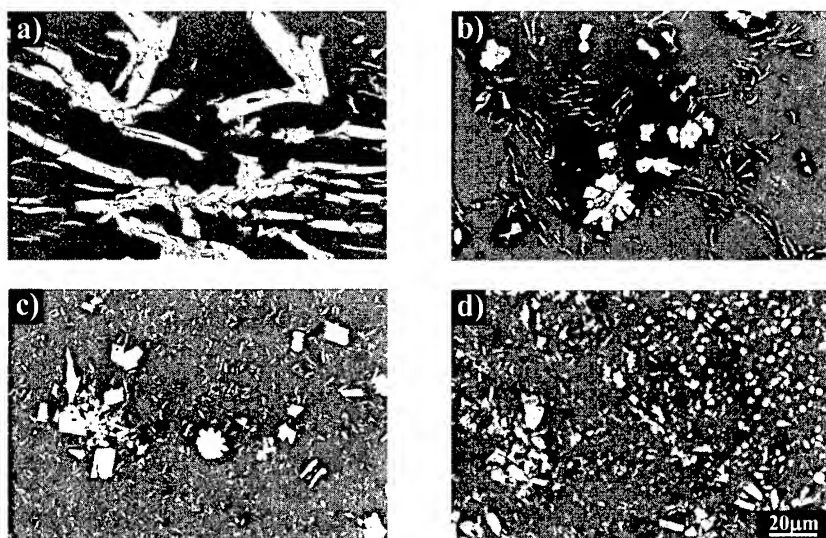


Fig. 4 SEM images of Al-5Fe alloy with cryogenic working at 77 K
(a) $\epsilon = 0.812$, (b) $\epsilon = 1.687$, (c) $\epsilon = 2.669$, (d) $\epsilon = 3.582$

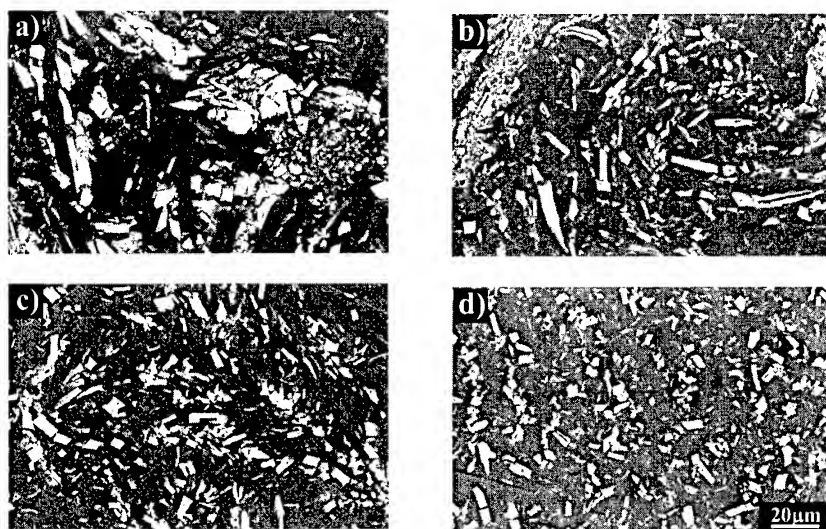


Fig. 5 SEM images of Al-7Fe alloy with working at 77 K
(a) $\epsilon = 0.812$, (b) $\epsilon = 1.687$, (c) $\epsilon = 2.669$, (d) $\epsilon = 3.582$

It is recently reported that severe plastic deformation causes the desolution of second phase in Al-Fe alloys [4], Al-Cu alloy [5]. Samples of Al-5Fe alloy deformed to the true strain of 3.582 at 77 K were aged at 150°C from 15 min to 10 hrs. The microstructure after aging treatment for 5 hrs is shown in Fig. 7. Recrystallization from the deformed structure occurs. The size of the recrystallized grain is very small, less than 0.5 μm. Fine precipitation occurred within the subgrain due to the aging treatment.

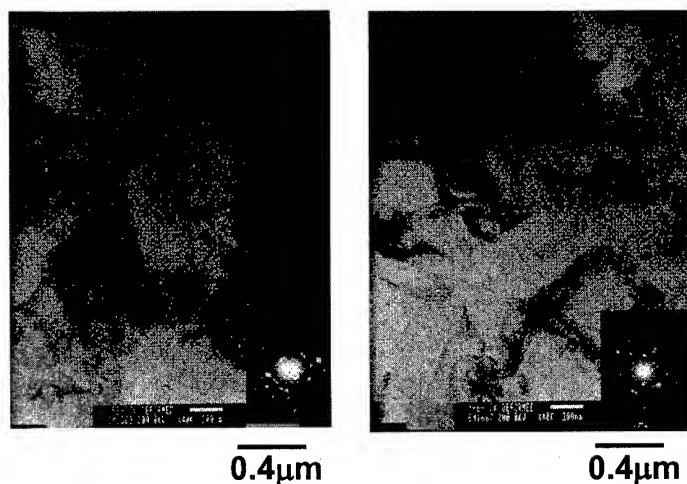


Fig. 6 TEM images of Al-5Fe alloy in as-deformed($\epsilon = 3.582$) condition at 77 K

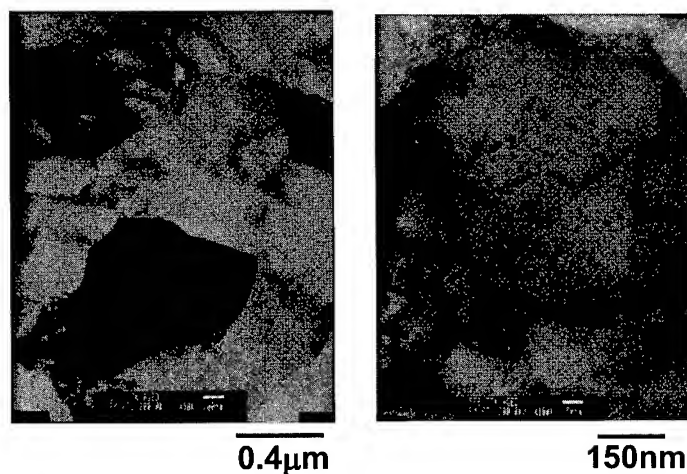


Fig. 7 TEM images of Al-5Fe alloy aged at 150°C for 5hr after swaging($\epsilon = 3.582$) at 77 K

3.2 Tensile Properties

The tensile properties of Al-Fe alloys after refinement of microstructure were investigated at room and high temperatures. At room temperature, the sample of Al-3Fe alloy deformed at 77 K has tensile strength of 230 MPa. With increasing test temperature, the tensile strength of all three alloys decreases. Tensile strength of sample deformed at 77 K is higher than that of sample deformed at RT. The ductility of the three alloys in the as-deformed condition is measured. The ductility of Al-Fe alloy increases with temperature. Al-5Fe has the elongation of 2.0 % at room temperature.

3.3 Microhardness

Fig. 8 shows the microhardness change of Al-Fe alloys with deformation at RT and 77 K. The hardness value of Al-Fe alloys increases with increasing the Fe content, with increasing the true strain, and with decreasing the deformation temperature. The changes of hardness during aging of the deformed (at 77 K) Al-5Fe alloy is shown in Fig. 9. The microhardness of deformed alloy increases with aging time due to the precipitation of small $\text{Al}_{13}\text{Fe}_4$ second phase (this is shown in TEM images of Fig. 7). The hardness goes through the peak value at 3 hrs, then decreases due to the coarsening of second phase and relaxation of the internal stress caused by deformation.

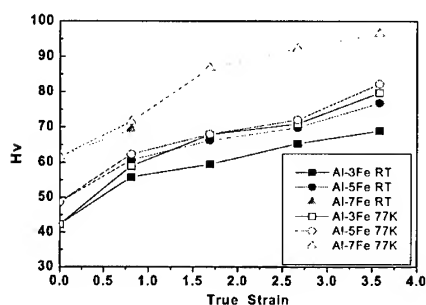


Fig. 8 Hardness (Hv) of Al-Fe alloys as a function of true strain.

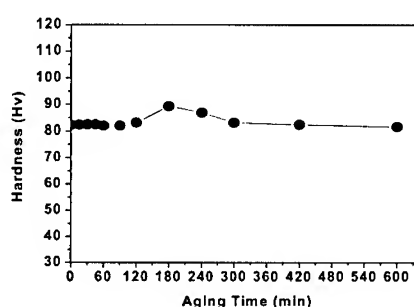


Fig. 9 Hardness of Al-5Fe alloy with aging time at 150°C.

4. CONCLUSIONS

Changes in the microstructure of Al-Fe alloys deformed at cryogenic temperature have been investigated using SEM and TEM. The following conclusions were obtained.

1. Cryogenic swaging deformation of Al-Fe alloys led to the refinement of intermetallic compound (primary and eutectic $\text{Al}_{13}\text{Fe}_4$ phases) and the homogeneous distribution of fragmented small intermetallic compound particles. The size of particles after swaging deformation to true strain 3.582 at 77 K is less than $10\mu\text{m}$.
2. The grain size of matrix phase is also refined by the swaging process at 77 K. The refined grain size is about $0.5\mu\text{m}$ in diameter.
3. Severe deformation causes some desolution of Fe element into the aluminum matrix. Aging the deformed Al-5Fe samples at 150°C led to the precipitation of the $\text{Al}_{13}\text{Fe}_4$ within the subgrain. The grain size is maintained less than $0.5\mu\text{m}$ in diameter.

REFERENCES

1. O. Roder, J. Albrecht and G. Lujering, Microstructure and Mechanical Properties of Metallic High-Temperature Materials, H. Mughrabi, G. Gottstein, H. Mecking, H. Riedel and J. Toboski eds., Research Report, WILEY-VCH, (1990), pp. 3-17.
2. P. Gilgien, A. Zryd and W. Kurz, Acta Mater., Vol. 43(1995), 3477-3487.
3. J.L. Estrada and J. Duszczek, J. Mater. Sci., Vol. 25(1990), 886-896.
4. O.N. Senkov, F.H. Froes, V.V. Stolyarov, R.Z. Variev, and J. Liu, NanoStructured Materials, Vol. 10(1998), pp. 691-698.
5. M. Murayama, Z. Horita and K. Hono, Acta Mater., Vol. 49(2001), pp. 21-29.

MECHANICAL PROPERTIES OF Al-Mg-Sc AND COMMERCIAL ALUMINUM ALLOYS AFTER EQUAL-CHANNEL ANGULAR PRESSING

Minoru Furukawa, Sungwon Lee*, Zenji Horita** and Terence G. Langdon***

Department of Technology, Fukuoka University of Education
Munakata, Fukuoka 811-4192, Japan

*Plate Rolling Department, Pohang Iron & Steel Co., Ltd.
P.O. Box 35, Nam-ku, Pohang 790-360, Korea

**Department of Materials Science and Engineering, Faculty of Engineering
Kyushu University, Fukuoka 812-8581, Japan

***Departments of Aerospace & Mechanical Engineering and Materials Science
University of Southern California, Los Angeles, CA 90089-1453, U.S.A.

ABSTRACT

Equal-channel angular pressing (ECAP) is a processing procedure in which a material is subjected to severe plastic deformation. This paper describes the use of ECAP in preparing materials with ultrafine grain sizes and the subsequent properties of these materials at room temperature and at elevated temperatures. It is shown that a very fine grain size of $\sim 0.2 \mu\text{m}$ with high-angle boundaries may be produced in an Al-3% Mg-0.2% Sc alloy by using ECAP to 8 passes at room temperature. These fine grains are stable to $\sim 773 \text{ K}$ due to a dispersion of fine Al_3Sc particles and the alloy exhibits superplastic elongations at high temperatures. Commercial 1100, 2024, 3004, 5083, 6061 and 7075 alloys were subjected to ECAP at room temperature giving fine grain sizes of $< 1 \mu\text{m}$. It is shown that the 0.2% proof stress and the UTS of these alloys increase abruptly in tensile tests after a single pass in ECAP but thereafter the increase is more gradual. By contrast, the elongations to failure decrease abruptly after one pass and then remain constant. The results show also the development of superplasticity in the 2024 alloy.

1. INTRODUCTION

Severe plastic deformation (SPD) is a processing tool that may be used to introduce very significant grain refinement in structural metals [1,2]. Several SPD methods are now available but the most promising technique appears to be Equal-Channel Angular Pressing (ECAP) [3,4] because this procedure may be used for processing relatively large bulk samples. Through the use of ECAP, it is possible to reduce the grain size to the submicrometer level and therefore to values that are smaller than generally achieved using conventional thermomechanical processing. This grain refinement has two potential advantages. First, it strengthens the material in the low temperature regime through the Hall-Petch relationship [5,6] as, for example, in tensile testing at room temperature. Second, in the high temperature regime where diffusion is reasonably rapid, there is a possibility of achieving a superplastic forming capability [7]. This paper examines the use of ECAP with a series of aluminum-based alloys.

2. EXPERIMENTAL MATERIALS AND PROCEDURES

The experiments were conducted using an Al-3% Mg-0.2% Sc alloy prepared by casting and a series of commercial alloys (1100, 2024, 3004, 5083, 6061 and 7075). The Al-Mg-Sc alloy was fabricated from 99.99% Al, 99.999% Sc and 99.9% Mg using the procedure described in detail in earlier reports [8-10] and including a solution treatment for 1 hour at 883 K in order to maximize the amount of scandium in solid solution [8]. The commercial 1100 and 5083 alloys were received after hot rolling, the 3004 alloy after cold rolling and the 2024, 6061 and 7075 alloys after appropriate heat treatments: detailed information about these various alloys, including their chemical compositions, was given in an earlier report [11]. Measurements showed that the initial grain sizes of these materials prior to ECAP were $\sim 200\text{ }\mu\text{m}$ in the Al-Mg-Sc alloy and ~ 30 , ~ 40 , ~ 15 , ~ 30 , ~ 50 and $\sim 30\text{ }\mu\text{m}$ in the 1100, 2024, 3004, 5083, 6061 and 7075 alloys, respectively.

All samples were subjected to ECAP at room temperature. In addition, some of the samples of the 2024 alloy were pressed at 373 K. The principle of ECAP is that a sample is pressed through a die contained within a channel bent into an L-shaped configuration. In this investigation, the ECAP used a solid die with a single channel bent through an angle of 90° . For a channel angle of 90° , it can be shown from first principles that the strain introduced into the sample on a single passage through the die is ~ 1 [12]. In practice, the cross-sectional dimensions remain unchanged during processing by ECAP and it is therefore possible to achieve very high total strains by pressing the same sample repetitively through the die. In this investigation, each sample was rotated by 90° in the same sense between consecutive pressings in the procedure termed route B_C [13] where this route was selected because it tends to be the optimum procedure for attaining an array of equiaxed grains separated by high-angle boundaries [14]. Following ECAP, specimens were examined using transmission electron microscopy and the thermal stability of the ultrafine microstructures was evaluated by annealing samples for 1 hour at selected elevated temperatures. Tensile specimens were machined from several of the as-pressed billets, with the gauge lengths of the samples cut parallel to the pressing direction. These specimens were tested in tension at room temperature and at 673 K using a testing machine operating at a constant rate of cross-head displacement.

3. EXPERIMENTAL RESULTS

3.1 Al-3% Mg-0.2% Sc alloy

Figure 1 shows a representative microstructure of the Al-3% Mg-0.2% Sc alloy after ECAP through a total of 8 passes at room temperature to a strain of ~ 8 : the selected area electron diffraction (SAED) pattern was taken from a region having a diameter of $12.3\text{ }\mu\text{m}$. Careful measurements showed that the average grain size in this condition was $\sim 0.2\text{ }\mu\text{m}$. In addition, the SAED pattern suggests the presence of high-angle grain boundaries. By recording the individual SAED patterns over a large area within the sample ($\sim 100 \times 100\text{ }\mu\text{m}^2$), it was estimated that the as-pressed condition contained an area fraction of $>90\%$ of equiaxed grains separated by high-angle boundaries and $<10\%$ of subgrains separated by boundaries having low-angles of misorientation. Thus, ECAP is exceptionally effective in introducing an

extremely small grain size into this alloy.

The grain stability of this alloy was evaluated by annealing small disks cut from the as-pressed rods. The result is shown in Fig. 2 together with similar data for samples of pure Al after pressing through 4 passes at room temperature [15], an Al-3% Mg alloy after 8 passes at room temperature [15] and an Al-0.2% Sc alloy after 8 passes at room temperature. These results show that the ultrafine grain sizes introduced by ECAP are remarkably stable in the alloys containing 0.2% Sc and this stability is attributed to the presence of fine secondary particles of Al_3Sc .

Tensile testing was conducted at 673 K and Fig. 3 shows the measured elongations to failure as a function of the initial strain rate for the Al-3% Mg-0.2% Sc alloy and for the other materials documented in Fig. 2. It is apparent from this plot that the Al-3% Mg-0.2% Sc alloy exhibits

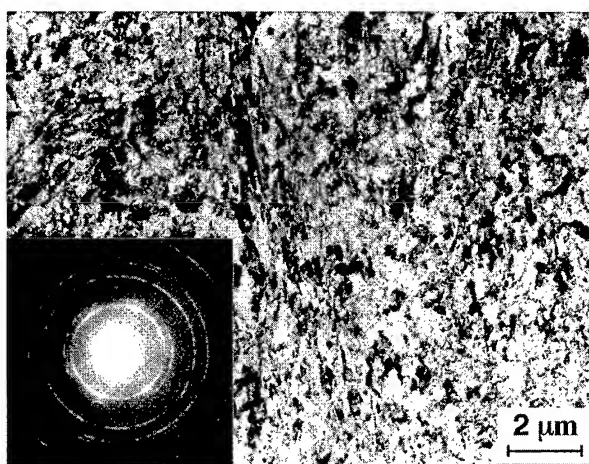


Fig. 1 Microstructure of the Al-3% Mg-0.2% Sc alloy after ECAP through 8 passes at room temperature:
SAED pattern taken with an aperture size of 12.3 μm .

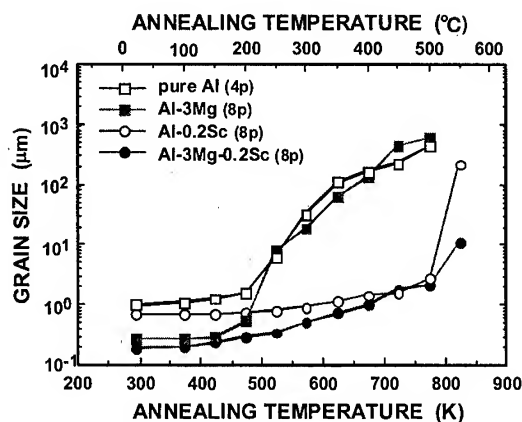


Fig. 2 Variation of grain size with annealing temperature for pure Al and various Al alloys after processing by ECAP.

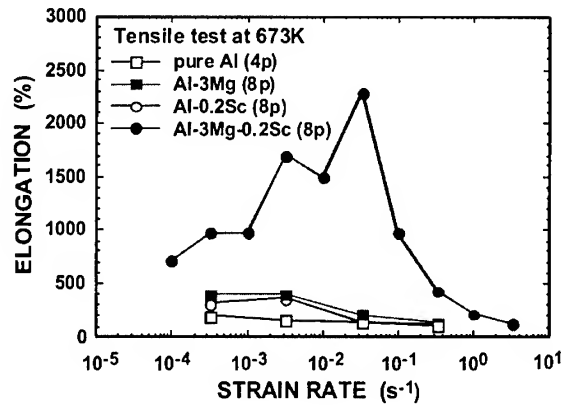


Fig. 3 Elongation to failure versus initial strain rate for tests conducted at 673 K after ECAP.

exceptionally high ductilities at strain rates in the vicinity of $\sim 10^{-3} - 10^{-1} \text{ s}^{-1}$, with a maximum elongation of 2280% at an initial strain rate of $3.3 \times 10^{-2} \text{ s}^{-1}$. Pure Al and the Al-3% Mg alloy do not exhibit superplastic elongations at this testing temperature because, as shown in Fig. 2, the grains grow to $>100 \mu\text{m}$; and the Al-0.2% Sc alloy fails to give high ductilities because the alloy is deforming by a conventional climb-controlled deformation mechanism with a relatively low strain rate sensitivity of ~ 0.2 . By contrast, the addition of 3% Mg introduces a glide-controlled deformation process together with the enhanced ductilities and higher strain rate sensitivity associated with Al-Mg alloys [16] and this behavior is further enhanced in the Al-3% Mg-0.2% Sc alloy because of the retention of an exceptionally fine grain size close to $\sim 1 \mu\text{m}$.

3.2 Commercial Al alloys

Processing by ECAP at room temperature leads to average grain sizes of $<1 \mu\text{m}$ in the commercial Al-based alloys [11]. As a consequence of this grain refinement, there is an increase in both the 0.2% proof stress and the ultimate tensile stress (UTS) in tensile testing at room temperature. This is illustrated in Figs 4(a) and (b) where the tests were conducted with an initial strain rate of $3.3 \times 10^{-4} \text{ s}^{-1}$ and the data are plotted as a function of the equivalent strain introduced by ECAP and thus to the number of passes through the ECAP die. These plots show the sharp increase introduced on a single pass through the die and the gradual increase thereafter, and Fig. 4(c) shows also the corresponding reductions in the elongations to failure that occur on the first passage through the die.

The commercial 2024 alloy was also tested in tension at a temperature of 673 K in both the unpressed condition and after ECAP for 8 passes at either room temperature or 373 K [17]. The results are shown in Fig. 5 where the elongations to failure are plotted against the initial strain rate in tension. Inspection shows the unpressed alloy yields elongations to failure that are generally $<200\%$ whereas the alloy exhibits elongations close to $\sim 500\%$ after ECAP at either 298 or 373 K. The highest elongation was achieved in this alloy at an initial strain rate of $1.0 \times 10^{-2} \text{ s}^{-1}$ after ECAP for 8 passes at 373 K.

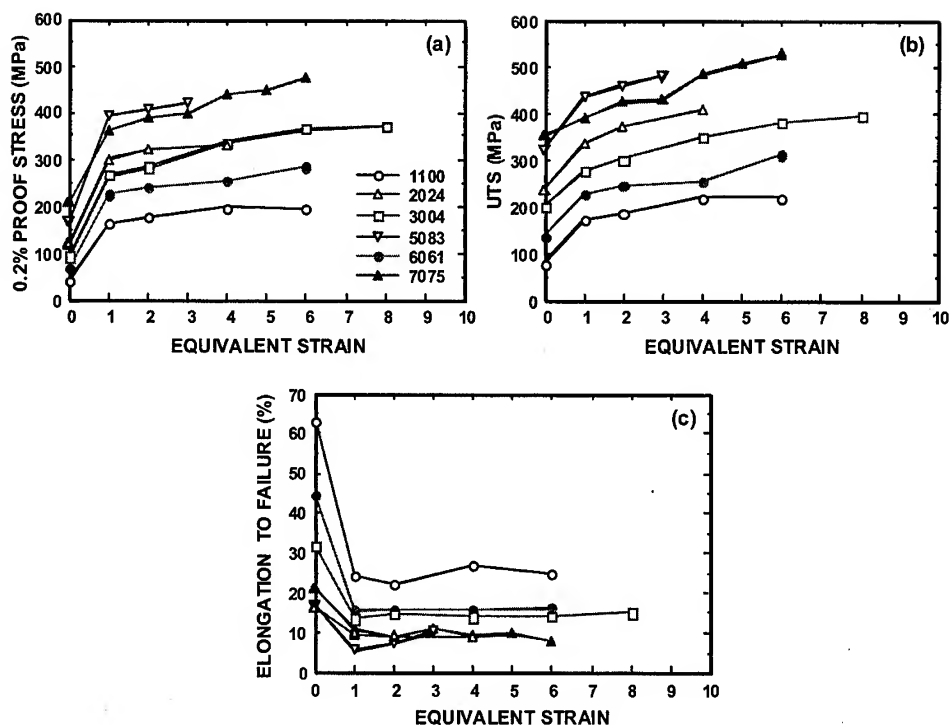


Fig. 4 Relationship between the mechanical properties and the equivalent strain in ECAP in tensile tests at room temperature using an initial strain rate of $3.3 \times 10^{-4} \text{ s}^{-1}$: (a) 0.2% proof stress, (b) UTS and (c) elongation to failure.

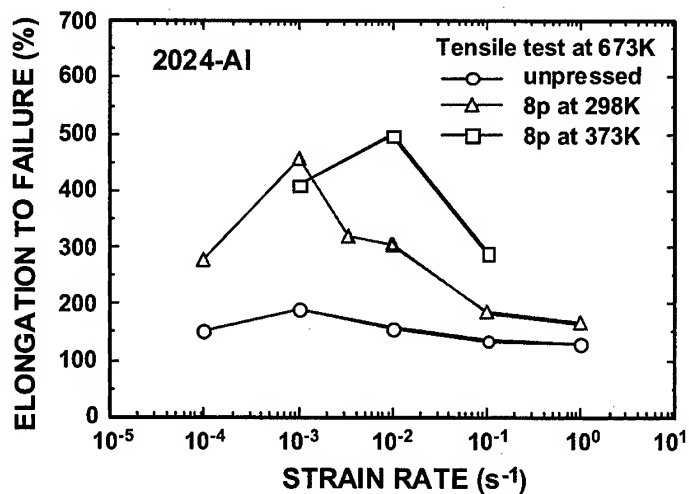


Fig. 5 Elongation to failure versus initial strain rate for tests conducted in tension on the commercial 2024 alloy in the unpressed condition and after ECAP.

4. SUMMARY AND CONCLUSIONS

Ultrafine grain sizes of $<1\ \mu\text{m}$ may be introduced into Al-based alloys through processing by ECAP at room temperature. These grains are reasonably stable at high temperatures if precipitates are present in the materials. The introduction of very small grains leads to strengthening of the alloys at low temperatures and there is a potential for achieving superplastic ductilities at elevated temperatures.

ACKNOWLEDGEMENTS

This work was supported in part by the Light Metals Educational Foundation of Japan and in part by the U.S. Army Research Office under Grant No. DAAD19-00-1-0488.

REFERENCES

1. T.C. Lowe and R.Z. Valiev (eds.), *Investigations and Applications of Severe Plastic Deformation*, Kluwer, Dordrecht, The Netherlands (2000).
2. R.Z. Valiev, R.K. Islamgaliev and I.V. Alexandrov, *Prog. Mater. Sci.*, Vol. 45 (2000), pp. 103-189.
3. V.M. Segal, V.I. Reznikov, A.E. Drobyshevskiy and V.I. Kopylov, *Russian Metall.*, Vol. 1 (1981), pp. 99-105.
4. V.M. Segal, *Mater. Sci. Eng.*, Vol. A197 (1995), pp. 157-164.
5. E.O. Hall, *Proc. Roy. Soc. B*, Vol. 64 (1951), pp. 747-753.
6. N.J. Petch, *J. Iron Steel Inst.*, Vol. 174 (1953), pp. 25-28.
7. Z. Horita, M. Furukawa, M. Nemoto, A.J. Barnes and T.G. Langdon, *Acta Mater.*, Vol. 48 (2000), pp. 3633-3640.
8. S. Komura, Z. Horita, M. Furukawa, M. Nemoto and T.G. Langdon, *J. Mater. Res.*, Vol. 15 (2000), pp. 2571-2576.
9. S. Komura, M. Furukawa, Z. Horita, M. Nemoto and T.G. Langdon, *Mater. Sci. Eng.*, Vol. A297 (2001), pp. 111-118.
10. S. Komura, Z. Horita, M. Furukawa, M. Nemoto and T.G. Langdon, *Metall. Mater. Trans. A* (in press).
11. Z. Horita, T. Fujinami, M. Nemoto and T.G. Langdon, *Metall. Mater. Trans.*, Vol. 31A (2000), pp. 691-701.
12. Y. Iwahashi, J. Wang, Z. Horita, M. Nemoto and T.G. Langdon, *Scripta Mater.*, Vol. 35 (1996), pp. 143-146.
13. M. Furukawa, Y. Iwahashi, Z. Horita, M. Nemoto and T.G. Langdon, *Mater. Sci. Eng.*, Vol. A257 (1998), pp. 328-332.
14. K. Oh-ishi, Z. Horita, M. Furukawa, M. Nemoto and T.G. Langdon, *Metall. Mater. Trans.*, Vol. 29A (1998), pp. 2011-2013.
15. H. Hasegawa, S. Komura, A. Utsunomiya, Z. Horita, M. Furukawa, M. Nemoto and T.G. Langdon, *Mater. Sci. Eng.*, Vol. A265 (1999), pp. 188-196.
16. E.M. Taleff, G.A. Henshall, T.G. Nieh, D.R. Lesuer and J. Wadsworth, *Metall. Mater. Trans.*, Vol. 29A (1998), pp. 1081-1091.
17. S. Lee and T.G. Langdon, *Mater. Res. Soc. Symp. Proc.*, Vol. 601 (2000), pp. 359-364.

Fracture toughness of various zones in weldments of 6082 Al alloys

V.A. Mosneaga*, T. Kobayashi**, H. Toda**

*Graduate School, Toyohashi University of Technology, Toyohashi 441- 8580, Japan

**Department of Production Systems Engineering, Toyohashi University of Technology, Toyohashi 441- 8580, Japan

ABSTRACT

Al-Mg-Si alloys are widely used as materials for welded structures. In this paper, the effects of Mn addition on toughness of welded Al-Mg-Si alloys have been investigated. To evaluate microstructural effects quantitatively, in-situ SEM observations of crack initiation and propagation behaviors through the weldment were carried out. When small amount of Mn is added, recrystallization is completely suppressed as compared to the specimen to which no Mn was added, thereby coarse grains appeared. Recrystallization of HAZ causes a drastic decrease in fracture toughness. With the extension of the main crack, many microcracks are formed at the grain boundaries ahead of crack-tip, where stress is relatively low. The microcracking are not attributed to so-called liquation cracks. The degradation is caused by the formation of film like Al-Mg intermetallic compounds at grain boundaries. The microcracks are aligned ahead of the crack-tip at an angle of 60 degrees from an initial notch direction. This is attributable to the direction of intermetallic compound films, which is confirmed by the numerical analysis.

Keywords: Al-Mg-Si alloy, Weldment, Charpy impact test, Fracture toughness, Liquation crack, In- situ observation.

1. Introduction

Medium to high-strength aluminum alloys represent attractive alternatives to steel for various applications. Of these, Al-Mg-Si alloys are superior to other high strength aluminum alloys in their weldability and corrosion resistance, but is reported to have a problem of low fracture toughness in the heat affected zone near a weldment due to the liquation cracking (1), (3). The liquation cracking is a defect of welded section on Al-Mg-Si alloys. The HAZ liquation cracking of 6082Al alloy is investigated using the instrumented Charpy impact testing and three-point bending tests. The sensitivity of HAZ liquation cracking was mainly evaluated by maximum crack length in the HAZ (2). In the previous paper, it became clear that the initiation of liquation crack depends on type of filler, cross section, grain structure of base material, density of alloying elements and welding conditions (2). These alloys are currently used for automobile, train and passenger/cargo ships, combining with other aluminum alloys

or composites. It is expected that the usage will be steadily increased in the future.

2. Experimental procedure

2.1 Welding conditions and specimens

Table one shows the chemical compositions of materials used in this study.

Table 1 Chemical compositions of the base materials (mass %)

Material	Mg	Si	Mn	Fe	Ti	Cu	Zn	Cr	Al
0.0%Mn	0.88	1.10	0.01	0.13	0.02	0.01	0.03	0.01	balance
0.4%Mn	0.91	1.11	0.40	0.13	0.02	0.01	0.02	0.01	balance
0.7%Mn	0.90	1.06	0.72	0.13	0.02	0.01	0.01	0.01	balance

The amount of Mn is changed from 0.01 to 0.72%. The base materials were homogenized (813K, 144ks), extruded at high temperature (743K, 10m/min) and artificially aged (453K, 21.6ks, T6 conditions). Finally plates with 6mm in thickness were obtained. The treatments were done outside. Filler material used was an A5356 Al-Mg with diameter of 1.6mm. Before welding, the base materials were fastened on a copper support and a groove was very precisely machined with an angle of 60 degrees and a depth of 5mm. The welding procedure is MIG and welding direction is perpendicular to the extrusion direction of the base material. The parameters of welding are: arc current 230V, arc voltage: 23V and welding speed: 400mm/min. The welding was finished by a single pass. This process was done by Furukawa Corporation.

2.2 Optical observations

Samples were prepared for optical observations. Longitudinal section of weld bead was polished to be like a mirror and after that etched with the Burger's etching agent (4). Optical observations were carried out using a Nikon microscope. Other observations were made using a SEM JSM 5600 equipped with EDX image analyzer.

2.3 Instrumented Charpy impact testing

Standard 10(thickness) x 10(width) x 55 mm³ Charpy V notch specimens were tested at room temperature. Specimens were produced so that it is perpendicular to the weld bead on loading direction. The direction of crack propagation is opposite to the welding direction. For the study of toughness, 5 types of specimen with different positions of notch were prepared. The notch positions were decided according to distribution of Vickers hardness shown in Figure 1. Notch position of the first sample is located in the center of the bead, for the second to the fifth notch position, distance from a fusion line is: 0.5, 4, 13 and 20mm, respectively. The crack propagation in the second material is mostly in weld metal and partially through HAZ. For the third position, crack propagation is mostly in the HAZ and partially in the weld metal. The instrumented Charpy impact-testing machine used has: a capacity of 98J, impact speed of 4.5m/s. E_i , E_p and E_t were evaluated from load- deflection curves (5).

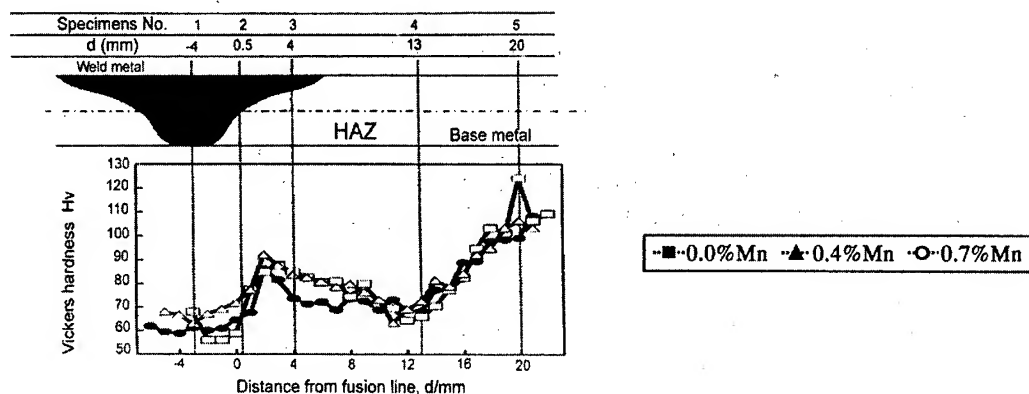


Fig.1 Variation of Vickers hardness as a function of distance from a fusion line with a schematic illustration of positions of notch- tip in the fracture toughness tests.

2.4 In situ SEM fracture toughness test

For the study of fracture behavior of HAZ, it was carried out in situ fracture toughness tests. 3 point bending specimen were used. The notch is located 400 μ m from fusion line, the direction of crack propagation is the same as Charpy impact specimen. Loading speed was 0.01mm/min and before breaking, the load deflection curve was recorded and finally in situ observations were carried out.

3. Experimental results

3.1. Microstructural observations

Figure 2 shows optical micrographs of cross sectional area near a fusion line. HAZ of 0% Mn material shows recrystallized grains. In HAZ of 0%Mn material, liquation crack was observed away at 350- 450 μ m from a fusion line (indicated by an arrow).

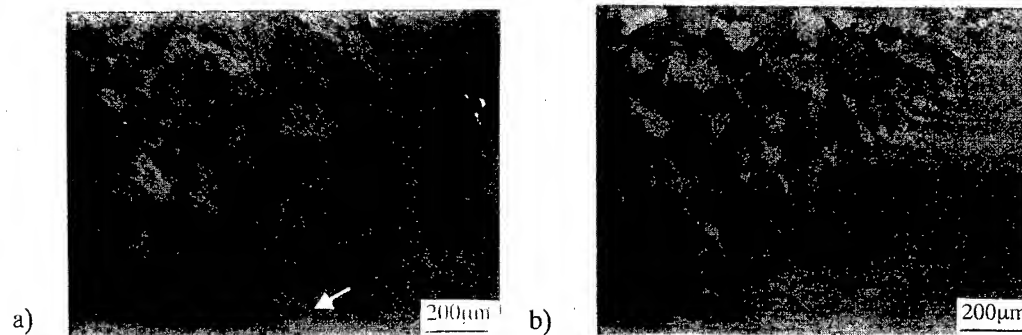


Fig.2 Optical microstructures of cross sectional areas near fusion line a) for 0%Mn material and b) 0.4%Mn material.

In the case of 0.4% and 0.7% Mn, the fibrous microstructure well remains and no evidence of recrystallization can be seen. Figure 3 shows SEM image with a corresponding EDX spectrum of Mg in the HAZ at about 240 μ m from a fusion line for the 0% Mn material. EDX analysis presents only a sharp peak of Mg; other elements like Si, Fe, Te, Zr and Cr were not identified. Grain boundary at about 420 μ m from a fusion line was also analyzed, where a liquation crack appeared and only a peak of Mg was observed. In both cases we confirmed the formation of intermetallic compound phases of the Al- Mg system.

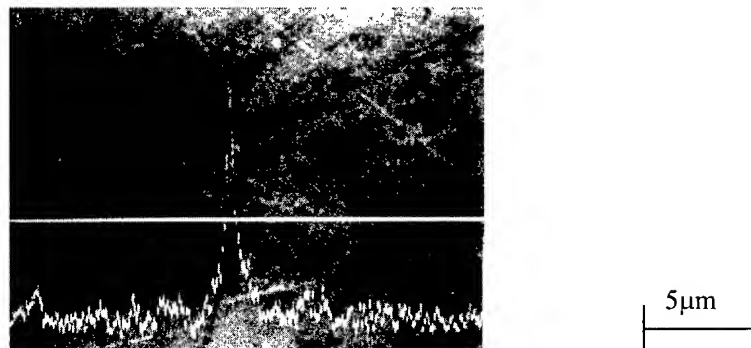


Fig.3 SEM image and corresponding EDX spectrum of Mg at around 240 μ m from fusion line in 0% Mn material

3.2 Instrumented Charpy impact testing results

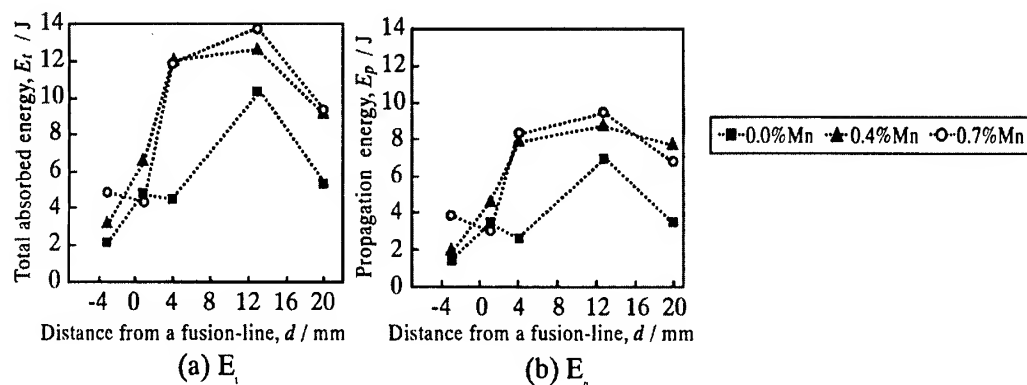


Fig.4 Variations of absorbed energy as a function of distance from a fusion line. Effects of the Mn content were shown for comparison.

According to Figure 4, toughness of matrix and HAZ of the 0%Mn material is smaller than those of the 0.4% and 0.7% Mn materials over a wide distance. The largest difference in the toughness between the 0%Mn material and other two materials was recorded at the third position of notch. For the 0.4 and 0.7% Mn materials, the levels of E_t and E_p are larger in the first position. Returning to the first position, weld metal has the lowest toughness because it has the casting structure (5), while the farthest position also has remarkably low fracture toughness comparing with the neighboring position simply because of overaging.

3.3. In situ observation of crack propagation process

Figure 5 shows SEM micrograph of specimen surface during the in-situ fracture toughness test together with the schematic illustration of microcrack distribution. In the case of the 0%Mn material in which a notch was introduced at 400 μ m ahead fusion line, i.e. in HAZ, only one liquation crack of 1 mm long was observed ahead of a crack-tip before starting the test. Crack initiated from the notch tip is propagated by 500 μ m and many microcracks with the maximum length of 1 μ m were also observed within 3mm ahead of the main crack tip at $P/P_{max} = 0.97$. The microcracks are oriented in a similar direction, inclined at an average angle of 60 degrees from the initial notch direction.

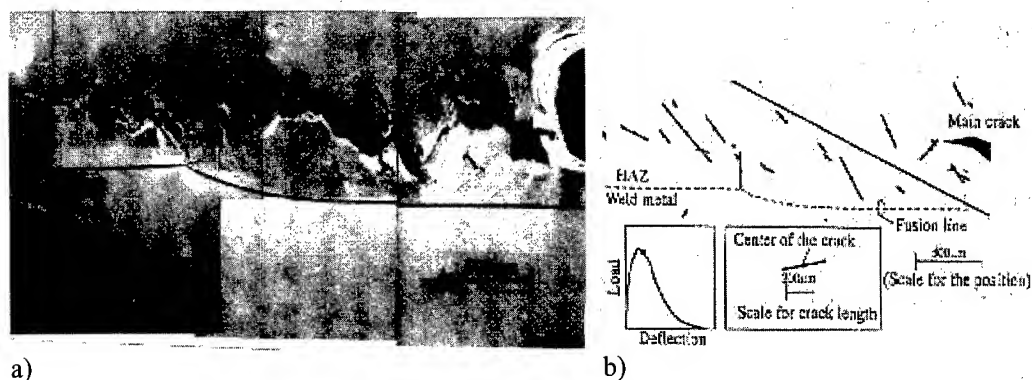


Fig.5 SEM micrograph of specimen surface during in-situ fracture toughness test a) and schematic illustration of microcrack distribution b).

4. Discussions

In Figure 3, recrystallization was suppressed in the HAZ in the case of materials with Mn addition. Even by a small amount of Mn added (0.1mass%), small Mn bearing particles suppressed grain boundary migration. On the other hand, grains are observed in the 0%Mn material. It is known that the behavior is affected by the welding conditions. According to Miyazaki (6) who used the Varestraint test, liquation cracking was developed within HAZ grains were coarsened. Before loading (Figure 5), liquation crack could not be observed, while, after loading, we observed extensive intergranular cracking ahead of a crack tip. This observation suggests that the grain boundary strength within the HAZ is extremely low in the vicinity of the fusion line. Usually, the liquation cracks are welding defects which are formed by opening of grain boundaries next to a melt pool at high temperature due to the local eutectic melting and subsequent impregnation of melt metal. Insufficient impregnation causes the liquation cracks especially when the fluidity is bad. However, in this case, no discernable welding defects were observed before tests. The grain boundary strength is lowered by the formation of the film-like brittle layer. Microcracks, which are formed ahead of a main tip were orientated in a specified direction. There seem to be two possibilities for the orientation of the microcracks: 1) Mechanism: The deformation behaviors of welded metal and HAZ are different, thus mode II deformation takes place. 2) Material: When the base metal is welded,

grain boundary opened in a specified direction. Figure 6 shows fracture surfaces after the in-situ SEM fracture toughness test. The intermetallic compounds can be observed at grain boundary. It indicates that the opening direction of grain boundary during welding mainly causes inclination of the microcracks formed.

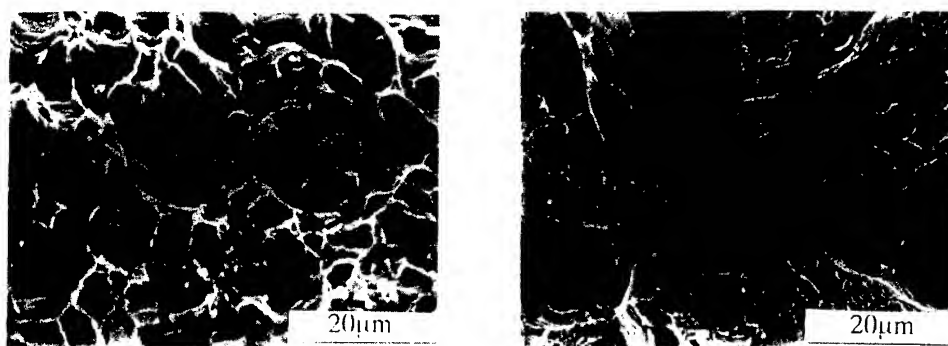


Fig.6 Fracture surface after in-situ fracture toughness test.

5. Conclusions

In this article the effects of the grain structure on toughness of the welded materials have been investigated. The following results were obtained:

- 1) Toughness of the weld metal is the always the lowest because it has the casting microstructures.
- 2) When no Mn was added, recrystallization occurred in the HAZ. Small numbers of liquation cracks are observed at 350- 450µm from a fusion line. However, the recrystallization is suppressed by a small amount of Mn addition.
- 3) In 0% Mn material many microcracks were initiated ahead of crack tip during loading. These microcracks are not pre-existing liquation cracks, and is formed by considerably low strength of grain boundary due to the formation of brittle intermetallic compound at grain boundary. These microcracks are limited within 500µm from a fusion line.
- 4) Microcracks were initiated at 60 degrees to the weld bead. It is due to the oblique opening of grain boundary in HAZ during welding.

6. References

1. T. Fukui and S. Sugiyama, Welding Institute Magazine, Vol.40(1997), pp. 868-870
2. H.V. Kerr and M. Katoh, Welding Research Supplement, September(1987), pp. 251-259
3. M.B.D. Willis, M.F. Gittos and I. Hadley, TWI Journal, Vol.6(1997), pp. 213-215
4. J.C. Blade and M. Katoh, J. Inst. Met., Vol.88(1959), pp. 356-358
5. P. Furrer and H. Warlimont, Aluminum, Vol.54(1978), pp.135-139
6. M. Miyazaki and K. Noshō , Welding Research Supplement, September(1990), pp. 362-370
7. H. Toda and T. Kobayashi, J. Jap. Inst. Met., Vol.59(1995), pp. 94-100.

Study on Microstructures and Mechanical properties in Electromagnetic Cast and Direct Chill Cast Al Alloys

Sug-Won Kim, Hai Hao, Ui-jong Lee, Kee-Do Woo, Jun-Ze Jin*

Division of New Materials Engineering & Research Institute of Advanced Materials
Development, Chonbuk National University, Chonju, 561-756, South Korea

*Dalian University of Technology, Dalian, 116-023, China

ABSTRACT

DCC has some demerits such as oscillation and subsurface segregation etc. The electromagnetic casting (EMC) technology was used to solve these problems. The 2024 Al alloys were made by EMC and DCC technology. OM, SEM, XRD and DSC etc. were carried out to contrast the microstructural and mechanical characteristics of EMC and DCC 2024 aluminum alloy before and after heat treatment. Compared to DCC ingot, the EMC ingot has better mechanical properties not only in as-cast condition but also in as-aged one. DSC curves show the EMC specimens have high enthalpy that means much more precipitation formed during the heating process. Even though after heat-treatment, the DCC ingot still can not get the same quality as EMC one. Moreover, considering the expensive scalping operation for DCC ingots, the EMC technique is one of the best manufacturing methods to get the high quality ingots of aluminum alloys.

1. INTRODUCTION

Owing to their impact on industrial casting processes, an increasing interest has been shown in fundamental and applied investigations on electromagnetic casting (EMC). EMC is a technology developed by combination of magnetohydrodynamics (MHD) and casting engineering. The main advantage of the EMC technology consists in the presence of stirring motions in the melt which lead to significant reduction of the grain size in the solidified product. Moreover surface quality and subsurface quality are improved due to the absence of ingot mould[1]. The surface finish of the ingot is usually smooth enough to be hot rolled without scalping operation that is required following direct chill casting[2]. Besides refining internal structures, electromagnetic stirring also has advantages of homogenized alloy elements, reducing porosity and segregation, and minimizing internal cracks[3]. Even though

many investigations have examined electromagnetic and magnetohydrodynamics phenomena in EMC of aluminum, the research about the microstructural and mechanical characterization are comparatively few. This paper is an attempt to remedy this deficiency. Comparing the DCC ingot, the EMC one has more fine microstructure and excellent properties. In this paper, an investigation of aluminum alloys EMC ingots will be described in this aspect.

2. EXPERIMENTAL PROCEDURE

2.1 The operation of EMC

After obtaining the distribution of the magnetic field, the solidification front and the height of the liquid column, the shaping experiment for an EMC ingot could be done. The technique procedures are as follows: (1) to melt metal; (2) to adjust the position of inductor, screen, water jacket and bottom block; (3) to operate cooling system; (4) to turn on power supply; (5) to cast on; (6) in steady stage, to keep withdrawal speed, casting and solidification rate with optimal value to make steady liquid column and solidification front until the end of casting. The manufacturing condition is: inductor current, 4800A; height of liquid column, 40mm; solidification front, 10mm up to bottom of inductor; pouring temperature, 710~730°C; flow rate of cooling water, 3m³/h; casting speed, 0.3~1.5mm/s. The experimental specimens could be obtained from these EMC ingots and DCC ingots.

2.2. Heat-treatment and Mechanical Properties

The metallographic specimens were prepared by cutting, grinding, polishing and etching. The etchant was Keller's solution. All specimens were examined by an optical microscope. 2024 specimens were solution-treated at 495 °C (salt bath) for 1 hour and then quenched in ice water. After this, they were immediately aged in the 190 °C silicon oil bath for various holding time. For contrasting the mechanical properties and response of the ageing effect, hardness tests were performed before and after heat-treatment by the load of 60kg with the Rockwell hardness tester

3. RESULTS AND DISCUSSION

3.1 Microstructures

Fig.1 shows the transverse sectional grain structures of the 2024 DCC and EMC specimens in as-cast state. It is clear that the grains of EMC are small and equiaxed, no matter at edge,

midthickness, 1/2 or center of ingots. In DCC condition, the grain size becomes coarse from surface to center of ingot. The conventional DCC process is known to generate non-uniform heat transfer due to air-gap formation. Therefore, local solidification times become extended due to the rapid loss of superheat. The grains move about in the pool for extended times, growing and coarsening all the while. Microstructural coarsening of the dendrites due to Ostwald ripening becomes significant in the center of DCC ingot[4]. However, it has different situation in EMC process. The grain of EMC ingots is more homogeneous over the entire cross section. It is well known, the skin-effect exists in the electromagnetic induction system.

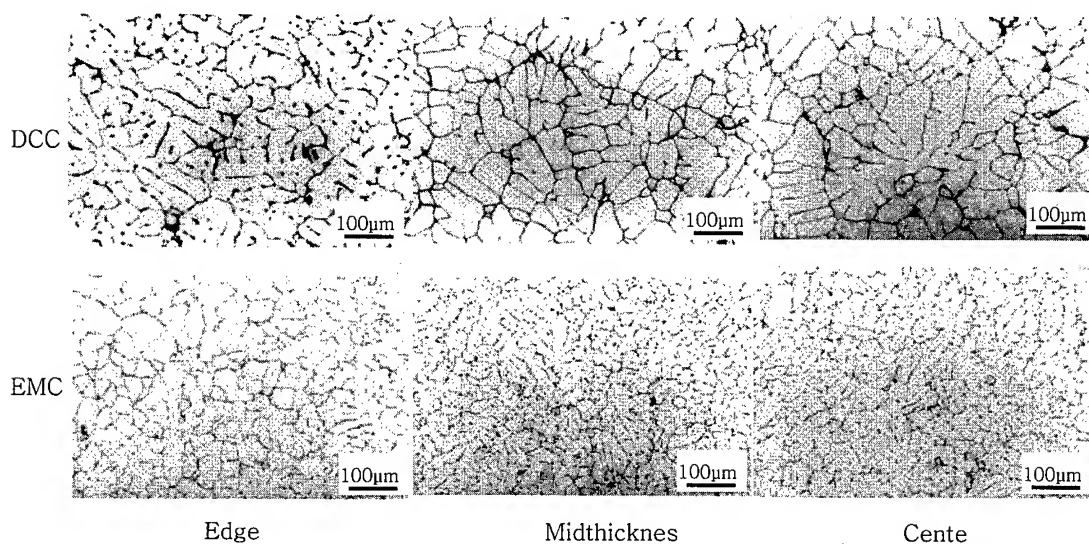


Fig.1 Microstructural comparison of 2024 DCC and EMC ingots (Ø180) at as-cast state

As shown in Fig.2, the induced current mainly distributes at the subsurface zone of the ingot, and the Joule heating will effect this zone strongly. This results in the decrease of the cooling rate in this zone and makes the grain grow up easily. On the other hand, there is the strong electromagnetic stirring in the liquid pool during the EMC solidification. Vives and Sakane investigated the melt flow in EMC system respectively[5,6], there are two main stable loops in the sump. The existence of these loops is explained by a viscous friction phenomenon caused by the radial and horizontal pouring jet running out of the float. It should be mentioned that the velocities are low in the proximity of the mushy zone and that the maximum velocities have been detected in the immediate vicinity of the dispenser outlet. The flow is obviously strongly turbulent between the two loops owing to the electromagnetic stirring. This intense forced convection promotes the evacuation superheat and breaks the dendrite arm, which leads to grain multiplication. The suspended nuclei localized in the near

vicinity of the solid interface are carried away and dispersed in a slightly under-cooled melt. The crystallization takes place simultaneous in most of the sump, around a number of floating nuclei, and this increasing nucleation results in the appearance of a fine grained equiaxed structure. Therefore, the grain size become more uniform from edge to center of EMC ingot.

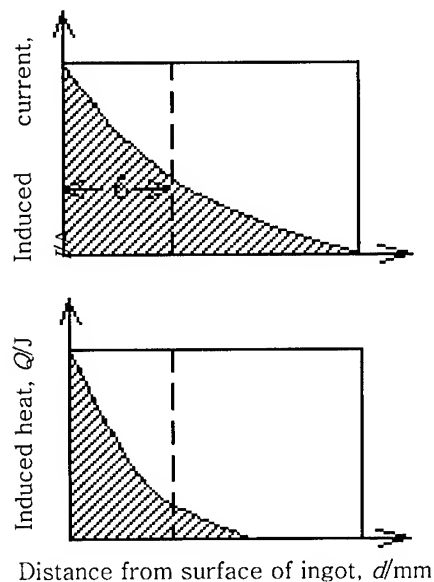


Fig.2 Distribution of Induced Current and Joule heating.

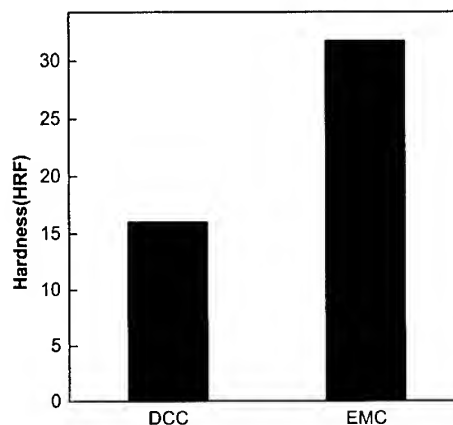


Fig. 3 Hardness comparison between EMC and DCC ingots at as-cast 2024 alloy

3.2. Mechanical characterization

As shown in Fig.4, the hardness of EMC specimens (HRF 31.72) is two times higher than DCC ones (HRF 16.02) at as-cast state, which is owing to the much finer grain structure of former. The age-hardening curves for the 2024 alloy are plotted in Fig.7. The increase in hardness with ageing time is due to precipitation of GP zones and other intermediate phases. The EMC specimens reached a peak value (HRF 48.52) at around 12h, while the DCC ones got the peak (HRF 44.4) after 36h artificial ageing. That means the EMC ingots have more obvious response to solution and ageing treatment, compared to DCC ones, because of difference in cooling rate.

Fig.5 shows the DSC curve, taken at a heating rate of $10^{\circ}\text{C min}^{-1}$. the exothermic peak centered at around 280°C are caused by G.P. zones or clusters formation. The exothermic peak at around 500°C should correspond to S' precipitation. The broad endothermic bump appeared around 230°C indicates some G.P. zones dissolved during the heating[7]. As shown in Fig.5(b), the lower heat flow indicates G.P. zones already existed in the as-aged sample.

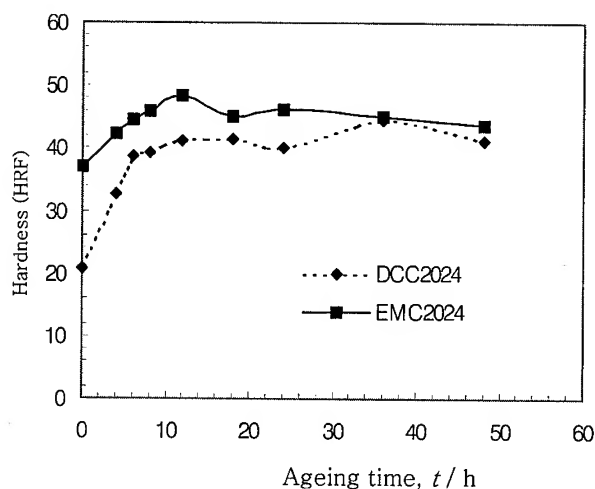


Fig. 4 Age-hardening curves of 2024 alloy.

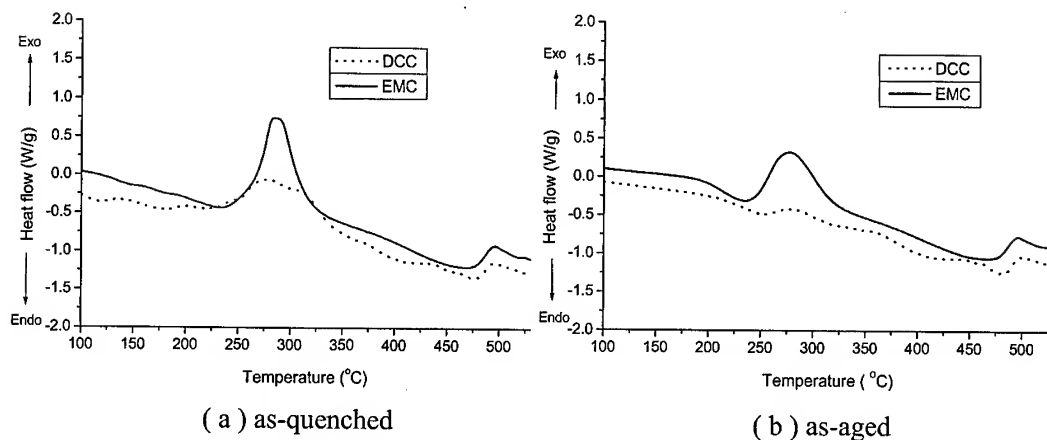


Fig.5 DSC thermograms of 2024 alloy (heating rate 10°C/min)

The principal features of the curves appear that the EMC specimens have higher exothermic precipitation peaks than DCC ones. Moreover, the peak broadness of the DCC specimens suggested that different kinds of zones/clusters existed, or that the sizes of the zones/clusters are far from being uniform. That is why the EMC specimens have more obvious precipitation-hardening effect. For as-quenched specimens, the reaction enthalpy of EMC specimen is 16.41J/g, and DCC is 14.24J/g at around 280°C. And the reaction enthalpy is 1.58J/g for EMC one and 0.14J/g for DCC one respectively at around 500°C. In as-aged condition, the reaction enthalpy of EMC specimen is 12.89J/g, and DCC is 1.58J/g at around 280°C. And the reaction enthalpy is 1.69J/g for EMC one and 1.62J/g for DCC one respectively at about 500°C. That means there are more precipitation formation in EMC specimens both in as-quenched and as-aged state

4. CONCLUSIONS

- 1) The optimal technique parameters for EMC are: power supply at a frequency of 2500Hz, inductor current from 4000 to 5000A, casting speed from 0.5 to 1.5 mm/s, height of liquid column from 30 to 40mm and the flow rate of cooling water from 2 to 3.5m³/h.
- 2) Electromagnetic stirring and Joule heating leads to the EMC ingot have much fine grain size and homogeneous structure, which makes it to be better mechanical properties not only in as-cast condition but also in as-aged one.
- 3) The hardness of EMC specimens is higher than that of DCC ones both in as-cast and heat-treated condition.
- 4) DSC investigation indicate that the precipitation is more easily formed in EMC specimens than in DCC ones

ACKNOWLEDGEMENTS

This work was supported by the grant of post-doctoral program, Chonbuk National University (2000), South Korea.

REFERENCES

1. M. Garnier: *Proceedings of International Symposium on Electromagnetic Processing of Materials* (ISIJ, Nagoya, Japan, 1994) pp.1-8.
2. D.C. Prasso, J.W. Evans and I.J. Wilson: *Metall. Trans.*, **26B** (1995) 1243-1251.
3. B.Q. Li: *JOM-e*, **50** (1998) 1-10.
4. N. Bryson: *Proceedings of the F. Weiberg International Symposium on Solidification Processing*, ed. by J.E. Lait and I.V. Samarasekera, (Pergamon Press, New York, 1990) pp69-73.
5. R. Ricou and C. Vives: *Metall. Trans.*, **16B** (1985) 377-384.
6. J. Sakane, B.Q. Li and J. W. Evans: *Metall. Trans.*, **19B** (1988) 397-408.
7. W.F.Miao, D.E. Laughlin, J. Mater. Sci. Letters **19** (2000) 201.

TENSILE DUCTILITY AND TEAR RESISTANCE OF A356 ALUMINUM ALLOYS FABRICATED BY CONVENTIONAL AND SEMI-LIQUID CASTING PROCESS

S. Kumai, T. Tanaka, S. W. Han, A. Sato and S. W. Kim*

Department of Materials Science and Engineering, Tokyo Institute of Technology
4259 Nagatsuta, Midori-ku, Yokohama 226-8502, Japan

*Faculty of Advanced Materials Engineering, Chonbuk National University
Chonju 561-756, Korea

ABSTRACT

Tensile tests and detailed microstructure observation were performed for A356 aluminum alloy castings with systematically controlled microstructure. The semi-liquid casting alloys showed improved ductility compared to the conventional cast alloys exhibiting ordinary dendrite structure. The microstructure of the semi-liquid alloy was characterized by colonies consisting of several globular dendrite cells. The EBSD analysis and slip line observation revealed that the misorientation among these colonies is large and so they can be recognized as "effective grains". Presence of refined effective grains reduces stress concentration at the grain boundaries and prevents the localized crack formation during tensile deformation. Conventional Kahn-type tear tests were also performed on the alloys. The energy required for both crack initiation and propagation was evaluated from the load-displacement curve. The effect of microstructure on the tear resistance was examined and correlation between tear resistance and tensile properties was discussed.

1. INTRODUCTION

Aluminum alloy castings have been popular as construction materials for automotive engines. With improvements in casting quality their usage spreads into nontraditional applications as a viable alternative of wrought or forged aluminum alloys[1]. Al-7mass%Si-0.4mass%Mg alloy (A356) is a representative casting material for such usage. Mechanical properties are affected by various microstructural features such as grain size, dendrite arm spacing (DAS), size and distribution of eutectic Si particles, intermetallic

particles originated from impurities, casting defects and non-metallic inclusions. Strengthening precipitates should also be taken into account since the alloy is age-hardenable. Complicated microstructure and difficulty in their systematic control have hindered clear understanding of relationship between mechanical properties and the solidified structure.

Recently application of HIP (Hot Iso-static Pressing) to the casting was found to be effective in reducing defects (mainly shrinkage cavities). A novel process called "Semi-liquid die-cast" has also been developed in recent years[2]. A molten metal is stirred at a solid-liquid coexistence temperature. The partially solidified melt is then injected to a mold cavity. The process provides a high quality casting with finer microstructure and lesser defects. In the present study, A356 alloy castings with systematically controlled microstructure were produced by means of several casting methods including the semi-liquid die-cast and HIP treatment. Tensile tests and detailed microstructure observation were performed to highlight the effect of individual microstructural factors on tensile properties.

Ductility is generally defined as the ability of a material to deform plastically rather than crack and fracture. On the other hand, this characteristic is called toughness in presence of micro- or macro-cracks or notches, which increase stresses locally. Macro- and micro-notches may significantly reduce fracture resistance (toughness) and are detrimental to crashworthiness, for example, of automobile components. Fracture toughness, K_{Ic} , is a measure of a material's toughness. However, the critical stress intensity for fracture, K_{Ic} , depends on specimen thickness. Experimental determination of K_{Ic} (the plane strain fracture toughness, K_{Ic} , a material property) is possible only when specimens exceed a certain thickness. In turn this thickness will depend on the material yield strength. Many aluminum alloys combine high toughness with low yield strength, so that K_{Ic} tests are neither practical nor useful. Therefore we need some other practical measures to evaluate toughness of such alloys even if it is not so sophisticated.

A procedure for determining the tear resistance of aluminum alloy sheet has been evolved from that suggested by Kahn. The Kahn-type tear test provides a measure of the energy required to initiate a crack in the specimen and the energy subsequently required for crack propagation to complete failure. It has been recognized that the tear test is more than just a relative rating, and in fact is a quantitative measurement of crack toughness[3]. In the present study, Kahn-type tear tests were performed on A356 alloys with different solidification structure.

2. EFFECTS OF SOLIDIFICATION STRUCTURE ON TENSILE DUCTILITY

Tensile tests were performed for A356 alloys with systematically controlled

microstructure. Their microstructures are shown in Fig.1. It should be mentioned that SS1 was produced by semi-liquid process, but the resultant microstructure was ordinary dendrite structure. The microstructure of the semi-liquid die-cast alloys (SS2 and SS3) was characterized by the colonies consisting of single or several globular dendrite cells (Fig.2). The EBSP analysis indicated that misorientation among these colonies were large enough to call them "effective grains" (Fig.3). Consequently grain refinement was achieved in the semi-liquid die-cast alloys. Quantitative data of microstructural parameters and tensile properties are summarized in Table 1 and 2, respectively.

Table 1 Quantitative data of microstructural parameters

	DAS (μm)	Dendrite cell size(μm)	Eutectic Si size (μm)	Aspect ratio of eutectic Si	Porosity area(%)	Rf	Grain size (μm)
Sm	60	—	8.7	2.15	0.23	—	1370
Pm	28	—	3.6	1.45	0.22	—	980
SS1	17	—	3.1	1.39	—	—	200
SS2	—	46	2.5	1.31	0.031	1.27	140
SS3	—	45	3.0	1.85	—	1.13	120

Table 2 Tensile properties of the five samples

	$\sigma_{0.2}$ (MPa)	UTS(MPa)	e (%)
Sm	182	217	2.3
Pm	286	322	6.3
SS1	298	339	7.4
SS2	285	342	11.3
SS3	266	322	15.7

The alloy with effective grain structure showed improved ductility compared to the sand and permanent mold cast alloys with ordinary dendrite structure. Specimen surface observation during the tensile test found that fine and homogeneous slip took place in each effective grain (Fig.4). Interrupted tensile tests and following structural observation for the mid-section of the gage part revealed crack initiation at triple grain junctions and void formation at the transgranular Si particles for the ordinary dendrite structure. While, crack initiation seldom takes place at triple grain junctions for the globular cell structure. Although crack initiation occurred at the Si particle clusters, crack initiation from such sites disturbs localized crack growth since the equivalent crack initiation sites are dispersed in the microstructure homogeneously. Refined effective grain structure is considered to be the origin of the improved ductility of the semi-liquid die-cast A356 alloys.

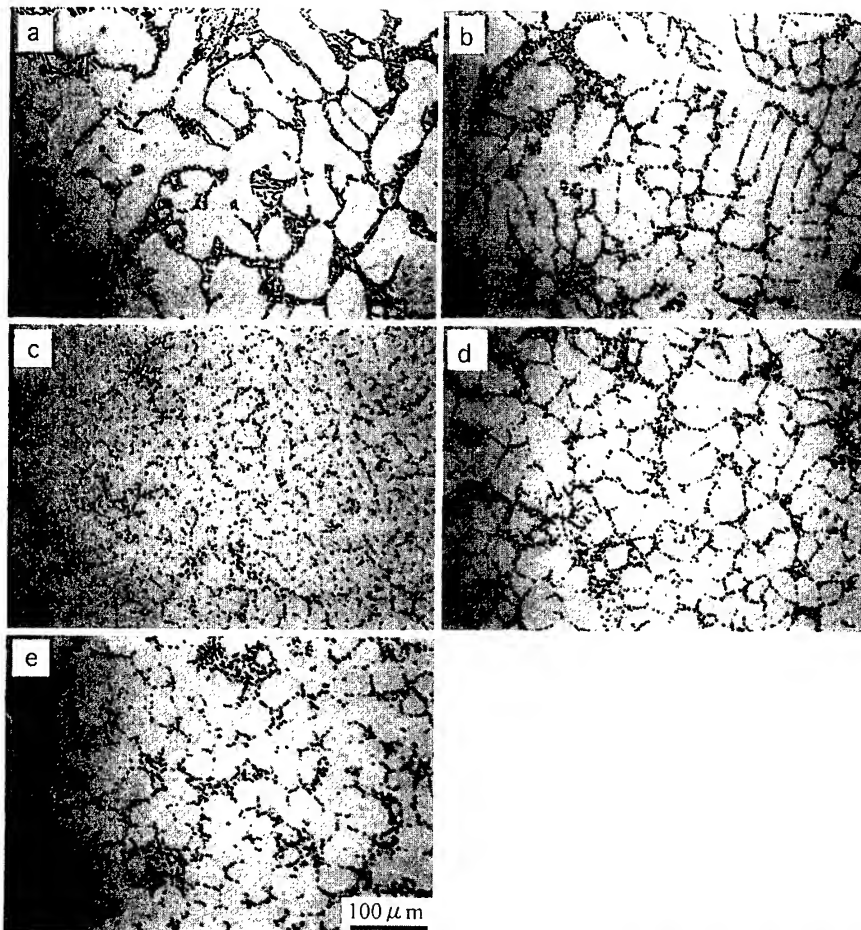


Fig.1 Optical micrographs of the five samples. (a)Sm, (b)Pm, (c)SS1, (d)SS2 and (e)SS3.

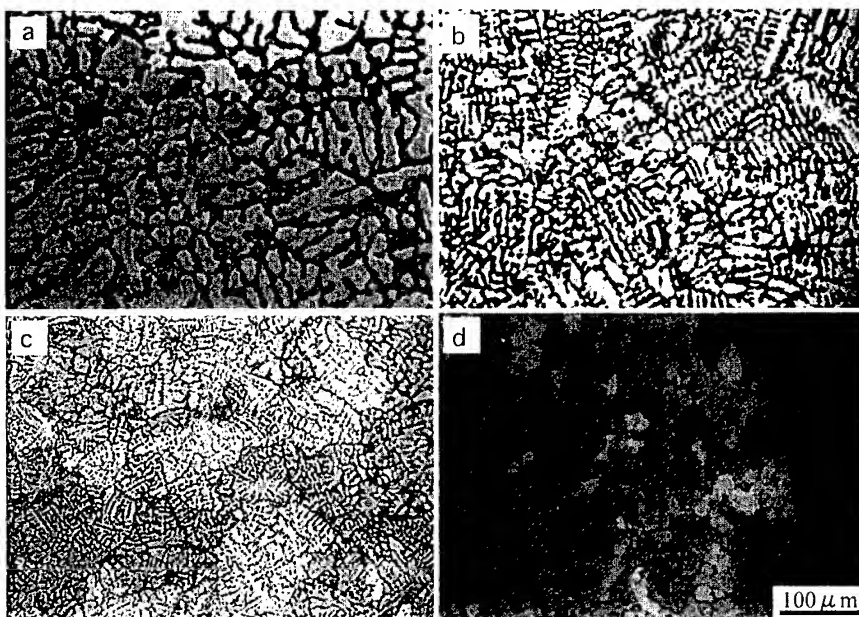


Fig. 2 Optical microscopy under polarized light for anodized specimens. (a)Sm, (b)Pm, (c)SS1 and (d)SS2.

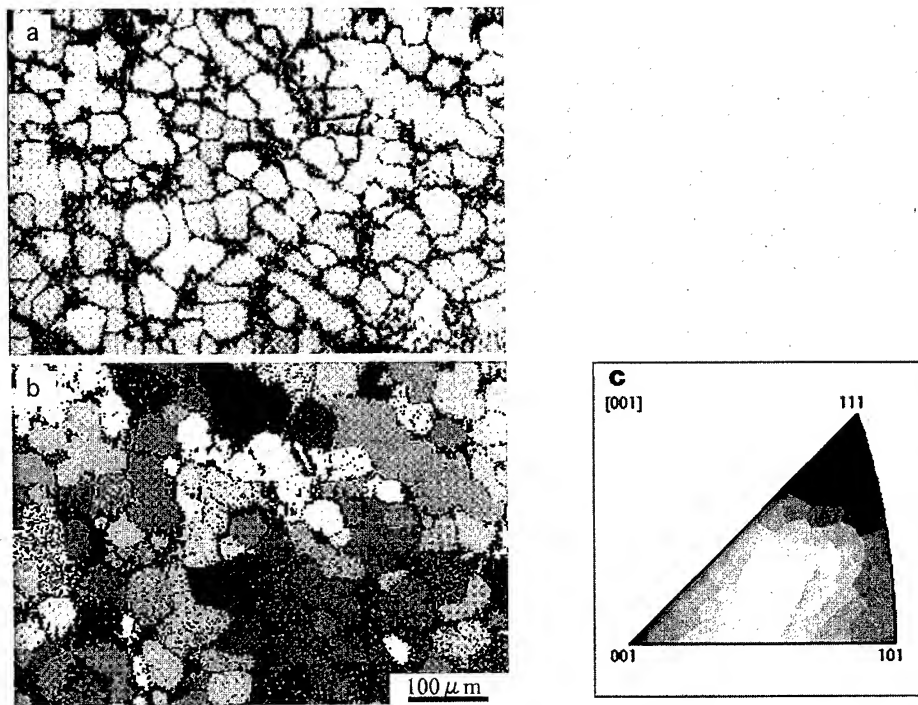


Fig. 3 The degree of misorientation among the effective grains.
 (a) SEM image of SS2, (b) inverse-pole figure of (a) and (c) reference for orientation.

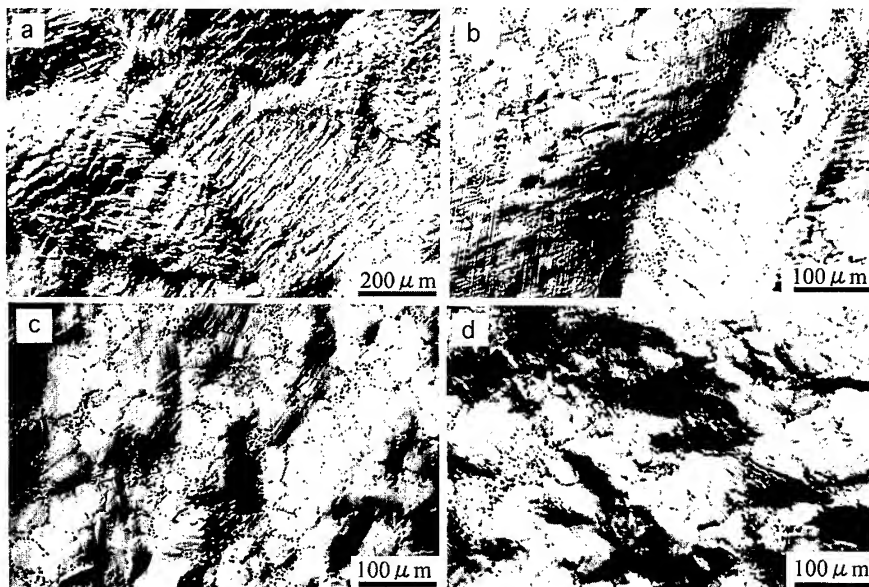


Fig. 4 Change in specimen surface topography with applied strain.

(a) Pm, $\epsilon = 0.03$, (b) Pm, $\epsilon = 0.06$, (c) SS2, $\epsilon = 0.03$, (d) SS2, $\epsilon = 0.06$

3. EFFECTS OF SOLIDIFICATION STRUCTURE ON TEAR RESISTANCE

The effect of solidification structure on tear toughness of A356 alloys was investigated by Kahn-type tear tests. Load-displacement curves of all the present materials exhibited pop-in indicating sudden crack extension and arrest. The pop-in was followed by stable crack growth and then went to fast fracture. A vertical line to the maximum load (P_{max}) divides the load-displacement curve into the areas associated with initiation and propagation of a crack, E_i and E_p . The E_p represents the energy necessary to propagate the crack across the specimen. A large area under the second part is associated with greater toughness or resistance to crack propagation. The unit propagation energy, UE_p is obtained by dividing the propagation energy by the net area of the specimen

For permanent mold cast materials, decrease in DAS improved tear toughness, i.e., increased UE_p . The influence of grain size was not clear in the specimens with ordinary dendrite structure. The casting defect was not a controlling factor of tear toughness in the present materials since the original quantity of casting defect was quite small both in size and volume fraction. Semi-liquid die-cast materials with fine effective grain structure showed larger tear toughness than that of the permanent mold castings. The obtained UE_p was about double that of the others. Deflected crack growth path was observed on the specimen side surface. Fracture surface contained more shear lips at the side surfaces than the other castings. It is considered that such a slant crack growth contributed to obtain larger crack propagation energy and the resultant improved tear toughness.

Acknowledgements

Thanks are due to Mr Ryoich Shibata, Hitachi Metals Ltd. for producing materials and Dr Osamu Umezawa, NRIM for the assistance of EBSP analysis. The authors are pleased to thank the Suzuki foundation and the Light Metal Education Foundation, Inc. for providing the financial support for a part of this work.

REFERENCES

1. T. L. Reinhart, ASM Handbook, Vol 19, (1996), pp. 813-822.
2. R. Shibata, T. Takeuchi, T. Souda and Y. Iizuka, Proc. of 4th Int. Conf. on Semi-Solid and Composite, England, (1996), pp. 296-300.
3. J. G. Kaufman and A. H. Knoll, Materials Research & Standards, April, (1964), pp.151-155.

A STUDY ON THE FABRICATION PROCESS, COMPRESSION STRENGTH AND SOUND ABSORPTION PROPERTIES OF AL FOAM IN POT FURNACE

Bo-Young Hur, Hyo-Joon Ahn, Dae-Chul Choi, Sang-Youl Kim,
NRL-ULSFoM LAB, ReCAPT, Gyeongsang National University
Chinju, 660-701 ,Korea

ABSTRACT

A new process for producing aluminum foam by a foaming technique has been developed. The apparent foam shape, foam height, density, pore size and their distributions in various section areas of the experimental samples have been investigated. They can be classified by different criteria such as pore size and pore shape. The foamed metal is not only light in weight, free of directionality and structurally strong but also excellent in sound absorbing and electromagnetic shielding properties, and is useful as constructional, structural or functional material.

A metal for producing the foamed are decomposing a foaming agent in a molten metal such that there is an initial and a subsequent expansion due to foaming agent. It has been found that the Al porous foaming with variation amount of 1~2wt% foam agent and at 2min holding time, which melting temperature has appeared homogeneous pore size at 700~710 °C.

The compression strength were 12-15 kg/mm² at 120ppi, and increased by higher pore density.

The acoustical performance of the panel made with the foamed aluminum is considerably improved; its absorption coefficient shows NRC 0.6-0.8.

1. INTRODUCTION

There has been extensive recent interest in the production [1-3] and mechanical and sound absorption properties of lightweight metallic foams. There is also interest in layered structures incorporation metallic foams[4-8]. Some information is now becoming available on the relationships between processing conditions and the size, shape, volume, fraction and spatial distribution of the cells within these foams. However, there is still some uncertainty about the role of these factors in determining the sound absorption properties. The apparent foam shape, foam height, density, pore size and their distributions in various section areas of the experimental have been investigated. The sample have been cast into metallic mold, using aluminum foam prepared from a precursor based on pure Al ingot mixed with increasing viscosity and foaming agent. The process provides for flexibility in design of foam structures via relatively easy control over the amount of hydrogen evolution and the drainage processes which occur during foam formation. This is fabricated by manipulating parameters such as the foaming agent. The acoustical performance of the panel made with the foamed aluminum is considerably improved. Two kind of noise barrier are developed. One is the single sided absorptive panel, the other is the double sided absorptive panel.

2. EXPERIMENT PROCEEDURE

Al alloy foams, all made by a hydride foaming process, the first material is produced by a melt route. Attention is concentrated both on the cell structures and the cell wall microstructures, which are significantly different in the three cases. The foamed aluminum is fabricated by adding foaming agent into thickened aluminum melt. The matrix materials is pure aluminum(Al, > 99.9 wt.%), the adjuster for the control of the viscosity of the aluminum melt is pure calcium(Ca, > 99.9 wt.%) and the foaming agent is hydride titanium powder(TiH_2 , 98wt.%, 300 mesh).

The foamed aluminum is fabricated in the following stages. Pure aluminum is melted in a crucible to 973K. Pure calcium is added to the melt and stirred at a constant speed to make the melt viscous. When the viscosity of the melt reaches a critical value [7], the foaming agent is added to the melt. At the same time, the mixture is stirred with a higher speed to homogeneously disperse the powder in the whole melt. Holding the mixture in the furnace to allow decomposition of the foaming agent. In this stage, bubbles in the melt are grown with the holding time until a cellular structure form. During the holding period, great changes in the structure of the melt take place. The structure of the finished product is determined by the evolution of the bubbles in the foaming melt in this period. Removing the mixture from the furnace and cooling the foamed melt to solidify cutting have been foamed ingot with saw cutter at half inch plate.

3. RESULTS AND DISCUSSION

Typical cell structures, as observed on cross-sections are shown in Fig. 1. It can be seen that all three materials contain heterogeneities and imperfections in their structure. Inhomogeneity was characterised by the width in the cell size and cell wall thickness distributions. Pores with fractured cell walls form large, non-equiaxed cells with their neighbors. Moreover, these elongated cells often contain buckles in the cell walls. The microstructural parameters of the samples such as porosity and pore size vary with the holding time. In order to obtain a parameter related to the structure of the foaming melt in the process, measuring the real time height of foaming melt is a feasible method, In a way, the degree of the growth of bubbles can be reflected by the real-time height, The higher the height of the foamed melt, the greater the number and size of bubbles.

Table. 1 Mechanical Properties, Density & Porosity of sound absorption panel

Pore size	Density(g/cm^3)	Porosity	Tensile-strength (Mpa)	Compress-strength (Mpa)
Small(<1.5mm ϕ)	0.8-0.9	75	150-160	240-250
Medium(1.5mm< sample<2.5mm ϕ)	0.3-0.5	96	130-140	160-180
Large(>2.5mm ϕ)	0.2-0.3	99	110-120	130-140

The specific energy absorbed by the foam up to densification was estimated from the area under the stress-strain curve. Average values are listed in Table 1, expressed per unit volume and per unit mass. The sound absorption sandwich panel was made by epoxy bond with foam Al plate, honeycomb and galvanised steel plate when it was varied with, honeycomb height (A: not gap, B: airgap 20mm, C: airgap 30mm, D: airgap 40mm). The honeycomb was purposed of eco-sounds. The D foam absorbs more energy than B and C foams, although its

densification strain is the lowest of the three. This is primarily because relatively high stresses are required for the D foam to density, which in turn is associated both with the porosity content being lower (than that of B) and the cell wall material being harder and more brittle than either of the other two foams. In practical terms, the energy-absorbing characteristics of the D foam may be less attractive than those of the other two, since behaviour in which progressive plastic deformation occurs at relatively low plateau stresses is more likely to ensure uniform and efficient collapse of the material over a also likely to be advantageous when tensile stresses are present

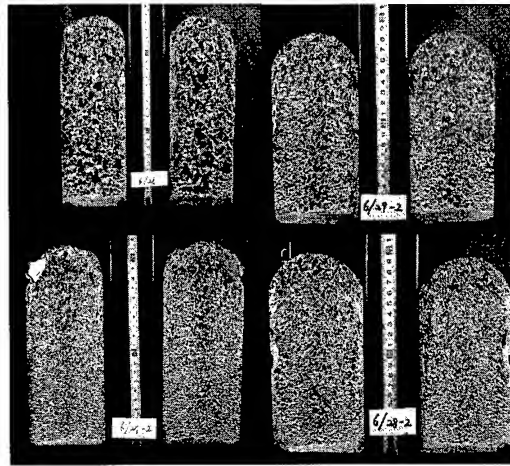


Fig. 1. Macrostructure varied by mixing temperature.
(a) 682 °C (b) 695 °C (c) 704 °C (d) 707 °C

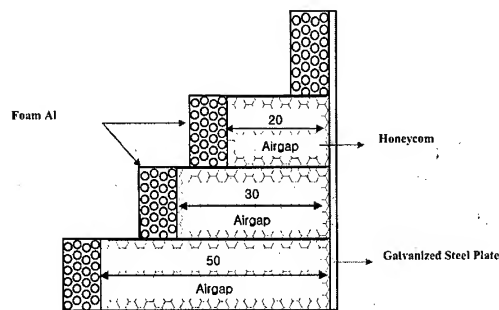


Fig. 2. Schematics diagram of airgap behind wall in composite sound Absorption panel

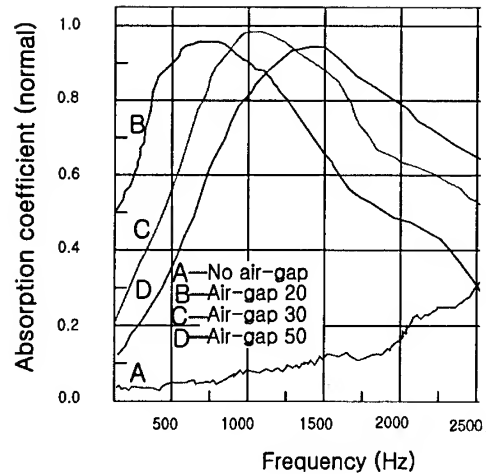


Fig. 3. The result of absorption coefficient, frequency and air-gap behind wall

4. CONCLUSION

1. The acoustic performance of the panel made with the foamed aluminum is considerably improved; its absorption coefficient shows NRC 0.6-0.8.
2. There is disclosed a panel for use in soundproofing walls, having a base organization in which an aluminum foam board containing numerous open pores and a noise-insulating metal board are attached to either side of an aluminum honeycomb structure via adhesive sheets.
3. The panel has the advantages of being semi-permanent in life span, highly resistant to corrosion and excellent in surface strength enough to be resistant to impact generating neither hazardous articles nor dust, and being reusable

5. REFERENCE

1. Gibson, L. J. and Ashby, M. F., Cellular Solids, 2nd ed. Cambridge University Press, 1997.
2. Markaki, A. E. and Clyne, T. W., in MetFoam '99, ed. j. Banhart, M. F. Ashby and N. Fleck. Verlag MIT publishing, Bremen, 1999, p. 359.
3. Gergely, V. and Clyne, T. W., adv. Eng. Mater., 2000, 2, 175.
4. Simone, A. E. and Gibson, L. J., Acta mater., 1998, 46, 3109
5. Bastawros, A. F. and Evans, A. G., in MetFoam '99, ed. J. Banhart, M. F. Ashby and N. Fleck. Verlag MIT Publishing, Bremen, 1999, p. 221.
6. Silva, M. J. and Gibson, L. J., Int. J. Mech. Sci., 1997, 39, 549.
7. B. Sosnick, U.S. Patent 2434775, 1948.
8. J. C. Elliott, U.S. patent 2751289, 1956.
9. H. Unno, S. Akiyama, Light Metal (in Japanese) 42, 1987, 37.

DEVELOPMENT OF LIGHT-WEIGHT Al SCROLL COMPRESSOR FOR CAR AIR CONDITIONER

Jongmin Park, Junkyu Ahn, Hobum Im, Changsik Ha
Ildong Choi*, Kyungmox Cho and Ikmin Park

Department of Metallurgical Engineering, Pusan National University
San 30 Jangjeon-dong, Keumjeong-ku, Pusan 609-735, Korea

* Department of Mechanical & Materials Engineering, Korea Maritime University
1 Dongsam-dong, Youngdo-ku, Pusan 606-791, Korea

ABSTRACT

The scroll compressor with high cooling efficiency and lower oscillating noise is applicable as a part of car air conditioner, household air conditioner and so on. In case high strength Al alloy has replaced cast iron for scroll compressor, rotation speed can be increased by weight reduction. To design Al alloy which has enough mechanical properties to replace cast iron, the effect of alloying elements such as Si(13~15%), Cu(4~5%), and Mg(0.5~1%) and cooling rates on the mechanical properties of squeeze cast Al alloy was studied. The influence of Sr and P modification treatment on Si morphology was also studied. An Al alloy over 400MPa of tensile strength and 2% of elongation was developed. Al scroll samples was fabricated by squeeze casting machine(UBE 800ton) with using 2 cavity mold. Flow-3D which is a three dimensional melt flow analysis program was used to find most proper mold design and optimum process conditions for squeeze casting before making samples. Relationship between secondary dendrite arm spacing(DAS) and cooling rate was simulated by Flow-3D and compared with experimental results.

1. INTRODUCTION

Recently, the scroll compressor with high cooling efficiency and lower oscillation noise is noticed as a part of car air conditioner, household air conditioner and so on. Considering various requirements for performance and low manufacturing cost of scroll compressor, the development and application of adequate material is important.[1] Cast iron was used for scroll compressor, but Al alloy is started to be considered as material of scroll compressor because of heavy weight of cast iron. In case of using Al alloy as material for scroll compressor, rotation speed of scroll can be increased by weight reduction. Al scroll compressor fabricated with various processes such as permanent mold casting, die casting, squeeze casting, hot forging, and powder metal forging is hard to obtain the stable quality, high strength and low fabrication cost in comparison with cast iron scroll compressor. To improve the quality and performance of Al alloy scroll compressor, more studies have to be done in fields of alloy design, modification, squeeze casting, solidification, machinability of Al alloy.[2~4] The improvement of these techniques are essential for weight reduction, noise reduction and enlargement of application of scroll compressor for air conditioner. In this study, to develop squeeze cast Al scroll compressor[5] which has similar quality with cast iron scroll compressor, several Al-Si alloys were designed, and the influence of modification treatment and cooling rate to microstructure was studied by Flow-3D solidification analysis.

2. EXPERIMENTAL

Al-(13,15wt%)Si-(4,5wt%)Cu-(0.5,1wt%)Mg alloys were made in high frequency melting furnace using 99.9% Al, 99.8% Mg, Al-25wt%Si, and Al-50wt%Cu.[6] These alloys were

degassed by Ar gas bubbling through alumina tube injected into melt maintaining at 800°C in electric resistance furnace and then squeeze cast. To study the effect of modification by alloying elements, 60ppm Sr (Al-10wt%Sr) and 60ppm P (Cu-15wt%P) was inoculated into molten Al-13Si alloy and Al-15Si alloy, respectively. Alloys were solution treated at 515°C for 8 hours in Ar gas atmosphere, water cooled and aged at 180°C for 8 hours. Also, to study the influence of cooling rate of unmodified alloy and Sr-modified alloy[7], K-type thermocouple was placed on cone type mold and obtained the cooling curve using X-Y recorder with chart speed of 1200mm/s. During squeeze casting, cooling curve was obtained by placing thermocouple at 20mm from bottom of mold(size 4×9×9cm). And microstructure was observed by optical microscope and SEM, and image analyzer was used to measure mean Si size and roundness. ASTM B557M tensile specimens were tested with crosshead speed of 1mm/min. To find optimum mold design and process conditions to get rid of solidification defects, the melt flow and solidification analysis was carried out before making test samples. The filling and solidification behavior of melt were analyzed by using Flow-3D that is 3-dimensional heat flow analysis program.[8-11] To find optimum gate speed, the filling behavior was tested with gate speed of 0.07m/sec and 0.15m/sec. After the filling test, secondary DAS was predicted by the secondary DAS mapping test of Flow-3D.[12] Molten alloy of 730°C was poured into preheated mold at 200°C and squeeze cast in UBE 800 ton squeeze casting machine. Two-cavity mold was used and pressure of 600kg/cm² and gate speed of 0.07m/sec were applied.

3. RESULTS AND DISCUSSION

Al-Si alloy and modified Al-Si alloy were cast in cone type mold to see the effect of cooling rate and inoculants on Si morphology, respectively. Fig. 1 shows microstructures of unmodified and Sr modified Al-13Si alloys at 15, 30, 45, 60 mm from bottom of metal mold. Point (a) is the point of the fastest cooling rate and point (d) is the point of the slowest cooling rate. It was observed that the size of primary Si and flake eutectic Si size become smaller as cooling rate increased, and the eutectic Si of Sr modified alloy is refined in compared to unmodified Al-13Si alloy. Also, same trend for cooling rate was observed in case of hypereutectic Al-15Si alloy, and primary Si size of P modified alloy is smaller than unmodified Al-15Si alloy. This result is shown in Fig. 2.

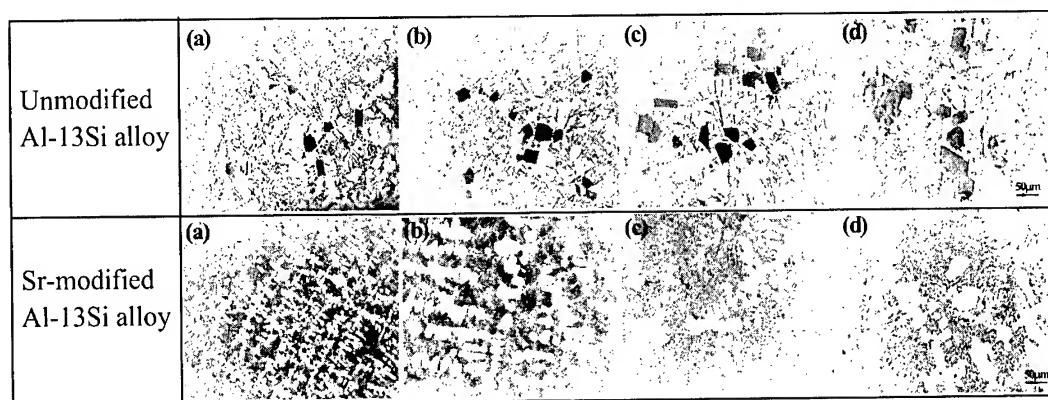


Fig. 1. Microstructural change with variation of cooling rate in unmodified and Sr-modified Al-13Si alloy : (a) 15mm, (b) 30mm, (c) 45mm, (d) 60mm from bottom of mold

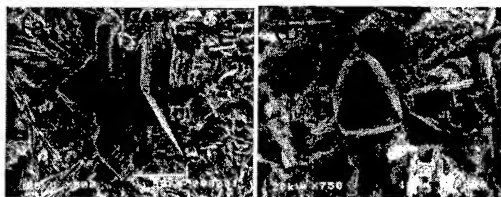


Fig. 2. SEM micrographs showing the morphology of primary Si in Al-15Si alloy (a) unmodified (b) P-modified



Fig. 4. SEM micrographs showing the morphology of eutectic Si in unmodified Al-13Si alloy (a) permanent mold cast, (b) squeeze cast

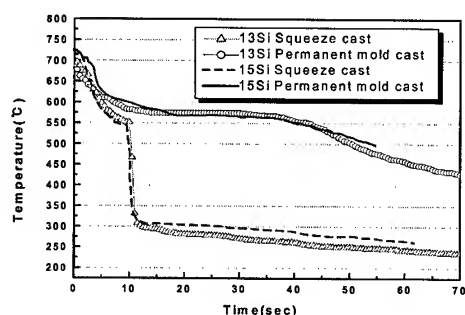


Fig. 3. Comparison of thermal analysis curves of permanent mold cast and squeeze cast in unmodified Al-13Si and Al-15Si alloys

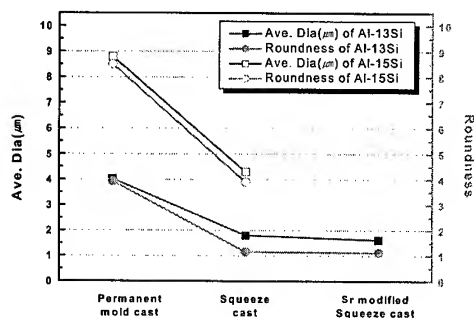


Fig. 5. Comparison of average diameter and roundness of eutectic Si in Al-13Si and Al-15Si alloys

Fig. 3 shows the result of thermal analysis during permanent mold casting and squeeze casting using the preheated mold at 200°C. Because of the rapid cooling rate of squeeze casting comparing with permanent mold casting, the transformation time of primary Si and eutectic Si in squeeze casting was decreased. It is considered that cooling rate in squeeze casting was increased due to the high heat transfer, that is, the increment of contact area between melt and mold because of high pressure squeeze casting. The change of morphology and the refinement of the eutectic Si by rapid cooling rate in squeeze casting were observed through SEM. Eutectic Si in permanent mold cast is large plate type in Fig. 4(a) and eutectic Si in squeeze cast is fine fibrous type in Fig. 4(b). The results of morphological analysis of unmodified permanent mold cast, unmodified and Sr modified squeeze cast are shown in Fig. 5. The size and roundness of eutectic Si in squeeze cast are smaller than that of permanent mold cast, and it was confirmed that the Si morphology is modified to rounded and fine fibrous type from coarse acicular or plate type. However, there was very small difference in morphology of eutectic Si between unmodified squeeze cast and Sr modified squeeze cast. Consequently, it is concluded that cooling rate is more efficient than modifier as a eutectic Si modification. The size and roundness of eutectic Si of squeeze cast Al-15Si alloys is smaller than those of permanent mold cast Al-15Si alloys but larger than those of Al-13Si alloys. Fig. 6 shows the results of tensile test of the squeeze cast Al alloys alloyed with Cu(4, 5 wt%) and Mg(0.5, 1 wt%), elements of age hardening to make material which has elongation and strength similar to cast iron. Tensile strength of as-cast specimens was almost similar, regardless of amount of Cu and Mg. In case of T6 treated specimens, there was little difference in tensile strength according to the amount of Cu, but Mg affected the tensile strength and alloy with 1wt% Mg was shown highest tensile strength. Alloy with 4wt%Cu-1wt%Mg has highest elongation in Fig. 6(b). Therefore, alloys with 4wt%Cu-1wt%Mg were chosen for the test to evaluate the effect of modifier. Fig. 7 shows the tensile test results of unmodified permanent mold cast, unmodified squeeze cast and modified squeeze cast Al-

(13,15)Si-4Cu-1Mg alloys. Tensile strength and elongation of squeeze cast alloys were increased and those properties were increased more by T6 treatment. However, The effect of modifier on the mechanical properties was not shown. This result was expected from microstructural observations. Tensile strength of Al-15Si alloys is lower than Al-13Si alloys because of big primary Si particles over 20 μ m in spite of smaller primary Si size by inoculating P. Elongation of Al-13Si and Al-15Si alloys after T6 treatment was 2.3%, 1.5% respectively. Therefore, Al-13Si-4Cu-1Mg is satisfactory for the Al scroll material because the material for scroll needs to have elongation of over 2%.

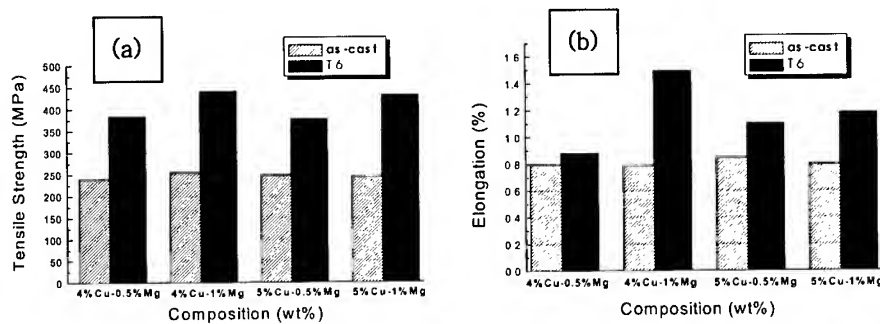


Fig. 6. Comparison of tensile strength and elongation with variation of Cu and Mg contents in Al-13Si alloy

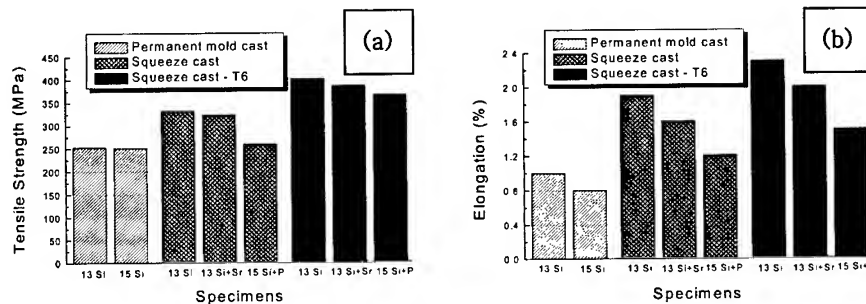


Fig. 7. Comparison of tensile strength and elongation with casting process and modification in Al-(13, 15)Si-4Cu-1Mg alloy

Before making Al scroll sample, Flow-3D solidification analysis was carried out to optimize mold design and cast scheme. Fig. 8 shows filling simulation results with two gate speed. It was predicted that air trap would happen with gate speed of 0.15m/sec, and no air trap would happen with gate speed of 0.07m/sec, and this simulation result coincided experimental result. Secondary DAS turned out to have direct relationship with solidification parameter experimentally and theoretically. So secondary DAS can be verify results of theoretical analysis, and predict mechanical properties of cast products. Fig. 9 shows the predicted results of secondary DAS by simulation. From the results of this analysis, it can be found that secondary DAS is decreased according to approaching upper wrap of scroll, and it is increased according to approaching flange above the bottom than other point in wrap. From simulation of the cooling curve in the 6 point on the wrap section of scroll, the sudden temperature drop at early cooling stage in each point was predicted. It was found that cooling rate of upper wrap is the fastest and flange part is the slowest. Fig. 10 shows the theoretical secondary DAS values predicted from cooling curves and experimental results obtained from image analysis. It is well-known that secondary DAS is related to cooling rate of melt. The relationship between secondary DAS (d) and cooling rate (C) is $d=K \cdot C^{-n}$. But K and n is changed a little by alloy composition and degree of overheating. The equations showing the

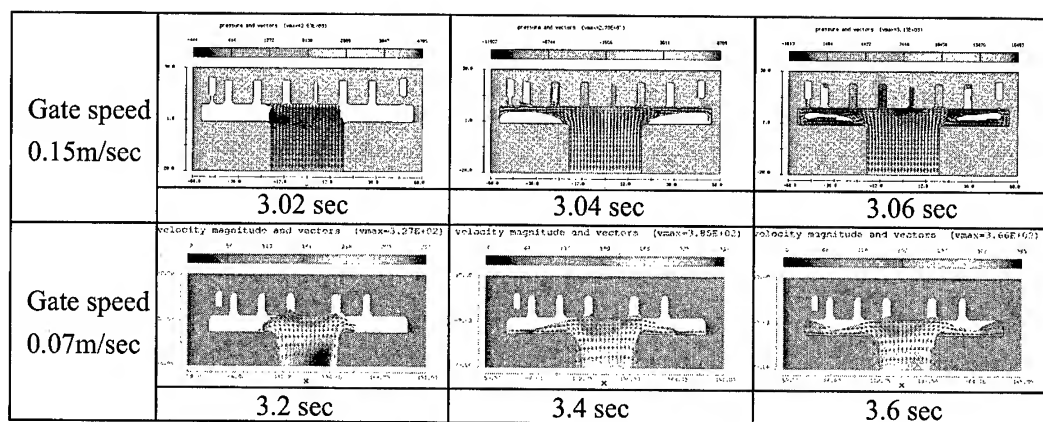


Fig. 8. Filling simulation results with variation of filling time (gate speed : 0.15m/sec and 0.07m/sec)

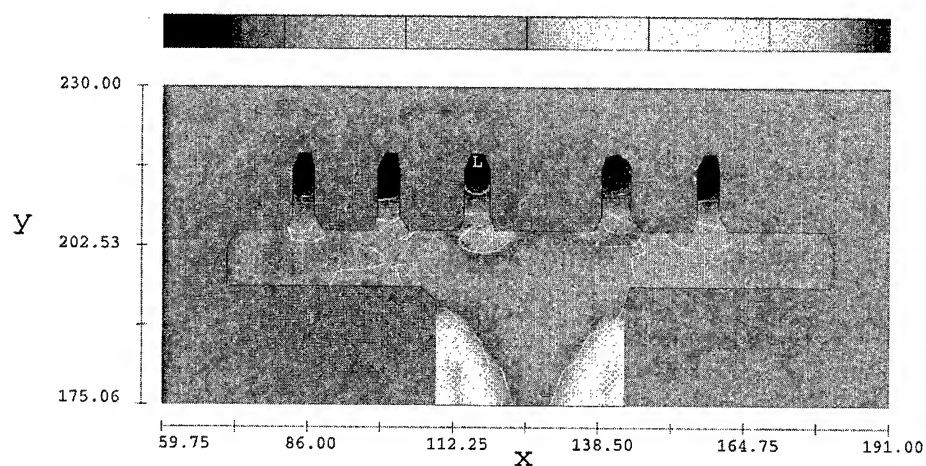


Fig. 9. Prediction of secondary dendrite arm spacing on scroll section

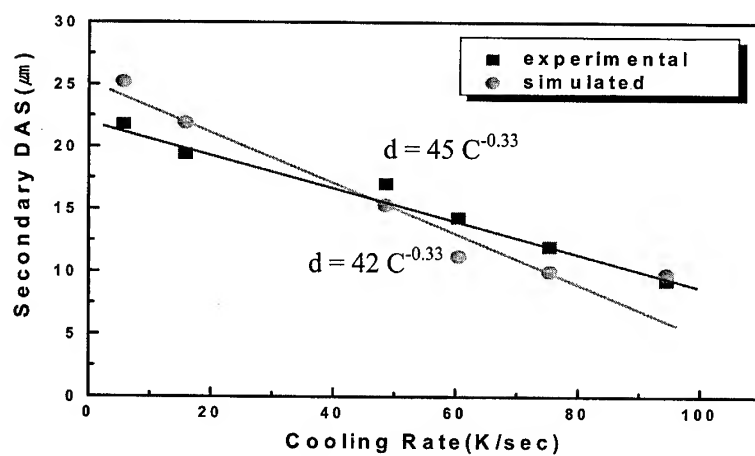


Fig. 10. Secondary dendrite arm spacing with variation of cooling rate

relationship between cooling rate and secondary DAS from flow-3D analysis and experimental analysis were $d=45 \cdot C^{-0.33}$ and $d=42 \cdot C^{-0.33}$, respectively. Consequently, secondary DAS is decreased as cooling rate is increased. And it is confirmed from the above equations that the result of flow-3D analysis and experimental analysis is nearly same. Comparing the results with wrap section of scroll, upper part of wrap section with fastest cooling rate has smallest secondary DAS and the part approaching flange section with slowest cooling rate has the largest secondary DAS.

The hardness of each point in wrap is decreased as secondary DAS is increased. Hardness in wrap section with secondary DAS of $9.3 \sim 19.4 \mu\text{m}$ is $106 \sim 135\text{Hv}$ and hardness in flange section with secondary DAS of $21.8 \mu\text{m}$ is suddenly dropped to 80Hv . As cooling rate is increased, secondary DAS and size of eutectic Si are decreased, and the morphology of eutectic Si turn into modified fibrous and hardness is increased consequently. And as cooling rate is decreased, secondary DAS and size of eutectic Si are increased, and the morphology of eutectic Si remain unmodified flake and hardness is decreased. Therefore, mechanical properties of each point of product can be predicted by the mapping of secondary DAS.

4. CONCLUSIONS

To develop Al-Si alloy for scroll compressor which has similar mechanical properties with cast iron, Al alloys were designed and the effect of cooling rate and modification by Sr and P was studied. Mold design and casting conditions were optimized by solidification analysis. From the analysis, the equation which represent the relationship between secondary dendrite arm spacing and cooling rate were made, and the microstructure and mechanical properties of the product were compared with simulation results.

1. Squeeze cast Al-(13-15)Si-4Cu-1Mg alloy which has tensile strength of over 400MPa and elongation of 2% was developed by changing alloy elements, cooling rate and modification treatment.
2. By the rapid cooling and modification, fine fibrous Si under $1 \mu\text{m}$ could be obtained. And cooling rate change was more efficient than modifier as a Si modification.
3. From the comparison of Flow-3D analysis with experimental results, it was found that secondary dendrite arm spacing and mechanical properties of scroll could be predicted from theoretical analysis.

REFERENCE

1. W.J.Park, I.M.Park, N.J.Kim, J.Korea Society of Automotive Engineers, Vol.16 (1994/04), pp.23-31
2. J.K.Aha, H.P.Yoon, H.S.Park, I.M.Park, Meeting abstract of Korea Institute of Metals (1998/04), pp.153
3. I.M.Park, Meeting abstract of Korea Foundrymen's Society, (1997/07), pp.89-106
4. M.L.V. Gayler, J. Inst. of Metals, Vol. 38(1927), pp.157
5. I.M.Park, B.S.Kim, the newsletter of Korea Institute of Metals (1996/06), pp.112-125
6. F.H.Samuel, A.M.Samuel, H.Liu, Journal of Materials Science, Vol. 30 (1995), pp.2531-2540
7. L.Wang, S.Shivkumar, J.Materials Science, Vol. 30 (1995), pp.1584-1594
8. E. Niyama, Imono, Journal of Japanese Foundry Engr. Society, Vol. 49 (1977), pp. 26-31
9. H.D.Brody and R.A.Stoeckl, J. Metals, Vol. 32 (1980), pp. 20-27
10. J. E. Welch, F.H.Harlow, P.J.Shannon and B.T.Dally, Tech. Report LA-3425, Los Alamos Scientific Laboratory, (1965)
11. A.A.Amsden and F.H.Harlow, Tech, Report LA-4370, Los Alamos Scientific Laboratory, (1980)
12. N.Fat-Halla, J. Materials Science, Vol. 25(1990), pp.3396

HYDROGEN-ASSISTED DEFORMATION AND FRACTURE BEHAVIOR OF Al 8090

Woo Kil Jang, Sang Shik Kim** and Kwang Seon Shin*

School of Materials Science and Engineering

*Center for Advanced Aerospace Materials

Seoul National University, Seoul 151-742, Korea

**Division of Materials Science and Engineering

Advanced Materials Research Center

Gyeongsang National University, Chinju 660-701, Korea.

ABSTRACT

In the present study, the hydrogen embrittlement (HE) and the hydrogen-assisted fracture (HAF) behavior of electrochemically hydrogen-charged Al 8090 with different specimen orientations and aging practices were examined using smooth bar and single-edge notch (SEN) specimens. It was found that the cathodic hydrogen charging substantially reduced the tensile ductility and the resistance to fracture of Al 8090. The susceptibility to HE and HAF of Al 8090 was strongly dependent on the specimen orientation and aging practice. Hydrogen attack was the most significant along the grain boundaries and, consequently, T-S oriented SEN and T-oriented smooth bar specimens showed the highest susceptibility among the orientations studied. The susceptibility to HE and HAF decreased from UA temper to OA temper. The formation and development of precipitate free zone along the grain boundaries, rather than the change in slip planarity, with prolonged aging appeared to be mainly responsible for the reduced susceptibility to HE and HAF.

1. INTRODUCTION

Numerous investigations have been conducted to identify the effect of external hydrogen-intake on the deformation and fracture behavior of precipitation hardened, high-strength Al and Al-Li alloys [1-3]. The resistance to hydrogen-assisted deformation and/or fracture have

been reported in a number of literatures to vary depending on a number of factors, including chemical composition, heat treatment condition, prior cold working, test temperature, specimen orientation, strain rate, the presence of notch, etc. However, the complete understanding of the effects of various metallurgical factors on the hydrogen-assisted deformation and fracture behavior is yet to come. Li-containing Al alloys are mainly strengthened by δ' (Al_3Li) precipitates and have a high slip planarity as a result of dislocation shearing of δ' particles. Such a high slip planarity tends to increase the susceptibility to hydrogen embrittlement (HE) and hydrogen-assisted fracture (HAF), by increasing the chance for hydrogen to be transported to the deleterious trapping sites. Recently, Smith and Scully have conducted rigorous hydrogen-charging experiments to obtain the fundamental understanding of the effects of hydrogen on the mechanical properties of some Al-Li and Al-Cu alloys. They reported that the peak-aged alloy showed higher propensity for HAF than the under-aged counterpart [4].

The main objective of the present study was, therefore, to characterize the fracture behavior of electrochemically hydrogen-charged Al 8090 with different specimen orientations and aging practices using smooth bar and single-edge notch specimens.

2. EXPERIMENTAL PROCEDURE

A 70mm thick Al 8090-T351 (Al-2.4Li-1.22Cu-0.86-Mg-0.12Zr) plate was purchased from ALCOA for the present study. Smooth bar tensile specimens with a gauge length of 24mm and single-edge notch (SEN) specimens with a thickness of 2.5 mm and an a/W of 0.4 with various orientations were prepared. The specimens were aged at 190°C for 4 (underaging, UA), 16 (peakaging, PA), 32 (overaging, OA), 64 and 96 hours. Some specimens were resolutionized at 530°C for 30 minutes and then peak-aged. The details of the microstructure of Al 8090 can be found in reference 6. The optical micrographs showed typical pancake shape grains and the grain structure on this scale was not notably affected with further aging treatment. Both tensile and SEN specimens were cathodically hydrogen-charged in a 0.1N HCl solution with an applied voltage of -2000mV vs. SCE for 12 to 48 hours. After hydrogen charging, the specimens were immediately tested to minimize the hydrogen loss. Tensile tests were performed on a universal materials testing machine at a nominal strain rate of 10^{-4} /sec. The crack growth resistance curves (K-R curves) were determined for fatigue precracked SEN specimens, utilizing a direct current potential drop (DCPD) method for in-situ crack measurement, at a displacement rate of 10^{-4} mm/sec. The fracture surfaces of the tested specimens were examined by using scanning electron microscopy (SEM).

Transmission electron microscopy (TEM) specimens were prepared by using a jet thinning

method in a 30% nitric acid-70% methanol solution at -20°C [5,6].

3. EXPERIMENTAL RESULTS

3.1 Effect of Cathodic Hydrogen Charging on Tensile Properties of Al 8090

With hydrogen charging, the change in yield and ultimate tensile strength of Al 8090 was not significant. However, the tensile elongation of Al 8090 decreased substantially with hydrogen charging. The magnitude of the pct decrease in tensile elongation of Al 8090 with hydrogen charging was strongly dependent on the specimen orientation and aging condition. Considering the pct change in tensile elongation of Al 8090-PA, for example, the HE sensitivity was the highest along the T-direction, followed by L- and S-direction. The effect of aging on the HE sensitivity was thoroughly examined with the T-oriented specimen, which showed the highest susceptibility to HE. It is clearly demonstrated that UA temper showed the highest HE susceptibility, while it decreased substantially with increasing aging time. The resolutionized and PA tempered Al 8090 showed an approximately 25% decrease in tensile elongation, which was better than the just PA tempered counterpart. The details of tensile test results could be found in reference 1. Figure 1 shows the low and high magnification SEM fractographs of the tensile tested T-oriented Al 8090-PA. A typical intergranular fracture mode was observed in both specimens. At high magnifications, the intergranular facets were found to be covered with very fine dimples, as shown in Figs. 1(b) and (d).

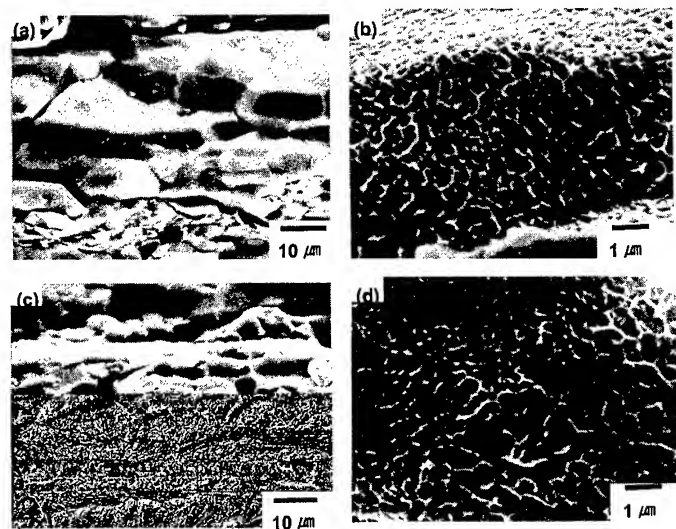


Figure 1. The low and high magnification SEM fractographs of the T-oriented specimens; (a)(b) uncharged and (c)(d) hydrogen-charged for 12 hours.

The morphology of dimples, however, changed with hydrogen charging. The average dimple diameters of the uncharged and the hydrogen-charged specimens were 0.26 and 0.4 μm , respectively, as shown in Fig. 1. It showed that the dimples found in the hydrogen-charged specimens to be larger and relatively shallower than those in the uncharged specimens, suggesting that the microvoid coalescence process was promoted by hydrogen charging.

3. 2 Effect of Hydrogen Charging on Fracture Behavior of Al 8090

The hydrogen charging significantly affects the fracture behavior of Al 8090, particularly the initial fracture toughness, K_{th} , which is defined as the corresponding K value for the initial rising point of the potential with propagating crack. The K_{th} value for the uncharged Al 8090-PA was, for example, 19.8 $\text{MPa}\sqrt{\text{m}}$, while it decreased to 16.4, 15.5 and 14.5 $\text{MPa}\sqrt{\text{m}}$ with hydrogen charging for 12, 24 and 48 hours, respectively.

As mentioned previously, the hydrogen charging affects the K_{th} value of Al 8090 significantly. The HAF behavior of Al 8090 was greatly affected by the specimen orientation and aging condition. The T-S orientation, for example, showed an almost two-fold increase in the pct decrease in K_{th} , compared to the other orientations. The effect of aging condition on HAF susceptibility of Al 8090 was examined using the T-S specimens, which showed the highest susceptibility to HAF in the present study. Figure 2 represents the change in the K_{th} values of the uncharged and 12hr hydrogen-charged Al 8090 as a function of aging time.

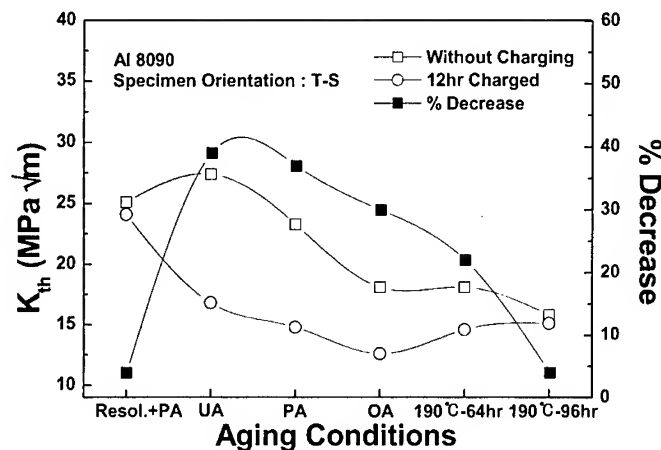


Figure 2. The change in the K_{th} values and the pct decrease of the T-S oriented Al 8090 with different aging practices.

The K_{th} values of the uncharged Al 8090 decreased from 23.3 MPa \sqrt{m} to 18.1 MPa \sqrt{m} with increasing aging time from 16 to 64 hours. The extreme case of 96 hour aging further reduced the K_{th} value to 15.8 MPa \sqrt{m} . Unlike the trend observed in the uncharged specimens, the K_{th} values of the hydrogen-charged specimen for 12hrs did not show a notable change with different aging time. In terms of the pct decrease in K_{th} value, however, the resistance to HAF of Al 8090 tended to decrease substantially with increasing aging time. In its PA temper, the pct decrease in K_{th} value was 37%. The pct decrease in K_{th} value decreased to 30%, 22% and 4% with aging for 32, 64 and 96 hours, respectively. The resolutionized and PA tempered Al 8090 showed only a 4% decrease in K_{th} with hydrogen charging.

4. DISCUSSION

The present study clearly demonstrates that the resistance to fracture, as well as the tensile ductility, of Al 8090 can be greatly reduced with an electrochemical hydrogen charging. The K_{th} values and the tensile elongation of Al 8090 decreased gradually with increasing hydrogen charging time. Many other previous papers [1,2] proposed that the maximum depth of embrittlement is proportional to the (charging time)^{1/2}, when metal is exposed to hydrogen-generating environments. Based on their hypothesis, the K_{th} data for Al 8090-PA were replotted as a function of (charging time)^{1/2} as shown in Figure 3. From the figure, it is seen that the K_{th} value decrease linearly to the (charging time)^{1/2}. As shown in Fig. 1 the hydrogen charging caused the dimples on the intergranular facets to be slightly larger and shallower. It is, therefore, hypothesized that the hydrogen, as redistributed to the fracture process zone by dislocation-assisted transport from the severely embrittled area, probably on the surface, tends to reduce the plastic flow required for microvoid coalescence process at the interface between the precipitates and the matrix along the grain boundaries of Al 8090.

Since the hydrogen charging affects the deformation and fracture behavior of Al 8090 predominantly in the grain boundary areas, the pct decrease in K_{th} values, as well as the tensile elongation, of Al 8090 with hydrogen charging was naturally dependent on the loading and crack propagation directions. Smith and Scully [4] have proposed that hydrogen trapping at high angle grain boundaries correlates with the preferred fracture path, but only when favorably oriented. Considering the pancake shape of the grain structures of Al 8090 and Smith's proposition, the T-S oriented specimens have the greatest chance for crack to follow the grain boundaries and consequently show the lowest resistance to HAF. The present study clearly demonstrates that the susceptibility to both HE and HAF decreases with aging time. The pct decrease in the K_{th} value of Al 8090 with hydrogen charging was the highest in the UA temper, while it gradually decreased with increasing aging time. The

improved resistance to HAF of precipitation hardened Al alloys is often explained by the reduced slip planarity with aging. It has been well established that δ' precipitates promote the slip planarity in Al-Li alloys.

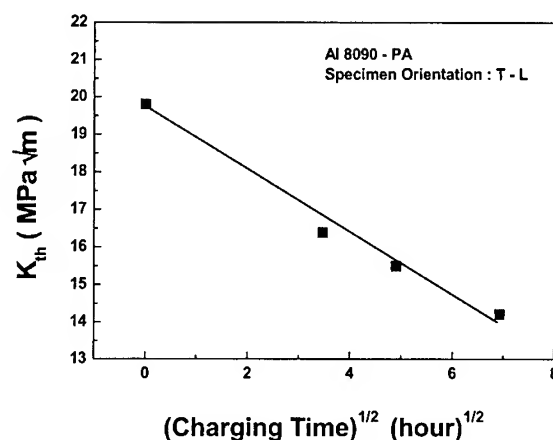


Figure 3. The change in the K_{th} values of the T-L Al 8090-PA as a function of (charging time)^{1/2}.

The δ' microstructured Al 8090 (resolutionized and aged), however, showed a better resistance to HAF and HE than the $\delta'+S'$ microstructured counterparts for the same temper. In the present study, the microstructure of Al 8090 was not significantly affected with prolonged aging at 190°C for 4 to 96 hours, other than the widening of PFZ along the grain boundaries. Moreover, the degree of slip planarity was not significantly affected with prolonged aging. It is, therefore, speculated that the slip planarity plays a secondary role in determining the HE and HAF behavior of Al 8090. Figure 4 clearly shows that the width of PFZ in Al 8090 increases substantially with increasing aging time from approximately 200 nm to 600 nm. The present study suggests that the main mechanism for HE and HAF of Al 8090 is the reduced plasticity required for the microvoid coalescence along the grain boundaries. With prolonged aging, the number of precipitates on the grain boundaries, which acts as the sources of microvoid, would be reduced due to the formation of PFZ. Conclusively, the formation and development of PFZ along the grain boundaries in Al 8090 is detrimental to the tensile and fracture properties. It is, however, beneficial for lessening the effect of hydrogen on the mechanical properties.

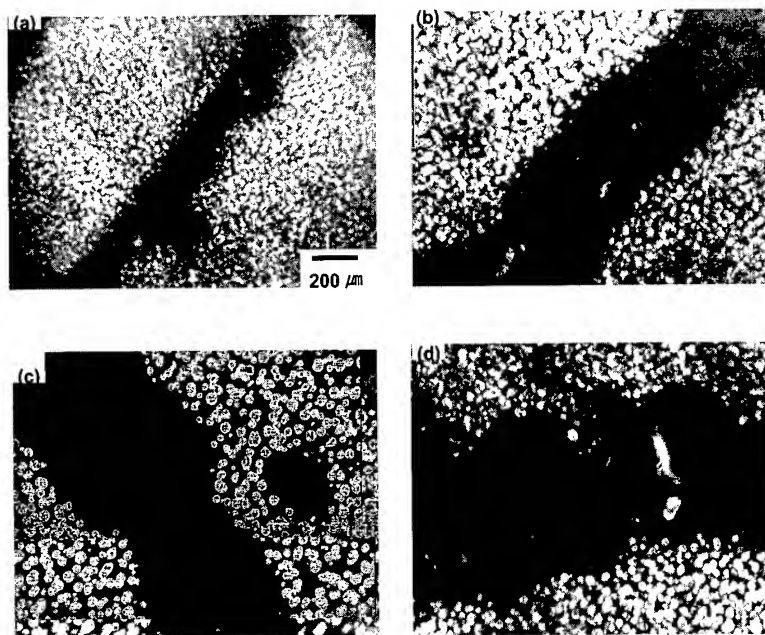


Figure 4. Dark field TEM micrographs of the Al 8090 aged at 190°C for (a) 16, (b) 32, (c) 64 and (d) 96 hours, showing well-developed precipitate free zones along the grain boundaries.

5. CONCLUSIONS.

1. The cathodic hydrogen charging substantially reduced the initial fracture toughness values, K_{th} , and tensile ductility of Al 8090, where the reduction was linearly proportional to $(\text{charging time})^{1/2}$.
2. The dominant fracture mode in Al 8090 was intergranular dimpled rupture. It was noted that the dimples on the intergranular facets tended to be larger and shallower with hydrogen charging.
3. The HAF sensitivity of Al 8090 were strongly dependent on the specimen orientation. The T-S oriented SEN specimens had the better chance for crack to follow the grain boundaries, where the hydrogen attack was the most significant, and showed the highest susceptibility.
4. The δ' microstructured Al 8090 (resolutionized and aged) showed a better resistance to HAF and HE than the $\delta'+S'$ microstructured counterparts, suggesting that the slip planarity plays a secondary role in determining the HE and HAF behavior of Al 8090.

-
5. The susceptibilities to HE and HAF of Al 8090 gradually decreased from UA temper to OA temper. The formation and development of precipitate free zone along the grain boundaries with prolonged aging is believed to be responsible for the reduced susceptibility to HE and HAF of Al 8090.

REFERENCES

1. N. J. H. Holroyd and D. Hardie: Corrosion Science, vol. 21, 1981, pp. 129-44.
2. S. S. Kim, E. W. Lee and K. S. Shin: Scripta metal., vol. 22, 1988, pp. 1831
3. W. K. Jang, S. S. Kim and K. S. Shin: Scripta mater., vol. 40, 1999, pp. 503-8.
4. S. W. Smith and J. R. Scully: *Hydrogen Effects in Materials*, A.W. Thompson and N.R. Moody eds., TMS, Warrendale, 1996, pp. 131-41.
5. T. H. Sanders, Jr. and E. A. Starke, Jr.: Met. Trans., vol. 7A, 1976, pp. 1407-17.
6. J. H. Kulwicki and T. H. Sanders, Jr.: *Aluminum-Lithium II*, T. H. Sanders Jr. and E. A. Starke, Jr., eds., AIME, Warrendale, 1983, pp. 31-51.

Fracture Behavior of AA6061 Aluminum Alloy under Resonant Vibration

J. H. Horng¹, J. L. Hu², T. S. Lui^{1*}, L. H. Chen¹

¹ Department of Materials Science and Engineering, National Cheng Kung University, Tainan 701, Taiwan

² Department of Industrial Safety and Hygiene, Chung Hwa College of Medical Technology, Tainan 701, Taiwan

Abstract

Fracture behavior of AA6061 aluminum alloy was investigated by varying aging conditions under resonant vibration. Experimental results showed that strength of alloy can be improved by aging, but it also influences the deflection amplitude of specimens. The peak-aged specimen, which possesses the highest strength, shows the largest deflection amplitude in six different aging treatments. Additionally, for naturally aged and underaged specimens, the crack propagation indicated a slip band cracking feature. Whereas, the slip band cracking was not observed in the peak-aged and overaged specimens. The propagation of the cracks were mainly transgranular. For six different aging treatments, the ratio of the yield strength (or matrix microhardness) to the largest deflection amplitude of specimens indicated the crack propagation resistance. The results of crack propagation resistance as a function of aging condition were discussed.

Keywords: AA6061, Logarithmic Decrement, Crack Propagation Resistance, Aging

1. INTRODUCTION

For the sake of energy conservation, aluminum alloys have been used extensively to reduce the weight of automobiles and aircrafts. Among these alloys, heat treatable AA6061 alloy has found wide application in transportation and structural components, owing to its strength, weldability and corrosion resistance [1]. In this study, a vibration equipment that can generate the resonant condition was used to explore the fracture behavior of AA6061 aluminum alloy in various aging conditions.

McGuire *et al.* [2, 3] have shown that the measurement of resonant frequency can be applied as a nondestructive tool to detect crack length. Dentsoras *et al.* [4] have also pointed out that material damping was the decisive factor for determining the crack growth rate in a resonant system. Additionally, our previous investigation [5] on the resonant fracture behavior showed that increasing the damping capacity reduced the deflection amplitude and then resulted in increasing the crack propagation resistance. The investigation of aging treatment of A356 alloy [6] indicated that changing the aging condition significantly influenced the crack propagation behavior under resonant vibration. Thus, the crack propagation resistance increased with increasing the yield strength and hardness of specimens. To have a better understanding of the effect of aging on the material damping and crack propagation resistance under resonant vibration, the aging condition of AA6061 aluminum alloy was investigated.

2. EXPERIMENTAL PROCEDURES

The composition of AA6061 aluminum alloy used in this study is shown in Table 1. The test specimens were solution-treated at 535°C for two hours, quenched in water and then subjected

to six different aging treatments. One specimen naturally aged at room temperature for 7 days and four other specimens underaged (UA1, UA2), peak-aged (PA) and over-aged (OA1) at 185°C for 1, 6, 12 hour and 7 days, respectively. One overaged treatment (OA2) was also conducted at 250°C for 10 hour.

Table 1. Chemical composition of AA6061 aluminum alloy (wt.%).

Si	Mg	Cu	Mn	Fe	Zn	Ti	Cr	Al
0.65	1.05	0.3	0.1	0.12	0.14	0.01	0.093	Bal

Fig. 1a schematically depicts the vibration apparatus applied for the resonant vibration test. The specimen has two V-notches on the lateral sides near the clamp according to the shape and dimensions provided in Fig. 1b. These notches were made to confine the crack initiation from the notch tip. The acceleration of the vibrating shaker was fixed at 1.5g and 1.7g ($g: 9.8 \text{ m}\cdot\text{sec}^{-2}$). The resonant frequency was in the range of $72 \pm 1 \text{ Hz}$ regardless of the aging condition. The specimens' deflection amplitude was recorded as a function of the vibration cycle during the testing process. The test was paused at various vibration cycles to observe the cracking features. An optical microscope equipped with an image analyzer was utilized for this observation.

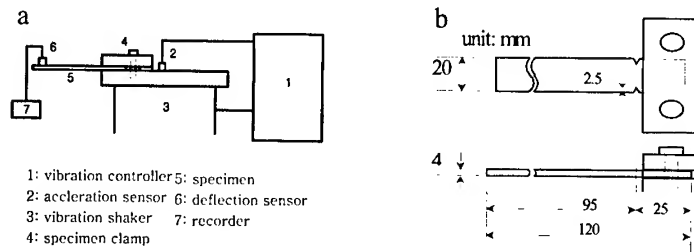


Fig. 1. a) Schematic diagram of the vibration equipment and b) shape and dimension of the resonant vibration test specimen.

Damping capacity is one measure of a material's ability to dissipate strain energy during vibration test. Logarithmic decrement, δ , is one of the method used to measure damping capacity, derived from deflection amplitude decay of specimen under free vibration is defined as [7]

$$\delta = \frac{1}{n} \ln \frac{A_i}{A_{i+n}} \quad (1)$$

where A_i and A_{i+n} are the deflection amplitude of the i th cycle and the $(i+n)$ th cycle, at times t_1 and t_2 , respectively, separated by n periods of oscillation. Schematic diagram of deflection amplitude decay of specimen is shown in Fig. 2. In this study, the vibration shaker acceleration was fixed at 1.5g and when the vibration was stopped, the amplitude decay of the specimen was measured.

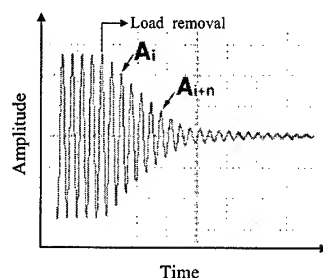


Fig. 2 Schematic diagram of deflection amplitude decay of specimen, showing the measurement of logarithmic decrement (δ)

3. RESULTS

3.1 Microstructure and Tensile Properties

Fig. 3 illustrates the optical metallography of the naturally aged specimen. The grain size of the specimens remained practically unchanged for the six different aging treatments, with the average grain size of about $210\ \mu\text{m}$. Summarized in Table 2 are the datum of tensile strength, elongation and microhardness for different specimens. The peak-aged (PA) specimen displayed the highest stress and microhardness compared to other specimens.

Table 2. Datum of tensile stress, elongation and Rockwell B hardness.

Designation	Yield stress (MPa)	UTS (MPa)	Elongation (%)	Microhardness (Hv)
NA	137	261	27.6	74.1
UA1	248	311	19.1	98.7
UA2	313	353	12.7	116.1
PA	325	360	10.7	126.5
OA1	319	345	8.0	116.4
OA2	208	261	8.1	83.1

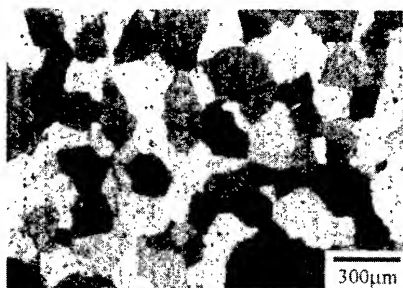


Fig. 3. Optical micrograph of the naturally aged specimen, showing the grain structure.

3.2 Deflection amplitude and vibrational life

The dependence of deflection amplitude (D) vs. the number of vibration cycles (N) can be described by D-N curve as shown in Fig. 4. As illustrated in the figure, all test materials exhibit a similar trend in the variation of deflection amplitude, which can be divided into three distinct stages throughout the test. The deflection amplitude at resonance increases with the number of vibration cycles in Stage I. An increase in deflection amplitude in Stage I should be correlated with the effect of work hardening [5-6]. Subsequently, the deflection amplitude in Stage II can be classified as a plateau region. According the observation of crack propagation path, the

crack predominantly propagates in this stage. Stage III delineates the deflection amplitude decreases significantly with increasing vibration cycles. The phenomenon of descending deflection amplitude in Stage III should be correlated with the deviation of resonant frequency [5-6]. Furthermore, due to the divergence of resonance condition, the vibrational life can be defined qualitatively from the D-N curve as that point corresponding to the transition between the plateau region (stage II) and the descending region (stage III), as depicted Fig. 4a.

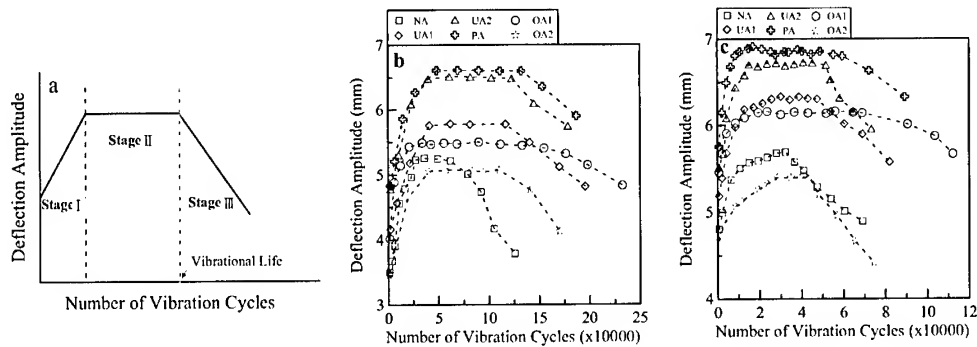


Fig. 4. Deflection amplitude vs. number of vibration cycles: a) schematic figure of D-N curve, b) 1.5g vibration shaker acceleration and c) 1.7g vibration shaker acceleration.

Fig. 4 indicated the deflection amplitude was significantly affected by aging. The deflection amplitude are in the following order: PA > UA2 > UA1 > OA1 > NA > OA2. According to the measurement of logarithmic decrement, as indicated in Table 3, it should be noted that there is an inverse relation between the logarithmic decrement and deflection amplitude. Fig. 5 shows the vibrational life of the specimens. This figure indicates that the vibrational life increases in turn from NA to OA2 to UA1 to UA2 to PA and to OA1.

Table 3. Logarithmic decrement (δ)

Designation	δ
NA	0.221
UA1	0.196
UA2	0.175
PA	0.171
OA1	0.207
OA2	0.223

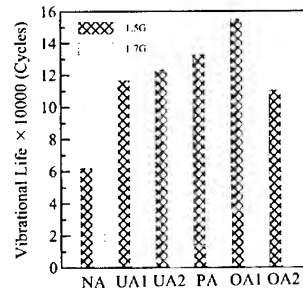


Fig. 5 Vibrational life of all specimens.

3.3 Crack Propagation Features

Under different vibration shaker acceleration (1.5g and 1.7g), the naturally aged (NA) and underaged (UA1 and UA2) specimens showed similar crack propagation paths. Fig. 6a shows the crack propagation feature observed on the surface of the naturally aged specimen, which indicates the slip band cracking feature. Whereas, the slip band cracking was not observed in the peak-aged (PA) and overaged (OA1 and OA2) specimens. Fig. 6b illustrates the crack propagation path of the OA2 specimen. This figure shows that the cracks propagation are mainly transgranular.

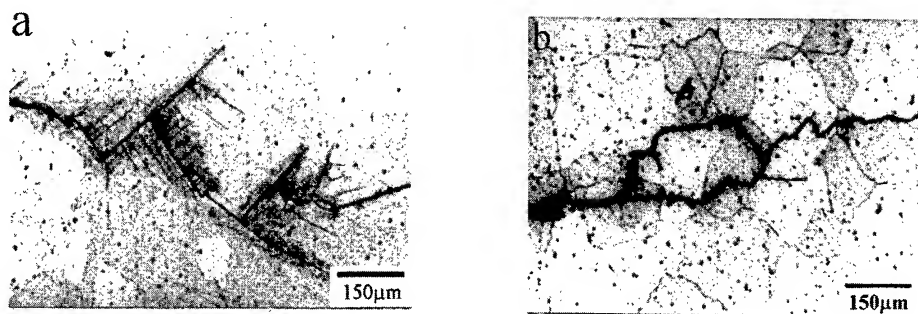


Fig. 6. Crack propagation feature: a) NA specimen and b) OA2 specimen

4. DISCUSSION

Fig.4 shows the deflection amplitude of specimens significantly influenced by aging treatment. The deflection amplitude of specimen in turn increases from NA to UA1 to UA2 and to PA specimens, subsequently the deflection amplitude decreases to OA1 and OA2 specimens. The mechanism by which the dislocations are generally considered to affect damping behavior is Granato-Lucke mechanism [7-9]. The internal friction (damping) from the motion dislocation break-way or the action of particle/matrix interfaces can release the vibration energy and result in the increment in the damping capacity of material. For the naturally aged (NA) and underaged (UA1 and UA2) specimens, coherency of the precipitation/matrix interfaces makes mobile dislocations in the plastic zone ahead of crack tip to glide by shearing the precipitates. Increasing the strength or hardness will increase the stress required for shearing the coherent precipitates; thus, the crack is harder to slip. Thus, the order of the damping capacity of specimens is: NA > UA1 > UA2 (Table 3). Whereas, for the peak-aged (PA) and overaged (OA1 and OA2) specimens, the gliding of mobile dislocations alters from shearing the precipitates to Orowan looping, if the precipitates are incoherent [10-12]. Increasing the matrix strength also raises the resolved shear stress for Orowan looping, that increase the resistance of crack propagation. Consequently, experimental result depicts the damping capacity order is: OA2 > OA1 > PA (Table 3)

The naturally aged (NA) and underaged (UA1 and UA2) specimens possess the slip band cracking feature. In some fatigue propagation, studies [10-12] have shown that the underaged 7XXX and Al-Li aluminum alloys with coherent precipitates also had the slip band cracking feature. Increasing the matrix strength or hardness will raise the stress required for shearing the coherent precipitates, then that is helpful to improve the crack propagation. Whereas, if the precipitates are incoherent, the increase in the matrix strength and hardness raises the resolved shear stress for Orowan looping, for the PA, OA1 and OA2 specimens. This is a factor for increasing the crack propagation resistance with increasing the strength and hardness. Thus, the crack propagation resistance shows a direct proportion to the yield stress and hardness. On the other hand, our previous study [5] showed that the suppression of deflection amplitude of specimen can significantly improve the crack propagation resistance and the crack predominantly propagates in stage II (displayed the largest deflection amplitude). Thus, the vibrational life should be correlated with the deformation resistance of matrix and deflection amplitude.

Furthermore, Fig. 7 shows a good linear relation between the vibrational life and the ratio of yield strength (or matrix microhardness)/largest deflection amplitude. The vibrational life increases with increasing the value of ratio. The ratio of the yield strength to the largest deflection amplitude, for the specimens used in this study, can be considered as the indication of the crack propagation resistance.

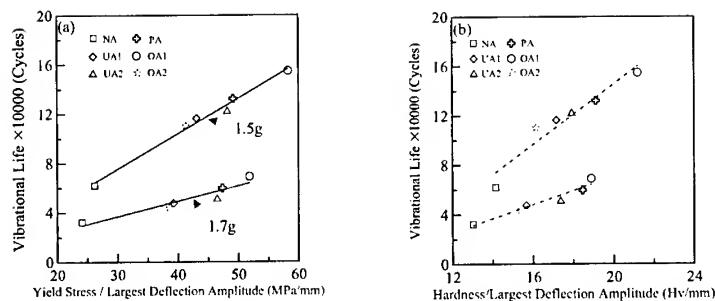


Fig. 7 Vibrational life vs. ratio of yield strength (or matrix microhardness)/largest deflection amplitude.

5. CONCLUSIONS

1. In six different aging treatments, the values of deflection amplitude of specimens had the following order: PA > UA2 > UA1 > OA1 > NA > OA2. Having an inverse relation between the logarithmic decrement and deflection amplitude, the logarithmic decrement values were arranged as: OA2 > NA > OA1 > UA1 > UA2 > PA. This showed the deflection amplitude of specimen could be suppressed with increasing the logarithmic decrement.
2. The naturally aged (NA) and underaged (UA1 and UA2) specimens showed similar crack propagation behavior. The observation of crack propagation indicated the slip band cracking feature. Whereas, the slip band cracking was not observed in the peak-aged (PA) and overaged (OA1 and OA2) specimens. This shows that the propagation of cracks are mainly transgranular and partly intergranular.
3. For the six specimens with different aging treatments used in this study, the ratio of the yield strength to the largest deflection amplitude can represent the crack propagation resistance. The crack propagation resistance increases in turn from NA to OA2 to UA1 to UA2 to PA and to OA1.

Reference

1. Metals Handbook, 10th edn., Vol. 2(1990), American Society for Metals, Metals Park, Ohio, USA, pp. 102-103.
2. S. M. McGuire, M. E. Fine and J. D. Achenbach, J. Mater. Res., Vol. 8(1993), pp. 2216-2223.
3. S. M. McGuire, M. E. Fine and J. D. Achenbach, Metall. Mater. Trans. A, Vol. 26A(1995), pp. 1123-1127.
4. A. Dentsoras and A. D. Dimarogonas, Eng. Fracture Mech., Vol. 17(1983), pp. 381-386.
5. J. H. Horng, T. S. Lui and L. H. Chen, Aluminum Trans., Vol. 2(2000), pp. 283-291.
6. D. S. Jiang, T. S. Lui and L. H. Chen, Mater. Trans. JIM, Vol. 41(2000), pp. 499-506.
7. S. S. Rao, Mechanical Vibrations, 2nd ed., Addison-Wesley Publishing Company, Inc., (1990), pp. 89-91.
8. A. Granato and K. Lucke, J. Appl. Phys., Vol. 27(1956), pp. 583-593.
9. J. Zhang, R. J. Perez and E. J. Lavernia, J. Mater. Sci., Vol. 28(1993), pp. 835-846.
10. J. T. Hartman, Jr., K. H. Keene, R. J. Armstrong and A. Wolfenden, J. Met., Vol. 38(1986), pp. 33-35.
11. K. T. V. Rao, W. Yu and R. O. Ritchie, Metall. Trans. A, Vol. 19A(1988), pp. 549-561.
12. R. D. Carter, E. W. Lee, E. A. Starke, Jr. and C. J. Beevers, Metall. Trans. A, Vol. 15A(1984), pp. 555-563.
13. D. C. Slavik, C. P. Blankenship, Jr., E. A. Starke, Jr. and R. P. Gangloff, Metall. Trans. A, Vol. 24A(1993), pp. 1807-1817.

DEFORMATION BEHAVIOR OF A SPRAY-CAST HYPEREUTECTIC Al-25Si ALLOY

Tae Kwon Ha, Joseph Kim, Woo-Jin Park*, Eon-Sik Lee*,
Sangho Ahn* and Young Won Chang

Center for Advanced Aerospace Materials

Pohang University of Science and Technology, Pohang 790-784, Korea

*Research Institute of Industrial Science and Technology, Pohang 790-600, Korea

ABSTRACT

This article reports the fabrication of a hypereutectic Al-25Si (wt.%) alloy, which is expected to be applied to the cylinder liner part of the engine block of an automobile due to its excellent wear resistance, low density and low thermal expansion coefficient, through a spray casting process and the characterization of the microstructure and the mechanical properties of this alloy. The OSPREY process used in this study is one of spray forming techniques, which can produce semi-finished products such as billet, tube and plate with rapid solidification structure and density in a single operation from molten metal. The obtained microstructure of the hypereutectic Al-25Si alloy consisted of Al matrix and equiaxed Si particles of average diameter of $\sim 6 \mu\text{m}$. To characterize the deformation behavior of this alloy, a series of load relaxation and compression tests have been conducted at temperatures ranging from RT to 500°C. The strain rate sensitivity parameter (m) of this alloy has been found to be very low (≤ 0.1) below 300°C and to reach the maximum value of about 0.2 at 500°C. During the compression tests, no strain hardening was observed even at RT. From the result of compression tests, the condition of hot-extrusion, a necessary process for application as the cylinder liner, was deduced. The extrusion has been successfully conducted at the temperatures of 300°C and above with the ratio of area reduction of 28 and 40 in this study.

1. INTRODUCTION

Hypereutectic Al-Si based alloys exhibit useful characteristics that make them as one of the most important, advanced material systems, such as good wear resistance, high stiffness, low thermal expansion coefficient and high temperature performance [1, 2]. Recently, hypereutectic Al-Si Alloys have been recommended as a strong candidate material for the cylinder liner of engine block in automotive industry in the light of automobile weight reduction.

The conventional ingot metallurgy (IM) and rapid solidification/powder metallurgy (RS/PM) processes have been employed for production of these alloys. The formation of coarse, primary Si particles and AlFeSi based intermetallic phases [3, 4] during IM process, however, have been restricted the application of this alloy. These problems from IM process can be solved by various RS/PM methods, which bring about a significant microstructural modification of the alloys in size, morphology and distribution of Si particles and AlFeSi based intermetallic compounds [5, 6]. The spray casting, although it offers somewhat slower

solidification rate than that of RS processes, can also produce a fine microstructure in which Si particles and AlFeSi based intermetallics are uniformly distributed [1, 7, 8]. It is, therefore, very interesting technologically and commercially to apply the spray casting for the production of Al-Si based alloys.

In the present study, it was attempted to produce a 180-mm-diameter billet of Al-25Si (wt.%) alloy using the OSPREY spray casting process. In an attempt to establish the optimum condition for extrusion process that is required for the preform to be formed into a cylinder liner, a series of high temperature compression and load relaxation tests have also been conducted.

2. EXPERIMENTAL PROCEDURE

The composition of the present alloy was Al-25Si (wt.%). The 15-kg-alloy-preform was prepared via the OSPREY spray casting process with melt temperature of 850°C. The schematic drawing of the apparatus used in this study is given in Fig.1. The alloy was melted in a graphite crucible using an induction-heating furnace. A thermocouple was placed at the bottom of the tundish to monitor the temperature of the melt prior to atomization. The melt stream was atomized into fine droplets by nitrogen gas at high pressure. The atomized droplets were deposited onto a substrate positioned at an appropriate distance from the tundish nozzle. The diameter of the billet thus obtained was 180 mm. After measuring the density distribution of the billet, specimens for compression test, load relaxation test, and extrusion were taken from the center part of the billet, having over 97 % of the ideal density. The gauge dimensions of specimens were 3 mm × 3 mm × 6 mm for compression tests and 3 mm × 4 mm × 27 mm for load relaxation tests, respectively. For extrusion, billets with 80 mm in diameter were machined.

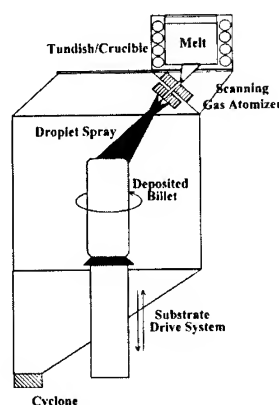


Fig. 1. The schematic drawing of the spray casting apparatus used in this study.

A series of compression and load relaxation tests were then carried out at the temperatures ranging from 24 to 500°C by using a computer controlled electro-mechanical testing machine (Instron 1361 model) attached with a furnace capable of maintaining the temperature fluctuation within $\pm 1^\circ\text{C}$. It is well known that load relaxation test can provide a much wider range of strain rates, applying a little amount of plastic strain, 1.5 % in this study, to the specimen without an appreciable change in microstructures [9]. Loading strain rate was $5 \times 10^{-2}/\text{s}$ in all cases. The flow stresses as a function of the inelastic strain rate were determined by

following the usual procedure described in the literature [10]. Compression tests were also carried out under the various strain rates ranging from 10^{-4} /s to 10^{-2} /s at the same temperature range. After constructing the diagrams of extrusion pressure vs. ram-speed from the compression test results, extrusion has been conducted under the various conditions.

3. RESULTS AND DISCUSSION

3.1. Spray-cast billet

The density of the spray-cast billet showed more than 97% of its ideal density. All specimens for mechanical testing and extrusion have been taken from the center part of the billet. Figure 2 shows the typical microstructure of the as-spray-cast billet together with the micrograph of IM processed Al-25Si alloy. As briefly mentioned earlier, coarse primary Si particles (P) and AlFeSi based intermetallic phases (I) are easily observed in the IM processed alloy, while the Si particles in the spray-cast alloy appear to be very uniform in their size ($\sim 6 \mu\text{m}$) and distribution. The AlFeSi based intermetallic phases can also be observed in Fig. 2(b) in the form of thin film type.

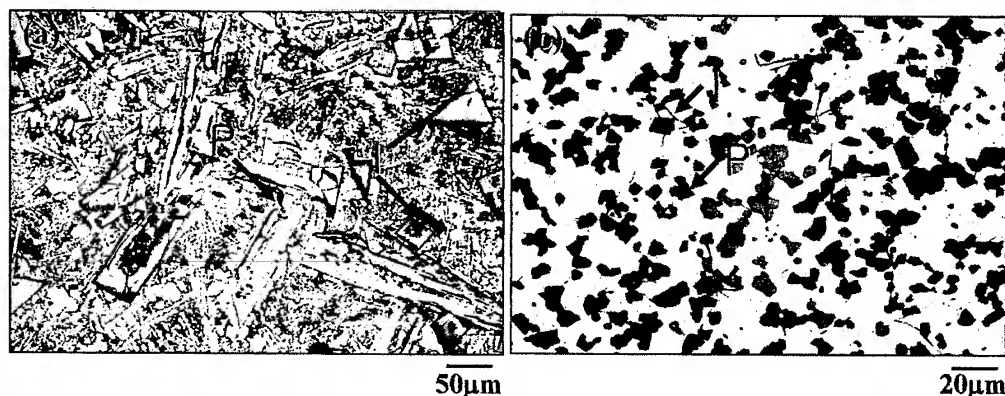


Fig. 3. Typical microstructures of Al-25Si alloys produced by (a) an ingot metallurgy and (b) spray casting.

3.2. Load relaxation behavior

The flow curves of strain rate ($\dot{\epsilon}$) vs. stress (σ) obtained from a series of load relaxation tests conducted at temperatures from RT to 500°C are given in Fig. 4 in a log scale, showing a wide range of flow data in more than four orders of the strain rates. The flow stresses are observed to be very sensitive to the test temperatures. The slope of the flow curve is well known as the strain rate sensitivity parameter (m), characterizing the strain rate dependency of the flow stress and also the measure of high temperature ductility [11]. The m values of spray-cast Al-25Si alloy are found very small at lower temperatures less than $m = 0.1$ below 300°C but appear to increase remarkably reaching upto about 0.2 at 500°C . It is very interesting to note that the flow curve obtained at 500°C can be divided into two regions with different m values, suggesting that two different deformation mechanisms might operate for each m value.

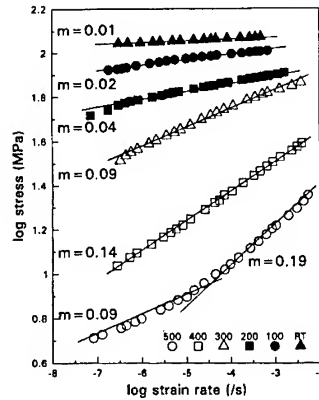


Fig. 3. Flow curves of a spray-cast Al-25Si alloy are obtained from load relaxation tests conducted at the various temperatures.

3.3. Compression test results

Some compression test results are given in Fig. 4 in terms of the true stress and true strain. It should be noted here that the strain-hardening rate is negligible even at RT. At higher temperatures, strain softening can be observed, though the degree of which is not remarkable. The flow curves of log strain rate ($\dot{\epsilon}$) vs. log stress (σ) can also be obtained from the compression test results, plotting the flow stresses evaluated at the strain level of 1% as a function of the initial strain rates as shown in Fig. 5. This result shows somewhat smaller m values than those calculated from load relaxation tests.

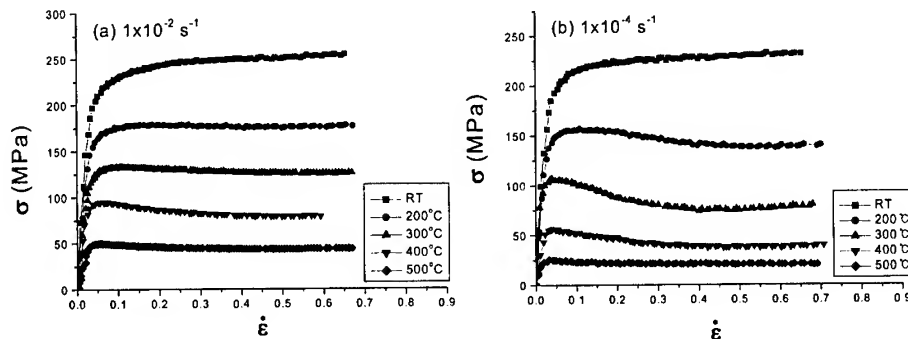


Fig. 4. True stress vs. true strain curves obtained from a series of compression tests under the initial strain rates of (a) 1×10^{-2} /s and (b) 1×10^{-4} /s.

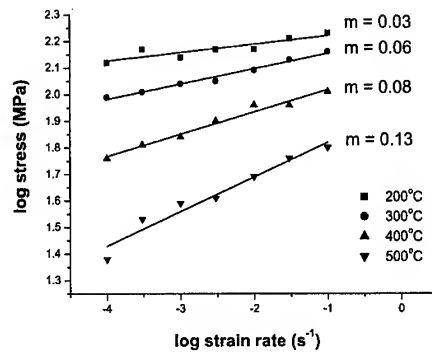


Fig. 5. The flow curves of a spray-cast Al-25Si alloy are obtained from compression tests conducted at the various temperatures.

3.4. Assessment of extrusion conditions

The extrusion pressure P_e (MPa) is expressed by the following equation:

$$P_e = \sigma_y (A + B \ln r) \quad (1)$$

where σ_y (MPa) and r are the yield stress of the feed material and the extrusion ratio, respectively. The coefficients A and B depend on the die shape and friction [12, 13], having the reported values of 0.8 and 1.5, respectively, for a non-hardenable material. Since the spray-cast Al-25Si showed negligible strain-hardening rate as shown in Fig. 4, these values are presumed to be applicable in this study.

On extrusion with a conical die with a hole of circular shape, the mean strain rate $\dot{\epsilon}$ (s^{-1}) is expressed by

$$\dot{\epsilon} = (6 V_e / D) \ln r \tan \theta \quad (2)$$

with V_e (mm/s) and θ (degrees) denoting the ram-speed and the half die angle, respectively [13]. In this study, the diameter D of the feeding billet and θ were 80 mm and 45 degrees, respectively.

Figure 6 shows the relations between the extrusion pressure and ram-speed for the extrusion ratios of $r = 28$ and 40, obtained from equations (1) and (2) using the flow data in Fig. 6. During extrusion, it is necessary to control the working pressure below the endurance pressure of the machine. The critical pressure is evaluated as 1072 MPa in the case of this study and marked by the horizontal lines in Fig. 6. A series of experimental extrusions were successfully conducted at the ram-speeds of 1~10 mm/s, for the extrusion ratios of $r = 28$ and 40 and at the various temperatures above 300°C. After an extrusion with the condition of $r = 28$ and $T = 400^\circ\text{C}$, Si particles were found to refine into an average size of about 2 μm .

4. SUMMARY

The 180-mm-diameter billet of a hypereutectic Al-25Si alloy with over 97% of ideal density,

was produced using the OSPREY spray casting process in this study. The Si particles were found to be uniform in both distribution and their size. The strain rate sensitivity parameter (m) of this alloy has been observed to be very low (≤ 0.1) below 300°C but to reach the maximum value of about 0.2 at 500°C from a series of load relaxation and compression tests. The diagrams of ram-speed vs. extrusion pressure for this alloy were constructed from the compression test results, providing the extrusion conditions. The effectiveness of these diagrams has been confirmed experimentally by conducting extrusions under the various conditions. After an extrusion, the Si particles were observed to refine into much smaller size of about 2 μm .

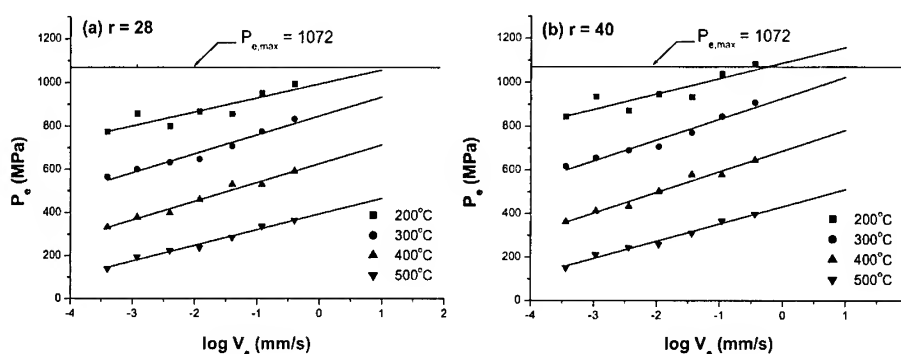


Fig. 6. The plot of extrusion pressure as a function of the ram-speed providing a means to determine the extrusion conditions.

REFERENCES

1. J. Zhou, J. Duszczek and B. M. Lorevaar, J. Mater. Sci., Vol. 26 (1991) pp.5275-5291.
2. H. Sano, N. Tokinano, Y. Ohkubo and K. Sibue, Powder Metallurgy, Vol. 36 (1993) pp.250-251.
3. A. M. Samuel, F. H. Samuel and H. W. Doty, J. Mater. Sci., 31 (1996) pp.5529-5539.
4. J.-S. Lee and H. Ra, J. the Korean Inst. of Met. & Mater., Vol. 34 (1996) pp. 1346-1352.
5. W.-W. Park, B.-S. You and N. J. Kim, Mater. & Design, Vol. 17, 5/6 (1996) pp. 255-259.
6. T. Satoh, K. Okimoto and S. Nishida, J. Mater. Pro. Tech., Vol. 68 (1997) pp.221-228.
7. J. L. Estrada and J. Duszczek, J. Mater. Sci., Vol. 25 (1990) pp. 1381-1391.
8. Y. Wu, W. A. Cassada and E. J. Lavernia, Metall. & Mater. Trans. A, Vol. 26A (1995) pp.1235-1247.
9. E. W. Hart, "Stress Relaxation Testing", A. Fox ed., ASTM, Baltimore, Md. (1979), p. 5.
10. D. Lee, and E. W. Hart, Metall. Trans., Vol. 2A (1971), p. 1245.
11. O. D. Sherby, and J. Wadsworth, Prog. Mater. Sci., Vol. 33 (1989), p. 169.
12. W. Johnson, J. Inst. Metals, Vol. 85 (1956), p. 403.
13. R. J. Wilcox and P. H. Witton, J. Inst. Metals, Vol. 87 (1958), p. 289.

ACOUSTIC EMISSION FROM FATIGUE CRACK EXTENSION IN CORRODED ALUMINUM ALLOYS

Ki-Woo Nam, Seok-Hwan Ahn and Ajit K. Mal*

Pukyong National University, Pusan, 608-739, Korea

*Mechanical and Aerospace Engineering Department, University of California, Los
Angeles, CA, 90095, USA

ABSTRACT

The main objective of this study is to determine if the sources of *AE* in corroded specimens of aluminum could be identified from the characteristics of the waveform signals recorded during fatigue loading. Coupons of notched 2024-T3 aluminum with or without corrosion (at the notch) were subjected to fatigue loading and the *AE* signals were recorded using non-resonant, flat, wide-band transducers. The time history and power spectrum of each individual wave signal recorded during fatigue crack growth were examined and classified according to their special characteristics. Five distinct types of signals were observed regardless of specimen condition. Three types of signals (identified as Types I, II and III), recorded by transducers located at relatively large distances from the notch-tip, were found to be similar in both as-received and corroded specimens, but the other two signals (Types IV and V) were different in their characteristics.

1. INTRODUCTION

Acoustic Emission (AE) is the phenomenon in which elastic waves are emitted from sudden release of the strain energy due to the extension of cracks and flaws in structural solids[1]. It is a common nondestructive methodology that has been used, with varying degrees of success, to monitor damage evolution in engineering structures subject to service loads. Microfracture events in loaded structures can be triggered by different mechanisms. The primary sources of *AE* are dynamic deformation and fracture while phase transformation, corrosion, friction, magnetic processes, among others, also give rise to detectable *AE*[2-6]. As a common nondestructive testing technique *AE* methods can be used in monitoring structural integrity, leak detection, initial fracture and in characterizing material behavior[7-9].

In plate-like structures a major portion of the energy released during microfracture events associated with damage is carried away from the source by multimode guided waves. The efficiency of the excitation and the relative strength of different guided wave modes can be used to interrogate the characteristics of the microfracture sources. This relationship between different types of microfracture and the guided waves generated by them in thin graphite/epoxy composite plates under fatigue loading has been established through laboratory tests and theoretical modeling[10]. Since the method monitors the dynamic processes associated with damage, its applicability does not depend on the size of the existing defects. Thus the onset of very small cracks that can not be detected by passive nondestructive methods can be detected by *AE* monitoring in general and the nature of the source can be characterized through wave-based analysis of *AE* signals.

In this paper, *AE* signals generated during a fatigue process in an as-received specimen and a corrosion pitted specimen of 2024-T3 aluminum alloy were recorded in real time. The energy released during fracture initiation and propagation were shown to be carried by guided waves in the plates. The signals were classified into several types based on their temporal as well as spectral characteristics, and were related to the characteristics of the microfracture. The signals from the corroded specimens were found to have distinct features that can, in principle, be used to detect the presence of early corrosion in rivet holes and other locations in aging metallic structures.

2. SPECIMEN PREPARATION

The specimens used in the experimental study were made of 2024-T3 (bare) Aluminum alloy of 1.6mm nominal thickness. The dimensions of specimens are shown in Figure 1. The grip sections of the specimens were covered by epoxy resin in order to reduce grip noise. The resin was cured by heat treatment for 20 minutes at 80° C. Two kinds of specimens, as-received and corroded, were used in the experiments. The corroded specimen was prepared by immersing it in a 0.5M NaCl solution, with approximately 7ppm of dissolved oxygen, for 16 days at room temperature. The specimen was coated with stop-off lacquer so that only the notch surface was exposed to the solution. The corrosion appearance of the notch surface is shown in Figure 2.

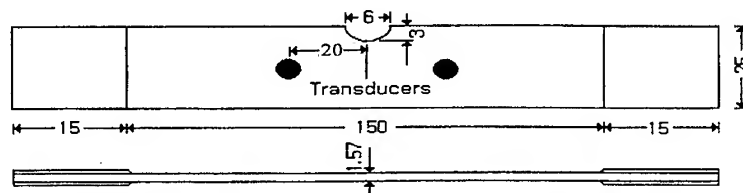


Fig.1 Dimensions of specimens ; all dimensions in mm

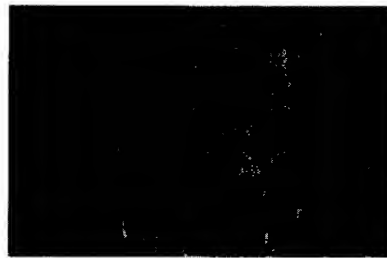


Fig.2 Corrosion pit appearance of notch tip (x300)

3. THE EXPERIMENTS

Fatigue tests were performed at room temperature using a servo-hydraulic testing machine (INSTRON model 8500), under a controlled loading cycle. The waveform was a sine wave with frequency 1Hz and the stress ratio was $R=0.1$. AE measurements were carried out using a Fracture Wave Detector (Model F4000, Digital Wave Corp., Englewood, Co.), which allows digitization of the total AE waveform in real time. The digitization rate was set at 12.5MHz with a 1024 point gate length for each channel using a threshold of 0.2V. Two

broadband transducers (DWC B1025), with reasonably flat response to about 1.5 MHz, were placed at equal distances of 20 mm from the source (notch) (see Figure 1). Two 40dB preamplifiers (AET 140B) with a 30kHz-2MHz plug-in filter were used in this experiment.

4. CHARACTERISTICS OF SIGNALS FROM FATIGUE TESTS

A large number of signals were recorded during the test; they were generated by fatigue crack propagation and also by other extraneous sources of noise. The signals were classified based on visual examination of their temporal and spectral features.

The general procedure followed in the visual classification of the signals is sketched in Figure 3, and its application to typical signals is illustrated in Figure 4 for as-received specimens, and in Figure 5 for corroded specimens. The signals from each specimen were found to be of five general types based on their spectral characteristics. Signals of Types I, II and III have similar characteristics for as-received and corroded specimens, while those of Types IV and V have different characteristics for both specimens. The percentage observed emissions from the two specimen are shown in Table 1.0

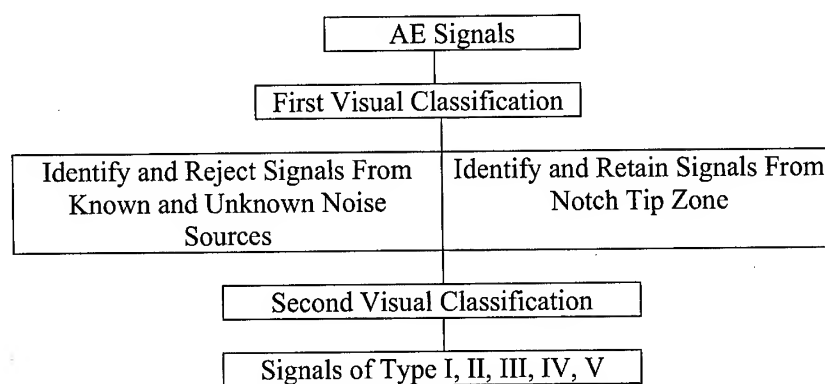


Figure 3. Flow chart of the visual classification of AE signals.

Table 1 Acoustic emission events classification

AE event	Type-I	Type-II	Type-III	Type-IV	Type-V
As-received(%)	3.1	12.5	15.6	25.0	43.8
Corroded(%)	12.1	10.3	28.2	13.0	15.4

The signals of Types I, II and III appear to have originated from the crack tip after the crack had propagated some distance away from the notch tip, and crossed the corrosion zone. Thus the sources of these emissions are not affected by corrosion. It can be seen in Figures 4 and 5 that Type-I signals have dominant peaks in their power spectra at approximately 0.25MHz and 0.75MHz. The power spectra of Type-II signals have a dominant peak at approximately 0.5MHz and a smaller peak at approximately 1.0MHz. Type-III signals have dominant peaks at approximately 0.25, 0.7 and 1.2MHz.

In contrast, the signals of Type-IV in Figure 4 (for the as-received specimen) have a dominant peak at approximately 1.0MHz and that in Figure 5 (for the corroded specimen) has a dominant peak at approximately 0.15MHz. The Type-V signal of Figure 4 has peaks at approximately 0.7 and 1.1MHz, and that in Figure 5 has significant peaks below 0.5MHz

followed by smaller peaks at higher frequencies. Signals of Types IV and V were produced during early stages of crack propagation, and for the corroded specimen, when the crack tip was within the corroded zone. Thus the source mechanism of signals of Types IV and V are different for the corroded and as-received specimens. In general, these waveform signals in as-received specimens have more high frequency content than those in the corroded specimens. The reason for this difference is not clear. However, it is possible that in as-received specimen the signals are generated by high energy, short duration transgranular cleavage caused by extrusion and intrusion under fatigue loading(Fig.6(a)). On the other hand, in the corroded specimen they are generated by intergranular cleavage due to embrittlement of the grain boundary in the vicinity of the notch tip(Fig.6(b)).

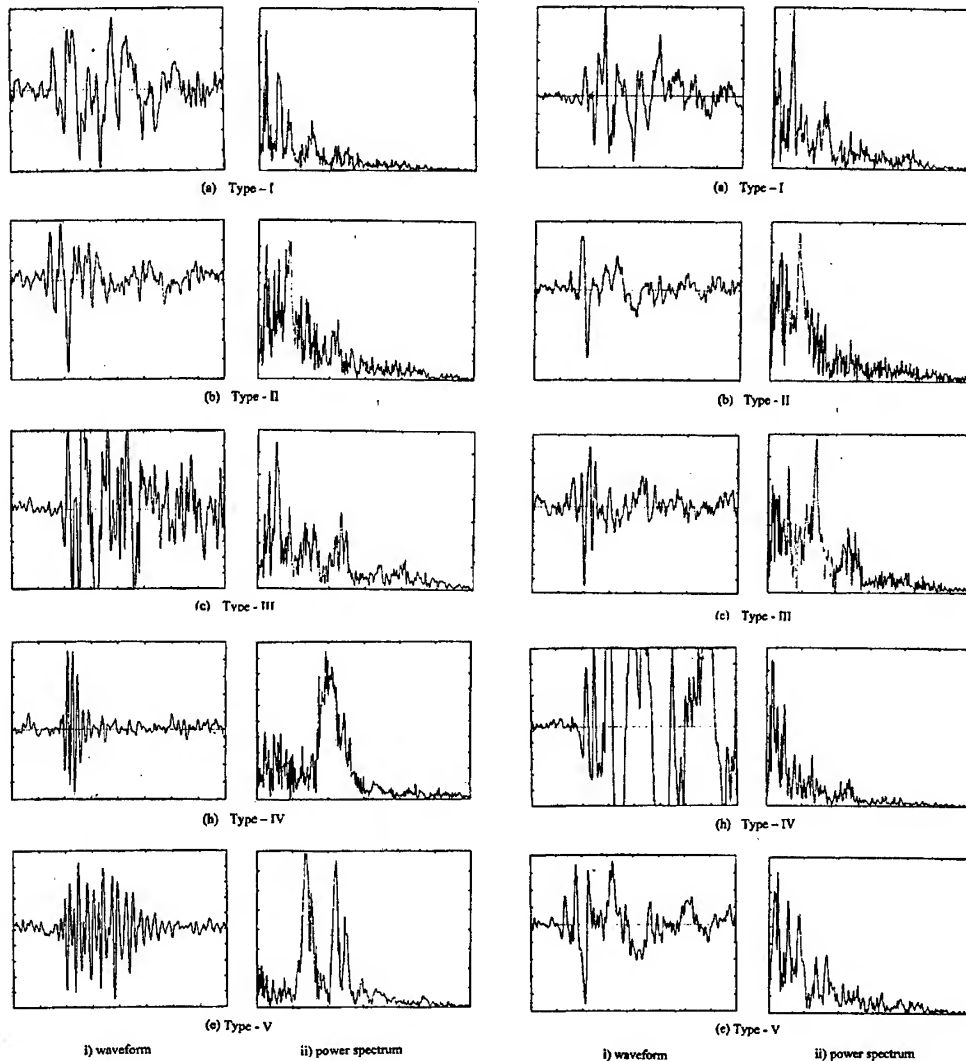


Fig. 4. AE events detected from as-received specimens. Fig.5 AE events detected from corroded specimens

Horizontal scale ; i) time : 5μs/div., ii) frequency : 0.5MHz/div.,
Vertical scale : arbitrary

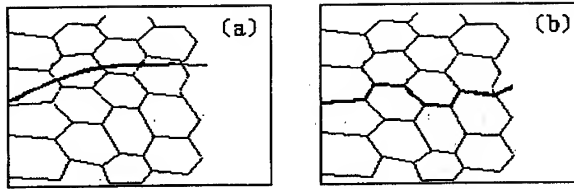


Figure 6. Possible microfractures associated with the AE signals:
(a) Transgranular fracture, (b) intergarnular fracture

5. DISCUSSIONS

Fatigue crack extension in high strength aluminum alloys has displayed numerous acoustic emission events that can be detected on the surface. The material tested was 2024-T3 (bare) aluminum alloy in two types of specimen, as-received and corroded. In the fatigue tests five types of signals were observed regardless of specimen condition. Type-I, Type-II and Type-III signals are similar regardless of the specimen condition, as-received or corroded, but signals of Types IV and V have different characteristics in their waveform and power spectra. It should be noted that the signals are carried by plate guided Lamb waves, and their reflections from the edges of the plate. The dispersion curves for the aluminum plates used in the experiment are shown in Figure 7. Since most of the spectral peaks of the signals are at frequencies below 1.2MHz, the waves consist of symmetric (S_0) and antisymmetric (A_0) waves of the lowest mode. At a frequency of 1MHz, the wave speeds are approximately, $v_{gs} = 4.4$ mm/ μ sec for S_0 , and $v_{ga} = 2.2$ mm/ μ sec for A_0 waves. It can be easily seen that the reflected S_0 waves start to arrive at the receiving transducer about 4 μ sec after the arrival of the direct S_0 wave, the direct A_0 wave arrives about a microsecond after this. Thus, only the first 4 μ sec of the recorded waveform is pure S_0 mode Lamb wave, the remainder is a combination of various other waves. It is difficult if not impossible to relate the entire time histories of the signals to the source mechanism at the advancing crack tip. However, the spectral content of the signals is not affected significantly by the reflections and multiple arrivals. Thus the observed differences in the spectral characteristics of the waves in the as-received and corroded specimens should be reliable, and can, in principle be used to detect the presence of corrosion in aging structures.

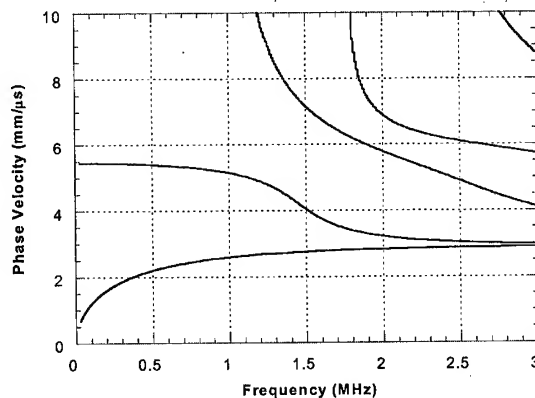


Figure 7. Dispersion curves for the aluminum plate.

6. SUMMARY

In this paper, *AE* signals generated during fatigue in an as-received and a corrosion pitted specimen of 2024-T3 aluminum alloy were recorded in real time and classified based on their temporal as well as spectral characteristics.

Five distinct types of signals were observed regardless of specimen condition. Three types of signals (identified as Types I, II and III), recorded by transducers located at relatively large distances from the notch-tip, were found to be similar in both as-received and corroded specimens, but the other two signals (Types IV and V) were different in their characteristics. The waveforms and power spectra were shown to be dependent on specimen condition. During the initial phase of crack growth, the signals obtained in the as-received specimens are most probably due to transgranular fracture caused by extrusion and intrusion under fatigue loading. In the corroded specimen the signals are probably generated by intergranular fracture or transgranular cleavage of the corrosion induced embrittled grains near the pit. Based on analysis of waveforms and power spectra it should also be possible to monitor in real-time the crack propagation and final fracture process resulting from various damages and defects in structural members.

REFERENCES

1. annual Book of ASTM Standards, Section 3, 1993
2. S.Carpenter and M.Gorman, J.of Acoustic Emission, Vol.13(1995), pp.s01-07.
3. D.Buttler and C.Scruby, J. of Acoustic Emission, Vol.9(1990), pp.243-254.
4. C.Heiple, S.Carpenter and D.Armentrout, J.of Acoustic Emission, Vol.10(1992), pp.103-106.
5. S.McBride, J.Maclachlan and B.Paradis, J.of Nondestructive Evaluation, Vol.2(1981), pp.35-41.
6. S.McBride and J.Harvey, Review of Progress in Qualitative Nondestructive Evaluation, Vol.6A(1987), pp.353-360.
7. M.Friesel, Materials Evaluation, No.47(1989), pp.842-848M.
8. C.Scala and S.Cusland, Materials Science and Engineering, Vol.76(1985), pp.83-88.
9. I.M.Daniel, J.J.Luo, C.G.Sifniotopoulos and H.J.Chun, Review of Progress in Quantitative Nondestructive Evaluation. Vol.16(1997), pp.451-458.
10. D.Guo, A.K.Mal and K.Ono, J. Acoustic Emission, Vol. 14(1996), pp. S19-46.

SHORT AND LONG FATIGUE CRACK GROWTH BEHAVIOR IN Al-7%Si-0.4%Mg ALLOY CASTINGS

Sang-Won Han, Shinji Kumai and Akikazu Sato

Department of Materials Science and Engineering Tokyo Institute of Technology 4259 Nagatsuta, Midori-ku, Yokohama 226-8502 Japan

ABSTRACT

Crack initiation and successive short fatigue crack behavior of the peak-aged Al-7%Si-0.4%Mg alloy castings were examined using rectangular smooth bar specimens under the axial loading condition. In the ordinary dendrite structure, grain boundaries acted as effective obstruction to the growing fatigue crack. On the other hand, the effective grain of the semi-liquid die-cast was a moderate obstruction to the crack growth. Short crack growth behavior in the semi-liquid die-cast was comparable to that of the long crack. Fine effective grain structure is considered to promote homogeneous cyclic deformation at the fatigue crack tip in spite of short crack length and the corresponding small plastic zone size.

1. INTRODUCTION

Aluminum alloy castings have been increasingly used in structural applications for aircraft and automobiles. This is due to great economic advantage of casting process in reducing fabrication costs of complex structure as well as great benefits of weight reductions for saving energy and reducing exhaust gas emission[1-2].

Fatigue resistance is essential in nontraditional load-carrying use for castings. Such a demand facilitates a basic research concerning microstructure/fatigue relationship of the cast alloys.

The objective of the present study is to examine growth behavior of naturally initiated short fatigue crack. The matters of interest here are as follows. (1) Growth behavior of microstructurally short crack and effectiveness of the grain boundary as an obstruction to the fatigue crack growth. (2) Transition of growth manner from a short crack to a long crack.

2. EXPERIMENTAL PROCEDURE

2.1 Materials

Three samples with an equivalent chemical composition but with different microstructure were prepared. For convenience these materials are called Pm, HPm and SS hereafter. The permanent mold cast material is called Pm. For some Pm samples, HIP(Hot Isostatic Pressing) was performed for reducing casting defect. These HIPed samples are called HPm. The specimen SS is fabricated by semi-liquid die-cast method.

Chemical compositions of three samples are equivalent to A356 cast alloys. The castings were cut into as rectangular smooth bar specimens with shoulders (gage section: $16 \times 5 \times 4 \text{ mm}^3$). They were T6 heat treated. Figures 1(a) and (b) show the microstructure of Pm and HPm. Both of them exhibit ordinary dendrite structure. Porosities were observed at the interdendritic region in Pm. In contrast to that HPm contains very few casting defects. The average length of major axis of the porosity was about $150 \mu\text{m}$ for Pm, $10 \mu\text{m}$ for HPm. The microstructure of SS is characterized by globular cell structure and refined eutectic Si particles as shown in Fig. 1(c). For such a structure cell size was used as a parameter instead of conventional DAS(Dendrite Arm Spacing). The average cell size of SS(D_2) is larger than DAS of Pm and HPm(D_1) as shown in Table 1, but Si particles are fine and globular as shown in Fig. 1.

Another important microstructural parameter is a grain size. Figures 2(a) and (b) are optical micrographs of the anodized specimens which are available for grain size measurement. Average grain size of Pm, HPm and SS were 980, 960 and $130 \mu\text{m}$, respectively. As for SS(Fig. 2(b)), colonies consisting of several dendrite cells are recognized as units of different color tones. The EBSD analysis confirmed that misorientation exists across neighboring colonies. Therefore, we call them as “effective grains” in the sense that the colonies act as usual grains in mechanical behaviors[3, 4].

2.2 Short fatigue crack growth tests

Tests were performed in fully reversed tension-compression (at a stress ratio, $R=-1$) or tension-tension ($R=0.1$) at a frequency of 19Hz with a sinusoidal load waveform in air at a room temperature. The maximum tensile stress level employed was 80% of the 0.2% proof stress of the material for the test at $R=-1$ and 100% for the test at $R=0.1$, respectively.

2.3 Long through-thickness fatigue crack growth tests

Constant load amplitude fatigue crack growth tests were performed using compact tension (CT) specimens (thickness: 8.5mm, width: 30mm). The tests were made under sinusoidal wave-form at a frequency of 10Hz with a stress ratio of $R=0.1$.

3. RESULTS AND DISCUSSION

3.1 Effects of porosities for fatigue crack initiation

Fatigue cracks mainly initiated at porosity located at the specimen surface in Pm[5~7]. For HPm and SS, the fatigue crack initiated at Si particle/matrix interface[8, 9].

Figure 3 shows growth behavior of several short surface cracks initiated in Pm and HPm, both of which exhibited ordinary dendritic structure. For short cracks initiated from the porosity, the crack length is defined as the distance between the center of porosity and the one side of the crack tip. Therefore, the initial length of each crack(the smallest crack length data for each series of data plot) corresponded roughly to a half of porosity size. Since larger porosity is prone to be the stress riser, the resultant initial length exceeded the average porosity size. On the other hand, the minimum crack length data for HPm is the half of dominant crack length, since the dominant crack was generated from the meshy crack aggregation generated at Si particle dense region and not from the porosity. If we tentatively define the crack initiation as the fatigue cycle at which the crack length reached $200\mu\text{ m}$, as indicated in Fig.6, the fatigue life for crack initiation of HPm was about 10 times larger than that of Pm. The result confirms the effectiveness of HIPing for extending crack initiation life.

3.2 Short fatigue crack growth behavior in effective grain structure

For the specimen Pm, an example of crack growth rate(da/dN)-crack (a) relationship for a short surface fatigue crack is shown in Fig.4. The crack growth occurred repeating the growth rate acceleration and deceleration. The crack retardation at the grain boundaries was evident as indicated by No. 1 to 5 when the crack was very short, less than $1000\mu\text{ m}$. Change in crack growth rates also took place at the grain boundaries. Large growth rates were obtained when the crack propagated through the grain as marked by A and B in the figures for instance.

Figures 5 shows the da/dN -crack length relationship in SS. In-situ crack path observation during the fatigue tests revealed that such a crack deflection took place at the boundaries of effective grains. Decrease in growth rates was observed at the effective grain boundaries, however, the extent of fluctuation in growth rate was smaller than that of Pm with the ordinary dendrite structure. These experimental results suggest that grain boundaries of the ordinary dendrite structure were strong obstruction to the growing fatigue crack tip. In contrast to that, boundaries of the effective grains acted as relatively weak obstructions as well as dendrite cell boundaries.

3.3 Transition from short crack growth behavior to that of long crack

The crack growth behavior of short and long cracks in Pm and SS is shown comparatively

in Figs.5(a) and (b). For naturally initiated surface short cracks $\log(da/dN)-\log(a)$ curves are given. Both $\log(da/dN)-\log(a)$ and corresponding $\log(da/dN)-\log(\Delta K)$ curves are presented for long through-thickness cracks initiated from the notch. Fig.5(a) shows fluctuation in growth rates was observed for the crack in Pm while its length was below 3000μ m. Figure 5(b) indicates that the short surface crack in SS exhibited monotonous increase of growth rates for the crack length over about 700μ m, which is comparable to that of the long through-thickness crack. This means that surface crack in the effective grain structure behaves like a long crack regardless of its small size. The degree of growth rate retardation depends on the crystallographic orientation of the neighboring grains. The short crack which experiences little orientation mismatch at the grain boundary may propagate smoothly, and achieve growth rates comparable to those of the long crack.

Considering those experimental facts fatigue crack growth behavior in SS result from its characteristic effective grain structure. In addition to small orientation mismatch at the neighboring effective grain boundary, fine effective grain size promotes homogeneous cyclic deformation at the fatigue crack although the crack length and the corresponding plastic zone size are small.

4. CONCLUSIONS

In the ordinary dendrite structure, grain boundaries acted as effective obstruction to the growing fatigue crack. Dendrite cell boundaries also hindered the crack advance as relatively weak barriers. On the other hand, the effective grain of the semi-liquid die-casting was a moderate obstruction to the crack growth. This resulted in higher growth rates of the short crack in the semi-liquid die-cast than those of the alloy with ordinary dendrite structure. Short crack growth behavior in the semi-liquid die-cast was comparable to that of the long crack. It is considered that the fine effective grain structure promotes homogenous cyclic deformation at the fatigue crack tip although the crack length and the corresponding plastic zone size are small.

REFERENCES

1. T. Reinhart, Fatigue and Fracture Properties of Aluminum Alloy Castings, ASM Handbook, 19 (1996), pp. 813-822.
2. J. Polmear, Light Alloys, Metallurgy of the Light Metals, 2nd edition, Edward Arnold, London, (1989), pp. 144-168.
3. S. W. Han, S. Kumai and A. Sato, submitted to Materials Transactions, JIM, Vol.42, No. 2, (2000), pp. 342-349.

4. S-W Han, S. Kumai and A. Sato: Materials Science and Engineering (2001), in print.
5. M.J.Couper, A.E.Neeson and J.R.Griffiths; Fatigue Fract. Engng. Mater. Struct. Vol.13, No.2, (1990), pp. 213-227.
6. J.C.Ting, and F.V.Lawrence: Fat. Fract. Eng. Mater.Struct., Vol.16(1993), pp. 631-647.
7. B.Skallerud, T.Iveland and G.Harkegard: Eng. Fract. Mech., Vol.44(1993), pp.857-874.
8. Y.Ochi, M.Kubota: Proc. 3rd Engng. Foun Int. Conf, Hawaii (1998), pp. 215-222.
9. A. Plumtree and S. Schafer: The Behaviour of Short Fatigue Crack, Edt.Cambridge K.J. Miller, E.R. de los Rios (1986) pp. 215-227.

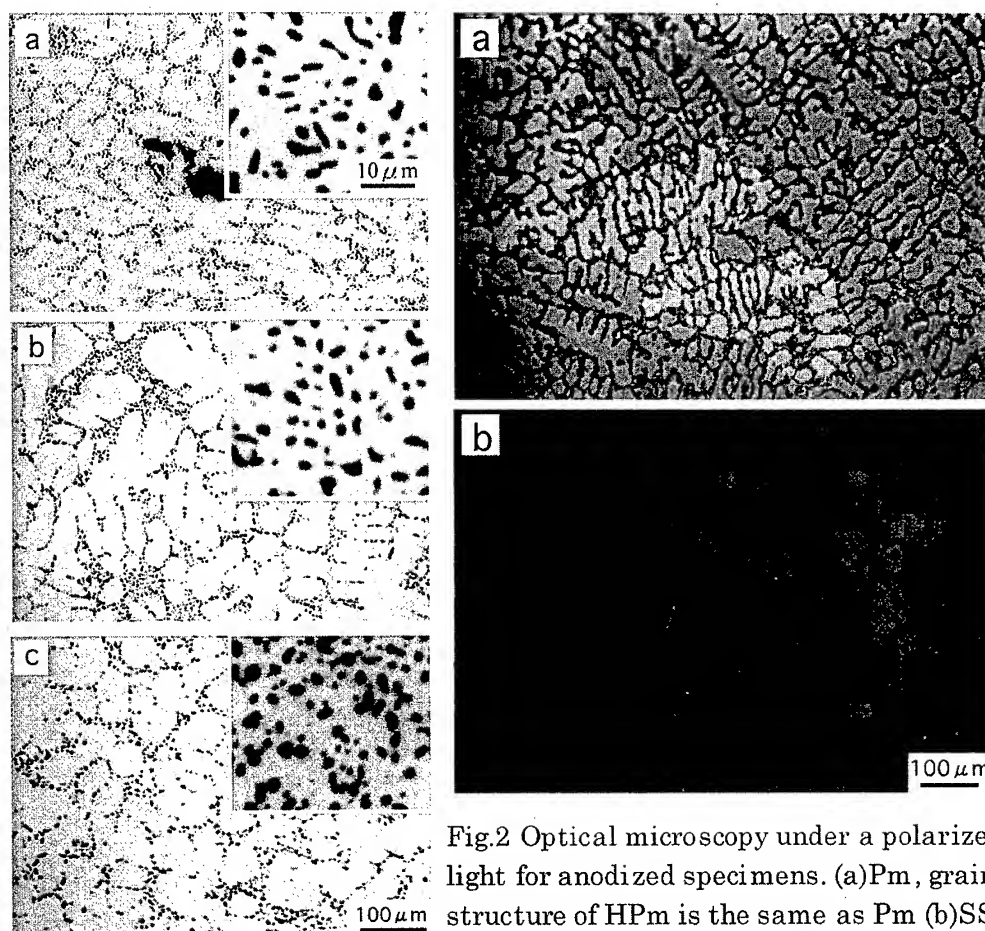


Fig.1 Optial micrographs of the A356 cast alloys (a) permanent mold cast but un-HIPed, (b) permanent mold cast and HIPed, (c) semi-liquid die-cast. High-magnification pictures in the windowsshow Si particle morphology.

Fig.2 Optical microscopy under a polarized light for anodized specimens. (a)Pm, grain structure of HPm is the same as Pm (b)SS.

Table 1 Quantitative data on microstructural factors and 0.2% proof stress, D:primary α -Al dendrite size (D_1 :dendrite arm spacing, D_2 :dendrite cell size), d:eutectic Si particle size

	Grain size(μm)	D(μm)	d(μm)	$\sigma_{0.2}$ (MPa)
Pm	980	28(D_1)	3.6	285
HPm	960	27(D_1)	3.7	236
SS	130	46(D_2)	2.5	283

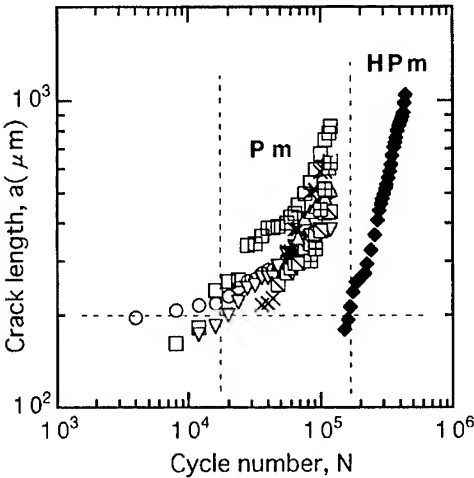


Fig.3 Growth behavior of several short surface cracks initiated in Pm and HPm

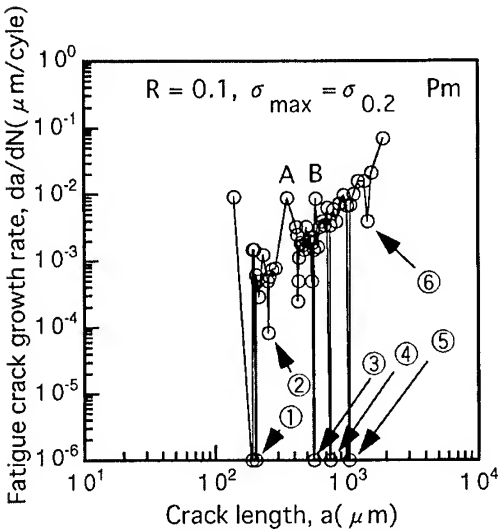


Fig.4 Relationship between the crack growth path and the crack growth rates in Pm.

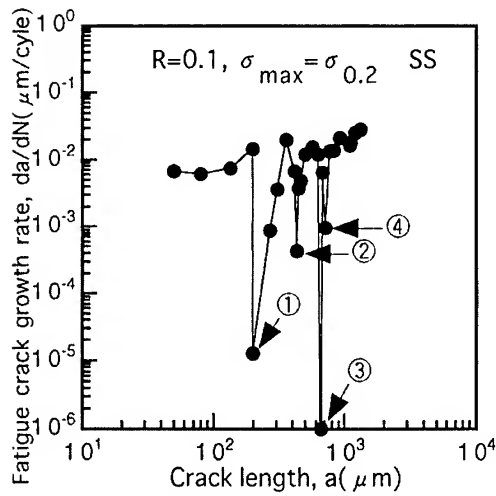


Fig.5 Relationship between the crack growth path and the crack growth rates in SS.

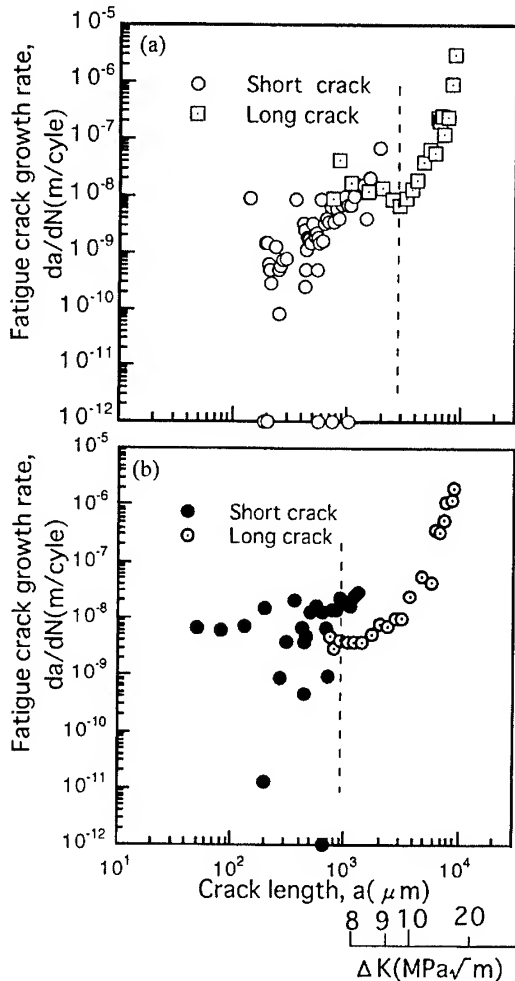


Fig.6 Transition from the short crack to long crack growth behavior in Pm(a) and SS(b)

FATIGUE CRACK PROPAGATION BEHAVIOR OF A356 SQUEEZE CAST ALLOY

Song Hee Kim* and Ki Ho Rhee

Department of Advanced Materials Science and Engineering,
Kangwon National University, Chuncheon 200-701, KOREA

* Jointly Affiliated with Center for Advanced Aerospace Materials,
Pohang University of Science and Technology

ABSTRACT

The fatigue crack closure was measured experimentally at various stress ratios(R) and the fatigue failure mechanism of A356 squeeze cast alloy was investigated. On the basis of crack closure concept, modeling the universal equations were proposed which enable us to predict the fatigue crack growth rate(da/dN), regardless of stress intensity factor range(ΔK) and stress ratio(R) and was compared to Newman's Equation. Surface examination were proposed on different stage of crack growth(near-threshold region, Paris region, final rupture) to model the fatigue failure mechanism. The fatigue crack prefers to propagate through the dendrite cell transgranularly in the near-threshold region. While in the Paris region, the fatigue crack followed the interdendrite cell. Cracking of the eutectic Si worked as an initiate site for the formation of dimple in final rupture.

1. INTRODUCTION

The Al-Si-Mg alloys are widely used as cast form in automotive and aircraft industries because of its excellent castability, good resistance to corrosion and high strength. In designing and using of such materials, fatigue phenomenon is mostly considered. Since many structural components are subjected to random loading rather than constant amplitude loading, it is very important to understand the fatigue crack growth behavior and to propose a way to predict the fatigue crack growth rate at various conditions.

In our early work[1,2], we have purpose an universal equation from effective stress intensity factor range ratio(U) and fatigue crack closure concept based on Elber proposed law(Equation 1). Regarding crack closure concept on fatigue crack growth rate, Elber[3,4] has

modified Paris and Erdogan's equation by introducing crack closure(Equation 1) and defined the effective stress intensity factor range ratio, U as below(Equation 2)

$$da/dN = C(U\Delta K)^n = C(\Delta K_{eff})^n \quad (1)$$

$$U = (K_{max} - K_{cl})/(K_{max} - K_{min}) = (\sigma_{max} - \sigma_{cl})/(\sigma_{max} - \sigma_{min}) \\ = (1 - (\sigma_{cl}/\sigma_{max}))/ (1 - R) \quad (2)$$

Other work like Newman model, is concerned with the development and application of an analytical model of cyclic crack growth that includes the effects of crack closure[5,6]. So our predicted universal equation results are compared to Newman equation results for investigation and further modification. Because there have been some limits in prediction of crack growth rate at variable stress ratios and amplitudes such as unfitting predicted data in near-threshold regions.

Finally, fatigue crack propagation was investigated to model the fatigue failure mechanism of A356 squeeze cast alloy.

2. EXPERIMENTAL MATERIALS AND PROCEDURES

Modified A356 alloy was supplied by CSIRO Divison of Manufacturing Technology in the form of step plate. The chemical composition of the alloy is shown in Table 1. The plates were manufactured by squeeze casting technique to produce near-net-shape high-quality components. Then solution heat treated at 540°C for 18 h, quenched in water at room temperature, pre-aged at room temperature for 20 h and aged at 170°C for 6 h in a salt bath. The average dendrite cell size is 40µm.

Table 1. Chemical composition of A356 alloy.

Element	Al	Si	Mg	Fe	Sr	Ti	Cr, Cu, Mn, Ni, Zn, Zr
wt%	bal.	7.0	0.36	0.08	0.024	0.01	< 0.01

Compact-Tension specimens were used for fatigue crack growth rate tests and ASTM E647-88 was referred to for calculating stress intensity factor. Sinusoidal loading of 20 Hz was applied at $R=0.1, 0.3, 0.5$ by using the MTS 810 servo-hydraulic dynamic testing machine. Fatigue cracks were measured by traveling microscope with a 0.01 mm minimum scale. Strain gauges with 5mm gauge length were used to measure crack closure by attaching the gauge onto the specimen surface in front of the crack tip on various ΔK and R . From the

results of load-displacement curve by X-Y recorder, K_{cl} and K_{op} were gained.

. On prediction modeling of universal equation of U , regression analysis was used. Fatigue crack growth rate was predicted with the consideration of a function of effective stress intensity factor range (ΔK_{eff}). Fracture toughness, K_{IC} was measured to compare predicted da/dN equation with Newman equation. Specimen surface and fracture surface was examined by optical microscope and SEM on different fatigue failure region (near-threshold region, Paris region, and final rupture.)

3. RESULTS AND DISCUSSION

The crack closing stress (σ_{cl}) and crack opening stress (σ_{op}) was measured from load-displacement curve and the relationship of K_{cl}/K_{max} vs. ΔK is presented on various stress ratios in Figure 1. Therefore, the change in U with ΔK could be easily re-plotted as in Figure 2 by referring to Equation 2. The effective stress intensity factor range (U) was obtained empirically, using linear relationship between U and ΔK . Equation of linear regression is as below.

$$U = A + B \Delta K \quad (3)$$

Where A and B are known to be polynomial functions for variable stress ratios, after the regression from the plotting A and B against stress ratios. Thus U becomes a function of R and ΔK , and the relationship between U , ΔK and R were obtained as Equation 4.

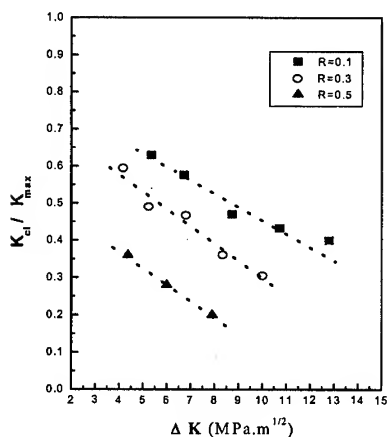


Fig.1. The relationship of ΔK vs K_{cl}/K_{max} for various R .

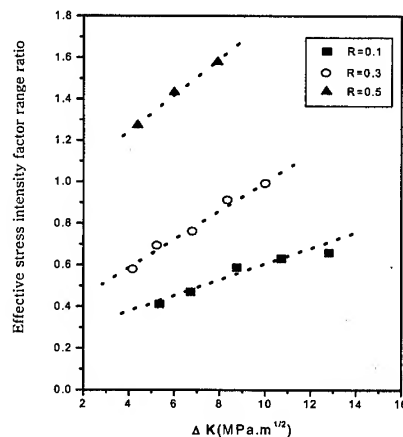


Fig.2. The relationship of U vs ΔK for various R .

Therefore effective stress intensity factor range ratio(U) is now predictable for various stress intensity factor range(ΔK) and stress ratios(R) on the basis of crack closure concept.

Figure 3 shows a comparison between experimental fatigue crack growth rates and crack growth rates calculated by Equation 1 from the results of Equation 4. The dash lines show factor-of-2 bands about the perfect agreement line. Most of the data fitted well within these bands except for very high or low crack growth rates. Figure 4 shows a comparison between experimental fatigue crack growth rates and crack growth rates calculated by Newman Equation.

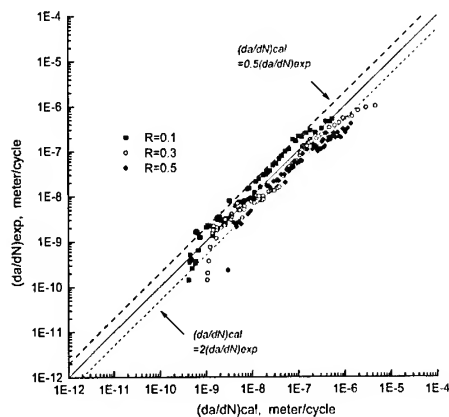


Fig.3. Comparison of experimental and calculated crack growth by predicted equation.

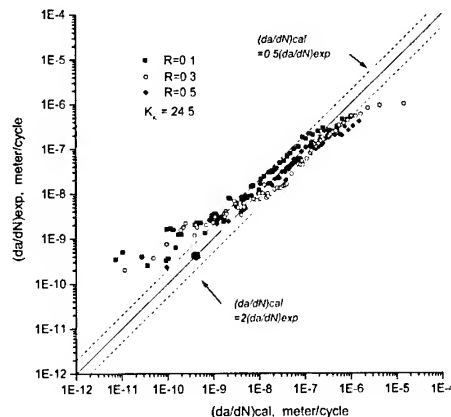


Fig.4. Comparison of experimental and crack growth by Newman equation

Fatigue crack propagation was investigated by optical microscope and SEM. The fatigue crack prefers to propagate through the dendrite cell transgranularly at the near-threshold region. Eutectic Si segregated on the dendrite cell boundary seems to link (arrow mark) the crack path propagating through the matrix (Figure 5-a). While in the Paris region, the fatigue crack followed the inter-dendrite cell (Figure 5-b). Branching of fatigue crack can be clearly observed (arrow mark) which also propagates along the dendrite cell boundary.

Figure 6 is the SEM micrographs of fatigue fracture surfaces at different fatigue propagate regions (near-threshold region, Paris region, final rupture). In Figure 6-a, debonding of Si particles can be observed and the distance of each eutectic Si seems to match the near net-shape of the dendrite arm spacing. While in Figure 6-b, clustered fractured Si particles are

observed(circle line) with rough surface corresponding to the inter-dendrite propagation. *Figure 6-c* shows the dimple fracture of A356 alloy. In each dimple, fractured eutectic Si is observed as being an initiate site for the final rupture. High volume fraction of fractured Si particles is considered to be the result of cracking of Si particle in the dendrite cell boundary since average dendrite arm spacing is 40um. Fatigue crack propagation mechanism of A356 alloy is illustrated at *Figure 7*.

4. CONCLUSION

By obtaining the relationship between da/dN vs. ΔK_{eff} it has been possible to predict da/dN in squeeze cast A356 alloy regarding crack closure concept for the variation of ΔK and R . The predicted equation model agreed well with experimental data and Newman model. The fatigue crack propagation mechanism of squeeze cast A356 alloy has been organized.

REFERENCE

1. S.H. Kim et al., J. Kor. Inst. Met. & Mater., Vol.36, No.8 (1998), pp. 1285-1289.
2. S.H. Kim and Young Ik Park, Metals and Materials, Vol.6, No.2 (2000), pp.133-138.
3. W. Elber, Eng. Fracture Mech., Vol.2, No.1 (1970) p.37-45.
4. W. Elber, ASTM STP 486 (1971) pp.230-242.
5. J.C.Jr. Newman, ASTM STP 605 (1976) pp.104-123.
6. J.C.Jr. Newman, ASTM STP 748 (1981) pp.53-84.

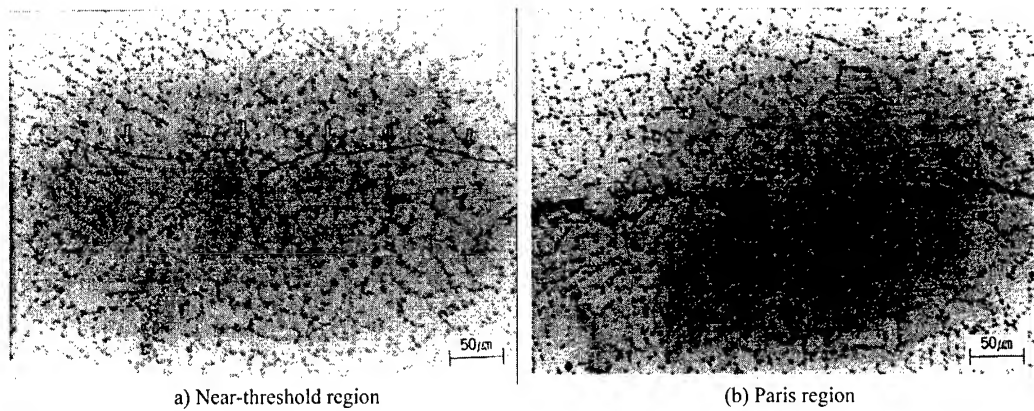


Fig.5. Optical micrographs of fatigue crack propagation path. ($\times 100$)

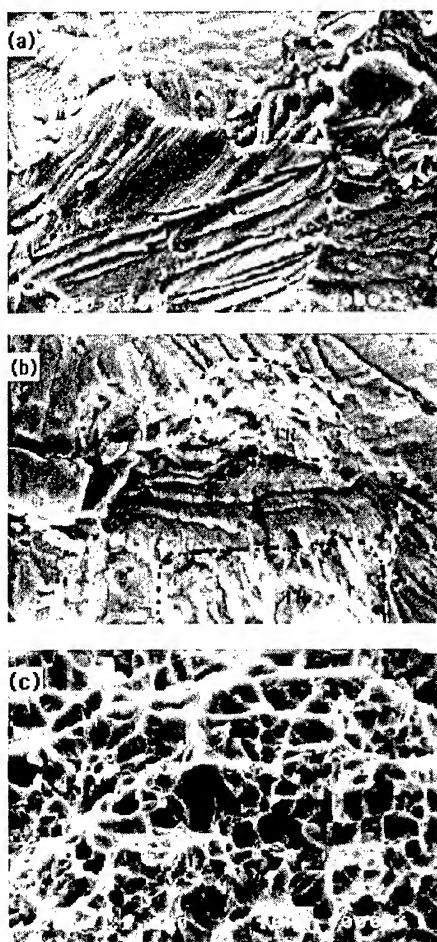


Fig.6. SEM images of fatigue fractured surface.
(a) near-threshold region (b) Paris region (c) Final Rupture

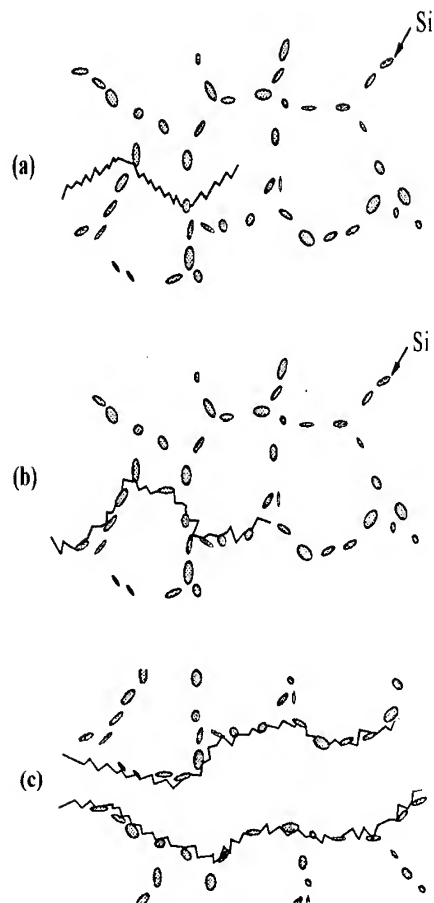


Fig.7. Schematic illustration model of fatigue crack propagation (near-threshold region \rightarrow final rupture)

Session VIII

INTERMETALLICS

GAMMA TITANIUM ALUMINIDES: ALLOYS, PROCESSING & SCALE-UP

Dennis M. Dimiduk, Harry A. Lipsitt* and Martin J. Blackburn†

Air Force Research Laboratory, Materials and Manufacturing Directorate
AFRL/MLLM, 2230 Tenth Street, Wright-Patterson AFB, OH 45433-7817

*Professor Emeritus, Wright State University, Dayton, OH 45435

†Department of Metallurgy & Materials Engineering, University of Connecticut,
Storrs, CT 06269-3136

ABSTRACT

The development and use of intermetallic alloys in aerospace has been very slow and difficult. The reasons for are briefly discussed in this manuscript, concentrating on the potential use of titanium-aluminide alloys in high-performance systems. Future growth of turbine engines and transportation systems depends upon the continued development of high-temperature, light-weight materials. It has been suggested that intermetallic alloys could contribute to the required efficiency gains. However, one must remember in making such a suggestion the new alloys are competing with well established current materials of construction that exhibit balanced properties, and intermetallic alloys are not simple extensions of conventional alloys. The properties of gamma depend strongly on the processing method selected to make components. Cast gamma alloys are not yet fully commercialized in part because of the uncertainty in property-related performance benefits and the cost of parts. Wrought gamma alloys show greater performance benefits on a laboratory scale, but there is no complete and demonstrated commercial-scale technology. The laboratory-scale demonstration of an attractive balance of alloy properties suggests there could be revolutionary opportunities for weight reduction, and perhaps increased operating temperatures in aerospace systems, but at a price. This price includes building new or refined design approaches, and an involved, time-consuming, and expensive sequence to build confidence in the reproducible performance of the material. The next decade should bring a systematic reduction of cost for gamma-alloy parts as familiarity builds and more are produced.

1. INTRODUCTION

Gamma titanium-aluminide alloys may be useful in a variety of structural applications in transportation and power generation systems [1,2]. The remarkable balance of properties offered by selected gamma alloys, together with projections for competitive costs, suggest that application of these alloys should continue to build. This manuscript provides a brief review of current alloy compositions, processing and scale-up status, and uses this information to identify some aspects of the technology that have made commercialization difficult. The examination suggests that gamma alloys are a potentially viable class of titanium alloys, the introduction of which is paced by the world-wide business climate, an incomplete design methodology, and a lack of production maturity. Further insights into these issues may be found elsewhere [3,4].

Why has the commercialization of gamma titanium aluminides been so slow? Why has it not happened in the traditional high-technology leading field of aerospace? Much application activity has been focussed on the potential use of these alloys in high-performance propulsion and power generation systems. Numerous successful prototype hardware demonstrations illustrate the viability of the materials technology [1,2,5,6]. Test results confirm the real potential to increase operating temperatures and reduce weight. However, many factors must be weighed before a new structural material is certified for use in an engineering system, and gamma alloys exhibit some characteristics that have delayed acceptance in the design and manufacturing com-

munities. These factors require a complex balancing between performance, affordability, and reliability. Further, it should be emphasized that reparability and field maintenance are important in life-cycle costs and present some special challenges for gamma alloys. In the present business-climate a quantifiable benefit for any technology investment is required from the outset. Often this is associated with a performance improvement based on increased properties, but cost reduction and reliability increases are becoming equally important drivers and combinations of improvements makes for a more compelling incentive.

Performance, affordability and reliability metrics depend on the specific end use for the material. For example, the application of gamma alloys in automotive engine turbocharger rotors involves only modest challenges to the material from the aspects of performance (properties) and reliability, but quite serious restrictions for cost. The cost factors impose a reliability requirement since a recall to repair or replace defective components can be extremely expensive.

The properties of the gamma alloys strongly depend on processing (cast, wrought etc.) and the specific levels achieved can set constraints on applicability. All gamma alloys exhibit low (but useful) ductility and a low cleavage stress, and the levels seem relatively insensitive to alloy composition. It seems unlikely that further research will substantially improve these properties. However, recent research at the laboratory-scale has demonstrated an attractive and improved balance of properties including ductility and toughness levels at the upper end of the range. This material may offer the revolutionary opportunities for weight reduction, and perhaps increased operating temperatures long sought in aerospace systems, but at a price. Part of this price will be continued refinement of design approaches, coupled with an involved, time-consuming, and expensive sequence to calibrate the design systems and to build confidence in the material. A second factor will be the need for robust, reproducible and larger scale manufacturing methods to make components—another expensive proposition.

2. ALLOYS AND PROPERTIES

Promising engineering alloys are emerging that have a good balance of physical and mechanical properties, and some of these are listed in Table I. Although called gamma alloys, they are in

TABLE I: ENGINEERING GAMMA ALLOYS AND THEIR COMPOSITIONS

ALLOY NAME	COMPOSITION (ATOMIC PERCENT)	BEST ATTRIBUTES	WEAKNESSES
4822:	Ti-47Al-2Nb-2Cr	Ductility, Fracture Toughness	Strength, Creep Resistance
45XD:	Ti-45Al-2Nb-2Mn-0.8vol%TiB ₂	Tensile & Fatigue Strength, Castability	Creep Resistance
47XD:	Ti-47Al-2Nb-2Mn-0.8vol%TiB ₂	Elevated Temp. Strength, Castability	Creep Resistance
WMS:	Ti-47Al-2Nb-1Mn-0.5W-0.5Mo-0.2Si	Creep Resistance	Ductility
ABB-2:	Ti-47Al-2W-0.5Si	Creep & Oxidation Resistance	Ductility, Toughness
TAB:	Ti-47Al-1.5Nb-1Mn-1Cr-0.2Si-0.5B	Castability, Property Balance	
IRC:	Ti-44Al-4Nb-4(Zr,Hf)-1B-0.2Si	Strength	
Daido:	Ti-48Al-2Nb-0.7Cr-0.3Si	Ductility	
IHI:	Ti-44.8Al-1.3Fe-1.1V-2.4B	Castability	Strength, Creep Resistance
3-95:	Ti-47Al-2Nb-2Cr-1Mo-0.2B	Creep Resistance, Wrought Processing	Oxidation Resistance
ONERA	Ti-47.3Al-1.0Re-1.0W-0.24Si	Castability	Strength, Creep Resistance
K5:	Ti-46.2Al-3Nb-2Cr-0.2W-(0.1-0.2B)-0.2C	Wrought Processing, Oxidation Resistance, Property Balance	

fact two-phase alloys, wherein the primary phase is γ -TiAl, and the second phase is α_2 -Ti₃Al. The aluminum contents of these alloys falls within the range of 44 to 48 atomic % Al, and the alloys contain other elements to enhance their performance. It is not possible to list all of the alloys currently under development, but those shown in Table I have achieved some level of application testing. With the exception of the IHI alloy, their compositions range within Ti-(44-48)Al -(0-2)Cr, Mn -(0-10)Nb -(0-4)Zr,Hf -(0-2)W,Re -(0-1)Mo -(0-1)B -(0-0.5)Si -(0-0.2)C. The major roles of Al are to vary strength and oxidation resistance, the former increasing and the latter decreasing as the Al-content decreases. Cr and Mn appear to increase ductility within the range specified, while the rest of the major alloying elements tend to reduce the ductility. The elements Cr, Mo, W, and Re promote β -phase formation, the importance of which is controversial and not well established. Nb, W and Si improve oxidation resistance, with Nb becoming synergistically more effective with W additions. Carbon is the most effective creep strengthener when it is present in the form of appropriately distributed carbides. Various methods of grain refinement exist; the most effective for both cast and wrought alloy microstructures being B additions. While some merits and disadvantages of most of the alloys in Table I are discussed elsewhere [7], it is important to recognize that only a few of these exhibit strength and creep-resistance levels that are particularly attractive to aerospace designers.

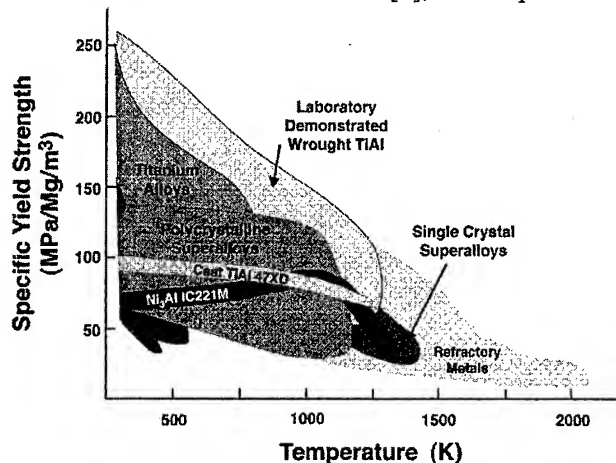


Figure 1. Specific yield strength versus temperature for gamma alloys and selected structural alloy classes.

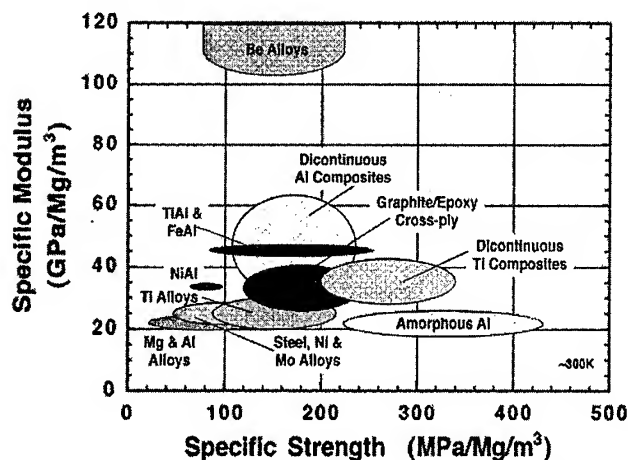


Figure 2. Specific modulus versus specific strength for a variety of structural materials, including gamma alloys.

2.1 Strength

Figure 1 shows broad bands of specific-yield strength versus temperature for structural alloys and gamma alloys. The best gamma alloys listed in Table I fall between the band shown in Fig. 1 for 47XD and the upper band for laboratory-scale wrought alloys; some alloys are actually below the 47XD band. It is clear from Fig. 1 that on the basis of specific-yield strength, most gamma alloys (especially most cast alloys) are likely to only serve in selected niche applications where they may offer a temperature or weight advantage over Ti and Ni alloys. Alternatively, the strengths achieved for wrought alloys are competitive on a direct basis, being in the range from 750 to 1050 MPa, and are quite outstanding on density-normalized basis, especially at high temperatures. However, to date these alloys have not been produced in quantities that are meaningful to the production of aerospace hardware, thus the performance potential for wrought alloys awaits production scale-up. Following production scale-up, there must be product development and testing that leads to designer confidence and, hopefully, material use.

Figure 2 shows a cross plot of the domains of specific-modulus versus specific strength (yield strength for ductile alloys, fracture or ultimate strengths for non-ductile materials) for a variety of structural materials, following Ashby. While some of the materials shown are experimental, the figure shows both a potential advantage for gamma alloys, and the fact that competing materials exist at this (~ 300 K) and other temperatures.

2.2 Ductility and Toughness

About four years ago the view emerged that failure processes in gamma alloys are dominated by the grain size, especially for lamellar microstructures in the absence of defects. Apparently, lamellar microstructures inherently constrain the cleavage-crack initiation size, perhaps by reducing the effective multiplicity of cleavage planes, relative to duplex microstructures. Further, knowledge gained over the last few years about processing and phase transformations became sufficient that the grain size could be reliably controlled in experimental lamellar materials at the laboratory level by thermomechanical processing (TMP) [8, 9]. Such control of lamellar microstructures tends to mitigate the effects of the "inappropriately oriented" lamellar colony which nucleates the failure process. These discoveries now make exploitation of the improved balance of properties for lamellar microstructures a practical reality. More recently, research has shown that the lamellar alloy strength has an extreme sensitivity to grain size and lamellar spacing [10]. Together, the two findings (ductility and strength sensitivity to grain size) indicate the possibility for a whole new class of gamma alloy technology, provided that grain size and lamellar spacing may be controlled in full-scale production hardware.

Research by Appel et al. [11], has shown that by control of both grain size and nearly-lamellar microstructures, one may develop a high-Nb gamma alloy having a room-temperature strength of greater than 1000 MPa and a plastic elongation greater than 2.5 %. Strengths drop only modestly through about $\sim 800^\circ\text{C}$. However, modern mechanical design demands control of fracture properties for structural materials used under both static and cyclic conditions, and usually at high temperatures. These properties directly set the limitations that must be considered in design with the material, even more so than the uniaxial yield strength. Thus, when measured, only the creep resistance and cyclic properties will reveal the useful advantage of these alloys.

2.3 Cyclic Properties

The challenge for the immediate future of gamma alloys is to build the knowledge of durability and life-limiting behavior under fatigue conditions while maturing component design approaches that have such knowledge at their foundation. Two key areas require focused study; i) the microstructural and metallurgical aspects of long-crack growth thresholds, and ii) the behavior of short-cracks having lengths below or comparable to the grain size under high-cycle fatigue environments [12,13]. A convenient insight into the use of threshold data for gamma alloys is depicted through the "Kitagawa Diagram" [14]. Such a graphical representation of durability and fatigue performance provides immediate feed-back to the development strategy by highlighting such important parameters as crack length in distinguishing regimes of mechanistic behavior. These alloy properties must also be reconciled with non-destructive evaluation capabilities to establish a design system for particular hardware.

2.4 Impact Resistance

The impact resistance of gamma alloys is generally poor. While these materials usually do not shatter into a large number of fragments during impact testing, the impact energy is measured at about 1 J. Such a low impact energy will continue to limit opportunities for hardware design. Further, there are no systematic studies of microstructural effects on impact energy for modern alloys. Such information is necessary to complete a design system for using gamma alloys. Thus, this topical area stands out as one needing further research.

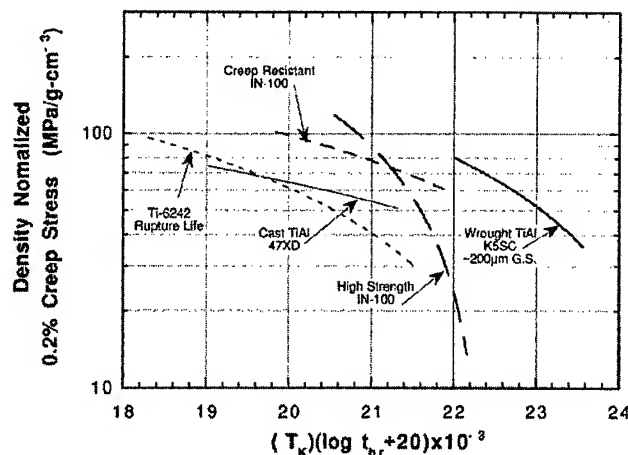


Figure 3. Specific creep stress versus Larson-Miller parameter for two gamma alloys, a titanium alloy, and two forms of a common superalloy.

Improved creep resistance centers on introducing carbide precipitation, and/or enrichments in Nb to levels of about eight atomic percent. Ultimately, the creep performance of these alloys must be compared to modern powder-metallurgy superalloys since those are the pertinent competitors. Unfortunately, since most modern superalloy data is proprietary, such comparisons are not made here.

2.6 Environmental Properties

The oxidation behavior of TiAl is intermediate between that of conventional Ti alloys and of Ni base superalloys. The most recent laboratory investigations indicate that alloying can significantly reduce weight gain during oxidation of gamma alloys. The best gamma alloys oxidize about twice as fast as Ni-based alloys at temperatures as high as 870°C [15-17]. However, the hot corrosion (sulfidation) resistance of gamma base alloys has had only limited study [18]. Clearly, as the temperature capability as set by the ability to carry load increases through composition selection and microstructural control, simultaneous evaluations of the environmental properties must be carried out to establish accurate temperature limitations for these materials.

3. SCALE-UP ISSUES

3.1 Wrought Products

Large-scale melting of gamma alloys is not fully implemented, but is under development. Initial attempts at large-ingot making (43-66 cm dia.) via the Plasma Arc Melting (PAM) process indicate that segregation and other defects may be a problem [19]. Among the defects observed were centerline porosity and/or pipe formation, grain size disparities, and high- and low-density regions related to insufficient melt homogenization. Examples of such inclusions are shown in Fig. 4. Qualitatively, both the macrostructures and microstructures obtained from various ingot processes are similar, presenting the same challenges in thermomechanical processing. Microstructures are both macroscopically and crystallographically textured as a result of the heat flow during solidification and the crystallographic constraints on the solid-state transformations. The structure is further complicated by dendritic segregation that results in interdendritic Al-rich, gamma-phase regions. While the residual beta-phase particles present no difficulty in subsequent processing, the Al-rich interdendritic gamma phase places severe constraints on the

2.5 Creep Resistance

The density-normalized high-temperature strength properties of the aluminides, as a function of the Larson-Miller parameter for creep rupture, are shown in Fig. 3 with those for selected other structural alloys. Gamma alloys offer competitive or improved creep properties over titanium alloys at temperatures above ~650°C. Current developments place an upper temperature limit for long-term use of gamma alloys at <800°C. However, laboratory investigations hold promise for raising the service temperature to at least 840°C in the near future, with the ultimate limit somewhat undefined from the current research base.

Development of alloys having im-

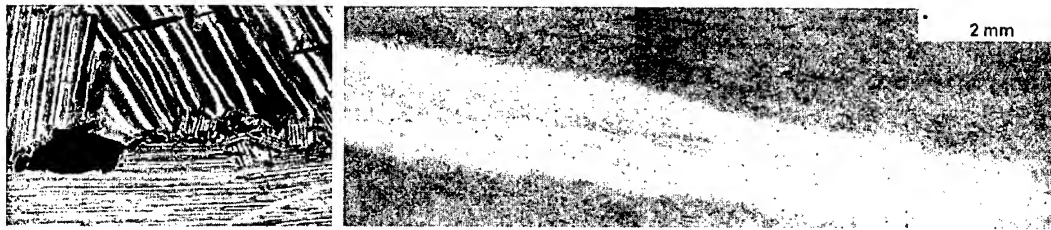


Figure 4. Examples of two defects found in a 43 cm dia. PAM ingot of a Ti-47Al-2Nb-1.5Cr-0.5Mo-0.2B gamma alloy. On left is a grain boundary pore; on right is a large high-density inclusion. These defects indicate a need for development of primary melting.

process window if banded structures are to be avoided that have been shown to exhibit poor properties [20].

Gamma alloys are, in general, processed using conventional titanium-alloy foundry practices, with one major exception. For gamma alloys, thermal control is much more critical, particularly at ingot surfaces. Thus, hot working is conducted either isothermally, or after encasing the ingots in a thermally protective can. Numerous investigations have established ingot break-down, isothermal forging, nonisothermal forging, sheet rolling, and superplasticity; the reader is referred to the broad literature for detailed discussions and reviews [20-22]. Processing scale-up efforts are backed by knowledge of failure mechanisms and failure criteria built from studies of process-induced defects as a component of microstructure [20]. Recently, heat transfer and grain-growth kinetic analyses provided a quantitative basis for controlling grain size and lamellar transformation products at useful material size scales. While the progression of technical challenges and scale-up continue to be addressed for wrought processing, the general constraints are established for selected mill products, including sheet. Fabrication, joining processes and efficient industrialization of products require several years of development.

Powder metallurgy (P/M) processing methods have been used for small-scale gamma technology development since at least the 1970's. However, there are several remaining problems, such as powder quality control, and production-scale equipment is currently not available [23]. The difficulties in obtaining homogeneous, fine-grain, large-width preforms using today's ingot processing technology, indicate that P/M preforms may provide an advantage in producing gamma alloy rolled sheet in large widths. Further, in the long term, the need for grain-size control may require the use of powder-metallurgy processing for high-durability material—a prospect that may not be viewed favorably in the cost-conscious business environment.

3.2 Cast Products

Cast gamma alloys also have a long and reasonably-successful history. Literally tens-of-thousands of cast parts have been produced and tested [24]. However, by-and-large, scale-up issues persist and there is remaining uncertainty over the performance, affordability, and reliability of manufactured cast products. This is especially true for aerospace-grade components. Figure 1 suggests that the alloys have only a minimal competitive advantage over conventional metal alloys. Experience has shown that grain refinement provides an advantage, but alloys and processes for refining grains are not widely commercially available. Further, the cost of machining components has not significantly changed, especially where hole drilling is concerned; this alone can lead to gamma alloys failing in the business environment. New processes that achieve even closer to net shape parts should be explored.

Cast shop technology relies on cheap sources of remelt stock. Small-diameter ingots, generally from 10-20 mm diameter, are required for investment casting. Recently this material was produced at a price of ~\$40/kg; however, a lack of a production market place seems to have caused an erosion of low cost material availability. For conventional titanium castings, ingot is gener-

ally converted from large diameter VAR ingots via thermal-mechanical processing, such as swaging or extrusion. These processes are currently not cost-effective for gamma remelt stock, so casting ingot is usually remelted and poured into steel or graphite molds of the appropriate size utilizing a cold-wall crucible VAR furnace (VAR pour). Induction-scul remelting (ISM) is the preferred method for melting and casting of smaller quantities.

Other casting processes currently being applied to produce gamma-alloy components include the ISR melting + counter-gravity casting process practiced by Daido Steel and Howmet [2, 24]. This process has the potential to have greater control over fill rates of molds versus conventional gravity casting, and the benefit of bottom filling molds, which tends to reduce turbulence related casting defects. The process has been implemented on limited production basis for turbocharger impellers [2]. In addition to investment casting, the Howmet Corporation has developed a gravity metal mold (GMM) process which utilizes a permanent metallic mold to form the casting, rather than an invested ceramic mold. This process appears advantageous for simple component shapes in fairly high volume applications. Because this process eliminates many of the process steps related to creating and removing invested ceramic molds, it should lead to cost reductions of between 15% - 40% versus investment casting, especially for components which require significant machining, such as automotive valves [25].

Today, the major barriers to production and use of gamma-alloy cast components are primarily remelt ingot cost, dimensional conformance control, and establishing a mature vendor base. Dimensional control of investment cast gamma-alloy components is similar to capabilities for other investment cast product. However, due to the limited room-temperature ductility of gamma alloys, cold straightening of components to achieve precise dimensions for aerodynamic shapes is not practical. Hot straightening techniques have been developed, but there are persistent cost concerns over their use.

4. SUMMARY & CONCLUSIONS

While not explicitly discussed herein, a general deficiency of funds for transitioning technologies to production has made it increasingly difficult to move gamma alloys from the laboratory to production. As discussed previously, the world-wide aerospace business community has changed its focus toward addressing the acquisition and life-cycle costs associated with engineering technologies, more than material performance. Gamma alloys are viable, but their introduction is paced by the emerging design knowledge for low ductility alloys, and by the lack of a full-scale production technology. To date, thousands of automotive valves and turbochargers have been made by casting methods and tested throughout the US, Japan and Europe, using both permanent-mold and investment casting processes. This accumulating experience indicates that gamma alloy casting technology holds significant promise when the business conditions are right for implementation. When the status of the development of gamma alloys and their progress toward full commercialization is examined, it is apparent that applying similar arguments to other new alloy possibilities would suggest that a great deal of development work is needed.

5. REFERENCES

1. C.M. Austin, T.J. Kelly, K.G. McAllister, and J.C. Chesnutt, in Structural Intermetallics 1997, ed. M.V. Nathal, R. Darolia, C.T. Liu, P.L. Martin, D.B. Miracle, R. Wagner, and M. Yamaguchi (TMS, Warrendale, PA, 1997), 413-425.
2. T. Tetsui, in Gamma Titanium Aluminides 1999, ed. Y-W. Kim, D.M. Dimiduk, and M. Lorretto (TMS, Warrendale, PA, 1999), 15-24.
3. H.A. Lipsitt, M.J. Blackburn, and D.M. Dimiduk, in Intermetallic Compounds Principles and Practice Vol. 3, ed. J.H. Westbrook and R.L. Fleischer, (Wiley, New York, NY, 2001), in press.

4. D.M. Dimiduk, Mater. Sci. and Engr. A, **A263**, 1999, p. 281-88.
5. Smarsley, in Structural Intermetallics 2001, submitted for publication.
6. P.A. Bartalotta and D.L. Krause, in Gamma Titanium Aluminides 1999, ed. Y-W. Kim, D.M. Dimiduk, and M. Lorretto (TMS, Warrendale, PA, 1999), 3-10.
7. D.M. Dimiduk, P.A. McQuay, and Y-W Kim, in Titanium '99 Proceedings of the Ninth World Conference on Titanium, St. Petersburg, Russia, June 1999, in press.
8. Y-W. Kim and D.M. Dimiduk, in Structural Intermetallics 1997, ed. M.V. Nathal, R. Darolia, C.T. Liu, P.L. Martin, D.B. Miracle, R. Wagner, and M. Yamaguchi (TMS, Warrendale, PA, 1997), p. 531-43.
9. P.A. McQuay, D.M. Dimiduk, and Y-W. Kim, US Patent No. 5,417,781, 23 May
10. D.M. Dimiduk, P.M. Hazzledine, T.A. Parthasarathy, S. Sriram, & M.G. Mendiratta, Metall. Trans A, **29A**, 1998, p. 37-47.
11. Appel, in Structural Intermetallics 2001, submitted for publication.
12. A.H. Rosenberger, B.D. Worth, and J.M. Larsen, in Structural Intermetallics 1997, ed. M.V. Nathal, R. Darolia, C.T. Liu, P.L. Martin, D.B. Miracle, R. Wagner, and M. Yamaguchi (TMS, Warrendale, PA, 1997), p. 555-62.
13. B.D. Worth, J.M. Larsen, and A.H. Rosenberger in Structural Intermetallics 1997, ed. M.V. Nathal, R. Darolia, C.T. Liu, P.L. Martin, D.B. Miracle, R. Wagner, and M. Yamaguchi (TMS, Warrendale, PA, 1997), p. 563-69.
14. J.M. Larsen, A.H. Rosenberger, B.D. Worth, K. Li, D.C. Maxwell, and W.J. Porter, in Gamma Titanium Aluminides 1999, ed. Y-W. Kim, D.M. Dimiduk, and M. Lorretto (TMS, Warrendale, PA, 1999), 463-472.
15. L. Singheiser, W.J. Quadakkers, and V. Shemet, in Gamma Titanium Aluminides 1999, ed. Y-W. Kim, D.M. Dimiduk, and M. Lorretto (TMS, Warrendale, PA, 1999), p. 743-752.
16. M. Yoshihara, and Y-W. Kim, in Gamma Titanium Aluminides 1999, ed. Y-W. Kim, D.M. Dimiduk, and M. Lorretto (TMS, Warrendale, PA, 1999), p. 753-760.
17. M. Yoshihara, and Y-W. Kim, in Proceedings from High Temperature Corrosion-2000, 2000, in press.
18. G.T Dowling and T.R. Bieler, in Gamma Titanium Aluminides 1999, ed. Y-W. Kim, D.M. Dimiduk, and M. Lorretto (TMS, Warrendale, PA, 1999), 775-782.
19. W. John Porter, III, Y-W. Kim; K. Li; A.H. Rosenberger; and D.M. Dimiduk, in Structural Intermetallics 2001, submitted for publication.
20. D.M. Dimiduk, P.L. Martin, and Y-W. Kim, Mater. Sci. Engr., **A243**, 1998, 66-76.
21. S.L. Semiatin, in Gamma Titanium Aluminides 1999, ed. Y-W. Kim, D.M. Dimiduk, and M. Lorretto (TMS, Warrendale, PA, 1999), p. 509-24.
22. H. Clemens, N. Eberhardt, W. Glatz, H-P. Martinz, W. Knabl, and N. Reheis, in Structural Intermetallics 1997, ed. M.V. Nathal, R. Darolia, C.T. Liu, P.L. Martin, D.B. Miracle, R. Wagner, and M. Yamaguchi (TMS, Warrendale, PA, 1997), p. 277-86.
23. U. Habel, C. F. Yoltan, and J.H. Moll, in Gamma Titanium Aluminides 1999, ed. Y-W. Kim, D.M. Dimiduk, and M. Lorretto (TMS, Warrendale, PA, 1999), p. 301-308.
24. McQuay, in Structural Intermetallics 2001, submitted for publication.
25. P.A. McQuay and D. Larsen, in Structural Intermetallics 1997, ed. M.V. Nathal, R. Darolia, C.T. Liu, P.L. Martin, D.B. Miracle, R. Wagner, and M. Yamaguchi (TMS, Warrendale, PA, 1997), p. 523-29.

ADVANCES IN SYNTHESIZING METHODS OF Ti-BASED INTERMETALLICS FROM ELEMENTAL POWDERS

H.S. Park¹, Y. Wu², Y. Park², D. Lee², and S.K. Hwang^{2,3}

¹Formerly Graduate Student at Inha Univ., Now at Korea Houghton Corp., Seoul, 156-010, Korea

²School of Materials Science and Engineering, Inha University, Incheon, 402-751, Korea

³Jointly Appointed by the Center for Advanced Aerospace Materials, Pohang University of Science and Technology, Pohang, 790-784, Korea

ABSTRACT

Powder metallurgy has been successfully adopted in synthesizing intermetallic compounds based on Ti-Al and Ti-Si. Direct hot extrusion of elemental powder mixtures resulted in rods of about 2cm in diameter with the compositions based on Ti-46.6Al-1.4Mn-2Mo (all in at.%). Among the processing parameters, degassing scheme, heating rate, extrusion can and die design, extrusion temperature and extrusion ratio were found to be crucial to ensure the sound mechanical properties such as tensile properties and creep strength. Further improvement in the mechanical properties was obtained by modifying the chemical composition with C or Y, which were effective in refining the microstructure, thus enhancing the tensile strength at elevated temperature. Electro-pressure sintering was also evaluated as an alternative consolidation route for Ti₅Si₃-(Cu-Nb-C). Through a balanced control of the heating scheme, sintering temperature and pressure, near full density state of the two Ti-based intermetallic compounds was obtained, in which a high fracture toughness and absence of porosity, respectively, were realized.

1. INTRODUCTION

Due to the low density and high melting point, the intermetallic compounds based on Ti receive increasing attentions of researchers in the field of high performance automobiles and aircrafts. Among the synthesis methods of the intermetallic compounds, elemental powder method is an attractive route because of the homogeneity in alloy chemical composition and the fine grain size in the final product. Employment of direct extrusion of the powder mixtures and electro-pressure sintering (EPS), resulted in a full density alloys in Ti-46.6Al-1.4Mn-2Mo and Ti₅Si₃-Nb-C [1-3], respectively. These methods, however, require a careful control of the processing parameters to ensure the soundness in the microstructure that is essential for the mechanical properties. The purpose of this paper is to address some of the crucial technical issues in the utilization of the proposed powder methods for synthesizing the two Ti-based intermetallic compounds.

2. EXPERIMENTAL PROCEDURE

Elemental powders used in this study were of 99.5% or better purity and 4 to 80 μm in the average particle size. For Ti-46.6Al-1.4Mn-2Mo (all in atomic percent) alloy, powders were mixed in a V-blender for 4 hrs without additive, and compacted into a Cr-Mo steel(AISI 4140) can of 40 mm and 73 mm in the ID and OD, respectively, and 180 mm in height. The cans were degassed sequentially at room temperature, 250 and 500°C for 1, 2 and 4 hrs, respectively, followed by vacuum sealing at 3×10^{-5} torr. For consolidation, either hot

extrusion or electro-pressure sintering was conducted. Hot extrusion was conducted at 1250°C with extrusion ratios ranging from 8 to 12. Prior to extrusion, cans were pre-heated for 12 hrs. The sketches of the can and extrusion die are shown in Fig. 1. In the case of $\text{Ti}_5\text{Si}_3\text{-(Cu-Nb-C)}$ alloy, additional milling was conducted in an attritor filled with ethanol. Stainless steel balls of 4.75 mm in diameter and 35 times the weight of powder were used for the mechanical milling. Milled powders were sieved and dried for 24 hrs in oven. Dried powder aggregates were further milled in a tubular shaker mixer for 30 min in argon atmosphere, which yielded powders of 37 μm in the average particle size. Powder mixtures were then cold compacted and were given an EPS treatment at 1200°C under a pressure ranging from 30 to 100 MPa and holding time ranging from 150 to 600 s.

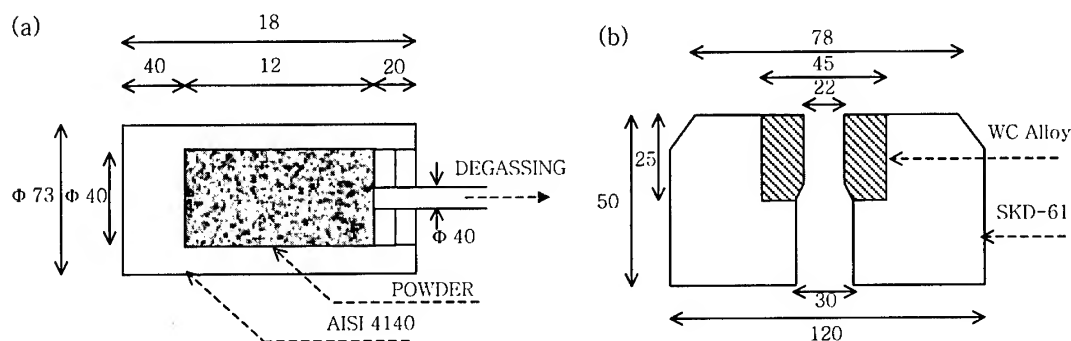


Fig. 1 Schematic drawings of (a) can and (b) die used for extruding elemental Ti-46.6Al-1.4Mn-2Mo alloys. Unit of the dimensions: mm.

3. RESULTS AND DISCUSSION

During preparation of powders, the average powder particle size, mixing conditions, degassing conditions and pre-extrusion heat treatment were important parameters affecting the final microstructure and porosity. The effect of the powder particle size on the relative density of $\text{Ti}_5\text{Si}_3\text{-Cu}$ alloy was previously studied by Park et al. [1] In this study the powder mixtures were milled for 12 hrs in an attritor at a speed of 250 rpm with the ball to powder charge ratio of 40:1 in weight and under hexane atmosphere. Two different Ti powders were used, with the different initial average particle size of 15 μm and 109 μm . Subsequently the mixtures were dried, cold compacted, degassed at 450 °C and reactively sintered at 1450°C for 3 hrs under a vacuum atmosphere of 10^{-3} torr. With increasing Cu content, from 0 up to 6 wt.%, the relative density of sintered specimens increased from about 70% to 90% of the theoretical density. The relative density was consistently higher by approximately 5% in the specimens made from the fine (15 μm) Ti powder at all levels of Cu addition. Although the mechanical milling reduced the initial size of Ti powders, there was presumably a significant gap in the average size of the two kinds of Ti powders prior to reactive sintering. It is surmised that fine particles provided a larger surface areas of sintering reaction and also provided a segregation of Cu at grain boundaries, which resulted in an increase in the capillary force to enhance diffusion of the mobile liquid phase [4].

Multi-step degassing was an essential step toward reduced porosity in the final material. Depending on temperature, the composition of the extracted gases differed. In the range of 25-200°C, the major gas component was water vapor that gradually decreased with temperature up to 450°C, which was followed by another increase of the gas release at higher temperatures. Hydrogen gas extraction occurred mainly in the temperature range of 200-400°C whereas CO_2 gas release peaked at 100°C, the former out-weighting the latter over the whole temperature range. Oxygen gas was persistent against degassing treatment, resulting in

approximately 1300ppm in the final materials of Ti-Al as well as Ti-Si alloy systems.

Control of the rate of reactive sintering among powder particles was based on the characteristics of the phase forming at the interfaces of powders. During heating Ti-Al powder mixtures above 600 °C, melting of Al powder occurred first, which was immediately followed by the formation of Ti-Al intermetallic compounds. This process involved adiabatic endothermic reaction and exothermic reaction in sequence. The major forms of the compounds were identified as Ti_3Al and Ti_2Al , $TiAl$ and $TiAl_3$. Since these phases form shells on pure Ti powder particles, they affect further diffusion of Ti. To maximize the gamma phase ($TiAl$), it was necessary to find a processing route to suppress the formation of the undesirable phases, particularly $TiAl_3$ since this phase exhausts Al and at the same time retards the diffusion rate of Ti. The heating rate was found to be a crucial parameter for this purpose. As shown in Fig. 2, the amount of the gamma phase increased with the heating rate. The reason for this result is thought to be the effect of the heating rate on the ignition temperature and the reaction finish temperature of the major reaction among the powder particles. While the ignition temperature was insensitive to the heating rate, the reaction finish temperature increased sensitively with the heating rate (from 650°C to 1400°C with the heating rate increase from 2 to 300°C/min), resulting in a suppression of $TiAl_3$ phase. Control of the heating rate affected the consolidation of Ti_5Si_3 -(Cu-Nb-C) also but in a different way from that of the $TiAl$ alloy. In this case, too rapid heating caused an explosion. Therefore it was necessary to keep the heating rate below 150°C/min.

Hot extrusion was effective in consolidating Ti-46.6Al-1.4Mn-2Mo alloy but not Ti_5Si_3 -(Cu-Nb-C) alloy. The main cause of the difference is considered to be the partial liquid phase sintering in the former, which was absent in the latter. The key processing parameters for hot extrusion were the preheating treatment, the extrusion ratio and the extrusion temperature. To evaluate the effect of the preheating treatment, three different heat treatments were designed over the temperature range of 1200 to 1250°C and the holding time of 1 to 2 hrs. Quantification of the preheating treatment was best described by the annealing parameter defined as follows:

$$A = \sum_{i=1}^n t_i \left(\frac{-Q}{RT_i} \right)$$

where Q is the activation energy for self diffusion of Ti in single phase $TiAl$, which was assumed to be 300kJ/mol [5] and the summation was taken over each heat treatment segment. Porosity was substantially reduced as the value of the parameter A increased from 1.0×10^{-10} to 1.7×10^{-10} . Further increase of the value up to 5.1×10^{-10} , however, was inconsequential. The extrusion ratio affected the final grain size in the extruded specimens, the grain size decreasing with the extrusion ratio although the capacity of the press, 700ton, limited it to about 11:1. From these considerations, the optimum consolidation process for Ti-46.6Al-1.4Mn-2Mo alloy was found to be preheating at 1250°C for more than 2hrs, followed by extrusion at this temperature with a ratio of 10:1. A similar consideration for the case of EPS identified the optimum consolidation process as a stepwise pressure increase up to 82MPa at 1200°C followed by holding for 150s as shown in Fig. 2(b)

The EPM approach brought several advantageous microstructural features as well as the mechanical properties derivable from the microstructures. Among these, the grain size refinement showed the most pronounced effect. The average grain size of Ti-46.6Al-1.4Mn-2Mo alloy produced by the EPM method was approximately 70 μm compared to about 300 μm in vacuum arc melted alloys [6] and around 58 μm in arc-melted and subsequently hot extruded alloys [7]. In Table 1, the average grain sizes of the microstructures in the gamma alloys made by various processing methods are compared. The fine grain size obtainable in the EPM process of $TiAl$ alloys is a great advantage in comparison to the IM alloys since it is known that the yield strength, room-temperature ductility as well as the fracture resistance can be enhanced by the fine grain size. To realize the fine grain size in the IM alloys thermo-mechanical processing like a two-step forging is required, which will add additional cost to the final product. Furthermore the EPM process can be potentially refined to reduce the final

grain size by optimizing the characteristics of the starting powder or the consolidation conditions although this was out of the scope of the present work.

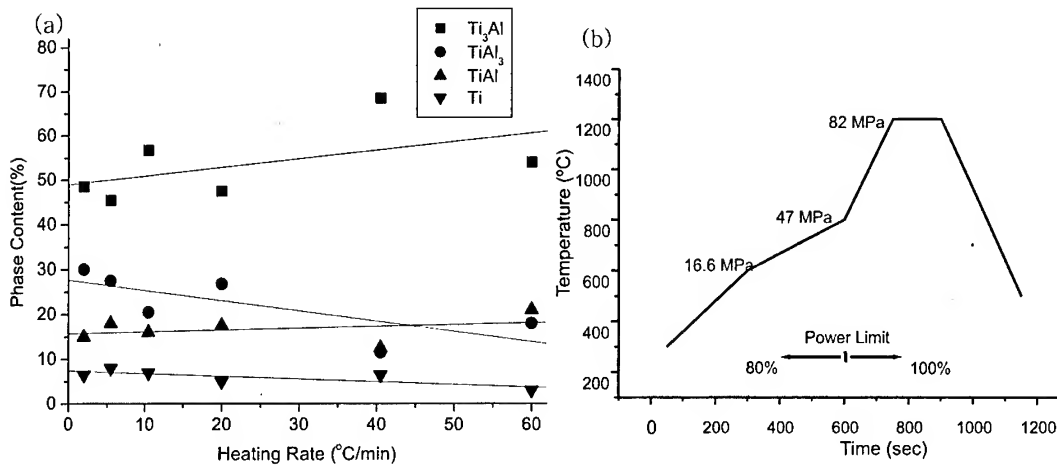


Fig. 2 Control of the consolidation parameters in Ti-base intermetallic alloys: (a) Effect of the heating rate on the amount of various intermetallic phases in reactively sintered Ti-46.6Al-1.4Mn-2Mo alloy, in which compacts of elemental powder mixtures were heated up to the reaction finish temperature identified by the differential thermal analysis and cooled immediately, and (b) Stepwise power enhancement scheme used for consolidating Ti_5Si_3 -(Cu-Nb-C) alloy.

Table 1 Grain sizes of gamma TiAl alloys produced by various methods.

Alloys	Process	Grain size (μm)	Ref.
TiAl -2.3V-0.9Cr	VAR	330	6
Ti-47Al-3.7(Cr, Nb, Mn, Si)-0.5B	VAR/Hot Extrusion ($T > T_\alpha$)	58	7
Ti-45Al-2Mn-2Nb +0.8vol% TiB_2 (XD45)	VAR /HIP	40-200	8
Ti-47Al-2Mn-2Nb +0.8vol% TiB_2 (XD47)	VAR /HIP	50-200	9
Ti-46.5Al-2Cr-3Nb-0.2W	Induction skull melting/HIP/2-step forging	10	10
Ti-46.6Al-1.4Mn-2Mo	EPM/Hot Extrusion	70	Present work

Alloying additions to the EPM produced gamma alloys resulted in further improvement in the microstructural refinement. Either C or Y additions reduced the grain size as well as the lath sizes in the fully lamellar microstructures. Variation of the lamellar dimension with C-addition in Ti-46.6Al-1.4Mn-2Mo alloys is shown in Fig. 3. The reason for the lamellar size refinement in the case of C containing alloy is two-fold: reduction in the stacking fault energy of the high temperature α phase [11,12], thus increasing the nucleation rate of the lamellae, and suppression of the growth rate by carbon segregation at grain boundaries and the lamellar interfaces [3].

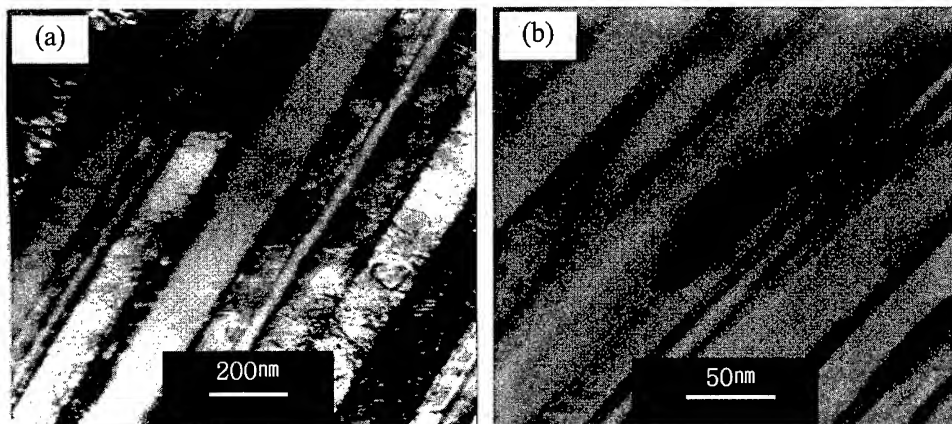


Fig. 3 Lamellar size refinement of Ti-46.6Al-1.4Mn-2Mo alloys with C addition: (a) C-free alloy and (b) C-modified (0.3%) alloy.

The microstructural refinement resulted in enhancement of the mechanical properties, particularly the tensile properties at both room temperature and at elevated temperatures. Room temperature elongation in the order of 2 to 4% together with the yield strength of approximately 500MPa was obtained in the Ti-46.6Al-1.4Mn-2Mo alloys. With the addition of C or Y, the elongation value was slightly decreased but, in contrast, the yield strength increased significantly. Particularly the high temperature yield strength increased considerably up to a temperature of 800°C. The tensile properties of C-modified and Y-modified Ti-46.6Al-1.4Mn-2Mo alloys are shown in Fig. 4. Evaluation of the creep properties of these alloys is currently underway with promising initial results [13].

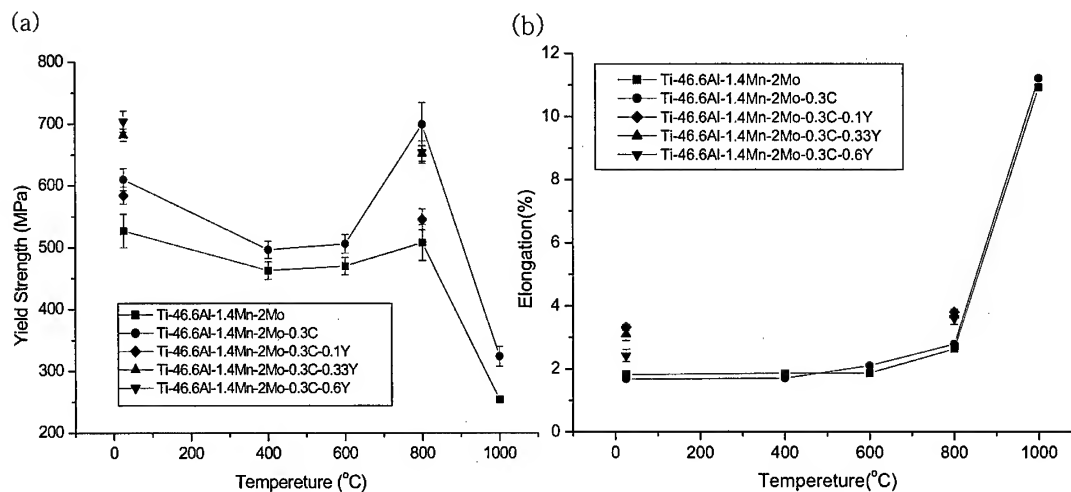


Fig. 4 Tensile properties of Ti-46.6Al-1.4Mn-2Mo alloys: (a) yield strength and (b) tensile elongation.

Particularly with addition of Y, the mechanical properties and the oxidation resistance of the TiAl alloy improved considerably. The first effect of Y addition is the grain refinement as shown above, which resulted in the improvement of the room-temperature ductility as well as

the yield strength although the brittle-to-ductile transition temperature was unaffected. As for the ductility improvement, there is also an oxygen-scavenging effect of Y. Y has a strong affinity to oxygen and, as such, it tends to absorb the interstitial oxygen atoms in the matrix and form oxides, Y_2O_3 . Since the interstitial oxygen is detrimental to ductility at room temperature, this enhances the room temperature ductility as shown above. Due to the difference in the equilibrium solubility of oxygen γ phase and α_2 phase showed different tendency in forming the oxide. In chemical analysis using TEM, it was found that the average concentrations of Y in γ and α_2 were 0.41wt.% and 0.31wt.%, respectively. This indicates that more Y_2O_3 formed in γ , which accords with the low solubility of oxygen in this phase compared to α_2 .

The second, yet more important effect of Y addition to Ti-46.6Al-1.4Mn-2Mo alloy was the oxidation resistance. As shown in Fig. 5, the alloys containing Y showed a significantly improved resistance to high temperature oxidation in air. The cause of this phenomenon is unclear at present. However it is thought that Y modifies the structure of the oxide on the surface exposed to the high-temperature air environment. It has been reported in other systems that Y reduces the concentration of oxygen vacancies in TiO_2 [14,15] and promotes Al_2O_3 formation rather than TiO_2 formation. Although there is no direct evidence, this explanation is plausible for the present system since Al_2O_3 is more resistant to oxygen penetration than TiO_2 .

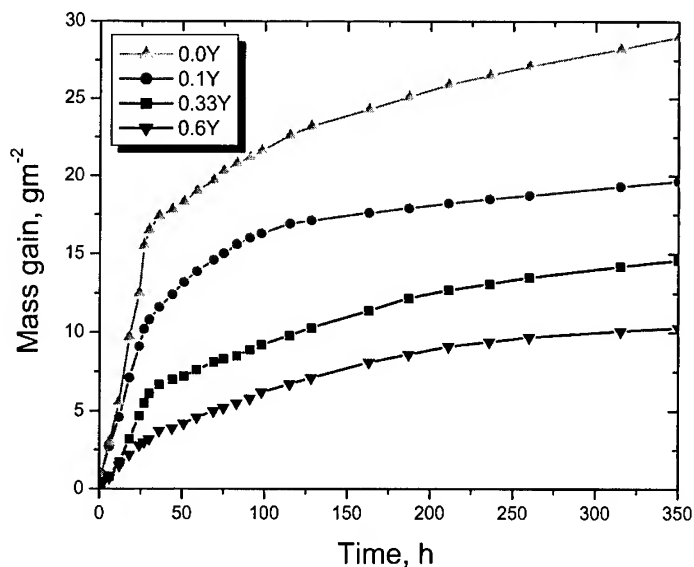


Fig. 5 Effect of Y-addition on the high temperature oxidation resistance of Ti-46.6Al-1.4Mn-2Mo alloy. Specimens were exposed to air at 800°C and the weight gains were measured as a function of time.

Beside the effects of Y as stated above, it also modifies the dislocation structure of Ti-46.6Al-1.4Mn-2Mo alloy at high temperature so that the mode of high temperature deformation is modified. There are, in general, two types of dislocations reported in TiAl alloys, $\langle 110 \rangle$ type super dislocations and $1/2\langle 110 \rangle$ type ordinary dislocations. In the present study, it was observed that the ordinary type dislocations were promoted in the Y-containing alloy compared to the super dislocations.

In case of Ti_5Si_3 -(Cu-Nb-C) alloys, the EPM process did not yield a marked grain size refinement. Rather, the microstructure consisted of a composite-like feature with islands of Nb-rich phase embedded in the hard Ti_5Si_3 matrix. In addition, it appears that Nb and C

enhanced the bonding strength of the matrix phase [16,17]. The role of C in improving the fracture resistance of the compound seems to be related to the reduction in the anisotropic thermal expansion characteristics of the alloy. As a result of these combined effects, the hardness and the fracture toughness of the final multi-phase intermetallic compound increased significantly as compared to the monolithic Ti_5Si_3 phase. In this alloy systems however, the effect of the alloying elements as a single addition or in combination were complex. Fig. 6 shows the effect of C addition on the fracture toughness of the compounds.

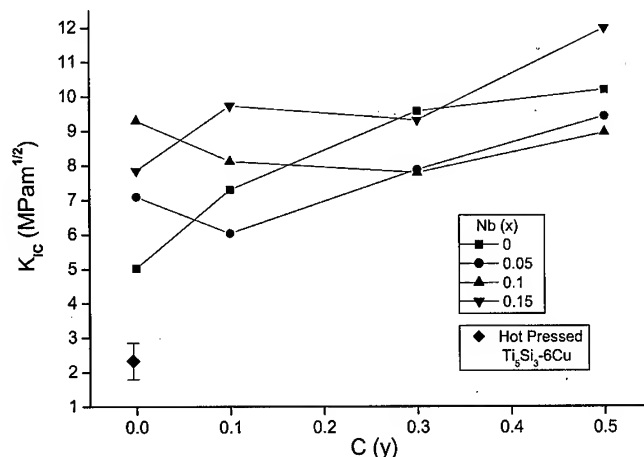


Fig. 6 Fracture toughness of $\text{Ti}_5\text{Si}_3\text{-(Cu-Nb-C)}$ alloys as a function of C content

4. CONCLUSION

In this work, we evaluated some of the key processing parameters in synthesizing Ti-base intermetallic compounds from elemental powders. Among others, the powder characteristics, mixing method, degassing procedure, extrusion can and die-design, pre-extrusion heat treatment, extrusion ratio and temperature are the most important variables to control. Control of these processing parameters, combined with proper additions of alloying elements such as C and Y in Ti-46.6Al-1.4Mn-2Mo alloys and Nb and C in $\text{Ti}_5\text{Si}_3\text{-(Cu-Nb-C)}$ alloys brought in enhanced mechanical properties at both room temperature and elevated temperatures. Particularly in the TiAl alloy, Y addition is of noteworthy since it also improved the high temperature oxidation resistance. The present work, therefore, demonstrates that the EPM process should be considered as a strong candidate processing technique alternative to the ingot metallurgy.

ACKNOWLEDGMENT

This work was supported by the Korea Science and Engineering Foundation through the Year 2001 ERC program at the Center for Advanced Aerospace Materials, POSTECH.

REFERENCES

1. K.J. Park, J.K. Hong and S.K. Hwang, Metall. Trans. A, Vol. 28A(1997), pp. 223-228.
2. K.L. Park and S.K. Hwang, Scripta Mater, Vol. 44(2001). pp. 9-16,
3. H.S. Park, S.K. Hwang, C.M. Lee, Y.C. Yoo, S.W. Nam and N.J. Kim, Metall. Trans. A, Vol. 32A(2001), pp.251-259.

4. R.M. German and B.H. Rabin, Powder Metall. Vol. 28(1985), pp. 7-12.
5. S. Kroll et al., Z. Metallkd., Vol. 83(1992), p. 591.
6. J.D. Shi, Z.J. Pu and K.H. Wu, in Gamma Titanium Aluminides, Y.W. Kim, R. Wagner and M. Yamaguchi, eds., TMS, Las Vegas, Nevada, (1995), pp. 709-716.
7. M. Oehring, U. Lorentz, R. Niefanger, U. Christoph, F. Appel, R. Wagner, H. Clemens and N. Eberhardt, in Gamma Titanium Aluminides, Y.W. Kim, D.M. Dimiduk and M.H. Loretto, eds., TMS, San Diego, CA, (1999), pp. 439-446.
8. V. Recina and D. Nilson, in Gamma Titanium Aluminides, Y.W. Kim, D.M. Dimiduk and M.H. Loretto, eds., TMS, San Diego, CA, (1999), pp. 447-454.
9. D.Y. Seo, T. Everard, P.A. McQuay and T.R. Bieler, in Interstitial and Substitutional Solute Effects in Intermetallics, I. Baker, R.D. Noebe and E.P. George, eds., TMS, (1998), pp. 227-234.
10. Z. Jin, C. Cady, G.T. GrayIII and Y.W. Kim, Metall. Trans. A, Vol. 31A(2000), pp. 1007-1016.
11. K. Kawahara, S. Tsunekawa and H. Nakashima, J. Jpn. Inst. Metals., Vol. 62(1998), pp. 246-254.
12. D. Blatte, P. Duval, L. Letellier and M. Guttman, Acta Mater., Vol. 44(1996), pp. 4995-5005.
13. S.W. Nam, H.S. Cho, S.K. Hwang and N.J. Kim, Metals and Materials, Vol. 6, No. 4(2000), pp. 287-292.
14. K. Hauffe: Oxidation of Metals, Plenum Press, New York, NY(1965), pp.217
15. M. Yoshihara and Y.W. Kim, in Gamma Titanium Aluminides, Y.W. Kim, D.M. Dimiduk and M.H. Loretto, eds., TMS, San Diego, CA, (1999), pp.753-760
16. A. J. Thom, M. K. Meyer, Y. M. Kim and M. Akins, in the Processing and Fabrication of Materials III, TMS, Warrendale, PA (1994), pp. 413-138.
17. Y. Murata, T. Higuchi, Y. Takeda, M. Morinaga and N. Yukawa, in the Proceedings of the International Symposium on Intermetallic Compounds, O. Izumi, eds. JIMIS-6, Sendai(1991), pp. 627.

MECHANICAL PROPERTIES AND MICROSTRUCTURE OBSERVATION OF TiAl +Nb ALLOY

Yun Qi Yan^{1,2}, Lian Zhou¹, Wen Sheng Wang^{1,2} and Guo Zhen Luo¹

¹ Titanium Research Center, Northwest Institute for Nonferrous Metal Research,
Xi'an, P.R.China, 710016

² Material School, Xi'an Jiaotong University, Xi'an, P.R.China, 710049

ABSTRACT

Recently, TiAl+Nb alloys have attracted much attention as potential high temperature (HT) structural materials because of their outstanding HT strength. Great progress has been gained in phase diagram, oxidation resistant studies. Nb addition maybe generate the prospective of engineering applications of TiAl based alloys containing high Nb. In this paper, two alloys were presented including fracture toughness and tensile properties at room temperature and elevated temperature. These alloys named as TAMBY and TAMWY were prepared through various annealing treatments after cladding insulting forging with homogeneous microstructures. Finally, OM, TEM and SEM observed the microstructures.

1. INTRODUCTION

Titanium aluminides based on both Ti_3Al (α_2) and TiAl (γ) have received considerable attention during the past few years as potential candidates for high temperature (HT) structural applications in the aerospace industry. This has been due to the attractive combination of mechanical properties such as low density, high specific modulus and strength, elevated temperature strength retention, and excellent creep resistance. But their relatively poor oxidation resistance and poor ductility have still handicapped the applications of these alloys. Refinement of grains size, addition of ternary and quaternary alloying element, and modifying microstructures through innovation heat treatment and thermo-mechanical processing have been explored to obtain optimal properties. [1~4] Amongst these methods, addition of alloying elements, especially of Nb, has been proven extremely beneficial. Recently, ternary Ti-Al-Nb alloys have also attracted much attention as potential HT structural materials. The phase constitution map, density-composition dependence, oxidation resistance map and general mechanical behavior of ternary TiAl+Nb alloys were systematically studied. [5~8] Those alloys coincide with the conventional TiAl alloys characterized as low density, simple lattice. However, gaining the optimal mechanical properties and excavating the ternary TiAl+Nb alloys' potential abundantly need to refine the microstructures of these alloys chiefly. In this paper, two TiAl based alloys containing high Nb were presented. There will be provided some experimental data for applications of TiAl alloys, through some tensile and three-point-bend tests.

2. EXPERIMENTAL PROCEDURES

Table 1 As-annealed condition vs. microstructure

Conditions	1310°C-0.5h	1250°C-1h
Microstructures	Full lamellae	Duplex

Ti-45Al-8.5Nb-0.3W-0.3B-0.05Y at% (TAWBY) alloy and Ti-45Al-8.5Nb-0.3W-0.2Mo-0.15Si-0.05Y at% (TAWMY) were prepared in the form of as-cast ingots after twice melting by VAR to reduce the composition segregation. The ingots with the size of $\phi 100\text{mm} \times 120\text{mm}$ was cladding insulating-forged into $\phi 165\text{mm} \times 35\text{mm}$ pancakes by type Y3314 hydro press with the pressure 200 ton after 1280°C-2h heat treatment. The samples gained from these pancakes have duplex (DP) microstructure after 1250°C-1h annealing and full lamellae (FL) microstructure after 1310°C-0.5h (Table 1). Investigation was taken through tensile tests and three-point-bend tests at ambient temperature and high temperature. All the tests were conducted using Instron-1185 mechanical machine. FL and DP microstructures were studied via OM and TEM. The factographs were observed through SEM.

The testing samples schematic as Fig.1 were cut from the forged pancake with electric charge machine.

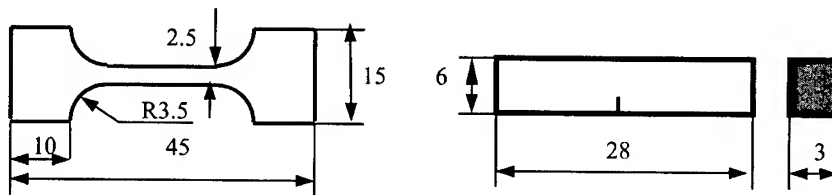


Fig. 1 Schematic diagrams of Tensile (a) and three-point-bend test samples (b).

3. RESULTS AND DISCUSSION

Table2 Tensile properties and fracture toughness of TAWBY and TAWMY alloys at room temperature.

Condition		1310°C-0.5h	1290°C-0.5h	1250°C-1h	1200°C-1h	1150°C-1h
Alloy and its properties						
TAWBY	UTS, MPa	532	-	789	-	-
	K_{Ic} , $\text{MPa} \cdot \text{m}^{1/2}$	16	11.2	10	-	-
TAWMY	UTS, MPa	454	440	514	621	731
	K_{Ic} , $\text{MPa} \cdot \text{m}^{1/2}$	20	18	12	-	-

Table 2 is the data for tensile strength and fracture toughness of TAWBY and TAWMY alloys. From table 2, the tensile strength decreases with the temperature rising while fracture toughness increases with the annealing temperature rising during mechanical testing. For example, UTS for TAWBY alloy as-annealed, 1310°C-0.5h is 532 M Pa, whereas that for the alloy as-annealed,

1250°C-1h is 789 MPa. It is reversed for fracture toughness vs. annealing temperature. Both to fracture toughness and also to UTS for these two alloys there exists the same results. Heat treatment in the α single-phase field, the α phase would decompose into full lamellae arraying with α_2 laths and γ laths (Fig. 2(a)). Therefore, the lamellae strengthening is another factor attributed to the UTS except solidifying strengthening. It is also the reason for higher UTS for TAWBY alloy as-annealed, 1310°C-30min. During annealing in the $(\alpha+\gamma)$ phase field, γ grains will disperse from α phase (Fig.2(b)). The grain boundary can be the other factor strengthening the alloys, especially in the ambient temperature. High UTS results from the higher solid heat treatment temperature. TAWMY alloy exhibits the same property such as UTS for this alloy as annealed, 1310°C-30min is higher than that for as-annealed, 1250°C-1h. The microstructures of this alloy were in the Fig. 2 (c) and Fig. 2 (d). Fig.2 is FL and DP microstructures of TAWBY ((a), (b)) and TAWMY ((c), (d)) alloys. Obviously, the respecting microstructures for TAWBY alloys are finer than those of TAWMY alloy.

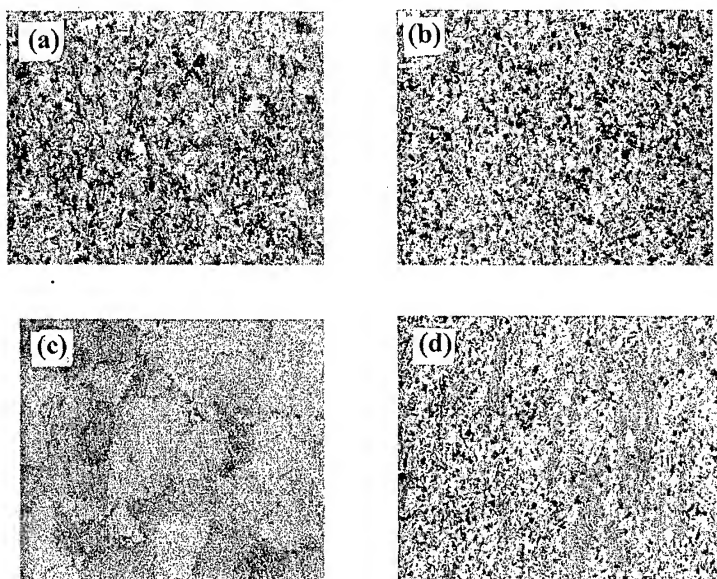


Fig. 2 FL and DP microstructures of TAWBY ((a), (b))and TAWMY ((c), (d)) x 200

Compared to these two alloys, UTS for TAWBY alloy as annealed in all temperatures is higher than that for TAWMY alloy. The thin atom such as B atom occupying the intrinsic location, alloys the grain boundary partially nevertheless they are too few (Fig. 3). Changing the feature if grain boundary there will exist the strengthening affect. So it is the reason that UTS for TAWBY alloy as-annealed in all temperatures is higher than that for TAWMY alloy.

Table 3 is the comparison with K5 alloy, TAWBY and TAWMY alloys for HT tensile tests. The tensile properties for TAWBY and TAWMY alloys are higher in HT, especially at 870°C. At 870°C, elongation (δ) amounts to above 10% whereas the tensile strength exhibits about 400MPa. TAWMY alloy exhibits the same property such as strength and elongation for this alloy as annealed at higher temperature is higher than that for as annealed at lower temperature.



Fig. 3 Existing form of TiB2 in TAWBY alloy.

Table 3 Comparison with TAWBY, TAWMY alloys and other alloys for HT tensile tests

Temperature Alloys and condition		800°C			870°C			
		UTS, MPa	YTS, MPa	δ, %	UTS, MPa	YTS, MPa	δ, %	
TAWBY	FL	520	-	2.8	405	-	9.4	
	DP	440	-	2.9	485	330	19	
TAWMY	FL	590	460	3.1	480	335	22	
	DP	540	410	3.6	405	285	46	
K5	FL	502	375	3.2	485	362	12	
	DP	468	345	40				
Ti47Al2Nb2Cr4Ta		DP	495	363	23.3	403	334	14.6

Table 4 Comparison with TAWBY and other alloys containing high Nb for HT tensile tests

Temperature Alloys, condition		RT			700°C			760°C		
		UTS, MPa	YTS, MPa	δ, %	UTS, MPa	YTS, MPa	δ, %	UTS, MPa	YTS, MPa	δ, %
Ti46Al5Nb-1W	FL	518	476	0.3 5	471	416	0.4 9			
Ti48Al8Nb1B	FL	699	569	0.6 1	641	506	105 8			
Ti44Al4Nb4Zr1B	FL	665	650	0.2	627	563	0.4 4			
TAWBY	FL	532	-	0.5				535	435	3.0
	DP	789	-	0.8				520	410	3.8

Table 3 and Table 4 exhibit the comparison of HT tensile strength among TAWBY, TAWMY and some 3rd generation TiAl alloys. These two alloys have better properties among these alloys. The development of these two alloys should be approved. Solid solution strengthening takes the chief role during application of HT alloys at HT. Solid atom addition enhances the recrystallization temperature. Strengthening matrix is through improving the force between atoms, and decreases the stack faults energy. And it also reduces the dispersing capability. In this paper, high Nb content addition enhances

the melting point and decreases the stacking fault energy. The sliding resistance is also enhanced. Furthermore, Nb addition changes the dislocation ability and improves strength at HT through restraining the dislocation climbing.

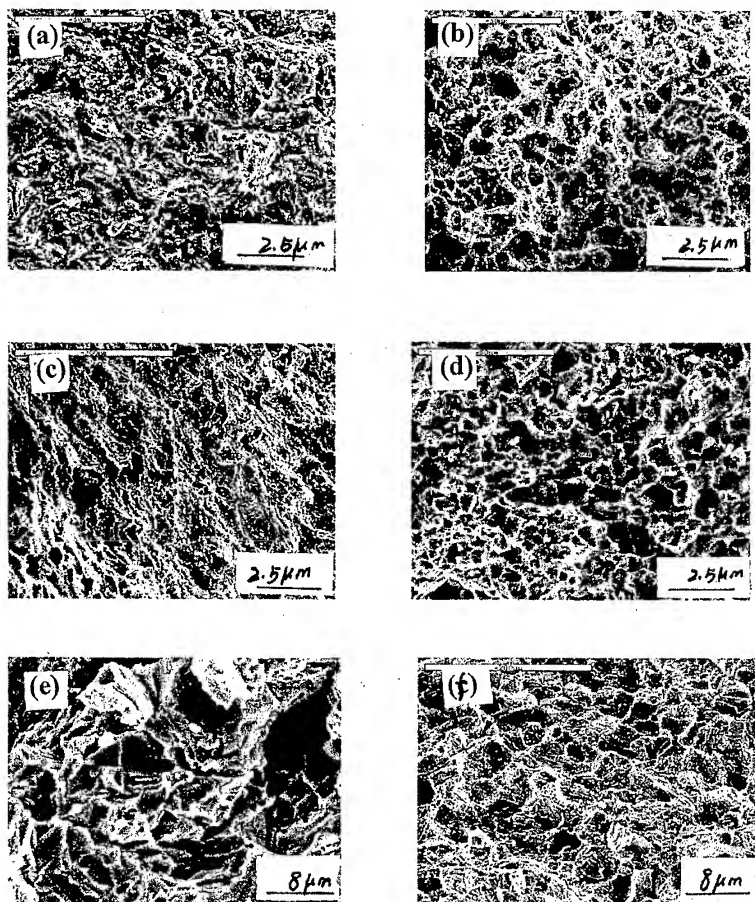


Fig. 4 Micrographs of TAMBY ((a) FL and (b) DP at 870°C, (c) FL and (d) DP at 800°C) and TAWMY alloy (e) FL and (f) DP at 800°C).

Fig.4 are the fractographs for TAWBY and TAWMY alloys after tensile tests as HT. The left side in Fig. 4 (Fig. 2 (a), (c) and (e)) exhibits the brittle fracture partially, for which is little elongation at that condition. The other side in Fig. 4 is ductile fracture. FL microstructure for those two alloys exhibits less ductile than DP microstructure. Plain grain boundary benefits the propagating crack. Lamellae enhance the resistance for the crack except the grain boundary. The interface between lamellae is also the barrier to propagate crack. Under the same condition, tensile strength for TAWMY alloy is higher than that for TAWBY alloy, for which the propagating crack is prolonged in TAWMY alloy.

4. CONCLUSIONS

- (1) For TAWBY and TAWMY alloys, tensile strength decreases with the temperature rising while fracture toughness increases with the annealing temperature rising during testing.
- (2) Under the same condition, fracture toughness for TAWMY alloy is higher than that for TAWBY alloy, for which the propagating crack is prolonged in TAWMY alloy, tensile strength opposite at ambient temperature.
- (3) Comparison of HT tensile strength among TAWBY, TAWMY and some 3rd generation TiAl alloys exhibits these two alloys have better properties among these alloys at high temperature.

ACKNOWLEDGEMENTS

This paper is supported by National Nature Science Foundation of China Contracted No.59895150 and “ 863 ” Hi-tech Project. The author thanks Engineer Qu Henglei and Professor Wang Keguang in Northwest Institute for Nonferrous Metal Research for their technical support and helpful discussions.

REFERENCES

1. Y. W. Kim. JOM, vol.41, No.7 (1989): pp. 24-30
2. Y. W. Kim, D. M. Dimiduk, JOM, vol.43, No.8 (1991): pp. 40-47
3. Y. W. Kim. Mater Sci Eng A, vol.192/193(1995): pp.519-524
4. K. S. Chan, Y. W. Kim. Acta Meta Mater, vol.43 (1995): pp.439-445
5. J. G. Wang, L. C. Zhang, G. L. Chen et al. Scripta Materialia, vol.37, No.2 (1997): pp. 135-140
6. Yan Y Q. Materials Science and Engineering A, vol.280, No.1 (2000): pp. 187-191
7. J. G. Wang. J Materials Sci and Tech, vol.10, No.2 (1994): pp. 18-26
8. Q. Hong, L. Zhou, G. Z. Luo et al. Proceedings of the Xi'an International Titanium Conference, L. Zhou etc. eds., Xi'an, China (1998), pp. 1019-1024

EFFECT OF B ADDITION ON THE CONTINUOUS COOLING TRANSFORMATION BEHAVIOR OF Ti-45.5at.%Al ALLOY

Seong Kon Kim, Jung Sun Kim* and Joong Keun Park

Dept. of Materials Science and Engineering,
Korea Advanced Institute of Science and Technology,
373-1 Kusong-dong, Yusong-gu, Taejeon 305-701, Korea

*Agency for Defense Development, Yusong P.O. Box 35, Taejeon 305-600, Korea

ABSTRACT

Effect of B addition on the continuous cooling transformation behavior of Ti-45.5at.%Al alloy was quantitatively measured using a real-time resistivity-temperature-time measurement apparatus modified to operate under high vacuum. The addition of small amount of B is believed not to alter the T_{α} transus temperature but to enhance the lamellar formation kinetics. At the same time, the B addition significantly raises the lamellar stability by enlarging the lamellar formation regime toward much faster cooling rates. This is believed to be closely related to the effect of B to enhance the chemical diffusivity of Ti-45.5at.%Al alloys. The addition of B tends to slightly lower the $\alpha \rightarrow \alpha_2$ ordering start temperature.

1. INTRODUCTION

Our previous study of the continuous cooling transformation behavior of γ -based Ti-Al alloys showed that the $\alpha \rightarrow \gamma$ transformation in a Ti-45.5at.%Al alloy predominantly occurs through a lamellar reaction[1]. At relatively fast cooling rates, the $\alpha \rightarrow \alpha_2$ ordering reaction directly competes with the lamellar reaction. No massive transformation occurs at this relatively low Al composition. We recently modified our real-time resistivity-temperature-time measurement apparatus to operate under high vacuum. Present study thus allowed to estimate the environmental effect, in particular, the oxygen effect on the $\alpha \rightarrow \gamma$ lamellar reaction.

The main purpose of the present research was to investigate the effect of B addition on the continuous cooling transformation behavior of Ti-45.5at.%Al alloy. Our previous work of Ti-47at.%Al-2at.%Cr-(2-4)at.%Nb alloys[2] showed that the B addition markedly accelerate the lamellar formation kinetics and enhances the thickening rates of γ plates, despite the fact that it increases both the misfit between α and γ plates and the α/γ interfacial energy. The acceleration of lamellar formation kinetics was thus believed to arise from the enhancement of chemical diffusivity as a result of B addition. However no quantitative information was available with regard to the B addition on the phase equilibria of α and γ phases.

2. EXPERIMENTS

The button-shaped ingots of Ti-Al binary alloy(Ti-45.5at.%Al) and B-doped Ti-Al alloy(Ti-45.5at.%Al-0.05at.%B) were casted in a vacuum arc melting furnace using high purity sponge Ti(99.99wt.%), granular Al(99.99wt.%) and flake B(99.5wt.%). The ingots

were remelted several times to ensure a homogeneous composition. They were encapsulated in a quartz tube which was evacuated to 1×10^{-5} torr and back filled with high purity Ar and hold at 1200°C , 24hr for homogenization. These homogenized ingots were machined into sheet specimens of $4 \times 38 \times 0.5\text{mm}$ using an electro-discharge machine. The sheet specimens were resistance-heated under high vacuum into an α -single phase region 1400°C for 1 min by applying a controlled currents through the grips attached to the both ends of specimen. The real time variation of the resistivity and temperature of the specimens was computer-monitored at high speeds at the various cooling rates of 0.2 - $1,000^{\circ}\text{C/s}$ using our previous assembled heating-rate and cooling-rate controlling apparatus; this instrument was at present study modified to operate under high vacuum, the degree of which was less than 1×10^{-5} torr. In the present vacuum-modified instrument, we used thin Nb($50\mu\text{m}$ thick) pad as an insert between the specimen and R-type thermocouple. Two differently sized thermocouples of ϕ $25\mu\text{m}$ and ϕ $75\mu\text{m}$ were tested for comparison and no appreciable difference was detected. And most of the presents works were performed using thermocouples of ϕ $75\mu\text{m}$. To monitor the emf variation, two fine Ta wires(ϕ $25\mu\text{m}$) were spot-welded onto the specimen surface at a distance 6mm apart.

3. RESULTS

Figure 1 illustrates the variation of resistivity of Ti-45.5at.%Al alloy with temperature upon heating at two different heating rates. The rapid rise in resistivity at temperatures from about 1050°C to about 1300°C is mainly due to the $\gamma \rightarrow \alpha$ reaction. The differential of resistivity with respect to temperature better indicated the temperature range for this $\gamma \rightarrow \alpha$ reaction. The finish temperature of this reaction was observed to diminish with the cooling rate and approaches about 1320°C at the cooling rate of 0.1°C/s . This temperature should, in principle, corresponds to the α -transus temperature. The examination of Ti-Al binary phase diagram indicates that this temperature is close to T_{α} of the Ti-45at.%Al alloy, which is close to the nominal composition of the present alloy.

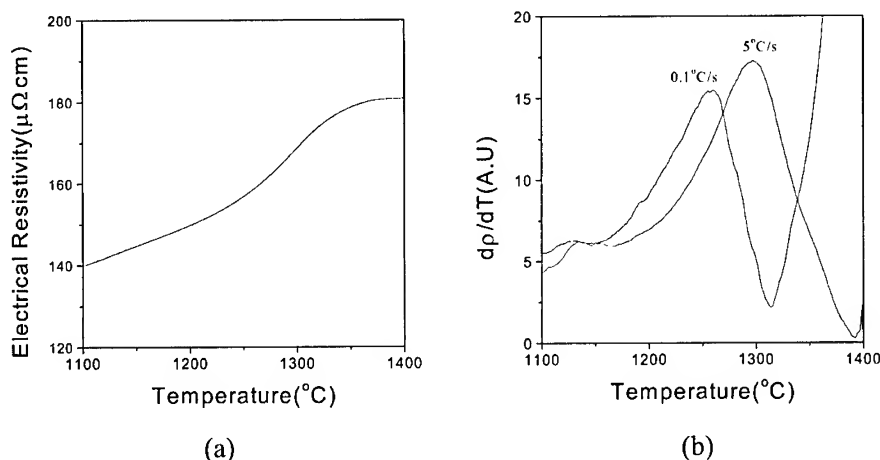


Fig. 1 Variation of resistivity of Ti-45.5at.%Al alloy during continuous heating at 5°C/s (a) and its differential curves (b).

More detailed examination of the differential curve indicated that the presence of another small reaction peak from about 1120°C to 1150°C. This is believed to arise from the eutectoid reaction of $\alpha_2 + \gamma \rightarrow \alpha$, primarily accompanying the disordering reaction of α_2 phase.

Figure 2 shows the variation of resistivity of Ti-45.5at.%Al alloy with temperature upon continuous cooling from the α single phase region 1400°C at various cooling rates. The rapid drop in resistivity at temperatures of about 1200-1000°C is due to the $\alpha \rightarrow \gamma$ transformation. No appreciable resistivity variation occurs at cooling rates faster than about 25°C/s. The temperature range for the $\alpha \rightarrow \gamma$ transformation depends on the cooling rates and shifts toward lower temperatures with cooling rate. The resistivity differential curve better differentiates the temperature range for the $\alpha \rightarrow \gamma$ reaction (Fig. 3). The reaction peaks clearly appear in these curves and generally shift toward lower temperatures with cooling rate. The reaction peaks were not detected at cooling rates faster than about 50°C/s because of little change in its resistivity. However, the temperature differential curves (Fig. 3b) exhibited the reaction peaks even at these fast cooling rates. The result further showed that the peak temperature little varies with the cooling rate in this cooling rate regime, suggesting that these peaks arise from the $\alpha \rightarrow \alpha_2$ ordering reaction.

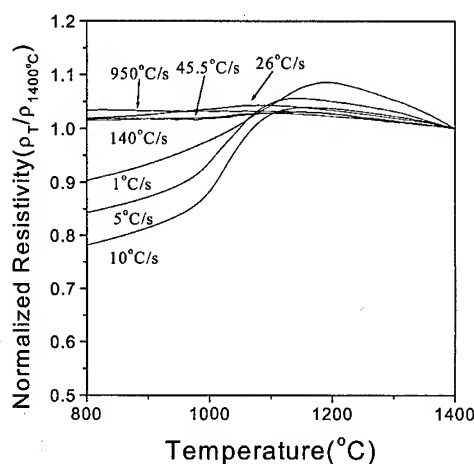


Fig. 2 Variation of normalized resistivity of Ti-45.5at.%Al alloy with temperature during continuous cooling at various cooling rates.

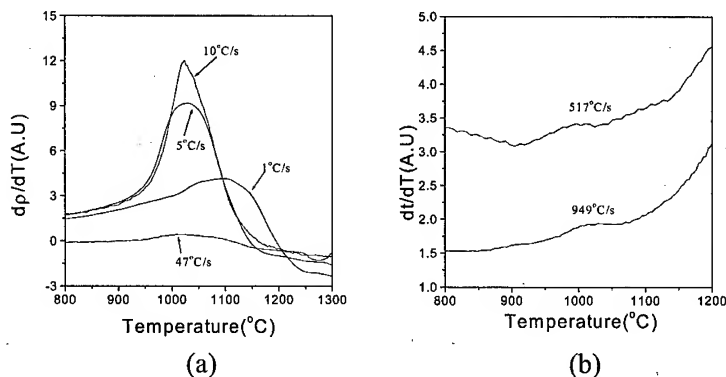


Fig. 3 The Resistivity differential curves (a) and the temperature differential curves (b) of Ti-45.5at.%Al alloy.

The reaction start temperatures are plotted in a continuous cooling transformation curve (Fig. 4). The reaction start temperature is measured to be about 1200°C. This temperature continuously decreases with the cooling rate up to about 75°C/s and remains nearly constant thereafter. The reaction peak temperatures follow a very similar trend. The curve from slow cooling rates represents the $\alpha \rightarrow \gamma$ lamellar reaction, whereas that from fast cooling rates represents the $\alpha \rightarrow \alpha_2$ ordering reaction. The comparison of the lamellar start temperature (1200°C) with the α -transus temperature T_α (1330°C) indicates that a significant amount of undercooling is required for the $\alpha \rightarrow \gamma_L$ lamellar reaction. The reaction start temperature is actually lower than T_0 of Ti-45.5at.%Al alloy. The ordering start temperature is measured to be about 1070°C, which is very close to the metastable $\alpha/\alpha+\alpha_2$ boundary line.

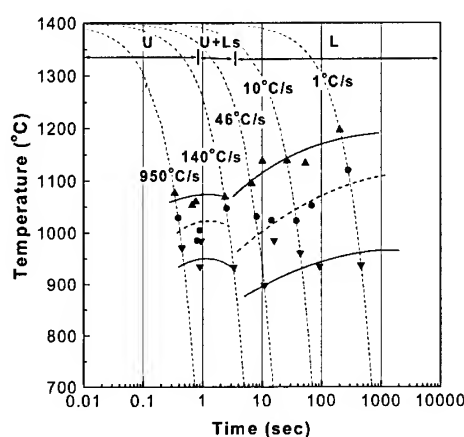


Fig. 4 Continuous cooling transformation curve of Ti-45.5at.%Al alloy :

▲ : reaction start ; ● : reaction peak ; ▼ : reaction finish
(L : Lamellar reaction ; U : Untransformed ; Ls : Short lamellar).

The results of the present study is in good agreement with our previous results measured under Ar+He gas atmosphere in Ti-45.5at.%Al alloy except the data at relatively slow cooling rates, i.e., at cooling rates less than about 20°C/s. The previous data showed significantly higher start temperatures at these slow cooling rates. This is believed to arise from the magnification of surface oxidation effect at slow cooling rates. The oxygen is well known to greatly raise the $\alpha+\beta/\alpha$ phase boundary line in pure Ti. A similar reasoning suggests the rise of T_α with the oxygen content. However no literature is available with regard to this point. Apart from this difference, two results are very close each other. Namely the lamellar start temperatures are similar each other at relatively fast cooling rates. Similar results were also obtained with respect to the transition cooling rate for the ordering reaction as well as to the ordering start temperature.

Figure 5 illustrates the variation of resistivity of B-doped 45.5Al alloy with temperature. A significant resistivity change occurs, in particular, up to the cooling rate of 250°C/s, differently from the 45.5Al alloy. The resistivity differential curve clearly shows this point (Fig. 6). Reaction peak appears in a relatively well defined form up to the cooling rates of 250°C/s. At cooling rates faster than about 300°C/s, the reaction peak becomes evident only in the temperature differential curves.

The peak start temperatures are plotted in a continuous cooling transformation curve (Fig. 7). The start temperature is measured to be about 1200°C at slow cooling rates, which is very

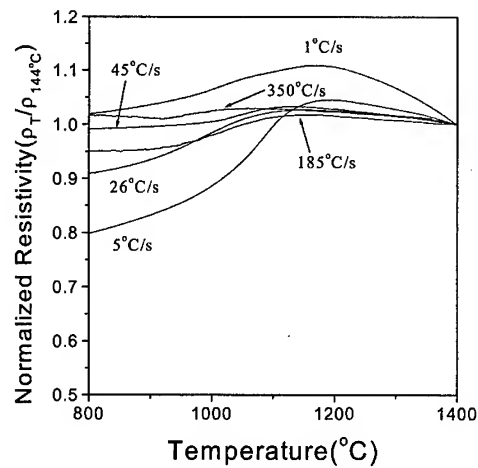


Fig. 5 Variation of normalized resistivity of Ti-45.5at.%Al-0.05at.%B alloy with temperature during continuous cooling at various cooling rates.

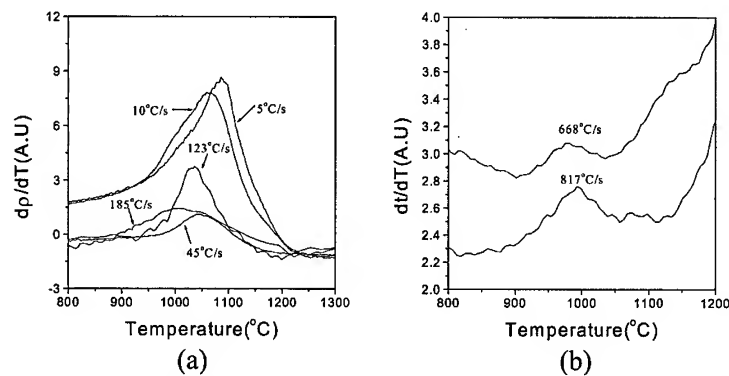


Fig.6 The Resistivity differential curves (a) and the temperature differential curves (b) of Ti-45.5at.%Al-0.5at.%B alloy.

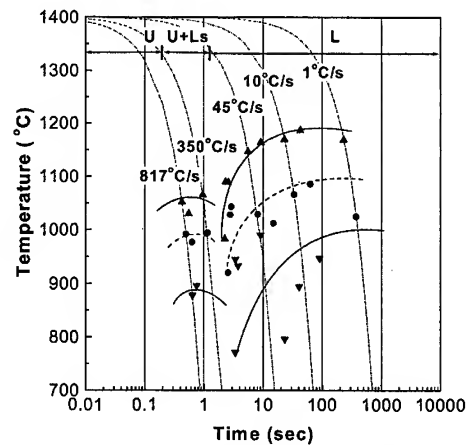


Fig. 7 Continuous cooling transformation curve of Ti-45.5at.%Al-0.05at.%B alloy :
 ▲ : reaction start ; ● : reaction peak ; ▼ : reaction finish
 (L : Lamellar reaction ; U : Untransformed ; Ls : Short lamellar).

similar to that in the binary alloy. This temperature, however, decreases very slowly with cooling rate and maintains comparatively higher temperatures up to the cooling rate of about 50°C/s. The starting temperature thereafter decreases rapidly with cooling rate up to about 300°C/s, after which it remains nearly constant. This indicates that the $\alpha \rightarrow \alpha_2$ ordering reaction occurs at this fast cooling rate regime and the ordering start temperature is measured as about 1050°C. The transition cooling rate from the lamellar to the ordering reaction thus largely shifts toward faster cooling rates as a result of B addition.

4. DISCUSSION

The comparison of the two CCT curves indicates that the lamellar start temperature at very slow cooling rates is very close each other regardless of B addition. This result suggests that the addition of B does not appreciably alter the α transus temperature T_α . Nevertheless, the lamellar reaction always starts to occur at higher temperatures over whole cooling rates except at very slow cooling rates, i.e., at slow cooling rates less than about 5°C/s. Furthermore, the range of cooling rate for the lamellar reaction largely extends toward fast cooling rates and transition cooling rates shifts from about 70°C/s to about 250°C/s. These results suggest that the B addition accelerates the nucleation as well as the growth kinetics of γ -lamellar plates. The large extension of lamellar reaction region toward fast cooling rate further suggest that $\alpha \rightarrow \gamma_L$ lamellar reaction is mainly controlled by the nucleation stage than by the growth stage. Namely, the growth proceeds instantaneously, once the nucleation occurs. Therefore a very fast cooling rate is necessary in order to be able to stop the growth of lamellar once nucleated.

Finally, the B addition slightly lowers the ordering start temperature by about 20°C. This temperature difference is believed to be large enough to be taken as a real difference. This indicates that the B addition has an effect to slightly depress the metastable $\alpha/\alpha+\alpha_2$ phase boundary. The origin of this effect is not known at the present time.

5. CONCLUSIONS

The addition of small amount of B significantly raises the lamellar start temperature at most cooling rates except at slow cooling rates where the lamellar start temperature is very similar to that of binary Ti-45.5at.%Al alloy. Furthermore, the small amount of B addition largely shifts the transition cooling rate for the lamellar to the ordering reaction from about 70°C/s to about 250°C/s. It is believed from these results that B addition does not significantly alter the α -transus temperature and that the addition of B enhances both the nucleation and growth rates of γ_L lamellar plates probably through the enhancement of chemical diffusivity. Finally, the B addition tends to slightly lower the $\alpha \rightarrow \alpha_2$ ordering start temperature.

REFERENCES

1. J. S. Kim and J. K. Park : Phil. Mag. A, 2001, in print.
2. J. Y. Jung and J. K. Park : J. Mater. Res., vol.12, No.3(1997), pp. 665-680.

Effects of Low Cycle Fatigue Test Parameters on $\alpha_2 \rightarrow \gamma$ Phase Transformation at the Grain Boundary in Lamellar TiAl Alloy

Young Sam Park and Soo Woo Nam¹

Department of Materials Science and Engineering, Korea Advanced Institute of Science and Technology, 373-1 Kusong-dong, Yusong-gu, Taejon, 305-701, KOREA

¹Jointly Appointed at the Center for Advanced Aerospace Materials.

E-mail: namsw@cais.kaist.ac.kr

Abstract

In order to investigate effects of low cycle fatigue test parameters on low cycle fatigue property, total strain range controlled low cycle fatigue tests were conducted at 1073K in an air environment. It is observed that fatigue life decreases and intergranular cracking mode becomes predominant with imposing tensile hold time or increasing applied strain range, which is induced by $\alpha_2 \rightarrow \gamma$ phase transformation at the grain boundary. Experimental result clearly confirms that the phase transformation weakens grain boundary to induce intergranular cracking.

1. Introduction

There has been an enormous increase in research and development activity on lamellar TiAl alloys, because the alloys have excellent high-temperature mechanical properties compared with conventional Ti alloys [1-3]. Applying only fracture concept to practical application condition, most researchers have been interested in high cycle fatigue damage tolerance and a number of papers investigating the effects of microstructure, temperature and environment on fatigue crack growth resistance have been reported [4-8]. However, lamellar TiAl alloys are generally exposed to low cycle fatigue damage when the alloys are designed for high-temperature engine components. Therefore, a database on low cycle fatigue property is necessary for the practical application. In the present study, total strain range controlled low cycle fatigue tests were conducted in order to investigate the effects of low cycle fatigue test parameters such as tensile hold time and applied strain range on low cycle fatigue property.

2. Experimental

Gamma TiAl alloy with a composition of Ti-46.6Al-1.4Mn-2Mo (at.%) was prepared by a hot extrusion of a blended elemental powder mixture to have an available room temperature ductility [9]. The testing material was heat treated at 1653K for 30min and then at 1223K for

5hr in an Ar environment in order to get lamellar structure, which has superior high-temperature mechanical properties to duplex structure [10,11]. After then, button-head typed fatigue specimens were machined to have a gauge diameter of 3mm with a gauge length of 5mm. Total strain range controlled low cycle fatigue tests ($R=-1$, strain rate= 4×10^{-3} /sec.) were conducted at 1073K in an air environment to simulate the practical application conditions. Number of cycles to failure, N_{cr} , was defined as the number of cycles leading to a 20% reduction in a saturated tensile peak. Scanning electron microscope (SEM, JEOL JSM 840A) and transmission electron microscope (TEM, Philips CM20) were used to observe fatigue crack growth behavior and grain boundary morphology, respectively. Auger electron spectroscopy (AES, PHI Model 4300 SAM) was also used to analyze the phases existing near fatigue cracks.

3. Results and Discussions

3.1. Low Cycle Fatigue Property

After the heat treatment, typical lamellar structure was obtained to have a grain size of $150\mu m$ with a lamellar spacing of $0.2\mu m$ as shown in Fig. 1. It is observed that dislocations can not penetrate α_2/γ interfaces, which implies that α_2/γ interfaces can block the dislocation movement [12]. It is also observed that the number of α_2/γ interface is the highest compared with those of other types of interfaces [13].

Fig. 2 shows a Coffin-Manson plot taken from hysteresis loops at the half of fatigue life ($N_{cr}/2$). This plot clearly indicates that fatigue life decreases with imposing tensile hold time or increasing applied strain range. This implies that low cycle fatigue property of lamellar TiAl alloy is closely dependent on low cycle fatigue test parameters such as tensile hold time and applied strain range which induce microstructural change. Therefore, it is necessary to investigate effects of low cycle fatigue test parameters on low cycle fatigue damage in terms of microstructural change in order to improve low cycle fatigue property of lamellar TiAl alloy.

3.2. Microstructural Analysis

In order to investigate the microstructural change induced by low cycle fatigue damage, fatigue fracture surfaces after low cycle fatigue tests were observed using SEM as shown in Fig. 3. In the case of tensile hold time considerations, it is observed that intergranular cracking mode becomes predominant with imposing tensile hold time and the mode is more pronounced with increasing tensile hold time in the fixed total strain ranges of ± 0.5 and $\pm 0.7\%$, respectively. In the case of applied strain range considerations, it is observed that intergranular cracking mode becomes more predominant with increasing applied strain range in the fixed waveforms of continuous fatigue and 5min tensile hold, respectively. This implies that increased plastic deformation by imposing tensile hold time or increasing applied strain range induces a weakness of a grain boundary rather than a matrix. It is well known that intergranular crack has a faster crack propagation rate compared with that of transgranular crack, which clearly indicates that the intergranular cracking mode is responsible for the reduction of fatigue life. However, the reason for grain boundary weakness with imposing tensile hold time or increasing applied strain range has not been investigated yet.

In order to investigate the reason for the grain boundary weakness, grain boundary

morphologies after low cycle fatigue tests were observed using TEM as shown in Fig. 4. In the case of tensile hold time considerations, it is observed that sphere γ phase is newly observed at the grain boundary with imposing tensile hold time and the generation of the γ phase is accelerated to form huge γ phase at the grain boundary with increasing tensile hold time in the fixed total strain range of $\pm 0.7\%$. In the case of applied strain range considerations, huge γ phase is observed near the grain boundary in higher applied strain range in the fixed waveform of continuous fatigue. This suggests that the huge γ phase formation is assisted by the application of tensile hold time and applied strain range and is proceeded by $\alpha_2 \rightarrow \gamma$ phase transformation at the grain boundary. Lever rule as shown in Fig. 5 [14] insists that the phase transformation is a spontaneous reaction, because volume fraction of γ phase at the low cycle fatigue testing temperature (800°C), 77.7vol.%, is higher than that of aging temperature (950°C), 76.0vol.%. Therefore, stress induced phase transformation from α_2 to γ phase can occur spontaneously when lamellar TiAl alloy is exposed to high-temperature low cycle fatigue test [15].

3.3. Compositional Analysis

It can be supposed that the phase transformation removes α_2/γ lamellar interface, a barrier to dislocation movement to induce easier dislocation movement and plastic deformation concentration, which suggests that the phase transformation causes the grain boundary fracture. In order to support the suggestion that the phase transformation leads to grain boundary fracture, the effect of the grain boundary γ phase on intergranular cracking must be investigated. Therefore, compositional analysis was conducted using AES to investigate the phases existing near fatigue cracks as shown in Fig. 6. In Fig. 6(a) where transgranular and intergranular cracks co-exist, it is observed that compositional ratios, at.%Al/(at.%Ti+at.%Al), near intergranular are in those of γ region, while those of transgranular cracks are in those of $(\alpha_2 + \gamma)$ region. In Fig. 6(c) and (e), where only intergranular cracks exist, the ratios near intergranular cracks are in those of γ region. This result implies the existence of only γ phase near intergranular cracks and the existence of α_2 and γ phase near transgranular cracks. This insists that intergranular cracks propagate along the γ phase in the grain boundary, while transgranular cracks propagate along the lamellar plate composed of α_2 and γ phase in the matrix. Therefore, it can be confirmed that grain boundary fracture with imposing tensile hold time or increasing applied strain range is induced by $\alpha_2 \rightarrow \gamma$ phase transformation at the grain boundary.

4. Conclusion

In low cycle fatigue of lamellar TiAl alloy, it is observed that fatigue life is reduced and intergranular cracking mode becomes predominant with imposing tensile hold time or increasing applied strain range, which is probably due to $\alpha_2 \rightarrow \gamma$ phase transformation at the grain boundary.

Acknowledgment

This research was sponsored by Korea Science and Engineering Foundation through the Center for Advanced Aerospace Materials, Pohang University of Science and Technology. The authors gratefully acknowledge its financial support. Also, the authors gratefully express

their appreciation to Prof. Sun Keun Hwang in Inha Univ. for supplying the testing materials.

References

1. Y. W. Kim, J. Metals, Vol. 41, No. 7 (1989), pp. 24.
2. Y. W. Kim and D. M. Dimiduk, J. Metals, Vol. 43, No. 8 (1991), pp. 40.
3. S. W. Nam, Y. S. Park, S. K. Hwang, in Proceedings of the 14th Conference on Mechanical Behaviors of Materials, S. I. Kwon and D. I. Kwon, eds., The Korean Institute of Metals and Materials, Seoul, Korea, (2000), pp. 15.
4. J. M. Larsen and T. Nicholas, Eng. Fract. Mech., Vol. 22 (1985), pp. 713.
5. K. T. Rao and R. O. Ritchie, Mater. Sci. Eng. A, Vol. 153 (1992), pp. 479.
6. A. M. James and P. Bowen, Mater. Sci. Eng. A, Vol. 153 (1992), pp. 486.
7. W. O. Soboyejo, J. E. Deffeyes and P. B. Aswath, Mater. Sci. Eng. A, Vol. 138 (1991), pp. 95.
8. D. L. Davidson and J. L. Campbell, Metall. Trans. A, Vol. 24 (1993), pp. 1.
9. I. S. Lee, S. K. Hwang, W. K. Park, J. H. Lee, D. H. Park, H. M. Kim and Y. T. Lee, Scripta Metall. Mater., Vol. 31 (1994), pp. 57.
10. B. D. Worth, J. W. Jones and J. E. Allison, Metall. Trans. A, Vol. 26 (1995), pp. 2947.
11. H. E. Deve, A. G. Evans and D. S. Shih, Acta Metall. Mater., Vol. 40 (1992), pp. 1259.
12. Y. Umakoshi, H. Y. Yasuda and T. Nakano, Mater. Sci. Eng., Vol. A192/193 (1995), pp. 511.
13. W. Wunderlich, T. Kremser and G. Frommeyer, Acta Metall. Mater., Vol. 41 (1993), pp. 1791.
14. C. McCullough, J. J. Calencea, C. G. Levi and R. Mehrabian, Acta Metall. Mater., Vol. 37 (1989), pp. 1321.
15. H. S. Cho: Ph. D. thesis, KAIST, (1999).

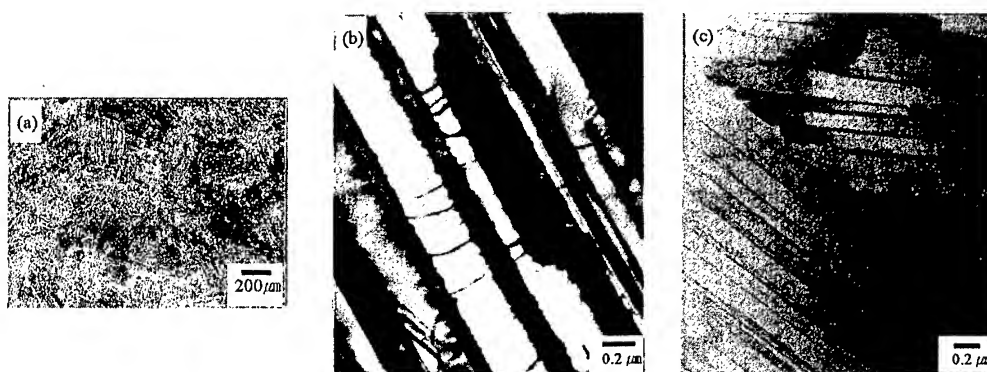


Fig. 1. Microstructure. (a) OM, (b) TEM (inner grain), (c) TEM (grain boundary).

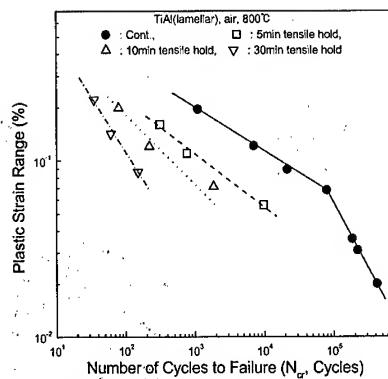


Fig. 2. A Coffin-Manson plot.

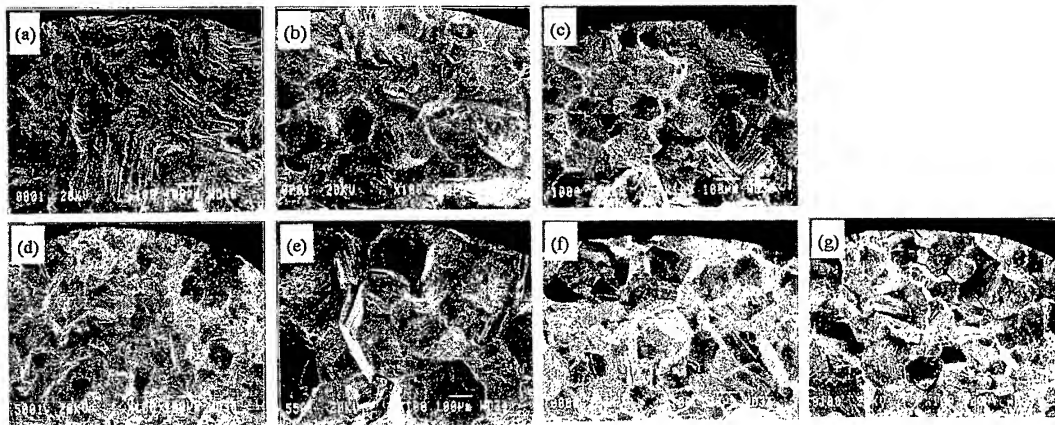


Fig. 3. Fatigue fracture surfaces. ($N=N_{cr}$) (a) $\Delta\epsilon_t=\pm 0.5\%$, cont., (b) $\Delta\epsilon_t=\pm 0.7\%$, cont., (c) $\Delta\epsilon_t=\pm 1.0\%$, cont., (d) $\Delta\epsilon_t=\pm 0.5\%$, 5min tensile hold, (e) $\Delta\epsilon_t=\pm 0.7\%$, 5min tensile hold, (f) $\Delta\epsilon_t=\pm 0.7\%$, 10min tensile hold, (g) $\Delta\epsilon_t=\pm 0.7\%$, 30min tensile hold.

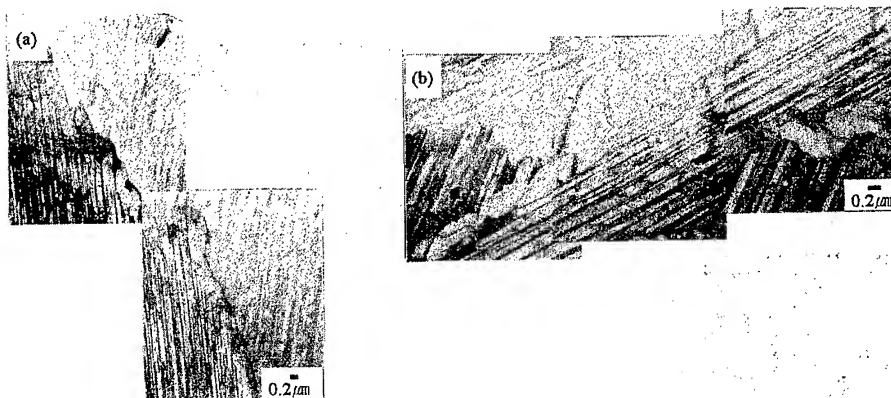


Fig. 4. Grain boundary morphologies ($N=N_{cr}$). (a) $\Delta\epsilon_t=\pm 0.7\%$, cont., (b) $\Delta\epsilon_t=\pm 1.0\%$, cont., (c) $\Delta\epsilon_t=\pm 0.7\%$, 10min tensile hold, (d) $\Delta\epsilon_t=\pm 0.7\%$, 30min tensile hold, (e) γ spot pattern.

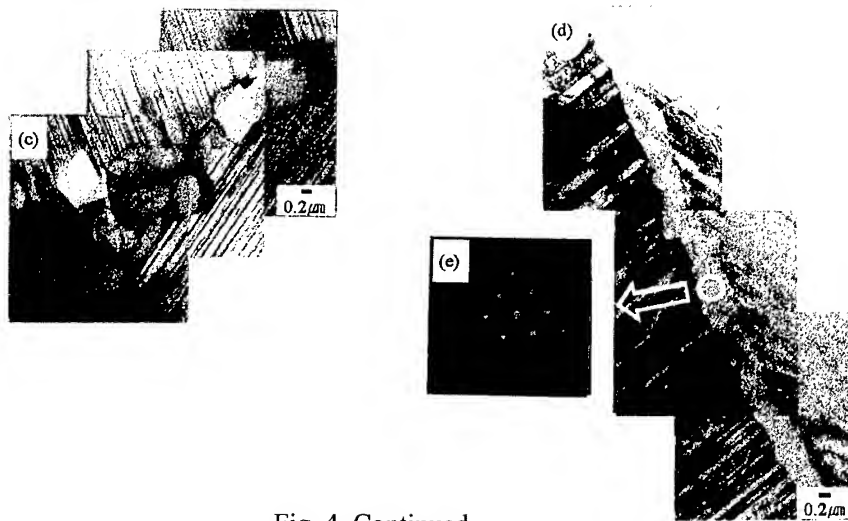


Fig. 4. Continued.

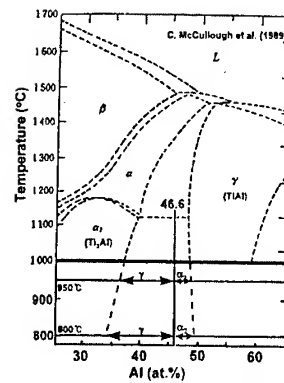


Fig. 5. A phase diagram from which volume fractions of α_2 and γ phase are calculated at aging temperature (950 °C) and low cycle fatigue testing temperature (800 °C) [14].

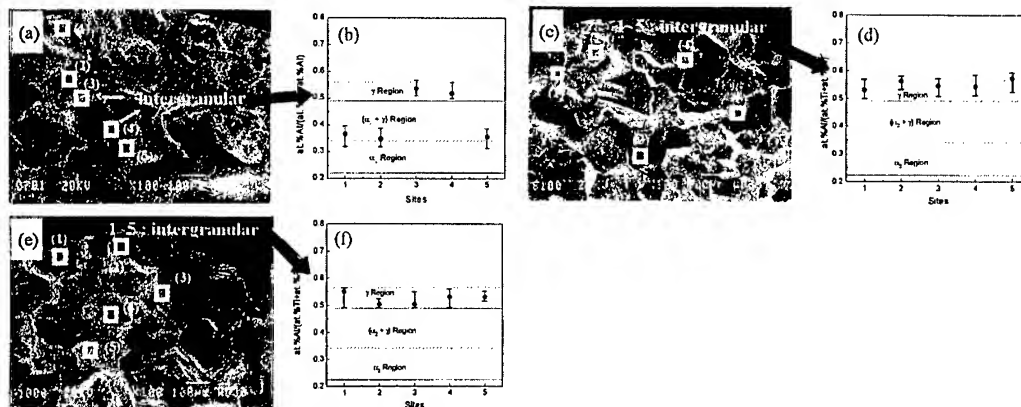


Fig. 6. AES analysis. ($N=N_{cr}$) (a) fatigue fracture surface ($\Delta\epsilon_i = \pm 0.7\%$, cont.), (b) AES result of (a), (c) fatigue fracture surface ($\Delta\epsilon_i = \pm 0.7\%$, 30min tensile hold), (d) AES result of (c), (e) fatigue fracture surface ($\Delta\epsilon_i = \pm 1.0\%$, cont.), (f) AES result of (e).

HIGH TEMPERATURE DEFORMATION BEHAVIOR OF FINE DUPLEX GAMMA TiAl ALLOY

J.H. Kim, D.H. Shin* and C.S. Lee

Center for Advanced Aerospace Materials
Department of Materials Science and Engineering
Pohang University of Science and Technology, Pohang 790-784, KOREA
* Hanyang University, Ansan, Kyunggi-Do 425-791, KOREA

ABSTRACT

The high temperature deformation behavior of two-phase gamma TiAl alloy has been investigated with the variation of temperature and γ/α_2 volume fraction. When the amount of deformation is small ($\epsilon \approx 0.04$) as in the load relaxation test, experimental flow curves of the fine-grained TiAl alloy are well fitted with the combined curves of grain matrix deformation and dislocation climb process. When the amount of deformation is large ($\epsilon \approx 0.8$), flow curves significantly changes its shape indicating that grain boundary sliding also operates at this stage, which has been attributed to the occurrence of dynamic recrystallization during the deformation. With the increase in the volume fraction of α_2 -phase, the flow stress for grain matrix deformation increases. It is considered that cavity initiation is more probable to occur at α_2/γ interface rather than at γ/γ interface.

1. INTRODUCTION

Gamma(γ)-TiAl alloys are nowadays receiving a great attention for high temperature structural materials because of their high strength-to-weight ratio, high Young's moduli. However, this alloy exhibits brittle fracture and poor ductility, which prevents so far commercial applications of these alloys. Although many investigations have been focused to enhance the ductility and hot workability, there still remain several vague points^[1].

Firstly, what are the predominant mechanisms operating at high temperatures? Among several possible mechanisms such as grain matrix deformation, dislocation creep and grain boundary sliding, which is most responsible for the high temperature deformation? Secondly, deformation characteristics with the variation of microstructure are not clarified. It is of great worth to investigate the influence of γ/α_2 volume fraction on high temperature deformation of γ -TiAl alloy^[2]. Thirdly, cavity initiation mechanisms and preferred sites are not clearly known.

The above information is important in optimizing the microstructure for best hot working performance. To investigate the aforementioned points, high temperature deformation characteristics of γ -TiAl alloy have been analyzed in view of inelastic deformation theory by conducting load relaxation tests.

2. INELASTIC DEFORMATION THEORY

A simple rheological model for the grain matrix deformation ($\dot{\alpha}$), dislocation climb ($\dot{\beta}$) and grain boundary sliding (\dot{g}) is schematically shown in Fig. 1. From the model, the stress relation and kinematic relation among the deformation rate variables $\dot{\alpha}$, $\dot{\alpha}$, $\dot{\beta}$ and \dot{g} can be obtained as follows.

$$\sigma = \sigma^I + \sigma^F \quad (1)$$

$$\dot{\epsilon}_T = \dot{\alpha} + \dot{\alpha} + \dot{\beta} + \dot{g} \quad (2)$$

The stress variables σ^I and σ^F are the internal stress due to a long-range interaction among dislocations and the friction stress due to short-range interaction between dislocation and lattice, respectively. The constitutive relation between σ^I and $\dot{\alpha}$ can be expressed in a form similar to that by Hart [3].

$$(\sigma^I / \sigma^F) = \exp(\dot{\alpha}^* / \dot{\alpha})^p \quad (3)$$

$$\dot{\alpha}^* = f_{\alpha}^I (\sigma_{\alpha}^* / \mu_{\alpha})^{n^I} \exp(Q_{\alpha}^I / RT) \quad (4)$$

Like the plastic strain rate $\dot{\alpha}$, dislocation creep strain rate $\dot{\beta}$ can be formulated as follow.

$$(\sigma_{\beta}^* / \sigma^I) = \exp(\dot{\beta}^* / \dot{\beta})^p \quad (5)$$

$$\dot{\beta}^* = f_{\beta}^I (\sigma_{\beta}^* / \mu_{\alpha})^{n^I} \exp(-Q_{\beta}^I / RT) \quad (6)$$

Considering GBS as a viscous drag process similar to the frictional glide process of dislocations, the following power law relations can be described for GBS. A more detailed description is given in the reference [4].

$$(\dot{g} / \dot{g}_0) = \exp(\sigma / \Sigma_g - 1)^{1/M_g} \quad (7)$$

$$\dot{g}_0 = f_g^g (\Sigma_g / \mu_g)^{n^g} \exp(Q_g^g / RT) \quad (8)$$

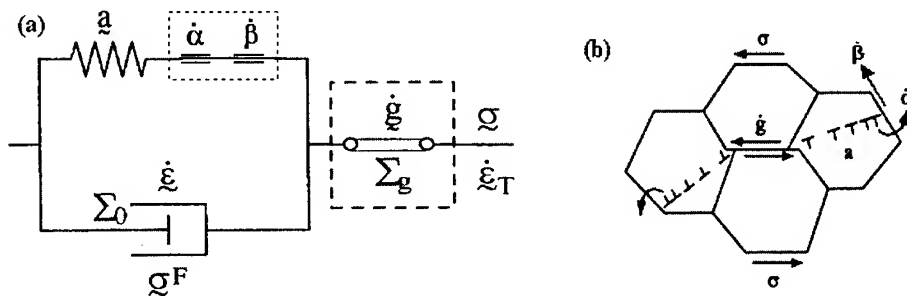


Fig.1 An internal variable model for describing the high temperature deformation:
(a) rheological model and (b) topological model.

3. EXPERIMENTAL PROCEDURES

Gamma-TiAl alloy used in this study was supplied by U.E.S. The alloy was skull-melted and isothermally forged at 1260°C with the pressure of 173 MPa for 4hrs. The chemical composition of this alloy is Ti-46.2 Al-2.0Cr-3.0Nb-0.18W-0.05B-0.12C. Specimens were

heat treated at 1280°C for 3hrs followed by furnace cooling to 800°C, air-cooling to room temperature and final aging at 900°C for 24hrs. The resulting microstructure was the duplex microstructure with average grain size of $\sim 12\mu\text{m}$. The volume fraction of α_2 -phase is about 5%. In order to vary the α_2 volume fraction, the specimen was heat treated at 1200°C for 3hrs followed by air-cooling, by which the volume fraction of α_2 -phase was increased to 30% without changing the average grain size.

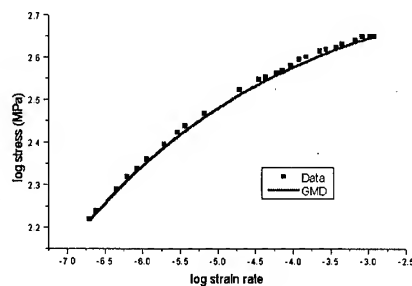
Load-relaxation test was carried out using an Instron 1361 testing machine attached to a three-heating-zone furnace capable of maintaining the temperature constant within $\pm 0.5\text{K}$ with respect to both the time and the position along the gauge length. In this investigation, load relaxation tests were conducted in Ar atmosphere at temperatures ranging from 800°C to 1020°C. Microstructures before and after the deformation were analyzed and it was confirmed that microstructures were not largely varied during the load relaxation tests.

4. RESULTS AND DISCUSSION

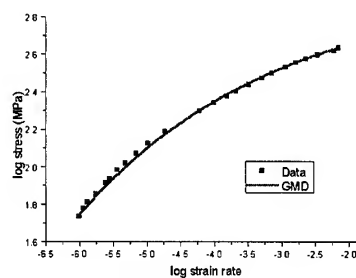
4.1. Flow curves obtained by load relaxation test

To determine the high temperature deformation mechanisms of TiAl alloys at the given small amount of deformation ($\epsilon \approx 0.04$), the flow curve data from load relaxation test have been fitted to the constitutive equation and the results are shown in Fig.2. The flow behavior of GMD shows a good agreement with the experimental data at 800 and 880°C over the entire strain rate region (Fig.2(a), 2(b)). At 980°C, experimental data points deviate with the GMD curve at low strain rate region. This is considered due to the operation of another high temperature deformation process such as dislocation climb^[5]. This dislocation climb process is observed to occur above 900°C (Fig.2(c)). All the flow curves at various temperatures do not reveal any concave shape, which is an indication of operation of GBS^[4,6]. Therefore, it is reasonable to assume that grain boundary sliding rate($\dot{\gamma}$) equals to zero in this analysis. The combined curves of GMD and dislocation climb in Fig.2(c) have been compared with the experimental data, and a good agreement is observed.

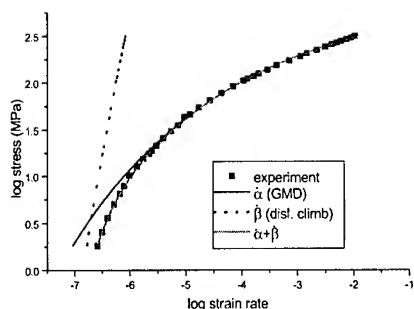
Fig.2(d) shows the result of load relaxation test (at 980°C) for heavily deformed ($\epsilon \approx 0.8$) specimen. The flow curves are very much different from those of lightly deformed ($\epsilon \approx 0.04$) specimens since the phenomenon of grain boundary sliding appears (concave upward portion) and prevails the flow behavior. Here the portion of dislocation climb creep is considered small. Then, the flow behavior is dominated by the GMD and GBS. The combined curve of GMD and GBS shows a good agreement with the experimental data in Fig.2(d).



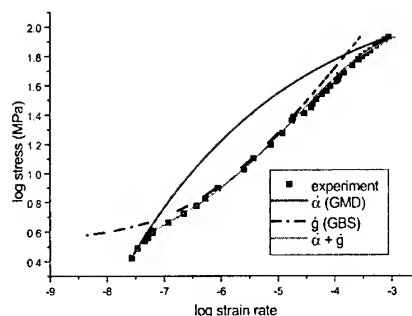
(a) 800°C



(b) 880°C



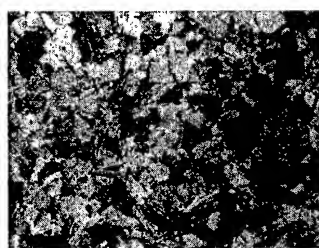
(c) 980°C ($\epsilon \approx 0.04$)



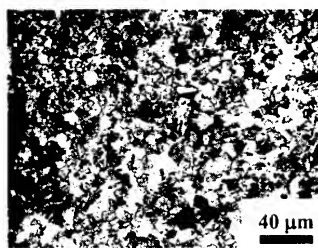
(d) 980°C ($\epsilon \approx 0.8$)

Fig.2. Comparison between experimental flow data obtained by load relaxation test and predicted curves based on the internal variable theory.

Fig.3 clearly shows the microstructural change of heavily deformed specimen. The fraction of recrystallized grains increases with the increase of the imposed strain. Thus, it is thought that grain boundary sliding would be enhanced by grain refinement due to dynamic recrystallization and contributes noticeably to total deformation of TiAl.



(a) grip area



(b) fracture area

Fig.3 Optical micrograph showing the microstructural change due to the dynamic recrystallization at a strain rate of 4×10^{-4} /s.

4.2 Flow behavior with the variation of α_2/γ phase ratio at 980°C

The flow curves of 5% and 30% α_2 microstructures at 980°C are compared. The flow curves of both microstructures can also be split into GMD and dislocation climb curves. As the volume fraction of α_2 -phase increases, flow stress of GMD slightly increases, and however, that of dislocation climb creep decreases at a fixed strain rate. It is suggested that the increase in the flow stress for grain matrix deformation in 30% α_2 microstructure is due to the higher hardness of α_2 -phase as compared to that of γ phase^[7]. As such, it is expected that total elongation would be reduced with the increase of α_2 -phase volume fraction, which has been manifested in this study as shown in Fig.4. This is in contrast to the earlier investigations^[7,8] on TiAl alloys reporting the benefit of having the large amount of α_2 phase to enhance the mechanical properties.

4.3. High temperature tensile test

Tensile tested specimens conducted at several initial strain rates and temperatures are shown in Fig.4. As the temperature increases and/or strain rate decreases, elongation increases. The largest elongation is obtained at 1050°C and 4×10^{-4} /sec. Also, it is observed that the elongation of 30% α_2 microstructure is smaller than that of 5% α_2 microstructure. The microstructures after the tensile tests are analyzed by optical microscopy. All specimens revealed that the γ grains were refined due to the dynamic recrystallization occurred during the heavy deformation.

4.4. Cavity initiation sites

To determine the cavity initiation sites, tensile specimens deformed by a 100% strain in tension at 980°C and strain rate of 4×10^{-4} /sec were investigated by back-scattered electron image. The number of cavities produced in α_2/γ , γ/γ and α_2/α_2 boundaries were quantitatively measured on the fracture area, and the results are listed in Table.1. Actually, a larger number of cavities were observed at γ/γ boundaries than α_2/γ boundaries. However, the normalized number of cavities, which was calculated by dividing the actual number of cavities with phase volume fractions of constituent phases, showed the frequency of cavity initiation at α_2/γ is 8 times higher than that of γ/γ . This implies that α_2/γ boundary is more susceptible for the cavity initiation than γ/γ boundary. This result is well agreed with that shown in Fig.3, which shows that the total elongation is reduced with increasing α_2 -volume fraction. Cavities at α_2/α_2 boundary are rarely observed due to the small volume fraction of α_2 phase in this specimen.

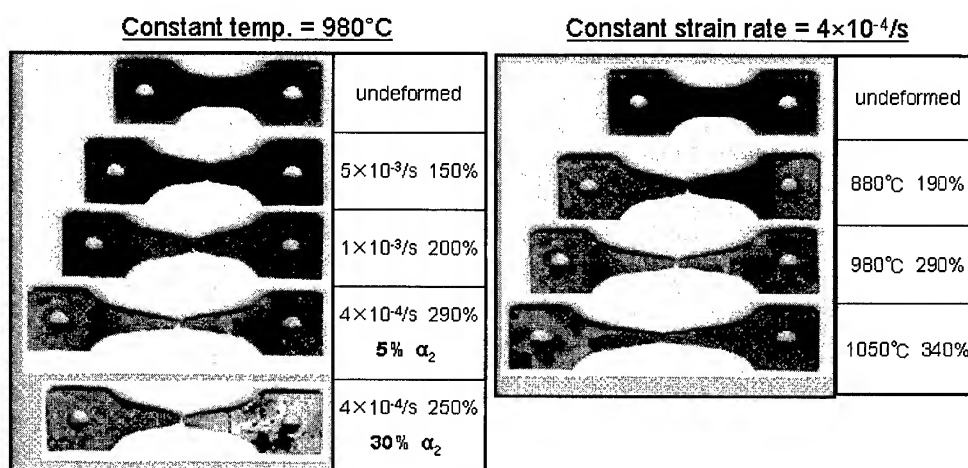


Fig.4 Superplastically deformed specimens showing the effects of strain rate, temperature and α_2 volume fraction.

Table.1 Measured and normalized number of cavities.

	γ/γ	α_2/γ
Actual numbers of cavities	55	22
Normalized numbers of cavities	0.119	0.881

5. SUMMARY

1. In the early stage of the deformation, flow curves of the fine-grained TiAl alloy are well agreed with the combined curves of grain matrix deformation and dislocation climb mechanisms. With the increase of strain, dynamic recrystallization takes place resulting in the grain refinement, and thereby, GBS is becoming dominant. At the large deformation, flow curves are well matched with the combined curves of grain matrix deformation and grain boundary sliding.

2. With the increase of α_2 -phase volume fraction, the flow stress for GMD at fixed strain rate has been increased presumably due to the high amount of stronger α_2 -phase. Correspondingly, the total elongation decreases with the increase of α_2 -phase.

3. The analysis of normalized numbers of cavities shows that the frequency of cavity initiation at α_2/γ is 8 times higher than that of γ/γ , implying that the α_2/γ boundary is more susceptible site for cavity initiation than the γ/γ boundary.

ACKNOWLEDGMENT

This work was supported by the Air Force Office of Scientific Research / Asian Office of Aerospace Research and Development. The authors are grateful for their support. One of the authors (D.H. Shin) also thanks to 2000 National Research Laboratory Program by Korea Ministry of Science and Technology. Special thanks are given to Dr. T.K. Ha for his helpful comments and discussion.

6. REFERENCES

1. W.B. Lee, H.S. Yang, Y.-W. Kim and A.K. Mukherjee, *Scripta metallurgica*, 29, (1993) pp.1403-1408.
2. Ji Sik Kim, Young Won Chang, Chong Soo Lee, *Metallurgical and Materials Transactions A*, 29A, (1998) pp. 217-226.
3. Hart, E.W., *J. Engng Mater. Tech.*, 106 (1984), pp.322.
4. T.K. Ha and Y.W. Chang, *Acta mater.* (1998), 46, pp.2741.
5. K.A. Lee, Y.N. Kwon, C.S. Lee and Y.W. Chang, *Proceedings of the 8th Int'l Conf. on Mechanical Behavior of Materials*, Vol. 3, pp.1083-1088, (1999)
6. Sung, H.J., Kim, K.S. and Chang, Y.W., *J. Korean Inst. Metals Mater.*, 31 (1993), pp.48.
7. R. Gnanamoorthy, Y. Mutoh, and Y. Mizuhara: *Mater. Sci. Eng. A197*, (1995), pp. 69-77.
8. Y.-W. Kim and Dennis M. Dimiduk, *JOM*, (August 1991), pp.40-47.

Creep, Creep-Fatigue and Continuous Fatigue Deformation

Characteristics of Lamellar TiAl Alloy

Soo Woo Nam¹, Young Sam Park and Seung Jin Yang

Department of Materials Science and Engineering, Korea Advanced Institute of Science and Technology, 373-1 Kusong-dong, Yusong-gu, Taejeon, 305-701, KOREA

¹Jointly Appointed at the Center for Advanced Aerospace Materials.

E-mail: namsw@cais.kaist.ac.kr

Abstract

By investigating research tendency on gamma TiAl alloys, it is understood that studies on gamma TiAl alloys are being conducted extensively and studies on creep, creep-fatigue and continuous fatigue properties are very urgent for the purpose of safety and performance improvement. In the case of creep considerations, it is observed that the rate controlling process of creep deformation is $\alpha_2 \rightarrow \gamma$ phase transformation accompanying dislocation generation at the lamellar interface. An intermediate Ti_2Al phase has also been observed during the phase transformation with a new atomic configuration model for $\alpha_2 \rightarrow Ti_2Al \rightarrow \gamma$ phase transformation process. In the case of creep-fatigue and continuous fatigue considerations, it is observed that fatigue life is drastically reduced in creep-fatigue test compared with that of continuous fatigue test. This reduction of fatigue life under creep-fatigue is probably due to $\alpha_2 \rightarrow \gamma$ phase transformation at the grain boundary, which induces intergranular cracking.

1. Introduction

Due to high specific strength and good creep resistance at elevated temperature, studies on gamma TiAl alloys have been conducted extensively since the first measurement of mechanical properties for the alloys in the early 1950's [1-4]. Because researches on the alloys have been conducted extensively throughout the world, it is very important to investigate the research tendency on the alloys in order to understand the importance of the studies on the mechanical properties such as creep, creep-fatigue and continuous fatigue properties. In the present study, the published papers on the alloys were analyzed in order to investigate the research tendency.

The reports concerning to creep deformation of gamma TiAl alloys have been concentrated on the study of deformation mechanism through the measurement of activation energy or stress exponent using steady state creep rates [5-8]. However, considering the fact that the size tolerance in designing high-temperature engine components is usually limited within primary

creep strain region, it is very valuable to investigate the primary creep deformation mechanism. In the present study, constant-stress tensile creep tests were conducted in order to investigate the primary creep deformation mechanism.

Gamma TiAl alloys designed for the engine components are generally exposed to low cycle fatigue deformation. Therefore, it is necessary to investigate low cycle fatigue deformation mechanism. However, studies on the mechanism were rarely investigated [4]. In the present study, total strain range controlled creep-fatigue and continuous low cycle fatigue tests were conducted in order to investigate creep-fatigue and continuous fatigue deformation mechanism.

2. Experimental

In order to investigate the research tendency, CD-ROM named Compendex Plus, a database of published papers on engineering fields, was mainly used as a source of published reports. In addition, the reports in KAIST central-library were also added to supplement the missed papers in the Compendex Plus. All the published papers on gamma TiAl alloys were classified by the published years, the nations and the research fields in order to investigate the research tendency.

The testing material mainly used in the present study, Ti-46.6Al-1.4Mn-2Mo (at.%) alloy, was processed by a hot extrusion of a blended elemental powder mixture to have an available room temperature ductility [9]. In order to get lamellar structure, which shows good creep resistance and high fracture toughness compared with duplex structure [10,11], the material was heat treated at the condition of 1653K/30min + 1223K/5hr in an Ar environment to show typical lamellar structure with a grain size of $150\mu\text{m}$ as shown in Fig. 1.

After the heat treatment, creep and fatigue specimens were machined to have a gauge diameter of 3.2 and 3mm with a gauge length of 15 and 5mm, respectively. Using the creep specimens, constant-stress tensile creep tests were conducted in an air environment over the testing temperature range from 1048 to 1173K under constant-stress ranging from 150 to 250MPa. Additionally, using the fatigue specimens, total strain range controlled creep-fatigue and continuous low cycle fatigue tests ($R=-1$, strain rate= $4\times 10^{-3}/\text{sec}$) were conducted at 1073K in an air environment. For creep-fatigue tests, tensile hold times of 5, 10 and 30min, respectively, were applied at the tensile peak strain. The number of cycles to failure, N_{cr} , was defined as the number of cycles leading to a 20% reduction of the saturated tensile peak load.

3. Results and Discussions

3.1. Research Tendency of Gamma TiAl Alloys

As of December, 2000, the total number of published papers for whole gamma TiAl alloys is 3095 and the papers were classified by the published years as shown in Fig. 2. It is observed that the numbers of the papers for whole TiAl alloys, for creep properties of TiAl alloys and for fatigue properties of TiAl alloys, respectively, increase since 1990 and extensive studies on the alloys are being conducted throughout the world. Through the classification of the reports by the nations as shown in Table 1, it is obtained that most researches have been conducted in U.S.A. and Japan. Table 2 shows the result of classification of the reports by the research fields. It is observed that most researches have been concentrated on mechanical properties as shown in Table 2-1. Concerning only mechanical properties, it is observed that tensile properties have been mainly investigated as shown in Table 2-2. These results clearly indicate

that studies on the mechanical properties are very important because the alloys were developed to be used for high-temperature engine components. Therefore, it can be inferred that the studies on creep and creep-fatigue and continuous fatigue deformation mechanisms are very urgent for the practical application of the alloys.

3.2. Primary Creep Deformation Mechanism

Fig. 3 [12] shows the relationship between creep rate and creep strain under the various creep test conditions. It is observed that creep rate in primary region decreases with creep strain, which implies that lamellar TiAl alloy shows the normal primary creep behavior [12,13]. It is also observed that steady state begins at the creep strain of $1.7 \pm 0.2\%$, regardless of test conditions. This indicates that the alloy can be regarded as "well-behaved material". It is well known that well-behaved materials have an identical substructure at any given creep strain in primary region even under different creep test conditions. Therefore, creep activation energy can be measured using the iso-strain concept. As shown in Fig. 4 [14], it is observed that apparent activation energy, Q_a , increases with normalized creep strain and is saturated to the value ranging from 380 ~ 390 kJ/mol at the beginning of steady state. It is also observed that the saturated value range is much higher than apparent activation energy for self-diffusion, 300 kJ/mol. This result clearly indicates that creep deformation is controlled by a different mechanism from diffusion mechanism [12-14].

In order to investigate primary creep deformation mechanism in viewpoint of microstructure, TEM microstructures after creep tests were observed as shown in Fig. 5 [15] and Fig. 6 [16]. Interfacial dislocation emission from α_2/γ lamellar interface accompanying α_2 phase dissolution is confirmed and the dislocations in γ lath were considered to be emitted to γ lath as shown in Fig. 5. Fig. 6 indicates that dislocations are generated at the α_2/γ lamellar interface by bowing process and the both sides of the bowed dislocations are single γ phase. Therefore, it can be confirmed that the dislocation generation process accompanying α_2 phase dissolution is the main source of dislocations and $\alpha_2 \rightarrow \gamma$ phase transformation accompanying dislocation generation becomes the creep rate controlling process. This is strongly supported by the higher values of the measured creep deformation activation energies than that of self-diffusion [12-18].

It has been currently reported that, after 0.05% creep deformation, Ti_2Al phase is newly observed during the phase transformation as shown in Fig. 7 and has been nucleated from the interaction between gliding dislocation and lamellar interface ledge [19]. In addition, an atomic configuration model for $\alpha_2 \rightarrow Ti_2Al \rightarrow \gamma$ phase transformation process has been newly proposed [19].

3.3. Creep-Fatigue and Continuous Fatigue Deformation Mechanism

Fig. 8 shows a Coffin-Manson plot taken from hysteresis loops corresponding to the half of fatigue life ($N_{cr}/2$) under the various low cycle fatigue test conditions. The plot indicates that fatigue life is drastically reduced in creep-fatigue test compared with that of continuous fatigue test. This reduction of fatigue life in creep-fatigue test is generally understood to be due to the creep damage during tensile hold time. Therefore, it can be seen that the creep-fatigue properties can be improved by inhibiting creep damage of lamellar TiAl alloy. Because the creep deformation of lamellar TiAl alloy leads to microstructural phase change [12-18], it is necessary to investigate the creep damage under creep-fatigue deformation in terms of

microstructural change.

As shown in Fig. 9, intergranular cracking mode is predominant under creep-fatigue deformation, while transgranular mode is predominant under continuous fatigue deformation. This insists that the introduction of creep damage during tensile hold time weakens a grain boundary rather than a matrix. In order to investigate the reason for the grain boundary weakness induced by the creep damage, grain boundary morphologies after low cycle fatigue tests were observed as shown in Fig. 10. Compared with the result of continuous fatigue, huge γ phase is newly observed along the grain boundary where α_2 phase has previously existed under 30min tensile hold. Therefore, it can be inferred that the generation of γ phase at the grain boundary is assisted by the creep damage and is proceeded by $\alpha_2 \rightarrow \gamma$ phase transformation at the grain boundary. Newly transformed γ phase at the grain boundary can be proposed to be responsible for grain boundary weakness due to the concentration of plastic deformation. Therefore, it can be suggested that intergranular cracking mode under creep-fatigue deformation is induced by $\alpha_2 \rightarrow \gamma$ phase transformation at the grain boundary. In order to support the suggestion that the creep-fatigue fracture behavior is controlled by $\alpha_2 \rightarrow \gamma$ phase transformation at the grain boundary, the effect of transformed γ phase on intergranular cracking must be investigated. Therefore, the compositional analysis was conducted to investigate the phases existing near fatigue cracks as shown in Fig. 11. Under continuous fatigue where transgranular and intergranular cracks co-exist, a great deal of differences are observed between compositional ratios, $\text{at.\%Al}/(\text{at.\%Ti}+\text{at.\%Al})$, near intergranular cracks and those of transgranular cracks. It is found that the ratios near intergranular cracks are in those of γ region, while the ratios near transgranular cracks are in those of $(\alpha_2 + \gamma)$ region. Under 30min tensile hold where only intergranular cracks exist, the ratios near the fatigue cracks are observed to be in those of γ region. These results evidently indicate the existence of only γ phase near intergranular crack and the existence of two phases such as α_2 and γ near transgranular crack. This implies that intergranular crack propagates along γ phase at the grain boundary, while transgranular crack propagates along lamellar plate composed of α_2 and γ phase in the matrix. Therefore, it can be inferred that grain boundary weakness and intergranular cracking under creep-fatigue deformation are induced by phase-transformed γ phase at the grain boundary. This confirms that creep-fatigue deformation mechanism is controlled by $\alpha_2 \rightarrow \gamma$ phase transformation at the grain boundary.

4. Summary

- 1) Research tendency on gamma TiAl alloys indicates that studies on gamma TiAl alloys, especially on creep, creep-fatigue and continuous fatigue deformation mechanisms, are very urgent for the purpose of safety and performance improvement.
- 2) In the case of creep considerations, the rate controlling process of creep deformation is observed to be $\alpha_2 \rightarrow \gamma$ phase transformation accompanying dislocation generation at the lamellar interface. An intermediate Ti_2Al phase is also observed during the phase transformation with a new atomic configuration model for $\alpha_2 \rightarrow \text{Ti}_2\text{Al} \rightarrow \gamma$ phase transformation process.
- 3) In the case of low cycle fatigue considerations, it is observed that fatigue life is drastically reduced in creep-fatigue test compared with that of continuous fatigue test. This reduction of fatigue life is probably due to $\alpha_2 \rightarrow \gamma$ phase transformation at the grain boundary, which induces intergranular cracking.

Acknowledgment

This research was sponsored by Korea Science and Engineering Foundation through the Center for Advanced Aerospace Materials, Pohang University of Science and Technology. The authors gratefully acknowledge its financial support. Also, the authors gratefully express their appreciation to Prof. Sun Keun Hwang in Inha Univ. for supplying the testing materials.

References

1. J. B. McAndrew and H. D. Kessler, *J. Metals*, (1956), pp. 1348.
2. Y. W. Kim, *J. Metals*, Vol. 41, No. 7 (1989), pp. 24.
3. Y. W. Kim and D. M. Dimiduk, *J. Metals*, Vol. 43, No. 8 (1991), pp. 40.
4. S. W. Nam, Y. S. Park, S. K. Hwang, *Proceedings of the 14th Conference on Mechanical Behaviors of Materials*, S. I. Kwon and D. I. Kwon, eds., The Korean Institute of Metals and Materials, Seoul, Korea, (2000), pp. 15.
5. M. Es-Souni, A. Bartels and R. Wagner, *Mater. Sci. Eng. A*, Vol. 171 (1993), pp. 127.
6. M. Es-Souni, A. Bartels and R. Wagner, *Acta Metall. Mater.*, Vol. 43 (1995), pp. 153.
7. R. W. Hayes and P. A. McQuay, *Scr. Metall. Mater.*, Vol. 30 (1994), pp. 259.
8. J. Trinatafillou, J. Beddoes, L. Zhao, W. Wallace, *Scr. Metall. Mater.*, Vol. 31 (1994), pp. 1387.
9. I. S. Lee, S. K. Hwang, W. K. Park, J. H. Lee, D. H. Park, H. M. Kim and Y. T. Lee, *Scripta Metall. Mater.*, Vol. 31 (1994), pp. 57.
10. B. D. Worth, J. W. Jones and J. E. Allison, *Metall. Trans. A*, Vol. 26 (1995), pp. 2947.
11. H. E. Deve, A. G. Evans and D. S. Shih, *Acta Metall. Mater.*, Vol. 40 (1992), pp. 1259.
12. H. S. Cho, S. W. Nam, S. K. Hwang and N. J. Kim, *Mater. Sci. Res. Inter.*, Vol. 3, No. 3 (1997), pp. 166.
13. H. S. Cho, S. W. Nam, Y. W. Kim, *Metals and Materials*, Vol. 4, No. 1 (1998), pp. 33.
14. S. W. Nam, H. S. Cho, S. K. Hwang and N. J. Kim, *Metals and Materials*, Vol. 6, No. 4 (2000), pp. 287.
15. H. S. Cho and S. W. Nam, *Metals and Materials*, Vol. 5, No. 3 (1999), pp. 255.
16. S. W. Nam, H. S. Cho, S. K. Hwang and N. J. Kim, *Mater. Sci. Eng.*, Vol. A239-240 (1997), pp. 457.
17. H. S. Cho, S. W. Nam, S. K. Hwang and N. J. Kim, *Scripta Mater.*, Vol. 36, No. 11 (1997), pp. 1295.
18. H. S. Cho, S. W. Nam, J. H. Yun and D. M. Wee, *Mater. Sci. Eng.*, Vol. A262 (1999), pp. 129.
19. S. J. Yang and S. W. Nam, *Mater. Sci. Eng. A*, (2001), in published.

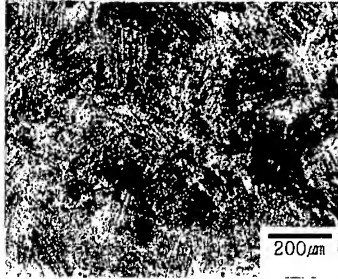


Fig. 1. Microstructure. (OM)

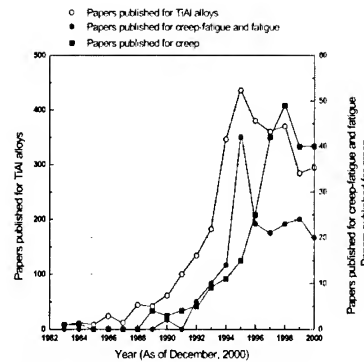


Fig. 2. Number of the published papers for whole TiAl alloys, for creep and for creep-fatigue and fatigue of TiAl alloys in each year. (As of December, 2000)

Table 1. Classification of the published reports by the nations. (As of December, 2000)

Nations	No. of Publications	%
U.S.A.	1248	40.3
Japan	796	25.7
Germany	232	7.5
China	203	6.6
U.K.	115	3.7
Korea	106	3.4
Others	395	12.8
Total	3095	100

Table 2-1. Classification of the published reports by the research fields. (As of Dec., 2000)

Fields	No. of Publications	%
Mechanical Property	1628	52.6
Alloying effect	450	14.5
Microstructure	404	13.1
Manufacturing process	216	7.0
Environment effect	195	6.3
Others	202	6.5
Total	3095	100

Table 2-2. Classification of the published reports concerning mechanical properties by testing methods. (As of December, 2000)

Fields	No. of Publications	%
Tensile test	621	38.1
Creep test	249	15.3
Toughness test	230	14.1
Creep-fatigue and fatigue test	185	11.4
Compressive test	109	6.7
Others	234	14.4
Total	1628	100

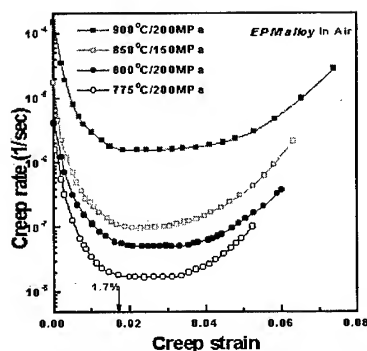


Fig. 3. Creep deformation rates under the various creep test conditions [12].

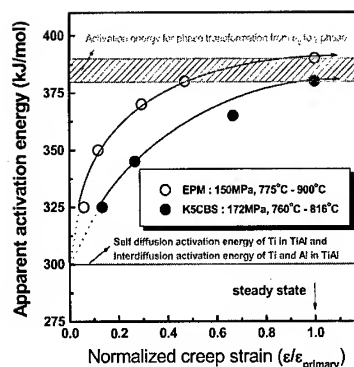


Fig. 4. Relationship between apparent activation energy and normalized creep strain [14].



Fig. 5. Microstructure after 0.05% creep deformation [15].

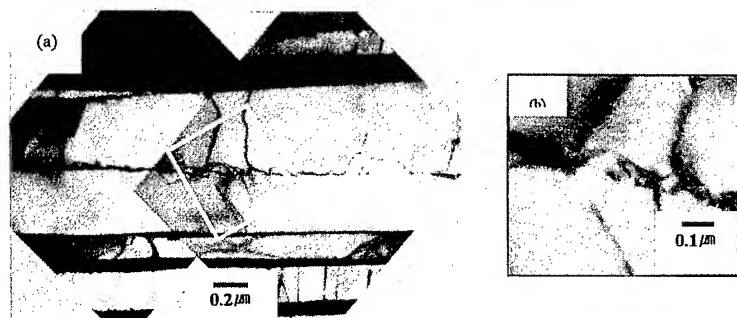


Fig. 6. Microstructure after 0.2% creep deformation [16]. (a) Dislocations are considered to be generated at α_2/γ lamellar interface, (b) Diffraction pattern of single γ phase.

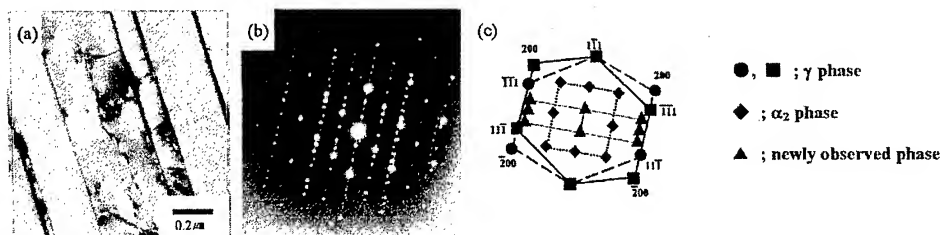


Fig. 7. Microstructure after 0.05% creep deformation [19].

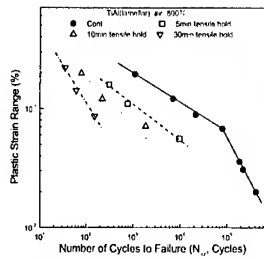


Fig. 8. Coffin-Manson plot.

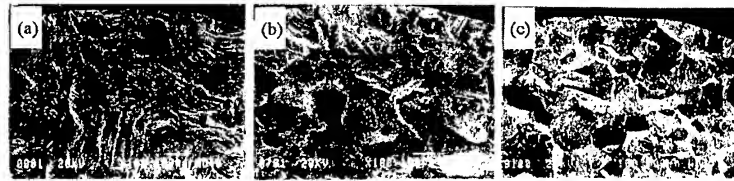


Fig. 9. Fatigue fracture surfaces. (a) $\Delta\epsilon_f = \pm 0.5\%$, cont., (b) $\Delta\epsilon_f = \pm 0.7\%$, cont., (c) $\Delta\epsilon_f = \pm 0.7\%$, 30min tensile hold.

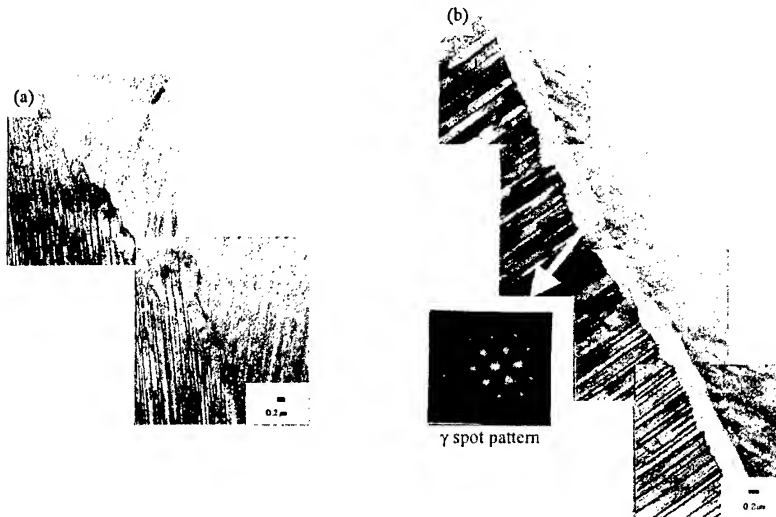


Fig. 10. G.B. morphologies ($N=N_{cr}$) (a) $\Delta\epsilon_f = \pm 0.7\%$, cont., (b) $\Delta\epsilon_f = \pm 0.7\%$, 30min tensile hold.

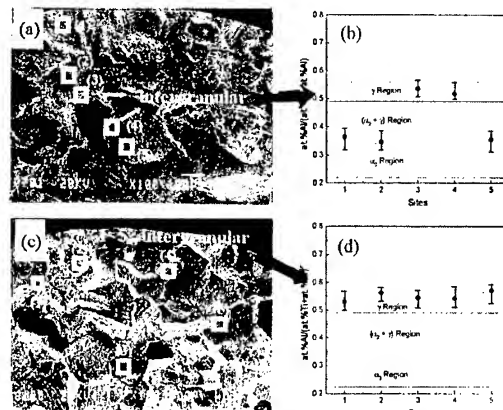


Fig. 11. AES (auger electron spectroscopy) analysis results. ($N=N_{cr}$, $\Delta\epsilon_f = \pm 0.7\%$)

(a) fatigue fracture surface (cont.), (b) AES result of (a),
(c) fatigue fracture surface (30min tensile hold), (d) AES result of (c).

A comparative study of the creep resistance improvement between the interstitial alloying elements and different heat treatments for TiAl alloys

Seung Jin Yang, Soo Woo Nam¹ and Sun Keun Hwang²

Dept. of Materials Science and Engineering
Korea Advanced Institute of Science and Technology

¹ Jointly appointed at the Center for Advanced Aerospace Materials

² Inha University, Jointly appointed at the Center for Advanced Aerospace Materials

Abstract

It is well known that TiAl alloy with a fully lamellar structure shows the highest creep resistance. In the fully lamellar structure, there exist abundant lamellar interfaces and the microstructure has an important role on the creep resistance. Recently, some efforts to improve the creep resistance of lamellar TiAl alloy have been reported. With decreasing lamellar spacing and an interstitial alloying (carbon addition) effect, the creep resistance of lamellar TiAl would be improved. However, the microstructure can be changed by carbon addition. The primary alloy has a composition of Ti-46.6Al-1.4Mn-2Mo (at.%), which was made by EPM method. Primary test alloys have three different lamellar spacing with different cooling process and three different amounts of carbon were added to the normal alloy (0.15, 0.3 and 0.6 at.%). To compare with creep resistance, constant tensile stress creep tests were conducted at the condition of 800/850/900°C/150MPa. In this investigation, the effective method to improve the creep resistance of lamellar TiAl will be discussed with different lamellar spacing and carbon contents.

1. Introduction

It is well known that TiAl alloy with a fully lamellar structure shows the highest creep resistance [1]. In the fully lamellar structure, there exist abundant lamellar interfaces. The lamellar spacing has an important effect on the creep behavior of TiAl alloy [2]. The relationship between lamellar microstructure and mechanical properties has been reported [3,4]. Recently, the improvement of creep resistance was reported with decreasing lamellar spacing [5] and the effect of interstitial atoms (carbon and nitrogen) [6-8]. In this investigation, the creep behavior of TiAl alloy which has different lamellar spacing and carbon composition will be compared and the effective method to improve creep resistance will be discussed.

2. Experimental details.

The primary alloy used for this study has a nominal composition of Ti-46.6Al-1.4Mn-2Mo (at.%). This alloy was prepared by EPM method. This alloy was heat treated to have a lamellar structure with the schedule of 1380°C/30min/ cooling + 950°C/5hr/ cooling with different cooling methods. A lamellar colony size is fixed in homogenization condition and the lamellar spacing is changed with cooling method. The characteristics of each sample are listed in table 1. Constant tensile stress creep tests were conducted at the conditions of 800/850/900°C/150MPa. An optical microscope and a TEM of Philips CM-20 were used to observe the microstructure.

Table 1. The characteristics of each prepared fully lamellar TiAl alloy.

Alloy	Composition (at.%)	Cooling method
Base alloy	Ti-46.6Al-1.4Mn-2Mo (Base)	Air cooling
Fine lamellar	Base	Compressed air blow
Low-carbon	Base + 0.15C	Air cooling
Intermediate-carbon	Base + 0.3C	Air cooling
High-carbon	Base + 0.6C	Air cooling

3. Results and discussion

The microstructures of test samples are shown in figure 1 and 2 with different cooling rate and carbon contents, respectively. It can be easily seen that the lamellar colony size is not changed in all cases, however the lamellar spacing is decreased with different cooling process and carbon contents. The measured lamellar colony size is around 90~110 μm and the lamellar spacing in each condition is shown in figure 3.

Figure 4 exhibits creep test results with various test conditions. Figure 5 and Table 2 shows creep resistance of each test sample. It is clear that the creep resistance of fully lamellar TiAl alloy is improved by decreasing lamellar interface and carbon addition. The most creep resistant alloy among test samples is the compressed air blown alloy that has the finest lamellar interfacing as shown in Fig. 3 and 5. The reduction of lamellar interfacing is occurred by carbon addition, too. Therefore test alloys would be made a list in the ascending creep resistance by the lamellar spacing. From the figure 3, the apparent creep activation energy is easily calculated. The calculated creep activation energy is from 370 to 390kJ/mol. That means all tested alloy do not have different creep deformation mechanism but have same creep deformation mechanism that is phase transformation controlling deformation process [9-11]. Considering the creep deformation mechanism of lamellar TiAl [9-11], the improvement of creep resistance with decreasing lamellar spacing may be easily understood.

Table 2. Time to constant creep strain in each condition (hr)

		Base alloy	Low carbon	Intermediate	High carbon	Fine lamellar
800 °C /150MPa	To 0.5%	1.7	3.59	6.78	11.52	10.58
	To 1%	6.4	23.89	52.80	77.83	93.94
	To 1.5%	13.41	77.10	114.15	176.87	209.87
850 °C /150MPa	To 0.5%	1.38	2.68	3.19	4.01	7.513
	To 1%	5.41	11.29	22.87	26.99	44.40
	To 1.5%	13.36	28.79	55.85	66.32	83.27
900 °C /150MPa	To 0.5%	0.07	0.12	0.26	0.39	0.59
	To 1%	0.33	1.24	2.311	3.06	4.44
	To 1.5%	1.23	3.96	5.92	7.93	11.10

According to the creep deformation mechanism, initial dislocations are disappeared at the lamellar interface in initial primary creep stage and new moving dislocations are generated by $\alpha_2 \rightarrow \gamma$ phase transformation at the lamellar interface in order to continue creep deformation. However, higher interface density in fine lamellar TiAl alloy may accelerate the disappearance of dislocation and restrict the dislocations movement by the narrow γ width. Additionally, densely interfacial boundaries may block the emission of dislocation that is necessary for continuous creep deformation because the shear stress for the emission of dislocations at the lamellar interface is increased with decreasing lamellar interface [12]. On that account, a fine lamellar spacing can hinder the movement of dislocation that is necessary for creep deformation. Therefore, the creep resistance can be improved by decreasing the lamellar spacing.

As seen in figure 4 and figure 5, the creep resistance of lamellar TiAl alloy is also increased by carbon addition. The effects of carbon on the creep resistance of TiAl intermetallics were reported in terms of the precipitation strengthening [13] or solute/dislocation interaction [14,15]. Anyway, the efficiency of carbon addition for the improvement of creep resistance is lower than fast cooling method in lamellar TiAl. As seen in figure 4, the creep resistance of fast cooled alloy is better than that of 0.6 at% carbon added alloy. In this study, it is not clearly investigated that the precipitation effect and the influence of solute/dislocation interaction by carbon on the creep behavior. However, when the tendency of lamellar spacing in different carbon added alloys is compared with another alloys, the major effect of carbon addition on the improvement of creep resistance in lamellar TiAl may be the reduction of lamellar spacing. Fig. 5 shows the relationship among the creep resistance, carbon content and lamellar spacing.

4. Summary and conclusion

The creep resistance of different carbon added alloy has been compared with fast-cooled alloy at the viewpoint of lamellar spacing. The most creep-resistant alloy among test samples is fast cooled alloy that has a most narrow lamellar spacing. From the results, more effective method

on the improvement of creep resistance is controlling the lamellar spacing with different heat treatment schedule than carbon addition (under 0.6at.%). Therefore, the optimized heat treatment schedule would be more effective way than carbon addition in the alloy design of lamellar TiAl alloy.

5. Acknowledgements

The authors wish to thank the Korea Science and Engineering Foundation (KOSEF) for the financial support this study (Korea-China joint project, No 968-0800-008-2) and Professor S-K Hwang, at the Inha University, Korea for supplying test material.

References.

1. SC. Huang, Metall. Trans., Vol. 23A(1998), pp. 375
2. J. Beddoes, W. Wallace and L. Zhao, Int. Mat. Rev., Vol. 40(5) (1995), pp. 197
3. K. Maruyama, R. Yamamoto, H. Nakakuki and N. Fujitsuna, Mater. Sci. and Eng. A, Vol. 239-240(1997), pp. 419
4. G. Cao, L. Fu, J. Lin, Y. Zhang and C. Chen, Intermetallics, Vol. 8(2000), pp. 647
5. C.E.Wen, K. Yasue, J.G.Lin, Y.G. Zhang and C.Q. Chen, Intermetallics, Vol. 8(2000), pp. 525
6. W.H. Tian, T. Sano and M. Nemoto, Phil. Mag. A, Vol. 68(1993), pp. 965
7. H.S.Cho, S.W. Nam, J.H. Yun, and D.M. Wee, Mater. Sci. and Eng. A, Vol. 262(1999), pp. 129
8. J.H.Yun, M.H.Oh, S.W. Nam and D.M. Wee, Mater. Sci. and Eng. A, Vol. 239-240(1997), pp. 702
9. S.W.Nam, H.S.Cho, S-K. Hwang and N.J. Kim, Mater. Sci. and Eng. A, Vol. 239-240 (1997), pp.457
10. S.W.Nam, H.S.Cho, S-K. Hwang and N.J. Kim, Metals and Materials, Vol. 4(1998), pp.33
11. S.W.Nam, H.S.Cho, S-K. Hwang and N.J. Kim, Metals and Materials, Vol. 5(1999), pp.255
12. P.M. Hazzledine, Intermetallics, Vol. 6(1998), pp. 673
13. G.B. Viswanathan, Y-W. Kim, Y-W and M.J. Mills, in Gamma Titanium Aluminides, Y-W. Kim, D.M. Dimiduk and M.H. Loretto, eds., TMS, San Diego, California,(1999), pp.653
14. P.I. Gouma, S.J. Davey and M.H. Loretto, Mater. Sci. and Eng. A, Vol. 241(1998), pp. 151
15. B.D. Worth, J.W. Jones and J.E., Allison, Metall. and Mater. Trans., Vol. 26A(1995), pp.2961

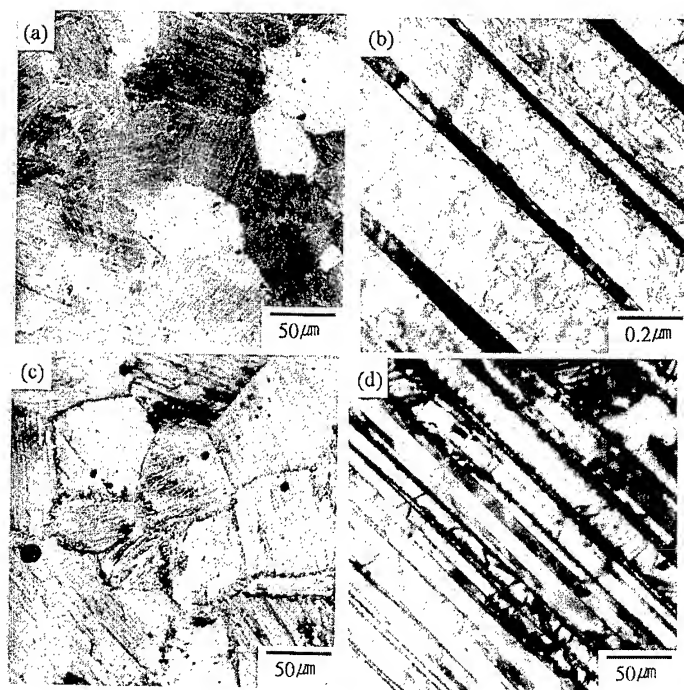


Fig. 1. The microstructure of fully lamellar TiAl alloy with different cooling rate (a) and (b) after normal heat treatment; (c) and (d) after fast cooling rate.

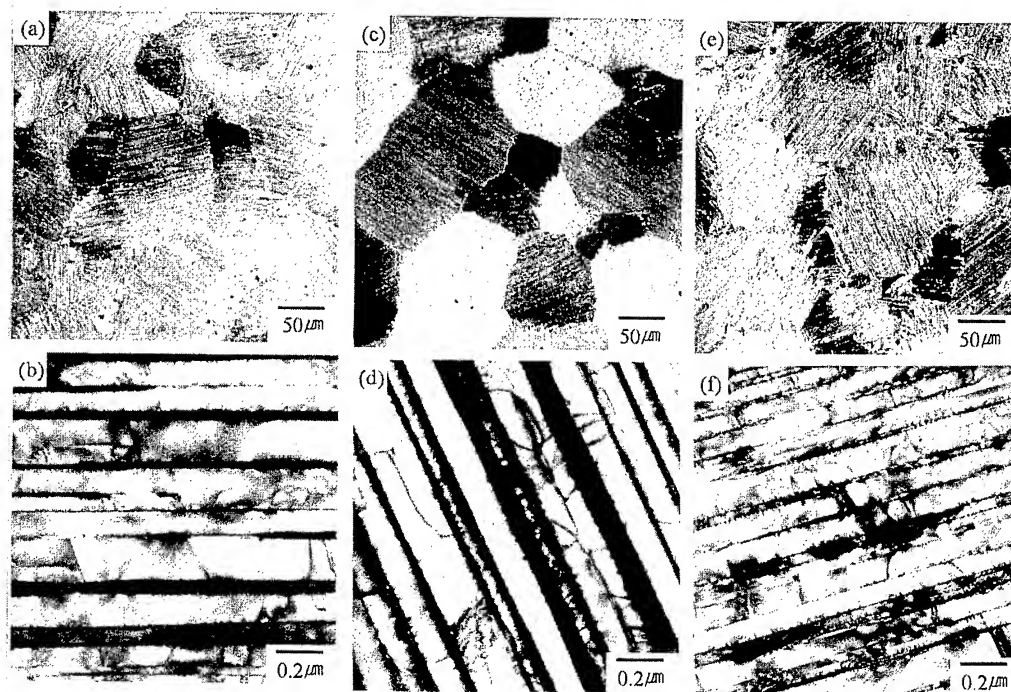


Fig. 2. The microstructure of fully lamellar alloy with different carbon contents. (a) and (b) 0.15 at.% C; (c) and (d) 0.3at.% C; (e) and (f) 0.6at.% C.

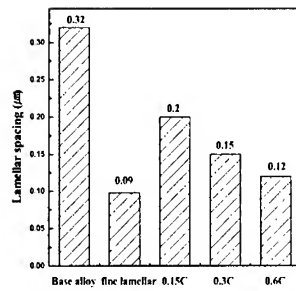


Fig. 3. The comparison of a lamellar spacing for each test condition.

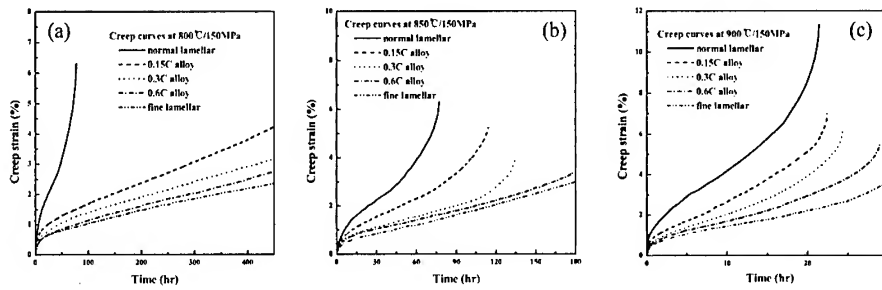


Fig. 4. The creep behaviors of lamellar TiAl alloy with different carbon addition and different cooling rate.

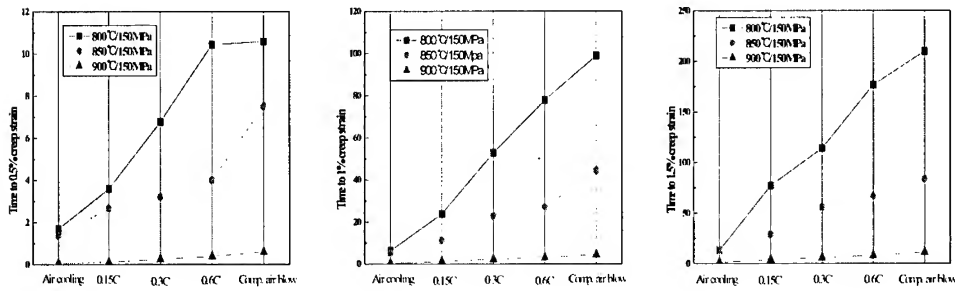


Fig. 5. Time to constant creep strain for each creep test condition

EFFECT OF LAMELLAR SPACING ON THE FATIGUE CRACK PROPAGATION RESISTANCE OF FULLY LAMELLAR γ -TiAl ALLOY

Hyun Jin Kim and Chong Soo Lee

Center for Advanced Aerospace Materials
Department of Materials Science and Engineering
Pohang University of Science and Technology
San 31, Hyoja-dong, Pohang 790-784, KOREA

ABSTRACT

The fatigue crack propagation resistance of Ti-46.2Al-2Cr-3Nb alloy associated with the variation of lamellar spacing (0.7 μ m and 0.1 μ m) was examined at ambient (25°C) and high (600°C, 800°C) temperatures. Particular interest was given to understand the role of lamellar interface on the fatigue crack growth resistance with the variation of temperature. The fine lamellar structure showed superior fatigue resistance as compared to the coarse lamellar structure not only at room temperature (25°C) but also at high temperature (800°C). It was mainly attributed to the excellent intrinsic fatigue resistance of the microstructure as well as the higher extrinsic closure effect.

However, in the case of 600°C, fatigue resistance of fine lamellar structure was significantly decreased to the level of coarse lamellar structure. Embrittlement of lamellar interface by the adsorption of hydrogen and/or oxygen at 600°C was considered to be responsible for the deterioration of fatigue resistance of fine lamellar microstructure, and however, the effect was not marked at 800°C due to the formation of thick oxide layer at the surface, hindering the adsorption of hydrogen.

1. INTRODUCTION

Previous studies [1-6] on FCP of γ -TiAl alloys have shown that the lamellar microstructure exhibits superior fracture toughness and fatigue crack growth resistance as compared to the duplex and near γ microstructures. The higher crack growth resistance of the lamellar structure can be attributed to the anisotropic nature of the microstructure itself and it is generally believed that the crack growth resistance of the lamellar microstructure is mainly governed by two microstructural factors such as colony size and lamellar spacing. However, until now, there has been very limited information as to the independent role of lamellar spacing on the fatigue crack propagation resistance. Therefore, the objectives of the present study are to investigate the effects of lamellar spacing on FCP properties and to understand better the FCP mechanism. Since these alloys are mainly intended for elevated temperature use up to about 800°C, there is obvious concern whether the lamellar spacing effects on FCP are kept at high temperature.

2. EXPERIMENTAL PROCEDURES

The material used in the present study was Ti-46.2Al-2Cr-3Nb-0.2W-0.16B-0.12C-0.18O (at.%) alloy and supplied by Universal Energy System. By applying different heat treatment, microstructures with different lamellar spacing but with constant colony size were produced. Their heat treatment conditions and microstructures are listed in Table 1.

Table 1. Heat treatment conditions and microstructural parameters for two microstructures of fully lamellar γ -TiAl alloys

Microstructures	Heat Treatment Conditions	CS(μ m)	LS(μ m)	C	n
Coarse Lamellar Width	1340°C/50min./CC/1000°C/AC	~250	~0.7	4.10×10^{-20}	12.07
Fine Lamellar Width	1340°C/60min./AC	~250	~0.1	1.66×10^{-18}	9.22

The as-received alloy was cast and isothermally forged materials at 1150°C with a pancake shape which has 12mm thickness. The alloy has boride particles in the microstructure, which can prevent effectively the colony coarsening during the cooling. Microstructures obtained after two different heat treatments are presented in Fig. 1.

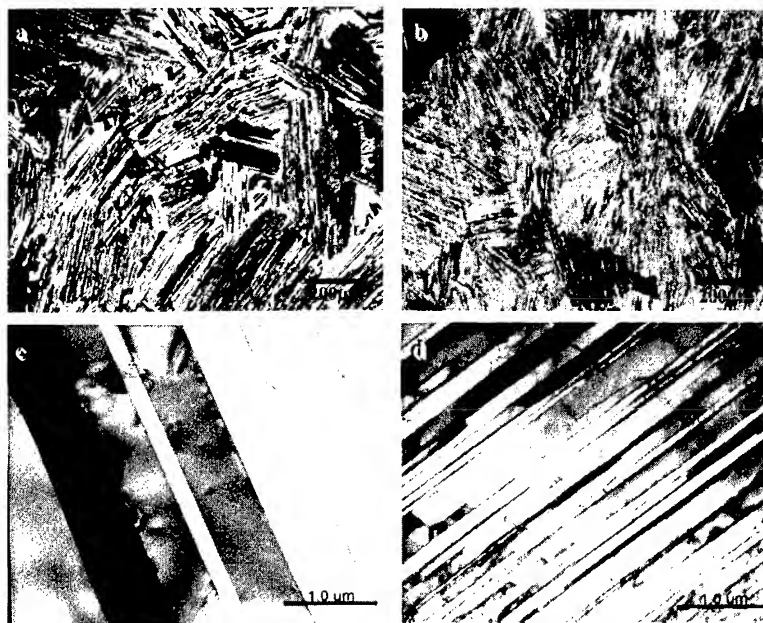


Fig. 1. Optical and TEM micrographs of coarse(a,c) and fine(b,d) lamellar microstructures : (a),(b) optical micrographs, (c),(d) TEM micrographs.

Fatigue crack growth tests were conducted at 25°C (room temperature), 600°C and 800°C in an ambient environment using compact tension (CT) specimens (31.15mm x 30mm x 5mm). Prior to the crack growth tests, precracks were produced to 1-2mm by load shedding procedures (K-decreasing) in accordance with ASTM E647-86a. The microstructures and

crack profiles were examined by optical and scanning electron microscopy (SEM) for each samples, and the lamellar spacing was investigated by transmission electron microscopy (TEM).

3. RESULTS AND DISCUSSIONS

3.1 Effect of lamellar spacing

Fig. 2 shows the variation of fatigue crack growth rates, the normalized crack closure levels and intrinsic fatigue crack growth rates for the fully lamellar microstructures with different lamellar spacing ($0.1\mu\text{m}$ and $0.7\mu\text{m}$). The crack growth rate of the coarse lamellar spacing is much higher than that of the fine lamellar spacing while the near threshold stress intensity ranges of both microstructures converge together within a narrow range of 7.8 to $8.5\text{ MPa}\sqrt{\text{m}}$. But, the constants of the Paris equation, $da/dN=C(\Delta K)^n$, for these two microstructures are largely different.

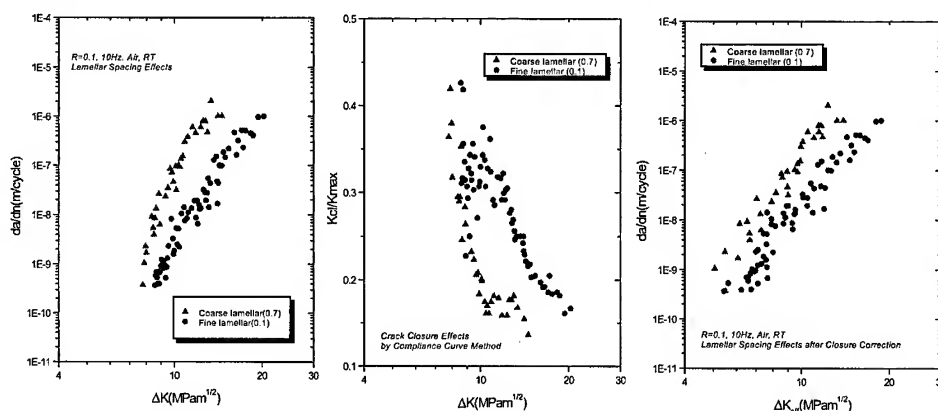


Fig. 2. Fatigue crack growth rates and normalized crack closure levels of two microstructures with different interlamellar spacings

Coarse lamellar microstructure shows n value of about 12, while fine lamellar microstructure shows n value of 9. Kim [10] has shown that, in his previous fracture tests, lamellar spacing is more significant microstructural variable than colony size for over the $100\mu\text{m}$ colony size range in the fully lamellar microstructure. Also, in our previous study [11–12], fatigue crack growth rates are almost same in two different microstructures which have similar lamellar spacing and different colony size. From the above results, it can be concluded that lamellar spacing is more dominant variable for controlling the fatigue crack growth rates than the colony size.

Crack propagation paths observed on the surface of specimens are shown in Fig. 3. As seen in this figure, several microcracks, crack deflections, lamellar interface delaminations and shear ligaments are observed in fine lamellar microstructure. On the other hand, coarse lamellar microstructure has lesser degree of crack deflection showing relatively flat crack paths.

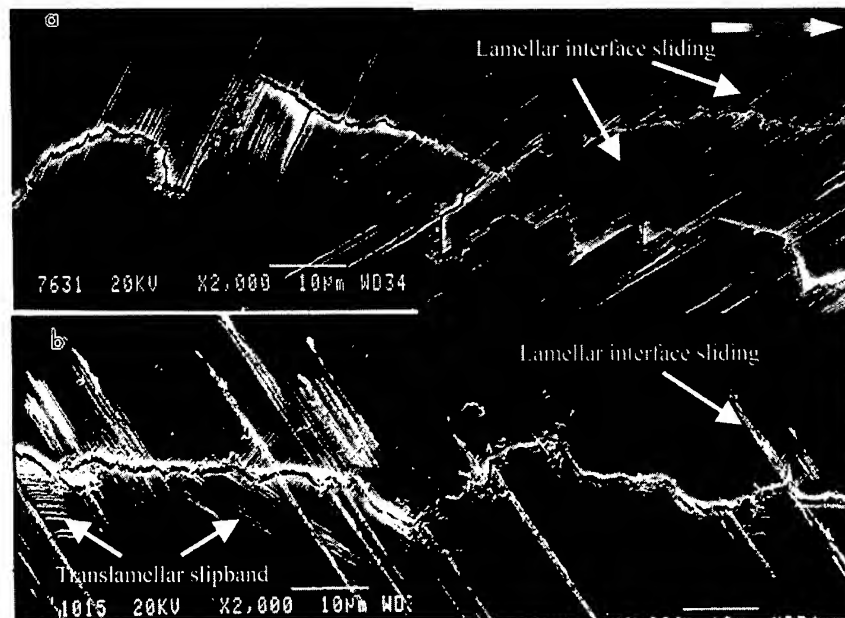


Fig. 3. Translamellar slip bands and/or lamellar interface sliding phenomenon (a) in the fine lamellar spacing and (b) in the coarse lamellar spacing microstructures. Horizontal arrows indicate the crack-growth direction.

3.2 Effect of temperature

Fig. 4 shows the effect of temperature on the fatigue crack growth behavior of two microstructures with different lamellar spacing. With increasing temperature, coarse lamellar spacing microstructure has shown gradual decrease of fatigue crack propagation resistance. However, fine lamellar spacing microstructure has shown significant decrease of near threshold stress intensity factor range ($\Delta K_{\text{near threshold}}$) at 600°C. In the cases of room temperature and 800°C, near threshold stress intensity levels converge to almost same levels, though crack propagation rate at 800°C is a little higher than that at room temperature. It is worthwhile to consider why the crack growth resistance at 600°C is inferior as compared also been reported at temperature range of 600 ~ 650°C. Our results on fatigue crack growth resistance with the variation of temperature also manifest the occurrence of the anomalous behavior.

It is thought that the anomalous behavior of fatigue crack growth resistance comes from two factors. One is the change of mechanical (tensile) properties with the temperature and the other is the environmental embrittlement effect. Tensile test results as shown in Fig. 5 represent that yield strength decreases gradually with increasing temperature both in the coarse and fine lamellar specimens.

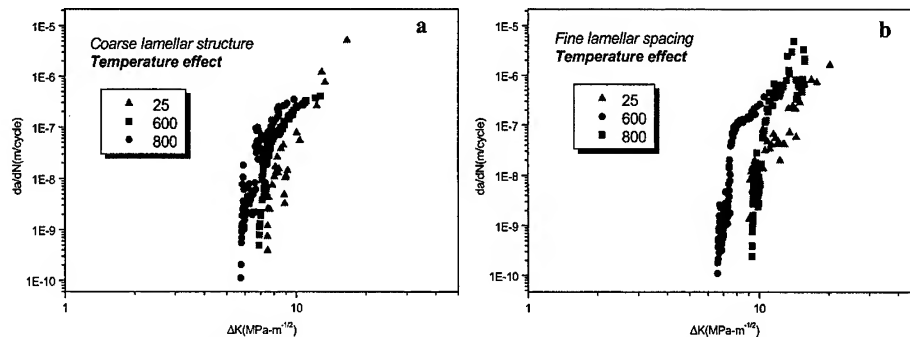


Fig. 4. Fatigue crack growth rates with the variation of temperature (a) coarse lamellar spacing and (b) fine lamellar spacing.

Considering the fact that fatigue crack growth rates are proportional to the plastic zone size near the crack tip, which is subsequently inversely proportional to the yield stress, it is not surprising to observe lower fatigue crack growth resistance at higher temperature. Also, the environmental embrittling effect would be accelerated with increasing temperature.

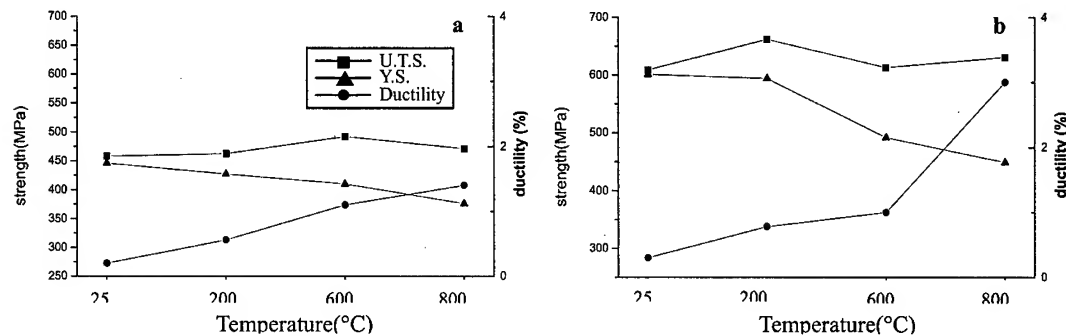


Fig. 5. Effects of interlamellar spacing and test temperature on the tensile properties (a) coarse lamellar spacing (b) fine lamellar spacing.

Then, the question arises as to the higher FCG resistance at 800°C observed only in the fine lamellar microstructures. The existence of ductile to brittle transition temperature (DBTT) observed at temperature range of 600 ~700°C in γ alloy would be one reason for the phenomenon. At a temperature of 800°C just above the DBTT, the material would reveal high ductility (inducing high toughness), in spite of its lower yield stress, resulting in the high resistance for fatigue crack propagation in the near threshold region. Another reason for the higher FCG resistance at 800°C may come from thick oxide layer formed on the crack surface during the cyclic loading (Fig. 6), which might have beneficial roles in the fatigue resistance. The $\Delta K_{\text{near threshold}}$ can be largely increased by the large amount of oxide induced crack closure. Also, hydrogen embrittlement, which is more pronounced in the fine lamellar microstructure, would be effectively inhibited by the formation of thick oxide layers.

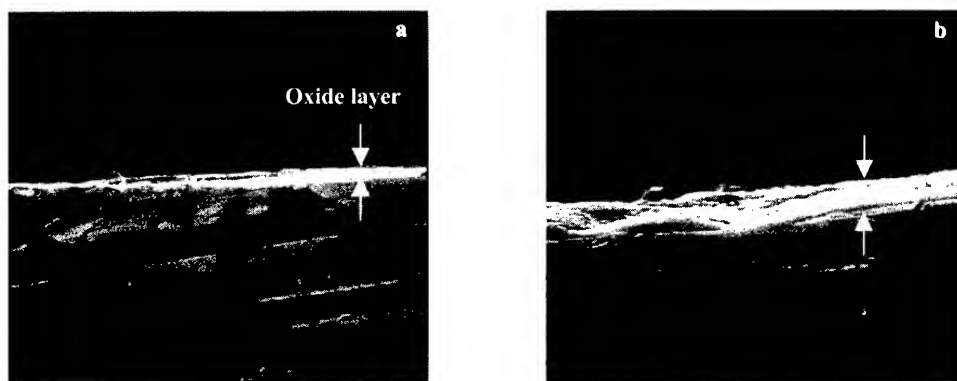


Fig. 6. SEM micrographs showing different oxide layer(Al_2O_3) thickness (a) 600°C (b) 800°C

4. CONCLUSION

Fine lamellar microstructure represents superior fatigue crack growth resistance as compared to the coarse lamellar spacing microstructure at all temperature ranges, which is mainly attributed to the higher intrinsic nature of the microstructure as well as to the higher extrinsic closure effects. Particularly, fine lamellar microstructure showed lowest ΔK_{th} due to marked environmental embrittlement at 600 °C. On the while at 800°C, thick Al_2O_3 oxide layer, which effectively inhibits the embrittlement by hydrogen on the specimen surface enables to restore the toughness of the alloy. However, the effect is minimized in the coarse lamellar spacing microstructure due to its smaller number of lamellar interface.

REFERENCES

1. Y.-W. Kim, J.Metals, Vol.41(1989), pp. 24
2. Y.-W. Kim and D.M.Dimiduk, J.Metals, Vol.43 (1991) pp.40
3. Y.-W. Kim : J.Metals, 46 (1994) 30
4. C.M.Austin and T.J.Kelly : Int'l Symp. On Gamma Titanium Aluminides, Y.-W.Kim, R.Wagner, and M.Yamaguchi (eds.), TMS, Warrendale, PA, (1995) 21
5. P.E.Jones, D.Smits, D.Eylon, and G.Covlin : Int'l Symp. On Gamma Titanium Aluminides, Y.-W.Kim, R.Wagner, and M.Yamaguchi (eds.), TMS, Warrendale, PA, (1995) 53
6. H.E.Deve, A.G.Evans, and D.S.Shih : Acta Metall. Mater., 40 (1992) 1259
7. S.L.Semiatin, D.C.Vollmer, S. El-Soudani, and C.Su : Scripta Metall. Mater., 25 (1991) 1409
8. Y.-W. Kim : Acta Metall. Mater., 40 (1992) 1121
9. C.Choi, Y.T.Lee and C.S.Lee : Scripta Metall., 36, (1997) 821
10. Y.-W. Kim : Mater. Sci. Eng., A192/193 (1995) 519
11. J.M.Larsen, B.D.Worth, S.J.Balson, and J.W.Jones : Gamma Titanium Aluminides, Y.-W.Kim, R.Wagner and M.Yamaguchi(eds.), TMS, Warrendale, PA, (1995) 717
12. K.T.Venkateswara Rao, Y.-W. Kim and R.O.Ritchie : Gamma Titanium Aluminides, Y.-W.Kim, R.Wagner and M.Yamaguchi(eds.), TMS, Warrendale, PA, (1995) 893

***In-situ* OBSERVATION OF FATIGUE CRACK PROPAGATION OF Ti-Al INTERMETALLICS**

H. Suzuki*, A. Nozue* and M. N. Tamin**

* Department of Mechanical Engineering, Sophia University,
7-1 Kioi-cho, Chiyoda-ku, Tokyo 102-8554, JAPAN

** Faculty of Mechanical Engineering, Universiti Teknologi Malaysia,
81310 UTM Skudai, Johor, MALAYSIA

ABSTRACT

Ti-Al intermetallics have been developed for high temperature structural material to be used in turbine or internal combustion engines. The relation between fatigue properties and microstructure in addition to the effect of environment is important in these applications. In this paper, fatigue crack propagation of Ti-48Al intermetallics is studied by means of *in-situ* observation of crack growth. Three types of microstructure, namely, as-cast, duplex and fully lamellar structure are used for fatigue experiment that is performed in vacuum and air condition. Fatigue crack propagation property is strongly dependent on the angle between direction of the crack and the orientation of lamellar layers. The observed crack growth behavior is classified into possible modes of crack propagation in lamellar structure, which is made possible by detailed *in-situ* observation of crack extension. The preferred path of crack propagation is found to go through the weakest phase of the structure with associated microcracking within plastic zone around the tip of the crack. Crack growth is accelerated in air compared with vacuum condition. This phenomenon is attributed to the effect of humidity in the crack tip plastic zone. The environmental effect is discussed through the observation of crack propagation and the resulting fractured surface.

1. INTRODUCTION

Intermetallics based on γ (TiAl) titanium aluminide have been developed as high temperature structural material because of their superior mechanical properties at high temperature and relatively low density compared to conventional heat resistant alloys [1]. Typical area of application of the material is turbine or internal combustion engines. The relationships between microstructure and mechanical properties, especially on fatigue and fracture properties have been reported by many researchers [2-4]. The microstructure of the material can be controlled by thermo-mechanical or heat treatment to obtain favorable microstructure for specific applications [5-7]. Typical microstructures of the alloy can be classified into three types [1]: as cast, fully lamellar and duplex structure. Fatigue and fracture properties of the material are strongly dependent on the orientation of lamellar structure and the direction of crack propagation [2, 3]. These phenomena are observed during fatigue test [2] and *in-situ* observation of crack propagation [8]. In the present study, fatigue crack growth in typical microstructure of TiAl intermetallics is examined in detail by means of *in-situ* observation of crack extension both in vacuum and air conditions. The relationship between microstructure and crack propagation properties is established through the crack propagation rate versus stress intensity factor range plots. The effects of crack closure and environment on the resulting crack propagation behavior are also discussed.

2. MATERIAL AND SPECIMEN

The material used in this study is a cast Ti-48Al alloy. The chemical composition of the material is shown in Table 1. Specimens are cut from the as-cast ingot and heat treated in a constant-flow argon gas chamber to obtain fully lamellar and duplex structure.

Table 1 Chemical composition of Ti-48Al intermetallics.

Element	Al	C	H	N	O	Ti
wt%	34.48	0.006	0.001	0.005	0.008	balance
at%	48.3	--	--	--	--	balance

The condition for the heat treatment was chosen according to the Ti-Al system phase diagram [9] and published reports on microstructure and heat treatment of Ti-Al intermetallics [1, 5, 7]. Fully lamellar structure is obtained by heating the sample at 1668 K for 80 minutes followed by furnace cooling to low temperature. The duplex structure is obtained by a heat treatment at 1543 K for 120 minutes and furnace cooled to low temperature.

Microstructure of the as-cast material is composed of equiaxed lamellar grains (200 to 300 μm) and small amount of γ grains (120 to 200 μm). Duplex structure consists of large (1000 to 4000 μm) lamellar grains and equiaxed γ grains (200 to 300 μm). The ratio of lamellar to γ grains in duplex structure material is estimated to be 7:3. Fully lamellar structure is composed of lamellar grains with nominal diameter of 400 to 700 μm . The size of lamellar grains is larger in the fully lamellar structure material when compared to the as-cast material. In addition, no γ grain is observed in the fully lamellar structure.

Compact tension specimens are used for fatigue crack growth tests. The geometry of the specimen follow the ASTM E399-90 specification with specimen width, $W = 35$ mm and thickness, $B = 6$ mm. The specimens were machined so that the plane of the fatigue crack agrees with the radial plane of the cast ingot.

3. EXPERIMENT

3.1 *In-situ* observation of crack growth in vacuum condition

Fatigue crack growth test in vacuum condition is carried out using an electro-hydraulic testing machine fitted with a scanning electron microscope. This set-up enables *in-situ* observation of the crack growth process. A vacuum of 10^{-3} Pa is established throughout the test. A sinusoidal load with a stress ratio (R) of minimum to maximum load of 0.1 and a frequency of 20 Hz is applied to the specimen. A higher stress ratio of $R = 0.5$ is utilized to examine the effect of crack closure on crack propagation behavior. In addition to the *in-situ* observation of the crack growth process, crack lengths, a , were recorded at prescribed interval of load cycles, N , and the resulting data is analyzed to obtain the crack propagation rate, da/dN . The corresponding applied stress intensity factor range, ΔK , is determined from the value of the applied load amplitude and the measured crack length.

3.1.1 Crack growth in lamellar structure

Both as-cast and fully lamellar structures are composed primarily of lamellar structure. The angle between the direction of crack growth and the orientation of lamellar layer is known to strongly affect the crack propagation behavior [2, 3]. Figure 1 shows an example of observed crack in vacuum condition, as found in the fully lamellar structure. In this figure, the angle between the orientation of the lamellar layers and the direction of main crack propagation is less than 45 degrees, resulting in translamellar fracture. We call this case (<45 degrees) "sharp angle" and the opposite case (>45 degrees) "blunt angle" in this paper. In Fig. 1, each arrow indicates the tip of the main crack at even interval of 600 fatigue cycles.

The crack extends along $\text{Ti}_3\text{Al}(\alpha_2)/\text{TiAl}(\gamma)$ interface of the lamellar structure where the

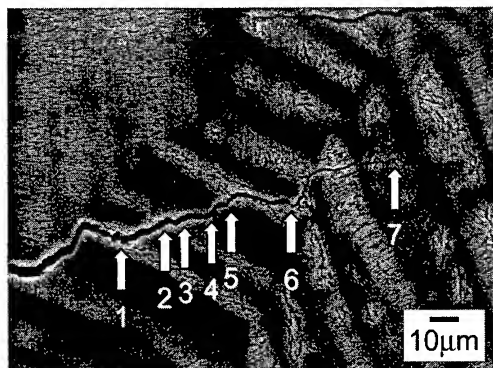


Fig. 1 Crack growth in lamellar structure where the direction of crack propagation and lamellar layer forms sharp (<45 degrees) angle. Stress intensity factor range is $14.5 \text{ MPa}\cdot\text{m}^{1/2}$. Stress ratio is 0.1. White arrows indicate position of the tip of main crack at even interval of 600 cycles of fatigue.

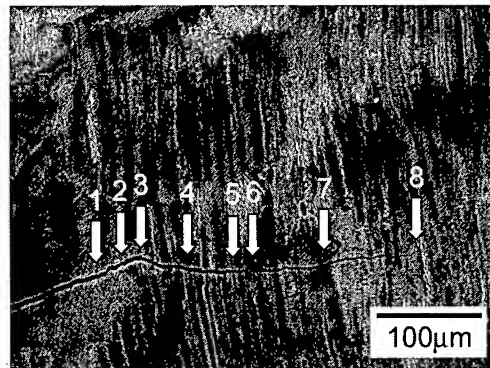


Fig. 2 Crack growth in lamellar structure where the direction of crack propagation and lamellar layer forms blunt (>45 degrees) angle. Stress intensity factor range is $16.0 \text{ MPa}\cdot\text{m}^{1/2}$. Stress ratio is 0.1. White arrows indicate position of the tip of main crack at even interval of 2000 cycles of fatigue.

cohesive force is expected to be low (arrow 1). The crack is deflected and grew across the γ layer (arrow 2). Crack retardation occurred at the next α_2/γ interface followed by initiation of microcracks in the vicinity of the main crack tip (arrows 3, 4). The microcrack is initiated within the plastic zone associated with the crack tip. With additional load cycles, the main crack extends and joins the microcrack and the process continues when the crack tip reaches the next neighboring lamellar grains (arrows 6, 7).

Figure 2 shows crack growth in lamellar structure when the direction of the main crack propagation and the orientation of lamellar layer forms blunt angle. In this case, crack growth is likely to be retarded between layers of lamellar structure (arrows 1-3, 5, 6). With additional fatigue cycles, the crack is deflected to extend across lamellar layers, resulting translamellar crack growth behavior.

3.1.2 Crack growth in duplex structure

An example of crack growth in duplex structure is shown in Fig. 3. The main crack propagates along γ and lamellar grain boundary of low resistance to crack growth (arrow 1). The crack propagation is retarded forming a zigzag profile of the crack extension. Simultaneously, a microcrack is initiated at γ and lamellar grain boundary ahead of main crack (arrow 2). With additional load cycles, the main crack propagates into the γ phase forming a shear ligament that connects with the microcrack. This leads to rapid crack extension.

The main crack that propagates along the γ grain boundary tends to halt when the crack encounters a material phase with higher crack growth resistance such as lamellar layers oriented perpendicular to the crack growth direction. In such a case, the crack extends with many microcracks initiated at boundaries of γ and lamellar grain, particularly in the crack tip region.

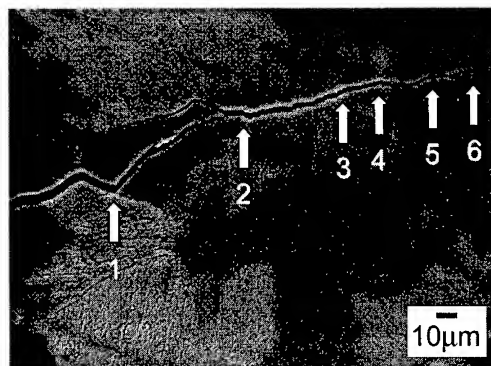


Fig. 3 Crack growth in duplex structure. Stress intensity factor range is $16.5 \text{ MPa}\cdot\text{m}^{1/2}$. Stress ratio is 0.1. White arrows indicate position of the tip of main crack at even interval of 100 cycles of fatigue.

3.2 Crack growth in air condition

Fatigue crack growth tests are conducted in laboratory air to determine the crack growth response and assess the effect of environment on the crack propagation property. An electrohydraulic testing machine is used in the experiment. The specimen is fatigued at a loading frequency of 20 Hz. Crack length are measured with the aid of an optical traveling video scope.

It was observed that many parallel microcracks are initiated on both sides of the main crack, as shown in Fig. 4. This cracking feature with large number of microcracks is observed only in specimen fatigued in air condition and at low stress intensity factor range. However, the feature prevails in all microstructures of the Ti-48Al alloy examined in the present study.

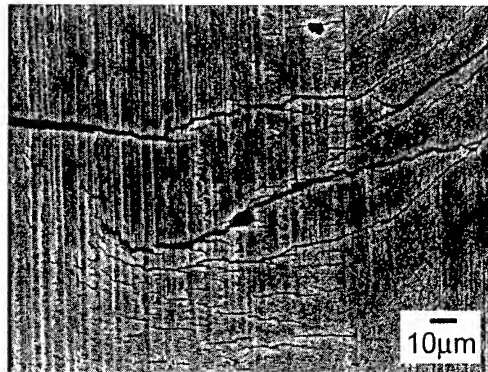


Fig. 4 An example of crack growth of as cast material in air condition. Stress intensity factor range is $11.0 \text{ MPa}\cdot\text{m}^{1/2}$. Stress ratio is 0.1. Many microcracks are initiated around the main crack.

4. DISCUSSION

The observed crack propagation behavior of Ti-48Al intermetallics is expressed in terms of crack propagation rate, da/dN , versus stress intensity factor range, ΔK , diagram. Obtained plot for the as-cast material in vacuum condition at $R = 0.1$ is shown in Fig. 5. Crack propagation process in the as-cast material occurs by initiation and growth of microcracks ahead of the main crack tip resulting in crack growth acceleration and deceleration, as described in the previous section. Consequently, a large scatter of data occurs in the intermediate crack growth region. An approximated trend line is determined to represent the nominal behavior of the crack. This nominal crack propagation property will be utilized in comparing and discussing crack propagation response in the different types of microstructure.

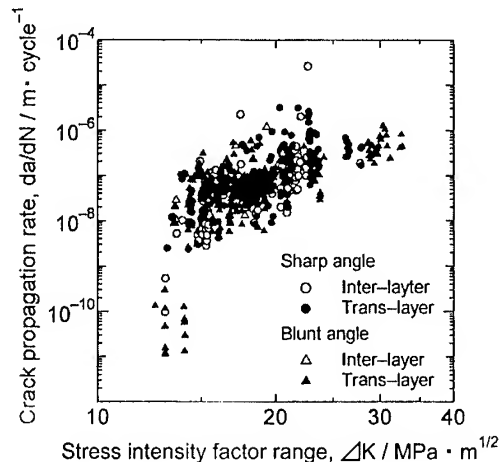


Fig. 5 Property of crack growth in lamellar structure. Instantaneous crack extension data are sorted according to the angle between the direction of fatigue crack and the orientation of lamellar layer.

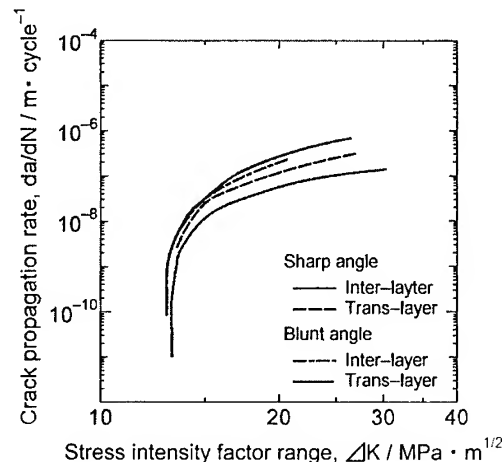


Fig. 6 Approximated crack growth property in lamellar structure obtained from data of Fig. 5. The lines correspond to modes of crack propagation in the structure.

4.1 Microstructure and crack growth in lamellar structure

Crack propagation in lamellar structure is strongly affected by the angle between the direction of crack propagation and the orientation of lamellar layer, as illustrated in Figs 1 and 2. *In-situ* measurements of crack growth rate, da/dN , and the corresponding stress intensity factor range, ΔK , are classified according to the angle and morphology of the microstructure. Approximated lines obtained from the sorted data in Fig. 5 are shown in Fig. 6. Results show that the number of occurrences for the blunt angle and inter-layer is the smallest, indicating that this type of crack growth is least possible. Other types of crack growth occur with almost equal possibility. The results also indicate that fatigue crack propagates faster between layers of lamellar structure (inter-layer) than across the layers (trans-layer) for both cases of sharp and blunt angles. When the angle is sharp, the crack propagates preferentially between layers of lamellar structure where the cohesive force between α_2 and γ phase is small. On the other hand, when the angle is blunt, the crack tends to stop between layers of lamellar causing blunting of the crack and simultaneous initiation of microcracks.

The good correlation of the *in-situ* observation of crack growth process and the measured crack growth rate behavior (da/dN - ΔK plot) suggests that fatigue crack propagates selectively through path of weakest cohesive bond in the structure. Otherwise, the crack growth is retarded and stopped to consume energy from the crack tip driving force.

4.2 Effect of environment on crack growth

The crack growth rate response for fully lamellar and duplex structure in vacuum and air is compared in Figs 7 and 8. Results show that the crack growth rate for the alloy is higher in air environment for both types of microstructure. This suggests accelerated crack growth in air environment. In addition, similar effect of environment holds for both conditions of stress ratios, $R = 0.1$ and 0.5 . It is worth noting in Figs 7 and 8 that the results of the test for stress ratio, $R = 0.5$, may demonstrates crack growth deceleration that could be due to crack closure effect.

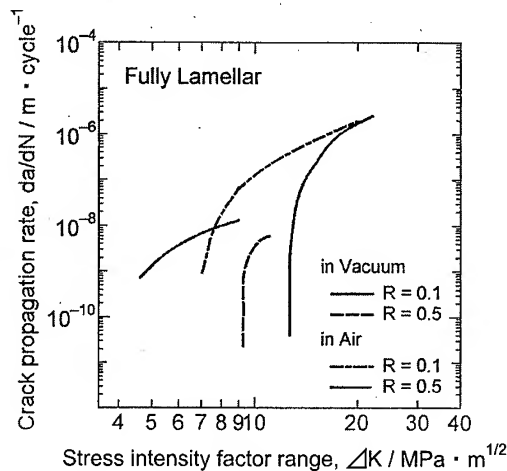


Fig. 7 Property of crack propagation in vacuum and air for fully lamellar structure. Properties of stress ratio of 0.1 and 0.5 are also compared.

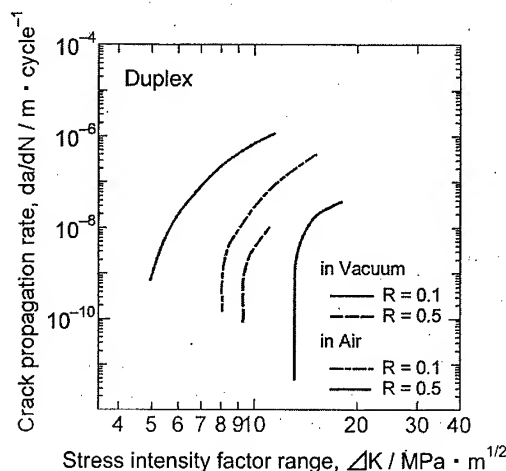


Fig. 8 Property of crack propagation in vacuum and air for duplex structure. Properties of stress ratio of 0.1 and 0.5 are also compared.

This environmental effect is caused by absorption of humidity from the atmosphere through the surface of the specimen and subsequent reaction with aluminum element in the plastic zone at the tip of the crack [10-12]. Figure 9 shows fracture surface of fully lamellar

structure specimen tested in air condition at locations near the free surface. Fracture surface near the edge of the specimen shows fine parallel lines that are independent of lamellar grains orientation. These lines that correspond to microcracks observed at the surface of the specimen are not observed in the bulk region of the specimen. In addition, the effect of environment diminishes at high stress intensity factor range, as illustrated in Figs 7 and 8. At high level of stress intensity factor range, the crack propagates at a faster rate. As a result, insufficient time is allocated for absorption of air humidity towards the crack tip, thus minimizes environmental embrittlement.

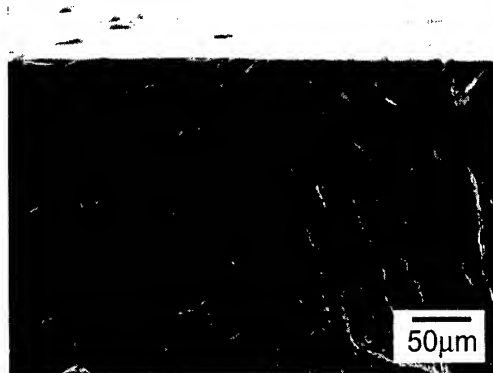


Fig. 9 Fracture surface observed at low stress intensity factor range of a compact tension specimen of fully lamellar structure tested in air. Note many fine parallel lines independent of lamellar structure.

5. CONCLUSION

Fatigue crack propagation behavior of Ti-48Al intermetallics is studied by *in-situ* observation of crack growth process under vacuum and air conditions. Three representative microstructures, namely, as-cast, fully lamellar and duplex structure of the TiAl intermetallics are used in the present study. Measurements of fatigue crack extension are correlated with types of microstructure. The effect of environment on the resulting crack growth behavior is examined. The results can be summarized as follows:

Crack propagation is strongly affected by microstructure and the angle between crack propagation direction and the orientation of lamellar colony, particularly in lamellar structure.

The observed crack growth response is classified into possible modes of crack propagation including inter-layer and trans-layer. The preferred path of crack propagation in lamellar structure has been established; it goes through the weakest phase of the structure with associated microcracking within the plastic zone around the tip of the crack.

Crack growth is accelerated in air condition. This phenomenon is attributed to the effect of absorption of air humidity to the crack tip plastic zone and subsequent reaction with aluminum. This environmental effect is apparent through the observation of crack propagation and the resulting fracture surface.

REFERENCES

1. Y.W. Kim, JOM, **14**(1989), 24.
2. R. Ganamoorthy, Y. Mutoh, K. Hayashi, and Y. Mizuhara, Scripta Metall., **33**(1995), 909.
3. S. Mitao, T. Isawa, and S. Tsuyama, Scripta Metall., **26**(1992), 1405.
4. M. Chen, D. Lin, and D. Chen, Scripta Metall., **36**(1997), 497.
5. B.D. Worth, J.M. Larsen, S.J. Balsone, and J.W. Jones, Metall. Materials Trans., **28A**(1997), 825.
6. Y.W. Kim, Acta Metall. Mater., **40**(1992), 1121.
7. T. Kumagai, E. Abe, M. Takeyama, and M. Nakamura, Scripta Metall., **36**(1997), 523.
8. K.W. Chan and D.S. Shih, Metall. Materials Trans., **28A**(1997), 79.
9. J.L. Murray in *Binary Alloy Phase Diagram*, edited by T.B. Massalski, ASM, 1986, p173.
10. H. Gilbert, M. Catherrine, T. Anne, and P. Jean, in *Structural Intermetallics*, edited by M.V. Nathal, et al., TMS, 1997, p469.
11. C.T. Liu, Scripta Metall., **23**(1989), 875.
12. C.T. Liu, Scripta Metall., **27**(1992), 599.

The Optimum Thickness of Coating Film for the Fatigue Strength of Surface Modified TiAl Intermetallic Alloy

Hideto Suzuki*, Yutaka Watanabe**,
Masaru Ikenaga* and Kaoru Ikenaga*

* Department of System Engineering, Faculty of Engineering,
Ibaraki University, 4-12-1 Nakanarusawa-cho, Hitachi-city,
Ibaraki 316-8511, Japan

** Dept. of Intelligent Machines and System Engineering, Faculty
of Science and Technology, Hirosaki University3 Bunkyo-Cho,
Hirosaki, Aomori 036-8561, JAPAN

ABSTRACT

The experimental study on the optimum thickness of coating film for the fatigue strength of surface modified TiAl intermetallic alloy was carried out. The main results were obtained as follows.

- (1) The fatigue strength of TiAl intermetallic alloy could be improved through the optimum thickness of TiAlN hard coating film, that is 3 μm .
- (2) From micro-fractography, two different types of fatigue fracture mechanisms were found. For the thinner coating film, the shear mode of fatigue initiation crack was occurred. On the other hand, for the thicker coating film, the TiAlN film cracking triggered off the tensile mode of the fatigue initiation crack.
- (3) Therefore, it could be comprehended that the optimum thickness of coating film for the fatigue strength of surface modified TiAl intermetallic alloy had been controlled through the two types of roles in the hard film. Then, the one effect is the constraint of slip deformation and the other is the Griffith crack of film cracking.

1. Introduction

Intermetallic alloys based on the TiAl matrix have received considerable interest in recent years because of their potential as elevated-temperature structural materials [1-5]. This is due to a number of property advantages, including low density, excellent oxidation resistance, and relatively good elevated temperature mechanical properties.

However, TiAl intermetallic alloy has also poor properties such as wear resistance, corrosion resistance and so on, and it is necessary for energy problem and environmental problem that elevated temperature structural materials (including TiAl intermetallic alloy) have superior properties at elevated temperature over the conventional material. Therefore, because of the improvement of poor properties (such as fatigue resistance, wear resistance, corrosion resistance and so on), the methods of surface modification will have important roles for TiAl intermetallic alloy [5].

Physical vapor deposition (PVD) coating and chemical vapor deposition (CVD) coating have received considerable interest in recent years [6]. Especially, it is known that (TiAl)N coating by PVD could be one of the prospective hard layers to enhance the wear and thermal oxidation resistances of tools overcoming the shortcomings of TiN and TiCN coatings.

The aim of this paper is to highlight surface modifications for the fatigue strength of TiAl intermetallic alloys. Especially, the experimental study on the optimum thickness of coating film, (TiAl)N hard coating film, for the fatigue strength of surface modified TiAl intermetallic alloy was carried out. The reason of this study was that the cracks of hard films that were not

optimum, as the case might be, result in surface modified material's inferior mechanical properties such as fatigue strength and fatigue life without optimal films.

2. Experimental Procedures

2.1 Materials

The material used in this investigation are Ti36wt.%Al (TiAl intermetallic alloy). The chemical compositions of the material are shown in Table 1. TiAl intermetallic alloy were prepared using skullmelting and casting techniques into ingots. Figure specimen was machined from TiAl intermetallic alloy casting to the shape shown in Figure 1.

Figure 2 show the microstructure of TiAl intermetallic alloy observed by an optical microscope. TiAl intermetallic alloy contained duplex microstructure consisting equaxed gamma grain (TiAl) and lamellar colonies (TiAl + Ti₃Al).

(TiAl)N film was deposited by Cathodic Arc Ion Plating (Physical Vapor Deposition). The e conditions for (TiAl)N coating process are shown in Table 2. The thickness of (TiAl)N film deposited on the substrates was 1μm (TiAlN/1μm), 3μm (TiAlN/3μm) and 10μm (TiAlN/10μm).

Table 1 Chemical composition of the materials in weight percent

Material	Al	C	N	O	H	Ti
Ti36wt.%Al	36.3	0.01	0.004	0.112	0.0024	Bal.

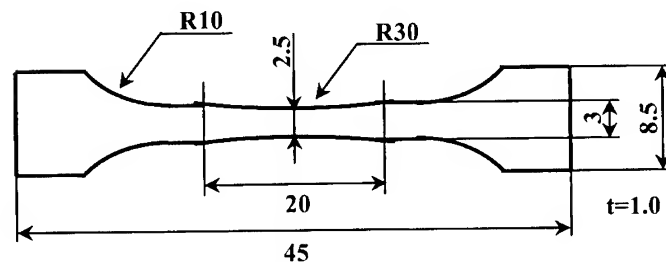


Fig.1 Geometry of specimen

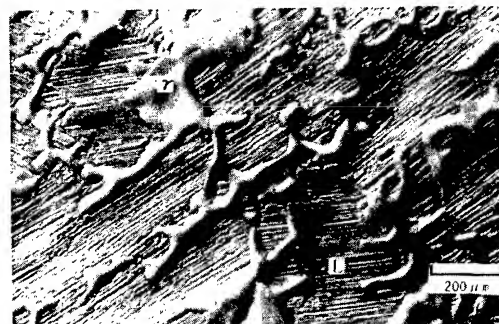


Fig.2 Microstructure of TiAl intermetallic alloy

2.2 Experimental Methods

Fatigue tests were conducted in vacuum at 1073K, using a servohydraulic testing machine

equipped with scanning electron microscope (SEM-servo testing machine). All tests were carried out in load control at a stress ratio R (minimum to maximum stress) of 0.1 using a frequency of 30 Hz.

In-situ observations using SEM-servo testing machine were employed to study the initiation and growth of surface fatigue cracks. The surface of failed specimens was examined using scanning electron microscopy.

Table 2 Coating condition

Processes	Conditions	
Cleaning	Ultrasonic Cleaning using Methylene chloride (CH_2Cl_2)	
Exhaust gas	4×10^{-5} Torr	
Pre-coating	Substrate sputter cleaning using Ti (Heating, 673K)	
Coating	Film	TiAlN
	Apparatus	Cathodic Arc Ion Plating (Physical Vapor Deposition)
	Temperature	723K
	Target	TiAl intermetallic alloy
	Process gas	N_2
	Film thickness	1, 3 and 10 μm

3. Experimental Results

The S-N curves of the TiAlN coated TiAl intermetallic alloy and TiAl intermetallic alloy (Virgin material) are plotted in the form of the stress amplitude (S) versus the number of cycles to failure (N_f) in Figure 3. The fatigue strength of TiAlN/1 μm and TiAlN/10 μm was lower than that of Virgin material. However, the fatigue strength of TiAlN/3 μm was higher than that of Virgin material.

It has been shown in recent studies that surface modified elevated-temperature structural

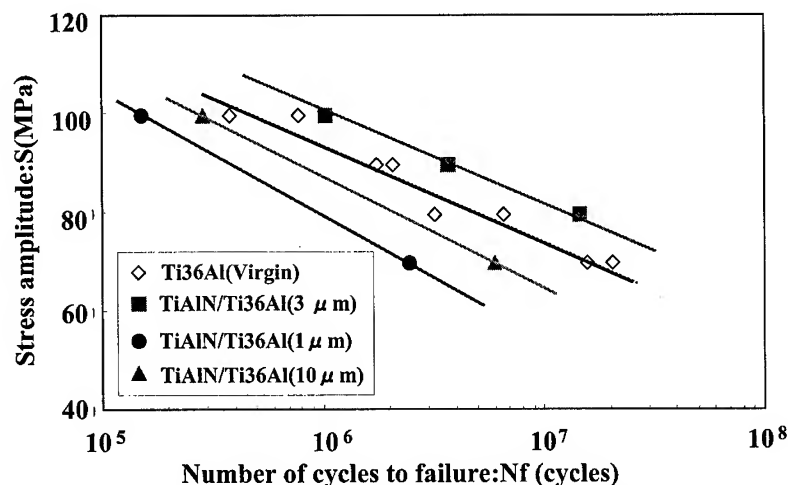


Fig.3 S-N curves of TiAlN coated TiAl intermetallic alloy

materials had adverse effects. For example, although surface modified elevated-temperature structural materials have excellent heat resistance, wear resistance and corrosion resistance, the fatigue strength of surface modified elevated-temperature structural materials is seriously lower than that of virgin materials. But, in this study, the fatigue strength of TiAl intermetallic alloy could be improved through the optimum thickness of TiAlN coating film, that is 0.3 μm .

Because little is known the effect of film thickness on fatigue property and fatigue mechanism, the relationship between film thickness and fatigue fracture mechanism was examined in next chapter.

4. Discussion

4.1 Fatigue mechanisms of TiAlN coated TiAl intermetallic alloy

The results of our recent research showed that the cleavage fracture in γ grain occurred over the fracture surface of virgin material [7]. The fatigue fracture of virgin material was dominated by the following many mesocracks growth mechanism: (1) Slip deformation of lamellae structure in the early stage of the life, (2) mesocrack initiation and growth in γ grain, (3) link with other mesocracks, (4) final fracture. Where, the small crack has been defined as mesocrack affected by microstructure which were initiated on the surface and several hundred μm length. Taking into account these experimental results, the fatigue mechanism of the TiAlN coated TiAl intermetallic alloy was investigated.

4.1.1 TiAlN/1 μm

Figure 4 show a low-magnification fracture surface and typical surface mesocracks of TiAlN/1 μm . The fracture surface of TiAlN/1 μm was rough, and many TiAlN film cracking were occurred. From the detail fractography, it was observed that slip deformation of lamellae structure by shear stress was occurred near the interface between TiAlN film and TiAl intermetallic alloy. In case of TiAlN/1 μm , TiAlN films did not reduce slip deformation and crack initiation in γ grain. TiAlN film cracking initiated by slip deformation triggered off initiation and propagation of main fatigue crack.

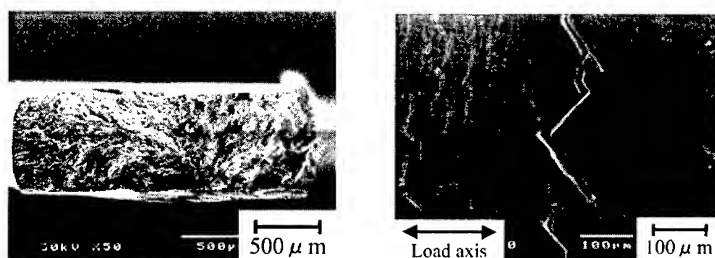


Fig.4 A low-magnification fracture surface and surface mesocracks of TiAlN/1 μm

4.1.2 TiAlN/10 μm

Figure 5 show typical fracture surface near the fracture origin and surface mesocracks of TiAlN/10 μm . The fracture surface of TiAlN/10 μm was divided into two types. There two types were smoothed featureless area and rough area. The fatigue crack was initiated and propagated by TiAlN film cracking. That is, TiAlN film cracking triggered off the fatigue fracture of TiAlN/10 μm . The fatigue crack was rapidly propagated from the surface to the inside of TiAl intermetallic alloy.

There have been such several fatigue crack on the fracture surface. Furthermore, there

has been several separation of TiAlN film and many perpendicular mesocracks to the loading axis. This perpendicular mesocracks induced the tensile mode of the fatigue initiation crack. It seemed that the fatigue crack linked with other fatigue crack, then the fatigue fracture rapidly occurred. In case of TiAlN/10 μ m, the slip deformation was not observed.

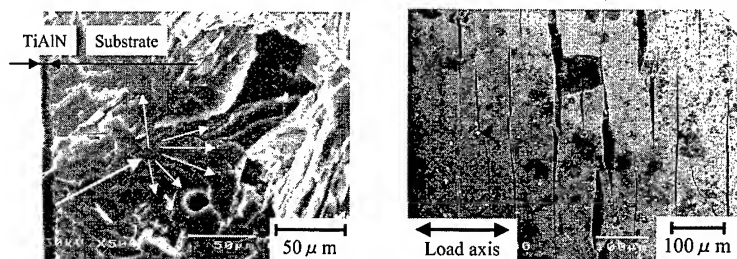


Fig.5 Fracture surface near the fracture origin and surface mesocracks of TiAlN/10 μ m

4.1.3 TiAlN/3 μ m

Figure 6 show typical fracture surface near the fracture origin and surface mesocracks of TiAlN/3 μ m. The fracture surface of TiAlN/3 μ m was divided into two types as TiAlN/10 μ m. There two types were smoothed featureless area and rough area. There has been several fatigue crack origins initiated from the smoothed featureless area. Especially, the fatigue crack was initiated and propagated by the cracking of the interface between γ grain and lamellae structure. The fatigue crack was rapidly propagated in γ grain, and propagated to the surface.

There has been several opening mesocracks, which was about 300 μ m length, on the surface of TiAlN/3 μ m. Therefore, it seemed that the fatigue process was dominated by initiation and growth mechanism of these mesocracks. In case of TiAlN/3 μ m, the slip deformation was not observe, and TiAlN film reduced mesocracks initiation, which was smaller than 100 μ m.

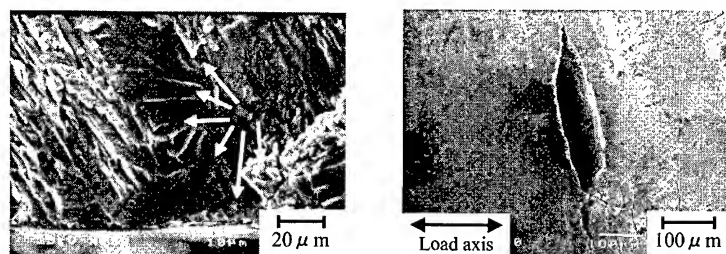


Fig.6 Fracture surface near the fracture origin and surface mesocracks of TiAlN/10 μ m

4.2 Constraint of slip deformation and Griffith crack

As a conclusion of this paper, the fatigue mechanism of TiAlN coated TiAl intermetallic alloy is shown schematically in Figure 7. In case of thinner TiAlN film, TiAlN film could not constrain the slip deformation because of thin film, and TiAlN film cracking was initiated. So, the fatigue strength of TiAlN/1 μ m was lower than that of virgin material because this TiAlN film cracking triggered off the shear mode of the fatigue initiation crack.

On the other hand, in case of thicker TiAlN film, TiAlN film could constrain the slip deformation because of thick film. But, because many perpendicular mesocracks to the loading axis occurred, the fatigue strength of TiAlN/10 μ m was lower than that of virgin material. That is, the brittle fracture of TiAlN film triggered off tensile mode of the fatigue

initiation crack, and the fatigue crack was rapidly propagated.

Especially, it seemed that the fracture mechanism of this case depended on the fracture strength (fatigue strength) σ_f ($= \sqrt{2E\gamma_s/\pi c}$) of Griffith crack. where E is the elastic modulus, γ_s is the surface energy and c is the length of one-half crack. That is, in case of thicker TiAlN film, c increased because of the brittle fracture of thick film, and the fracture strength σ_f and fatigue strength decreased.

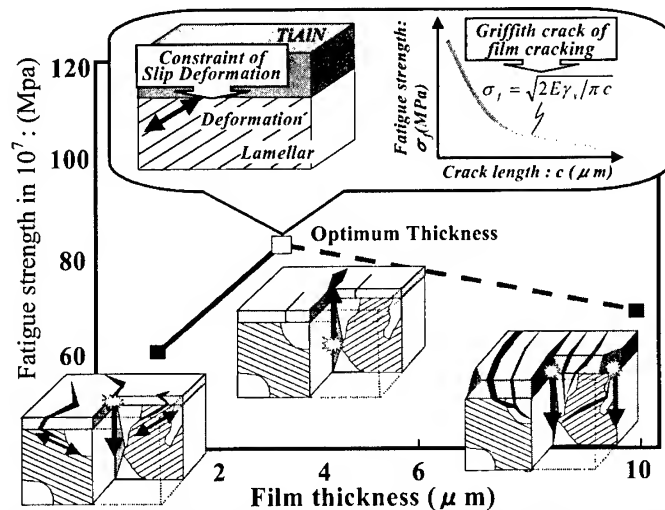


Fig.7 Relationship between fatigue strength and fatigue mechanism

5. Conclusions

- (1) The fatigue strength of TiAl intermetallic alloy could be improved through the optimum thickness of TiAlN hard coating film, that is 3 μm .
- (2) From micro-fractography, two different types of fatigue fracture mechanisms were found. For the thinner coating film, the shear mode of fatigue initiation crack was occurred. On the other hand, for the thicker coating film, the TiAlN film cracking triggered off the tensile mode of the fatigue initiation crack.
- (3) Therefore, it could be comprehended that the optimum thickness of coating film for the fatigue strength of surface modified TiAl intermetallic alloy had been controlled through the two types of roles in the hard film. Then, the one effect is the constraint of slip deformation and the other is the Griffith crack of film cracking.

References

1. S. Numata, K. Katahira and H. Suzuki, Transactions of the Japan Society of Mechanical Engineers A, Vol.65, No.629, A (1999), pp.55-61.
2. S. Numata, K. Katahira and H. Suzuki, Transactions of the Japan Society of Mechanical Engineers A, Vol.64, No.619, A (1998), pp.597-602.
3. S. Numata and H. Suzuki, Proc. Of the 11 th international conference on experimental mechanics, I. M. Allison (ed), Oxford, UK (1998), pp.939-944.
4. T. Nanpo, J. Fujioka, H. Hino, T. Miyashita and T. Araki, Technical reports of Kawasaki Heavy Industries, LTD, Vol.111, (1991), pp.37-44.
5. Jeon G. Han, Joo S. Yoon, Hyung J. Kim and Keon Song; Surface and coatings technology, 86-87, (1996), pp.82-87.
6. M. Ikenaga, Heat Treatment, Vol.37, No.3, (1997), pp.148-153.
7. H. Suzuki, S. Numata, K. Katahira and M. Ikenaga, Transactions of the Japan Society of Mechanical Engineers A, Vol.66, No.649, A(2000), pp.1689-1694.

SURFACE STRENGTHENING FOR OPTIMIZING FATIGUE PERFORMANCE OF GAMMA TITANIUM ALUMINIDES AT AMBIENT AND ELEVATED TEMPERATURES

J. Lindemann*, D. Fagaraseanu** and L. Wagner*

*Chair of Physical Metallurgy and Materials Technology
Technical University of Brandenburg at Cottbus, 03013 Cottbus, Germany

**Rolls-Royce Deutschland, 15827 Dahlewitz, Germany

ABSTRACT

To improve the fatigue performance of gamma titanium aluminides, shot peening as a method of surface strengthening was applied. Results on $\gamma(\text{TiAl})$ were compared to those on a conventional high-temperature near- α titanium alloy TIMETAL 1100. Fatigue tests were performed in fully reversed loading ($R = -1$) on smooth specimens at frequencies of about 60 Hz. Compared to electropolished references, the ambient temperature 10^7 cycles fatigue strength of $\gamma(\text{TiAl})$ could be improved much more than that of TIMETAL 1100. While shot peening-induced residual compressive stresses played the dominant role in ambient temperature fatigue, surface roughness and dislocation strengthening became more important when process-induced residual stresses were relieved by an annealing treatment at temperatures of 600°C and 650°C for 50 hours before testing.

1. INTRODUCTION

Gamma titanium aluminides are attractive candidates for application as blade material in the high-pressure part of the compressor of gas turbines. Compared to the yield stress values at both room temperature and elevated temperature (650°C), the 10^7 cycles fatigue strengths at these temperatures are extraordinarily high, particularly if related to the material's density being only half that of the commonly used Ni-superalloys [1,2]. To further improve the fatigue performance of $\gamma(\text{TiAl})$, mechanical surface treatments such as shot peening or roller-burnishing can be utilized. These treatments induce high dislocation densities in near-surface regions owing to local plastic deformation, change the surface topography and generate residual compressive stresses. The present work is part of a project which was undertaken to determine potential improvements in ambient and elevated temperature applications of $\gamma(\text{TiAl})$ by mechanical surface treatments.

2. EXPERIMENTAL

The $\gamma(\text{TiAl})$ base ingot with the chemical composition Ti - 47Al - 3.7 (Nb, Cr, Mn, Si) - 0.5B was received from Duriron (USA). The material was hipped, extruded and forged to turbine blades. After forging, the turbine blades were heat treated to achieve fully lamellar microstructures. Specimens for mechanical tests were machined from the turbine blade

forgings with the load axis in longitudinal blade direction as indicated in Fig. 1. The TIMETAL 1100 material was received from TIMET (USA) as a Ø200 mm forged bar stock. The material was thermomechanically processed to achieve a fine grained fully lamellar microstructure. Details are given in [3]. Tensile tests were performed on electropolished specimens having a gage length of 20 mm and a gage diameter of 4 mm. The initial strain rate was $8.3 \times 10^{-4} \text{ s}^{-1}$. Compression tests were done on cylindrical specimens with a length of 8 mm and a diameter of 4 mm. The initial strain rate was $2.1 \times 10^{-3} \text{ s}^{-1}$. Tensile test results are listed in Tab. 1 comparing the data of both alloys.

Table 1 Tensile test results of the fully lamellar microstructures in $\gamma(\text{TiAl})$ and TIMETAL 1100

Alloy	$\sigma_{0.2}$ [MPa]	El [%]	E [GPa]
$\gamma(\text{TiAl})$	440	~1	170
TIMETAL 1100	935	11	116

Fatigue tests were performed on hourglass shaped specimens with a gage diameter of 2.5 mm in rotating beam loading ($R = -1$) in air. Shot peening was performed by means of an injector type system using spherical zirconia based ceramic shot with an average diameter of 0.5 mm. The Almen intensities were kept constant at 0.40 mmN and 0.20 mmA for $\gamma(\text{TiAl})$ [4] and TIMETAL 1100 [5], respectively. Some specimens of TIMETAL 1100 were shot peened at a higher intensity of 0.33 mmA. The change in surface layer properties was characterized using profilometry, microhardness and residual stress measurements by means of the hole drilling method. The diameter of the drill was 1.7 mm. The oscillating drill was driven by an air turbine with a rotational speed of about 200.000 rpm. The shot peening induced strains in the surface layer were measured with strain gage rosettes at drilled depths of about every 20 μm . The measured strains were converted into stresses by using Young's moduli of 170 GPa and 116 GPa for $\gamma(\text{TiAl})$ and TIMETAL 1100, respectively. The fatigue results after shot peening were compared with the electrolytically polished reference. Roughly 150 μm were removed from the machined surface by electrolytic polishing to make sure that any machining effect that could mask the results was absent.

The thermal stability of the shot peening-induced residual compressive stresses at anticipated application temperatures of 600°C and 650°C was determined by comparing measurements before and after annealing treatments at these temperatures for 50 hours which corresponds to the exposure time for run-outs (10^7 cycles at 60 Hz).

3. RESULTS AND DISCUSSION

The typical microstructure of $\gamma(\text{TiAl})$ within the blade section of the forgings (Fig. 1) is shown in Fig. 2a indicating a fully lamellar structure with a packet size of γ and α_2 lamellae of about 150-200 μm . The microstructure of TIMETAL 1100 (Fig. 2b) is characterized by α and β lamellae with packet sizes similar to those in $\gamma(\text{TiAl})$. The monotonic stress-strain curves of both materials are plotted in Fig. 3 comparing the differences in mechanical behavior between tensile and compressive loading for $\gamma(\text{TiAl})$ (Fig. 3a) and TIMETAL 1100 (Fig. 3b). The 0.2 % yield stress of $\gamma(\text{TiAl})$ in compression (580 MPa) is significantly higher than the corresponding value in tension (440 MPa). This apparently lower yield stress in tension might be the result of early crack nucleation and propagation which is also indicated by the low

tensile ductility of only about 1 %. On the other hand, the stress-strain relationship in compression illustrates the marked work-hardening capacity of the material which obviously can not be seen in tensile loading due to premature failure. No significant differences were observed between tensile and compressive stress strain curves for TIMETAL 1100 (Fig. 3b). Obviously, the work-hardening capacity in TIMETAL 1100 is much smaller than in $\gamma(\text{TiAl})$ (compare Fig. 3a with 3b).

Due to the process-induced plastic deformation, the microhardness values in near-surface regions of both alloys significantly increase to a maximum value at the surface (Fig. 4). However, the maximum microhardness in $\gamma(\text{TiAl})$ is twice the value of the unaffected material in the bulk while the hardness increase in TIMETAL 1100 is only roughly 20% (Fig. 4). This again illustrates the extraordinarily high work-hardening capacity of $\gamma(\text{TiAl})$ (compare Fig. 4 with Fig. 3). The residual stress profiles as measured by the hole drilling method are plotted in Fig. 5 indicating residual compressive stresses in near-surface regions for both $\gamma(\text{TiAl})$ and TIMETAL 1100. On average, the magnitude of the process-induced residual stresses in $\gamma(\text{TiAl})$ is higher than in TIMETAL 1100.

The resulting S-N curves are shown in Fig. 6 comparing the fatigue performance between the shot peened conditions and the electropolished references for $\gamma(\text{TiAl})$ (Fig. 6a) and TIMETAL 1100 (Fig. 6b). As seen in Fig. 6a, the 10^7 cycles fatigue strength of $\gamma(\text{TiAl})$ in the electropolished condition is about 550 MPa. Taking the yield stress in compression, the ratio $\sigma_{a_{10^7}} / \sigma_{0.2}$ amounts to 0.95 compared to a values of only 0.58 for TIMETAL 1100. From the

very marked work-hardening of $\gamma(\text{TiAl})$ as observed in the compression tests, pronounced cyclic hardening is expected which can explain the comparatively high fatigue strength. This fatigue strength of 550 MPa increases after shot peening to 675 MPa (Fig. 6a) while no increase in the 10^7 cycles fatigue strength was observed for TIMETAL 1100 (Fig. 6b). Presumably, the shot peening-induced residual compressive stresses in $\gamma(\text{TiAl})$ are cyclically more stable than in TIMETAL 1100.

Although no elevated temperature fatigue tests were done in this investigation, a few critical tests were performed which may shed some light on the materials response to shot peening in fatigue at 600°C and 650°C. The effect of an annealing treatment at 600°C and 650°C for 50 hours on the shot peening induced microhardness in the surface layer of $\gamma(\text{TiAl})$ is shown in Fig. 7. Compared to the as-peened condition, there is only a slight decrease in microhardness which indicates that the shot peening-induced high dislocation density is thermally quite stable up to 650°C. On the contrary, the process-induced residual compressive stresses exhibit marked decays by the same treatments (Fig. 8). Obviously, creep deformation at 600°C and 650°C can transform most of the near-surface elastic strains to plastic strains, thus leading to a marked residual stress relief. While the microhardness in the shot peened surface layer of TIMETAL 1100 even somewhat increased after thermal exposure at 600°C and 650°C presumably owing to additional age-hardening effects, the temperature dependent residual stress decay was very similar as in $\gamma(\text{TiAl})$. Again, most residual stresses in TIMETAL 1100 were relieved after an annealing at 600°C for 50 hours.

Not surprisingly, the annealing treatment at 650°C for 50 hours significantly deteriorates fatigue performance of shot peened specimens of $\gamma(\text{TiAl})$ as seen in Fig. 9. Since both conditions SP and SP+A have a rough surface which contains process-induced microcracks, the fatigue strengths are crack propagation controlled. Owing to the residual stress decay in the annealed condition, the threshold value for microcrack growth ΔK_{th} decreases which reduces the fatigue strength by about 100 MPa (Fig. 9). However, polishing shot peened and subsequently annealed specimens can markedly improve fatigue performance as also seen in

Fig. 9. For a smooth surface, the fatigue strength is crack nucleation controlled. Therefore, the work-hardened surface layer which is still present after the anneal (see Fig. 7) can increase the resistance to fatigue crack nucleation and thus, improve the fatigue strength [6]. Regarding fatigue performance of shot peened γ (TiAl) specimens at $T = 650^\circ\text{C}$, it may be derived from the annealing experiments that the work-hardened surface layer will be beneficial for improving elevated temperature fatigue strength. However, the peened surface will need polishing to take advantage of the beneficial effect of the high strength of the surface layer on fatigue crack nucleation. Compared to γ (TiAl), the drop in fatigue strength of shot peened TIMETAL 1100 after thermal exposure is much more pronounced (Fig. 10). These results are very similar to those previously reported on fully lamellar Ti-6Al-4V [6]. The significantly higher 10^7 cycles fatigue strength in shot peened and thermally exposed γ (TiAl) (550 MPa) as compared to TIMETAL 1100 (300 MPa) is argued to stem from a higher threshold value for microcrack growth in γ (TiAl) as compared to the conventional titanium alloys Ti-6Al-4V and TIMETAL 1100. This higher threshold value could be the result of the Young's modulus amounting to 170 GPa for γ (TiAl) as opposed to about 115 GPa for Ti-6Al-4V and TIMETAL 1100.

ACKNOWLEDGEMENTS

Part of this work was supported by the German Research Society (DFG).

REFERENCES

1. William E. Dowling et al., *Microstructure/Property Relationships in Titanium Aluminides and Alloys* (Y.-W. Kim and R. R. Boyer eds.) TMS, Warrendale, PA (1991), 123.
2. J. Kumpfert, Y.-W. Kim, and D. M. Dimiduk, "Effect of Microstructure on Fatigue and Tensile Properties of the Gamma TiAl Alloy Ti-46.5Al-3Nb-2.1Cr-0.2W", *Mat. Sci. and Eng.*, A192/193 (1995), 465.
3. J. Lindemann and L. Wagner: "Mean Stress Sensitivity of the Near- α Titanium Alloy TIMETAL 1100: Effects of Test Temperature", *Microstructure and Mechanical Properties of Metallic High-Temperature Materials* (H. Mughrabi, G. Gottstein, H. Mecking, H. Riedel and J. Tobolski, eds.) Wiley-VCH, 144.
4. J. Lindemann, D. Fagaraseanu and L. Wagner: "Effect of Shot Peening on Fatigue Performance of Gamma Titanium Aluminides", 3rd International Symposium on Structural Intermetallics, Sept. 2001, Jackson Hole, Wyoming, in press.
5. T. Dörr and L. Wagner: "Fatigue Response of the Various Titanium Alloys Classes to Shot Peening", *Surface Treatment IV* (C.A. Brebbia and J.M. Kenny, eds.) WIT Press (1999), 349.
6. L. Wagner: "Mechanical Surface Treatments on Titanium Alloys: Fundamental Mechanisms", (J. K. Gregory, H. J. Rack and D. Eylon, eds.) TMS-AIME (1996) 199.

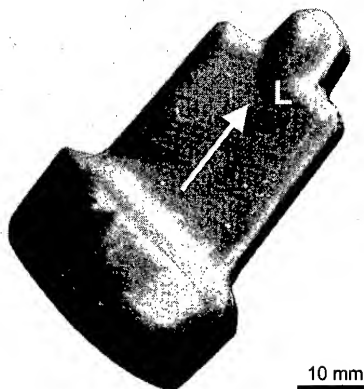
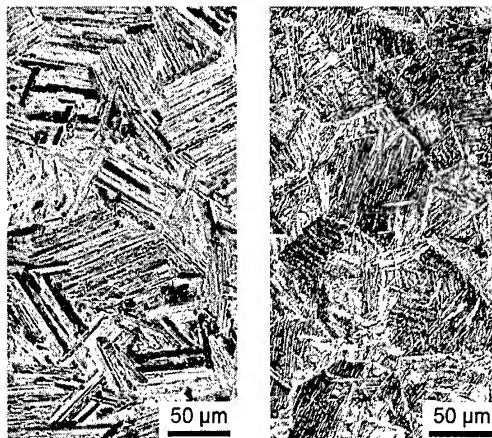


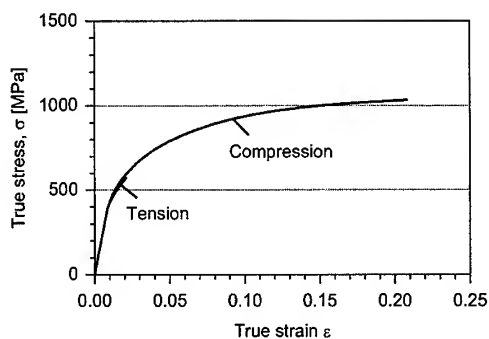
Fig. 1: Turbine blade forging



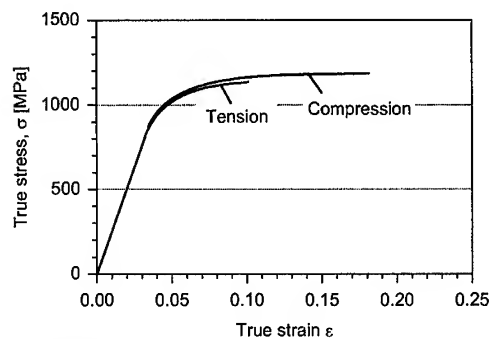
a) γ (TiAl)

b) TIMETAL 1100

Fig. 2: Fully lamellar microstructures



a) γ (TiAl)



b) TIMETAL 1100

Fig. 3: σ - ϵ curves with tensile and compression test results

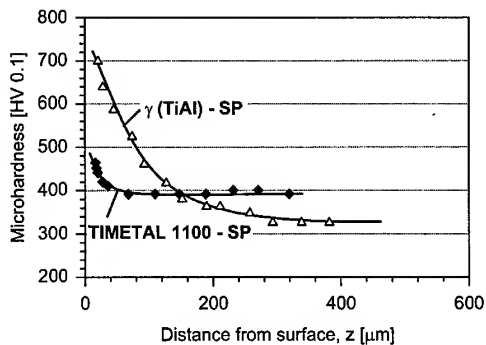


Fig. 4: Microhardness profiles after shot peening of γ (TiAl) and TIMETAL 1100

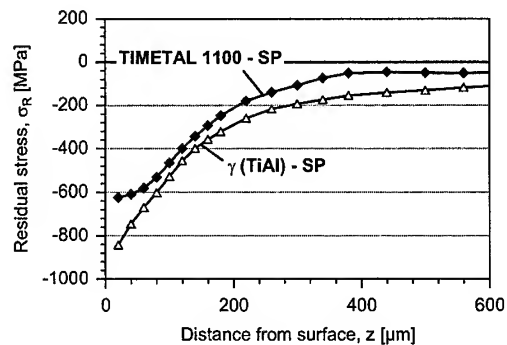
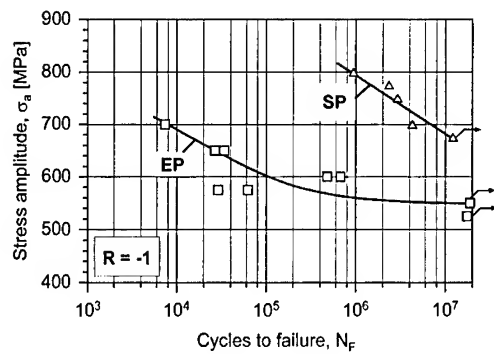
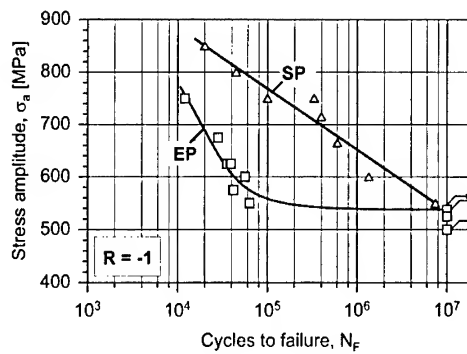


Fig. 5: Residual stress profiles after shot peening of γ (TiAl) and TIMETAL 1100



a) γ (TiAl)



b) TIMETAL 1100

Fig. 6: Effect of shot peening in rotating beam loading ($R = -1$)

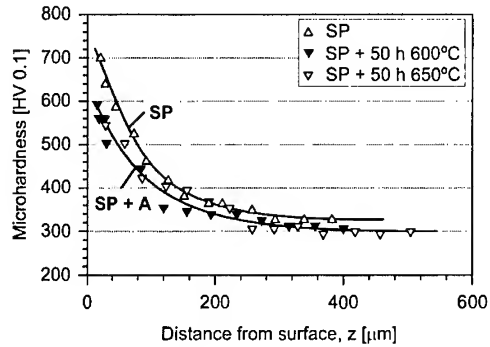


Fig. 7: Change in shot peening-induced microhardness profile in γ (TiAl) due to annealing

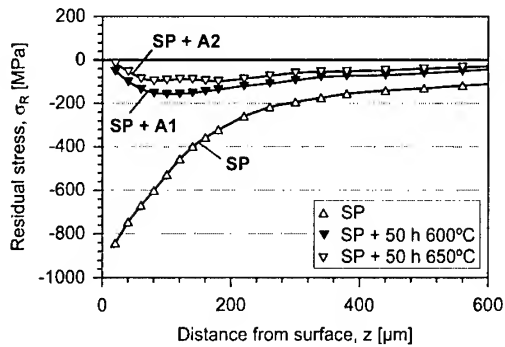


Fig. 8: Change in shot peening-induced residual stress profile in γ (TiAl) due to annealing

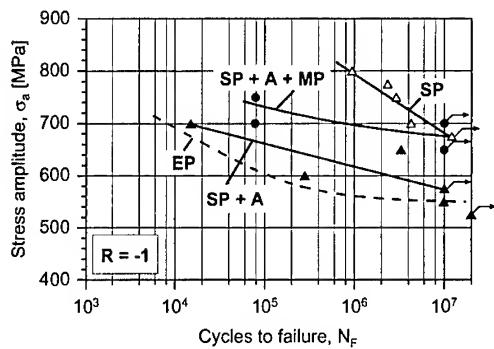


Fig. 9: S-N curves in rotating beam loading ($R = -1$) of the various conditions in γ (TiAl) (A: 50 h 650°C)

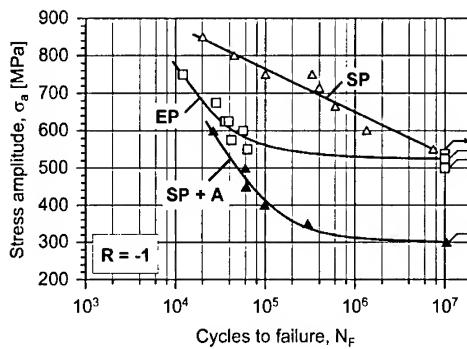


Fig. 10: S-N curves in rotating beam loading ($R = -1$) of the various conditions in TIMETAL 1100 (A: 50 h 600°C)

ALLOY DESIGN OF GAMMA TITANIUM ALUMINIDES

Keizo Hashimoto

Department of Materials Science and Engineering, Teikyo University
1-1 Toyosatidai Utsunomiya 320-8551 JAPAN

ABSTRACT

Gamma titanium aluminides (γ -TiAl) have been studied extensively, since they have been considered as a candidate material for advanced jet engine, automobile exhaust valves, turbo-charger and so on. Alloy design of γ -TiAl is still in progress for developing advanced alloy compositions and microstructures. In order to design materials, survey of phase diagrams is essential. Phase stability in the Ti-Al-Cr system at 1200°C has been investigated. Additions of Cr stabilize the β phase in the ternary phase diagrams. Based on the ternary phase diagrams, a unique microstructure; $\alpha+\beta+\gamma$ phases TiAl alloys with the capability of the super-plastic deformation have been developed. Fine γ grains and surrounding β phase grains are attributed to more than 400% tensile elongation at 1200°C. Using this property, a pack rolled process has been applied to the conventional hot rolling mill and as hot rolled sheet material can be deformed as a honeycomb structure. Then Cr doped γ -TiAl exhibit improvements of tensile strength at room to elevated temperatures after duplex microstructure changed to nearly full lamellar microstructure by a specific heat treatment.

1. INTRODUCTION

There is a strong demand for materials featuring high strength at temperatures at which conventional heat-resistant materials cannot satisfactorily perform, for future aircraft and energy applications. Gamma titanium aluminides (γ -TiAl) feature low density and superior high-temperature strength, so that they are extensively investigated as the lightweight heat-resistant materials for jet engines, automotive exhaust valves, and similar applications. Many investigations have been conducted to improve the mechanical properties of γ -TiAl at ambient temperature as well as at high temperatures. Recent researches have succeeded in controlling phases and microstructures by means of the hot working and heat treatment processes, resulting in a significant improvement of its workability or ductility [1-4]. However, there are still many problems to be solved. One is material affordability; although turbochargers made of γ -TiAl have been commercialized recently, production cost of γ -TiAl is still expensive comparing with other conventional titanium alloys. In order to reduce the fabrication cost of γ -TiAl, it is very crucial that the γ -TiAl must be manufactured by the conventional metallurgical process routes, such as forging, hot rolling and heat treatments in the industrial furnaces.

In this study, the alloy design of Cr doped γ -TiAl has been proposed based on the Ti-Al-Cr ternary phase diagram. Sheet forming process utilizing a conventional hot rolling facility has been studied. Mechanical properties of Cr doped γ -TiAl have been investigated in conjunction with the phase stability and microstructures.

2. PHASE STABILITY OF Ti-Al-Cr

It is reported that certain additions of Cr in γ -TiAl improve the room temperature ductility and the hot workability [5,6]. Cr is known as a β stabilizer in Ti base alloys. Figure 1 shows a calculated Ti-Al-Cr ternary phase diagram at 1200°C based on our current quenching experiments. Closed squares(■) indicate a single phase, open circles(O) indicate two phases and open triangles(Δ) present three phases. Experimentally determined compositional tie lines are drawn as the straight lines. The features of this phase diagram are i) β phase stabilizes by additions of Cr. ii) Solubility limit of Cr in α phase is about 8at%Cr and that in γ phase is less than 5at%Cr. Difference in solubility in α and γ phases causes inclined tie line between α and γ phases in the ternary phase diagram. These results indicate that the volume fractions of phases (α , β and γ) change entirely as a function of Al and Cr concentrations. The volume fractions of each phase can be controlled by both alloy compositions and heat treatment conditions. Based on the Ti-Al-Cr ternary phase diagram, Ti-47at%Al-3.0at%Cr compositions have been selected as a sheet forming material, since it requires the capabilities of the super plastic deformation and the high temperature strength. Figure 2 illustrates a calculated quasi-binary Ti-Al phase diagram at 3at% Cr by Thermo-Calc program. According to the quasi-binary phase diagram, Ti-47at%Al-3.0at%Cr specimen does not show $\alpha+\beta+\gamma$ three phases at any given temperatures. However, it has been reported that metastable β phase precipitates during the melting and the hot working process in this compositions [7].

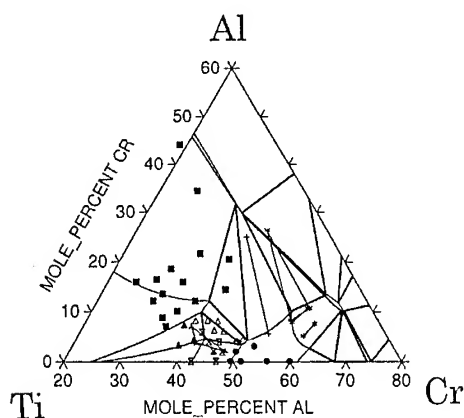


Fig. 1 Proposed Ti-Al-Cr ternary phase diagram at 1200°C

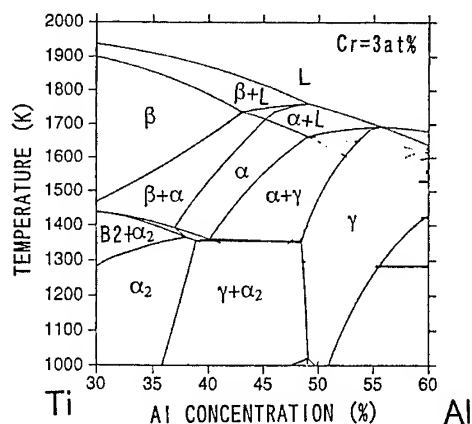


Fig. 2 Quasi-binary Ti-Al phase diagram at 3at% Cr

3. SHEET FORMING PROCESS

The ingot metallurgy and the hot rolling have been developed to produce γ -TiAl sheet. The sheet material can be fabricated into any shape using the super plastic forming (SPF). Plasma arc melting processes (PAM) were applied to produce a high purity γ -TiAl whose oxygen level was kept less than 400wtppm. The physical properties of γ -TiAl are very sensitive to small shifts of the alloy compositions. To get a fine grain size microstructure, ingots were homogenized at 1050°C for 96hrs and isothermally forged at 1200°C with an initial strain rate $1 \times 10^{-4} \text{ s}^{-1}$ until 70% reduction in a vacuum atmosphere.

Hot rolling is the most advantageous process among other sheet forming process [8].

It is very difficult to directly perform the hot rolling of γ -TiAl using a conventional mill, because γ -TiAl shows the poor deformability at the rolling temperature. Following three conditions should be maintained to overcome it; i) high temperatures, ii) low strain rate and iii) inert atmosphere. Isothermal hot rolling process in a vacuum atmosphere has been developed [9]. The isothermal rolling process requires an additional expensive facility; therefore, a more affordable process must be developed, that is pack rolling method.

Isothermally forged Ti-47at%Al-3.0at%Cr samples ($39 \times 39 \times 4.6 \text{ mm}^3$) were embedded in the SUS304 pack materials ($80 \times 180 \times 25 \text{ mm}$), then pack materials welded by means of the electron beam welding technique in a vacuum atmosphere. Figure 3 illustrates the pack rolling process. A conventional hot rolling facility that was fabricating steel products was utilized for the current hot rolling experiments. Table 1 lists the key conditions of the hot rolling at present experiments.

Table 1 Rolling conditions for pack rolling experiments

Sample	Furnace temperature (°C)	Roll velocity (m/min)	Strain rate (s^{-1})	Deformation Ratio
1	1250	10	1.92	30%(25 16.8)
2	1250	1	0.19	30%(25 16.8)
3	1250	5	0.96	30%(25 16.8)
4	1085	10	1.92	30%(25 16.8)

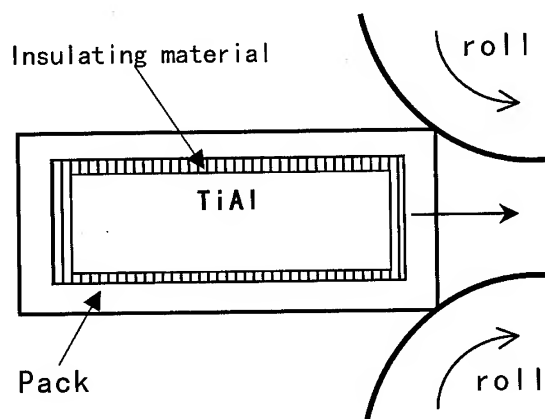


Fig. 3 Illustration of the pack rolling process

All four samples have been rolled successfully, but sample #4 showed severe delamination from the welded backside after rolling. Although heat loss from the SUS container during rolling was quite large, temperatures of the inner γ -TiAl have been preserved more than 1100°C from the start to the finish. As rolled packs were cut and the inner γ -TiAl plate samples were taken out. Inner γ -TiAl plates were sound and separated from the pack materials easily, since alumina insulator which prevented solid state reaction between γ -TiAl and the pack materials were inserted. As rolled samples (#1, 2 and 3) showed similar microstructures to that of the isothermally forged Cr doped γ -TiAl. X-ray diffraction analyses

from the as rolled samples were revealed that $\alpha_2+\beta+\gamma$ phases exist and their phase ratio was maintained to be constant during the rolling process.

4. MECHANICAL PROPERTIES

Previous researches have reported that microstructure controlled Ti-47at%Al-3.0at%Cr specimen shows more than 400% elongation and the strain rate sensitivity factor exceeds 0.5. Detailed investigations of this alloy have revealed that β phase precipitates around γ grains and those microstructures continuously generate during deformation above 1000°C. Uniform dynamic recrystallization plays an important role in the super-plastic deformation of γ -TiAl. The volume fraction of each phase can be controlled by alloying compositions and process temperatures those are determined by the quasi- binary Ti-Al phase diagram (in Fig. 2).

After fabrication, γ -TiAl would be applied in a severe environment such as elevated temperatures more than 600°C and an oxidation atmosphere. Therefore, much importance must be taken into account to the high temperature strength and the oxidation resistance of γ -TiAl. It is known that high temperature strength of full lamellar microstructure ($\alpha_2+\gamma$) is superior to that of duplex microstructure. According to Fig.2, $\alpha_2+\beta+\gamma$ duplex microstructure is able to transform to single α phase at 1350°C, then, it is decomposed to $\alpha_2+\gamma$ full lamellar microstructure during cooling down to room temperature. Tensile test specimens heated up to α transition temperature (1350°C), subsequently cooled down by introducing helium gas into the furnace. Microstructures of as heat-treated and as forged reference specimens show in Fig. 4. After heat treatment, nearly full lamellar microstructure whose colony size is 60 μ m was obtained. Tensile tests have been carried out from room temperature to 1100°C with a strain rate 5×10^{-4} in a vacuum atmosphere. Figure 5(a) summarizes the yield stresses of the heat-treated specimens at various temperatures. High temperature yield stresses of γ -TiAl are improved by the heat treatment. Tensile elongation is plotted as a function of test temperature in Fig.5(b).

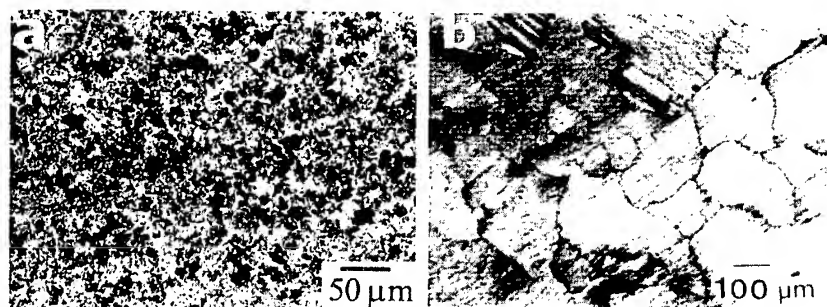


Figure 4 Optical micrograph of (a) duplex microstructure (before heat treatment) and (b) near lamellar microstructure (after heat treatment).

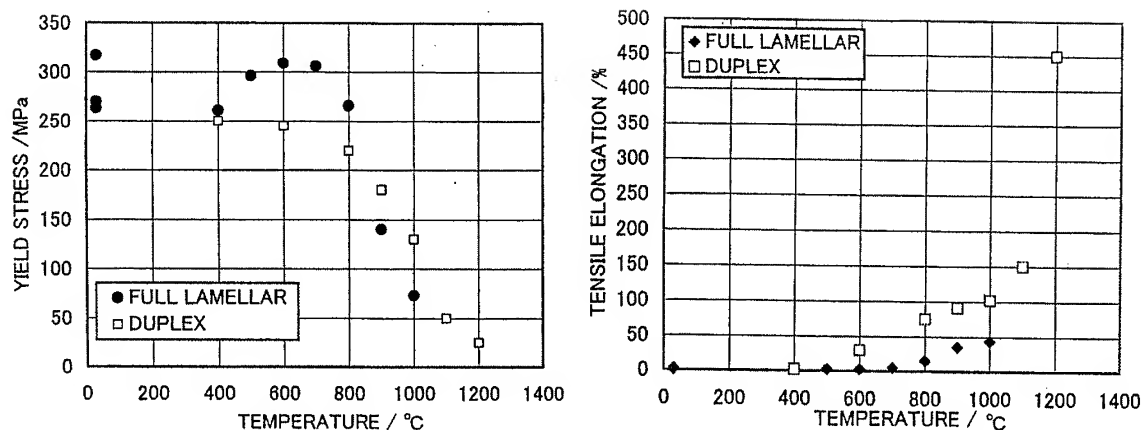
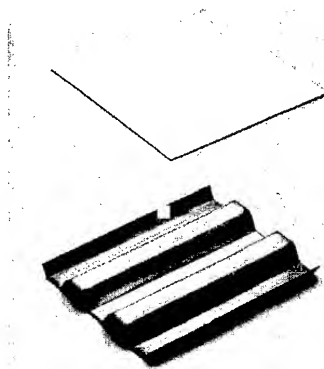


Figure 5 (a) Yield stress, (b) tensile elongation at temperature between 20°C and 1200°C.
 Nearly lamellar material is represented by filled symbols, duplex with open symbols

5. APPLICATION

Cr doped γ -TiAl is designed based on the Ti-Al-Cr ternary phase diagrams. Figure 6 shows the sheet material and honeycomb structure of Ti-47at%Al-3.0at%Cr. Sheet material is one of the basic shape of commercial products and opens many possibilities. For instance, titanium aluminide foils which were ground to 100 μ m thickness from the sheet material (0.5mm) prepared, and fabricated the CVD SiC fiber reinforced titanium aluminide composite materials by HIP process [10].

Figure 6 Honeycomb structure produced by the γ -TiAl sheet



6. SUMMARY

Phase stability in Ti-Al-Cr system at 1200°C has been investigated. Additions of Cr stabilize the β phase in the ternary phase diagram. Based on the ternary phase diagrams, a unique microstructure; $\alpha+\beta+\gamma$ phases TiAl alloys with the capability of the super-plastic deformation have been developed. Fine γ grains and surrounding β phase grains are attributed to more than 400% tensile elongation at 1200°C. Using this property, a hot rolling process has been established. Then Cr doped TiAl exhibits improvement of tensile strength at room to elevated temperatures after $\alpha_2+\beta+\gamma$ microstructure changed to full lamellar $\alpha_2+\gamma$ structure by the specific heat treatment.

7. ACKNOWLEDGEMENTS

The author wishes to thank Mr. Youji Mizuhara of the Nippon Steel Corporation for

manufacturing sheet of titanium aluminides for this investigation. A part of this work was supported by the JSPS 97R1201.

REFERENCES

- [1] H.A. Lipsitt, D. Shechtman and R.E. Schafrik, *Met.Trans.*, 6A, (1975) 1991
- [2] Y-W. Kim, *JOM* 41, No.7, (1989) 24
- [3] Y-W Kim and D.M.Dimiduk, *Structural Intermetallics*. Eds. by M.V.Nathal et al. TMS (1997) 531
- [4] C.T. Liu and P.J. Maziasz, *Intermetallics*, 6, (1998) 653
- [5] T. Kawabata, T. Tamura and O. Izumi, *MRS Symp. Proc.* 133 (1989) 329
- [6] M.Matsuo, *ISIJ International*, 31, (1991) 1212
- [7] N. Masahashi, Y.Mizuhara, M.Matsuo, K.Hashimoto, M.Kimura, T.Hanamura, H.Fujii, *Mat.Res.Soc.Symp. Proc.* .213, (1991) 795
- [8] H.Clemens et. al., *Gamma Titanium Aluminides 1999*, Eds. Y-W. Kim et. al. TMS (1999) 209
- [9] N. Fujituna, Y. Miyamoto and Y. Ashida, *Structual Intermetallics* Eds. by R. Darolia et. al. TMS (1993) 187
- [10] Y. Mizuhara , K. Hashimoto, H. Nakatani, Y. Shimada, *Structural Intermetallics* Eds. by M.V.Nathal et al (TMS), (1997) 929

FABRICATION OF Ti_3Al -XNB (X=0, 3, 7, 11, 13 AT%) POWDER COMPACTS MANUFACTURED BY PULSE DISCHARGE SINTERING

Wei Fang, Se-hyun Ko, and Yong-ho Park

National Institute of Advanced Industrial Science and Technology,
Tohoku National Industrial Research Institute,
4-2-1 Nigatake, Miyagino-ku, Sendai 983-8551, Japan

ABSTRACT

Powder compacts for Ti_3Al -xNb (x=0, 3, 7, 11, 13 at%) alloys were prepared by pulse discharge sintering at 1173-1573 K and their microstructures, oxidation resistance and mechanical properties were evaluated. The microstructure changed with sintering temperature and Nb content. At lower sintering temperatures, unreacted Ti and Nb were identified by X-ray diffraction and SEM-EDX, and Nb-rich phase primarily existed in the boundaries of Ti_3Al grains. Increasing sintering temperature obviously improved homogeneity of microstructure. Microhardness, oxidation resistance of compacts increased with sintering temperature and Nb content. For Ti_3Al , only pillar-like TiO_2 formed after oxidized at 1273 K in air. Adding Nb to Ti_3Al , oxide scale was dense and composed of fine particles of TiO_2 doped with Nb.

1. INTRODUCTION

Alloys based on the Ti_3Al -Nb system are currently the most advanced engineering intermetallics. These alloys have attractive properties which make them good candidates for application in gas turbine engines and airframe structures in advance aircraft. The primary advantages of Ti_3Al alloys are low density, high strength to weight ratio, good creep rupture strength, high moduli. Several compositions have been developed to achieve specific strength and stress rupture properties which exceed those of nickel base alloys such as INCO 718 over the temperature range 823-973 K [1]. The major disadvantages are their low ductilities and toughness at room temperature. Since they have poor workability, it is difficult for them to be deformed plastically even at elevated temperatures by conventional methods such as hot forging, hot rolling and hot extrusion, after conventional melting processing [2].

Recently, as one of hot-pressing processes, pulse discharge sintering (PDS) process technique has successfully developed to manufacture net shape TiAl valves [3]. The advantage of this technique is that the samples can be sintered in a short time to attain full density, so it can minimize grain growth. The present research is aimed at investigating microstructural properties of Ti_3Al and Ti_3Al alloyed with Nb prepared by PDS method. The effect of varying Nb content on oxidation resistance of Ti_3Al -Nb alloys are also examined to compare the results with those already reported by other investigators [4, 5].

2. EXPERIMENTAL PROCEDURES

The powders of elemental titanium (99.9% pure, less than 125 μm), aluminum (99% pure, less than 150 μm) and niobium (99.9% pure, less than 75 μm) were mixed to the desired composition of $\text{Ti}_{75-x}\text{Al}_{25}\text{-Nb}_x$ ($x=0, 3, 7, 11$ and 13 at %) for 48 hours prior to sintering. The powder was filled in a graphite mold with two graphite punches pressed at both ends. The sintering system is evacuated to a vacuum of about 3×10^{-5} torr prior to sintering with a diffusion vacuum pump. Disc-shaped compacts with a diameter of 50 mm and a thickness of 5 mm were sintered. To evaluate the effect of sintering temperature, the compacts were resistance-heated to fixed temperatures (1173-1573 K) under an applied uniaxial punch pressure of 38 MPa. Sintering temperatures were estimated using radiation thermometer by measuring the temperature of the graphite mold at the position 5 mm from the compact during sintering.

Density measurement by Archimedes' method was performed. X-ray diffraction was used for phase identification of the sintered compacts. The sintering compacts were sectioned to observe the microstructure using optical microscopy and scanning electron microscopy with EDX analysis. The microhardness was measured by MVK-G3 hardness tester. Resistivity measurement of sintered compacts was carried out from room temperature to 473 K by ULVAC ZEM-1 equipment. Four point bending specimens were prepared to a size of $40 \times 4 \times 2$ mm by electrical discharged machining (EDM) from the sintered compacts. Specimen surfaces were carefully ground using silicon carbide paper through 1500 grit and polished to a uniform finish of 0.3 μm alumina suspension. Mechanical testing was performed on an Instron universal testing machine at a load rate of 8.3×10^{-6} m/s.

3. RESULTS AND DISCUSSION

3.1 Microstructural observation and X-ray diffraction analysis

Table 1 shows the results of density of compacts. When sintering temperature is higher than 1173 K, the density of sintered compact of Ti_3Al is almost constant and is equal to the theoretical value. In the case of $\text{Ti}_3\text{Al-Nb}$ alloys, although there are not data of density of $\text{Ti}_3\text{Al-Nb}$ alloys, since the measured values are almost constant, we can consider that full density was obtained through sintering at above 1173 K. Lower sintering temperature is of importance for preventing grain growth and decreasing costs in industry. Fig. 1 shows XRD patterns for Ti_3Al

Table 1 Density of $\text{Ti}_3\text{Al-Nb}$ compacts sintered at various temperatures

Density ($\text{g}\cdot\text{cm}^{-3}$)	Ti_3Al	$\text{Ti}_3\text{Al-3Nb}$	$\text{Ti}_3\text{Al-7Nb}$	$\text{Ti}_3\text{Al-11Nb}$	$\text{Ti}_3\text{Al-13Nb}$
1173 K	4.24		4.55	4.71	4.78
1273 K	4.26	4.39	4.56	4.71	4.80
1373 K	4.29		4.57	4.72	4.80
1473 K		4.39	4.57	4.72	4.81
1573 K				4.73	4.81

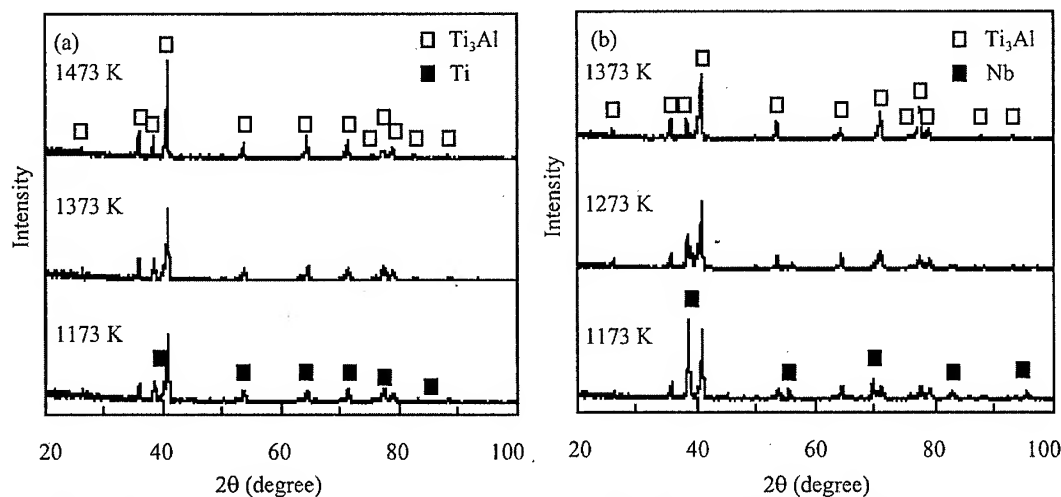


Fig. 1 X-ray diffraction patterns of Ti_3Al (a) and Ti_3Al -13Nb (b) compacts sintered at various temperatures.

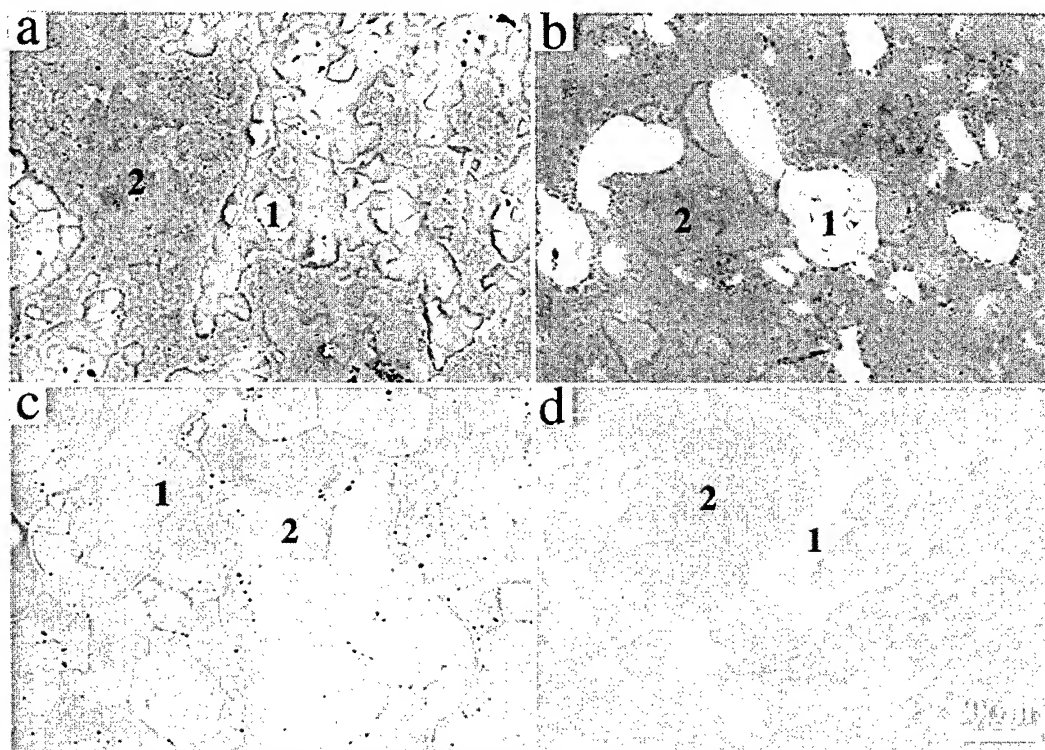


Fig. 2 SEM micrographs of Ti_3Al (a, c) and Ti_3Al -11Nb (b, d) compacts sintered at 1173 K (a, c) and 1373 K (b, d).

and Ti_3Al -11Nb compacts sintered at 1173 K and 1373 K. The XRD pattern indicates that Ti_3Al is a major phase and peaks of α -Ti (an unreacted phase during sintering) are detected when sintering at 1173 K, and only Ti_3Al peaks appear when sintering at 1373 K for Ti_3Al compact. For Ti_3Al -11Nb compact, the XRD pattern consists of unreacted Nb and Ti_3Al phases when sintering at 1173 K and only Ti_3Al peaks when sintering above 1373 K. SEM microstructures of Ti_3Al and Ti_3Al -11Nb are shown in Fig. 2. There is unreacted α -Ti and Nb in Ti_3Al and

Table 2 The compositions obtained from EDX for Ti_3Al and $\text{Ti}_3\text{Al-11Nb}$ compacts sintered at various temperatures (corresponding to the microstructures in Fig. 2)

at %	Ti_3Al		$\text{Ti}_3\text{Al-11Nb}$	
	1173 K	1373 K	1173 K	1573 K
	Ti : Al : Nb	Ti : Al : Nb	Ti : Al : Nb	Ti : Al : Nb
Point 1	96.8:3.2:0	78.2:21.8:0	2.1:2.8:95.1	47.2:29.3:23.5
Point 2	82.5:17.5:0	71.3:28.7:0	62.2:36.9:0.6	68.2:29.3:2.5

$\text{Ti}_3\text{Al-11Nb}$ sintered at 1173 K respectively, and microstructure clearly became homogeneous with increasing sintering temperature. Table 2 shows composition of phases denoted as 1 and 2 in Fig. 4. This is consistent with the results of XRD patterns, i.e. unreacted Ti and Nb were left over when sintered at 1173 K and only single phase Ti_3Al existed for Ti_3Al and $\text{Ti}_3\text{Al-11Nb}$ alloys sintered at 1373 K and 1573 K, respectively. Although compacts with high density can be obtained when sintering at 1173 K, it is difficult to obtain homogeneous compacts sintered with elemental powder size of about 100 μm [6], and especially, the diffusivity of Nb in Ti_3Al is very sluggish [7]. With increasing sintering temperature, microstructure became more homogeneous in comparison to sintering at 1173 K but there is still Nb-rich phase in $\text{Ti}_3\text{Al-11Nb}$ alloy sintered at 1573 K. The composition of Nb-rich phase is Ti-29Al-24Nb (in at%). This composition is the same as that of Ti_2AlNb phase with an orthorhombic structure, but peak of Ti_2AlNb phase can not be identified in XRD pattern.

3.2 Specific resistivity of compacts

Due to exposure of mixed powders in air prior to sintering, oxide film can form on the powder surface. One of advantages of PDS method is the dielectric breakdown of the oxide film on powder surface during sintering. It is suggested that the in situ ability of dielectric breakdown between powder particles and the heat generation in the metallic contact area between particles during heating process leads to improving particle sinterability; in other words, this enhances diffusion during subsequent densification. Therefore, magnitude of resistivity of compacts can be used to evaluate sintering characteristic of compacts. Specific resistivity of $\text{Ti}_3\text{Al-xNb}$ ($x=0, 3, 7, 11, 13$ at%) sintered at various temperatures was measured at 300 K, 373 K and 473 K. Fig. 3 shows the result of resistivity of compacts of Ti_3Al , $\text{Ti}_3\text{Al-7Nb}$ and $\text{Ti}_3\text{Al-13Nb}$ compacts at 300 K.

The value of resistivity clearly increased with increasing sintering temperature. In fact, the metallic contact shows extremely low resistivity compared to an oxide film, so it is suggested that the dielectric breakdown between powder particles has finished when sintered at 1173 K.

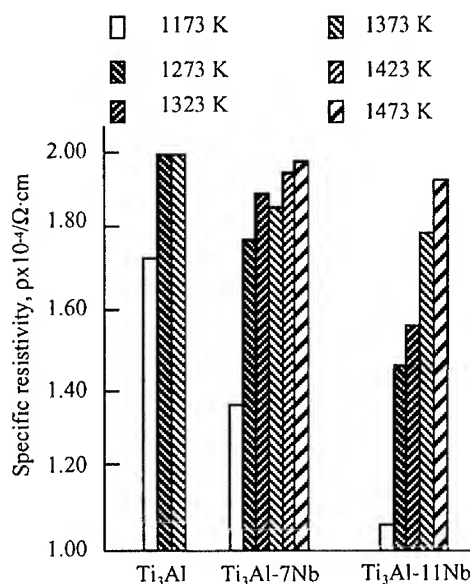


Fig. 3 Specific resistivity of $\text{Ti}_3\text{Al-Nb}$ compacts at various temperatures.

The reason why resistivity of the compact increased with increasing sintering temperature can be explained that unreacted metallic phase which is a better conductor than intermetallics, is remained after sintering and the amount of them is decreased as the sintering temperature increases. For Nb added Ti_3Al alloys, resistivity of compact clearly decreases with increasing Nb content.

3.3 Microhardness and bent test

Fig. 4 shows the dependence of microhardness of Ti_3Al , $Ti_3Al-3Nb$, $Ti_3Al-7Nb$ and $Ti_3Al-11Nb$ compacts on sintering temperature. Microhardness test was carried out at a load of 25g for 10s. It can be seen that the microhardness increases with sintering temperature and Nb contents. Since the microhardness of Ti_3Al is higher than that of Ti and TiAl [8], this agrees with the result obtained from X-ray diffraction and microstructural observation, which shows the amount of Ti_3Al increases with increasing sintered temperature. Single phase Ti_3Al microstructure could be obtained when sintering temperature increased. It can be considered that Nb increases microhardness of Ti_3Al by means of solid solution strength. Four point bent test of Ti_3Al-Nb compacts was carried out on Instron universal machine. The results show that sintering temperature and Nb contents do not show clear effect on bent stress of Ti_3Al-Nb compacts sintered by elemental powder.

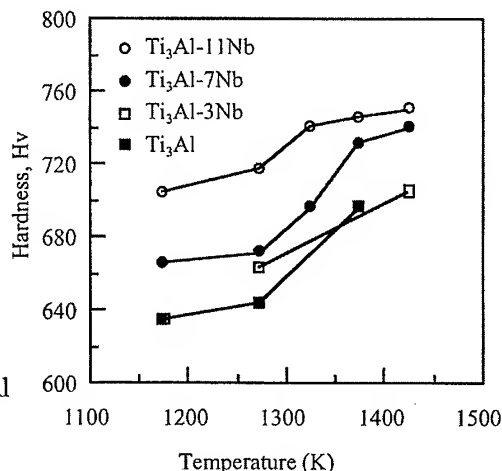


Fig. 4 Relation between microhardness and sintering temperature of Ti_3Al-Nb compacts.

3.4 Oxidation test

Fig. 5 shows oxidation-induced weight change of Ti_3Al-Nb compacts sintered at different temperatures in air. The result shows that oxidation resistance of Ti_3Al increases with sintering temperature and Nb contents. The oxidation resistance of $Ti_3Al-13Nb$ sintered at 1573 K is found to be the best among the alloys investigated in this study. The alloying of Nb improves the oxidation resistance of Ti_3Al , which also agree with other investigators [4,5]. Fig. 6 shows a scanning electron microscope of oxide surface of Ti_3Al and $Ti_3Al-13Nb$ oxidized at 1273 K. In the case, X-ray diffraction reveals the pillar-like oxide of Fig 6 (a) to be TiO_2 . The structure of oxide layer on the $Ti_3Al-13Nb$ compact (Fig. 6(b)) is completely different from that of Ti_3Al compact (Fig. 6(a)). The oxide scale formed on $Ti_3Al-13Nb$ alloy composed of TiO_2 containing Nb. Comparing with the porous structure

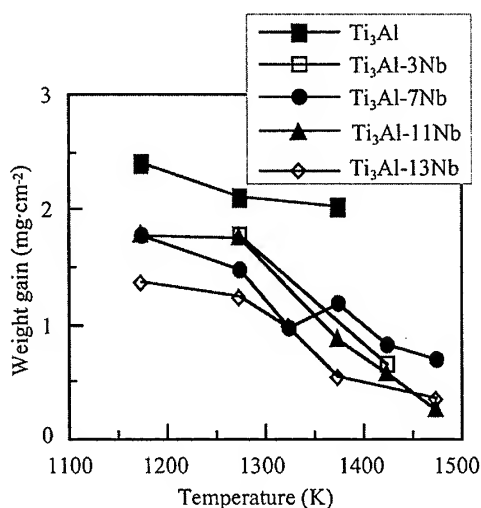


Fig. 5 Weight gain versus sintering temperature for Ti_3Al-Nb compacts oxidized in air up to 1273 K at a rate of 10 K/min.

ure of the oxide layer on Ti_3Al compact surface, the oxide particles on $Ti_3Al-13Nb$ compact surface are fine (less than a few micros) and dense, and the oxygen molecules would have more difficulty to pass through. More detailed investigation is needed before clarifying the oxidation mechanism. This dense-oxide layer means the Nb in the alloy may change the oxide structure and efficiently improve the oxidation resistance in Ti_3Al alloys.

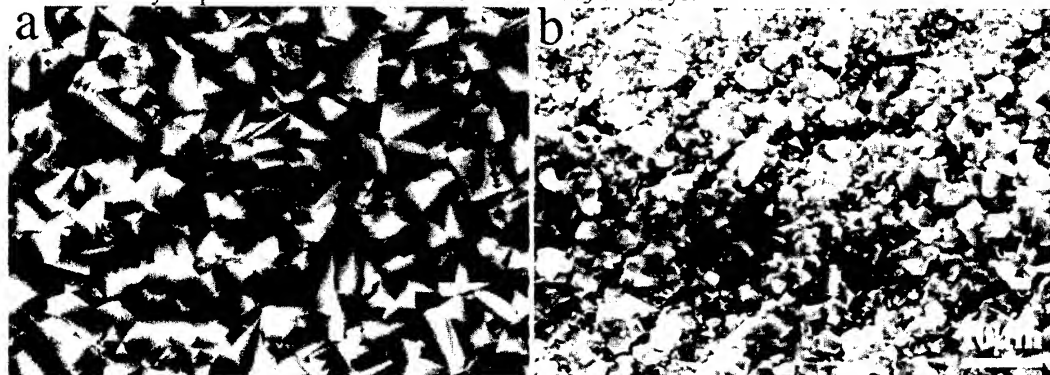


Fig. 6 Surface of oxide scale formed on Ti_3Al (a) and $Ti_3Al-13Nb$ (b) after exposure to air up to 1273 K at a rate of 10 K/min.

4 CONCLUSIONS

The microstructure, mechanical properties and oxidation resistance of Ti_3Al-Nb powder compacts produced by pulse discharge sintering at 1173-1573 K were investigated. The following are conclusions of the present investigation.

- 1) Compacts with high density can be attained when sintering temperature above 1173 K. At lower sintering temperature, unreacted Ti and Nb remained. Increasing sintering temperature clearly improved microstructural homogeneity of compacts. Nb-rich phase primarily existed in Ti_3Al grain boundaries.
- 2) Microhardness, oxidation resistance of compacts increased with sintering temperature and Nb contents. For Ti_3Al , only pillar-like TiO_2 formed after oxidized at 1273 K in air. Adding Nb to Ti_3Al enables the formation of a relatively dense layer of finer Nb doped TiO_2 particles and thereby improves the scale's protectiveness.

REFERENCES

1. D. Banerjee, A.K. Gogia, T.K. Nandy, K. Muraleedharan and R.S. Mishra, Structural Intermetallics, R. Darolia, J.J. Lewandowski, C.T. Liu, P.L. Martin, D.B. Miracle and M.V. Nathal ed., The Mineral, Metals & Materials Society, (1993), pp. 19-33.
2. D. Shechtman, M.J. Blackburn and H.A. Lipsitt, Metall. Trans., 5(1974), pp. 1373-1781.
3. H. Hashimoto, H. Sato, S and T. Abe, J. Japan Soc. Powder Metall., 44 (1997), pp. 542-546.
4. G.H. Meier, D. Appalonia, R.A. Perkins and K.T. Chiang, Oxidation of High Temperature Intermetallics, T. Grobstein and J. Doychak ed., Cleveland, (1988), pp. 185-193.
5. T.A. Wallace, R.K. Clark and S.N. Sankaran, Oxid. Met., 37(1992), pp. 111-124.
6. S. Emura and M. Hagiwara, J. Japan Institute of Metals, 10(1999), pp. 1269-1276.
7. J. Breuer, T. Wilger, M. Frisel and Chr. Herzig, Intermetallics, 7(1999), pp. 381-388.
8. K. Matsugi, N. Ishibashi and O. Yanagisawa, Intermetallics, 4(1996), pp. 457-476.

SYNTHESIS OF Ti-BASED INTERMETALLIC COMPOUNDS AND THEIR COMPOSITE USING SHOCK COMPRESSION

J-S. Lee, K. Hokamoto* and K. Siva Kumar**

Graduate School of Science and Technology,
Kumamoto University, Kumamoto 860-8555, Japan
*Shock Wave and Condensed Matter Research Center,
Kumamoto University, Kumamoto 860-8555, Japan

**Department of Mechanical Engineering and Materials Science, Kumamoto
University, Kumamoto 860-8555, Japan (Presently, D.M.R.L., India)

ABSTRACT

The synthesis of Ti-based intermetallic compound and the making of their composite materials by using shock compression technique were investigated. In the experiments to obtain Ti_5Si_3 compound, Ti-Si mixture powders, shock compressed at above 5.5 GPa, show porous structure by an excessive melting due to the exothermic reaction of the powders. Shock compression experiments, in order to obtain bulk composite materials were also carried out for mechanically milled Ti-Si powders mixed with relatively large Ti or TiAl powders. The Ti or TiAl powders acts as a heat sink for quenching excessive reaction heat. One of the experimental results shows that the fully reacted Ti_5Si_3 is confirmed and a composite of having a good cross-sectional area without any voids and cracks is obtained. A very high Vickers hardness above 10 GPa is measured at the reacted Ti_5Si_3 area. Also, some compacts composed of mixed Ti and Si plus TiAl powders obtained under a low pressure condition, which is not generating reaction between Ti and Si powders, the following heat-treatment for reaction between Ti and Si successfully made a moderate TiAl/ Ti_5Si_3 composite.

1. INTRODUCTION

Synthesis of materials using shock compression of powders is one of the quite unique techniques for making novel bulk materials [1-4]. The making of intermetallic compounds and their composites through shock-induced and shock-assisted reaction is investigated. The present investigation tries to synthesize Ti_5Si_3 and the composites employing the following two processes. One is using shock-induced reaction of Ti and Si elemental powder mixture, and the other is by heat treatment followed by shock compression of Ti and Si powder mixture. Since the generation of large amount of exothermic reaction heat induces undesired microstructure due to an excessive energy release, another inert powder, which act as heat sink, are added to the Ti and Si powder mixture.

The present investigation developed a new method for shock compression of powders using underwater shock wave. The system is quite easy to control as the pressure applied to the powders can be adjusted changing the height of water layer. Some experiments were performed to synthesize Ti_5Si_3 and its composites using (1) direct shock-induced reaction and (2) shock compression and heat treatment techniques.

2. EXPERIMENTAL

A schematic illustration of the explosive shock compression assembly is shown in Fig. 1. The powder mixture was filled in a mild steel container of having 30 mm inner diameter. The pressure, which acts just above the powders, can be controlled by changing the thickness of water, t_w . The height of explosive container was fixed at 50 mm and the explosive was ignited through an explosive lens for obtaining a plane shock wave as a purpose of compressing the prepared powders simultaneously. The main explosive used in our experiment was SEP, produced by Asahi Chemical Industry Co., Ltd., whose detonation velocity was 7 km/s and the density was 1300 kg/m³.

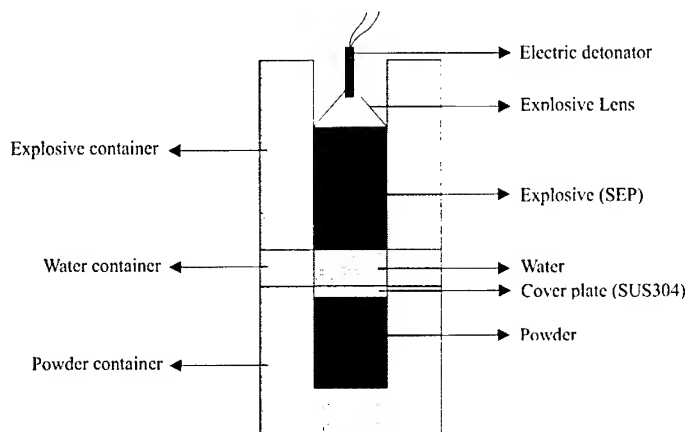


Fig.1 Schematic illustration of shock compression system using underwater shock wave.

The experimental conditions were listed in Table 1 and the thickness of water t_w was fixed at 5 mm. In the present investigation, elemental Ti (Sumitomo Sitix Co., - 45 μ m) and Si (CERAC, - 315mesh) powders were blended in an atomic ratios 5:3 under an argon atmosphere, and mixed in a conventional ball mill for 48 h. The milled powders were not mechanically alloyed well but mechanically mixed making thin layers of Ti and Si. The Ti-Si powders were mixed again with Ti or TiAl (Sumitomo Sitix Co., - 150 μ m). The mixed powders were packed to 10-15mm in height and the initial theoretical density was about 0.6. Only the experiments #U1, #M1, #M2 and #M3, a thin mechanically mixed Ti-Si layer was placed above the mixed powders as a purpose of activating the reaction between Ti and Si. Some of the non-reacted compacts obtained under low pressure condition, were heat treated at 1000°C for 1h in argon atmosphere to induce the reaction between the elemental powder mixture for making intermetallic compound composites.

Table 1 Experimental conditions and results.

Experiment Number	Powders (atomic ratio)	Recovered condition
#U1	Ti : Si (5:3) (50mass%) + Ti (50%)	Good, Fully reacted
#M1	Ti : Si (5:3) (40mass%) + TiAl (60%)	Good, Partially reacted
#M2	Ti : Si (5:3) (50mass%) + TiAl (50%)	Good, Partially reacted
#M3	Ti : Si (5:3) (60mass%) + TiAl (40%)	Porous, Fully reacted
#M4	Ti : Si (5:3) (30mass%) + TiAl (70%)	Good, non-reacted

3. RESULTS AND DISCUSSION

3-1. The making of composites through direct shock-induced reaction

After a series of experiments, it was confirmed that the shock-synthesized Ti_5Si_3 showed porous microstructure due to a large exothermic reaction heat [1]. Therefore, another powder Ti and TiAl, which are not expected to react the Ti and Si powder mixture, are blended to the mechanically mixed powders. Some of the experiment showed reaction between the Ti and Si as expected and the results are shown in Table 1. Fig. 2 shows the cross-sectional area for an experiment #U1, and a quite good microstructure without defects is observed. Mechanically mixed Ti and Si is fully reacted and only Ti_5Si_3 phase is confirmed through X-ray diffraction. Also, the reacted Ti_5Si_3 layer shows very high hardness about 10.2 GPa. The hardness value is quite high in comparison with Ti_5Si_3 commercially available [4].

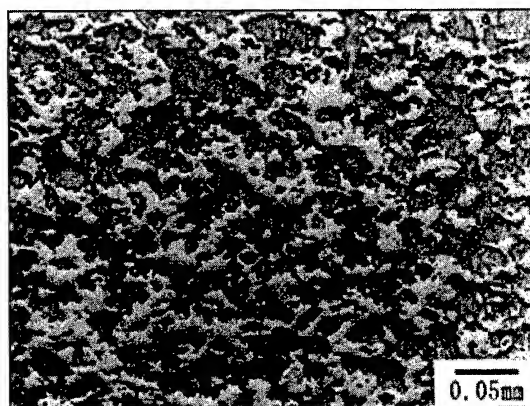


Fig. 2 Cross-section for experiment #U1.

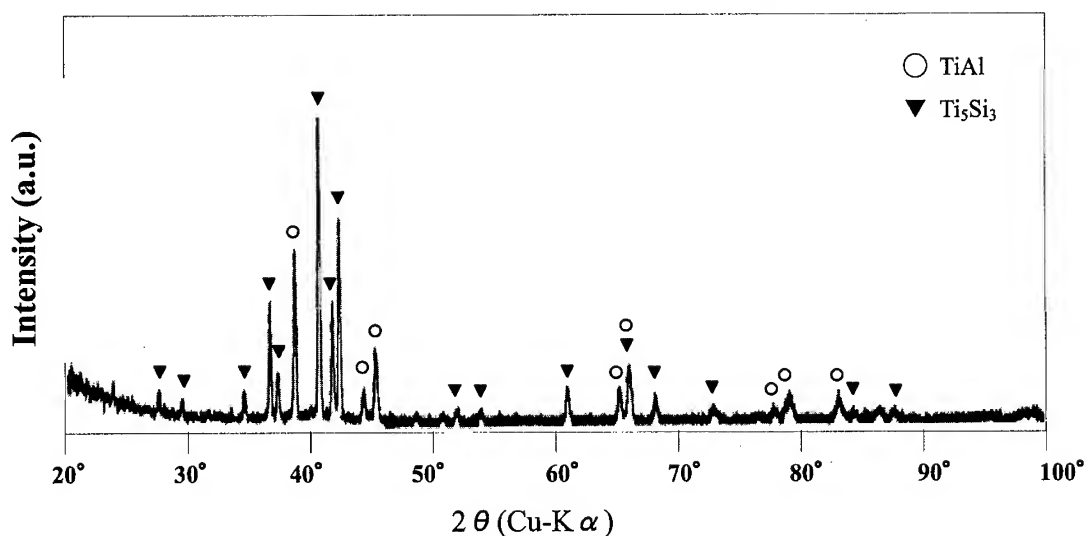


Fig. 3 X-ray diffraction pattern after shock compressed and reacted sample #M3.

For TiAl powders, the results are slightly different with the result obtained for using Ti

powders. Using the same powder mass ratio between TiAl and (Ti+Si) as experiment #U1, only partial reaction has been confirmed as suggested in table 1. By using large amount of mechanically mixed Ti and Si powders, the Ti and Si are fully reacted as listed in Table 1, but resulted in porous microstructure due to an excessive reaction heat. The X-ray diffraction pattern shows that no ternary compound is confirmed and it suggests only the existence of Ti_5Si_3 and TiAl as shown in Fig. 3, even the original TiAl particles are destroyed during shock processing. The authors originally expected to make a desired composite of Ti_5Si_3 and TiAl as obtained for a composite of Ti_5Si_3 and Ti (#U1) through a Route 1 as illustrated in Fig. 4. In this case, only the difference in the experimental condition is the size and shape of the powders employed Ti or TiAl. One explanation is that the reaction is enhanced for a case by the use of relatively fine Ti powders, which have large contacting surface area.

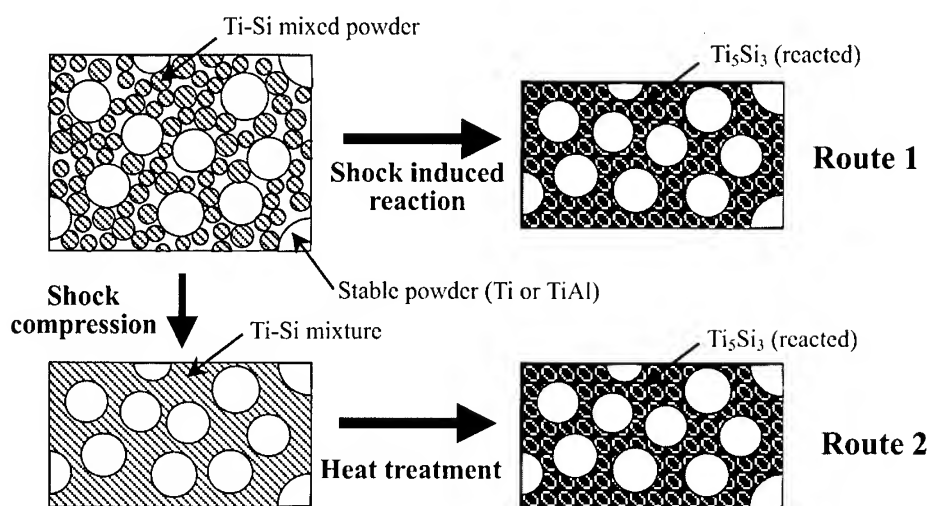


Fig. 4 Desired model for synthesis of various composites of intermetallics.

3-2. The making of composites by heat treatment after shock compression

For the sample #M4 just shock compressed without reaction, which shows no defects such as cracks or pores, a heat treatment is performed as a purpose to accomplish the reaction between the mechanically mixed Ti and Si powders. Normally, a high temperature above 1200°C is required for the reaction [4-6], but the shock compressed sample is activated through shock processing and is successfully reacted through a heat treatment at 1000°C for 1h. The SEM image in the cross-section is shown in Fig. 5. Table 2 shows the chemical compositions in the areas A, B and C suggested by arrows in Fig. 5 using EDS analysis. Ti element is almost distributed equally in whole area, and Al is gradually diffused into the reacted Ti + Si layer. In this SEM image, we confirmed one reacted layer between TiAl and Ti-Si mixture. It is thought to be generated due to the diffusion of Al from TiAl to Ti-Si region. This process, as suggested in a Route 2 in Fig. 4, is an alternative way to make composites of intermetallics though shock or explosive materials processing. The reacted Ti_5Si_3 area shows high Vickers hardness in the range of 9-11 GPa, and a high hardness close to 11 GPa is measured especially in the area B which is close to TiAl particles. Since the measured concentration of the contacting area C, suggested in Fig. 5, includes aluminum about 14.81 at.%. It suggests that some part of Si in the reacted Ti_5Si_3 is replaced with the solute Al which is diffused from TiAl.

So far, some reports have suggested [7-10] that such high hardness for shock-induced and shock compressed and heat treated Ti_5Si_3 and other intermetallics. The present investigation also shows the high hardness by the use of shock processing, and the present method have an advantage to make an uniform bulk material without defects by using a controlled shock pressure of having relatively long duration.

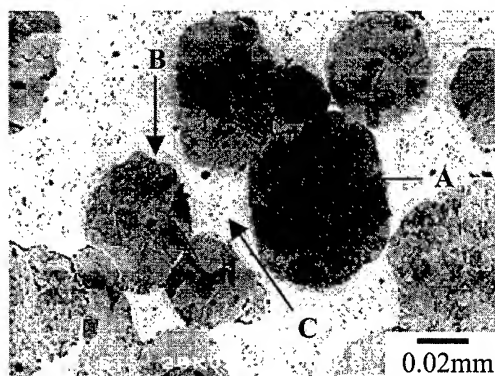


Fig. 5 SEM micrographs of heat treated sample #M4 at 1000°C for 1h.

Table 2 Chemical compositions of sample #M4 for each areas suggested in Fig. 5.

Point	Chemical composition (at.%)		
	Ti	Si	Al
A	50.40	0.08	49.52
B	64.34	1.82	33.84
C	62.89	22.30	14.81

4. CONCLUSIONS

The possibility to synthesize Ti_5Si_3 and the making of their composites of Ti-base intermetallics through the use of underwater shock wave assembly is suggested. Due to a large exothermic reaction heat of the mixed Ti and Si powders by shock-induced reaction, the addition of the other powder to release the excessive heat is requested for obtaining a bulk material without defects. Also, a heat treatment after shock compression for non-reacted mixed Ti and Si powders is available for obtaining composites of intermetallics. The Ti_5Si_3 layer synthesized through both processes shows very high hardness value in comparison with the Ti_5Si_3 commercially available.

REFERENCES

1. N.N. Thadhani, Shock-induced chemical reactions and synthesis of materials, Prog. Mater. Sic. Vol. 37(2)(1993), pp. 117-226.
2. R.A. Graham and N.N. Thadhani, in: A.B. Sawaoka (Ed.), Shock Waves in Materials Science, Springer, Berlin(1993), pp. 35-65.
3. T. Yamasaki, T. Ogino, K. Morishita, K. Fukuota, T. Atou and Y. Syono, Mater. Sci. Eng., Vol. A179/A180(1994), pp. 220-223.

4. N.N. Thadhani, S. Namjoshi, P.J. Counihan and A. Crawford, J. Mater. Process. Technol., Vol. 85(1999), pp. 74-78.
5. S. Kirihaara, Y. Tomota and T. Tsujimoto, Mater. Trans., JIM, Vol. 38(7)(1997), pp. 650-652.
6. K.P. Rao and Y. Du, Mater. Sci. Eng., Vol. A277(2000), pp. 46-56.
7. N.N. Thadhani, R.A. Graham, T. Royal, E. Dunbar, M.U. Anderson and G.T. Holman, J. Appl. Phys., Vol. 82(3)(1997), pp. 1113-1128.
8. P.J. Counihan, A. Crawford and N.N. Thadhani, Mater. Sci. Eng., Vol. A267(1999), pp. 26-35.
9. L.H. Yu and M.A. Meyers, J. Mater. Sci., Vol. 26(1991), pp. 601-611.
10. S.S. Shang and M.A. Meyers, Metall. Trans., Vol. 22A(11)(1991), pp. 2667-2676.

IMPROVED ROOM AND HIGH TEMPERATURE MECHANICAL PROPERTIES OF AN ORTHORHOMBIC Ti_2AlNb -BASED ALLOY

M. Hagiwara, S. Emura and F. Tang

National Institute for Materials Science
1-2-1 Sengen, Tsukuba 305-0047, Japan

ABSTRACT

A study was conducted to improve room and high temperature mechanical properties of an orthorhombic Ti_2AlNb -based Ti-22Al-27Nb alloy by microstructural and compositional modifications. The pinning effect of spherical α_2 particles, which were formed during hot deformation and subsequent annealing, was successfully utilized to refine B2 grains. The average size of final B2 grains ranged from 10 μm to 200 μm in diameter depending on the hot deformation and annealing conditions. The finer-grained materials showed an excellent combination of room temperature tensile strength and ductility.

An attempt was also made to substitute transition metal elements such as W, Mo or V for a portion of Nb in a Ti-22Al-27Nb alloy where the beta phase stability in the modified alloy is equal to that in Ti-22Al-27Nb. It was found that the substitution of 2 %W for 7 %Nb substantially increased the tensile strength at temperatures above 650°C and reducing the steady state creep rate and primary creep strain.

1. INTRODUCTION

A new class of titanium intermetallic alloys based on the Ti_2AlNb phase has been receiving much attention as candidate materials for high temperature applications [1-4]. These alloys are often called orthorhombic alloys because of the ordered orthorhombic structure of Ti_2AlNb phase.

A wide range of microstructures and hence a variety of properties can be developed in orthorhombic alloys through control of their chemistry and processing. Of various orthorhombic alloys so far studied, GE researchers have shown that a Ti-22Al-27Nb alloy which consists mainly of the O phase and B2 phase has the best balance of tensile, creep, and fracture properties[1]. A primary disadvantage of a Ti-22Al-27Nb alloy is, however, that the room temperature tensile elongation is very low, which ranges from 0 % to 7 % depending on microstructures. Another disadvantage of this alloy is that it exhibits a relatively large primary creep strain, as compared to that of nickel-based super-alloys. Furthermore, its yield stress drops sharply at temperatures higher than 650°C.

The purpose of the present research was therefore to overcome these drawbacks and develop novel orthorhombic alloys for temperatures above 650°C by microstructural and compositional modifications.

2. MICROSTRUCTURAL MODIFICATION

Microstructural modification was aimed to improve room temperature ductility and tensile strength of a Ti-22Al-27Nb alloy. To achieve this goal, the possibility of refining prior B2 grains was examined.

1.1 Sample preparation

Since a Ti-22Al-27Nb alloy contains a large amount of Nb, the gas atomization powder metallurgy (PM) processing route was employed to ensure homogeneity of the alloy. The as-atomized Ti-22Al-27Nb powder with the diameter ranging between 45 μm and 150 μm was compacted by hot isostatic pressing (HIP) at 1100°C under the pressure of 200 MPa.

1.2 Microstructures and creep property relationship

Since creep is one of the most important properties for high temperature use, microstructures and creep property relationship was first evaluated for a Ti-22Al-27Nb alloy.

Three typical microstructures observed in a Ti-22Al-27Nb alloy are shown in Fig.1. When the alloy is slowly cooled from above the B2 transus temperature, a coarse lamellar microstructure with large prior B2 grains is formed (Fig.1a). A very fine (O+B2) two phase microstructure is formed by quenching the alloy from above the B2 transus temperature and subsequent annealing at around 800°C (Fig.1b). The equiaxed O phase microstructure can be obtained by annealing the heavily deformed alloy at around 800°C (Fig.1c).

Fig.2 shows the creep curves for these three typical microstructures tested at 650°C with an applied stress of 310 MPa. It was demonstrated that the lamellar microstructure has the best creep property among the microstructure studied. However, the room temperature tensile ductility of 4 % for the lamellar structure, as shown in Fig. 3, was not so encouraging.

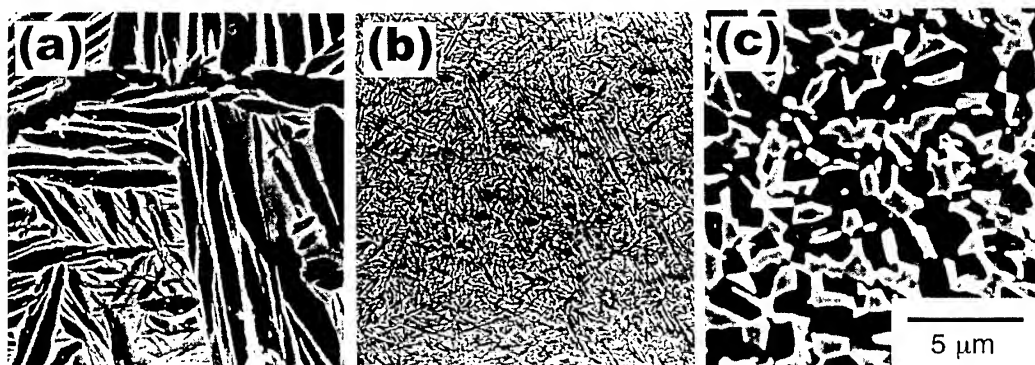


Fig.1 Three typical microstructures observed in a Ti-22Al-27Nb alloy:
(a) Lamellar microstructure, (b) Fine microstructure, and (c) Equiaxed microstructure

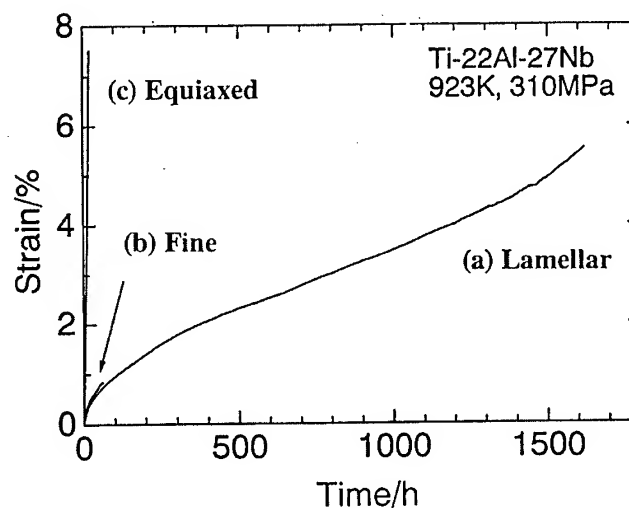


Fig.2 Creep curves for three typical microstructures in a Ti-22Al-27Nb alloy.

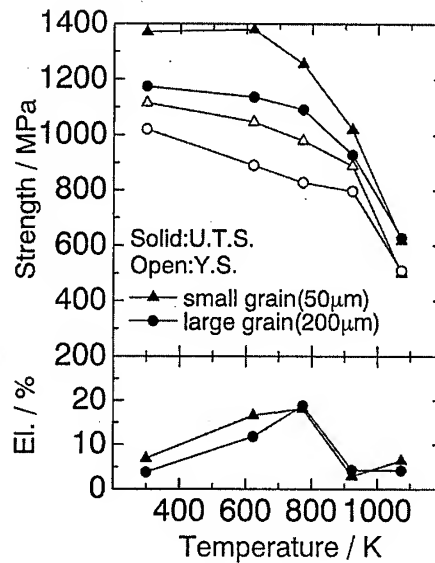


Fig.3 High temperature tensile property of a Ti-22Al-27Nb with a lamellar microstructure.

1.3 Refining prior B2 grains to improve room temperature ductility

From the standpoint of material's reliability, Ti-22Al-27Nb alloy should have an excellent combination of creep property and room temperature ductility. As previously mentioned, the creep property was the best for the lamellar microstructure. For the improved room temperature tensile ductility, it is necessary to reduce the size of prior B2 grain in the orthorhombic alloy, as is the case for many metallic materials. The microstructure modification should, therefore, need to be done in such a way for the alloy to have smaller prior B2 grains and a lamellar microstructure within grains.

An attempt was made to reduce prior B2 grains by using spherical α_2 particles as obstacles against grain growth. The actual B2 grain size control was done in the following three manners.

(1) Hot rolling in the (α_2+B2) phase region and annealing in the (α_2+B2) phase region

It was found that the hot rolling of a Ti-22Al-27Nb alloy in a (α_2+B2) two phase region (1000 to 1070°C) could be easily done. The elongated α_2 phases formed after hot rolling tended to become spherical during subsequent annealing in the (α_2+B2) two phase region, even though the alloy was not subjected to heavy deformation during hot rolling.

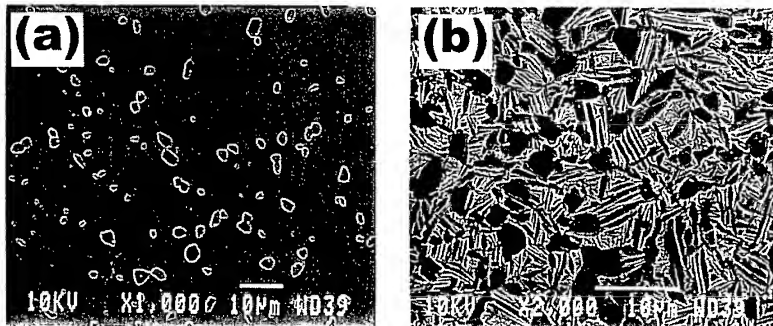


Fig.4 Distribution of the spherical α_2 phases. The material was hot rolled at 1000°C and annealed at 1050°C. (a): Water quenched from 1050°C. (b): Slowly cooled from 1050°C.

Fig.4 shows the distribution of the spherical α_2 phases after hot rolling at 1000°C and subsequent annealing at 1050°C (Fig.4a). These uniformly dispersed α_2 phases acted as obstacles against grain growth, and therefore fine B2 grains ranging from 10 μm to 50 μm in diameter were obtained. As shown in Fig.4b, the lamellar microstructure could be formed within these small B2 grains by slow cooling from the annealing temperature.

(2) Hot rolling in the (α_2 +B2) phase region and annealing in the B2 phase region

The resolution rate of these spherical α_2 phases was found to be quite slow when the spherical α_2 particles-containing material was heated in the B2 single phase region. Relatively fine B2 grains could therefore be obtained due to the pinning effect of these α_2 particles on the B2 grain growth. Fig.5 shows that there is a linear relationship between the average size of B2 grain ranging from 50 μm to 80 μm in diameter and the Larson-Miller parameter for a Ti-22Al-27Nb alloy which was hot-rolled at 1273 K (1000°C) and subsequently annealed in the B2 single phase region with various combinations of temperature and time.

(3) Hot rolling in the B2 phase region and annealing in the B2 phase region

During slow cooling after hot rolling in the B2 single region (e.g., 1423 K), a small amount of spherical α_2 particles were found to form. These particles were therefore used to control the B2 grains for the size above 80 μm in diameter by annealing the hot-rolled material in the B2 single phase region, as shown in Fig.5.

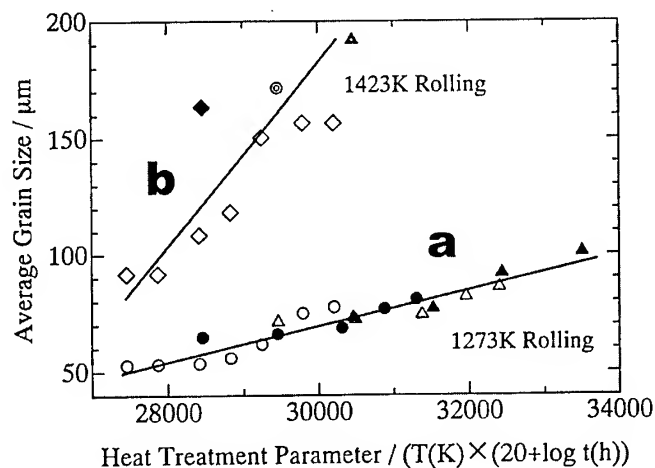


Fig.5 The relationship between the average B2 grain size and the Larson-Miller parameter. Line a and b: Material was hot-rolled at 1273 K and 1423 K, respectively, and annealed in the B2 single phase region with various combinations of temperature and time.

Tensile data for a Ti-22Al-27Nb alloy with smaller B2 grain size of 50 μm and a lamellar microstructure within the grains is also included in Fig.3. It was clearly demonstrated that by reducing the grain size from 200 μm to 50 μm , an excellent combination of room temperature tensile strength of 1371 MPa and elongation of 7 % could be obtained.

3. COMPOSITIONAL MODIFICATION

The compositional modification was aimed to improve tensile and creep strength at temperatures above 650°C by substituting transition metal elements such as W, Mo or V for a portion of Nb in a Ti-22Al-27 Nb alloy.

3.1 Guideline for alloy modification

The guideline governing the alloy modification is based on the fact that the total sum of β phase stability from each β -stabilizing element in the modified alloy should correspond to a baseline Ti-22Al-27Nb alloy. This guideline suggests that the phase diagram for the modified alloy need to be equal or very similar to that of a baseline alloy, and therefore the same phase constitutions may be obtained with the same heat treatment for both modified and baseline alloys.

Fig.6 shows the critical concentration of various beta stabilizers necessary to retain a 100 % β phase at room temperature for a number of alloying elements in titanium [5], indicating that the β phase stabilizing ability becomes strong in the order of Nb, V, W, and Mo. For example, Mo is $\text{Nb} (22.5) / \text{Mo} (5.3) = 4.25$ times stronger than that of Nb. Therefore it is reasonable to consider that one atomic percent addition of Mo corresponds to the replacement of 4.25 atomic percent of Nb. Similarly, one atomic percent addition of W corresponds to the replacement of $\text{Nb} (22.5) / \text{W}(6.7) = 3.36$ atomic percent of Nb. According to this guideline, various modified alloys were newly composed.

3.2 Sample preparation, heat treatment and density

The modified alloys and a baseline Ti-22Al-27Nb alloy were prepared using a non-consumable electric arc furnace. The ingots, which weighed 200g each, were first forged at 1150°C in the B2 single phase region. These forged ingots were subjected to the same BA treatment to produce lamellar microstructure. The lamellar morphology was highly dependent on the cooling rate. Slower cooling rate of 0.03 K/s resulted a coarsely aligned side plate at the prior B2 grain boundaries, and similarly aligned laths within the grains (See Fig.1a).

The composition and density of each modified alloy are shown in Table 1. The density of these modified alloys was in the range of 4.9 to 5.4 g/cm³, which are almost equal or somewhat lower than that of a Ti-22Al-27Nb alloy.

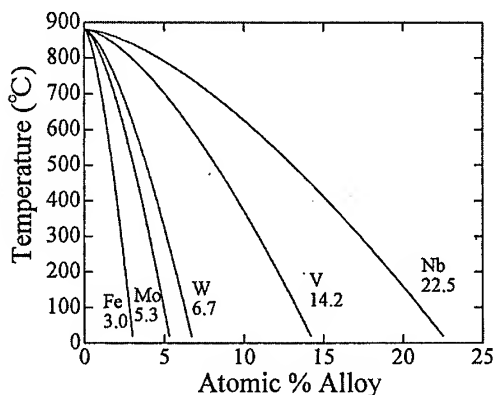


Fig.6 Concentration of alloying elements necessary to obtain the 100 % β phase at room temperature.

Table 1 Compositions and density of modified alloys.

Alloy	D (g/cm3)
Ti-22Al-27Nb (O+B2)	5.4
Ti-22Al-19Nb-2Mo	5.1
Ti-22Al-11Nb-4Mo	4.9
Ti-22Al-20Nb-2W	5.3
Ti-22Al-14Nb-4W	5.4
Ti-22Al-24Nb-2V	5.3
Ti-22Al-21Nb-4V	5.2

3.3 Creep properties

Fig.7 shows the creep curves of modified alloys and a Ti-22Al-27Nb alloy. A creep test was conducted at 650°C at an applied stress of 310 MPa. It was demonstrated that the Ti-22Al-20Nb-2W alloy exhibited a marked decrease in a primary creep strain as well as steady state creep rate as compared to those of other modified alloys and a baseline alloy.

3.4 High temperature tensile properties

The 0.2 % yield stress of W-modified Ti-22Al-20Nb-2W alloy was compared with that of a Ti-22Al-27Nb alloy, and represented in Fig.8. Since the yield strength of these two alloys changed depending on the alloy's lamellar morphology, yield strength data were depicted as a scatter-band. In this scatter-band, a coarser lamellar morphology resulting from the slower cooling rate corresponded to the lower boundary whereas a finer lamellar morphology resulting from the faster cooling rate exhibited the highest yield strength.

It is obvious that the critical temperature above which the yield stress began to decrease rapidly is 100°C higher in a Ti-22Al-20Nb-2W alloy than in a Ti-22Al-27Nb alloy.

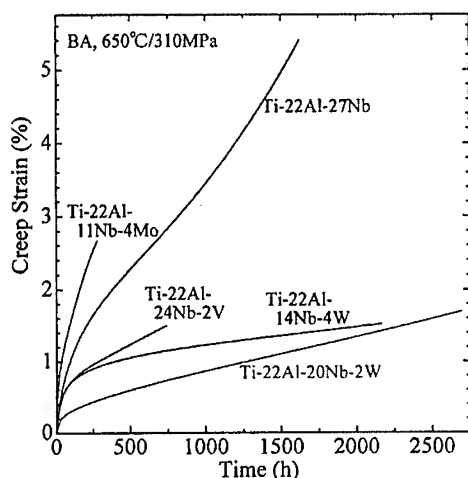


Fig.7 Creep property of modified alloys with lamellar microstructure.

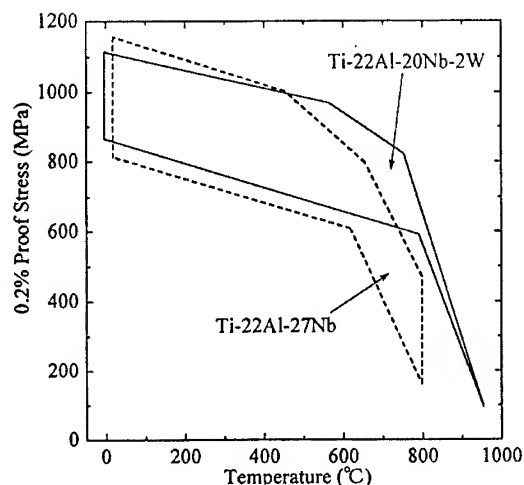


Fig.8 The 0.2 % yield stress of W-modified Ti-22Al-20Nb-2W alloy.

4. CONCLUSION

A Ti-22Al-27Nb alloy with prior B2 grain size ranging from 10 μm to 200 μm were successfully obtained by using spherical α_2 particles as obstacles against grain growth. An alloy with B2 grain size of 50 μm and a lamellar microstructure within the grains exhibited higher tensile strength (1371 MPa) and elongation (7%) at room temperature.

Substitution of 2 %W for 7 %Nb in a Ti-22Al-27Nb was quite effective in increasing tensile strength at temperatures above 650°C. This substitution was also effective in reducing the steady state creep rate and primary creep strain.

REFERENCES

1. R.G.Rowe, Microstructure/Property Relationship in Titanium Aluminides and Alloys Y.-W. Kim and R.R.Boyer, eds., TMS, Warrendale, PA, (1991), pp.387-398.
2. J. Kumpfert and C. Leyens, Structural Intermetallics, B.D. Miracle, R. Wagner and M. Yamaguchi, eds., TMS, Warrendale, PA, (1997), pp.895-904.
3. A.K. Gogia et al, Intermetallics, 6(1998), pp.741-748.
4. C.J. Boehlert, B.S. Majumdar, V. Seetharaman and D.B. Miracle, Met. Trans., 30A(1999), pp.2305-2329.
5. S. Ankem and S.R. Seagl, Beta Titanium Alloys in the 1980's, R.R. Boyer and H.W. osenberg, eds., TMS-AIME, Warrendale, PA, (1983), pp.107-126.

MICROSTRUCTURE AND TENSILE DUCTILITY OF FE-40AL WITH HIGH BORON CONTENT

J.H. Lee, S.I. Kwun, W.S. Lee*, Y.H. Kim and Jai Won Byeon
Dept. of Metallurgical Engineering, Korea University, Seoul, 136-701, Korea
*Korea Institute of Industrial Technology, Hongchonri, Chonan, Choongnam,
330-825, Korea

ABSTRACT

The effect of a large amount of B addition to Fe-40at%Al intermetallic alloy on microstructure and mechanical properties was investigated. The alloys with or without B were cast, hot extruded, homogenized and subsequently vacancy annealed at 400°C for 7 days. The microstructure consisted of FeAl matrix with B2 structure and Fe₂B borides with tetragonal structure along grain boundaries. Neutron irradiation was employed for the analysis of B atoms and borides distribution. Tensile properties at room temperature in air were determined under the initial strain rate of $1 \times 10^{-4} \text{ s}^{-1}$ and $1 \times 10^0 \text{ s}^{-1}$. For a given strain rate, The alloys with B demonstrated improved ductility over the alloy without B. Especially, The Fe-40at%Al-1.21at%B alloy exhibited the elongation of 16.4% under the strain rate of $1 \times 10^0 \text{ s}^{-1}$. The addition of a large amount of B resulted in grain refinement and changed the fracture mode from intergranular to transgranular to increase the ductility.

1. INTRODUCTION

The FeAl intermetallic compound has many attractive properties such as low density, excellent oxidation and corrosion resistance, and high temperature strength. However, it is lacking in room temperature ductility even though FeAl has more than the five independent slip systems [1]. It has been reported that the main causes for low ductility in FeAl are grain boundary brittleness [2,3,4,5], hydrogen embrittlement [3,4,5,6,7] and excess vacancies [5,8,9,10,11]. Previous research [12] found that a large amount of B addition (1.21%) to Fe-40Al (all composition are in at. %) could improve the elongation to 8.1% at room temperature in air.

This research intended to investigate the distribution of B atoms and borides to find the effect of high B content on the microstructure and mechanical properties of Fe-40Al.

2. EXPERIMENTAL PROCEDURES

The alloys with the nominal compositions were prepared by vacuum induction melting from high purity Fe, Al and granular B. Alloy designation and its nominal compositions are shown in Table 1. The alloy ingots were first homogenized at 1000°C for 1 hr and then clad in low carbon steel sheet in vacuum atmosphere and hot extruded at 1100°C with an extrusion ratio of 16:1. The alloys were again held at 1000°C for 1 hr homogenization heat-treatment and subsequently annealed at 400°C for 7 days to reduce the excess vacancies. It has been reported [11] that vacancies can be reduced by furnace cooling [10] followed by vacancy annealing at low temperature for a long time [8] in spite that vacancies are difficult to remove due to low vacancy formation energy and high vacancy migration energy in FeAl intermetallic alloy. The distribution of B atoms in the alloys was identified by neutron beam irradiation in Korea Atomic Energy Research Institute. The CBED (convergent

beam electron diffraction) method was used to analyze the structure of borides in the annealed specimens. The tensile properties were measured at room temperature in air under the constant initial strain rate of $1 \times 10^{-4} \text{ s}^{-1}$ and $1 \times 10^0 \text{ s}^{-1}$.

3. RESULTS AND DISCUSSION

The extra peaks at 2θ values of 31° and 55° due to superlattice of FeAl alloy were observed in the X-ray diffraction of the hot extruded alloy (Fig. 1).

Fig. 3 is the optical microstructures of the vacancy annealed alloys, which shows the decreased grain size with increasing B content. The grain sizes of the alloys without B (FA) and with 0.41B (FA-0.1B) were $310 \mu\text{m}$ and $60 \mu\text{m}$, respectively, and these with 1.21B (FA-0.3B) and 1.61B (FA-0.4B) were similar to be about $30\text{--}35 \mu\text{m}$. It is reported that the B addition refines the grains slightly [4,13]. Coarse borides along grain boundaries hinder the dynamic recrystallization grain growth during hot extrusion.

Image contrast in Fig. 4 is determined by the amount of B contents exposed to neutron beam. Both interstitial B atoms and coarse borides were seen in the Fe-0.1B and FA-0.4B alloys (Fig. 4 (b), (c)). The B atoms were segregated along grain boundaries (Fig. 4 (a)) and the borides in FA-0.4B alloy were coarser and more densely distributed than those in the FA-0.1B alloy. According to the previous analysis by SIMS (secondary ion mass spectroscopy), the solubility of B in FeAl is less than 80 wppm [13]. The excess B atoms are reported to segregate to grain boundaries [3,9]. From the structure analysis of these borides by CBED method, it was found that the borides were Fe_2B with tetragonal structure ($a=5.1103\text{\AA}$, $c=4.2494\text{\AA}$), which agreed well with previously published result [7,14].

The microhardness increased with B content in the vacancy annealed alloys as shown in Fig. 2. However, the decreasing rate of hardness by vacancy annealing was steeper in FA alloy than in the alloys with B, which implies that interstitial B atoms suppress the mobility of vacancies. Deevi et al [8] also observed that the strength of the FeAl without B decreased after vacancy annealing and suggested that the strength of the FeAl with B were insensitive to vacancy annealing as the alloy without B.

Results of tensile test under the initial strain rate of $1 \times 10^{-4} \text{ s}^{-1}$ and $1 \times 10^0 \text{ s}^{-1}$ are given in Table 2. The alloys with B exhibited not only higher strength but also higher elongation in both strain rates. It is noticed that both strength and elongation increased as the strain rate increased. By increasing the strain rate 10^4 times, the elongation increased by 4.5% in the FA alloy while by 10% in the alloys with B. Especially, the FA-0.3B alloy showed the elongation as high as 16.4% with the tensile strength of 880 MPa. Pike and Liu [5] attributed the decreased elongation at slower strain rate to the time-dependent hydrogen embrittlement in the Fe-40Al alloy. George et al [15] reported that interstitial B atoms prevented or slowed down the diffusion of hydrogen atoms in Ni_3Al alloy. Baker et al [9] observed that the increase of elongation by increased strain rate was higher in the Fe-45Al alloy with B than in the alloy without B.

The fracture surfaces of the specimens fractured under different strain rates are shown in Fig. 5 and Fig. 6. When the strain rate was $1 \times 10^{-4} \text{ s}^{-1}$, the alloy without B showed the complete intergranular fracture while the alloys with B showed the transgranular fracture. The fracture mode did not change in FA, FA-0.3B and FA-0.4B alloy by increasing the strain rate to $1 \times 10^0 \text{ s}^{-1}$ except that in the FA-0.1B alloy showed the mixed fracture surface. This result indicates that the B content higher than 0.41 is needed to strengthen grain boundaries under the strain rate of $1 \times 10^0 \text{ s}^{-1}$. Considering that the borides became coarser and distributed more densely along the grain boundaries (Fig. 3, 4) and showed transgranular fracture surface as B content increased, it is evident that borides strengthen grain boundaries. However, grain boundary strengthening did not always

increase the elongation. Research on the role of borides in Fe-40Al alloy has been seldom published. Pang et al [16] observed that lath perovskite carbides inside grains and along grain boundaries increased the elongation in Fe-40Al-0.6C alloy. They suggested that carbides could influence the characteristics of crack path grain boundaries and that the carbide interface trap the diffusing hydrogen atoms. It is thought that similar mechanism might be applied to borides in present alloys.

4. CONCLUSION

1. High content of B resulted in grain refinement due to coarse borides along grain boundaries.
2. The interstitial B atoms suppress the mobility of vacancies.
3. The alloys with B exhibited not only higher strength but also better elongation than the one without B. Especially, the Fe-40Al-1.21B alloy showed 16.4% elongation at the strain rate of $1 \times 10^0 \text{ s}^{-1}$.

REFERENCE

1. I. Baker and D.J. Gaydosch, Mater. Sci. eng., Vol.96(1987) pp. 147-158
2. M.A. Crimp and K.M. Vedula, Mater. Sci. Eng., Vol.78(1986) pp. 193-200
3. C.T. Liu and E.P. George, Scripta metall. Mater., Vol.24(1990) pp. 1285-1290
4. J.W. Cohron, Y. Lin, R.H. Zee and E.P. George, Acta Mater., Vol.46(1998) pp. 6245-6256
5. L.M. Pike and C.T. Liu, Scripta Metall., Vol.38(1998) pp. 1475-1480
6. C.T. Liu, E.H. Lee and C.G. McKamey, Scripta Metall. Mater., Vol.23(1984) pp. 875-880
7. L. Pang and K.S. Kumar, Mater. Sci. & Eng. A., Vol.258(1998) pp. 161-166
8. S.C. Deevi, V.K. Sikka, B.J. Inkson and R.W. Cahn, Scripta Metall., Vol.36(1997) pp. 899-904
9. I. Baker, O. Klein, C. Nelson and E.P. George, Scripta Metall., Vol.30(1994) pp. 863-868
10. P. Nagpal and I. Baker, Metall. Trans. A, Vol.21A(1990) pp.2281-2282
11. O. Klein and I. Baker, Scripta. Metall., Vol. 30(1994) pp. 627-632
12. M.H. Kim and S.I. Kwun, Scripta Metall., Vol.35(1996) pp. 317-322
13. G. Webb, P. Juliet and A. Lefort, Scripta. Metall., Vol.28(1993) pp. 769-772
14. D.J. Gaydosch, S.L. Draper, and M.V. Nathal, Metall. Trans., Vol.20A(1989) pp.1701-1714
15. E.P. George, C.T. Liu and D.P. Pope, Scripta Metall., Vol.28(1993) pp. 857-862
16. L. Pang and K.S. Kumar, Intermetallics, Vol.8(2000) pp. 693-698

TABLE 1

Specimen designation and its nominal composition (at%)

Designation	Fe	Al	B
FA	Bal.	40	0
FA-0.1B	Bal.	40	0.41
FA-0.3B	Bal.	40	1.21
FA-0.4B	Bal.	40	1.61

TABLE 2
The tensile properties of experimental alloys as a function of strain rate

strain rate	1×10^{-4}			1×10^0		
	elong. (%)	UTS(MPa)	Frac. Mode	elong. (%)	UTS(MPa)	Frac. Mode
FA	4.9	412.8	IG	9.4	456.7	IG
FA-0.1B	6.2	546.8	TG	16.4	788.8	TG/IG
FA-0.3B	6.1	676.8	TG	16.4	880.1	TG
FA-0.4B	5.5	664.7	TG	13.4	856.5	TG

*IG – intergranular, TG – transgranular, TG/IG – mixed transgranular and intergranular

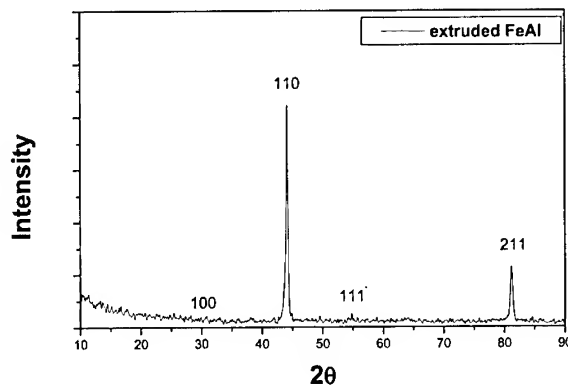


Fig. 1 X-ray diffraction pattern of hot extruded FA

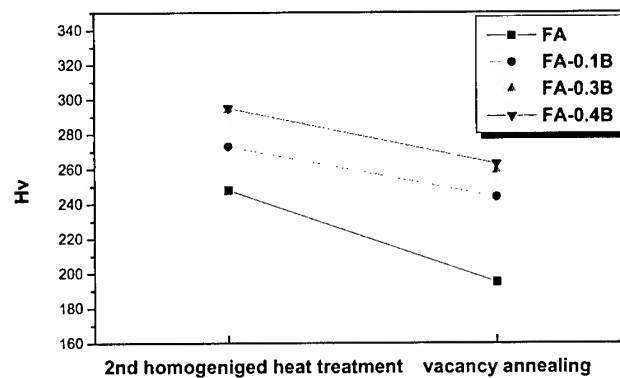


Fig. 2 Microhardness value of the 2nd homogenized and vacancy annealed specimens

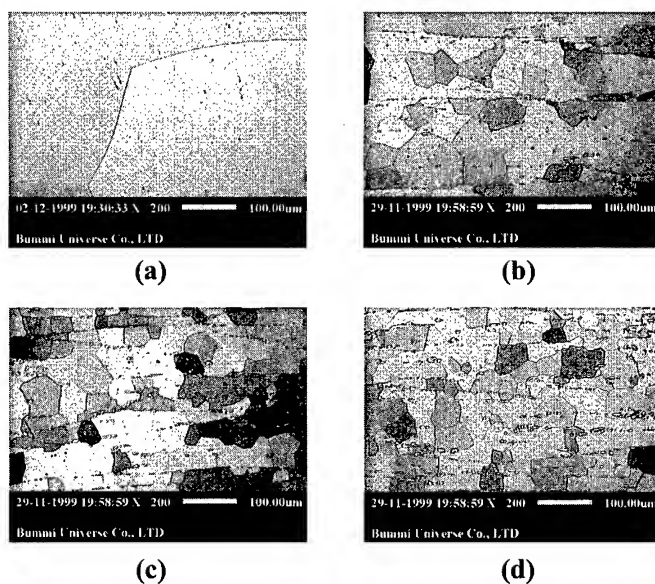


Fig. 3 The optical micrographs of the vacancy annealed alloys
 (a) FA (b) FA-0.1B (c) FA-0.3B (d) FA-0.4B

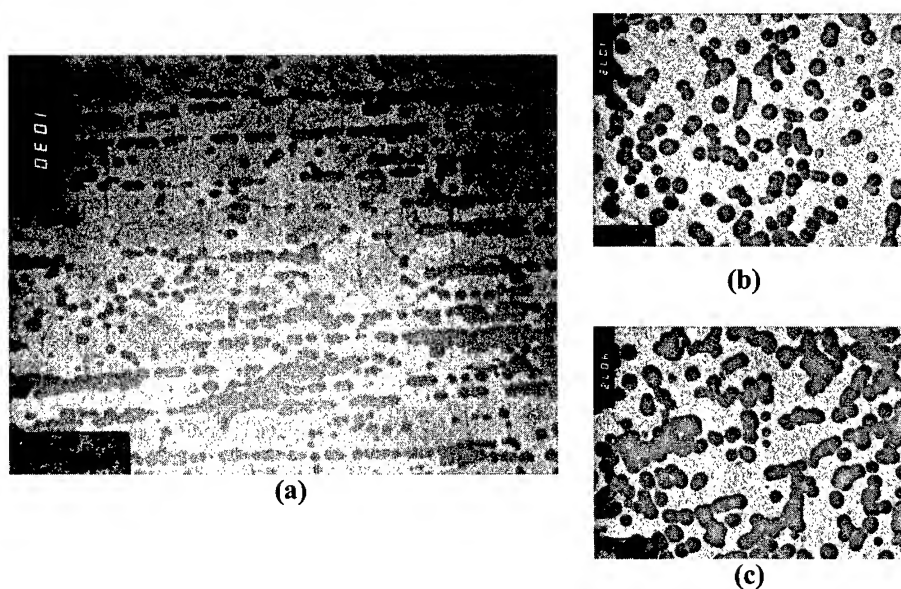


Fig. 4 The micrographs of Neutron irradiation (30sec/22MW)
 (a) FA-0.1B (extrusion direction),
 (b) FA-0.1B (c) FA-0.4B (The vertical direction of extrusion)

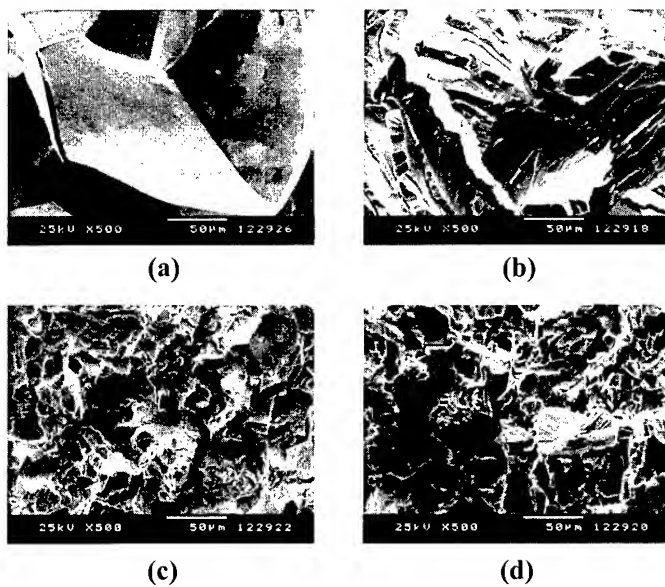


Fig. 5 Scanning electron micrographs of fracture surfaces (strain rate 10^{-4})

(a) FA (b) FA-0.1B
(c) FA-0.3B (d) FA-0.4B

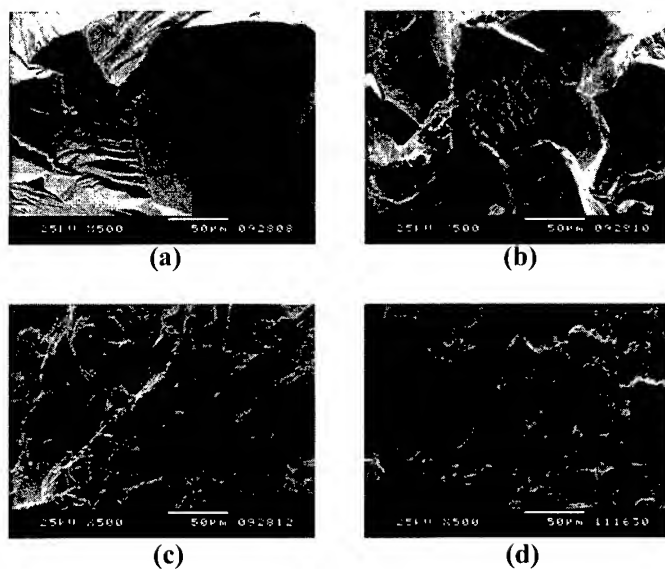


Fig. 6 Scanning electron micrographs of fracture surfaces (strain rate 10^0)

(a) FA (b) FA-0.1B
(c) FA-0.3B (d) FA-0.4B

SYNTHESIS OF NICKEL ALUMINIDES VIA VACUUM PLASMA SPRAYING WITH SELF-PROPAGATING HIGH-TEMPERATURE SYNTHESIS

Yong Gi Jeong, Su Jeong Park and Hyun Kyu Lee

Division of Metall. & Mat. Engineering, Chosun University, Gwangju 501-759, Korea

ABSTRACT

The feasibility of combining self-propagating high-temperature synthesis(SHS) with vacuum plasma spraying to produce near full density structural nickel aluminides has been demonstrated. A dual phase nickel aluminide consisting of a lamellar Ni_3Al and $\text{Ni}_3\text{Al}/\text{NiAl}$ microstructure with <5V% residual nickel and 2-3% porosity has been repeatedly produced. Control of the exothermic SHS reaction is critical in order to obtain complete conversion of the elemental powders and near full density deposits. Vacuum plasma spraying is used to initiate the exothermic reaction as well as simultaneously densify and form the synthesized material.

1. INTRODUCTION

The demand for increased thrust to weight ratios and higher operating temperatures for gas turbine engines has lead to consideration of intermetallic materials as matrices for high temperature structural applications. Nickel aluminides, i.e. NiAl and Ni_3Al , have been the focus of many investigations considering these materials as alternatives to nickel based superalloys currently used in gas turbine engines. The nickel aluminides have lower densities and therefore, have the potential of improved strength to weight ratios over nickel based superalloys. However, monolithic nickel aluminides are difficult and costly to process via conventional methods due to their inherently low room temperature ductility and high melting temperature. Therefore, before nickel aluminides can be used as high temperature structural materials a cost effective way of producing near net shape, full density, ductile materials in large quantities must be developed.

Self-propagating high-temperature synthesis(SHS) has been shown to be an effective, simple, low energy input and therefore, low cost method of producing high purity

intermetallics and intermetallic matrix composites. Low cost raw materials can be utilized since impurities are often volatilized at the high temperatures obtained during processing. The geometries typically produced by SHS reactions are relatively simple and may require considerable machining to obtain a useful structural component.

Vacuum plasma spraying(VPS) is a thermal spray process capable of producing near full density deposits of metallic and ceramic materials. VPS has been used extensively in the aerospace industry both as a coating process and spray forming process. Near net shapes with densities >98% can be produced, and the capability of producing free standing bodies of NiAl has been demonstrated[1].

Dual phase nickel aluminides($\text{Ni}_3\text{Al}/\text{NiAl}$) are an attractive candidate as matrix materials for intermetallic matrix composites. Monolithic nickel aluminides are hindered either by low room temperature ductility (NiAl) or high temperature embrittlement and relatively high density (Ni_3Al).

The goal of this investigation is to demonstrate the feasibility of combining vacuum plasma spraying with self-propagating high-temperature synthesis to produce full density, high temperature, structural intermetallic materials. Through process development and material characterization an understanding of the effects of processing conditions on the reaction mechanisms and microstructural development will be obtained.

2. EXPERIMENTAL PROCEDURE

2.1 Processing

2.1.1 Raw materials

Powders were selected primarily on their flow characteristics which will determine how well they can be fed into the plasma torch. Typical vacuum plasma spray feeders are capable of effectively feeding powders $>10\mu\text{m}$ [2]. Irregular or spherical powders may be used provided they flow well. Nickel powders was obtained from Novamet Specialty Powder Corp.. It is produced by thermal decomposition of nickel carbonyl which results in a spherical powder. The powder was screened to -400mesh and the mass mean particle size, $d_{50\%}$, determined by microtrac was $9.5\mu\text{m}$. The aluminum powder was obtained from Valimet, Inc. and is an atomized powder with a mass mean particle size of $65\mu\text{m}$ (microtrac). XFORM, Inc. provide the NiAl powder used as diluent. This powder was produced by mechanically alloying Ni and Al powders and allowing an SHS reaction to completely convert the elementals to NiAl. The mass mean particle size determined by microtrac analysis was $27\mu\text{m}$.

The amount of each powder needed to produce the proper composition was placed in a twin shell V blender for 12-24 hrs to obtain uniform mixing of the powders. Initial blends consisted of elemental Ni and Al at a composition of Ni-54at%Al. This composition was used to compensate for expected Al loss during spraying in order to obtain a Ni-50at%Al final composition. Later blends reduced the amount of elemental Al to 50at% and added 20V% NiAl.

2.1.2 Vacuum plasma spraying

The powder blends were vacuum plasma sprayed according to the parameters listed in Table 3.1. The spray chamber was evacuated to $200-300 \times 10^{-3}$ Torr and then backfilled with argon to 200 Torr. Upstream powder injection was utilized and a schematic of a VPS chamber is shown in Fig. 3.1. Deposits approximately 3" long, 1" wide, and 1/2" high were eventually produced. All characterization was conducted on as sprayed material.

2.1.3 Material characterization

Bulk samples were sectioned and subjected to x-ray diffraction to determine the phases present. A Cu x-ray source was used and phases were determined by matching peak intensities to the corresponding 2θ angles for a $30-90^\circ$ scan. Cross section of the bulk deposits were mounted either in epoxy or bakelite, polished, and examined with a light optical microscope. The scanning electron microscope (SEM) operated in backscattered mode was very good at revealing the variation in composition throughout the deposit. Quantitative energy dispersive spectroscopy (EDS) of the polished surfaces was conducted in the SEM to determine bulk composition as well as the composition of each phase.

Table 3.1 VPS spray parameters

Plasma Gun	EPIO3CA
Arc Gas	Ar-66SLM
	He-28SLM
Voltage	37 Volts
Current	1000 Amps
Carrier Gas Flow Rate	Ar-14SLM
Powder Feed Rate	6.6 kg/hr
Spray Distance	6"
Atmosphere	200 Torr

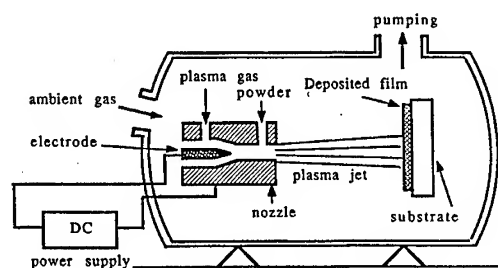


Fig. 3.1 Schematic of typical vacuum plasma spray chamber[3]

3. RESULTS AND DISCUSSION

3.1 Laminated nickel aluminide

3.1.1 Reaction sequence

The exothermicity of the reaction can be tailored by adding either diluents to lower ΔH_r or by adding more exothermic reactants to increase ΔH_r [4]. Therefore, to control the Ni-Al reaction 20V% NiAl was added to a Ni-50at%Al mixture thereby lowering the overall heat of combustion. The aluminum content was reduced from 54at% to 50at% since aluminum rich phases such as NiAl_3 and Ni_2Al_3 were found after the thermal explosion reactions. The anode was also changed to an EPI#170 which produces a narrower spray pattern than the EPI#93 and should reduce the amount of particle segregation within plasma. The diluted blend was vacuum plasma sprayed with the same parameters as before except for substrate cooling. The substrate was placed on a water cooled chill block without any water flowing through it, and the entire assembly was repeatedly traversed a distance of 4.6cm at a speed of 6cm/sec during spraying.

EDS microprobe measurements of the cross section were used in conjunction with the Ni-Al binary phase diagram to determine the phases present. A typical microstructure produced from the Ni-Al-NiAl blend found in the center of the deposit is shown in Fig. 4.10. The microstructure in the center of the deposit consists of laminated layers of Ni_3Al (74-77at% Ni) adjacent to layers of a NiAl/ Ni_3Al (60-66at% Ni) mixture. XRD indicates that the center of the deposit is NiAl and Ni_3Al (Fig. 4.12). which further indicates that the amount of nickel in the deposit is below the detection limit of X-ray diffraction(<5V%)[5]. The layered structure is typical of thermal spray deposits and results from the repeated traversing of the substrate during spraying. Quantitative EDS of the region shown in Fig. 4.10 indicates that the bulk composition is 67at%Ni \pm 2at%.

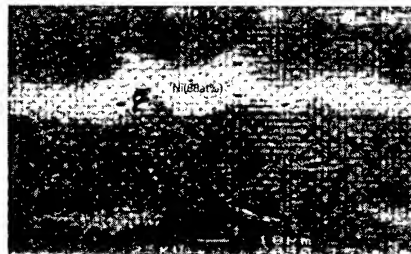


Fig. 4.10 Backscattered electron image of laminated Ni_3Al / NiAl microstructure

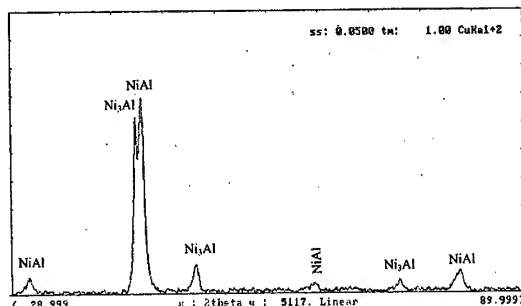


Fig. 4.12 X-ray diffraction pattern

To obtain complete conversion a substantial amount of preheating was needed which lead to thermal explosion and self destruction of the deposit. Attempts at cooling the deposit either with inert gas or a water cooled substrate were unsuccessful. Therefore, 20V%NiAl was added to the Ni-50at%Al blend to reduce the exothermicity of the reaction. The addition of 20V%NiAl has decreased the violence of the exothermic reaction between Ni and Al, and the initial temperature can now be raised sufficiently high enough to ensure complete conversion of the reactants. The ability to raise the temperature of the deposit also allows a liquid phase to be formed at the substrate. A continuous network of liquid is necessary for complete conversion of the elementals and as will be discussed below it is also necessary for densification of the deposit.

3.1.2 Densification

SHS theory tells us that a transient liquid phase is necessary for densification to occur. In the previous section it was noted that densification did not occur due to the lack of this transient liquid phase. In order to obtain dense VPS deposits incoming particles must be molten[6,7] and as the substrate temperature increases the porosity level decreases[7,8]. Therefore, if the temperature of the substrate is raised to the point where the surface is partially molten, as in our case, densification should occur more readily due to easier "hammering down" and increased liquid flow into pores. Addition of 20V%NiAl therefore, serves two functions; 1) it reduces the overall exothermicity of the reaction preventing explosive SHS from occurring in the extreme environment of the plasma jet, 2) it enables the overall temperature of the substrate and deposit to be raised ensuring the presence of a transient liquid phase which facilitates densification.

4. FINALLY

The feasibility of combining self-propagating high-temperature synthesis(SHS) with vacuum plasma spraying to produce near full density structural nickel aluminides has been demonstrated. A nickel aluminide material consisting of laminated layers of Ni_3Al and a mixture of $\text{Ni}_3\text{Al}/\text{NiAl}$ with <5V% residual nickel and 2-3% porosity(by area) has been repeatedly produced. The center of the deposits have an average bulk composition of 69at%Ni.

Control of the exothermic reaction diluting with product phase (NiAl) to reduce the overall exothermicity of the reaction and thermal management of the substrate is critical in order to obtain near full conversion of the elementals as well as near full density deposits.

REFERENCES

1. A.Giebel, P.Verstreken, L.Delaey, L.Froyen, Thermal Spray: International Advances in Coating Technology, ed. C.Berndt, ASM Intl.(1992), pp.363-368.
2. R.Knight, Personal Communication, Dept. Mater. Engr., Drexel Univ., Philadelphia, PA, Sept.(1993).
3. J.Heberlein, "Introduction to Vacuum Plasma Spraying Shortcourse," Huntsville, Alabama, Dec.(1991).
4. J.Subrahmanyamanam, M.Vijayakumar, J. Mater. Sci., 27(1992), pp.1-25.
5. M.J. Koczak, Personal Communication, Dept. Mater. Engr., Drexel Univ., Philadelphia, PA, Sept.(1993).
6. B.Champagne, S.Dallaire, Thermal Spray:Advances in Coatings Technology, ed. D.L. Houck, ASM Intl.(1988), pp.25-33.
7. H.Liu, E.J. Lavernia, R.H. Rangel, E. Mühlberger, A.Sickinger, 1994 Thermal Spray Industrial Applications, eds. C.C. Berndt, S. Sampath, ASM Intl.(1994), pp.375-380.
8. D.J. Varacalle, Jr., R.A. Neiser, M.F. Smith, Thermal Spray: International Advances in Coatings Technology, ASM Intl.(1992), pp. 781-785.

Session IX

COMPOSITE MATERIALS

METHODOLOGIES TO DESIGN THE INTERFACES IN SiC/Al COMPOSITES

Jae-Chul Lee

*Div. of Materials Science and Engineering, Korea Institute of Science and Technology (KIST)
P.O. Box 131, Cheongryang, Seoul, Korea 136-132 (jclee@kist.re.kr)*

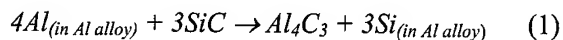
ABSTRACT

Methodologies to control interfacial microstructures, while suppressing formation of Al_4C_3 in Al alloy composites reinforced with SiC, were demonstrated. Thermodynamic calculations were carried out to elucidate how one can select process parameters in terms of alloy composition and fabrication temperature to obtain intended interfaces. Experimental verifications were conducted using SEM and TEM to validate calculated results. The reaction mechanisms for forming various interfaces were identified both theoretically and experimentally. Evaluations of the interfacial bonding strengths and interfacial stability at elevated temperatures were also carried out for various interface types.

Keywords : SiC/Al composite, Interface design, Passive oxidation

1. INTRODUCTION

In SiC/Al composites, a direct reaction between Al and SiC can occur during the fabrication stage to form Al_4C_3 and Si according to the reaction given by



In the presence of Al_4C_3 as in Fig.1, such composites can be very susceptible in a moist environment to accelerated fatigue crack growth, due to the hydrophilic nature of Al_4C_3 [1]. Therefore, the interfacial reaction in SiC/Al composites should be avoided both during the fabrication and subsequent forming stages.

Among the various methods proven to be effective in preventing the interfacial reaction is the Si addition into various Al matrices. This method has been employed widely to produce SiC/Al composites [2-5]. The principle behind this methodology is based on thermodynamics. According to the Le Chatelier's principle, the interfacial reaction can be avoided by simply dissolving equilibrium amounts of Si into the matrices of composites. One processing

technique based on this method is the melt-stir cast (or compocast). This method, due to its simplicity and economy for the actual processing, has been adopted for producing most commercial SiC/Al composites. A major drawback of this process is that it can be applied only to certain composite systems, where prolonged contact at elevated temperatures does not degrade SiC. These composites, therefore, usually contain 10-12% of Si to avoid the interfacial reaction. This limits applications of resultant composites for casting.



Fig.1 Al_4C_3 crystals formed on the surface of the SiC particle, which was extracted from the Duralcan SiC/6061Al composite

Another alternative to avoid the formation of Al_4C_3 is the passive oxidation of SiC combined with matrix modification. When SiC is exposed at temperatures above 800°C in air, SiC begins to be oxidized to form a thin SiO_2 layer on its surface. The SiO_2 layer formed as a result of the passive oxidation not only could be effective for prohibiting a direct contact between SiC and the matrix, but also acts as the reactant required to form a stable interface serving as a protective barrier. The objective of the present work is to study a methodology to tailor the interfacial characteristics in SiC/Al composites by controlling their interfacial microstructures. Thermodynamics were employed to elucidate how one can select process parameters to obtain intended interfaces. Experimental verifications were made to validate calculations. Measurement of the interfacial bonding strengths and assessment of interfacial stability at elevated temperature were also carried out for various interfaces.

2. THERMODYNAMICS

2.1 Calculation of the equilibrium Si contents

Considering eq. 1, the interfacial reaction in SiC/Al composites can be avoided either by adding an adequate amount of Si or processing composites at the lowest possible temperatures. The question then are how much Si is required to avoid the interfacial reaction and, under a given Si content, what temperature range is appropriate for the composite forming? In this

section, possible suggestions are proposed on the basis of theoretical and experimental analyses.

Although procedures to calculate equilibrium Si contents differ slightly depending on whether the reaction occurs in the liquid or solid state, equilibrium Si contents at a given temperature and alloy system can be calculated using the free energy change associated with eq. 1. In this study, equilibrium Si contents were calculated for liquid, solid, and semi-solid regions by incorporating simultaneous variations in Al and Si activities as well as Gibbs free energy changes associated with the formation of other compounds. All calculations were made by assuming the crystallographic structure of the reinforcing phase to be α -SiC(6H) rather than β -SiC(3C). Since the basic schemes and thermodynamic data used for calculations are reported elsewhere [6-8], only calculated results are presented and discussed here.

Equilibrium Si contents were also measured experimentally to confirm the calculated results : The amount of the elemental Si formed as a result of the interfacial reaction increases with increasing holding temperature and time, resulting in decrease in the liquidus temperature of the composite. Therefore, measurement of the liquidus temperature can be used as a means for measuring the Si content. The measured liquidus temperatures were then converted into the Si contents. Detailed experimental procedures for measuring the equilibrium Si contents are discussed elsewhere [6,8]. The matrix alloy considered in this study was 2014Al.

Calculations of equilibrium Si content in the SiC/2014Al composite based on eq.1 require activity values for Al and Si in the 2014Al alloy. However, calculations of the equilibrium Si content based on eq.1 are not possible, since activity values for Al and Si in this multicomponent system are not known. Therefore, the 2014Al alloy was simplified as a Al-0.94Si-4.5Cu ternary alloy, assuming that minor alloying elements, such as Mg, Fe, Mn, etc. within the alloy would not have a significant effect on the activities of Al and Si. Such an assumption may obscure phase equilibria at low temperatures, especially prediction of precipitates. Nevertheless, it is considered to be reasonable enough for predicting phase equilibria in the liquid and the semi-solid state, since phase equilibria concerned in this study are not influenced significantly due to the ignorance of minor alloying elements, such as Mg, Mn, and Zn.

Fig.2 is the graphical illustration of the calculated and experimentally determined Si contents plotted on the Al-4.5Cu-xSi phase diagram. Although the general trend was similar to that in the SiC/Al-Si composite, the transition temperature was located near 600°C, which is not only lower than that of the SiC/Al-Si composite, but also is not as clear. The indistinct transition temperature is due to the fact that tie lines between the α -Al and the ternary liquid vary with varying temperature.

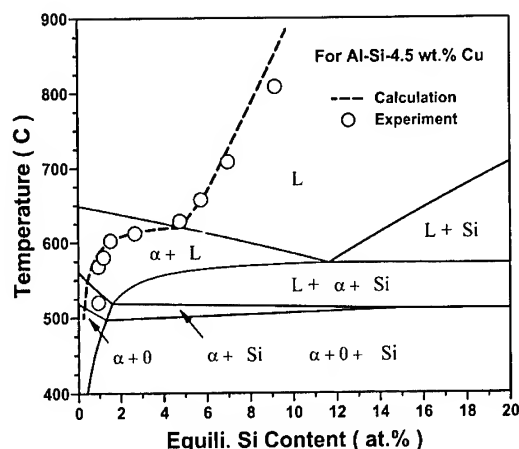
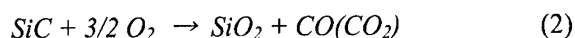


Fig.2 Equilibrium Si content profiles in the SiC/2014Al composite. The profiles are superposed with phase diagrams corresponding to those of the matrix alloys

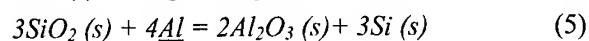
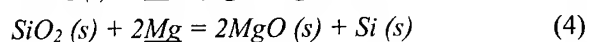
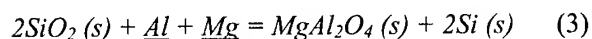
2.2 Design of the interfaces

2.2.1 Model formulation

When SiC is exposed at temperatures above 800°C in air, SiC reacts with oxygen to form a SiO₂ layer on the surface of SiC according to the reaction given by eq. (2).

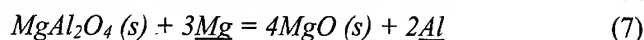
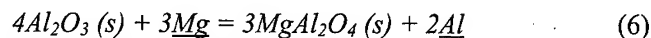


If Al alloy composites reinforced with oxidized SiC particles (SiC_{ox}/Al composites) are held at sufficiently high temperatures, SiO₂ thin layers enveloping SiC particles in Al alloy matrices tend to transform into more stable oxide layers by reacting with Al and Mg dissolved in the matrices. This is because, from the point of view of thermodynamics, oxygen affinities of Al and Mg are high enough to reduce SiO₂ layers [9]. A composite system, i.e., SiC_{ox}/(2014Al+xMg) composites having thin SiO₂ layers on SiC, was considered for calculations. In order to evaluate the interfacial reaction between SiO₂ and Al/Mg, the following three interfacial reactions to form oxides as reaction products were considered.



where all the compounds Al₂O₃, MgAl₂O₄, MgO and free Si are in solid state and Al and Mg are in dissolved state, i.e. in the α-Al and liquid matrices. The above three reactions are spontaneous, since the Gibbs energies of Al₂O₃, MgAl₂O₄ and MgO are much lower than that of SiO₂ and the interface is free from Si at the initial stage of the reactions. Therefore, the above three reactions would compete one another.

Considering that Mg has higher oxygen affinity than Al, the reaction product might be gradually changed from Al_2O_3 to either $MgAl_2O_4$ or MgO depending on process temperatures and Mg content in an Al alloy. To evaluate the phase equilibria among Al_2O_3 , $MgAl_2O_4$, and MgO , equations (6) and (7) were obtained by manipulating equations (3)-(5).



The reaction directions of equations (6) and (7) depend on the Gibbs energy changes associated with the reactions assuming the presence of local thermodynamic equilibrium at the interface. When the Gibbs energy change is a negative quantity, the reaction proceeds along the forward direction. When positive, the backward reaction occurs. Assuming that the activity values of the compounds are unity, the Gibbs energy changes associated with reactions (6) and (7) can be expressed, respectively, as follows:

$$\Delta G_1 = \Delta^\circ G_1 + RT \ln \frac{a_{Al}^2}{a_{Mg}^3} \quad (8)$$

$$\Delta G_2 = \Delta^\circ G_2 + RT \ln \frac{a_{Al}^2}{a_{Mg}^3} \quad (9)$$

where $\Delta^\circ G_i$, R , T and a_i denote the Gibbs energy change of reaction i in the standard state, gas constant, absolute temperature, and activity of component i , respectively.

The Gibbs energy changes in the standard state of equations (8) and (9) consist of the Gibbs energies of the pure substances in the standard state, respectively, as follows:

$$\Delta^\circ G_1 = 3^\circ G_{MgAl_2O_4} + 2^\circ G_{Al} - 4^\circ G_{Al_2O_3} - 3^\circ G_{Mg} \quad (9)$$

$$\Delta^\circ G_2 = 4^\circ G_{MgO} + 2^\circ G_{Al} - ^\circ G_{MgAl_2O_4} - 3^\circ G_{Mg} \quad (10)$$

At a given temperature, thus, the Gibbs energy change of the reaction, ΔG_i depends solely on the activities of Al and Mg in the solid solution and liquid, since the Gibbs energy change in the standard state is a function of temperature only.

2.2.2 Analyses of the calculated results

The stable interfacial reaction products within the $SiC_{ox}/(2014Al+xMg)$ composites are predicted by evaluating equations (8) and (9). All thermodynamic calculations in the present

work have been carried out using the computer software Thermo-Calc developed by Sundman et al [10].

Phase equilibria calculated for the $\text{SiC}_{\text{ox}}/(\text{Al}+x\text{Mg})$ and the $\text{SiC}_{\text{ox}}/(2014\text{Al}+x\text{Mg})$ composites are shown graphically in Fig.1. As can be seen from the graphs, when composite systems containing low Mg contents are exposed at high temperatures, the formation of MgAl_2O_4 according to reaction (3) is favored. On the other hand, composite systems containing high Mg contents tend to form MgO even at low temperatures according to reaction (4).

Fig.2 is the graphical illustration of the calculated results for the $\text{SiC}_{\text{ox}}/(2014\text{Al}+x\text{Mg})$ composite, showing that the formation of Al_2O_3 is possible only when matrices contain very low Mg. However, the interfacial reaction describing the formation of Al_2O_3 can be ignored, since most Al matrices used for commercial SiC/Al composites contain more than 0.4% Mg. Therefore, the major interfacial reactions, which will be considered in this study, are those reactions associated with the formation of MgAl_2O_4 and MgO.

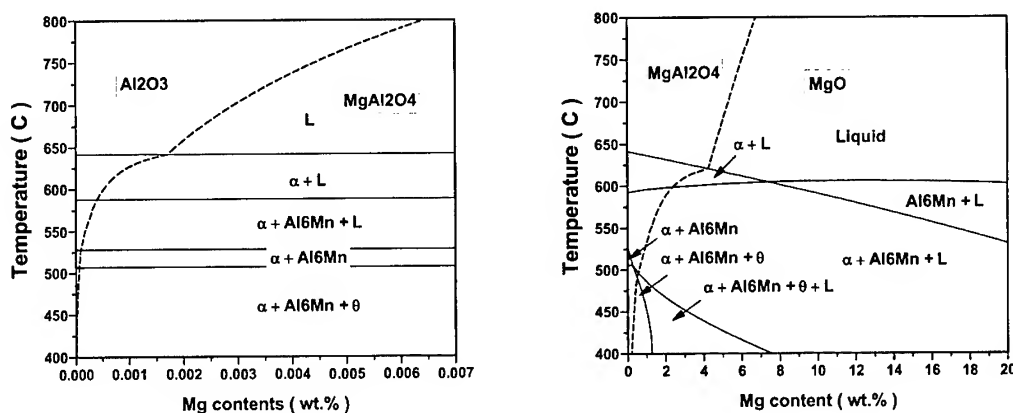


Fig.2 Calculated results showing conditions for forming $\alpha\text{-Al}_2\text{O}_3$, MgAl_2O_4 , and MgO in the $\text{SiC}_{\text{ox}}/(2014\text{Al}+x\text{Mg})$ composite. Note that Al_2O_3 can form only under very low Mg contents within matrices.

2.2.3 Interfacial modification in $\text{SiC}_{\text{ox}}/(2014\text{Al}+x\text{Mg})$ composites

Observations of interfacial reaction products were also carried out on $\text{SiC}/(2014\text{Al}+x\text{Mg})$ composites to study the effect of Mg contents on the interfacial reactions. Trends similar to those observed from $\text{SiC}/(\text{Al}+x\text{Mg})$ composites were obtained from $\text{SiC}/(2014+x\text{Mg})$ composites. As can be seen in Fig.3, the interfacial reaction products observed from the composites were identified as either MgAl_2O_4 or MgO depending on the Mg contents within the composites. In addition, the size of the reaction products becomes finer with increasing Mg contents.

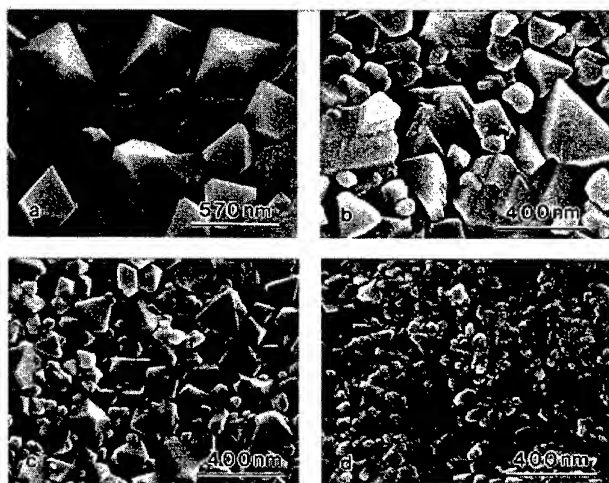


Fig.3 A series of SEM micrographs showing morphological changes of SiC surfaces. SiC were extracted from the (a) $\text{SiC}_{\text{ox}}/\text{2014Al}$, (b) $\text{SiC}_{\text{ox}}/(\text{2014Al}+1\text{Mg})$, (c) $\text{SiC}_{\text{ox}}/(\text{2014Al}+2\text{Mg})$, and (d) $\text{SiC}_{\text{ox}}/(\text{2014Al}+4\text{Mg})$ composites after holding at 610°C for 2 h.

Experimental verifications of the theoretical calculations in Fig.2(b) were conducted and shown in a graphical form as in Fig.4. In general, analytical results obtained from this study were good enough to pre-depict the nature of the interfaces in $\text{SiC}_{\text{ox}}/(\text{2014Al}+x\text{Mg})$ composites; MgAl_2O_4 crystals tend to form within the composites having low Mg contents at high temperatures, while MgO crystals form within the composites having high Mg contents at low temperatures.

3. CONCLUSION

Based on theoretical and experimental results, a certain amount of Si was required to prevent the interfacial reaction. Such Si contents were also observed to increase with increasing temperature such that, when the composite is exposed at temperatures below the solidus of the matrix, less than 1 at.% of Si was found out to be enough for preventing the interfacial reaction. However, Si contents required to prevent the interfacial reaction was observed to increase substantially at temperatures near 600°C such that more than 5 at.% of Si was required to prohibit the interfacial reaction even at 620°C .

Modifications in the interfaces of the SiC/Al composites were made using the passive oxidation of SiC combined with the matrix modification. Passive oxidation of SiC resulted in the formation of amorphous SiO_2 layers on SiC. The SiO_2 layers were then transformed into either MgO or MgAl_2O_4 depending on the Mg contents and temperatures by reacting with Mg in Al matrices.

In general, based on theoretical and experimental results, nano-sized MgO particles were observed to form at the interface of the $\text{SiC}_{\text{ox}}/(\text{2014Al}+x\text{Mg})$ composites containing high Mg. On the other hand, formation of nano MgAl_2O_4 crystals was observed to be favored in the $\text{SiC}_{\text{ox}}/(\text{2014Al}+x\text{Mg})$ composites containing low Mg.

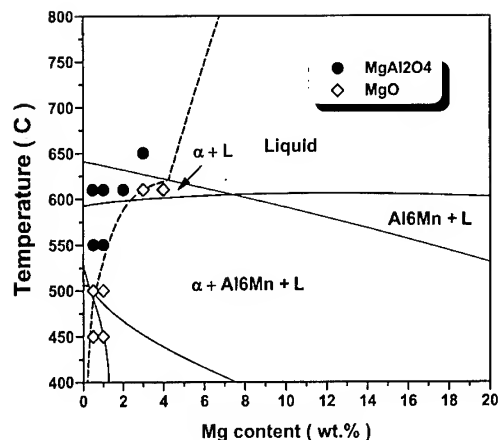


Fig.4 Equilibrium phase diagrams of the $\text{SiC}_{\text{ox}}/(2014\text{Al}+x\text{Mg})$ composite showing combination of the alloy composition and temperature required to form MgAl_2O_4 and MgO .

Reference

1. S.S. Yau and G. Mayer, Mater. Sci. Eng. **A82**, 45 (1986).
2. A.C. Ferro and B. Derby, Acta Metall. Mater. **43**, 3061 (1995).
3. J.C. Viala, P. Fortier and J. Bouix, J. Mater. Sci. **25**, 1842 (1990).
4. J. Narciso, C. Garcia-Cordovilla and E. Louis, Mater. Sci. Eng. **B15**, 148 (1992).
5. H. Ribes, M. Suery, G. L'sperance, and T.G. Legoux, Met. Trans. A. **21**, 2489 (1990).
6. J.C. Lee, J.Y. Byun, S.B. Park, and H.I. Lee, Acta Metall. Mater. **46**, 1771, (1998).
7. J.C. Lee, J.Y. Byun, C.S. Oh, H.K. Seok, and H.I. Lee : Acta Metall. Mater. **45**, 5303, (1997).
8. J.C. Lee, C.S. Oh, S.B. Park, and H.I. Lee, Acta Metall. Mater. vol.46(8), 2635-2643 (1998).
9. D.R. Gaskell, *Introduction to Metallurgical Thermodynamics*, 2nd Ed., McGraw-Hill Book Co., New York, NY, 1981, p.287.
10. B. Sundman, B. Jansson and J.O. Andersson, *Calphad*, 1985, **9**, 153.

TENSILE PROPERTIES AND MICROSTRUCTURES OF 7075 AL/SiC_p COMPOSITE FABRICATED BY PRESSURELESS INFILTRATION TECHNIQUE

Kon Bae Lee, Ho Seop Sim and Hoon. Kwon

School of Metallurgical and Materials Engineering, Kookmin University,
Seoul 136-702, KOREA

* jointly appointed at the Center for Advanced Aerospace Materials

ABSTRACT

AA7075 alloys reinforced with SiC and without SiC particles were fabricated by pressureless infiltration method and then their tensile properties and microstructures were analyzed. A significant strengthening even in the control alloy occurred due to the formation of *in-situ* AlN particle even without an addition of SiC particles. Composite reinforced with SiC particles exhibited higher strength values than the control alloy in all aging conditions (UA, PA, and OA) as well as solution treated condition. Spontaneous infiltration was further prompted owing to combined effect of both Mg and Zn. This may lead to an enhancement of wetting between molten alloy and reinforcement. Consequently, strength improvement in composite may be attributed to good bond strength via enhancement of wetting. The grain size of the control alloy is greatly decreased to about 2.5 μ m compared to 10 μ m for the commercial alloy. In addition, the grain size in the composite is further decreased to about 2.0 μ m. This grain refinement contributed to strengthening of the control alloy and composite.

1. INTRODUCTION

Metal matrix composites (MMCs) reinforced with ceramic phase have emerged as an important class of materials for structural, wear, thermal, transportation, and electrical applications, not needing a high ductility and toughness, because of their excellent properties relative to those exhibited by the corresponding monolithic alloy. Thus various fabrication methods have been developed, such as powder metallurgy, stir casting and pressure infiltration method, etc.^[1-3]

Many metals have been considered as a possible matrix: magnesium, silicon, aluminum, titanium, and copper, etc. Among them, discontinuously reinforced aluminum (DRA) a technologically maturing materials system capable of competing with conventional aluminum and titanium alloys and organic matrix composites. DRA is an extremely versatile class of material with an attractive balance of specific stiffness and strength and a host of other properties, including good wear resistance, thermal conductivity, and low thermal expansion, all of which makes them good multifunctional materials as well.^[4]

However, so far most of the alloys that have been employed as matrices in DRA have been focused on the A356, 2xxx, and 6xxx series alloy. Although very few studies have been reported on 7xxx series alloys reinforced with SiC particles, much less attention has been paid to the 7xxx Al alloys matrix composites, which show the highest strength of all commercial Al alloys and widely used for structural applications.^[5-8] In addition, most of 7xxx Al composites reported in literature were primarily fabricated by powder metallurgy method. Furthermore, it should be noted that tensile properties (yield and tensile strength) in 7xxx Al

matrix composites were nearly the same or lower than that of unreinforced materials while a higher increase in strength was often observed in lower strength matrix composites such as 2xxx and 6xxx Al alloys. No data is available on 7xxx Al/SiC_p composites fabricated by pressureless infiltration technique. Therefore, in this study, 7xxx/SiC_p composite was fabricated by the pressureless infiltration method, and the tensile properties and microstructures were investigated.

2. EXPERIMENTAL PROCEDURE

Both composite and control alloy used in this study was fabricated by pressureless infiltration method. Fabrication process is given elsewhere.^[9-12] Both of fabricated ingots were extruded at 450°C into a bar 16mm in diameter (extrusion ratio 22:1). Tensile specimens having a gauge length of 25mm and 2mm thickness were machined from the extruded bars, parallel to the extrusion direction. Those specimens were solution treated at 510°C for 2h and water quenched and artificially aged. The underaged (UA) and peakaged (PA) condition were obtained by heat treating for 30 min and 24 h at 120°C, while the overaged (OA) condition was obtained by heat treating at 120°C for 24h, followed by heat treating at 177°C for 36h. Both the commercial and control AA7075 was also heat treated using the same aging practices as in the composite. Tensile testing was performed at room temperature, using a cross-head speed of 1mm/min. Average tensile data were obtained from at least five tests for each condition. The resulting microstructures and reaction products were investigated using optical microscopy, scanning electron microscopy (SEM), and transmission electron microscopy (TEM).

3. RESULTS

3.1. Tensile properties

The spontaneous infiltration of molten metal at 800°C for 1 hour under a nitrogen atmosphere made it possible to fabricate 7075 Al matrix composite reinforced with SiC_p as well as control alloy without SiC_p. The spontaneous infiltration behavior of molten metal was explained in detail in previous papers.^[9-12]

Table I show the variation of tensile properties with aging condition in commercial AA7075, control AA7075 and composite which were solution treated for 2hours at 510°C. The tensile strength in the control AA7075 was 45-81 MPa greater than the commercial AA7075. These values were an additional 31-78 MPa higher in the composite reinforced with SiC_p compared to the control alloy. A large increase in strength in the case of the control AA7075 is related to the in-situ formation of AlN particles. When the MMCs were fabricated by pressureless infiltration technique, AlN is formed as a result of the *in-situ* reaction ($\text{Mg}_3\text{N}_2 + 2\text{Al} = 2\text{AlN} + 3\text{Mg}$).^[9-12]

It should be noted that composite reinforced with SiC_p exhibited higher strength values than the control alloy in all the aging conditions as well as solution treated condition. This result is different from many other studies reported in literature, which showed a decrease in the strength of Al-Zn-Mg-Cu alloy matrix composites with the addition of SiC reinforcement.^[17-23] This will be discussed later.

3.2. Aged Microstructure

Fig. 1 show the microstructure observed by TEM in PA condition. Very small precipitates (GP zones), about 5nm in size, were seen throughout the matrix in the PA condition. In addition, precipitate free zones (PFZ) and some large grain boundary precipitates were frequently observed at grain boundaries. The width of the PFZ along the grain boundaries in the composite (80nm) was larger than that of unreinforced materials at this stage. However, there is no appreciable difference both the size and amount of the precipitates (GP zones) observed in the matrix in the PA condition.

Table I. Tensile properties of alloys and composite

Material Designations		UTS (MPa)	YS (MPa)	El (%)
Commercial alloy	ST	417	217	20.4
	UA	520	368	15.2
	PA	604	550	10.6
	OA	453	345	11.8
Control alloy	ST	483	302	13.8
	UA	565	489	10.4
	PA	695	611	3.8
	OA	527	441	7.6
Composite	ST	555	320	11.2
	UA	630	545	9.0
	PA	726	650	3.7
	OA	605	518	7.0

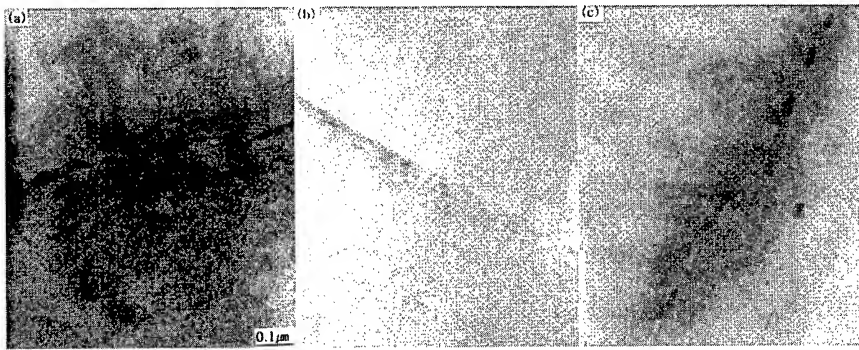


Fig.1 Bright field TEM images showing GP zones and PFZ in peakaged condition: (a) commercial, (b) control alloy, and (c) composite, respectively

Fig. 2 show the microstructure observed by TEM in OA condition. TEM revealed precipitation of metastable η' plates (less than 30nm in length) and equilibrium η (MgZn_2) phases (about 50-80nm in length). Similarly to the result obtained in PA condition, the width of the PFZ in the composite was wider than that of unreinforced materials. In addition, PFZs in OA condition were slightly larger than in PA condition.

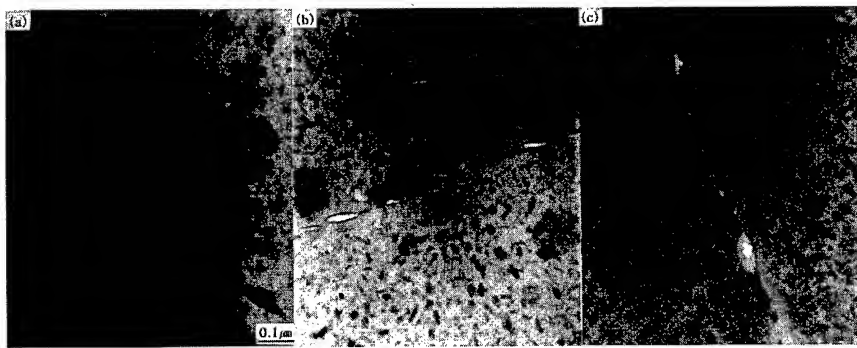


Fig.2 Bright field TEM images showing precipitates and PFZ in overaged condition: (a) commercial, (b) control alloy, and (c) composite, respectively

Fig. 3 shows the grain structure of the commercial, control alloy, and composite observed by TEM in OA condition, respectively. Even though the grain size did not uniform, equiaxed

grains with an average size of $10\mu\text{m}$ are observed in the commercial alloy. The grain size greatly decreased to about $2.5\mu\text{m}$ in the control alloy and further decreased to about $2.0\mu\text{m}$ in the composite reinforced with SiC. In addition, grain morphology in control alloy without SiC reinforcement was further elongated along the extrusion direction when compared to composite.

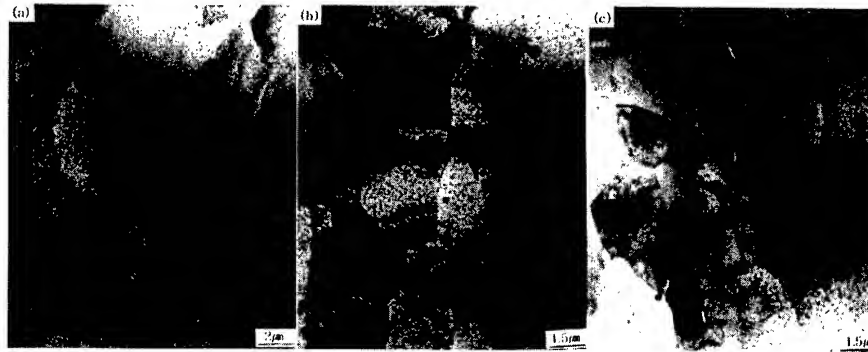


Fig. 3 Bright field TEM images showing grain structure: (a) commercial, (b) control alloy, and (c) composite, respectively.

3.3. Reaction Products

Fig. 4 shows SEM micrographs showing the reaction product obtained in both the control alloy and composite, after dissolving away the Al alloy matrix with a solution of methanol bromine. According to the analytical results obtained from EDS analysis, this phase coincided with stoichiometry of AlN. A great amount of reaction product (AlN, the size of which about $1.0\mu\text{m}$) was originally formed on the surface of the old Al particles that had comprised the powder bed prior to infiltration. After extrusion, this was aligned along the extrusion direction as shown in Fig. 4.

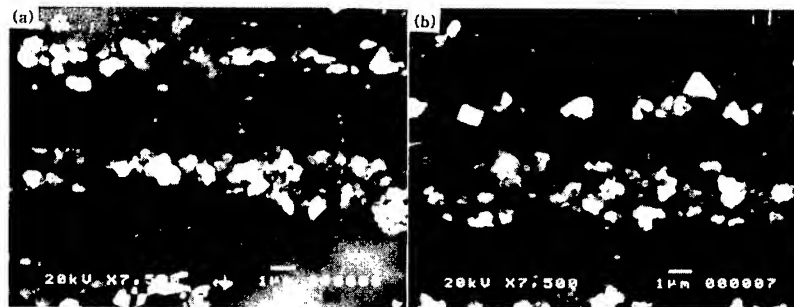


Fig. 4 SEM micrographs showing the AlN reaction products, after dissolving away the Al alloy matrix: (a) control alloy and (b) composite.

4. DISCUSSIONS

As previously mentioned, strength values in 7xxx Al matrix composites reported in literature were nearly the same or lower than that of unreinforced materials while a higher increase in strength was often observed in lower strength matrix composites such as 2xxx and 6xxx Al alloys. Particularly, it should be noted that most of researcher cited Humphreys's suggestion in order to explain decreasing of strength in 7xxx Al matrix composites.^[5-8] Humphreys has indicated that the addition of a brittle reinforcement in high strength Al alloys may even decrease the yield stress. One plausible explanation is that as composites with these

high strength matrices are strained, the stresses on the reinforcement become large. Fracture can then occur in the reinforcement in the presence of a pre-existing flaw in the reinforcement, probably formed during earlier processing. Once the reinforcement fractures, the net load carrying capacity of the composite decreases and thus yield stress might decrease.

It is also possible that the mismatch between reinforcement and matrix leads to a large stress concentration near the reinforcement and the matrix in that region fails prematurely, while loss of alloying elements (e.g. Mg) during processing may also contribute to these observations. In lower strength matrices, however, the stresses reached locally might not be large enough for either of these effects to occur, leading to strength improvement.

Fig. 5 shows tensile strength in 7xxx matrix composites fabricated by various methods. It is seen that tensile properties depend on fabrication method. As mentioned above, it should be noted that tensile strengths in composites fabricated by both P/M and casting methods were nearly the same or lower than that of unreinforced materials while composite fabricated by pressureless infiltration method used in this study showed higher strength than the unreinforced material. In addition, strength values in materials fabricated by pressureless infiltration method (control alloy and composite) were higher than that of materials fabricated by other methods. It is believed that this result is mainly caused by difference in fabrication method. The fact that the spontaneous infiltration of molten metal in this study occurred means that the problem of wetting between the ceramic reinforcement and molten metal is solved. However, since wetting between molten metal and reinforcements is often poor, mechanical stirring or pressure infiltration has been applied in order to obtain improved wetting between the matrix and reinforcements during fabrication of composites.

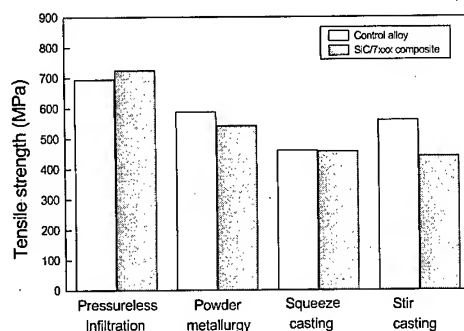


Fig. 5 Tensile strength in 7xxx matrix composites fabricated by various methods.

It was observed that Zn could serve as Mg to induce spontaneous infiltration of molten metal. Actually, when pure Al was placed in the powder bed consisting of Al-3Zn-20 vol pct SiC without Mg and it was heated to 800°C under the nitrogen atmosphere, spontaneous infiltration occurred. Therefore, because the 7xxx alloy used in this study contains relatively large amount of Zn (6.1 wt pct) compared to Mg content (2.9 wt pct), spontaneous infiltration may be further prompted owing to combined effect of both Mg and Zn. This may lead to an enhancement of wetting between molten alloy and reinforcement. Consequently, it is believed that strength improvement in composite may be attributed to superior bond strength via enhancement of wetting.

In addition, fine AlN particles *in-situ* formed led to a significant enhancement of strength in the control alloy and composite. Furthermore, because AlN particles *in-situ* formed are thermodynamically stable in the matrix, these fine AlN particles intimately contact with the matrix and also show clean interface. Therefore, fine AlN particle *in-situ* formed can serve as additional reinforcement and thus contribute to improvement in strength. Finally, grain size refinement may contribute to strengthening of the control alloy and composite.

5. Conclusions

1. A significant strengthening even in the control alloy occurred due to the formation of *in-situ* AlN particle even without an addition of SiC particles.
2. Composite reinforced with SiC particles exhibited higher strength values than the control alloy in all aging conditions (UA, PA, and OA) as well as solution treated condition.
3. Spontaneous infiltration was further prompted owing to combined effect of both Mg and Zn. This may lead to an enhancement of wetting between molten alloy and reinforcement. Consequently, strength improvement in composite may be attributed to good bond strength via enhancement of wetting.
4. The grain size of the control alloy is greatly decreased to about 2.5 μ m compared to 10 μ m for the commercial alloy. In addition, the grain size in the composite is further decreased to about 2.0 μ m. This grain refinement contributed to strengthening of the control alloy and composite.

Acknowledgements

This work was supported by the Korea Science and Engineering Foundation (KOSEF: 97-0300-07-01-3).

References

1. A. Mortensen and I. Jin: Int. Mater. Rev., vol. 37(1992), pp. 101-28.
2. A. Ibrahim, F.A. Mohamed, and E.S. Lavernia: J. Mater. Sci., vol. 26(1991), pp. 1137-56.
3. M.J. Koczak and M.K. Premkumar: J. Metall., vol. 45(1993), pp. 44-8.
4. B. Maruyama and W. H. Hunt, Jr: JOM, vol. 51(1999), pp. 59-64.
5. S.I. Hong, G.T. Gray III: Acta Metall. Mater., vol. 40(1992), pp. 3299-3315.
6. M. Manoharan and J.J. Lewandowski: Acta Metall. Mater., vol. 38(1990). pp. 489-496.
7. J.K. Shang and R.O. Ritchie: Acta Metall., vol. 37(1989), pp. 2267-78.
8. N.V. Ravi Kumar and E.S. Dwarakadasa: Composites Part A, vol. 31(2000), pp. 1139-45.
9. K.B. Lee and H. Kwon, Metall: Mater. Mater. Trans. A, vol. 29A(1998), pp. 3087-95.
10. K.B. Lee and H. Kwon, Metall: Mater. Mater. Trans. A, vol. 30A(1999), pp. 2999-3007.
11. K.B. Lee, J.P. Ahn, and H. Kwon: Mater. Mater. Trans. A, vol. 32A(2001), pp. 1007-1018.
12. K.B. Lee, H.S. Sim, S.Y. Cho, and H. Kwon: Mater.Sci. Eng., vol. A302(2001), pp. 227-34.

MICROSTRUCTURE AND THERMAL PROPERTIES OF COMPOSITIONALLY GRADED Al-SiCp COMPOSITES

**Nak Bong Choi¹, Jin Ill Hwang¹, Ik Min Park¹, Ildong Choi²
and Kyung-mox Cho^{1*}**

¹Department Metallurgical Engineering,
Pusan National University, Pusan 609-735, Korea

²Department of Materials Science
Korea Maritime University, Pusan 606-791, Korea

*Member of Center for Advanced Aerospace Materials

ABSTRACT

Compositionally graded Al-SiCp composites were fabricated on the route of pressureless infiltration process. Microstructure was examined and thermal properties were characterized for Al-SiCp composites. Fairly uniform distribution and compositional gradient of SiCp reinforcement in Al matrix were observed though the thickness direction of the Al-SiCp composite plate fabricated. The thermal conductivity of Al-SiCp composites was measured using laser flash method. The thermal conductivity of monolithic Al-SiCp composites increases non-linearly with decreasing the volume fraction of SiC. The thermal conductivity of compositionally graded Al-SiCp composites was tried to estimate using the conductivity of the monolithic composites. Cyclic thermal shock fatigue test was performed by immersing Al-SiCp FGM into a water bath (25°C) from the different heating temperatures of 400°C, 300°C and 200°C, repeatedly. The microcrack formation behavior in Al-SiC composites was also investigated. From the crack observation, the critical number of cycle for thermal crack initiation was 130 at $\Delta T=375^\circ\text{C}$, 150 at $\Delta T=275^\circ\text{C}$. No evidence of crack initiation was found below $\Delta T=175^\circ\text{C}$. Cracks were initiated on the surface of high SiC volume fraction side. The cracks propagated through the thickness direction and then changed its direction perpendicularly to the surface of the plate. The path of crack propagation was found to have a close relationship with the distribution of the internal thermal stresses in Al-SiCp composites.

1. INTRODUCTION

The concept of FGM is gradual changes in composition or microstructure at the interface between two different kinds of materials bonded together, for example metal and ceramic[1,2]. Comparing to the sharp interface of a layered structure composed of different kinds of materials, the thermal mismatch could be greatly relieved especially at the graded interface of FGMs. In terms of materials category, FGMs are composite materials. Among metal matrix composites, Al-SiCp composites have been considered as one of the most potential structural materials. Studies have been performed for Al-SiCp extensively for the years of period, and a number of technological information on Al-SiCp are available presently[3,4]. In this study, Al-SiCp FGM was tried to fabricate employing pressureless infiltration technique. Microstructure and thermal properties of the Al-SiCp FGM were characterized.

2. EXPERIMENTAL

Pressureless infiltration method was used for the fabrication of Al-SiCp FGMs. Al and SiC powder mixtures with nine different volume fractions, namely from 90%Al-10%SiC to 10%Al-90%SiC with an interval of 10% of both powders, were prepared for Al-SiCp FGM. Average size of powders used were $50\mu\text{m}$ -Al and $44.6\mu\text{m}$ -SiC. Powder mixtures were stacked sequentially to get the compositional gradient of Al and/or SiC in a compaction mould and consolidated to obtain the preform. Al-10%Mg alloy was infiltrated into the preforms placed in a tube furnace at 920°C . Fig. 1 shows the whole fabrication process of Al-SiCp FGM schematically. Microstructure of Al-SiCp FGM was examined using SEM.

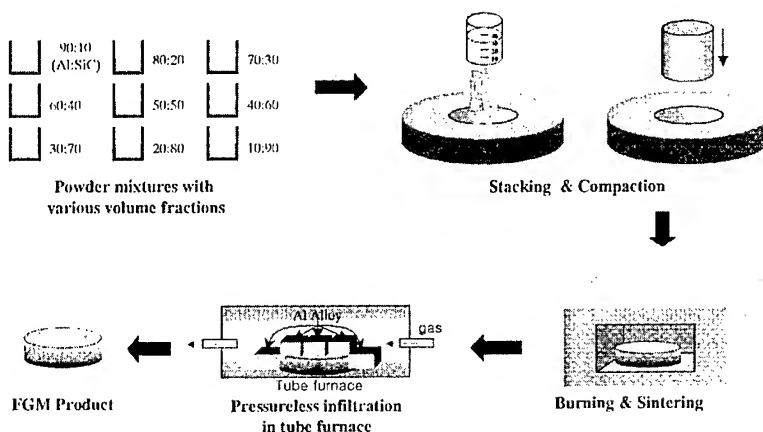


Fig. 1. Fabrication process of FGM

The thermal conductivity of Al-SiCp composites was measured using laser flash method. Thermal conductivity was measured at three different temperatures (25, 200, 400 °C). Thermal conductivity was tried to calculate theoretically using Maxwell model[5] for composite materials and the calculated values were compared with the experimentally measured values.

Thermal shock fatigue property of Al-SiCp FGM was evaluated. Al-SiCp FGM was heated up to 400 °C, 300 °C and 200 °C respectively and dropped to the quenching water bath(25 °C). Heating-quenching cycles have been repeated until microcracks were observed. Micro-cracks formed in Al-SiCp FGM were observed with SEM.

3. RESULTS AND DISCUSSION

Fig. 2 shows the microstructure of Al-SiCp FGM which reveals fairly uniform distribution of the constituent phases, Al and SiC. The compositional gradient along the thickness direction of the plate can be seen. Microstructure of three layers (58%Al-42%SiC, 70%Al-30%SiC and 90%Al-10%SiC) is presented with enlarged magnification in this figure. Noticeable defect was not found in the microstructure of Al-SiCp FGM.

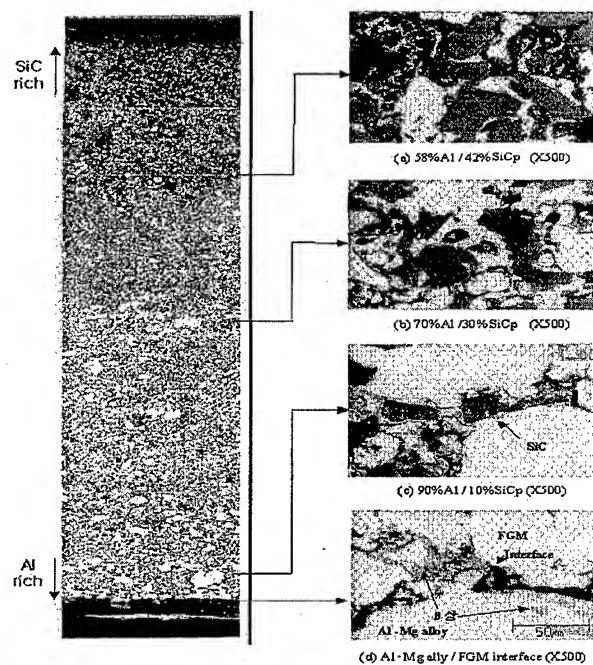


Fig. 2. Photograph of the functionally graded layers of the Al-SiCp functionally graded material

Thermal conductivity of Al-SiCp composites was measured. Results are summarized in Fig. 3. For the monolithic Al-SiCp composites, thermal conductivity decreases with increasing the volume fraction of SiC up to about 40%. Thermal conductivity tends to become plateau above the volume fraction of 40% SiC. It might be due to the fact that the thermal conductivity of Al-SiCp composites is largely governed by that of SiC with higher volume fraction as Al phase loses the microstructural continuity. Other factors such as microstructural defects also possibly might affect the thermal conductivity of Al-SiCp composites. Note the experimentally measured thermal conductivity is quite lower than the theoretically expected value based on the Maxwell's model for composite materials[5].

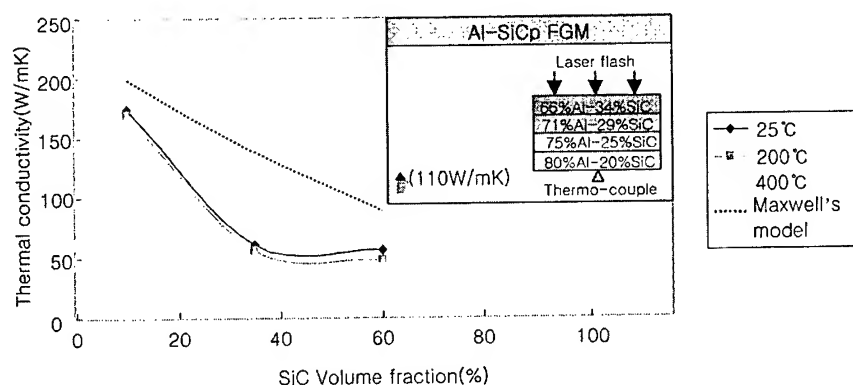


Fig. 3. Thermal conductivity of Al-SiCp composites and Al-SiCp FGM(inset)

Thermal conductivity of Al-SiCp FGM (a four layer-structure: 66%Al-34%SiC/ 71%Al - 29%SiC /75%Al-25%SiC/80%Al-20%SiC) was measured as 110W/mK. It is noted that the range of the SiC volume fraction is 20 to 34%. The value of Al-SiCp FGM is close to that of monolithic 80%Al-20%SiC composite. Thermal conductivity could be controlled mainly by the layer with the richest Al of Al-SiCp FGM. The thermal conductivity of Al-SiCp composites and Al-SiCp FGM is not very dependent on temperature up to 400°C despite minor decrease with increasing temperature.

Thermal shock fatigue behavior was investigated by the examination of microcrack formation in Al-SiCp FGM. No microcrack was observed for the temperature drop, $\Delta T=175^\circ\text{C}$ until 1000 cycles of thermal shock, while 150 and 130 cycles were the critical numbers of cycles for the temperature drop of $\Delta T=375^\circ\text{C}$ and $\Delta T=275^\circ\text{C}$ respectively. Microcrack propagation behavior was investigated by continued thermal shock cycles after the initial microcrack formation. As it is shown in Fig. 4, microcracks initiated on the surface of high SiC volume fraction layer of Al-SiCp FGM plate and propagated through the thickness direction of the plate in the early stage. The path of microcrack changes the

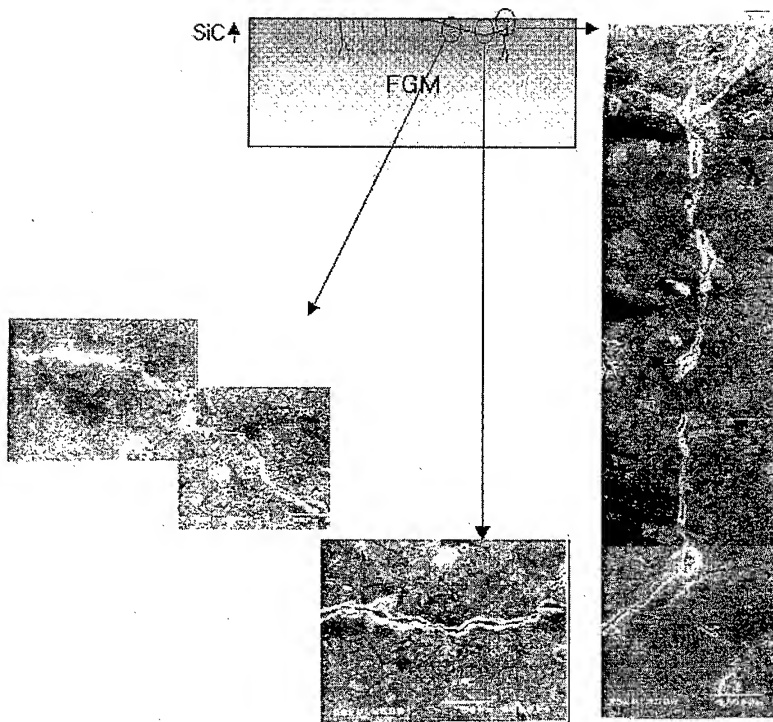


Fig. 4. Crack propagation behavior of Al-SiCp FGM during cyclic thermal shock test

propagation direction parallel to the surface as well as continues to the direction through thickness of plate in the later stage. The path of microcrack propagation is believed to have a close relationship to the internal thermal stress distribution developed during temperature change in Al-SiCp FGM and will be discussed later.

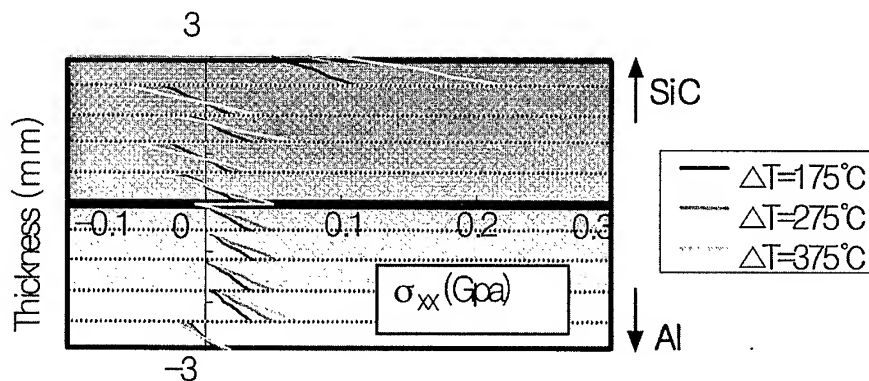


Fig. 5. Calculated thermal internal stresses for Al-SiCp FGM

From the thermo-mechanical analyses[6,7], the thermal internal stress distribution within each layer of Al-SiCp FGM can be calculated. Micro-crack propagation behavior of Al-SiCp FGM shown in Fig. 4 could be explained by the aid of the thermal stress analyses shown in Fig. 5. Micro-cracks would be initiated on the surface of SiC rich side where the tensile stress developed. The micro-cracks propagate through the thickness direction beneath the surface where the tensile stresses exist. It is found the deflection of crack propagation parallel to the surface of Al-SiCp FGM plate occurs at the depth where stress state changes from tensile to compressive.

4. CONCLUSIONS

Al-SiCp FGM with fairly uniform distribution and compositional gradient of the constituent phases, Al and SiC, was fabricated on the route of pressureless infiltration process. Thermal conductivity of Al-SiCp composites is controlled by the more conductive Al phase. The critical numbers of cycles for the formation of cracks in Al-SiC FGM were 150 and 130 for $\Delta T=275^{\circ}\text{C}$ and $\Delta T=375^{\circ}\text{C}$ respectively. However thermal shock fatigue crack was not observed for the temperature drop of $\Delta T=175^{\circ}\text{C}$. Micro-cracks were initiated on the surface of the high SiC volume fraction side. Propagation behavior of micro-cracks could be explained by the thermal stress analyses for Al-SiCp FGM plate.

ACKNOWLEDGEMENTS

This work was supported by CAAM(2000), POSTECH.

REFERENCES

1. M. Niini, T. Hirai and R. Watanabe, *J. Jan. Soc. Comp. Mater.* **13**, 257(1987).
2. A. Mortensen and S. Suresh, *Int. Mater. Rev.* **40**, 239 (1995).
3. P. Rohatgi, *JOM* **43**, 10 (1991).
4. C. Zweben, *JOM* **44**, 15 (1992).
5. J. C. Maxwell, *A Treatise on Electricity and Magnetism*, vol. I, 3rd ed., Dover, New York (1954).
6. D. Nam, K. Baek, H. Lee and K. Cho, *J. Kor. Inst. Met. and Mater.* **36**, 760 (1998).
7. J. Yoo, K. Cho, W. S. Bae, M. Cima and S. Suresh, *J. Am. Ceram. Soc.* **81**, 21 (1998).

PREPARATION OF SiC/2024 COMPOSITES BY SEMISOLID CASTING

Xianyun Meng, Hua Ding, Yanbo Chen, Jinglin Wen

School of Materials and Metallurgy
Northeastern University, Shenyang, P.R.China

ABSTRACT

Aluminium based matrix reinforced with SiC particles appears as the promising candidate for low-weight high strength applications. In the present study, a SiC/2024 composite was made by semisolid casting. The wetting between SiC and Al matrix was improved by treating SiC particles at a high temperature and coating K_2ZrF_6 and adding Mg to Al melt. An effective way to remove the gas around the SiC particles was also found. Microstructures were observed under optical microscope and SEM. The results showed that the bonding between SiC particles and Al matrix was close and there were no gaps or cavities around the particles. SiC particles were distributed on the Al matrix homogeneously.

1. INTRODUCTION

Al-ceramic particle composites have been recognized as candidate materials in the aerospace and automobile industry due to the improvement in yield strength and tensile strength as compared with the matrix as well as an improvement in the wear resistance. It was reported that the method to prepare metal-ceramics composites is mainly power metallurgy [1]. Some work has been done in preparing the composites by in-situ reaction method [2]. Power metallurgy method is relatively complex and it takes much time and the costs are usually high. There are also limitations in in-situ reaction method since it can be only used for some certain particles. With respect to the conventional casting process, the viscosity of metal is higher when metals are in semisolid state so that the particles can be drawn into the metal matrix more easily, which is good for making composites. In the present paper, SiC/2024 composites were prepared by semisolid casting and wetting between SiC particles and 2024 alloy was discussed.

2. EXPERIMENTAL

The size of SiC particles was 2 – 5 μm and the particles were treated by the following process before the compounding process. SiC particles were treated at a high

temperature, 1200°C, for one hour at first, coated with K_2ZrF_6 and then mixed with some pure Al powder. The matrix is 2024 alloy, and the contents of the elements were shown in Table 1.

Table 1 The composition of 2024 Al alloy

2024	Cu	Mg	Mn	Ti	Zn	Fe	Si	Ni	Al
%	3.8-4.9	1.2-1.8	0.3-0.9	≤0.15	≤0.3	≤0.5	≤0.5	≤0.1	balance

The testing apparatus is shown in Fig.1. The inside is the stirring furnace, heating elements being set around it. Adjustable rotating magnetic field can be added with power of 0 – 22 kw. The temperature was controlled by digital automatic control meter.

The 2024 alloy was heated at 730°C, and then the melt was poured into the stirring furnace after degassing. Pure Mg was added to the melt and prepared SiC particles mentioned earlier were added when the temperature of the Al alloy reached liquidus (melting temperature range of 2024 being 502°C – 638°C). The melt was stirred while the particles were added. The slurry was put into the mold and then it was quickly water quenched to room temperature. The microstructure of the ingot was observed by optical microscope and SEM. The volume fraction of SiC was measured by IAS-4 image analyzer.

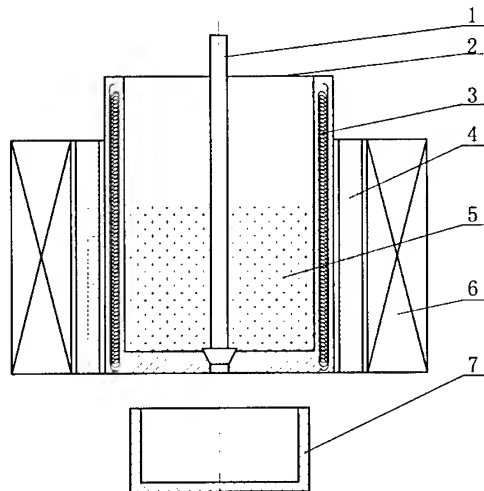


Fig.1 Electromagnetic stirring equipment of the semisolid casting
1- stopper; 2- stirring furnace; 3- heating elements; 4- insulating layer;
5- melt; 6 - electromagnetic stick; 7 - cooling mold

3.RESULTS AND DISCUSSION

The composites with different SiC volume fraction were received. The microstructures of the composites are shown in Fig.2. Quantitative analysis indicates the volume fractions of the SiC particles in Fig.2(a) and (b) are 4.6% and 11.7% respectively. It can be seen that the distribution of SiC particles was homogeneous and dispersed on the Al matrix and there is not much assemble of the particles.

Fig. 3 shows the microstructure under SEM. It indicates that the bonding between the particles and the matrix was close , the interface was clear and there aren't gaps and cavities.

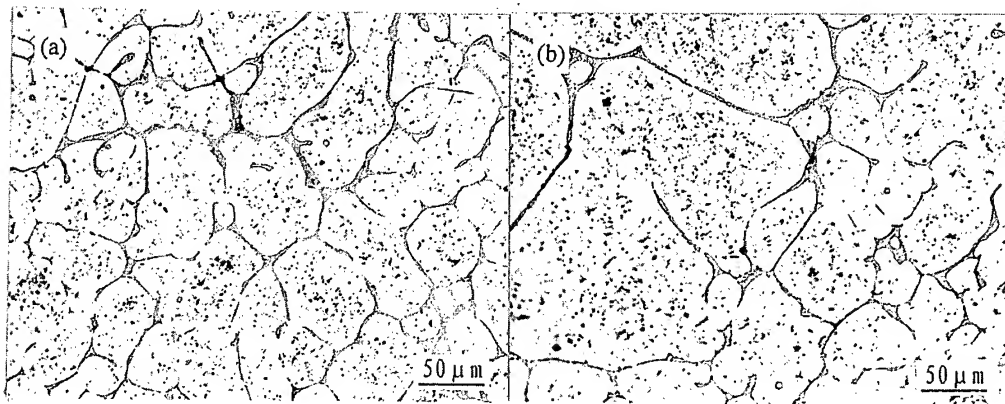


Fig.2 Microstructure of the SiC/2024 (OM)
(a) 4.6%SiC; (b) 11.7%SiC

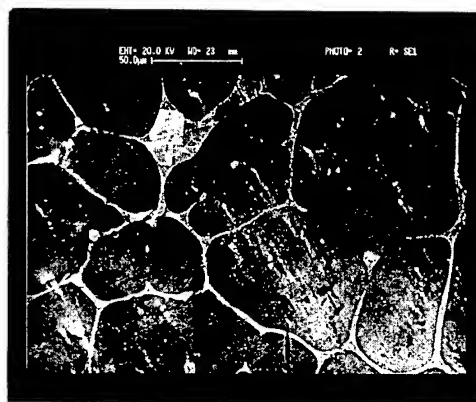


Fig.3 Microstructure of SiC/2024 (SEM)

For particle reinforced materials, one key technique is to solve the wetting problem between particles and metal matrix. In semisolid casting, the viscosity of the melt is high and the melt has some flowability. Adding SiC while stirring can prohibit the floating and sinking

of the particles and increase the reaction time for SiC and the melt, which makes SiC particles distribute homogeneously in 2024 melt. In the present study, several methods were used such as high temperature treatment of SiC, K_2TiF_6 surface treatment and addition of Mg to improve the wetting between SiC and 2024 alloy.

The surface of SiC was often contaminated by different organic compounds or absorbed by some water, which is not good for mixing and wetting during the composite preparation and also increases the gas content in the melt. Therefore, the surface of SiC must be treated to remove the gas and water and improve its wetting with metal matrix. In the present work, SiC particles were heated before the compounding process. During the heating process, detrimental substances were removed and SiC particles were oxygenated, forming a continuous and compact SiO_2 layer. In the compounding process, SiO_2 reacted with Al melt as the follows [5]:



The formation of Si restrains the occurrence of Al_4C_3 and is good for improving the chemical compatibility between metal matrix and SiC particles. The boundary reaction can also facilitate the boundary bonding and improve wetting.

J.P.Rocher reported [3,4] that the wetting between Al matrix and SiC could be improved by treating SiC fiber or particle surface in K_2ZrF_6 liquid. The reason is that the exothermal reaction occurred between K_2ZrF_6 and Al melt and the surface temperature of fibers or particles increases so that the contact angle decreased. The method was used here and also in our earlier work in making SiC/2017 composites [6]. The results indicate that the wetting was improved by the treatment.

Adding Mg into 2024 melt can decrease the boundary tension between Al melt and solid particles so that the wetting can also be improved.

Gas is a major factor which affects the wetting between the SiC particles and the matrix. Because the wetting angle between gas and SiC is smaller than the one between Al matrix and SiC, the gas around the SiC particles becomes the barrier for the further bonding. In semisolid processing, the viscosity of the metal liquid is relatively high and the temperature is relatively low. Therefore, the gas is difficult to escape from the metal liquid. This problem can be solved by preparing the composites in vacuum, but it is expensive and the operation is complex. In the present study, we mixed SiC particles and a certain amount of Al powder. They were added into the Al melt while stirring. The method not only removed the gas surrounding the particles, but also made particles more disperse when the composites were made.

In the experiment, we also found that changing the stirring power of the magnetic field has a positive effect. Besides, the stirring time is very important to the compounding process. The time is not enough for SiC particles to disperse when the stirring time is too short, while the SiC particles would be drawn to the side of stirring furnace by the centrifugal force when the stirring time is too long. The optimal stirring time is about 10 – 12 min for this equipment.

4. CONCLUSION

1. Semisolid casting is a good way for preparing SiC/2024 composites. The distribution of SiC particles on the Al matrix is homogeneous and disperse and there aren't obvious gaps and cavities around SiC particles.
2. The wetting between the SiC particles and Al matrix can be improved by treating SiC particles at a high temperature, coating K_2ZrF_6 and adding Mg to the 2024 melt.

REFERENCES

1. S.S.Xie, S.H.Huang: Semisolid Processing Technique and Application, Metallurgical Industry Publisher, Beijing, 1999
2. Shoukui Zhang, Danhong Wang, Foundry, (1996), No.234, pp.4-7
3. J.P.Rocher, J.M.Quenisset, R.Naslain, J.Mater.Sci.letters, Vol.4 (1985), pp.1527-1529
4. J.P.Rocher, J.M.Quenisset, R.Naslain, J.Mater.Sci., Vol. 24 (1989), pp.2697-2703
5. D.J.Lloyd, International Materials Reviews, Vol. 39 (1994), pp. 1-22
6. X.Y.Meng, J.W.zhang, Y.B.Cheng, J.L.Wen, in press

Influence of ECA Pressing on Microstructure and Mechanical Properties of P/M SiCw/6061 Al Alloy Composite

Si-Young Chang, Seung Kyun Ryu*, Dong Hyuk Shin,
Hiroyasu Tezuka** and Tatsuo Sato**

Department of Metallurgy and Materials Science, Hanyang University,
Ansan, Kyunggi-do, Korea 425-791

*Digital Plating Co., Yangjae-dong, Seocho-ku, Seoul, Korea 137-130

**Department of Metallurgy and Ceramics Science, Tokyo Institute of
Technology, O-okayama, Meguro-ku, Tokyo, Japan 152-8552

ABSTRACT

The 6061(Al-1.01wt%Mg-1.07wt%Si) Al alloy based composites reinforced with 10 vol% SiC whiskers were fabricated by powder metallurgy, and then subjected to equal channel angular pressing at various temperatures. Their microstructure and microhardness were compared with those of the equal channel angular pressed P/M 6061 Al alloy. For P/M 6061 Al alloy with an initial grain size of approximately 20 μm , an equiaxed ultra-fine grained structure with the mean grain sizes of $\sim 0.5 \mu\text{m}$ was obtained after 4 repetitive equal channel angular pressing using route A and C. The microstructure of P/M SiCw/6061 Al composites consisted of the aggregated whiskers and matrix. The aggregated SiC whiskers were uniformly distributed by the hot extrusion, whereas, after equal channel angular pressing, they remained aggregated. The aggregation of SiC whiskers were aligned parallel to the shear direction and well distributed after equal channel angular pressing. This microstructural evolution became stark with the repetitive pressings and lower pressing temperature. Both as-received P/M 6061 Al composite and the equal channel angular pressed one revealed different microhardness between the aggregation region of SiC whiskers and matrix, whereas the extruded one showed uniform microhardness.

1. Introduction

Metal matrix composites (MMCs) have received much attention as potential structural materials for their high specific strength and stiffness. Such MMCs are expected in high performance applications such as in aircraft and automotive parts. Among such MMCs, MMCs reinforced with short fibers have been produced by squeeze casting [1]-[5] and powder metallurgy [6]-[8], to obtain the higher specific mechanical properties necessary to achieve better performance. In the squeeze casting, the reinforcements are easy to be damaged by the high infiltration pressure and the decrease of strength occurs due to reaction products at the reinforcement/whisker interface. In contrast, the powder metallurgy has been used for producing composites because of the several merits that no reaction at the interface results from mixing at lower temperature than melting temperature, and that the volume fraction of reinforcements can be controlled. In general, however, the subsequent processes such as hot press and extrusion are necessary to compact completely and to improve the mechanical

properties of P/M MMCs.

Recently, equal channel angular (ECAP) technique have been used as an attractive method to obtain a sub-micrometer ultra-fine grained (UFG) structure, because it gives large bulk metallic materials without residual porosity [9]-[13]. Therefore, it is of interest to apply the ECAP technique as the subsequent process after powder metallurgy of the MMCs.

Accordingly, the aim of this work is to investigate the effect of ECAP on microstructure and mechanical properties of P/M SiCw/6061 Al composite in comparison with those of ECA pressed matrix.

2. Experimental procedure

Air atomized 6061 Al alloy (Al-1.01%Mg-1.07%Si-0.35%Cu-0.25%Fe-0.05%Mn-0.12%Cr (in wt.)) powder with an average size of 30 μm and SiC whiskers with an average diameter of 0.45 μm and a length of $\sim 5 \mu\text{m}$ were mixed by stirring under a stirring speed of 3000 rpm for 20 min. The obtained powders with 10 % in the volume fraction of SiC whiskers were hot-pressed at 773 K under a pressure of 100 MPa. The hot-pressed samples with a dimension of $\phi 32 \times 80$ mm were machined to cylindrical samples of $\phi 10 \times 80$ mm as-received materials for ECAP. The ECAP was carried out using a press speed of 2 mms^{-1} with MoS_2 as a lubricant at 373~573 K. The present ECAP die was designed to yield an effective strain of ~ 1 by a single pass: the inner angle and the arc of curvature at the outer point of contact between channels of the die were 90 and 20°, respectively [14]. During the ECAP, the samples were repetitively pressed using two processing routes: route A in which the sample is repetitively pressed without any rotation and route C in which the sample is rotated 180° around its longitudinal axis between individual pressings [15]. In addition, a part of as-received sample was hot-extruded at an extrusion ratio of 12:1 and at 673 K instead of ECAP.

Microhardness was measured using a Vickers microhardness tester at a load of 0.05 kg for 15 s. Microstructure examination of samples before/after ECAP was carried out using an optical microscope (OM), a field emission scanning electron microscope (FE-SEM, JSM6330F, JEOL, Japan) and a transmission electron microscope (TEM, JEOL 2010, Japan) operated at 200 keV.

3. Results and Discussion

3.1 Microstructural Characteristics

Figure 1 represents TEM micrographs of ECA pressed P/M 6061 Al alloy. For P/M 6061 Al alloy with an initial grain size of approximately 20 μm , after two pressings at 373 K using route A, the grains were elongated and had a length of $\sim 0.8 \mu\text{m}$ and a width of $\sim 0.3 \mu\text{m}$. The selected area diffraction (SAED) pattern showed the appearance of the diffused spots and the extra spots indicating the formation of a high angle boundary. In contrast, the grains after two pressings at relatively high temperature of 573 K became larger above 1 μm in length and width. Its corresponding SAED pattern was characterized by relatively clear spots. This implies that most of the boundaries in the grains formed by a single pressing would be low-angled. Near equiaxed ultra-fine grains of approximately 0.5 μm were obtained by 4 pressings. In addition, the number of rings in the SAED pattern increased and the spots became more diffused compared to one pressed at 573 K. There was no microstructural difference in the

samples pressed using route A and route C.

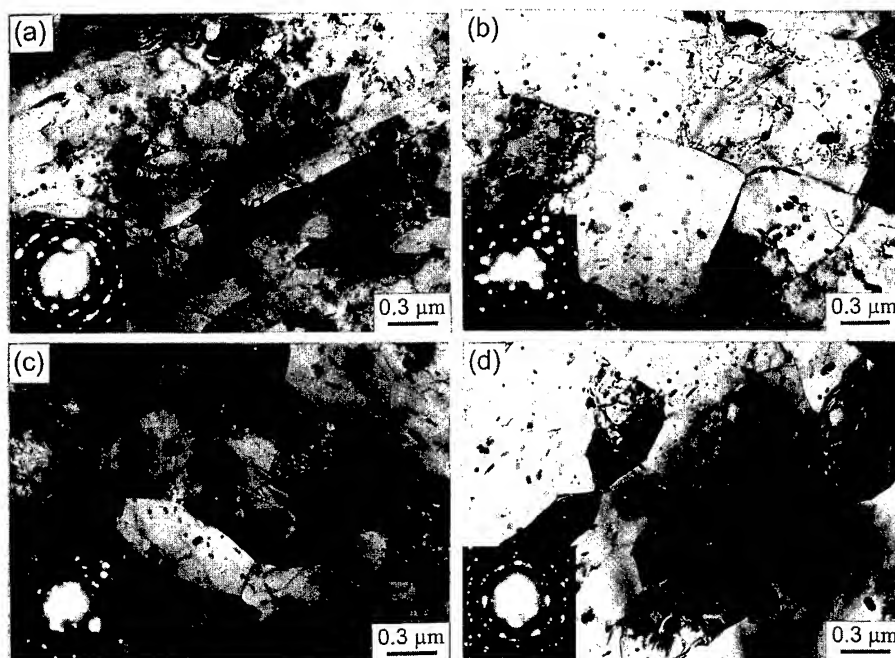


Fig.1 TEM micrographs of the ECA pressed P/M 6061 Al alloys; 2 pressings at (a) 373 K and (b) 573 K, 4 pressings using (c) R_A and (d) R_C at 473 K.

The optical microstructure of ECA pressed P/M SiCw/6061 Al composites is shown in Fig. 2. The as-received P/M SiCw/6061 Al composites showed the microstructure consisting of the black region of the aggregation of SiC whiskers and the white region of matrix. The aggregated SiC whiskers were uniformly distributed by the hot extrusion (Fig.2 (e)), whereas, after ECAP, they still remained aggregated. The aggregation of SiC whiskers was aligned parallel to the shear direction and distributed more homogeneously after ECAP. In addition, the large aggregation with the irregular island shape was separated to small ones with the round island shape. These microstructural characteristics became stark with the repetitive pressings and lower pressing temperature. The alignment and distribution of SiC whiskers in the black region were shown in Fig. 3, together with those in the as extruded composite. The SiC whiskers in the black region were densely aggregated before ECAP, whereas, after ECAP, they became more distant. This tendency obviously appeared with the repetitive pressings. On the other hand, in the as extruded composite, they were well distributed totally and aligned parallel to extrusion direction as shown in Fig.3 (d).

3.2. Microhardness

The microhardness of the ECA pressed P/M 6061 Al alloy and P/M SiCw/6061 Al composites is shown in Fig.4, together with that of the as extruded composite. The microhardness of P/M 6061 Al alloy drastically increased from 46 Hv to 80 Hv and to 55 Hv after two pressings at 373 K and at 573 K, respectively. The as-received P/M SiCw/6061 Al

composite had different microhardness between the aggregation region of SiC whiskers and matrix. The microhardness in the aggregation region and matrix increased respectively after ECAP, and slightly decreased with increasing the pressing temperature. In contrast, the extruded P/M SiCw/6061 Al composite showed uniform microhardness. In general, the increase of microhardness after ECAP is because of the work hardening that is caused by the formation of subgrain bands and the density increase of dislocation occurring with the shear deformation in the initial grain interior. Additionally, the reason why the microhardness decreases with increasing the press temperature is deduced to be due to the dynamic recovery occurring during the pressing [16] at higher temperatures.

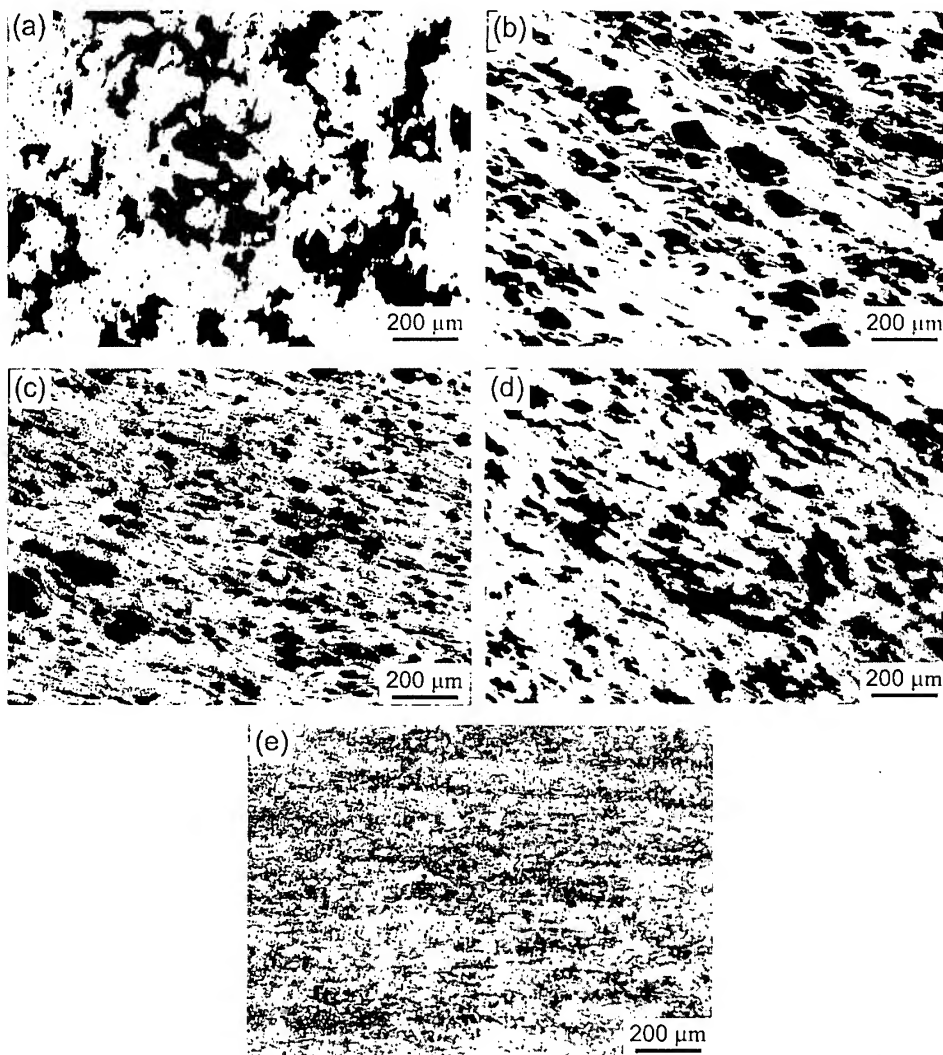


Fig.2 Optical micrographs of the ECA pressed P/M SiCw/6061 Al composites; (a) 0 pressing, (b) 1 pressing and (c) 2 pressings at 373 K, (d) 1 pressing at 573 K, (e) as extruded.

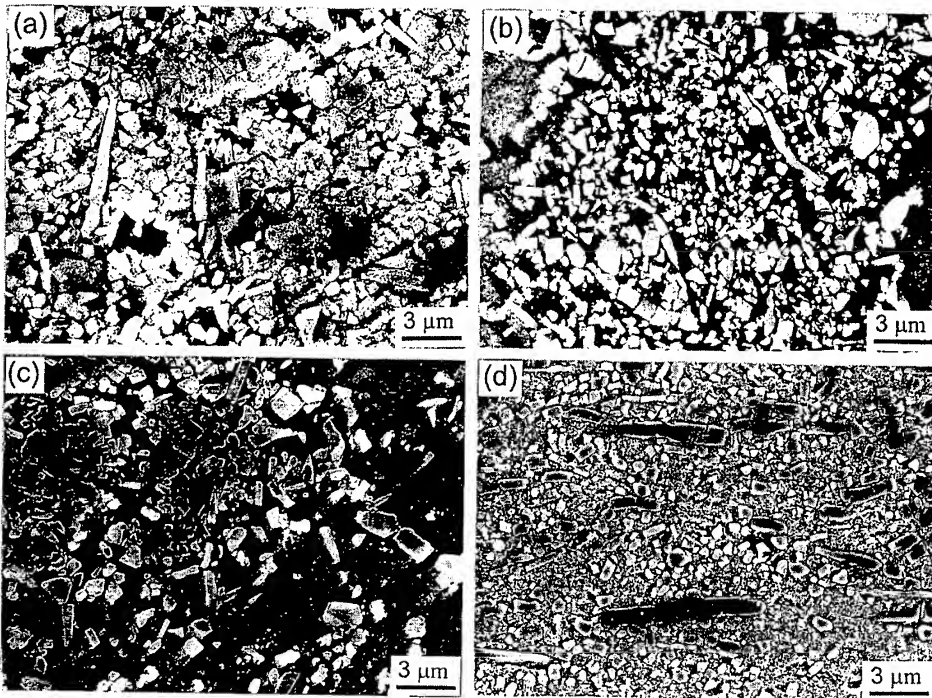


Fig.3 FE-SEM micrographs of the aggregated whiskers in the ECA pressed P/M SiCw/6061 Al composites; (a) 0 pressing, (b) 1 pressing and (c) 2 pressings at 373 K, and (d) as extruded.

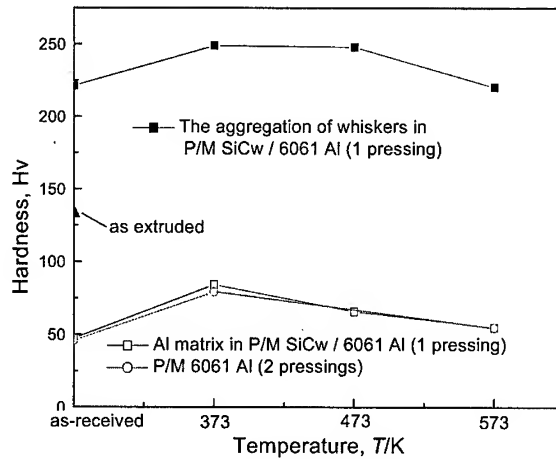


Fig.4 Microhardness of the ECA pressed P/M 6061 Al alloys and SiCw/6061 Al alloy based composites.

4. Summary

1. For P/M 6061 Al alloy with an initial grain size of approximately 20 μm , an equiaxed (UFG) structure with the mean grain sizes of $\sim 0.5 \mu\text{m}$ was obtained after 4 ECAPs using

route A and C.

2. The P/M SiCw/6061 Al composites consisted of the aggregated SiC whiskers and matrix. The aggregated SiC whiskers were uniformly distributed by the hot extrusion, whereas they still remained aggregated after ECAP. The aggregation of SiC whiskers were aligned parallel to the shear direction and well distributed after ECAP. This microstructural evolution became stark with the repetitive pressings and lower pressing temperature.
3. The microhardness of P/M 6061 Al alloy drastically increased from 46 Hv to 80 Hv and to 55 Hv after two pressings at 373 K and at 573 K, respectively. The as-received P/M SiCw/6061 Al composite and the ECA pressed one revealed different microhardness between the aggregation region of SiC whiskers and matrix, whereas the extruded one showed uniform microhardness.
4. In applying the ECAP technique as the subsequent process after powder metallurgy of the MMCs, many repetitive pressings at relatively low temperatures are necessary to obtain the structure of uniformly well-distributed SiC whiskers resulting in high microhardness.

Acknowledgements

This work was supported by the 'National Research Laboratory Program' of Korea Ministry of Science and Technology.

REFERENCES

1. T. W. and J. F. Mason, Metal. Trans. A, Vol.18A(1987), pp. 1519-1530.
2. J. F. Mason, C. M. Warwick, P. J. Smith, J. A. Charles and T. W. Clync, J. Mater Sci., Vol.24(1989), pp. 3934-3946.
3. K. Purazarang, K. U. Kainer and B. L. Mordike, Composites, Vol.22(1991), pp. 456-462.
4. S. K. Hong, H. Tezuka, A. Kamio, B. S. Chun and S. S. Cho, J. Japan Inst. Metals, Vol.60(1996), pp. 218-224.
5. S. Y. Chang, D. H. Shin, S. K. Hong and J. C. Choi, J. Korean Foundrymen's Soc., Vol.20(2000), pp. 167-172.
6. B. A. Mikucki, W. E. Mercer and W. G. Green, Light Met. Age, Vol.48(1990), pp. 12-16.
7. A. P. Divecha, S. G. Fishman and S. D. Barmacha, J. Metals, Vol.33(1981), pp. 12-17.
8. F. H. Froes, J. R. Pickens, J. Metals, Vol.36(1984), pp. 14-28.
9. R. Z. Valiev, R. K. Islamgaliev and I. V. Alexandrov, Progress in Materials Science, Vol.45(2000), pp. 103-189.
10. D. H. Shin, Y. S. Kim and E. J. Lavernia, Acta Materialia, Vol.49(2001), in press.
11. D. H. Shin, I. Y. Kim, J. Kim and K. T. Park, Acta Materialia, Vol.49(2001), pp. 1285-1292.
12. D. H. Shin, B. C. Kim, K. T. Park and W. Y. Choo, Acta Materialia, Vol.48(2000), pp. 3245-3252.
13. D. H. Shin, B. C. Kim, Y. S. Kim and K. T. Park, Acta Materialia, Vol.48(2000), pp. 2247-2255.
14. K. Nakanishi, Z. Horita, M. Nemoto and T. G. Langdon, Acta Mater., Vol.46(1998), pp. 1589-1599.
15. Y. Iwahashi, M. Furukawa, Z. Horita, M. Nemoto and T. G. Langdon, Metall. Mater. Trans., Vol.29A(1998), pp. 2245-2252.
16. S. Ferrasse, V. M. Segal, K. T. Hartwig and R. E. Goforth, Metall. Mater. Trans., Vol.28A(1997), pp. 1047-1057.

IN-SITU SYNTHESIS OF Al/Al₃Ti COMPOSITES BY MA-PDS PROCESS

ZhengMing Sun, Qian Wang, Hitoshi Hashimoto,
Yong-Ho Park and Toshihiko Abe

AIST Tohoku
National Institute of Advanced Industrial Science and Technology
4-2-1 Nigatake, Miyagino-ku, Sendai 983-8551, Japan

ABSTRACT

In-situ synthesis of Al/Al₃Ti composites by Mechanical Alloying and Pulse Discharge Sintering (MA-PDS) process was studied. The powder with size smaller than 75 μm was recovered at a recovery rate of higher than 70 percent. The X-ray diffraction (XRD) profiles of as milled powders showed that Ti can be completely dissolved into Al and formed super saturated Al (Ti) alloy. Full density compacts were obtained when powders were sintered at 873K for 600 seconds with the pulse discharge sintering (PDS) process. The peaks of Al and DO₂₂ Al₃Ti were found in XRD patterns of as sintered specimens. In additional, small amount of Al₄C₃ was also found in the as sintered samples. The microstructure of as-sintered compacts showed that Al₃Ti particles with size of about 20 μm dispersed homogeneously in the Al matrix. It is concluded that Al₃Ti reinforcement particles can be in-situ formed during the sintering process. It is found that the samples with composition of 5 at. % Ti have Young's modulus of 110 GPa and tensile strength of 550 MPa, much higher than conventional Al alloys. The results of high temperature tensile tests showed that the composites possess high strength at the temperature higher than 673K. The stability of Al₃Ti reinforcement particle at high temperature and high bonding strength at interface between Al₃Ti particles and Al matrix are believed to contribute to the excellent mechanical properties of this composite.

1. INTRODUCTION

Mechanical alloying (MA) has been proven an effective method for synthesizing aluminum alloys or aluminum-based composites containing a large quantity of transition metals such as Ti, Fe and Ni, *et al* [1]. As a non-equilibrium solid-state process, MA can result supersaturation of the transition metals in Al during the milling process and the formation of fine Al-based intermetallic compound phases in the following heating process [2, 3]. Due to high diffusivity in liquid state, the intermetallic phases easily grow and form coarse grains. Thus it is difficult to obtain fine intermetallic dispersoids in the Al alloys with high content of transition metals by conventional melting process [4]. Among the aluminum-rich intermetallic compounds, Al₃Ti is attractive for its high Young's modulus (~220 GPa) and

high melting point (~ 1623 K) and relatively low density (~ 3.3 g/cm³). But extreme brittleness of bulk Al₃Ti limits its practical structural applications [5]. However, if the Al₃Ti phase appears by fine dispersoids in a ductile matrix, it is predicted that the dispersoids are effective in strengthening the matrix alloys [6].

The Al alloys with a significant content of fine Al₃Ti dispersoids have been successfully produced by MA process [7]. The Al-Al₃Ti alloys show excellent combination of low density, good thermal stability and high modulus and strength. Especially, compared with conventional Al based alloys or composites such as 7075 alloy and Al/SiC_p composite, the Al-Al₃Ti alloys exhibit a superior elevated temperature strength, ~ 200 MPa at 623 K [8].

However, almost all synthesis of MA Al-Al₃Ti alloys was carried out on laboratory scale, in which only several grams of MA powder were formed in one process circle. The small yield scale is not suitable for industrial applications. Further the excellent mechanical properties were obtained in the Al-Al₃Ti alloys by multi-step process including high temperature (~ 873 K) sintering for long time (~ 3.6 ks) and hot extrusion [9]. The severe processes will decrease the lifetime of moulds and consume more energy, meanwhile hot extrusion raises difficulty in the process, which all increase the cost of the alloys.

In this paper, the mechanical alloying and pulse discharge sintering (MA-PDS) technology was applied for fabricating the Al-Al₃Ti alloy. In every process circle, the yield of MA Al-Ti powder can be maintained at about 1 kg. The bulk Al-Al₃Ti composites with full density were successfully manufactured by single-step sintering process with short soaking time (0.6 ks) and low temperature (< 773 K). The microstructures and mechanical properties of the alloys were also studied.

2. EXPERIMENTAL

2.1 Mechanical alloying (MA) process

The elemental aluminium powder (purity: 99.9%; maximum particle size: 0.18 mm) and titanium powder (purity: 99.9%; maximum particle size: 0.15 mm) with composition of Al-12 mass % Ti were used as starting materials in milling process. The powder and 1 mass % of stearic acid as process control agent (PCA) were firstly pre-mixed with a Turbula mixer for 7.2 ks. Then the mixture was put in middle-scale powder synthesis unit consisting of a gas/vacuum system and a tumbling ball mill with 0.3 m in inner diameter and 0.35 m in inner length, where more than 50 kg of steel balls with diameter ranged from 6.35 mm to 19.05 mm were contained as grinding media. Such synthesis unit is able to deal with at least 1 kg of starting materials in one process circle. The MA process was carried out in argon atmosphere for 720 ks. After milling, the media balls and as-milled powder were separated by a vibration sieve and the MA powder were graded and collected by three different particle sizes: smaller than 33 μ m (-33μ m); between 33 μ m and 75 μ m ($+33\mu$ m/ -75μ m); over 75 μ m ($+75\mu$ m). According to Japanese Industrial Standard (JIS) only the powder with particle size less than 75 μ m can be used in industrial applications.

2.2 Pulse discharge sintering (PDS) process

The as-milled powders with particle size less than 75 μ m were recovered for PDS. The powder was filled in graphite die with two graphite punches and then the sintering chamber was evacuated to a high vacuum of about 6×10^{-3} Pa. At the beginning of sintering process, a pulse current with an intensity of 800 A was applied for 30 seconds and then the direct electric current and load were applied on the die by the temperature and pressure programme. A maximum pressure of 110 MPa and a maximum temperature ranged from 748 K to 873 K

for 0.6 ks soaking time were adopted in the sintering process. Billet-shaped compacts with $\phi 50\text{mm}$ were sintered.

2.3 Materials characterization

The X-ray diffraction (XRD) analysis (Cu-K α radiation) was conducted to examine the crystal structure of as-milled powder and as-sintered specimen. The composition of as-milled powder was examined by chemical analysis. The microstructures of as-sintered specimens were observed by scanning electron microscopy (SEM). The density of sintered materials was measured by the Archimedes' method, and the Young's modulus was determined with an ultrasonic pulse echo method using an ultrasonic measuring instrument. The Young's modulus E (GPa) can be calculated with the following equation,

$$E = \frac{(3V_L^2 - 4V_T^2)V_T^2}{V_L^2 - V_T^2} \rho$$

where V_L and V_T , in km/s, are the velocities of the longitudinal and transverse waves transmitted in the test piece, respectively, and ρ (Mg/m^3) is the density of the measured materials.

The sintered billets were machined to specimens with gauge dimension of $20 \times 4 \times 2 \text{ mm}^3$ for tensile test at temperature ranged from 293 K to 793 K. Mechanical tests were carried out on an Instron universal testing machine with a strain rate of $3 \times 10^{-4} \text{ s}^{-1}$. The fracture surfaces after tensile tests at various temperatures were observed with a scanning electron microscope.

3. RESULTS AND DISCUSSIONS

3.1 Mechanical alloying process

Table 1 Particle size distribution of MA powder

According to JIS, the powder with size less than $75 \mu\text{m}$ can be applied in the Powder Metallurgical industry. The distribution of particle size of

size	-33 μm	+33/-75 μm	+75 μm
Recovery rate, %	4.65	82.3	13.05

MA powder after 720 ks milling is summarised in Table 1, which shows more than 80 per cent of powder with particle size ranged from $33 \mu\text{m}$ to $75 \mu\text{m}$. The proportions of finer powder ($< 33 \mu\text{m}$) and coarser powder ($> 75 \mu\text{m}$) are both low. The total recovery rate of more than 90 percent proved that the high stable yield of MA Al-Ti powder was realized after milling process. It means that at least 900g of MA powder can be produced in every milling process recycle, which is suitable to industrial scale. Figure 1 showed the XRD profiles of MA powder at different milling time. It is found that the structural evolution during milling process was similar with other results from laboratory planetary ball mill [2,3]. In the milling, the dissolution of Ti atoms into Al powder can be responsible for the intensity of Ti peaks weakened in XRD profiles. At the milling time of 720 ks, the peaks of Ti cannot be identified due to formation of Al(Ti) supersaturated solid solution. The broadening and weakening of Al peaks is attributed to crystalline distortion and refining of grain size introduced by heavy plastic deformation in aluminium.

3.2 Microstructure and mechanical properties of as-sintered composites

Variation in the density of sintered alloys with sintering temperature is shown in Fig.2. It is found that the powder can be consolidated to bulk specimens with full density by PDS at 773K, which is 100K lower than by conventional hot press. As well known, the surface of

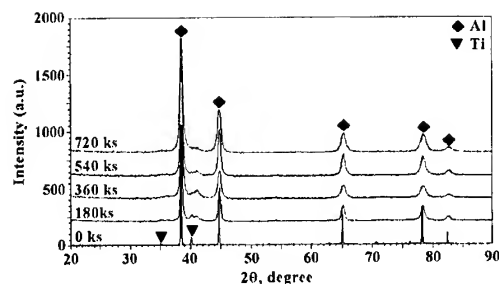


Fig.1. X-ray diffraction profiles of MA powder at different milling time

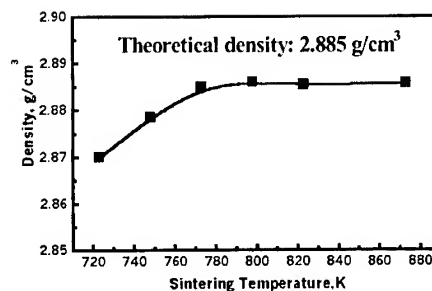


Fig.2 The variation of density of sintered alloys with sintering temperature

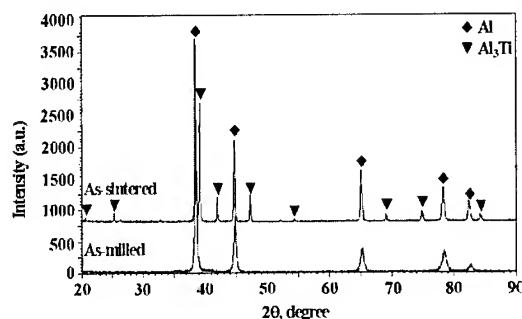


Fig.3 X-ray diffraction profiles of the MA powder and sintered alloy.

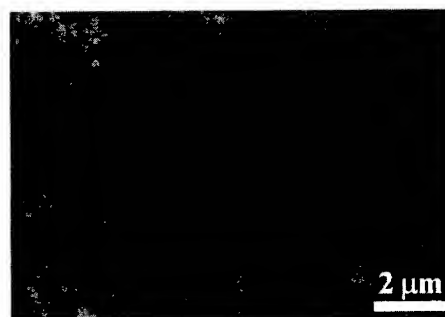


Fig.4 Back scattered electron microscopic image of the alloy sintered at 773K

MA Al powder is generally coated by oxide, which will increase the sintering temperature. As aforementioned description of PDS process, a gigantic current (800 A) pulse applied on the powder can break the oxide surface to prompt the activated sintering process. The Young's modulus of sintered specimen is 112 GPa, slightly higher than the theoretical value of 109 GPa due to existence of small amount of oxide and carbide, as shown by chemical analysis in Table 2.

The XRD profile in Fig.3 shows the sintered alloy consisted with Al matrix and in-situ formed Al_3Ti intermetallic compound. Due to small amount, the peaks corresponding to oxide Al_2O_3 and carbide Al_4C_3 can not be identified in the XRD profiles. Figure 4 shows the backscattered electron image of microstructure in alloy sintered at 723K. In the micrograph the dark area represents the Al matrix and the grey particles represent Al_3Ti phase. Al_3Ti phase appears as equiaxed particle with average diameter less than 1 μm . In addition, it is found that Al_3Ti phase disperses homogeneously in Al matrix.

Table 2. Chemical composition (in mass %) of the Al- Al_3Ti composite and the calculated volume fractions (F) of Al_3Ti

Al	Ti	C	O	$F_{\text{Al}_3\text{Ti}}$
Bal.	11.62	0.70	0.73	0.28

* assuming that the titanium are fully reacted with aluminium to form the Al_3Ti .

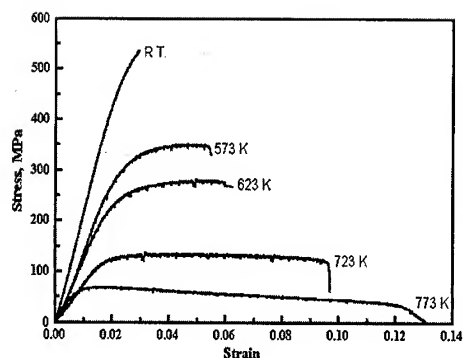


Fig.5 The stress-strain curves of Al-Al₃Ti alloys tested at different temperature

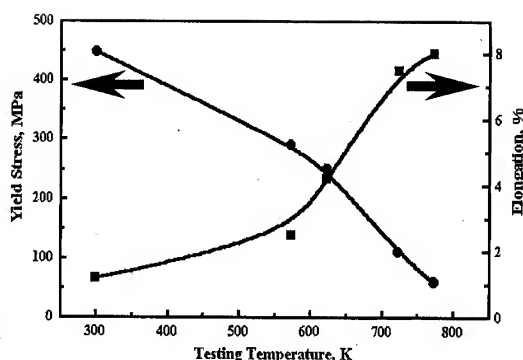


Fig.6 The relation curves of yield strength and elongation with temperature

Table 3 mechanical properties of Al-Al₃Ti composite, compared with 7075-T6 Al alloy*

Alloy	293 K				573K		
	E, GPa	UTS, MPa	YS, MPa	El.(%)	UTS, MPa	YS, MPa	El.(%)
7075-T6	71	559	471	11 %	85	75	46 %
Al-Al ₃ Ti	112	550	460	1 %	350	300	3%

*data of 7075 alloy from Japanese Industrial Standard Handbook (JIS-H-4100)

The tensile stress-strain curves, the tensile yield strength and elongation of the Al-Al₃Ti alloy sintered at 773 K as functions of testing temperatures are summarized in Fig.5 and Fig.6, respectively. High ultimate tensile strength of 550 MPa was obtained at room temperature, meanwhile, the alloy showed significant plastic deformation behaviour. The strength decreased with increasing testing temperature, meanwhile the strain or elongation showed opposite tendency. It is worthy to notice that yield strength maintained 300 MPa at 573 K.

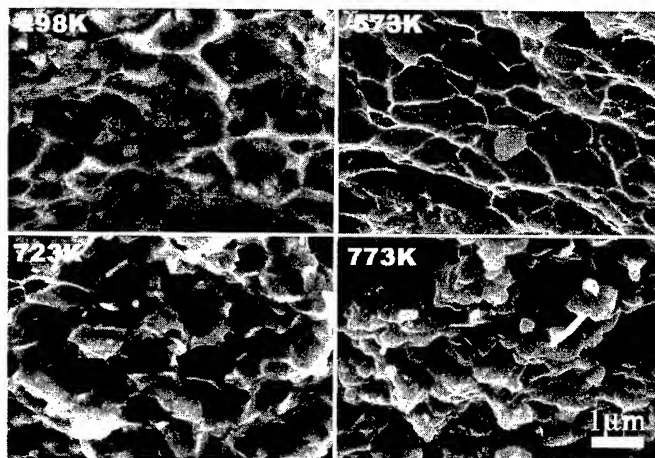


Fig.7 Fracture surfaces after tensile testing at different temperatures of 298K, 573K, 723K and 773K, respectively.

Compared with mechanical properties of 7075-T6 aluminium alloy, as can be seen in Table 3, the present Al-Al₃Ti composite shows same level of strength at room temperature and much higher strength at elevated temperatures. The excellent mechanical properties can be attributed to fine Al₃Ti reinforcement in the Al matrix, which can be explained by load-sharing effect of Al₃Ti particles [8]. The Al-Al₃Ti composites have potential application as lightweight heat-resistant alloys.

3.3 Fractography

The scanning electron micrographs in Fig. 7 represent the fracture surfaces of the Al-Al₃Ti alloy after tensile testing at room temperature, 573K, 723K and 773K, respectively. It can be seen from the fractography of the specimen tensile tested at room temperature that though brittle fracture characteristic due to the reinforcement phase prevails, matrix aluminium still showed substantial plastic deformation feature. With an increase in testing temperature, the constraint of reinforcement phase on the plastic deformation of matrix aluminium is reduced and more plastic deformation features are seen in the fracture surface, which is consistent with the result shown in Fig.5 and Fig.6.

4. SUMMARY

The in-situ Al-Al₃Ti composites were successfully fabricated on kilogram scale by MA-PDS process. The Al powder and Ti powder was completely alloyed to form Al(Ti) supersaturated solution after 720 ks milling in a middle scale mill. The recovery rate of MA powder conforming to Japanese Industrial Standard was more than 80 percent and ~1 kg MA powder can be synthesized in one process circle. The MA powders were consolidated to bulk specimens with full density by short time and low temperature sintering process in a PDS system. The characteristic microstructure of sintered alloy is an Al matrix composite with homogeneously distributed fine Al₃Ti dispersoids with particle size less than 1 μm. Compared with 7075-T6 aluminium alloys, the strength of Al-Al₃Ti composites shows same level of strength at room temperature and much higher strength is obtained at elevated temperatures.

REFERENCE

1. Froes, F.H., Suryanarayana, C. Russell, K. and Li, C.-G. (1995) 'Synthesis of intermetallics by mechanical alloying', Mater. Sci. Eng. A, Struct. Mater., Prop. Microstruct. Process., Vol.A192-A193, pp. 612-623.
2. Kim, G.H., Kim, H.S. and Kum, D.W. (1996) 'Determination of titanium solubility in alpha-aluminum during high energy milling', Scr. Mater., Vol.34, No.3, pp. 421-428.
3. Fujii, T. Sodeoka, S. and Ameyama, K. (1998) 'Phase transformation of heptane added Ti-Al mechanically alloyed powders during heating', J. Jpn. Inst. Met., Vol.62, No.10, pp. 945-951
4. John, H.St. and Hogan, L.M. (1980) 'Thermal stability in the Al-Al₃Ti system', J. Mater. Sci., Vol. 15, pp. 2369-2373
5. Nic, P., Zhang, S. and Mikkola, D.E. (1990) 'Observation of systematic alloying of Al₃Ti with fourth period elements to yield cubic phase', Scr. Mater., Vol.24, pp. 1099-1107.
6. Liao, S.H., Kao, P.W. and Chang, C.P. (1997) 'The Bauschinger effect in fine-grained Al-Ti alloys prepared by mechanical alloying', Scr. Mater., Vol.36, No.11, pp. 1227-1232.
7. Lee, K.M. Kim, J.C. and Moon, I.H. (1991) 'Fabrication of Al-Ti alloy by mechanical alloying. I', J. Korean Inst. Met., Vol.29, No.2, pp.158-164.
8. Wang, S.H. and Kao, P.W. (1997) 'High temperature deformation of a submicron grained Al-12 wt.% Ti alloy', Scr. Mater., Vol.36, No.12, pp. 1397-1402.
9. Jia, D.C. Zhou, Y. and Lei, T.C. (1997) 'Microstructure and mechanical properties of Al-12Ti-6Nb prepared by mechanical alloying', Mater. Sci. Eng. A, Struct. Mater., Prop. Microstruct. Process., Vol.232, pp. 183-190.

MICROSTRUCTURAL EVOLUTION OF AL/AL₃FE COMPOSITES BY PLASMA SYNTHESIS METHOD

J. M. Lee, S. B. Kang, C. Y. Lim, C. Y. Eum,
T. Sato*, H. Tezuka* and A. Kamio*

Korea Institute of Machinery and Materials, Changwon, 641-010, Korea

* Tokyo Institute of Technology, Tokyo, 152-8552, Japan

ABSTRACT

The present work was undertaken to highlight a novel in-situ process in which electromagnetic stirring plus plasma spraying techniques were used to produce Al/Al₃Fe composites consist of angular shape of Al₃Fe intermetallic compounds of about 20 μm in size. The microstructures of fabricated materials depended mainly on the plasma spraying conditions such as input current, gas flow rate of plasma and distance from plasma gun to melt surface. This seemed to be due to the difference of instant temperature and velocity of iron particle on the melt surface. The temperature and velocity of iron particles in the plasma arc were calculated and the results were compared with the fabricated microstructures. In addition, the mechanism for formation of Al₃Fe intermetallic compounds in the melt was analyzed by spherical shell model incorporating of diffusion kinetics.

1. INTRODUCTION

MMCs have been developed from the motive for making materials that exhibits good combination of mechanical properties such as strength, elastic modulus, hardness and resistance to wear [1]. Ceramic particles such as SiC, TiC and Al₂O₃ have been recognized as potential reinforcement for metal [2]. However, production costs, machinability and incompatibility with environment have so far hampered ceramic particle reinforced MMCs to be utilized for their commercial applications in spite of their superior physical and mechanical properties [3]. In recent years, metal particle reinforced MMCs have been taken great attention due to their easy fabrication and variety of property selection. Recently, much work has been reported on the development of metal particle reinforced MMCs: in-situ Al/Al₃Ti composites with centrifugal casting of Al-Ti alloy [4], squeeze casting of A380/Fe [5], A201/Al-Fe-V-Si particles [6], stir-casting of Al/quasicrystalline Al-Cu-Fe particles [7] and in-situ Al/Al₃Fe composites with plasma synthesis method [8]. Plasma synthesis method (PSM) is a kind of in-situ formation of intermetallic compounds in the matrix and it involves incorporation of metallic particles into a molten metal using a plasma jet. In the process, the particles are heated and accelerated in the plasma arc, which helps the incorporation of the particles into the molten metal.

The objectives of the present work were to investigate the effects of plasma spraying conditions on the microstructures of Al/Al₃Fe composites and to verify the mechanism for formation of Al₃Fe intermetallic compounds in the matrix when Al/Al₃Fe is produced by plasma synthesis method.

2. EXPERIMENTAL

The fabrication processing was carried out by a ValuPlazTM Plasma spray system with Ar as plasma spraying gas and powder carrier gas. Aluminum (99.9% purity) ingots of 1000g placed in a clay-graphite crucible with argon flux cover were heated by high frequency induction furnace. The crucible with the molten aluminum was taken out from the chamber of high frequency induction furnace, and put into the chamber under the plasma spraying nozzle. As the spray processing began, the electromagnetic stirring equipment was switched on to distribute particles homogeneously in the molten aluminum. While the injection of iron particles reached a required value, the melt was poured into a steel mould 85mm in diameter. The Fe powder used in the experiment was 99.9% purity and its mean particle size was about 90 μ m. Fabrication experiments were carried out under the various plasma spraying conditions; input current 200, 300 and 400A, gas flow rate 50, 65 and 80 l/min, and powder feeding rate 40 and 60g/min.

Standard metallographic techniques were employed to examine the microstructures of the as-cast ingots of Al/Al₃Fe composites. The microstructures were characterized using an optical microscope, a scanning electron microscope equipped with energy dispersive X-ray spectrometer. Phase identification was carried out using an X-ray diffractometer with Cu K α radiation at 40kV and 30mA. The volume fraction and size distribution of intermetallic compounds were estimated with the help of an image analyzer.

3. RESULTS

3. 1 Microstructures

Fig. 1 shows the X-ray diffraction pattern of the as-cast specimen fabricated at the plasma spraying condition of input current 300A, gas flow rate 65 l/min and powder feeding rate 40g/min. From the diffraction pattern, iron aluminide was identified as Al₁₃Fe₄ and no other phases such as AlFe, Al₂Fe, Al₆Fe and AlFe₃ were identified.

Fig. 2 shows the optical micrographs of as-cast specimen fabricated at the plasma spraying condition of input current 300A, gas flow rate 65 l/min and powder feeding rate 40g/min. The microstructure consisted of angular shape and needle-like Al₁₃Fe₄ (sometimes referred to as Al₃Fe) embedded in α -Al matrix.

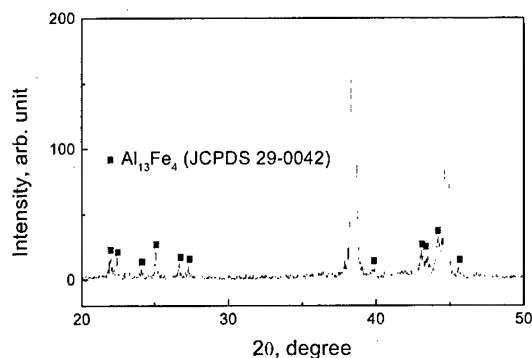


Fig. 1 X-ray diffraction pattern of the as-cast specimen

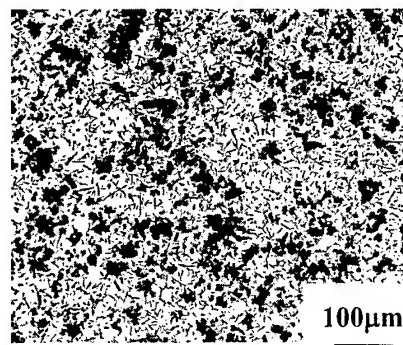


Fig. 2 Optical micrographs of the as-cast specimen

The similar microstructures were obtained with the specimens fabricated at different plasma spraying conditions. However, the size distributions of angular and needle-like intermetallic compound, and volume fractions of total, angular and needle-like Al_3Fe were different with plasma spraying conditions.

Fig. 3 shows the results of image analysis with input current. At input current 300A, the fraction of needle-like intermetallic compounds in the microstructures is lower and the fraction of angular intermetallic compounds is higher compared with those fabricated at input current 200A and 450A, while the total fraction of intermetallic compounds is nearly the same for different input current. Further, the size of needle-like intermetallic compounds is smaller compared with those fabricated at input current 200A and 450A. While, there are no much variations in the size distribution of angular intermetallic compounds with the variation of input current.

Fig. 4 shows the results of image analysis with gas flow rate. With increasing gas flow rate, the total fraction of intermetallic compounds and the fraction of angular shape of intermetallic compounds increase while the fraction of needle-like intermetallic compounds decreases. In addition, the size of needle-like intermetallic compounds decreases with gas flow rate. While, there are no much variations in the size distribution of angular intermetallic compounds with gas flow rate.

It was confirmed that the microstructural features with powder feeding rate was similar with that for gas flow rate.

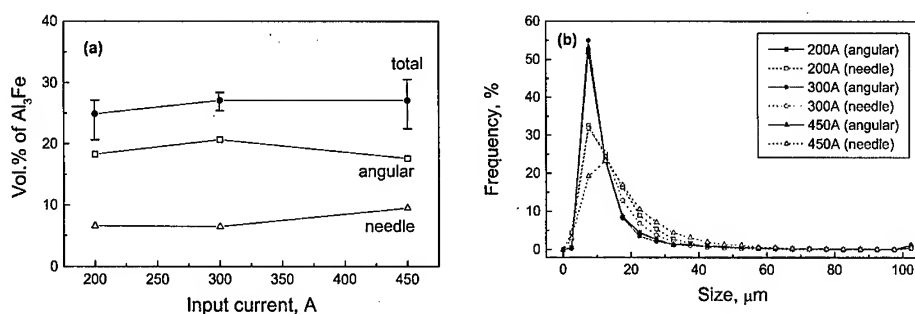


Fig. 3 Results of image analysis of microstructures with input current
(a) volume fraction of Al_3Fe (b) size distribution of Al_3Fe

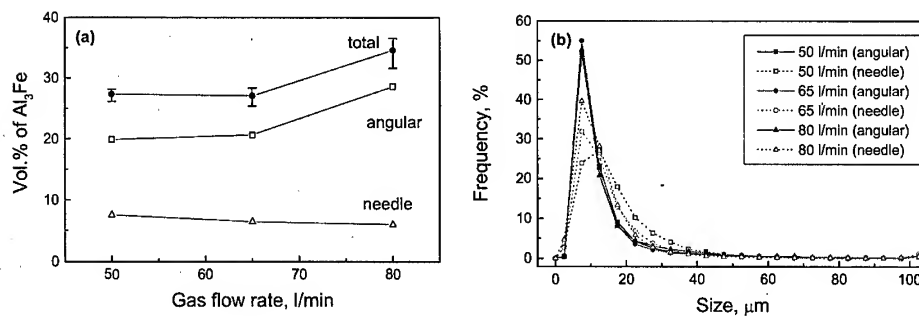


Fig. 4 Results of image analysis of microstructures with gas flow rate
(a) volume fraction of Al_3Fe (b) size distribution of Al_3Fe

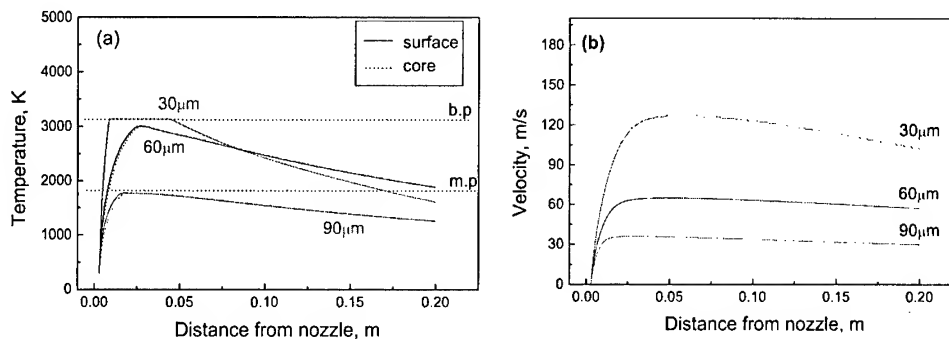


Fig.5 Temperature (a) and velocity (b) profile for Fe particle along the axial distance.

3. 2 Temperature and velocity of Fe particles

The temperature and velocity of particle was simulated based on momentum transfer and heat transfer between plasma gas and particle in the plasma arc. Fig. 5 shows the temperature and velocity profile for Fe particle along the axial distance from the plasma nozzle. The temperature and velocity of the Fe particle were calculated on the plasma spraying condition of 300A and 65 l/min. The temperature and velocity increase sharply to reach its maximum and decrease smoothly with plasma spraying distance. In addition, it can be observed that the phase of particle at the moment of impact on the melt surface depends on the initial particle size.

4. DISCUSSION

Al-rich Al-Fe alloys exhibit a simple eutectic between Al and Al_3Fe under the equilibrium conditions. The morphology of primary phase of Al_3Fe is plate-like, needle-like or star-shaped under the conventional melting and casting of the hypereutectic composition of the alloys [9]. Unlike the Al_3Fe morphology obtained by the conventional melting and casting of hypereutectic Al-Fe alloys, the Al_3Fe intermetallic compounds obtained by PSM was composed of angular and small needle-like shapes. From the comparison of morphology of Al_3Fe between the microstructures of conventional melting and casting and those of PSM, it can be induced that the needle-like shapes of intermetallic compounds might come from crystallization followed dissolution of the Fe particles into the Al melt and the angular shape of intermetallic compounds might come from reaction of the Fe particles with the Al melt.

The spherical shell model [10] in Fig.6 was applied to the reaction of liquid Al and Fe particle. This model consisted of a Fe particle with an initial diameter of r_0 surrounded by Al melt, and that the Fe particle size decreased to r_1 as the reaction proceeded. It can be assumed that no other compounds such as FeAl and FeAl_2 formed from the microstructural observations. Further, as shown in Fig. 5, the temperature of Fe particle is higher or same as that of the Al melt and due to high thermal conductivity, the temperature of Fe particle and the Al melt becomes local equilibrium. Thus, it can be assumed that no temperature gradient exists between liquid Al and Fe particle.

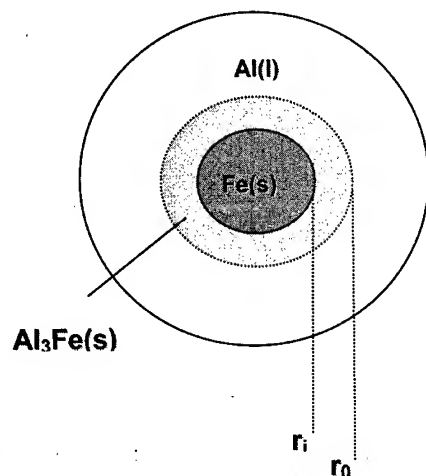


Fig. 6 Schematic illustrations of spherical shell model

The diffusion of Al occurred in Al_3Fe to the $\text{Al}_3\text{Fe}/\text{Fe}$ layer and the reaction occurred between Al and Fe at this layer. The diffusion velocity, $v_d(\text{mol/s})$, of Al in Al_3Fe at the spherical plane with a radius of r is represented by equation (1),

$$V_d = 4\pi r^2 \frac{D_{\text{Al}}}{\gamma_{\text{Al}}} \left(\frac{da_{\text{Al}}}{dr} \right) \quad [\text{mol/s}] \quad (1)$$

where D_{Al} , γ_{Al} and a_{Al} are diffusion coefficient, activity coefficient and activity of Al in Al_3Fe , respectively. Equation (1) can be obtained by integrating with respect to r on the condition that v_d is constant between r_i and r_o ,

$$V_d = 4\pi \frac{D_{\text{Al}}}{\gamma_{\text{Al}}} \frac{r_o r_i}{r_o - r_i} (1 - a_{\text{Al}}) \quad [\text{mol/s}] \quad (2)$$

If the radius of the unreacted Fe particle decreases from r_i to $r_i - dr$ in the duration of dt , the decrease velocity, $v_r(\text{mol/s})$, in the Fe volume is represent by equation (3),

$$v_r = \frac{4\pi}{3} \frac{\{r_i^3 - (r_i - dt)^3\}}{dt} \frac{\rho_{\text{Fe}}}{M_{\text{Fe}}} = 4\pi r_i^2 \frac{\rho_{\text{Fe}}}{M_{\text{Fe}}} \frac{dr_i}{dt} \quad (3)$$

where ρ_{Fe} and M_{Fe} are the density and molecular weight of Fe, respectively. In a steady state and considering the law of conservation of mass at $\text{Al}_3\text{Fe}/\text{Fe}$, the overall reaction velocity, $v(\text{mol/s})$, may be equal to v_d and v_r .

Thus, from equation (2) and (3), the time for complete reaction of liquid Al and solid Fe can be obtained by integrating from r_o to zero of r_i ,

$$t = \left(\frac{1}{6} \right) \left(\frac{\gamma_{\text{Al}}}{D_{\text{Al}}} \right) \left(\frac{1}{1 - a_{\text{Al}}} \right) \left(\frac{\rho_{\text{Fe}}}{M_{\text{Fe}}} \right) r_o^2 \quad (4)$$

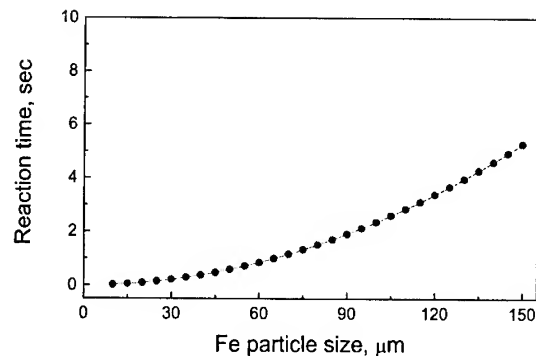


Fig. 7 Variation of complete reaction time with initial Fe particle size at 1073K

The time for complete reaction of Al and Fe at 1073 K are calculated using equation (4) (taking $\gamma_{\text{Al}}=0.52$, $a_{\text{Al}}=0.4$, $\rho_{\text{Fe}}=7.87\text{g/cm}^3$, $M_{\text{Fe}}=55.85\text{g/mol}$, $D_{\text{Al}}=D_0\exp(-Q/RT)$, $D_0=4.21\times 10^3$ and $Q=273\text{kJ/mol}$ [11,12]) and the calculated results are plotted in Fig. 7 as a function of initial Fe particle size. The reaction between the Al melt and Fe particle completes within a few seconds.

5. CONCLUSIONS

MMCs of Al/Al₃Fe intermetallic compounds were fabricated by injection of Fe powder into the Al melt through plasma synthesis method under the various processing parameters, and the results obtained are as follows:

(1) The as-cast microstructures consisted of α -Al and Al₃Fe intermetallic compounds. The morphology of Al₃Fe intermetallic compounds was mixed with angular and small needle-like and the fraction depended on the processing parameters such as input current, gas flow rate, spraying distance, powder feeding rate.

(2) The reaction between Fe particle and the Al melt occurred very rapidly to complete within a few seconds.

REFERENCES

1. D. J. Lloyd, *Int. Mater. Revs.* 39 (1994), 1.
2. J. Eliasson, R. Sandstrom, *Key Eng. Mater.* 104-107 (1995), 3.
3. V. M. Kevorkijan, *J. of Met.* 51 (1999), 54.
4. Y. Watanabe, N. Yamanaka, Y. Fukui, *Z. Metallkud.* 88 (1997), 717.
5. R. P. Baron, C. Jones, F. E. Wawner, J. A. Wert, *Mater. Sci. Eng. A259* (1999), 308.
6. C. C. Yang, W. M. Hsu, E. Chang, *Mater. Sci. Tech.* 13 (1997), 687.
7. E. Fleury, S. M. Lee, W.T. Kim, D.H. Kim, *Met. Mat.* 6 (2000), 415.
8. J. M. Lee, C.G. Lee, S. B. Kang, A. Kamio, *Met. Mat.* 6 (2000), 389.
9. D. Liang, P. Korgul, H. Jones, *Acta. Mater.* 44 (1996), 2999.
10. A. Hibino, R. Watababe, *J. Jpn. Inst. Met.* 55 (1991), 1256.
11. J. Eldridge, K. L. Komarek, *Trans. Met. Soc. AIME* 230 (1964), 226.
12. Y. Mizuno: Ms. Thesis, Tokyo Institute of Technology, (2001)

DYNAMIC SOFTENING OF Al-18Si COMPOSITE DURING HOT DEFORMATION

Sung-Il Kim, Chang-Hoon Han, Ho-In Lee* and Yeon-Chul Yoo

Department of Materials Science and Engineering, Inha University, Incheon 402-751, Korea

*Korea Institute of Science and Technology, Seoul, Korea

ABSTRACT

The high-temperature deformation behavior of Al-18wt.%Si composite was studied by torsion tests in the temperature range of 350 - 500°C and the strain rate range of 1×10^{-3} - 1×10^0 /sec. The metal matrix composite showed the characteristics of dynamic softening transition. The transition from dynamic recovery (DRV) to dynamic recrystallization (DRX) occurred at the deformation conditions of 400°C and 1×10^{-2} - 1×10^{-1} . Also, the dynamic transition behavior was investigated with multi-pass deformation test. The relationship among the processing variables, strain rate ($\dot{\epsilon}$), temperature (T) and flow stress (σ), can be expressed as constitutive equations that can be considered with the transition behavior.

Keywords: metal matrix composite, constitutive equations, dynamic softening transition, multi-pass deformation

1. INTRODUCTION

The spray-formed Al-Si composite has emerged as advanced materials owing to its good wear resistance and low thermal expansion properties [1,2]. For expanding the practical application of the composite, the conventional hot working processes such as rolling, forging, and extrusion can be used to produce products. However, during the forming process of the composite, the flow behavior would be significantly different from that of the monolithic Al alloy because of the presence of hard Si particles, which strongly affect the microstructure and mechanical properties of the composite [2-4]. Therefore, it is very important to understand the microstructural evolution and to predict the optimum hot working condition for the composite during hot deformation.

In the last few years, many workers have studied for the hot softening mechanisms of Al matrix composites [4-6]. Especially, some researchers have reported that Al matrix composites were softened by the both dynamic recovery (DRV) and dynamic recrystallization (DRX) during hot deformation. The composites showed the transition of softening mechanisms [5,6]. It is difficult to determine optimum deformation conditions due to their transition behavior.

The aim of this work is to study the hot softening mechanism of Al-18wt.%Si composite and to predict conditions for optimization of hot workability using analysis of flow stress curves and microstructures. Also, the transition of dynamic softening was investigated with multi-pass deformation test and then discussed.

2. EXPERIMENTAL PROCEDURES

The materials used in this work are spray-formed Al-18wt.%Si composite. The composite was fabricated by spray forming process. And the spray-formed rod was hot extruded. The torsion specimens with a gauge length of 10 mm and a diameter of 7 mm were machined from the extruded bars.

To investigate the hot deformation behavior of Al-18wt.%Si composite, hot torsion tests were conducted in the temperature range 300 - 500°C and in the strain rate range 0.001-1/sec. Subsequently, the torsion-tested specimens were quenched immediately in the water at 25°C. The effective stress (σ) and effective strain (ϵ) of the composites were calculated by the von Mises criterion [7] using the torque moment (M) and angular displacement (θ) measured from the torsion tests. The microstructures of the hot-deformed composites were investigated by the scanning electron microscopy (SEM, Hitachi 420) and transmission electron microscopy (TEM, Philips CM200).

3. EXPERIMENTAL RESULTS

3.1 Flow stress curves and transition of dynamic softening

Fig. 1 shows the flow stress curves of Al-18wt%Si composite obtained under several deformation conditions. The deformation variables, such as strain rate ($\dot{\epsilon}$), temperature (T) and strain (ϵ) affected the variation of flow stress (σ). It is interesting to note that the flow curves show the both features of the metals, softened by DRX or DRV. Generally, the flow stress curves of metals show the two different shapes with their softening mechanisms. For example, the flow stress curves by which softened dynamic recrystallization (DRX) exhibit the peak value and gradually reduce with strain to steady state. On the other hand, the flow curve of some metals, e.g., pure aluminum with a characteristic of dynamic recovery (DRV) due to their high stacking fault energy (SFE) shows that the peak value is equal to the steady state value in flow stress curve [2,4-8].

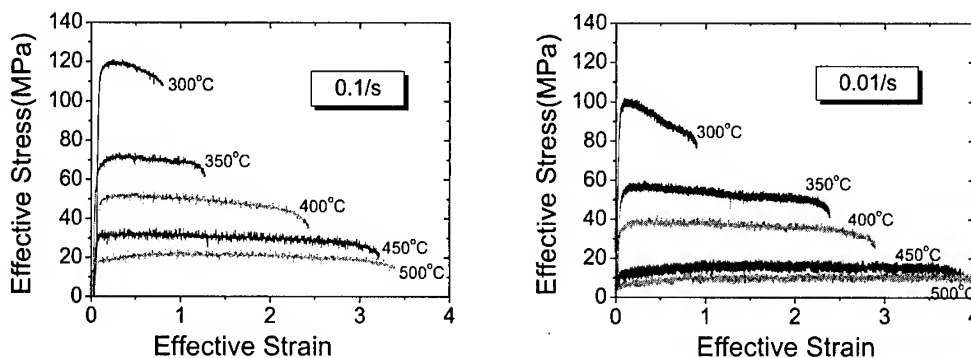


Fig. 1. Effective stress – effective strain curves obtained from hot torsion test under various temperatures at (a) 0.1/sec and (b) 0.01/sec.

From the type of flow stress curves, it could be noticed that DRX occurs in the temperature

range of 300 - 400 °C, which DRV occurs in the temperature range of 400 - 500 °C. Also, the flow stress depends on the deformation temperature. Therefore, it is necessary to express exactly the dependence of flow stress on process variables, such as temperature and strain rate. The flow stress increased with increasing strain rate and decreasing temperature due to the increase of strain rate and the decrease of temperature. First, the relationship between the flow stress and strain rate can be expressed as follows;

$$\dot{\epsilon} = a \sigma_p^n \quad (1)$$

where, $\dot{\epsilon}$ is the strain rate and σ_p is the peak stress corresponding peak strain. The experimental constant, a is about 9.5×10^{-13} . The exponent, n , means a reciprocal of strain rate sensitivity (m) and can be determined as a mean slope, 6.4, analyzed in Fig. 2(a). The n values have a tendency to decrease with increasing temperature. Especially, when the temperature decreased from 400 °C to 350 °C, the value increased in three times (Fig. 2(b)). This big difference was due to the transition of softening mechanism. Generally, the transition of softening mechanism has been reported in Al matrix composites [4-6]. In this case, the transition occurs at about 400 °C.

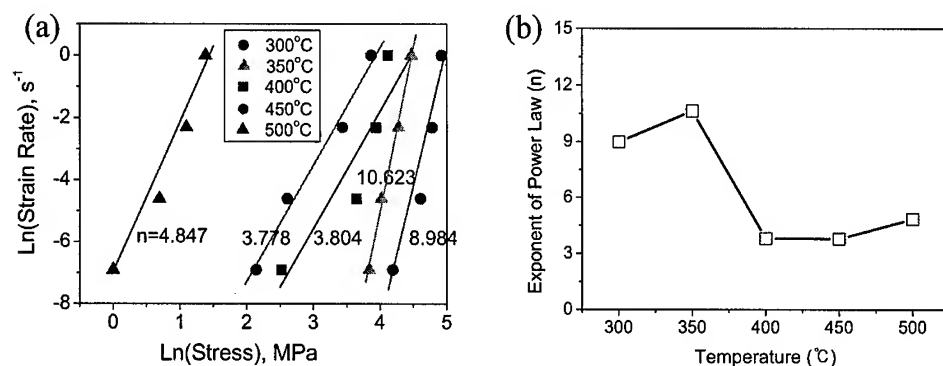


Fig. 2. (a) Relationship between the peak stress and strain rate and (b) the exponent of power law as a function of temperature.

In order to consider the effect of temperature simultaneously on strain rate, a temperature compensated strain rate parameter (Zener-Hollomon parameter, $Z = \dot{\epsilon} \exp(Q/RT)$) was substituted with the strain rate term of equation (1) [2,4-8].

From this stress-strain curve, σ_p is plotted with $\ln(1/T)$ to determine the activation energy (Q) shown in Fig. 3(a). As a result, the effects of strain rate and temperature (T) on peak stress can be determined as;

$$\begin{aligned} \dot{\epsilon} &= A \sigma_p^n \exp(-Q/RT) \\ n &= 9.80, \quad Q = 177 \text{ kJ/mol (at } < 400^\circ\text{C and } > 0.1/\text{s)} \\ n &= 4.41, \quad Q = 312.8 \text{ kJ/mol (at } > 400^\circ\text{C and } < 0.01/\text{s)} \end{aligned} \quad (2)$$

where, T is the absolute temperature and experimental constant, A is 1.76×10^8 . From these results, it is found out that Q strongly depends on the deformation conditions. Q shows a high

value at the condition of lower level strain rate. Especially, the change of strain rate from 0.1/sec to 0.01/sec increases significantly the values of Q (Fig.3 (b)).

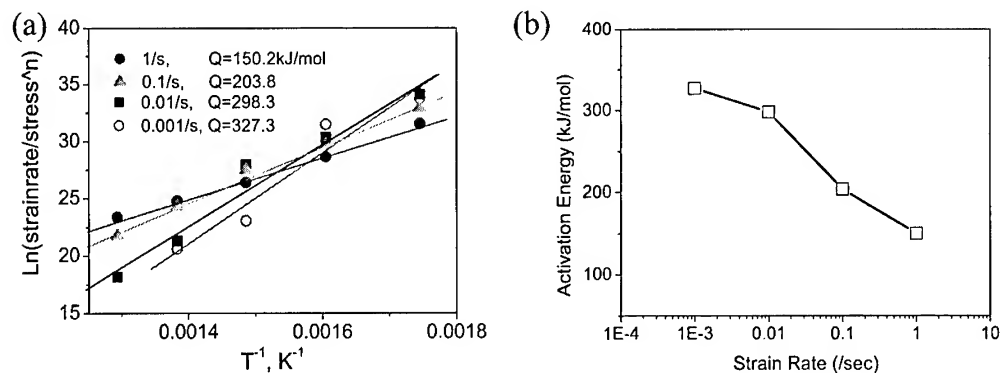


Fig. 3. (a) Relationship between the peak stress and temperature and (b) the change of activation energy as a function of strain rate.

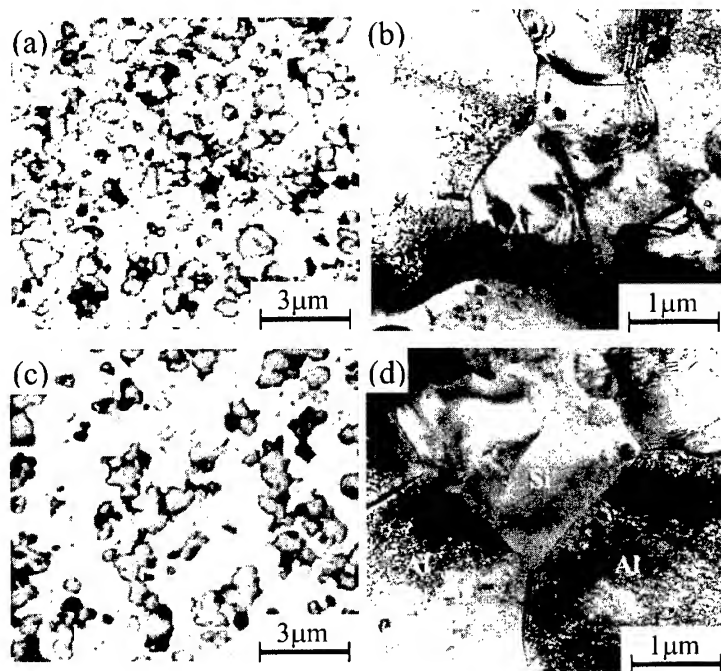


Fig. 4. SEM micrographs (a, c) and TEM bright field images (b, d) of the composite deformed at different deformation conditions : (a), (b) 300 °C, 1/sec and (c), (d) 500 °C, 0.001/sec.

The transition behavior of Al-18wt%Si composite could be confirmed from microstructural evolution. Fig. 4 shows the comparison of the microstructures deformed at the DRV region of 500 °C and 0.001/s and at the DRX region of 300 °C and 1/s. Figs. 4(a) and (b) show dynamically recrystallized microstructures. The small size grains of 1 - 2 μm were found along the Si particles. Figs. 4(c) and (d) indicate the characteristics of DRV whose grain size

was constant with that of non-deformed specimen. The grain refinement of Al-18Si composite was obtained from the hot deformation at high Zener-Hollomon parameter conditions.

3.2 Multi-pass deformation

The dynamic transition behavior could be investigated from the flow stress curves obtained from multi-pass deformation. Fig. 5 shows the flow stress curves and effective stress – temperature curve of Al-18wt%Si composites obtained from multi-pass deformation. The flow stress in each pass increases smoothly in response to decreasing temperature from 500 °C to 250 °C. In this continuous cooling torsion test, the specimen is multi-pass deformed as it is cooling. The mean flow stress in each pass increased gradually with a constant slope due to the work hardening and strain accumulation [8,9]. The slope of mean flow stress curve ($d\sigma/dT$) has the change from 44.38 to 27.83 with increasing strain rates from 0.01/sec to 0.1/sec. The decrease of mean flow stress occurs due to DRX which new grains are generated along the initial grain boundaries [4-8]. This result means that the softening mechanisms of Al-18wt%Si composite are altered from dynamic recovery (DRV) to dynamic recrystallization (DRX) in multi-pass deformation.

We may, therefore, reasonably conclude that the transition of softening behavior for Al-18wt%Si composite occurs at the deformation condition of 350 - 400 °C and 0.01 – 0.1/sec. Also, under a multi-pass deformation, the transition behavior of the composite occurred at the lower temperature due to static softening during interpass time. For the improvement of mechanical properties of Al-18wt%Si composite, the optimum hot working temperature and strain rate for DRX are 350 °C and 0.1/sec respectively.

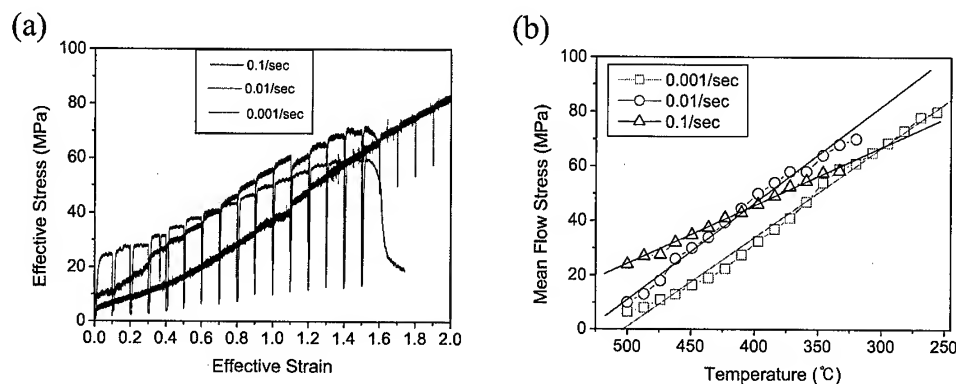


Fig. 5. (a) Flow stress curves obtained from multi-pass deformation with decreasing temperature (b) the change of mean flow stress slope obtained from (a).

4. CONCLUSIONS

The spray-formed Al-18wt%Si composite showed the transition behavior of softening mechanisms. Dynamic recrystallization occurs at the deformation range of 300 - 400 °C and 0.1 - 1/s. Under a multi-pass deformation, the transition behavior occurred at the lower temperature than that of continuous deformation due to the static softening during interpass

time. The optimum hot working condition for DRX of the composite can be suggested to be 350°C and 0.1/sec.

5. REFERENCES

1. D. M. Schuster, M. D. Skibo, R. S. Bruski, R. Provencher and G. Riverin : JOM, A Publication of The Minerals, Metals & Materials Society, (1993) p.26.
2. N. D. Ryan and H. J. McQueen : High Temp. Tech., Vol.8 (1990) pp. 27-34.
3. T. Satoh, K. Okimoto, S. Nishida and K. Matsuki, Scripta Metal. Mater., Vol.33 (1995), pp. 819-824.
4. Byung-Chul Ko and Yeon-Chul Yoo, Comp. Sci. and Technol. Vol.58 (1998), pp. 479-485.
5. Byung-Chul Ko and Yeon-Chul Yoo, J. of Mater. Sci. Lett., Vol.18 (1999), pp.1277-1279.
6. Byung-Chul Ko and Yeon-Chul Yoo, J. of Mater. Sci., Vol.35 (2000), pp. 4073-4077.
7. Sang-Hyun Cho, Yeon Chul Yoo, J. of Mater. Sci. Lett., Vol.18 (1999), pp. 987-989.
8. Sang-Hyun Cho Sung-Il Kim and Yeon-Chul Yoo, J. of Mater. Sci. Lett. Vol.16 (1997), pp. 1836-1837.
9. L.N. Pussegoda, and J. J. Jonas : ISIJ Inter. Vol.31 (1991) pp. 278-288.

TAILORING THE HYPEREUTECTIC Al-Si-Xs COMPOSITES AS A STRUCTURAL MATERIAL REQUIRING HIGH YOUNG'S MODULUS

Hyun-Kwang Seok¹, Jin-Yoo Suh¹, Don-Soo Shin², Ho-In Lee¹,
and Jae-Chul Lee¹

1. Div. of Materials Science and Engineering, Korea Institute of Science and
Technology, Seoul, 136-791, Korea (drstone@kist.re.kr)
2. R&D Center, Dooray Air Metal Ltd., Seoul, 345-11, Korea

ABSTRACT

If fine Si particles within the hypereutectic Al-Si-Xs (Xs are minor elements) alloys are dispersed in the matrix, the alloys can be used as an alternative for ceramic reinforced composites, which can be achievable via spray forming and extrusion process. The advantages of the hypereutectic Al-Si-Xs composites over the conventional composites are their superb wear resistance, high modulus, ease of shaping, and low production cost. Such properties make these composites suitable for structural applications. However, the reinforcement Si particle is known to have lots of habit planes, which degrades the mechanical properties of the Al-Si-Xs composites. Therefore careful design of matrix alloy system, heat treatment conditions, and Si particle size is required to improve the mechanical properties of spray formed and extruded Al-Si-Xs composites. In this study, the effects of matrix alloy systems, heat treatment conditions, spray forming and extrusion parameters on the Young's modulus and mechanical properties are estimated for the application of the composites as a structural material.

1. INTRODUCTION

Extensive studies on metal matrix composites(MMCs) reinforced with ceramic particulates or short fibers have been carried out due to their attractive mechanical properties suitable for structural applications. Although a considerable increase in properties, such as strength, modulus, wear resistance etc., could be achieved by adding ceramic reinforcements, these improvements are always accompanied by a substantial decrease in ductility and enhanced wear rate on opposite parts. In addition, another practical problems in these types of MMCs are relatively high production costs as well as difficulties in machining and recycling.

In recent years, spray formed hypereutectic Al-Si-Xs (Xs are minor elements) alloys[1-4], due to their low fabrication cost and ease of mechanical shaping, are gaining a commercial significance for

various structural applications that do not require a very high unidirectional strengthening. These composites not only exhibit high strengths equivalent to those of conventional MMCs, but also possess superior wear resistance and high modulus with reasonable ductility. Up to date, most research works on the hypereutectic Al-Si-X composites are centered on wear properties. Several parts such as compressor rotor[3-6], VCR head[4], cylinder liner[7,8], etc., have been commercialized successfully. An effort to develop hypereutectic Al-Si-X composites suitable for moving(rotating) structural parts, such as propeller shaft for passengers cars, was made recently[9]. Such a component requires materials with high specific modulus to enhance the resonant frequency of the part, thereby reducing noise caused by vibration during service. Also, the component requires reasonably high ductility in addition to high strength.

In the present study, several hypereutectic Al-Si-Xs composites were fabricated via spray forming and subsequent extrusion and the effects of matrix alloy systems, heat treatment conditions, process parameters on the mechanical properties are evaluated for the application of the composites as structural materials requiring high Young's modulus, high strength, and reasonable elongation all together. The fracture mechanisms of the samples were also investigated in order to know how to design the mechanical properties of the composites.

2. EXPERIMENTAL PROCEDURES

2.1 Preparation of the hypereutectic Al-Si-Xs composites

Hypereutectic Al-Si-Xs composite preforms were spray formed in rod shapes with dimensions of $\phi 300\text{mm} \times h 800\text{mm}$, in which the contents of minor elements were varied in the range of Cu(<4.5%), Mg(<2%), Zn(<1.5%), and Fe(<1.5%). The process parameters used to fabricate the preforms were melt temperature of 850-900°C, spray distance of 450mm, substrate withdrawal velocity of 0.2-0.8mm/s at a fixed spray angle of 30°, gas pressure of 6-8 atm, and G/M ratio of 0.8-1.0 m³/Kg[9]. Spray formed rods were then extruded into tubes with the outer diameter and the wall thickness of $\phi 120\text{mm} \times t 2\text{mm}$ at 500°C using a 2300ton capacity hydraulic press[9].

2.2 Characterization

Pieces were cut out from the extruded tubes along a direction parallel to the extrusion and machined into the specimens to measure Young's modulus and tensile properties. Samples were subjected to various heat treatments, such as T4 (495°C for 3 hrs & quenching) and T6 (T4 & 175°C for 10 hrs). Young's modulus was measured by the sonic resonant test method designated by ASTM C848-78. ASTM tensile test pieces with a rectangular cross-section(W 6.25mm) were machined and tested at a room temperature under the constant strain rate of 0.1/min. Fractured specimens were polished along a direction parallel to tension using standard metallographic procedures and observed using a scanning electron microscope (SEM) to study the crack initiation and propagation behaviors.

3. EXPERIMENTAL RESULTS AND DISCUSSIONS

3.1 Mechanical properties of the hypereutectic Al-Si-Xs composites

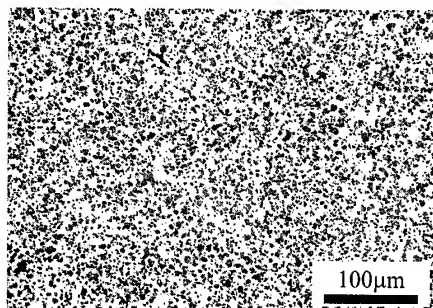


Fig. 1 Optical micrographs of spray formed and extruded Al-18Si-Xs composite.

As fine Si particles are dispersed in the matrix by spray forming process, spray formed hypereutectic Al-Si-Xs preforms can be easily extruded and become smart MMC as shown in Fig.1.

The elastic modulus of the hypereutectic Al-(18-25)Si-Xs composites, which were measured using the sonic resonance test method, increased in linear relationship with Si contents, however, addition of Fe elements even in a small contents(1-1.5wt%) increased greatly the Young's Modulus as shown in Fig.2. This is thought because Fe in

Al-Si-Xs alloys forms various kind of intermetallic compounds with high Young's modulus. The critical rotation velocity(N_c) of a tubular-shaped rotating shaft increases as the specific Young's modulus(E/ξ , E ;Young's modulus, ξ ;weight) increases with the relationship of

$N_c = \alpha(F_s)(E/\xi)^{0.5}$ (where, α ; constant, F_s ; shape factor). When the rotation velocity of the shaft

approaches the critical velocity, frequency caused by the shaft revolution resonate with the natural frequency of the part and the shaft produces noise due to the resonant vibration. Regarding the specific Young's modulus, hypereutectic Al-Si-Xs composites with Young's modulus of 85-90GPa reveal specific modulus higher than that of steel parts and comparable to that of Duralcan composite(20%Al₂O₃/6061Al). These experimental results show that the hypereutectic Al-Si-Xs composite is suitable for a high Young's modulus material.

The tensile strength and elongation of the Al-(18-25)Si-Xs composites, which were fabricated with different contents of minor elements, different spray forming conditions, and different heat treatment conditions, are plotted in Fig.3. The composites can be classified in three different groups; 1) Al-25Si-Xs composites(solid line), 2) Al-18Si-Xs composites(dot line), and 3) the other Al-18Si-Xs composites(dashed line). In each case, higher contents of minor elements and severe heat treatment result in higher strength and lower elongation. As the amount of Si decreases from 25vol.%(solid line group) to 18vol.%(dot line group), the mechanical properties are improved because lower content of Si makes less internal defects such as pores in matrix between Si particles which are formed during extrusion due to bad metal flow obstructed by Si particles. The mechanical properties of Al-18Si-Xs composites along dashed line(with higher gas/metal ratio and higher gas pressure) are superior to those of another Al-18Si-Xs composites along dot line, this is because higher gas/metal ratio and higher gas pressure form fine microstructure of the composites. Details on the compositions, spray forming conditions, and heat treatment conditions of the tested samples are available elsewhere[9]. These experimental results show that tailoring of the mechanical properties of the hypereutectic Al-Si-Xs composites is possible by designing the composition, process parameters and heat treatment path,

which could be assisted by the studies on the fracture mechanism of the composites.

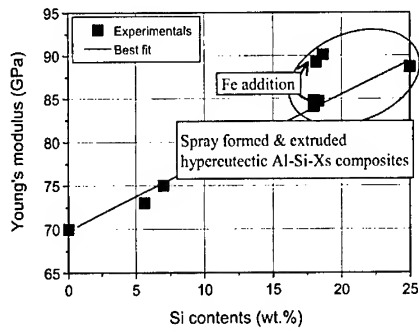


Fig. 2 The variation of Young's modulus with respect to varying Si contents in Al-Si-Xs composites.

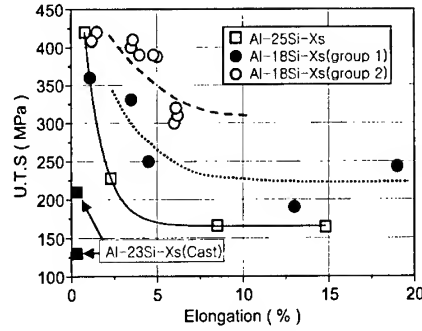


Fig. 3 Tensile properties of S.F. & extruded Al-Si-Xs composites.

3.2 Fractographic observations

As shown in Fig.3, fracture elongations of the composites decreased rapidly with increasing tensile strength. Among these composites, two different types of composites, sample **A**(hard/brittle) and sample **B**(soft/ductile) as characterized by the stress-strain curves in Fig.4, were selected and tested under tension to investigate the fracture mechanisms operative in these composites. The preparation conditions and mechanical properties of the sample **A** and sample **B** are listed in table 1.

Table. 1 Physical properties of the sample A and sample B.

	Chemical composition	UTS (MPa)	ϵ_f (%)	E (GPa)	Heat treatment
Sample A	Al-25Si-3.67Cu-1.11Mg-0.4Fe	420	0.8	90	T6
Sample B	Al-25Si	164	15.8	89	F

(ϵ_f (%); elongation, F: as-fabricated, T6: 495°Cx 3hrs, quenching, 190°Cx 10hrs)

After fracture test, the microstructures were recorded from the side surfaces of the fractured samples using SEM. In sample **A**, which was fractured under the tensile stress of 420MPa, most cracked Si particles were seen in the vicinity of the main crack as shown in Fig.5(a) and (b). On the other, in sample **B**, which experienced only about 165MPa of the tensile stress, cracks have been developed uniformly through out the gage length of the specimen as shown in Fig.5(c) and (d). It is of interest to know the reason why Si particles were fractured under the low tensile strength of 165MPa.

3.3 Fracture Mechanism of the Sample A and Sample B

As shown in Fig. 5, cracks are initiated inside of the Si particles because Si particle has many habit planes, which is different from the ceramic reinforced MMCs. When a crack is developed inside of a Si particle in sample A, both matrix around the Si particle and the neighboring Si particle should experience higher stress which was transferred from the cracked Si. Therefore, sequential cracks can be developed in another Si particles nearby the previously cracked Si particle due to the load transfer from

the cracked one, and then, the matrix between both cracked Si particles should fail under ultimately high tensile stress which was transferred from the both cracked Si particles as can be shown in Fig.6.

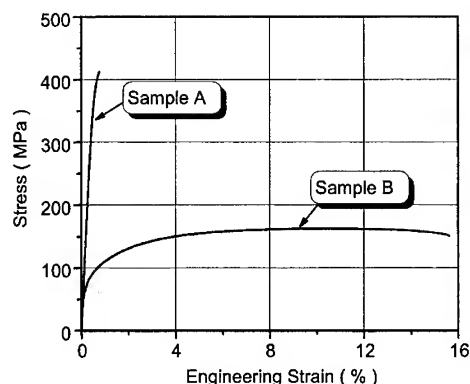


Fig. 4 The stress-strain curves of the two different Al-25Si-Xs composites.

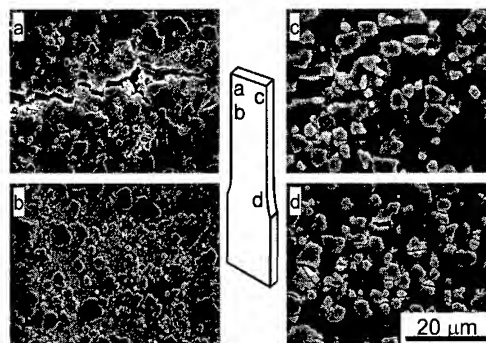


Fig.5 SEM images observed (a),(b) from sample A, and (c),(d) from sample B, after fracture test.

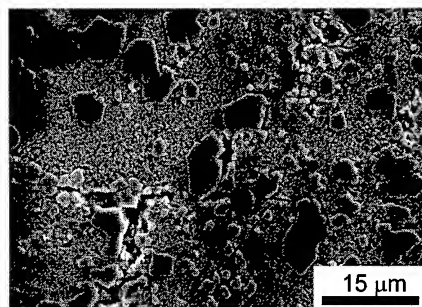


Fig. 6 SEM micrographs showing the frontier of main crack developed in the sample A.

In the case of the sample B with soft/ductile matrix, lots of cracks are developed inside of Si particles all over the sample, which experienced only 165MPa tensile stress. However, ultimate stress can be imposed on the Si particles even under low stress as shown in Fig. 7 when the strain is increased. The microstructures of the test samples were observed after interrupting the tensile test at elongation of 3%, 5%, 7%, and 9% using SEM. Few cracked Si particles are observed in the composite at the engineering elongation of 3%(Fig.8(a)) and 5%(Fig.8(b)), however, some Si particles begin to be cracked under 7%(Fig.8(c)) elongation. Furthermore, numerous cracked Si particles are seen when the sample has been elongated up to 9%(Fig.8(d)). Eventual fracture takes place at about 16% engineering elongation, therefore, lots of cracks can be developed inside Si particles all over the sample after 7~9% elongation because ultimate stress is imposed on Si particles from plastic-deformed matrix.

3.4 How to improve the tensile properties of the composites?

Soft/ductile matrix is not desirable for high-strength Al-Si-Xs composites as Si particles should be damaged with high strain even under low stress. Hard/brittle matrix is not also acceptable because a developed crack makes sequential cracks in neighboring Si particles, resulting in sudden fracture of the composite. If hard/tough alloy is used as a matrix of the composite, it would be helpful to achieve a composite with high strength as well as reasonable elongation because the developed or existing crack could not propagate through the matrix easily. Fine Si particles are also desirable because small crack inside of small-sized Si particle cannot propagate through matrix easily, which has been certificated by experiments as shown in Fig. 3 by using high gas/metal ratio and high gas pressure during spray

forming.

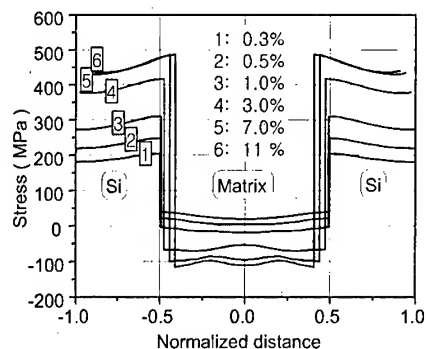


Fig. 7 Internal normal stress distribution imposed on Si particles and matrix with increasing elongation.

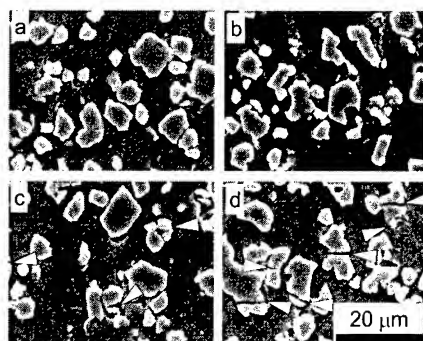


Fig. 8 SEM images observed in sample B after (a) 3% elongation, (b) 5% elongation, (c) 7% elongation, and (d) 9% elongation.

5. CONCLUSIONS

Various hypereutectic Al-Si-Xs composites were prepared and evaluated for the application as a structural material requiring high Young's modulus as well as reasonable tensile properties. The specific Young's modulus of the composite was high enough to be comparable to that of steel and Duralcan composite which have drawbacks of heavy weight and high production cost, respectively. It was also known that the tensile properties were possible to be tailored by varying matrix system, spray forming conditions, and heat treatment conditions.

REFERENCES

1. P. Van Mourik, E.J. Mittemeijer, Th.H. De Keijser, J. of Mater. Sci. 18 (1983) 2706-20
2. S. P. S. Sangha, D.M. Jacobson, A. J. W. Ogilvy, M. Azema, A. Arun Junai, and E. Botter, Materials, 1 (1997) 195-201
3. H. Sano, N. Tokizane, Y. Ohkubo, and K. Sibue, Powder Metall. 36 (1993) 250-1
4. H. Sano, N. Tokizane, Y. Ohkubo, and K. Shibue, Sumitomo Light Metal Technical Reports (1994) 123-130
5. T. Hayashi, Y. Takeda, K. Akechi, and T. Fujiwara, SAE Tech. Paper Series, no. 900407 (1990)
6. E. Koya, Y. Hagiwara, S. Miura, T. Hayashi, T. Fujiwara, and M. Onoda, SAE Tech. Paper Series, no. 940847 (1994)
7. Scarlett, Engine Technology International, 3 (1998) 54-7
8. P.J. Ward, H. V. Atkinson, P.R.G. Anderson, L.G. Elias, B. Garcia, L. Kahlen, and J-M. Rodrigue-Ibabe, Acta Mater. 44 (1996) 1717-27
9. H. K. Seok, H.I. Lee, B.J. Kim, and J.C. Lee, J. Kor. Inst. Met. Mater., 38 (2000) 892-8

PARTICLES REFINEMENT IN ALUMINUM COMPOSITE SLURRY FORMED BY LIQUID/PARTICLES REACTION AND ITS WEAR PROPERTIES

Masato Tsujikawa*, Makoto Hino** and Makoto Kawamoto*

*College of Engineering, Osaka Prefecture University
Gakuen-cho 1-1, Sakai-shi, 599-8531 JAPAN

**Industrial Technology Institute of Okayama Government
5301 Haga, Okayama, 701-1296 JAPAN

ABSTRACT

A new method is introduced to prepare the fine alumina particles dispersion Al-Si alloy composite slurry for casting. The method involves thermit reaction in molten Al-Si alloy with charging coarse silica particles into stirred vortex of molten alloy. The particles change into firm and fine sponges of alumina filled with melt, without changing their size or shape. By continuous stirring after the reaction, these fine alumina network become spheroidally independent, during the grain growth process. Then, the separation and the dispersion of these small alumina occur in the shear flow. In the optimized condition, average particle size of 2.6 μm was achieved using 160 μm silica particles. The dry sliding wear test revealed the excellent anti-wear property of the composite specimens prepared by this method.

1. INTRODUCTION

Ceramic particle dispersion Al_2O_3 alloy composite is one of the best wear resistant material because of its high abrasion resistance, anti seizure properties and high thermal conductance. Simultaneously, casting is an ideal forming method for these materials with poor machinability. For net shape forming by casting, we need particles dispersion Al alloy slurries as raw material.

The stirred vortex method is the simplest way to disperse the ceramic particle into molten metal. However, the dispersion of non-metallic particles into the molten metal is not easy due to the poor wettability between them. The difficulty increases with decrease in particles size.

To overcome this problem of wetting, active elements such as Mg and Ca etc. were added for improvement of the wettability, and the partially solidified state of matrix has been used to incorporate particles compulsory by its high viscosity. However, the composites prepared by these methods have weak and dirty interface of spinel, insufficient adhesiveness at the metal/particle interface.

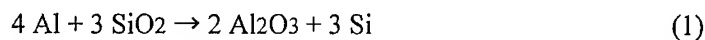
A method to prepare smaller Al_2O_3 particle dispersion Al alloy slurry by large SiO_2 particles addition is introduced in this paper. The method contains two steps: (1) in situ

preparation of Al₂O₃ in molten aluminum by reaction of coarse SiO₂ and the melt [1-8], and (2) dispersion of fine Al₂O₃ particles into matrix during isothermal stirring. Small surface area of coarse SiO₂ particles to be wet contributes to easy incorporation of particles into melt, with the help of thermit reaction. Though the volume of particles should reduce to 73 % after the reaction, the shape and size of particles remain same as charged silica, in appearance. This means the internal microstructure of reacted particle is porous [2, 6, 8]. The TEM observation of reacted SiO₂ revealed that the reacted particles have a fine network of alumina filled with aluminum [6].

Therefore, there is a possibility of the isolation of smaller Al₂O₃ from reacted network driven by the high interfacial energy of such a fine network of Al₂O₃ during isothermal holding at the proper temperature under the shear flow condition.

2. EXPERIMENTAL PROCEDURE

700 g of Al-12mass%Si alloy was melted in the alumina crucible for each of the batches. Then they were stirred to make a vortex at specific temperature from 1023K to 1273K. Preheated SiO₂ particles with 160 μm in average diameter were charged into the vortex. The following reaction begins.



This exothermic reaction generates 608 J per one mole of SiO₂. The SiO₂ is reduced, and the Al₂O₃ is formed. Produced Al₂O₃ is the α-Al₂O₃ [2]. The slurries with molten alloy and reacted particles were kept stirring at specific temperature until the pouring into a graphite mold. The duration of the longest experiment was 43.2 ks. During isothermal stirring; small amounts of composite slurry were scooped several times for microscopic observations.

3. RESULTS

3.1 Effect of temperature on small alumina dispersion

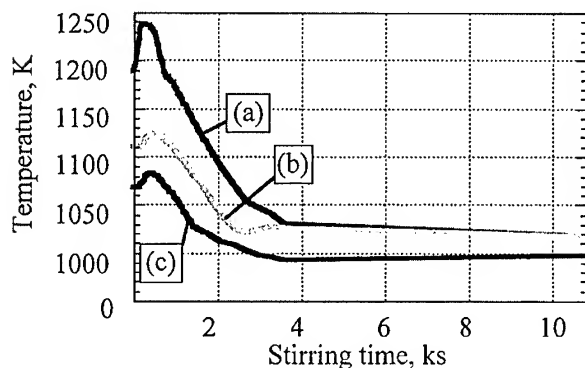


Fig. 1 Examples of thermal cycle during stirring (15 Hz).

The result of three typical experiments with different thermal conditions is shown in Fig. 1, and Fig. 2. The input of silica particle was 10 vol% for each of the batches. When silica particle was put into the melt, the temperature gradually increases by exothermic reaction. After the peak temperature, the samples were kept isothermally at specific temperature under

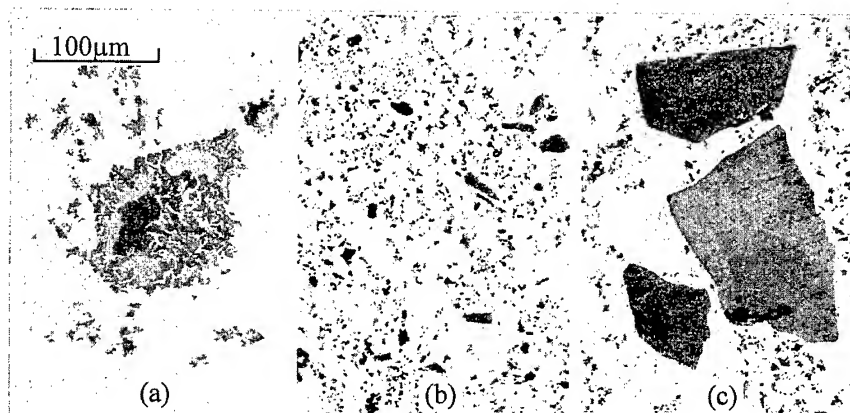


Fig. 2 Influence of thermal condition on dispersion of fine alumina particles. Photos correspond to the thermal cycles in Fig. 1.

stirring.

The microstructures of these samples, stirred for 3.6 ks, are shown in Fig. 2. The sample (c), which had been exposed to lowest thermal condition, has large particles after reaction. The clear outline around the particles is observed. Inside of the particle is fine structure. The shape and size of these large particles are almost same as that of material silica particles [2]. The breakup of a large particle is obvious in sample (a)[9]. However, even after the these long isothermal stirring, large part of the reacted particles were large. On the other hand, there are almost no large particles in Fig. 2(b). Small dispersion of Al_2O_3 in the matrix is observed. Fig. 3 shows the particle size distributions of specimen Fig. 2(b) and SiO_2 particles before reaction. It was possible to disperse small alumina of 2.6 μm in diameter by large 160 μm SiO_2 particles addition.

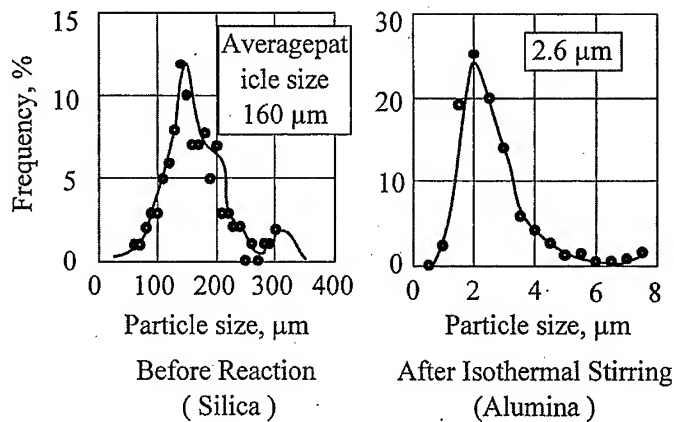


Fig. 3 An example of change in particle size at before and after the treatment

3.2 Microstructure of reacted particles

In the reaction of equation (1), the volume of produced Al_2O_3 is only 73 vol% of material SiO_2 . Simultaneously, the shape and the size of reacted particles were almost equal to those of the material silica particles. Therefore, the reacted particle is not solid alumina, but a complex particle of produced alumina and Al alloy melt.

Fig. 4 (a) and (b) shows optical micrographs of reacted silica just after reaction (a) and isothermally held for 3.6 ks (b) at 1123 K. In Fig. 4.(b), we can see the thick transparent

alumina phases tangled each other in the aluminum matrix. Clearly, the reacted microstructure is coarsened during isothermal holding. The TEM micrograph of sample (a) is shown in (c) with electron beam diffraction pattern. It shows that the structure of particles just after the reaction is consist of fine Al_2O_3 grains of 100 nm size and aluminum [6].

Fig. 4(d) is a SEM micrograph of the fracture surface of the reacted particles isothermally held at 1123 K. Aluminum metal was removed by the alkali aqueous solution before the SEM observation. We can see the grain growth process in which the fine Al_2O_3 network at the left hand side change too thickly tangled mass as shown in the right hand side. At the center of the micrograph (d), there is a zone of independent particles with diameter about 10 μm .

3.3 Effect of stirring speed on the dispersion of Al_2O_3

The experiment to investigate the effect of stirring speed on the refinement of the alumina particle is shown in Fig. 5 and 6. Frequency of rotation of the stirrer was 15 Hz or 20 Hz. Microstructures of these samples are shown in Fig. 6. At 15 Hz, complete dispersion of the alumina did not occur. Reacted particles has coarse inner microstructure by the excess grain growth, and the shape of the silica particle has

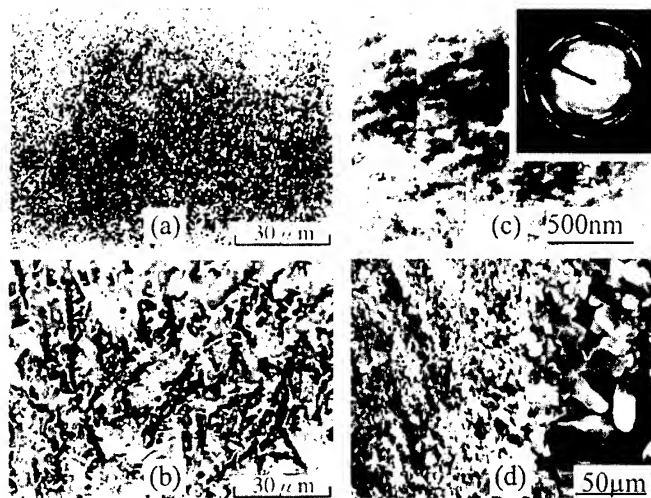


Fig. 4 Microstructures of reacted particles. (a), (b) Cross section view after isothermal stirring. (a):at 1123K for 0.3 ks, (b): at 1123K for 3.6 ks. (c); TEM micrograph immediately after the reaction. (d); SEM micrograph of fracture surface after reaction.

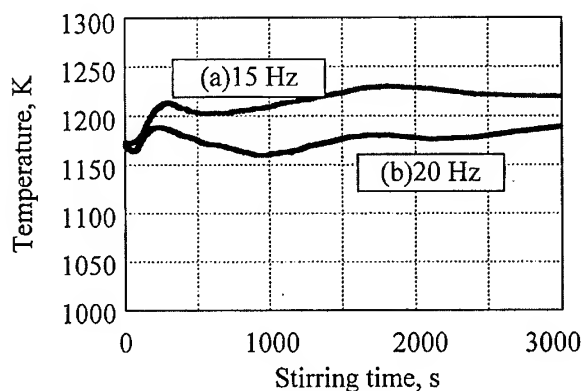


Fig. 5 Thermal cycles for experiment on stirring speed dependence in dispersion.

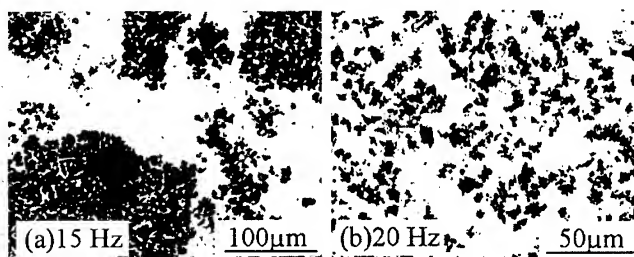


Fig. 6 Effect of stirring speed on dispersion of fine alumina particles. Photos correspond to thermal cycle in Fig. 5.

mainly remained. Contrary, it is proven at 20 Hz that reacted particle has finely dispersed in the matrix under the almost equal temperature condition at the 15 Hz experiment.

3.4 Wear property

Wear rates of pin specimens against annealed 0.6%C steel discs are shown in Fig. 7 compared with the result of Al-Si alloy and pure aluminum. The sliding speed was 3 m/s, and the load was 49 N. Tests were carried out in atmospheric environment under dry condition. Composite materials show great anti-wear property.

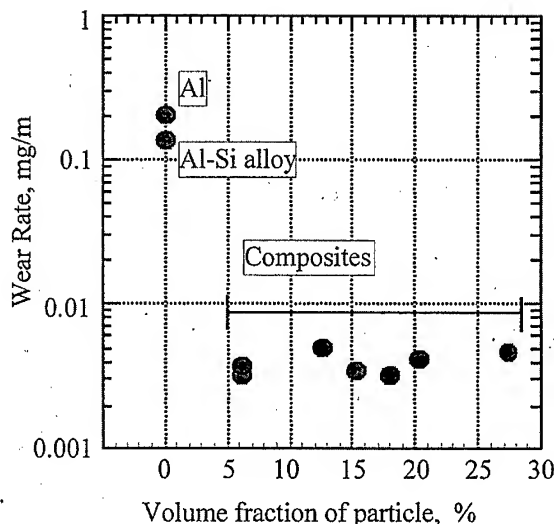


Fig. 7 Wear of materials

4. DISCUSSION

As shown in Fig. 4, the small dispersion mechanism of reacted particle under stirring at high temperature is based on the independence of alumina particles during grain growth. This is a process by the diffusion similar to the spheroidizing of tabular cementite in the pearlite of carbon steels during spheroidizing annealing.

The degree of diffusion of some stirring experiments is shown in Fig. 8. The time-temperature curve of each experiment was translated to the time-diffusion rate curve. Then the

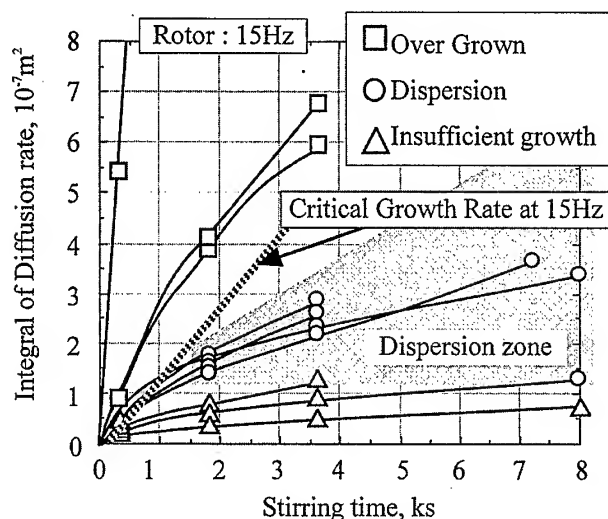


Fig. 8 Effect of grain growth rate on small alumina particle dispersion.

time-diffusion rate curves were integrated with time. Consequently, the Y-axis indicates the degree of diffusion. It is proven that lower limit of the Y-axis value exists for the small dispersion of alumina. This lower limit is the necessary condition of the grain growth for being independent in spheroidal shape of which the dispersion is possible.

However, it is also proven that the thick tangling of Al_2O_3 has been formed by the excess grain growth [10], when the diffusion is too fast. There is the critical growth rate, beyond which the

excess growth lead to tangling, the dispersion of small particles does not happen.

In the investigation of the effect of stirring speed, it was shown that small dispersion of Al_2O_3 was possible by higher stirring speed even at higher temperature. This is shown in Fig. 9. The critical grain growth rate increases with increasing stirring speed. It is shown the possibility of shortening the processing time for the small dispersion within 1000 s.

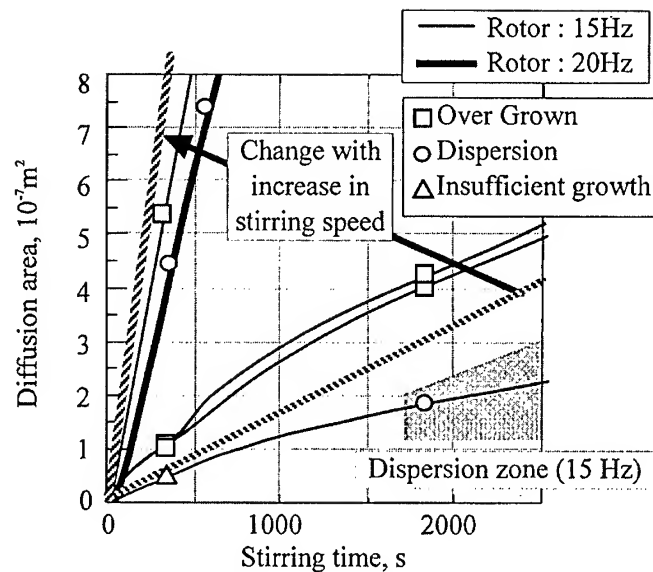


Fig. 9 Small alumina dispersion by high speed stirring at higher temperature in short period.

6. CONCLUSIONS

The composite material with dispersion of the small alumina particle was obtained by mixing coarse silica particle into Al alloy melt. The alumina particle of 2.6 μm in average size dispersed using the silica of 160 μm . It was clarified that higher stirring speed can shorten the small dispersion process with higher processing temperature. It was clarified that the composite prepared by the method mentioned in this paper have excellent wear property under dry sliding condition.

REFERENCES

1. M. Kobashi and T. Choh, "KEI-KINZOKU", Vol. 42(1992), pp. 138-142, in Japanese.
2. M. Tsujikawa, T. Hashimoto, M. Kawamoto, Trans. The Japan Foundrymen's Society, Vol. 12(1993), pp. 82-87.
3. S. G. Fishman, In-Situ Composite Science and Technology, ed. by M. Singh and D. Lewis, The Minerals, Metals & Materials Society, Pittsburg, PA (1994).
4. W. Liu, U. Koester, Mater. Sci. Eng. A, Vol. 210(1996), pp. 1-7.
5. M. R. Hanabe and P. B. Aswath, J. Mater. Res., Vol. 11(1996), pp. 1562-1569.
6. N. Yoshikawa, A. Kikuchi, S. Taniguchi, Mater. Trans., JIM, Vol. 41(2000), pp. 399-405.
7. W. G. Fahrenholtz, D. T. Ellerby, K. G. Ewsuk, R. E. Loehman, J. American Ceramic Soc., Vol. 83(2000), pp. 1293-1295.
8. T. Watari, T. Torikai, W. P. Tai, O. Matsuda, J. Mater. Sci., Vol. 35(2000), pp. 515-520.
9. R. Asthana, Solidification Processing of Reinforced Metals, Trans Tech Publications Ltd (1998) p. 325.
10. N. Mizutani, T. Ogihara, M. Kondo, M. Ikeda, K. Shinozaki, J. Materials Sci., Vol. 29(1994) pp. 366-372.

DRY SLIDING WEAR BEHAVIOR OF ALUMINUM ALLOY MATRIX COMPOSITES REINFORCED WITH CARBIDE PARTICLES PRODUCED BY A PRESSURELESS INFILTRATION TECHNIQUE

Seung-Hyun Kim, Hyoung-Chul Park, Hoon Kwon, and Yong-Suk Kim

School of Metallurgical and Materials Engineering
Kookmin University, Seoul 136-702, Korea

ABSTRACT

Dry sliding wear behavior of Al-3 wt. % Mg and 6061Al matrix composites reinforced with SiC, TiC, and B₄C particles manufactured by a pressureless infiltration technique was investigated. Pin (Ball)-on-disk wear tests under various applied load conditions were carried out using hardened steel and alumina balls as counterpart materials. The effects of the varying size and volume fraction of the carbide particle, kinds of carbides, and heat treatment of the composites together with the effect of the different counterpart materials on the wear were studied. Worn surfaces of the composite as well as cross sections of them were examined with optical and electron microscopy. Wear resistance of the composite increased with the increase of the size and volume fraction of the reinforcing particle. Among the composites tested, the SiC reinforced composite showed the lowest wear resistance. Mild abrasive-like wear was accompanied with low wear rates, while massive and severe delamination wear resulted in high wear rates. Matrix hardening by a heat treatment was found to play an important role in increasing wear resistance of the composites. At low loads the steel counterpart gave rise to lower wear rate than the alumina ball for the composites.

1. INTRODUCTION

The use of aluminum-matrix MMCs with hard ceramic particles increases in many applications including automobile, aerospace, and electrical industries due to their high specific strength and stiffness, thermal and electrical conductivity. Their excellent wear resistance is also known and the composites are becoming very appealing wear-resistant materials. Many research works have been done on wear-behavior characterization of the composite [1-8]. It is now generally accepted that composites are more wear resistant than monolithic alloys and wear resistance of the composite increases with the increase of volume fraction and size of the reinforcing particles.

Wear characteristics are quite changeable depending on system variables such as test methods and test conditions. A manufacturing process of the composite will also affect the wear behavior and characteristics of it. Most of the previous works on wear of the composite treated composites fabricated through conventional powder metallurgy or casting processes and wear-test equipments used were typically pin-on-disk or block-on-ring type testers [1-7]. Therefore, it is necessary to carry out different type wear tests of composites manufactured by different processing methods to understand wear characteristics of the composite more generally. The present work discusses wear characteristics of Al alloy matrix composites that were manufactured by a pressureless infiltration technique (the PRIMEX process). A ball-on-disk (round-ended pin-on-disk) type wear tests were performed on the composites. The manufacturing technique employs spontaneous infiltrations of a molten Al alloy into a ceramic (carbide) perform at a nitrogen atmosphere under a pressureless condition. The process is known to be effective in reducing reinforcement damage and segregation of carbide particles during fabrication. However, many reaction products are reported to form at the

interface between the reinforcing carbide particle and the Al alloy matrix [8].

In the present work, dry sliding wear behavior of Al-3 wt.% Mg and 6061 Al matrix composites reinforced with SiC, TiC, and B₄C particles manufactured by a pressureless infiltration technique was characterized. The size and volume fraction of the reinforcing carbides were varied and their effects on the wear behavior were investigated, especially, relating wear characteristics with the interface reaction and matrix-microstructure modification by the carbides. Dry sliding wear tests were carried out using a ball-on-disk type wear tester at room temperature varying applied load. The effects of the varying size and volume fraction of the carbide particles, carbide species, and heat treatment of the composites together with the effect of the different counterpart materials on the wear were studied. Few works are reported regarding the counterpart-material effect until now. Worn surfaces as well as subsurface were examined and the wear mechanism of the composites was also investigated.

2. EXPERIMENTAL PROCEDURES

Al-3 wt.% Mg alloy reinforced with SiC particles (SiC/Al-3Mg) and 6061Al alloy reinforced with SiC, TiC, and B₄C particles (SiC/6061Al, TiC/6061Al, and B₄C/6061Al) were used as experimental composites. Monolithic alloys of Al-3Mg and 6061Al were also tested. The composites and the monolithic alloys were fabricated through the pressureless infiltration method (the PRIMEX process). Size and volume fraction of the reinforcing carbides were varied from 7μm to 40μm and from 10% to 30%, respectively. The manufactured composite ingots were cut to 100 x 70 x 70mm blocks and then hot-extruded with the extrusion ratio of 8:1 at 450°C. Wear test specimens were consequently machined from the hot-extruded composite bars. The wear specimen had a disk shape with a diameter and thickness of 25mm and 7mm, respectively. The 6061Al matrix composites and the monolithic 6061Al alloy specimens were tested in an as-extruded state and also after a T6 heat treatment. The T6 heat treatment condition was a solution treatment at 529°C for 2 hours followed by a peak aging at 177°C for 8 hours. The disk specimens were grinded and polished before the test.

Dry sliding wear tests were carried out in the air at room temperature by using a ball-on-disk wear tester. As a mating material to the composite disk specimen, heat-treated AISI 52100 bearing steel and alumina balls were used. Their hardness values were HV 845 and HV 1800, respectively. A new ball was used for each test and diameter of a wear track on the disk was maintained constant so that a uniform wear test condition was maintained. Applied load (wear load) was varied from 1N to 12N. Sliding speed and sliding distance were kept constant as 0.2m/s and 1000m, respectively. Friction coefficient (μ) was measured continuously during the test. Wear rates of the composite disk specimen were calculated by dividing the weight loss of the specimen by the density of the specimen and the sliding distance. The weight loss was measured to the accuracy of 10⁻⁵ g using an electronic balance.

We also observed worn surfaces and cross sections of the composite disk specimens by SEM to examine the nature of wear and subsurface deformation and cracking.

3. EXPERIMENTAL RESULTS AND DISCUSSIONS

3.1 Mechanical Properties

Table 1 provides room-temperature hardness and 0.2% offset yield strength of the composites and monolithic alloys used in the present study. The table shows that increasing volume percent of the reinforcing carbide results in the increase of the yield strength as well as the hardness. It is to be noted that composites with the same carbide volume percent but with different size have similar mechanical properties. The larger SiC particles do not always improve the mechanical properties of the composite. Among the composites tested, the TiC reinforced composites showed superior mechanical properties to SiC and B₄C reinforced

composites, which confirmed the previously reported result [6]. The strengths of all the 6061Al matrix composites and the 6061Al monolithic alloy are shown to increase nearly about two times after peak aging heat treatments.

Table 1 Mechanical Property of the specimens used in the present study

Material	As-Extruded		T6-heat treatment	
	0.2% σ_y (Mpa)	Hardness (H_{RB})	0.2% σ_y (Mpa)	Hardness (H_{RB})
Al-3 wt.% Mg	131	58 (H_{R15T})	-	-
Al-3Mg- (20 μm , 10%) SiC _P	164	25	-	-
Al-3Mg- (10 μm , 20%) SiC _P	191	38	-	-
Al-3Mg- (20 μm , 20%) SiC _P	190	35	-	-
Al-3Mg- (40 μm , 20%) SiC _P	200	38	-	-
6061Al alloy	123	55 (H_{R15T})	304	61
6061Al- (10 μm , 10%) SiC _P	133	67 (H_{R15T})	421	76
6061Al- (10 μm , 20%) SiC _P	187	27	437	83
6061Al- (20 μm , 10%) SiC _P	135	71 (H_{R15T})	393	76
6061Al- (20 μm , 20%) SiC _P	174	9	414	79
6061Al- (7 μm , 10%) TiC _P	145	17	439	80
6061Al- (7 μm , 20%) TiC _P	205	42	439	80
6061Al- (24 μm , 10%) B ₄ C _P	171	71 (H_{R15T})	395	76

3.2 Wear Test Results

Figure 1 shows the wear-rate variation of the SiC/Al-3Mg composites with different SiC particle size as a function of applied load. Wear rates of the monolithic Al-3Mg alloy are also given in the figure. Wear rates of all specimens increase as the applied load increases, though each has a different wear-rate-increase slope. The wear rate of the Al-3Mg alloy is higher than all the composites under the given test conditions. Among the composites, the Al-3Mg-SiC (40 μm , 20%) specimen shows the highest wear resistance. The figure reveals that there exist different wear rate regimes depending on specimens. The Al-3Mg alloy and the Al-3Mg-SiC (10 μm , 20%) specimens have two regimes of wear-rate increase: one is a slow-increase regime below the applied load of 7N and the other is an abrupt increase regime at high loads. On the other hand, the two specimens, Al-3Mg-SiC (20 μm , 20%) and Al-3Mg-SiC (40 μm , 20%), show two different wear-rate regimes. The first one is characterized by very low wear rates occurring at low loads. The low rates at the first regime increase to about $5 \times 10^{-13} \text{ m}^3 \text{ m}^{-1}$ and remain relatively constant at the second regime. The different wear rates at the first and the second regime indicate that different wear mechanisms prevail at both regimes. It is also to be noted that the transition from the first regime to the second one occurs at different loads for the two composites. The effect of the reinforcing particle size on the wear rate is also shown in Fig. 1. It is evident that bigger SiC particles result in superior wear resistance. The effect is more significant at low loads.

Figure 2 shows the wear-rate variation as a function of applied load for the SiC/6061Al composites. As in Fig. 1, all composites have higher wear resistance than the monolithic alloy. The composite with larger SiC particle and higher volume fraction shows lower wear rate. The 6061Al-SiC (20 μm , 20%) composite maintains very low wear rate at all test loads. Some researchers have reported that wear rates of a composite and a matrix alloy become comparable at high loads due to cracking and fracture of the interface between the matrix and the reinforcing particle [2, 5]. In the present study wear rates of all composites are always lower than that of the monolithic alloy, which shows that the pressureless infiltration technique produces composites with good mechanical properties and a sound interface. The effect of volume fraction of reinforcing particles on wear of the composite is well displayed in

Fig. 2. Increasing volume fraction of a reinforcing particle seems to be more efficient than increasing the size of it to improve wear resistance of a composite.

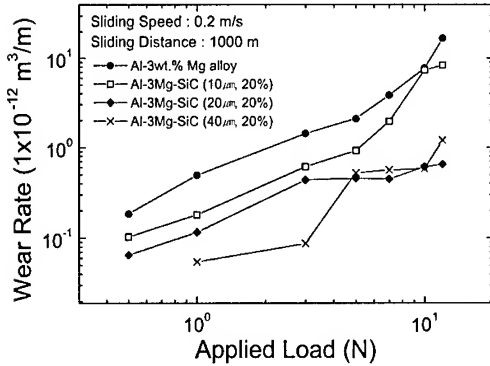


Fig. 1. Variation of wear rate with applied load for Al-3Mg alloy and Al-3Mg-SiC composites.

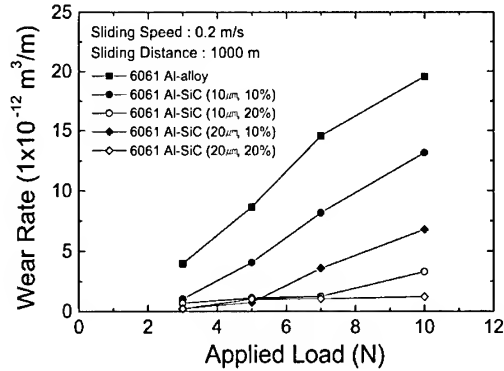


Fig. 2. Variation of wear rate with applied load for 6061Al alloy and 6061Al-SiC composites.

Wear rates of 6061Al matrix composites reinforced with different carbide particles are compared in Fig. 3. Both of the 6061Al-SiC (10 μ m, 10%) and 6061Al-SiC (20 μ m, 10%) specimens show rapidly increasing wear rates with applied loads. On the other hand, the wear rate of the 6061Al-TiC (7 μ m, 10%) remains low until the load of 7 N and the 6061Al-B₄C (24 μ m, 10%) exhibits the lowest wear rate at all test loads. Figure 3 indicates that the wear rate of a composite is strongly influenced by a species of reinforcing particle. It was observed that the matrix hardness of the TiC_p reinforced composite is higher than that of the other two composites. A reaction between the carbide and the 6061Al matrix, which produces reaction products in the matrix, is postulated to give the high matrix hardness in the system, since the hardness increased with the volume fraction of the TiC particle. TiC is also known to have higher fracture toughness than SiC. It was considered that the high matrix hardness and the fracture toughness of the TiC/6061Al composite resulted in the lower wear rate than the SiC/6061Al composite. Previous work has also reported that the reaction between a SiC particle and Al alloy produces brittle reaction products [8]. They partly are postulated to result in the low wear resistance of the system. It is interesting to note that the 6061Al-B₄C (24 μ m, 10%) specimen has high 0.2% yield strength, while it shows a low hardness. The high wear resistance of the 6061Al-B₄C (24 μ m, 10%) specimen at all loads seems to be related partly with the large particle size. However, considering that the effect of particle-size increase is not

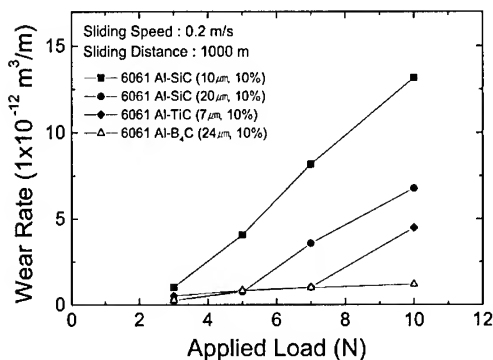


Fig. 3. Variation of wear rate with applied load for 6061Al-SiC, TiC, and B₄C composites.

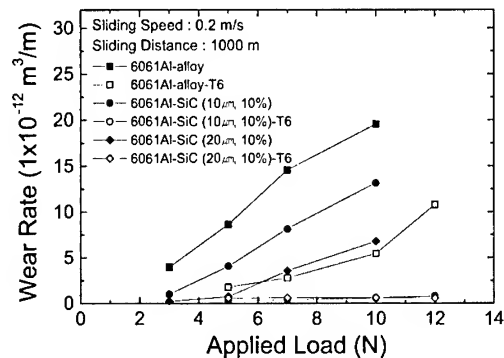


Fig. 4. Variation of wear rate with applied load for 6061Al and 6061Al-SiC composites. The effect of T6 heat treatment on wear is illustrated.

very significant in increasing wear resistance as shown in Fig. 2, the high yield strength and high hardness of the B_4C particle seem to be the main cause of the low wear rate of the B_4C_p reinforced composite.

Figure 4 compares wear rates of 6061Al alloy and SiC/6061Al composites in as-extruded and T6 heat-treated states as a function of applied load. The effect of the heat treatment on decreasing the wear rate is remarkable. The heat-treated 6061Al matrix alloy even exhibits higher wear resistance than the composites at loads higher than 5 or 6 N. The composites that previously showed high wear rates in an as-extruded state possess higher wear resistance after the heat treatment. These results strongly indicate that the matrix hardness plays an important role in determining wear rate of a composite.

The effect of the counterpart material on wear of the composites is also investigated. Figure 5 compares wear rates of SiC/6061Al composites with two different carbide-volume % tested against AISI 52100 steel and alumina ball counterparts. The figure shows that composites with the same volume % of carbides exhibit similar wear rates at high loads regardless of the counterpart material. However, the wear rate of composites tested against the steel counterpart is shown to be lower than that tested against alumina ball at low loads. The lower wear rate of the composites against the steel is explained by the formation of the mechanically mixed layer (MML) on the wearing surface of them. The layer is composed of transferred steel and oxides formed during the wear, which is known to lower the wear rate of a composite. Such a layer formation could be confirmed through SEM observations of worn surfaces and the friction-coefficient measurement during wear tests. Figure 6 shows the variation of the friction coefficient of Al-3Mg-SiC ($10\mu m$, 20%) specimens tested against the steel ball at the load of 1 N (Fig. 6 (a)) and 10 N (Fig. 6 (b)) as a function of sliding distance. The high and uniform friction coefficient of the specimen tested at 1 N indicates a metal transfer between the two materials and the formation of the MML layer.

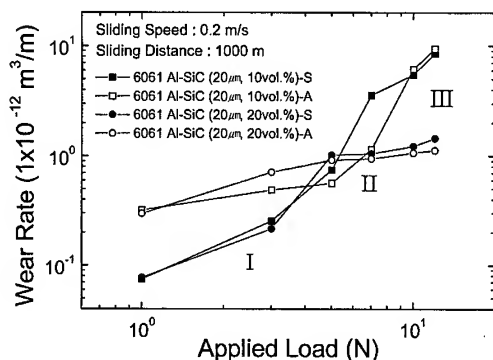


Fig. 5. Variation of wear rate with applied load for 6061Al-SiC composites. The effect of counterpart materials on wear of the composite is illustrated.

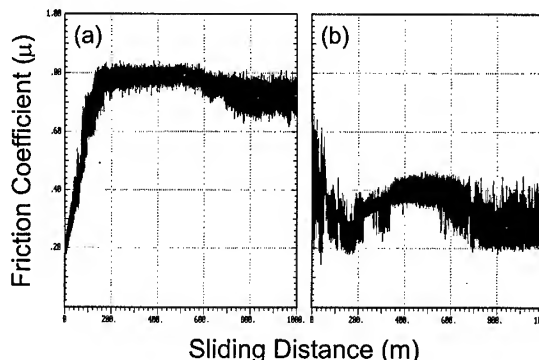


Fig. 6. Variation of friction coefficient with sliding distance for Al-3Mg-SiC (10mm, 20%) specimens tested at the load of: (a) 1 N and (b) 10 N.

3.3 SEM Micrographs of Worn Surfaces and Cross Sections

Typical SEM micrographs of worn surfaces and cross sections of the composites that experienced mild and severe wear are shown in Fig. 7. The mild-wear surface (Fig. 7 (a)) is flat and contains many abrasive-wear like scratch marks. A ferrous element was detected on the worn surface through an EDS analysis. The cross section of the specimen (Fig. 7 (b)) reveals undamaged carbide particles and confirmed the active iron transfer from the steel ball counterpart. On the other hand, the severely worn surface of the 6061Al-SiC ($10\mu m$, 10%) specimen (Fig. 7 (c)) shows galling-wear like surface with extensive deformation of the matrix. Longitudinal cross section of the specimen demonstrates that the wear occurred

through a subsurface cracking and delamination of a zone where large strain is accumulated.

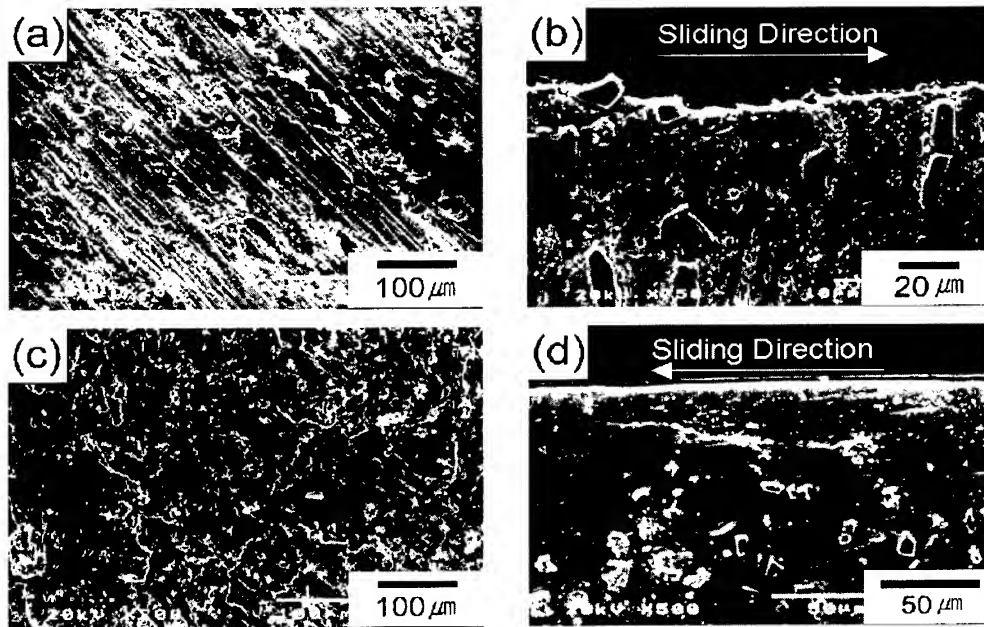


Fig. 7. SEM micrographs showing (a) worn surface and (b) cross section of Al-3Mg-SiC (20μm, 10%) specimen tested at 5 N; (c) worn surface and (d) cross section of 6061Al-SiC (10μm, 10%) specimen tested at 10 N.

4. CONCLUSION

The sliding wear behavior of the SiC, TiC, and B₄C particle reinforced Al alloy matrix composites manufactured by the pressureless infiltration technique is found to be similar to that of those by powder metallurgy and casting routes. Wear resistance of the composites increased with the increase of carbide-particle size and volume fraction. Increasing volume fraction of the carbide was more efficient in increasing wear resistance of the composite. Among the composites tested, wear resistance of the composite with the SiC particle was the lowest and the B₄C reinforcement resulted in the highest wear resistance. Matrix hardening was found to be very effective in increasing wear resistance of the composites. The AISI 52100 steel counterpart gave rise to lower wear rate of the composite than that with the alumina ball at low loads, however, at high loads similar wear rates of the composites were measured with both counterpart materials.

REFERENCES

1. A. Wang and H.J. Rack, *Mater. Sci. Eng.*, Vol.A147 (1991), pp.211-224.
2. J. Zang and A.T. Alpas, *Mater. Sci. Eng.*, Vol.A161 (1993), pp.273-284.
3. S. Wilson and A.T. Alpas, *Wear*, Vol.196 (1996), pp.270-278.
4. P.H Shipway, A.R. Kennedy and A.J. Wilkes, *Wear*, Vol.216 (1998), pp.160-171.
5. A.T. Alpas and J. Zhang, *Metall. Trans.A*, Vol.25A (1994), pp.969-983.
6. M. Roy et al., *Metall. Trans.A*, Vol.23A (1992), pp.2833-2847.
7. B. Venkataraman and G. Sandrajan, *Acta Metall. et Mater.*, Vol.44 (1996), pp.451-459.
8. K. B. Lee, Y. S. Kim, and H. Kwon, *Metall. Trans.A*, Vol.29A (1998), pp.3087-3095.

Effect of Residual Stress on the Wear Properties of SiCp/6061Al Composites

Heon-Joo Kim, Chang-Gyu Kim, Lee-Sik Oh and Jin-Ho Cheon

Department of Metallurgical Engineering
Pukyong National University
San100, Yongdang-dong, Nam-gu, Pusan 608-739, Korea

ABSTRACT

Wear properties of the 6061Al alloys reinforced with 0, 5, 10 and 20% SiC particles were studied for dry sliding against a SM45C counterface.

It was widely known that wear properties of MMCs are mainly affected by size, shape and volume fraction of reinforced materials. However, much attention has not been paid on the role of residual stress due to thermal mismatch induced between metal matrix and reinforced particle in the evaluation of wear properties of MMCs.

This study concerned with the variation of wear behaviors and residual stress according to various heat treatment conditions. Effect of residual stress in the matrix measured by X-ray diffraction method on the wear behaviors has been investigated as a function of SiC particle volume fraction, load and sliding speed for differently heat treated SiCp/6061Al composites. The highest compressive residual stress was recorded for the liquid nitrogen(LN) quenched specimen from solution temperature. Wear rate was turned out to decrease with increasing compressive residual stress. Also high compressive residual stress in the metal matrix affected wear mechanism to transit from a severe wear to a mild wear.

According to the results of present study, amount of compressive residual stress was a dominant factor in the wear properties of MMCs, in which it acts as a restraint stress to SiC particles coming off by remaining it within the matrix.

1. INTRODUCTION

In addition to their superior properties such as high specific strength, specific modulus, and creep strength, metal matrix composites(MMCs) exhibit excellent wear resistance. Interest in the tribological properties of MMCs has increased substantially because of the potential for weight savings, particularly in automotive industry. MMCs are, now, being used as the replacement for steel components. Among the MMCs, particulate reinforced MMCs have the advantage of low cost, good workability and high machinability compared with continuous fiber reinforced composites.

It is generally known that wear behaviors of MMCs are mainly affected by the shape, size, volume fraction and it's inherent fracture strength of the reinforcement, and the nature of the bond between matrix metal and the reinforcement, etc[1].

Understanding of strengthening mechanism of MMCs is helpful to comprehend general properties of MMCs. It can be explained as generation and working of dislocations formed by thermal stress due to the big difference of coefficients of thermal expansion between matrix metal and reinforcement. In other words, it means that consideration of residual stress is necessary in the evaluation of various properties of MMCs.

Effect of residual stress on wear properties was validated for hyper-eutectic Al-Si alloy in our preliminary study[2]. Many researchers have studied the influence of residual stress in the field of metal matrix composites[3-9]. However, there has been very little work on the effect of residual stress on tribological properties of particulate reinforced MMCs.

This work concerned with the variation of wear behaviors and residual stress according to various heat treatment conditions in SiCp/6061 Al composites.

2. EXPERIMENTAL PROCEDEURE

2.1 Materials and Heat treatment

The materials used were SiCp/6061 Al composites (where SiCp indicates SiC particles) manufactured by extruding a mixture of 6061 Al alloy powder and SiC particles at 843K. The volume fractions of SiC particles are 0, 5, 10 and 20% as shown in Table 1.

To investigate the effect of residual stress due to the difference of coefficients of thermal expansion between matrix metal and reinforcement, the materials were heat treated to give different level of residual stress. Four types of heat treatment procedure were devised to vary the magnitude of compressive residual stress as follows: (1) T6 aging(T6), (2) water quenching(WQ), (3) repetition of rapid heating and quenching(R.H&Q) and (4) liquid nitrogen quenching(LN) treatment[10,11] as shown in Table 2. Samples were heat treated after machining to eliminate the effect of stress induced by machining.

Table 1 Volume fraction and measurement result by an image analyzer

Material	Volume Fraction, V_f (%)	Average Size, D_p (μm)	Standard Deviation, (μm)	Average spacing*, d_p (μm)
5% SiCp/6061	4.9	6.2	4.92	119.4
10% SiCp/6061	11.2	8.6	5.56	68.4
20% SiCp/6061	21.5	11.9	7.87	43.6

*Computed from $d_p = D_p (1 - V_f) / V_f$

Table 2 Heat treatment conditions for variation of compressive residual stress.

Treatment	Treatment Procedure
T6 aging(T6)	530°C 2hr solution treatment → Water quenching → 175°C 8hr holding
Water Quenching(WQ)	530°C 2hr solution treatment → Water quenching
Rapid Heating and Quenching(R.H&Q)	530°C 2hr solution treatment → Water quenching → 5 times repeating (530°C 1min. holding → Water quenching)
Liquid Nitrogen Quenching(LN)	530°C 2hr solution treatment → Liquid nitrogen quenching

2.2 Wear Tests

Wear tests were conducted using a pin-on-disk type machine. The samples were machined to blocks of $10 \times 10 \times 10 \text{ mm}^3$ and polished to obtain an average surface roughness(R_a) of $0.35 \mu\text{m}$. The counterface disk(S45C steel plate) was heat treated to have a uniform surface hardness value of $45 \pm 2 \text{ HRC}$ and its average R_a was $0.5 \mu\text{m}$. After each test, the counterface disk was ground prior to using it again for the next test.

Wear tests were conducted in air at loads of 19.6, 49N and a sliding speed of 0.2, 1, 2m/sec for a constant distance of 4000m. Samples were cleaned with acetone in ultrasonic cleaner and weight losses were calculated from the differences in weight of samples measured before and after tests to an accuracy of 0.1mg using an electronic balance.

Unit of wear rate in this study was used volumetric wear rate(mm^3/m), that is, the wear rates measured in weight units were converted to volumetric wear rates using the density of the composites(6061Al: 2.71 g/cm^3 , SiC: 3.22 g/cm^3).

Microstructural observations were conducted using a scanning electron microscope(SEM) on worn surface.

2.3 Residual stress measurement

Residual stress was measured at the surface of wear samples before a wear test to determine the magnitude of residual stress. 2θ - $\sin^2\psi$ method by X-ray diffractometry was used on condition as shown in Table 3. It is the utilizing principles that diffracted X-rays are detected at differing diffraction angles according to variation of lattice constants of crystals if residual stress exists in materials[12].

Residual stress was calculated by the following equation[13], and the slope, $d(2\theta)/d(\sin^2\psi)$ was determined by a least square method.

$$\sigma = -\frac{E}{2(1+\nu)} \cos\theta \frac{\pi}{180} \frac{d(2\theta)}{d(\sin^2\psi)}$$

where E : Young's modulus (7.03×10^3 kgf/mm²)

ν : Poisson's ratio (0.345)

θ : standard Bragg's angle (diffraction angle of Al(331) plane : 148.7)

Table 3 Experimental conditions for X-ray stress measurement.

Method	2θ - $\sin^2\psi$ method
Characteristic X-ray	Co-K α
Diffraction plane	Al(3 3 1)
Size of irradiation mask	5mm \times 3mm
Determination mask	Half-value width method
X-ray incident beam (ψ)	0, 15, 30, 45 deg.

3. EXPERIMENTAL RESULTS AND DISCUSSION

As a result of measuring the residual stress of these SiCp/6061Al composites, the stress was turned out to be compressive.

Figure 1 shows the variation of compressive residual stress according to different heat treatment conditions. The magnitude of compressive residual stress increased in the order of T6 < WQ < R.H&Q < LN heat treatments regardless of volume fraction of SiCp. This is considered as due to the increase in dislocation density and the variation of stress state in metal matrix according to the difference in the coefficients of thermal expansion(6061Al: 23.6×10^{-6} K⁻¹, SiC particle: 4.6×10^{-6} K⁻¹) between Al matrix and SiC particle during quenching from high temperature[14-16]. Compressive residual stress also increased with increasing volume fraction of SiCp.

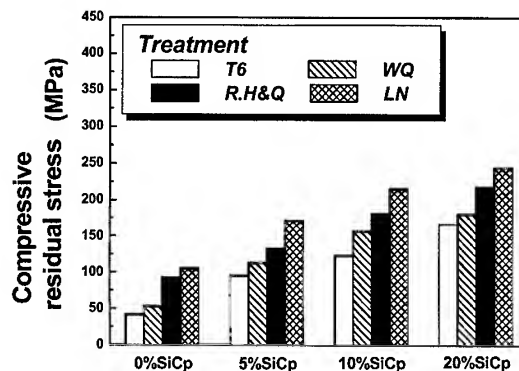


Fig.1 Effect of heat treatment condition on the residual stress of SiCp/6061Al composites.

Figure 2 shows effect of heat treatment conditions on wear rate of 5%SiCp/6061Al composite with the variation of applied loads and sliding speeds. Wear rates of T6 and WQ treated samples increased with increasing sliding speed, but wear rates of R.H&Q and LN treated samples decreased with increasing sliding speed. The improvement of wear resistance is probably ascribe to the inherent strengthening effect of matrix metal due to the increase in restraint stress against SiC particles with increasing compressive residual stress in addition to strain hardening as the sliding speed increases[17]. This phenomenon was more apparent when the applied load was increased to 49N.

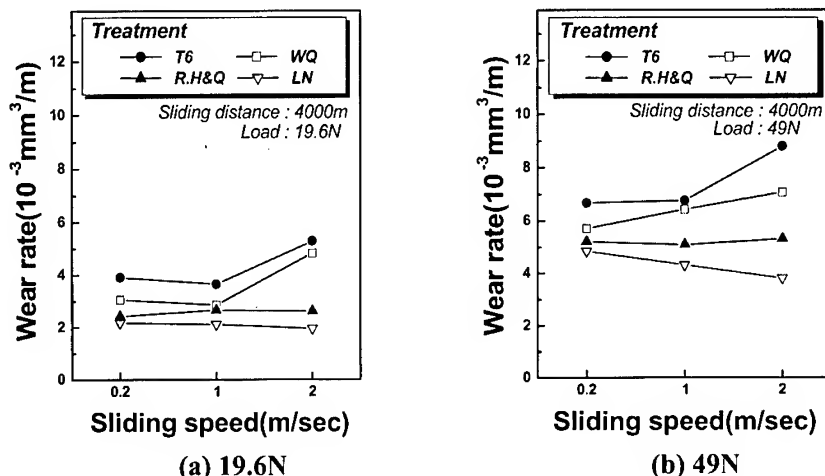


Fig.2 Effect of heat treatment on wear rate of 5%SiCp/6061Al composite tested at various applied loads and sliding speeds.

Figure 3 indicates the worn surface of the sample of 5%SiCp/6061Al composite tested at 49N, 1m/sec. In cases of T6 and WQ treated samples, severe wear is observed, in which the traces of plastic deformation of the matrix metal is shown on the worn surfaces. While, mild wear is observed for R.H&Q and LN treated samples. It could be considered that high compressive residual stress in the matrix metal affected wear mode to transit from a severe wear to a mild wear.

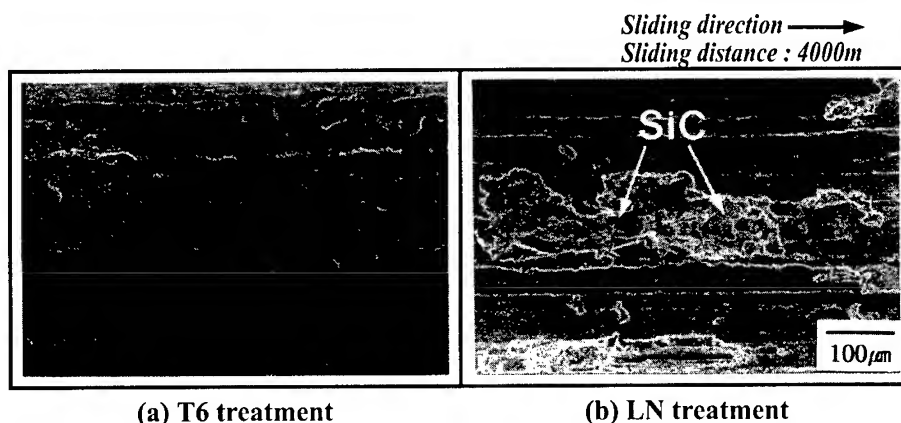


Fig.3 Effect of heat treatment condition on worn surface of 5%SiCp/6061Al composite tested at 49N, 1m/sec.

Figure 4 shows, depending on heat treatment conditions, the variation of wear rate of 20%SiCp/6061Al composite as a function of applied loads and sliding speeds. Similar to the

sample of 5%SiCp/6061Al composite, wear rate decreased for the specimen being heat treated to increase compressive residual stress. Wear rate also decreased as sliding speed increased in all heat treatment conditions. In comparison with 5%SiCp/6061Al composite, this is attributed to the high stress condition of residual stress, which hinders the breaking away of SiC particles from the sample surface, and wear debris acts a lubricant at this condition.

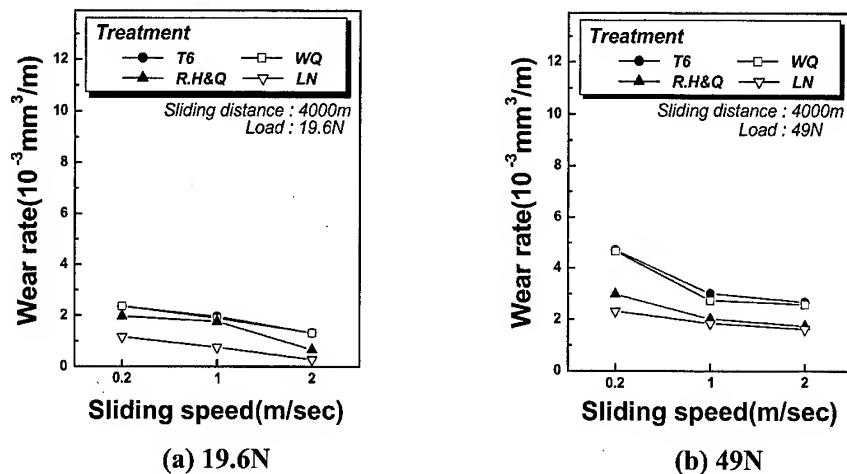


Fig.4 Effect of heat treatment on wear rate of 20%SiCp/6061Al composite tested at applied load and sliding speed.

Figure 5 exhibits the worn surface of 20%SiCp/6061Al composite sample tested at 49N, 2m/sec. Delamination and abrasive wear mode observed at T6 and LN treated samples, respectively. While deep scratches appeared on the worn surface of T6 treated sample, trace of abrasive wear was found at LN treated sample, in which compressive residual stress measured to be the highest among SiCp/6061Al composites used in this study.

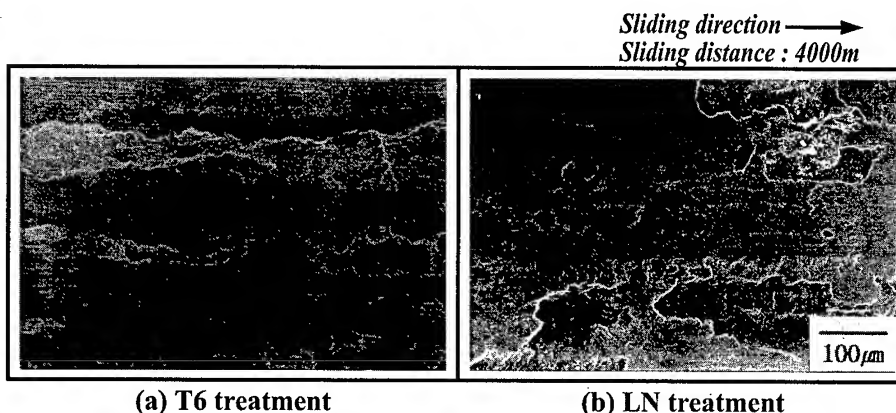


Fig.5 Effect of heat treatment condition on worn surface of 20%SiCp/6061Al composite tested at 49N, 2m/sec.

In view of the results so far achieved, it could be concluded that improvement of wear resistance is possible in SiCp/6061Al composites through the process of heat treatment which could increase compressive residual stress of matrix metal.

4. CONCLUSION

1. As the volume fraction of SiC particle increased at the same heat treatment condition, compressive residual stress increased, and it made wear rate decreased.
2. The magnitude of compressive residual stress in the composites of constant volume fraction of SiC particle increased in the order of T6 < WQ < R.H&Q < LN heat treatments. Wear rates decreased with increasing compressive residual stress in the matrix metal.
3. In case of T6 treated condition, mild wear observed in every material used for all sliding speeds at the wear load of 19.6N.
As the wear load increased to 49N, mild wear and severe wear observed at low sliding speed and high sliding speed conditions, respectively for 6061Al alloy and 5%SiCp/6061Al composite. However, mild wear always appeared in for all sliding speeds in 20%SiCp/6061Al composite.
4. In case of LN treated condition, mild wear observed in every material used for all sliding speeds at the wear load of 19.6N.
As the wear load increased to 49N, mild wear and severe wear observed at low sliding speed and high sliding speed conditions, respectively for 6061Al alloy. However, mild wear always appeared in for all sliding speeds in 5%SiCp/6061Al composite and 20%SiCp/6061Al composite.
5. High compressive residual stress of the matrix metal acts as a restraint stress to SiC particles coming off by remaining it within the matrix.

REFERENCES

1. T. W. Clyne and P. J. Withers: An Introduction to Metal Matrix Composite, Cambridge University Press, (1993), 294
2. Heon-Joo Kim and Chang-Gyu Kim: J. Korean Foundrymen's Society, 20(2000), 89
3. P. Van Houtte and L. De Buyser: Acta Metall. Mater., 41 (1993), 323
4. S. D. Tsai, D. Mahulikar, H. L. Marcus, I. C. Noyan and J. B. Cohen: Mater. Sci. Eng., 47 (1981), 145
5. K. Wakashima, B. H. Choi and T. Mori: Mater. Sci. Eng. A, 146 (1991), 291
6. K. Tanaka and T. Mori: Acta Metall., 21 (1973), 571
7. C. T. Kim, J. K. Lee and M. R. Plichta: Metall. Trans. A, 21A (1990), 673
8. H. M. Ledbetter and M. W. Austin: Mater. Sci. Eng., 89 (1987), 53
9. P. J. Withers, W. M. Stobbs and O. B. Pedersen: Acta Metall., 37 (1989), 3061
10. Sung-Kil Hong, Hiroyasu Teauka and Akihiki Kamio : Materials Transactions, JIM, Vol. 37, No. 3 (1996), 230
11. Sung-Kil Hong, Hiroyasu Teauka and Akihiki Kamio : Materials Transactions, JIM, Vol. 37, No. 5 (1996), 975
12. H. R. Shetty and Twu-Wei Choo : Metall. Trans., 16A (1985) 853
13. S. I. Tanaka : J. Japan Inst. metals, Meteria, 29 (1990) 924
14. D. C. Dunand and A. Mortensen : Acta metall. Mater., 39 (1991) 127
15. D. J. Lloyd : Acta metall. Mater., 39 (1991) 59
16. T. Christman and S. Suresh: Acta Metall., 36 (1988), 1691
17. J. Zhang and A. T. Alpas: Acta metall. Mater., 45 (1997) 513

ACTIVE CONTROL OF CRACK CLOSURE ACTS BY THE SHRINKAGE EFFECT OF SHAPE MEMORY TiNi FIBER EMBEDDED/POLYMER MATRIX COMPOSITE

Akira Shimamoto, Cheong Cheon Lee and Hiroshi Isui*

Saitama Institute of Technology, Saitama 369-0293, Japan

*Nihon University, Tokyo 641-010, Japan

ABSTRACT

As TiNi shape memory TiNi fiber-reinforced epoxy matrix composite with given prestrain ε_i in TiNi fiber at room temperature is subjected to temperature increase so as to exceed austenitic finish temperature (A_f), the TiNi fiber shrinks to its original length by ε_i resulting in compressive stress in the epoxy matrix. This compressive stress in the matrix was utilized to reduce K_I of a side-notched TiNi fiber/epoxy matrix composite and TiNi fiber/CFRP (Carbon fiber) matrix composite, which was confirmed by the present experiment with two types of temperature control: subjecting the composite to a constant temperature using an iso-temperature furnace. The experimental trend that $|\Delta K_I|$ increases with prestrain ε_i was in good agreement with the predictions based on the present model.

1. INTRODUCTION

Enhancement of the mechanical strength (stiffness, yield strength and fracture toughness) and suppression of the degradation damage (crack, delamination) during in service time are very important subjects in the development of engineering composite systems. Recently, the authors developed a new type of "smart" composite where shape memory TiNi fiber was used as a reinforcement and actuator to improve the mechanical properties of the composite at higher use temperatures above the inverse transformation temperature ($T > f$) of TiNi alloy [1,2,3,4] up to the present, the enhancing effects of the tensile yield strength, the suppression effect of fatigue crack propagation in TiNi fiber reinforced Al matrix composite (TiNi/Al) [5] and the increase of the fracture toughness (K-value) in a TiNi/epoxy composite have been experimentally confirmed because of the large compressive stresses in the matrix by the shape memory shrinkages of embedded fibers (refer to Fig.1).

In the present paper, shape memory TiNi fiber reinforced/epoxy matrix composites and TiNi fiber reinforced/Carbon fiber (CF) matrix composites are fabricated to re-verify the active damage control for cracks in the composite by using experimental photoelasticity method. The suppression effect of crack tip stress concentration and the increase of fracture toughness (K) are investigated. Especially, the dependencies of K value on not only the restrains of TiNi fibers but also the compressive stress domain size between a crack tip and the embedded fibers are discussed based on the analytical equivalent inclusion model for a composite.

2. TEST SPECIMEN

The experimental processing, as well as mechanical tests of TiNi/epoxy composite and TiNi/CFRP composite are described. The shape memorized TiNi fibers (Ti-50 at %Ni) of 400 μm diameter were first annealed for 30 minutes at 500°C, then quenched in ice water. Four transformation temperatures of TiNi fiber were determined: Martensite start $M_s=31^\circ\text{C}$, Martensite finish $M_f=15^\circ\text{C}$, Austenitic start $A_s=57^\circ\text{C}$, and Austenitic finish $A_f=63^\circ\text{C}$. The geometry of the composite specimen is shown in Fig.2. In order to determine the

transformation temperatures and stress-strain relations of TiNi fiber, tensile test of TiNi fiber at different temperatures (T) were implemented. The stress vs. strain curves at constant temperature: $T=20, 40, 60, 80$, and 100°C were obtained as shown in Fig.3. During the process, TiNi fibers were kept in tension with four different prestrains of 0, 1, 3, and 5%. Both ends of the TiNi fiber were fixed with the jig to prevent danger to which the shrinkage of the TiNi fiber in the matrix happened at the stage before experiment, and epoxy resin was cast with the prestrain had been maintained. CFRP (8131 TORAYCA and Toray Ltd.) used for the matrix for TiNi fiber reinforced/CFRP composite which is fiber weight 175g/m^2 and resin content rate 33%.

TiNi fiber reinforced/CFRP composite is made until the prepreg accumulated to ten layers is paved, three fibers are put, prepreg is piled up by one layer afterwards and the fiber side becomes three layers similarly. Prestrain of 0, 1, 3, and 5% were given, and made by compressing the high temperature with the hot press. Photoelastic sensitivity of the matrix in case of TiNi fiber reinforced/epoxy composite is $\alpha=0.116\text{ mm/N}$ and the fiber content rate of TiNi fiber reinforced/CFRP composite is $V_f=0.32$. CFRP used the photoelastic coating method as opaque material. The coating material used the plate material of 3mm in thickness (PS1, Measurement Group, and Inc.) and adhesives (PC1 bipax, Measurement Group, and Inc.). One side notch processed the point, processed the notch depth to three stages (3 and 4mm) by 0.3mm in thickness for TiNi fiber reinforced/epoxy composite with a miller cutter which finished up grinding in 60° , and after the coating material had been bonded, 7mm in the notch depth was processed for TiNi fiber reinforced/CFRP composite material.

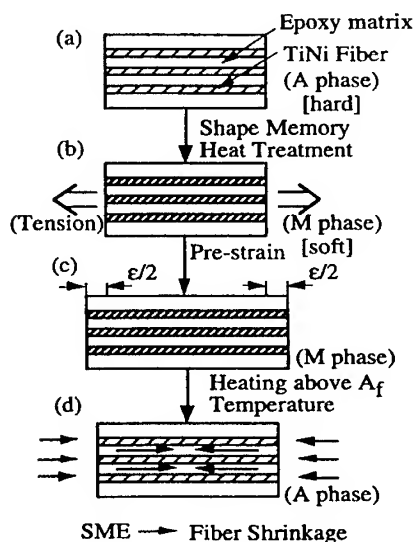


Fig.1 Design concept of shape memory alloy(SMA) smart composite

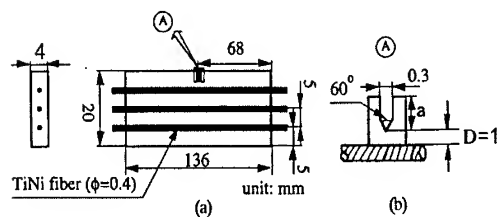


Fig.2 Dimension and shape of test specimen (TiNi/epoxy and TiNi/CFRP composite)

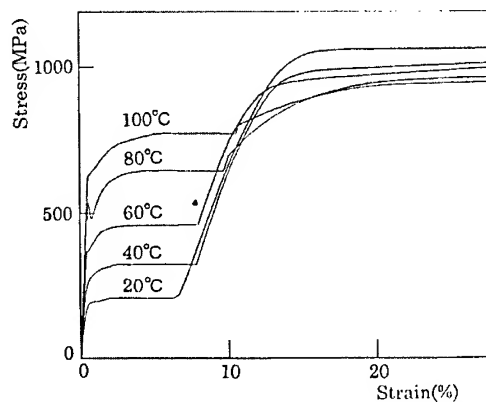


Fig.3 Stress-strain curves of TiNi fiber at different temperature

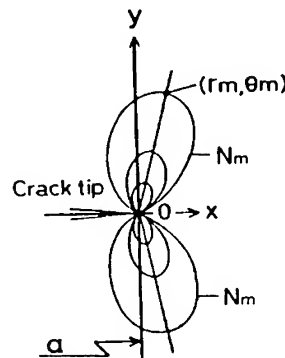


Fig.4 Photoelastic fringe pattern schematically developed in front of a crack size a

3. EXPERIMENTAL METHOD

The composite specimens were loaded by a Tensilon/RTM-1T machine in which a iso-temperature furnace and a photoelastic analysis apparatus were combined. When experimenting, a top and bottom of the test specimen edge is placed with the zipper and the constant load 392N in case of TiNi fiber reinforced/epoxy composite and constant load 4903N in case of Ti Ni fiber reinforced/CFRP composite was loaded and the 4-5th photoelastic fringe caused the stress concentration the notch tip of the extent to be caused. Not only the TiNi fiber but also the entire test specimen is changed to the ninth steps of 20, 30, 40, 50, 60, 70, 80, 90, and 100°C in the room temperature in the iso-temperature furnace and the shape memory inverse transformation is caused more than the A_f temperature and the decrease of the stress concentration of the crack tip according to the heating shrinkage of the TiNi fiber and K_I value is observed and the change in the photoelastic fringe pattern of crack point is observed. It took a picture of the photoelastic fringe pattern of each pattern one by one. From the Fig.5, shape memory effect of the embedded TiNi fibers reduce the stress concentration with increasing prestrain value. Stress intensity factor K_I can be computed from

$$K_I = \frac{n\sqrt{2\pi}r_m}{\alpha t \sin \theta_m} \left[1 + \left(\frac{2}{3 \tan \theta_m} \right)^2 \right]^{-0.5} \left[1 + \frac{2 \tan(3\theta_m/2)}{3 \tan \theta_m} \right] \quad (1)$$

where, n is the number of the fringe, t is the composite plate thickness, α is the epoxy photoelastic sensitivity constant, r_m and θ_m are respectively, the distance and angle in polar coordinates at point M, shown schematically in Fig.4. When K_I value was determined, the range of $73.5^\circ < \theta_m < 134^\circ$ that the error is few was measured, and doing 2-3 calculated the average value obtaining each K_I value from the fringe loop. The stress intensity factor of TiNi fiber reinforced/CFRP composite by the photoelastic coating method in equation (1) calculated at t obtained thickness of the coating material and photoelastic sensitivity α obtained from equation (2).

$$\alpha = 1 / \left(\frac{\lambda}{K} \frac{E}{1+\nu} \right) \quad (2)$$

Where, λ is wave length of light (it is 0.577×10^{-6} in white light), K is optical strain coefficients, E is young's modulus and ν is Poisson's ratio.

4. RESULTS AND DISCUSSION

4.1 Reduction of crack tip stress concentration by TiNi shape memory shrinkage force

Fig.5(a) shows the photoelastic fringe pattern of around the crack tip (domain size $D=0.2\text{mm}$) in the room temperature 80°C in the iso-temperature furnace of each test specimen under the constant load 392N (amount of tensile prestrain $\varepsilon_t = 0, 1, 3$, and 5% at TiNi fiber). It was confirmed that photoelasticity fringe order decreased gradually with an increase in the amount of the prestrain of the TiNi fiber by distance's r_m to the apogee where each isochromatic line pattern loop from crack point projected most rapidly decreasing more than the A_f point (about 60°C) along with the rise of the room temperature in the iso-temperature furnace from Fig.5. Fig.6 shows the relation of K_I value rate of change and the room temperature on each domain size according to an increase in the room temperature in the iso-temperature furnace. From Fig.6, the decrease in a clear K_I value was confirmed so that the temperature of the TiNi fiber may rise along with the room temperature rising (20-100°C) in the iso-temperature furnace and the TiNi fiber shrinkage may happen more than inverse transformation temperature A_f point. Moreover, the decrease in K_I value compared with the prestrain amount 0% was confirmed as 27.4% at prestrain amount 1%, 35.5% at 3% and 42.9% at 5% in a case of the domain size at 1mm. According to results of examining the change of K_I value with the room

temperature-rise in the iso-temperature furnace when the domain size is changed into $D=2, 1\text{mm}$ (for the notch depth $a=3, 4\text{mm}$) and the prestrain to the TiNi fiber is changed into $\varepsilon_i=0, 1, 3$ and 5% , K_I value level is different from an initial stage, because the sample always receives elastic compression strength from the TiNi fiber which corresponds to the amount of the prestrain and the domain size (compression region D) for the room temperature 20°C in the iso-temperature furnace. When the prestrain is 0% , K_I value and ΔK_I value (difference between a value at the room temperature-rise in the iso-temperature furnace and a standard value) were assumed to be a parameter and the effect of the decrease of the crack tip stress concentration by the shape memory shrinkage strength of burial TiNi fiber was examined according to the rise of the room temperature in the domain size and the iso-temperature furnace based on the case of the room temperature 20°C in the iso-temperature furnace in each test specimen with a different domain size. As for Fig.7 in the room temperature 80°C in the iso-temperature furnace, K_I value decreases as the amount of the prestrain increases under the relation of K_I value and the amount of the prestrain for each domain size, the decrease of the value of 0.075 and $0.087\text{MPa}\sqrt{\text{m}}$ can be confirmed by the domain size 2 and 1mm for the prestrain amount 5% test specimen, and the effect of the domain size was confirmed. ΔK_I value have compared and examined with FEM analysis value (refer to Fig.7) by using data in the room temperature 80°C in the iso-temperature furnace.

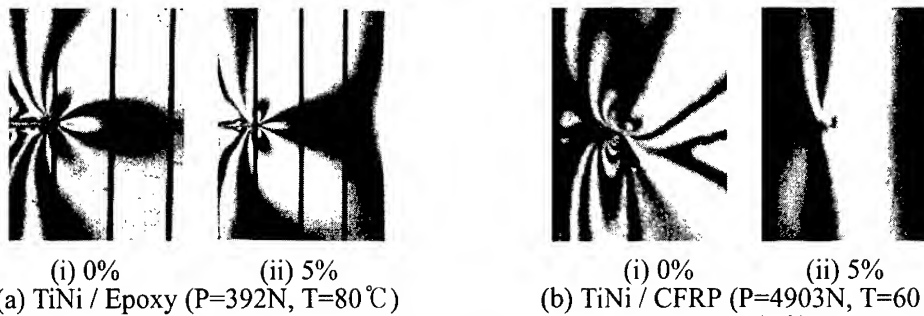


Fig.5 Photoelastic fringe patterns around the notch of TiNi/Epoxy and TiNi/CFRP specimens with different prestrain

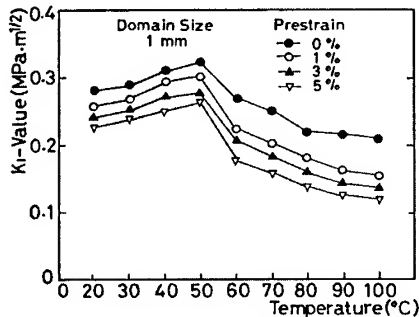


Fig.6 Relation between K_I value and different temperature (TiNi/Epoxy composite)

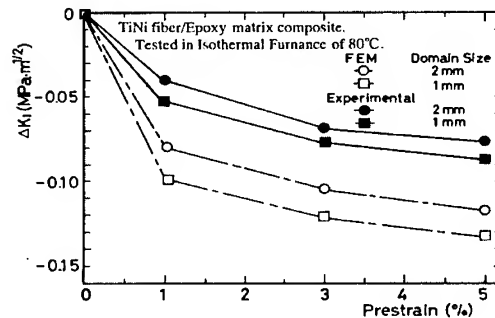


Fig.7 Stress intensity factor change ΔK_I of a side notched TiNi/Epoxy composite vs. prestrain

4.2 Dependence of Stress Intensity Factor (K value) on the Domain Size (D)

The reduction in stress intensity factor due to prestrain and shape memory effect is estimated by the analytical modeling which generally consists of the steps: (1) computation of the compressive residual stress in the matrix, (2) prediction of crack tip stress intensity factor change K_I . Following Eshelby's [6] equivalent inclusion method [7,8] by using eigen strain concept as well as the equation of force between TiNi fiber stress and average matrix (q) can

be calculated. When a crack tip is subjected to compressive stress q , then, the stress intensity factor K_I is given by following equation.

$$\Delta K_I = 2q\sqrt{\frac{2D}{\pi}} \quad (3)$$

where D is the length of the compressive stress domain between a crack tip and the embedded fiber. Eq.(3) was originally formulated by Tada et al. and has been used by several researchers [9,10]. The values of D in the present experiment are 2, 1mm respectively for two notch depths model for matrix. The analysis of the fracture toughness improvement mechanism of the FEM model calculated stress intensity factor ΔK_I value of mode I in the crack tip by virtual crack closure technique for the energy open rate. As a result, the predicted values of K_I are plotted as solid points in Fig.7. From Fig.7, the decrease in ΔK_I occurs to an increase in the fiber prestrain and it was confirmed that the tendency of the experimental result and the FEM analysis of the effect by the domain size were almost in agreement. Moreover, the experiment value's indicating a high value from FEM analysis value ΔK_I is thought that the strain with epoxy resin shrinkage was not taken in to the calculation of the residual stress; the value of K_I weaken the decrease tendency to around the fiber and the finite width correction factor $Y(a/w)$ showed the gradual increase tendency because finite width correction factor $Y(a/w)$ was not considered for the photoelasticity method of K_I value calculation. If the shrinkage strain is considered, it seems that the experimental value approaches to the FEM analysis value by the original amount of the prestrain caused by the austenite transformation according to $T \geq A_f$ of the TiNi fiber being eased by the shrinkage of epoxy resin and average residual stress in the matrix decreased.

4.3 Crack closure acts in TiNi fiber reinforced/CFRP composite

Fig.5(b) shows the reflex photoelastic fringe pattern of around the crack tip in the room temperature 60°C in the iso-temperature furnace of each specimen (tensile prestrain of TiNi fiber $\varepsilon_t = 0, 1, 3, 5\%$) in constant load 4903N. The closure action of the crack was confirmed by stress intensity factor K_I value's and the crack tip fringe order's reduction as well as TiNi fiber reinforced/epoxy composite along with the rise of the temperature from Fig.5. Fig.8 shows the relation of the value of stress intensity factor K_I of TiNi fiber reinforced/CFRP intelligent composite and the room temperature in the iso-temperature furnace in the amount of each prestrain. K_I value decreases as well as TiNi fiber reinforced/epoxy composite along with an increase in the amount of the prestrain and the rise in the room temperature in the iso-temperature furnace from Fig.8. However, in case of the prestrain amount 1, 3 and 5%, it was confirmed that K_I value recovered almost in the room temperature 60°C in the iso-temperature furnace. Fig.9 shows the relation between the value of stress intensity factor K_I and the amount of the prestrain of TiNi fiber reinforced/CFRP intelligent composite in the room temperature in the iso-temperature furnace at 30, 40, 50, and 60°C. In case of the prestrain amount 5%, the decrease in K_I value was confirmed by 0.89MPa \sqrt{m} at 50°C, 0.65MPa \sqrt{m} at 40°C, and 1.2MPa \sqrt{m} at 30°C in the room temperature in the iso-temperature furnace from Fig.9. If an intelligent composite (metal, polymer) by which the shape memory shrinkage and the recovery stress appearance mechanism to which the TiNi fiber reinforced by rule of the high temperature which was proposed here in the future and the elasticity improvement happen at the same time are given from this can be achieved; an active control of the fracture toughness and the fatigue crack spread speed can be contained, and long-life the machine structural material and research development into the safety design be expected. The compressive stress in the intelligent composite caused because the temperature rises can reduce stress concentration in the crack tip and the design of a recovery transformation of the stuff of doing and the machine and the structure and driving element be expected. Moreover, the design of the material can do the fracture control, that is, the self-recovery becomes possible when the crack occurs by setting the amount of the prestrain of the TiNi fiber in an appropriate amount in the design stage. Therefore, it has been understood to be able to offer a new safe material.

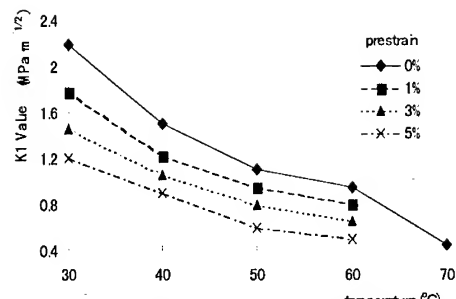


Fig.8 Realation between K_I value and different temperature (TiNi/CFRP composite)

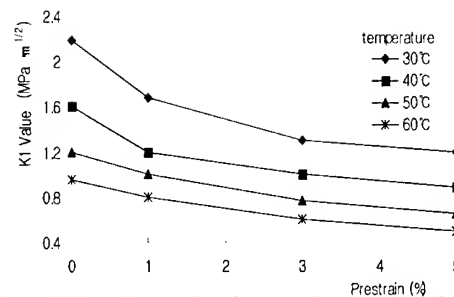


Fig.9 Stress intensity factor change K_I of a side notched TiNi/CFRP composite vs. prestrain

5. CONCLUSION

- (1) Not only the TiNi fiber but also the specimen was confirmed and the effect of the fracture resistance improvement of the decrease of the stress intensity factor was confirmed by the rise of the room temperature in the iso-temperature furnace.
- (2) The decrease in K_I value was confirmed to generate a big recovery force (compressive force) in the TiNi fiber as an increase of the amount of the prestrain and the domain size became small (as it approached the TiNi fiber) and it was confirmed greatly that the decrease tendency to K_I value was almost corresponding compared with the analytic value of the theoretical model (effect of the domain size) by the Eshelby equivalent inclusion method.
- (3) In TiNi/CFRP intelligent composite by which matrix is assumed to be CFRP, it has been understood for the crack closure acts to be able to work and to improve a further fracture resistance and the fatigue life.

This work was supported by High-Tech Research Center of Saitama Institute of Technology.

REFERENCES

1. Rogers, C. A., et al., Active Damage Control of Hybrid Material Systems Using Induced Strain Actuator, Proc. 32nd Structures, Structural Dynamics and Materials Conference, (1991), 1190-1197. Furuya, Y., Sasaki, A. and Taya, M., Vol.19A(1988), pp. 646-658.
2. Akira Shimamoto and Minoru Taya, Crack Closure Acts of Composites by Shrinkage Effect of Shape Memory TiNi Fiber Embedded, JSME 63-605, A (1997), pp. 26-31 (in Japanese)
3. Akira Shimamoto, Minoru Taya and Yasuhumi Furuya, Crack Closure Acts of Composites by Shrinkage Effect of Shape Memory TiNi Fiber Embedded (effect of crack depth), JSME, Strength of Materials Lecture Vol.B(1996-10), pp. 363-364 (in Japanese)
4. Akira Shimamoto, et al., Fatigue Crack Spread Control by Shape Memory Fiber Reinforced Composite, JSME, the 74th's Usual Rally Lecture (I), (1997-3), pp. 667-667. (in Japanese)
5. Composite date of TORECA, Tore Co., Ltd.
6. Eshelby, J. D., The Determination of the Elastic Field of an Ellipsoidal Inclusion and Related Problems, Proc. Roy. Soc. Lond., A, 224 (1957), pp. 376-396.
7. Yamada, Y., Taya, M. and Watanabe, R., Strengthening of Metal Matrix Composite by Shape Memory Effect, Mater. Trans., JIM, 34-3 (1993) pp. 254-260.
8. Taya, M., Yamada, Y., Furuya, Y., Watanabe, R., Shibata, S. and Mori, S., (Varadan, V. K. Volume), Strengthening the Mechanism of TiNi Shape Memory Fiber/Al Matrix Composite, Proc. Smart Mater., SPIE 1916, (1993), pp. 373-383.
9. Tada, H., Panis, P. C. and Irwin, G. R., The Stress Analysis of Cracks Handbook, (1973), 3.7., Del Research, Corp. Hellertown, P.A.
10. Taya, M., Hayashi, S., Kobayashi A. S. and Yoon, H. S., Toughness of a Pacriculate Residual Stress, J. Am. Ceram. Soc., 73-5 (1990), pp. 1382-1391.

THE PROPERTIES AND MICROSTRUCTURES OF TiC_p PARTICLE REINFORCED TITANIUM MATRIX COMPOSITES

Zhou Lian, Mao Xiaonan, Zhao Yongqing, Zeng Liying, Alain Vassel*

Northwest Institute for Nonferrous Metal Research, Xi'an 710016, China

*Materials Systems and Composites Department, ONERA, FRANCE

ABSTRACT

The property and the microstructure have been researched for TiC particle reinforced titanium matrix composite. Result shows that the properties for the composite at ambient temperature were different with varying heat treatment conditions. The comprehensive properties of as-annealed composite with furnace cooling were superior to that of with oil cooling and air cooling. And the service temperature for TP-650 composite was 50~100°C higher than that of ordinary Ti alloys. It possessed the better heat stability at high temperature. The varying relation between strength and elongation can be expressed as a straight-linear rule approximately over 500°C. The TiC particles were distributed uniformly in the Ti matrix, and the microstructure of the composite was homogeneous. There is a favorable metallurgical connection between the TiC particle and the matrix. The interface was narrow.

1. INTRODUCTION

Titanium alloy possesses the higher specific strength, specific stiffness and the better corrosive resistance. It has been widely used in aerospace. When a certain property of the ordinary Ti alloys had developed to a limitation, and it approached the highest value and faced the urgent requirement for developing the high property Ti alloy, it forced that the research of material science diverted from the ordinary non-orderly Ti alloy to the orderly inter-metallic

compound, from solid-solution reinforced Ti alloy to Ti alloy matrix composite^[1].

Ti matrix composite composed of the particle and the fiber reinforced Ti matrix composite. The development for fibre reinforced Ti matrix composite has been restricted by the following several factors. At first, the price of the continuous fibre is expensive, then the processing method is complicated and property is non-homosexuality. Therefore, the particle reinforced Ti matrix composite, which possesses the character of homosexuality and easily processing, had been greatly paid attention by people. When the particle of the lower density and the higher modulus and strength have been mixed diffusely to Ti alloy matrix, The specific strength, specific modulus and the creep strength of Ti alloy would be elevated greatly. The using temperature of Ti alloy have been elevated greatly to content the requirement for developing the aerospace material further. The other is that the wear resistance of Ti alloy had been elevated and combined the higher corrosive resistance, it can content the requirement for the material possessed the wear and corrosion resistance in developing high-new technology. In the past several years, It was found the there is a better metallurgical compatibility between TiCp and the Ti matrix in TiC particle reinforced Ti matrix composite. It has better heat expansion match between TiCp and Ti matrix. Comparing with the Ti matrix, the specific strength and modulus can be elevated greatly for the composite with TiC particle. The comprehensive properties of the composite can be adjusted by varying the volume fraction of TiCp and heat treatment conditions. This paper discussed the microstructure and the property treated at different heat treatment condition for TiC particle reinforced Ti matrix composite.

2. EXPERIMENTAL METHOD

The experimental material is the TiC particle reinforced Ti matrix composite (TP-650) (3vol%TiC, TiCp size: 5 μ m or so), which had been fabricated by PTMP (pre-treatment melt process). The ingot of TP-650 had been processed to ϕ 13mm bars by the opening mould forging and the turning forging.

The composite had been heat treated at 800⁰C~1050⁰C for 1h, and then treated at 700⁰C for 2h. The blank samples of the post-heat treatment had been machined to the tensile samples. Then it had been tested in the INSTRON 1185 electron tensile machine. The testing results were compared with that of the famous high temperature Ti alloys IMI834 and Ti-1100. The microstructure of the composite was analyzed by the optical micrography and SEM.

3. RESULT AND DISCUSS

3.1 The property's varying in the different solid- solution treatment temperature

Fig.1 shows the properties at room temperature varying after different post-treatment. The strength varied from 1270MPa to 1350MPa with heat treatment temperature's varying from 800°C to 1050°C. The highest value (1350MPa) created at B and the valley value (1270MPa) is at D. Span from peak to valley is 70 MPa. The rate of growing is just 6%. So the heat treatment's varying do a little influence to the room temperature strength of TP-650. This little influence may be related to the varying of interface at the different temperature^[2]. However, the plastic of TP-650 shows a varying rule clearly with the different heat treatment conditions. With the solid-solution temperature's elevating, the plastic declined clearly. The declining rate of elongation and reducing area reached at 125% and 248%, respectively. It may be due to the microstructure of matrix varying to effect the plastic greatly at the different heat treatment temperature^[4]. Therefore, for the as-annealed composite at 800°C to 1050°C, a little influence has been done to the strength, a great influence to the plastic.

3.2 The property's varying in the different cooling rate

Fig.2 shows the property at room temperature after the post-treatment at E~G. The cooling rate declined, the room temperature strength tapered. The declining rate is 11%. The plastic

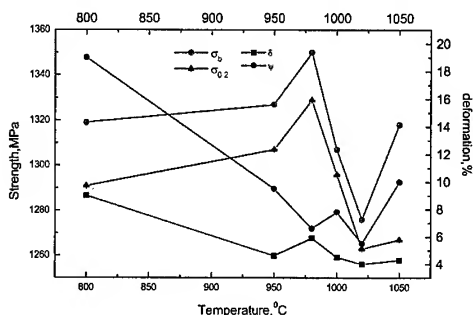


Fig.1 The tensile properties of TP-650 at different heat treatment rule

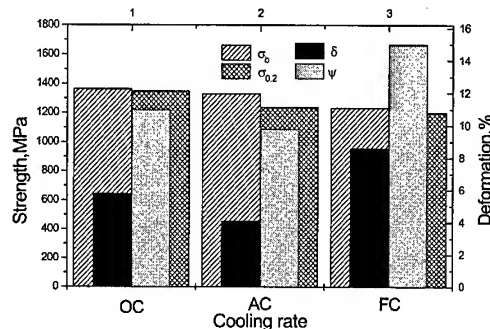


Fig.2 The tensile properties of TP-650 at different cooling rate

for composite treated with oil cooling is the same as one with the air cooling. But for furnace cooling, plastic is much higher than the former. The elongation and reducing area increased 100% and 53%, respectively from the oil cooling to furnace cooling. The analysis learned the equivalent grains formed by the furnace cooling possessed the better comprehensive properties than the one treated at oil cooling and air cooling [3].

3.3 The heating softening character of TP-650 composite

Fig.3 shows the strength varying of TP-650 composite tested at R.T., 300°C, 500°C, 600°C, 650°C, and 700°C. And it was compared with the strength of the IMI834 and Ti-1100 Ti alloys tested at the same conditions. The curve shows the strength of TP-650 declined quickly from R.T. to 300°C and then declined slowly at over 300°C.

It indicated that TP-650 Ti matrix composite had the better high temperature characters. Comparing with IMI834 and Ti-1100 Ti alloys, the strength of TP-650 is 50~100MPa higher tested from R.T. to 700°C. The strength of TP-650 tested at 700°C is equal to the one of IMI834 and Ti-1100 tested at 650°C. So it can reach a conclusion that the servicing temperature of TP-650 composite is 50~100°C higher than that of the ordinary Ti alloys.

Fig.4 shows the varying relation between the strength and the elongation tested at the different temperatures. From R.T. to 500°C, the strength declined quickly with the elongation's increasing smoothly. However, the strength of TP-650 declined slowly with the elongation's

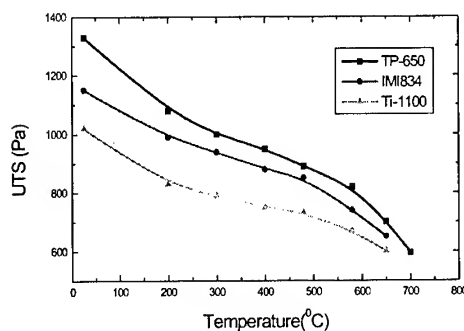


Fig.3 The tensile strengths of TP-650 at different testing temperature and compared with that of IMI834 and Ti-1100

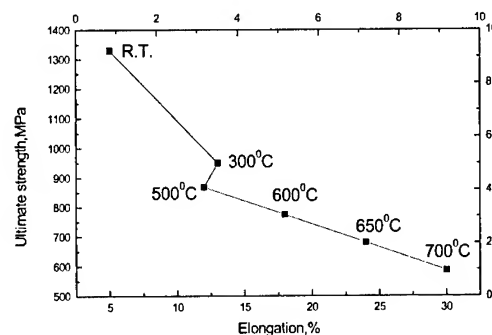


Fig.4 The varying relation between the strength and the elongation tested at different temperatures

increase smoothly at over 500⁰C. This shows that TP-650 possesses better heat stability at elevated temperature. When the temperature was over 500⁰C, the varying relation between strength and elongation can be expressed as a straight linear rule approximately, that is: $\sigma_b(1/100) = -0.156 \delta + 10.55$. The slope K for straight linear is -0.156, the angle between the straight linear and the abscissa α is 150⁰. This varying relation of the linear confirmed that TP-650 Ti matrix composite possessed better property at high temperature.

3.4 The microstructure of TP-650 composite

Fig.5 shows the microstructure of TP-650 composite. The composite possesses homogenous microstructure. The TiC particle distributed uniformly in the matrix (as shown in Fig.5a). The microstructure of the composite consists of ballad TiC particle and homogeneously Ti alloys matrix phases. Heterogeneous structure had not been seen by adding the TiC particle in TP-650 composite (as show in Fig.5b).

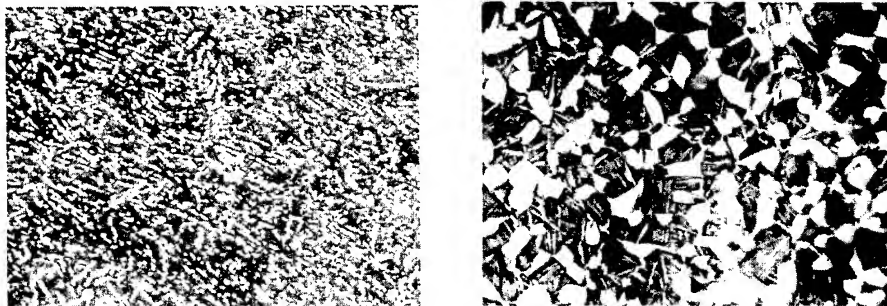


Fig.5 The structure of TP-650 composite, uniform distribution of TiC particle(a), homogeneous microstructure of the composite(b)

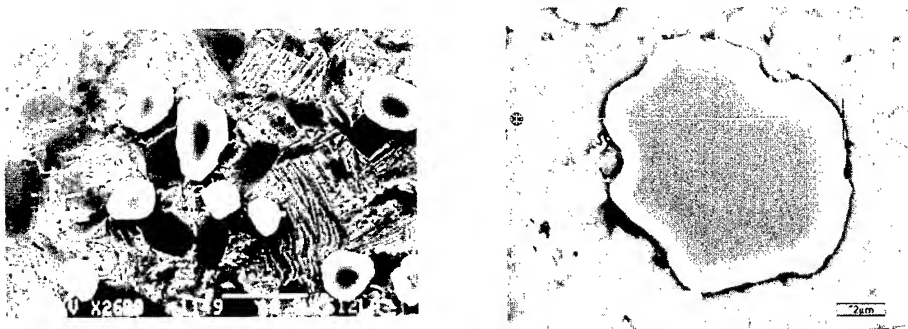


Fig.6 Interface between TiC particle and the matrix, smooth (a) and narrow (b) interface

Fig.6 shows the interface between TiC particle and the Ti alloy matrix. Smoothly interface existed between the particle and the matrix. The outline of interface was clear. The particle and the matrix combined metallurgical. The width of the interface was below $1\mu\text{m}$ [5].

4. CONCLUSION

- (1) The different heat treatment condition has little influence to strength of TP-650 at room temperature. But it did a great influence to the plastic, which declined greatly tested from 800°C to 1050°C .
- (2) The better comprehensive properties for the as-annealed composite with furnace cooling were superior to that of with oil cooling and air cooling.
- (3) The servicing temperature of TP-650 was $50\sim 100^{\circ}\text{C}$ higher than ordinary Ti alloys.
- (4) TP-650 possesses better heat stability at high temperature. The varying relation between strength and elongation can be expressed as a straight linear rule approximately over 500°C .
- (5) The TiC particle distributed uniformly in the Ti matrix, the structure of Ti matrix was homogenous. The interface between the TiC particles and Ti matrix was metallurgical uniting, and the width of which is narrow.

REFERENCE

- [1] Zhang Li, *Acta Metallurgica Sinica*, Vol. 33(1) (1997), pp.85.
- [2] Mao Xiaonan, Zhou Lian, Wei Hairong, *Acta Metallurgica Sinica*, Vol.35(Suppl. 1)(1999), pp.S339.
- [3] Mao Xiaonan, ZengQuanpu, Zhang Tingjie, *Titanium'98 Proceeding of Xi'an International Titanium Conference (XITC'98)*, L. Zhou, D. Eylon, eds., Beijing, China, (1999), pp.1025.
- [4] Mao Xiaonan, Zhou Lian, Wei Hairong: Master Thesis, Northeast University, (1999).
- [5] ZengQuanpu, Mao Xiaonan, *Titanium'98 Proceeding of Xi'an International Titanium Conference (XITC'98)*, L. Zhou, D. Eylon, eds., Beijing, China, (1999), pp. 896~901.

MECHANICAL PROPERTIES OF SCS-6/Ti-15V-3Cr- 3Sn-3Al TITANIUM MATRIX COMPOSITES

Hiroshi Izui, Atsushi Tada, and Takao Furukawa

Department of Aerospace Engineering
College of Science and Technology
Nihon University, Funabashi, Chiba, 274-8501, Japan

ABSTRACT

The mechanical and brazed joint properties of SCS-6 SiC fiber reinforced Ti-15V-3Cr-3Sn-3Al (Ti-15-3-3-3) titanium matrix composite (TMC) were investigated. TMC was manufactured by using a foil-fiber-foil technique in alternating layers of the titanium foil and SCS-6 fiber mats were consolidated into laminates by hot pressing. The TMCs were consolidated at the temperatures of 660°, 730°, or 800°C and at pressures of 20, 40, 60, or 80 MPa. The effects of these consolidating conditions on the mechanical properties, SiC/Ti-15-3-3-3 interactions, and failure modes were investigated. The TMC specimens were tested in air at room temperature, 200°, 400°, 600°, or 800°C.

Brazed joint specimens were fabricated from TMC using three types of Ag-Pd-Ga braze alloys, Ag-10Pd-5Ga, Ag-9Pd-9Ga, and Ag-8Pd-17Ga. The brazed joint specimens were tested in air at room temperature and 600°C using single overlap tensile shear (OLTS) tests. Metallurgical analyses were used to characterize the microstructure, and braze alloy/TMC interactions.

The TMC consolidated at 730°C and 40 MPa had high tensile strengths of 767 to 1346 MPa from room temperature to 800°C. The joints brazed with the Ag-10Pd-5Ga braze alloy at room temperature and 600°C had shear strengths of 146 and 40 MPa, respectively.

1. INTRODUCTION

The low structural mass fraction required for future aerospace vehicle necessitates the development of new materials having improved specific properties at elevated temperatures that can be incorporated into highly efficient advanced structural components.

Fiber-reinforced titanium matrix composites (TMC) offer significant improvements in strength and in stiffness over their monolithic counterparts and are prime candidates for use in elevated temperature advanced airframe structures.

This study was undertaken to investigate the tensile properties of SCS-6/Ti-15V-3Cr-3Sn-3Al TMC and the joint strength of TMC. SCS-6 fibers fabricated by Textron System Division were used as reinforcements. The matrix alloys used in this study were Ti-15V-3Cr-3Sn-3Al (Ti-15-3-3-3). Unidirectional composites containing SCS-6 fibers were consolidated using the vacuum diffusion bonding technique. The consolidation temperatures were from 660° to 800°C and in the subsequence cool down. The consolidation pressures were from 20MPa to 80MPa. To investigate the tensile strengths of the composites, tensile tests were carried out using an Instron material test machine at room temperature, 200°, 400°, 600°, and 800°C.

The development of joining processes capable of incorporating TMC into efficient structural components is essential to the successful development of advanced aerospace vehicles. Brazing is one of the candidate joining processes being considered for airframe structural components because it requires bonding temperatures similar to those used to consolidate the composite and can be used to join complex parts. The desired combination of good wetting and flow properties minimal base metal erosion and intermetallic formation, and good joint mechanical properties at elevated service temperatures limits it's the choise of available braze alloy. Based on these criteria, the Ag-Pd-Ga braze alloys have shown good potential to produce consistently sound and ductile brazed joints [1]. Three types of Ag-Pd-Ga braze alloys, Ag-10Pd-5Ga, Ag-9Pd-9Ga, and Ag-8Pd-17Ga were used in this study. The brazed joint properties were evaluated in air at room temperature and 600°C using single overlap tensile shear (OLTS) tests.

2. EXPERIMENTAL

2.1 Materials and processing

The TMC used in this study was SCS-6/Ti-15V-3Cr-3Sn-3Al (Ti-15-3-3-3), which consisted of a Ti-15V-3Cr-3Sn-3Al titanium matrix reinforced with continuous SCS-6 SiC fibers. The 0.14-mm diameter SCS-6 fibers were in the form of unidirectional mats with Ti-Nb wire cross weave.

The composite was manufactured by using a foil-fiber-foil technique in alternating layers of 0.15-mm thick the titanium foil and SCS-6 fiber mats were consolidated into laminates by hot pressing as shown in Fig.1. All processing was conducted in a high-frequency heated vacuum furnace at a vacuum less than 10^{-5} torr (1.3 mPa). The composites were

consolidated at temperatures of 660°, 730°, or 800°C and at pressures of 20, 40, 60, or 80 MPa. Once attained, these conditions were maintained for an hour. These composites were always heated to full temperature prior to the application of the full pressure.

2.2 Brazing

Newly developed palladium-containing braze alloys for TMC were Ag-10Pd-5Ga, Ag-9Pd-9Ga, and Ag-8Pd-17Ga. The TMC brazed joints shear behaviors were evaluated with single lap specimens. Brazing was conducted by infrared heating in a vacuum furnace at a vacuum less than 10^{-5} torr (1.3 mPa). Brazing temperatures of Ag-10Pd-5Ga, Ag-9Pd-9Ga, and Ag-8Pd-17Ga were 1030°, 1000°, or 960°C, respectively. A thermo-couple was attached to the TMC specimens in the vicinity of the brazed joints to monitor brazing temperature. The TMC temperature was held at these temperatures for 5 min.

2.3 Mechanical Testing

The tensile tests of TMCs were conducted in air at room temperature, 200°, 400°, 600°, or 800°C. Brazing joint properties of TMC were evaluated at room temperature and 600°C using single OLTS specimens. For the elevated-temperature tests, the specimens were heated by infrared heating.

2.4 Metallurgical Analysis

Brazed joint microstructures were characterized using optical microscopy and scanning electron microscopy (SEM). Metallurgical specimens were cross-sectioned using diamond saw cutting and mounted in an epoxy medium. Fracture surfaces of tensile test specimens were examined using SEM microscopy.

3. RESULTS AND DISCUSSION

3.1 Metallurgical analyses

Figure 1 show the micrographs of transverse sections through the TMCs consolidated at the temperatures of 660°, 730°, or 800°C and at pressures of 20, 40, 60, or 80 MPa. They show the distribution of fibers and the joining of fibers to matrix or matrixes. At the consolidation pressure of 20 MPa, the matrix to matrix and matrix to fibers did not adhere well at all consolidation temperatures because of low consolidation pressure. At the consolidation pressure of 40 MPa, matrix to fibers adhered well at the consolidation temperatures of 730° or 800°C, and the interfaces of matrixes disappeared by diffusion bonding. At the consolidation pressure of 60MPa, matrix to matrix and matrix to fibers adhered well at the

consolidation temperatures of 660° or 730°C. When the TMCs were consolidated at 800°C and 60 MPa, the arrangement of fibers was disturbed by plastic flow. At the consolidation conditions of 80 MPa , matrix to matrix and matrix to fibers adhered well at 660° or 730°C.

High magnification SEM photomicrographs and elemental maps of the fiber/matrix interface are shown in Fig.2. The observation indicates that carbon diffused from the carbon-rich surface of SiC fibers toward titanium. Increasing the consolidation temperature promoted the diffusion of carbon into titanium.

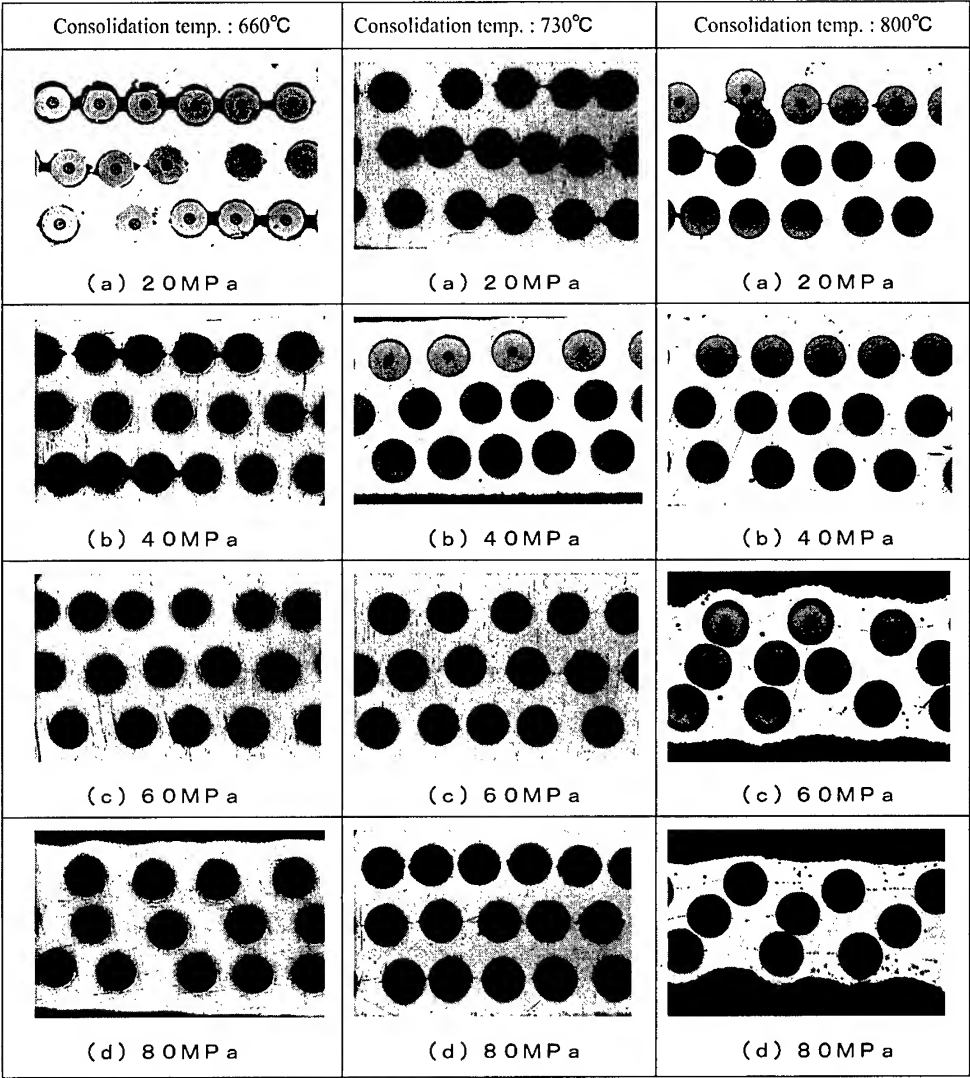


Fig.1 Micrographs of transverse sections through the TMCs at each consolidation condition

3.2 Mechanical testing

Figure 3 shows the ultimate tensile strengths (UTSs) of TMCs consolidated at the temperatures 660°, 730°, or 800°C and at pressures of 20, 40, 60, or 80 MPa. The TMCs consolidated at the temperature of 730°C and at the pressure of 40 or 60 MPa or at the temperature of 660°C had high tensile strengths. At the consolidation temperature of 800°C, as the consolidation pressure was increased, the UTSs were decreased. The arrangement of the fiber, such as the fiber concentration or distribution, has a significant influence on the tensile strength of the TMC. As shown in Fig.1, the fibers of the TMC consolidated at 800°C and at 60 or 80 MPa neared or contacted. Therefore, the tensile load could not be transmitted to the fibers by the matrix phase.

The relationship between the fiber volume fraction (Vf) and the UTSs of TMC consolidated at 730°C and 40 MPa is shown in Fig.4. The broken line indicated the theoretical longitudinal tensile strength of TMC. It is evident that, as the fiber volume fraction was increased, the tensile strengths of TMCs were increased. The highest UTS shows at the volume fraction of 35 %. The UTSs of TMCs agreed well with the theoretical value under the fiber volume fraction 22 %.

Figure 5 shows the average UTSs of TMCs at elevated temperature. Compared to the UTSs of the matrix, TMC shows high UTSs of 767 to 1346 MPa from 20 to 800°C.

The results of the shear tests of brazed joints are shown in Fig.6. As the overlap length was increased, the shear strengths of brazed joints were decreased. The TMC brazed joints with Ag-10Pd-5Ga had high shear strength of 146

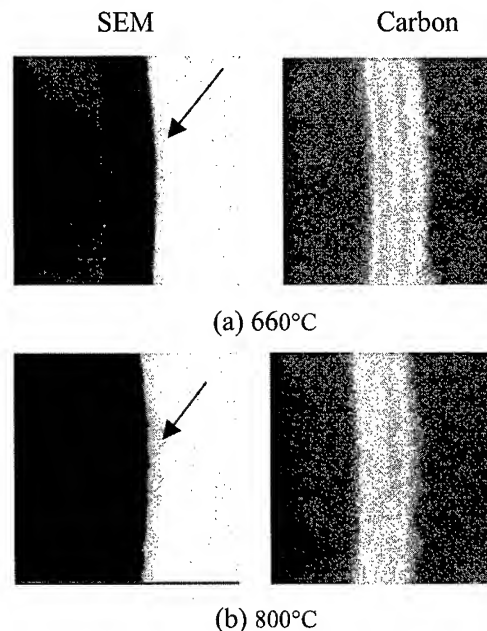


Fig.2 SEM micrograph and x-ray elemental map (Carbon) of TMC consolidated at the pressure of 40 MPa

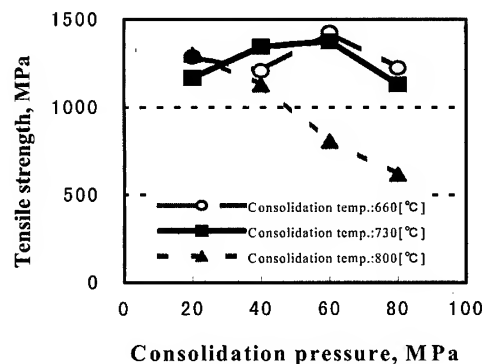


Fig.3 Relationship between consolidation pressure and UTS at each consolidation temperature

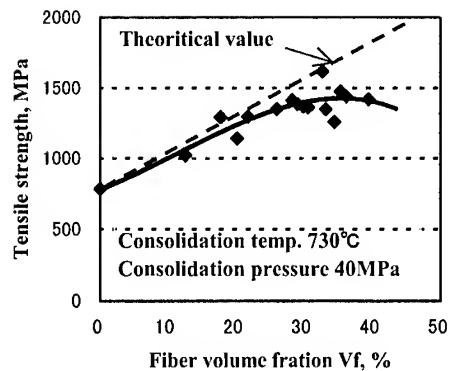


Fig.4 Relationship between fiber volume fraction and UTS

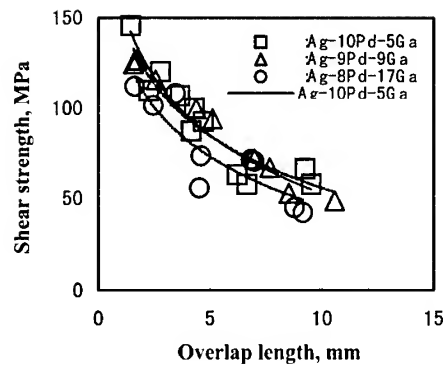


Fig.6 Shear strengths of the TMC brazed joints

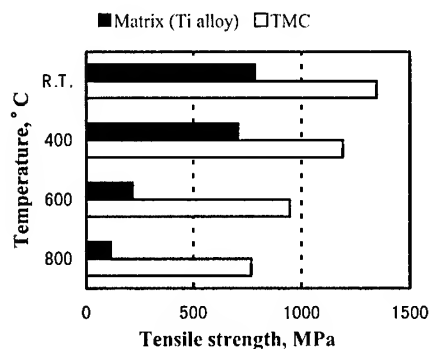


Fig.5 Tensile strengths of TMCs at elevated temperatures

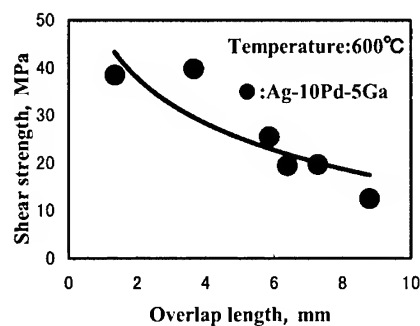


Fig.7 Shear strengths of brazed joints with Ag-10Pd-5Ga.

MPa at overlap length 1.45 mm.

Figure 7 shows the shear strength at 600°C of the brazed joints with Ag-10Pd-5Ga. The brazed joint had the highest shear strength of 40 MPa.

4. CONCLUSIONS

Based on the experimental evidences presented, the following conclusions were made:

- 1) The TMC consolidated at 730°C and 40 MPa had high tensile strengths of 767 to 1346 MPa from room temperature to 800°C.
- 2) The joints brazed with the Ag-10Pd-5Ga braze alloy at room temperature and 600°C had shear strengths of 146 and 40 MPa, respectively.

REFERENCE

1. D. Douglas Berger, Welding Journal, Vol.74, pp.35-37

Mechanical and Fracture Behaviors of (Al₂O₃+SiC_p)/AZ91 Hybrid Mg Matrix Composite

Ikmin Park, Kyung-mox Cho, Ildong Choi* and Changsik Ha

Department of Metallurgical Engineering,
Pusan National University, Pusan 609-735, Korea

* Department of Mechanical & Materials Engineering,
Korea Maritime University, Pusan 606-791, Korea

ABSTRACT

Hybrid AZ91 Mg matrix composites reinforced with ceramic short fiber (Al₂O₃) and particle (Si or SiC_p) simultaneously were fabricated by squeeze casting method. Microstructure of hybrid Mg matrix was examined and mechanical and fracture properties were characterized. It was found that squeeze casting is effective method for the fabrication of hybrid Mg matrix composites with fairly well distributed reinforcement and near defect-free solidification microstructure. Enhanced mechanical properties of strength and wear resistance were obtained with hybridization of reinforcements. To investigate fracture properties of hybrid Mg matrix composites, in-situ micro-fracture experiment was performed in SEM. Crack initiated and propagated mainly by decohesion of interfaces between Mg matrix and reinforcements. Large ceramic particles tend to fracture and thus seem to be undesirable for mechanical and fracture behavior of hybrid Mg matrix composites.

1. INTRODUCTION

Mg alloys, the lightest commercial structural alloys (density: 1.75g/cm³) are considered as environmental friendly and energy saving materials.[1-3] Advantageous properties such as damping capacity, castability and machinability are key factors for the recent increasing consumption of Mg alloys.[4-5] Mg matrix composites also have been investigated these days for the application to various engineering fields.[3] One of the potential applications of Mg matrix composite is the material for automotive parts. Strength and wear resistance of Mg matrix composites is expected to have those of commercial age hardened Al alloys.[6] Selection of reinforcements and manufacturing technique are two main things for the fabrication of Mg matrix composites. Hybridization of reinforcements, namely reinforcing two kinds of materials together, for Mg matrix composites has been considered to develop most recently.[7-9] In this paper hybrid Mg matrix composites fabricated by squeeze casting process are summarized. Squeeze cast fabrication and mechanical and fracture property of hybrid Mg matrix composites of AZ91 Mg/(Al₂O₃+Si) and AZ91 Mg/(Al₂O₃+SiC_p) are presented. Research objectives of Al₂O₃+Si hybridization is to investigate the formation of Mg₂Si intermetallic compound during squeeze casting. And Al₂O₃+SiC_p hybridization is to investigate the effect of SiC_p particle size on hybrid Mg MMC.

2. SQUEEZE CAST FABRICATION AND MICROSTRUCTURE

AZ91D Mg was used as matrix to fabricate hybrid composites reinforcing (10vol% Al₂O₃+5vol% Si) or (10vol% Al₂O₃+5vol% SiC_p). Saffil short fiber of δ -Al₂O₃ (3 μ m in diameter and 200 μ m in length) and three different sizes of SiC particles (45, 29, 9 μ m) were

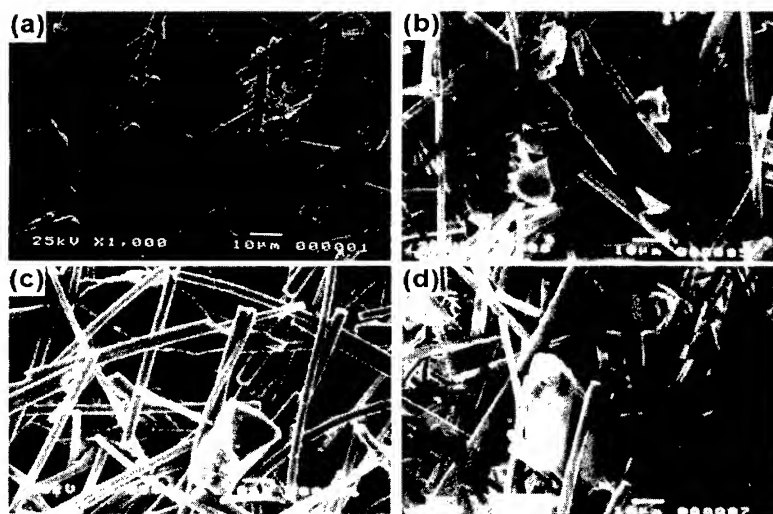


Fig. 1 SEM morphology of preforms.

(a) $\text{Al}_2\text{O}_3+\text{Si}$ (b) $\text{Al}_2\text{O}_3+\text{SiC}_p(45\mu\text{m})$ (c) $\text{Al}_2\text{O}_3+\text{SiC}_p(29\mu\text{m})$ (d) $\text{Al}_2\text{O}_3+\text{SiC}_p(9\mu\text{m})$.

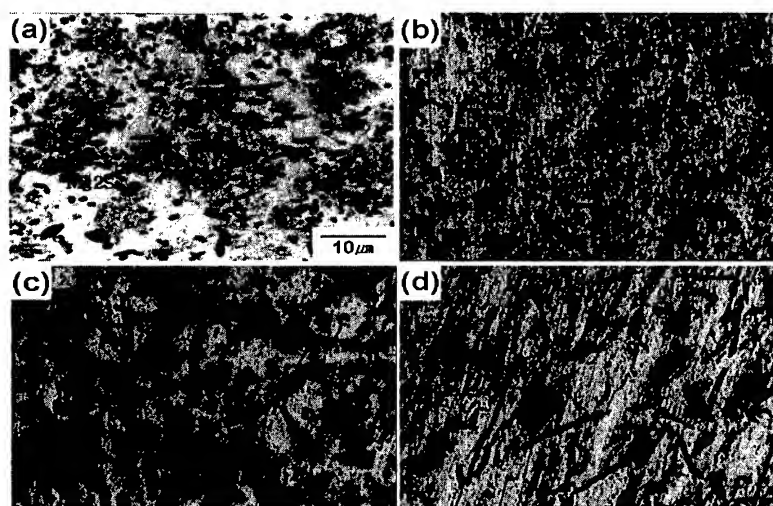


Fig. 2 Optical microstructure of hybrid composites.

(a) $\text{Al}_2\text{O}_3+\text{Si}$ (b) $\text{Al}_2\text{O}_3+\text{SiC}_p(45\mu\text{m})$ (c) $\text{Al}_2\text{O}_3+\text{SiC}_p(29\mu\text{m})$ (d) $\text{Al}_2\text{O}_3+\text{SiC}_p(9\mu\text{m})$.

chosen for reinforcements.

Preforms of reinforcements ($\text{Al}_2\text{O}_3+\text{Si}$) and ($\text{Al}_2\text{O}_3+\text{SiC}_p$) were prepared and molten Mg was infiltrated into the preforms by applying pressure to fabricate hybrid composites. To prepare preforms, reinforcements mixed with silica colloidal binder were dispersed in distilled water and consolidated using vacuum suction method.[10-11] Preforms dried and calcinated at 1100°C to obtain enough strength for squeeze casting. Fig. 1 shows preforms of reinforcements.

For squeeze casting, a perform was placed in a steel mold of 450°C preheated and molten Mg of 800°C was poured. The pressure of 35Mpa was applied and held for 60 seconds to fabricate hybrid Mg matrix composites by squeeze casting. Delayed time of the applied

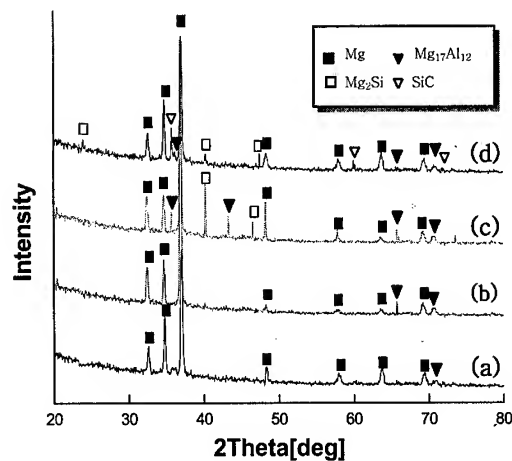


Fig. 3 X-ray diffraction patterns.
(a) AZ91 (b) $\text{Al}_2\text{O}_3/\text{AZ91}$ (c) $\text{Al}_2\text{O}_3+\text{Si}/\text{AZ91}$ (d) $\text{Al}_2\text{O}_3+\text{SiC}_p/\text{AZ91}$.

pressure was 7 seconds.[12-14]

Squeeze cast hybrid Mg matrix composites are shown in Fig. 2. Fairly uniform distribution of reinforcements, $\text{Al}_2\text{O}_3+\text{Si}$ and $\text{Al}_2\text{O}_3+\text{SiC}_p$, in Mg alloy matrix can be seen in the microstructure of hybrid Mg matrix composites. Any noticeable casting defects were not observed in the composites fabricated. From X-ray diffraction analyses, Mg_2Si and $\text{Mg}_{17}\text{Al}_{12}$ were detected at the interfaces between Mg matrix and reinforcement of Si and SiC_p (Fig. 3).

3. MECHANICAL PROPERTIES

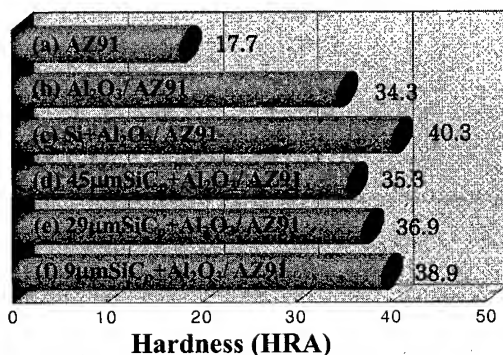


Fig. 4 Hardness of squeeze cast AZ91 and AZ91 matrix composites.

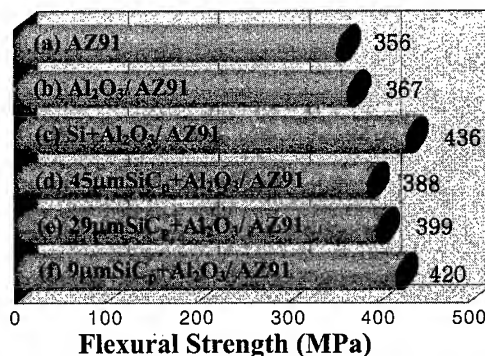


Fig. 5 Flexural strength (MPa) of squeeze cast AZ91 and AZ91 matrix composites.

Fig. 4 shows hardness values for AZ91 Mg and AZ91 Mg matrix composites. Hardness increases more than twice with reinforcing ceramic materials. Composites reinforced with $\text{Al}_2\text{O}_3+\text{Si}$ and $\text{Al}_2\text{O}_3+9\mu\text{mSiC}_p$ revealed the most effective results to obtain high value of hardness. Large size of SiC_p is not recommended for reinforcement. Similar trend can be seen in flexural strength (Fig. 5) and tensile strength (Fig. 6) measurements except relative value of AZ91 Mg is higher in strength than in hardness. It is noted that the volume fraction of reinforcements is same for all composites mentioned here (15vol%).

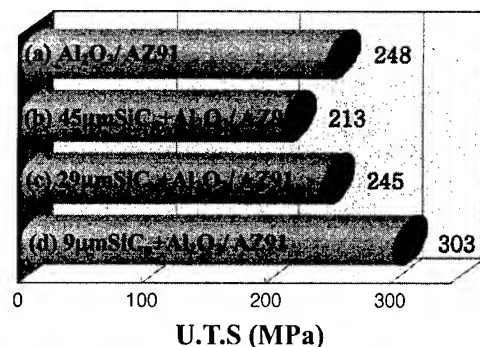


Fig. 6 Tensile strength of Mg matrix hybrid composites.

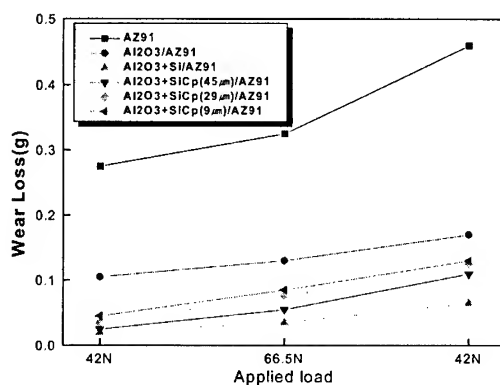


Fig. 7 Wear loss of AZ91 and AZ91 composites as a function of applied load.

Fig. 7 shows wear property of AZ91 Mg and AZ91 Mg matrix composites. Wear resistance of hybrid AZ91 Mg matrix composites, regardless of the size of SiC_p , reveals similar values. Wear resistance of AZ91 Mg/ $(\text{Al}_2\text{O}_3 + \text{Si})$ is higher than SiC_p reinforced hybrid composites possibly due to in-situ formation of Mg_2Si . For all materials, wear loss increases with sliding speed almost linearly.[15]

4. IN-SITU FRACTURE BEHAVIOR

Hybrid AZ91 Mg matrix composites reinforced with $(\text{Al}_2\text{O}_3 + \text{SiC}_p)$ were tested with notched CP(Compact tension) type specimen employing the loading stage equipped in SEM for the investigation of the fracture behavior. Fig. 8 shows the loading stage and specimen geometry of the in-situ fracture experiment. The series of SEM micrographs in Fig. 9 showing cracks formed near the notch of the in-situ fracture test specimens are for hybrid AZ91 Mg/(10% $\text{Al}_2\text{O}_3 + 5\% \text{SiC}_p$) with different SiC_p sizes, (1) $45\mu\text{m}$, (2) $29\mu\text{m}$ and (3) $9\mu\text{m}$. Fracture of SiC_p is seen in the composites containing large size of SiC_p , i.e., $45\mu\text{m}$ and $29\mu\text{m}$ whereas SiC_p particles are not fractured with $9\mu\text{m}$. Crack propagates mainly along the interfaces between Mg matrix and reinforcing ceramics (Al_2O_3 and SiC_p). Even though the cracks tend to propagate along the weak interfaces, fracture of the composites could be somewhat delayed with hybridization. If SiC_p are small enough and fracture of SiC_p does not occur, the crack front meets shorter Mg/ SiC_p interfaces frequently instead of consecutive encounter of longer

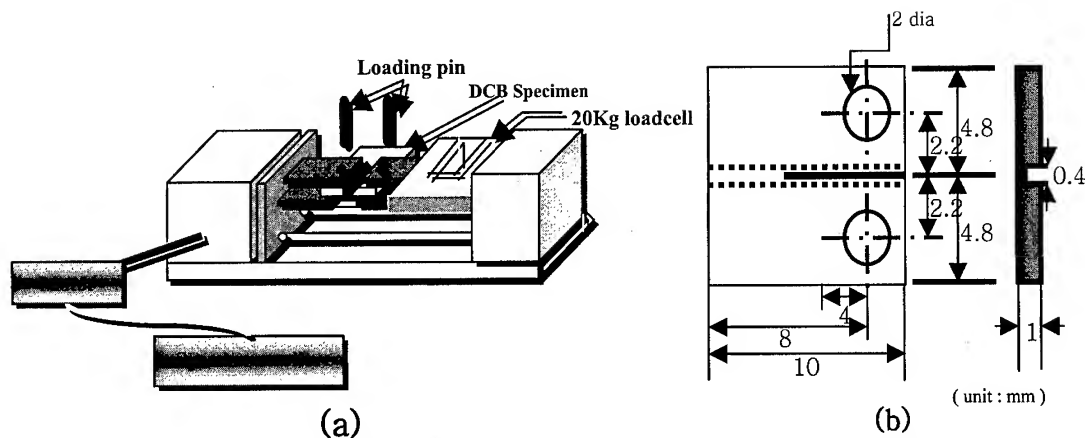


Fig. 8 (a) The loading stage used for in-situ fracture observation in SEM.
(b) sub-size DCB specimen (ASTM E 399-83)

Mg/ Al_2O_3 interfaces. However the effectiveness of hybridization is not achieved with large size of SiC_p . Localized shear band formed in Mg matrix can be seen also along the propagated cracks.

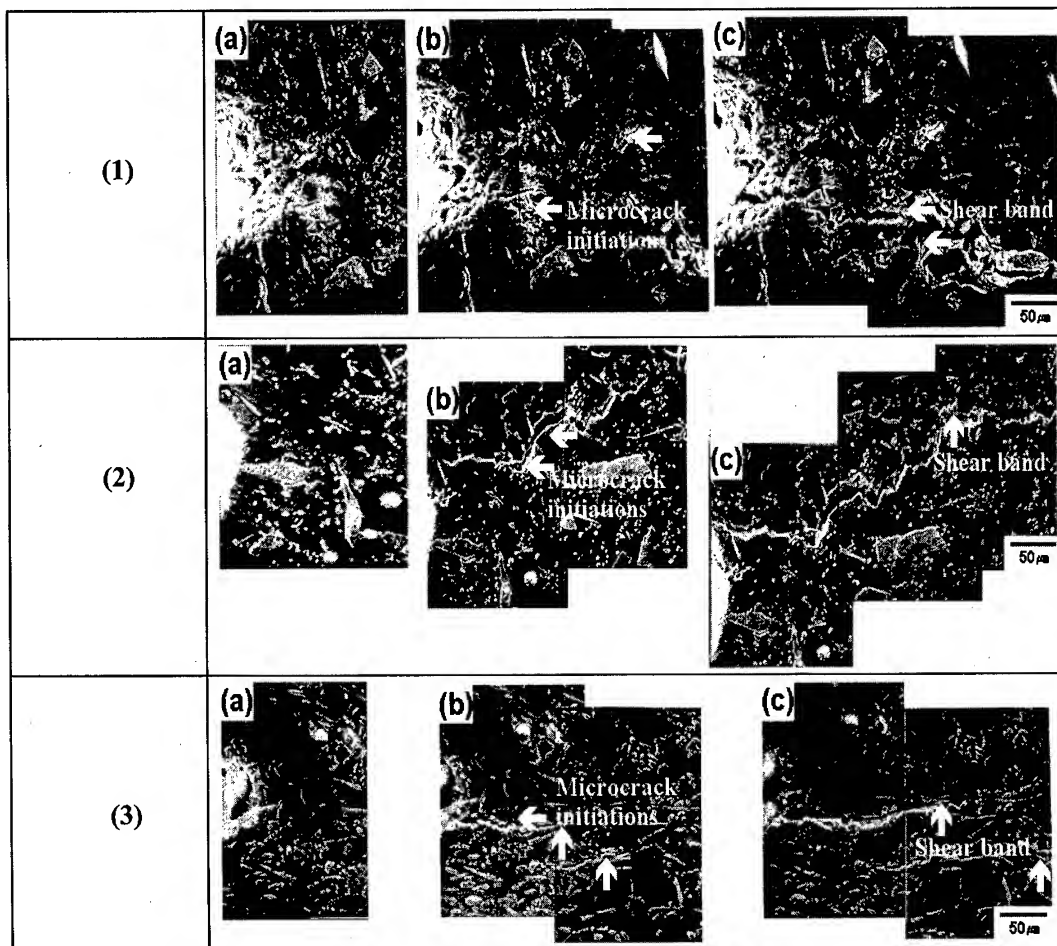


Fig. 9 Series of SEM micrographs near notch tips of hybrid composites.
(1) $\text{Al}_2\text{O}_3 + \text{SiC}_p(45\mu\text{m})/\text{AZ91}$ (2) $\text{Al}_2\text{O}_3 + \text{SiC}_p(29\mu\text{m})/\text{AZ91}$ (3) $\text{Al}_2\text{O}_3 + \text{SiC}_p(9\mu\text{m})/\text{AZ91}$.

5. CONCLUDING REMARKS

Fundamental studies on hybrid Mg matrix composites are summarized with the system of AZ91 Mg/(Al₂O₃+Si) and AZ91 Mg/(Al₂O₃+ SiC_p). Squeeze casting method could be prospective processing technique for the fabrication of the hybrid Mg matrix composites. Microstructure, mechanical properties and fracture behavior of hybrid Mg matrix composite are surveyed in this paper.

ACKNOWLEDGMENT

This work was supported by Korea Science and Engineering Foundation (2000).

REFERENCE

1. M. Kobashi and T. Choh, Proc. ICCM-12, Metal Matrix Composites, (1999), pp. 454.
2. S.Lim, T. Imai, Y. Nishida and D. Jiang, Proc. ICCM-11, Metal Matrix Composites and Physical Properties, (1997), pp. 486.
3. John E. Allison and Gerald S. Cole, JOM, Vol.1, (1993), pp. 19.
4. S. K. Hong, S. H. Hwang, J. C. Choe, I. M. Park, H. Tezuka, T. Sato and A. Kamino, Materials Science Forum, vol. 242, (1997), pp.165-172.
5. E. Jeon, M. Kim, I. Choi, K. Cho and I. Park, Proc. of the 2nd Pacific Rim Intern. Conf. on Advanced Materials and Processing, K. S. Shin, J. K. Yoon and S. J. Kim, eds., KIM, Kyungju, (1995), pp. 2675.
6. I. Horsfall and S.I Cundy, Ceram. Eng. Sci. Proc., 13(9-10) (1992), pp. 605-613.
7. Kim, J.S., Kaneko, J. and Sugamata, M., J. Japan Inst. Metals, Vol. 56, No.7, (1992), pp. 819-827.
8. Luo, A., Processing, Metall. Mater. Trans.A, Vol. 26A (1994), pp. 2445-2455.
9. Martin, A. and Llorca, J., Mater. Sci. Eng., Vol. A201(1995), pp. 77-87.
10. P. Abachi, B. L. Mordike and K. U. Kainer, Proceedings of ICCM-11, Vol. II (1997), pp. 424.
11. I. M. Park, I. D. Choi and K. M. Cho, Proceedings of the 3rd Korea-China Joint Workshop on Advanced Materials-Transportation Materials, Cheju, Korea, (1999/08), pp138-151.
12. I. M. Park, K. S. Sohn, K. J. Euh and S. H. Lee, Metallurgical and Materials Transactions A, Vol. 29A, (1998/10), pp. 2543-2553.
13. I. M. Park, C. O. Son, I. D. Choi, K. M. Cho and S. H. Lee, The Third Pacific Rim International Conference on Advanced Conference on Advanced Materials and Processing, (1998/07), pp. 287-294.
14. Y. G. Cho, S. Y. Kim, I. M. Park and K. M. Cho, TMS, Orlando, USA, (1997/02), p981.
15. David A. Rigney: Fundamentals of Friction and Wear of Materials, ASM, (1980), pp. 13, 43, 187.

Session X

**CORROSION &
SURFACE TREATMENT**

CORROSION ATTACKS OF ALUMINUM WIRE IN A SOLUTION CONTAMINATED BY COMBUSTION GAS OF CHEMICAL WASTE

Osami Seri

Department of Mechanical System Engineering,
Muroran Institute of Technology, Muroran, 050-8585, Japan

ABSTRACT

An attempt has been made to clarify influence of environmental solution contaminated by combustion gas of polyvinyl-chloride and chemical disposals on corrosion behavior of aluminum wire. Electrochemical measurement and metallurgical observation by SEM show that the environments, which have absorbed exhaust gas of polyvinyl-chloride matter, are detrimental to corrosion resistance of aluminum and cause the corrosion degradation severely.

1. INTRODUCTION

Aluminum wire alloys are used in power electric transmission cable for their light weight, better conductivity and superior corrosion properties. There been various investigations of corrosion behaviors for aluminum and its alloys. It is well known that aluminum materials are pitting-attacked in a solution containing chloride ions [1]. There has been few report for the corrosion behavior of aluminum used in power electric transmission cable. We had severe accident of the power electric transmission cable at Shimoda City, Shizuoka Prefecture in summer, 1998[2]. The residents there had a whole day blackout due to an interruption of the power supply. The cable, twisted together to make aluminum wires, which has been damaged and interrupted. The snapping of the main and reserve cables cause the stoppage. The newspaper said that most of aluminum wires of the cable were corroded by exhaust gas of a chemical wastes from an industrial disposal plants. It was the aim of this investigation to prove data relevant to an basic understanding of the corrosion behavior of aluminum which is exposed to contaminated circumstances, especially contaminated by exhaust gas of chemical wastes.

2. EXPERIMENTAL METHOD

2.1 Specimen

The specimen is aluminum wire for the purpose of power electric transmission cable under standardization of JIS H2110. And its chemical composition is high purity aluminum of 99.7%. After degreasing by acetone, the specimen was pickled in a 10% NaOH solution at 353K for 1min. After rinsing with water, specimens were finally passivated in a 30% HNO₃ solution at room temperature (about 298K) for 1min. To remove corrosion products adhering after tests, specimens were dipped into a cleaning solution (4% Na₂CrO₄·4H₂O + 10% H₃PO₄ aqueous solution) at 353K for 4min.

2.2 Solution

The test solution was prepared by using a special apparatus: the 750ml of tap water was bubbled up through combustion gas made by burning 12g of a polyvinyl chloride electric cord

(PVC cord). The test solution sucked combustion gas at a rate of about 6l/min. The combustion temperature is about 873~1073K and the period of burning time is 25min.

2.3 Measurement

The polarization curves have been potentiodynamically measured. A scanning rate of 0.5mV/s was selected. The reference electrode was Ag/AgCl electrode in saturated KCl solution. The potential are quoted with respect to the Ag/AgCl unless otherwise stated. The platinum counter electrode and working electrode were placed in the same solution. The reference electrode was connected to the measuring cell with a salt bridge and Luggin capillary at the distance of 2mm from the specimen. This distance makes the iR drop negligibly small. No corrections to the polarization curves for iR drop were necessary. A scanning electron microscope(JSM-T100 of JEOL Ltd.) was utilized for the observation of the specimen surfaces.

3. EXPERIMENTAL RESULTS

3.1 pH changes of test solution

The pH value of the test solution when has been absorbed exhaust gas of PVC with time is measured for the period of 30min. The value of pH indicated about 7.6 at first. The value gradually decreases with absorption time, and indicates about constant value of 2.5 at the time of more than 18min. It is confirmed that the combustion gas of PVC makes the solution acidic in quick manner.

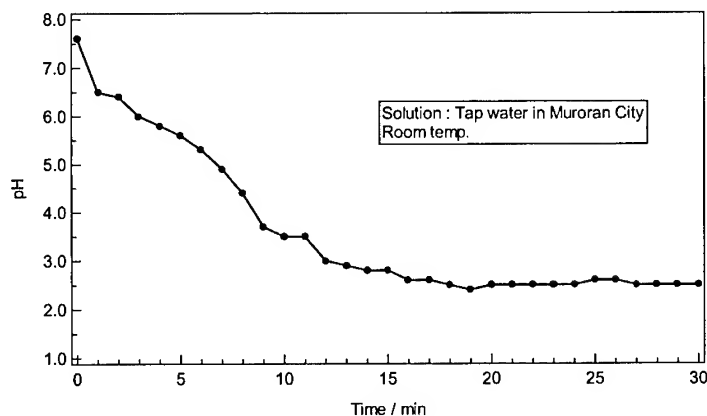


Fig.1 the pH change of test solution contaminated by exhaust gas of PVC

3.2 Change of corrosion potential

Corrosion potential of aluminum wire, which is corroded in the acidic solution made by in 3.1, is measured for the period of 1800min. The early corrosion potential indicated about -620 mV. Then the potential shifts to noble direction and shows the maximum value of -549 mV at 250min. The constant value of 549mV shows for the period of more than 1000min.

3.3 Surface observations

The surface of the specimen corroded in 3.2 was observed by the SEM. The results are shown in Fig.2 (a) and Fig.2 (b).

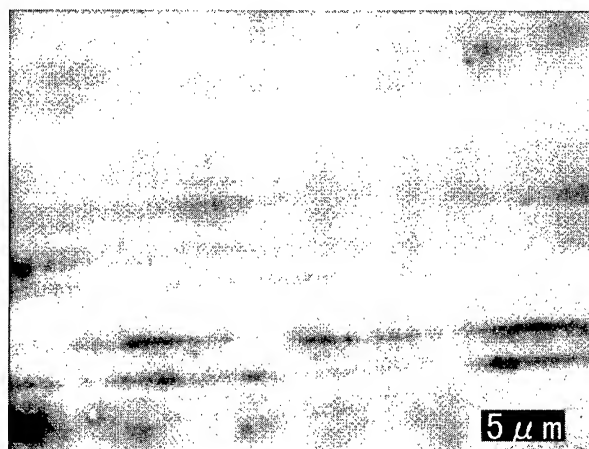


Fig.2 (a) Surface observation of specimen (before corrosion test)



Fig.2 (b) Surface observation of specimen (after corrosion test)

The Fig.2 (a) shows original surface, which is not corroded, for the sake of comparison. No particles such as intermetallic compounds are observed. The Fig.2 (b) shows corroded surface mentioned in 3.2. There are many pitting attacks forming facet dissolution [3].

3.4 Polarization curves

The polarization curves of aluminum wire specimen dipped in to the acidic test solution were measured. The anodic polarization curve shows the typical shape of aluminum pitting-attacked in a chloride solution: about -600mV of the pitting potential, at which the anodic current density increases rapidly, is observed. The cathodic polarization curve characteristically shows that the plateau area, which is a sign of the limiting cathodic current density for dissolved oxygen reduction reaction, is observed around $-650\text{mV}\sim 950\text{mV}$.

4. DISCUSSIONS

4.1 Metallurgical phase of aluminum wire used

The aluminum wire specimen used contains 99.7% aluminum purity. The chemical species and their volumes may not be enough to form the second phases such as intermetallic compounds. And the surface observation by SEM (Fig.1 (a)) shows that there is no particle on the surface. So phases in aluminum wire specimen used can be treated as single phase of high purity aluminum matrix.

4.2 Characteristics of test solution contaminated by PVC exhaust gas

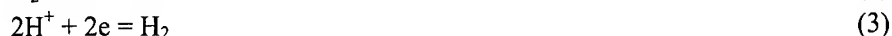
It is well known that the exhaust gas after burning PVC contains chlorine or hydrogen chloride. This hydrogen chloride when reacts with water rapidly changes into hydrochloric acid. The reason why the pH value of the test solution in Fig.1 indicates low value is due to producing strong acid substances such as hydrochloric acid. Some parts of the PVC combustion gas have hydrogen chloride matter. It is found that the test solution used has suitable atmosphere for occurrence of pitting attacks of aluminum. The solution contains chloride ions provides easy occurrence of pitting attacks and acidic circumstances for hard forming of oxide film.

4.3 Chemical forms of aluminum wire in test solution

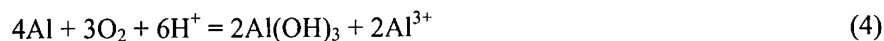
Aluminum ions is electrochemically stable species when aluminum is corroded in the test solution because of the electrochemical position in E-pH diagram, both the electrode potential of -575mv and the pH value of 2.5 will make aluminum corroded by the test solution into aluminum ions.

4.4 Corrosion behavior of aluminum wire in a contaminated solution by PVC gas

The discussion in 4.3 indicated decidedly that anodic reaction is dissolution reaction of aluminum wire and cathodic reaction is oxygen reduction reaction or hydrogen ion reduction reaction as follows:



Overall reactions are following reactions by adding eq.(1) + eq.(2) or eq.(1) + eq.(3).



Aluminum ions produced by eq.(4) and eq.(5) is hydrolyzed into aluminum hydroxide as follows:



Hydrogen ions produced by eq.(6) may contribute to promote further pitting attacks of aluminum wire. When the polarization behaviors are characterized by an approximately linear relationship between electrode potential and current density, following relation can be ex-

pressed[4].

$$I_g = (E_c^0 - E_a^0) / (h_c / S_c + h_a / S_a + \rho l) \quad (7)$$

where, I_g is galvanic current (A), E_c^0 is corrosion potential of cathode (V), E_a^0 is corrosion potential of anode (V), h_c is polarized resistance of cathode ($\Omega \text{ cm}^2$), h_a is polarized resistance of anode ($\Omega \text{ cm}^2$), S_c is area of cathode (cm^2), S_a is area of anode (cm^2), ρl is solution resistance (Ω).

Since the test solution used shows high solution conductivity, the term of $(h_c / S_c + h_a / S_a)$ is larger than that of ρl . So, the eq. (7) will be simplified into flowing equation with an acceptable error.

$$I_g = (E_c^0 - E_a^0) / (h_c / S_c + h_a / S_a) \quad (8)$$

The values of E_c^0 , E_a^0 , h_c , h_a will be calculated by the anodic and cathodic polarization curves. However it is difficult to estimate the values of S_a and S_c because their values change from moment to moment during the corrosion process. Then, eq.(8) is expressed to the follow:

$$i_g = I_g / S_a = (E_c^0 - E_a^0) / \{h_c(S_a / S_c) + h_a\} \quad (9)$$

The value of i_g is current density of galvanic couple and depends on the ratio of S_a/S_c . The experimental data from measurements are drawn in Fig.3 in order to clarify the electrochemical placement among corrosion potential-time curve, anodic/cathodic polarization curves and ratio of S_a/S_c . The cross point of anodic/cathodic polarization curves shows corrosion potential of -590mV , which is under the condition of $S_a/S_c = 1$ ($S_a = S_c = 1\text{cm}^2$). As the experimental data of corrosion potential measured shows about -580mV , the cross point of anodic/cathodic polarization curves should be shift to noble direction. The ratio of S_a/S_c must be $S_a/S_c < 1$ to satisfy the cross point. The region of the cross point above lay on the region of pitting attack occurrence. This leads that the aluminum wire specimen in the test solution may suffer from severe pitting attacks.

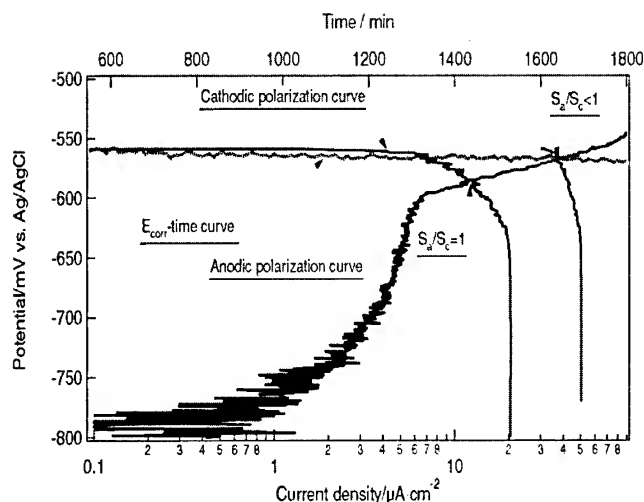


Fig.3 Schematic relationship between corrosion potential measured and anodic/cathodic area ratio by superimposing polarization curves

5. CONCLUSION

Aluminum wire which used as cable for power electronic transmission in Japan was corroded in a solution contaminated by the exhaust gas of a polyvinyl chloride cord. By the electrochemical measurements and metallurgical observation it is found that the solution contaminated by the exhaust gas of a polyvinyl chloride is detrimental to corrosion of the aluminum wire and then causes the pitting attacks severely.

REFERENCES

1. ASM International: Metals Handbook, 9th edition, Vol.13 (1987), pp.583-609.
2. Shizuoka Shimbun: Sept.1st (1998)
3. O.Seri and M.Imaizumi: Corrosion Science, Vol.30 (1990), pp.1121-1133.
4. S.Michael ed.:Materials and Technology, Vol.19, Wiley-Vch,(2000),pp113-132.

CHANGES IN OXIDE FILM CHARACTERISTICS OF MAGNESIUM ALLOY BY THE ADDITION OF CALCIUM AND MINOR ELEMENT

Bong-Sun You, Moon-Hoe Kim, Won-Wook Park and In-Sang Chung*

Korea Institute of Machinery & Materials,
66 Sangnam-dong, Changwon, Kyungnam, Korea 641-010

* Dept. of Metallurgical Engineering, Kyungpook National University,
1370 Sangkyuk-dong, Puk-ku, Taegu, Korea 702-701

ABSTRACT

Morphological and compositional characteristics of oxide films were investigated in Ca-containing magnesium alloys oxidized at high temperatures. And, the effects of Al and Y additions on the oxidation behavior of the molten alloys were also studied in Ca-containing magnesium alloys. The oxide films of pure magnesium formed at high temperature were porous, whereas those in Ca-containing alloys were compact, thin and dense. The oxide films of Ca-containing alloy formed after solid and liquid oxidation were basically in an amorphous state. However, in the oxidation at 700°C, Mg-Ca binary alloy was ignited and burned, whereas the Mg-Ca alloy containing Al and Y showed the improved oxidation resistance because of the protective oxide layers on the molten alloys. The surface analyses indicated that the thin oxide layer of Mg-Ca-Al alloy consisted of the mixed structure of MgO, CaO and Al₂O₃, with the single-layered oxide layer. On the other hand, the oxide layer of the Mg-Ca-Y alloy had a double-layered structure composed of two distinct MgO/CaO and Y₂O₃, playing a role of very effective barriers to improve the high temperature oxidation resistance.

1. INTRODUCTION

The extensive structural application of the magnesium alloys is limited by the poor corrosion and oxidation resistance at elevated temperature[1,2]. The high affinity to oxygen and the high vapor pressure of magnesium alloys have caused rapid oxidation and ignition with flame. However, the non-combustible magnesium alloys with high ignition temperature were recently developed to draw significant attention as promising oxidation resistant alloys. According to the previous works[3-6], Ca addition to magnesium alloy was very effective to suppress continuous oxidation and spontaneous ignition followed by violent combustion at high temperature. It is noticeable that the microstructural change from porous to compact oxide layer could be induced by Ca addition. Thus, calcium addition to magnesium alloy was known as one of the challenging methods to avoid the use of environmentally harmful SF₆ + CO₂ mixture gas in melting and casting process (1 kg of SF₆ in the atmosphere gives approximately the same contribution to the greenhouse effect as 24 tons of CO₂ [7]). However, the microstructural and compositional characteristics of the oxide layer in Ca-containing magnesium alloys have not fully understood.

This study is concerned with the analyses of the oxide films formed at high temperature, of which oxidation treatments were carried out in both solid and liquid state of Ca-containing

magnesium alloy. And, the effects of aluminum and yttrium additions on the oxidation behavior of Ca-containing magnesium alloys were also investigated. The microstructural and compositional characteristics of the oxide layers in Mg-Ca-Al and Mg-Ca-Y alloys were analyzed in detail, and compared with those of Mg-Ca binary alloy.

2. EXPERIMENTAL PROCEDURE

Magnesium alloys were melted and cast under a mixed gas ($\text{SF}_6 + \text{CO}_2$) atmosphere in the steel crucible and mold. The SF_6/CO_2 ratio and flow rate were constantly controlled by a MFC (mass flow controller). Table 1 shows the chemical compositions of the Mg-Ca and Mg-Ca-X(Al,Y) alloys. The amounts of Al and Y added to Mg-Ca alloy were varied from 0.3 to 1.0wt%.

Mg-Ca and Mg-Ca-X(Al,Y) alloys were oxidized at 440~750°C in the air. The weight changes of the binary and ternary alloys were measured after oxidation treatment in the air. After the oxidation treatment, the surface and cross-sectional morphologies of oxide films of the alloys were investigated using FE(Field-emission)-SEM and TEM.

Table 1. Chemical compositions of the Mg-Ca and Mg-Ca-X alloys.

Designated		Measured(wt%)
Mg-2.0Ca		2.32Ca
Mg-Ca-Al	Mg-2.0Ca-0.3Al	Mg-1.71Ca-0.28Al
	Mg-2.0Ca-1.0Al	Mg-2.10Ca-1.16Al
Mg-Ca-Y	Mg-2.0Ca-0.3Y	Mg-1.74Ca-0.27Y
	Mg-2.0Ca-1.0Y	Mg-2.07Ca-1.03Y

3. RESULTS AND DISCUSSION

From the previous works [3,4] on the oxidation behavior of Mg-Ca alloys, it was reported that the oxidation resistance of magnesium alloy was improved remarkably by calcium addition at high temperature. In this study, the cross-sectional view of oxide films in pure magnesium and Ca-containing alloy oxidized at 500 °C showed a considerable difference in microstructure, as shown in Fig. 1. The oxide film of pure magnesium consisted of discrete loose oxide particles (Fig. 1(a)), whereas that of Mg-Ca alloy showed thin, dense and compact oxide films (Fig. 2(b)). The thickness of oxide films in Mg-Ca alloy was approximately 200 nm, which was less than a half of that in pure magnesium. TEM micrograph (Fig. 1(c)) and SADP (Fig. 1(d)) taken from the cross-section of Mg-Ca alloy oxidized at 500 °C revealed that the oxide films were basically in an amorphous state. The amorphous structure of MgO films in pure magnesium generally plays an important role as a protective layer to prevent further oxidation at low temperature, however the films easily become to be porous and loose with the increase of oxidation temperature. On the contrary, since the amorphous oxide films in Mg-Ca alloy formed at 500 °C were more protective/thermally-stable compared to pure magnesium, it is suggested that the stable amorphous structure of oxide films in Ca-containing alloy could effectively contribute to high temperature oxidation resistance.

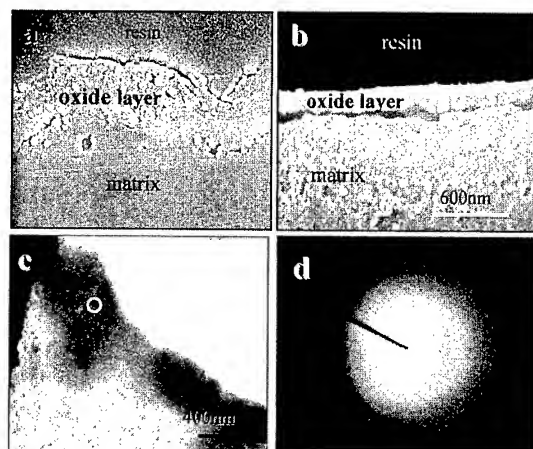


Fig.1 FE-SEM(a,b) and TEM(c,d) micrographs of pure Mg(a) and Mg-Ca alloy(b,c,d) oxidized at 500 °C

On the other hand, the protective oxide films could also be found on the surface of Mg-Ca alloy after the liquid oxidation treatment. Fig. 2 shows the microstructural and compositional investigations on the fractured surface (Fig. 2(a)) and the sectioned surface (Fig. 2(b)) of the oxide films formed after oxidation at 700 °C. The protective layer was composed of Mg, Ca and O (Fig. 2(c)), and the matrix mainly consisted of Mg and Ca (Fig. 2(d)). The oxide films formed in Ca-containing alloy were dense and enriched with Ca in part. The average thickness of oxide films of the molten alloy was in the range from 200 nm to 300 nm which is slightly thicker than those formed after the solid oxidation of 500 °C. And, it is very remarkable that the oxide films obtained after the liquid oxidation treatment were analyzed as

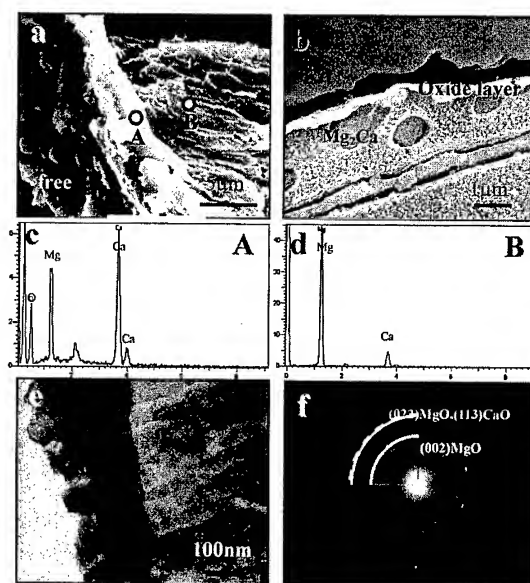


Fig. 2 FE-SEM(a,b), EDS results(c,d) and TEM micrographs(e,f) of oxide layer in Mg-Ca alloy oxidized at 700 °C

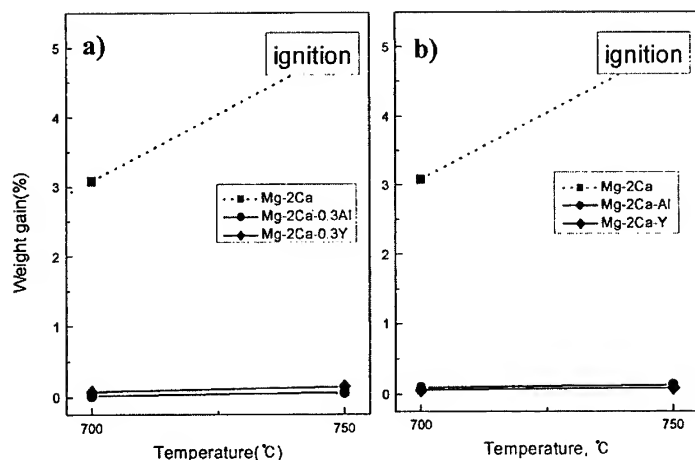


Fig. 3 Weight gains of the Mg-Ca, Mg-Ca-Al and Mg-Ca-Y alloys oxidized at 700(a) and 750°C (b)

the mixture of amorphous and microcrystalline structure through TEM micrograph (Fig. 2(e)) and SADP (Fig. 2(f)) in Mg-Ca alloy.

The additions of Al and Y to the Mg-Ca alloys were very effective to further increase of the oxidation resistance. The weight gain of the Mg-Ca alloy measured after the oxidation at 700°C was quite higher than that of the ternary alloys (Fig. 3(a)). The Mg-Ca alloy ignited and evaporated violently to be white-colored oxide with the increase of oxidation temperature to 750°C. However, there were little change in weight gains after the oxidation of the ternary alloys regardless of Al and Y contents (Fig. 3(a,b)).

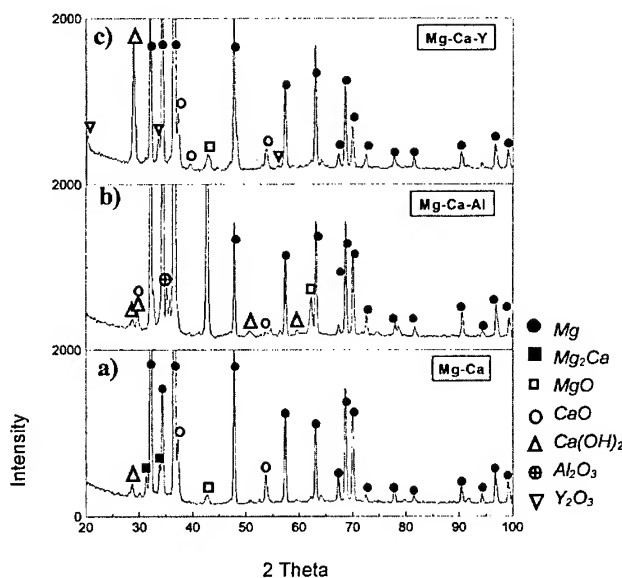


Fig. 4 Low angle XRD peaks taken from the surface of Mg-2Ca base alloys containing 1.0 wt% of Al and Y oxidized at 700°C

Phase identification using a low angle XRD was done on the oxide films of Al and Y containing alloys, as shown in Fig. 4. The oxide layers of Mg-Ca binary alloy formed at 700°C (Fig. 4(a)) were analyzed as MgO and CaO. In the ternary alloy, it was found that the oxide layer consisted of Al_2O_3 , MgO, CaO and $\text{Ca}(\text{OH})_2$ in the Mg-Ca-Al alloy (Fig. 4(b)), and Y_2O_3 , MgO and CaO in the Mg-Ca-Y alloy (Fig. 4 (c)). It is obvious that these Al_2O_3 in Mg-Ca-Al alloy and Y_2O_3 in the Mg-Ca-Y alloy contribute to the prevention of the ignition on the surface of the molten alloys.

The sectioned surface of oxide layer in the Mg-Ca-Al alloys oxidized at 700°C were shown in Fig. 5. The single-layered oxide of the Mg-Ca-Al alloy with excellent oxidation resistance was relatively thin and compact without any defects such as pore and grain boundary. The oxide layers of the Mg-Ca-Y alloy formed at 700°C (Fig. 6) were quite different from that of the Mg-Ca-Al alloy. The oxide layer of the Mg-Ca-Y alloy consisted of two distinct layers as shown in Fig. 6(a). The EDS analyses for element mapping showed that the outer layers contained a high fraction of Ca, and the inner layers contained a high fraction of Y instead. Based on these results together with Fig. 4, it was confirmed that the

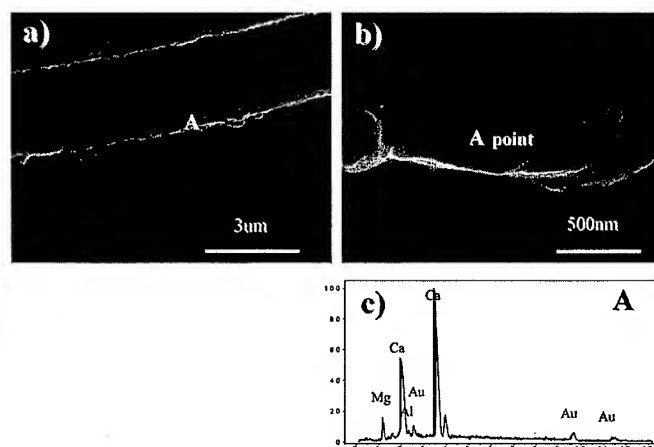


Fig. 5 Cross-sectional micrographs(a,b) and EDS result(c) of oxide layer in Mg-2.0Ca-1.0Al alloy oxidized at 700 °C

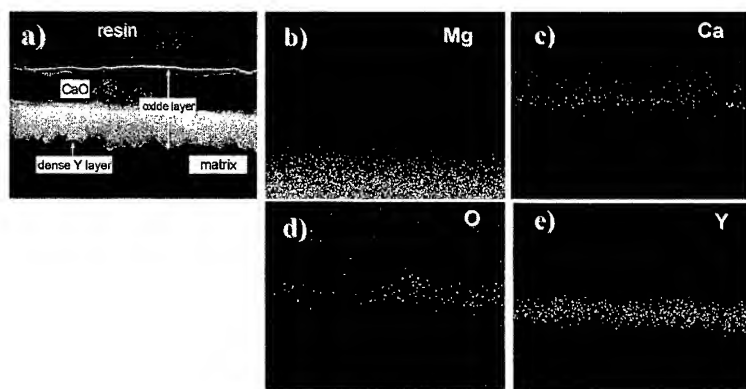


Fig. 6 Cross-sectional micrograph(a) and EDS mapping results of (b) Mg, (c) Ca, (d) O and (e) Y in the oxide layers of Mg-2Ca-1.0Y alloy oxidized at 700 °C

outer layer was the mixture of MgO and CaO, and the inner layer was Y_2O_3 in the Mg-Ca-Y alloy.

The addition of Ca to pure magnesium improved oxidation resistance because Ca made the oxide layer compact and dense. However, the oxidation resistance of Ca-containing alloy is not sufficient to retard oxidation rate at high temperature, which resulted in ignition and combustion at around 700°C. In the ternary alloys containing Al and Y, the oxidation resistance remarkably improved by forming thermally-stable oxide layers on the surface. Accordingly, it was suggested that the protective oxide layer of Ca-containing magnesium alloy improves the oxidation resistance, and the additions of Al or Y to the Mg-Ca alloy showed a good possibility that magnesium alloys can be melted and cast without using SF_6 + CO_2 mixture gas.

4. CONCLUSIONS

1. The oxide films of Ca-containing alloys were basically in an amorphous state. The suppression of continuous oxidation in Ca-containing magnesium was caused by the formation of amorphous and compact oxide films on the surface.
2. The Mg-Ca molten alloy easily ignited during oxidation at about 700°C in the air, whereas the Mg-Ca molten alloys containing Al and Y showed the remarkably improved oxidation resistance due to the formation of more protective oxide layer than the binary alloy.
3. In the ternary alloys oxidized at 700°C, the single-layered oxide of the Mg-Ca-Al alloy consisted of the mixed structure of MgO, CaO and Al_2O_3 . On the contrary, the oxide layer of the Mg-Ca-Y alloy possessed the double-layered oxide of MgO/CaO and Y_2O_3 acting as very effective oxide barriers to improve oxidation resistance at high temperature.

REFERENCES

1. A. Luo, M. O. Pekguleryuz, *Material Science*, 29(1994) p5259.
2. B. L. Mordike, W. Henning, in *Third International Magnesium Conference*, G.W.Lorimer, eds., Manchester, (1997) p54.
3. B. S. You, W. W. Park and I. S. Chung, *Scripta Mater.*, 42 (2000) p1089
4. B. S. You, W. W. Park and I. S. Chung, in *2nd Israel Int. Conf. on Magnesium Sci. & Technology*, E. Aghion and D. Eliezer, eds., Israel,(2000) p377
5. M. Sakamoto, S. Akiyama, T. Hagio and K. Ogi, *Japan Foundry Eng. Soc.*, 69 (1997) p227
6. S. Y. Chang, M. Matsushita, H. Tezuka and A. Kamio, *Int. J. Cast Metals Res.*, 10 (1998) p345
7. H. Gjestland and H. Westengen, in *Third International Magnesium Conference*, G.W.Lorimer, eds., Manchester(1996)) p33

CORROSION MODELS IN Mg ALLOYS WITH RESIDUAL AND CONCENTRATED STRESSES

Shun-ichiro TANAKA and Shuichi IWATA

Research into Artifacts, Center for Engineering, The University of Tokyo
4-6-1 Komaba, Meguro-ku, Tokyo 153-8904, Japan

ABSTRACT

The effect of stress on a corrosion mode of a thixomolded Mg-Al-Mn alloy in a NaCl aqueous solution was studied in order to elucidate the corrosion mechanism, the time-dependent characteristics of corrosion products and an actual concentrated stress value in a grain (α -Mg) and a grain boundary ($\text{Mg}_{17}\text{Al}_{12}$) around an artificial notch. The residual stress values of both phases in the lapped Mg alloy were balanced and reached about 30 MPa with opposite sign. The mechanism of corrosion in the lapped plate was proposed as a microscopic anode-cathode reaction based on the concept of the localized cell. The corrosion mode in the stress concentrated area was quite different depending on the sign of the stresses; a fine and dense amorphous hydro-oxide formed in the region of tensile stress, whereas a coarse amorphous oxide formed in that of compressive stress. The concentrated tensile stress at the notch root relaxed due to the corrosion followed by gradual relaxation to zero.

1. INTRODUCTION

The development of molding techniques for complicated shapes is expected to lead to the application of magnesium alloys for automobile components. Such components will be required to withstand as long as 10 years in severe environmental and mechanical conditions while running. Although Mg alloys have high specific strength, their reliability in such conditions has not been thoroughly confirmed yet. Stress corrosion cracking (SCC), which is induced as inter- or intra-granular mode, is a well-known phenomenon in steel. It has been explained in terms of the complex reaction of stress and electrochemical factors. However, SCC has not been discussed on the basis of actual measured stress values for a small area of interest such as one in which stress is concentrated or which is welded. The recent development of a stress measurement in a localized area carried out by one of the authors, S.-I. Tanaka, will provide an explicit relationship with the corrosion mode of the material. Using the μ -X-ray $\sin^2\psi$ method, Tanaka has evaluated detailed actual distributions of residual stress around ceramic/metal interface [1] and also measured a concentrated stress distribution to discuss non-linearity around an artificial notch in the ceramic [2], and it is convenient to evaluate such a stress value in the poly-crystalline materials. This method clarified the contribution of each phases of the alloy to corrosion separately, and revealed time-dependent characteristics of the concentrated stress and the corrosion products around an artificial notch [3,4]. This paper aims firstly to clarify the effect of actual residual/concentrated stress values on the corrosion mode of magnesium alloy in an aqueous solution quantitatively, and secondly to propose the model of stress corrosion in Mg alloy.

2. EXPERIMENTAL

The magnesium alloy used in this experiment is Mg-Al-Mn, also known as AM-60, and applied in automobile components. The specimen was prepared from a lapped thixomolded plate, 2 mm in thickness and having a 4×40 mm bending bar shape, and on which V notch was introduced with the dimensions of 1.5 mm in depth, 20 deg in opening angle and 12 μ m in tip radius [2-4]. A load was applied by 3 point bending to open the notch as a Mode I. Stress distributions were measured by the μ -sin² ψ method [1] using a highly powered collimated Cr-K α irradiation by which distributions of the residual stress before loading and the concentrated stress ahead of the notch root after loading were successfully evaluated. The measuring conditions are listed in Table 1 by which the stress value in the grain and the grain boundary can be evaluated separately. An area of irradiation was optimized using a collimator having a pinhole of 0.5 - 1.0 mm in diameter, taking into account diameter and randomness of grains in the specimen [3,4].

A specimen bar loaded Mode I was immersed in 0.9 % NaCl aqueous solution at room temperature and time-dependent corrosion features on the surface were observed by an optical microscope. Dynamic change of the surface was also observed and recorded *in-situ* by VCR equipped with an optical microscope. Distributions of the normal stress across the notch were obtained at each stage of the introduction of the notch, the loading and the immersion. The change of stress values at the area neighboring the notch root was monitored over time.

Table 1 Conditions for stress measurement by the μ -sin² ψ method

	Mg	Mg ₁₇ Al ₁₂
apparatus	Rigaku PSPC-MDG	
X-ray	Cr-K α , V-filter, max 50kV-160mA	
collimator (mm)	ϕ 1.0 (ϕ 0.5, ϕ 0.1)	
ψ -angle (deg)	0, 10, 15, 20, 25, 30, 35, 40, 45	
tilt	side-inclination	
$2\theta_0$ (deg)	140.0	133.4
lattice plane	(202)	(660)
stress constant K (MPa/deg)	-110	-160

3. DISTRIBUTION OF RESIDUAL AND CONCENTRATED STRESSES

3.1 Residual stress distribution

Microstructure of the specimen, thixomolded AM-60, consisted of primary α -Mg grains with Al atoms in solid solution and eutectic Mg₁₇Al₁₂ phase with α -Mg at the grain boundary. The diameter of grain is about 30 μ m and the number of grain is pseudo-sufficient to be regarded as polycrystal in the X-ray irradiation area 1.0 mm in diameter. The X-ray sin² ψ

method provides a stress value for each phase in the irradiation area separately, and $2\theta_0$ values were selected as 140.0 deg for α -Mg (202) and 133.4 deg for $Mg_{17}Al_{12}$ (660) from a micro-area diffraction profile as listed in Table 1. A stress constant was estimated using elastic constant and Poisson's ratio as -110 and -160 MPa/deg, respectively.

The residual stress values in the surface area of lapped thixomolded AM-60 bar measured at the positions 0.5, 1.5 and 2.5 mm from the notch root ranged 20-40 MPa compressive (-) in α -Mg grains as shown in Figure 1 and about 30 MPa tensile (+) in $Mg_{17}Al_{12}$ phase at the grain boundary. Although stress values it was possible to measure were limited to the volume of disk, 1.0 mm in diameter \times 20 μ m in depth, into which Cr-K α penetrates from the surface, stresses in both micro-phases were balanced (see Fig. 5 in Section 6).

3.2 Concentrated stress distribution

After loading by bending to the notched specimen, the distribution of the concentrated stress sensing by α -Mg was measured from the notch root to the opposite end of the specimen. A measured distribution of the concentrated stress is shown in Fig. 1 with the residual stress. Stress intensity factor, K_I , of loading in this case is about 6 MPa·m^{1/2}. The stress value changed from tensile to compressive apart from the root having neutral point at 1.2 mm. The averaging effect appeared remarkably around notch root because of the steep gradient of the stress. In Fig. 1, the measured stress value was 50 MPa tensile at the position of $x = 0.5$ mm from the root in the case of 1.0 mm X-ray collimation, whereas it was 100 MPa tensile at $x = 0.25$ mm from the root in the case of 0.5 mm X-ray collimation. These stress values have error bar of max. 20 MPa. The origins of error are as follows: firstly, an average grain size of 30 μ m which is slightly large to be treated as an ideal polycrystal having sufficient number of grains even in the area irradiated through a 1.0 mm collimator; secondly, slightly fibrous structure of grains caused by the thixomolding process; and thirdly, a statistical error based on small yield of their diffraction peak. An extrapolated stress value of the distribution to the position $x = 0$ mm matches 0.2 % proof stress of magnesium alloy, which indicates a possible plastic deformation at the notch root.

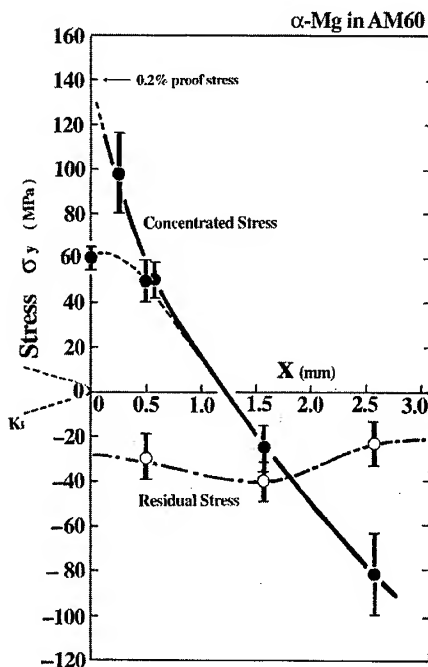


Fig. 1 Residual and concentrated stress distributions measured using the μ -X-ray $\sin^2\psi$ method in α -Mg grains of Mg-Al-Mn alloy, AM-60. The irradiation area was confined to 1.0 mm in diameter. The curve of distribution can be extrapolated to 140 MPa at the notch root, matching 0.2% proof stress of AM-60.

4. MODE OF CORROSION DEPENDING ON THE STRESS DISTRIBUTION

Next, we attempted to elucidate the corrosion characteristics in the case that the stress was present. Mg alloy, AM-60, having distribution of the concentrated stress shown in Fig. 1 was immersed in 0.9%NaCl aqueous solution and the change of its surface was observed by an optical microscope. This composition of aqueous solution is similar to perspiration from a human body. The surface changed drastically within only two minutes and two kinds of corrosion products formed as shown in Fig. 2: a fine but dense compound close to the notch root and a coarse and black one at the opposite end. It is interesting that such morphologies match well with the stress sign shown in Fig. 1, the former corresponding to tensile stress and the latter to compressive stress. They are amorphous phases impossible to identify by micro-area X-ray diffraction, but their compositions are considered to be hydro-oxide and oxide, respectively, presuming from the products immersed in a long term. The latter one may be related to the product of the galvanic corrosion at the contact between the Mg alloy and the stainless steel of the loading jig. As time elapsed the former did not change, whereas the latter grew to cover the entire specimen (Fig. 2).

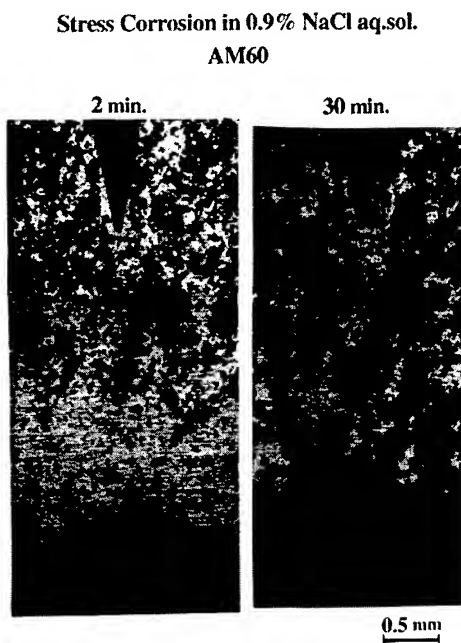


Fig. 2 Corrosion products on the surface of AM-60 in a 0.9% NaCl aqueous solution depending on the stress sign. It was a fine but dense amorphous hydro-oxide in the region of tensile stress, whereas it was a growing coarse amorphous oxide in the region of compression.

5. MODEL OF STRESS CORROSION IN Mg ALLOY

In-situ observation by an optical microscope revealed that corrosion had occurred and propagated with hydrogen bubbling at the grain boundary in the lapped Mg-Al-Mn alloy plate immersed in 0.9% NaCl aqueous solution [5]. The mechanism of the corrosion is explained from the viewpoint of localized anode-cathode reaction based on the micro-stress balance in the alloy as stated in Section 3. Figure 3 shows the schematic model of the corrosion. A grain made of α -Mg in the compression state acts as an anode providing Mg^{2+} ions, whereas a grain boundary made of $Mg_{17}Al_{12}$ in the tensile state acts a cathode where electrons are supplied to H^+ ion to nucleate hydrogen gas. Electron transfer occurs from a grain to adjacent boundary area. This corrosion model resembles the pitting corrosion in stainless steel, but, to our knowledge, this is the first time that the actual stresses in each

micro-phase of the material have been investigated separately. Even in the lapped specimen, a localized cell as small as 30 μm in size exists and acts as a corrosion system when a human holds the Mg alloy housing of a mobile apparatus and it comes into contact with perspiration, or automobile components are splashed while the vehicle running along a road whose surface is icy.

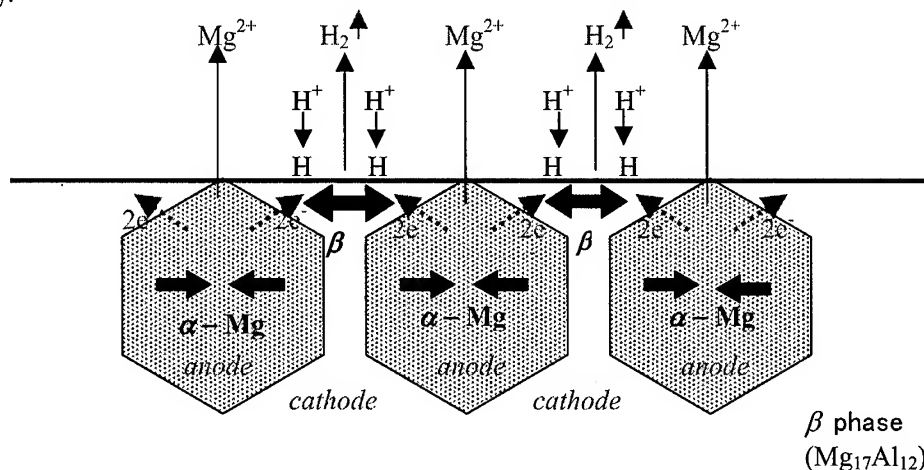


Fig. 3. Model of stress corrosion in a lapped Mg-Al-Mn alloy. α -Mg (grain) with compressive stress acts as an anode where Mg^{2+} ion dissolves, whereas $\text{Mg}_{17}\text{Al}_{12}$ (grain boundary) with tensile stress acts as a cathode where H_2 gas bubbles nucleate.

6. CORROSION INDUCED STRESS RELAXATION IN Mg ALLOY

The stressed specimen immersed for 30 min and the change of the normal stress value was monitored every ten minutes. Figure 4 shows the rapid stress relaxation in a short time at the notch root. The concentrated stress relaxed within two minutes with the formation of amorphous hydro-oxide on Mg alloy, in view of the morphology of the corrosion product stated in section 4. The stress value in $\text{Mg}_{17}\text{Al}_{12}$ phase at grain boundary changed almost to zero as shown in Fig. 5. The redistribution of the concentrated stress also occurred. We call this phenomenon "corrosion induced stress relaxation" whose nature seems to be the relaxation of the lattice spacing by the site-selective corrosion product [3, 4]. It is necessary to check further eliminating the effect of the galvanic corrosion.

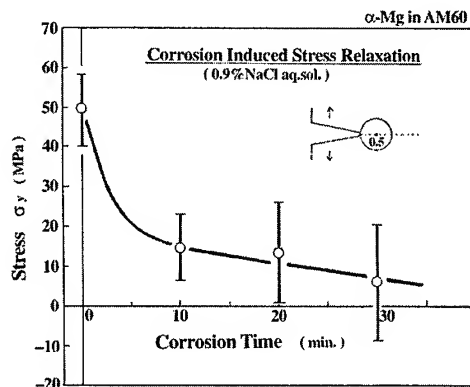
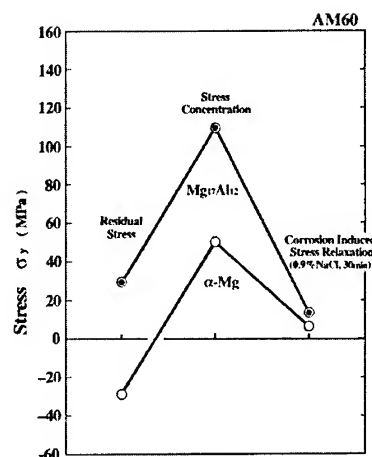


Fig. 4 Corrosion induced relaxation of concentrated stress in 0.9% NaCl aqueous solution at the notch root of AM-60 bar. It occurred in a very short time.

Fig. 5 The change of stress value in α -Mg and $Mg_{17}Al_{12}$ phases. A tensile residual stress in $Mg_{17}Al_{12}$ phase at grain boundary increased when loaded, and it relaxed to zero after being immersed in 0.9% NaCl aq. sol. for 30 min. We call this phenomenon "corrosion induced stress relaxation".



7. CONCLUSIONS

- (1) Stresses in α -Mg and $Mg_{17}Al_{12}$ phases existing in a thixomolded Mg alloy (AM-60) plate can be measured separately using the X-ray $\sin^2\psi$ method in the Cr-K α irradiation area of 1.0 mm in diameter. The recommended $2\theta_0$ values for stress measurement are 140.0 deg for α -Mg (202) and 133.4 deg for $Mg_{17}Al_{12}$ (660).
- (2) The measured residual stresses in a thixomolded AM-60 plate were about 30 MPa compressive in α -Mg and about 30 MPa tensile in $Mg_{17}Al_{12}$ phase balancing microscopic region. A concentrated stress ranged from 100 MPa tensile to 80 MPa compressive ahead of the V notch root when loaded $KI = 6 \text{ MPa}\cdot\text{m}^{1/2}$ by three point bending.
- (3) Even in a lapped Mg-alloy a localized micro-cell exists between α -Mg grain in compressive stress state and grain boundary made of $Mg_{17}Al_{12}$ in tensile stress state. The proposed model explains well the fact that the grain provides Mg^{2+} ions for solution whereas grain boundary acts as a nucleation point of the hydrogen gas bubbles. Corrosion in Mg alloy occurs essentially while it is in contact with any aqueous solution.
- (4) Corrosion mode of AM-60 in 0.9% NaCl aqueous solution was quite different depending on the sort (sign) of the stresses: a fine and dense amorphous hydro-oxide formed in the region of tensile stress whereas a coarse amorphous oxide formed in that of compressive stress. The former reaction product formed in a short time, but the latter grew gradually.
- (5) Concentrated tensile stress in α -Mg phase at the notch root relaxed within two minutes due to the corrosion followed by gradual relaxation of the stress to zero. This phenomenon is considered to be the compensation effect of the lattice spacing in α -Mg phase.

ACKNOWLEDGEMENT

The authors are indebted to the Japan Steel Works Limited for supplying a thixomolded specimen plate.

REFERENCES

1. S.-I. Tanaka and Y. Takahashi, ISIJ International, vol.30, (1990), pp.1086-1091
2. S.-I. Tanaka, Materials Science Forum, vol.347-349 (2000), pp.586-591
3. S.-I. Tanaka, and S. Iwata, Materials Science Forum, vol.350-351 (2000), pp.283-288
4. S.-I. Tanaka and S. Iwata, Int. J. of Materials and Product Technology (2001) in press
5. S.-I. Tanaka, N. Oka and S. Iwata, Acta Materialia to be submitted.

THE EFFECT OF SiC AND Si₃N₄ ADDITIONS ON THE OXIDATION RESISTANCE OF TiAl ALLOYS

Dong-Bok Lee, Ki-Boem Park, and Jae-Jin Moon

School of Metallurgical and Materials Engineering,
Sungkyunkwan University, Suwon 440-746, Korea

ABSTRACT

Alloys of TiAl containing dispersed particles of either (5,10,15wt%) SiC or (3,5wt%) Si₃N₄ have been manufactured by mechanical alloying followed by spark plasma sintering process. The oxidation behavior was studied between 900 and 1200°C in atmospheric air. Both SiC and Si₃N₄ dispersoids were unstable in the TiAl matrix, so that some of them reacted with Ti to form Ti₅Si₃ during sintering. These Si-containing particles oxidized to SiO₂ during oxidation. The oxide scales formed on TiAl-SiC and -Si₃N₄ alloys consisted TiO₂, Al₂O₃, and SiO₂. The drastic improvement obtained by the addition of SiC and Si₃N₄ dispersoids originated primarily from the enhanced alumina-forming tendency, the incorporation of SiO₂ within the oxide scale, and oxide grain refinement owing to the beneficial effect of dispersoids.

1. INTRODUCTION

The ordered L1₀ intermetallic γ -TiAl has low density and high specific strength. However, major obstacles restricting its use are poor ductility at room temperature, low strength and poor oxidation resistance at high temperatures [1,2]. One approach to overcome these drawbacks is to reinforce the TiAl matrix with various continuous or discontinuous ceramics such as ZrO₂ toughened Al₂O₃ fibers [3], TiNb particles[4,5], TiB₂ particles [6,7], and SiC fibers[8,9]. Accordingly, these second-phase-reinforced TiAl alloys have been evaluated in terms of chemical stability of reinforcing materials in the matrix [3,6-8], mechanical property [4,6,9], and oxidation behavior [3,5]. However, no attempts were made to utilize SiC- and Si₃N₄-particles in TiAl alloys until now.

The purpose of this study is to manufacture SiC- and Si₃N₄-particle-reinforced TiAl alloys, and investigate their high temperature oxidation behavior. The high temperature oxidation resistance is an important factor for practical applications. Thermogravimetric analyses and various analytical techniques including XRD, and SEM equipped with EDS were used to determine the oxidation resistance and mechanism of the prepared alloys.

2. EXPERIMENTAL

Alloys of Ti-50at.%Al with and without (5,10,15wt.%)SiC and (3,5wt.%)Si₃N₄ dispersed particles were prepared by mechanical-alloying (MA) and spark-plasma-sintering (SPS) method. The compositions of the prepared specimens are given in terms of the atomic

percentage for metallic components, based only on the metallic components, while the dispersed phase is given in weight percentage based upon the total weight of the composite. The starting powders were Ti (<150 μ m, 99.9% pure), Al (70~180 μ m, 99.9% pure), SiC (2~3 μ m, >99.0% pure) and Si₃N₄ (<50 μ m, >99.0% pure).

Initially, Ti and Al powders were mixed and mechanical alloyed under Ar+1%N₂ atmosphere. Argon was used to eliminate oxygen contamination, and dilute nitrogen was used to facilitate the mechanical alloying of elemental powders [10]. Onto the MA'ed Ti-Al powders, either SiC or Si₃N₄ particles were added in predetermined ratios, and subsequently mixed using a mill. The mixed powders were compacted and then sintered using a SPS apparatus. The sample fabrication process is described elsewhere in detail [11,12]. The sintered specimens of 20mm Φ x5mm were cut into sizes of 10x5x5mm³, polished, and oxidized isothermally.

The oxidation tests were performed between 900 and 1200 $^{\circ}$ C in atmospheric air. The weight changes were continuously monitored using a thermogravimetric analyzer (TGA). The oxidized specimens were inspected by scanning electron microscopy (SEM) to evaluate surface topography and transverse sections of oxide layers. Energy-dispersive spectrometer (EDS) and X-ray diffraction (XRD) techniques were employed to evaluate the qualitative analyses of elemental distribution and phase identification of the oxides. Marker experiments using fine platinum powders (1-7 μ m) were conducted on TiAl alloys with and without Si₃N₄ particles to elucidate the oxide growth mechanism.

3. RESULTS AND DISCUSSION

Fig. 1 shows the isothermal oxidation kinetics for the prepared alloys. The oxidation temperatures for TiAl-(3,5wt.%)Si₃N₄ alloys were chosen as 900 and 1000 $^{\circ}$ C, whereas those for TiAl-(5,10,15wt.%)SiC alloys were chosen as 1000, 1100 and 1200 $^{\circ}$ C. The higher oxidation temperatures employed for TiAl-SiC alloys were mainly due to their better oxidation resistance compared to TiAl-Si₃N₄ alloys. The high amount of SiC particles in TiAl-SiC alloys yielded quite small weight gains below 900 $^{\circ}$ C, so that oxidation tests were performed above 1000 $^{\circ}$ C. Nevertheless, it is clear that the oxidation resistance of TiAl alloys effectively increases with the increase in the content of dispersoids. Under an identical oxidation temperature, the more the dispersoids were added, the better the oxidation resistance was. The ability to form protective oxide scales clearly increased with the increase in the content of dispersoids. In contrast with the pure TiAl which displays no oxidation resistance particularly above 1100 $^{\circ}$ C, TiAl-(5,10,15wt.%)SiC alloys still have superior oxidation resistance, with a maximum weight gain of 6.0 mg/cm² in case of TiAl-5wt.%SiC at 1200 $^{\circ}$ C. The weight gain of TiAl-(10,15wt.%)SiC alloys were less than 0.6 mg/cm² after oxidation at 1000 $^{\circ}$ C for 60 hr. For the same alloy composition, the higher the oxidation temperature was, the poorer the oxidation resistance was, as expected. The only exception was TiAl-5wt.%SiC at 1000 $^{\circ}$ C, whose weight gain was larger than that at 1100 $^{\circ}$ C. The increment in oxidation temperature increases the oxidation rate or the growth rate of possible oxides such as TiO₂, Al₂O₃ and SiO₂. The last two oxides inherently have quite slow growth rates, and play a decisive role in protecting the alloy matrix.

Typical X-ray diffraction patterns of the scales formed on the prepared alloys are shown in Fig. 2. It is well known that the oxide scales on TiAl alloys consist of layers of TiO₂ and Al₂O₃, as shown in Fig. 2a. The outer layer is always essentially pure TiO₂, and the inner

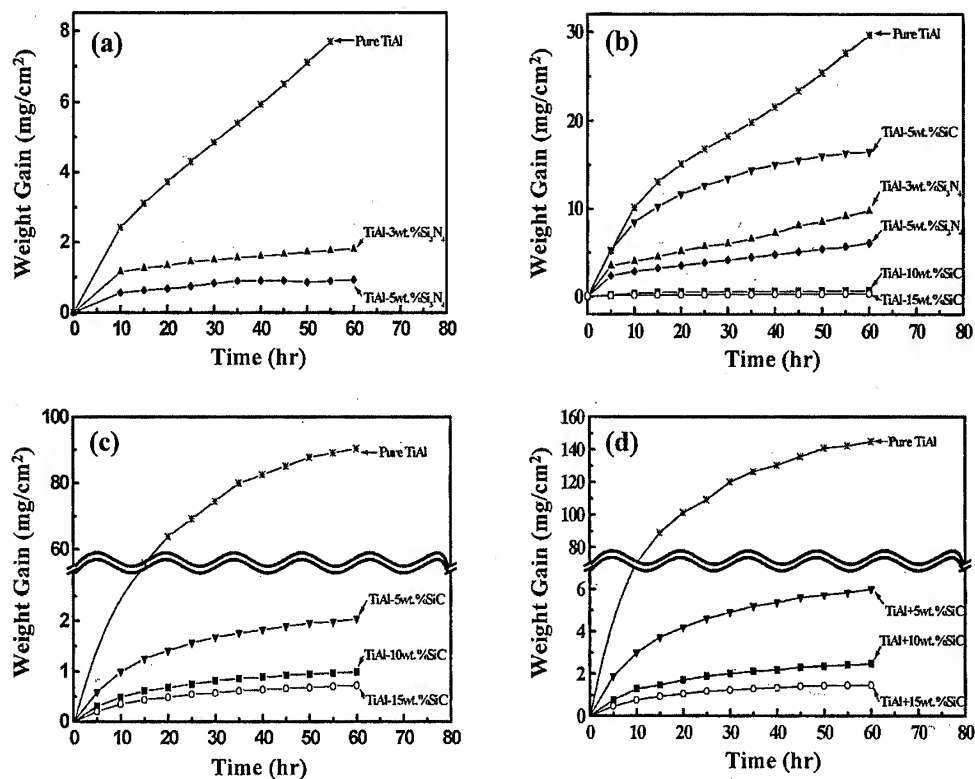


Fig. 1. Isothermal-oxidation curves for pure TiAl, TiAl-(3,5wt.%)Si₃N₄, and TiAl-(5,10,15wt.%)SiC alloys in air: (a) 900°C, (b) 1000°C, (c) 1100°C, (d) 1200°C.

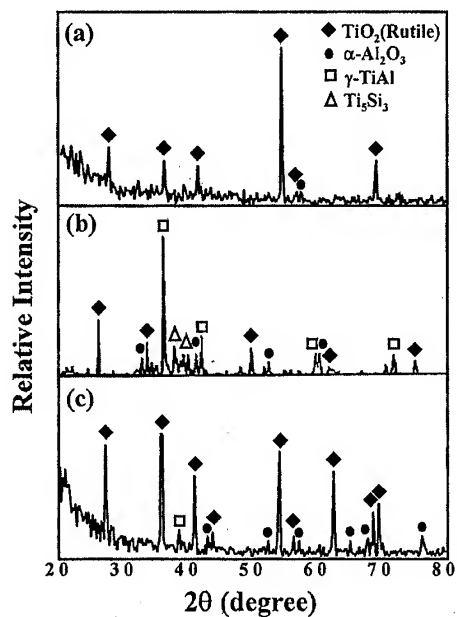


Fig. 2. XRD patterns after oxidation for 60 hr: (a) pure TiAl at 1000 °C, (b) TiAl-15wt.%SiC at 1100 °C, (c) TiAl-3wt.%Si₃N₄ at 1000 °C.

layer is a porous mixture of TiO_2 and Al_2O_3 . Between these two layers, there is an intermediate Al_2O_3 layer which is thin and discontinuous [13,14]. The oxidation resistance of TiAl alloys depends primarily on the thickness and continuity of the intermediate Al_2O_3 layer. The oxide scales formed on TiAl-SiC and Si_3N_4 alloys were also composed of TiO_2 and Al_2O_3 (Figs. 2b-c). But, the oxide scales were comparatively thin, so that the matrix phases such as TiAl and Ti_5Si_3 were observable. It should be noted that silica is not seen in Figs. 2b-c because of its amorphous nature. The formation of amorphous silica within the oxidation scale was confirmed by TEM studies [12].

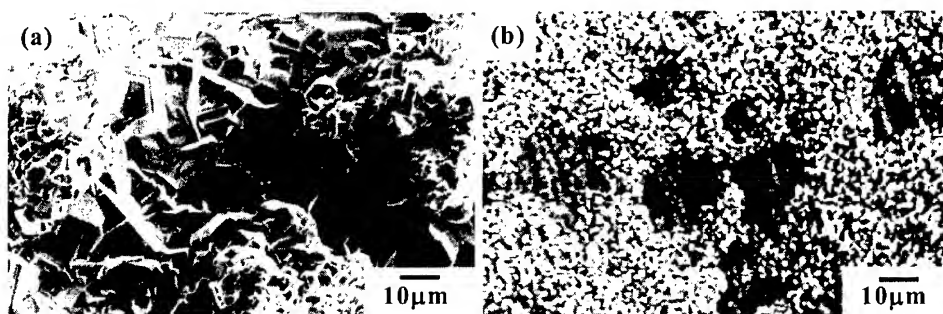


Fig. 3. SEM top view of the scales after oxidation for 60 hr in air: (a) pure TiAl at 1000 °C, (b) TiAl-15wt.%SiC at 1100 °C.

From the observation of top view of oxide scales, it was found that the oxide grains formed on TiAl-SiC and Si_3N_4 alloys were inevitably finer than those formed on pure TiAl. The oxide scale formed on pure TiAl has rod-like TiO_2 crystals (Fig. 3a). Partial sintering of small crystallites as globules is also seen on the surface oxide layer. On the other hand, the external surfaces of TiAl-SiC and Si_3N_4 alloys were covered with much finer oxide grains (Fig. 3b). Thus, it is clear that unreacted dispersoids and fine particles such as Ti_5Si_3 are acting as oxide nucleation sites by providing high surface areas to the oxygen, and thus lead to a decrease in oxide grain size. It is well to note that the ability to obtain uniformly distributed dispersoids is more feasible following the powder metallurgical routes. The increase in nucleation rate allows more rapid formation of a protective scale and, consequently, slows down the oxidation rate.

The oxide scales formed on pure TiAl are generally thick, porous and fragile, consisting of an outer TiO_2 layer, an intermediate Al_2O_3 layer, and an inner ($\text{TiO}_2 + \text{Al}_2\text{O}_3$) mixed layer. The outer layer of TiO_2 , n-type semiconductor, is known to grow primarily by outward diffusion of interstitial Ti ions, whereas the growth of inner mixed layer is dominated by inward oxygen diffusion [11,12]. As depicted in Fig. 4a, the oxide scale formed on TiAl-5wt.% Si_3N_4 is relatively thin and dense. Strong Al_2O_3 -formation throughout the whole oxide layers is clearly noticeable, except the surface TiO_2 layer (Fig. 4b). Beneath this surface layer, Pt markers initially placed on the specimen surface prior to oxidation is seen. Hence, it is proposed that, for TiAl- Si_3N_4 alloys, the surface TiO_2 layer grows primarily by the outward transport of Ti ions, whereas the inner ($\text{TiO}_2 + \text{Al}_2\text{O}_3$) mixed layer by inward oxygen diffusion, being analogous to pure TiAl. The Pt marker test was not performed on TiAl-SiC alloys. But, an experiment on $\text{Ti}_3\text{Al-SiC}$ alloys [13] indicated that the oxidation mechanism of this alloys was basically the same as that of TiAl- Si_3N_4 alloys. Interestingly, SiO_2 is mainly confined at the

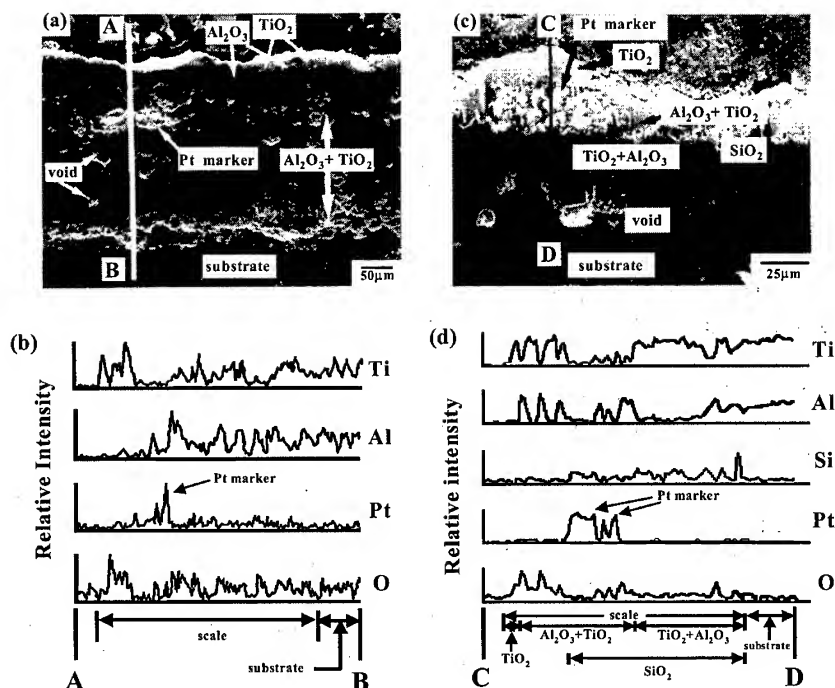


Fig. 4. Cross-sections of the scales after isothermal oxidation at 1000 °C for 40 hr in air: (a) pure TiAl, (b) EDS line profile across AB of (a), (c) TiAl-5wt.% Si_3N_4 , (d) EDS line profile across CD of (c).

lower part of the oxide scale. Initially added SiC and Si_3N_4 dispersoids oxidized to SiO_2 and became immobile. The formation of a silica phase protects the substrate from further attack by oxygen, giving a much thinner scale formation.

The major difference of TiAl-SiC and - Si_3N_4 alloys from dispersoids-free TiAl alloys is the formation of silica and more alumina within the oxide scales. Silica is a protective oxide scale, and can give a chance for Al to diffuse outward from the matrix, without being oxidized at the oxide-alloy interface. This resultantly makes the oxide layer rich in alumina, as observed in Fig. 4. Finer initial oxide grain size can also promote the outward diffusion of aluminum ions by providing more easy diffusion paths such as grain boundaries. It is noted that the strong alumina-forming tendency was also observed in $\text{Ti}_3\text{Al-SiC}$ alloys [13].

4. CONCLUSIONS

- (1) Drastic increment in oxidation resistance of TiAl alloys was achieved by the initial addition of SiC and Si_3N_4 dispersoids. Some of the dispersoids reacted with Ti to form Ti_5Si_3 during sintering. The dispersoids and Ti_5Si_3 oxidized to SiO_2 .
- (2) The scales formed on the TiAl-SiC and - Si_3N_4 alloys consisted TiO_2 , Al_2O_3 and SiO_2 . Reduction in the oxide-growth rate or the thin scale formation may be attributed to the rapid formation of a protective scale because of the dispersoid's role as oxide nucleation sites, the enhanced alumina-forming tendency, and the presence of another barrier layer of SiO_2 .

ACKNOWLEDGEMENT

This study was supported by the Center for Advanced Plasma Surface Technology at Sungkyunkwan University, and the BK 21 program of the Ministry of Education, Korea.

REFERENCES

1. T. Kawabata, T. Kannai and O. Izumi, *Acta Metall.*, 33(1985), 1335.
2. Y. W. Kim, *JOM*, 46(7), (1994), 30.
3. S. Nourbakhsh, O. Sahin and H. Margolin, *Acta Metall.*, 43(1995), 3035.
4. K. T. Venkateswara Rao, G. R. Odette and R. O. Ritchie, *Acta Metall.*, 40(1992), 353.
5. S. A. Kekare, J. B. Toney and P. B. Aswath, *Metall. Trans.*, 26A(1995), 1835.
6. D. E. Larsen, M. L. Adams, S. L. Kampe, L. Christodoulou and J. D. Bryant, *Scripta Metall. Mater.*, 24(1990), 851.
7. M. Saqib, I. Weiss, G. M. Mehrotra, E. Clevenger, A. G. Jackson and H. A. Lipsitt, *Metall. Trans.*, A22(1991), 1721.
8. J. Sorensen, in *Structural Intermetallics*, R. Darolia, J. J. Lewandowski, C. T. Liu, P.L.Martin, D. B. Miracle, and M. V. Nathal, eds., TMS, Warrendale, PA, (1993), p. 717.
9. S. E. Hsu, H. Y. Chou, K. L. Wang, S. C. Yang, J. Y. Wang, and C. I. Chen, in *Structural intermetallics*. R. Darolia, J. J. Lewandowski, C. T. Liu, P. L. Martin, D. B. Miracle, and M. V. Nathal, eds., TMS, Warrendale, PA, (1993), p. 749.
10. H. Hashimoto, *Materia*, 38(1999), 68.
11. D. B. Lee, J. H. Park, Y. H. Park and Y. J. Kim, *Mater. Trans., JIM*, 38(1997), 306.
12. D. B. Lee, Y. C. Lee, Y. J. Kim and S. W. Park, *Oxid. Met.*, 54(2000), 575.
13. D. B. Lee, S. W. An and Y. J. Kim, *Mater. Trans. JIM*, 40(1999), 1050.
14. D. B. Lee, *Bulletin of the Korean Inst. of Met. & Mater.*, 10(1997), 312.

TEM OBSERVATION OF INITIAL OXIDATION BEHAVIOUR OF Nb ION IMPLANTED TiAl

Shigeji Taniguchi*, Yao-Can Zhu**, Kazuhisa Fujita** and Nobuya Iwamoto**

*Department of Materials Science and Processing, Graduate School of Engineering,
Osaka University, 2-1 Yamadaoka, Suita, Osaka 565-0871, Japan

**Ion Engineering Research Institute Corporation, 2-8-1 Tsuda-yamate, Hirakata,
Osaka 573-0128, Japan

ABSTRACT

Coupon specimens of TiAl were implanted with Nb at an acceleration voltage of 50 kV with a dose of 10^{21} ions·m⁻². Their oxidation resistance was assessed by cyclic oxidation with temperature varying between room temperature and 1200 K in purified oxygen under atmospheric pressure. The implanted specimens and oxidised specimens for short periods were characterised and observed by AES, X-ray diffractometry, TEM, SEM, EDS, and EPMA. The implantation improves the oxidation resistance significantly by forming virtually Al₂O₃ (α -Al₂O₃) scales. The implanted layer is about 75 nm thick; outer part of 30 nm thickness is β -Ti and the rest of 45 nm thickness is amorphous. The heating to 900 K in O₂ results in partial crystallisation of the amorphous layer and to 1200 K results in oxide scales of 270-400 nm thickness consisting mainly of Al₂O₃. Nb seems to be incorporated in TiO₂ (rutile). The fraction of Al₂O₃ in the scale increases toward the substrate. The oxidation at 1200 K for 3.6 ks results in Al₂O₃-rich scales of about 400 nm thickness. Each oxide grain is very fine such as about 80 nm in size and becomes smaller toward the outer scale surface. This implies that the implantation enhanced the nucleation of Al₂O₃ grains. This finding and the formation of β -Ti phase together with doping of Nb to TiO₂ are thought to be responsible for the excellent oxidation resistance obtained.

1. INTRODUCTION

The potential application of γ -TiAl based materials as engine components and turbine blades has often been discussed and accordingly extensive research is being performed [1,2]. As a result of this, it was found that at least a few alloying elements are needed for controlling their microstructure and improving their mechanical properties. However, it is quite difficult to maintain compatibility between these and oxidation resistance by single alloying additions. For instance, a small addition of Cr improves the plasticity of TiAl [3], but it enhances high-temperature oxidation [4]. In addition, it is necessary to improve castability by further alloying additions, when such engine parts are to be produced by casting. Therefore, there seems to be no room for further addition to improve high-temperature oxidation resistance. The necessary resistance to environmental attack would be performed successfully by surface treatments.

With the above background we have been concerned with ion implantation [5-8] and found that the implantation of Nb, Mo, Ta or W is effective to improve oxidation resistance of TiAl by forming virtually Al₂O₃ scales. These elements worked similarly. In order to understand

the mechanism by which Nb implantation improved the oxidation resistance [5], we have carried out a detailed transmission electron microscopy (TEM) study in addition to studies using glancing angle X-ray diffractometry, AES and SEM.

2. EXPERIMENTAL PROCEDURES

2.1 Specimen and oxidation test

TiAl coupon specimens were prepared from a forged pan-cake consisting mainly of γ -TiAl grains and a small fraction of grains composed of γ -TiAl and α_2 -Ti₃Al phases. The chemical composition of the specimen is shown in Table 1.

Table 1 Chemical composition of the specimen (mass %)

	A l	F e	C	H	O	N	T i
TiAl	36.5	0.079	0.005	0.0027	0.034	0.0030	Bal.

Coupon specimens measuring 15 x 10 x 1 in mm were cut out of a slice and polished to a mirror finish with a series of SiC polishing paper of increasingly finer size and finally alumina powders of 0.3 μ m in size. The polished specimens were ultrasonically washed in acetone and methanol, and dried. Then, they were implanted with Nb at an acceleration voltage of 50 kV with a dose of 10^{21} ions \cdot m⁻². Their oxidation resistance was assessed by cyclic oxidation test with temperature varying between room temperature and 1200 K in a flow of O₂ under atmospheric pressure. Specimens placed in an alumina boat were put in a quartz reaction tube which was positioned in a horizontal electric furnace. Oxygen gas was purified by passing it through towers of silica gel, phosphorus pentoxide and CO₂ remover in this order. The specimens for TEM observations were oxidised for short periods similarly.

2.2 Characterisation and observation

The implanted specimens and oxidised specimens were examined with glancing angle X-ray diffractometry (XRD) for identifying phases and depth profiles of relevant elements were obtained with AES. Outer surfaces and fractured sections were observed and characterised by SEM equipped with an EDS unit. Specimens for TEM observations were thinned using an FIB unit. TEM investigations were performed at an acceleration voltage of 200 kV. Selected area diffraction patterns were obtained and EDS analyses were also performed in addition to the standard observations.

3 RESULTS

3.1 Depth profiles

Figure 1 shows the AES depth profiles of the relevant elements of as-implanted specimen. The implantation depth of Nb is about 70 nm with peak concentration of about 42 mol.% at a depth of 20 nm. The Nb profile shows near Gaussian distribution. The O profile indicates a slight penetration of oxygen during the implantation. Ti and Al vary similarly with Ti a little higher than Al. Figure 2 shows the depth profiles of the specimen heated to 1200 K in O₂ in

about 3 ks (0 ks oxidation). From the O distribution we can predict that the oxide scale is about 300 nm thick and a thin layer where O is present is formed beneath it. The Al distribution indicates that Al_2O_3 is enriched at two places in the scale: outer part and near the interface to the substrate.

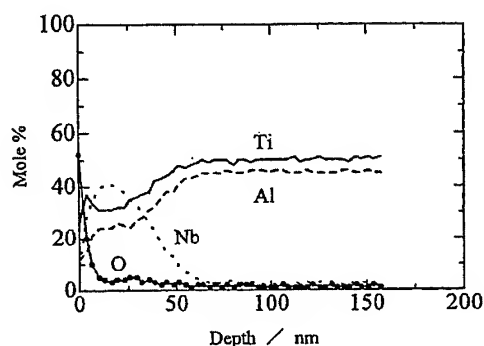


Fig. 1 AES depth profiles of as-implanted specimen.

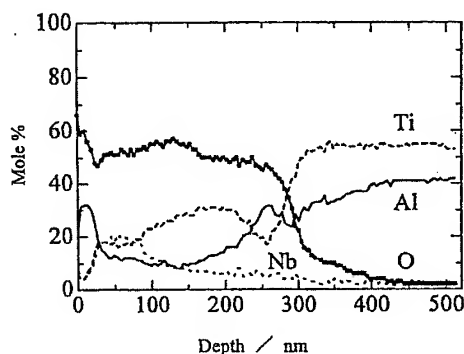


Fig. 2 AES depth profiles of the specimen heated to 1200 K in O_2 .

TiO_2 (rutile) is enriched in middle part of the scale with Nb. The XRD indicated no Nb oxides, so Nb is thought to be dissolved in TiO_2 lattice. When the specimen was oxidised at 1200 K for 20 ks, well developed Al_2O_3 scales of about 1 μm thickness were formed as Fig. 3 shows.

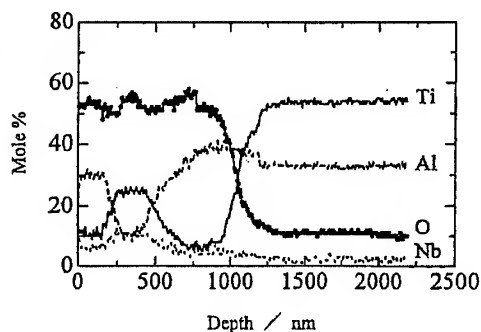


Fig. 3 AES depth profiles of the specimen oxidised at 1200 K for 20 ks.

The fraction of Al_2O_3 in the scale is very large, indicating the formation of virtually Al_2O_3 scales. It is noteworthy that Nb is still present where TiO_2 is enriched in the scale. The dissolution of Nb in TiO_2 lattice means that the growth of TiO_2 is slowed according to the doping effect, i.e. oxygen vacancy concentration in TiO_2 is decreased according to the valence control rule. This makes the situation more favourable to enrich Al_2O_3 in the scale. It is noteworthy again that an Al-depleted layer containing certain amount of oxygen is formed beneath the scale.

3.2 TEM investigations

Figure 4 shows a bright-field image of cross section of as-implanted specimen and the numbers in the figure show positions where diffraction patterns were taken and EDS analyses were performed. The outer thin layer (1) of about 30 nm thickness was found to be β -Ti by diffraction pattern and EDS results, and the next layer of about 45 nm thickness (2) was identified as amorphous. Position (3) is the interface between implanted and intact substrate (4). These results agree well with the AES analysis (Fig. 1) and XRD result.

Figure 5 shows a cross section of the specimen heated to 900 K in O_2 and cooled immediately. The outer β -Ti layer remains almost intact. However, crystallisation started already at the



Fig. 4 Bright field image of as-implanted specimen.

interface between the amorphous layer and the substrate. The crystallisation front is moving outwards. However, there is a sign showing that crystallisation also started at the interface to the β -Ti layer. There seems to be no structural change in the substrate. The oxidation at 1200 K for 3.6 ks resulted in a well developed scale which consists mainly of Al_2O_3 grains as Fig. 6 shows. The oxide grains are very small such as around 80 nm

and they become finer toward the outer scale surface. The scale thickness is very uniform and is about 400 nm. There is the so-called Z-phase layer of about 1 μm thickness beneath the scale. This was confirmed by diffraction patterns and EDS analyses which indicated a composition of $\text{Ti}_5\text{Al}_3\text{O}_2$ in good agreement with the literature[9-11]. This layer consists of relatively large near columnar grains such that one grain occupies almost whole layer thickness.



Fig. 5 Bright field image of the specimen heated to 900 K in O_2 .

4. DISCUSSION

In general, high-temperature oxidation of TiAl results in scales consisting of two layers: outer TiO_2 layer and inner layer which is porous mixture of TiO_2 and Al_2O_3 grains. Al_2O_3 is enriched between the two layers, however it is not sufficiently dense and continuous. Therefore, it cannot be a protective layer. It is prerequisite to form an Al_2O_3 scale for obtaining sufficient

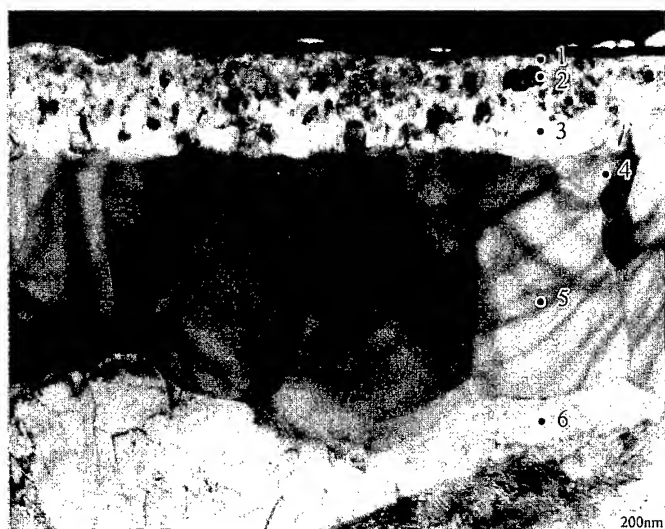


Fig. 6 Bright field image of the specimen oxidised at 1200 K for 3.6 ks in O_2 .

oxidation resistance for TiAl-base materials, because the diffusion of oxygen and cations through TiO_2 is much faster than through Al_2O_3 . It was found [12] that a very thin Al_2O_3 layer is formed during heating to high temperature or in short oxidation period at temperature and an Al-depleted layer or Z-phase layer beneath it. However, TiO_2 grains start to grow at the interface of the two with the progress of oxidation and break the Al_2O_3 scale. Then TiO_2 grains overgrew it.

The present study,

however, showed that the implantation of Nb formed very protective Al_2O_3 scales and they are maintained during the subsequent oxidation. The significant points of the Nb implantation are (a) formation of β -Ti layer and (b) grain refining of Al_2O_3 . The formation of β -phase can contribute the enrichment of Al_2O_3 during the initial oxidation period, since the diffusion of Al is faster than in γ -TiAl. The initial enrichment of Al_2O_3 in the scale slows the diffusion of oxygen toward the substrate and this enables the accumulation of Al_2O_3 near the substrate. Thus, Al_2O_3 is enriched in the initial scales. If oxygen diffuses fast, Ti will also be oxidised simultaneously, leading to mixture of the both oxides.

The enrichment of Nb in the initial scales is also important, since Nb is dissolved in TiO_2 lattice and decreases its oxygen vacancy concentration according to the valence-control rule.

The fine Al_2O_3 grains composing the scale implies that the nucleation of Al_2O_3 is enhanced during the initial oxidation period, although the mechanism for it is unclear now.

4 CONCLUSIONS

The initial oxidation stages of Nb implanted (50 kV , $10^{21} \text{ ions} \cdot \text{m}^{-2}$) TiAl have been studied mainly by TEM observations and the following main conclusions are derived.

- (1) The implanted layer consists of two parts; outer layer of about 30 nm thickness consists of β -Ti and inner amorphous layer of about 45 nm thickness.
- (2) During heating to 900 K crystallisation of the amorphous layer starts at the interface to the substrate.
- (3) The oxidation at 1200 K for 3.6 ks results in scales consisting of Al_2O_3 , virtually Al_2O_3 scales consisting of very fine grains such as 80 nm. So-called Z-phase is well developed beneath the scale.

Acknowledgements

The present study was supported by New Energy and Industrial Technology Development Organization (NEDO), Japan.

REFERENCES

1. Gamma Titanium Aluminides, Y-W Kim, R. Wagner and M. Yamaguchi, eds., TMS Las Vegas, (1995).
2. Gamma Titanium Aluminides, Y-W Kim, D. M. Dimiduk and M. H. Loretto, eds., TMS San Diego, (1999).
3. S. C. Huang, D. W. Mackee, D. S. Shih and J. C. Chesnutt, in *Intermetallic Compounds*, O. Izumi, ed., JIM, Sendai, (1991), pp. 363-370.
4. Y. Shida and H. Anada, *Corros. Sci.*, Vol. 35(1993), pp. 945-953.
5. S. Taniguchi, K. Uesaki, Y.-C. Zhu, H.-X. Zhang, T. Shibata, *Mater. Sci. & Eng.*, Vol. A249(1998), pp. 223-232.
6. S. Taniguchi, K. Uesaki, Y.-C. Zhu, Y. Matsumoto, T. Shibata, *Mater. Sci. & Eng.*, A266(1999), 267-275.
7. S. Taniguchi, T. Kuwayama, Y.-C. Zhu, Y. Matsumoto, T. Shibata, *Mater. Sci. & Eng.*, Vol. A277(2000), pp. 229-236.
8. S. Taniguchi, T. Fujioka, M. Nakajima, Y.-C. Zhu, T. Shibata, M. Yoshihara and Y.-C. Zhu, in *High-temperature Corrosion and Protection 2000*, T. Narita, T. Maruyama & S. Taniguchi, eds., Hokkaido (2000), pp. 495-501.
9. Y. F. Cheng, F. Dettenwanger, J. Mayer, E. Schumann and M. Rühle, *Scripta Mater.*, Vol. 34(1996), pp. 707-711.
10. V. Shmet, P. Karduck, H. Hoven, B. Grushko, W. Fischer and W. J. Quadakkers, *Intermetallics*, Vol. 5 (1997), pp. 271-280.
11. V. Shemet, H. Hoven and W. J. Quadakkers, *Intermetallics*, Vol. 5(1997), pp. 311-320.
12. S. Taniguchi, S. Fujimoto, T. Katoh and T. Shibata, *Materials at High Temperatures*, Vol. 17(2000), 35-40.

Investigation of Passivity and Its Breakdown on Al₃Ti Alloys in 3.5 wt.% NaCl Solution

Yong-Jae Yu, Jung-Gu Kim

Department of Advanced Materials Engineering
Sung kyun kwan University , Suwon, 440-746, Korea

ABSTRACT

Al₃Ti alloys have received a lot of attention as potential lightweight materials because of their low density and high strength at elevated temperatures. Induction melting method followed by the thermomechanical treatment was used for preparation of L1₂-typed Al₃Ti-Cr alloys, i.e. Al₆₇Ti₂₅Cr₈, Al₆₆Ti₂₄Cr₁₀ and Al₅₉Ti₂₆Cr₁₅. The corrosion behavior of Al₃Ti-Cr alloys in deaerated 3.5 wt.% NaCl solution was investigated by electrochemical corrosion tests and surface analysis. Particular attention was paid to the effects of Cr addition on the surface film composition and its breakdown related to the corrosion behavior. The result of cyclic potentiodynamic polarization test showed that E_{pit} and E_{prot} increased with increasing Cr content. This indicates that Al₃Ti-Cr alloys with higher Cr content are effective in improving relative resistance to pit initiation and propagation. In EIS, an increase of Cr content increased polarization resistance(R_p) and decreased the depressed angle which is strongly related to pitting resistance. AES analyses were performed in order to characterize in-depth distribution of constituents in the passive film and EDS techniques were used to examine the effect of alloying elements inside pit.

1. Introduction

The ordered intermetallic compounds of Al₃Ti are attractive as a potential lightweight materials for aircraft. Some of the positive characteristics of these compounds are their good oxidation resistance, high strength and low density[1-3]. However, Applications are limited because it exhibits brittle behavior at ambient temperature. This behavior can be due to the low symmetry DO₂₂ structure which has few slip systems. Therefore, successful development of aluminide alloys depends on overcoming their brittleness at ambient temperature. One possible approach to improve the ductility of Al₃Ti is to transform its structure to cubic ordered structure with higher symmetry by adding a ternary element to the Al₃Ti. In fact, by the substitution of several fourth to sixth period transition elements such as Cr, Mn, Fe, Co, Ni, Cu, Ag and Au preferentially for some Al atoms, the cubic L1₂ phases can be formed. In recent years, many studies[4-7] have been made on the microstructures and mechanical properties. e.g., microhardness, bend ductility, tensile strength at ambient temperature, in a number of ternary L1₂ compound alloys on the Al-Ti-Cr system. However, very little works have been done on the corrosion behavior of these modified Al₃Ti intermetallic alloys. Hence, the purpose of this paper is to investigate corrosion characteristics of Al₃Ti-Cr alloys in deaerated 3.5 wt.% NaCl solution by electrochemical techniques(electrochemical impedance spectroscopy, cyclic potentiodynamic polarization test). Surface analysis techniques(auger electron spectroscopy, electron probe microanalysis) were used to provide information on the passive film and inside pits of Al₃Ti-Cr alloys.

2. Experimental procedures

The preparation of the specimens was described previously[8]. Table 1 lists the chemical compositions of the prepared samples that are designated as $\text{Al}_{67}\text{Ti}_{25}\text{Cr}_8$, $\text{Al}_{66}\text{Ti}_{24}\text{Cr}_{10}$ and $\text{Al}_{59}\text{Ti}_{26}\text{Cr}_{15}$. All specimens were mounted in a cured epoxy resin and polished to 600 grit prior to immersion. All solutions were made from reagent grade NaCl with distilled water and were thoroughly deaerated by bubbling high purity nitrogen. For most the specimens, a paint adequate for saline environments was used to mask the specimens perimeter in order to prevent any crevice formation. The cyclic potentiodynamic polarization test[9] was carried out at room temperature in a typical three-electrode with the specimen as the working electrode, a saturated calomel reference electrode(SCE), and a pure graphite counter electrode. The specimen was scanned potentiodynamically at a rate of 0.166mV/s to a potential corresponding to a current density of 10^{-3}A/cm^2 . At this point, the scan direction was reversed. The downscan was continued until the protection potential was identified. EIS measurements were carried out in the passive region and in the pitting region, respectively. EIS method was used in the frequency range from 100kHz to 5mHz using a logarithmic sweeping frequency of 5 steps/decade. EIS involved the imposition of a 10mV amplitude sine-wave. The EIS results were analysed with analysis software Z-view. The nature of passive film formed on the surface was studied by auger electron spectroscopy(AES). The pits were examined in a scanning electron microscope(SEM) equipped with an energy dispersive X-ray spectroscopy(EDS).

3. Results and discussion

Cyclic anodic polarization curves are presented in Fig. 1 for three kinds of $\text{Al}_3\text{Ti-Cr}$ alloys. From these data, E_{corr} , E_{pit} , E_{prot} and the difference ($E_{\text{prot}}-E_{\text{corr}}$) are given in table 2. All alloys lead to spontaneous passivation. The addition of Cr decreased the anodic current density with polarization potential, and therefore open-circuit potentials of these alloys were shifted in the noble direction with increase in the Cr content. E_{corr} , E_{pit} and ($E_{\text{prot}}-E_{\text{corr}}$) increased with increasing Cr content, indicating increased relative resistance to localized, Cl^- induced, aqueous corrosion. However, it has been reported that the sputtered-deposited Al-Cr alloys with 10-35at.% Cr exhibit no appreciable change in the pitting potential and the sputtered-deposited Al-Ti alloys with 10-20at.% Ti are independent of pitting potential with Ti content[10]. Accordingly, it can be said that the simultaneous addition of Cr and Ti is more effective in improving the corrosion resistance rather than the single addition of Cr or Ti to Al[11]. For a better understanding of the effect of alloying elements on the passivity and pitting, EIS measurements were performed for $\text{Al}_3\text{Ti-Cr}$ alloys. Fig. 2 shows Nyquist plots of $\text{Al}_3\text{Ti-Cr}$ alloys after immersion for 6h in deaerated 3.5wt.% NaCl solution at room temperature. The impedance spectra obtained at the passive states represent a single and perfect semicircle. This behavior can be interpreted according to the Randles circuit for a simple electrochemical cell[12-13]. Here, the diameter of arc represents polarization resistance(R_p) or charge transfer resistance at the electrode/solution interface and the low intercept at real-axis shows solution resistance(R_Ω) between the working and reference electrodes. Solution resistance measured from Fig. 2 was almost close to zero and Polarization resistance increased with increasing Cr content. The increasing values of R_p suggest that the corrosion resistance of $\text{Al}_3\text{Ti-Cr}$ alloys increase with Cr content and should be also consistent with the results of cyclic anodic polarization curves(Fig. 1) in which passive current density decreases with increasing Cr content. Fig. 3 shows Nyquist plot at the transpassive states. All specimens were polarized anodically from equilibrium potential(E_{corr}) until 60mV in the pitting region. This applied potential was based on the pitting potential of $\text{Al}_{59}\text{Ti}_{26}\text{Cr}_{15}$. The impedance diagram spectra obtained at the transpassive states still represent a single semicircle but are not perfect semicircle. Some authors have demonstrated experimentally that the semicircle depression and deformation originate from the microscopic roughness of the surface[14-16]. From such a conclusion, it was normal to extrapolate that the surface modifications, introduced by the formation and propagation of localized pits, should be somewhat related to the calculated depression angle. Table 3

represents an attempt that was made to correlate both R_p and depression angle with pitting resistance as a function of Cr content. R_p values obtained from the analysis of experimental results in Fig. 3 increased with increasing Cr content and depression angles increased with decreasing Cr content. In particular, $Al_{67}Ti_{25}Cr_8$ represented the highest depression angle (-25.4°), indicates decreased relative resistance to pitting corrosion. Fig 4(a)-(c) shows the results of an AES analyses at the passive states. All alloys formed Al and Ti oxide on the surface, which act as a protective film. In a previous paper[8], these protective films were known as Al_2O_3 and TiO_2 . In addition, AES analyses revealed that Cr was detected earlier from the outer surface as Cr content increases. This behavior increased the possibility of formation of Cr oxide on the outer surface. In other words, Cr can act as a protective barrier on pit initiation. Fig. 5(a)-(c) shows three micrographs obtained using SEM for polarized specimens in the pitting region. Pit morphology exhibits larger and deeper pit with decreasing Cr content. Table 4 shows the results of EDS analysis obtained inside pit of Fig. 5(a)-(c). The presence of Al, Cr and Ti was observed. Compared to the bulk compositions of Al_3Ti -Cr alloys, the chemical compositions inside pit seem to be lower concentration in Al, while higher concentration in Ti with increasing Cr content. These results support that the Ti enrichment inside pit on alloys with higher Cr contents contributes to an increased resistance to pit propagation.

4. Conclusions

- 1) Cyclic potentiodynamic polarization curves showed that all Al_3Ti -Cr alloys lead to spontaneous passivation after immersion in deaerated 3.5 wt.% NaCl solution at room temperature and E_{corr} , E_{pit} and $(E_{prot}-E_{corr})$ increased with increasing Cr content, indicating increased relative resistance to localized corrosion.
- 2) Nyquist plot showed a single and perfect semicircle at the passive states. Here, the high R_p values were due to a protective passive film formed on the surface of Al_3Ti -Cr alloys.
- 3) The shape of Nyquist plot exhibited a depressed semicircle at the transpassive states. The R_p parameter increased and the depression angle, which is strongly related to microscopic roughness of the interface, decreased with increasing Cr content. It means increased relative resistance to pitting corrosion as Cr content increased.
- 4) From AES and EDS analyses, it was evident that Cr in Al_3Ti -Cr alloys inhibited pit initiation and Ti in Al_3Ti -Cr alloys also prevented pit propagation. That is, it can be said that the simultaneous Cr and Ti addition of Al_3Ti -Cr alloys exhibits synergistic effect on improving pitting resistance.

REFERENCES

1. Shipu Chen, Wei Zhang, Yuanhu Zhang and Gengxiang Hu, Scripta Metall. Mater., Vol. 27(1992), pp. 455-460.
2. Hiroshi Mabuchi, Hiroshi Tsuda, Toshiyuki Matsui and Kenji Morii, Materials Transactions, JIM, Vol. 38(1997), pp.560-565.
3. D. B. Lee, S. H. Kim, K. Ninobe, C.W. Yang and M. Nakamura, Materials Science and Engineering, A290(2000), pp.1-5.
4. M. Kogachi and A. Kameyama, Intermetallics, Vol. 3(1995), pp.327-334.
5. H. Mabuchi, A. Kito, M. Nakamoto, H. Tsuda and Y. Nakayama, Intermetallics, Vol. 4(1996), pp.193-199.
6. L. J. Parfitt, J. L. Smialek, J.P. Nic and D. E. Mikkola, Scripta Metall. Mater., Vol. 25(1991), pp.727-731.
7. H. Mabuchi, K. Hirukawa, H. Tsuda, T. Nakayama, Scripta Metall. Mater., Vol. 24(1990), pp.505-508.
8. J. G. Kim, Y. J. Choi, and D. B. Lee, Scripta Mater., Vol. 43(2000), pp.579-584.

9. ASTM G 61, Annual book of ASTM standards, 1995.
10. G. S. Frankel, M. A. Russak, C. V. Jahnes, M. Mirzamaani and V. A. Brusic, J. Electrochem. Soc., Vol. 136(1989), pp.1243-1244.
11. E. Akiyama, H. Habazaki, A. Kawashima, K. Hashimoto, Materials Science and Engineering, A226-228(1997), pp.920-924
12. EG&G Princeton Applied Research : Impedance measurement, Application Note, Princeton, NJ(1989), pp.1-13
13. Robert Cottis and Stephen Turgoose : Electrochemical Impedance and Noise, NACE International, Houston, TX(1999), pp.36-49.
14. John R. Scully, David C. Silverman, Martin W. Kendig : Electrochemical Impedance-Analysis and Interpretation, ASTM STP 1188, Philadelphia, PA(1993), pp.54-72.
15. P. R. Roberge, E. Halliop and M. Asplund, J. Applied Electrochem. Vol. 20(1990), pp.1004-1008.
16. P. R. Roberge, E. Halliop and V. S. Sastri, Corrosion, Vol .48(1992), pp.447-454.

Table 1. Chemical compositions of the prepared Al₃Ti-Cr alloys

Designation	Al(at.%)	Ti(at.%)	Cr(at.%)
Al ₆₇ Ti ₂₅ Cr ₈	66.8	25.5	7.7
Al ₆₆ Ti ₂₄ Cr ₁₀	65.5	24.4	10.1
Al ₅₉ Ti ₂₆ Cr ₁₅	59.0	25.9	15.1

Table 2. Electrochemical corrosion characteristics in deaerated 3.5wt.% NaCl solution

Material	E _{corr} (mV)	E _{prot} (mV)	E _{pit} (mV)	E _{prot} -E _{corr} (mV)
Al ₆₇ Ti ₂₅ Cr ₈	-599.00	-504.00	-186.00	95.00
Al ₆₆ Ti ₂₄ Cr ₁₀	-587.00	-468.00	-52.01	119.00
Al ₅₉ Ti ₂₆ Cr ₁₅	-556.00	-177.00	53.99	379.00

Table 3. Results of the analysis of impedance diagrams at the transpassive states

Material	R _p (kΩcm ²)	Depression angle(degree)
Al ₆₇ Ti ₂₅ Cr ₈	638	-25.4
Al ₆₆ Ti ₂₄ Cr ₁₀	940	-11.9
Al ₅₉ Ti ₂₆ Cr ₁₅	1431	-7.0

Table 4. Results of EDS analysis inside pits

Material	Al(at.%)	Ti(at.%)	Cr(at.%)
Al ₆₇ Ti ₂₅ Cr ₈	67.82	25.85	6.33
Al ₆₆ Ti ₂₄ Cr ₁₀	57.93	30.10	11.97
Al ₅₉ Ti ₂₆ Cr ₁₅	44.33	40.17	15.50

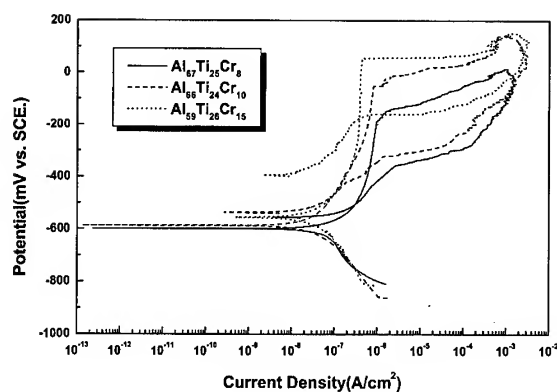


Fig. 1. Cyclic anodic polarization curves of Al_3Ti -Cr alloys in deaerated 3.5 wt.% NaCl solution.

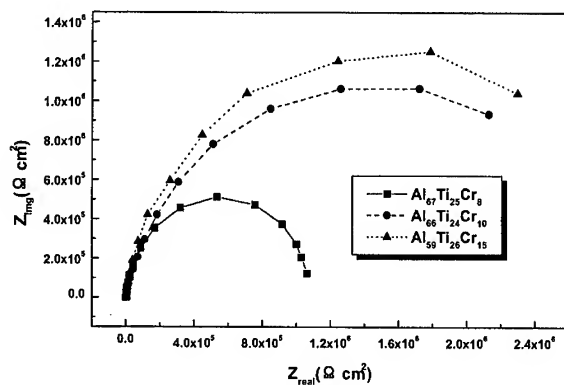


Fig. 2. Nyquist plots for Al_3Ti -Cr alloys at the passive states.

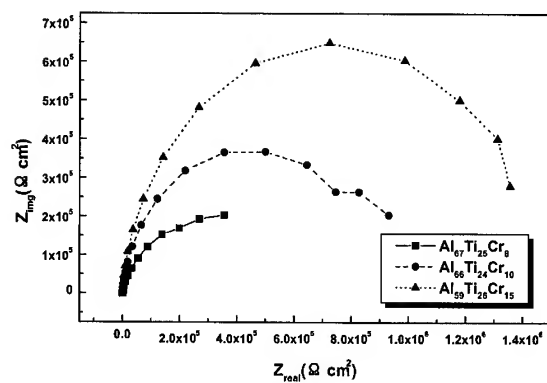


Fig. 3. Nyquist plots for Al_3Ti -Cr alloys at the transpassive states.

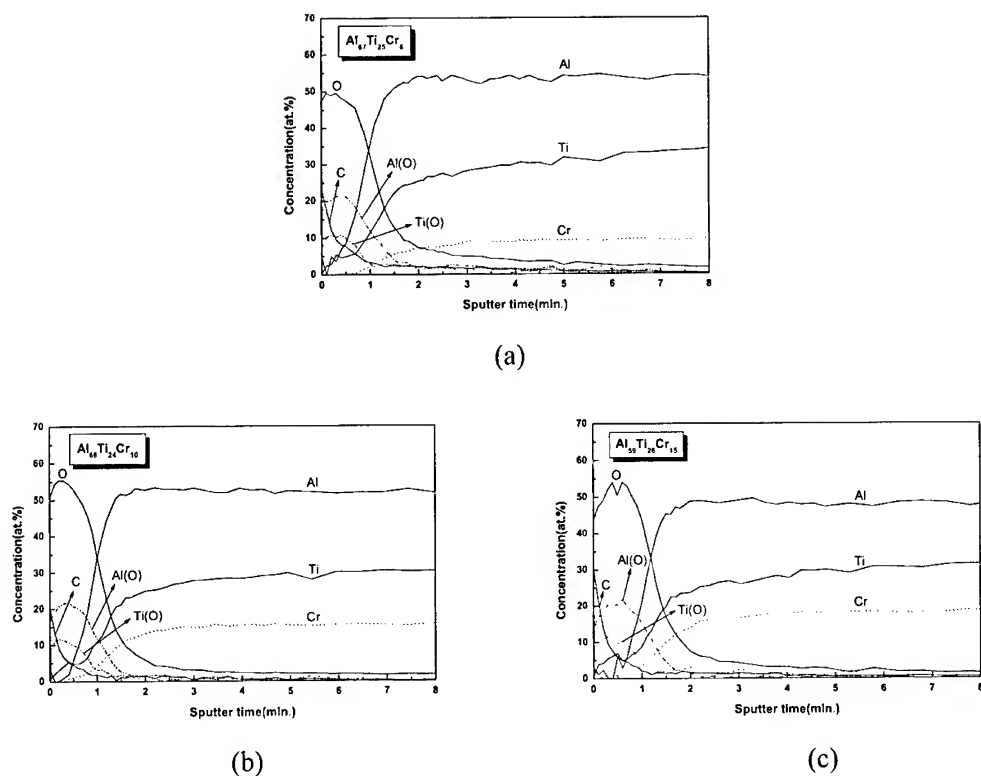


Fig. 4. Depth profile of elements of Al_3Ti -Cr alloys at the passive states (a) $\text{Al}_{67}\text{Ti}_{25}\text{Cr}_8$ (b) $\text{Al}_{66}\text{Ti}_{24}\text{Cr}_{10}$ (c) $\text{Al}_{59}\text{Ti}_{26}\text{Cr}_{15}$.

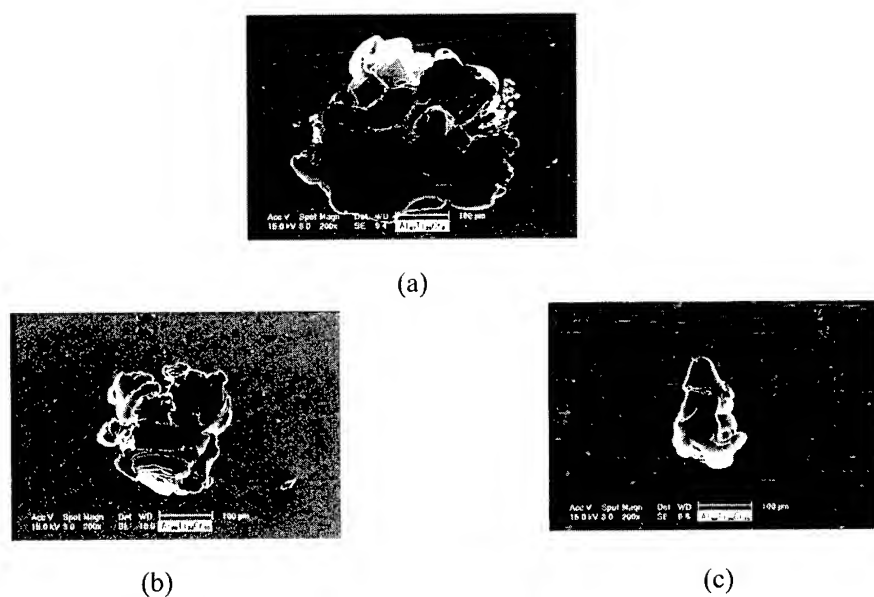


Fig. 5. SEM micrographs of Al_3Ti -Cr alloys in the pitting region (a) $\text{Al}_{67}\text{Ti}_{25}\text{Cr}_8$ (b) $\text{Al}_{66}\text{Ti}_{24}\text{Cr}_{10}$ (c) $\text{Al}_{59}\text{Ti}_{26}\text{Cr}_{15}$.

HIGH TEMPERATURE SULFIDATION AND OXIDATION OF SPUTTER-DEPOSITED Nb-Al-Si COATINGS

Dong-Bok Lee, Gi-Young Kim, Woung-Shik Shim

Department of Metallurgical Engineering, Sungkyunkwan University,
Suwon 440-746, Korea

ABSTRACT

The sulfidation and oxidation behavior of an amorphous 58Nb-38Al-4Si(at.%) coating sputter-deposited by a d. c. magnetron sputtering has been studied over the range of 700-900°C under 0.1 atm of pure S₂(g) and 1 atm of air, respectively. The coating approximately followed the parabolic sulfidation and oxidation rate law, and displayed superior resistance to sulfidation and oxidation. The coating sulfidized to Al₂S₃ and NbS₂ which protects the substrate. The coating oxidized to TiO₂, AlNbO₄ and κ -Al₂O₃ which acts as an oxidation barrier.

1. INTRODUCTION

In many branches of modern technologies such as high-temperature gas turbines, petrochemical units, and coal gasification systems, structural components are exposed to gases containing both sulfur and oxygen. Thus, it is of considerable industrial interest to develop new sulfidation- and oxidation-resistant alloys or coating. Conventional oxidation-resistant metallic materials have poor sulfidation resistance [1,2]. Interestingly, niobium has exceptionally high resistance to sulfidation, because its sulfide, NbS₂, has surprisingly low growth rate owing to the very low defect mobility in spite of its large defect concentrations [3]. However, niobium unfortunately oxidizes very fast even from moderate temperatures, because of high volatility of Nb-oxides [4].

Based upon the previous works on the sputter-deposited amorphous Al-Nb(-Si) alloys [5-9], we have recently reported sulfidation and oxidation behavior of sputter-deposited amorphous Nb-Al-Si coatings [10,11]. It would therefore be of interest to compare and discuss the similarities and differences in sulfidation and oxidation behavior of amorphous Nb-Al-Si coating. The characteristics of the scales, and the mutual interaction between the coating and the substrate materials during sulfidation and oxidation will be discussed.

2. EXPERIMENTAL

A ternary amorphous coating, the composition of which being 58Nb-38Al-4Si(at%), was applied on both sides of substrates by using a d. c. magnetron sputter under a purified Ar

atmosphere of about 10^{-3} torr. The substrate used for sulfidation tests was austenitic stainless steel (SUS 304; Fe 70.9%, Cr 20.3%, Ni 7.5%, Mn 0.9%, Si 0.4%), whereas that used for sulfidation tests was titanium (Ti balance, H<0.013%, O<0.20%, N<0.05%, Fe<0.25%). The sputtering targets were composed of pure aluminum, niobium, and silicon plates. The substrate size was about $10 \times 10 \times 0.1 \text{ mm}^3$.

Sulfidation tests were performed over a range of 700-900°C under 0.1 atm of pure $\text{S}_2(\text{g})$ for up to 30 hr [10]. Oxidation tests were performed at the same temperatures in atmospheric air for up to 240 hr [11]. The weight changes during tests were continuously monitored using thermogravimetric analyzer (TGA). The chemical composition and morphology of tested specimens were examined by X-ray diffraction (XRD), and scanning electron microscopy (SEM) equipped with an energy dispersive X-ray spectroscopy (EDS).

3. RESULTS AND DISCUSSION

Fig. 1a shows the sulfidation kinetics, and Fig. 1b shows the oxidation kinetics of Nb-38Al-4Si coating in the temperature range of 700-900°C. For comparison, the kinetics of uncoated specimens is also included. Decrease in sulfidation/oxidation resistance of both uncoated and coated specimens with an increase in temperature is clearly seen. The kinetics of the coated specimens, except the sulfidized one at 900°C (Fig. 1a), approximately follows the parabolic rate law, indicating that the kinetics is controlled by a diffusion process. It is evident that the coated specimens display excellent resistance compared with uncoated specimens which show almost no sign of protective scale formation at high temperatures. This suggests that the coating enables broad utilizations in hostile environments containing both oxygen and sulfur.

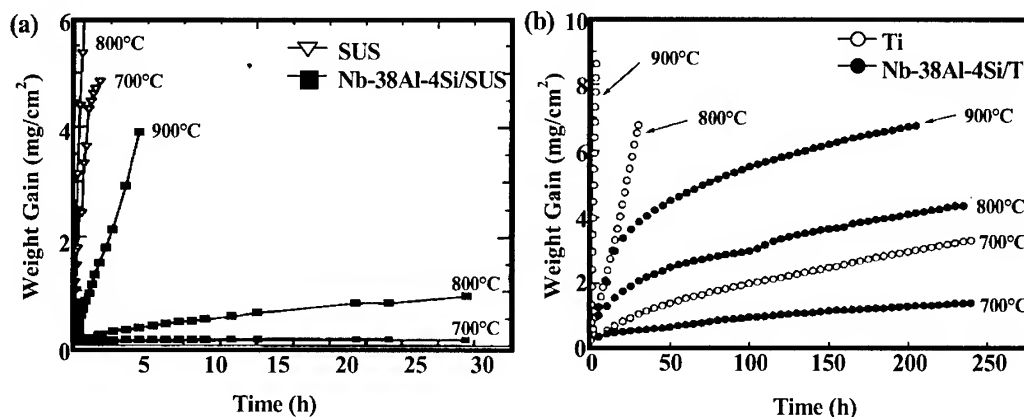


Fig. 1. (a) Sulfidation kinetics of a stainless steel with and without Nb-Al-Si coating, (b) oxidation kinetics of a Ti substrate with and without Nb-Al-Si coating.

X-ray diffraction tests revealed that the sulfide scale consisted primarily of 3s-NbS_2 , Al_2S_3 and FeCr_2S_4 ($\text{FeS} \cdot \text{Cr}_2\text{S}_3$), whereas the oxide scale was composed of TiO_2 and some $\kappa\text{-Al}_2\text{O}_3$ and AlNbO_4 . Though silicon ions within the oxide scale were detected by EDS analyses,

neither Si-oxides nor silicates were detected, probably due to their amorphous nature.

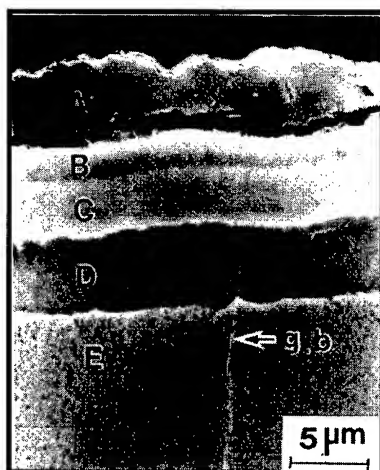


Fig. 2. Cross-sectional scale. SEM image of Nb-Al-4Si coating sputter-deposited on a stainless substrate after sulfidation at 900°C for 1 h.

Fig. 2 shows a typical cross-sectional scale after sulfidation at 900°C for 1 h. The etched microstructure was divided into areas of A-E. The corresponding EDS analyses revealed an outer scale of less-adherent Al_2S_3 (area A), and an inner scale of protective NbS_2 (area B). Beneath these sulfide scales, a retained Nb-Al-Si coating existed (area C). All these three layers had some of dissolved Fe, Cr and Ni, which evidently came from the substrate. Below the area C, a distinct depleted zone of substrate elements was seen (area D), which have arisen due to the preferential outward diffusion of substrate elements.

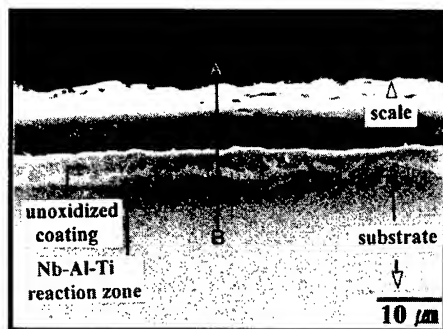


Fig. 3. Cross-sectional scale. SEM image of Nb-Al-4Si coating sputter-deposited on a Ti substrate after oxidation at 900°C for 30 h.

Fig. 3 shows a typical cross-sectional microstructure after oxidation at 900°C for 30 h. The microstructure can be divided into an oxide layer, a retained coating, Nb-Al-Ti reaction zone, and a Ti substrate. The reaction zone exists at the interface of the coating and substrate.

Unlike the bilayered sulfide scale, the oxide scale is rather single-layered, consisting of mixtures of TiO_2 , AlNbO_4 and $\kappa\text{-Al}_2\text{O}_3$.

4. CONCLUSIONS

A ternary amorphous coating of 58Nb-38Al-4Si (at%) was sulfidized and oxidized between 700 and 900°C in air. The coating displayed significant increase in sulfidation and oxidation resistance. The sulfide scale was bilayered, consisting of an outer nonprotective Al_2S_3 layer, and an inner protective NbS_2 layer. The oxide scale was single-layered, consisting of mixed oxides of TiO_2 , AlNbO_4 and $\kappa\text{-Al}_2\text{O}_3$. The activity, growth rate, and availability of Nb and Al from the coating seem to be responsible for the observed scale structure. Silicon inside the coating was not detected in the sulfide scale, but was found in the oxide scale.

ACKNOWLEDGEMENT

This study was supported by the Center for Advanced Plasma Surface Technology at Sungkyunkwan University, and the BK 21 program of the Ministry of Education, Korea.

REFERENCES

- [1] P. Kofstad, High Temperature Corrosion, Elsevier Applied Science, London and New York, (1988), p. 425.
- [2] G. Wang, R. Carter, D. L. Douglass, Oxid. Met., 32(1989), 273.
- [3] F. Gesmundo, F. Viani, Y. Niu, Oxid. Met., 38(1992), 465.
- [4] N. Birks, G. H. Meier, Introduction to High Temperature Oxidation of Metals, Edward Arnold, London, (1983), p. 126.
- [5] K. Hashimoto et al., Mat. Sci. Eng., A198(1995), 1.
- [6] H. Habazaki, K. Takahiro, S. Yamaguchi, K. Hashimoto, J. Dabek, S. Mrowec, M. Danielewski, Mat. Sci. Eng., A181(1994), 1099.
- [7] H. Mitsui, H. Habazaki, E. Akiyama, A. Kawashima, K. Asami, K. Hashimoto, S. Mrowec, Mater. Trans., JIM, 37(1996), 379.
- [8] H. Mitsui, H. Habazaki, K. Asami, K. Hashimoto, S. Mrowec, Corro. Sci., 38(1996), 1431.
- [9] H. Mitsui, H. Habazaki, K. Hashimoto, S. Mrowec, Corro. Sci., 39(1997), 9.
- [10] D. B. Lee, H. Mitsui, H. Habazaki, A. Kawashima, K. Hashimoto, Corro. Sci., 38(1996), 2031.
- [11] D. B. Lee, H. Habazaki, A. Kawashima, K. Hashimoto, Corro. Sci., 42(2000), 721.

EFFECT OF MOLYBDENUM ON THE CORROSION BEHAVIOR OF IRON-ALUMINIDES IN THIOSULFATE-CHLORIDE SOLUTION

Yoon Seok Choi, Jung Gu Kim

Department of Advanced Materials Engineering
Sungkyunkwan University
300 Chunchun-dong, Jangan-Gu, Suwon 440-746, Korea

ABSTRACT

Aqueous corrosion characteristics of iron aluminides in thiosulfate-chloride solution were studied as a function of Mo addition. Four kinds of iron aluminides, namely, FA-72(Fe-28Al-4Cr), FA-138(Fe-28Al-4Cr-0.5Mo), FA-139(Fe-28Al-4Cr-1Mo) and FA-140(Fe-28Al-4Cr-2Mo), were prepared by arc melting followed by thermomechanical treatment. An aerated thiosulfate-chloride solution was used to simulate a sulfur-bearing environment. The corrosion behavior in thiosulfate-chloride solution for the prepared alloys was investigated by electrochemical corrosion tests(cyclic polarization test; potentiostatic test and electrochemical impedance spectroscopy(EIS) measurement) and surface analysis(AES). The results of the cyclic polarization test indicated that the breakdown potential and the protection potential increased with increasing Mo content. EIS measurements showed that Mo addition to iron aluminides creates dramatic increase in impedance values by a repassivation process. The SEM observations of surface morphology after corrosion tests showed that the iron aluminides containing Cr and Mo had far fewer pits than that only containing Cr. The AES results gave evidence that the thiosulfate ions are reduced on the metallic surface, which inhibits the repassivation process.

1. INTRODUCTION

Intermetallic alloys are one of the most interesting new classes of metallic materials by virtue of their superior characteristics. For example, the ordered intermetallic iron aluminides represent attractive candidates for high temperature applications because they have excellent oxidation and sulfidation resistances at high temperatures due to protective aluminum oxide(Al_2O_3) scales[1]. Another strong point of iron aluminides is their low density ($\rho = 6.6 \text{ g/cm}^3$) compared to steels($\rho = 7.8 \text{ g/cm}^3$) and nickel-based alloys($\rho = 8.5 \text{ g/cm}^3$). However, the major limitations of these materials are their low ductility at room temperatures and a sharp drop in mechanical strength above 600°C [2]. These properties can be improved by adding ternary elements such as Cr, Mo, and Mn[3-5]. Iron aluminides have a wide range of uses where more expensive stainless steels and nickel-based alloys are being used(e.g., automobile exhaust system, gas clean-up system, and fossil energy production area in sulfur-bearing environments). In these environments, thiosulfate anions may be present with chloride ions. It was proved that these species exert a detrimental influence on the pitting behavior of Fe-Cr-Ni alloys[6]. Furthermore, in sodium chloride solution with the addition of sodium thiosulfate, enhanced pitting corrosion as compared with that found in pure sodium chloride solution was reported[7]. Although thiosulfate anions alone have not been found aggressive enough to cause damage to stainless steel, they have been shown to act in synergy with other common ions, such as chlorides to cause severe localized corrosion[8]. In order to increase the application of iron aluminides, it is important to evaluate their aqueous corrosion properties in a sulfur-bearing environment. The purpose of this research is to investigate the effect of molybdenum on the corrosion characteristics of the iron aluminides in thiosulfate-chloride solution. Electrochemical methods and surface analysis techniques were used to determine the pitting resistance of iron aluminides.

2. EXPERIMENTS

2.1 Materials and preparation

Alloy specimens of 500g were prepared by arc-melting the constituent elements in a water-cooled copper crucible in a chamber backfilled with argon. The specimens were remelted six times for homogeneity and then were drop cast into a copper mold to form ingots. The ingots were hot-forged 50% at 1,000 °C, hot-rolled 50% at 800 °C, and warm-rolled 70% at 650 °C to a final thickness of 0.75mm. Chemical compositions of the iron aluminides (at.%) used for experiments are given in Table 1. Heat treatment was stress relieving at 750 °C for 1hour, followed by an oil quench, which produced the B2-ordered structure.

2.2 Electrolytes

It was suggested earlier that the ratio of chloride to thiosulfate concentration would control the occurrence of pitting as the overall ionic strength is valid[9,10]. In the present study, an aerated thiosulfate-chloride solution was used to simulate a sulfur-bearing environment. The chloride-thiosulfate ratio was 5 (Chloride 50ppm / thiosulfate 10ppm). Solution was aerated with pure air at a flow rate of 10cc/min.

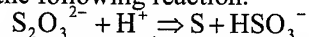
2.3 Investigation methods

Each specimen was mounted in a cured epoxy resin and polished to 600-grit silicon carbide paper. To prevent the initiation of crevice corrosion between the epoxy and the specimen, the epoxy-specimen interface was painted, leaving an exposed area of 1cm² on the material surface. For each material and electrolyte combination, the corrosion sample was allowed to stabilize in the electrolyte, until the potential change was < 1mV/min. This potential then was taken as the open-circuit potential(OCP). To insure reproducibility, at least three replicates were run for each specimen. The cyclic potentiodynamic polarization test was carried out at room temperature in a typical three-electrode with the specimen as the working electrode, a saturated calomel reference electrode(SCE), and pure graphite counter electrodes. The specimen was scanned potentiodynamically at a rate of 0.166mV/s to a potential corresponding to a current density of 10⁻³ A/cm². At this point, the scan direction was reversed. The downscan was continued until the protection potential was identified. The potentiostatic tests were performed to examine the tendency of breakdown(pit propagation) as a function of Mo content. After potentiostatic test, electrochemical impedance spectroscopy(EIS) measurements were investigated to compare the impedance behavior. EIS measurements were performed in the frequency range between 10kHz and 10mHz. Sinusoidal voltage of ± 5mV was supplied and DC potential was set to corrosion potential. To investigate the relationship between the repassivation behavior and surface morphology of pitting, the surfaces were examined by scanning electron microscopy(SEM) after EIS measurement. Elemental concentration profiles through the repassivated pits were obtained using Auger electron spectroscopy(AES) in conjunction with argon ion sputtering. A Perkin-Elmer Physical Electronics Model PHI 680 was used for AES analyses. The sputter rate was calibrated to 33 Å/min on SiO₂.

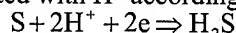
3. RESULTS AND DISCUSSION

The cyclic anodic polarization curves of the four iron aluminides are presented in Fig. 1. From these data, E_{corr} , E_{pit} , E_{prot} are given in Table 2. All the alloys passivated in these thiosulfate-chloride solutions. However, polarization above the breakdown potential resulted in a marked increase in current density as the result of the initiation of pitting. The passive current densities are shown to be decreased by increasing Mo content, which was a result of more stable passive film on the surface. E_{corr} and E_{prot} increased with increasing Mo content, indicating increased relative resistance to pitting corrosion. While little difference in E_{pit} is seen between FA-72, FA-138 and FA-139, Mo clearly prevents pitting entirely in the passive range of potential. For a better understanding of the effect of Mo on the pitting corrosion, potentiostatic tests and EIS measurements were performed. Fig. 2 shows the result of

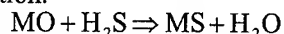
potentiostatic tests performed at an applied potential of 592mV_{SCE}. The applied potential was based on the data from polarization curves in Fig. 1, corresponding to the breakdown potential of FA-140. The current density increased and then it remained almost constant through the experiment. The current density revealed that the addition of Mo to iron aluminides increased the resistance to pitting corrosion. The increased current density would be directly related to the pit initiation and propagation. The current density in the steady state decreases with an increase in Mo content and the values are 9, 3, 1.5 and 1.3 mA/cm² for FA-72, FA-138, FA-139 and FA-140, respectively. EIS measurements were first performed just after potentiostatic test and then accomplished every 24 hours for 2 days to investigate the repassivation process. Fig. 3(a) shows Nyquist plots of iron aluminides just after potentiostatic test. The diameter of arc increased with Mo content. The increase in diameter of the arc indicated an increase in the R_p value. Such an increase in R_p is attributed to a improved pitting resistance. Fig. 3(b) and (c) show Nyquist plots, measured after 24 hours and 48 hours. And Fig. 3(d) represents the R_p values as a function of exposure times. These results indicated that the addition of Mo creates dramatic increase in R_p by a repassivation process. In the absence of Mo, the barrier layer was not formed so efficiently following repassivation. Fig. 4 shows the scanning electron micrographs of pitting after the EIS measurements. Some pits, caused by $S_2O_3^{2-}$ and Cl^- were formed on FA-72, and the number of pits was reduced for FA-138, and few pits on FA-139 and FA-140. The size and the number of pits decreased with increasing Mo content. Fig. 5 presents the results of an AES analysis of the repassivated surfaces and shows their in-depth profiles of Cr and Mo contents. Repassivation for Mo bearing alloys did not indicate evidence of Mo enrichment in the film or metal interface. Instead, it appears that only Cr is enriched. This is because passive film formation subsequent to the repassivation stage leads to retention of Cr in the oxide phase and loss of Mo, thus reducing the total Mo concentration near the oxide surface[11,12]. Mo promotes the enrichment of Cr inside the pit and passive film on alloys, which contributes to an increased resistance to pit propagation. AES analyses also detected sulfur species on the surfaces of specimens(Fig. 6). The results gave the evidence that the thiosulfates are reduced to absorbed sulfur, which inhibits the repassivation process once pitting has initiated. The sequence of reaction is explained as following[13,14]. At first, $S_2O_3^{2-}$ was oxidized to form S by the following reaction.



S was further oxidized and incorporated with H^+ according to the following reaction.



It was possible that the pre-existing metal oxide reacted with H_2S to form sulfide in accordance with the following reaction.



After sputtering, sulfur species decreased in the case of Mo bearing iron aluminides. This means that the enriched Cr interrupted the absorbed sulfur species to diffusion into the oxide or metal. Thus, the absorbed depth of sulfur species was different as a function of Mo content. Consequently, the benefit of alloying with Mo appears to be in segregating the Cr to the oxide, preventing pitting corrosion caused by $S_2O_3^{2-}$ and Cl^- .

4. CONCLUSIONS

- 1) The pitting corrosion resistance was improved by adding Mo, which increased the pitting and repassivation potential compared with the case not containing Mo.
- 2) The addition of Mo to iron aluminides containing Cr had a synergistic effect on the pitting resistance of iron aluminides.
- 3) EIS measurements showed that Mo additions to iron aluminides creates dramatic increase in impedance(R_p) by a repassivation process.
- 4) The presence of sulfur species on the corroded surface indicated that the thiosulfates are reduced to absorbed sulfur, which inhibits the repassivation process. However, the penetration depth of the absorbed sulfur species decreased with Mo addition.
- 5) By enhancing the Cr in oxides, Mo additions aid in the development and stability of a repassivated layer which further provided resistance against Cl^- and $S_2O_3^{2-}$ ions attack and, therefore, subsequent pitting corrosion.

REFERENCES

1. C.G. Mckamey, J.H. Devan, *Mater. Sci. Eng.* **A153** (1992) 573.
2. C.G. Mckamey, J.H. Devan, P.F. Tortorelli and V.K. sikka, *J. Mater. Res.* **6** (1991) 1779.
3. C.G. Mckamey, J.A. Houston and C.T. Liu, *J. Mater. Res.* **4** (1989) 1156.
4. C.G. Mckamey, C.T. Liu, *Scripta Metall. Mater.* **24** (1990) 2119.
5. D.G. Morris, M.M. Dadras and M.A. Morris, *Acta Metall. Mater.* **41** (1993) 97.
6. J. Gutzeit, in "Process Industries Corrosion", Edited by B.J. Moniz, W.I. Pollock (NACE, Houston, TX. 1987) p. 171.
7. R. Roberge, *Corrosion* **44** (1988) 274.
8. R.C. Newman, *Corrosion* **41** (1985) 450.
9. A. Garner, *Corrosion* **41** (1985) 587.
10. J.O. Park, M. Verhoff and R. Alkire, *Electrochimica Acta* **42** (1997) 3281.
11. C.R. Clayton and Y.C. Lu, *J. Electrochem. Soc.*, **133** (1986) 2465.
12. A.R. Brooks, C.R. Clayton, K.Doss and Y.C. Lu, *J. Electrochem. Soc.*, **133** (1986) 2459.
13. C. Duret-thual, D. Costa, W.P. Yang and P. Marcus, *Corrosion Sci.* **39** (1997) 913.
14. H.S. Kuo, H. Chang and W.T. Tsai, *Corrosion Sci.* **41** (1999) 669.

Table 1. Chemical compositions of iron aluminides (at.%)

	Fe	Al	Cr	Mo
FA-72	68	28	4	-
FA-138	67.5	28	4	0.5
FA-139	67	28	4	1
FA-140	66	28	4	2

Table 2. Electrochemical corrosion characteristics in thiosulfate-chloride solution

	E_{corr} (mV)	E_{pit} (mV)	E_{prot} (mV)
FA-72	-304	323	-595
FA-138	-68	316	-271
FA-139	-26	366	-174
FA-140	-8	592	-60

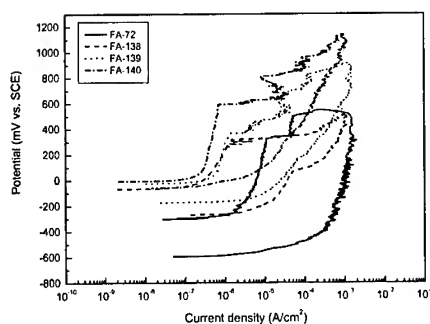


Fig. 1. Cyclic polarization curves of iron Aluminides in thiosulfate-chloride solution

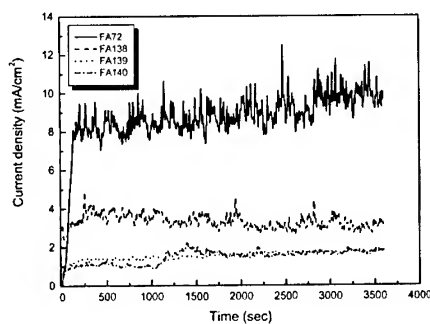
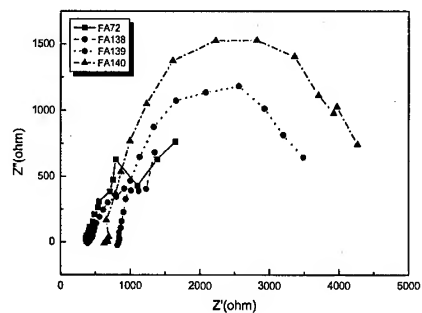
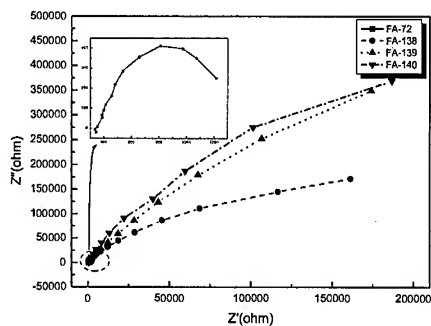


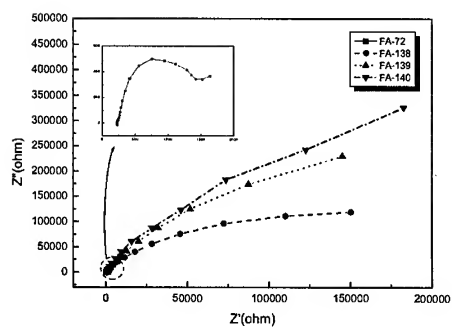
Fig. 2. Current variation with time at a breakdown potential of 592mV_{SCE}.



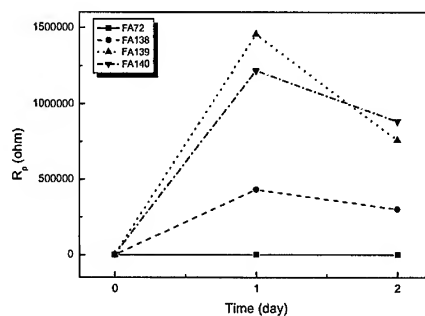
(a)



(b)

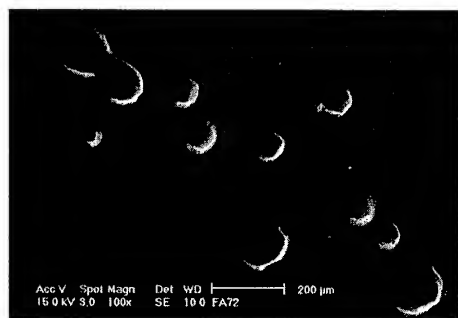


(c)

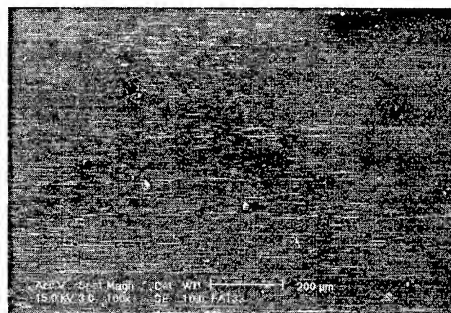


(d)

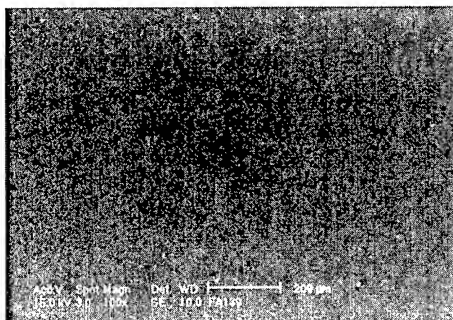
Fig. 3. Nyquist plots for iron aluminides for 2 days: (a) Just after potentiostatic test, (b) After 1 day, (c) After 2 days and (d) Polarization resistance as a function of exposure time.



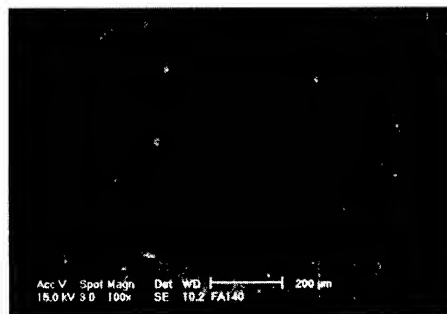
(a)



(b)

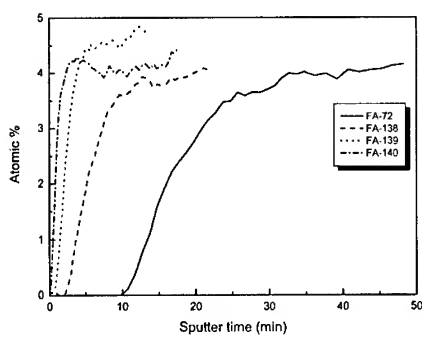


(c)

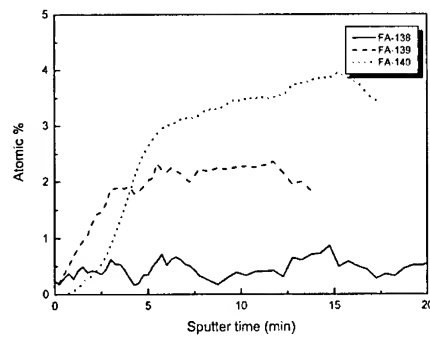


(d)

Fig. 4. Surface morphologies of pitting: (a) FA-72, (b) FA-138, (c) FA-139 and (d) FA-140.



(a) Cr



(b) Mo

Fig. 5. Depth profiling of Cr and Mo on iron aluminides after corrosion tests.

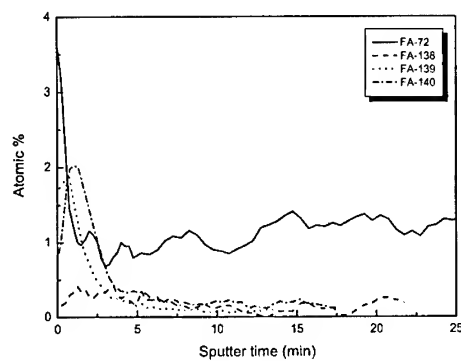


Fig. 6. Depth profiling of S on iron aluminides after corrosion tests.

A STUDY OF COMPOSITE COATING OF Cr EVAPORATION AND PACK CEMENTATION TO IMPROVE HIGH TEMPERATURE OXIDATION RESISTANCE OF TiAl ALLOYS

D. J. Jung, H. G. Jung and K.Y. Kim
Dept. of Materials Science and Engineering
Center for Advanced Aerospace Materials
Pohang University of Science and Technology, Pohang 790-784, Korea

ABSTRACT

TiAl alloys are coated by two different processes with a simple aluminide coating and a Cr+Al-type composite coating for the improvement of oxidation resistance of TiAl alloy. The simple aluminizing is applied to TiAl-XNb(X=1,2,4,6at%) alloys. The Cr+Al-type composite coating is performed by Cr evaporation on the TiAl alloys substrate followed by pack aluminizing. The simple aluminide coating applied to the Nb-added TiAl alloys shows considerable improvement of ductility and oxidation resistance. This is mainly due to grain refinement of Nb-added coating layer. The Cr+Al-type composite coating forms two layers of the inner TiAl₃ and the outer Al₄Cr. However, after 200h isothermal oxidation, these coating layers are changed to L1₂-type Ti(Al,Cr)₃ layer. This layer shows much better ductility out of other coating layers and excellent oxidation resistance through cyclic oxidation test. Also, the amount of imperfections such as crack in the coating layer was reduced considerably

1. INTRODUCTION

The poor oxidation resistance of TiAl alloys may be improved to a certain extent by addition of alloying elements such as Nb, Mo, and W. However, improvement of oxidation resistance by addition of these elements is not enough for practical applications and these elements may have a deleterious effect on the mechanical properties of TiAl alloys. Therefore, surface coating is considered as more attractive method to improve the oxidation resistance of TiAl alloys. Out of various surface coating technologies available commercially, pack aluminizing is widely used as a coating method for high temperature alloys because of its practical advantages over other coating methods. The pack aluminizing of TiAl forms TiAl₃ coating layer. Due to the sufficient amount of Al in the TiAl₃ coating layer, stable Al₂O₃ is formed as exposed to high temperature oxidation atmosphere¹. But TiAl₃ coating layer formed on the TiAl alloy, is quite brittle and has poor cracking resistance under mechanical and thermal stress during pack process, which limits the oxidation resistance of TiAl alloy by pack cementation².

In fact, much work has been conducted on the transformation of the crystal structure through addition of ternary alloying elements to improve ductility of TiAl₃. Ternary alloying elements such as Ni, Fe, Cu, Mn, Ag, and Nb and Cr were confirmed to change crystal structure of TiAl₃ from low symmetry DO₂₂ to high symmetry L1₂³⁻⁷. Especially, TiAl₃ alloys modified with Cr addition were reported to have better oxidation resistance and compressive ductility than those alloyed with other ternary elements⁸⁻¹⁰. Furthermore, this L1₂ type Ti(Al,Cr)₃ and L1₀ type TiAl alloys resemble each other very closely in crystal structure and lattice parameter¹⁰⁻¹². Therefore, the formation of L1₂ Ti(Al,Cr)₃ on TiAl substrate can be considered as quite desirable structure for minimizing defects formation in the coating layer during pack process.

In this study, to improve the oxidation resistance of TiAl alloy by increasing ductility of TiAl₃,

TiAl alloys were coated by two different processes with simple aluminide coating and a Cr+Al-type composite coating. Simple aluminizing was applied to TiAl-XNb(X=1,2,4,6at%) alloys. The Cr+Al-type composite coating was performed by Cr evaporation on the TiAl alloys substrate followed by pack aluminizing.

2. EXPERIMENTAL PROCEDURE

The button ingots were prepared by vacuum-arc melting. The arc melted ingots were homogenized at 1150°C for 72h in a vacuum quartz tube and then furnace cooled to room temperature. Each ingot was sliced to obtain 10× 13× 2mm in size by EDM (electrical discharge machining) and all sliced specimens were polished to No.1500 with SiC paper and ultrasonically cleaned in acetone. The specimens in this study were TiAl and Nb-added TiAl alloys. The content of Nb was controlled as 1, 2, 4 and 6 atomic percent (a/o).

2.1. simple aluminide coating

Pack aluminizing was done by a high activity process. In the pack cementation, NH_4Cl powder was used as an activator, Al_2O_3 powders as a filler material, and Ar gas as a carrier gas. Pack composition was composed of 15%Al+3% NH_4Cl +82% Al_2O_3 and pack aluminizing was performed at 900°C for 6hrs.

2.2. Cr+Al-type composite coating

This Cr+Al composite coating was applied to TiAl alloys with no Nb. For Cr evaporation. Cr source (purity 99.9%) was placed in a copper crucible and vaporized by heating with an electron-beam source. The initial vacuum level of the chamber and the substrate temperature were set at 10^{-5} torr and 360°C, respectively. The acceleration voltage of the electron beam was 10KV and emission current was 80mA. The 10~15 μm thickness of Cr layer was obtained by depositing for 1hr. After Cr evaporation on TiAl alloy, the specimens were pack aluminized as the same condition as the simple aluminizing.

For the analysis of microstructure and compositional distribution of coating layer, OM (optical microscopy) and SEM (scanning electron microscopy) were used, respectively. Sometimes, for analysis of small precipitates in the coating layer, FESEM (field emission SEM) was used. Toughness of the coating layer was determined by using a microhardness tester. Evaluation of the oxidation resistance of the specimen was carried out by isothermal and cyclic oxidation tests at 1000°C. Cyclic oxidation was performed in a tube furnace equipped with a program controller. For each cycle, the specimens were exposed at 1000°C for 2h and cooled to 140° for 1h.

3. RESULTS & DISSCUSION

3.1. Simple aluminide coating

As shown in Figure 1, the Nb addition to TiAl affects microstructure of the coating layer. As the content of Nb is increased, the number of cracks in the coating layer becomes reduced, the grain size of coating layer becomes finer and the coating thickness becomes thicker. As shown in Table 1, the microhardness test reveals that addition of Nb in TiAl alloys improves the ductility of the coating layer and cracking resistance. To understand the effect of Nb addition on the improvement of coating ductility, all the specimens were analyzed using X-ray diffractometry and Unit Cell program (Tim Holland and Simon Redfern, Cambridge University,UK) for calculation of lattice parameter. Table 2 lists lattice parameters of the coating layer formed on each specimen. The value of c/a ratio must be less than 2 or more than 2.4 for the transformation from DO_{22} to L1_2 structure¹³. As shown in Table 2, however, c/a ratios of coating layers do not meet the condition for the transformation from DO_{22} to L1_2

structure. Therefore, it is clear that the Nb addition didn't have any effect on the transformation from DO_{22} to $L1_2$ structure of the coating layer. Improvement of ductility and cracking resistance of coating layer through Nb addition seems to be due the fact that Nb in $TiAl_3$ refines grain size of the $TiAl_3$ coating layer.

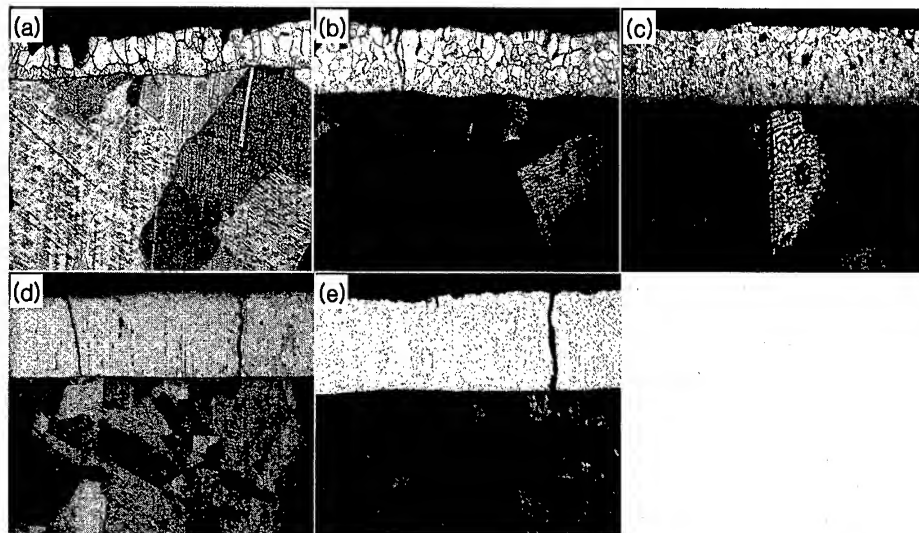


Figure 1. Microstructures of aluminide coating on TiAl alloys
(a) TiAl, (b) TiAl-1Nb, (c) TiAl-2Nb, (d) TiAl-4Nb, (e) TiAl-6Nb

Table 1. Vickers microhardness readings of aluminized coating layer

TiAl alloy	H _v	Crack load
TiAl	540 (20g)	50
TiAl-1Nb	427 (100g)	150
TiAl-2Nb	401 (100g)	200
TiAl-4Nb	397 (100g)	200
TiAl-6Nb	384 (100g)	300

Table 2. The c/a ratio of TiAl₃ structure

TiAl-alloys	Lattice Parameter	c/a ratio
TiAl	a: 3.844±0.001 c: 8.598 ±0.001	2.237
TiAl-1Nb	a: 3.852±0.002 c: 8.617 ±0.002	2.237
TiAl-2Nb	a: 3.844±0.002 c: 8.602 ±0.004	2.237
TiAl-4Nb	a: 3.853±0.02 c: 8.598 ±0.01	2.235
TiAl-6Nb	a: 3.856±0.007 c: 8.618 ±0.004	2.235

Cyclic oxidation test was performed to evaluate the stability of the coating layer. Figure 2 shows a plot of the weight change per unit area of the specimen vs. the number of cycles after test performed at 1000°C. As shown in Figure 2, in general, the Nb addition to TiAl alloys improves oxidation resistance. As the content of Nb is increased, the weight gain of TiAl alloys tends to be reduced. Especially, the TiAl alloys with Nb content of 4-6at% show excellent thermal stability of coating layer even after 1600cycles. On the other hand, TiAl without Nb addition is degraded less than 100 cycles. Figure 3 shows a typical surface morphology and cross-sectional analysis on the coating layer with protrusion of TiO₂ which forms on TiAl alloys. Cracks were observed in the immediate vicinity of TiO₂ beneath which Al₂O₃ and Al₂O₃+TiO₂ layers were formed. It is clearly seen that the TiAl substrate was oxidized directly by oxygen penetration through the crack. TiO₂ formation by direct oxidation of the TiAl substrate causes volume expansion in the coating layer, and this leads to spallation of the TiAl₃ coating layer and consequently, a faster degradation of the coated TiAl alloy with no Nb. On the other hand, in case of the Nb-added TiAl alloys, no protrusion of TiO₂ was observed.

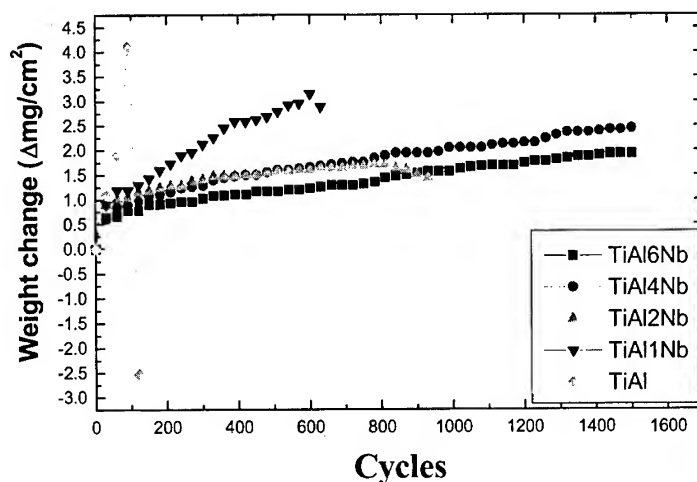


Figure 2. Cyclic oxidation test result of aluminized TiAl alloys at 1000°C

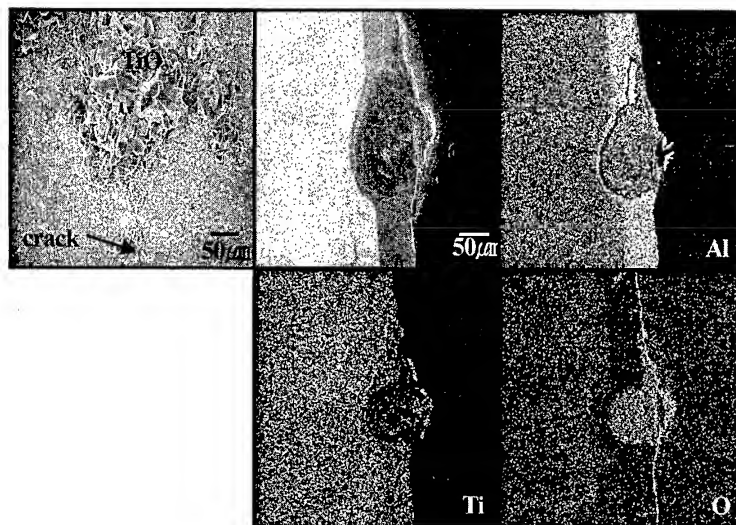


Figure 3. Surface image and cross sectional analysis on the coating layer with protrusions of TiO_2

3.2. Cr+ Al type composite coating

Figure 4 shows the cross-sectional microstructures of the composite coating layer after the isothermal oxidation test at 1000°C . The identification of phases in the coating layer was confirmed by EDS data and ternary phase diagrams of Ti-Al-Cr system in the literatures¹⁹⁻²¹. Initial coating layer was composed of two layers; the inner layer of TiAl_3 and the outer layer of Al_4Cr . As shown in Figure 4, the desirable coating layer of L_{12} -type $\text{Ti}(\text{Al,Cr})_3$ was not obtained after two-step coating, but it was obtained during isothermal oxidation. The L_{12} -type $\text{Ti}(\text{Al,Cr})_3$ was formed in the coating layer by interdiffusion among all the elements in the composite coating layer. After 50h oxidation, TiAl_2 layer between substrate TiAl and TiAl_3 was formed by the inward diffusion of Al and the outward diffusion of Ti. Also, the outer Al_4Cr layer formed after two-step coating was found to be changed to $\text{Al}_{17}\text{Cr}_9$ through EDS analysis. This is considered to be mainly due to the inward diffusion of Al from Al_4Cr layer. The inward diffusion of Cr was not significant. The compositional distribution and microstructure after 50h oxidation were similar to those after 100h oxidation except small decrease in thickness of $\text{Al}_{17}\text{Cr}_9$ layer and small increase in thickness of inner two layers. But after 200hr oxidation, inward diffusion of both Al and Cr from the outer $\text{Al}_{17}\text{Cr}_9$ layer changed effectively the outer layer to L_{12} -type $\text{Ti}(\text{Al,Cr})_3$, but with higher rate of Al diffusion. This coating layer is desirable for improvement of ductility of coating layer.

To evaluate mechanical property of coating layers, Vickers microhardness test was performed. The measured hardness values of coating layers were roughly consistent to those in the literatures^{6,10,19,22}. Especially, in case of L_{12} -type $\text{Ti}(\text{Al,Cr})_3$ coating layer, this showed the lowest value (about 170) and the best ductile structure among others. Comparing with the hardness reading of bulk L_{12} -type $\text{Ti}_{25}\text{Al}_{67}\text{Cr}_8$ reported in the literature, the difference was about 20. Considering experimental error and difference in specimen preparation, this difference was thought to be comparable. This result strongly suggests that formation of L_{12} -type $\text{Ti}(\text{Al,Cr})_3$ layer on TiAl is the most desirable structure for improvement of ductility of coating layer, and consequently for improvement of oxidation resistance of coated TiAl alloy.

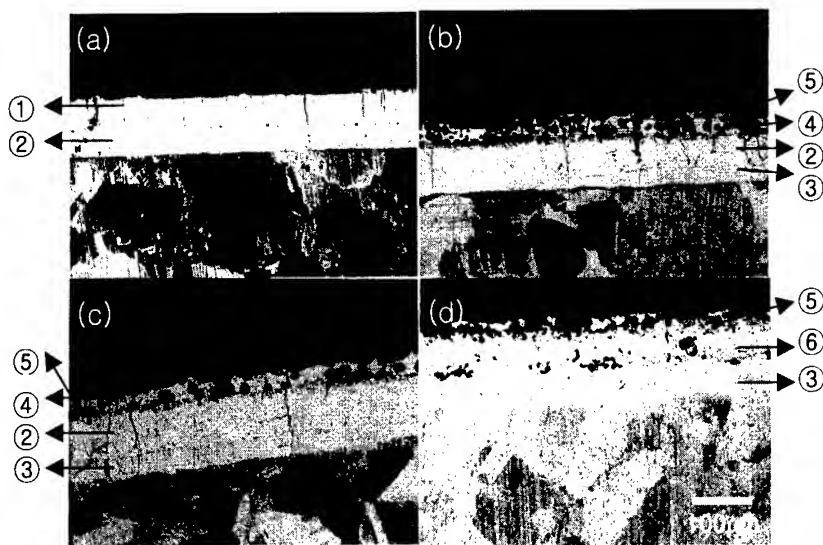


Figure 4. Cross-sectional microstructure of TiAl alloy with Cr+Al composite coating.

(a) after composite coating (b) after 50h oxidation
(c) after 100h oxidation (d) after 200h oxidation
① Al_4Cr , ② TiAl_3 , ③ TiAl_2 , ④ $\text{Al}_{17}\text{Cr}_9$, ⑤ Cr_2Al , ⑥ $\text{L}_{12}\text{-Ti(Al,Cr)}_3$

Figure 5 shows cyclic oxidation test result. It was found that composite-coated TiAl alloy shows 5 times better oxidation resistance than that of simple pack aluminized TiAl alloy.

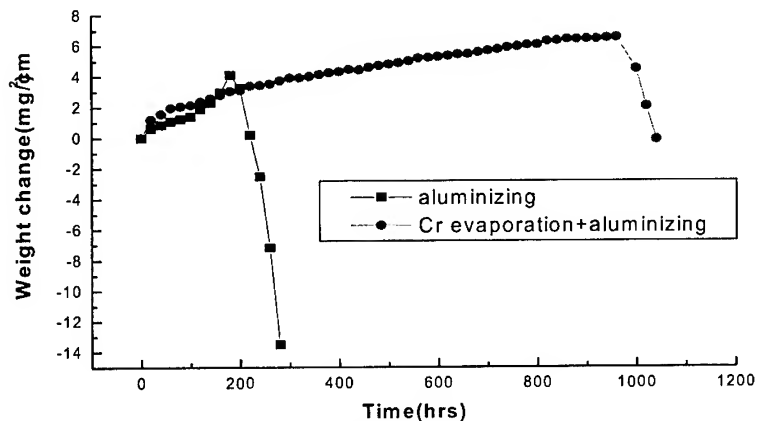


Figure 5. cyclic oxidation test result.

Figure 6. shows elemental maps of surface oxide formed on the coating layer after cyclic oxidation test. Most outer layer is dense and stable Al_2O_3 which acts as an effective diffusion barrier against the ingress of oxygen. Compared to the result shown in Figure 3, neither microcracks nor TiO_2 protrusions were observed. It demonstrates clearly that formation of

$\text{Ti}(\text{Al,Cr})_3$ layer with L1_2 structure can suppress development of crack formation under cyclic thermal stress, and thus can improve the oxidation resistance of TiAl alloys.

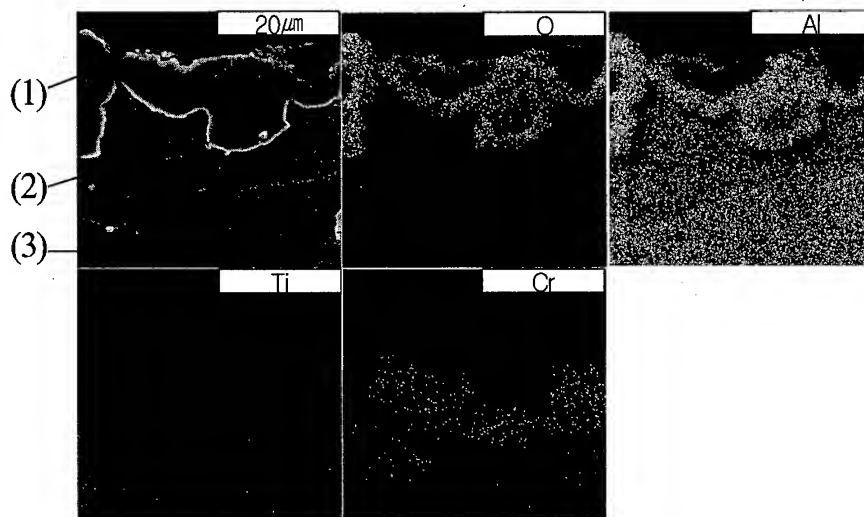


Figure 6. Elemental maps of surface oxide formed on the coating layer after cyclic oxidation test: (1) Al_2O_3 , (2) L1_2 -type $\text{Ti}(\text{Al,Cr})_3 + \text{Cr}_2\text{Al} + \text{TiAl}$, (3) TiAl_2

4. SUMMARY

1. Simple aluminide TiAl_3 coating layer becomes thicker and microstructure becomes finer as the content of Nb is increased.
2. The microhardness test of simple aluminide TiAl_3 coating layer reveals that the Nb addition to TiAl alloy improves the ductility of the coating layer and cracking resistance by refining grain size of TiAl_3 coating layer forming on TiAl substrate during pack aluminizing.
3. Composite coating (Cr evaporation+ aluminizing) on TiAl forms two layers; the outer Al_4Cr layer and the inner TiAl_3 layer. However, during oxidation, the microstructure of composite coating layer was changed to ductile L1_2 -type $\text{Ti}(\text{Al,Cr})_3$ mainly due to inward diffusion of aluminium & chromium from outer layer.
4. Formation of ductile L1_2 -type $\text{Ti}(\text{Al,Cr})_3$ layer in the composite coating reduced considerably crack formation in the coated layer during oxidation and showed significant improvement of oxidation resistance TiAl alloy.

5. REFERENCE

1. M. Yoshihara, T. Suzuki, and R. Tanaka, ISIJ Int, vol.31(1991)p1201
2. H.G.Jung, C.H.Oh, K.Y.Kim, J.Kor.Inst.Met & Mater.vol.38,No.8,(2000)p.1062
3. K.S.Kumar and J.R.Pickens, Scripta Metall.,vol.22(1988) p.1015
4. E.P.George, W.D.Porter, H.M.Henson, W.C.Oliver, and B.F.Oliver, J.Mater.Res.4(1989)p.78
5. H.Mabuchi, K.Hirukawa, and Y.Nakayama, Scripta Metall.,vol.23(1989)p.1761
6. S.Zhang, J.P.Nic, and D.E.Mikkola, Scripta Metall.Mater.vol.24(1990)p.57
7. W.O.Powers and J.A.Wert, Metall.Trans.21A(1990)p.145
8. K.Hirukawa, H.Mabuchi, and Y. Nakayama, Scripta Metall.Mater. vol.25,(1991)p.1211
9. M.B. Winnicka and R.A.Varin, Metall Trans A, vol 24,(1993)p.935

10. J.P.Nic,S.Zang, and D.E. Mikkola, Scripta Metall. Mater. vol.24(1990) p.1099
11. D.G. Morris,R.Lerf and M.Leboerf,Acta Metall.Mater., vol. 43,(1995) p.2825
12. Selected Powder Diffraction Data for Metals and Alloys, Data Book1, ed. By JCPDS Int. Center for Diffraction Data. Pennsylvania,(1978)
13. D.M.Nicholson, G.M.Stocks,W.M.Temmerman,P.Sterne and D.G.Pettifor: Proceeding of High Temperature Ordered Intermetallic alloys III,133,(1989)p17
14. W.Da Costa,B.Gleeson, and D.J.Young, J.Electrochem.Soc, vol .141,No 6,(1994)p.1464
15. W.Da Costa,B.Gleeson, and D.J.Young, J.Electrochem.Soc, vol .141,No 10,(1994)p.2690
16. W.Da Costa,B.Gleeson, and D.J.Young, Surface and Coating Tech. Vol.88,(1996)p.165
17. Robert Bianco,Mark A.Harper, and Robert A. Rapp, JOM, Nov,(1991)p.68
18. Si-Cherg Kung and Robert A. Rapp. Oxidation of Metals, vol.32. Nov. 1/2(1989)p.89
19. J.P.Nic,J.L.Klansky, D.E.Mikkola, Mat.Sci.Eng, A152(1992)p.132
20. Y.Nakayama and H.Mabuchi, Intermetallics. 1 (1993)p.41
21. T. J. Jewett, B.Ahrens ans M.Dahms, Intermetallics 4,(1996)p. 543
22. J.L.Klansky, J.P.Nic, and D.E.Mikkola, J.Mater.Res,vol. 9,No. 2,(1994)p.255

TITANIUM AND ALUMINUM COATINGS WITH SUPERSONIC FREE-JET PVD

Atsushi Yumoto, Fujio Hiroki, Ichiro Shiota* and Naotake Niwa

Dept. of Mechanical Systems Engineering, Kogakuin University, Tokyo 163-8677, JAPAN

*Dept. of Materials Science and Technology, Kogakuin University, Tokyo 192-0015, JAPAN

ABSTRACT

This paper presents Supersonic Free-Jet PVD (SFJ-PVD) as a new coating technology for structural materials. In SFJ-PVD, coating film is formed by high velocity impact of solid ultra-fine particles to base materials. This method composed of evaporation and deposition processes. In the evaporation process, the source material is evaporated to form ultra-fine particles in an inert gas atmosphere. In the deposition process, ultra-fine particles are deposited on base materials to form a film with supersonic gas flow. The gas flow is caused by pressure difference between each evaporation chamber and the deposition chamber. The flow of the gas is accelerated through a specially designed supersonic nozzle at the supersonic flow of 3.6 Mach number.

Ti and Al films obtained through SFJ-PVD showed a metallic luster as grown and no voids were observed in the coating films with SEM. And, the effects of control parameters of SFJ-PVD on film condition were elucidated.

1. INTRODUCTION

Improvement of the properties of structural materials is important for the development of industrial technology. Many experimental investigations have been conducted on overlay coating for structural materials. However, it is very difficult that the formation of a high-density film at low temperature is made to be compatible with high deposition rate.

Thin film using ultra-fine particles and ultra-fine particle itself have been studied as functional materials¹⁻⁴⁾ until now. However, studies that apply ultra-fine particles to structural material are very little. Because, it is due to the difficulties that the grain boundaries of individual ultra-fine particles do not disappear and ultra-fine particles do not bond each other easily. Thus, synthesized solid ultra-fine particles do not behave as conventional bulk materials, i.e., they do not have enough strength and properties comparing to those of conventional bulk structure materials⁵⁾.

We have investigated Ultra-fine Particle Deposition method⁶⁾ in order to solve the defects of other overlay coating methods for structural materials. This study aimed to develop Supersonic Free-Jet PVD (SFJ-PVD) method that accelerates the depositing velocity of ultra-fine particles in the Ultra-fine Particle Deposition method to solve the defects and the difficulties mentioned above through a specially designed supersonic nozzle.

This paper focuses on the properties of titanium and aluminum coatings with the SFJ-PVD and the evaluation of control parameters of the method.

2. EXPERIMENT

2.1 Supersonic Free-Jet PVD (SFJ-PVD)

The schematic diagram of Supersonic Free-Jet PVD (SFJ-PVD) is shown in Fig. 1. SFJ-PVD apparatus is composed of two evaporation chambers and one deposition chamber. Two evaporation chambers are equipped with a rotary pump, and the deposition chamber has a mechanical booster pump with a rotary pump. Each evaporation chamber and deposition chamber have been connected by two transfer pipes. There are two physical stages in SFJ-PVD: gas evaporation and vacuum deposition. In the gas evaporation, source material is evaporated to form ultra-fine particles in an inert gas atmosphere. Then, ultra-fine particles are carried with the inert gas through transfer pipe where gas flow is caused by pressure difference between the evaporation and deposition chambers. In the deposition stage, the particles are deposited on the substrate in the deposition chamber with gas flow that is accelerated to the supersonic velocity by a specially designed supersonic nozzle joined the transfer pipe tip. In the evaporation chambers, evacuation tubes with needle valves are equipped to evacuate the excess gas that is not suctioned through transfer pipes and to suppress gas stagnancy caused by the excess gas.

A nozzle for producing supersonic gas flow is designed on the assumption of one-dimensional isentropic flow. Actually, it is designed based on the evacuation ability of vacuum pumps and pressure ratio between the evaporation and deposition chambers of 66 to attain the velocity of the gas flow of 3.6 Mach number at the outlet of the nozzle.

Evaporation chamber 1 holds an electric resistance heating system where a material in a graphite crucible is heated in surrounding tantalum band heater. Evaporation chamber 2 holds an electric arc plasma heating system where a material in a water-cooled copper crucible is heated by arc plasma using non-consumable tungsten electrode. The maximum electric powers for heating are 1.8kW for the evaporation chamber 1 and 9kW for the evaporation chamber 2 respectively. A substrate in deposition chamber is mounted in a X-Y movable stage. A substrate holds an electric resistance heating system of tantalum heater and a nozzle also holds an electric resistance heating system of coil heater.

It is useful to list the key features of the SFJ-PVD.

1. High deposition rate and high-density thick film at low temperature.
2. Controllability of the growth rate of a film by evaporation rate and depositing time.
3. Many combinations of depositing materials (metals, ceramics and inter-metallic compounds).
4. Graded coating by varying the composition of evaporating materials continuously
5. Efficiency of evaporated materials to a deposited film.
6. Coating without crack and columnar boundaries.

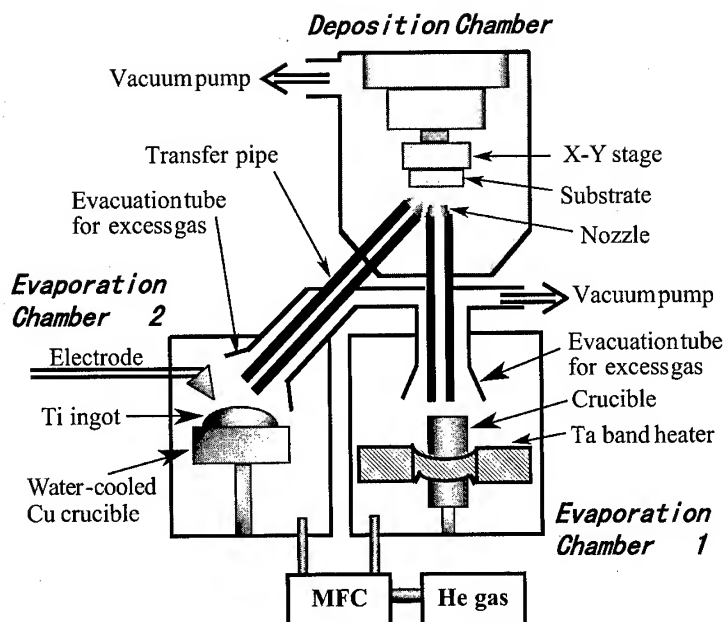


Fig. 1 Schematic diagram of Supersonic Free-Jet PVD apparatus.

2.2 Experimental Procedure

All chambers are evacuated at 0.4Pa or less and filled with helium gas. The pressure ratio between the evaporation chamber where the helium gas is fed continuously and the deposition chamber evacuated continuously is fixedly kept in order to keep the flow with supersonic velocity. Differential pumping is achieved during experiments and pressure range was 50-80kPa for the evaporation chamber and 0.3-1kPa for the deposition chamber.

In this experiment, the evaporation chamber1 is for the evaporation of aluminum, the evaporation chamber2 is for that of titanium and a substrate is aluminum or titanium. The chemical fineness of source aluminum and titanium for evaporation are over 99.999 mass%. Size of the substrate is 53 mm length, 27 mm width. Non-consumable tungsten electrode including the thoria of 2 mass%(YWTh-2) was used for arc plasma heating. Stage was designed to move in X-Y directions with 0.2 mm interval and coated area is 2mm². Main control-parameters of the SFJ-PVD are electric power for heating, pressure difference between evaporation chamber and deposition chamber and substrate temperature.

Table 1 Preparation conditions of titanium and aluminum films.

	Evaporation Chamber 1	Evaporation Chamber 2
Source materials	Pure Al (>99.999)	Pure Ti (>99.999)
Heat power source (A)	300, 330, 360	30, 40, 50
Pressure difference between chambers. (kPa)	50 ~ 80	

In the SFJ-PVD, we should especially pay attention to oxygen. Ultra-fine particles are easily oxidized because the particles have very large surface area to volume. Especially, both Al and Ti are the metals that react with oxygen very actively. One of the aims of this study is to qualify the method using these aluminum and titanium as source materials to overcome the difficulties and to extend the usage of the method.

As an inert gas, helium gas is chosen because the sonic flow of helium gas is the fastest among those of other inert gases (Velocity of sound in helium is about 970m/s: 1atm, 273K) and size of the ultra-fine particles generated in helium gas atmosphere is smaller than in other inert gases.

Surface of films was observed with a scanning electron microscope (SEM) and film thickness was measured with an optical microscope (OM).

3. RESULTS and DISCUSSION

3.1 Experimental condition and film properties

Without adequate evacuation of excess gas in the evaporation chamber, films contained cracks and coarse particles that were produced by agglomeration of the ultra fine particles. The excess gas that was not suctioned through transfer pipes caused the agglomeration. Thus, it is necessary to evacuate excess gas adequately and to suppress gas stagnancy caused by the excess gas for getting the uniform metallic films of aluminum and titanium.

Figure 2(a) and (b) show the photographs of the surface of aluminum and titanium films formed on substrates. EPMA line analysis indicated that the oxygen content of a Ti film on the substrate was from 2 to 2.5mass%. No cracks were formed by indenting the diamond indenter of micro Vickers hardness tester at the interface between substrate and coated film with the force of 4.9N, which indicates strong adhesion between them.

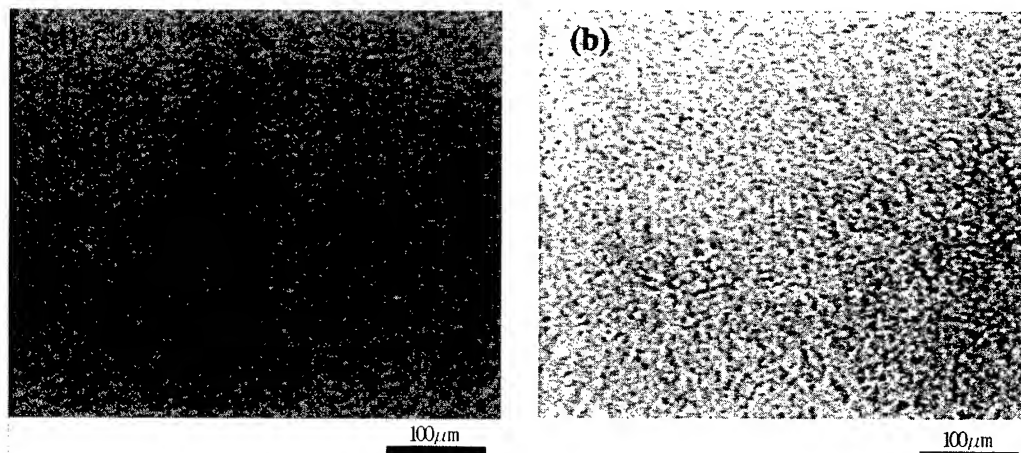


Fig. 2 Photograph of surface of Al film (a) and Ti film (b).

3.2 Growth rate

The growth rate of film increases with increase in electric power for heating that is the one of control parameters for the SFJ-PVD.

Figure 3(a) and (b) show the dependence of film growth rate on electric power for evaporation and pressure difference between chambers from 50 to 80kPa. The growth rate of film increases with increase in electric power for heating as shown in both Figure 3(a) and (b). In case of titanium films, the growth rate of film increases with increase in pressure difference [Fig. 3(b)], on the other hand, in case of aluminum films, the growth rate of film decreases with increase in pressure difference [Fig. 3(a)]. It is probably because the flow rate of cold helium gas around heating unit (crucible and band heater) increases by the increase of pressure difference between the evaporation chamber1 and the deposition chamber and the evaporation rate decreases with cooling of the heating unit. On the other hand, the arc plasma heats directly titanium ingot in the evaporation chamber2. Thus, the evaporation rate did not affected so much by the increase in the flow rate of helium gas with the increase of the pressure difference. The growth rate of titanium film increases with the increase in the pressure difference because the increase of the flow rate causes the increase of the particles carried into the deposition chamber.

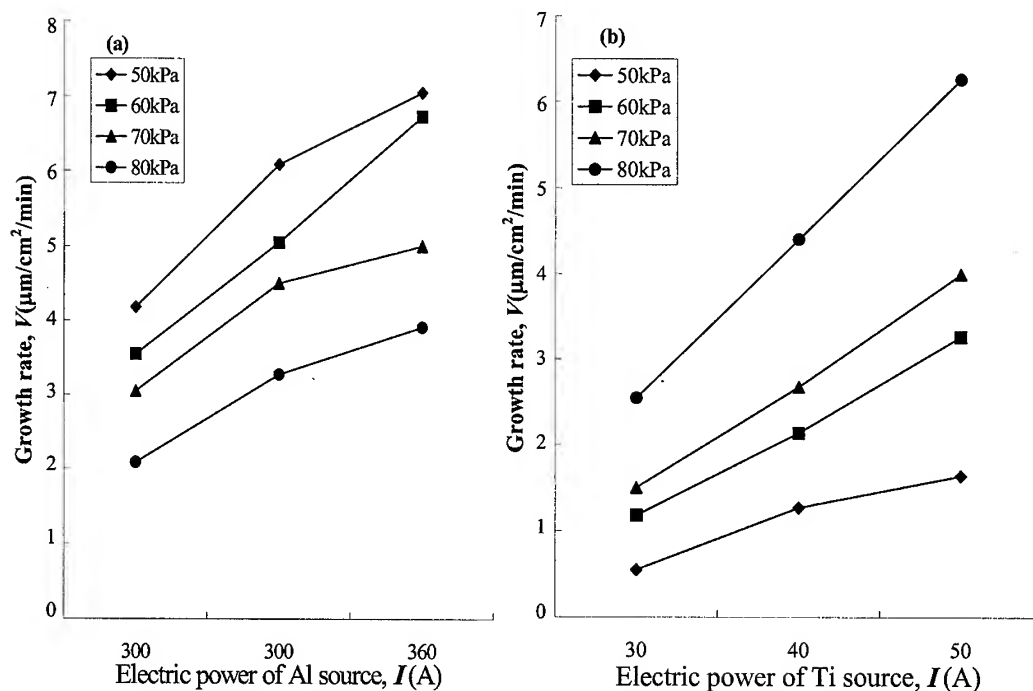


Fig. 3 Dependence of growth rate on electric power for the evaporation and the pressure difference between chambers from 50 to 80kPa. (a)Al, (b)Ti.

4. CONCLUSIONS

The results obtained in this experiment are as follows:

- (1) Reduction of coarse particles by suppressing the stagnancy and secondary agglomeration of particles is necessary for producing metallic films of titanium and aluminum.
- (2) Growth rate of film increases in proportion to electric power to evaporate source metal.
- (3) No cracks were formed by indenting the diamond indenter of micro Vickers hardness tester at the interface between substrate and coated film with the force of 4.9N, which indicates strong adhesion between them.

ACKNOWLEDGEMENTS

This study was supported, in part, by the Sasakawa Scientific Research Grant from The Japan Science Society, Iketani Science and Technology Foundation and Grant-in-Aid for Scientific Research (C).

REFERENCES

1. E. R. Buckle, P. Tsakirooulos and K. C. Pointon, *International Metals Reviews*, 31(1986), pp. 258-288.
2. S. Ono and M. Uda, *J. Japan Inst. Metals*, 48(1984), pp. 640-646.
3. K. Saito, *J. Japan Inst. Metals*, 60(1996), pp.1125-1129.
4. S. Okuda, M. Kobiyama and T. Inami, *Mater. Trans., JIM*, 40(1999), pp.412-415.
5. K. Suzuk, *Seminar text ofJIM* (Hakumaku Zairyou no Kiso to Oyo, 1987), pp. 1-9.
6. A. Yumoto, F. Hiroki, I. Shiota and N. Niwa, *Mass and Charge Transport in Inorganic Materials*, P. Vincenzini and V. Buscaglia, Eds., TECHNNA, Venice, Italy, (2000), pp. 991-998.

FABRICATION AND THERMO-MECHANICAL PROPERTIES OF FUNCTIONALLY GRADED THERMAL BARRIER COATINGS

J. H. Kim, Y. M. Rhyim and C. G. Park

Center for Advanced Aerospace Materials
Pohang University of Science and Technology, Pohang 790-784, Korea

ABSTRACT

As a new approach, an excellent functionally graded thermal barrier coating (FGM TBC) has been fabricated by the detonation gun spray process with a newly proposed 'shot-control method' in the present study. FGM TBCs were sprayed as multi-layered coatings having the compositional gradient along the thickness direction from 100% NiCrAlY metal on the substrate to 100% ZrO_2 -8wt.% Y_2O_3 ceramic for the topcoat, and exhibited a finely mixed microstructure of metal and ceramic without any certain interfaces between the layers. Various thermo-mechanical properties of FGM TBCs were also investigated and compared with those of traditional duplex TBCs.

1. INTRODUCTION

Thermal barrier coatings (TBCs) have been applied to high temperature components of gas turbine engines for improved performance, efficiency and extended component life. The major limitation to expanding application range of TBCs lies in their premature failure and consequently in their poor reliability. It has been reported that the failure of TBCs is mainly caused by the thermal expansion mismatch between the ceramic and metal coating layers of the 'duplex TBC' systems [1-3].

One way to overcome this problem is to introduce the concept of functionally gradient material (FGM) into TBCs, which are so-called 'FGM TBCs'. FGM TBCs are sprayed as multi-layered coatings with the composition varying in the thickness direction from 100% metal applied directly to the substrate to 100% ceramic for the topcoat. While the concept of FGM TBC itself is rather intuitive and simple, it is quite difficult to fabricate a fine mixture of ceramic and metals with a compositional gradient. Several processing techniques have been explored, e.g., plasma spraying, powder metallurgy, *in situ* synthesis, etc., but the optimum process for the fabrication of FGM TBCs is still a challenging task [2-5].

In the present study, detonation gun (d-gun) spray technique was applied to the fabrication of FGM TBCs. Since d-gun sprayed coatings have inherently higher adhesive/cohesive strength than the other thermal-sprayed coatings due to the higher kinetic energy of the powder particles [6], d-gun spraying can be a promising thermal spray technique for high quality coatings. A new approach of 'shot control method' to make an excellent FGM TBC was also proposed in this study. For characterization of the d-gun sprayed FGM TBCs, X-ray diffractometer (XRD), optical and scanning electron microscope (SEM) and were utilized. Thermal barrier property and thermal shock resistance of the FGM TBCs were also evaluated by using a burner rig tester, and compared with those of duplex TBCs.

2. SHOT CONTROL METHOD

In d-gun spraying, coatings are deposited in a discrete way; that is, by each shot (or each explosion), molten particles spread out and splatter as they strike the surface to form about $10\mu\text{m}$ thick coating deposit with diameter of 20-25mm, as shown in Fig. 1. The nominal working rate of the machine is 4 shots per second, and for spraying wide areas, the substrate is moved using a specimen manipulator as shown in this figure. The 'shot control method' proposed in the present study utilizes this unique feature of d-gun spraying, and cannot be applied to the plasma spray techniques, in which cases the spray process is continuous.

The basic concept of the method is that: the ceramic and metal powders are sprayed alternately in each shot by using two powder feeders to deposit a half and half mixture of ceramic and metal, as shown in Fig. 1. In the area overlapped by the successive shots, an excellent mixture of ceramic and metal could be produced on the level of each particle splat with this method. The area overlapped by each shot can be controlled by the moving speed of the manipulator, and the optimum speed of the manipulator for a fine mixture of ceramic and metal was set as 2cm/sec by several pre-experiments.

Various spraying parameters of the d-gun machine used in the present study can be precisely controlled for each shot. Therefore, the 'shot control method' has an excellent merit of spraying both ceramic and metal powders with their optimum spraying parameters, because with this method basically only one kind of powder is deposited per each shot to produce a coating mixture of ceramic and metal. In other fabrication methods of FGM TBCs such as mixed powder method, it is difficult to optimize spraying parameters for a mixture coating of ceramic and metal due to the large difference in their material properties, e.g., melting temperature [3].

By changing the ratio of the ceramic powder shot to the metal powder shot, it is possible to control the volume ratio of the coating mixtures of ceramic and metal. For instance, spraying with the shot ratio of 1:3, which means the spraying sequence consisting of three shots of metal powder followed by one shot of ceramic powder, produced a mixture of ceramic and metal with the ceramic to metal volume ratio of approximately 25:75. Therefore, the FGM coating having the compositional gradient in the thickness direction could be produced in the manner of spraying several coating layers with increasing the ratio of metal to ceramic shots in sequence as shown in Fig. 2.

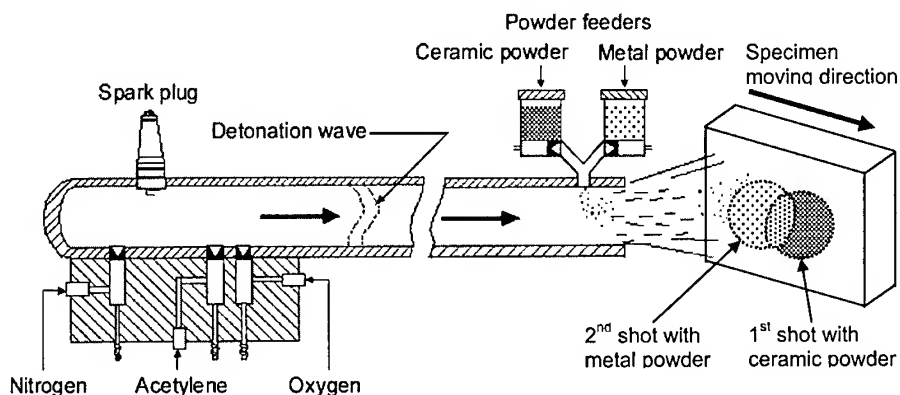


Fig. 1. Schematic illustration showing the basic concept of the 'shot control method'.

3. EXPERIMENTAL DETAILS

TBC specimens were produced with a Russian OB d-gun machine [5] using an explosive gas mixture of acetylene and oxygen. The yttria-stabilized zirconia (YSZ) power (ZrO_2 -8wt.% Y_2O_3) was used for ceramic coating and NiCrAlY powder (Ni-22Cr-10Al-1Y) was used for metal coating.

In order to evaluate and compare the thermal shock resistance of both FGM and duplex TBCs, thermal shock tests were conducted using the burner rig test system. The surfaces of the coated specimens were heated by acetylene-oxygen combustion flame, and a cycle of 10min. of heating followed by a forced air cooling to room temperature was repeated with the thermal load step-likely raised for each cycle from 1000°C to 1600°C.

The thickness of the YSZ and the NiCrAlY coating layers was the same for both FGM and duplex TBC specimens as about 600µm and 200µm, respectively. In the FGM TBC specimen, a functionally graded coating of a YSZ/NiCrAlY mixture (called FGM layer) with the thickness of about 300µm was added between YSZ and NiCrAlY layers. The FGM layer was produced by spraying five coating layers with the metal to ceramic shot ratios of 3:1, 2:1, 1:1, 1:2 and 1:3 in sequence, as shown in Fig. 2.

4. RESULTS AND DISCUSSION

4.1. Microstructure

Figure 3 shows the cross-sectional microstructure of the FGM layer of d-gun sprayed FGM TBCs using the 'shot control method'. The NiCrAlY deposits have a light contrast while the YSZ deposits have a dark contrast under an optical microscope. As clearly shown in this figure, the FGM layer had finely mixed microstructure and the volume ratio of YSZ to NiCrAlY was increased gradually in the thickness direction inside the FGM layer. In addition, despite that the FGM layer was produced by spraying five coating layers different in their volume ratios of metal to ceramic, no specific interface was observed inside the FGM layer. These results indicated that the fabrication of the d-gun sprayed FGM TBCs using the 'shot control method' proposed in the present study was successful.

The FGM layer of the d-gun sprayed FGM TBCs exhibits a lamellar structure of NiCrAlY and YSZ deposits. The lamellar structure is one of the typical features of thermal sprayed

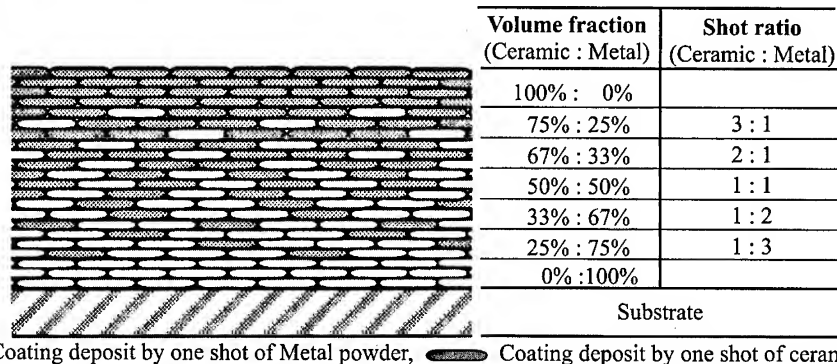


Fig. 2. Schematic illustration showing the deposition scheme to produce a 7-layer FGM TBC by applying the 'shot control method'.

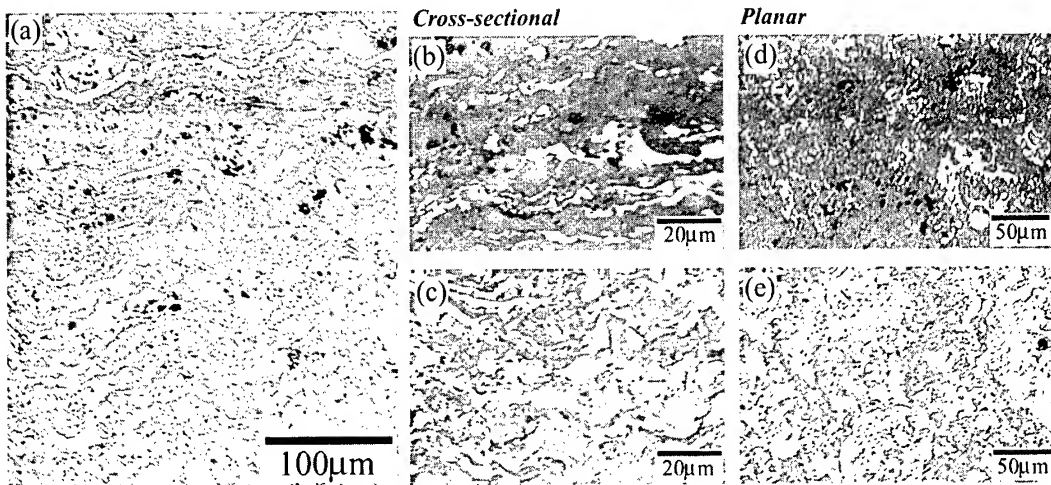


Fig. 3. Optical micrographs showing the FGM coating layer of the d-gun sprayed FGM TBC fabricated by using the 'shot control method'.

coatings and the plasma sprayed FGM TBCs were also reported to exhibit the same structure as this case [2-4]. The ceramic-rich area of the FGM layer seems to be a poor mixture of YSZ and NiCrAlY with stripes of NiCrAlY deposits due to this lamellar characteristic of d-gun sprayed coatings. However, the enlarged micrographs of both areas taken from cross-sectional and planar viewpoints show that both ceramic-rich and metal-rich areas of the FGM layer also finely mixed on the level of each particle splat, as shown in Fig. 3 (b)-(e).

Figure 4 shows the results of XRD analysis from the d-gun sprayed FGM TBC specimens. The intensity of both YSZ and NiCrAlY peaks was changed proportionally with their volume fractions, but no other peaks were detected, which implied that no phase transformation nor severe oxidation occurred during the d-gun spraying process. In case of the plasma sprayed FGM TBCs, it was sometimes reported that the severe oxidation and even phase transformation of metallic phases occurred due to the high processing temperature [1].

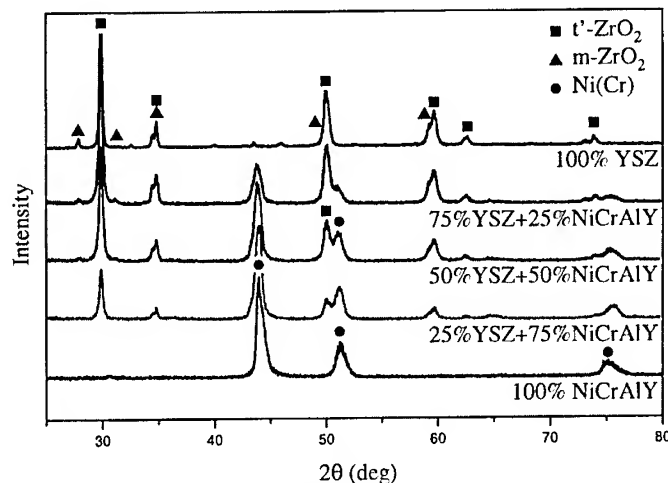


Fig. 4. The variation of the intensity of XRD peaks as a function of the YSZ and NiCrAlY volume fractions.

4.2. Thermal shock resistance

In order to evaluate and compare the thermal shock resistance of both FGM and duplex TBCs, thermal shock tests were conducted using the burner rig test system. During the tests, both the input flame temperature at the front surface and the back surface temperature of the coating were measured in real time, and the difference between these two temperatures when the steady state was achieved (after heating for about 10 min.) was defined to be ΔT of the coated specimen at that input flame temperature, as shown in Fig. 5(a). With a 600 μm thick YSZ top coating layer, d-gun sprayed FGM TBC specimens showed an excellent thermal barrier property with ΔT values reaching as high as about 800°C.

The results of the thermal shock tests for both the FGM and duplex TBCs were compared with regards to the measured values of ΔT in Fig. 5(b). At all the input flame temperatures, FGM TBCs exhibited a larger value of the ΔT than duplex TBCs due to the thermal barrier effect of YSZ ceramic in the FGM layer. No visible delamination occurred in both FGM and duplex TBC specimens till the input temperature reached as high as 1600°C, but the thermal barrier property (or ΔT values) of duplex TBC specimens was drastically degraded as the input temperature was raised above 1300°C.

Figure 6 shows the microstructure of both FGM and duplex TBC specimens after the thermal shock tests. FGM TBC specimens were apparently stable up to the high input flame temperature of 1600°C; on the contrary, a lot of defects and even partial spalling of coating were observed in the YSZ layer of duplex TBC specimens after the thermal shock test. These severe defects in duplex TBC specimens were caused by the repeated and raised thermal loads of the thermal shock tests, resulting in the degradation of thermal barrier property as shown in Fig. 5. These results demonstrate that FGM TBCs have higher thermal shock resistance than duplex TBCs.

In addition, the degradation behavior of duplex and FGM TBCs were also different. In case of duplex TBC, the horizontal cracks, which could cause the delamination of the coatings, were formed near the interface between the YSZ and NiCrAlY layers while the horizontal cracks inside the FGM TBCs were mainly observed inside the FGM layer near the interface between the YSZ and FGM layers, as shown in Fig. 6 (indicated by arrows). In case of the FGM TBCs, therefore, it seems that the ceramic-rich area of the FGM layer is a weak point

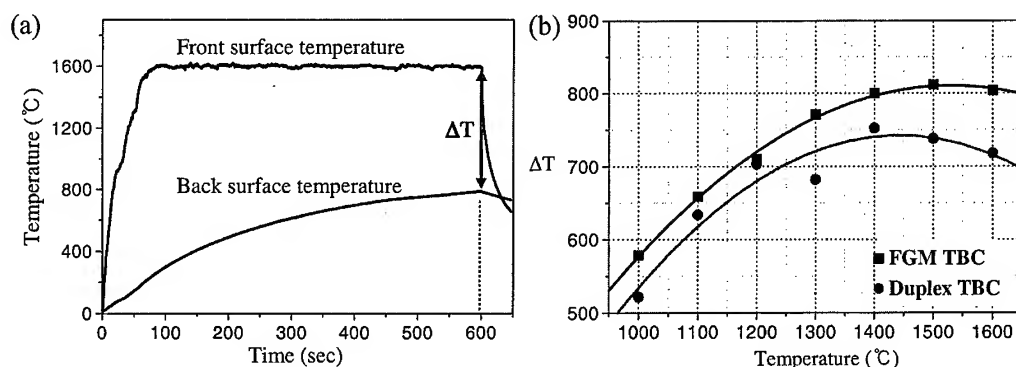


Fig. 5. (a) Temperature profiles of the d-gun sprayed FGM TBC specimens measured by using the burner rig test system. (b) Comparison of the thermal shock resistance between FGM and duplex TBCs with regards to the ΔT values measured during the thermal shock tests.

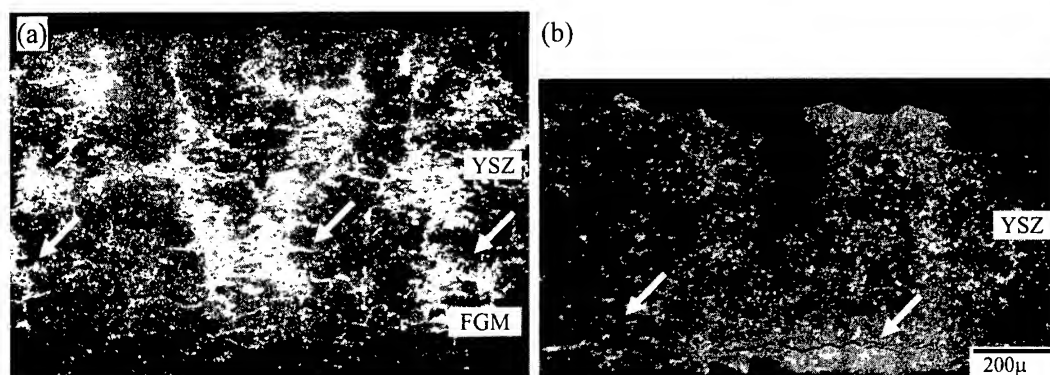


Fig. 6. SEM micrographs showing the degradation behavior of (a) FGM TBC and (b) duplex TBC specimens after the thermal shock tests.

against the thermal shock. It could be explained by the fact that this area lacks of metal deposits, which accommodate the thermal strain developed by a thermal load even though the thermal expansion mismatch between the YSZ and FGM layers is relatively small.

5. SUMMARY

In the present study, FGM TBCs were fabricated using the d-gun spray technique. As a new approach to make an excellent FGM TBC, the 'shot-control method' was proposed and found to be successful; The FGM layer of d-gun sprayed FGM TBCs exhibited finely mixed microstructure of metal and ceramic with the compositional gradient in the thickness direction, and XRD analysis results revealed that the ceramic and metal mixed in the FGM layer kept their own properties and no phase transformation occurred during the spraying process. The expected improvement of the thermal shock resistance due to the realization of a functionally graded layer between the ceramic coat and the metal coat in TBC systems was also proven by the thermal shock tests using a burner rig tester.

ACKNOWLEDGEMENTS

This work was supported financially by the Agency for Defense Development (ADD) under the contract No. UD980014AD.

REFERENCES

1. R. A. Miller and C. E. Lowell, *Thin Solid Films*, 95(1982), pp.265-273.
2. A. Kawasaki, R. Watanabe, M. Yuki, Y. Nakanishi, and H. Onabe, *Mater. Trans. JIM*, 37(1996), pp.788-795.
3. J. Musil and J. Fiala, *Surf. Coat. Technol.*, 52(1992), pp.211-220.
4. Y. Shinohara, Y. Imai, S. Ikeno, I. Shiota, and T. Fukushima, *ISIJ Int.*, 32(1992) pp.893-901.
5. A. Ş. Demirkiran and E. Avcı, *Surf. Coat. Technol.*, 116/119(1999) pp.292-295.
6. R. C. Tucker, Jr., *J. Vac. Sci. Technol.*, 11(1974), pp.725-734.
7. H. W. Jin, Y. M. Rhyim, M. C. Kim, and C. G. Park, *J. Kor. Inst. Met. Mater.*, 36(1999) pp.707-714.

Low Pressure Carburizing of Ti-6Al-4V Alloy

J. H. Kim, C. H. Shin, and S. W. Kim

Korea Institute of Industrial Technology
35-3, HongChonRi, IbJangMun, ChonAnSi 330-820, KOREA

Abstract

For the improvement of wear performance of Ti alloy, vacuum carburizing technique was applied using propane atmosphere. Like in the plasma carburizing carbide was also formed at the surface and carbon transfer from the carbide to the matrix was influenced by the temperature. The obtained surface hardness is increased with the reduction of operating pressure and time. Optimum hardness distribution could be obtained with proper choice of temperature and carbon flux control. Case depth was largely influenced by not the times about temperature. For the thick case depth and high surface hardness, two steps process was recommended.

1. INTRODUCTION

Titanium and titanium alloys possess the high specific strength, fracture toughness, corrosion resistance, biocompatibility, and low density of 4.51g/cm^3 . Therefore, they are widely used as light material components in the field of aerospace, military, transportation, and nuclear industries. But, poor wear characteristics, such as seizure problem due to high reactive surface properties limits the use of titanium alloys for the mechanical parts such as automobile valve, etc. So many efforts have been done to improve the surface properties using plating, oxidation, boronizing, nitriding, and carburizing. But, none of them could satisfy customers.

Recently, there was an interesting report in which plasma carburizing process could be successfully applied to the titanium alloy for the tribological use. But, plasma carburizing has still some disadvantages such as high initial investments and intrinsic difficulties to get the uniform plasma density, and to set up the charge efficiently. Low pressure carburizing was invented as an innovative process in the 1970's, but it has not been widely adopted, in contrary to the expectation, due to maintenance problem by the sooting and difficulty to get high speed quenching.

Recent technical progress of vacuum carburizing and logical design of equipment have renewed the low pressure carburizing as one of the promising, next generation technologies for the production of automobile parts in Japan and Europe. The advantage of low pressure carburizing is that it is possible to do high speed carburizing with uniform gas distribution in vacuum, and that it is to get internal oxidation free structure. The important thing is that low pressure carburizing is done through high flux of carbon by the instantaneous formation of thin layer carbide at the interface of Fe alloy in oxygen free atmosphere.

The purpose of this work is to provide the basic information of low pressure carburizing of

the titanium alloy for the tribological applications such as effects of process variable on the characteristics of carburized layer of titanium alloy.

2. EXPERIMENT

Carburizing treatment was done at less than 1000Pa with mass flow control of gases using propane and acetylene in the vacuum furnace in Fig.1. Pure titanium and Ti-6Al-4V samples with 10mm length×15mm diameter were prepared and polished to the 0.3 μ m alumina powder before treatment. As experimental variables, temperature, time, and operating pressure using different flux had been taken as shown Fig. 2. The results were examined by scanning electron microscope and X-ray diffraction.

3. RESULTS

3.1 Hardness distribution

In order to see the effects of gas species and operating pressure on the carburizing characteristics of Ti-6Al-4V, carburizing treatment was carried out for Ti-6Al-4V at 900°C for 1hour holding with different dosage of propane and acetylene(different operating pressure). Fig.3 shows the distribution of Microvickers hardness in carburized titanium. As the operating pressure is lowered (decrease the flux), the surface hardness is increased. Acetylene and propane show the similar tendency in hardness distribution. But, acetylene provoke the soot and non-uniformity of colors on the surface of specimen. Fig. 4 shows the hardness distribution with different operating pressure and time for the carburized titanium at 800°C and 900°C. As the carburizing pressure is lowered and the holding time is increased, the surface hardness is increased in general but at 900°C with time the surface hardness is decreased, and the diffusion depth is increased. These tendencies are the same for the Ti-6Al-4V. That is, at 800°C, the surface hardness of carburized specimen is increased with lowering of operating pressure and holding time and for 900°C the surface hardness of alloy is decreased, and diffusion depth is increased with carburizing time.

3.2 Microstructure evolution

Microstructure examination of specimen before and after carburization shows no grain growth even 7hours carburization treatment at 900°C. Fig. 5 shows one example of the evolution of carburized layer for the Ti-6Al-4V under SEM. The thickness of layer gradually increases as carburizing time goes by. And, this tendency is equal to pure titanium.

3.3 X-ray diffraction(XRD) analysis

According to the XRD analysis in Fig. 6, the surface white layer could be identified as titanium carbide for the carburized titanium and titanium alloy. The intensity of titanium carbide peak is sharpened with carburized time.

3.4 Thickness of TiC layer

Fig. 7 shows the evolution of carbide layer thickness which is measured under scanning

electron microscope(SEM) with 10,000 times magnification versus square root times. The thickness of carbide layer linearly increases in general. And, at higher temperature, the rate of increment of carbide layer is higher than that at lower temperature. Therefore, the growth of carbide layer is thought as the thermally activated process.

3.5 Summary

In terms of carburized case depth and hardness distribution, there were no differences between propane and acetylene gas, but apparently there were some problems of sooting and non-uniformity of colors for the acetylene usage. So, in this work, low pressure carburizing has been mainly done with propane gases. Concerning effect of operating pressure and treating time on the surface hardness, surface hardness of carburized layer is increased with lowering of pressure and holding time at 800 °C for pure titanium and Ti-6Al-4V. But, on the contrary, the surface hardness of carburized layer pure titanium and Ti-6Al-4V is decreased with time at 900 °C.

Contrary to the cases of carburization of steel for the case of the carburizing of Ti-6Al-4V, the titanium carbide layers were always formed and grown on the carburized surface.

4. DISCUSSION

To understand the dependence of surface hardness upon the operating pressure and temperature, two-steps carburizing with pressure change or temperature change during process were made as in Fig. 8. This experiment shows again that final surface hardness value of carburizing of titanium alloys is influenced largely by the second step.

From Fig. 9 of the wavelength dispersive spectroscopy(WDS) analysis of elements variation on the carburized layers, it seems that carbon is almost segregated in the carbide layer for the 800 °C carburized case, and, from surface carbide layer, carbon is penetrated to the substrate of titanium alloy for the 900 °C carburized specimen.

According to the phase diagram of TiC in Fig. 10, it can be seen that TiC at 900 °C has a wide gradient of carbon composition than TiC at 800 °C. And the diffusion of carbon in beta(β) phase is much faster than that in alpha(α) phase due to lattice structure even though the solubility of carbon in titanium is somewhat higher in alpha phase compared to that of beta phase.

Therefore, the evolution of surface hardness of carburized layer with time, and temperature could be understood qualitatively as follows. During carburization, the carbide is first formed at the surface of sample and grown with composition gradient mainly in carbon. For the carburization of Ti-6Al-4V at 900 °C, diffusion of carbon is expected from the carbide to the matrix. It will have less gradient of carbon in the carbide layer with time.

So, the surface hardness of carbide layer will decrease with time, and case depth of hardened layer will be thick. But, for the carburization of Ti-6Al-4V at 800 °C, carbon is blocked in the carbide layer by the difficulty of diffusion in alpha phase. So, carbon gradient in the surface layer is sharpened. Then surface hardness is increased with time. As the decomposition of hydrocarbon occurs more rapidly, with reduction of operating pressure, carbon flux will be higher. Therefore, the hardness of carbide layer is increased with reduction of operating pressure for the 800 °C carburization.

Fig. 11 shows the dependence of surface hardness on the operating pressure. According to the works of C.HAYAUD, et. al., the dissociation of propane increases with pressure to form

more stable hydrocarbon(C_2H_2) and hydrogen[1]. So it is thought that higher flux carbon increases the hardness of carbon layer.

Comparing with the results of plasma vacuum carburizing in Japan, the following remarks can be made from Fig. 12[3]. In the plasma vacuum carburizing, surface carbide is first formed by the recombination of ions of carbon and titanium under glow discharge and deposition. But, in this work, surface carbide is also formed without plasma in the low pressure carburizing, and the thickness of carbide layer is increased with time and temperature. The growing behavior of carbide layer in both carburizing is similar, but, for the carburizing at $900^\circ C$, it is shown that plasma carburizing make much thicker carbide layer compared to the low pressure carburizing. And the hardness values obtained in both carburizing is about Hv1200. Have compared with hardness on the PVD or CVD coated sample, it seems these values are half of hardness of coated sample. Further studies are needed to understand this discrepancy.

5. CONCLUSION

From the above studies, we obtained the following conclusions. By low pressure carburizing of Ti-6Al-4V, we can obtain the same result as plasma carburizing. The different evolution of surface hardness of carburized Ti-6Al-4V with temperature, time, and operating pressure could be understood by the gradient of carbon in the carbide and diffusion difficulty. For the practical use two steps heat treatment, for example, short time pre-carburizing at $900^\circ C$ and final low temperature carburizing at $800^\circ C$ could be used to get deep hardening and high surface hardness for the wear and load bearing capacity. Here, we obtained only qualitative results. For the more understanding of carbon evolution during low pressure carburizing, more works such as TEM(Transmission Electron microscope) studies are needed.

REFERENCES

1. C. Hayaud et al., in ATTT, (1997), pp. 99-103.
2. T.B. Massalski et al.: Binary alloy phase diagram, Vol.1, W. Scott, Jr.(APIC),(1990), pp. 889.
3. Z.S. Okamoto, H.S. Hoshika and M.S. Yakushiji, The Japan Society for heat Treatment, Vol.40, No.2(2000), pp.88-93.

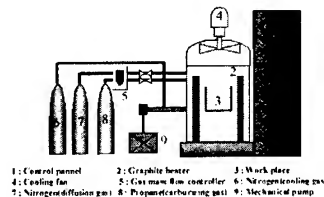


Fig. 1 Schematic of carburizing furnace

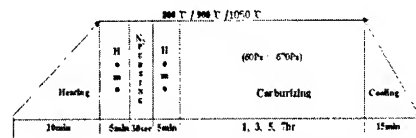


Fig. 2 Experimental variables

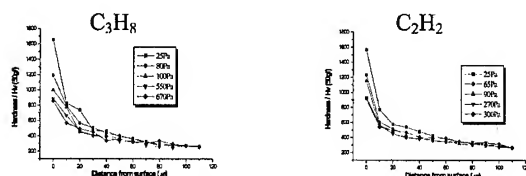


Fig. 3 Hardness distribution of carburized Ti-6Al-4v with different operating pressure and gases

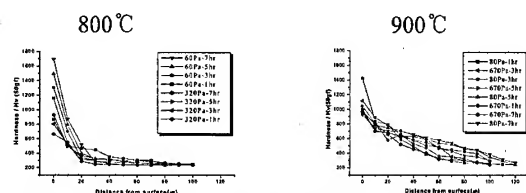


Fig. 4 Hardness distribution of carburized layer of Ti with furnace pressure, time, and temperature

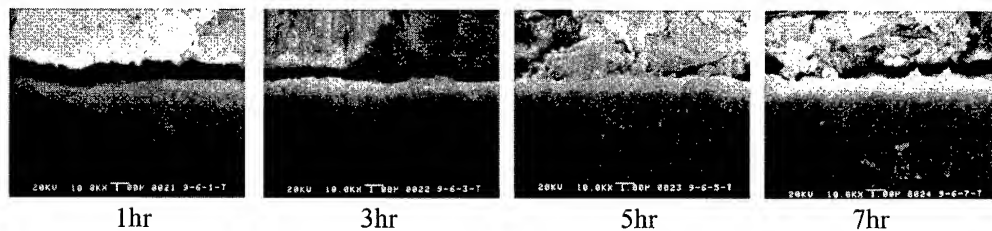


Fig. 5 Evolution of carburized layer (Ti-6Al-4V alloy, 900 °C, 670Pa, ×10,000)

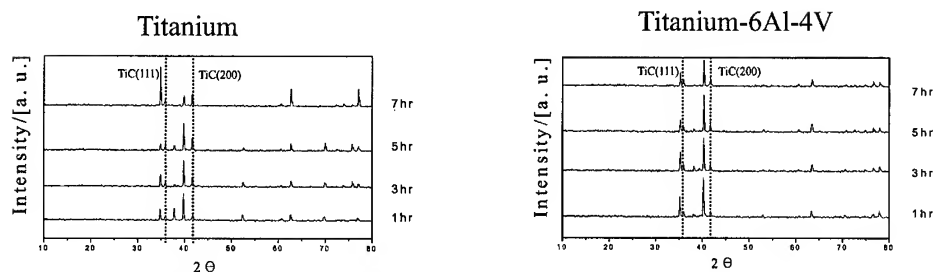


Fig. 6 X-ray diffraction of the carburized Ti & Ti-6Al-4V surface (900 °C, 670Pa)

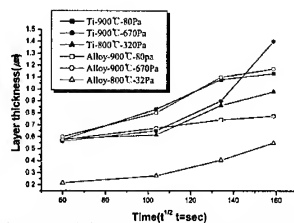


Fig. 7 The evolution of TiC layer thickness with the carburized time and pressure

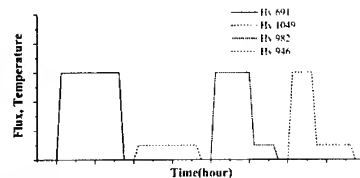


Fig. 8 The step carburizing process

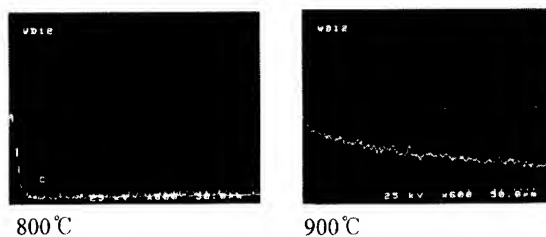


Fig. 9 WDS line mapping carbon analysis of carburized Ti-6Al-4V

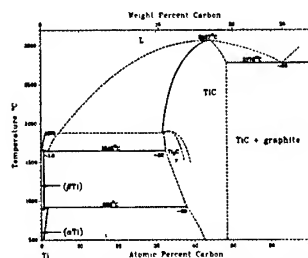


Fig. 10 Phase diagram of Ti-C[2]

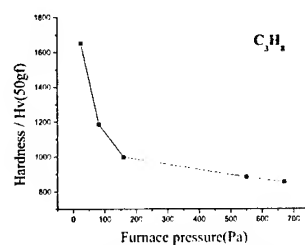


Fig. 11 The dependence of surface hardness with the operating pressure

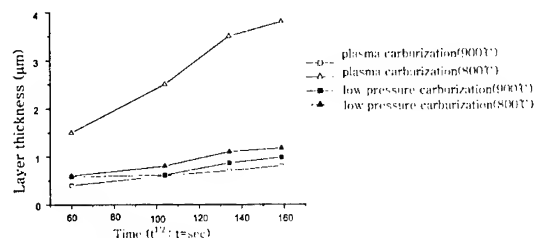


Fig. 12 The evolution TiC layer thickness with time in plasma carburization and low pressure carburization versus plasma carburized time[3]

NITRIDING AND BORONIZING OF TITANIUM AND TITANIUM ALLOYS AND EVALUATION OF SURFACE STRENGTH

Keiji Nakasa, Xu Yan and Masahiko Kato

Faculty of Engineering, Hiroshima University, 1-4-1 Kagamiyama
Higashi-Hiroshima 739-8527, Japan

ABSTRACT

Pure titanium, Ti-6Al-4V, Ti-15V-3Cr-3Al-3Sn and Ti-13V-11Cr-3Al alloys, were nitrided using N_2 gas or borozed in molten $Na_2B_4O_7$ salt. The microstructures, hardness, strength of the titanium nitrides or titanium borides layers as well as wear and hydride formation resistance were examined. The thickness of boride layer increased with increasing boronizing temperature and time, and increased with increasing charging current density to take a maximum at a certain current density. The thickness of boride layer and the hardness were larger for pure titanium than other titanium alloys. The bending strength of the boronized layers measured by using a crack-interval extrapolation method was much larger than that of nitrided layer for pure titanium. The application of nitriding to pure titanium increased the wear resistance and the hydride formation resistance.

1. INTRODUCTION

Titanium and titanium alloys are often used for many transportation vehicles because of high specific strength and corrosion resistance. However, titanium is one of the most active metals, and once the protective oxide film is destroyed under frictional load the sticking to counter metal can occur. In addition, the small heat conductivity of titanium accelerates the fretting and wear. Moreover, the hydride is formed under the hydrogen environment, and the heat resistance is low compared with stainless steels and super alloys because of the rapid oxidation at high temperature. These demerits prevent the titanium alloys from the application to important parts, such as landing gears and jet engine parts.

In order to solve these problems, various kinds of surface modification processes, such as diffusion-permeation process, PVD, CVD, thermal spray coating and ion implantation, have been carried out [1-5]. Among them, the surface modification using gas or molten salt is more effective especially for the machine parts with large size and complex shape than PVD and thermal spraying methods. Moreover, because the elastic modulus of titanium is low compared with steels while that of hard coating materials is generally larger, the modification layer receives high stress under the applied load. Thus, the diffusion method using gas or melting salt is superior to CVD and ion implantation because both methods provide thicker modification layer. Although the methods are rather classical, the process does not need complex and expensive apparatus.

In the present research, the boronizing and nitriding are applied to titanium and titanium alloys to obtain the surface with high hardness, and the effect of the modifications on the wear and hydride formation characteristics were examined comparing with other surface modification methods.

2. EXPERIMENTAL METHOD

The materials used are as-received pure titanium (α -phase), Ti-6Al-4V ($\alpha + \beta$ phase), Ti-15V-3Cr-3Al-3Sn, Ti-13V-11Cr-3Al (β -phase) alloys. After machining the alloys to the specimens with 60mm length \times 10mm width \times 3mm thickness, the surface was polished using

emery papers to #800. The apparatus used for boronizing is shown in Fig.1. The specimens were immersed into melted $\text{Na}_2\text{B}_4\text{O}_7$ salt kept at a temperature of $T=1073\text{--}1273\text{K}$ for $t=0\text{--}36\text{ks}$. The electric current of $i_c=0\text{--}5.4\text{kA/m}^2$ was applied between specimen and platinum electrode. The apparatus for gas nitriding is shown in Fig.2. The specimens were kept at a temperature of $T=1153\text{K}$ or 1223K in vacuum of $4\times 10^{-3}\text{Pa}$, and the nitrogen gas of 99.999 % purity was introduced with flow rate of $Q=0.017\text{L/s}$. After holding for $t=3.6\text{--}86.4\text{ks}$, the specimen was cooled in the chamber.

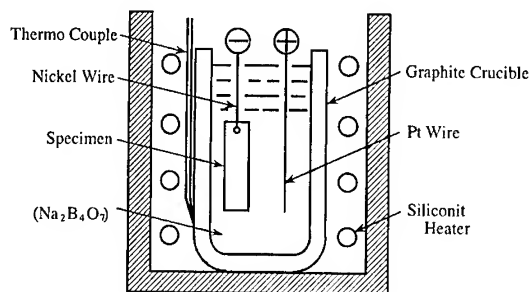


Fig.1 Apparatus for boronizing.

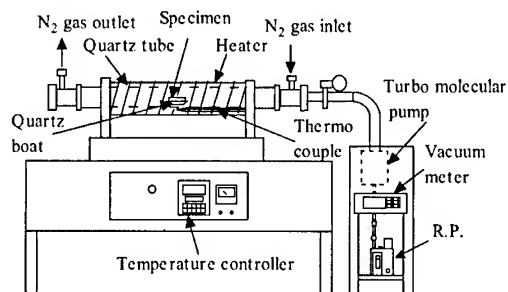


Fig.2 Apparatus for gas nitriding.

3. RESULTS AND DISCUSSION

3.1 Surface hardness and microstructure of boronized or nitrided layers

Figure 3 shows the structures of cross section of specimens after boronizing. The optical microstructure of pure titanium (Fig.3(a)) reveals the white continuous layer of TiB_2 and discontinuously distributed granular TiB which corresponds to the X-ray diffraction analysis shown in Fig.4. The optical structures of Ti-6Al-4V alloy is shown in Fig. 3(b). The boride layers becomes irregular at higher charging current density than 1200A/m^2 .

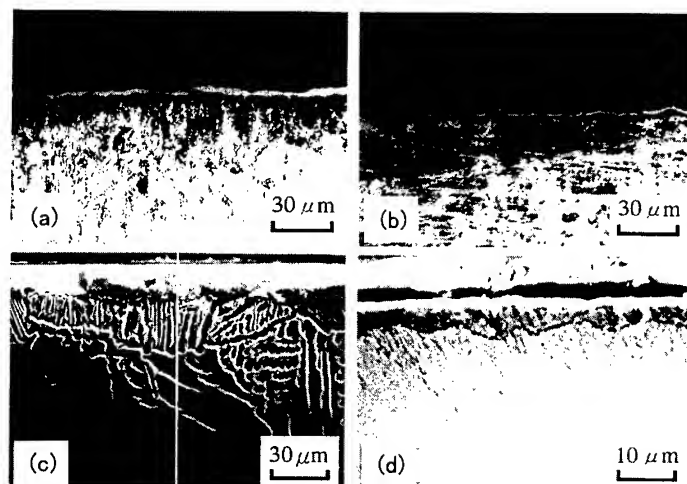


Fig.3 Micro structure of titanium and titanium alloys after boronizing.
(a) Pure titanium (charging current density $i_c=230\text{A/m}^2$), (b) Ti-6Al-4V alloy ($i_c=4211\text{A/m}^2$), (c) Ti-15V-3Cr-3Al-3Sn alloy ($i_c=230\text{A/m}^2$), (d) Ti-15V-11Cr-3Al alloy ($i_c=1068\text{A/m}^2$)

Figure 3(c) is the structure of Ti-15V-3Al-3Sn alloy observed by SEM, where the plate-like phase appears in substrate under the TiB_2 and TiB layers. From the X-ray analysis of the surface after removing the boride layers, the structure was identified as α phase. Fig.5 shows the line analysis of the structure using EPMA. Boron exists only in the boride layer and does not diffuse into titanium, which corresponds that boron does not dissolve into α and β phases of titanium according to binary equilibrium phase diagram. In boride layers, there exist Cr and V from substrate while Al and Sn are extruded near the boundary between layer and substrate. In the plate-like α phase, the concentration of V, Cr and Al is low while that of Ti and O are high. These distribution of elements means that the formation of boride layer occurs taking following process; Boron diffuses into the alloy to form borides, which partly dissolve V and Cr, and at the same time extrude Sn and Al, which are α phase stabilizing element, to substrate. On the other hand, the oxygen atoms, which is also α phase stabilizing element and have large binding energy with titanium, diffuse from surface into substrate and extrude V and Cr, which are β phase stabilizing elements, to form α phase during boriding process. Fig.3(d) shows the optical structure of Ti-13V-11Cr-3Al alloy. The string-like α phase seems to exist in the substrate near boundary. Fig. 6 shows the X-ray diffraction patterns of the specimen. The peaks from VB_2 or CrB_2 appears with TiB_2 peaks when the current density is $i_c=1.9kA/m^2$ where the thickness of boride layer is maximum.

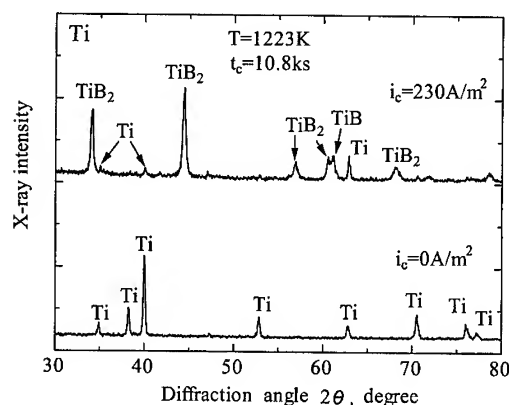


Fig.4 X-ray diffraction patterns of boronized pure titanium.

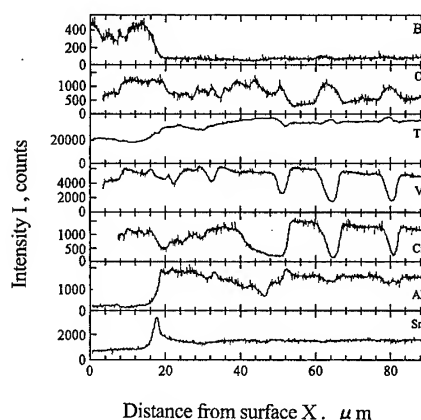


Fig.5 Line analysis Ti-15V-3Cr-3Al-3Sn alloy by EPMA

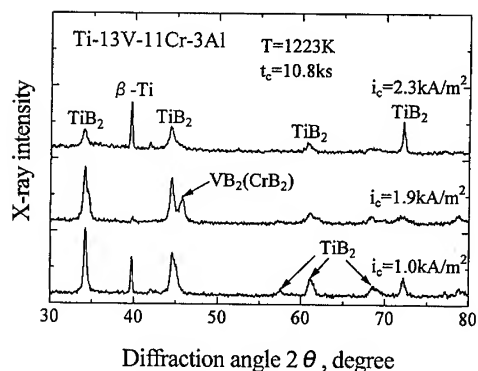


Fig.6 X-ray diffraction patterns of boronized Ti-13V-11Cr-3Al alloy.

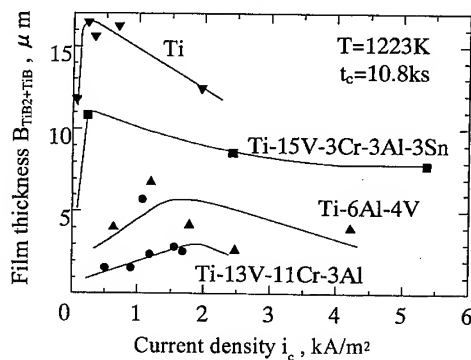


Fig.7 Effect of charging current density on the boronized layer thickness.

Figure 7 shows the relationship between current density and boride layer thickness for all the alloys. The thickness is the largest for pure titanium and the peak of current density taking maximum thickness is smaller for the alloy with larger boride layer thickness. Figure 8 shows the relationship between current density and micro Vickers hardness measured at an indentation load of 1, 2 and 5N for titanium specimen boronized at 1223K for 10.8ks. The hardness takes a maximum of 40GPa at a certain current. The similar tendency was observed for titanium alloys and the maximum hardness of the boride layers (0.1N indent force), are about 37GPa for Ti-6Al-4V alloy and about 24GPa for Ti-15V-3Al-3Sn and Ti-13V-11Cr-3Al alloys. Although the hardness of boride layer of β type alloys are not large perhaps Cr or V dissolves in borides substituting for Ti, they are still larger than that of Fe_2B of boronized steels (20GPa). Moreover, the boronizing temperature of about 1223K is so high for pure titanium or near α type alloys that grain growth occurs, while the temperature corresponds to the solution treatment temperature for $\alpha+\beta$ and β type alloys. Thus, the boronizing treatment is rather suitable for $\alpha+\beta$ and β type alloys.

Gas nitriding was carried out for pure titanium. Fig.9 shows the relation between nitriding time and the thickness of nitride layers. The microstructure in Fig.10 and X-ray diffraction pattern in Fig.11 shows that TiN and Ti_2N layers are formed on the substrate.

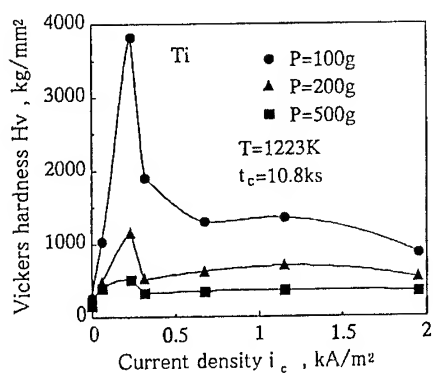


Fig.8 Effect of electric current density on the micro-Vickers hardness of boronized pure titanium.

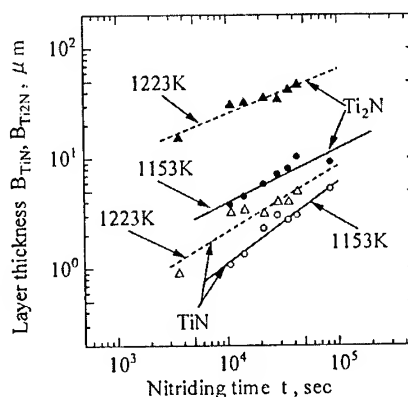


Fig.9 Effect of nitriding time and temperature on the thickness of nitride layers.

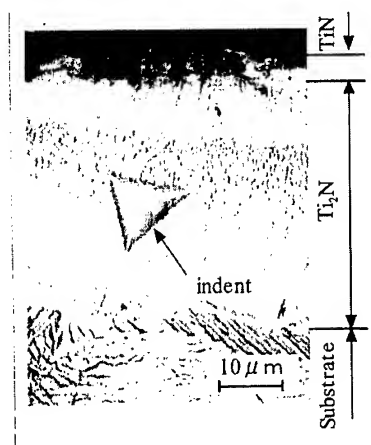


Fig.10 Optical micro-structure of nitrided layers ($T=1223\text{K}$, $t=28.8\text{ks}$).

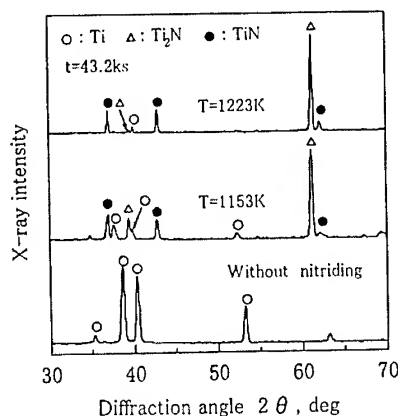


Fig.11 X-ray diffraction patterns of nitrided pure titanium.

3.2 Strength of boride and nitride layers

Four-point bending tests were carried out on the boronized or nitrided pure titanium specimens. The true bending strength σ_c was calculated by using the equation: $\sigma_t = E_1 I \sigma / (2(E_1 I_1 + E_2 I_2) + E_3 I_3)$. Here, σ is nominal bending stress, σ_t is true stress, E_1 , E_2 and E_3 , and I_1 , I_2 , I_3 , are the elastic moduli and second moment of area of surface layer, middle layer and substrate. B_1 , B_2 and B_3 are the thickness of each layer and substrate. During the bending tests, the average interval between cracks, L , were measured and plotted as a relation between σ and inverse of L . Fig.12 shows the results for TiN layer. Although the true stress is not exact after the cracking has occurred in the layer, the true stress just when the first cracking occurred, or the stress at $1/L=0$, corresponds to the σ_c . According to the estimation, the σ_c of TiN is about 630MPa. Fig.13 shows the relationship between thickness of titanium-boride layer and true bending strength σ_c , nominal bending stress σ and residual stress σ_R obtained from X-ray measurement. The σ_c of TiB₂ layer is almost constant irrespective of layer thickness. The existence of residual compressive stress seems to increase the strength of TiB₂ layer. The σ_c of TiB₂ layer is much larger than that of TiN layer and the hardness of TiB₂ (HV4000) is also larger than that of TiN (HV2400), so that the boronizing has a merit to improve surface properties of titanium.

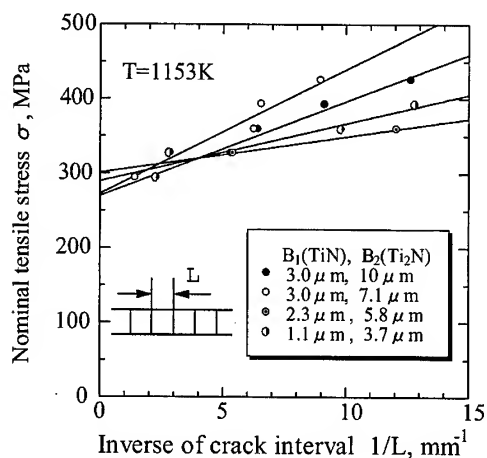


Fig.12 Relationship between inverse of crack interval and nominal tensile stress.

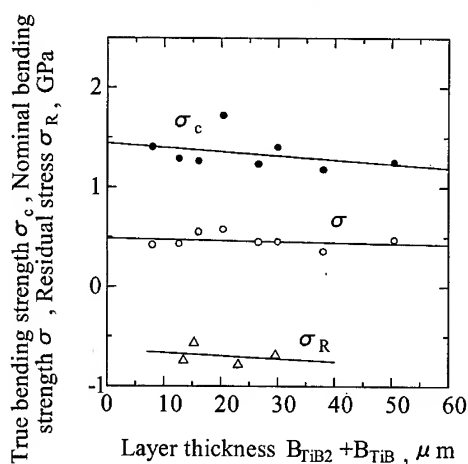


Fig.13 Relationship between boride layer thickness and nominal, true bending strength and residual stress.

3.3 Wear and hydride formation resistance of nitrided titanium

Pin-on-disk type wear tests were carried out for the nitrided pure titanium. The loading pin was SiC ball. The example of the results is shown in Fig.14 with the results for sputtered TiN film. The wear property is largely improved by nitriding. Although the delamination of TiN layer occurred at a certain wear cycles, the Ti₂N layer does not delaminate from substrate and prevent wear of titanium. On the other hand, the sputtered TiN film delaminates within a shorter period and the wear of substrate increases largely.

The hydrogen charging test was carried out for pure titanium in 40mass% sulfuric acid aqueous solution under the charging current density of 500A/m². Fig.15 shows the relationship between thickness of nitride layer or film and delamination time, where the data obtained for sputtered TiN film, N₂⁺ ion implanted titanium, TiO₂ film coated by sol-gel method and by anodic oxidation are also shown. The nitriding prevents delamination of nitride layers as well as hydride formation on titanium, while the coated films are easily delaminated and hydride was formed in the N₂⁺ ion-implanted titanium after the charging of 1ks. Thus, gas nitriding is more effective than the coating methods when the titanium is used for hydrogen environment.

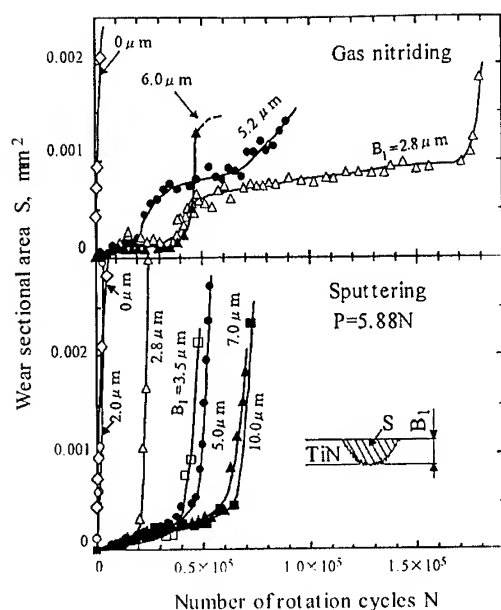


Fig.14 Relationship between number of rotation cycles and wear area for nitrided or sputtered pure titanium.

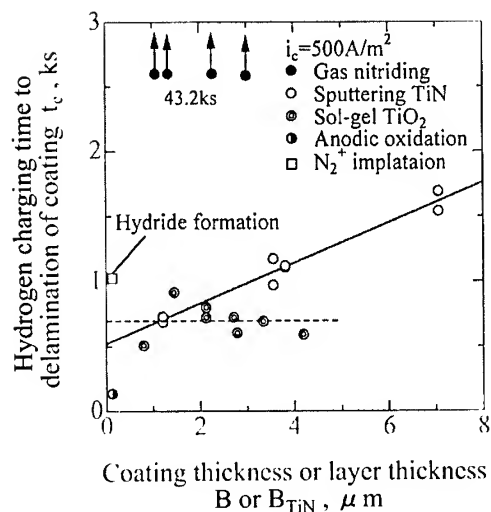


Fig.15 Relationship between layer or film thickness and delamination time under hydrogen charging.

It is concluded that the boronizing and nitriding are applicable for titanium alloys to form thicker hard layers. This is important for the material with small elastic modulus like titanium and aluminum alloys, because the thin modification layer can not bear the large contact load, and the layer or film is easily cracked and delaminated due to the large difference in elastic modulus between film and substrate.

4. CONCLUSION

Pure titanium, Ti-6Al-4V, Ti-15V-3Cr-3Al-3Sn and Ti-13V-11Cr-3Al alloys are boronized using $\text{Na}_2\text{B}_4\text{O}_7$ melted salt and nitrided using N_2 gas, and the micro-structures, micro-hardness, strength of the layers as well as wear and hydride formation resistance are examined. Titanium borides, TiB_2 and TiB , are formed by the boronizing. The thickness of boride layer increases with increasing boronizing temperature and time, and takes a maximum at a certain charging current density. The thickness of boride layer and the hardness are larger for pure titanium than other titanium alloys. Titanium nitrides, TiN and Ti_2N , are formed by N_2 gas nitriding. The bending strength of the boronized layers measured by using a crack-interval extrapolation method is much larger than that of nitrided layer for pure titanium. The application of nitriding to pure titanium increases the wear resistance and the hydride formation resistance.

REFERENCES

1. Surface Performance of Titanium, L.K.Gregoty, H.J.Rack and D.Eylon eds., TMS (1996).
2. K.Nakasa, M.Kato and H.Matsuyoshi, J.Japan Inst. Metals, Vol.61(1997), pp.311-318.
3. M.Kato, R.Wang and K.Nakasa, Proc. Xi'an Int. Titanium Conf. (XITC' 98), Titanium'98, L.Zhou, D.Eylon, G.Lutjering and C.Ouchi eds., Int. Academic Pub., Vol.1(1998), pp.533-539.
4. R.Wang, M.Kato and K.Nakasa, J.Japan Inst. Metals, Vol.63 (1999), pp.1015-1021.
5. R.Wang, M.Kato and K.Nakasa, J.Japan Inst. Metals, Vol.64 (2000), pp.887-894.

INTENSIFIED PLASMA-ASSISTED PROCESSING OF PURE Ti AND Ti-6Al-4V ALLOY

Efstathios I. Meletis

Materials Science and Engineering program
Mechanical Engineering Department
Louisiana State University
Baton Rouge, Louisiana 70803 USA

ABSTRACT

Intensified Plasma-Assisted Processing (IPAP) is a surface engineering method developed in our laboratory that has been utilized for low-temperature, low-pressure nitrogen diffusion treatments and coating deposition. Plasma intensification and energetic flux bombardment of the work piece is accomplished by using a triode glow discharge. IPAP utilizes high cathode current densities at low pressures, allowing enhanced flow and controlled energies of the particles bombarding the work piece leading to formation of desired nanostructured nitrides and deep diffusion zones. Recent studies show that IPAP can achieve enhanced plasma nitriding kinetics at relatively low temperatures even in materials that are difficult to nitride by conventional means such as Ti-based and Al-based alloys. A brief summary of the fundamentals behind this method is presented along with experimental results on IPAP-treated pure Ti and Ti-6Al-4V alloy. IPAP treatment was found to achieve a marked increase in hardness (3.5 and 4.5 times higher for Ti and Ti-6Al-4V, respectively) and tribological experiments have shown significantly greater wear resistance and lower friction coefficients. Anodic polarization and fatigue experiments revealed that corrosion and fatigue resistance of IPAP-treated specimens is also slightly increased. The present results suggest that IPAP is a high potential surface treatment for Ti-based alloys.

1. INTRODUCTION

During the last three decades, there have been tremendous advancements in the area of surface engineering by developing novel diffusion, coating (composite, multilayered, functionally gradient) and duplex treatments. Intensified plasma-assisted processing (IPAP) is a patented surface modification technique that has been developed in our laboratory [1,2]. The IPAP technique allows a combination of plasma diffusion treatments with plasma-assisted vapor deposition and chemical-reaction synthesis. Plasma intensification is accomplished by using a triode glow discharge allowing low-pressure, low-temperature treatments (typically $<500^{\circ}\text{C}$). Figure 1 presents the experimental set-up and the principle behind the technique. The system involves an ion gun and two magnetron sputter sources and is capable of conducting several treatment combinations.

A major portion of our work has been concerned with intensified plasma nitriding utilizing the IPAP technique. Considering energy levels during plasma or ion beam treatments, it is evident that previous studies have concentrated on either end of the energy spectrum of participating particles. For example, ion implantation is at the high-energy spectrum (5-500 keV) and conventional plasma nitriding at the low energy end of the spectrum (particle energy <200 eV). Energetic particle bombardment during IPAP takes place at an intermediate energy level (200-2000 eV). In the past, beneficial effects by energetic bombardment have been realized in processes such as ion plating (triode ion plating) [3] and ion beam enhanced deposition [4] and these developments motivated research in the area of intensified plasma nitriding [5].

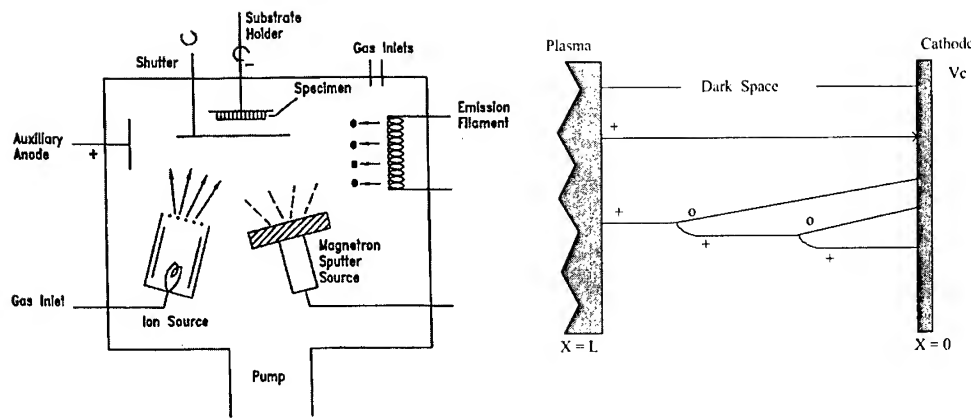


Fig.1 Experimental set up of IPAP and dominating mechanism of charge exchange collisions [(+) represent ions and (o) represent neutrals].

Plasma intensification during IPAP provides several fundamental advantages compared to the diode process. These advantages include (i) higher ionization efficiency; (ii) lower operating gas pressures; (iii) highly energetic flux of ions and neutrals; and (iv) flux bombardment can provide the activation energy for chemical reaction and compound synthesis. These advantages result in: (i) less contamination and cleaner surfaces; (ii) highly desirable nitrides and microstructural control; (iii) treatment at relatively low temperatures; (iv) significantly enhanced diffusion kinetics; and (v) diffusion zones can be produced to serve as a precursor to subsequent coating treatments (duplex treatments or functionally-graded coating treatments) that can be performed in the same system. The majority of our work has been focused on applying IPAP to nitride systems that are difficult to be processed by the conventional plasma nitriding (i.e. Al- and Ni-based alloys, stainless steels, etc.) [5,6]. This paper provides a summary of the theoretical background behind IPAP and achievements obtained for the Ti system.

2. THEORETICAL BACKGROUND AND MECHANISM

IPAP operates in the cathode dark space of the abnormal regime of the glow discharge. In the dark space, energetic ions and neutrals bombarding the work piece are generated through collisions, Figure 1. This results in three types of energetic particles: ions that escape collisions and arrive at the cathode with their full energy, and ions and neutrals produced from collisions within the dark space having a distribution of energy that has been previously described [7]. An approximate estimate of the average ion (E_i^a) energy is given by [8]:

$$E_i^a = V_c \left[2 \left(\frac{\lambda}{L} \right) - 2 \left(\frac{\lambda}{L} \right)^2 + 2 \left(\frac{\lambda}{L} \right)^2 e^{-\frac{L}{\lambda}} \right] \quad (1)$$

where V_c is the cathode voltage, λ is the mean free path for charge exchange collisions and L is the dark space length. The neutrals bombarding the cathode can be either energetic or low-energy thermal neutrals (1-2 eV). The average energy (E_n^a) of energetic neutrals is expressed as:

$$E_n^a = V_c \frac{\lambda}{L} \left[1 - 2 \left(\frac{\lambda}{L} \right) + 2 \left(\frac{\lambda}{L} \right)^2 - 2 \left(\frac{\lambda}{L} \right)^2 e^{-\frac{L}{\lambda}} \right] \quad (2)$$

The above equations show that the ratio L/λ has a controlling effect on the flux energies as has been previously suggested [9,10]. IPAP is characterized by low L/λ ratios ($L/\lambda < 10$) whereas high L/λ values ($L/\lambda > 10$) prevail in the conventional process. A decrease in L/λ causes an increase in the average ion and neutral energies. Low L/λ ratios are obtained under low pressure and discharge intensification conditions that reduce the number of collisions and increase average energy of ions and neutrals. Decreasing L/λ increases the total ion energy but reduces the number of energetic neutrals and their total energy. A balance of these counter acting factors produces an optimum energy distribution that occurs at a critical value of $L/\lambda = 2$ [8,11]. Figure 2 presents surface microhardness values of pure Ti IPAP-nitrided at various L/λ ratios. These experiments were conducted at the same cathode current density ($j = 3.5 \text{ mA/cm}^2$), temperature (440°C) and bias voltage ($V = 2,000 \text{ V}$). Varying the chamber pressure varied the L/λ ratio. The results show a hardness increase over that of pure Ti ($\sim 400 \text{ H}_V$) by 3.5 times and that the highest hardness is obtained for the critical value of $L/\lambda = 2$.

As noted earlier significantly higher average ion and neutral energies exist in IPAP compared to the diode process. Also, in spite of the higher dose pertaining in the diode process (due to higher neutral dose), IPAP-treated specimens exhibit higher surface hardness. Considering the various energy-dependent physical processes that take place during bombarding particle/material surface interaction (sputtering, implantation, defect generation, diffusion, etc.), it is evident that a beneficial effect is expected from the energetic flux pertaining in IPAP compared to the conventional low energy process. Similar beneficial effects by ionic bombardment on film deposition have been previously recognized [3,4]. The above observations clearly suggest that beneficial surface conditions (vacancies and surface defects) develop during the higher energy bombardment of the surface. Recent theoretical predictions using TRIM show that energetic particle bombardment beyond a threshold energy level of $\sim 200 \text{ eV}$ (upper limit of conventional plasma nitriding) would be required for significant vacancy generation in the outer surface layer [12]. Previous experimental results however, on a large number of metals show a reduction of point defects produced in cascades when the bombarding particle energy is beyond a certain level (a few keV) [13]. Thermal spikes can cause localized melting in cascades where all of the vacancies lie, causing vacancy annihilation. Thus, energetic particle bombardment at the intermediate energy levels pertaining during IPAP may be causing significant vacancy formation whereas lower or higher energies are either not sufficient or cause annihilation. It has been proposed [14] that vacancies generated in the near-surface region by particle bombardment, can couple with N atoms and undergo long-range migration. Our results are consistent with this N diffusion mechanism and recent modeling work in our laboratory [12] provides good predictions with experimental nitrogen diffusion profiles.

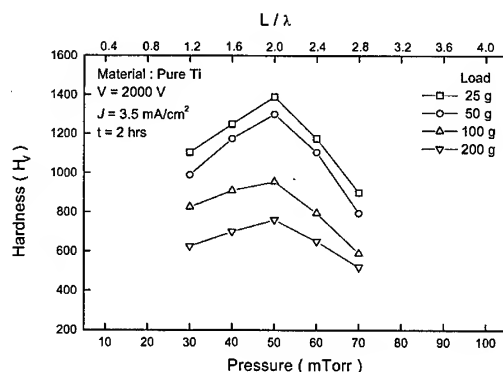


Fig.2 Surface hardness of pure Ti specimens nitrided in pure nitrogen discharge at different chamber pressures.

3. IPAP NITRIDING OF Ti-6Al-4V ALLOY

Titanium and Ti-based alloys exhibit an attractive combination of properties (excellent strength-to-weight ratio, fracture toughness, corrosion resistance, etc.) but suffer in terms of wear performance. Thus, surface-hardening treatments for Ti-based alloys are of significant importance. Recent high-resolution transmission electron microscopy (TEM) studies have shown that IPAP nitriding of Ti-based alloys produces a three-layer structure at the surface region. A thin outer TiN_x compound layer followed by a Ti_3N layer and a diffusion zone exhibiting a hardness gradient. The Ti_3N structure has been found to be a superstructure and the diffusion zone to be a Ti-matrix/ Ti_3N composite with the volume fraction of the Ti_3N phase gradually decreasing with depth. Such microstructure results in a significantly higher hardness (Knoop hardness, H_K , ~4.5 times higher) and a hardness gradient that can alleviate problems expected at hard coating/soft substrate interfaces. It should also be noted that conventional plasma nitriding is conducted at high temperatures (usually above the α/β transition temperature) that may result in distortion and prevents treatment of temperature sensitive microstructures. IPAP treatments of Ti-based alloys can be performed at significantly lower temperatures (<450° C) offering a significant advantage.

Table 1 Hardness (H_K) and wear results of PMMA pin on Ti-6Al-4V in 0.1M NaCl solution.
(sliding velocity: 0.1 m/s, load: 5 N, sliding distance: 1 km)

Test	Material (processing time)	H_K	f (f_i/f_f)	W_D ($\times 10^{-3} \text{ mm}^3 \text{ N}^{-1} \text{ m}^{-1}$)	W_P ($\times 10^{-5} \text{ mm}^3 \text{ N}^{-1} \text{ m}^{-1}$)
1	Ti-6Al-4V (unprocessed)	600	0.5	0.44	10.5
2	IPAP-Nitrided Ti-6Al-4V (1 h)	1700	0.33/0.3	0.0015	9.1
3	IPAP-Nitrided Ti-6Al-4V (2 h)	2250	0.36/0.24	0.0201	16.7
4	IPAP-Nitrided Ti-6Al-4V (4 h)	2800	0.34/0.24	0.018	14.6

f_i and f_f : initial and final coefficient of friction, respectively; W_D : Wear rate of disk;
 W_P : Wear rate of pin; PMMA pin diameter = 12.5 mm;

Table 1 presents results from pin-on-disc experiments that were conducted on IPAP-nitrided Ti-6Al-4V alloy processed for a time period of 1, 2, and 4 hours. Table 1 shows that significant improvements in the wear resistance of Ti-6Al-4V can be achieved by IPAP nitriding. Wear rates can be reduced by more than one order of magnitude (20 times lower) but equally important is the significant reduction (~50% reduction) in the value of the final coefficient of friction (f_f). SEM examination of the wear track region of the IPAP-treated specimens revealed no signs of gross wear damage but rather the initiation of a surface polishing effect (roughness reduction) in the wear-track region. It is believed that the slightly higher f values observed initially are due more than likely, to the wear-in behavior of the as-processed surface. After that initial break-in period and as polishing of the asperity contacts occurs a smoother surface is produced resulting in a lower f value.

Further more, it is important to note that the above surface treatment can serve as a precursor to deposition of hard wear-resistant coatings providing a functionally graded interface (FGI). This duplex system can provide a solution to the problem of abrupt strain change at the coating/substrate interface, which is one of the major sources of coating failure in systems involving hard coatings on soft metallic substrates. Experiments have been conducted recently in such a system in our laboratory. Diamondlike carbon coatings (DLC) deposited on Ti-6Al-4V substrates with FGI were found to exhibit significant improvements in wear resistance (2-3 times longer lifetime) especially at high-applied loads due to the better substrate support. At the same time these systems enjoy a very low coefficient of friction ($f < 0.05$) resulting from the presence of the DLC coating.

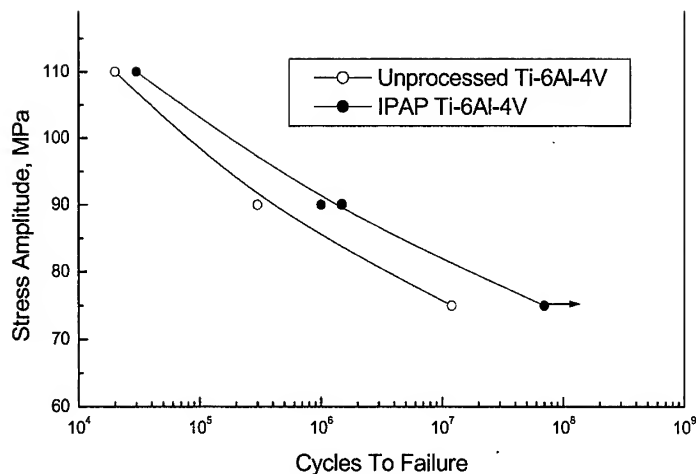


Fig.3 High cycle fatigue behavior of IPAP-treated and unprocessed Ti-6Al-4V alloy.

Surface modification methods have been used extensively in the past as a surface strengthening method to delay onset of cracking during cyclic loading. In the present study, fatigue tests were carried out on "hourglass" specimens in tension and full compression ($R = -1$), at 50 Hz frequency. The particular type of specimen used is very sensitive to fatigue crack initiation (failure occurs immediately upon crack initiation), which is the stage that can potentially be affected by the surface treatment. The results of the fatigue experiments are shown in Figure 3 and suggest that IPAP treatment has a beneficial effect on the fatigue behavior of Ti-6Al-4V. The fatigue life of the IPAP-treated specimens was longer for all levels of stress amplitude, with probably a larger improvement at lower stress amplitudes. These effects are attributed to improvement in surface strengthening, homogeneity of slip and development of residual stresses at the surface region.

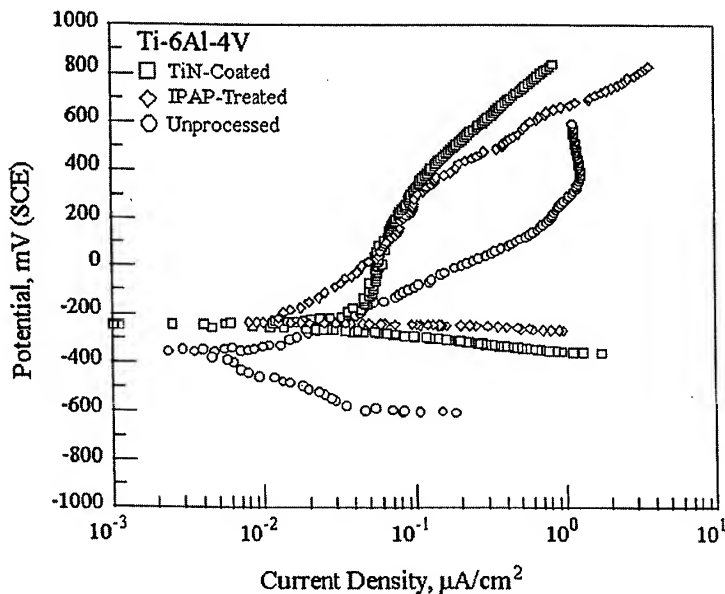


Fig.4 Anodic polarization behavior of IPAP-treated, TiN-coated and unprocessed Ti-6Al-4V alloy in 0.1M NaCl solution (36°C).

Figure 4 presents results from anodic polarization experiments conducted in 0.1M NaCl solution (pH=6.8) at 36° C. In addition to unprocessed and IPAP-nitrided Ti-6Al-4V alloy, TiN-coated samples were also tested. The results show that the presence of TiN either as a discrete coating or formed by IPAP within the original substrate, raises the corrosion potential by about 100 mV (SCE). The unprocessed alloy exhibited an initial activation polarization stage followed by passivation at higher current densities. Both IPAP-treated and TiN-coated alloys exhibited passivation with the TiN-coated alloy showing somewhat lower corrosion current densities. However all three corrosion rates are considered very low. Similar low corrosion rates have been determined previously in NaCl solution [15]. The present results also show that the surfaces where TiN was present (either TiN coating or TiN produced by IPAP) in general exhibited lower passive current densities. These results are in general agreement with previous reports on corrosion behavior of TiN coatings and have been attributed to inhibition caused by the presence of N in the outer surface layer. Nevertheless, the present results demonstrate that the corrosion resistance of the material is maintained after IPAP treatment while tribological performance is significantly improved.

4. CONCLUDING REMARKS

IPAP is an emerging surface engineering technique that can provide effective surface treatments at relatively low-temperatures. IPAP treatment of Ti and Ti-6Al-4V alloy at temperatures <450°C was found to achieve a marked increase in surface hardness. IPAP treatment was also found to cause significant improvements in tribological performance while maintaining or even slightly improving fatigue and corrosion resistance. The present results demonstrate that IPAP is a high potential surface treatment process for Ti-based alloys.

5. ACKNOWLEDGMENT

This work was supported in part by the Army Research Office (Grant Number: DAAG55-98-1-0279) and Louisiana Board of Regents. The author thanks Dr. E.W. Lee (NAWC) for the invitation and his students S. Yan, J. Xu, T.M. Muraleedharan and A.A. Adjaottor for their contributions.

REFERENCES

1. E.I. Meletis, U.S. Patent and Trademark Office, Patent No. 5,334,264, Aug. 2, 1994.
2. E.I. Meletis, U.S. Patent and Trademark Office, Patent No.: 5,443,633, Aug. 22, 1995.
3. R.D. Bland, G.J. Kominiak and D.M. Mattox, J. Vac. Sci. Technol., Vol.11(1974), pp. 671-674.
4. F.A. Smith, Intern. Mater. Rev., Vol. 35(2)(1995), pp. 61-128.
5. E.I. Meletis and S. Yan, J. Vac. Sci. Technol., Vol. 9(4)(1991), pp. 2279-2284.
6. A.A. Adjaottor and E.I. Meletis, in Surface Modification Technologies IX, T.S. Sudarshan, W. Reitz and J.J. Stiglich, eds., TMS, Warrendale, PA, (1996), pp. 421-436.
7. J. Rickards, Vacuum, Vol. 35(5) (1984), pp. 559-562.
8. J. Xu and E.I. Meletis, in Beam Processing of Advanced Materials, J. Singh and S.M. Copley, eds., TMS, Warrendale, PA, (1993), pp. 551-560.
9. K.S. Fancey and A. Matthews, Surf. Coat. Technol., Vol. 33(1987), pp. 17-29.
10. A. Leyland, K.S. Fancey and A. Matthews, Surface Engineering, Vol. 7(3)(1991), pp. 207-215.
11. J. Xu: M.Sc. thesis, Louisiana State University, (1993).
12. A.A. Adjaottor, Ph.D. thesis, Louisiana State University, (1998).
13. R.S. Averback, T. Diaz de la Rubia, H. Hsieh and R. Benedek, Nucl. Instr. Meth. Phys. Res., Vol. B59/60 (1991), pp. 709-717.
14. A. Brokman and F.R. Tuler, J. Appl. Phys., Vol. 52(1)(1981), pp. 468-471.
15. T. M. Muraleedharan and E. I. Meletis, Thin Solid Films, Vol. 221 (1992), pp. 104-113.

EVALUATION OF CORROSION ON ALUMINUM ALLOY AIRFRAME STRUCTURES UNDER PROTECTIVE COATINGS USING ACOUSTIC AND THERMOGRAPHIC TECHNIQUES

Jochen Hoffmann, Shamachary Sathish, Norbert Meyendorf

Center for Materials Diagnostics, University of Dayton, Dayton, OH 45469-0121

ABSTRACT

The goal of this work is to develop a multi-sensor nondestructive evaluation (NDE) approach to characterize aluminum alloy airframe structures under polymeric corrosion protective coatings. Two main efforts are highly relevant: (i) studying different degradation processes in the polymers to estimate the coating performance in service; and (ii) detecting and quantifying early stages of corrosion beneath an intact coating. To address these tasks we employed acoustic and thermographic NDE techniques, including Scanning Acoustic Microscopy (SAM) and Fan Thermography. SAM can be utilized to map either coating or interface properties (C-scans). The method revealed potential to determine the curing quality of the coatings. It was also possible to detect small corrosion pits under delaminated areas. Furthermore, we evaluated the reflections of surface waves, which are generated and detected by the same probe. This enabled us to examine the substrate/coating interface and to detect sites of weak adhesion or corrosion pitting underneath an intact coating. Fan Thermography (hot air heating) was applied to detect corrosion under the coatings and sites of delamination.

1. INTRODUCTION

Nondestructive characterization of corrosion protective coatings is of exceptional importance to enhance usability of coating systems and thus, to reduce the costs of aircraft maintenance and to avoid extensive environmental pollution. The possible failure of the coating leads to insufficient corrosion protection and finally to the failure of the Al alloy. Determination of mechanical and physical properties of the coating and the condition of the interface are required, both under different types of load and environmental exposure. Furthermore, it is necessary to detect corrosion damage in the aluminum alloy below the coating¹. To achieve this, the employment of high-resolution nondestructive evaluation (NDE) is necessary.

Military aircraft coatings have to be multi-functional. Only a multi-layer coating-system can satisfy all requirements. Currently used coating-systems consist of surface pretreatment (chromate conversion coatings), primer (mainly epoxies) and topcoat (e.g. polyurethane elastomers) [1, 2, 3]. We examined a series of epoxy primer-coatings applied on Al 2024-T3 plates. Al 2024-T3 is currently one of the most popular aluminum-alloy, especially due to its good specific strength and stiffness [1,2]. Insufficient curing is essentially non-uniform distribution of crosslinking agents leading to density variations in the coating; high density regions are brittle and susceptible to cracking while low density regions may allow migration of environmental particles (e.g. hydrogen) to the metal substrate. Ultraviolet (UV) radiation,

present in sunlight, causes photooxidation processes in the coating that destroy the polymer chains. This leads to embrittlement and fracture. Another problem for coating applications is weak bonding or even delamination at the interface, as a result of improper metal surface treatment or insufficient adhesion capability of the polymer chains. Eventually, these mechanisms lead to an environmentally exposed metal surface where corrosion pits can occur. Under mechanical load the pits act as initiation sites for metal fracture.

2. EXPERIMENTS

2.1. Scanning Acoustic Microscopy

The characterization of multi-layered structures using SAM is classically performed by time-of-flight spectroscopy in the pulsed regime. An ultrasonic wave generated by a piezoelectric transducer is sent into the test material; the same probe detects the reflected waves [4,5]. The coupling between transducer and sample is achieved by submerging both in a water bath (figure 1). Since probe and sample are not in contact, the transducer can be moved with a x-y-z-manipulator.

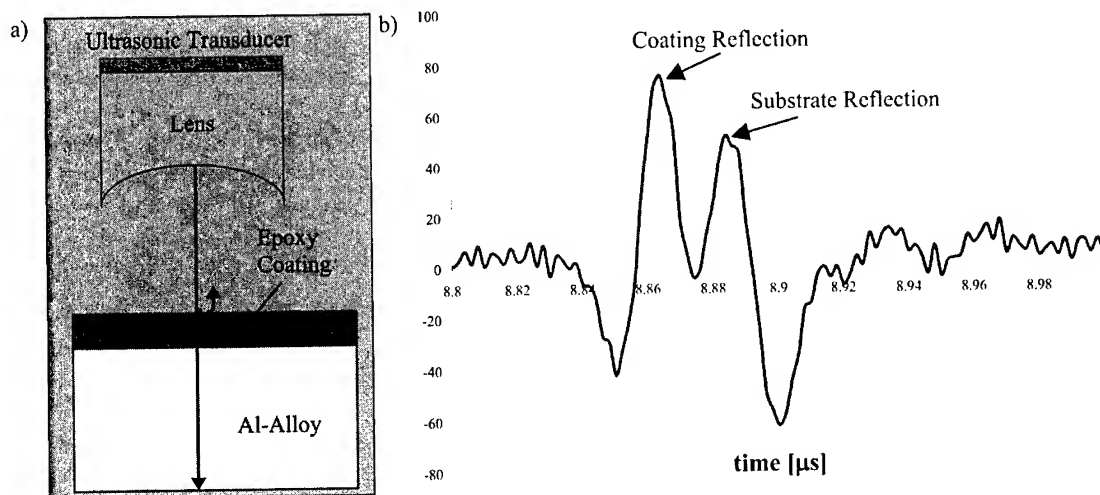


Fig. 1. a) scheme of SAM Pulse/Echo measurements b) A-scan of longitudinal bulk wave reflections at the interfaces; focal point on coating/substrate-interface

Alternatively, A-, B-, or C-scans can be obtained. In our experiments we employed a broadband 10-200 MHz transducer with a spherical focusing lens. Focusing and high frequency of the excited wave provide two important advantages: high lateral resolution measurements (order of wavelength in water: down to approx. 10 μm) and time resolving of the different interface reflections (figure 1). These interface reflections are due to longitudinal bulk waves. Most reflection is achieved, when the probe lens is focused on the coating/substrate interface, because all normal and oblique incident waves add up to one reflection amplitude.

2.2. Fan Thermography

An alternative application is the use of thermal techniques. Due to high-energy radiation (e.g. laser radiation, hot air) the specimen heats up. Certain properties or imperfections of the material influence the spatial patterns of temperature values. The measuring parameters can be correlated to material properties like thermal conductivity or thermal diffusivity. The thermal techniques are based on the thermal diffusion equation allowing quantified measurements.

A well-established method is flash thermography that provides a quantitative characterization of defects under coatings. Using this technique a high-energy (approx. 12 kJ) light pulse is deposited on the surface of examination. A part of the light is absorbed and converted into heat. An infrared (IR) camera with up to 1 kHz frame rate observes the cooling process of the material. The material properties of coatings as well as possible interface or substrate defects influence heat diffusion and thus cause changes in the surface temperature with time [6].

In our approach, we replaced the flash lamps with a hot air gun or fan. The IR-camera observes the heating process of the material. In comparison to the flash lamps this heating method deposits considerably less energy per time on the surface of examination. The sample heats up much slower, which allows observing the material response over longer periods of time. The lower heat deposition energy reduces the risk of destroying the coating. An additional advantage is the very simple and inexpensive set-up.

2.3. Scanning Vibrating Electrode Technique

Scanning Vibrating Electrode Technique (SVET) is used to investigate corrosion events under coatings at the metal/coating interface with adequate spatial resolution. The technique detects the minute variations in d.c.-corrosion currents that are associated with localized anodic or cathodic corrosion activity. The corrosion may be related to coating defects or galvanic coupled regions of the metal surface. SVET allows identification of defects and conductive pathways through the coating and can detect initiation and progress of corrosion activity in-situ [7]. Other advantages include the ability to quantify corrosion progression with time and the high resolution in current measurements on the order of 0.5 A/cm^2 .

3. RESULTS

3.1. Acoustic mapping of Interface Imperfections

SAM was employed to obtain C-scans on samples with different thickness or interface defects. The possibility of gating certain signals enabled us to measure amplitude variations over the scanning area for different reflections. Thus, we obtained several C-scans per measurement improving the correspondence between the measurement and the material property of interest. Since corrosion pits can be detected with SAM, we tried to correlate the acoustic C-scans with electrochemical mapping obtained by SVET. Some resulting C-scans and corresponding electrochemical scans for 38 μm thick Epoxy JJ coatings (90 hours exposure to corrosive environment) are presented in figures 2 and 3. The difference between the two samples is the application of a newly developed thin sol-gel interface layer prior to coating the epoxy primer. The sol-gel layer includes pre-formed, self-assembled nano-phase silane particles (SNAP). These SNAP coatings are considered to enhance corrosion resistance and adhesion to the

primer [8]. Our results indicate that the SNAP-coatings basically improve adhesion. As shown in figure 2a, several spots of delamination can be observed, which eventually lead to some severe accumulated corrosion activity. However, the measured current density does not show high peaks (maximum approx. $100 \mu\text{A}/\text{cm}^2$) and is rather homogeneously distributed (fig. 2b). Due to micro-scale delamination all over the sample, the corrosion activity can be equalized over large areas.

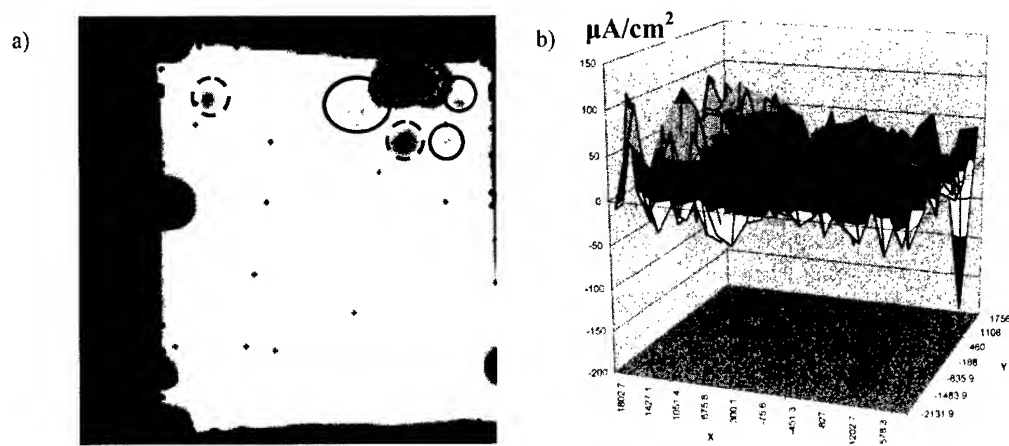


Fig.2. 38 μm thick epoxy JJ coating, no SNAP layer

- a) SAM C-scan scan area: $6 \times 6 \text{ mm}^2$, stepwidth: $50 \mu\text{m}$, substrate reflection
 full line circles: hidden corrosion - - dashed circles: hidden delamination
 large visible delamination in upper right corner
 b) SVET scan: $5 \times 5 \text{ mm}^2$, 20×20 steps

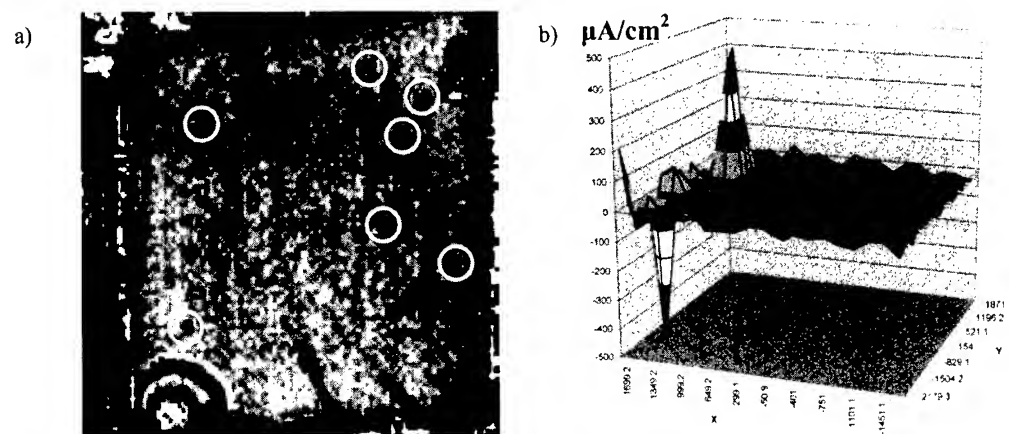


Fig.3. 38 μm thick epoxy JJ coating, with SNAP layer

- a) SAM C-scan scan area: $6 \times 6 \text{ mm}^2$, stepwidth: $50 \mu\text{m}$, substrate reflection
 white circles: hidden corrosion
 b) SVET scan: $5 \times 5 \text{ mm}^2$, 20×20 steps

In comparison, the SVET scan for the sample with additional SNAP layer shows no significant current density over almost the complete scan-area, except one negative (cathodic) peak (approx. $-500 \mu\text{A}/\text{cm}^2$) and one positive (anodic) peak (approx. $400 \mu\text{A}/\text{cm}^2$). The SAM C-scan also detects these spots, but also several additional positions. This is because of much higher lateral resolution.

The sample without SNAP pretreatment shown in figure 2 is more severely damaged; the good adhesion capability for the SNAP sample causes high local current density. This corrosion activity, however, may not be as severe as indicated. A lot of image processing needed to be done, to visualize the minute detection in figure 3a. These results indicate that SNAP pretreatment definitely improves adhesion capability and generally the corrosion resistance. However, if the primer coating fails, high localized corrosion activity can lead to its failure.

3.2. Comparison of Acoustic and Thermographic Mapping

Measuring a similar sample (Epoxy JJ, 50 μm thick, 125 hours exposure to corrosive environment, no SNAP layer) figure 4 shows SVET, Fan Thermography and SAM images of the same sample area. First SVET measurements are carried out. Figure 4a presents a vector overlay mapping of electrochemical current density superimposed over a video image. Delamination can be observed in the video image. The longer vectors indicate corrosion activity underneath these delaminated regions.

Coating delamination or sites of corrosion are thermal barriers. If the test object surface is heated the heat diffusion into the aluminum plate is inhibited in the delaminated or corroded region. A thermal response appears. The time for the maximum contrast at the surface is called response time. This time depends upon the thermal properties of coating and substrate and the coating thickness. Figure 4b shows a thermal contrast for corrosion below a polymeric coating. The spatial resolution was improved with a microscopic optic used in combination with the camera. The bright spots (higher surface temperature) indicate regions of reduced heat diffusion and correlate well with the SVET image. Furthermore, the actual grid structure of the substrate surface is visible providing the possibility to detect sites of corrosion as disturbances in a well-defined surface topography.

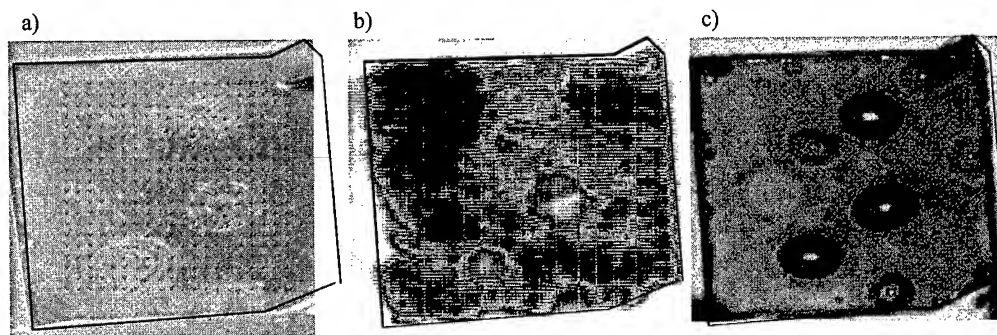


Fig. 3. NDE imaging of same sample: 50 μm thick artificially damaged epoxy JJ coating
a) SVET video image + current density vector overlay (vector area: $4 \times 4 \text{ mm}^2$)
b) Fan Thermography image (image area: $6 \times 6 \text{ mm}^2$)
c) SAM substrate reflection C-scan (scan area: $6 \times 6 \text{ mm}^2$, stepwidth: 50 μm)

The sample was then measured with SAM. In figure 4c the substrate reflection C-scan is presented. The same delamination as in 4a and 4b can be observed as well as newly created delaminated sites. This is due to the rather poor performance of this coating and the fact that repeated heating and additional exposure in a water bath has a deteriorating effect on the sample. However, this shows that the different methods can detect similar effects. The results can be compared and verified.

SUMMARY

We employed successfully thermal and acoustic techniques to measure polymeric coating properties, sites of delamination and small size corrosion of aluminum alloy substrate under the coating. Scanning Acoustic Microscopy (SAM) has proven to be an excellent laboratory technique. However, it reveals two major disadvantages: (i) highly resolved C-scans are only possible due to the accurate scanning system and (ii) a couple medium (e.g. water, oil) between sensor and sample is needed. These facts reduce the changes to develop an in-field technique. Fan Thermography, on the other hand, is an easy to apply non-contact technique with high in-field capability. In the process of developing this technique, SAM and SVET are useful reference methods. Ongoing work is concentrated to distinguish corroded and delaminated regions.

ACKNOWLEDGMENTS

The work presented in this paper is sponsored by the Defense Advanced Projects Agency (DARPA) Multidisciplinary University Research Initiative (MURI), under Air Force Office of Scientific Research grant number F49620-96-1-0442. The authors would like to thank Ms. Angela Mahan, Dr. Andrew Vreugdenhil, Dr. Joel Johnson, Dr. Mohammad Khobaib and Dr. Daniel Eylon for their contributions and support.

REFERENCES

1. M. Khobaib, final report for US Air Force, contract-number F 33615-94-C-58-04, (1997).
2. J. Hoffmann et al., 3rd Annual Report for DARPA-MURI, Grant Number F49620-96-1-0442, (1999).
3. C.S. Jeffcoate et al., in Proceedings of 43rd International SAMPE Symposium and Exhibition , Vol.43, (1998), pp. 2113-2122.
4. V.K. Kinra, V.R. Iyer, Ultrasonics, Vol.33, (1995), pp. 95-109.
5. A. Briggs, Acoustic Microscopy, Oxford University Press, New York, (1992).
6. U. Netzelmann, G. Walle, Photoacoustic and Photothermal Phenomena, 10th International Conference, Rome, Italy, 1998, published in AIP Conference Proceedings, Vol.463, American Institute of Physics, Woodbury, New York, (1999), pp. 401-403.
7. A. Buchanan, MS Thesis, University of Dayton, (1999).
8. A. Vreugdenhil et al., to be published in Polymeric Materials: Science & Engineering, Vol.85, (2001).

MICROSTRUCTURE AND MECHANICAL PROPERTIES OF Ti-6Al-4V ALLOY SURFACE-ALLOYED MATERIALS FABRICATED BY HIGH-ENERGY ELECTRON BEAM IRRADIATION

Kwangjun Euh, Jongmin Lee, and Sunghak Lee

Center for Advanced Aerospace Materials
Pohang University of Science and Technology, Pohang, 790-784 Korea

ABSTRACT

The present study is concerned with fabrication and microstructural analysis of Ti-6Al-4V alloy surface-alloyed materials using irradiation of high-energy electron beam. Mixtures of TiB_2 or MoB boride powders and CaF_2 flux were placed on a Ti-6Al-4V alloy substrate, and then electron beam was irradiated on these mixtures using an electron beam accelerator. In the specimens processed with a flux mixing ratio of 40wt.%, the melted region of 1.1~1.5 mm in thickness was homogeneously formed without defects, and contained a large amount of TiB borides. The formation of TiB borides in the melted region greatly improved hardness, high-temperature hardness, and wear resistance, two or three times higher than the Ti alloy substrate. Besides, the addition of MoB powders into the powder mixtures made the fabrication of the surface-alloyed materials having various properties possible through controlling the kind, size, and volume fraction of TiB borides and the characteristics of the matrix.

1. INTRODUCTION

Titanium alloys have many attractive properties such as high specific strength and stiffness, but their poor resistance to wear and oxidation at high temperatures has required surface treatments. Conventional thermochemical processes such as nitriding and deposition techniques such as plasma spraying, sputtering, and plating have been used in order to improve surface properties of titanium alloys [1,2]. In the former processes, a substrate may be distorted or surface properties may deteriorate because of the high fabrication temperatures. The latter processes are disregarded under repeated loading conditions because of weak interfacial bonding. To overcome these shortcomings, researches on surface-alloying have been conducted by depositing ceramic powders such as TiN, TiC, and TiB_2 powders on a titanium alloy substrate and by irradiating high-energy heat sources such as laser or electron beam [3-5]. Upon irradiation of the material surface on which ceramic powders are evenly deposited, the material surface and ceramic powders are either partially or completely melted, and then ceramic elements are precipitated again during solidification, thereby fabricating a surface-alloyed material. This study is concerned with the fabrication of boride/Ti-6Al-4V surface-alloyed materials by high-energy electron beam irradiation. Borides added for the surface-alloying are TiB_2 and MoB powders, and flux has to be used to protect these powders from air and to promote homogeneous melting.

2. EXPERIMENTAL

A substrate material used in this study is a Ti-6Al-4V titanium alloy, and its chemical composition is Ti-6.19Al-4.05V-0.02C-0.19Fe-0.12O-0.01N-0.0035H (wt.%). Borides used for the surface-alloying are TiB₂ and MoB powders having high hardness, excellent resistance to heat and abrasion, high thermal conductivity, and high melting point [6]. CaF₂ powders (density; 3.18 g/cm³, melting temperature; 1423 °C) were used as flux [7], and were mixed with TiB₂ or MoB powders at a flux mixing ratio of 40wt.%. These boride/flux mixtures were evenly deposited on the titanium alloy substrate of 70×50×25 mm, and then pressed with a 300 N load. For convenience, specimens containing TiB₂ or MoB powders mixed with 40% flux are referred to as 'T' and 'M', respectively, while a specimen containing TiB₂ and MoB powders (1:1) mixed with 40% flux, *i.e.*, 30TiB₂-30MoB-40CaF₂, as 'TM'. A high-voltage electron accelerator of Budker Institute of Nuclear Physics, Novosibirsk, Russia, was used for high-energy electron beam irradiation. Irradiation was conducted under conditions of beam energy of 1.4 MeV, beam traveling speed of 2.45 cm/s, scanning width of 5 cm, beam size of 1.15 cm, and beam current of 26 mA.

The microstructure of the melted region was observed by an optical microscope. Hardness was measured from the surface down to the substrate by a Vickers hardness tester under a load of 500 g. High-temperature hardness was also measured by a high-temperature Vickers hardness tester in the temperature range from room temperature to 750 °C. Abrasive wear resistance test was conducted using a ring-on-disc type wear tester in accordance with DIN 50320 [8]. The disc specimen was worn in contact with the ring (SUS 420 J2 stainless steel) under a testing load of 25 kgf. Wear testing was performed at room temperature for 30 minutes without using a lubricant, and revolution speed was 100 rpm. Wear amount was evaluated from the weight measurement of the disc specimen.

3. RESULTS AND DISCUSSION

3.1. Microstructure

Figures 1(a) through (c) are low-magnification optical micrographs of boride/Ti-6Al-4V surface-alloyed specimens. Boride powders and the substrate surface were melted, showing a clear interface between the melted and the unmelted regions. The specimens show evenly thick melted regions without pores since melting occurs homogeneously by the addition of flux. Beneath the interface lies the heat affected zone (HAZ) of about 2 mm in thickness due to heat transfer from the melted region. Average thickness of the melted region is measured to be 1.1~1.5 mm, and slightly decreases in the order of the M-, T-, TM-specimens, as shown in Table 1.

Optical micrographs of the melted region are shown in Figures 2(a) through (c). The melted region was formed as boride powders and the surface of substrate were completely melted and then solidified. A considerable amount of large hexagonal-pillar-shaped primary borides with diameters of 10~20 μm and lengths of 50~300 μm and fine needle-shaped eutectic borides with lengths of 5~30 μm are observed in the T- and TM-specimens, whereas only eutectic borides are found in the M-specimen (Figure 2(c)). The primary borides are reported to be TiB phases [9], which are formed inside the melted metal and grown in a hexagonal pillar shape. Volume fraction and size of primary TiB of the T-specimen are measured to be 21.2% and 9.3 μm, respectively, and are considerably larger than those of the

TM-specimen (9.9% and 5.0 μm , respectively) as shown in Table 1. The HAZ is mainly composed of martensite because of rapid heat transfer into the substrate (Figure 2(d)).

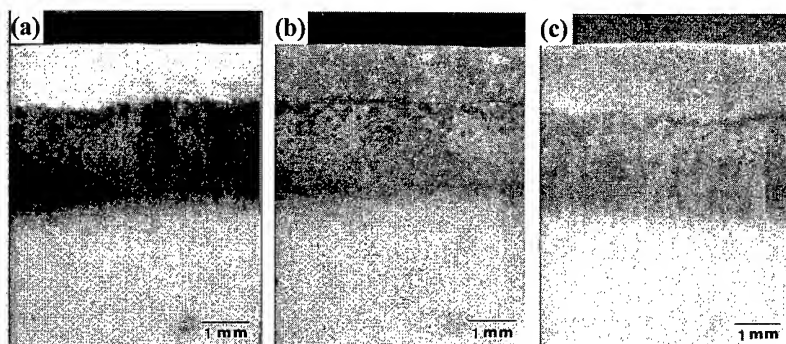


Fig.1 Low-magnification optical micrographs of boride/Ti-6Al-4V surface-alloyed materials irradiated with high-energy electron beam: (a) T-, (b) TM-, and (c) M-specimens.

Table 1. Average thickness of the melted region, volume fraction and size of primary TiB particles, and approximate concentration of boron in the melted region.

Specimen	Thickness of Melted Region (mm)	Primary TiB		Concentration of Boron in Melted Region (wt.%)
		Vol. Fraction (%)	Size (μm)	
T	1.25 ± 0.18	21.2	9.3	4.7
TM	1.14 ± 0.14	9.9	5.0	3.0
M	1.46 ± 0.18	-	-	1.0

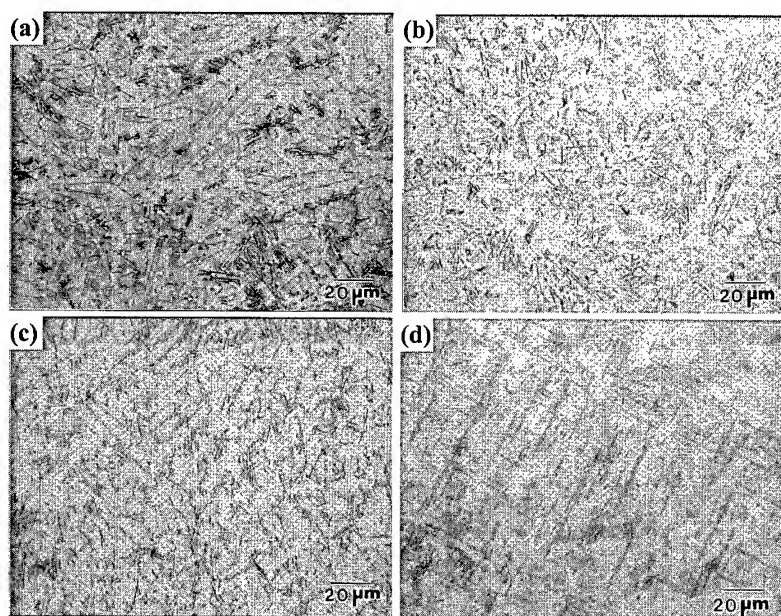


Fig. 2. Optical micrographs of the melted region of the (a) T-, (b) TM-, and (c) M-specimens. (d) is an optical micrographs of the heat affected zone of the T-specimen.

The concentration of boron present in the melted region was approximately calculated by measuring the weight change of specimen before and after irradiation, and is shown in Table 1. The boron concentration is measured to be 4.7% in the T-specimen, and decreases in the order of the T-, TM-, and M-specimens. A Ti-B phase diagram is shown in Figure 3, and a eutectic reaction occurs at the temperature of $1540 \pm 10^\circ\text{C}$ and the boron content of 1.7% [10]. The solubility of boron in Ti is nearly zero, and thus TiB phases are always formed during solidification. Since the boron contents in the T- and TM-specimens are 4.7% and 3%, respectively, which exceed the eutectic concentration, primary TiB borides are formed first, and then eutectic TiB borides are formed by the eutectic reaction. However, only eutectic TiB borides are formed in the M-specimen because of the low boron content (1%).

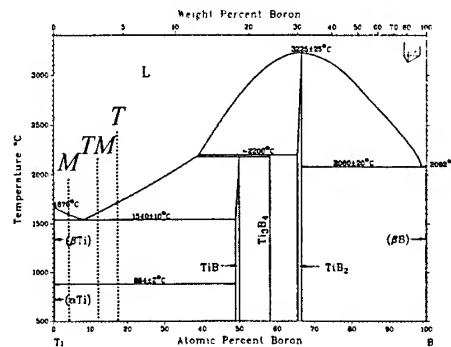


Fig. 3. Ti-B Phase diagram, showing the approximate concentration of boron in the melted region [10].

3.2. Hardness

Table 2 shows the microhardness data of primary TiB borides and matrix in the melted region. The hardness of the primary TiB is very high (about 1680 VHN). The hardness of the matrix increases in the order of the T-, TM-, and M-specimens, and is about 50% higher than that of the Ti substrate (about 300 VHN) because the matrix consists of martensite or β -Ti. Microhardness was measured from the surface down to the substrate, and the results are shown in Figures 4(a) through (c). Maximum hardness of the T-specimen is about 760 VHN because of the high volume fraction (21 vol.%) of primary TiB, showing an increase of two or three times over that of the substrate (Figure 4(a)). The hardness stays steady at 700 VHN down to the interfacial region, where the hardness drops to 370 VHN. The HAZ composed of martensite shows slightly higher hardness than that of the substrate. The hardness of the melted region of the TM- and M-specimens is somewhat lower (570~610 VHN) than that of the T-specimen (Figures 4(b) and (c)).

Table 2. Vickers microhardness of primary TiB particles and matrix, wear resistance, and surface roughness in the melted region. (load : 10g)

Specimen	Vickers Hardness (VHN)		Weight Loss (mg)	Surface Roughness
	Primary TiB	Matrix		
T	1689	421	32.5	3.02
TM	1676	474	84.7	0.69
M	-	489	91.5	0.87

Since primary TiB borides have very high hardness, they directly affect on hardness, depending on their shape, volume fraction, and distribution. It is interesting to note that only TiB borides are precipitated in the melted region of the TM- and M-specimens, although MoB powders were added into powder mixtures before electron beam irradiation. B atoms interact with Ti atoms, which exist in TiB₂ powders or the Ti-6Al-4V alloy substrate, to form TiB borides because Ti has larger chemical affinity for boron atoms than Mo [6]. Mo atoms are solved in the matrix without forming MoB borides, and contributes the β -Ti transformation since Mo is a strong β -Ti stabilizer [11]. This β -Ti is harder than α -Ti or α' -Ti (martensite) [12], and thus the matrix hardness of the TM- and M-specimens is higher than that of the T-specimen as shown in Table 2, thereby affecting the overall hardness. Particularly in the M-specimen which contains only eutectic TiB borides, its hardness reaches about 600 VHN due to the β -Ti matrix, somewhat comparable to that of the TM-specimen (Figures 4(b) and (c)).

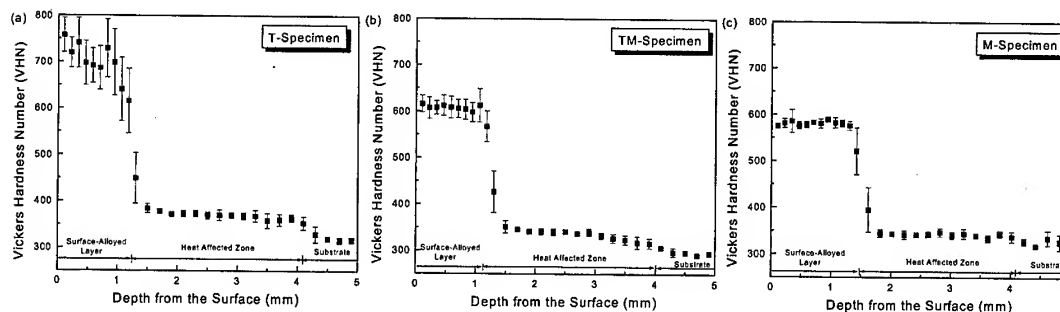


Fig. 4. Vickers hardness vs depth from the irradiated surface of the (a) T-, (b) TM-, and (c) M-specimens.

Figure 5 shows the high-temperature hardness results of the melted region and the Ti substrate. The high-temperature hardness of the melted region of the three specimens gradually decreases with increasing the test temperature since the hardness of the matrix significantly decreases, but is considerably high (over 400 VHN) up to 450 °C. At 600 °C, the hardness is about 300 VHN, maintaining the hardness two or three times that of the substrate. TiB borides play a role in improving high-temperature properties because they are insoluble and chemically stable even at high temperatures over 1000 °C.

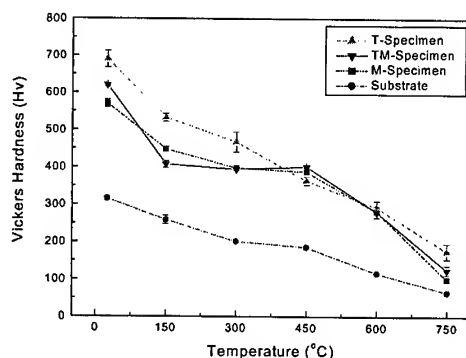


Fig. 5. Vickers hardness of the melted region and the Ti alloy substrate of the three specimens vs test temperature.

3.3. Wear Properties

Table 2 provides the wear resistance and surface roughness of the melted region. The T-specimen shows the best wear resistance, deteriorating in the order of the TM- and M-specimens. These data indicate that the wear resistance improves as the TiB volume fraction or hardness in the melted region increases. However, the TM-specimen shows the best surface roughness of the three specimens.

Figures 6(a) through (d) are SEM micrographs of the worn surface and the cross-section of the T- and TM-specimens. Scratches are deeper in the T-specimen than in the TM-specimen (Figure 6(a)), revealing the worse surface roughness (Table 2). This might be associated with the cracking and falling-off of primary TiB borides from the matrix as indicated by arrows in Figure 6(b). In the TM-specimen, however, homogeneously worn scratches are observed on the overall surface (Figure 6(c)). Almost flat surface is maintained, and the cracking or falling off of primary TiB borides is hardly found (Figure 6(d)).

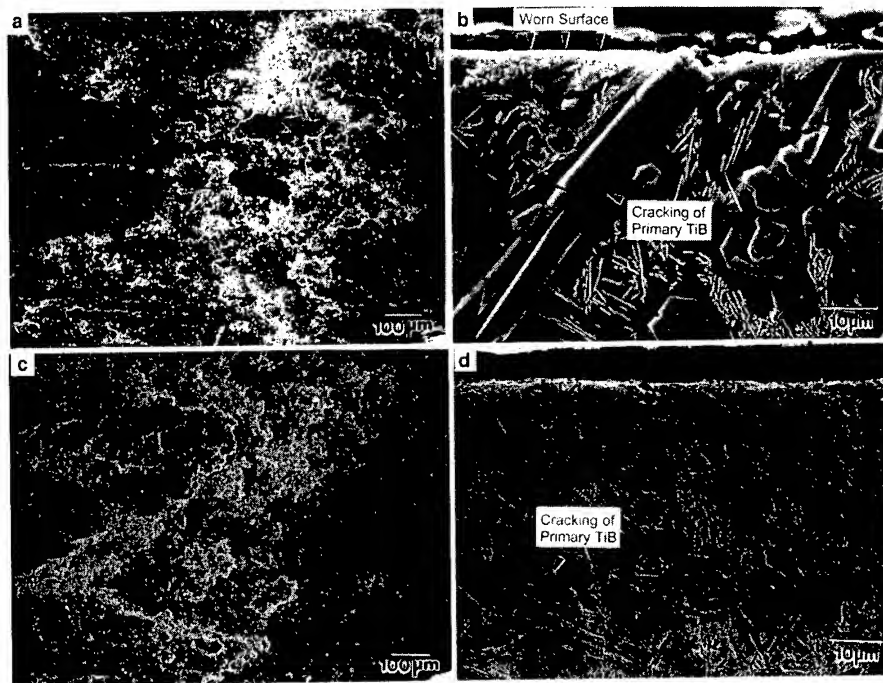


Fig. 6. SEM micrographs of the worn surface of the (a) T- and (c) TM-specimens and the cross-section of the (b) T- and (d) TM-specimens after the wear test.

In order to improve the wear resistance, it is desirable to homogeneously form hard primary TiB borides in the matrix. In this respect, it is quite obvious that the T-specimen has the better wear resistance than the other specimens (Table 2). However, the surface roughness of the T-specimen is worse than those of the TM- and M-specimens. This requires comparative analyses on the wear mechanisms of the T- and TM-specimens. In the wear process of the T-specimen, scratching wear predominates, and its surface becomes rougher as wear proceeds. The comparatively soft matrix is first worn because of a large hardness difference between borides and matrix (Table 2), and creates surface prominences around hard borides. Primary TiB borides can be easily cracked and fallen off from the matrix (Figure

6(b)). The fallen borides work as wear debris, and cause abrasive wear in addition to scratching wear, thereby resulting in the poor surface roughness. In the TM-specimen where both the size and volume fraction of primary TiB borides are smaller than those of the T-specimen, very few TiB borides are cracked or fallen off (Figure 6(d)). This is associated with a relatively small hardness difference between borides and matrix, and thus its surface roughness is much improved (Table 2). In terms of a wear application, the importance of the surface roughness sometimes overrides that of the wear resistance. Despite the T-specimen's excellent wear resistance over the TM-specimen due to the large fraction of primary TiB borides, the TM-specimen can be more desirable than the T-specimen, when the wear resistance and surface roughness are both taken into consideration. In addition, the TM-specimen can be improved by properly controlling the mixing ratio of TiB₂ and MoB powders because the size and volume fraction of primary TiB borides and the characteristics of the matrix phase are easily changed, although the fixed powder mixing ratio of 50:50 was used in the present study.

4. SUMMARY

When electron beam was irradiated on the boride powder mixtures containing 40% flux, melting occurred evenly without defects, and the resulting melted region was homogeneous in its thickness (1.1~1.5 mm). The melted region was composed of large hexagonal-pillar-shaped primary TiB borides and fine needle-shaped eutectic TiB borides. These borides improved the room-temperature hardness of the melted region two or three times higher than that of the substrate. High hardness above 400 VHN maintained up to 450 °C because TiB borides were chemically stable and insoluble without being melted at high temperatures over 1000 °C.

The surface-alloyed material fabricated by the deposition of TiB₂ powders had a larger fraction of primary TiB borides, and showed the better hardness and wear resistance than the other materials. In the surface-alloyed material fabricated by the deposition of both TiB₂ and MoB powders had the better surface roughness than the surface-alloyed material fabricated with TiB₂ powders, because very few TiB borides were cracked or fallen off during the wear process. Thus, the appropriate addition of MoB powders could improve the overall properties of the boride/Ti-6Al-4V surface-alloyed materials because of the thicker melted region, the transformation of the matrix to β -Ti, and the formation of relatively small primary TiB borides in the melted region.

ACKNOWLEDGMENTS

This work was supported by the Korea Research Foundation made in the program year of 1998. The authors would like to thank Mr. M. Golkovski and Mr. A.F. Vaisman, and Dr. N. Kuksanov of Budker Institute of Nuclear Physics for their helpful discussion on the fabrication of the boride/Ti-6Al-4V surface-alloyed materials.

REFERENCES

1. J. Magnan, G.C. Weatherly, and M.-C. Cheynet: *Metall. Mater. Trans. A*, 1999, vol. 30A, pp. 19-29.
2. A. Bloyce: *J. Eng. Tribol.*, 1998, vol. 212, pp. 467-76.

-
3. C. Hu, H. Xin, L.M. Waton, and T.N. Baker: *Acta Mater.*, 1997, vol. 45, pp. 4311-22.
 4. J.S. Selvan, K. Subramanian, and A.K. Nath: *Adv. Perf. Mater.*, 1999, vol. 6, pp.71-83.
 5. J.H. Abboud and D.R.F. West: *J. Mater. Sci. Lett.*, 1994, vol. 13, pp. 457-61.
 6. M. Baucchio: *ASM Engineered Materials Reference Book*, 2nd ed., ASM Intern., Materials Park, OH, 1994, pp. 301-11.
 7. R.C. Weast: *Handbook of Chemistry and Physics*, 70th ed., CRC Press, FL, 1989, p. B-80.
 8. DIN 50320: Wear, Definitions and Terminology, Beuth-Verlag, Berlin, 1980.
 9. M.E. Hyman, C. McCullough, J.J. Valencia, C.G. Levi, and R. Mehrabian: *Metall. Trans. A*, 1989, vol. 20A, pp. 1847-59.
 10. T.B. Massalski: *Binary Phase Diagrams*, vol. 1, ASM Intern., Metals Park, OH, 1986, p. 392.
 11. R. Boyer, G. Welsch, and E.W. Collings: *Materials Properties Handbook: Titanium Alloys*, ASM Intern., Materials Park, OH, 1994, pp. 5-11.
 12. Metals Handbook: *Properties and Selection: Nonferrous Alloys and Special-Purpose Materials*, 10th ed., vol. 2, ASM Intern., Metals Park, OH, 1990, pp. 592-633.

Session XI

MELTING/CASTING

Session XI MELTING/CASTING

The Expanding Family of Aluminium Grain Refiners for the Wrought and Foundry Industries

D. A. Boot and P. Fisher

London & Scandinavian Metallurgical Co Limited
Rotherham, England

ABSTRACT

There are several grain refiners available today based on the Al-Ti-B system. The traditional grain refiners contain a Ti:B ratio above the stoichiometric requirement to form TiB_2 particles of 2.2:1. These were developed for the wrought alloy systems. Stoichiometric grain refiners are now available and for casting alloys in the Al-Si system, substoichiometric refiners have been shown to perform well and are now a commercial reality. Non Ti based refiners are also discussed.

A review of all these refiners is presented here, with particular emphasis in the casting of Al-Si alloys.

INTRODUCTION

During cooling of a melt of aluminium, solidification occurs as aluminium grains are nucleated on suitable nucleant particles, such as TiB_2 , then growth is retarded by elements in solution, particularly titanium¹. In the wrought industry both the nucleant particles and the titanium are usually introduced as a grain refiner [titanium may be a separate addition]. In the foundry industry occasionally the melt may have impurities sufficient for grain refinement but because this cannot be guaranteed in every melt, a grain refiner is usually employed.

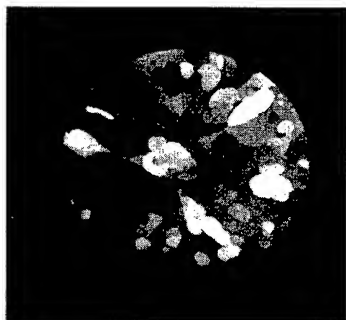


Fig. 1a Unrefined Aluminium

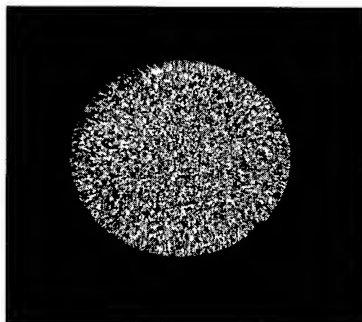


Fig. 1b Refined Aluminium

A fine, equiaxed grain structure is preferred [Fig. 1a & b], to give benefits such as:

- improved feeding characteristics and increased casting speed
- a uniform distribution of elements and improved homogeneity
- reduced porosity and the elimination of hot tearing
- enhanced response to subsequent heat treatment
- superior mechanical properties and increased machinability.

This paper sets out the different grain refiners that are available, the theories of grain refining and gives particular reference to the Al-Si alloys used in foundries.

Commercial Grain Refiners

Grain refining is achieved using various commercial additions. The most common grain refiners are Al-Ti alloys and Al-Ti-B alloys, though an increasingly popular grain refiner for the wrought special alloys is Al-Ti-C alloy. Grain refining may also be achieved using Al-B alloys or Al-Sr-B alloys, but their use is dependant on the application of the final product.

The most commonly used Al-Ti grain refiners contain between 5 and 10wt% Ti.

Al-Ti-B alloys have various ratios of Ti to B greater than stoichiometry. The most common are Al-5%Ti-1%B, Al-3%Ti-1%B, Al-5%Ti-0.2%B. However, stoichiometric alloys such as Hydloy [Al-1.2%Ti-0.5%B] have been found to give useful grain refinement. In the foundry industry substoichiometric alloys, such as TiBloy [Al-1.6%Ti-1.4%B], are becoming increasingly popular.

Based on several years experience of use in the foundry and also collaborative work with universities, TiBloy has been proven to provide many benefits to the foundry. In particular, lower porosity levels have enabled significantly lower cost to be achieved through reduced reject levels. Mix borides, having low density, provide benefits for long holding times and also for remelt ingot such as reduced boride settling. Users have found that TiBloy gives improved mould filling and fewer shrinkage defects.

Al-Ti-C has been recognised as a wrought aluminium grain refiner for many years but has only been commercially available recently. Benefits of Al-Ti-C over other grain refiners include:

- less interaction with filter systems
- less agglomeration of grain refiner particles
- better ingot surface
- more uniform grain size in billet sections
- resistance to poisoning by Zr.

Al-Ti-C is not recommended for grain refining Al-Si alloys as Tronche's³ work shows.

Other grain refiners, such as Al-B and Al-Sr-B alloys are not as common as Al-Ti, Al-Ti-B and Al-Ti-C alloys and are used for special applications.

Theory of Grain Refining and Grain Growth Restriction

Academics and grain refiner producers, such as London & Scandinavian Metallurgical Co Limited, have studied the behaviour of grain refiners in order to achieve better, more efficient products. A number of theories as to the mechanisms by which inoculant additions of Ti and/or B refine have been postulated.

The most widely accepted theory is that by Backerud⁴. He suggests that at solidification, the TiB_2 particle reacts with liquid aluminium to form a mixed boride, around which a shell of TiAl_3 forms. Nucleation of primary aluminium then occurs by a peritectic reaction. More recently, Schumacher and Greer⁵ have established the probable presence of a TiAl_3 layer on TiB_2 [Fig. 2]. There is good crystal lattice matching between TiAl_3 and $\alpha - \text{Al}$. The stretching of the TiAl_3 lattice would match that of the mixed boride. This theory is supported by the need to have Ti in solution in excess of stoichiometry to achieve good grain refinement. The stoichiometric alloy Hydloy and substoichiometric alloy TiBloy require additions of Ti for efficient grain refinement. The matching of TiB_2 and TiAl_3 lattices may well explain why there is a fade in performance of Al-Ti-B grain refiners when holding inoculated melts over a long period [in excess of 6 hours]. It is thought that boride particles are 'glued' together by the TiAl_3 , thereby reducing the number of effective nucleation sites.

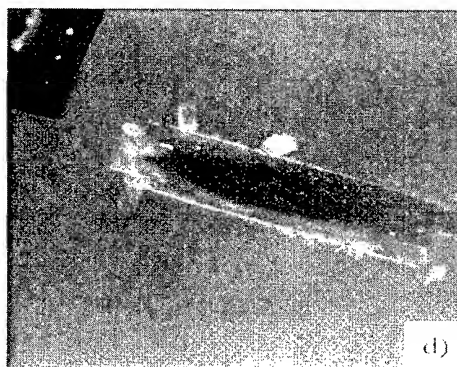


Fig. 2 t.e.m photo showing TiB_2 particle end on with thin TiAl_3 layer, and Al nucleation

Grain growth is restricted by the constitutional supercooling effect of Ti. Tiller⁶ arrived at a quantitative theory of constitutional supercooling for the freezing of a solid solution. Assuming a planar solid solution interface and the only transport mechanism is solute diffusion in the liquid, an enriched solute layer is formed ahead of the solid/liquid interface as the solid grows. This enriched layer has a lower liquidus temperature than the bulk of the liquid and further nucleation may be more favoured than growth.

Tiller developed a calculation of the effects of various solute elements in aluminium, the Growth Restriction Factor, based on the binary phase diagrams. Of the common solute elements in aluminium, titanium is by far the most effective for this supercooling effect and this explains grain refining by Al-Ti alone [table 1].

Table 1 Growth Restriction Factor [m]

Element	m
B	17
Cu	2.8
Fe	2.9
Mg	3.0
Mn	0.1
Si	6.1
Ti	246
V	30
Zr	6.8

The Effect of Silicon on Grain Refining

Grain refiners are added to Al-Si casting alloys to aid castability, improve porosity distribution and reduce hot tearing susceptibility as well as optimise mechanical properties.

Al-Si alloys appear to be different to other alloy systems in terms of grain refinement. Spittle⁷ found that between 0 and approximately 3% Si they show the expected behaviour, in that as Si increases they become easier to grain refine. However, above 3% Si they become more difficult [Fig. 3].

[Note that increased Si means less α – Al and therefore less grain refiner is required].

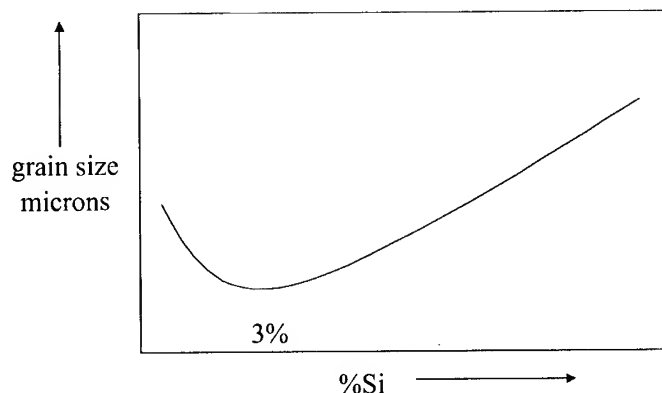


Fig. 3 Schematic Curve showing increased grain size over 3% Si

Various theories have been postulated to explain this phenomenon but in essence there appears to be a poisoning of the $TiAl_3$ by Si, thereby rendering the nucleating $TiAl_3$ layer less effective. It has also been suggested by Mohanty and Gruzleski⁸ that the solubility of titanium decreases with increasing Si addition such that the Ti is more likely to exist as an aluminide that has not contributed to grain refining or growth restriction. It may be for this reason that substoichiometric Al-Ti-B grain refiners are proving useful in foundry alloys.

Grain Refiner Effects on Castability

Improvements in castability of Al-Si alloys in the foundry industry can be achieved using grain refiners.

Without grain refiners large dendritic grains may form and grow. During solidification these dendritic grains interlock reducing the flow of the melt causing blockages in thin moulds. As solidification progresses there is some volumetric shrinkage which is usually counteracted by the feed of liquid metal. Again, large dendritic grains of aluminium can restrict this feed, leading to shrinkage porosity. With a finer dendritic network, mass feeding can occur for longer. Grain refiners are used to ensure only fine grains are nucleated.

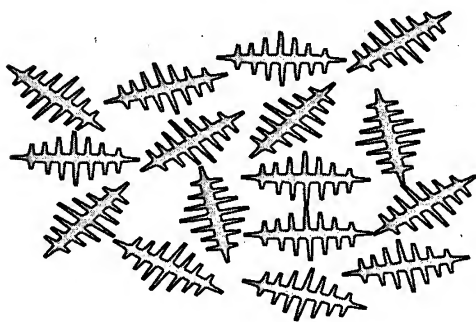
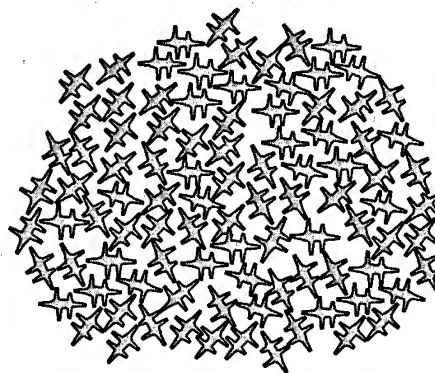


Fig. 4a Schematic of Coarse Dendritic Network



4b Schematic of Fine Dendritic Network

Gas porosity will also be affected in the same way as shrinkage porosity, resulting in fine and uniform porosity dispersion throughout a casting.

It should be noted that in hypoeutectic Al-Si alloys the final solidification of the melt is the eutectic phase. Flaws in any casting will usually be a result of this final solidification. Grain refining of the primary aluminium phase is essential to allow good distribution of the eutectic phase. Modifiers, such as Al-Sr alloys, improve the properties of the eutectic phase.

SUMMARY

A casthouse or foundry manager is looking to make a product that is homogeneous with a good distribution of elements. Cost must be minimised, as well as reduction of scrap and waste. Superior mechanical properties and finish have to be achieved. Grain refiners assist in producing aluminium alloys with required properties.

There are several grain refiners available commercially. Each has its benefits from cost to quality. The most common grain refiners used in both wrought and foundry industry are Al-5%Ti-1%B or Al-3%Ti-1%B. However, there has been an increased usage in recent years of TiBloy [Al-1.6%Ti-1.4%B] in foundry applications such as wheel manufacturer and Al-3%Ti-0.15%C in wrought applications.

REFERENCES

1. M. Johnsson "A Critical Survey of the Grain Refining Mechanisms of Aluminium" PhD Thesis, 1993, University of Stockholm.
2. A. Hellawell "Solidification and Casting of Metals", The Metal Society, 1979.
3. A. Tronche "Investigation and Modelling of Inoculation of Aluminium by TiC", PHD Thesis, 2000, University of Cambridge.
4. L. Backerud Jern. Kont Ann Vol 155, 1971.
5. P. Schumacher, A.L.Greer "Light Metals", 1995, Ed J Evans, TMS, Warrendale.
6. W.A. Tiller "Solidification in: Physical Metallurgy", 2nd Edition, Wiley Ltd, 1970.
7. J.A. Spittle, S.G.R. Brown "Acta Metallurgica", Vol 37, 1989
8. P.S. Mohanty, J.E. Gruzleski. "Acta Metallurgica", Vol 44, No 9, 1996

FILLING LIMITATION AND MECHANICAL PROPERTIES FOR DIFFERENT GATE POSITIONS IN SEMI-SOLID FORMING PROCESS OF ALUMINUM ALLOYS

Chung Gil Kang, Pan Ki Seo* and Young Ik Son*

School of Mechanical Engineering, Pusan National University, Pusan 609-735, Korea,
E-mail : cgkang@pusan.ac.kr

*School of Mechanical Engineering, Graduate School, Pusan National University,
Pusan 609-735, Korea

ABSTRACT

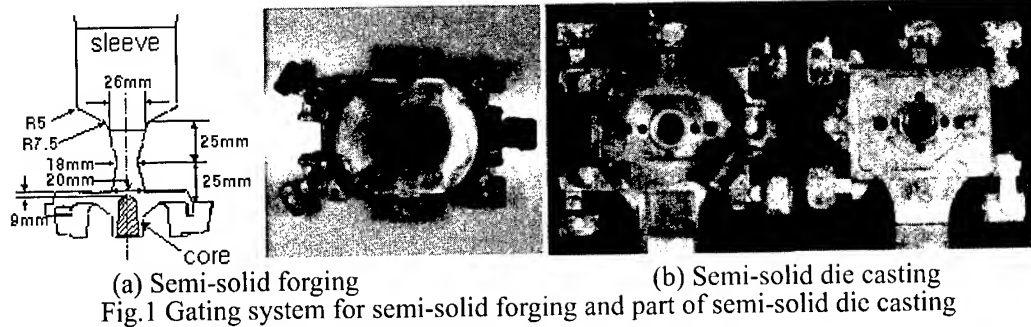
To obtain high quality component with semi-solid forging process, it is important to obtain the homogeneous distribution of solid particles without liquid segregation. In closed-die semi-solid forging process, liquid segregation is strongly affected by injection velocity than process parameters such as pressure and solid fraction because the material has to travel relatively long distance to fill the cavity through a narrow gate before solidification begins. The mechanical properties for forged semi-solid component with good filling situation were tested with the specimen before and after heat treatment. The mechanical properties of semi-solid die castings for varying die temperatures, injection velocity and applied pressure were investigated, and the relationship between applied pressure and stroke to assess the semi-solid die castability was proposed. In this study, the possibility of their use for compressor parts was verified.

1. INTRODUCTION

The products fabricated by casting and forging process need much machining, therefore it is one of reasons in cost-rise. But, if compressor parts with wear-resistance by semi-solid forming are developed, they can be obtained with low porosity, and machining process can be shortened. In the semi-solid forging process that produces complicated shape, it is known that semi-solid material with globular microstructure (the size of grain: 60~80 μ m) can be filled completely into a die. Viscosity of slug in semi-solid temperature is higher than that of liquid phase, therefore flow type will not develop into turbulence and velocity field and filling will be found, and gas defect by flow of pouring is lower. Semi-solid forging which produces component with alloys in the semi-solid state is gaining attention as a new manufacturing technology because of fewer defects such as porosity and low deformation resistance[1]-[3]. Semi-solid die casting is a net shape manufacturing method using a material co-existing in the solid and the liquid state. This process is capable of fabricating complex-shaped components in one process. Due to the high viscosity (i.e. greater than that of liquid), the material flow pattern will not become turbulent flow during die filling. Thus, gas defects such as porosity are diminished, and only small shrinkage defects for on-going solidification. As mentioned above, having various advantages compared with conventional metal semi-solid die casting processes, semi-solid die casting process has been studied around the world [4]-[9]. In this study, A357 material was used and mechanical properties were investigated with tensile, wear resistance and hardness test to the semi-solid forging and the semi-solid die casting to evaluate the suitability of semi-solid formed component.

2. FORMABILITY OF SEMI-SOLID ALLOYS

Gating system and Al frame for semi-solid forging and semi-solid die casting are shown Fig. 1. In the semi-solid forging, the sleeve was tapered and the diameter of gate was widened so that pressure should be transmitted sufficiently. In the semi-solid die casting, one of the most deleterious defects is the oxide skin either formed during die filling or dragged into the component from the skin of the billet. So, the runner system and overflow were designed to prevent the oxide skin from entering the product.



As shown in Table 1, the higher is temperature of initial billet, the more liquid segregation is investigated at the end portion of fabricated part. In the case of over 580°C of billet initial temperature, the flow phenomena of semi-solid alloy is improved because the liquid fraction is remarkably increased. Therefore, the unfilling defects were found at the final filling position and also investigated the liquid segregation at the final filling step. Consequently, it is proper to be formed under 580°C . In the case of $T_p=577^{\circ}\text{C}$, $V=300\text{mm/s}$, and $T_d=250\sim 300^{\circ}\text{C}$, there was no wide difference of the quality of forged part. But, the problems such as failure to eject pin occurred during semi-solid forging process. For that reason, under 300°C of die temperature is most suitable.

Table 1 Experimental conditions for semi-solid forging
(pressing pressure :80MPa, pressing holding time:20sec)

Exp. No.	Die Temp. $T_d(^{\circ}\text{C})$	Material Temp. $T_m(^{\circ}\text{C})$	Injection Velocity $V(\text{mm/s})$	Filling	Defects phenomena
1	200	577	160	U.F.	
2	200	582	160	U.F.	
3	200	577	300	D.F.	Liquid segregation
4	250	577	160	U.F.	
5	250	577	300	C.F.	
6	250	580	300	D.F.	Liquid segregation
7	250	582	300	D.F.	Liquid segregation
8	280	577	160	D.F.	Liquid segregation
9	280	580	160	D.F.	Liquid segregation
10	300	577	160	D.F.	Crack
11	300	580	160	D.F.	Liquid segregation
12	300	577	300	C.F.	
13	300	580	300	D.F.	Liquid segregation
14	350	580	160	U.F.	
15	350	580	300	D.F.	

* U.F.:unfilling, D.F.:defective filling, C.F.:filling complete

Fig. 2 (a) shows the load variation for production of the aluminum frame part on the condition of billet temperature 577°C, die temperature 250°C, injection velocity 370mm/s. Region ① is the billet reheating stage. In this stage, the punch is inserted into the sleeve to preheat the punch. In region ②, the punch is lifted up to the upper dead point to insert the reheated billet. Region ③ is time that billet is inserted into the sleeve. Region ④ is semi-solid forging stage. Region ⑤ is holding stage after semi-solid material completely filled. The holding time takes 20 second in region ⑤.

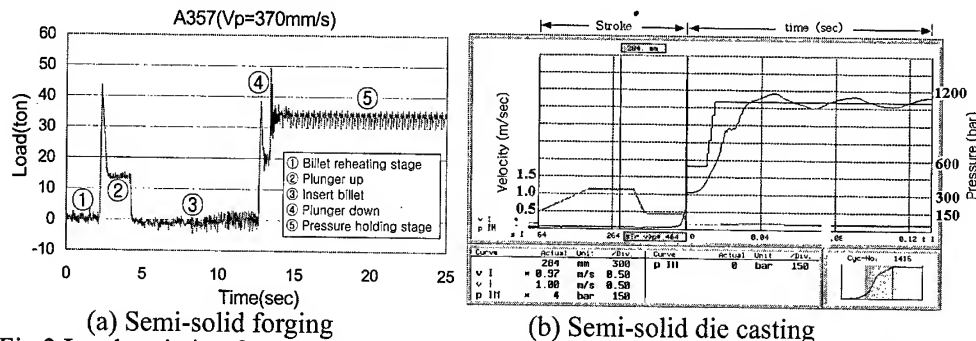


Fig.2 Load variation for semi-solid forging and injection curve for semi- solid die casting

In semi-solid die casting, the die was heated up to the set temperature between 180°C and 190°C by using an easily-handled cartridge heater. A horizontal type induction heating system was used for the reheating of the billet. This induction heating system is equipped with a digital control system that provides real-time data. The user can control a number of process parameters as a function of heating-holding time and temperature for its application. A real time controlled Buhler 42N die casting machine was used for the semi-solid die casting experiment.

The experiments of semi-solid die casting were performed by varying the process parameters such as the velocity profile (v) and displacement (s) of the plunger during the billet injection into the die cavity, the temperature (T_d) of the fixed and moving dies, the applied load (p), the billet temperature (T_m) and the time duration (t) of its application (see Table 2). Fig.2 (b) shows the relationship between displacement-velocity and injection velocity-pressure for the semi-solid die casting conditions of experiment 2 in Table 2.

Table 2 Experimental conditions for semi-solid casting of Al frame with A357

Exp. No.	$T_d(^{\circ}\text{C})$		$T_m(^{\circ}\text{C})$	s(mm)		Injection Conditions					
	Fixed	Moving				v(m/s)		t(s)		P(bar)	
1	110	110	581	200	320	1.0	1.0	0.0	0.010	550	550
				350	390	0.3	0.3		0.015		1100
					450		0.3				
2	128	138	581	200	320	1.0	1.0	0.0	0.010	550	550
				350	390	0.3	0.3		0.015		1100
					450		0.5				

3. MECHANICAL PROPERTIES

The specimen for tensile test is machined as shown in Fig.3. Fig.4 (a) shows the ultimate strength for variation of injection conditions and heat treatment. Products for injection Exp. No. 12 had the best ultimate tensile strength of 285MPa. The ultimate strength has increased by 13% with T5 heat treatment and 38% with T6 heat treatment. Fig.4 (b) shows the results of the tensile test for semi-solid die casting conditions (Table 2). On a tensile test, it was observed that the ultimate strength of the T6 heat-treated A357 (experiment 2) was highest.

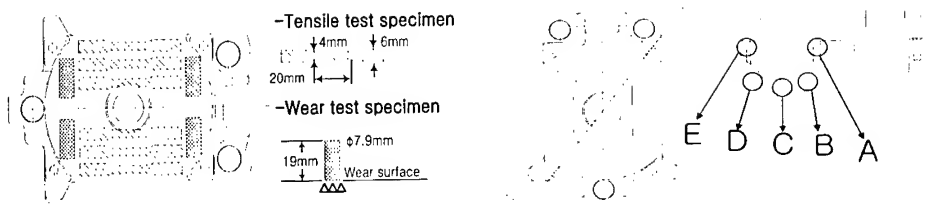


Fig.3 Specimen for tensile and wear test and the measured points of hardness test

The specimen for wear resistance test is machined as shown in Fig.3 (b). The disk is made of SKD61. The both specimens and disks were grinded to the 6-S surface toughness degree. The compressor force of disk and specimens is 100N. The quantity of wear is measured for 30 minutes.

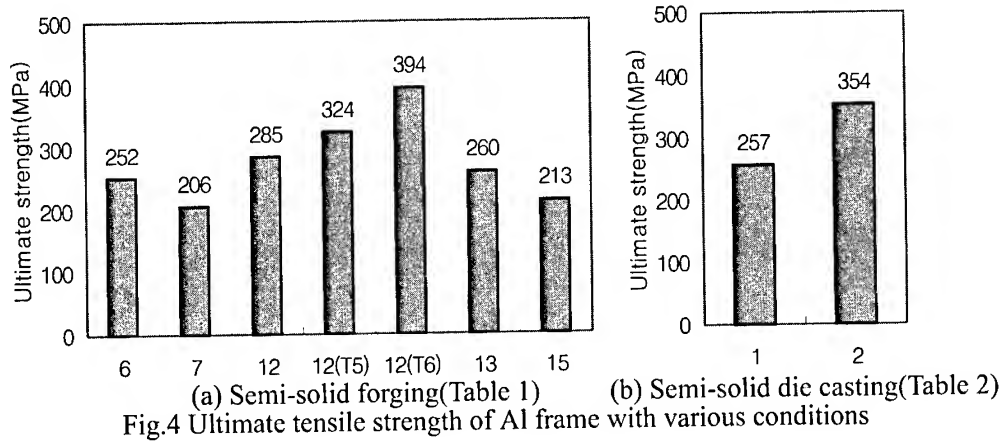


Fig.4 Ultimate tensile strength of Al frame with various conditions

Fig.5 shows the result of wear resistance test. The wear quantities of products of Exp. No. 7 and 15 of Table 1 were similar or higher than that of raw material. As shown in Fig.4 (a), products of Exp. No. 7 and 15 showed the lowest ultimate tensile strength and also have the most wear quantities. From the results of these experiments, it is considered that the desired formability and mechanical properties can be obtained, as the die temperature and billet initial temperature is lower than of 300°C and 580°C, respectively.

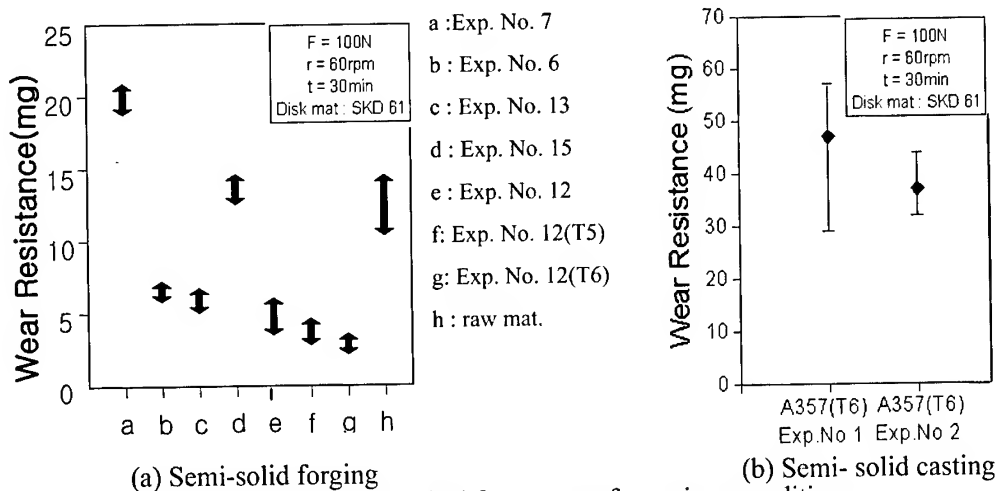


Fig.5 Wear resistance of Al frame parts for various conditions

Fig.3 (b) shows the position for the hardness tests. The hardness test was performed with A357 billets at the Exp. No. 7 and 12 of Table 1. Fig.6 (a) shows the result of hardness test. It shows comparatively uniform hardness in spite of variation of measuring position. The hardness of the forged parts at Exp. No. 7 and 12 of Table 1 is about 65~70. The average hardness with T5 and T6 heat treatment is 81 and 105, respectively. The hardness for T5 and T6 has increased about 15% and 45% compared with and without heat treatment, respectively. Fig.6 (b) shows the results of the hardness test for various semi-solid die casting conditions and heat-treatment conditions. The hardness tests showed that the hardness of the T6 heat-treated aluminum frame components fabricated at the semi-solid die casting conditions of experiment 2 was approximately 50 Hv higher than the T6 heat-treated components produced at the conditions of experiment 1.

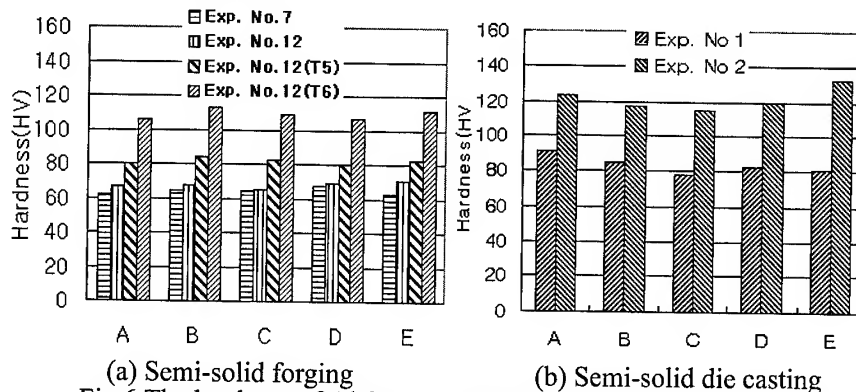
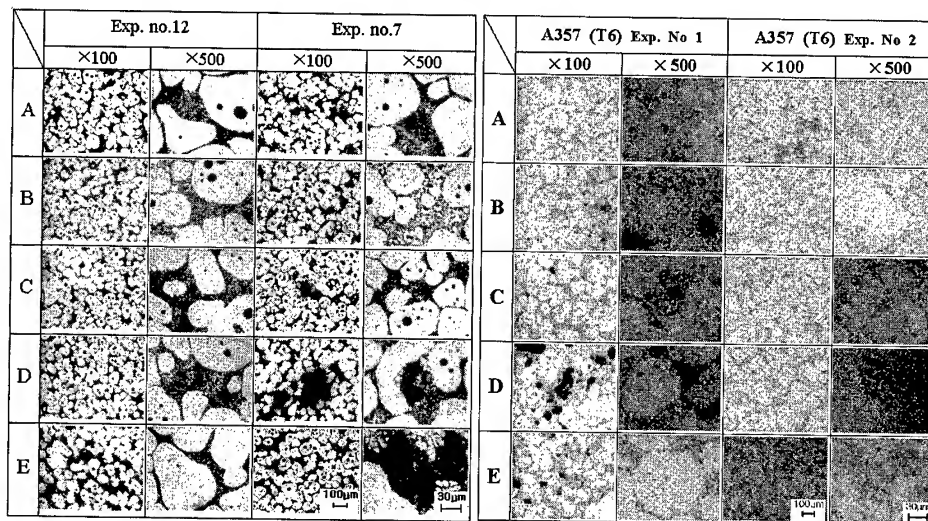


Fig.6 The hardness of Al frame products for the various conditions

4. MICROSTRUCTURE OF DEVELOPED PRODUCTS

Fig.7 (a) shows the comparison of globular and eutectic microstructure after the semi-solid forging. Exp. No. 12 shows totally uniform solid distribution and fine eutectic structure. Porosity was observed at point C, D, and E of Exp. No. 7. The injection velocity in semi-solid forging process is very important parameter that is affected with liquid segregation in cross section area of parts as well as filling phenomena.



(a) Semi-solid forging (Table 1) (b) Semi-solid die casting (Table 2)

Fig.7 Comparison of spheroidization and eutectic structure after semi-solid forming

Fig.7 (b) shows a fine globular microstructure and the micrograph magnified to the scale of 500 to observe the eutectic microstructure obtained at the conditions of experiments 1 and 2 prescribed in Table 3. A uniform distribution of both the solid and liquid phase was obtained. However, much porosity was observed at the conditions of experiment 1. The reason is that the final solidification pattern corresponding to the plunger velocity for completing filling affects the mechanical properties. Furthermore, it is considered that due to the rapid solidification at the conditions of experiment 1 the product shows pronounced susceptibility to formation of porosity. Internal defects such as this porosity may have a highly deleterious effect on the mechanical properties. As shown in Fig.4 through 6, the mechanical properties of the product fabricated at the conditions of experiment 1 prescribed in Table 2 are lowest. This phenomenon is explained by the formation of porosity, as shown in Fig.7 (b).

5. CONCLUSIONS

To eliminate air inside the overflow after the semi-solid billet had been fully filled, the pressing velocity at the final stage should be increased to guarantee better surface of the fabricated products. In semi-solid forging, uniform solid distribution and complete filling phenomena were found at billet temperature 577°C, die temperature 250°C and injection velocity 370mm/s. In semi-solid die casting, experiment was carried out under the conditions of the die temperatures of the fixed and moving dies at 128°C and 138°C and billet temperature at 581°C. The final velocity of the plunger tip at the stage to eliminate air inside the overflow out of the die cavity was changed up to 0.5 m/s. From the relationship between pressing force and time, the aluminum frame part with better surface was manufactured. The mechanical properties of semi-solid forming for varying die temperatures, injection velocity and applied pressure were investigated, and the relationship between applied pressure and stroke to assess the semi-solid formability was also proposed.

ACKNOWLEDGEMENTS

This work has been carried out with funding from the Engineering Research Center for Net Shape and Die Manufacturing (ERC/NSDM), which is an excellent center sponsored by the Korea Science and Engineering Foundation (KOSEF). The authors express heartfelt thanks for their financial support to the ERC/NSDM and KOSEF.

REFERENCES

1. R. Moschini, Proc. 2nd Int. Conf. on Semi-Solid Processing of Alloys and Composites, S. B. Brown, M. C. Flemings, eds., MIT, Cambridge MA, (1992), pp. 149-158.
2. K.P. Young, R. Fitze, Proc. 3rd Int. Conf. on Semi-Solid Processing of Alloys and Composites, M. Kiuchi, eds., Institute of Industrial Science, Univ. of Tokyo, Tokyo Japan, (1994), pp. 155-189.
3. T. Witulski, A. Winkelmann, G. Hirt, Sheffield, Proc. 4th Int. Conf. on Semi-Solid Processing of Alloys and Composites, D. H. Kirkwood, P. Kapranos, eds., Univ. of Sheffield, Sheffield, UK, (1996), pp. 242-247.
4. C.G. Kang, H.K. Jung, J. Mater. Eng. Performance Vol.9, (2000), pp. 530-535.
5. K.P. Young, Proc. 4th Int. Conf. on Semi-Solid Processing of Alloys and Composites, University of Sheffield, Sheffield, UK, (1996), pp. 229-233.
6. P. Giordano, F. Boero, G. Chiarmetta, Proc. 6th Int. Conf. on Semi-Solid Processing of Alloys and Composites, Unione Industriale di Torino, Turin, Italy, (2000), pp. 29-34.
7. E. Nussbaum, Light Met. Age, (1996), pp. 6-22.
8. R. Mehrabian, M.C. Flemings, Die casting of partially solidified alloys, Trans. AFS, Die Casting Engineer 80, (1973), pp. 173-182.
9. C.G. Kang, H.K. Jung, Semisolid forming process-numerical simulation and experimental study, Metall. Mater. Trans. B, 32B (2), (2001), in Press.

COMPARISON OF INNOVATIVE INDUCTION HEATING FOR ALUMINUM ALLOYS AND METAL MATRIX COMPOSITES IN SEMI-SOLID FORMING PROCESS

Hong Kyu Jung* and Chung Gil Kang**

School of Mechanical Engineering, Engineering Research Center for Net Shape and Die Manufacturing (ERC/NSDM), Pusan National University, Pusan 609-735, Korea,

* E-mail: hongkyuj@lycos.co.kr

** E-mail: cgkang@pusan.ac.kr

ABSTRACT

In this work, the fabrication processes of particulate metal matrix composites (PMMCs) with a homogeneous distribution of reinforcement and their reheating for thixoforming have been studied. Electromagnetic stirring was used to fabricate particulate reinforced metal matrix composites (PMMCs) for the variation of particle size. The compocasting conditions for fabricating the PMMCs are also suggested. For the thixoforming of PMMCs, fabricated billets are reheated by using the optimal coil designed as a function of the length between PMMC billet and coil, and coil diameter and billet diameter. The effects of the dispersion state of the reinforcements on the reheating temperature and microstructural morphology were investigated.

1. INTRODUCTION

Recently, it is an important subject to improve fuel efficiency in the transportation fields such as automobile, vessel, and aircraft because of an environmental point of view. From this point of view, the manufacturing process of lightweight products coinciding with the requirements of the parts must be developed. [1-7] For such objectives, the outstanding necessity for transportation weight reduction has led to a major increase in MMC production of engine parts for automobile applications. Particulate reinforced MMCs (PMMCs) combine metallic properties such as toughness and ductility with ceramic properties such as high strength, wear resistance and high modulus, leading to superior strength in shear and compression. A 50 pct increase in modulus, achieved by substituting a discontinuous silicon carbide reinforced aluminum matrix composite for an unreinforced wrought aluminum alloy, resulted in a 10 pct reduction in weight. [8] The fabrication method of MMCs by squeeze casting process has some problems, including the homogeneous dispersion of the particulates, extensive interfacial reactions, and particulate fracture during mechanical stirring, while powder metallurgy makes easy the homogeneous dispersion of the reinforcements and the control of interfacial reaction. However, squeeze casting process has lower cost and is nearer net shape manufacturing than powder metallurgy. [9] As a solution to improve the mechanical properties and to reduce manufacturing costs, particulate reinforced MMCs (PMMCs) provide an opportunity for thixoforming, which is one of the processes manufacturing net-shaped components. So, in this present study, the compocasting conditions for fabricating the PMMCs are suggested for the variation of particle size. For the thixoforming of PMMCs, fabricated billets are reheated. The present work focuses mainly on the effects of the dispersion state of the SiCp particles on the reheating temperature and microstructural

morphology.

2. EXPERIMENTS

2.1 The Fabrication Process of PMMCs

The matrix material used for the fabrication of PMMCs was an aluminum alloy, A357, fabricated by the electromagnetic stirring process and made by Pechiney (Voreppe, France). The chemical composition of the A357 is shown in Table 1. The silicon carbide particles used in these experiments were provided by Showa Denko Company (Japan) and the chemical composition and PH are shown in Table 2. Fig. 1 shows a schematic diagram of the composite stirrer designed and manufactured to obtain the homogeneous stirring. Mixing of SiC particles with the molten aluminum alloy, A357 was performed in a clay graphite crucible placed inside a high frequency furnace. The particles had an average size of 14 μm and 25 μm and were mixed into the melt with an impeller, manufactured from graphite, driven by a variable DC motor. The matrix was heated up to the molten metal state (over 630 $^{\circ}\text{C}$). After oxide films generated by the contact with atmosphere were removed, the cover fixing motor was driven for making the cover contact with the crucible. After driving the stirring impeller, the melted matrix was held and stirred at 595 $^{\circ}\text{C}$ for 1 min. The SiC particles of 10 g per unit minute were added uniformly for approximately 15 mins. The stirring impeller was coated with a fiberfrax coating cement made by Carborundum Company in the United States, and preheated up to 500 $^{\circ}\text{C}$ to prevent a rapid decrease in temperature by the contact with the matrix. After the particle addition, the impeller was driven for 15 mins, and the melted PMMCs were poured in the preheated graphite mold. The poured melt was cooled in the mold for 1 min and then was water-quenched. The fabricated PMMC billets are 40 mm in diameter and 180 to 200 mm in height. The billets for reheating are machined to $d \times l = 40 \times 50$ mm.

2.2 Inductive Coil Design for Uniform Reheating of PMMCs

In the case of heating the PMMC billet by using an induction heater, because the reheating conditions are different for the variation of PMMC and billet size, the inductive coil design and construction of a quantitative reheating data base for the thixoforming of the PMMC are very important. [10, 11] In commercial induction heating systems including the induction heating of aluminum billets, the induced heat is normally not equally distributed over the length of the PMMC billet. Non-uniformity of the heating profile at the coil and billets ends is related to the distortion of the electromagnetic field in those areas. This distortion is called the electromagnetic end effect. In general, electromagnetic end effect is one of the most complicated problems in induction heating. This effect can result in either overheating or underheating of the billet ends. So, the desired temperature distribution may be obtained only with a particular coil dimension. For uniform reheating of PMMCs (for minimizing electromagnetic end effect) in this present work, the effective coil length H and coil inner diameter D_i of the induction heating device were designed by using a new optimal inductive coil design method suggested by Jung and Kang. [1, 10, 11]

2.3 Reheating of PMMCs

The reheating experiments were carried out by using an induction heating system with a capacity of 20 kW. As shown in Fig. 2, to achieve uniform heating, the heating coil of the induction heating system was made by machining to $D_o \times H = 80 \times 100$ mm. Thermocouple holes to measure the temperature accurately are machined to 2 mm diameter at the position of 10 mm from the surface of the billet and 2 mm diameter at the position of 25 mm from the lateral of the billet. To accurately control the temperature of the PMMCs, K-type CA thermocouples of $\phi 1.6$ mm are inserted into the billet. A data logger TDS-302 (Tokyo Sokki Kenkyuio Co., Ltd., Tokyo) was used to receive the data, and the heating temperature was set

to the data as a thermocouple position "main" in Fig. 2. The reheating experiments were carried out for the conditions in Tables 3 and 4. The meanings of the symbols used in Tables 3 and 4 are the same as those shown in Fig. 3.

3. EXPERIMENTAL RESULTS AND DISCUSSION

3.1 Fabrication Experiments of PMMCs

The most important point in the fabrication process of PMMCs is the uniform dispersion of the reinforcements. The interaction parameters between SiCp and a growing solid/liquid interface are the alloying elements and the cooling rate. Particle capture or rejection is governed mainly by the Si content in the matrix. [12] In these experiments, the temperature of the matrix-particulate mixture was maintained at 595 °C. The fabricating conditions were set to obtain uniform dispersion for various stirring speeds. Agglomerated SiCp particles were observed at a stirring speed of 600 rpm with SiCp (15 vol. pct). At low stirring speeds, the semisolid stirring process had no influence on the uniformity of dispersion of the reinforcements. Figs. 4 and 5 present micrographs showing the dispersion state for an increased stirring speed of 1200 rpm. As shown in Fig. 4, in the case of the particle size of 25 µm, reasonably uniform dispersion was obtained, independent of volume fractions. In the case of the particle size of 14 µm, the dispersion state of the reinforcements was not more uniform than that of the particle size of 25 µm. This may be explained by the particles rejected by the solid/liquid interface. As a result of this phenomenon, the particles segregated to the interdendritic region.

3.2 SEM Fractograph

Fig. 6 shows the SEM fractographs of A357/SiCp tensile specimen for two different particle sizes of 25 µm and 14 µm. The preceding results show the weakness of the bonding force at the interface between the matrix and the SiCp particles in the region of clusters (position "A" in Fig. 6). This may be explained by many porosities (position "C" in Fig. 6) generated by air entrance in pouring the melt. Therefore, through the use of air vent, the interfacial bonding force was considered to be improved.

3.3 Results of Reheating Experiments

The microstructure of PMMCs after reheating must be a globular one. Furthermore, when the PMMCs are fed from the reheating device to the die, the shape of the PMMCs must be maintained. So, the volume fraction of the reinforcement and SiCp particle size were considered as parameters of the reheating experiment to obtain the globular microstructure and a small temperature gradient. The unreinforced A357 billets reach the set temperature with a small temperature difference (about 2 °C). In the case of A357 with 15 vol. pct (a particle size of 14 µm), the reheating temperature of PMMCs was approximately 13 °C higher than unreinforced A357. The effects of dispersion state of the reinforcements were observed remarkably during the reheating process of PMMCs. Moreover, in the case that the SiCp particle dispersed uniformly, the total reheating time of the PMMCs was reduced and the reheating temperature of the final step was low. Fig. 7 presents the reheating conditions of PMMCs according to the dispersion state. In the case that the reinforcement dispersed uniformly, the set temperature of the final reheating step was approximately 11 °C lower than that of the non-uniformly dispersed reinforcements and the total reheating temperature of the final step was also approximately 3 minutes shorter than that of the non-uniformly dispersed state. Figs. 8 and 9 show the microstructures after the reheating process of metal matrix composites fabricated by the semisolid stirring process. Uniform globular microstructures with a grain size of 100 µm as well as uniformly dispersed reinforcements were observed at all positions. From the preceding results, it was found that the most

important factor regarding the reheating process of PMMCs is the dispersion state of the reinforcements during stirring process. At the present time, research to obtain more uniform dispersion state of the particles by the control of solid fractions is being performed.

4. CONCLUSIONS

The particular conclusions are summarized as follows. In the case of the particle size of 25 μm , reasonably uniform dispersion was obtained, independent of volume fractions. In the case of the particle size of 14 μm , the dispersion state of the reinforcements was not more uniform than that of the particle size of 25 μm . The SEM fractographs of A357/SiCp tensile specimen show the weakness of the bonding force at the interface between the matrix and the SiCp particles. This may be explained by many porosities generated by air entrance in pouring the melt. In the case that the reinforcement dispersed uniformly, the set temperature of the final reheating step was approximately 11 $^{\circ}\text{C}$ lower than that of the non-uniformly dispersed reinforcements and the total reheating temperature of the final step was also approximately 3 minutes shorter than that of the non-uniformly dispersed state. Through the microstructure observation after the reheating process of metal matrix composites fabricated by the semisolid stirring process, uniform globular microstructures with a grain size of 100 μm as well as uniformly dispersed reinforcements were observed at all positions. It was found that the most important factor regarding the reheating process of PMMCs is the dispersion state of the reinforcements during stirring process.

ACKNOWLEDGEMENTS

The financial assistance of the Engineering Research Center for Net Shape and Die Manufacturing (ERC/NSDM) and Korea Science and Engineering Foundation (KOSEF) is gratefully acknowledged.

REFERENCES

1. C.G. Kang and H.K. Jung, Metall. Mater. Trans. B, Vol. 32B(2001), pp. 363-372.
2. C.G. Kang and H.K. Jung, J. Mater. Eng. Performance, Vol. 9(2000), pp. 530-535.
3. C.G. Kang and H.K. Jung, Metall. Mater. Trans. B, Vol. 32B(2001), pp. 119-127.
4. C.G. Kang and H.K. Jung, Metall. Mater. Trans. B, Vol. 32B(2001), pp. 129-136.
5. A. Zavaliangos, Int. J. Mech. Sci., Vol. 40(1998), pp. 1029-1041.
6. E. Nussbaum, Light Met. Age, June(1996), pp. 6-22.
7. E. Tzimas and A. Zavaliangos, Acta Mater., Vol. 47(1999), pp. 517-528.
8. I.A. Ibrahim, F.A. Mohamed and E.J. Lavernia, J. Mater. Sci., Vol. 26(1991), pp. 1137-1156.
9. T. Yamauchi and Y. Nishida, J. Japan Inst. Met., Vol. 58(1994), pp. 1436-1443.
10. H.K. Jung and C.G. Kang, Metall. Mater. Trans. A, Vol. 30A(1999), pp. 2967-2977.
11. H.K. Jung, C.G. Kang and Y.H. Moon, J. Mater. Eng. Performance, Vol. 9(2000), pp. 12-23.
12. H.J. Rack: Processing and Properties of Powder Metallurgy Composites, The Metallurgical Society, Warrendale, PA(1988), pp. 155.

Table 1 Chemical composition of A357

Content	Si	Fe	Cu	Mn	Mg	Ni	Zn	Ti	Pb	Sn
wt pct	7.5	0.15	0.03	0.03	0.60	0.03	0.05	0.20	0.03	...

Table 2 Chemical composition of silicon carbide particle

Content	SiC	F C	F SiO ₂	T Fe	PH
wt pct	99.0	0.04	0.55	0.07	5.0 to 7.0

Vol. pct	Test specimen (mm)	Heating time t_a (mm)			Heating temp. T_h (°C)			Holding time T_b (mm)		
		t_{a1}	t_{a2}	t_{a3}	T_{h1}	T_{h2}	T_{h3}	t_{b1}	t_{b2}	t_{b3}
0	d×l= 40×50	3	2	1	451	576	582	1	1	2
5		3	1	1	501	575	580	1	2	1
10		3	1	1	501	575	582	1	2	1
15		3	1	1	501	575	594	1	2	2

Vol. pct	Test specimen (mm)	Heating time t_a (mm)			Heating temp. T_h (°C)			Holding time T_h (mm)		
		T_{a1}	t_{a2}	t_{a3}	T_{h1}	T_{h2}	T_{h3}	t_{h1}	t_{h2}	t_{h3}
0	d×l= 40×50	3	2	1	451	576	582	1	1	2
5		3	1	1	501	575	582	1	2	1
10		3	1	1	501	575	583	1	2	1
15		3	1	1	501	575	595	1	2	2

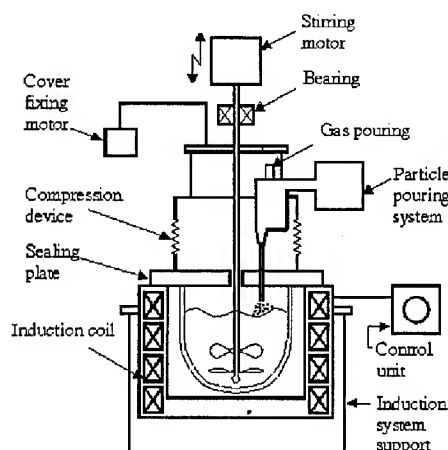


Fig. 2 Thermocouple positions to measure the temperature during the reheating process of metal matrix composites

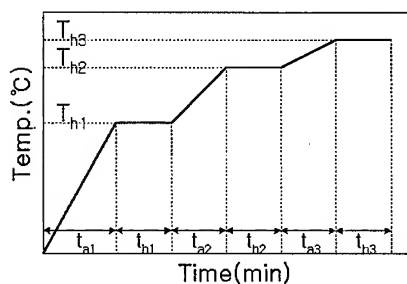


Figure 1 consists of four TEM micrographs arranged in a 2x2 grid. The top row (a) shows membranes with 10% and 15% PAAI content. The bottom row (b) shows membranes with 10% and 15% PAAI content, with an additional 10% PAAI content. The images show a porous structure with labels A, B, and C indicating different regions. Scale bars are 100 nm.

1053

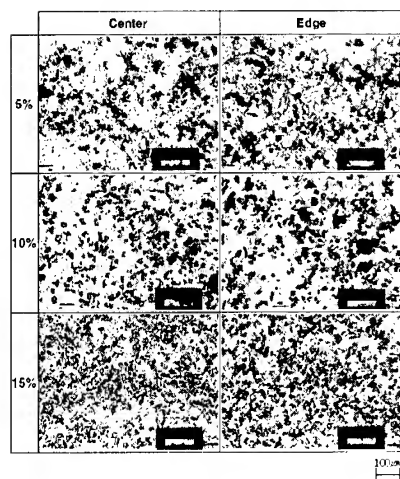


Fig. 4 Microstructure of metal matrix composites fabricated by the semisolid stirring process (matrix temperature 595 °C, a particle size of 25 μm and stirring speed 1200 rpm)

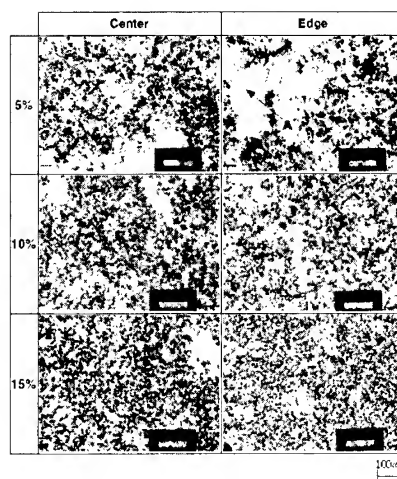


Fig. 5 Microstructure of MMCs fabricated by the semisolid stirring process (matrix temperature 595 °C, a particle size of 14 μm and stirring speed 1200 rpm)

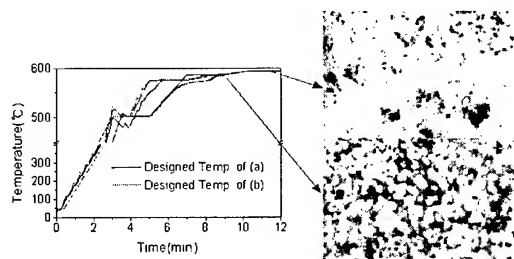


Fig. 7 Temperature profile during the reheating process and microstructure of PMMCs after reheating process (a) inhomogeneously dispersed state of reinforcements (b) homogeneously dispersed state of reinforcements

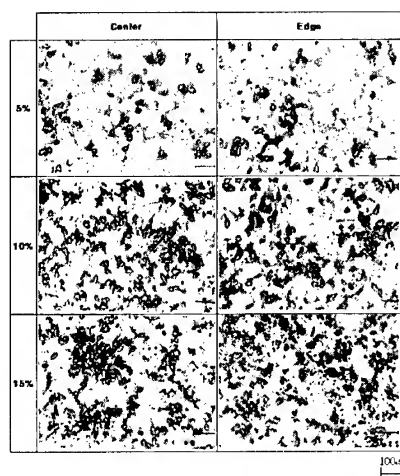


Fig. 8 Microstructure after the reheating process of metal matrix composites fabricated by the semisolid stirring process (a particle size of 25 μm)

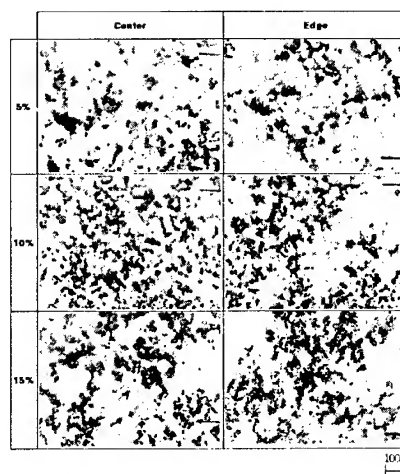


Fig. 9 Microstructure after the reheating process of metal matrix composites fabricated by the semisolid stirring process (a particle size of 14 μm)

MICROSTRUCTURAL EVOLUTION AND DEFORMATION BEHAVIOUR OF 2014 ALUMINIUM ALLOYS IN THE SEMI-SOLID STATE

D. S. Han*, I. C. Stone** and B. Cantor**

*Materials Research Team, Research & Development Division
For Hyundai Motor Company & Kia Motors Corporation

**Oxford Centre for Advanced Materials and Composites
Department of Materials, University of Oxford, Parks Road
OXFORD, OX1 3PH, U.K.

ABSTRACT

AA 2014 aluminium alloys were produced by different manufacturing processes such as wrought, as spray formed, spray formed & consolidated, spray formed & extruded, continuous cast & extruded and squeeze cast in order to obtain the various initial microstructures. The wrought, as spray formed, spray formed & consolidated materials possessed non-dendritic equiaxed grains of around $18\mu\text{m}$ while the spray formed & extruded and continuous cast & extruded materials exhibited deformed and elongated grains, and squeeze cast materials consisted of approximately equiaxed dendrites. The dendrite arm spacing and grain size were around $30\mu\text{m}$ and $115\mu\text{m}$ respectively. Cylindrical specimens of the materials were compressed under the constant load at 560 ($f_s=0.90$), 580 ($f_s=0.86$), 600 ($f_s=0.78$) and 610°C ($f_s=0.70$), respectively, to obtain strain versus time curves. The as spray formed or spray formed & consolidated material showed much higher strain rates in the initial stage and greater strain at all temperatures compared to the other materials. A semi-empirical constitutive model has been proposed for the steady state strain rate developed during semi-solid deformation under the present study. The model incorporates a stress component, a component based on the inter-relationship of grain size, solid fraction and grain boundary liquid film thickness, and a thermally activated diffusion. The thermally activated diffusion component yields an activation energy of approximately 150KJ/mol for all the materials, which is similar to the value for self-diffusion in solid aluminium.

1. INTRODUCTION

Recent legislative and environmental pressures on the automotive industry to produce light-weight fuel efficient vehicles with lower emissions have led to a requirement for traditional steel components to be replaced by aluminium alloy alternatives. This has led to a complete re-analysis of the design and manufacturing routes, with the emergence of semi-solid forming as a viable process for the production of high volume, low cost, high integrity automotive components [1]. Semi-solid forming is an attractive process because it combines the low costs of die-casting and the enhanced mechanical properties and shape replication associated with forging, and has the added benefits of enhanced die life, energy efficiency, and low scrap rates [2,3]. The present research was carried out to understand fundamental effects of variations in initial microstructure, such as grain size, grain morphology and second phase particles etc.,

temperature, solid fraction and applied stress on the ability to deform semi-solid Al alloys, to understand the mechanisms of semi-solid deformation in the solid fraction range ($f_s=0.70-0.90$), and to develop a constitutive model for the deformation behaviour. The study of the variation in initial microstructure is achieved by deformation testing of alloys of the same composition which have been made in different ways.

2. EXPERIMENTAL

The semi-solid deformation behaviour and microstructural evolution were investigated using a thermomechanical analyser as described in literatures [1,4,5] for AA2014 Al alloys. Small cylindrical samples of the alloys were compressed between top and bottom compression plates which were flat machined from Macor machinable ceramic, with the whole assembly located in a 60mm long, 40mm outer diameter and 20mm inner diameter tube furnace, and with an external LVDT to monitor sample dimension changes and the strain variation with time was measured using a linear voltage displacement transducer. Deformation tests were carried out on equiaxed non-dendritic alloys, dendritic alloys and elongated extruded alloys to investigate the effects of initial microstructure. Compressive deformation tests were carried at 560, 580, 600 and 610°C which is correspondent to solid fraction of 0.90, 0.86, 0.78, 0.70 respectively.

3. RESULTS and DISCUSSION

3.1. Deformation Behaviour

Fig.1 shows a true strain versus time curves for 2014 Al alloys with different initial microstructures. The strain varied significantly with the initial microstructure. Specimens with initially elongated or dendritic structure deformed less than specimens with initially non-dendritic microstructures. This is likely to be due to the increased mechanical interlocking

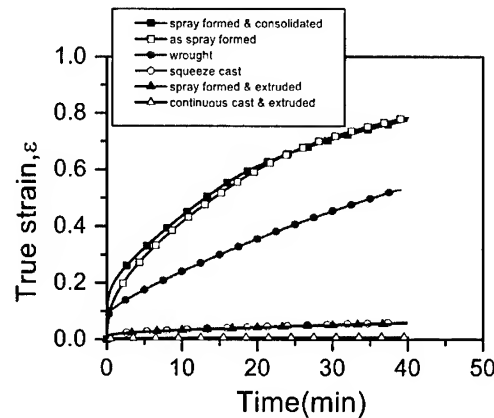


Fig.1 True strain versus time curves for 2014 Al alloys under the constant load of 100g at 610°C ($f_s=0.70$).

of elongated and dendritic grains, larger grain size and a greater portion of intragranular liquid droplets.

The alloy with initially equiaxed non-dendritic microstructures all had similar grain sizes, but their deformation behaviour varied. The strain of as spray formed alloy was higher than wrought alloy. There are three possible reasons for this. They are presence of 3.5% porosity, less intragranular liquid and more grain boundary liquid in as spray formed alloy. The dominant effect is probably the 3.5% of porosity present in the as spray formed alloy. The alloy yield stress σ_R can be given by the following equation [6]:

$$\sigma_R = \sigma_o(\rho - \rho_c / 1 - \rho_c) \quad (1)$$

where σ_o is the yield stress of the fully consolidated alloy, ρ = density of the porous alloy relative to the fully consolidated alloy, ρ_c = critical density at which the yield stress of a porous material becomes zero. Assuming that ρ_c is 0.7 for as spray formed 2014 Al alloy [6], according to eqn (1) $\sigma_R = 0.88\sigma_o$. Reduction of yield stress can make a large contribution to semi-solid deformation in the as spray formed 2014 Al alloy. In addition, the porosity may also provide short circuit paths to enhance diffusion rates in the grain boundary liquid and the solid grains. There were more intragranular liquid in the wrought alloy. This may be associated with the following microstructural observation. Second phase particles in wrought alloy were distributed along the grain boundaries and through the grains. On the other hand, most of second phase particles in as spray formed alloy were concentrated as a semi-continuous network along the grain boundaries. In the case of wrought alloy, on partial remelting second phase particles melted at the grain boundaries and interior grains while the second phase particles of as spray formed alloy were melted to form a grain boundary liquid film. The intragranular liquid droplets may have been left behind from the rapidly moving grain boundary liquid films as proposed by Annavarapu et al [7]. However, another possible explanation in the case of wrought 2014 is that the presence of second phases in the interior grains could have melted in the semi-solid regime to form the intragranular droplets.

As shown in Fig.1, the strain of spray formed & consolidated alloy was higher than wrought alloy. There are two possible reasons for this. Firstly, the effective grain boundary liquid of spray formed & consolidated alloy is larger than wrought alloy. This could be associated with the microstructural observation that almost second phase particles concentrated at the grain boundaries as a semi-continuous network, which melted in the semi-solid regime for spray formed & consolidated alloy unlike the wrought alloy. Second effect is the grain boundary structure. The fraction of low angle boundaries in wrought alloy increased from 5% to 10% in annealed state. The average misorientation angle in wrought alloy decreased slightly from 40° to 35° in the annealed state. This suggests that a slight preferred orientation developed during isothermal holding and this may have enhanced the grain boundary strength. On the other hand, the area fraction of low angle boundaries in spray formed & consolidated alloy decreased from 17% to 3% in the annealed state. The average misorientation angle in spray formed & consolidated alloy increased slightly from 34° to 40° in the annealed state. This suggests that no preferred orientation developed during isothermal holding and this may have enhanced grain boundary wetting.

3.2. Semi-empirical constitutive model

The rate controlling mechanisms for deformation behaviour can be investigated by using

strain rate relationship such as strain rate-temperature, strain rate-solid fraction and strain rate-stress etc. Steady state strain rate increases with roughly exponentially with absolute temperature which suggests plotting $\ln \dot{\epsilon}_{ss}$ versus $1/T$ in order to obtain the activation energy associated with the deformation mechanisms. The activation energy for semi-solid deformation was determined from the following Arrhenius type equation:

$$\dot{\epsilon}_{ss} = A_o \exp(-Q_o / RT) \quad (2)$$

where A_o is applied stress and microstructure dependent, Q_o is the apparent activation energy and R is the universal gas constant. In each case, the Arrhenius plot revealed a straight line relationship following this equation. The activation energy for the different alloys were quite similar, and were approximately 300KJ/mol. This activation energy is much higher than the reported value of Al self-diffusion, 144KJ/mol. It should be noted that the activation energy in this equation is a just apparent activation energy which is a combination of activation energy for self-diffusion adjusted by other temperature dependent parameters such as grain boundary film thickness and solid fraction. For the stress-strain rate relationship, a power-law equation has usually been used in the interpretation of the deformation mechanisms. The stress exponent was determined from the power-law equation. In each case, the plot revealed a straight line relationship. The values of stress exponent for 2014 alloys were similar and approximately unity for all the alloys in the temperature range 560-610°C ($f_s=0.90-0.70$). Grain boundary sliding is characterized by low stress exponent typically 1 or 2 and their values were quite consistent with values observed in the present work ($n \approx 1$). The grain size is clearly very important in determining the extent of deformation. The grain size exponent was

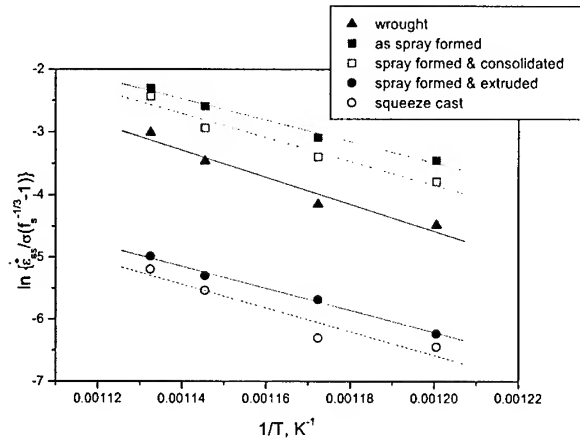


Fig.2 $\ln\{\dot{\epsilon}_{ss} / \sigma(f_s^{-1/3} - 1)\}$ versus $1/T$ curves for 2014 Al alloys.

determined from a power-law equation. The grain size exponent was 1.7 which is close to 2 associated with diffusion controlled deformation mechanisms. Semi-solid deformation in the 2014 alloys used in the present study occurs by grain boundary sliding accompanied by diffusion with a stress exponent close to unity and grain size exponent close to 2.

The plots that were described before gave indications of the individual effects of temperature,

stress and initial grain size on $\dot{\epsilon}_{ss}$ independently each other. A through description of $\dot{\epsilon}_{ss}$ requires accounting for the combination and inter-relation of these individual parameters, plus the incorporation of other inter-dependent parameters such as solid fraction and liquid film thickness. The constitutive equation should therefore contain an initial applied stress

Table 1 Calculated parameters from eqn (4) and Fig.2

Alloy	$\ln A$	Q (KJ/mol)	Q/R
wrought	21.2	172	21498
as spray formed	16.8	133	16915
spray formed & consolidated	18.9	151	18971
spray formed & extruded	15.1	141	17772
squeeze cast	16.4	152	19110

contribution and an Arrhenius contribution. The activation energy obtained from eqn (1) was higher than the expected value for Al lattice self-diffusion, but it should be noted that this high activation energy was only an apparent value which compensated for the effects of other temperature dependent parameters, namely, solid fraction, liquid film thickness, and *in-situ* diameter of the solid grains. These parameters are inter-related as following equation [8]:

$$\frac{\delta}{d_i} = f_s^{-1/3} - 1 \quad (3)$$

i.e. the ratio of the liquid film to the *in-situ* solid grain diameter is constant for a given solid fraction. The equation is based on an average spherical grain of average diameter, d_i , surrounded by a continuous film of liquid of average thickness δ [8]. δ and d_i are not convenient to use as input parameters for the constitutive equation because they are not readily known. The constitutive equation should therefore include the $(f_s^{-1/3} - 1)$ term. So, the proposed constitutive equation for semi-solid deformation under the conditions of the present study is therefore as follows:

$$\dot{\epsilon}_{ss} = A \sigma (f_s^{-1/3} - 1) \exp(-Q/RT) \quad (4)$$

Fig.2 shows $\ln[\dot{\epsilon}_{ss} / \{\sigma(f_s^{-1/3} - 1)\}]$ versus $(1/T)$ for wrought, as spray formed, spray formed & consolidated, spray formed and extruded, and squeeze cast 2014 Al alloys. As shown in Fig.2 and Table 1, results for all the alloys give good agreement with eqn (4). The activation energy for semi-solid deformation is in the range 133-172 KJ/mol, i.e. close to the expected value for self-diffusion of Al (144KJ/mol). As shown in Fig.2, the straight lines are parallel, indicating that the activation energy is not dependent on prior processing or initial microstructures, but they are shifted slightly. This shift is associated with the initial microstructural parameters such as aspect ratio or smoothness of the grains etc, affecting A values as shown in Table 1. These are non-temperature dependent parameters and thus do not affect the activation energy value, i.e., A is a function of microstructure (equiaxed, elongated and intragranular liquid droplets etc.).

4. SUMMARY

A given alloy was more deformable when it consisted of equiaxed, non-dendritic microstructures. The alloy was least deformable when the initial microstructure was highly elongated. When a large proportion of the liquid was present as intragranular droplets then the alloy became harder to deform because the effective liquid fraction between solid grains decreased. A larger deformation was achieved with higher grain boundary misorientations because of enhanced wetting of grain boundaries with liquid. A semi-empirical constitutive model has been proposed for the steady state strain rate developed during semi-solid deformation under the conditions of the present study. The model incorporates a stress component, a component based on the inter-relationship of grain size, solid fraction and grain boundary liquid film thickness, and a thermally activated diffusion component: $\dot{\epsilon}_{ss} = A\sigma(f_s^{-1/3} - 1)\exp(-Q/RT)$, where $\dot{\epsilon}_{ss}$ is steady state deformation rate, A is microstructure dependent, σ is initial applied stress, f_s is the solid fraction, Q is the activation energy, R is the universal gas constant and T is deformation temperature. The stress component comprises of the initial stress raised to a power $n \approx 1$. This is similar in nature to the relationship between stress and strain rate for solid state creep dominated by grain boundary sliding and solute diffusion, or self-diffusion. The thermally activated diffusion component yields an activation energy of approximately 150KJ/mol, which is similar to the value for self-diffusion in solid aluminium.

ACKNOWLEDGEMENTS

One of authors, D.S Han would like to thank the Hyundai Motor Company for leave of absence and financial support to carry out this work and would like to give deepest appreciation to the British Government for her financial support throughout the Chevening Scholarships.

REFERENCES

1. D. S. Han, D.Phil Thesis, University of Oxford, (2000) p1.
2. D. H. Kirkwood, Int. Mat.Rev. vol. 39 No.5 (1994) p173.
3. M. C. Flemings, Metall. Trans. 22 A (1991) p957.
4. D. S. Han, G. Durrant and B. Cantor, in 5th International Conference on Semi-Solid Processing of Alloys and Composites, Colorado School of Mines, U.S.A. (1998) p45.
5. D. S. Han, I. C. Stone and B. Cantor, in Advanced Forming and Die Manufacturing Technology, Pusan, Korea (1999) p65.
6. D. N. Lee and H. S. Kim, Powder Metall., No.35 (1992) p275.
7. S. Annavarapu and R. D. Doherty, Acta Metall., No. 43 (1995) p3207.
8. E. D. Manson-Whitton, I. C. Stone, P. S. Grant, B. Cantor and S. Blackman, TMS (1998) p415.

MICROSTRUCTURAL CONTROL FOR THIXOTROPIC Al ALLOY BY HORIZONTAL CONTINUOUS CASTING PROCESS USING ELECTROMAGNETIC STIRRING

Kibae Kim, Duckyoung Lee, Yongkyu Seon, Hoin Lee and *Donsoo Shin

Division of Materials, Korea Institute of Science and Technology

P.O.Box 131, Cheongryang, Seoul 130-650, KOREA

*Technical Research Institute, Dooray Air Metal Co. Ltd

345-11, Kasan-dong, Kumchun-ku, Seoul 153-023, KOREA

ABSTRACT

Semisolid forming process is getting established as a technology for fabricating the lightweight parts for transportation system. Thixoforming processes are being used for producing parts of Al and Mg alloys. These processes need a special billet of a microstructure having globular solid particles in the solid-liquid state to get the thixotropic property.

Thixotropic Al alloy billet with non-dendritic structure was fabricated by using horizontal continuous casting process where melt was electromagnetically stirred during solidification. Microstructures of billet were examined as a function of stirring strength and casting speed. The morphology, size, and distribution of primary crystal to be influenced on the thixotropic behavior of the billet were measured using image analyzer. Behavior of primary crystal on solidification with electromagnetic stirring was analyzed in order to predict the morphology, size, and distribution of primary crystal.

1. INTRODUCTION

The fuel consumption and environmental compatibility will continue to need for significant weight reduction in the design of transportation systems. Among the range of low-weight design approaches, the use of light alloys has come to play an increasingly important role despite higher materials costs. The target of a 50% weight reduction using aluminum as a substitute for classical steel forged or nodular cast iron parts only can be achieved, if the design of the parts can be optimized according to the loading conditions. This implies that there may not be too many design restrictions related to the manufacturing process. This often results in part geometries with complex shape. With conventional forging processes these complex geometries cannot be produced at competitive cost. On the other hand, conventional casting processes cannot guarantee the required mechanical properties.

In this context, thixoforming is gaining growing importance as an alternative to classic manufacturing routes. Thixotropic behavior of semisolid metals was discovered 30 years ago at MIT.[1-3] It is characterized by a high viscosity at rest and by a remarkably low viscosity upon shearing in a semisolid state. This drastic drop in viscosity permits shaping at relatively low pressure in a diecasting process. Furthermore, the semi-solid metal shows good flow behavior, comparable rather to plastic injection molding than to pressure diecasting. Laminar mold filling and little solidification contraction lead to low gas porosity and shrink holes. This

process certainly is very competitive with gravity diecasting and forging.[4-6] Combined with using high quality casting alloys (with low iron content) or wrought alloys, thixoformed parts combine high strength with appropriate elongation. First series productions have been concentrated on pressure tight parts but current developments are extending the technology to safety parts, thin walled parts for body structure components and tailored alloys like metal matrix composites for wear resistant components.[7,8]

The preconditions for the realization of thixoforming are a suitable alloy and an appropriate structural state in the feedstock, producing a slurry or solid-liquid matrix during the forming process. A number of different process variants have been developed to achieve the desired structure.[9] In the casting processes introduced for aluminum alloys, the melt is stirred intensively during solidification to obtain a suitably fine-grained globular dendritic structure, which then forms the desired structure on reheating. One alternative process is the modified chemical grain refinement with the use of a higher amount of grain refiner during continuous casting, which leads after a short period of time in the solid-liquid region to the necessary microstructure of the perform. An other variant of feedstock material manufacturing is the thermomechanical treatment for the use of conventional perform, which allows formation of a suspension of spherical solid particles and matrix melt during reheating into the solid-liquid region after appropriate plastic deformation. This feedstock route is suitable for all sufficiently formable materials, i.e. also for steel.

In this study the thixotropic aluminum alloy billets were produced in the horizontal continuous casting process utilizing the electromagnetic stirrer, which imparts the necessary motion to the melt in mold during solidification. In order to establish the quantitative relationships between microstructure and the process parameters, the morphology and grain size of billet were observed according to the withdrawal speed and electromagnetic force.

2. HORIZONTAL CONTINUOUS CASTING SYSTEM

A horizontal continuous casting process has been developed to produce the thixotropic aluminum alloy billet. The advantages of horizontal continuous casting system lie mainly in its superior economic efficiency under continuous manufacturing conditions. This asymmetry inherent in horizontal continuous casting due to the difference between the direction of gravity and the casting direction must be offset by a suitable design of the mold and the hot top system. Fig. 1 shows the pilot plant at Technical Research Institute of the Dooray Air Metal Co. Ltd for industrial scale production. Building on established continuous casting technology as developed by Dooray Air Metal, electromagnetic stirring in combination with special mold design facilitates the production of the fine grained billets necessary for thixoforming. In the first step casting of Al alloy(A356) billet of 3 in. in diameter has been evaluated and the work will be continued on other diameters and alloys. Fig. 2 shows the commercially mass-produced billets. The horizontal continuous casting system consists of the following elements: inductive melting furnace, runner, tundish, ceramic foam filter, die assembly (graphite or metal mold with electromagnetic stirring device), strand withdrawal machine for continuous or pull-back-stop mode, billet cutting station, billet collector.

The degassed and cleaned molten metal of melting furnace is transferred through a ceramic filter to a tundish where the temperature is stabilized and controlled before being passed into the casting mold. When the strand has formed within the mold, it passes through the zone of secondary cooling, where the strand is cooled by direct water spray to room temperature. The cold strand is withdrawn from the mold through the two pinch roll sets driven by an electric

withdrawal machine. In the first step of casting the cold strand is withdrawn by a dummy bar, which has the same diameter of the strand. The exact motion can be programmed to pull in continuous manner or do individual combination of pulling, pushing and stops with different speeds and for different duration times.



Fig. 1. The pilot plant at Dooray Air Metal Co. Ltd for industrial scale production



Fig. 2. The mass-produced Al alloy billets

Cutting is done using a flying saw. Length of the billets is chosen individually or depending on the needed shot weight. At high casting speed only long billet may be cut since the cutting time is too long to allow individual slug length. At the billet collector all billets can be stored or feed to the induction heating system to be prepared for casting in the thixoforming machine.

3. CASTING MOLD AND ELECTROMAGNETIC STIRRER

A horizontal continuous casting system in combination with special mold design and electromagnetic stirring was established. Both water-cooled graphite and metal mold have been designed and evaluated. In the graphite mold the liquid metal is solidified in a graphite tube, surrounded by a water-cooled copper tube. The graphite mold has less effective primary cooling and is suitable for casting speed between 100 and 200 mm/min. Advantages are its easy use during start or stop of the casting and its safety during casting. The metal mold has direct water-cooled walls and requires continuous oil lubrication. This is a so-called D.C. (Direct Chill) mold. The metal mold is designed for high casting speeds, 400 to 600 mm/min, and achieves a high cost effectiveness of the casting process. Start and stop have to be done carefully. The cooling affectivity is about three times higher than that of the graphite mold.

The mold comprises a structure having a low heat conductivity inlet portion defined by the hot top and a high heat conductivity portion by the exposed portion of the mold wall. A hot top made from alumina board conforms to the internal shape of the mold and is held to the mold wall. The low heat extraction rate associated with the hot top generally prevents solidification in that portion of the mold. The cooling manifold is arranged circumferentially around the mold wall. The cooling water serves to carry heat away from the molten metal via the inner wall of mold and exits through slot discharging directly against the solidifying ingot. A valve system is provided to control the flow rate of the water in order to control the rate at which the slurry solidifies.

An electromagnetic(EM) stirrer was designed and developed for horizontal continuous casting process as shown in Fig. 3. In order to get a non-zero field across the entire cross section of the mold a two-pole three-phase inductor was utilized. The magnetic stirring force

vector is normal to the heat extraction direction and is therefore normal to the direction of dendrite growth from the mold wall. By obtaining a desired average shear rate over the solidification range, i.e. from the center of the slurry to inside of the mold wall, improved shearing of the dendrites as they grow may be obtained. A rotating magnetic field generated by the EM stirrer is used to achieve the required high shear rates for producing thixotropic semi-solid alloy slurries. In particular, the stirring force field associated with the EM stirrer should preferably extend over the full length and cross section of the solidification zone with a sufficient magnitude to generate the desired shear rate. The stirring of the molten metal and the shear rates are functions of the magnetic induction at the periphery of the molten metal. Fig. 4 shows the magnetic flux density measured at the mold wall and medium position of EM stirrer. The cooling of the coils is done by water.

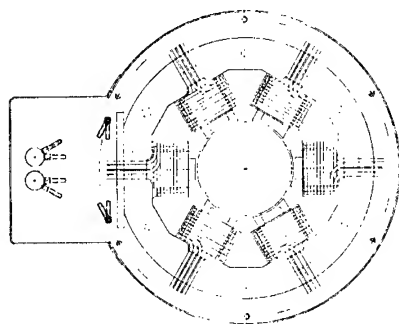


Fig. 3. An electromagnetic(EM) stirrer for horizontal continuous casting.

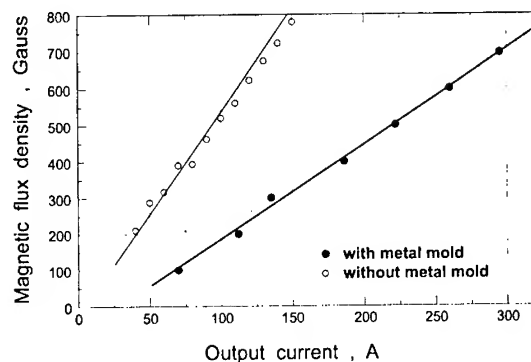


Fig. 4. The measured magnetic flux density of electromagnetic stirrer.

4. MICROSTRUCTURAL CONTROL THROUGH THE PROCESS

To form a thixotropic billet utilizing the horizontal continuous casting apparatus, molten metal is poured into mold cavity while EM stirrer is energized by a suitable three phase AC current of a desired magnitude and frequency. The molten metal is stirred continuously by the rotating magnetic field produced by EM stirrer. Solidification begins from the mold wall. The highest shear rates are generated at the stationary mold wall or at the advancing solidification front. By properly controlling the rate of solidification, desired thixotropic slurry is formed in the mold cavity. As a solidifying shell is formed on the casting, the withdrawal mechanism is operated to withdraw casting at a desired casting speed. Fig. 5 shows the macrostructures from the cross sections of billet produced at a magnetic flux density of 500Gauss and a different casting speed. A thickness of the solidifying shell was decreased with increasing the casting speed, but a breakout may be occurred when the solidifying shell is too thin.

The prerequisites for the thixotropic behavior are a special microstructure and a certain quality of the EM stirred billets. Fig. 6 shows the microstructures of the billet produced at a casting speed of 500mm/min and a different electromagnetic force. Conventionally solidified alloys have branched dendrites, which develop interconnected networks as the temperature is reduced and the solid fraction increases, as shown in Fig. 6 (a). In contrast, thixotropic metal slurries consist of discrete primary degenerate dendrite particles separated from each other by a liquid metal matrix. Because of the circulation of the melt in the stirring zone, the nuclei

formed during solidification are unable to grow in the normal way to coarse heavily branched dendrites. On the contrary, the nuclei are torn away from the solidification front and partially remelted in contact with the hotter metal entering the center of the mold. The primary solid particles are degenerate dendrites approaching an spheroidal configuration as shown in Fig. 6 (b). Strong electromagnetic forces come to bear during solidification, fragmenting the crystalline growth of the dendritic network into fine globular shaped particles bedded within the eutectic.

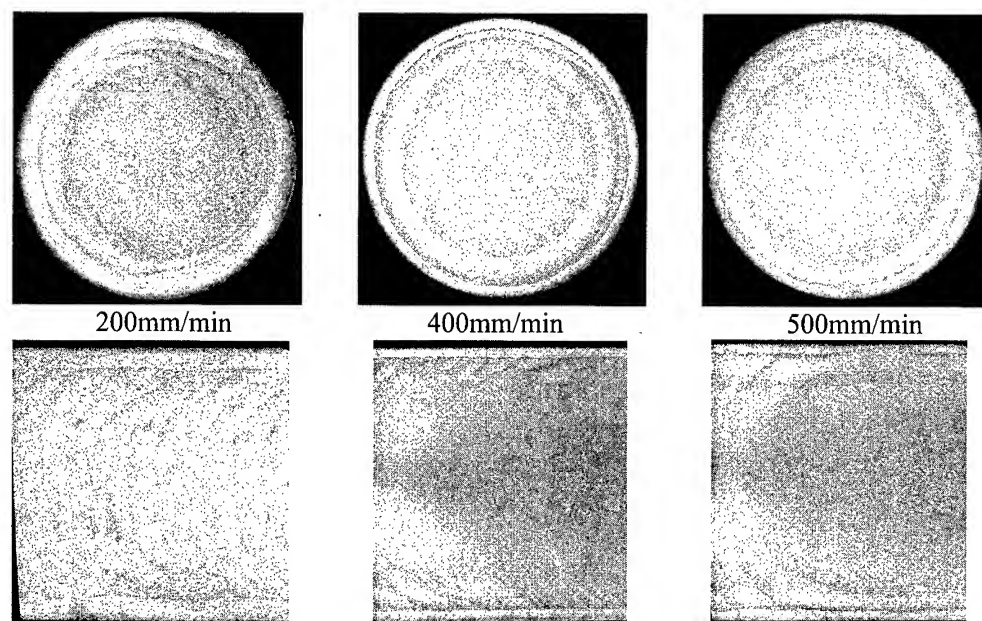


Fig. 5. Macrostructures from the cross sections of billet produced at a different casting speed

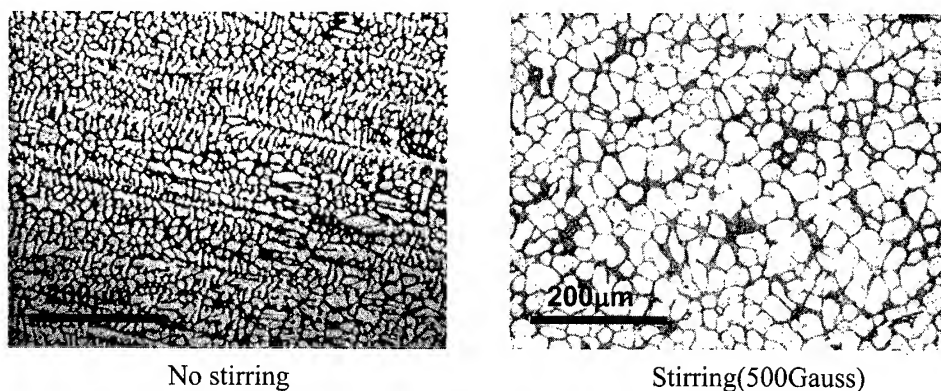


Fig. 6. Microstructures of the billet produced at a casting speed of 500mm/min.

Fig. 7 show the microstructures of the billets obtained at a different casting speed and the size and shape factor(aspect ratio) of primary crystal measured from those billets is shown in Fig. 8. The microstructure of the billet at lower casting speed was composed of more or less coarsened dendrite fragments, which are not perfectly spherical and the established fine

grained equiaxed dendritic microstructure was appeared at higher casting speed. The desired spheroidal morphology in the solid phase would be obtained only after reheating the billet into the solid-liquid region just before the thixoforming process.

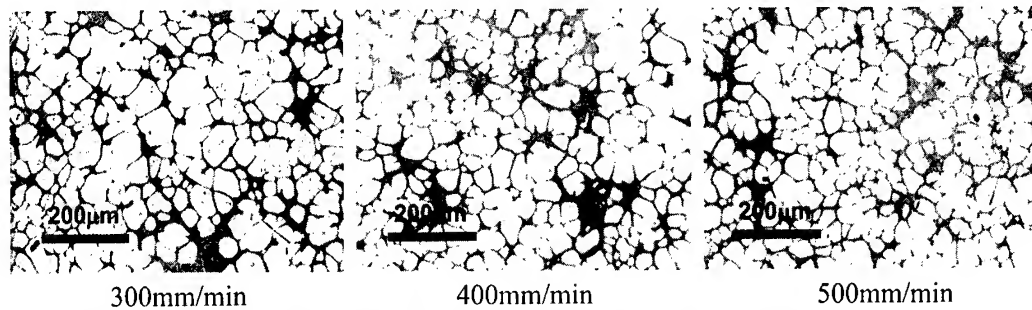


Fig. 7. Microstructures of the billets obtained at a different casting speed.

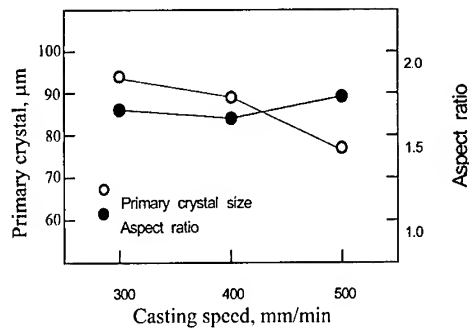


Fig. 8. The size and shape factor of primary crystal as a function of the casting speed.

5. CONCLUSIONS

A horizontal continuous casting process in combination with special mold design and electromagnetic stirring has been developed and evaluated to produce the thixotropic Al alloy billet of 3 in. in diameter and the billets were examined. A thickness of the solidifying shell was decreased with increasing the casting speed. By the stirring influence the primary crystal became to the degenerate dendrites approaching an spheroidal configuration. The established fine grained equiaxed dendritic microstructure was appeared at higher casting speed.

6. REFERENCE

1. D.B.Spencer et. al: Metallurgical Transactions, 3(1972), p.1925-32.
2. M.C.Flemings : Metallurgical Transactions B, 22B(1991), p.269-293.
3. M.P.Kenney et. al : Metals Handbook 9ed., Vol. 15, p.327-338.
4. A.I.Nussbaum : Light Metal Age, June(1996), p.6-22.
5. S.P.Midson : Proc. 4th Int. Conf. on Semi-solid processing of Alloys and Composites, The University of Sheffield, 19-21 June(1996), Sheffield, England, p.252-255.
6. H.I.Lee : Ph.D. Thesis, University of Sussex, Sussex, U.K., 1982.
7. P.A.Joly and R.Mehrabian : J. Mater. Sci., 11(1976), p.1393-1418.
8. H.K.Moon : Ph.D. Thesis, MIT, Cambridge, MA, 1990.
9. S.P.Midson and K.Brissing : Modern Casting, February(1997), p.41-43.

INTERFACIAL REACTIONS BETWEEN MOLD MATERIALS AND MOLTEN TITANIUM ALUMINIDE

Myoung-Gyun Kim, Si-Young Sung, Tae-Whan Hong, Young-Il Bae* and Young-Jig Kim

School of Metallurgical and Materials Engineering

Sungkyunkwan University, Suwon 440-746, Korea

*Hyunwoo Precision Corporation, Kyungsan 712-860, Korea

ABSTRACT

The effects of mold materials and preheat temperature during casting of titanium aluminide on metal-mold interfacial reaction were investigated. The extent of the interfacial reaction of titanium castings was determined by optical micrography, SEM, EPMA and hardness profiles. The mold materials being examined included ZrO_2 , $ZrSiO_4$, Al_2O_3 , and calcia partially stabilized ZrO_2 .

When the extent of metal-mold reaction was compared with conventional titanium alloy, the high aluminum content of Ti-47Al alloys helps to lower their reactivity in the molten state against alumina. Alumina mold is a promising mold material for investment casting of titanium aluminide in considering the thermal stability at high temperature, formability and cost of oxide.

1. INTRODUCTION

Titanium aluminide have the potential for high temperature applications because of their high specific strength, excellent creep and oxidation resistance[1]. Despite of their many advantages, potential exploitation has been hindered by the low ductility at ambient temperature and poor workability. One mean of avoiding these difficulties is through the use of investment casting.

Investment casting[2-3] is regarded as an economic processing technology for manufacturing net shape of titanium aluminide. However, the most serious barrier to use investment casting is the high reactivity of TiAl alloys in the molten state[4-5]. They are extremely reactive to mold materials at high temperature, resulting in a chemical reaction

affected-surfaces. The interstitial elements from the ceramics have a great tendency to enter into the titanium aluminide and cause the deterioration of mechanical properties of castings such as ductility, hardness and toughness[6]. However, there is little information with the interfacial reaction of metal-mold during casting of titanium aluminide.

In this study, we carried investigation into the effect of the interfacial reactions between mold materials and molten titanium aluminide on the mold materials during casting of titanium aluminide. Also, attempts have been made to evaluate the relative stability of alumina and zircon mold casting with mold preheat temperature.

2. EXPERIMENTAL PROCEDURES

2.1 Mold production

The oxides examined included ZrO_2 , Al_2O_3 , calcia partially stabilized ZrO_2 and $ZrSiO_4$. The molds were built up a wax pattern with an opening diameter of 15 mm and a height of 30 mm. Buildup was achieved by dipping the pattern in the appropriate slurry, sprinkling with a stucco, and allowing it to dry in a controlled humidity chamber, as is typical in an investment casting process. The shell were dried at controlled temperature ($23 \pm 2^\circ C$) and relative humidity ($50 \pm 10\%$) for least 4 hours. This was followed by dewaxing in an autoclave at about $150^\circ C$ at a pressure of about 0.5 MPa and then firing at $950^\circ C$ for 1 hour.

2.2 Melting and casting experiment

Titanium aluminide material of nominal composition Ti-47Al(at.%) specimen has been prepared by plasma arc melting furnace under argon atmosphere as mentioned earlier[7]. Casting experiment was carried out using 35 kHz and 30 kW vacuum induction melting furnace. The pressure of the furnace atmosphere can be controlled in the range 1.33×10^{-1} Pa by vacuum pump, and then subsequent backfilled with high purity argon at a pressure of 4.9×10^3 Pa. This cycle of evacuation and flushing with argon was repeated at least two times. The furnace was switched on and the temperature was gradually increased until the charge was melted. The power was turned off 60 s after complete melting as judged by the visual inspection and the melt was poured into the mold by tilting the crucible.

3. RESULTS AND DISCUSSIONS

3.1 Metal/mold reaction

It has been suggested earlier[8] that the relative difference of metal-mold reaction in microhardness and optical microscopy provide a good index of evaluating the relative stability of the molds. The molds for evaluating their thermal stability against Ti-47Al alloy melts were commercially used colloidal silica bonded ZrOSi_4 , ZrO_2 , calcia partially stabilized ZrO_2 and Al_2O_3 molds.

Fig. 1 illustrated the as-cast microstructure of the regions below the surfaces of the castings with different mold materials at room temperature. The hardness profiles of Ti-47Al alloy rod cast into investment mold with different mold materials are given in Fig. 1(e). The titanium aluminide castings into ZrO_2 mold show a little reaction layer, however little reaction with that occurred into ZrOSi_4 , calcia partially stabilized ZrO_2 and Al_2O_3 molds. Those results of hardness profiles correspond well with the metallographical observations as shown in Fig. 1.

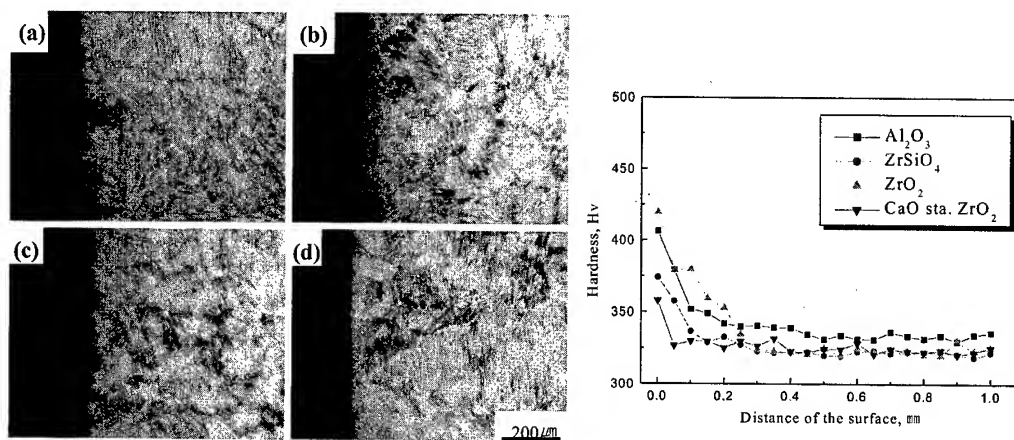


Fig. 1. Photographs showing the microstructures of regions below the surface of the as-cast of Ti-47Al alloys; (a) Al_2O_3 , (b) ZrSiO_4 , (c) ZrO_2 and (d) CaO stabilized ZrO_2 mold, and their's hardness profiles near the surface of castings.

In the similar study of R.L. Saha et al.[9], they showed the increase of bulk hardness is affected not only the stability of mold material itself but also the effect of the binder as colloidal silica. However, there is no evidence that the difference of thermal stability is influenced by the effect of binder, as mentioned by R.L. Saha et al.[9].

Especially, it is worth to note that the castings produced in Al_2O_3 mold have no reaction layer, as shown in Fig. 1(b). But, M.G. Kim[7] and T. Yoneda et al.[10] showed that the interaction of the Al_2O_3 molds for pure titanium and Ti64 alloy had clear reaction layer in the castings. This result could be explained by the work of A.K. Misra[11]. It shows that Al_2O_3 would be chemically stable in TiAl-based alloys with about 50 atomic percent Al. The high

aluminum content of Ti-Al alloys helps to lower their reactivity in the molten state against alumina.

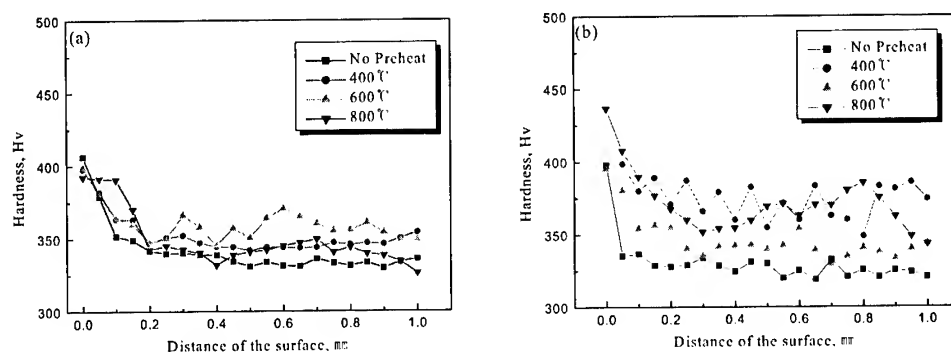


Fig. 2. Hardness profiles of Ti-47Al alloy castings produced into (a) Al₂O₃ and (b) ZrSiO₄ mold with preheat temperature.

From the these results, we chose Al₂O₃ and ZrSiO₄ mold as a candidate for mold material of titanium aluminide investment casting except for calcia partially stabilized ZrO₂ due to high cost of oxide. Fig. 2 show microhardness profiles of the Ti-47Al castings made into colloidal silica bonded alumina and zircon mold. Castings were produced in molds at room temperature and in molds preheated to 400, 600 and 800 °C. As the mold preheat temperature rises, it cannot be observed the increase of internal hardness into alumina mold(Fig. 2(a)). In Fig. 2(b), on the other hand, it can be observed that as the mold preheat temperature rises, there is a considerable increase in the internal hardness of Ti-47Al castings into zircon mold. This could be explained by the effect of mold material itself, as well as the binder with high preheat temperature.

Fig. 3 represent the EPMA elemental profiles of Ti-47Al castings made into alumina mold with the preheat temperature. In the case of 800 °C preheat temperature, silicon fluctuate in the internal of Ti-47Al castings due to an indication of silicon contamination in colloidal silica which, is used as a binder. This could be related to the hardness profiles, as shown in Fig. 2(a). On the other hand, Fig. 4 shows the EPMA elemental profiles of castings made into zircon mold with preheat temperature. As the preheat temperature of mold rises, the peaks of zirconium and silicon were obviously detected. Detection of this element in the internal castings strongly suggests that the constituents of mold materials and binder, zirconium and silicon diffuse through the surface of castings at high temperature. The increase of internal hardness supports the EPMA elemental profiles.

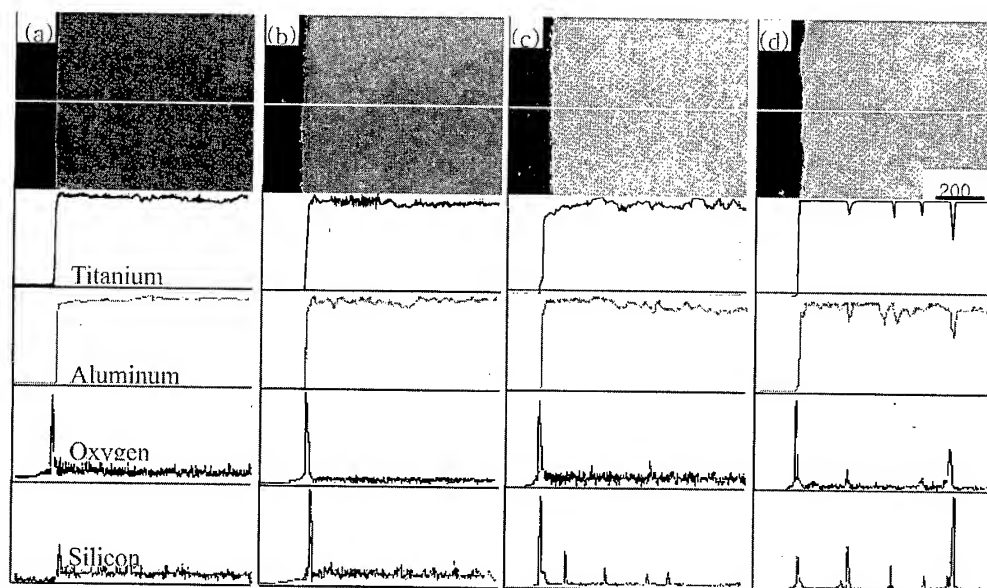


Fig. 3. EPMA elemental profiles of Ti-47Al alloy castings produced in zircon mold with preheat temperature; (a) no preheat, (b) 400 °C, (c) 600 °C, and (d) 800 °C

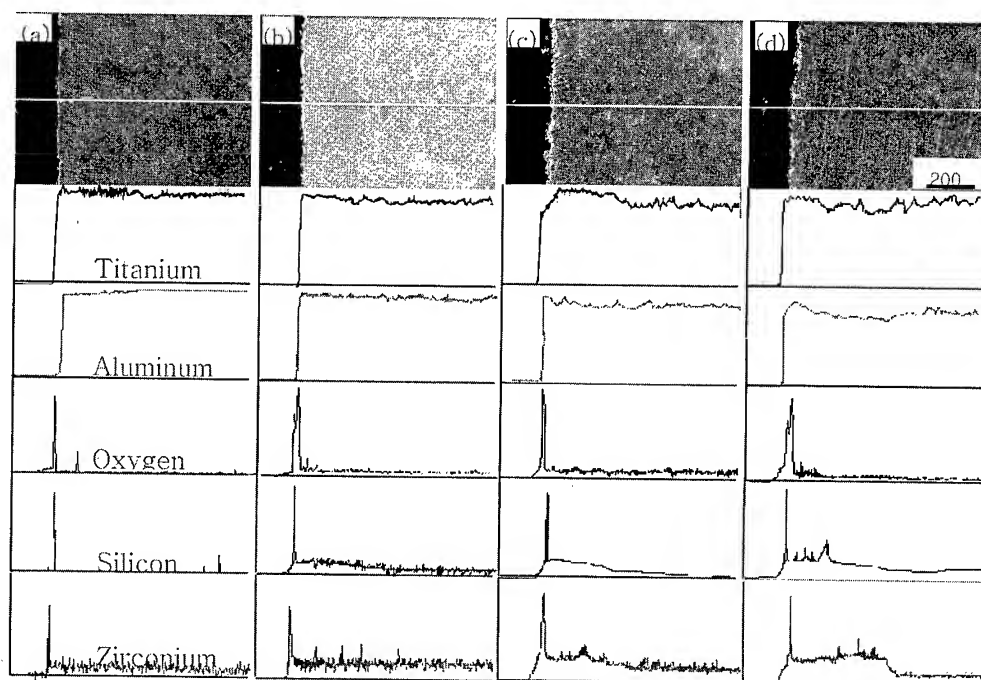


Fig. 4. EPMA elemental profiles of Ti-47Al alloy castings produced in alumina mold with preheat temperature; (a) no preheat, (b) 400 °C, (c) 600 °C, and (d) 800 °C

The selected Ti-47Al alloys in this study, but has low fluidity in pouring into investment mold. Therefore, it is necessary to consider the centrifugal casting and alloy design to improve the castability of titanium aluminide.

4. CONCLUSIONS

The major points that this paper attempts to show are the followings:

1. When compared with conventional titanium alloy, Ti-47Al alloys could be chemically stable with alumina mold.
2. Alumina mold is regarded as a promising mold material for titanium aluminide investment casting because of the thermal stability, cost of oxide and sufficient handling strength.
3. As higher temperature of mold preheat, the interfacial reaction between titanium aluminide and zircon mold is strongly affected by the zirconium and silicon of mold material itself as well as binder.

REFERENCE

1. W.Y. Kim, JOM, Vol. 6, (1989), pp. 24-30.
2. S. Isobe, Materia Japan, Vol. 25, (1996), pp. 1114-1117.
3. D.E. Larsen, L. Christodoulou, S.L. Kampe and P. Sadler, Mat. Sci. Eng. A, Vol. A144, (1991), pp. 45-49.
4. J.P. Kuang, R.A. Harding and J. Campbell, Mat. Sci. Tech., Vol. 15, (1999), pp. 840-850.
5. J.P. Kuang, R.A. Harding and J. Campbell, Mat. Sci. Tech., Vol. 16, (2000), pp. 1007-1016.
6. K. Suzuki, S. Watakabe and K. Nishikawa, J. of Japan Institute Metals, Vol. 60, (1996), pp. 734-743.
7. M.G. Kim, T.K. Kim, T.W. Hong, S.K. Kim and Y.J. Kim, J. of the Korean Inst. of Met. & Mater., Vol. 40, (2001), pp. 429-434.
8. R.L. Saha, T.K. Nandy, R.D.K. Misra and K.T. Jacob, AFS Trans., Vol. 98, (1990), pp. 253-260.
9. R.L. Saha, T.K. Nandy, R.D.K. Misra and K.T. Jacob, Metall. Trans. B, Vol. 21B, (1999), pp. 550-565.
10. T. Yoneda, T. Sato and E. Niyama, Imono, Vol. 67, (1995), pp. 619-625.
11. A.K. Misra, Metall. Trans. A, Vol. 22A, (1991), pp. 715-721.

POSTER PRESENTATION

EFFECT OF SILICON ON MICROSTRUCTURE AND MECHANICAL PROPERTIES OF TiAl BASE ALLOYS

Seung Eon Kim, Fusheng Sun*, Yong Tai Lee and Masaharu Yamaguchi**

Korea Institute of Machinery and Materials
66, Sangnam, Changwon, Kyungnam 641-010, Korea

*Beijing Institute of Aeronautical Materials, Lab.15
P.O. Box 81, Beijing 100095, China

**Department of Materials Science and Engineering, Kyoto University
Sakyo-ku, Kyoto 606-8501, Japan

ABSTRACT

Effect of silicon on microstructure and mechanical properties of $\text{Ti}_{52}\text{Al}_{48}$ base alloys was studied in a silicon range of 0.5~3at%. Distribution and formation behavior of silicide were characterized using electron microscopy, X-ray diffraction, differential thermal analysis technique. Addition of Si to the $\text{Ti}_{52}\text{Al}_{48}$ alloy yielded Ti_5Si_3 type silicide phase. Coarse primary and eutectic silicides formed during solidification. Fine secondary silicides formed at lamellar boundaries after heat treatment. Volume fraction of the α_2 phase was decreased and that of the Ti_5Si_3 phase was increased with Si content. In order to clarify the relationship between microstructure and mechanical properties, tensile tests at room and elevated temperature were carried out. In addition, creep rupture tests were also conducted at 800°C, 240MPa condition. The alloy having 0.5% Si exhibited prominent peak in creep strength as well as in tensile strength. It is believed that the peaks are related to the optimum combination in volume fraction of the α_2 and Ti_5Si_3 as well as the solubility limit of silicon in TiAl.

1. INTRODUCTION

Gamma TiAl base alloys are prospective materials for high temperature structural applications in the future. The fascinating advantages of these alloys are high specific strength, high specific creep strength, excellent stiffness retention up to high temperature and fire resistance, compared with heat resistant steels and nickel base superalloys. Unlikely this attraction, poor ductility at low temperature range, low fracture toughness and oxidation resistance drop at high temperature over 800°C have been major roadblocks to implementations [1-3]. Mechanical properties of the TiAl alloys can be improved either by alloying or by microstructure modification [4,5]. Recently, the advantage of Si in TiAl alloys has been paid attention, which is to enhance oxidation resistance and creep property of the TiAl alloy [6-8]. Some studies have been done to examine the microstructure and elevated temperature tensile deformation of the 1.4~2.7at% Si bearing TiAl alloys by powder processing [9,10], and to investigate cast microstructure and compressive behavior of the 3.0~10.0 at% Si-bearing TiAl alloys [11]. The alloying with less 0.5 at% Si to Ti-Al-Cr-Si, Ti-Al-Nb-Si, and Ti-Al-Nb-Mn-W-Mo-Si alloys have also been determined to improve the creep resistance [12-14].

However, the effect of Si itself as the third element on microstructure and mechanical properties in $\text{Ti}_{52}\text{Al}_{48}$ base alloys has been never investigated systematically yet. In the present

study, the influence of Si on characteristics of silicide formation, α_2 phase volume fraction, tensile and creep rupture properties in $\text{Ti}_{52}\text{Al}_{48-x}\text{Si}$ alloys was intensively investigated. The aim of this study is eventually to characterize the microstructural change by silicon addition, and to clarify the relationship between microstructure and mechanical properties.

2. EXPERIMENTAL PROCEDURE

Ternary alloys with the composition of $\text{Ti}_{52}\text{Al}_{48-x}\text{Si}$ ($x = 0, 0.5, 1, 2, 3\text{at}\%$) were produced by arc melting under argon atmosphere. High-purity Ti (99.9%wt.), Al (99.9% wt) and Al-Si master alloy were used. The ingots were hot-isostatic-pressed (HIPed) at 1200°C under an argon pressure of 200MPa for 3 hours, and subsequently heat-treated at 1200°C for 12 hours followed by air cooling. The tensile and creep specimens, with a size of 5 mm in diameter and 25mm in gauge length, were machined from the ingots. Tensile tests were carried out at both room temperature and 900°C using an Instron machine. Creep tests were conducted under a condition of $800^\circ\text{C}/240\text{MPa}$.

Metallographic samples were prepared by mechanical grinding and polishing. Microstructural examination was performed using SEM and TEM. For the phase identification, X-ray diffraction technique was employed with a $\text{Cu K}\alpha$ radiation and a scan rate of 0.2 degree per minute. The volume fraction of constituent phases was measured in a LECO 300 image analyzer. Differential thermal analysis (DTA) was conducted to characterize the silicide formation. The sample size for DTA experiment was 5 mm in diameter and 5 mm in height. Measurement was done during heating at a rate of $10^\circ\text{C}/\text{min}$ to 1500°C .

3. RESULTS

3.1. Microstructures

Optical microstructures of $\text{Ti}_{52}\text{Al}_{48-x}\text{Si}$ ($x=0, 0.5, 1, 3\text{at}\%$) alloys after heat treatment were shown in Fig. 1. The heat treatment at 1200°C for 12 hours resulted in a duplex microstructure of the binary $\text{Ti}_{52}\text{Al}_{48}$ alloy, consisting of equiaxed γ and $\alpha_2+\gamma$ lamellar microstructure. With the addition of Si, lamellar microstructure was maintained and amount of the coarse silicides was increased. The coarse silicides can be distinguished into two different morphologies as shown in Fig. 2a. One is a big isolated rod shape (P) and the other is a eutectic whisker shape (E). Besides the coarse silicides, fine silicides (S) were also found at the lamellar boundaries as shown in Fig. 2b. All silicides were identified to be Ti_5Si_3 type regardless of morphology and size.

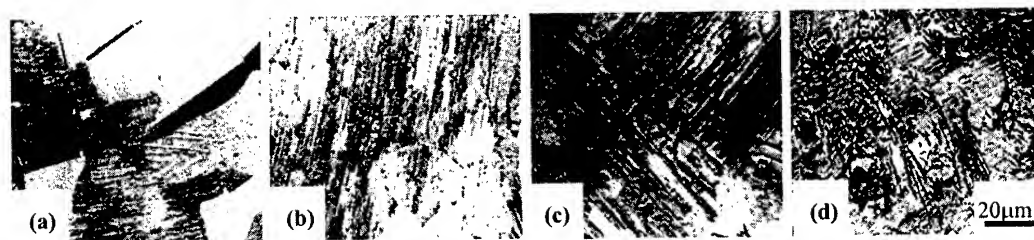


Fig. 1. Optical micrographs of $\text{Ti}_{52}\text{Al}_{48-x}\text{Si}$. (a) 0Si, (b) 0.5Si, (c) 1Si, and (d) 3Si.

X-ray diffraction analysis was performed at the 2θ range of $40\sim 42^\circ$ so as to show up the strongest (121) and (030) peaks of Ti_5Si_3 phase in contrast to α_2 peaks. As shown in Fig. 3, only (201) peak of α_2 was seen in the $\text{Ti}_{52}\text{Al}_{48}$ binary alloy. With the addition of Si up to 2at%, the two peaks of Ti_5Si_3 were presented, while the (201) peak of α_2 was weakened. With further addition of Si up to 3at%, no (201) peak of α_2 was found. This indicates that the addition of Si shifts the alloy composition to Al-rich side.

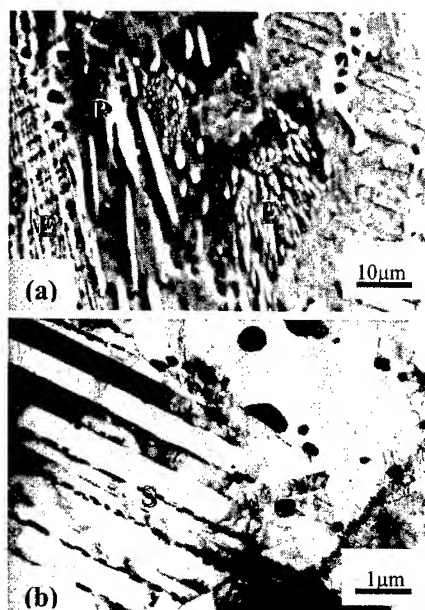


Fig. 2. Morphology and distribution of (a) coarse and (b) fine silicides.

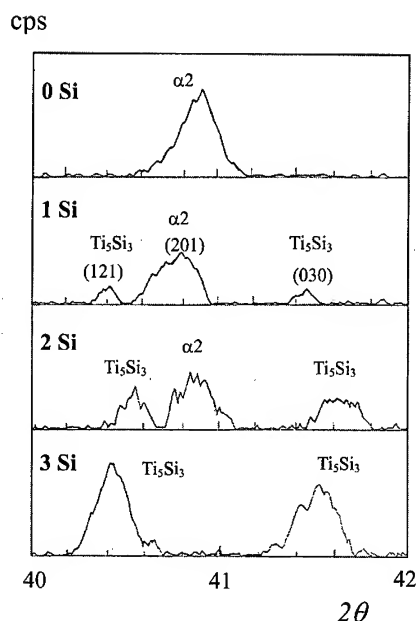


Fig. 3. Major peaks of α_2 and Ti_5Si_3 in the X-ray diffraction traces for the $\text{Ti}_{52}\text{Al}_{48-x}\text{Si}$ alloy.

Table 1 represents the variation in volume fraction for constituent phases of the $\text{Ti}_{52}\text{Al}_{48-x}\text{Si}$ alloys. The volume fraction of Ti_5Si_3 phase is increased and that of α_2 phase is decreased, respectively, with increasing Si content. Note that amount of the α_2 phase approached zero in the $\text{Ti}_{52}\text{Al}_{48-3}\text{Si}$ alloy.

Table 1. Variation in volume fraction for constituent phases of the $\text{Ti}_{52}\text{Al}_{48-x}\text{Si}$ alloys.

Si content (at%)	0	0.5	1	2	3
Ti_5Si_3 (vol%)	0	2.14	3.64	6.36	9.28
α_2 (vol%)	14.5	14.0	8.6	5.2	0

3.2. Tensile and creep rupture properties

The tensile properties at both room temperature and 900°C were determined as a function of Si content in $\text{Ti}_{52}\text{Al}_{48-x}\text{Si}$ ternary alloy as shown in Fig. 4a and 4b. The yield and ultimate tensile strengths at room temperature were remarkably increased up to 550 and 560 MPa respectively with the addition of 0.5 at% Si, which is about 120 and 150 MPa improvement compared with binary $\text{Ti}_{52}\text{Al}_{48}$ alloy. With further addition of Si, the strengths were gradually reduced. The $\text{Ti}_{52}\text{Al}_{48-3}\text{Si}$ alloy has the lowest strengths. The ductility was a little decreased with the addition of Si at room temperature. Note that $\text{Ti}_{52}\text{Al}_{48-0.5}\text{Si}$ shows virtually excellent enhancement in yield and ultimate tensile strengths at 900 °C, which maintains almost 430 and 530 MPa respectively. Strength drop with increasing Si over 1% was observed at 900°C also. Nevertheless, the $\text{Ti}_{52}\text{Al}_{48-(1\sim2)}\text{Si}$ alloys exhibit better strengths than the binary alloy and the $\text{Ti}_{52}\text{Al}_{48-3}\text{Si}$ alloy keeps almost same strengths as the binary alloy at 900°C. Fig. 5 shows creep rupture life and deformation curve against Si under a condition of 800°C/240 MPa. Excellent creep rupture strength was obtained in the $\text{Ti}_{52}\text{Al}_{48-0.5}\text{Si}$ alloy. Its creep rupture life is more than 450 hours, compared with 25.5 hours for the binary $\text{Ti}_{52}\text{Al}_{48}$ alloy in a same creep condition. A remarkable drop in the creep rupture life occurred with further addition of Si. The $\text{Ti}_{52}\text{Al}_{48-1}\text{Si}$ alloy has better creep rupture strength than the binary $\text{Ti}_{52}\text{Al}_{48}$ alloy, while the $\text{Ti}_{52}\text{Al}_{48-(2\sim3)}\text{Si}$ alloys have the almost same strength level as the binary alloy.

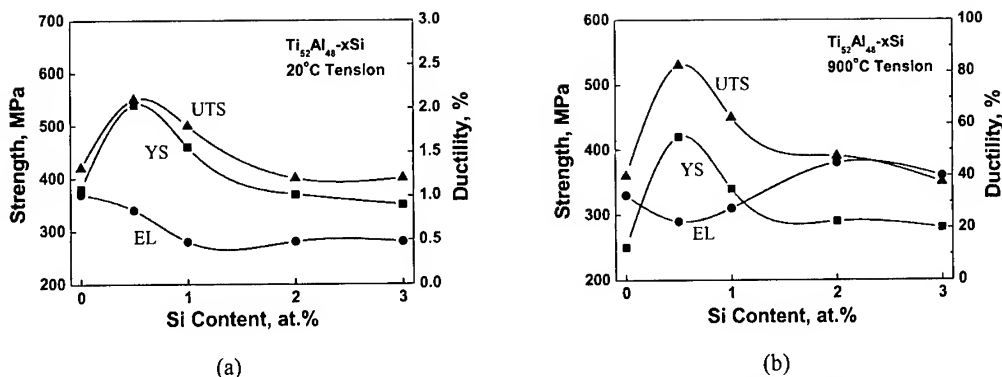


Fig. 4. Tensile properties of the $\text{Ti}_{52}\text{Al}_{48-x}\text{Si}$ alloys at room and elevated temperature.

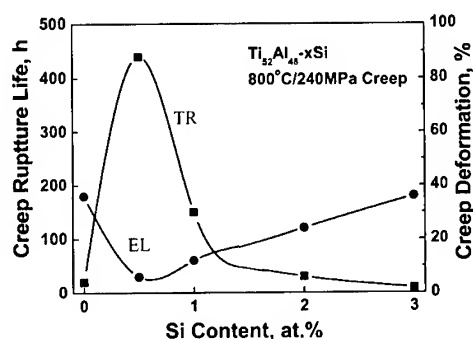


Fig. 5. Creep rupture properties of the $\text{Ti}_{52}\text{Al}_{48-x}\text{Si}$ alloys at 800°C/240MPa condition.

4. DISCUSSION

It was recognized that the addition of Si influences the microstructure of Si-bearing alloys either in silicide morphology and phase constituent. Owing to the solubility limit of Si in γ phase, addition of Si to TiAl alloys results in silicide phase. The silicide can be classified into three types based on morphology and distribution. The first one is a big isolated rod shape in matrix and the second one is a eutectic whisker shape at interdendritic region. The final one is a fine silicide at γ/γ boundaries. The former two types of coarse silicides are formed from liquid. It can be recognized from the DTA curves as shown in Fig. 6 that the primary rod shape of silicide is formed at higher temperature than the liquidus ($L=\text{Ti}_5\text{Si}_3$), and the whisker shape of silicide is formed by eutectic reaction ($L_1=\alpha+\text{Ti}_5\text{Si}_3$). The solidification sequence of Si bearing TiAl alloy can be interpreted from the DTA curve for the $\text{Ti}_{52}\text{Al}_{48-2}\text{Si}$ alloy on behalf of other alloys. Before the matrix solidification, the primary silicide formation takes place at 1468°C (P), and then the primary α phase begins to solidify at 1453°C (T_L). Eutectic silicide is formed at 1432°C (E) before the solidification of the primary phase is finished at 1411°C (T_S).

The similar solidification behavior happened in the $\text{Ti}_{52}\text{Al}_{48-1}\text{Si}$ and $\text{Ti}_{52}\text{Al}_{48-3}\text{Si}$. However, the two different peaks related to silicide formation in the $\text{Ti}_{52}\text{Al}_{48-0.5}\text{Si}$ alloy were hardly detected. Unlike coarse silicides, fine silicides at lamellar boundary are formed during heat treatment as well as solidification, and those are found in all Si bearing alloys. The fine silicides play a role of effective barrier to hinder the lamellar or grain boundary migration

during heat treatment. Therefore, after heat treatment at 1200 °C for 12 hours, the Si bearing alloys do not undergo recrystallization and maintain lamellar microstructure, while the Si free binary alloy is recrystallized and have a typical duplex microstructure, as shown in Fig.1.

In this study, the volume fraction of α_2 phase was decreased with Si content and eventually approached zero in the $\text{Ti}_{52}\text{Al}_{48}$ -3Si alloy, as depicted in Table 1. This is interpreted as follows. Ti combines with Si to make silicide and thus actual matrix composition moves toward Al rich side with Si addition, although the average alloy composition maintains $\text{Ti}_{52}\text{Al}_{48}$. For this reason, it is obvious that the actual matrix composition of $\text{Ti}_{52}\text{Al}_{48}$ -3Si alloy is very close to single γ phase.

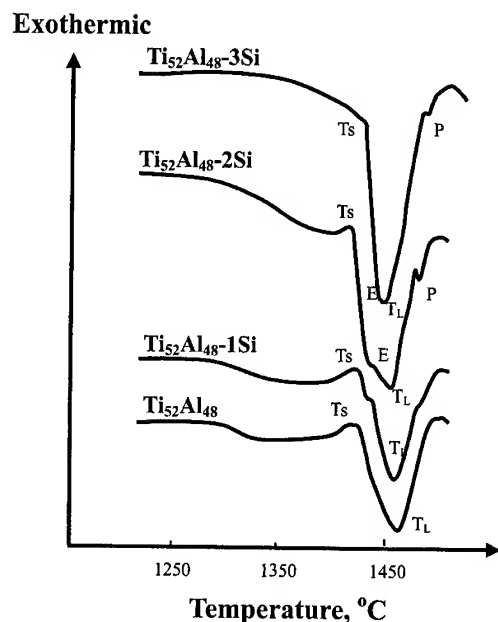


Fig. 6. DTA curves of the $\text{Ti}_{52}\text{Al}_{48}$ -xSi.

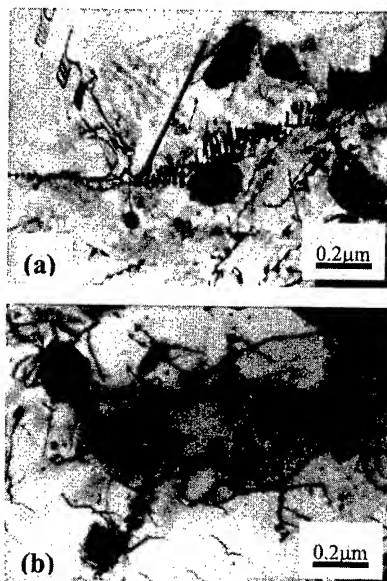


Fig. 7. Interaction between silicide and dislocations at (a) 20°C tension and (b) 800°C creep.

The significant improvement of yield and ultimate strengths at room and elevated temperature by addition of 0.5at% Si can be attributed by two factors. Firstly, the precipitation strengthening of fine Ti_5Si_3 particles plays the most important role in enhancing the strengths. Fig. 7a demonstrated the interaction of Ti_5Si_3 particles and dislocations in the $\text{Ti}_{52}\text{Al}_{48}$ -0.5Si alloy after room temperature deformation. The twinning and mostly the $a/2[110]$ dislocation are dominant. Occasionally can be seen the $a/6[112]$ partial dislocations and $[111]$ stacking fault. Plenty of fine Ti_5Si_3 particles impede dislocation slip, which benefits the improvement of strengths. Secondly, the optimum volume fraction of α_2 phase in the $\text{Ti}_{52}\text{Al}_{48}$ -0.5Si, which is comparable to that in the binary $\text{Ti}_{52}\text{Al}_{48}$ alloy, may give rise to good strengths. Therefore, the prominent jump in strength at 0.5%Si must be related to a synergy effect of the two factors, that is, precipitation hardening and γ/α_2 lamellar boundary strengthening. The present study showed that the addition of Si causes the decrease of α_2 volume fraction with increasing Si over 1%. The evident decrease of strengths with further Si addition up to 1.0~3.0 at% at both room and elevated temperature can be mainly elucidated by the reduction of α_2 volume fraction. Meanwhile, the coarse silicides abundant at higher Si content over 1% are presumed not to decrease the strengths, but to decrease the elongation.

The excellent creep resistance of $\text{Ti}_{52}\text{Al}_{48}$ -0.5Si alloy results from the precipitation of Ti_5Si_3 particles in γ phase. From the creep mechanism, diffusion, dislocation climb and dislocation slip would affect the creep rupture life of the TiAl alloys. The Ti_5Si_3 particles provide effective barrier to hinder the dislocation slip. The dislocation pinning by Ti_5Si_3

particles is the most important factor to enhance the creep rupture life because that the dislocation slip is the main creep mechanism at 900 °C under a high stress level of 240MPa. Figure 7b shows the micrograph of the pinning of dislocation by Ti_5Si_3 particles in 0.5% Si bearing alloy during creep. Most of the dislocations have the burgers vector of $1/2\langle 110 \rangle$, with a few of $1/2\langle 101 \rangle$ dislocations. In addition to the dislocation pinning by Ti_5Si_3 , some curved dislocation lines were observed. It was most possibly hindered by Si-rich region. The impeding of Ti_5Si_3 particles to the movement of creep dislocation also be found in other TiAl alloys [14]. Furthermore, the stabilized lamellar microstructure by silicide particle would benefit the creep resistance. With further increase of Si content, the reduction of α_2 volume fraction is responsible for the decrease of creep rupture life.

5. CONCLUSIONS

Effect of silicon on microstructure and mechanical properties of TiAl base alloys can be summarized as follows.

- 1) The addition of Si to $\text{Ti}_{52}\text{Al}_{48}$ alloy results in Ti_5Si_3 type silicide phase. Coarse primary and eutectic silicides are formed during solidification. Fine secondary silicides are formed at lamellar boundaries after heat treatment. The volume fraction of α_2 phase is decreased with increasing Si. The Ti_5Si_3 particles effectively stabilize the lamellar microstructure during heat treatment even at $\alpha+\gamma$ two phase region.
- 2) The addition of 0.5% Si to $\text{Ti}_{52}\text{Al}_{48}$ alloy enhances not only creep resistance but also tensile strengths at room and elevated temperature. This must be related to the optimum combination in volume fraction of the α_2 and Ti_5Si_3 . The decrease of tensile strengths and creep rupture life with further addition of Si over 1% results from the decrease of α_2 phase.

REFERENCES

1. M. Yamaguchi and H. Inui, in Structural Intermetallics, R. Darolia, J. J. Lewandowski, C. T. Liu, P. L. Martin, D. B. Miracle and M. V. Nathal, eds., TMS, Warrendale, PA, (1993) pp.127-142
2. C.M. Austin and T.J. Kelly, in Structural Intermetallics, R. Darolia et al., eds., TMS, Warrendale, PA, (1993) pp.143-150.
3. Y.-W. Kim, J. Met. Vol.46 (1994) pp.30-39.
4. Y.-W. Kim and F.H. Froes, in High Temperature Aluminides and Intermetallics, S.H. Whang, C.T. Liu and D. Pope, eds., TMS, Warrendale, PA, (1990) pp.465-492.
5. E.L. Hall and S.C. Huang, in Microstructure/Property Relationships in Titanium Aluminides and Alloys, Y.W. Kim and R.R. Boyer, eds., TMS, Warrendale, PA, (1991) pp.47-64.
6. S. Mitao and S. Tsuyama, in the 2nd Japan Int. SAMPE Symposium, (1991) p.410.
7. K. Maki, M. Shioda, M. Sayashi, T. Shomizu and S. Isobe, in High Temperature Aluminides and Intermetallics, S.H. Whang, C.T. Liu and D. Pope, eds., TMS, Warrendale, PA, (1991) pp.591-596.
8. B.G. Kim, G.M. Kim, and C.J. Kim, Scripta Metall., Vol.33, (1995) p.1117.
9. G.-X. Wang, B. Dogan, F.-Y. Hsu and M. Dahms, Metall. Trans. A, Vol. 26A, (1995) p.691.
10. F.-Y. Hsu, G.-X. Wang, H.-J. Klaar, Scripta Metall., Vol.36, (1997) p.497.
11. L.T. Zhang, G.H. Qiu and J.S. Wu, Scripta Metall., Vol.33, (1995) p.1683
12. G. Frommeyer, W. Wunderlich, Th. Kremser and Z.G. Liu, in High Temperature Aluminides and Intermetallics, S.H. Whang, C.T. Liu and D. Pope, eds., TMS, Warrendale, PA, (1991) pp.166-172.
13. S. Tsuyama, S. Mitao and K.N. Minakawa, in High Temperature Aluminides and Intermetallics, S.H. Whang, et al., eds., TMS, Warrendale, PA, (1991) pp. 451-456.
14. D.Y. Seo, S.U. An, T.R. Bieler, D.E. Larsen, P. Bhowal, and H. Merrick, in Gamma Titanium Aluminides, Y.W. Kim, R. Wagner, and M. Yamaguchi, eds., TMS, Warrendale, PA, (1995) pp.745-752.

Development of Fine Microstructure of B.390 Casting Alloy by the Modification of Ca Amount

Heon-Joo Kim, Moo-Kil Kim, Byong-Ho Jung and Kwang-Jin Son

Department of Metallurgical Engineering
Pukyong National University
San100, Yongdang-dong, Nam-gu, Pusan 608-739, KOREA

ABSTRACT

Refinement of primary silicon particles of hypereutectic Al-Si alloy, B.390 alloy, was examined.

This work focused on the modification processes of B.390 alloy for the refinement of primary silicon particles, and its effects on tensile properties and impact property. In the present investigation, a very effective and new method, that is, a control of calcium content in the melt was developed. Control of calcium content by addition of Ti_2Cl_6 degassing agent in the melt was successful in the refinement of primary silicon particles of the alloy. Minimum size of primary silicon particles obtained in this study was about $20\ \mu m$ when residual amount of Ca element in the alloy was 4 ppm. Application of this method gave a satisfactory result to refine the particles; the microstructure composed of very fine $20\ \mu m$ primary silicon particles as compared to that of $40\ \mu m$ primary silicon particles by AlCuP method which is known as the most effective method at present.

Refinement of primary silicon particles led to the improvement of mechanical properties of the alloy, especially in elongation.

1. INTRODUCTION

Hypereutectic Al-Si alloys are widely studied in detail because of their excellent properties, such as favorable tribological behaviors, high temperature strength, low coefficient of thermal expansion and high strength to weight ratio. The hypereutectic Al-Si alloys, therefore, are recognized to be potential candidates material for automotive applications such as engine block, piston and cylinder block, etc[1].

In order to ensure their reliable application in such a service condition and develop the alloy as a candidate for new composite material, in which inexpensive and simple processing is required, a research is indispensable on a microstructure with an uniformly distributed very fine primary silicon particles in modified eutectic matrix of Al-Si alloy.

Various methods to refine the primary silicon particles have been utilized up to the current point such as a rapid cooling, a low temperature casting or a high pressure casting. However, because of the problems such as the rapid cooling method becoming difficult to control its cooling speed uniformly in a material and the rest of the methods processes being complicated, the microstructure control with a minor-element addition is being popularly utilized.

Phosphorus has been mostly used as a refinement of primary silicon for hyper-eutectic Al-Si alloy that provides nucleation sites for silicon crystals by forming AlP in the melts. The AlCuP refiner in which AlP was already formed by sintering CuP with Al powder is now being widely utilized.

It is still a fact that the study falls short in applying the realistic operation.

With attention to the availability of this alloy, consistent researches have been performed by this researcher specially aimed at enhancing the degree of a refinement of the particles and tribological behaviors. In company with a study of calcium effect on the modification of eutectic Al-Si alloy[2] recently, attention has been directed to the effect of calcium which is already contained in metallic silicon as impurity. In process of the study of refining treatment

in hypereutectic Al-Si alloy, a very effective and new method to control calcium content in the melt was developed.

This work focused on the new modification processes in B.390 alloy for the refinement of primary silicon particles, that is, control of calcium content only by the addition of Ti_2Cl_6 degassing agent in the melts. Refining effect was also reviewed from the results of tensile and impact tests besides microstructural observation.

2. EXPERIMENTAL PROCEDURES

The material used in this study was B.390 alloy, whose chemical composition in wt.% is 18.7Si, 4.0Cu, 0.56Mg, 0.68Zn, 0.13Mn, 1.0Fe and balance of Al. The temperature was held at 750°C after melting, and degassing treatment was subsequently carried out by adding titanium chloride (Ti_2Cl_6) to be equal to 1.5% of the molten metal per each degassing treatment. Then, the molten metal maintained at 750 °C for 30 min. was poured into a metal mold for tensile specimen preheated at 100°C with dimensions of 260 (wide) \times 300 (height) \times 35mm (thick).

To investigate the effect of calcium content on the refinement of primary silicon, calcium content in each casting alloy was changed to be contained 45 ppm, 140 ppm or 190 ppm in the melts, along with reducing calcium content through the numerous treatments of the chloride agent within the melts.

Refining treatment of primary silicon and degassing treatment of the melt were done at the same time as one process in this study. The number of adding times of degassing agent, titanium chloride in each casting alloy was changed as shown in table 1.

Optical microscope equipped with a computer image analyzer was employed to observe the microstructure of specimen. Every data of primary silicon size was measured from the image of 5 pieces photographs taken 100 magnifications by a computer image analyzer. Tensile tests were performed at room temperature at a strain rate of $2.7 \times 10^{-4} \text{ s}^{-1}$ using an Instron type machine. The ultimate tensile strength and elongation were measured from the tensile test results.

Charpy impact tests were conducted on a standard size specimen using a Computer Aided Instrumented tester[3], and E_i (crack initiation energy) and E_p (crack propagation energy) energy were characterized from the test result. Fracture surfaces of the specimens were also characterized using SEM.

Table 1 Modification procedure and Retained Ca amount.

Modification procedure		Retained Ca content*
4 times degassing	4 times of degassing treatment	4ppm Ca
1 time degassing	1 time of degassing treatment	11ppm Ca
Ca addition	Addition of Al-Ca	45ppm Ca
Ca addition	Addition of Al-Ca	140ppm Ca
Ca addition	Addition of Al-Ca	190ppm Ca

* Measured by ICP method from test specimen

3. EXPERIMENTAL RESULTS AND DISCUSSION

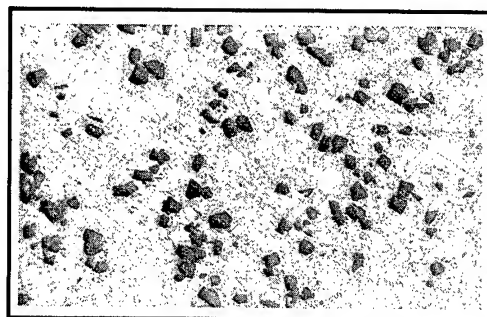
3.1 Refinement of primary silicon

The microstructure of this B.390 alloy was composed of α dendrite, eutectic silicon, α compound with Chinese script form and β intermetallic compound ($\text{Al}_3\text{Fe}_2\text{Si}$) as well as primary silicon with the shape of polygon.

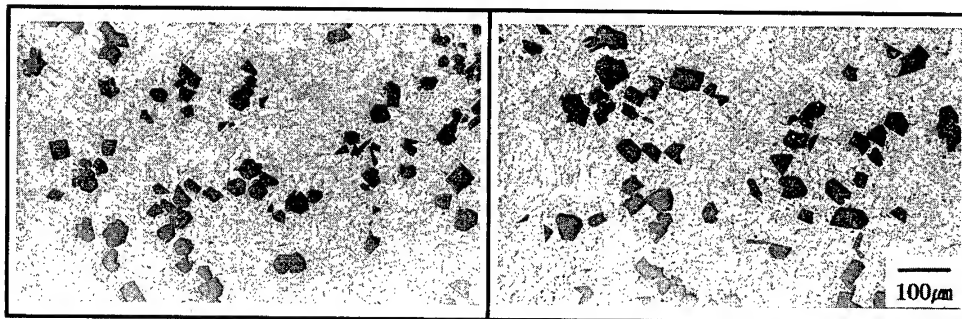
To observe the effect of calcium content on refining primary silicon, calcium content was

changed as shown in Table 1. Typical microstructures of B.390 alloy containing various amounts of calcium are shown in Fig.1. Fig.2 indicates the effect of number of times of degassing treatment on the refining primary silicon.

These figures show that control of calcium in the melts refines the primary silicon particles. The particles become more fine and uniformly distributed as the calcium content decreases. On the other side, it is found that the shape of eutectic silicon changes to needle type and the eutectic portion is uniformly distributed with decreasing calcium content.



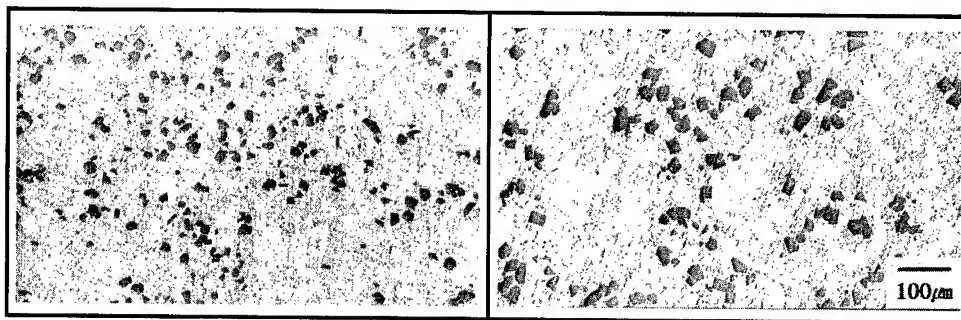
(a) 45ppm Ca



(b) 140ppm Ca

(c) 190ppm Ca

Fig.1 Effect of Ca content on primary Si size in steel mold cast B.390 alloys.



(a) 4 times of degassing treatment
(4ppm Ca)

(b) 1 time of degassing treatment
(11ppm Ca)

Fig.2 Effect of number of times of degassing treatment on primary Si size in steel mold cast alloys.

Figure 3 shows the effects of calcium on the refining primary silicon particles. When calcium was intentionally added as in case of the specimen being calcium content of 190 ppm, diameter of the particles appeared to be 54.7 μm . Whereas, for the specimen being calcium content of 4 ppm that was degassing treated for 4 times with chloride degassing agent,

diameter of the particles was 20.3 μm , and it was the most fine in this study. As can be seen from this figure, notable refinement of primary silicon particles was accomplished with decreasing calcium content.

It is generally known that a small addition of calcium is effective in the modification of eutectic silicon shape, as well as sodium[2, 4]. The experimental results of S. Z. Lu et al showed that this modification effect is due to a decrease in the eutectic temperature[5]. According to the results of thermal analysis in the present work as shown in Table 2, a slight decrease in the eutectic temperature was also found as the calcium content increased. Reducing calcium content in the melts that was accomplished through the numerous treatments of the chloride degassing agent within the melts caused to the refinement of primary silicon particles in B.390 alloy. Under the influence of chloride reacting with calcium during degassing treatment[6], it is assumed that the calcium content decreases in the melt. Chloride is known to have a strong affinity with calcium and sodium. However, phosphorus is effective element as a refiner for the primary silicon particles, and phosphorus combines with calcium to form Ca_3P_2 and slag-off when calcium content is high in the melt.

Sodium also acts as harmful element in refining the primary silicon particles because of the consumption of phosphorus by the formation of NaP during refining treatment.

From the viewpoint of phosphorus conservation, control of sodium and calcium content in the melts by the chloride degassing agent can be considered as to be beneficial for the refinement of primary silicon particles.

Examination of the exact correlation between the refinement of primary silicon particles and calcium content in hypereutectic Al-Si alloy is left unsolved yet. This new method is, for all that, a very effective and convenient in refining primary silicon particles of hypereutectic Al-Si alloys.

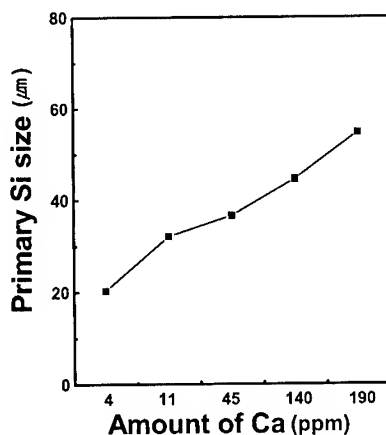


Fig.3 Effect of Ca amount on primary Si size in steel mold cast B.390 alloys.

3.2 Mechanical properties

Figure 4 and Fig.5 show the effect of calcium content on tensile strength and elongation, respectively. The tensile strength increases a little, while the elongation, although very small, increases remarkably as the calcium content decreases. Depending on the results of previous work about hypereutectic Al-Si alloy, improvement of tensile properties was accomplished mainly by the modification of eutectic silicon rather than the refinement of primary silicon particles[7]. Despite of general trend toward the degradation of properties by needle shape of eutectic silicon, these improvements could be considered to attribute the prominent refinement of primary silicon particles by the control of calcium content. And the refinement effect of large hard phases such as primary silicon that occur stress concentration in the matrix was reflected sensitively in the increase of elongation rather than tensile strength[7].

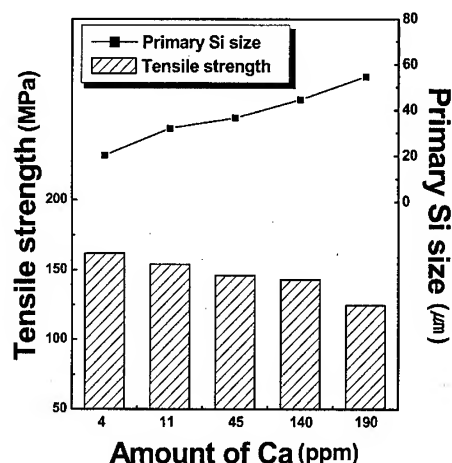


Fig.4 Effect of primary Si size on tensile strength in steel mold cast B.390 alloys.

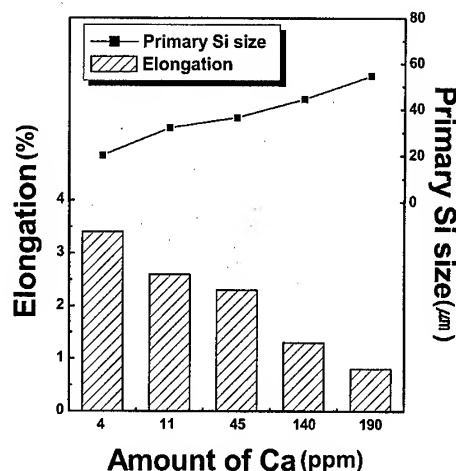


Fig.5 Effect of primary Si size on elongation in steel mold cast B.390 alloys.

Impact absorbed energy obtained from standard V notch specimens is shown in Fig.6 as a function of calcium content. The energy increases as the calcium content decreases. The refinement of primary silicon particles due to the decrease in calcium content increases the absorbed energy. While the total absorbed energy increases as the calcium content decreases, the value of absorbed energy for crack propagation is nearly the same. Even though the particles are refined relatively, the hypereutectic Al-Si alloy has still the characteristic of brittleness. Once crack initiates, it easily connect to a catastrophic fracture of overall specimen. It means that the energy for crack propagation is almost constant in this study. Therefore, the refinement of primary silicon contributes to the increase in the absorbed energy for crack initiation.

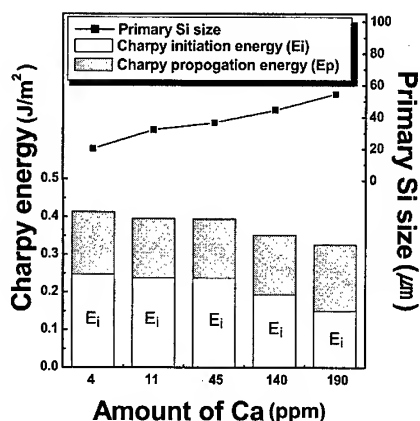


Fig.6 Effect of primary Si size on Charpy energy in steel mold cast B.390 alloys.

Figure 7 exhibits the effect of the particles size on the appearance of fracture surface in Charpy impact test.

Fracture occurs by the decohesion of the interface between the particles and the eutectic matrix being the weakest link[8]. As the mean free path between the particles decreases with decreasing the particle size, absorbed energy increases, and the fracture surface looks fine.

Refinement of primary silicon particles led to the improvement of mechanical properties of the alloy, especially in elongation.

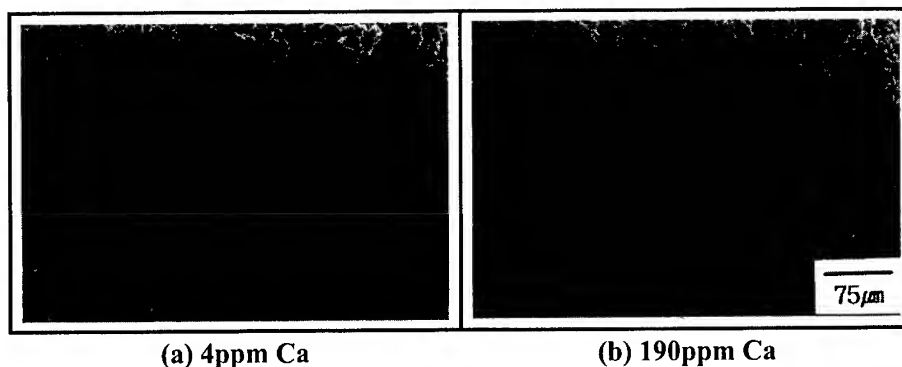


Fig.7 SEM fractographies of the Charpy test specimens with different Ca content.

4. CONCLUSION

From an experiment about the primary silicon refinement in purpose of improving the mechanical properties of hypereutectic Al-Si alloy, the following results were obtained.

1. Control of calcium content in the melt was successful in the refinement of primary silicon particles of B.390 aluminum casting alloy.
2. The refinement of primary silicon particles of the alloy by lowering calcium content was accomplished only through the numerous treatments of the chloride degassing agent within the melts.
3. The minimum size of primary silicon particle obtained in this study was about 20 μm when residual amount of calcium in the alloy was 4 ppm.
4. Refinement of primary silicon particles led to the improvement of mechanical properties of the alloy: tensile strength, elongation and Charpy absorption energy increased as the size of primary silicon particles decreased.
5. This method for the refinement of primary silicon particles has the characteristics of inexpensiveness and convenience.

REFERENCES

1. N. Tenekedijiev and J. E. Gruzleski, *Cast Metal*, Vol.3(1990), p.96.
2. T. Kobayashi, H. J. Kim and M. Niinomi, *Mater. Sci. and Tech.*, Vol.13(1997), pp.497-502.
3. T. Kobayashi, I. Yamamoto and M. Niinomi, *J. Test Eval.*, Vol.21(1993), pp.145-153.
4. John E. Hatch: *Aluminum properties and physical metallurgy*, ASM, Metals Park, Ohio(1984), p.349
5. S. Z. Lu and A. Helawell, *Metall. Trans. A*, Vol.18A(1987), pp.1721-1735.
6. C. J. Osborn, *J. Met. Trans, AIME*, Vol.188(1950), p.600.
7. N. Tenekedijiev D. Argo and J. E. Gruzleski, *AFS Trans.*, Vol.97(1989), pp.127-136.
8. P. Mandal, A. Saha and M. Chakraborty, *AFS Trans.*, Vol.99(1991), pp.643-651.

Plasma Nitriding Properties of Ti-aluminide Intermetallic Compounds Fabricated by Hot-Pressing

J. Y. Son* and Y. W. Park

College of Metals & Materials Engineering
Sungkyunkwan University
300 Chunchun-dong, Suwon, Korea, 440-746

ABSTRACT

The purpose of this study is to investigate the effect of plasma nitriding on TiAl by fabricated hot-pressing. This work was to analysis surface characteristics of the sintered Ti-aluminide intermetallic compounds by hot-pressing and surface hardening by plasma nitriding treatment.

The composite powders were pressed at 4500psi in room temperature and then sintered by hot-pressing. Hot-pressing were carry out at temperature ranges from 1200°C to 1250°C under pressure of 45MPa for 1hour in vacuum condition(10^{-2} torr). Plasma nitriding was performed for TiAl at temperature ranges from 800°C to 900°C, for 1 and 4hours, in case of atmosphere of N₂/H₂ ratio is 25%, 50%, 75% and then gas pressure is 3torr.

Surface hardening of TiAl Intermetallic Compounds improved by plasma nitriding and increasing plasma treatment time. Diffusion layer increased with increasing plasma nitriding time.

1. INTRODUCTION

TiAl is an intermetallic compound with L₁₀ structure which exists over a wide range of Ti-Al composition. It is very difficult to work this material plastically, even at temperatures > 1273K when conventional methods such as hot forging, hot rolling and hot extrusion can used. A futher method of overcoming the poor workability is fabrication of near net shaped bulk components using powder metallurgy techniques. These techniques also have the advantage of microstructural control. Nitriding techniques are commonly used to improve the fatigue and wear resistance of metals and alloys[1]. In particular, plasma nitirding has a number of advantages over conventional nitriding including faster growth rates of nitirding layers, easier control over the crystal structure of nitrided layers and fewer environmental problems[2]. Several investigations on plasma nitriding have been done for titanium and titanium alloys[3-4], but so far there have been few investigations on titanium aluminides.

In the present work, the plasma nitirding of titanium aluminides fabricated by hot-pressing is investigated. The sintering, nitriding parameters and characteristics of the nitrided layers are discussed[5-10].

2. EXPERIMENTAL PROCEDURES

Titanium (purity : 99.7%, -325mesh) and aluminium (purity : 99.9%, -200mesh), totaling 40g, were mixed with ratio of 52 at% to 48 at%. These powders were mixed at least during 48 hr by mixer and the composite powders were pressed at 4500psi in room temperature.

2.1. Sintering

Pouring the specimen into graphite mold, heating the graphite mold in approximately 1hr to temperature of 1523K in a vacuum of 3×10^{-2} Torr, holding for 1hr at this temperature, pressing for at pressures of 45Mpa during holding and finally cooling in the furnace.

The densities of hot-pressing sintered specimens were determined via the Archimedes method by weighing in alcohol and air. Metallographic cross-sections were examined in optical and scanning electron microscopes (SEM). X-ray diffraction patterns were obtained from polished specimens in the Bragg-Brentano geometry using a Cu. A hardness were examined in Vickers hardness (100g load, 10s dwell time)[11-12]

2.2. Plasma nitriding

Specimens with dimensions of 20mm×30mm×10mm were then cut from sintered TiAl using a low speed diamond saw. This specimen surface was then polished with 1500grit emery paper. Before plasma nitriding, all specimens were cleaned ultrasonically in acetone to remove surface grease.

Plasma nitriding was carried out in self-production furnace. Before nitriding, the specimens were sputtered with Ar gas (1.5×10^{-1} Torr) to remove compound of oxygen. After nitriding, the specimens were cooled in a vacuum. In order to investigate the relation between treatment parameters and surface properties, three treatment parameters were considered : nitriding temperature, nitriding time, and nitrogen-to-hydrogen (N_2/H_2 ratio).

The microstructures of the nitrided layers were studied by X-ray diffraction , optical microscopy (OM), scanning electron microscopy (SEM), and micro-vickers tester[13-14].

3. RESULTS

3.1. Sintered TiAl

Fig. 1. shows the cross-section of sintered TiAl. This fig show pores, lamellar structures and α -TiAl. The relative density was measured using the Archimedes method. Density was measured at 98%. The microhardness of sintered TiAl was about Hv 287.

XRD results shown in Fig. 2. indicate that cross-section is mainly composed of TiAl and Ti_3Al .

3.2. Plasma nitrided TiAl

The detailed reaction mechanism in the plasma nitriding process has not been clarified yet. However, to explain the plasma nitriding reaction in TiAl and Ti_3Al , we propose the four-step mechanism. One step : when the N^+ ions hit the surface of workpiece, metal atoms (Ti and Al) are detached and the workpiece is heated, allowing N^+ ions to be sputtered onto the clean

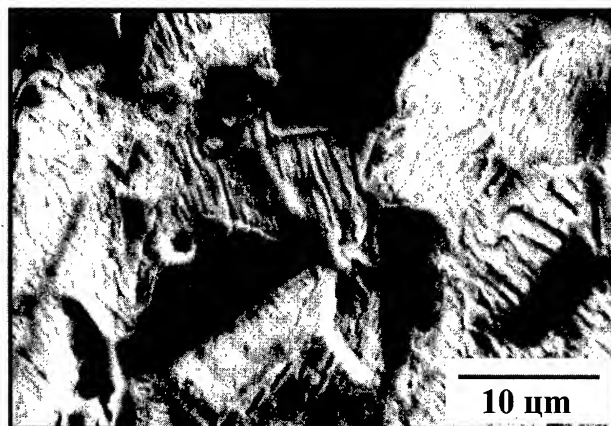


Fig. 1. Cross-section of sintered TiAl.

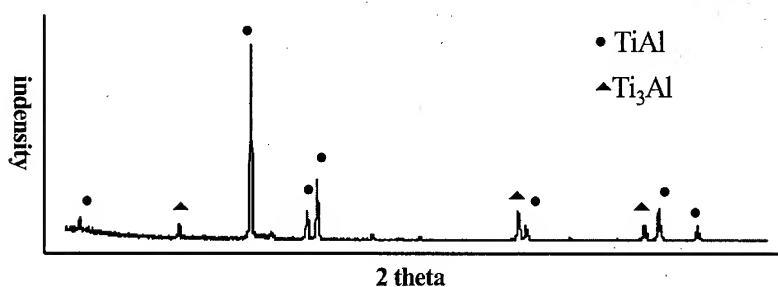


Fig. 2. XRD patterns of sample sintered at 1523K for 1hr.

surface. Two step : Ti and Al atoms which are detached from the surface can react with reactive nitrogen atoms in the plasma region near the surface of workpiece. Three step : TiN and AlN deposited on the workpiece surface is composed of a greater amount of TiN than AlN (Because the chemical affinity of Ti and N is stronger than that of Al and N). Four step : TiN becomes the main phase in the outer surface and then N atom diffuse into workpiece.

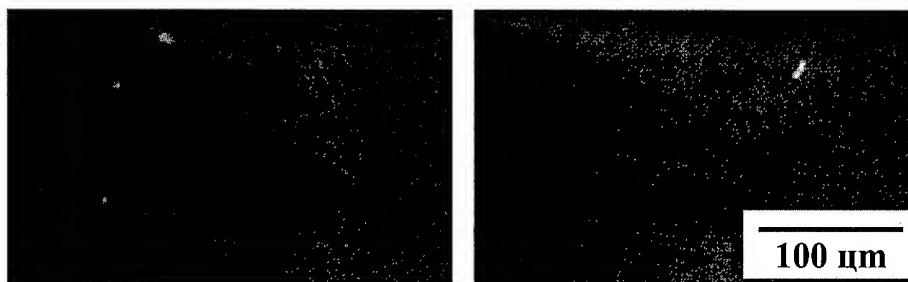


Fig. 3. The color of nitrided TiAl surface a) Nitriding for 1073K, 1hr, 25% (N_2/H_2 ratio)
b) Nitriding for 1073K, 1hr, 75% (N_2/H_2 ratio)

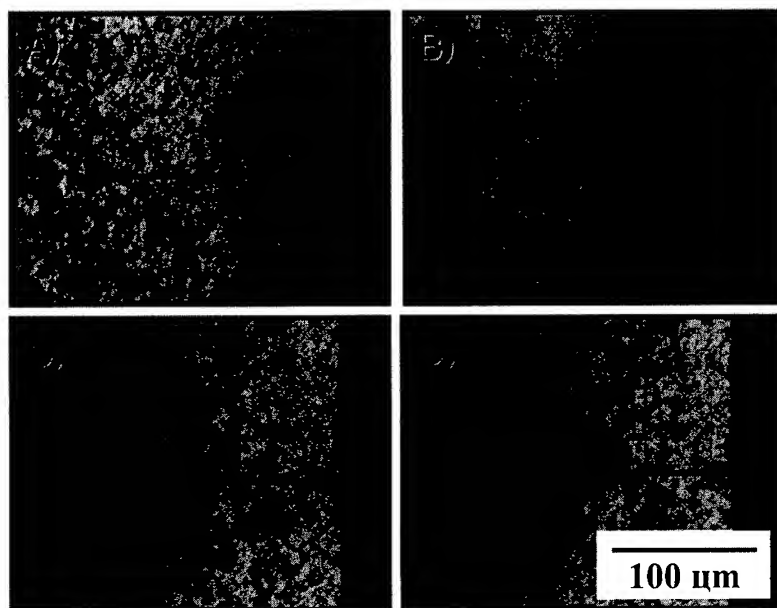


Fig. 4. Cross-section of nitrided TiAl

(a) Nitriding for 1173K, 4hr, 75% (N_2/H_2 ratio), b) Nitriding for 1173K, 1hr, 75% (N_2/H_2 ratio), c) 1173K, 1hr, 25% (N_2/H_2 ratio), d) Nitriding for 1073K, 1hr, 75% (N_2/H_2 ratio))

Fig. 3. show the color of nitrided surface which depend on gas ratio. The increase of nitrogen ratio change the color of surface from brown (Fig. 3. a) to golden yellow (Fig. 3. b)), because of formed TiN increased in the nitrided surface.

Fig. 4. show the depth of diffusion layer according to three process parameters. To compare Fig. 4. b) with Fig. 4. a), according as nitriding time increased ranges from 1hr to 4hr, nitriding rayer increased ranges from 144 μ m to 177 μ m. To compare Fig. 4. c) with Fig. 4. a), according as gas ratio increased ranges from 25% to 75%, nitriding rayer increased ranges from 118 μ m to 177 μ m. To compare Fig. 4. d) with Fig. 4. b), according as nitriding temperature increased ranges from 1073K to 1173K, nitriding layer increased ranges from 110 μ m to 144 μ m.

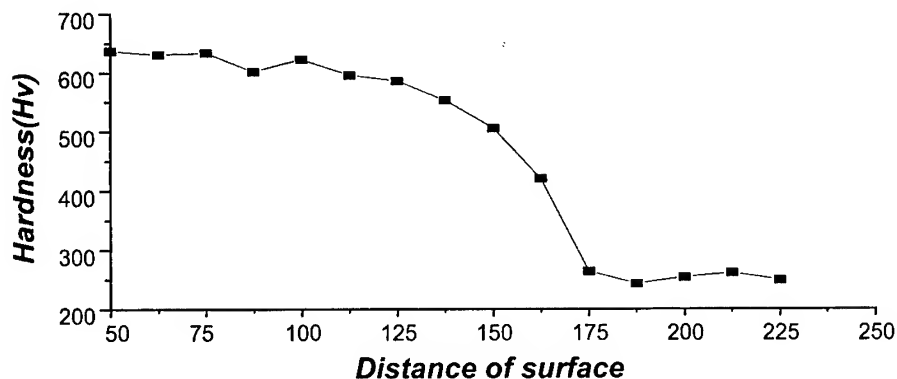


Fig. 5. Hardness distributions of Nitrided TiAl
(Nitriding for 1173K, 4hr, 75% (N_2/H_2 ratio))

4. CONCLUSIONS

The plasma nitriding of titanium aluminides fabricated by hot-pressing with 48at% Al under N_2 - H_2 atmosphere has been investigated. The results obtained by means micro-Vickers hardness test, XRD, OM, SEM can be summarized as follows.

- (1) When TiAl specimens fabricated by hot pressing at 1523 K under pressure of 45Mpa, from the Archimedes method, sintered TiAl were measured at 98% (relative density). And at the sintering TiAl few small pores, laminated structure and α -TiAl were observed. The microhardness of sintered TiAl was about Hv 287 by the micro-Vickers hardness test.
- (2) The three process parameters, namely nitriding temperature, nitriding time and N_2/H_2 ratio, the plasma nitriding parameters of TiAl with respect to depth of diffusion layer mainly depend on temperature and time. In case of the same temperature, depth of diffusion layer depend on N_2/H_2 ratio. The ratio of N_2 to H_2 increased, depth of diffusion layer was more deeper. In case of the same N_2/H_2 ratio, according to the temperature's higher, depth of diffusion layer was increased.
- (3) After plasma nitriding, the specimens' surface shows different color, ranging from brown to golden yellow which depends on nitriding parameters.
- (4) The surface hardness of nitrided TiAl independ on condition of the three process parameters, only surface hardness increase because of plasma nitriding. But the hardness distributions of nitrided TiAl depend on condition of the three process parameters, temperature, time, ratio increase, depth of hardness distribution was increased (Show the Fig. 5.).
- (5) XRD results show TiN, Ti_3AlN and AlN compound formed in surface and diffusion layer.

REFERENCES

1. ASM Handbook, vol. 4. 9th edn, American Society for Metals. Metals Park, OH, 1991, p.387.
2. W. Kovacs and W. Russell, Proc. ASM Int. Conf. On Ion Nitriding, American Society for Metals Park, OH. 1986. p. 9.
3. L.H. Chang, L.K. Lee, H.C. Peng and C.Y. Wang, Acta Metall. Sin., 20 (1984) A211-A228 (In Chinese).
4. A. Raveh, P.L. Hansen, R. Avni and A. Grill, Surf. Coat Technol., 38 (1989) 339-351
5. T. Telbizova, S. Paracandola, F. Prokert, E. Richter and W. Moller, Nuclear Instruments and Methods in Physics Research B, 161-163, 2000, 690-693
6. F. Perdrix, M. F. Trichet, J. L. Bonnentien, M. Cornet and J. Bigot, Intermetallics, 9, 2001, 147-155
7. Edward Rolinski, Materials Science and Engineering, 100, 1988, 193-199
8. H. Michel, T. Czerwicz, M. Gantois, D. Ablitzer and A. Ricard, Surface and Coatings Technology, 72, 1995, 103-111
9. C. L. Chu and S. K. Wu, Surface and Coating Technology, 78, 1996, 211-218
10. J. Musil, J. Vlcek and M. Ruzicka, Vacuum, 59, 2000, 940-951
11. M. Nakamura and Y. Kaieda, Powder Metallurgy, 31, 3, 1988, 201-208
12. M. Nakamura and Y. Kaieda, Powder Metallurgy, 33, 2, 1990, 133-139
13. Zlatanovic M, Kunosic and Tomcik B, Proceeding of the International Conference on Ion Nitriding, Cleveland, USA, September 15-17, 1986. p. 47.
14. T. Bell, H. W. Bergmann, J. Lanagan, P. H. Morton and A. M. Staines, Surface Engineering, 2, 2, 1986, 133-143

High Resolution Electron Microscopic Study of the δ' /G.P. zone Complex Precipitate Structure in an Al-Li-Cu-Mg-Zr Alloy

K. H. Lee, Y. H. Lee, Y. J. Lee* and K. Hiraga**

Department of Metallurgical Engineering, Chungnam National University,
Taejeon 305-764, Korea

* Propulsion Department, Agency for Defense Development, Yusong P.O.Box
35-4, Taejeon, Korea

** Institute for Materials Research, Tohoku University, Sendai 980-8577, Japan

Abstract

A typical G.P. zone structure was found to be the well-known single layer of Cu atoms on (001) planes. The δ' /G.P. zone complex precipitate structure in an Al-Li-Cu-Mg-Zr alloy was studied by means of high resolution electron microscopy and simulation with the following results: (a) The δ' /G.P. zone complex precipitate is formed by epitaxial growth of the δ' phase on both faces of the G.P. zone during the aging at 190°C. (b) In the δ' /G.P. zone complex precipitate, the G.P. zone consisted of three layers containing a single layer of Cu between layers of two pure Al. (c) An out of phase or antiphase correlation occurs between the δ' phase on opposite faces of the G.P. zone because of the attraction between Cu and Li atoms in the G.P. zone and δ' phase.

1. Introduction

It is well known that the complex precipitates such as δ'/β' and δ'/θ' are formed in Al-Li-Cu-Zr based alloys in an aging process[1, 2]. The δ' /G.P. zone complex precipitate formed by the precipitation of the δ' on the faces of larger G.P. zones is also found in weldalite 049 alloy[3], but the corresponding atomic arrangement is thus far unclear.

The metastable δ' (Al_3Li) phase is known to be homogeneously formed before the formation of the stable δ (AlLi) phase with a B32-type (NaCl) structure in Al-Li binary alloys. Silcock[4] studied the crystal structure by the X ray diffraction technique and reported that the δ' phase had a $L1_2$ -type ordered structure having cube/cube orientation relationship between the matrix. This cubic phase has a very small misfit with the Al matrix[5] and forms with a spherical morphology. The atomic arrangement in the $L1_2$ -type ordered structure is illustrated in Fig. 1(a).

The Guinier-Preston (G.P.) zone, one of the transformation products in Al-Cu alloy systems, is that a sort of atom clusters is formed at the early stage of phase separation during the decomposition of supersaturated solid solutions. The first model of a G.P. zone proposed [6, 7] consisted of single Cu-rich plane coherent on the {100}

Al matrix planes. Because of the smaller size of Cu atoms ($\gamma_{Al} = 0.143\text{nm}$, $\gamma_{Cu} = 0.128\text{nm}$) a little closer to the zone origin than the normal spacing. On the contrary, Gerold[8, 9] demonstrated that the structure was composed of only one layer of 100% Cu with lattice distortion from the center to the fifteenth layer of the range about 10-0.2%. Gerold's model can well explain the diffuse X-ray scattering intensities and is widely accepted as a G.P.I zone model. His model is referred to as a single-layer G.P. zone because it consisted of only one Cu layer. Nicholson and Nutting[10] and Hornborgen[11] observed directly G.P. zone with a conventional electron microscope. They found the characteristic strain field contrast around G.P.I zones and concluded that the observed image was consistent with the structure proposed by Gerold. Though many studies were carried out previously, the structure of G.P.I zone is illustrated in Fig. 1(b). But Karlik et al.[12, 13] observed that Cu content in the G.P. I zone is not uniform and that G.P. I zone having composition in the range from say 40 to 100% Cu co exist. And Fontaine et al.[14] presented a new model with an averaged 50% Cu composition of the G.P. zone by EXAFS method. But we assume that the Cu content in the G.P. zone is 100% in this study. In addition to G.P.I zone, the G.P.II zone consisting of two Cu rich layers separated by three Al layers are also observed [8, 10, 15].

In the present study, the interfacial structure of the δ' /G.P. zone precipitate in Al-Li-Cu-Mg-Zr alloy has been examined by a high resolution transmission electron microscopy(HRTEM) in order to understand the mechanism responsible for the development of the δ' /G.P. zone complex precipitate.

2. Experimental Procedure

The Al-1.86wt%Li-2.95wt%Cu-0.11wt%Mg-0.16wt%Zr alloy specimen was solution treated at 530°C for 1h and cold water quenched. The quenched specimen was aged at 190°C for 30min, 1h and 12h. Thin foil specimens for TEM study were thinned by twin jet-polishing using an electrolytic solution of 70ml CH₃OH and 30ml HNO₃ cooled to -40°C. High resolution observations were made using transmission electron microscopes of JEM-4000EX and JEM-200CX operated at 400kV and 200kV, respectively. Interpretation of the high resolution images were assisted by comparing experimental images with simulated ones. The simulated images were conducted by the usual multi-slice method using the software package, MacTempas, on a Power Macintosh personal computer.

3. Results

Fig. 2 shows an electron diffraction pattern with the [001] zone axis of a specimen aged at 190°C for 30min after quenched from 530°C. The super lattice reflections originated in the L1₂-type ordered structure appear at 100, 110 and their equivalent positions. In addition, continuous streaks run toward the [100] and [010] directions and no intensity maxima appear on streaks. The above mentioned streaks are similar to those of the diffraction pattern for the G.P.I zone in the early stage of aging in an Al-Cu alloy[16, 17].

A HRTEM image corresponding to Fig. 2 is shown in Fig. 3, which is taken using a JEM-4000EX microscope operated at 400kV. The bright dots with the spacing of about 0.2nm corresponding to the {200} planes of the Al

matrix are observed periodically along the [100] and [010] directions. The δ' particles having brighter dots with twice period of the {200} planes appear locally in the matrix, as marked A and B. The arrangement of the brighter dots surrounding four bright dots in the δ' phases seems to correspond to the Li atom position in the $L1_2$ -type ordered structure with the spacing of about 0.4nm. The isolated δ' particle with 8nm in size is observed at A in the matrix. The δ' /matrix interface is maintained coherent across the interphase boundary. The δ' phase was coated on the faces of a 12nm diameter G.P. zone on (010) plane it is shown at B. The G.P. zone appears in darker contrast than the δ' phase surrounding it, as indicated by an arrow.

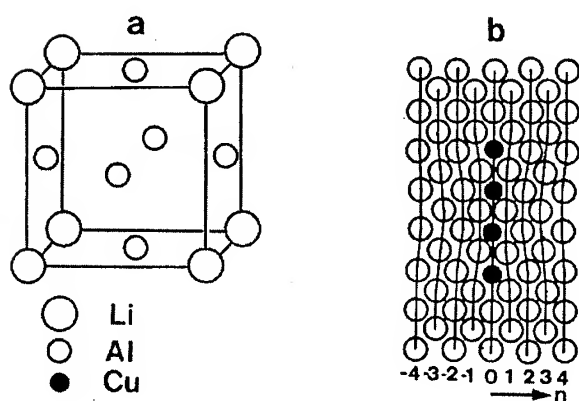


Fig. 1 Schematic illustration of a unit cell of the $L1_2$ -type ordered structure(a) the typical single-layer G.P. zone(b).

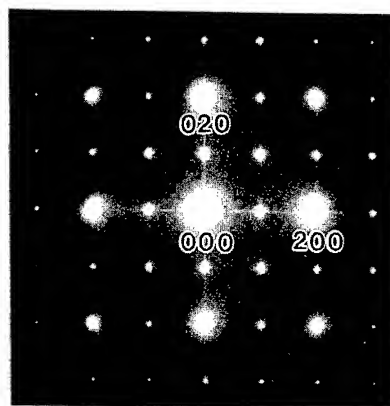


Fig. 2 Electron diffraction pattern with the [001] zone axis of the specimen aged at 190°C for 1hr after quenched from 530°C, which shows $L1_2$ -type superlattice reflections associated with δ' and streaking associated with G.P. zone.

The coupled δ' /G.P.I zone precipitate is clearly different from the δ'/θ' complex precipitates observed in an Al-Cu-Li alloy[18] or an Al-Li-Cu-Zr alloy[2]. According to the mechanism of the θ' growth in the Al-Cu alloys[19], the smallest θ' plate has two unit cells thick(1.16nm) along the $\langle 100 \rangle$ directions to reduce the volume strain in the f.c.c. \rightarrow b.c.t. transformation. However, the width of the G.P. zone in the present image is thinner than the one unit cell thick of the θ' plate. The δ' /G.P. zone interface boundary appears atomically sharp and flat on both faces of the G.P. zone and the shape of the δ' phase on both sides of the G.P. zone is asymmetrical in size. Especially, the arrangement of the brighter dots on the δ' phases on opposite faces of the G.P. zone is translated exactly by one-half of the unit cell dimension with respect to each other. The atomic arrangement of the interphase boundary in the δ' and G.P. zone is analyzed appropriately with a simulation image later.

The coupled δ' /G.P.I zone precipitates grew with increasing aging time. A HRTEM image of the specimen with the [001] zone axis aged at 190°C for 1h is shown in Fig. 4, which was taken by a JEM-200CX microscope operated at 200kV. The isolated δ' phases with a spherical shape were observed in the matrix, the bright dots correspond to the minority atom(Li) positions of the $L1_2$ -type superstructure. In the coupled δ' /G.P. zone precipitates, G.P. zones appeared in dark contrast with a few atomic layers and were not surrounded completely

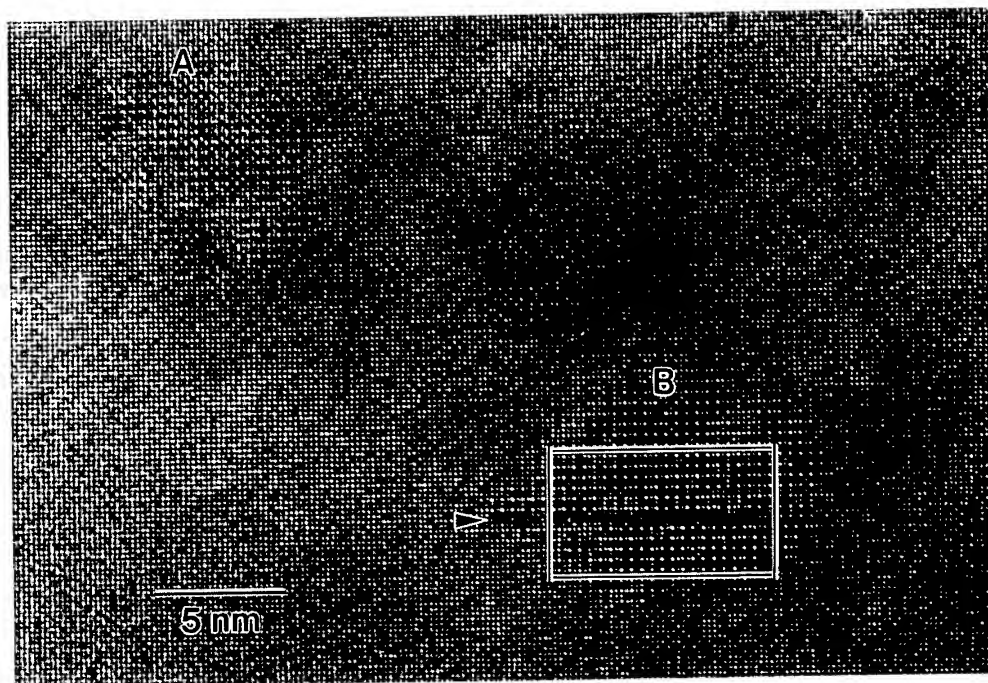


Fig. 3 HRTEM image corresponding to Fig 2. The isolated δ' particle and the $\delta'/\text{G.P. I}$ zone complex precipitate appear at A and B, respectively. The G.P. I zone is indicated by an arrow at B.

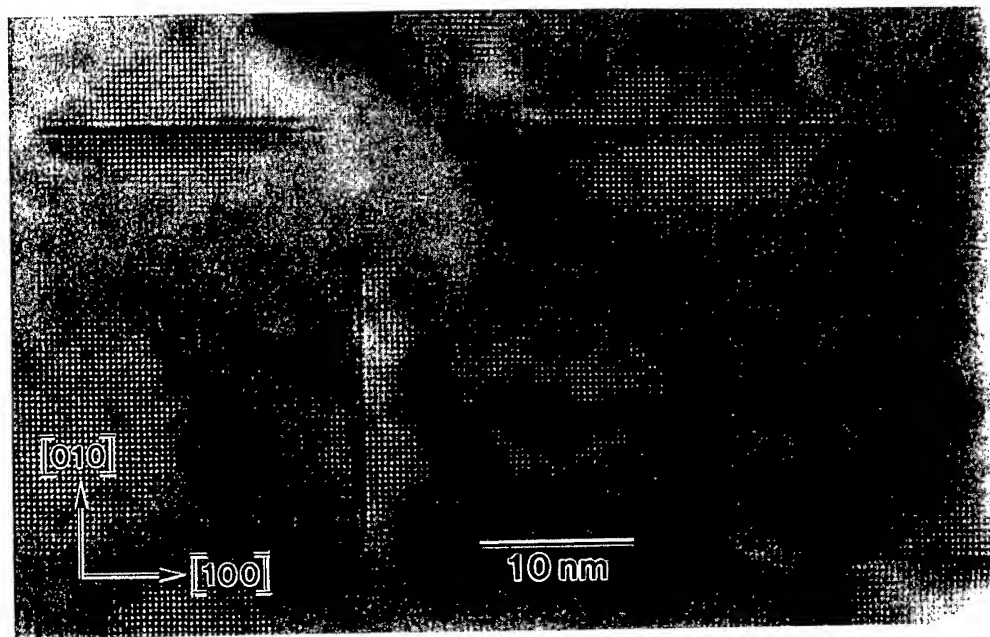


Fig. 4 HRTEM image of the specimen aged at 190 °C for 1 hr. The G.P. I zone appears as dark contrast in the $\delta'/\text{G.P. I}$ zone complex precipitates.

by the δ' phase; i.e., the δ' phase does not appear to grow around the edges of the G.P. zone. The $\delta'/\text{G.P. zone}$ precipitate is considered to be formed by the epitaxial growth of the δ' phase on both faces of the G.P. zone on the (100) and (010) planes. An out of phase or antiphase correlation appears clearly between the δ' phases with shape of spherical cap on the opposite faces of the G.P. zones each other.

With further aging at 190°C , a well-defined $\delta'/\text{G.P. zone}$ complex precipitates were developed as observed in Fig. 5, a HRTEM image of the specimen aged at 190°C for 12h.



Fig. 5 HRTEM image of the specimen aged at 190°C for 12hr, showing the well developed $\delta'/\text{G.P. zone}$ complex precipitate.

4. Discussion

The present result is discussed of the image contrast of the $\delta'/\text{G.P. zone}$ interface compared with computer simulation by the multi-slice method. Figure 6 is a magnified image of the marked area in Fig. 3 and the structure model (a) obtained from the observed HRTEM image and a simulated image (b) are both insetted. In a structure model (a), open circles represent Li atom positions. Large and small solid layer of Cu between two layers of pure Al, which correspond to $n = 0$ and $n = \pm 1$ layers in Fig. 1(b). The spacing between the Cu atom layer and Al atom layer in the G.P. zone was determined to be about 0.19nm from the observed image, which is a little smaller than 0.202nm corresponding to the (100) lattice spacing (d_{100}) of the Al matrix. the unit cell of the L1_2 ordered structure is marked by solid lines on both faces of the G.P. zone. Fig 6(b) is the simulated image based on a structure model in which the specimen thickness $t = 9\text{nm}$ and defocus value $\Delta f = 20\text{nm}$ are used. The parameters used for the calculation are listed in Table 1. The unit cells of the L1_2 ordered structure are outlined in Fig 6. The Positions of Li atom row in the L1_2 ordered structure are clearly seen as the brighter dots

surrounding four dots of the Al atom sites. The contrast of a Cu atom layer in the G.P. zone appears as an array of dots with darker contrast. The result of the image simulation clearly shows that the $L1_2$ ordered structure on opposite faces of the G.P. zone is translated exactly by one-half of the unit cell dimension with respect to each other. This forms an antiphase boundary in the $L1_2$ ordered structure across the G.P. zone. the same feature is observed of all the $\delta'/G.P.$ zone complex precipitates. In addition, the δ' phase appears to form in such a way that the Li atoms are adjacent to Cu atoms in the G.P. zone. The reason for the alignment of the Li and Cu atoms across the $\delta'/G.P.$ zone interface, can be explained by considering the mechanisms of epitaxial growth of the δ' phase on a pre-existing G.P. I zone, and comparing bond energies among the Al, Li and Cu atoms, as discussed in formation of the δ'/θ' complex precipitate in an Al-Li-Cu alloy[18].

The atomic arrangements projected in the $[100]$ direction of the δ' and the G.P. zone structure are shown in Fig. 7(a) and (b), respectively. In Fig. 7(b), the f.c.c. unit cells are enclosed by broken lines, and solid and broken circles present Cu atoms at $n = 0$ layer and Al atoms at $n = \pm 1$ layers in Fig. 1(b), respectively. When the δ' phase grows on the surface of G.P. zone, Li atoms in the $L1_2$ ordered structure will not lie at the atom positions in the $n = \pm 1$ layers on the G.P. zone, because this is not a favourable packing situation. Therefore Li atoms in the $L1_2$ ordered structure lie above Cu atom positions on the G.P. zone even of the atom positions have a little displacement, and there is either of two positions over the Cu atoms indicated by A and B in Fig. 7(b). If the Li atoms reside over position A on the G.P. zone, Li atoms in the $L1_2$ ordered structure should lie above all Cu atoms except centered Cu atoms in the f.c.c. unit cell on the G.P. zone. While, if the Li atoms reside over position B, Li atoms in the $L1_2$ ordered structure lie above all centered Cu atoms in the f.c.c. unit cell. However, the Li atoms do not lie together at positions A and B on one side of the G.P. zone and reside not in same position on both faces of the G.P. zone, as shown in HRTEM images. The preferred formation of this configuration can be

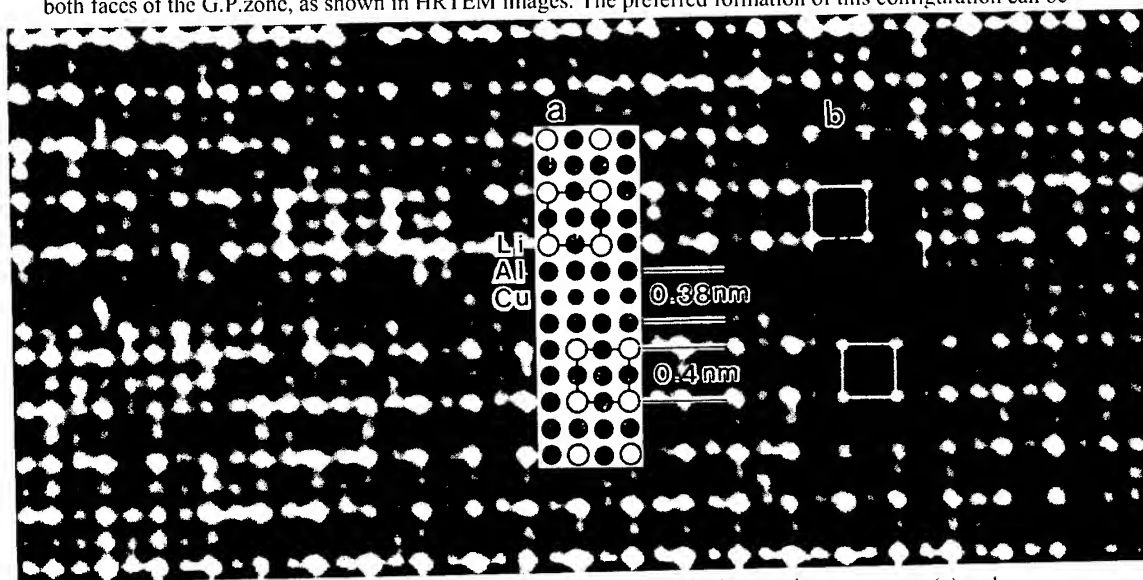


Fig. 6 Magnified image of the marked area in Fig. 4. The atomic arrangement(a) and its simulated image(b) of the $\delta'/G.P.$ zone interphase boundary are insetted. A unit cell of the $L1_2$ -type ordered structure is outlined.

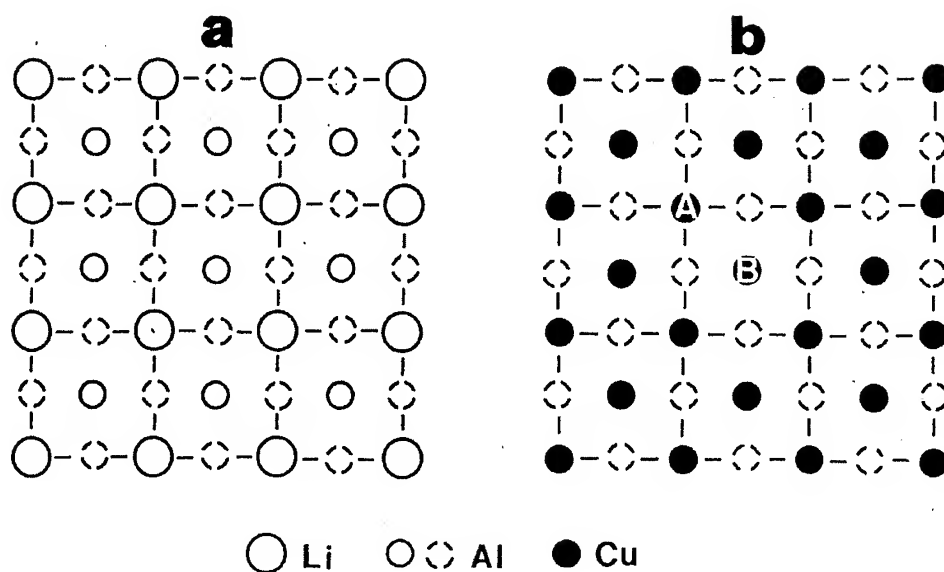


Fig. 7 The atomic arrangements projected in the $[100]$ direction of the $L1_2$ -type ordered Structure(a) and the G.P. I zone structure(b). In (b), solid and broken circles represent Cu atoms at $n = 0$ layer and Al atoms at $n = \pm 1$ layers in Fig 1(b), respectively.

Table 1. Parameters used in the image calculations

Accelerating voltage	400kV
Slicing interval	0.4nm
Spherical aberration constant(C_s)	1.0mm
Defocus due to Chromatic aberration	15nm
Objective aperture radius	7.0nm^{-1}

explained by considering the bond energies among Al, Li and Cu atoms, or by examining the electronegativities of those elements. First, reference to the Cu-Li[20] and Cu-Al[21] phase diagrams, the solubility of Li and Al in Cu at 190°C are about 22 at% and 8 at%, respectively. The higher solubility of Li in Cu than of Al in Cu indicates that the Cu-Li bond energy is greater than that of Cu-Al. Comparison of the electronegativities for these elements give a qualitative indication of the magnitude of the relative differences in bond energies. The electronegativities of Al, Cu and Li are 1.5, 1.9 and 1.0, respectively[22]. Since an electronegativity difference of 1.7 is considered to approach an ionic bonding situation, there is a strong attraction between Cu and Li atoms where the electronegativity difference is 0.9, compared with Al and Cu or Al and Li where the electronegativity differences are 0.4, and 0.5, respectively. Therefore, it appears that the δ' phase grows on the G.P. zone with Li atoms adjacent to Cu atoms because of the strong attraction between Cu and Li atoms.

5. Conclusions

The atomic structure of the δ' /G.P. zone complex precipitate in an Al-1.86wt%Li-2.95wt%Cu-0.11wt%Mg-0.16wt%Zr alloy was investigated by high resolution transmission electron microscopy, and the following results were obtained;

(1) The δ' /G.P. zone complex precipitate is formed by epitaxial growth of the δ' phase on both faces of the G.P.I zone during the aging at 190°C.

(2) In the δ' /G.P. zone complex precipitate, the G.P.I zone consisted of three layers containing a single layer of Cu between layers of two pure Al.

(3) An out of phase or antiphase correlation occurs between the δ' phase on opposite faces of the G.P. zone because of the attraction between Cu and Li atoms in the G.P. zone and δ' phase.

References

1. P. L. Markin and B. Ralph, *J. Mat. Sci.*, 19, 3835 (1984).
2. M. H. Tosten, A. K. Vasudevan and P. R. Howell, *Metall. Trans.*, 19A, 51 (1988).
3. F. W. Gayle, F. H. Heubaum and J. R. Pickens, *Scripta Metall. et Mater.*, 24, 79.
4. J. M. Silcock, *J. Inst. Met.*, 88, 357 (1959-1960).
5. S. F. Baumann and D. B. Williams, *Aluminum Lithium Alloys II*, (edited by T. H. Sander and E. A. Starke Jr.), p. 17. *Metall. Soc. AIME*, Warrendale, Pa, (1984).
6. G. D. Preston, *Proc. R. Soc.*, A167, 526 (1938).
7. A. Guinier, *Ann. Phys.*, 12, 161 (1939).
8. V. Gerold, *Z. Metallkd.*, 45, 593, 599 (1954).
9. V. Gerold, *Acta Cryst.*, 11, 230 (1958).
10. R. B. Nicholson and J. Nutting, *Phil. Mag.*, 3, 531 (1958).
11. E. Hornbogen, *Aluminum*, 43, 41, 115, 163 (1967).
12. M. Karix and B. Jouffrey, *Acta Mater.*, 45, 3251 (1997)
13. M. Karix, B. Jouffrey and S. Belliot, *Acta Mater.*, 46, 1817 (1998)
14. A. Fontaine, P. Lagarde, A. Naudon, D. Raoux and D. Spanjaard, *Phil. Mag.*, 40, 17 (1979)
15. T. Sato and T. Takahashi, *Trans. JIM*, 24, 386 (1983).
16. J. R. Parsons, M. Rainville and C. W. Hoelke, *Phil. Mag.*, 21, 1107 (1970).
17. V. A. Phillips : *Acta Metall.*, 23, 751 (1975).
18. J. M. Howe, D. E. Laughlin and A. K. Vasudevan, *Phil. Mag.*, A57, 955 (1988).
19. U. Dahman and K. H. Westmacott, *Phys. Status Solidi*, (a)80, 249 (1983).
20. A. D. Pelton, *Bulletin Alloy Phase Diagrams*, 7, 142 (1986).
21. L. M. Mondolfo : *Aluminium Alloys, Structure and Properties*, London, Butterworths, p. 253. (1979)
22. K. M. Ralls, T. H. Courtney and J. Wulff, *Introduction to Materials Science and Engineering*, New York, Wiley, p. 54. (1976)

EUTECTIC BONDING OF AL6061 ALLOY USING CU INSERT METAL

*Seung Yong Shin, Dong Choul Cho, Chi Hwan Lee, *Mung Wan Ko **and Kee Sam Shin

*Korea Institute of Industrial Technology, Chunan 330-825, Korea
Inha University, Inchun 402-751, Korea

**Changwon National University, Changwon 641-010, Korea

ABSTRACT

Al 6061 alloy has been brazed with conventional filler metal like Al-12Si alloy. However, if brazing temperature is not closely controlled, erosion and bad wettability is appeared due to little difference in melting temperature between the base metal and filler metal.

In this study, The eutectic bonding characteristics of Al 6061 alloy using pure Cu foil(8 μ m in thickness) has been investigated at lower temperature. The eutectic temperature of Al-Cu alloy is 548 $^{\circ}$ C. Differential temperature analysis was carried out with Al 6061/Cu/Al 6061 clad to investigate the starting temperature of eutectic reaction between Al 6061 alloy and pure Cu.

The alloy melt, which has the eutectic composition, started to form at 510 $^{\circ}$ C. It seems to be ternary or quaternary eutectic reactions by Al-Cu-Mg-Si system. Therefore, the bonding can be accomplished above 510 $^{\circ}$ C. The investigation on the effect of temperature was done at the temperature range between 510 $^{\circ}$ C and 575 $^{\circ}$ C. The results showed that the bonding strength increased as the bonding temperature increased. The base materials of bonded part, which was bonded at 575 $^{\circ}$ C, was fractured at 172MPa. Therefore, the bonding strength could be estimated over it. The bonding structure showed isothermal solidification structure at longer bonding time because it has enough time for copper to diffuse into aluminum matrix. As a result of interfacial analysis of microstructure using TEM, oxide layer through the interface was observed as amorphous structures.

1. INTRODUCTION

Expanded application of Al6061 alloy to heat exchanger is expected for its excellent machinability, high specific strength and good heat conductivity. However, alloy Al6061 just like 2xxx and 7xxx alloys is difficult to braze neither in furnace not to mention in vacuum, because of its low solvus temperature close to the melting point of the commonly used filler metal of 4xxx (Al-Si alloy). [1, 2]

Studies on joining the alloys of low solvus temperature are getting more and more attention and reports on the development of filler metals of low melting point are gradually increased in recent years.[2, 3, 8] Those newly proposed filler metals are mainly Al-Cu-Ni-Si, Al-Cu-Si, and Al-Ge-Si-Mg type. However, these filler metals are ternary or quaternary eutectic composition. Therefore, they are brittle and hard to form to foil shape and the price is higher than those of Al-Si filler metals. Eutectic brazing or bonding using Cu interlayer is another method of low temperature joining for aluminum brazing. [4, 5, 6, 7] In this method, Cu is electroplated on one surface of base metal or inserted between two base metals as a foil which forms a filler melt by eutectic reaction which in turn diffuses into the base metals followed by isothermal solidification. In the process, the formation of brittle CuAl_2 compound (eutectic crystals) during solidification is avoided and promotes the formation of a solid joint whose mechanical property and composition are close to those of the base materials. Though it has not been used yet, the method might be applicable for Al6061 base metal, in which case the joined part fabricated as such should show a comparable increase in strength by precipitation hardening such as T6 treatment.

Using Cu foil, this study investigated the applicability of low temperature eutectic brazing process for joining of Al6061 by focusing on 1) eutectic melt formation by diffusion between Al6061 matrices and Cu filler via eutectic reaction, and 2) isothermal solidification accompanied by Cu diffusion.

2. EXPERIMENTAL PROCEDURES

2.1 Base and filler metals

Table 1. shows the chemical composition of Al6061 used for the base metals, which was fabricated in Alusuisse Swiss Aluminum Ltd. The Cu foil used for filler metal was about $8\ \mu\text{m}$, $100\ \mu\text{m}$ thick and the purity was higher than 99.99%.

For the removal of the surface oxides, the surface of base metal was ground by 600 mesh sand paper and then electropolished at 12V for 3min. with a solution of methyl alcohol 600ml, glycol 360ml and perchloric acid 60ml. Cu foil was cleaned with acetone, 2 min. submerged in 5% Nital, and then rinsed in water. Fig.1 shows the shape and dimensions of the tensile

specimen of the joined part.

2.2 Joining equipment and introduction

The joining equipment was composed of a high frequency heating system, cold wall vacuum chamber, and pressing system by ball screw with an AC motor driver.(Fig.2) The predetermined load at the indicator was applied by a load cell attached on the lower ram, which was driven by the high and low contact points. Precise joining temperature was measured and controlled by an R-type thermocouple of wire diameter of 0.3mm which was percussion welded directly to the specimen. The vacuum was pumped by sequential connection of rotary and diffusion pumps.

2.3 Joining and characterization

The joining was performed with 0.5 MPa, at 510-575°C for 1~20min. Degree of vacuum is 5×10^{-5} torr. The heat treatment was carried out in $\text{KNO}_3 + \text{NaNO}_3$ salt bath and the solution treatment was carried out at 530°C for 1 hour and the aging was done at 175°C for 2~1000hrs

The tensile test was performed with Instron 8516 at the cross head speed of 1 mm/min. To observe the beginning temperature of eutectic reaction between Al6061 and Cu, differential calorimeter was used at a heating speed of 10°C/min. which was the same as the heating cycle. The joined regions were etched with Keller solution and then their microstructure and compositional mapping and line profile were analyzed using optical microscope and electron probe microanalyzer (EPMA).

3. RESULT AND DISCUSSION

3.1 Eutectic reaction between Al6061 and Cu

Al6061 is precipitation strengthened alloy by Mg_2Si and the contents of Mg and Si are 0.8~1.2% and 0.4~0.8%, respectively. Thus, the eutectic reaction of Al6061 and Cu is expected to influence on the other eutectic reactions of such elements as Mg and Si with Cu. The possible quaternary eutectic reaction in Al-Cu-Mg-Si system is listed in Table 2. The table shows, as the reactions become complicated ternary and quaternary, the reaction temperature gradually decreases from 548°C of the Al and Cu binary reaction temperature. In this study, differential thermal analysis was performed to examine reaction temperature of the clad and

the result is shown in Fig.3. The Al6061/Cu clad was fabricated by inserting $8\mu\text{m}$ Cu foil between $100\mu\text{m}$ Al6061 foils and through solid diffusion at 490°C for 2 min. in vacuum. Fig.3 shows that the endothermic reaction start at about 510°C . Thus, reactions such as D, O, P, and Q appear to have the highest probability of the first liquid formation. All the results indicate that the eutectic melting in Al-Mg-Si type Al6061 alloy, whose temperature was lower than that of Al-Cu, took place due to the presence of matrix precipitates such as Mg_2Si and Si. From that, it is conceivable that the presence of Mg_2Si and Si promotes the infusion of Cu into the matrix and promotes the formation of eutectic melting of filler by steady erosion of matrix.

3.2 Effect of joining parameters on the characteristics of the joined interface.

Fig.4 shows the strength of the joint, which was carried out at $510\sim 575^\circ\text{C}$. The strength was low when the joining was performed at $520\sim 530^\circ\text{C}$ for 1 min, 4 min. As the time of joining increased above 10 min, the strength linearly increased. Base metal rather than the joined region was fractured when the joining was performed at 575°C for 1 min.

Fig.5 shows the microstructural evolution of the joined region at various joining temperature with a fixed duration time of 10 min. The joining region widened as the joining temperature increased and reached to $300\mu\text{m}$ at 570°C . On the contrary to the dark elongated grains to the direction of rolling, equiaxed grains are observed in the joined region which was clearly distinguished from the matrix grains. The big contrast in brightness is attributed to the presence of Mg_2Si in the matrix. The dark mid-regions of the specimens joined at 510°C , 530°C appear to be due to the remnant of melt existing at the last stage of inward solidification from periphery. At the specimen of 560°C joining, the mid-region of fine microstructure is in clear contrast with that of the surrounding. In case of the specimen joined at 575°C , the fine particles observed in 560°C specimen are further refined and present along the grain boundary which are attributed to the migration/dispersion of the fine particles during the recrystallization and subsequent growth of grains.

Fig.6 is EPMA line-profiles of the diffusion brazing joined at various temperatures. The result shows relatively high concentration of Cu and Si at the joined regions of 530°C and 545°C specimens. The joined region widens as the joining temperature increases.

Fig.7 and 8 are results of TEM observation and elemental analysis of the joined region of 560°C . For TEM observation, 1.5 mm thick plate was obtained from a region tilted about 30° from joined plane and then ground to $100\mu\text{m}$ with #1500 grit paper. Twin jet polishing was carried out using electrolyte composed of 5% methyl alcohol, 5% perchloric acid.

The results indicate that the fine particles are oxides composed of Al, Si, Mg and O, whose structures are amorphous as shown by the diffraction pattern.

In short, the joining strength increased with the increase of the joining temperature with clearer appearance of isothermal solidification structure. The fine particles are found to be oxides of Al-Si-Mg-O.

Fig.9 shows the dependence of strength on aging time upon the 175°C aging after joining at 560°C for 10 min. The results show similar aging characteristics for both matrix and joint body with a maximum strength at 8 hr. ~ 32 hr. The maximum strength of 280 MPa was obtained when the specimen was aged at 175°C for 8 hr ~ 32 hr.

3.3 Figures and tables

Table 1 Chemical composition of Al6061 base metal

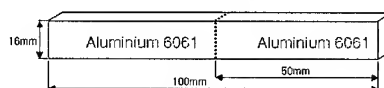
Al6061	Si	Fe	Cu	Mn	Mg	Cr	Zn	Ti	Al
composition	0.6	0.48	0.22	0.049	0.99	0.19	0.009	0.025	remainder

Table 2 The invariant reactions at the aluminum corner of the Al-Cu-Mg-Si system

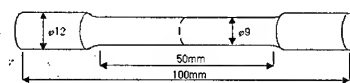
Reaction(s)		C	Temperature F	Cu	Composition, % Mg Si	
Binary						
A	Liq. → Al + CuAl ₂	548	1018	33.2	-	-
B	Liq. → Al + Mg ₂ Si	451	844	-	35.0	-
C	Liq. → Al + Si	577	1071	-	-	12.6
Ternary						
D	Liq. → Al + CuAl ₂ + CuMgAl ₂	507	944	30.0	6.0	-
E	Liq. → Al + CuMgAl ₂ (b)	518	964	24.5	10.1	-
F	Liq. → CuMgAl ₂ → Al + CuMg ₂ Si ₃	467	862	10.0	26.0	-
G	Liq. → Al + Mg ₂ Si + CuMg ₂ Si ₃	448	838	2.7	32.0	-
H	Liq. → Al + Mg ₂ Si + Mg ₂ Si	450	842	-	32.0	0.35
I	Liq. → Al + Mg ₂ Si (b)	595	1104	-	8.15	4.75
J	Liq. → Al + Si + Mg ₂ Si	575	1066	-	4.96	12.95
K	Liq. → Al + CuAl ₂ + Si	525	976	27.0	-	5.0
Quaternary						
L	Liq. → Al + Mg ₂ Si + Mg ₂ Si + CuMg ₂ Si ₃	446	835	1.5	33.0	0.3
M	Liq. → CuMgAl ₂ → Al + Mg ₂ Si + CuMg ₂ Si ₃	466	870	10.0	25.5	0.3
N	Liq. → Al + CuAl ₂ + CuMgAl ₂ (c)	516	960	23.0	10.5	0.3
O	Liq. → Al + CuAl ₂ + CuMgAl ₂ + Mg ₂ Si	500	932	32.0	6.6	0.4
P	Liq. → Al + CuAl ₂ + Mg ₂ Si (c)	515	958	31.5	3.9	2.3
Q	Liq. → Mg ₂ Si → Al + CuAl ₂ + CuMg ₂ Si ₃ Al ₃	512	954	31.0	3.3	3.3
R	Liq. → Al + CuAl ₂ + Si + CuMg ₂ Si ₃ Al ₃	507	945	28.0	2.2	6.0
S	Liq. → Mg ₂ Si + Si → Al + CuMg ₂ Si ₃ Al ₃	529	984	13.8	3.3	9.6

a. The letters refer to points in Fig. 4-29a. b. Quasi-binary eutectic. c. Quasi-ternary eutectic.

a. The letters refer to points in Fig. 4-29a. b. Quasibinary eutectic. c. Quaternary eutectic.



(a) diffusion brazed joint body



(b) dimension of a specimen for tensile test

Fig.1 Dimension and shape of specimen

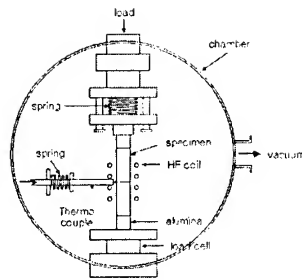


Fig.2 Schematic diagram of bonding apparatus

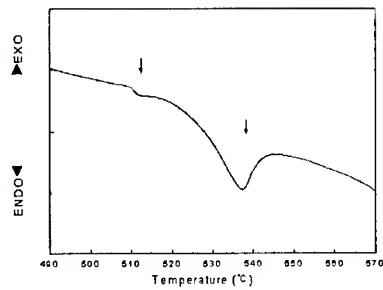


Fig.3 DAT result of Al6061/Cu/Al6061 clads

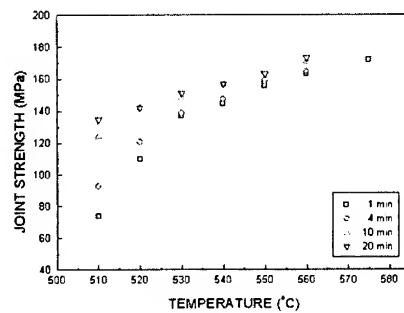


Fig.4 Tensile strength of the braze joint as a function of brazing temperature and brazing time

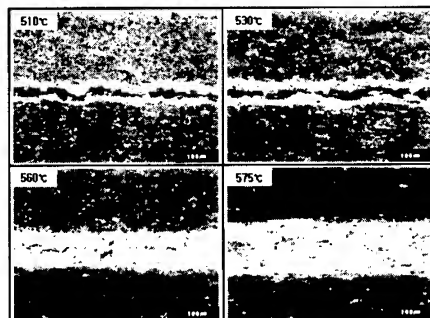


Fig.5 Micrographs of diffusion brazed joint

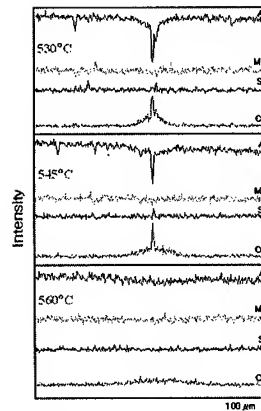


Fig.6 EPMA results in diffusion brazed joint

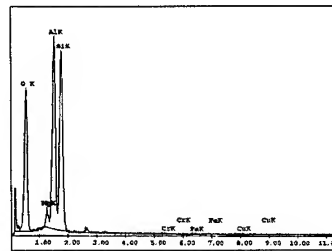


Fig.7 EDS/TEM results of interface

◆ 560 °C, 10min.

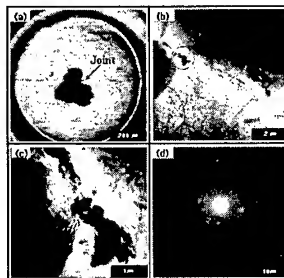


Fig.8 TEM results of diffusion brazed joint

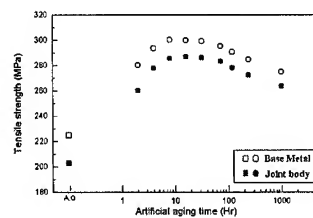


Fig.9 Variation of joining strength with artificial ageing time

4. CONCLUSIONS

As an effort for low temperature diffusion brazing of Al6061 using Cu insert, the eutectic reaction, the effect of heat treatment, and the characteristics of the joined region were studied and we reached to the following conclusions:

1. The eutectic reaction between Al6061 alloy and Cu occurred at 510°C, which was lower than the Al-Cu binary eutectic temperature of 548°C. The lower temperature eutectic melting of Al6061 was attributed to the presence of matrix precipitates such as Mg₂Si and Si.
2. Diffusion brazing of Al6061 using Cu insert showed isothermal microstructure of the joined region which showed higher stability as the joining temperature increased. The specimen joined at 575°C exhibited a high tensile strength of 172 MPa with a fracture occurring in the matrix.
3. The inclusions observed in the center of the isothermally solidified joined region were found to be amorphous oxides of Al-Si-Mg-O by TEM analysis.
4. When the joined region was T6 treated, it showed the maximum bonding strength of 280 MPa, which was about 93% of the base metal strength.

REFERENCE

1. Y. Sugiyama, Brazing of aluminum alloys, *Welding International*(1989), pp.700-710.
2. T Kayamoto,T Onzawa, Development of low melting temperature fillers for aluminum alloy, *Welding International*(1996), pp.363-369.
3. T.Chuang, et al., *Metall. and Materials Trans. A*, Vol.31(2000),pp.2239-2245.
4. J. T. Niemann, and R. A. Garrett, Eutectic bonding of born-aluminum structural components, *Welding Research Supplement*(1974), pp. 175-184.
5. T. Osawa, Change in the interface structure and strength of diffusion brazed joint of Al-Si system alloy castings, *Welding Research Supplement*(1995), pp. 206-212.
6. J. T. Niemann, and G. W. Wille, 1978, Fluxless diffusion brazing of aluminum castings, *Welding Research Supplement*(1978), pp.285-291.
7. A. Sunwoo, *Scripta Metallurgica et Materialis*, vol31,No.4(1994), pp.407-412.
8. Uk patent GB 2,270,086

ROTATION-CYLINDER METHOD FOR MASS-PRODUCTION OF LIGHTWEIGHT Mg-Ni HYDROGEN ABSORBING ALLOYS

Won Ha, Tae-Whan Hong, Shae-Kwang Kim, Sung-Gon Lee and Young-Jig Kim

School of Metallurgical and Materials Engineering, Sungkyunkwan University,
300 Chunchun-dong, Jangan-gu, Suwon, Gyungi-do 440-746, Korea

ABSTRACT

Mg-based alloys have been considered as one of potential candidates for hydrogen absorbing materials because of their large hydrogen capacity and lightweight. Various methods to produce Mg-based hydrogen absorbing alloys have been investigated, but mass-production methods have not been developed.

The aim of this study was to develop mass-production method of Mg-Ni alloys in ambient atmosphere and to evaluate hydrogenation and degradation properties. Mg-Ni alloys with various nickel compositions were produced by a mass-production of Rotation-Cylinder Method.

1. INTRODUCTION

Magnesium is a promising hydrogen absorbing material due to its high storage capacity, low cost and abundance. Particularly, Mg based alloys are quite suitable media for hydrogen transportation and on-board system of hydrogen fueled vehicle since they are the lightest among the most widely used alloys [1]. It has been recognized, however, that magnesium requires high temperature for the reversible hydriding and dehydriding reaction because of its lower equilibrium pressure and poor surface activity [2]. Nickel has been widely study as most effective catalytic elements for improving hydrogenation properties of Mg hydride [3]. But, as the amount of nickel increases, the specific gravity of alloys increases, and the hydrogen storage capacity decreases.

Many attempts, such as mechanical alloying, melt-spinning, and combustion synthesis, have been made to produce Mg based alloys [4~6]. However, melting process for mass-production in ambient atmosphere has not been developed.

The present paper discussed the mass-producibility of Mg-Ni alloys by RCM (Rotation-Cylinder Method) and the hydrogenation and degradation properties of them.

2. EXPERIMENTAL PROCEDURES

Pure magnesium (99.93%, Xuzhou Changhong Magnesium Co.) and nickel (99.92%, Inco Co. Ltd) ingots were used as raw materials. Nickel chips were prepared from nickel ingots by drilling without cutting oil. About 800g of pure magnesium were melted in a steel crucible in an electric resistance furnace under HFC-134a-CO₂ protective atmosphere. The melt was then rotated at 953K and the desired amount of nickel (1, 5, 10mass%) chips was added a feed rate of about 4g/min under a rotating speed of 800 rev/min. As-cast alloys were chipped by drilling and crushed by mechanical milling under hydrogen atmosphere to enlarge the surface area. RCM was originally developed to manufacture SiC particulate reinforced magnesium composites and is being used for producing particulate reinforced alloy composites as well as for alloying low-melting point metals with high-melting point chips homogeneously in short time [7].

Noran 217Z-1SPS electron probe microanalysis was used to identify the phases. X-ray diffracted patterns of specimens were measured by Macscience M18XHF-SRA XRD. And the hydrogenation and degradation properties were evaluated by Sievert type apparatus. Philips XL30 SEM was used to observe the change of specimen morphology after given cycles.

3. RESULTS AND DISCUSSION

3.1 Microstructure and phase analysis

The as-cast microstructures of Mg-Ni alloys are shown in Fig. 1 in comparison with the microstructure of pure magnesium. A typical hypoeutectic structure of primary α dendrites plus an interdendritic eutectic phase is seen except for pure magnesium. Much finer primary phases are obtained with increasing nickel composition. Especially, the as-cast microstructure of Mg-10mass%Ni alloy consists of the island-like hydride forming α -Mg phase and the eutectic phase. It has been generally accepted that nickel has a catalytic effect on hydrogen dissociation reaction. So the eutectic phase, which is rich in nickel composition compared with α phase, may act as a hydrogen dissociation site and a channel for diffusion of hydrogen atoms. These microstructures may promote hydrogenation reaction. Figure 2 displays the schematic illustration of hydrogen dissociation and diffusion. Figure 3 shows the XRD patterns of each specimen after 4 hr crushing under hydrogen atmosphere of 2 MPa. For all specimens, magnesium peaks are major. Nickel and Mg₂NiH_{0.3} peaks are shown in Mg-5mass%Ni alloy and Mg₂NiH₄ peak is found in Mg-10mass%Ni alloy with the increased intensity of nickel and Mg₂NiH_{0.3} peaks. EPMA results of the nominal and the later-frozen compositions of Mg-Ni alloys are summarized in Table 1.

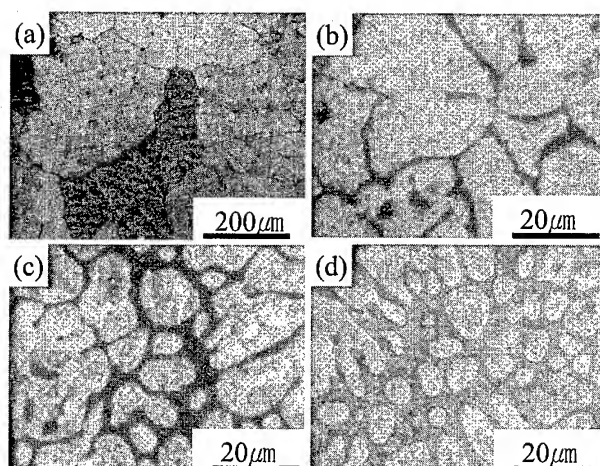


Fig. 1 Microstructures of (a) Pure Mg (b) Mg-1mass%Ni alloy, (c) Mg-5mass%Ni alloy, and (d) Mg-10mass%Ni alloy.

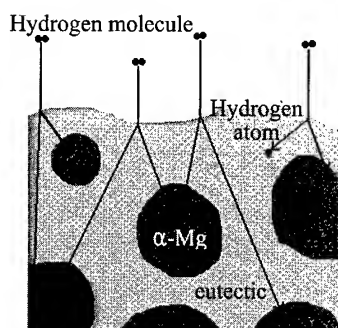


Fig. 2 Schematic illustration of hydrogen dissociation and diffusion of hydrogen atom for hypoeutectic Mg-Ni alloy

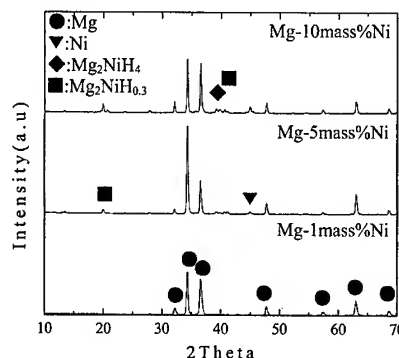


Fig. 3 XRD patterns of crushed Mg-Ni alloys under hydrogen atmosphere (2 MPa) for 4 hr

Table 1. Nickel composition of Mg-Ni alloys

Alloys		Mg-1mass%Ni alloy	Mg-5mass%Ni alloy	Mg-10mass%Ni alloy
Ni content (mass%)	Nominal	1.57	5.62	10.48
	Eutectic	20.93	21.00	24.45

3.2 Hydrogenation properties

Fig. 4 shows the PCT curves of hydriding and dehydriding for Mg-xmass%Ni alloys at 523, 573 and 623K. Hydrogen capacity of Mg-1mass%Ni alloy is about 4.5mass% at 573 and 623K. There is no plateau in hydriding reaction and a valley in dehydriding reaction of Mg-1mass%Ni alloy due to the poor kinetics of this alloy.

The hydrogen capacity and reversible capacity of Mg-5mass%Ni alloy increases in comparison with Mg-1mass%Ni alloy and the measured hydrogen capacity of Mg-5mass%Ni alloy is 83% of THSC (Theoretical Hydrogen Storage Capacity). About 0.3mass% hydrogen is remained in specimen without dehydriding at 523K. Figs. 4 (c) and (f) display the PCT curves of Mg-10mass%Ni alloy. The hydrogen capacity and reversible capacity are about 6.3mass% and 4mass% at 623K respectively. The hydrogen capacity of 6.3mass% corresponds to 92% of THSC. This high hydrogen capacity is attributed mainly to the microstructure of Mg-10mass%Ni alloy, which consists of island-like α -phase and the eutectic phase. Mg-1 and 5mass%Ni alloys have higher THSC than Mg-10mass%Ni alloy, but α -Mg of those alloys cannot form hydride entirely because the eutectic phase is not enough

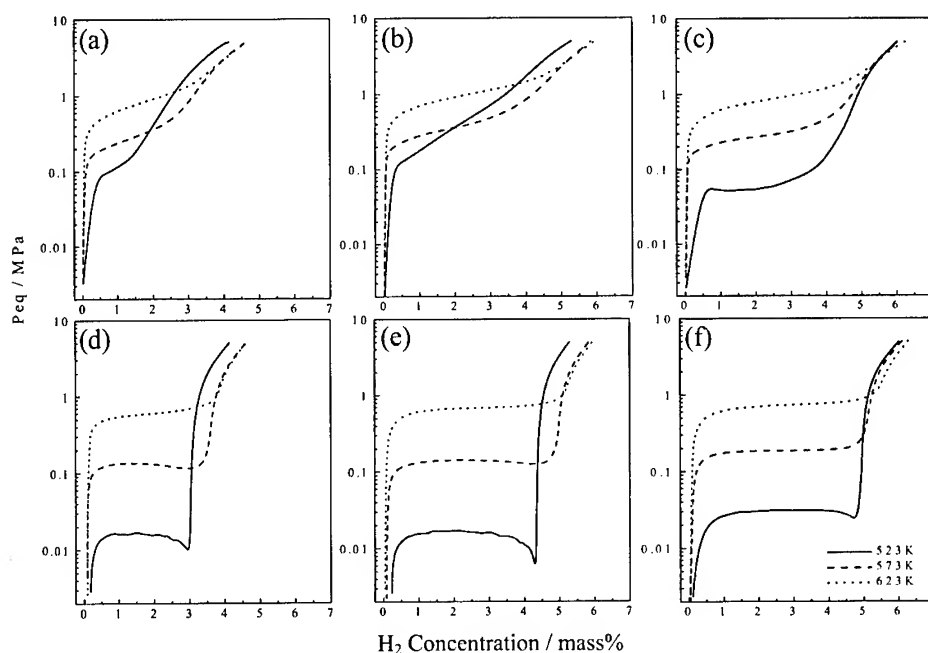


Fig. 4 PCT curves of Mg-1mass%Ni alloy (a) hydriding (d) dehydriding, Mg-5mass%Ni alloy (b) hydriding (e) dehydriding, and Mg-10mass%Ni alloy (c) hydriding (f) dehydriding.

to supply dissociated hydrogens to α -Mg sufficiently. The results of Image analysis done by Image Pro[®] PLUS, Media Cybernetics, shows that the eutectic fraction of Mg-10mass%Ni alloy is about 47.6%, which surround the primary hydride forming α -Mg and act as the dissociated hydrogen supplier. So, the α -Mg of Mg-10mass%Ni alloy can form hydride easily. The measured dehydriding plateau pressure is 0.18MPa at 573K and 0.1mass% hydrogen is remained without dehydriding at 523K. The calculated reaction enthalpy of Mg-1, 5, 10mass%Ni alloy is -53.98 ± 2.89 , -55.28 ± 0.00 , and -67.31 ± 2.14 kJ/mol, respectively. Reilly *et al.* reported that reaction enthalpy of Mg₂Ni, which was fabricated by induction

melting, is -64.5kJ/mol [8]. In spite of small amount of nickel contents and easy producing method, Mg-10mass%Ni alloy produced by RCM achieves excellent reaction enthalpy records.

3.3 Degradation behaviors of Mg-10mass%Ni alloy by cycling

The morphology change of Mg-10mass%Ni alloy after given cycles are shown in Fig. 5. The morphology without cycling of Fig. 5 has flat surface and sharp edge (a) and after 10 cycles, specimens started to be crushed (b). After 350 cycles, specimens were pulverized into fine particles of 100 nm (c). It may be originated from the volume change of specimens during hydriding and dehydriding reaction. Fig. 6 shows the changes of hydrogen capacity and the plateau pressure with the number of cycles. Hydrogen capacity increases rapidly up to 160 cycles, then decreased slowly. After 350 cycles, hydrogen capacity is lowered about 20% of THSC. The fine particles, which have large specific surface area, are highly reactive with hydrogen. So, at the initial stage of hydriding reaction, the hydrogen capacity increases sharply. After 160 cycles, however, the extreme pulverization may occur and cause the phase separation of $\alpha\text{-Mg}$ of the primary hydride former and the eutectic of the dissociated hydrogen supplier. The eutectic phase do not have to supply hydrogen to the $\alpha\text{-Mg}$, therefore hydrogen capacity decreased after 160 cycles (a) and all over the cycles, the hydriding plateau pressure decreased, and dehydriding plateau pressure increased.

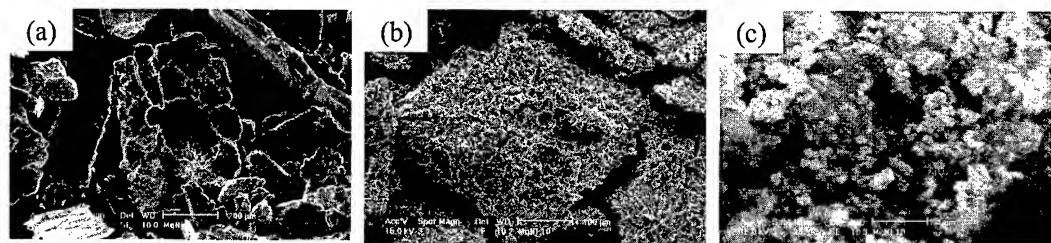


Fig. 5 Morphology of the specimens after the given cycles of (a) 0 cycle, (b) 10 cycles, and (c) 350 cycles

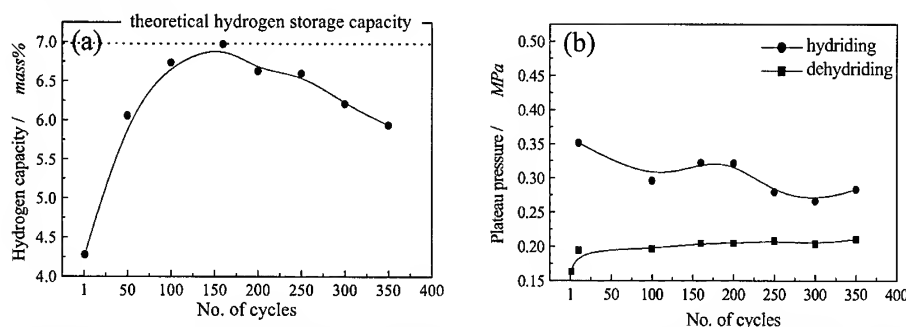


Fig. 6 Variations of (a) the hydrogen capacity and (b) the plateau pressure of Mg-10mass%Ni alloy during cyclic test

4. CONCLUSIONS

1. Magnesium-nickel alloys with various nickel composition were produced by a new alloying method, RCM in ambient atmosphere. It is supposed that mass-production of Mg-Ni alloy, which nearly closed to the desired composition, is possible. Hydrogen capacity and reversible capacity of Mg-10mass%Ni alloy were measured about 6.3mass% and 4mass% at 623K, respectively.
2. High hydrogen capacity of Mg-10mass%Ni alloy is attributed mainly to the microstructures of Mg-10mass%Ni alloy which consists of island-like α -Mg phase of the primary hydride former and the eutectic phase of the dissociated hydrogen supplier.
3. Degradation behavior of Mg-10mass%Ni alloy was estimated by hydriding / dehydriding cyclic test. After 350 cycles, specimens were pulverized into fine particles of 100 nm. During the cyclic test, hydriding plateau pressure decreased and dehydriding plateau pressure increased. Hydrogen capacity increased sharply up to 160 cycles and decreased slowly. This results may indicates that phase separation of α -Mg and the eutectic occurs during cycles.

REFERENCES

1. E. F. Emley: Principles of Magnesium Technology, 1st ed., Pergamon Press Ltd., Oxford, (1966), p.1.
2. Ed. By L. Schlapbach: Hydrogen in Intermetallic Compounds II, Springer-Verlag, New York, NY(1992), pp. 69-70, p.80.
3. L. Zaluski, L. Zaluska and J. O. Ström-Olsen, J. Alloys Comp., Vol.217 (1995), pp. 245-249
4. T. W. Hong, S. K. Kim, G. S. Park, and Y. J. Kim, Materials Transactions, JIM, Vol.41 (2000), pp.393-398.
5. G. Friedlmeier, M. Arakawa, T. Hirai, E. Akiba, J. Alloys Comp., Vol.292 (1999), pp. 107-117.
6. T. Akiyama, H. Isogai, J. Yagi, J. Alloys Comp., Vol.252(1997) L1, pp.11-14.
7. S. K. Kim, W. Ha, C. H. Bae, and Y. J. Kim, in Magnesium Technology 2001, J. Hryn, eds., TMS, Warrendale, PA, (2001), pp.205-210.
8. J. J. Reilly, R. H. Wiswall, Jr. Inorg. Chem., Vol.7 (1968), pp.2254

DRILLING OF MAGNESIUM AM60B ALLOY BY USE OF PVD COATED TOOLS

E. Gariboldi, P. Locati, M. Vedani

Politecnico di Milano, Dipartimento di Meccanica
Piazza L. da Vinci 32, 20133 Milano (Italy)

ABSTRACT

The present paper illustrates a research study on machinability in drilling operations of a magnesium alloy and on the opportunity offered by the use of coated tools. Twist drills in HSS steel (10 mm diameter) were used for the experimental work. Two different ZrN coatings were produced by means of an arc evaporation PVD process, using different deposition parameters. Each coating was characterised as far as thickness and surface finish are concerned. Dry machining drilling tests consisting in machining holes 40 and 60 mm deep were performed. Three sets of drilling tests were carried out with a fixed peripheral speed (63 m/min) and with feed speed of 0.27, 0.37, 0.5 and 0.7 mm/rev. In each test condition the tool life has been evaluated and the evolution of tool wear and of hole surface finish (roughness) were also monitored each 50 machined holes. The experimental results allowed to state that an optimal range of feed speeds for each drill surface finish exists, higher for ZrN coated tools.

1. INTRODUCTION

A great deal of magnesium components is required by the automotive market where the choice of materials is increasingly dictated by weight saving and recycling needs [1]. Further, the high fluidity, low specific heat per unit volume and very low solubility of iron from the dies made it an ideal material for die cast production [2] and counterbalance the complexity of die-casting equipment imposed by the reactivity of this metal [3]. Up to now, the advantages brought about by die casting Mg alloys have been used above all in the production of thin-walled, complex shape products. The opportunity to produce bulk parts in Mg alloys is also being taken into consideration. The amount of machining operations, such as milling, drilling or boring will gain importance on these parts. The machinability of magnesium alloys has been referred as very good, with low cutting forces and well broken chips [4], but the reactivity of magnesium has often restrained manufacturers from machining it. Further, the use of lubrication has widely been discussed in literature [3, 5]. Despite the good machinability of magnesium alloys, attention has to be paid to tool wear and surface finish. Under certain operating conditions, i.e. at high cutting speeds, dry machining was reported to favour flank built up (FBU) on tools (i.e. the adhesion of the material being machined on the clearance face of the tool) and to increase both cutting forces and machined surface roughness [5-7]. FBU is a characteristic feature in machining Al-containing Mg alloys having significant amounts of the eutectic Mg-Mg₁₇Al₁₂ at grain boundaries. The main reason for FBU was proved to be the local rise to the eutectic temperature (437°C for Mg-Al alloy) at which the eutectic melts, thus steeply increasing the alloy plasticity [5-6]. Some characteristics of tools have been reported to have positive effects on FBU formation: a low friction coefficient between tool and material being machined, high thermal conductivity (both factors concurring

in lowering temperature in the cutting zone) and a sharp cutting edge. The present paper illustrates a study carried out on the machinability in drilling operations of AM60B alloy and on the opportunity of using PVD coated twist drills and heavy dry machining conditions.

2. MATERIALS AND EXPERIMENTAL PROCEDURES

Twist drills in M2 grade HSS steel were used for the experimental work. Drills, corresponding to DIN 388 standard, had a diameter of 10 mm, an helix angle of about 35°, a point angle of 130°. In order to evaluate the machinability of a magnesium alloy and, at the same time the opportunities offered by coatings, three series of drills were coated with zirconium nitride (ZrN) by an arc evaporation PVD process. For this nitride two sets of process parameters have been used and the corresponding coatings will be hereafter referred as ZrN-a and ZrN-b. The coating process (PUSK Process) is characterized by a steered arc, by three cathodes and a three axes rotation system that minimize the shadow effects allowing an almost homogeneous thickness to be obtained. During PVD coating the tool substrate reached temperatures of 480-500°C. Coatings were characterized by SEM examination of surface finish and by the thickness evaluation in different locations on longitudinally sectioned twist drills. The influence of substrate surface finish on the coating surface characteristics has been estimated on sets of cylindrical samples cut from the straight shank of drills and polished by conventional metallographic techniques up to different roughness levels.

The widely used AM60B die casting Mg-alloy, was chosen to perform machinability tests. The alloy was supplied as ingots measuring 320 X 130 X 100 mm³. The microstructure of ingots was made of a Mg-matrix containing eutectic Mg-Mg₁₇Al₁₂ and AlMn particles. The hardness values (52HV) and microstructural features were similar (apart from grain size) to those of die cast products made of the same alloy [8], and results of machinability tests can reasonably be transferred to die cast products. Two sets of drilling tests were carried out on the above ingots. In the first set, performed using uncoated (UC) and ZrN-a coated tools, 40 mm deep holes were machined in two steps. The total depth was increased to 60 mm (machined in three steps) in a second set of tests on uncoated and ZrN-b coated tools in order to obtain heavier working conditions. The drilling parameters and the number of test tools used for machining tests are listed in Table 1. All drilling tests were performed at a fixed peripheral speed (63 m/min, in the low range suggested in literature [9]) and with different feed speed: 0.37, 0.5 mm/rev were chosen for both sets of tests, while 0.27 and 0.70 mm/rev feed speed have been investigated only for the first and second set, respectively. By this way the thickness of chips was greater than 0.25, as usually suggested for safety reasons. For each test, every 50 machined holes (20 at 0.7 mm/rev feed speed) pictures of the drill were taken to follow the wear evolution by means of observation on a stereomicroscope and, in particular cases, SEM analysis. Roughness profiles of the 0-6 mm from the surface of the holes and, for the second series of tests, also of the region at 12-18 mm deep were also taken in order to correlate the hole finish to the tool condition.

3. RESULTS

The SEM observation of the coated samples surfaces revealed traces of impacts and metallic droplets, typical features of arc evaporation process, particularly evident in ZrN-a coating, where some large droplets (up to 50µm long) were observed. The surface finish of the second

coating (ZrN-b) was more homogeneous and the maximum size of droplets was 8 μm . The surface features of coated tools corresponded to those previously mentioned on the clearance face of drills, while the presence of some craters, as well as of droplets, characterized the surface of the flutes. Both SEM observations and roughness measurements highlighted that the presence of the above irregularities were of particular importance when well-finished surface were coated, as discussed in a previous analysis [10]. The presence of large droplets on ZrN-a coating significantly increased R_a roughness values of twist drills, as reported in Table 2. The different surface finish of the tools is better underlined by a second roughness parameter, R_{pm} (expressed in μm , in Table 2), the average of the 5 maximum peaks of the roughness profile measured in 5 corresponding partial measurement sections. Despite the measurement of roughness on the rake face was prevented by geometrical reasons, its visually higher roughness reasonably smoothed the differences between coated and uncoated tools. The thickness of the coating layer, reported in Table 2, reflects the location of cylindrical samples inside the coating chamber and a partial shadow effect.

Table 1. Machining parameters and corresponding tool life and hole surface roughness for drilling tests on uncoated (UC), ZrN-a and ZrN-b coated tools.

Test reference number	Peripheral speed (m/min)	Feed speed (mm/rev)	Tested tools	(Average) tool life (m)	Standard deviation	Average R_a roughness of holes (0-6 mm)	Average R_a roughness of holes (12-18 mm)
ZrN _a -40-0.27	63	0.27	1	1.4	-	0.76	-
UC-40-0.27				4.2	-	0.63	-
ZrN _a -40-0.37	63	0.35	1	16.1	-	0.83	-
UC-40-0.37				20	-	1.35	-
ZrN _a -40-0.50	63	0.50	1	16.8	-	0.72	-
UC-40-0.50				10.3	-	1.08	-
ZrN _b -60-0.37	63	0.35	3	12.2	0.28	0.53	0.54
UC-60-0.37				15.4	0.19	0.62	0.91
ZrN _b -60-0.50	63	0.5	5	21.7	0.28	0.49	0.49
UC-60-0.50				10.3	0.29	0.54	0.80
ZrN _b -60-0.70	63	0.70	1	1.2	-	-	-
UC-60-0.70				3.6	-	-	-

The results of machining tests expressed in terms of distance machined by twist drills in each coating/feed speed conditions are listed in Table 1. Focusing on the first set of three drilling tests, even if the reported values represent the results of single tests (and thus no statistical evaluation on tool life can be performed), significant effect of the machining conditions can be observed. The tool life of both tools at the minimum feed speed was very short. It displayed a better behaviour at intermediate feed speed for the uncoated tools. The best results in terms of tool life for ZrN-a twist drills correspond to medium and high feed speed, where this tool behave better than the uncoated one. An analogous tool life evolution of the ZrN-b twist drills, with long machined length at 0.5mm/rev resulted from the second series of tests at increased hole depth. On the contrary in this second series of tests, life of uncoated tools reduced as the feed speed increased. The repeatability of tool lives can be observed by standard deviation values given in table 1.

Table 2. Thickness and roughness of the coatings on samples and twist drills.

Coating	Thickness			Roughness of Clearance face			
	Samples (μm)	Clearance face (μm)	Rake face (μm)	R _a // cutting edge (μm)	R _a ⊥ cutting edge (μm)	R _{pm} // cutting edge (μm)	R _{pm} ⊥ cutting edge (μm)
ZrN-a	2.0	3	1.8	0.52	0.21	1.89	0.94
ZrN-b	1.3	2.0	1.85	0.45	0.12	1.26	0.70
UC	-	-	-	0.44	0.14	1.08	0.40

The examination of twist drills every 50 holes allowed to monitor the wear evolution of the tool. When considering the minimum feed speed, 0.27 mm/rev in drilling holes 40 mm deep, the formation of a magnesium FBU was observed both on the cutting edge and on the margin of the drill. Further drilling led to the formation of a continuum layer of Mg that covered the whole flutes. The formation of FBU at the cutting edge corresponded to an increase of cutting forces, vibrations and to a modification in the chip geometry (from short to longer and curled, with evidence of extensive plastic deformation). The low feed speed of this set of tests reasonably caused machining of hardened magnesium alloy layers and thus increased cutting force, high local temperatures or even partial fusion of this alloy.

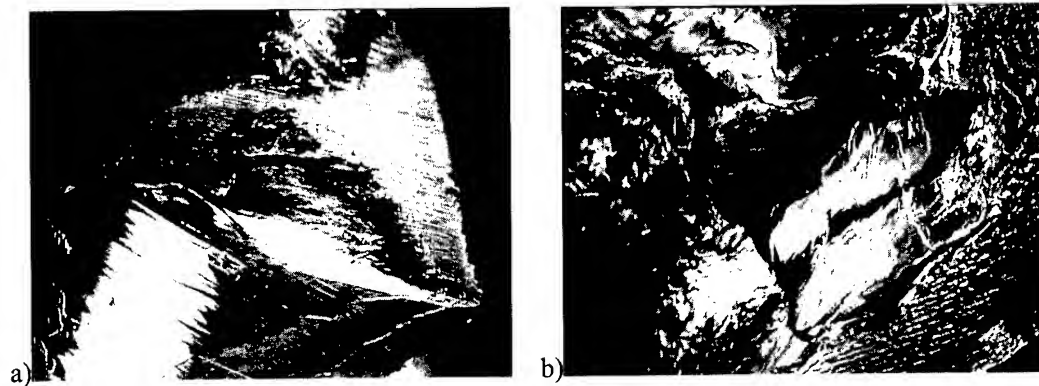


Figure 1. Typical adhesion of Mg alloy on twist drills during machining 60 mm deep holes with a feed speed of 0.5 mm/rev: a) on the clearance face of a ZrN-b twist drill, after 160 holes (9.6 m); b) on the surface of the flutes of an uncoated twist drill after 200 holes (12 m).

Greater feed speed of 0.37 mm/rev modified the wear characteristics of the tools and, consequently, the tool life. An earlier formation of a built-up layer on the margin and the extension of magnesium layer from the margin to all the clearance face characterized these tests (Figure 1a). It was also observed the presence of a continuum magnesium layer inside the flutes and progressively, the adhesion on them of fragments of chips displaying extensive plasticity (Figure 1b). The onset and the progress of each of the above features varied with the coating and machining conditions. In drilling of 40mm deep holes, the retarded onset of the above adhesive wear forms produced during most of the test short and well broken chips. Up to the final holes machined no difficulty of chip evacuation was observed. Machining deeper holes increased the difficulty to evacuate chips, that partially adhered to subsequent chips and then on the flute surface. Both the partial break-off of the hardened magnesium layer from the tool margins and the presence of long curled chips have deleterious effects on the hole surface

finish, particularly on the external region of the holes, as confirmed by comparisons of 0-6mm and 12-18 mm deep roughness measurements. A reduced break-off of magnesium particles from ZrN-b twist drills generally corresponded to lower roughness of machined holes than that of UC tools, as clearly appears in Figure 2.

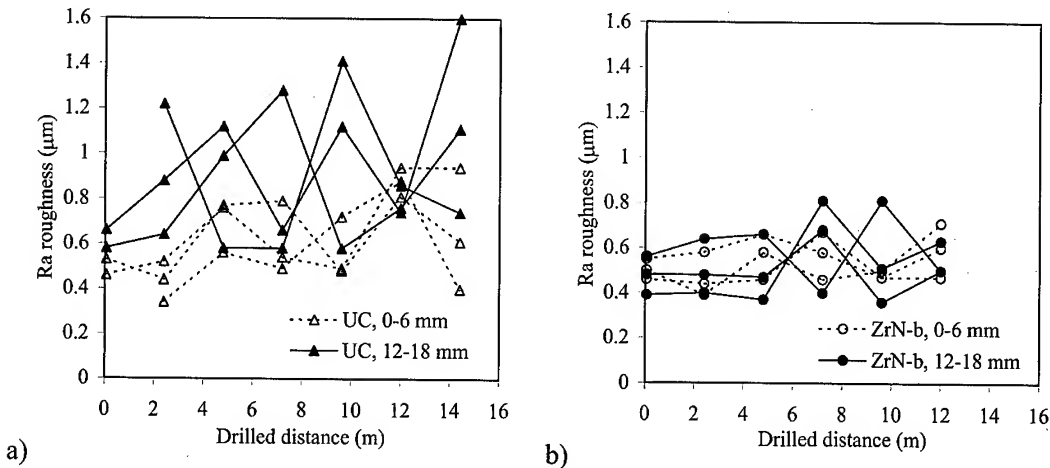


Figure 2. R_a roughness measured on the first and every 50th machined 60 mm hole (feed speed 0.37 mm/rev) at depth of 0-6 mm and 12-18 mm for UC (a) and ZrN-b (b) coated tools.

At the feed rate of 0.50 mm/rev the formation and evolution of magnesium built-up layer was similar to the medium feed speed. Under these machining condition the duration of the step corresponding to external surfaces kept free from the machined alloy was generally reduced and the same was true for the period of generation of broken chips. At the same time, the presence of magnesium on flutes was more significant and the evacuation of chips, of increased thickness and showing signs of great plastic deformation, was very difficult. An opposite behaviour under this machining parameters was found for the ZrN-b tool, displaying its longest life. The absence of a continuum Mg layer on the margin as well as break-off from it (Figure 3) and the formation, during most of the tool life, of broken chips, led also to low roughness values of holes, even in their portion near the external surface.

At the greatest feed speed, the tool life decreased due to the anticipated onset of the features of adhesive wear already reported for the first series of test.

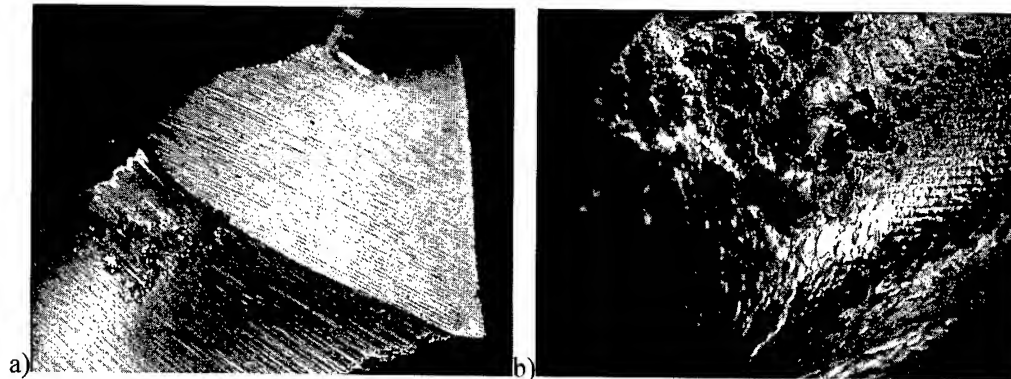


Figure 3. ZrN-b twist drills after machining 60mm deep holes with a feed speed of 0.5 mm/rev: a) clearance face after 160 holes, b) flute after 120 holes.

4. DISCUSSION AND CONCLUSIONS

The preliminary evaluation of the coating characteristics evidenced that the thin layers produced by arc evaporation PVD technique had different surface finish and displayed the presence of droplets typical of this PVD process, of larger size in ZrN-a coating. Due to the initial roughness values of the uncoated tools, the initial R_a and R_{pm} roughness parameters of ZrN-b twist drills were not significantly increased by the nitride deposition.

Under the investigated range of machining parameters all the examined tools reached the end of life due to extensive adhesion of magnesium. The present machining tests showed that there is an optimal range of feed speed that guarantees at the same time long tool life and good surface finish of the holes. Even if, for a correct definition of the tool life, dependence on the feed speed a more extensive number of tests should be performed, it is clearly demonstrated from the present tests the improved behaviour of ZrN-b coated tools at higher feed speeds, both in terms of machined length and hole surface finish. The improvement brought about by zirconium nitride coating when heavy machining parameters are used is confirmed by the ZrN-a coating, despite its surface finish. Longer tool lives were found for uncoated tools in the low-medium range of feed speed.

Several factors play their role in determining tool life and their combination led to the optimal range of machining parameters: the heat generated during the formation of chip, high both at high and at low feed speed (in this latter case because an hardened layer of magnesium is machined and because of the formation of FBU on the cutting edge), the heat removal from the machined zone, the thermal barrier effect of coatings, the tendency of magnesium to adhere to the tool and the friction characteristics of the tool surface. This latter two factors can be reduced by the presence of a suitable coating and on tool surface roughness.

The results presented in this paper offer a contribution to the improvement of machining parameter for drilling operations on a magnesium alloy. In order to determine the best drilling parameters for coated and uncoated tools a wider set of experimental tests should be performed, also taking into consideration different tool geometry.

ACKNOWLEDGEMENTS

The authors would like to thank A. Korovkin (SORI) for the PVD coating of tools, D. Bisi (Meridian) for supplying magnesium alloy, A. Bagnalasta for his contribution to drilling tests.

REFERENCES

1. T.K. Aune, H. Westengen. SAE Technical Paper 950424, SAE, Detroit, MI, (1995).
2. D.L. Albright, Proc. IMA San Francisco (1995), pp. 30-37
3. Holta, H. Westengen, D. Albright. SAE Technical Paper 940413, SAE, Detroit, MI, (1994).
4. H.J. Morales. SAE Technical Paper 800418, SAE, Detroit, MI, (1980).
5. M. Videm et. al., SAE Technical Paper 940409, SAE, Detroit, MI, (1994).
6. N. Tomac, K. Tønnesen, Annals of the CIRP, Vol. 40/1, (1991), pp. 79-82.
7. T. Friemuth, J. Winkler, Advanced Engineering Materials, 1, (1999), pp. 183-186
8. M. Vedani, Key Engineering Materials, Vol. 188 (2000), pp. 129-138.
9. Metals Handbook Ninth Edition, Vol. 16, p. 820-830.
10. E. Gariboldi, A. Korovkin, Proc. AIMAT Conference, Spoleto (2000), pp. 259-264.

High Efficient Drilling of Aluminum Alloys

Keizo Sakurai¹, Katsushige Adachi¹, Gosaku Kawai¹ and Koichi Ogawa²

¹ Osaka Sangyo University, Faculty of Engineering, 1-1 Nakagaito 3-Chome, Daito
Osaka 574-8530 Japan

² University of Osaka Prefecture, College of Integrated Arts and Sciences, 1-1
Gakuenmachi, Sakai Osaka 593-8231 Japan

ABSTRACT

With the prime objective of contriving an effective method of drilling on conventional machine tools with conventional drills, the high feed rate drilling of aluminum alloy A1050, A2017 and A6061 is attempted with titanium nitride coated SKH56 drills under cutting conditions (1500rpm, 1.0mm/rev) harsher than those generally employed. Results obtained of cutting characteristics such as cutting forces, chip shape, burr shape, drill life, etc were examined in order to determine the critical cutting condition for conventional drills. From results obtained it is found that the high feed drilling of aluminum alloy A1050 is difficult practically. While high feed drilling in A2017 and A6061 alloys is very feasible.

1. Introduction

Established custom from time past to employ the conventional norm to the drilling operation is very important since 1/3 of all machining operations is made up of drilling, thus, high efficiency and stability of the drilling operation are important requisites for enhancing production. From this standpoint, various studies into enhancing the efficiency of the drilling operation are undertaken. For instance, super high speed drilling that became possible due to advances made in rotating the spindle of machine tools at super high speed and research into high feed drilling using special drills with a web thickness 3 times that of conventional drills and having a second cutting edge instead of a chisel edge [1]. Super high speed drilling and the use of special drills are also important methods that can be used to enhance drilling efficiency, however, there are machining cost related problems that need to be solved before these methods are widely accepted.

As mentioned earlier, recently great strides have been in drill strength, cutting edge strength and heat resistance etc of conventional drills, conventional drills are now believed capable of withstanding harsher cutting conditions than conditions generally used at the moment. In this light, conventional drills and a conventional machine tool are employed in this study with the prime objective of contriving a high drilling efficiency, to attain this goal, TiN coated SKH56 drills are employed in the high feed drilling of three types of aluminum alloy workpiece and variables such as cutting forces, chip shape, burr shape and drill life etc are examined and the critical cutting condition of conventional drills is investigated.

2. Experimental Method

2.1 Drilling Device, Workpiece and Drill

Tests were performed on a CNC drilling machine (FANUC) driven by a 5.5kW motor. A piezo-electric dynamometer attached to the chuck of the drilling machine was used to measure cutting forces (thrust, torque). Rectangular blocks 20mm thick of three types of aluminum alloys (A1050, A2017 and A6061) were used as workpiece. TiN coated SKH56 drills of diameter 6mm were used in the study.

2.2 Cutting Conditions

The following rotational speeds 500, 750, 1000, 1250 and 1500rpm were employed in experiments to investigate the critical cutting conditions and at each cutting speed drilled under wet conditions using an emulsion type (JIS W1-1) water-soluble cutting fluid.

3. Results and Discussion

3.1 Cutting Forces

3.1.1 Workpiece A1050 Fig.1 shows cutting forces (the maximum thrust force and torque values) for alloy A1050 drilled at the various cutting speed ranging from 500~1500rpm using the following feed rates $F=0.15, 0.5$ and 1.0mm/rev . The plot shows that the thrust force is roughly 250N, while torque is about 1Nm for a normal feed rate $F=0.15\text{mm/rev}$ and stays almost constant with subsequent increases in cutting speed. In the case of feed rate $F=0.5\text{mm/rev}$, the observed trend is that thrust force and torque increase with increases in cutting speed. In the case of high feed rate $F=1.0\text{mm/rev}$, at a cutting speed of 500rpm a high thrust force roughly 2500N is revealed while at a cutting speed of 750rpm there is a sharp drop in thrust force to approx 1600N and torque to 9.5Nm. As cutting speed increases further the thrust force and torque increase once again.

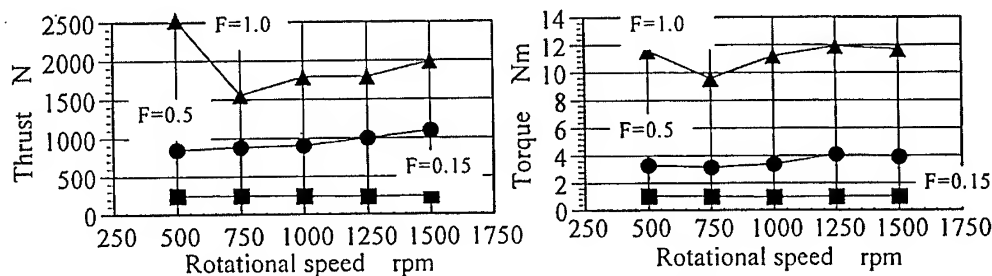


Fig.1 Relation between cutting force and rotational speed. (A1050)

Fig.2 shows plots of the measured results of the thrust force and torque for cutting speed 1500rpm at feed rates $F=0.15, 0.5$ and 1.0mm/rev . The plots show that at feed rate $F=1.0\text{mm/rev}$, thrust force and torque show a rapid increase at a hole depth of about 10mm, the rapid rise is believed attributed to a decrease in chip disposal rate. Beside, at a cutting speed of 1500rpm, thrust force and torque for high feed $F=1.0\text{mm/rev}$ are 8 times and 11 times respectively larger than values for the normal feed $F=0.15\text{mm/rev}$. It is discovered that a large load acts on the drill when machining a ductile material such as alloy A1050.

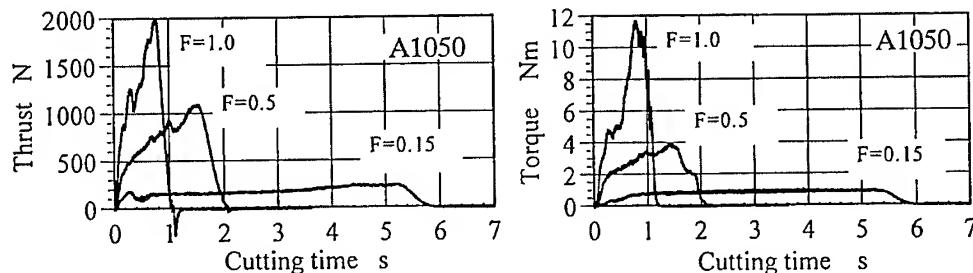


Fig.2 Comparison of cutting force. (1500rpm)

3.1.2 Workpiece A2017 Fig.3 shows the same relationship as in Fig.1 for alloy A2017. The plot shows that for feed rate $F=0.15\text{mm/rev}$, that even with increases in cutting speed a constant thrust force of about 400N and torque of 1 Nm is obtained. In the case of feed rate $F=0.15\text{mm/rev}$, the thrust force approx 900N and torque about 3Nm is constant when drilling at each cutting speed. Likewise, in the case of feed rate $F=1.0\text{mm/rev}$ the thrust force approx 1900N and torque about 5.5Nm is constant. In the case alloy A2017, overall, cutting forces are constant irrespective of the cutting speed.

Fig.4 shows the plot of measured results of cutting forces at speed of 1500rpm and feed rates of $F=0.15, 0.5$ and 1.0mm/rev . Though a large dynamic component can be observed in both the thrust and torque at feed rate $F=1.0\text{mm/rev}$, the cutting state is relatively steady. Whereas, for feed rate $F=0.5\text{mm/rev}$ the dynamic component is small which is indicative of

the excellent state of the drilling. Even in the case of high feed rate $F=1.0\text{mm/rev}$ the thrust force and torque are both 4.8 times those for feed rate $F=0.15\text{mm/rev}$.

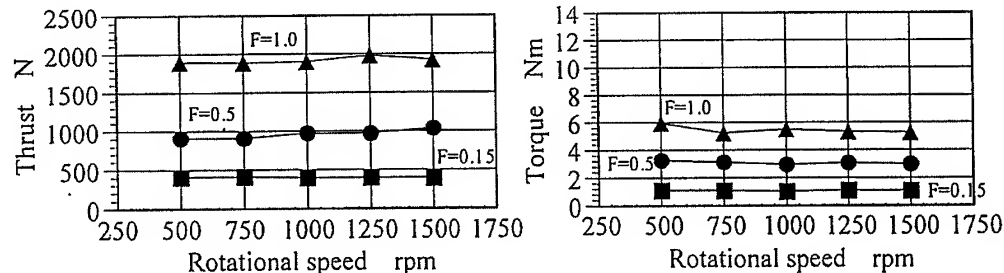


Fig.3 Relation between cutting force and rotational speed. (A2017)

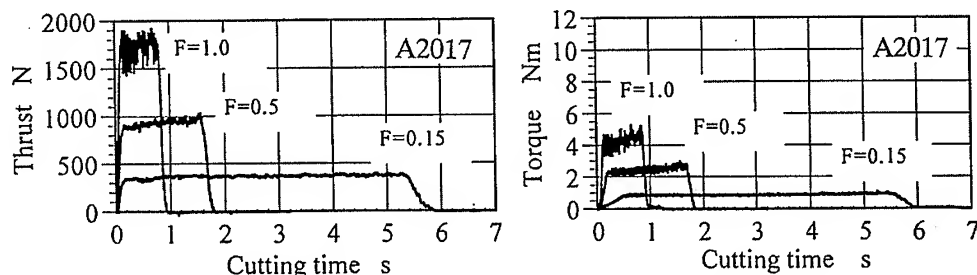


Fig.4 Comparison of cutting force (1500rpm).

3.1.3 Workpiece A6061 Just as in Fig.1, results for alloy A6061 are given in Fig.5. As can be seen in the plot, cutting forces show a similar trend to those of A2017. At all the cutting speeds employed, the thrust force and torque for alloy A6061 is 1/3 those of alloy A2017. However, torque shows a decreasing trend with an increase in cutting speed.

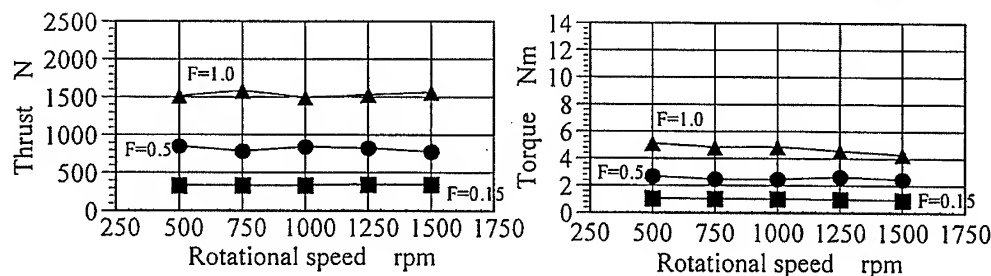


Fig.5 Relation between cutting force and rotational speed. (A6061)

Cutting forces measured at a cutting speed of 1500rpm are given in Fig.6. The plot shows that at feed rate $F=1.0$ the dynamic component of cutting forces is smaller than for alloy A2017, the smaller dynamic component indicates an excellent state of drilling. The thrust force and torque for high feed rate $F=1.0\text{mm/rev}$ are respectively 4.2 and 4 times those for feed rate $F=0.15\text{mm/rev}$. It can be gathered from measured results of cuttings forces stated above that a large load is exerted on the drill during high feed drilling and as result breaking strength is a problem. As a consequence, the focus was shifted to investigating the breaking strength. The experimental formula for deriving the torsion breaking torque T_b of HSS drills is generally given by Eq.1 [2].

$$T_b = 1.26 D^{2.72} \quad (1)$$

where D = diameter of drill

Using the above equation, the torsion breaking torque of the 6mm in diameter drills is about 16.2Nm. When alloy A1050 is drilled at a speed of 1500rpm and feed of $F=1.0\text{mm/rev}$ the maximum instantaneous torque is about 11.5Nm whereas, the maximum torque for alloy A2017 and A6061 is roughly 5Nm. This value is approximately 31% of the maximum instantaneous torque value. Breaking of the drill can be thought of when drilling alloy A1050 whereas when drilling in alloy A2017 and A6061 a drill is thought to have sufficient strength.

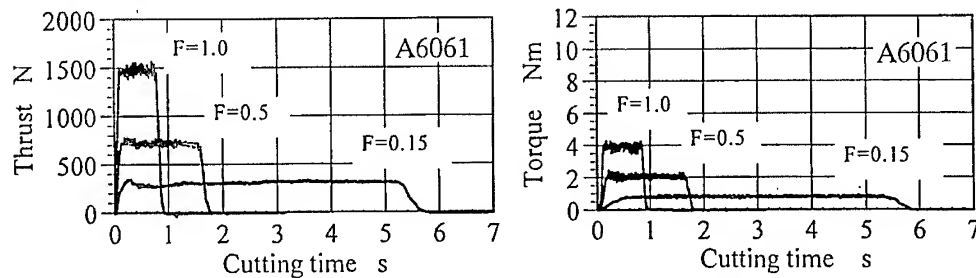


Fig.6 Comparison of cutting force (1500rpm).

3.2 Chip Shape

3.2.1 Workpiece A1050 Fig.7 shows the typical chips produced when holmaking in alloy A1050 at a speed of 1500rpm and at the various feed rates $F=0.15, 0.5$ and 1.0 mm/rev . At a normal feed rate $F=0.15\text{mm/rev}$, thin long pitched chips are formed. Chips of this nature are not influenced by the strong restraining action of the wall of the drilled hole and as result are easily flow through the drill flute leading to low cutting forces and subsequently an excellent drilling state.

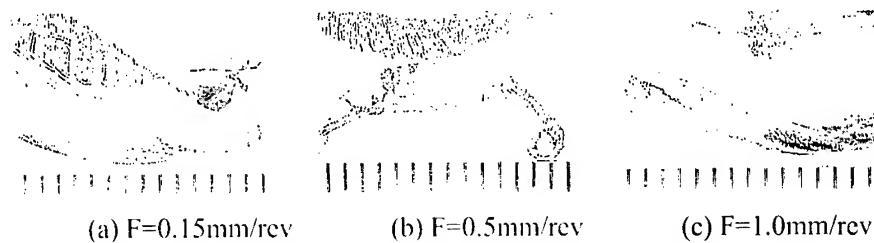


Fig.7 Comparison of chip shape (A1050).

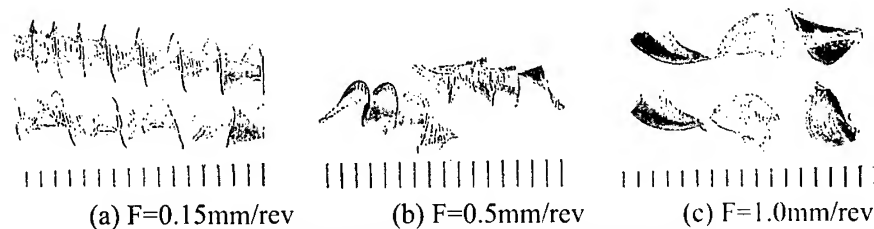


Fig.8 Comparison of chip shape (A2017).

However, in the case of high feed rate $F=0.5$ and $F=1.0\text{mm/rev}$, long pitched chips of length about 70~100mm that are extremely thick are formed. The strong restraining force of the wall of the drilled hole is exerted on chips of this nature as the chips flow throw the hole but as the ductility of alloy A1050 is large chips are able to withstand severe deformation without breaking into bits as evident from the long pitched chips produced. In the case of feed rate $F=1.0\text{mm/rev}$, the thickest portion of some of the chips exceed 1.5mm and judging from the size of the drill flute, chip elimination is believed to be difficult. The plot of cutting forces in Fig.2 discussed earlier substantiates this argument, thus the cutting condition is considered severe.

3.2.2 Workpiece A2017 Fig.8 shows chips formed when drilling alloy A2017 under conditions similar to that of Fig.7. In the case of the normal feed rate $F=0.15$, cone shaped helical chips are formed at a shallow depth of the drilled hole but as the hole depth increases transitional cone shaped chips are eliminated. Whereas, in the case of high feed rate $F=0.5$ and $F=1.0$ mm/rev, fan shaped chips are eliminated, this is due to the large depth of cut that causes thick chips to be formed, though the wall of the drilled hole exerts a strong restraining force on the chips formed, the breaking strain is small in the case of alloy A2017 compared to alloy A1050 because of its small ductility and is believed to break easily due to the formation of cracks on the chip surface along the furrows. Chips formed this way have excellent disposal rate as is evident from the large decrease in torque as compared to the torque for alloy A1050.

3.2.3 Workpiece A6061 Fig.9 shows chips formed when drilling alloy A6061 under conditions similar to that of Fig.7. In the case of high feed rate $F=1.0$ long pitched chips of length 20~30mm are eliminated. The ductility of alloy A6061 is a bit bigger than that of alloy 2017 and as a result chips formed in alloy A6061 are not fan shaped but rather having a long pitch, this sort of long pitched chips of suitable length have good chip exposal because the wall of the drilled hole exerts a much smaller restraining force on the long pitched chips formed. The smaller restraining force exerted is believed responsible for the lowest cutting forces compared to the other two alloy types.

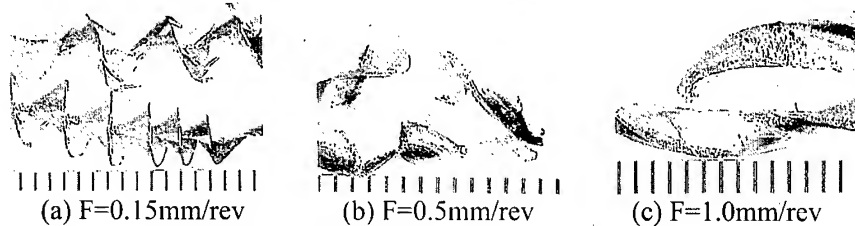


Fig.9 Comparison of chip shape (A6061).

3.3 Burr Shape

The burr shape formed at the exit of the drilled hole when drilling the various alloys at a cutting speed of 1500rpm and feed rate of 1.0mm/rev is shown in Fig.10. The burr shape for alloy A1050 is dome shaped with the workpiece material thrust out. As can be observed from the cutting force and shape of chips formed, this is attributed to the occurrence of severe clogging of chips and as a result there is little or no cutting action by the cutting edges around the hole exit and that has led to a large ductile portion of the workpiece material to thrust out. Judging from the burr shape, cutting forces and chip shape it is not practical to drill in alloy A1050 at high feed rate $F=0.5$ or $F=1.0$. In the case of alloy A2017, the height of the burr formed is low and the thickness of the base of the burr is also small. The size of the burr formed is of the same size as that formed under normal feed conditions. Whereas for alloy A6061, the height of the burr formed as well as the thickness of the base of the burr is large compared to those formed when drilling in alloy A2017.

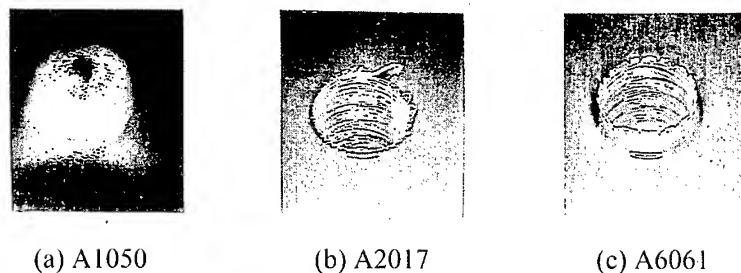


Fig.10 Comparison of burr shape.

The shape of the burr formed in alloy A6061 resembles a petal. This is attributed to a much higher ductility when drilling in A6061 compared to A2017 and as a result, immediately the chisel edge penetrates through the workpiece the uncut portion at the underside of the workpiece is thrust out. A burr of this extent is believed acceptable in practical machining situations.

3.4 Drill Life

From examining the cutting force, chip shape and burr shape results, drilling in A1050 was considered not feasible at feed rates of $F=0.5$ and $F=1.0$ mm/rev. However, since drilling at high feed rates was deemed possible in A2017 and A6061, drill life test at cutting speed of 1500rpm and a feed rate $F=1.0$ mm/rev. Since it was discovered from preliminary tests that drill life exceeded 5000 holes the drill life test entailed drilling 500 holes continuously and the relation between the number of holes drilled and cutting force was examined.

The relation between number of holes drilled and cutting force for alloy A2017 and alloy A6061 workpiece are displayed respectively in Fig.11. As can be seen in Fig.11, the thrust force of alloy A2017 is about 1600N while the torque is about 4.3Nm. It can be seen from the plot that the thrust and torque are almost constant and that cutting force does not vary with an increase in the number of holes drilled. On the contrary, in the case of alloy A6061 the thrust force obtained at the 1st hole approx 1400N and the torque about 4Nm which is smaller than the values for alloy A2017 mentioned earlier however, in the case of alloy A6061 cutting force increases with increases in the number of holes drilled and at the 500th hole the thrust force is about 1500N and the torque is about 4.5Nm. From the above results, it has been clearly shown that at high feed rate $F=1.0$ mm/rev drilling is still possible in both workpiece types after drilling continuously.

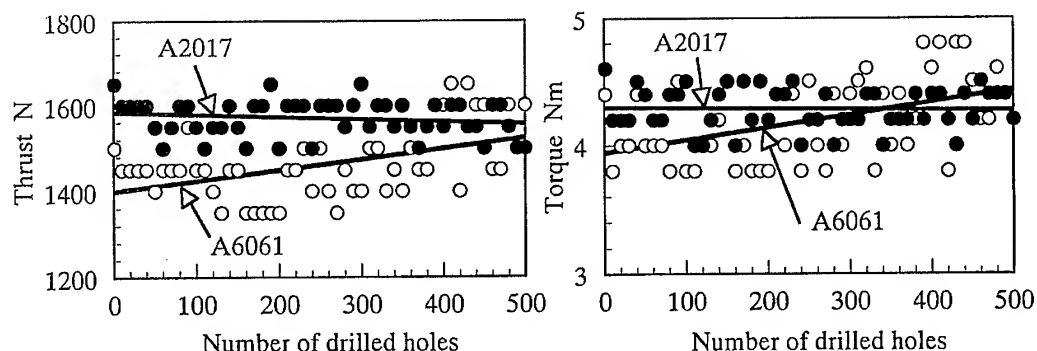


Fig.11 Relation between no. of drilled holes and cutting force.

4. Conclusion

The following facts are clarified from the study of results of cutting characteristics such as cutting forces, chip shape, burr shape, and drill life etc.

- (1) The cutting force when high feed drilling alloy A1050 at a cutting speed of 1500 rpm and feed rate of $F=0.5$ or 1.0 mm/rev is high resulting in the creation of large burrs making it practically difficult.
- (2) In the case of alloy A2017 and A6061, results of cutting variables such as cutting force, chip shape, burr shape, and drill life indicate that drilling is possible at high feed rates.

REFERENCES

- [1] T. Hosoi, Y. Hosoi, S. Hanasaki, Y. Hasegawa, Journal JSME 99-930(1996), p.340.
- [2] S. Okimoto, Tool Eng. 35-6(1994), p.100.

SELECTION OF OPTIMUM WELDING CONDITIONS FOR A6061ALUMINUM ALLOY FRICTION WELDING BY NEURAL NETWORKS

Gosaku Kawai*, Takeshi Sawai*, Toshiro Kurozawa, ** Yoshiaki Yamamoto**,
Hiroshi Yamaguchi*** and Koichi Ogawa***

- * Osaka Sangyo University, Daito Osaka 574-8530 Japan
- ** Setsunan University, Neyagawa Osaka 572-8508 Japan
- *** Osaka Prefecture University, Sakai Osaka 599-8531 Japan

ABSTRACT

This paper describes, by neural network technique, the optimum welding conditions friction welding of A6061 aluminum alloy. A lot of seven input parameters, three output parameters for axial length, five output parameters for heat input and one output parameter for tensile strength are required for successful implementation of this approach. An extended Kalman filtering algorithm was used to determine the synapse weights of the neural network.

From results learned by combining the various input and output parameters, seven factors of welding condition were selected as inputs and three factors of welding behavior as outputs for the network. These inputs and outputs were then interchanged, utilizing a characteristic of neural networks, in order to obtain the optimum welding conditions. As a result, the neural network was shown to provide a method that can successfully determine the optimum welding condition, despite being limited by the range of experimental data used for training.

1. INTRODUCTION

Friction welding [1] is a pressure welding process that employs heat generated by the sliding of friction faces to produce a weld. Possible uses of this technique include the joining of various machine and electric parts. It is a process controlled by few factors and as a result, it is simple to set up. However, the quality, shape and dimensions of the base material can have a significant impact, and, as a result, the optimum welding conditions are usually determined from a trial and error approach based upon both experience and experimentation. Consequently, it is often difficult to determine optimum welding conditions within a realistic frame.

Neural networks are now an established modeling technique with many applications in the field of engineering. It is a method that can determine if a parameter value is suitable for an application, using a pattern presentation obtained by learning data consisting of complex relationship with many variables.

In this study, a neural network technique is used to determine welded joint performance based upon certain inputs (weld conditions and heat inputs). Using results obtained by reverse calculation, the suitability of this method to determine optimum welding conditions is examined.

2. PARAMETERS OF FRICTION WELDING

There are a large number of input parameters and controlling factors in the friction welding processing. The fundamental factors that can be easily fixed on most welding machines are the friction pressure P_1 , the up-set pressure P_2 , the friction time t_1 (or the friction burn-off quantity δ_1), and the rotating speed N . From experimentation of these input parameters, the burn-off quantity δ and the heat input q were selected as middle stage parameters.

The burn-off quantity δ is represented by the friction burn-off quantity δ_1 , the up-set burn-off quantity δ_2 and the total burn-off quantity δ_t ($\delta_1 + \delta_2$). The heat input q is divided into four inputs which can be calculated using the following equations [2]:

$$q_{if} = 6.283 \times N T_i \quad (\text{J/s}) \quad (2.1), \quad q_{id} = (P_1 d^2 \pi \delta_1) / (4 \times 10^3 t_1) \quad (\text{J/s}) \quad (2.2)$$

$$q_{uf} = 6.283 \times N T_f \quad (\text{J/s}) \quad (2.3), \quad q_{df} = (P_2 d^2 \pi \delta_2) / (4 \times 10^3 t_B) \quad (\text{J/s}) \quad (2.4)$$

$$q_t = q_{if} + q_{id} + q_{uf} + q_{df} \quad (\text{J/s}) \quad (2.5)$$

Where, q_{if} : friction input under friction stage, q_{id} : deformation input under friction stage,
 q_{uf} : friction input under up-set stage, q_{df} : deformation input under up-set stage
 q_t : total input, T_i : friction torque under friction stage (Nm),
 T_f : friction torque under up-set stage (Nm), d : diameter of base material (mm),
 t_B : braking time (s).

A diagram of the friction welding process is presented in Fig.1.

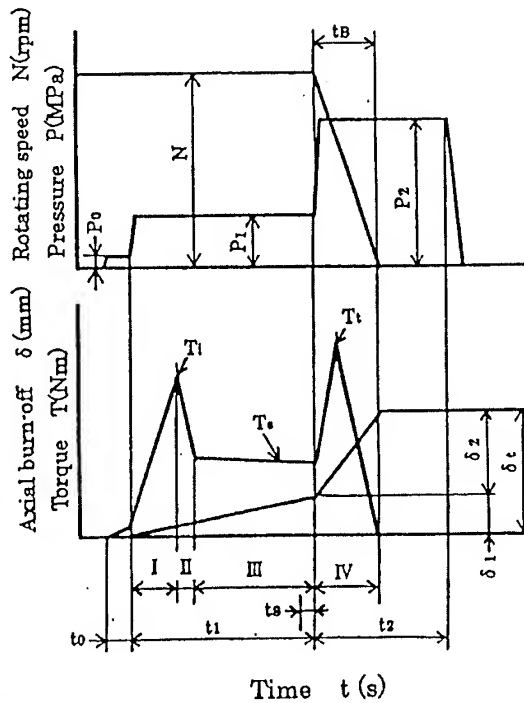


Fig.1 Schematic diagram of brake type friction welding process

3. WELDING DATA USED

The base material used in this experiment was A5056 aluminum alloy. The machined diameter of the welding specimen (base material) was 14 mm and the end face span was 20 mm. Friction welding was carried out under a brake type welding process and the range of welding condition was as follows:

Friction pressure (P_1) \rightarrow 5~45 MPa ; Upset pressure (P_2) \rightarrow 15~135 MPa ;

Rotating speed (N) \rightarrow 16.7~66.7 (rps) ; Friction time (t_1) \rightarrow 2 (s) ;

Braking time (t_B) \rightarrow 0.1 (s) ; Upset timing (t_s) \rightarrow 0 (s) ;

Diameter of base material (ϕd) \rightarrow 14 (mm).

During the welding process, the burn-off quantity and heat input were measured and calculated by photo-recorder. The welded joint was then machined to the dimension of a JIS-14 test piece and the tensile strength σ_B (MPa) from a tensile test conducted using an Amuslar testing machine with a 30 KN ability. Some of these results are presented in Table.1.

Table 1 Example Data

Welding condition							
No.	P_1	P_2	N	t_1	t_B	t_s	ϕd
3P3	15	45	16.7	2	0.1	0	14
3P20	20	60	33.3	2	0.1	0	14
3P25	45	135	33.3	2	0.1	0	14
3P40	40	120	50	2	0.1	0	14
3P55	35	105	66.7	2	0.1	0	14

Measuring & Calculation data									
No.	δ_1	δ_2	δ_3	q_{if}	q_{id}	q_{rf}	q_{rd}	q_t	σ_B
3P3	0.3	0.3	0.6	558	0.3	194	52	804	82
3P20	1.2	4.2	5.4	2076	1.9	309	384	2771	230
3P25	16.8	12.3	29.1	2892	58	488	2552	5990	270
3P40	13.1	14.0	27.1	2692	40	479	2579	5790	264
3P55	6.6	15.7	22.3	2343	18	499	2540	5400	236

4. LEARNING BASED ON NEURAL NETWORKS

The network structure used in the learning process is formed from three structures, consisted of the input layer (variable), the middle layer and the output layer as illustrated in Fig.2. The learning technique employed by the neural network is such that when an output signal was given, the teaching signal was adopted. This technique is usually called a reverse problem, and reverse analysis (the identical algorithm) can be used. This is equivalent to the problem of synapse weights. The problem was analyzed using a method based on expanded Kalman filtering [3], as a neural network is usually expressed as a non-linear system.

This method deals with synapse weights as a quantity of state by considering the neural network with a state space. The main advantage of this is that the convergence of learning is

faster than most usual back propagation algorithms. In addition, a sigmoid function with a slope of 1 (Equation 4-1) was adopted as the transfer function.

$$Y = 1 / (1 + e^{-x}) \quad (4-1)$$

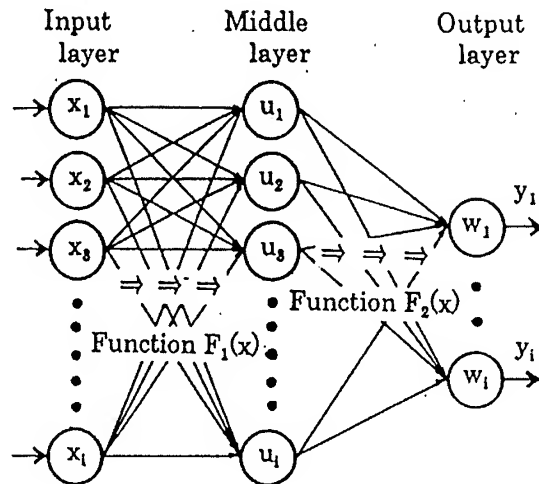


Fig.2 Structure of neural network

4.1 Teaching data

With friction welding, the principal welding conditions are likely to be friction pressure (P_1), friction time (t_1) or friction burn-off quantity (δ_1), rotating speed (N), up-set pressure (P_2), up-set timing (t_s) and braking time (t_B).

The characteristics of the neural network utilized in this study were as follows:

- ① The number of inputs (variables) in the input layer was equivalent to or greater than the number of outputs (variables) in the output layer.
- ② The number of units in the middle layer was fixed by the number of inputs.
- ③ Fifty iteration were used in the learning process.

With consideration of these conditions, the method was implemented in order to obtain optimum welding conditions using a variety of the following factors, $P_1, P_2, t_1, \delta_1, N, t_B, t_s, \phi d, \delta_2, \delta_t, q_{if}, q_{id}, q_{ff}, q_{fd}, q_t, \sigma_B$.

In the first, implementation of the method ($P_1, P_2, t_1, N, t_B, t_s, \phi d$) and nine output factors ($\delta_1, \delta_2, \delta_t, q_{if}, q_{id}, q_{ff}, q_{fd}, q_t, \sigma_B$) were selected. Next, seven input and three output factors were used. The optimum combination – namely, the highest correlation coefficient between input and output – was then calculated. As a result, it was found that there was a strong correlation coefficient between seven inputs ($P_1, P_2, t_1, N, t_B, t_s, \phi d$) and three outputs ($\delta_2, q_{fd}, \sigma_B$). These results are presented in Table 2, where r is correlation coefficient and ϵ is mean absolute deviation. No significant differences were observed between the tests using 50 or 100 learning iterations. Comparison between experimental data (teaching data) and calculated values is shown in Fig.3.

Table 2 Learning results

Data	Middle Layer	Learning	Input	Output	r	ϵ
36	One Layer Seven Units	100	P_1, P_2, N	δ_2	0.993	0.53
			t_1, t_B, t_s	q_{fd}	0.996	66
			ϕd	σ_B	0.983	11

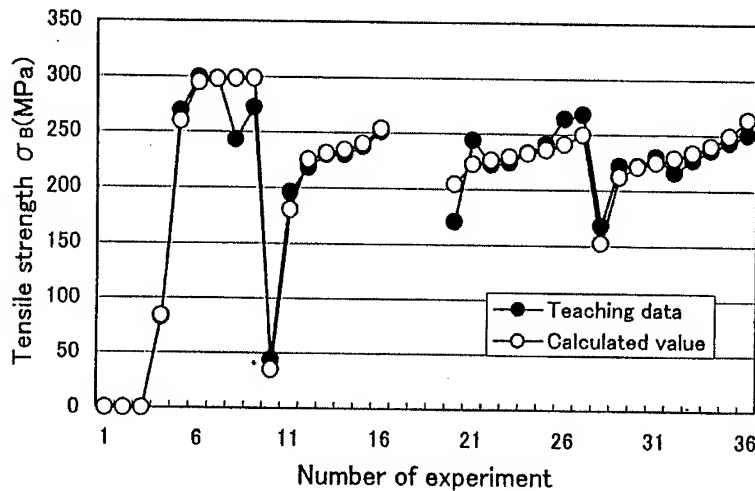


Fig.3 Comparison of teaching data with calculated values

4.2 Selection of optimum welding conditions

From Table 2, it can be seen that there was a strong correlation between welding condition and tensile strength σ_B . Hereupon, inputs and outputs are interchanged, utilizing a characteristic of neural networks, and the method examined to determine its suitability for obtaining optimum welding conditions.

Tensile strength σ_B was selected as an input, and friction pressure P_1 and up-set pressure P_2 selected as outputs, and the learning process was executed. Learning conditions and results are presented in Table 3. From Table 3, it is suggested that neural networks can be used for the inputs and outputs because of the strong correlation coefficients obtained from the study.

Table 3 Learning results

Data	Middle Layer	Learning	Input	Output	r	ϵ
36	One Layer Six Units	100	σ_B, N, t_1	P_1	0.92	3.7
			$t_B, t_s, \phi d$	P_2	0.92	11
				σ_B	0.991	7.3

Verification of this approach was conducted under varying welding conditions ($P_1, P_2, N, t_1, t_B, t_s, \phi d$), and the tensile strength σ_B of the resulting weld determined using a testing machine. The results are shown in Table 4, which shows that the values of calculated tensile strength σ_{BCal} and experimental tensile strength σ_{BExp} are almost identical.

Table 4 Verification conditions and results

No.	Given welding conditions						Results of calculation			Result of experiment
	σ_B	N	t_1	t_B	t_s	ϕd	P_1	P_2	σ_{BCal}	σ_{BExp}
1	100	66.7	2	0.1	0	14	10	32	136	130
2	150	66.7	2	0.1	0	14	8	24	165	162
3	200	33.3	2	0.1	0	14	9	27	199	201
4	200	50	2	0.1	0	14	16	48	204	208
5	200	66.7	2	0.1	0	14	10	28	196	200
6	250	16.7	2	0.1	0	14	38	113	253	248
7	250	33.3	2	0.1	0	14	35	105	256	252
8	250	50	2	0.1	0	14	33	98	246	250
9	250	66.7	2	0.1	0	14	43	130	258	260
10	299	16.7	2	0.1	0	14	33	98	286	290
11	299	33.3	2	0.1	0	14	44	133	284	292
12	299	50	2	0.1	0	14	45	135	288	295
13	299	66.7	2	0.1	0	14	45	135	291	295

5. CONCLUSION

In this study, a neural network technique was used to determine weld joint performance using various inputs (welding conditions and heat input), and results obtained by reverse calculation. Allowing for the performance of the friction welding equipment, the selection of appropriate inputs and outputs makes it possible to determine optimum welding conditions, despite being limited by the region of the network model. In this study, base material shape and quality were fixed, and variation of these parameters will from the basis of future research.

REFERENCES

- [1] S.Noda : Yosetsu-Gijutsu, 5, (1985), pp.19-45.
- [2] T.Sawai, K.Ogawa, H.Yamaguchi, H.Ochi, Y.Yamamoto and Y.Suga ; Effect of heat input on joint performance in 6061 aluminum alloy friction welding, Journal of Japan Institute of Light Metals, Vol.50, No.10, (2000), pp.505-511.
- [3] H.Murase, S.Koyama and R.Ishida : Kalman Neural Computing by Personal Computer, Morikita, (1994), pp.24-83.

Evaluation of Corrosion Fatigue Pitting Damage on 2024-T3

Y.I. Yoon, V. chandrasekaran, D.W.Hoeppner, and Y.H. Hwang

ROK Air Force Aero Technological Research Laboratory

Abstract

In all of the experiments, the resultant fracture occurred because of the formation and propagation of crack(s) from pits before and after coalescence and this is very important because there is a challenge to deal with not only with the individual pits but also to consider developing an estimation of pitting corrosion fatigue life of corrosion fatigue prone aircraft structural components with regard to multiple pit damage (MPD). In all but one of the experiments conducted in the present study, fractography revealed that the origin of fracture was from the deepest pit measured at the location within the group of pits that were joined. Moreover, it was observed that fracture path always followed the location of corrosion fatigue nucleated pits.

Another important finding from this study is that the origin of fracture was dependent on the location of corrosion pits. It was clearly observed that the location of corrosion fatigue nucleated pits resulted in the change of structurally significant location (SSL) with regard to the origin of fatigue fracture.

1. Introduction

Many types of corrosion mechanisms such as intergranular, exfoliation, pitting, crevice, fretting, microbiologically influenced corrosion, stress corrosion cracking, and hydrogen embrittlement have been found to occur in aircraft structural aluminum alloys. The synergistic effects of corrosion and the loading conditions have been found to initiate the corrosion fatigue failure process in aircraft structural components and recommendations to consider corrosion fatigue in materials selections and engineering design were proposed by Hoeppner in 1971 [1]. Nucleation of cracks from corrosion pits was observed by many researchers including the works of Hoeppner [2], Goto [3] in heat-treated carbon steel, and Muller [4] in several steels. As well, in NaCl environment, lowering of the fatigue life due to the generation of pits in carbon steel and 7075-T6 aluminum alloy was observed under corrosion fatigue conditions. Furthermore, recent studies also illustrated the effect of prior corrosion induced pits on the fatigue life as well as "short" crack behavior of 2024-T3 and 7075-T6 aluminum alloy materials [5,6]. In addition, pitting corrosion has been shown to affect the fatigue life of cold worked fastener hole in 2024-T3 and 7075-T6 aluminum alloy as well [7].

Once the pit forms, the rate of pit growth is dependent mainly on the material, local solution conditions and the state of stress. Cracks have been observed to form from pits under cyclic loading conditions. This work will remain for future research.

2. Experimental Methodology

An interrupted corrosion fatigue experimental methodology was developed to generate pit growth rates in 2024-T3 aluminum alloy. The specimens were prepared for artificial corrosion to produce pits on the surface. The specimens were masked except for a small square of approximately 1 mm by 1 mm at the center section of the specimen. A horizontal fatigue machine with MTS servo-controlled and electro-hydraulic system was used in conducting corrosion fatigue experiment. Environmental chambers were machined with Plexi Glass. The environment used was 3.5% NaCl solution. The same solution was used until the specimen fractured. The solution pH varied from 6.5 ("fresh" solution at the beginning of the experiment) to 6.9 (before fracture). The solution was introduced into the environmental chamber by gravity. Inlet and outlet flow regulators controlled the flow rate of solution into the chamber during testing. A maximum load of 312 lb or 1.4 kN (produced a stress of 20 ksi at the reduced center section of the specimen) was applied at the reduced cross section of the specimen at $R = 0.1$ and at a frequency of 10 Hz. In this research, corrosion fatigue induced pits were allowed to form on the exposed area of the specimen only on the upper surface of the specimen. The area of the exposed surface was approximately a square of 1 mm x 1 mm at the center of the specimen for specimen# 2, 3, 4, and 5. The testing was interrupted periodically to remove the specimen for analysis of corrosion fatigue induced pits using the optical microscope, scanning electron microscope, and confocal microscope (ZEISS LSM-510). The specimen was removed periodically from the fatigue test machine to analyze and to quantify the growth of pits. In general, the specimen was removed for analysis every 20,000 corrosion fatigue cycles. Depth of corrosion fatigue nucleated pits was quantified using the confocal microscope as well as the distribution of the depth for each pit also was recorded. After fracture, fractography was performed to correlate the origin of fracture to the "failure pit(s)" that caused the fracture.

3. Results and Discussion

While counting the number of pits as well as classifying the pits with certain depth periodically, the following procedure was used consistently for all of the pits monitored in all of the specimens. Once a group of pits joined, all of the pits in that group were counted as the pits having the depth corresponding to the pit of maximum depth measured in that group. For example, in specimen #3, as shown in Figure 1, after 60,000 corrosion fatigue cycles, pit# 19 and 21 were individual pits growing at a random location with depths of 21 and 30.8 μm respectively. After 80,000 cycles, as shown in Figure 1, the pits 19 and 21 joined together, and when the depth was measured at this location where the pits joined, naturally there would be a distribution of the depth. The maximum depth that was measured at this location was considered as the depth for all of the pits that were joined within that group. Figure 1 shows the distribution of the depth of pits (# 19 and 21) that were joined. This procedure was employed because once the pits joined, it was difficult to identify the boundary of the pit(s) when the pits remained as individual pits before they joined. The group of pits that were found to be joined when analyzed periodically was indicated clearly in pit depth for all of the section.

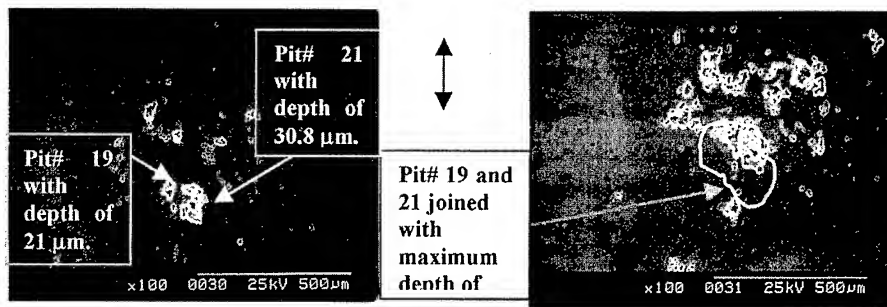


Figure 1: SEM pictures showing pits developed under corrosion fatigue conditions after 60,000 cycles, (top) and after 80,000 cycles, (bottom).

The discussion of these results is provided in the next specimen. Pit growth rates measured in terms of the depth (μm) using the confocal microscope clearly illustrate that pits once nucleated indeed grow to a critical depth resulting in the fracture of 2024-T3 aluminum alloy specimens tested in this study. The pits were randomly distributed with different sizes and shapes. It can be concluded that there is no standard morphology for pits. The factors that may decide the morphology of pits may include localized distribution of material composition such as Al-Cu distribution in 2024-T3 alloy, composition and the availability of electrolyte inside and outside of the pits, structure and composition of oxide film, temperature, stress conditions to name a few. As stated by Smialowska [7], since pitting is an electrochemical process, these variations in the morphology of pits may depend on the uneven distribution of current density within the pit. This also may occur because of the local changes in the thickness of the salt layer as well. Therefore, it is important to characterize the distribution of the depth within a pit in addition to quantifying the maximum depth of a pit. In all of the experiments, the resultant fracture occurred because of the formation and propagation of crack(s) from pits before and after coalescence and this is very important because there is a challenge to deal with not only with the individual pits but also to consider developing an estimation of pitting corrosion fatigue life of corrosion fatigue prone aircraft structural components with regard to multiple pit damage (MPD). This observation is supported by the charts of pit depth vs. number of corrosion fatigue cycles for all of the pits monitored in specimen# 2, 3, 4, and 5 tested in this study. Only 7 pits were monitored in specimen# 1. An example is provided in Figures 2 for specimen #2. For example, in specimen# 4, even though the maximum depth ($46.2 \mu\text{m}$) was recorded at a location where pit# 24, 25, 27A, 28, and 29 joined together, but the origin of fracture resulted from the location where pit# 15, 16, 17, 18, 19A, 19B, 19C, 20, 21, and 22 joined resulting in the maximum depth of $41.5 \mu\text{m}$. This is because, the greater number of pits join, the larger the aspect ratio of the group of pits. This observation is shown in Figure 3. Once the pits are nucleated under corrosion fatigue conditions, at some point of time or after certain number of corrosion fatigue cycles, crack(s) first form from inside the bottom of the pits as Hoepfner had observed this in his earlier research, as is the case in the present study as well. Examples of cracks developing within the pits were captured in this study and they are shown in Figure 4. According to Payer and Staehle [9], there is an analogy between an electrochemical cell and a growing pit.

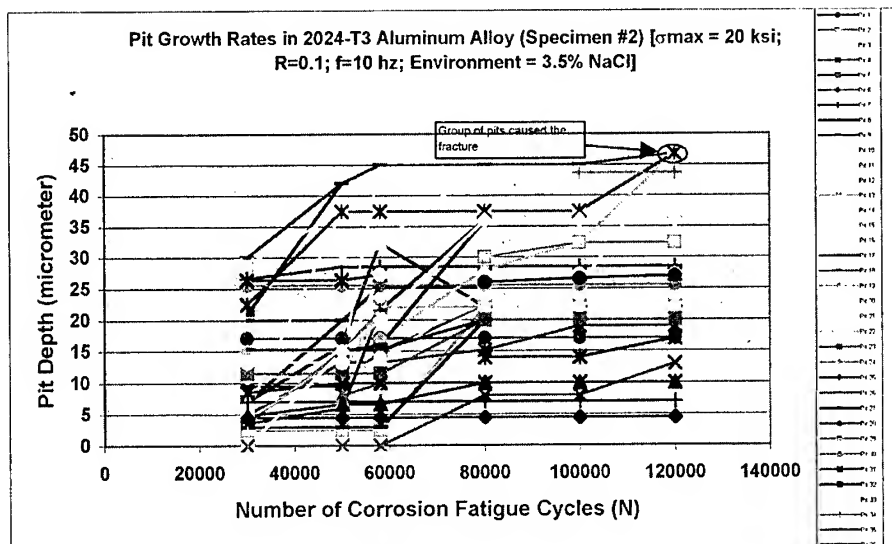


Figure 2: Pit growth rates for Specimen# 2 .



Figure 3: SEM and Confocal Images Showing the Origin of Fracture from the "Failure Pit" of Maximum Depth 41.5 mm for Specimen 4 -- 2024-T3 Aluminum Alloy.

The bottom of the pit is an anode, and the surface of the material and the surrounding walls of the pit are the cathodes. It is believed that the bottom of the pits is electrochemically active as the aggressive chemical solution is dragged in to the pit by capillary action. As a result, the pits grow deeper and also because of the applied cyclic load, fatigue cracks could very well originate from the location where the stress concentration is the largest, that is, at the bottom of the pit. Therefore, it can be stated that in a corrosive environment, with the simultaneous application of fatigue loading, the process of corrosion fatigue is dependent largely on the rate at which pits form and grow to a critical depth to nucleate the Mode-I fatigue crack that now becomes visible outside the pits. Furthermore, it is believed that the deeper the pits, the faster the crack emanates from the bottom of the pits and the faster the cracks that would form as surface cracks or as part through cracks from the pits. Is this a significant issue with regard to the safety of the aging aircraft structural component? Of course it is, because if the metrics with regard to the growth or development of corrosion pits are ignored

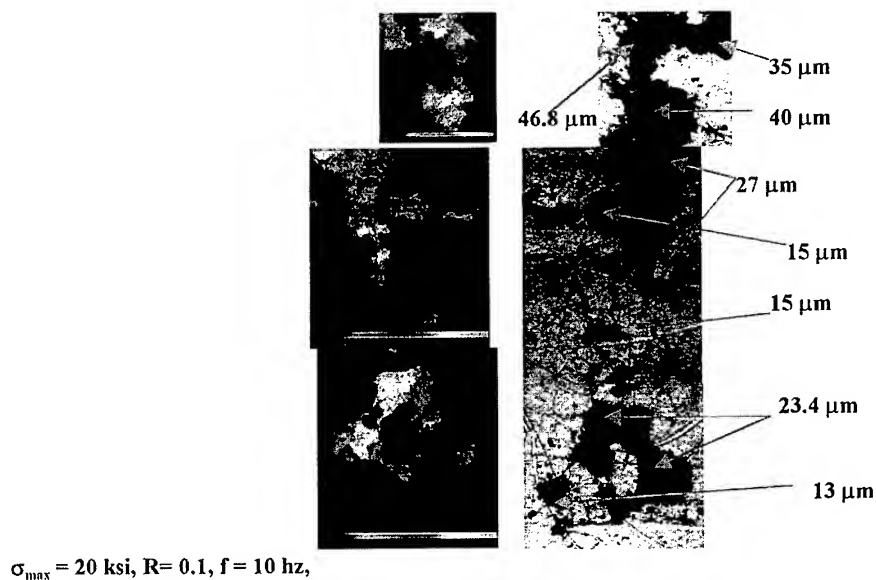


Figure 5: Confocal images showing the crack path through corrosion fatigue nucleated pits -of Specimen#2.

References

1. Hoepfner, D.W., Corrosion Fatigue: Chemistry, Mechanics, and Microstructure, NACE, 1972, pp. 3-11.
2. Hoepfner, D.W., Fatigue Mechanisms, Proceedings of an ASTM-NBS-NSF Symposium, J.T. Fong, Ed., ASTM STP 675, American Society for Testing and Materials, 1979 pp. 841-870.
3. Goto, M., and Nisitani, Fatigue Fracture Engineering Material Structure, Vol. 15, No. 4, 1992, pp. 353-363.
4. Corsetti, L.V., and Duquette, D.J, Metallurgical Transactions, Vol. 5, 1974, pp. 1087-1093.
5. Chandrasekaran, V., Taylor, A.M.H., Yoon, Y., and Hoepfner, D.W., Presented as a poster paper at the ASIP'99, Proceedings of the 1999 USAF Aircraft Structural Integrity Program Conference, San Antonio, TX, December 1999.
6. Chandrasekaran, V., Taylor, A.M.H., Yoon, Y., and Hoepfner, D.W., Presented as a poster paper at the ICAF'99, Bellevue, Washington, July 1999 – to be published in the ICAF'99 proceedings.
7. Cook, R., Clinos, N., and Wagstaff, P., Proceedings of the 21st ICAS Congress, Melbourne, 1998.
8. Smialowska, Z.S., Pitting Corrosion of Metals, National Association of Corrosion Engineers, Houston, Texas, 1986, pp. 127-140.
9. Payer, J.H. and Staehle, R.W., Corrosion Fatigue: Chemistry, Mechanics, and Microstructure, NACE, 1972, pp. 211-218.

Characteristics of Semi-Solid Processed Al-based Alloys for Automobile Applications

SangYul Lee, BomSok Kim, BoYong Lee*, SangYong Lee**, and HanJung Lee***

Materials Processing Laboratory, Department of Materials Engineering

*School of Aerospace and Mechanical Engineering,

HanKuk Aviation University, 200-1, KyungKi-Do, 412-791 KOREA,

**Korea Institute of Machinery and Metals, ChangWon, KyungNam, 641-010, KOREA,

***SungYong Hi-Tech, Kyungki-do, 415-860 KOREA

ABSTRACT

Microstructure and mechanical properties of semi-solid processed Al parts for automobile application were analyzed and were compared with those of die-cast parts and forged parts. While it is known to be impossible for die-cast part, in addition, heat treatment on the semi-solid processed part was performed so that the effect of heat treatment on the improvement of mechanical properties of semi-solid processed part could be evaluated in terms of tensile strength, wear properties, etc.

Microstructure of semi-solid processed Al part did not show any noticeable micro pores as compared to the microstructure of die-cast part. T6 heat treatment on A319 alloys has greatly improved the hardness as well as the wear resistance. Semi-solid processed A319 part showed slightly higher hardness value than and similar wear resistance to that of forged A332-T4 part. Abrasive type wear behavior was observed in both types of alloys and the friction coefficients of two alloys were similar to be approximately lower than 0.5. In any cases, the heat treated semi-solid processed Al parts showed much improved properties compared to the die-cast parts and could be competitive with forged Al parts. Experimental details will be presented.

1. INTRODUCTION

The automotive industry pays a great deal of attention to making parts as low cost, light weight and reliable as possible and therefore the automotive industry is now using much more aluminum than before. Recently Production of Al automotive parts using semi-solid forming(SSF) process receives more and more attention from auto manufacturers, especially in Europe and U.S.A.

The forming of metals is commonly performed in fully solid state (i.e. forging) or in fully liquid state (casting). Whilst solid state forming produces high performance parts, it is generally associated with long process lines, high energy consumption and limitation on shape. On the other hand castings offers the possibility to produce complex shapes with few process steps but does not enable the production of the same high performance quality as solid state forming does.

SSF, a new forming technology of semisolid metals, allows to combine the formability of liquid metals with the quality of solid-state formed products. The key to the process is in producing a non-dendritic microstructure, consisting of small, interconnected solid phase globules suspended in the liquid matrix. This particular microstructure is also at the origin of

the thixotropic behavior of the semi-solid alloys, allowing them to be handle as a solid when at rest and attaining fluid-like properties when sheared during the forming operation. Some of the advantages of SSF processing include near net shape, the ability to form thin walls, excellent surface finish, tight dimensional tolerances and excellent dimensional repeatability as well as good weldability. Compared to 100% liquid processing, such as used in conventional high pressure die or squeeze casting, semi solid metal flow is laminar, contains less thermal energy and shrinks less during solidification. Mechanical properties are comparative with those of other premium casting processes such as squeeze and low pressure. It is outgoal to get a basic understanding for the relationship between microstructure and mechanical properties of the SSF parts. This work includes preliminary results on microstructure and mechanical properties of semi-solid processed Al parts for automobile application were compared with those of die-cast parts and forged parts.

2. EXPERIMENTAL

In this experiment, Al parts for automobiles which are subject to relatively extensive wear were made from various processing methods such as forging, die casting, semi-solid forming and the types and chemical compositions of the specimens used in this work is summarized in Table 1. The microstructure was studied using SEM and EDS analysis was done using Oxford Link ISIS with Li-doped Si window at an accelerating voltages of 20 kV. The quantitative analysis was made using ZAF method. Microvickers hardness was measured using a load of 0.05kgf and the load was applied for 10 seconds. An average of seven hardness readings was taken. Ball-on-disk type wear tests were performed at room temperature. Applied load was 0.3kgf and the sliding distance was 250 km with a linear velocity of 3.75cm/sec. Alumina ball with 8 mm in diameter was used as counterface ball and the relative humidity was 50 - 60%. and no lubricant was used. The wear track was analyzed using a profiler meter and the friction coefficient and the weight change were measured.

Table 1 Chemical composition of specimens

Specimen	Process	Chemical composition								
		Si	Fe	Cu	Mn	Mg	Ni	Zn	Sn	Ti
A332	Forging, T4	12		1.0		1.0	2.5			
A332	SSF									
A319	SSF	5.5~6.5	0.15	2.5~3.5	0.03	0.3~0.4	0.03	0.05	0.03	0.2
A319	SSF, T6									
ADC-10	Die-Casting	10	0.15	0.03	0.03	0.5~0.6	0.03	0.05	0.03	0.2

3. RESULTS AND DISCUSSION

3.1 Microstructure and Microhardness

Microstructure from various specimens are summarized in Fig. 1. Fine microstructure with flow lines could be seen from the forged and T4-treated specimens in Fig. 1 a) and a non-dendritic microstructure, consisting of small, interconnected solid phase globules suspended in the eutectic matrix could be seen from the semi-solid formed specimens in Fig. 1b)-d). SSF A319-T6 specimen showed much finer microstructure with small precipitates of Fe₂Si₂Al₁₉.

Micro pores observed from the die-cast ADC-10 specimen as shown in Fig 1e) were not detected from either forged specimen or SSF specimens.

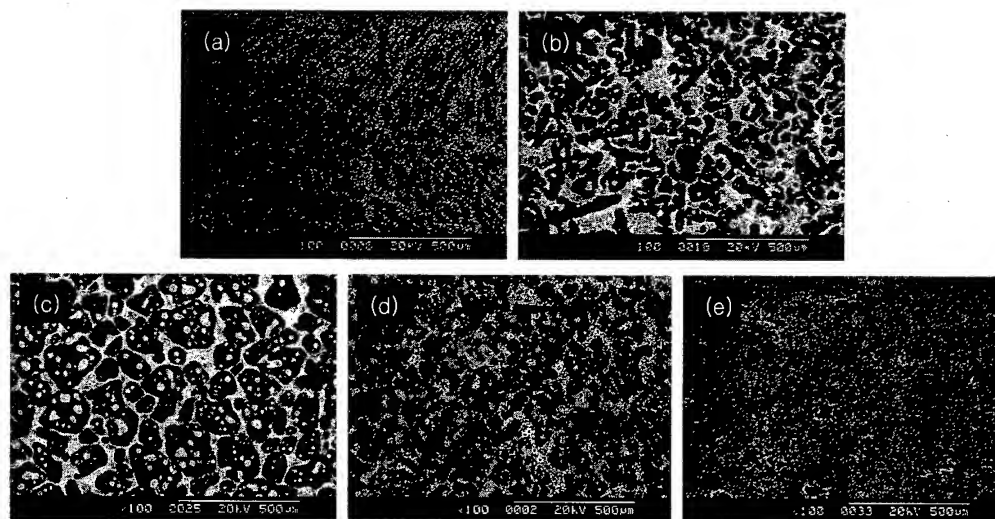


Fig.1 Microstructure of various specimens

(a) Forged A332-T4 specimen, (b) SSF A332 specimen,
(c) SSF A319 specimen, (d) SSF A319-T6 specimen, (e) Die-Casting ADC-10 specimen

Results from the microhardness measurement were summarized in Fig. 2. Slightly higher microhardness observed from the forged A332-T4 comparing with SSF A332 could be attributed to the finer microstructure and heat treatment. A319 specimen, containing approximately one half amount of Si content comparing with A332 specimen showed lower microhardness, but T6 heat treatment on SSF A319 alloys has improved the hardness so that SSF A319-T6 specimen showed slightly higher hardness value of 130Hv than that of forged A332-T4 specimen. Die cast ADC-10 specimen with approximately 10%Si showed similar microhardness of 120Hv with forged A332-T4 specimen.

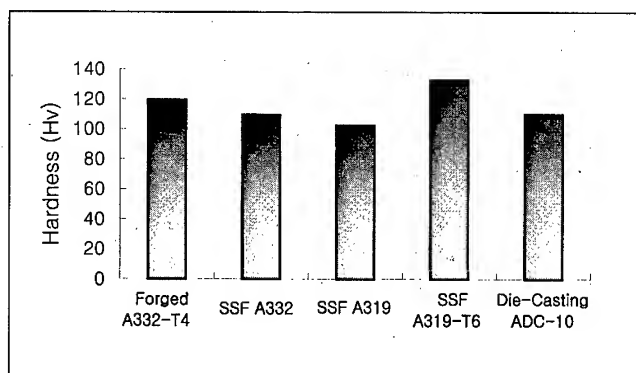


Fig.2 Microvickers hardness

3.2 Wear tests

The results from the ball-on-disk type wear test at room temperature were summarized in Fig.

3. The wear volume in Fig. 3 was calculated from the wear track using a profilometer. The ADC-10 die-cast specimen showed the worst wear resistance and the forged A332-T4 and SSF A319-T6 showed similar wear volume as shown in Fig. 3. Although ADC-10 specimen showed similar microhardness with forged A332-T4, micro pores observed from the die cast ADC-10 specimens (Fig. 1e) are believed to have effect on deteriorating the wear resistance. Extensive adhesion type wear behavior observed from the surface of the worn ADC-10 specimen supports this explanation. A332-T6 heat treatment on the SSF A319 specimen showed improved wear resistance comparing with SSF A319 without heat treatment and it could be attributed to the finer microstructure and higher microhardness from the SSF A319-T6 specimen.

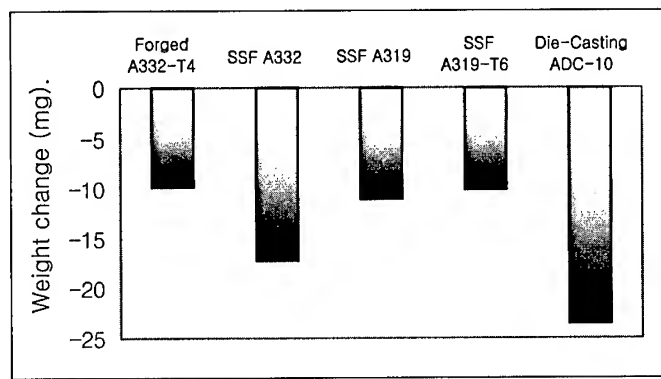


Fig.3 Results from wear test (weight change)

Fig. 4 showed the wear tracks from various specimens. The wear tracks from the of forged A332-T4 (Fig 4a) and SSF A319-T6 specimen (Fig. 4d) not only were narrower than those from other specimens, but showed abrasive type wear, comparing with the adhesive type wear observed from the die cast ADC-10 specimen.

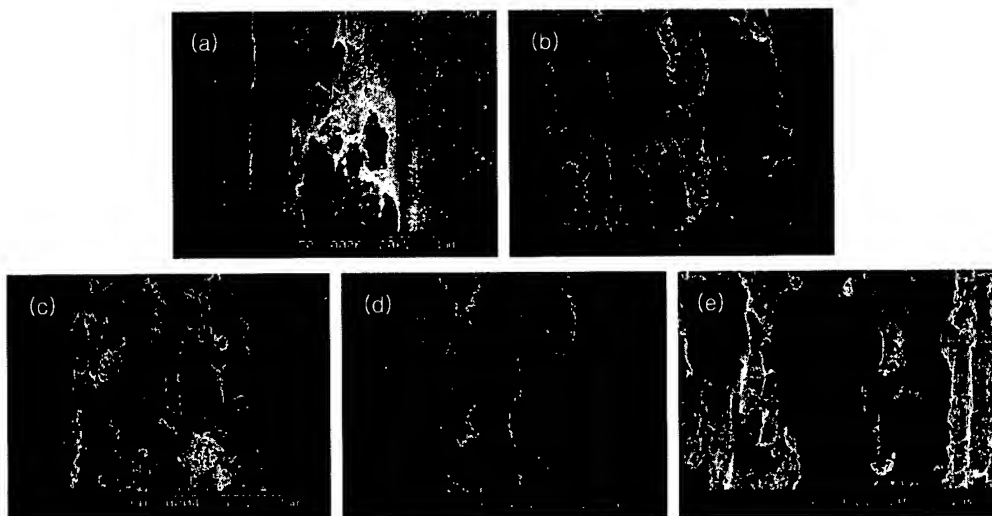


Fig.4 SEM micrographs of wear tracks

(a) Forged A332-T4 specimen, (b) SSF A332 specimen, (c) SSF A319 specimen, (d) SSF A319-T6 specimen, (e) Die-Casting ADC-10 specimen

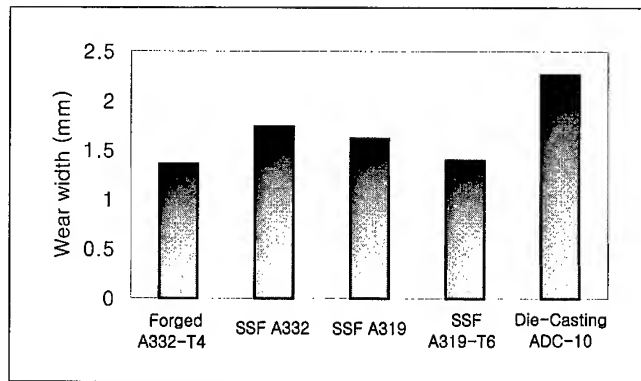


Fig.5 Results from wear test (wear width)

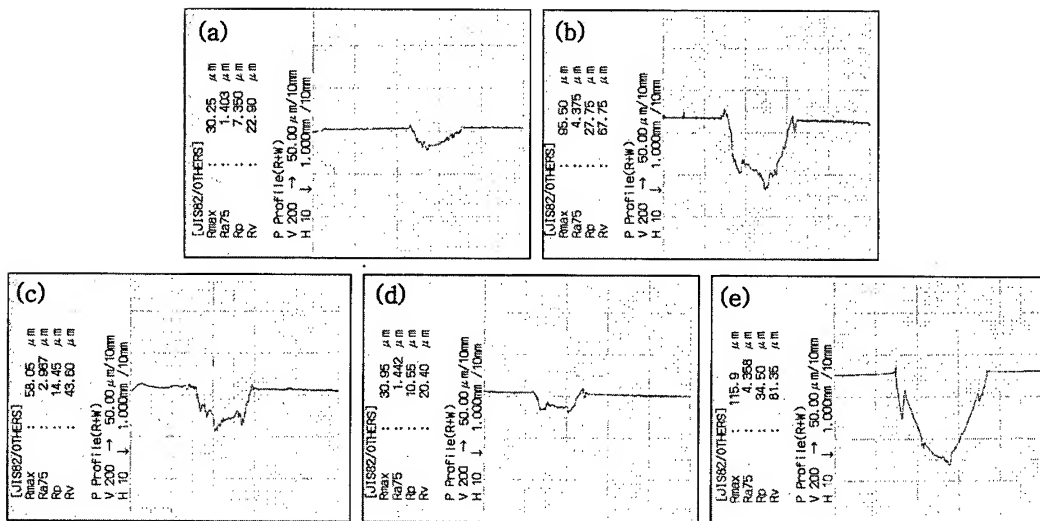


Fig.6 Results of the wear profile after wear test

(a) Forged A332-T4 specimen, (b) SSF A332 specimen,
(c) SSF A319 specimen, (d) SSF A319-T6 specimen, (e) Die-Casting ADC-10 specimen

Average wear width and wear depth profiles were measured and summarized in Fig. 5 and Fig. 6, respectively. Fig. 7 showed friction coefficients measured from various specimens and after initial steep increase, forged A332-T4 specimen and SSF A319-T6 specimen showed lower values of approximately 0.44 and 0.42 respectively. Friction coefficients of higher than 0.6 were observed from the die cast ADC-10 and other SSF specimens without heat treatment. It is noted that Si content in the alloy did not affect the friction coefficients very much. Instead, the degree of the fineness of microstructure was appeared to be a deciding factor.

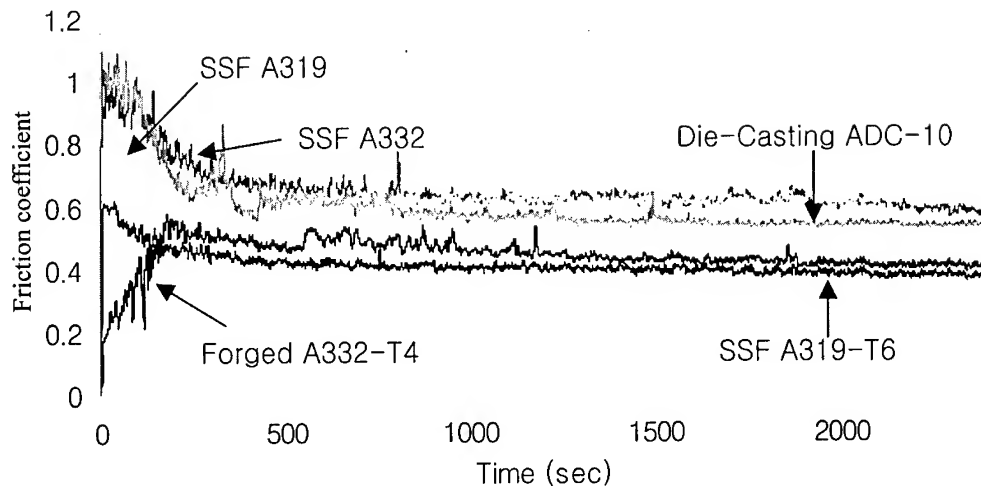


Fig.6 Friction coefficient

4. SUMMARY AND CONCLUSIONS

1) Results from the microhardness measurement showed that slightly higher microhardness observed from the forged A332-T4 comparing with SSF A332 could be attributed to the finer microstructure and heat treatment. Die cast ADC-10 specimen with approximately 10%Si showed similar microhardness of 120Hv with forged A332-T4 specimen.

2) The wear volume calculated from the wear track using a profilometer indicated that die cast ADC-10 showed the worst wear resistance and the forged A332-T4 and SSF A319-T6 showed similar wear volume.

Wear tracks from the forged A332-T4 and SSF A319-T6 specimen not only were narrower than those from other specimens, but showed abrasive type wear, comparing with the adhesive type wear observed from the die cast ADC-10 specimen. Si content in the alloy did not affect the friction coefficients very much but the degree of the fineness of microstructure was appeared to be a deciding factor.

REFERENCES

- (1) S.Y.Lee, Semi-Solid Forming Process for Light weight Automobile Part, KIMM Report, (1997)
- (2) C.G.Kang, Reheating of Semi-Solid Aluminum Alloys and Its Forging Process, Bulletin of the Inst. of Met.& Mat. vol. 10, No. 2, (1997)
- (3) J.C.Lee, H.I.Lee, Recent R&D trend in Thixoforming Process, Bulletin of the Inst. of Met.& Mat. vol. 10, No. 2, (1997)
- (4) William F.Smith, Structure and Properties of Engineering Alloys, McGraw-Hill, (1993)
- (5) E. Rabinowicz, Friction and Wear of materials, 2nd Ed., A Wiley -interscience Publication, (1995)
- (6) H.J.Park, Studies on the wear and the oxidation resistance of CrN surface layer formed by chromizing and plasma nitriding processes, Hankook aviation university, (1999)

AUTHOR INDEX

A

Abe, T.,	869
Adachi, H.,	597
Adachi, K.,	1121
Aghion, E.,	175
Ahn, H.J.,	671
Ahn, J.H.,	247
Ahn, J.K.,	675
Ahn, S.H.,	695
Ahn, S.H.,	701
An, C.W.,	503
Ankem, S.,	153
Asahina, T.,	457

B

Bae, Y.I.,	1067
Baeck, S.M.,	621
Balmuth, E.S.,	589
Bardi, F.,	361
Bieler, T.R.,	79
Blackburn, M.J.,	721
Bong, H.H.,	469
Boot, D.A.,	1037
Burvill, C.,	281, 287
Byeon, J.W.,	823

C

Cantor, B.,	1055
Cavaliere, P.,	361
Ceschini, L.,	361
Cha, S.I.,	469
Chandrasekaran, V.,	1133
Chang, S.N.,	105
Chang, S.Y.,	627, 863
Chang, Y.W.,	423, 695
Chatterjee, U. K.,	571
Chen, L.H.,	547, 689
Chen, Y.,	857
Cheon, J.H.,	905
Cho, D.C.,	1101
Cho, K.M.,	675, 851, 929

Cho, W.S.,	3
Choe, B.H.,	65
Choh, T.,	411
Choi, C.J.,	615
Choi, D.C.,	671
Choi, I.D.,	675, 851, 929
Choi, N.B.,	851
Choi, Y.,	247
Choi, Y.S.,	331
Choi, Y.S.,	977
Chung, C.S.,	503
Chung, I.S.,	943
Chung, S.W.,	417

D

Das, K.,	571
Davila, G.,	559
Dimiduk, D.M.,	721
Ding, H.,	857
Doraiswamy, D.,	153
Dutkiewicz, J.,	387

E

Eliezer, D.,	175
Emura, S.,	817
Eom, J.P.,	221
Es-Said, O.S.,	305, 559
Euh, K.J.,	1027
Eum, C.Y.,	875
Evangelista, E.,	361
Eylon, D.,	111, 127, 133, 141

F

Fagaraseanu, D.,	793
Fang, W.,	805
Fisher, P.,	1037
Fleck, P.,	559
Fountain, C.,	305
Fox, S.,	57
Foyos, J.,	559
Frazier, W. E.,	5

Fromer, E.,	559	Horita, Z.,	399, 647
Frouin, J.,	141	Horng, J.H.,	689
Fujishiro, S.,	111, 127	Hu, J.L.,	689
Fujita, K.,	961	Hur, B.Y.,	221, 671
Fukagawa, H.,	489	Hur, S.M.,	97
Fukunaga, K.,	111, 127	Hwang, J.I.,	851
Furukawa, M.,	399, 647	Hwang, S.K.,	729, 769
Furukawa, T.,	923	Hwang, Y.H.,	1133
		Hyun, Y.T.,	41, 91
G			
Gao, M.C.,	509	I	
Gariboldi, E.,	375, 1115	Igarashi, A.,	235
Garmestani, H.,	305	Ikeda, M.,	73
Ghosh, K.S.,	571	Ikenaga, K.,	787
Gunawarman,	127	Ikenaga, M.,	787
		Ikeno, S.,	535
H			
Ha, C.S.,	675, 929	Im, H.B.,	675
Ha, T.K.,	423, 695	Im, Y.R.,	583
Ha, W.,	1109	Imai, T.,	411
Hackenberg, R.E.,	509	Imose, T.,	73
Hagiwara, M.,	817	Imuta, M.,	489
Han, C.H.,	881	Inagaki, Y.,	337
Han, D.S.,	1055	Inoue, A.,	609
Han, J.H.,	317	Inoue, K.,	73
Han, S.W.,	665, 707	Isui, H.,	911
Han, Y.H.,	405	Ito, Y.,	477
Hanada, S.,	31	Ivanov, E.,	261
Hao, H.,	659	Ivasishin, O.M.,	57
Hashimoto, H.,	869	Iwamoto, N.,	961
Hashimoto, K.,	799	Iwata, S.,	949
Higashi, K.,	255, 451	Izui, H.,	923
Hilpert, M.,	205	J	
Hino, M.,	893	Jang, W.K.,	681
Hiraga, K.,	1093	Jata, K.V.,	15
Hirano, M.,	603	Jeong, H.W.,	41, 91
Hiroki, F.,	991	Jeong, Y.G.,	829
Hirose, Y.,	489	Jin, H.W.,	517
Hoeppepner, D.W.,	1133	Jin, J.Z.,	659
Hoffmann, J.,	1021	Jinishi, T.,	495
Hokamoto, K.,	811	Jo, Y.J.,	343
Hong, S.H.,	469	Ju, D.,	147
Hong, T.W.,	1067, 1109	Jung, B.G.,	65
Hong, W.P.,	167	Jung, B.H.,	1081

Jung, D.J.,	983	Kim, S.E.,	41, 91, 1075
Jung, H.C.,	215	Kim, S.H.,	119
Jung, H.G.,	983	Kim, S.H.,	297
Jung, H.K.,	1049	Kim, S.H.,	463
K		Kim, S.H.,	529
Kadoya, M.,	483	Kim, S.H.,	713
Kalidindi, S. R.,	305	Kim, S.H.,	899
Kamio, A.,	875	Kim, S.I.,	881
Kang, C.G.,	1043, 1049	Kim, S.J.,	65
Kang, S.B.,	641, 875	Kim, S.K.,	743
Kankawa, Y.,	275	Kim, S.K.,	1109
Kato, M.,	1009	Kim, S.S.,	681
Kato, K.,	445, 457	Kim, S.W.,	439
Kawai, G.,	1121, 1127	Kim, S.W.,	565, 659, 665
Kawai, H.,	603	Kim, S.W.,	1003
Kawamoto, M.,	893	Kim, S.Y.,	671
Kikukawa, H.,	483	Kim, W.J.,	381, 417, 503
Kim, B.K.,	615	Kim, W.T.,	199
Kim, B.S.,	1139	Kim, Y.H.,	823
Kim, C.G.,	905	Kim, Y.J.,	1067, 1109
Kim, D.H.,	199	Kim, Y.S.,	241, 343
Kim, D.I.,	621	Kim, Y.S.,	899
Kim, G.Y.,	973	Kim, Y.Y.,	463
Kim, H.C.,	167	Kimm, K.W.,	221
Kim, H.J.,	775	Kimura, H.M.,	609
Kim, H.J.,	905, 1081	Ko, M.W.,	1101
Kim, H.S.,	355	Ko, S.H.,	805
Kim, H.W.,	641	Kobayashi, S.,	577
Kim, J.,	695	Kobayashi, T.,	653
Kim, J.G.,	967, 977	Kohyama, M.,	255
Kim, J.H.,	755	Kohzu, M.,	255, 451
Kim, J.H.,	997	Koike, J.,	111
Kim, J.H.,	1003	Komatsu, S.,	73
Kim, J.K.,	503	Konishi, H.,	349
Kim, J.S.,	743	Konstanchuk, I.G.,	261
Kim, K.B.,	381	Kosugi, K.,	489
Kim, K.B.,	1061	Koziar, K.,	559
Kim, K.H.,	297	Kuan, S.L.,	547
Kim, K.Y.,	983	Kumai, S.,	541, 665, 707
Kim, M.G.,	1067	Kumar, K.S.,	811
Kim, M.H.,	943	Kurozawa, T.,	1127
Kim, M.K.,	1081	Ku?nierz, J.,	387
Kim, Nack J.,	225, 529, 553	Kusui, J.,	597
		Kwon, D.,	247

Kwon, H.,	845, 899	Lee, S.H.,	119, 1027
Kwon, S.C.,	463	Lee, S.H.,	191
Kwon, S.W.,	583	Lee, S.H.,	311, 635
Kwun, S.I.,	823	Lee, S.W.,	399, 647
		Lee, S.Y.,	343, 1139
L		Lee, S.-Y.,	1139
Langdon, T.G.,	399, 647	Lee, T.H.,	65
Lavernia, E.J.,	523	Lee, U.J.,	659
Leal, M.,	559	Lee, W.S.,	823
Leary, M.,	281, 287	Lee, Y.H.,	247
Lee, B.H.,	65	Lee, Y.H.,	1093
Lee, B.Y.,	1139	Lee, Y.J.,	1093
Lee, C.C.,	911	Lee, Y.S.,	331
Lee, C.G.,	65	Lee, Y.T.,	41, 65, 91, 1075
Lee, C.H.,	439	Lei, C. S. C.,	5
Lee, C.H.,	1101	Lesuer, D.R.,	369
Lee, C.S.,	119, 269, 755, 775	Lian, Z.,	23, 917
Lee, C.-S.,	119	Lim, C.Y.,	641, 875
Lee, D.,	729	Lim, H.K.,	199
Lee, D.B.,	955, 973	Lim, H.T.,	423
Lee, D.G.,	119	Lim, K.M.,	517
Lee, D.J.,	167	Lim, S.G.,	221
Lee, D.N.,	297	Lim, S.W.,	411
Lee, D.Y.,	1061	Lindemann, J.,	793
Lee, E.S.,	695	Lipsitt, H.A.,	721
Lee, E.W.,	5, 305, 559	Liyang, Z.,	917
Lee, H.C.,	583, 621	Locati, P.,	1115
Lee, H.I.,	317, 881, 887, 1061	Lui, T.S.,	547, 689
Lee, H.J.,	1139	Luo, G.Z.,	737
Lee, H.K.,	829		
Lee, J.,	317	M	
Lee, J.C.,	621, 837, 887	Mal, A.K.,	701
Lee, J.G.,	627	Malczewski, P.,	387
Lee, J.H.,	331	Mao, J.,	411
Lee, J.H.,	823	Matoba, M.,	495
Lee, J.M.,	641, 875	Matsuda, K.,	535
Lee, J.M.,	1027	Matsui, H.,	535
Lee, J.S.,	565	Matsuura, Y.,	577
Lee, J.S.,	811	Maurer, J.L.,	141
Lee, K.B.,	845	Meletis, E.I.,	1015
Lee, K.H.,	1093	Meng, X.,	857
Lee, M.Y.,	343	Meyendorf, N.,	1021
Lee, S.B.,	529	Mishra, R.S.,	405
Lee, S.G.,	1109	Miyauchi, H.,	431

Moon, I.G.,	393	Park, J.M.,	675
Moon, J.J.,	955	Park, J.S.,	97
Morri, A.,	361	Park, J.S.,	269
Mosneaga, V.A.,	653	Park, J.W.,	393
Motegi, T.,	185	Park, K.B.,	955
Mukherjee, A.K.,	405	Park, K.T.,	627
Muraishi, S.,	541	Park, S.H.,	269
		Park, S.J.,	829
N		Park, S.S.,	225
Nagura, Y.,	235	Park, T.Y.,	503
Nakai, K.,	577	Park, W.J.,	695
Nakasa, K.,	1009	Park, W.W.,	943
Nakata, J.,	431	Park, Y.,	729
Nam, K.W.,	701	Park, Y.H.,	393, 805, 869
Nam, S.W.,	749, 761, 769	Park, Y.S.,	225, 553
Nieh, T.G.,	387	Park, Y.S.,	749, 761
Niinomi, M.,	111, 127	Park, Y.W.,	1087
Nishida, Y.,	411	Pech, H.,	559
Nishikawa, N.,	185		
Niwa, N.,	991	Q	
Noda, K.,	349	Qu, H.L.,	161
Nomura, N.,	31		
Nozue, A.,	781	R	
		Rhee, K.H.,	713
O		Rhyim, Y.M.,	997
O'Brien, M.J.,	369	Ryu, K.H.,	583
Ochi, M.,	495	Ryu, S.K.,	863
Ogawa, K.,	1121, 1127		
Oh, K.H.,	621	S	
Oh, L.S.,	905	Saito, Y.,	311, 325, 635
Ohashi, S.,	495	Sakai, T.,	311, 635
Ohmori, Y.,	577	Sakurai, K.,	1121
Osamura, K.,	597	Sarkar, B.,	559
Ouchi, C.,	127	Sasamori, K.,	609
		Sathish, S.,	141, 1021
P		Sato, A.,	541, 665, 707
Park, C.G.,	517, 997	Sato, T.,	863, 875
Park, E.S.,	199	Sawai, T.,	1127
Park, H.C.,	565	Semiatin, S.L.,	79
Park, H.C.,	899	Senda, T.,	275
Park, H.L.,	105	Seo, M.H.,	355
Park, H.S.,	729	Seo, P.K.,	1043
Park, I.M.,	675, 851, 929	Seok, H.K.,	317, 621, 887
Park, J.K.,	615, 743	Seon, Y.K.,	1061

Seri, O.,	937	Takeda, M.,	235
Shan, A.,	393	Tamin, M.N.,	781
Shell, E.B.,	133	Tanaka, S.I.,	949
Sherby, O.D.,	369	Tanaka, T.,	665
Shiflet, G.J.,	509	Tang, F.,	817
Shim, W.S.,	973	Taniguchi, S.,	961
Shimamoto, A.,	911	Terayama, K.,	535
Shin, C.H.,	1003	Tezuka, H.,	863, 875
Shin, D.H.,	523, 627, 755, 863	Toda, H.,	653
Shin, D.S.,	887, 1061	Tokisue, H.,	445, 457
Shin, H.H.,	105	Tono, G.,	111
Shin, K.S.,	191, 215, 681	Tsuji, N.,	635
Shin, K.S.,	1101	Tsujikawa, M.,	893
Shin, S.Y.,	1101	Tsujimoto, T.,	489
Shinoda, T.,	431		
Shiota, I.,	991	U	
Sim, H.S.,	845	Ueda, M.,	73
Sohn, S.M.,	343	Uesugi, T.,	255
Sohn, W.H.,	469	Uetani, Y.,	535
Somekawa, H.,	451	Ueyama, M.,	325
Son, J.Y.,	1087	Utsunomiya, H.,	325, 635
Son, K.J.,	1081		
Son, Y.I.,	1043	V	
Song, J.H.,	423	Vassel, A.,	917
Song, J.M.,	547	Vedani, M.,	375, 1115
Souba, R.,	325		
Spigarelli, S.,	361	W	
Stone, I.C.,	1055	Wagner, L.,	205, 793
Suh, D.W.,	583	Wang, Q.,	869
Suh, J.Y.,	317, 887	Wang, W.S.,	737
Sun, F.,	1075	Watanabe, Y.,	787
Sun, Z.,	869	Wen, J.,	857
Sung, S.Y.,	1067	Wendt, J.,	205
Suryanarayana, C.,	261	Williams, L.,	305
Suzuki, H.,	781	Won, S.Y.,	241
Suzuki, H.,	787	Woo, K.D.,	565, 659
Suzuki, H.G.,	49	Wu, H.,	161
Suzuki, K.,	275	Wu, Y.,	729
Suzuki, T.,	31		
Syn, C.K.,	369	X	
		Xiaonan, M.,	917
T			
Tada, A.,	923	Y	
Takaki, Y.,	349	Yahata, A.,	483, 495

Yamaguchi, H.,	1127	Yoon, Y.I.,	1133
Yamaguchi, M.,	1075	Yoshimi, K.,	31
Yamamoto, Y.,	1127	You, B.S.,	943
Yan, X.,	1009	Yu, Y.J.,	967
Yan, Y.Q.,	737	Yumoto, A.,	991
Yang, C.H.,	565		
Yang, J.K.,	583	Z	
Yang, S.J.,	761, 769	Zhao, Y.Q.,	161
Yano, E.,	185	Zhentao, Y.,	147
Yim, C.D.,	191	Zhou, F.,	523
Yim, H.J.,	463	Zhou, L.,	161, 737
Yokoe, K.,	597	Zhu, K.Y.,	161
Yongqing, Z.,	917	Zhu, Y.C.,	961
Yoo, Y.C.,	881		